NOνA

NuMI Off-Axis ν_e Appearance Experiment

Technical Design Report

Contacts:
Gary Feldman, Co-Spokesperson, feldman@physics.harvard.edu
Mark Messier, Co-Spokesperson, messier@indiana.edu
John Cooper, Project Manager, jcooper@fnal.gov
Ron Ray, Deputy Project Manager, rray@fnal.gov
Nancy Grossman, Associate Project Manager, grossman@fnal.gov

October 8, 2007

Preface

This Technical Design Report (TDR) describes the preliminary design of the NOνA accelerator upgrades, NOνA detectors, detector halls and detector sites. Compared to the March 2006 and November 2006 NOνA Conceptual Design Reports (CDR), critical value engineering studies have been completed and the alternatives still active in the CDR have been narrowed to achieve a preliminary technical design ready for a Critical Decision 2 review.

Many aspects of NOνA described this TDR are complete to a level far beyond a preliminary design. In particular, the access road to the NOνA Far Detector site in Minnesota has an advanced technical design at a level appropriate for a Critical Decision 3a review. Several components of the accelerator upgrade and new neutrino detectors also have advanced technical designs appropriate for a Critical Decision 3a review.

Chapter 1 is an Executive Summary with a short description of the NOνA project.

Chapter 2 describes how the Fermilab NuMI beam will provide a narrow band beam of neutrinos for NOνA.

Chapter 3 gives an updated overview of the scientific basis for the NOνA experiment, focusing on the primary goal to extend the search for $\nu_\mu \rightarrow \nu_e$ oscillations and measure the $\sin^2(2\theta_{13})$ parameter. This parameter has not been measured in any previous experiment and NOνA would extend the search by about an order of magnitude beyond the current limit. A secondary goal is to measure the dominant mode oscillation parameters, $\sin^2(2\theta_{23})$ and Δm^2_{32} to a more precise level than previous experiments. Additional physics goals for NOνA are also discussed.

Chapter 4 describes the Scientific Design Criteria which the Fermilab accelerator complex, NOνA detectors and NOνA detector sites must satisfy to meet the physics goals discussed in Chapter 3.

Chapter 5 is an overview of the NOνA project. The changes in the design relative to the NOνA CDR are discussed.

Chapter 6 summarizes the NOνA design performance relative to the Design Criteria set out in Chapter 4.

Chapter 7 presents the Work Breakdown Structure dictionary at Level 3 and the Milestone dictionary.

Chapters 8 through 17 then take each Level 2 WBS element of the NOνA project and present each part of the design in more detail than the overview given in Chapter 5. Specific technical design criteria are delineated for each part of the project in addition to the scientific design criteria outlined in Chapter 4. Changes in the design since the NOνA CDR are discussed in detail. The work remaining to bring each part of this preliminary design to a final design is outlined.

Appendix A is a guide to other NOνA Project documentation with links to those documents.

Author List

D. S. Ayres, G. R. Drake, M. C. Goodman, J. J. Grudzinski, V. J. Guarino, R. L. Talaga, A. Zhao
Argonne National Laboratory, Argonne, IL

P. Stamoulis, E. Stiliaris, G. Tzanakos, M. Zois
University of Athens, Athens, Greece

J. Hanson, C. L. Howcroft, L. M. Mualem, H. B. Newman, R. B. Patterson, C. W. Peck, J. Trevor
California Institute of Technology, Pasadena, CA

D. B. Cline, K. K. Lee, X. Yang
University of California, Los Angeles, CA

C. R. Ader, M. P. Andrews, R. H. Bernstein, V. Bocean, G. J. Bock, D. Bogert, S. J. Brice, D. R. Broemmelsiek, D. P. Capista, S. Childress, J. W. Cooper, P. F. Derwent, J. E. Dey, S. J. Dixon, K. A. Domann, R. J. Ducar, H. P. Ferguson, W. S. Freeman, N. L. Grossman, C. P. Grozis, G. M. Guglielmo, L. L. Hammond, D. Harris, R. W. Hatcher, B. Haynes, M. J. Hu, P. G. Hurh, J. Hylen, C. C. James, C. C. Jensen, D. Jensen, D. E. Johnson, H. Jostlein, K. M. Kephart, O. J. Kiemschies, T. R. Kobilarcik, D. Koolbeck, I. Kourbanis, R. Kwarciany, T. W. Lackowski, A. Lee, P. W. Lucas, P. T. Lukens, M. A. Martens, E. G. McCluskey, S. J. Parke, S. L. Pasek, V. Pavlicek, A. Pla-Dalmau, R. K. Plunkett, D. R. Pushka, R. Rameika, R. E. Ray, B. J. Rebel, R. E. Reilly, N. Saoulidou, R. L. Schmitt, K. W. Schuh, P. Shanahan, P. Spentzouris, A. M. Stefanik, S. Tariq, D. Tinsley, L. R. Valerio, K. Vaziri, M. E. Votava, R. Wands, A. A. Wehmann, D. W. Wildman, K. E. Williams, M. Xiao, R. J. Yarema, T. Zimmerman, R. Zwaska
Fermi National Accelerator Laboratory, Batavia, IL

T. Patzak
College de France, Paris, France

J. A. Boehm, S. Cavanaugh, G. J. Feldman, N. F. Felt, J. N. Oliver, M. C. Sanchez
Harvard University, Cambridge, MA

B. Adams, B. Armstrong, C. R. Bower, C. Busch, W. Fox, M. Gebhard, M. Ishitsuka, N. Mayer, M. D. Messier, S. L. Mufson, J. A. Musser, J. Paley, A. Raval, D. Scott, J. E. Urheim, G. Visser
Indiana University, Bloomington, IN

S. Kotelnikov, V. Ryabov
Lebedev Physical Institute, Moscow, Russia

C. M. Bromberg, J. W. Huston, R. J. Miller, B. Page, R. A. Richards
Michigan State University, East Lansing, MI

A. Habig
University of Minnesota, Duluth, MN

K. E. Arms, T. R. Chase, D. P. Cronin-Hennessy, S. Dorsher, W. J. Gilbert, K. J. Heller, S. Kasahara, Z. Krahn, P. J. Litchfield, M. L. Marshak, A. M. McGowan, W. H. Miller, B. Nitti, N. M. Pearson, E. A. Peterson, D. A. Petyt, R. Poling, K. Ruddick, R. W. Rusack, A. B. Smith, B. Speakman, M. L. Strait, P. Zweber
University of Minnesota, Minneapolis, MN

M. Lindner
Technische Universität München, Munich, Germany

R. Shrock
State University of New York, Stony Brook, NY

C. H. Albright
Northern Illinois University, DeKalb, IL

J. F. Beacom
Ohio State University, Columbus, OH

H. Nunokawa
Pontifícia Universidade Católica do Rio de Janeiro, Rio de Janeiro, Brazil

A. R. Godley, J. Kim, J. Ling, S. R. Mishra, C. Rosenfeld
University of South Carolina, Columbia, SC

T. E. Coan
Southern Methodist University, Dallas, TX

G. M. Irwin, S. Murgia, S. G. Wojcicki, T. Yang
Stanford University, Stanford, CA

E. Tetteh-Lartey, R. C. Webb
Texas A&M University, College Station, TX

S. E. Kopp, K. Lang — ***University of Texas, Austin, TX***
R. F. Burkart, A. Cunningham, A. Farago, E. J. Fenyves — ***University of Texas, Dallas, TX***
H. R. Gallagher, T. Kafka, W. A. Mann, J. Schneps, N. Tagg — ***Tufts University, Medford, MA***
E. C. Dukes, N. E. Fields, Y. Masui, A. J. Norman — ***University of Virginia, Charlottesville, VA***
J. K. Nelson — ***The College of William and Mary, Williamsburg, VA***

Table of Contents

1. Executive Summary

1.1 Introduction

Fermi National Accelerator Laboratory and the NOνA Collaboration composed of 181 scientists and engineers from 26 Universities and Laboratories have collaborated to create this preliminary design for a new study of neutrino oscillations using the existing Department of Energy investment in the NuMI neutrino beam at Fermilab. NOνA is designed to search for oscillations of muon neutrinos to electron neutrinos ($\nu_\mu \rightarrow \nu_e$) by comparing electron neutrino rates at Fermilab with electron neutrino rates observed 810 kilometers from Fermilab.

1.2 Project Components

This technical design for the NOνA Project consists of four main elements:

1. **An upgrade of the Fermilab accelerator complex from 400 kW to one capable of 700 kW of beam power.** The Recycler will be converted from an anti-proton to a proton 8 GeV storage ring. New proton injection and extraction lines will be built using five new kicker systems and recycled magnets. The Main Injector cycle time will be reduced from 2.20 seconds to 1.33 seconds via the addition of two new additional RF cavities. The NuMI neutrino line will be upgraded to handle the increased beam power with small changes to the primary beam line and upgrades to cooling systems. The NuMI Target Hall will be changed to the medium energy neutrino beam configuration, requiring a new target, and horn 2 will be moved downstream 13 meters with an extended strip line transmission line. Commissioning of the upgraded accelerator complex is not part of the project since the complex is used by other experiments and must be scheduled by the Fermilab Directorate.
2. **A 222 ton Near Detector.** This detector will be placed in a small new underground cavern adjacent to the existing NuMI tunnel on the Fermilab site and will measure the inherent NuMI beam backgrounds relevant to a search for electron neutrino appearance in the NuMI muon neutrino beam.
3. **A new building on a site near the US-Canadian border in Ash River, Minnesota.** This building will house a new NOνA Far Detector. This site is 810 kilometers from Fermilab. The new building is 20.4 meters wide by 113.8 meters long with the detector section sunk 16 meters below the existing grade into granite rock at the site. The excavated granite is used as a cosmic ray shield on the above grade sides of the building. The roof of the building over the detector is composed of 1.37 meters of concrete covered with 0.15 meters of barite (barium sulfate) to complete the cosmic ray shield.
4. **A 15,000 ton (15 kiloton) NOνA Far Detector.** This detector will be composed of 385,000 cells of extruded PVC plastic in a cellular structure. Each cell is 3.9 centimeters wide by 6.0 centimeters deep and is 15.5 meters long. The cells are filled with a total of 3.3 million gallons of liquid scintillator. The liquid scintillator comprises 70% of the total detector mass, making this a totally active tracking calorimeter detector optimized for identification of electron neutrino (ν_e) interactions. The detector is read out via 13,000 kilometers of 0.7 millimeter diameter optical wave-shifting fiber into 12,000 avalanche photodiodes with associated electronics. The 222 ton Near Detector will be constructed with components identical to the ones used in the Far Detector.

1.3 Use of Existing Facilities

The NuMI beam is used in a new way by placing the NOνA detector at an angle 14.6 milliradians off the beam axis to obtain a muon neutrino (ν_μ) beam sharply peaked at 2 GeV in

energy. Following some modifications for 700 kW of beam power, the Fermilab NuMI beam transport, target, focusing horns, vacuum decay pipe, and absorber will be utilized to provide the neutrino beam for NOνA. The NOνA Near detector will be accessed via the existing NuMI underground tunnel at a depth 105 meters below grade.

1.4 Capabilities

The Accelerator and NuMI Upgrades portion of the NOνA Project is designed to deliver 6×10^{20} protons per year to the NuMI Target. In a six year run with a total of 36×10^{20} protons delivered by the Fermilab Main Injector, NOνA would measure the probability for muon neutrino to electron neutrino oscillations ($\nu_\mu \rightarrow \nu_e$) down to a value ten times smaller than the existing experimental limit.

The existence of neutrino oscillations means that neutrinos have mass. In a six year run equally split between neutrino and anti-neutrino beams, NOνA can resolve the neutrino mass ordering in a significant portion of the available parameter space for these oscillations. This capability is a unique aspect of NOνA not duplicated by any other formally proposed experiment.

1.5 Scope, Cost, and Schedule

The technical scope of the NOνA Project includes the Fermilab accelerator complex upgraded for 700 kW capability, a 15 kiloton Far Detector in a new building at Ash River, Minnesota, and a 222 ton Near Detector at Fermilab.

The Total Project Cost (TPC) of the NOνA Project is $ 260 M. The TPC includes $ 54.6 M in costs in a DOE Cooperative Agreement with the University of Minnesota to construct the Far Detector Building.

The NOνA Project Schedule calls for 68 months of construction from May, 2007 through January, 2013.

2 Using the Fermilab NuMI Beam for NOνA

2.1 The NuMI Beam

The NOνA project will upgrade the existing NuMI neutrino beam [1] to accommodate intensities of 700 kW. The NuMI beamline brings 120 GeV protons extracted from the Main Injector onto a 0.95 meter-long graphite target. Two parabolic magnetic horns focus the resulting secondary beam directing them toward the Soudan mine in northern Minnesota which houses the MINOS far detector. Neutrinos are produced from pion and kaon decay in an evacuated pipe 675 meters in length and 2 meters in diameter.

A unique feature of the NuMI neutrino beam is the ability to reconfigure the target and horn locations to produce neutrino energy spectra ranging in energy from 3 to 15 GeV on-axis. These configurations are illustrated in Figure 2.1, together with the spectra for three possible beam element arrangements, referred to as low, medium, or high energy beam tunes. Our calculations indicate that the medium energy tune will give the best performance for the NOνA experiment.

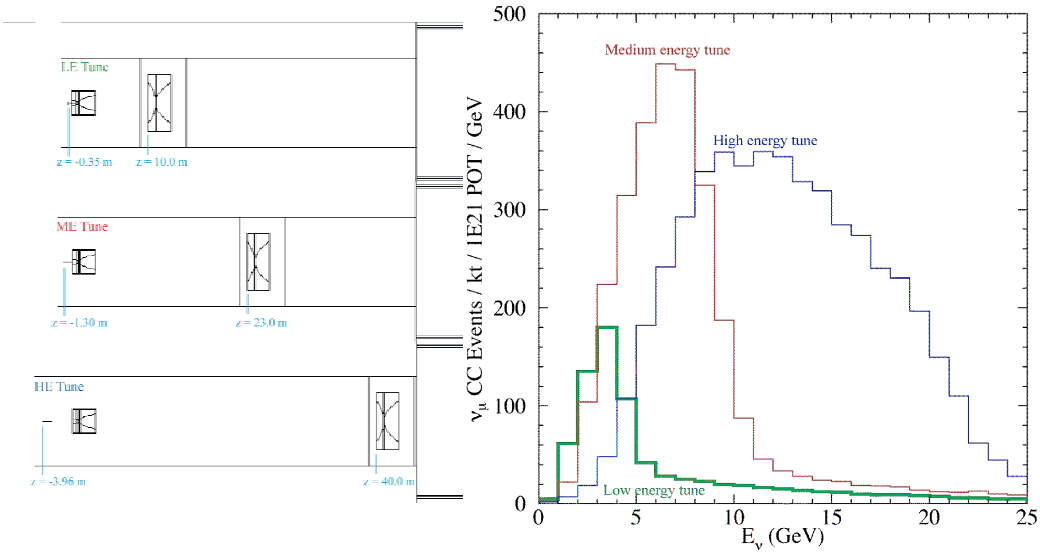

Fig. 2.1: Left: The locations of the target and second horn for the three NuMI beam configurations. Locations along the beam axis are referenced to *z=0* located at the front face of the first horn. The vertical scale is a factor 10 larger than the horizontal scale. Right: The expected neutrino interaction rates at the MINOS far detector site (on-axis at a distance of 735 km) for each of the three beam tunes.

2.2 Off-Axis Concept

The NOνA Far Detector will be sited 14.6 mrad off the NuMI beam axis, in contrast to the MINOS Far Detector which is sited on the center of the NuMI beam. The rationale for this choice is explained below.

In their rest frame, pions and kaons decay isotropically producing mono-energetic neutrinos. When these pions and kaons are boosted, the neutrino energy spectrum seen in the lab frame has a broad distribution, falling off as the angle between the boost direction and neutrino production angle increases. For small angles, the flux and energy of neutrinos produced from the decay $\pi \rightarrow \mu + \nu$ in flight and intercepted by a detector of area A and located at distance z are given in the lab frame by:

$$F = \left(\frac{2\gamma}{1+\gamma^2\theta^2} \right)^2 \frac{A}{4\pi z^2} \tag{2.1}$$

$$E_\nu = \frac{0.43 E_\pi}{1+\gamma^2\theta^2}, \tag{2.2}$$

where θ is the angle between the pion direction and the neutrino direction, E_π the energy of the parent pion, m_π the mass of the pion and $\gamma = E_\pi/m_\pi$. The expressions for neutrinos from the corresponding charged kaon decays are identical except that 0.43 is replaced by 0.96 resulting in a more energetic and broader distribution for identical meson energies.

The functions in Equations 2.1 and 2.2 are plotted in Fig. 2.2. The right portion of Fig. 2.2 shows that at 14 mrad the energy of the neutrino does not have a strong dependence on the energy of the parent pion. This is further demonstrated in Fig. 2.3, which shows the resulting number of neutrino events as a function of energy and off-axis angle. At 14 mrad, the medium energy beam produces a narrow energy beam with approximately five times more neutrinos at 2 GeV. This peak is well matched to the oscillation maximum which is expected to be 1.6 GeV for Δm_{32}^2=2.4 meV^2.

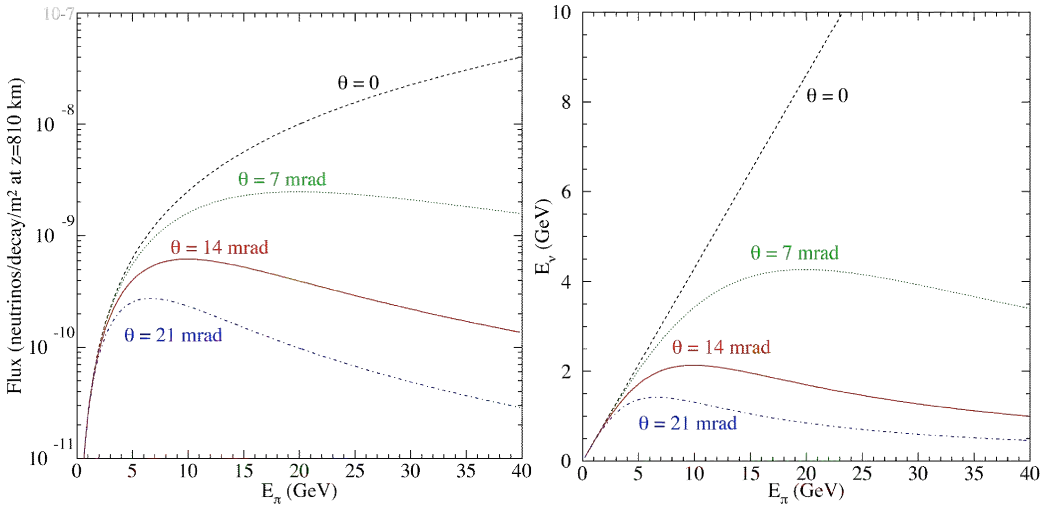

Fig. 2.2: Left: The neutrino flux from a pion of energy E_π as viewed from a site located at an angle θ from the beam axis. The flux has been normalized to a distance of 800 km. Right: The energy of the neutrinos produced at an angle θ relative to the pion direction as a function of the pion energy.

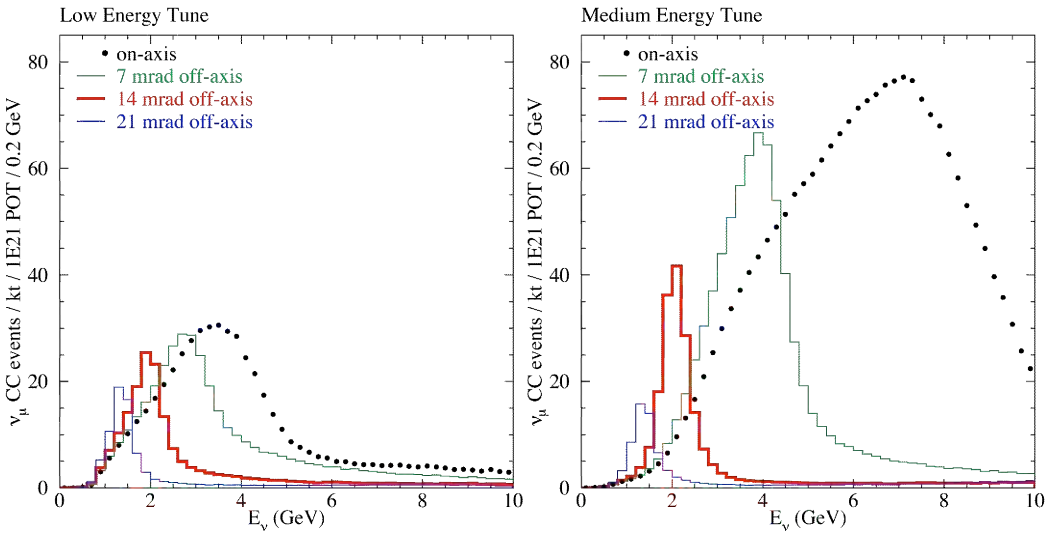

Fig. 2.3: Charged-current ν_μ event rates prior to oscillations calculated for a distance of 810 km from Fermilab and at various off-axis locations in the NuMI beam. The spectra are for the NuMI low-energy (left) and medium-energy (right) configurations.

In addition to the increased flux, the narrowness of the off-axis spectra enhances background rejection. One important source of background events are neutral-current events where the outgoing lepton (the neutrino) is not observed. The topologies of these events can fake the electron showers produced by ν_e charged-current events. As the neutrino carries much of the event energy away, the visible energies of neutral-current events tends to "feed down" to lower energies. In a wide band beam this feed down into the signal region is much larger than it is in a narrow band off-axis beam where the feed down tends to push the neutral-current events outside the signal energy window. Figure 2.4 shows the number of neutral-current events as a function of their visible energy, illustrating this effect.

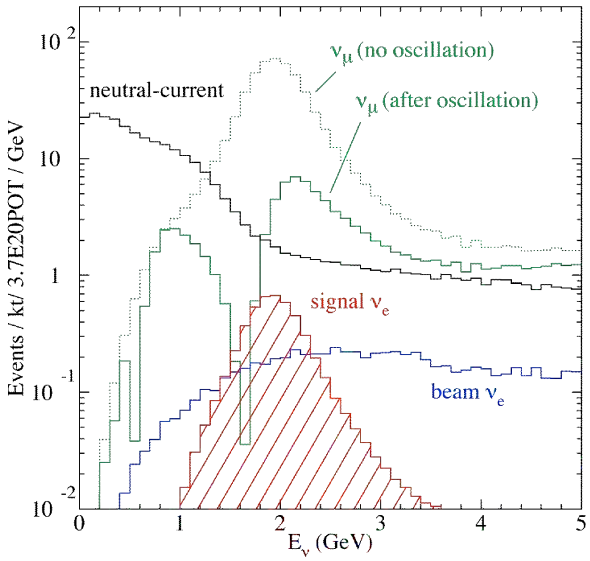

Fig.2.4: Simulated energy distributions for the ν_e oscillation signal, intrinsic beam ν_e events, neutral-current events and ν_μ charged-current events with and without

oscillations. The simulation used $\Delta m^2_{32} = 2.5 \times 10^{-3}$ eV^2, $\sin^2(2\_{23}) = 1.0$, and $\sin^2(2\_{13}) = 0.10$. An off-axis distance of 12 km at 810 km was assumed.

Another important source of backgrounds to the electron-neutrino appearance search is the intrinsic ν_e component of the NuMI beam which arise from muon and kaon decay. As these neutrinos result from three-body decays they are more broadly distributed in energy than the ν_μ's produced by two-body decays. The spectra of the ν_e's in the NuMI beam off-axis are shown in Fig. 2.4. The relative narrowness of the off-axis ν_μ beam compared to the ν_e beam is an additional advantage of the off-axis approach.

2.3 The NuMI Beam in the Post -Tevatron Collider Era

The NuMI beam line is currently in its third year of operation. It has achieved periods of 192 kW average beam power with 2.5 x 10^{13} protons/spill and achieved a peak of 320 kW and 4.0 x 10^{13} protons/spill. As of the spring of 2007, approximately 3.1 x 10^{20} protons have been delivered to the MINOS experiment.

Fermilab is engaged in a staged program to increase the number of protons delivered to the NuMI target (see Table 2.1). The first stage of these upgrades is called the Proton Plan and has the goal of slip-stacking 9 batches in the Main Injector. The second stage of these upgrades is part of the NOνA project and the details are presented in Chapter 8. Once the NOνA work is completed, the Main Injector (MI) is expected to deliver 4.9 x 10^{13} protons every 1.3 seconds to the NuMI target, yielding a total power of 700 kW. Approximately 6 x 10^{20} protons can be delivered to the experiment per year, assuming a reasonable level of accelerator inefficiencies [2].

A possible next stage of accelerator and NuMI upgrades would bring the beam power to 1.2 MW. This design concept is called SNuMI (Super NuMI) and would use the Accumulator (currently part of the anti-proton source) to momentum stack 3 Booster batches prior to transfer to the Recycler. This plan would fill the Main Injector with 8.3E13 protons every cycle. Extraction of these pulses at a repetition rate of 1.333 s would increase the NuMI beam power to 1.2 MW, and deliver 10 x 10^{20} protons to the experiment in one year. Another possible upgrade path under study is the construction of an 8 GeV linear proton accelerator to replace the existing 8 GeV Booster [3]. Construction of this new accelerator, "Project X", would increase the MI power to 2.3 MW, doubling the protons on target available for NOνA.

	Present Operating Conditions (May 2007)	**Proton Plan Multi-batch Slip-stacking in MI**	**NOνA Multi-batch Slip-stacking in Recycler**	**Conceptual SNuMI Accumulator Momentum Stacking**	**Conceptual Project X linear accelerator**
8 GeV Intensity (p/Batch)	4.3 - 4.5x10^{12}	4.3x10^{12}	**4.3x10^{12}**	4.5x10^{12}	5.6x10^{13}
Number of 8 GeV Batches to NuMI	7	11	**12**	18	3
MI Cycle Time (sec)	2.4	2.2	**1.3**	1.3	1.4
MI Intensity (protons per pulse or ppp)	3.3x10^{13}	4.5x10^{13}	**4.9x10^{13}**	8.3x10^{13}	1.6x10^{14}
MI to NuMI (ppp)	2.45x10^{13}	3.7x10^{13}	**4.9x10^{13}**	8.3x10^{13}	1.6x10^{14}
NuMI Beam Power (kW)	192	320	**700**	1169	2314
Protons/year to NuMI	2x10^{20}	3x10^{20}	**6x10^{20}**	10x10^{20}	20x10^{20}
MI Protons/hour	4.95x10^{16}	7.3x10^{16}	**1.3x10^{17}**	2.2x10^{17}	1.0x10^{18}

Table 2.1: Present accelerator operating conditions and future upgrades. The Present Operating Conditions and Proton Plan values are given for mixed mode cycles including Collider running. The SNuMI and Project X columns are shown in lighter gray since they are conceptual and not part of the NOνA Project.

2.4 Integrated Protons on Target Assumed for the NOνA Experiment

The sensitivity of the NOνA experiment depends on the product of three numbers, the number of protons delivered to the experiment per year of operation, the mass of the NOνA detector in kilotons, and the number of years the experiment is operated. The projected sensitivities of the NOνA experiment are shown in Chapter 3 for a 15 kiloton (kt) detector and 36×10^{20} protons delivered to the NuMI target. This corresponds to 6 years of running in the 700 kW beam expected following the NOνA Project accelerator upgrades (see Table 2.1).

Chapter 3 also presents the increased sensitivities NOνA would have with 60×10^{20} and 120×10^{20} protons delivered to the NuMI target, corresponding to 6 years of running 15 kt with 1.2 MW and 2.3 MW beams respectively. These are the projected proton intensities for the conceptual SNuMI and Project X upgrades; they are not, however, part of the NOνA Project. Chapter 3 is intended to demonstrate the increased reach of the NOνA experiment if SNuMI or Project X were accomplished.

2.5 Chapter 2 References

[1] The NuMI Technical Design Handbook, http://www-numi.fnal.gov/numwork/tdh/-tdh_index.html.
[2] R. Zwaska, NOVA-doc-1698.
[3] Fermilab Steering Group Report, http://www.fnal.gov/directorate/ Longrange/ Steering_Public.

3 Science Case for the NOνA Experiment.

3.1 Overview of Neutrino Oscillations

The standard picture of neutrinos consists of three different types: ν_e, ν_μ, and ν_τ, each of which is a partner to a charged lepton: e (electron), μ (muon), and τ (tau lepton). We know that the neutrinos have mass and as a result, one type of neutrino can transform (oscillate) into another type. Oscillations of ν_e into $\nu_\mu + \nu_\tau$ have been observed in solar neutrino experiments [1] and in a long baseline reactor neutrino experiment [2] with an oscillation length of approximately 15,000 km/GeV. Oscillations of ν_μ into ν_τ have been observed in atmospheric neutrino experiments [3], in a Japanese accelerator experiment [4], and in the MINOS experiment now running in the Fermilab NuMI beam [5] with an oscillation length of approximately 500 km/GeV, known as the "atmospheric oscillation length." Oscillations between ν_μ and ν_e have yet to be observed at the atmospheric oscillation length. There is an upper limit on the rate of this oscillation from a reactor neutrino experiment [6]. The primary goal of the NOνA experiment is to observe and study $\nu_\mu \rightarrow \nu_e$ oscillations at the atmospheric oscillation length.

The rate of the $\nu_\mu \rightarrow \nu_e$ oscillation is expressed mathematically in terms of a mixing angle, θ_{13}, and the number of signal events observed in the oscillation is roughly proportional to $\sin^2(2\theta_{13})$. For neutrino beams that pass through the earth, the rate of the $\nu_\mu \rightarrow \nu_e$ oscillation also depends on the ordering of the masses of the three species of neutrinos. If the two neutrinos that cause the solar oscillations have lower masses that the third neutrino, called the "normal mass ordering," then neutrino oscillations are enhanced and antineutrino oscillations are attenuated. If the mass ordering is reversed, call "inverted mass ordering," then the antineutrino oscillations are enhanced and the neutrino oscillations are attenuated. Currently, we have no information on the mass ordering. Additionally, the rate of $\nu_\mu \rightarrow \nu_e$ oscillations depends on a phase angle that violates charge-parity (CP) symmetry. A non-zero value of this phase angle, δ, leads to CP violation in the lepton sector and may have a bearing on the origin of the matter-antimatter asymmetry of the universe.

The goal of the NOνA experiment is to extend the search for $\nu_\mu \rightarrow \nu_e$ oscillations by roughly an order of magnitude beyond the sensitivity of the MINOS experiment. Additionally,

NOνA can begin to study the mass ordering and search for the effects of the CP violating phase angle δ. NOνA is particularly well suited to the study of the mass ordering due to the large amount of earth between the neutrino source and the detector. No other planned experiment can attack this problem.

This chapter outlines the neutrino oscillation formalism in more mathematical detail and describes the reach of NOνA for this physics.

3.2 Details of Neutrino Oscillations

3.2.1 Neutrino Mixing

Neutrino oscillations come about because the weak eigenstates are rotated from the mass eigenstates. The unitary matrix that rotates the mass eigenstates into flavor eigenstates is

$$\begin{pmatrix} \nu_e \\ \nu_\mu \\ \nu_\tau \end{pmatrix} = \begin{pmatrix} c_{13}c_{12} & c_{13}s_{12} & s_{13}e^{-i\delta} \\ -c_{23}s_{12} - s_{13}s_{23}c_{12}e^{i\delta} & c_{23}c_{12} - s_{13}s_{23}s_{12}e^{i\delta} & c_{13}s_{23} \\ s_{23}s_{12} - s_{13}c_{23}c_{12}e^{i\delta} & -s_{23}c_{12} - s_{13}c_{23}s_{12}e^{i\delta} & c_{13}c_{23} \end{pmatrix} \begin{pmatrix} \nu_1 \\ \nu_2 \\ \nu_3 \end{pmatrix}, \qquad (3.1)$$

where $c_{jk} \equiv \cos\theta_{jk}$ and $s_{jk} \equiv \sin\theta_{jk}$. With this labeling, the atmospheric neutrino oscillations are primarily determined by the θ_{23} and Δm^2_{32} parameters, whereas the solar neutrino oscillations depend on θ_{12} and Δm^2_{12}, where $\Delta m^2_{ij} = m^2_i - m^2_j$. If the phase δ is neither 0 nor π, then neutrinos exhibit CP violation.

3.2.2 Present Knowledge of the Mixing Parameters

The SuperKamiokande[7], KEK[4], and MINOS[5] experiments have all measured the atmospheric oscillation parameters $|\Delta m^2_{atm}| \approx |\Delta m^2_{31}| \approx |\Delta m^2_{32}|$ and $\sin^2 2\theta_{23}$. The results are summarized in Fig. 3.1. The combined analysis[2] of the SNO[2], SuperKamiokande[4] and KamLAND[3] experiments give $\Delta m^2_{21} = +7.9 \pm 0.6 \times 10^{-5}$ eV^2 and $\sin^2 2\theta_{12} = 0.82 \pm 0.07$ for the solar parameters. The CHOOZ experiment [6] provides a limit of $\sin^2 2\theta_{13} < 0.15$ for $\Delta m^2_{32} = 0.0024$ eV^2, the central value of the MINOS measurement.

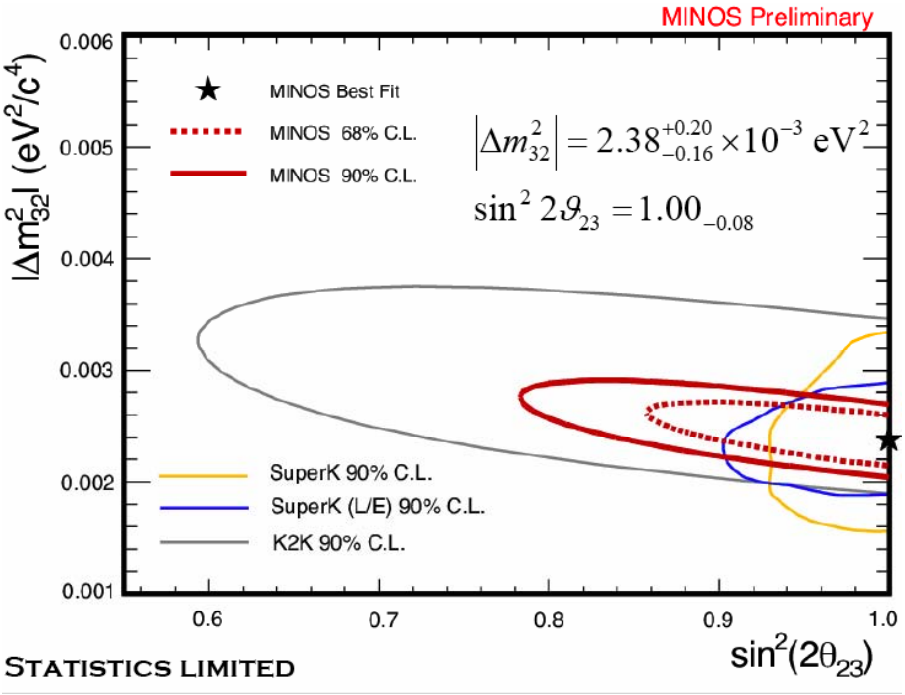

Fig. 3.1 Confidence intervals from the SuperKamiokande[7], K2K[4], and MINOS[5] experiments. The plot is from Ref. 5.

3.2.3 ν_e Appearance Probability

The appearance probability of ν_e in a ν_μ beam in vacuum is given by the sum of three terms,

$$P_{vac}\left(\nu_\mu \rightarrow \nu_e\right) = P_{atm} + P_{sol} + P_{int} \,. \tag{3.2}$$

P_{atm} represents the oscillation governed by the atmospheric oscillation length,

$$P_{atm} = \sin^2\theta_{23} \sin^2 2\theta_{13} \sin^2 \Delta_{31} \,, \tag{3.3}$$

where

$$\Delta_{ij} \approx 1.27\left(\frac{\Delta m^2_{ij} L}{E}\right) \tag{3.4}$$

where Δm^2_{31} is measured in eV^2, L is measured in km, and E is measured in GeV. P_{sol} represents the oscillation governed by the solar oscillation length,

$$P_{sol} = \cos^2\theta_{13} \cos^2\theta_{23} \sin^2 2\theta_{12} \sin^2 \Delta_{21} \,. \tag{3.5}$$

And P_{int} represents the interference between the solar and atmospheric oscillation lengths. It has both a CP conserving and CP violating term,

$$P_{int} = J\,[\cos\delta \cos\Delta_{32} \sin\Delta_{31} \sin\Delta_{21} \;\; \mu \sin\delta \sin\Delta_{32} \sin\Delta_{31} \sin\Delta_{21}], \tag{3.6}$$

where

$$J = \cos\theta_{13} \sin\theta_{12} \sin\theta_{13} \sin\theta_{23} \,, \tag{3.7}$$

and the top sign in the CP violating term refers to neutrinos and the bottom sign to antineutrinos. While the solar term, P_{sol}, is insignificant for the NOνA, the interference term, P_{int}, is comparable to the atmospheric term,. Further, since P_{int} is first order in the small parameter θ_{13} while P_{atm} is second order in θ_{13}, the significance of the CP-violating asymmetry between neutrino and antineutrino oscillations is roughly independent of θ_{13}.

3.2.3 Matter Effects

The neutrinos in the NuMI beam propagate through the earth and a coherent charged-current forward scattering of electron-type neutrinos with electrons in the earth induces a significant change in the oscillation probabilities. These matter effects have opposite sign for neutrinos and antineutrinos and for the normal versus inverted neutrino mass orderings. The matter effects can thus be used to distinguish the two possible three-neutrino mass orderings shown in Figure 3.2.

The matter effects modify $\sin\Delta_{21}$ and $\sin\Delta_{31}$ in Eqs. 3.3, 3.5, and 3.6 by the substitution

$$\sin\Delta_{ij} \rightarrow \frac{\Delta_{ij}}{\Delta_{ij} \mp aL}\sin(\Delta_{ij} \mp aL) \tag{3.8}$$

where the top sign refers to neutrinos and the bottom sign to antineutrinos and

$$a = \frac{G_F \rho_e}{\sqrt{2}} \approx (3700\ \mathrm{km})^{-1}\left(\frac{\rho}{2.8\ \mathrm{g\ cm^{-3}}}\right), \tag{3.9}$$

where ρ_e is the electron density in the earth and ρ is the density of the earth. If the experiment is performed at the first oscillation peak, the matter effects are primarily a function of the energy of the neutrino beam and the transition probability in matter can be approximated by

$$P_{mat}\left(\nu_\mu \rightarrow \nu_e\right) \approx \left(1 \pm \frac{E}{6\,GeV}\right) P_{vac}\left(\nu_\mu \rightarrow \nu_e\right). \tag{3.10}$$

For the normal hierarchy, matter effects enhance (suppress) the transition probability for neutrinos (antineutrinos) and vice versa for the inverted hierarchy. For the NOνA experiment, matter effects give approximately a 30% enhancement or suppression in the transition probability.

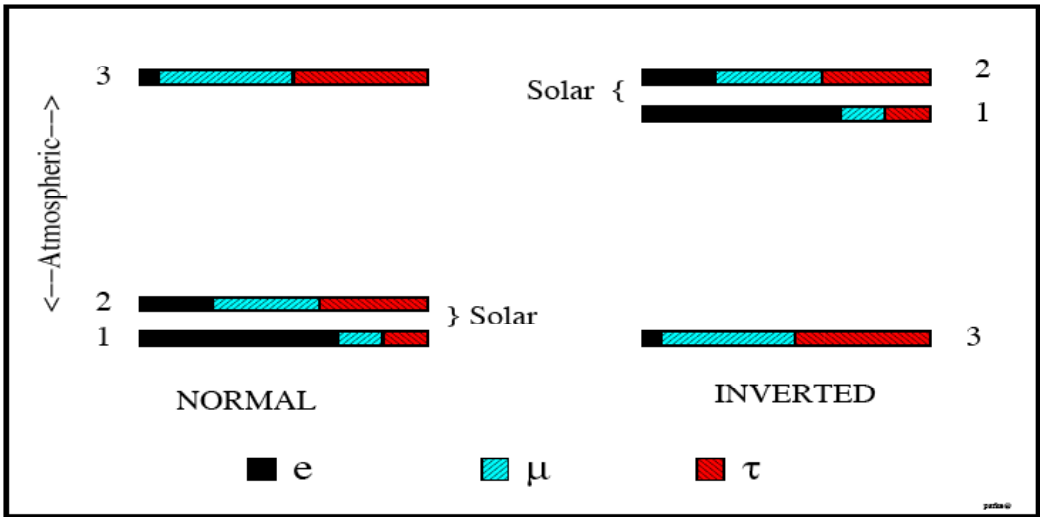

Fig. 3.2 The two allowed three-neutrino mass squared spectra that account for the oscillations of solar and atmospheric neutrinos. The normal spectrum has $\Delta m^2_{32} > 0$ and the inverted spectrum has $\Delta m^2_{32} < 0$. The ν_e fraction of each mass eigenstate is indicated by the black solid region, whereas the ν_μ (ν_τ) fraction is indicated by the blue-green right-leaning (red left-leaning) hatching. The ν_e fraction in the mass eigenstate labeled 3 has been enhanced for clarity.

3.2.4 Ambiguities

Since the matter effect is caused by the interaction of electron-type neutrinos with electrons in the earth, it has the opposite sign for neutrinos and antineutrinos and can be confused with a true CP-violating effect. This leads in some cases to an inherent ambiguity between the CP phase δ and the mass ordering.

Figure 3.3 shows an illustration of this ambiguity. It illustrates the parameters consistent with a NOνA measurement of a 2% $\nu_\mu \rightarrow \nu_e$ oscillation probability for $|\Delta m^2_{atm}| = 0.0024$ eV^2. Possible values of $\sin^2(2\theta_{13})$ are shown on the vertical axis, the CP-violating phase δ is shown by the ellipses, and the two mass orderings are shown by the two ellipses. The result of a $\bar{\nu}_\mu \rightarrow \bar{\nu}_e$ oscillation measurement is shown on the horizontal axis. If the signs of the CP violation effect and the matter effect are the same, for example δ near 3π/2 for the normal mass ordering or δ near π/2 for the inverted mass ordering, then there is no ambiguity and NOνA can determine the mass ordering. However, if δ is such that the ellipses overlap, then there is an inherent ambiguity can only be resolved by a third measurement, either at a different baseline, such as will be done by the T2K experiment, or by a measurement a different point in the dynamic phase, such as at the second oscillation maximum.

Since the relative size of the asymmetry due to CP violation increases as $\sin^2(2\theta_{13})$ decreases and the relative size of the matter effect stays constant, the fraction of possible δ values for which there is an ambiguity increases with decreasing values of θ_{13}

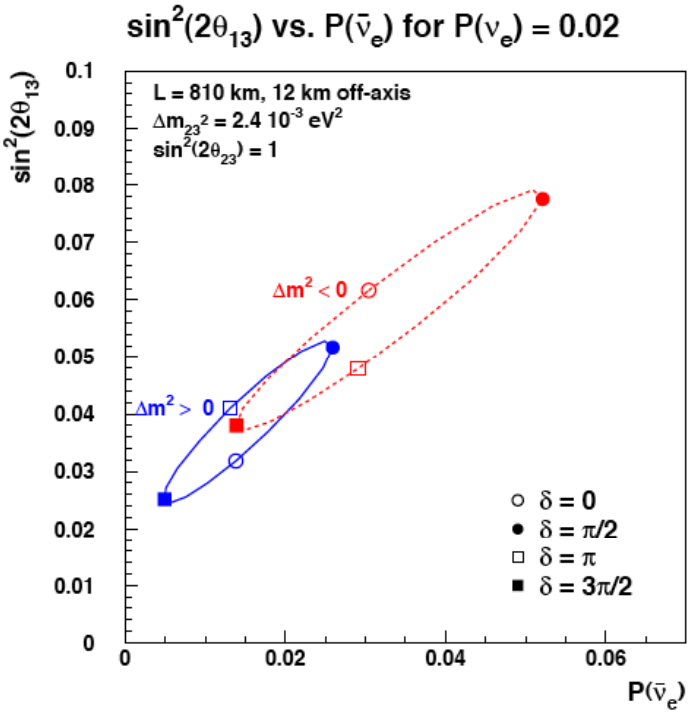

Fig. 3.3: Plot of the possible results for $\sin^2(2\theta_{13})$ vs. the oscillation probability observed for antineutrinos given a perfectly measured 2% neutrino oscillation probability. The solid (blue) curve is for the normal mass ordering, and the dashed (red) curve is for the inverted mass ordering. The values of the CP-violating phase δ are indicated in each case by the open and closed circles and squares with the key on the figure.

3.3 NOνA Capabilities in $\nu_\mu \rightarrow \nu_e$ Oscillation Measurements

NOνA plans to split its running time equally between with the horns focusing positive particles (neutrino running) and negative particles (antineutrino running). Even though the rates are higher for neutrino running than antineutrino running, there are two reasons for this strategy. First, it makes the sensitivity to seeing a signal less dependent on the value of δ and the sign of Δm^2_{atm}. Second, without antineutrino running, NOνA would have no ability to measure δ or the sign of Δm^2_{atm}.

In the following, we will show the capabilities of the NOνA experiment assuming a 15 kT detector with both 36×10^{20}, 60×10^{20}, and 120×10^{20} protons on target (pot). The first corresponds to 6 full years (44 weeks per year) of running at 700 kW beam power, assuming the NuMI and accelerator upgrades included in the NOνA project as discussed in Chapter 2 and Chapter 8. The last two corresponds to 6 full years of running at 1.2 MW and 2.3 MW beam power with the conceptual SNuMI and Project X upgrades, also discussed in Chapter 2, Sections 2.3 and 2.4. These latter beam powers are included to illustrate the potential of the NOνA experiment if either of these projects were to be accomplished. The sensitivity calculations have been done using the results of the simulations discussed in Chapter 6 assuming a systematic uncertainty in the background extrapolation from the near to far detector of 10%. These calculations take into account the antineutrinos in the neutrino running (1.5%) and the neutrinos in the antineutrino running (3.8%).

3.3.1 Sensitivity to $\sin^2(2\theta_{13})$

Figure 3.4 shows the sensitivity to $\theta_{13} \neq 0$ at the three standard deviation level as a function of δ for each of the mass orderings. A way of comparing the difference between 700 kW, 1.2 MW, and 2.3 MW beam power is to note the fraction of the parameter space for which the NOνA three-standard deviation sensitivity is more than an order of magnitude greater than the Chooz experiment 90% upper limit. The 2.3 MW and 1.2 MW sensitivities meet this criterion for 64% and 22% of the parameter space, respectively, while the 700 kW sensitivities meet it for only 9.5% of the parameter space.

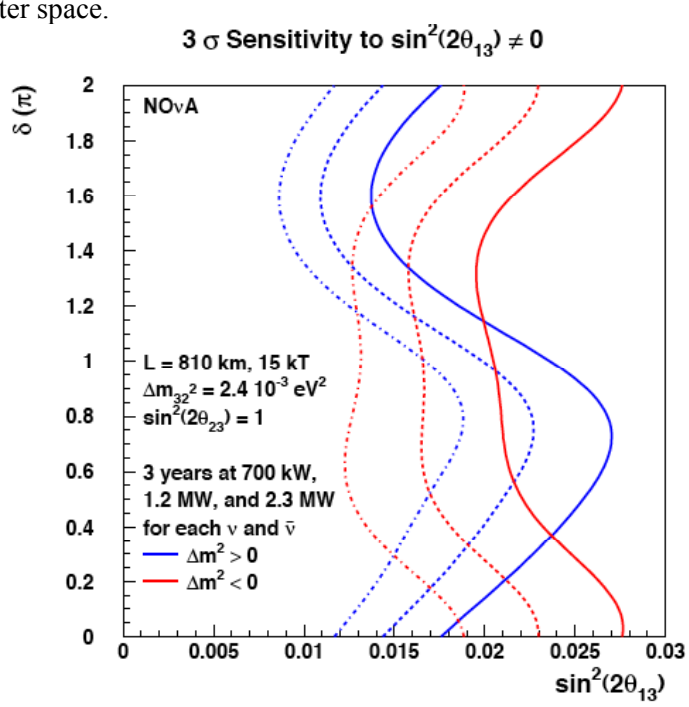

Fig. 3.4: Three standard deviation sensitivity to $\theta_{13} \neq 0$ as a function of the CP-violating phase δ for a 6-years of NOνA running split evenly between neutrino and antineutrino running. The solid curves are for 700 kW beam power, the dashed curves are for 1.2 MW beam power, and the dot-dashed curves are for 2.3 MW beam power. The blue (more S-shaped) curves are for the normal mass ordering and the red curves are for the inverted mass ordering.

3.3.2 Sensitivity to the Mass Ordering

Figure 3.5 shows the sensitivity to the mass ordering at the 95% confidence level as a function of δ for each of the mass orderings. The dot-dashed and dashed lines show the sensitivity for 2.3 MW and 1.2 MW running, respectively, and the solid lines show the sensitivity for 700 kW running. As explained above, the mass ordering can only be resolved by NOνA alone for the portion of the parameter space in which the matter effect and CP violation affect the oscillation in the same manner. For the remainder of the parameter space, a third measurement is required to resolve the mass ordering. One possibility is to combine NOνA data with data from T2K, which has a much shorter baseline. Figure 3.6 shows the effect of combining NOνA results with those from a 6-year neutrino run from the T2K experiment. It is assumed that the T2K beam power will upgrade in a similar way to the possible NOνA beam upgrades.[8]

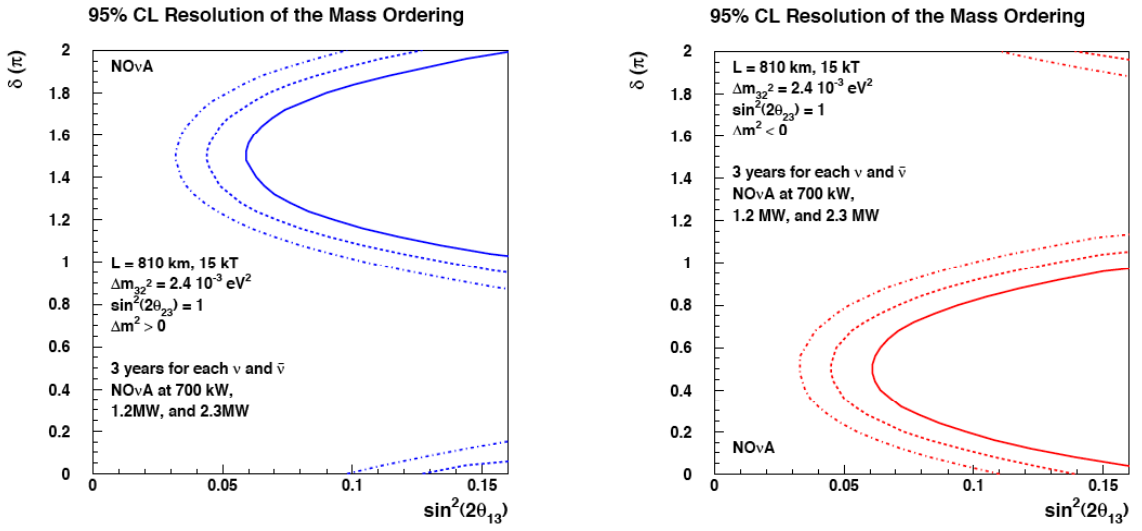

Fig. 3.5: 95% resolution of the mass ordering as a function of the CP-violating phase δ for 6-years of NOνA running split evenly between neutrino and antineutrino running. The dot-dashed and dashed curves are for 2.3 MW and 1.2 MW beam power, respectively, and the solid curves are for 700 kW beam power. The left graph is for the normal mass ordering and the right graph is for the inverted mass ordering.

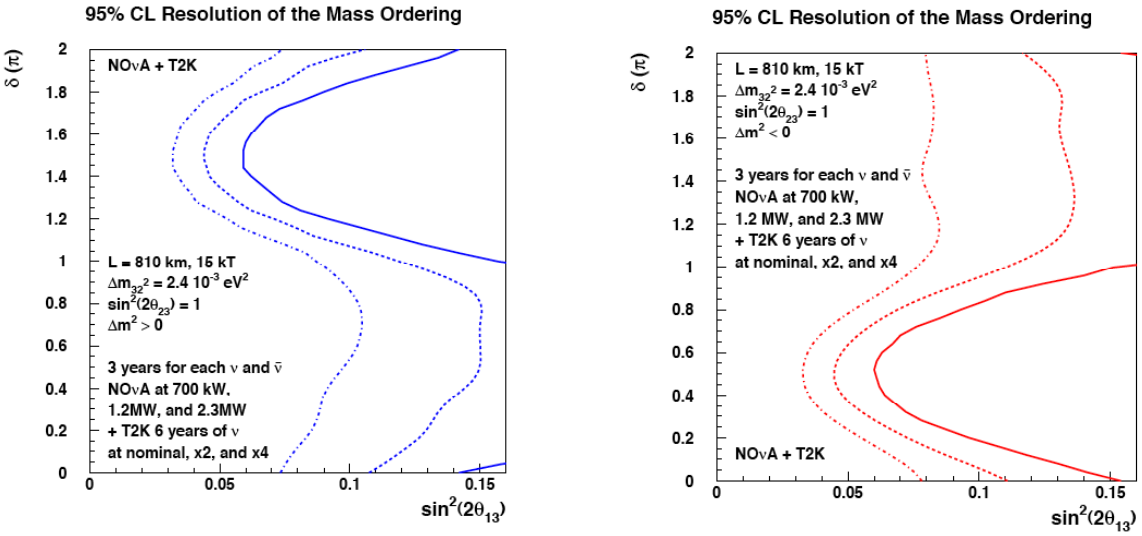

Fig. 3.6: 95% resolution of the mass ordering as a function of the CP-violating phase δ for 6 years of NOνA running split evenly between neutrino and antineutrino running combined with 6 years of T2K running on neutrinos. The dot-dashed and dashed curves are for 2.3 MW and 1.2 MW beam power, respectively, and the solid curves are for 700 kW beam power for NOνA. It is assumed that T2K will upgrade it beam power in parallel with NOνA. Thus, the 1.2 MW NOnA plot is paired with twice nominal T2K power and 2.3 MW NOνA plot is paired with four times nominal T2K power. The left graph is for the normal mass ordering and the right graph is for the inverted mass ordering.

3.3.3 Sensitivity to the CP-Violating Phase δ

Figures 3.7 and 3.8 show contours in the $\sin^2(2\theta_{13})$ -δ plane for a sample point, $\sin^2(2\theta_{13}) = 0.06$ and $\delta = 3\pi/2$. Figure 3.7 shows the one standard deviation contour for 2.3 MW, 1.2 MW and 700 kW running. Figure 3.8 shows the one, two, and three standard deviation contours for 2.3 MW running. There is not enough statistical power to demonstrate CP-violation at three standard deviation level, but there is enough sensitivity to give an indication of the type of future experiments that will be necessary. For cases in which the mass ordering is not determined, there will also be contours for the alternative mass ordering hypothesis.

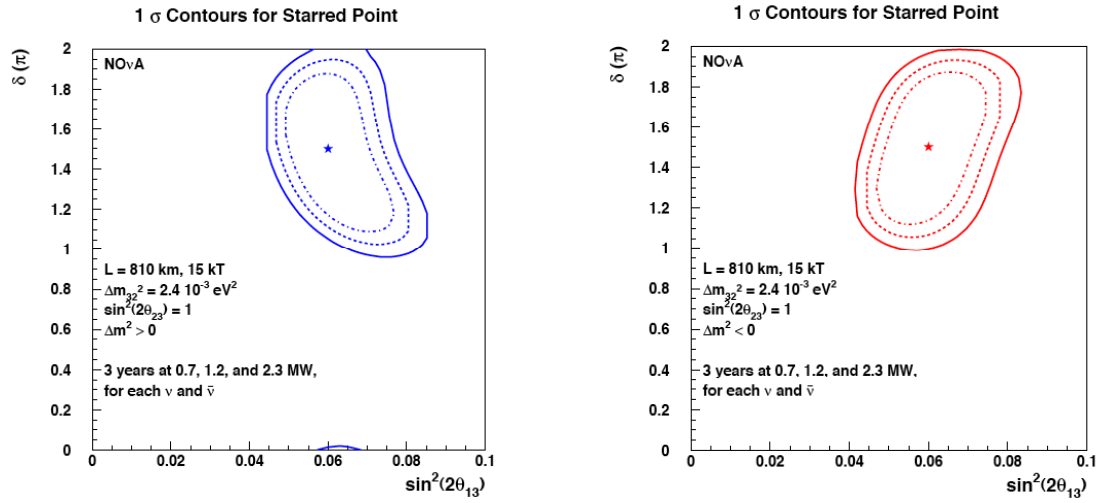

Fig. 3.7: Expected 1-standard deviation contour for a sample point, $\sin^2(2\theta_{13}) = 0.06$, $\delta = 3\pi/2$, for 6-years of NOνA running split evenly between neutrino and antineutrino running. The solid contour is for 0.7 MW beam power, the dashed contour is for 1.2 MW beam power, and the dot-dashed cure is for 2.3 MW beam power. The left graph is for the normal beam ordering and the right graph is for the inverted mass ordering.

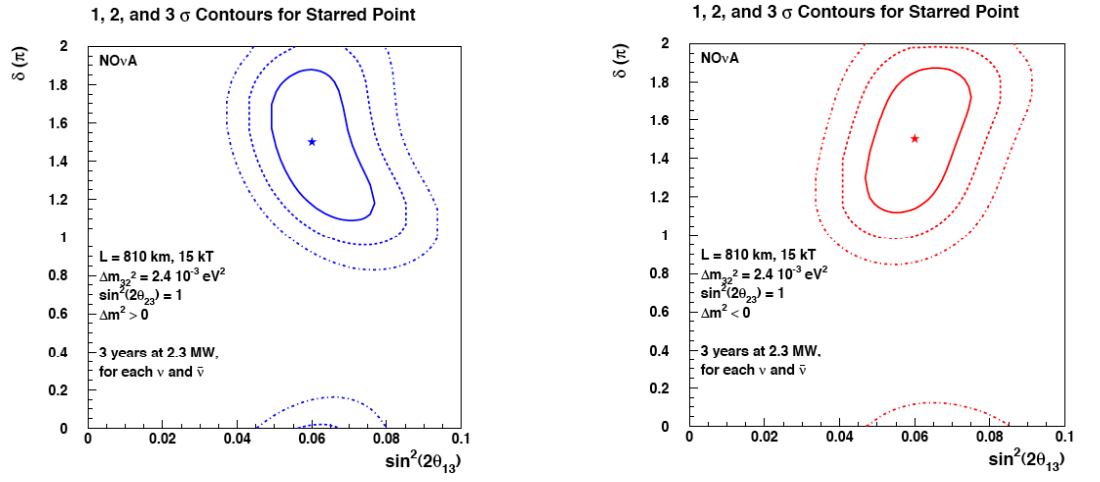

Fig. 3.8: Expected 1, 2, and 3-standard deviation contours for the sample point and conditions of Fig. 3.7 for 2.3 MW beam power.

3.4 Measurement of the Dominant Mode Oscillation Parameters Via ν_μ Disappearance.

Although the primary NOνA physics goal is the study of $\nu_\mu \to \nu_e$ oscillations, NOνA will also be able to make significant measurements of the dominant mode oscillation parameters, $\sin^2(2\theta_{23})$ and Δm^2_{32}. The best current measurement of $\sin^2(2\theta_{23})$ comes from the SuperKamiokande study of atmospherically produced neutrinos [7] and is shown in Fig. 3.1. This measurement is consistent with maximal mixing, $\sin^2(2\theta_{23}) = 1$, but with a considerable uncertainty. At the 90% confidence level, $\sin^2(2\theta_{23}) > 0.92$, which translates into a rather large range of possible values of $\sin^2\theta_{23}$, namely $0.36 < \sin^2\theta_{23} < 0.64$.

There are three reasons why determining $\sin^2(2\theta_{23})$ is of high interest:

(1) If the mixing is maximal, it might be due to some currently unknown symmetry.

(2) The $\nu_\mu \to \nu_e$ oscillation is mostly proportional to $\sin^2(\theta_{23})\sin^2(2\theta_{13})$ while $\bar{\nu}_e$ disappearance, measured by reactor experiments, is proportional to $\sin^2(2\theta_{13})$. Thus, if the mixing is not maximal, there is an ambiguity in comparing accelerator and reactor experiments.

(3) Conversely, whether θ_{23} is greater than or less than $\pi/4$, which measures whether the third neutrino mass eigenstate couples more strongly to ν_μ's or ν_τ's, can best be measured by comparing precise accelerator and reactor measurements. (See Section 3.5.)

The deviation of $\sin^2(2\theta_{23})$ from unity is measured by the depth of the oscillation dip in the ν_μ disappearance spectrum. Thus, precision in this quantity requires good statistics in this region, excellent neutrino energy resolution, and good control of systematics. NOνA offers the possibility of satisfying all of these requirements.

It appears that the best way to meet these requirements is to limit the analysis to totally contained quasielastic events, i.e., those events in which the geometrical pattern of energy deposition is consistent with the presence of only an energetic muon and a possible recoil proton. We have performed a preliminary study of how well NOνA can use these events to measure $\sin^2(2\theta_{23})$ and Δm^2_{32} using a parametric representation of the energy. This procedure is justified by the nature of these events, which are extremely clean.

The calculated one and two standard deviation contours are displayed in Figure 3.9 for assumed values of $\sin^2(2\theta_{23})$ of 0.95, 0.98, and 1.00 and a six-year run equally divided between neutrinos and antineutrinos for beam powers of 700 kW, 1.2 MW, and 2.3 MW. The energy resolution has been assumed to be 2%, but the contours do not change markedly as one increases the resolution to 4%.

Note that the precision of the $\sin^2(2\theta_{23})$ measurement increases as the value of $\sin^2(2\theta_{23})$ approaches unity. For maximal mixing, the error on the measurement of $\sin^2(2\theta_{23})$ is about 0.003 for 700 kW power and somewhat smaller for the other beam powers.

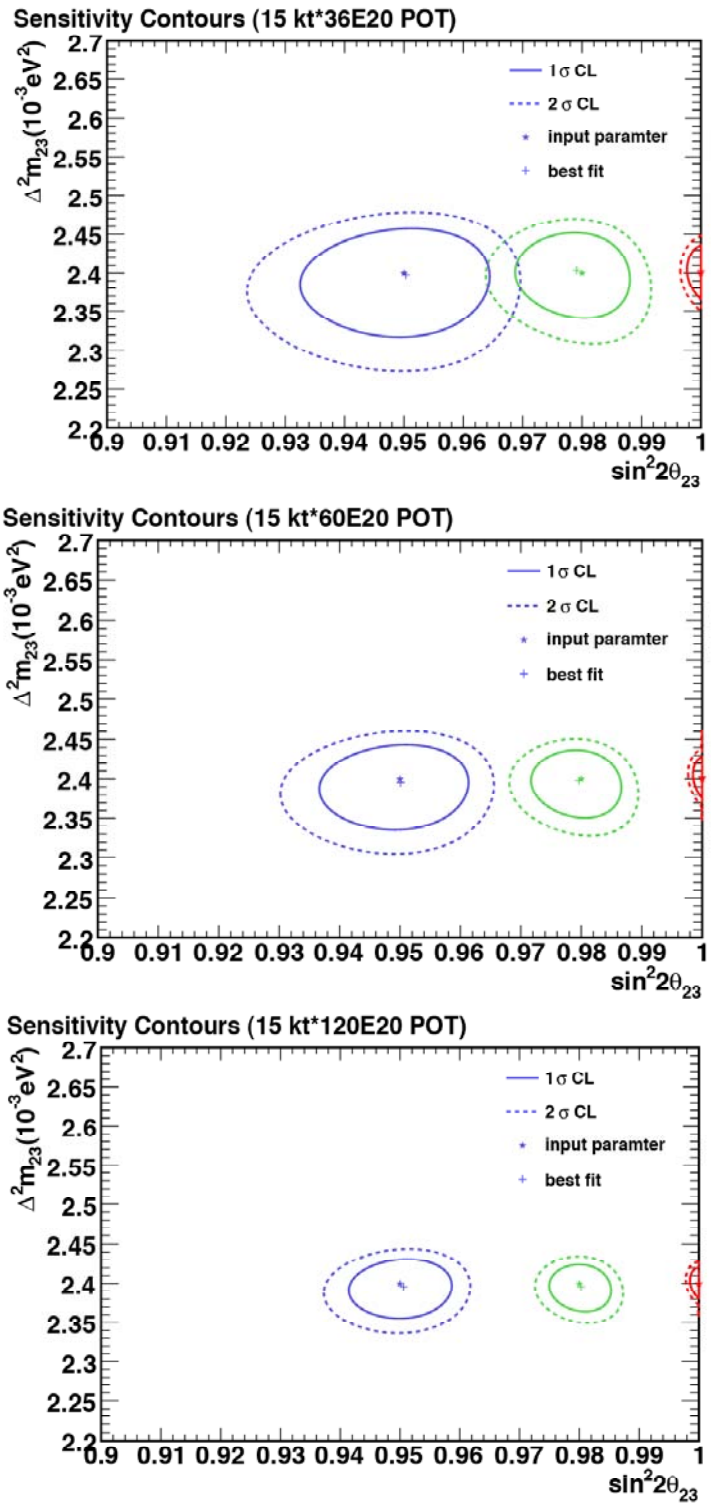

Fig. 3.9: One and two standard deviation contours for a simultaneous measurement of Δm^2_{32} and $\sin^2(2\theta_{23})$ for a six-year run at equally divided between neutrinos and antineutrinos. The three input values are indicated by a star and the best fit for each is indicated by a plus sign. The top plot is for 700 kW beam power, the middle for 1.2 MW, and the bottom for 2.3 MW.

3.5 Measurement of the Sign of $\cos(2\theta_{23})$

As mentioned in the previous section, if the dominant atmospheric oscillation is not maximal, it is interesting to determine whether θ_{23} is greater than or less than $\pi/4$, which measures whether ν_e's oscillate more strongly to ν_μ's or ν_τ's. This can be done most easily by comparing the results of the NOνA experiment with a reactor experiment, such as Daya Bay[9], since a reactor experiment will measure the oscillation of $\bar{\nu}_e$'s into the sum of $\bar{\nu}_\mu$'s and $\bar{\nu}_\tau$'s while an accelerator experiment will measure the oscillation of ν_μ's into ν_e's.

Figure 3.10 shows the region of $\sin^2(2\theta_{23}) - \sin^2(2\theta_{13})$ parameter space for which this measurement can be made at the 95% confidence level assuming that a reactor experiment can reach a one standard deviation precision of 0.005. The limits are functions of the CP-violating phase δ, the mass ordering, and the sign of $\cos(2\theta_{23})$; the values in Fig. 3.10 are averages over the parameter space.

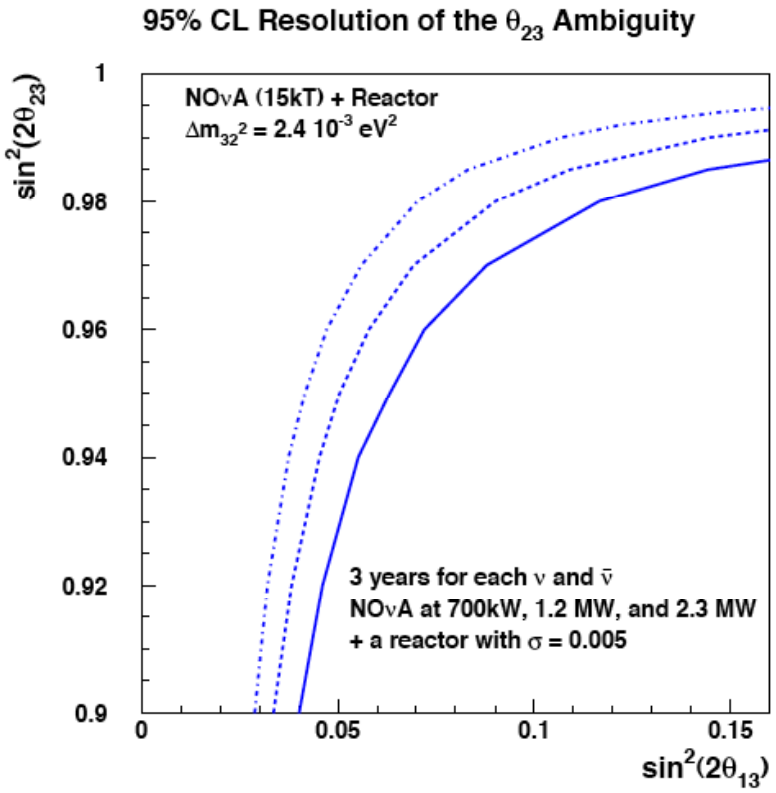

Fig. 3.10: The $\sin^2(2\theta_{23}) - \sin^2(2\theta_{13})$ regions to the right of the curves are those in which the sign of $\cos(2\theta_{23})$ can be resolved at the 95% confidence level by a comparison of data from NOνA and a reactor experiment that can achieve a one standard deviation sensitivity of 0.005 in $\sin^2(2\theta_{13})$. The solid curve represents a 6-year NOνA run divided equally between neutrino and antineutrino running at 700 kW beam power and the dotted and dash-dotted curves represents the same run at 1.2 MW and 2.3 MW beam power, respectively. The regions are somewhat sensitive to δ, the mass ordering, and the sign of $\cos(2\theta_{23})$; the curves represent an average over the parameter space.

3.6 Search for "atmospheric" sterile neutrinos

The Super-Kamiokande, K2K, and MINOS experiments each study neutrino oscillations via muon neutrino disappearance. Of these experiments, only Super-Kamiokande has any indications that the oscillations are in fact due to τ neutrinos, [10] leaving open the possibility that oscillations at the atmospheric scale could involved a fourth light neutrino. To be consistent with LEP measurements of Z^0 decays, this fourth neutrino state would have to sterile, that is, to have zero coupling to the Z and W bosons. Super-Kamiokande has ruled out the possibility that oscillations at the atmospheric scale could be entirely due to oscillations to sterile neutrinos[11]. Allowing for the possibility that muon neutrinos oscillate to a neutrino state which is an admixture of ν_τ and ν_s, Super-Kamiokande limits the sterile content to below 23% at the 90% confidence level [12].

In NOνA, participation of a sterile neutrino state in the oscillations of muon neutrinos would suppress the neutral-current event rate as measured at the far detector. Based on detailed simulations, the NOνA detector can select a neutral-current (NC) event sample of 91% purity with an efficiency for retaining neutral-current events with 56% efficiency. Figure 3.11 shows the resulting visible energy spectrum for the reconstructed NC sample. As seen in the Figure 3.11, increasing the sterile admixture only affects the spectrum significantly below 2 GeV in visible energy. The ratio of the number of NC events below 2 GeV to those above 2 GeV provides measure of the sterile admixture. In this ratio, we expect systematic uncertainties in the detection efficiency, neutrino cross-sections, and neutrino flux to largely cancel, leaving a 5% systematic uncertainty on the sterile admixture. In this way, NOνA can limit the sterile admixture to below 11% at 90% C.L., an improvement of slightly more than a factor of two on the limit from Super-Kamiokande.

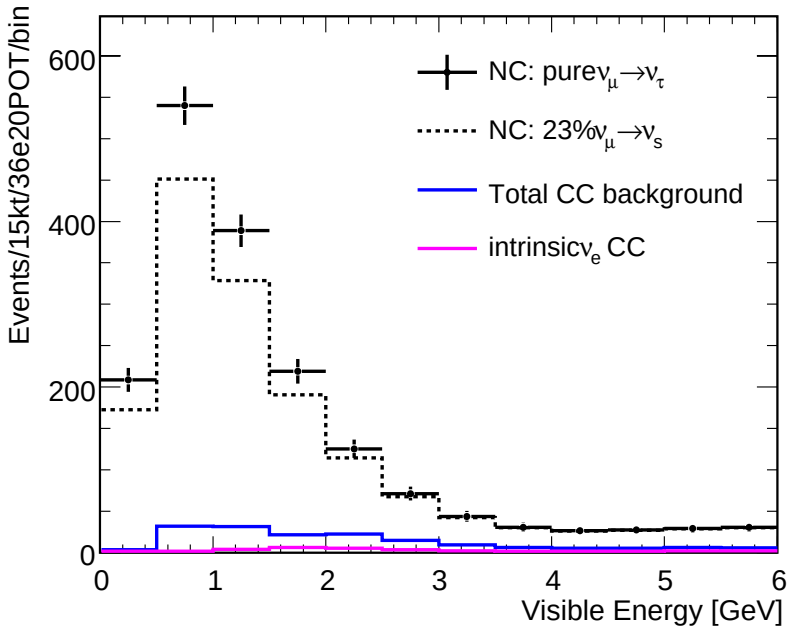

Fig. 3.11: The visible energy spectrum of neutral-current events reconstructed in the NOνA detector. Points show the expected spectrum for oscillations to a pure tau neutrino state, while the dotted curve shows the expectation for a sterile admixture at the current Super-Kamiokande limit. The blue and red curves show the background from charged-current muon and electron neutrino events in the neutral-current sample.

3.7 Chapter 3 References

[1] Q. R. Ahmad et al. [SNO Collaboration], *Phys. Rev. Lett*. **87**, 071301 (2001); S.N. Ahmed et al. *Phys.Rev.Lett.* **92**, 181301 (2004).

[2] K. Eguchi et al. [KamLAND Collaboration], *Phys. Rev. Lett*. **90**, 021802 (2003); T. Araki et al., *Phys.Rev.Lett.* **94**, 081801 (2005).

[3] S. Fukuda et al. [Super-Kamiokande Collaboration], *Phys. Lett.* **B539**, 179 (2002).

[4] M. H. Ahn et al. [K2K Collaboration], *Phys. Lett.* **B511**, 178 (2001); Phys. Rev. Lett. **90**, 041801 (2003); E. Aliu et al., hep-ex/0411038 (2004).

[5] D. G. Michael et al. [MINOS Collaboration], *Phys.Rev.Lett.* **97**, 191801 (2006); J. Thomas, "Accelerator Neutrino Experiments," to appear in the proceedings of the XXIII International Symposium on Lepton and Photon Interactions at High Energy, August 13-18, 2007, Daegu, Korea, (http://chep.knu.ac.kr/lp07/htm/s11_01_01.htm).

[6] CHOOZ collaboration, M. Apollonio *et al.*, Phys. Lett. B **466** (1999) 415; Eur. Phys. J. **C27** (2003) 331

[7] Y. Ashie et al. . [Super-Kamiokande Collaboration], *Phys. Rev. Lett.* **93,** 101801 (2004); Phys. Rev. D **71**, 112005 (2005).

[8] M. Zito, "The T2K neutrino oscillation experiment," to appear in the proceedings of the 2007 Europhysics Conference on High Energy Physics, July 19-25, 2007, Manchester, England, (http://www.hep.man.ac.uk/HEP2007/index.html).

[9] Daya Bay Proposal, hep-ex/0701029v1 (2007).

[10] K. Abe et al., Phys.Rev.Lett.**97**:171801,2006

[11] S. Fukuda et al., Phys. Rev. Lett. **85**, 3999 - 4003 (2000)

[12] W. Wang, Ph.D. Thesis, Boston University (2007).

4 NOνA Scientific Design Criteria

4.1 NOνA Goals

The primary goal of the NOνA experiment is to use the existing Fermilab NuMI muon neutrino (ν_μ) beam described in Chapter 2 to measure electron neutrino (ν_e) appearance due to $\nu_\mu \rightarrow \nu_e$ oscillations. A secondary goal is a greatly improved measurement of the ν_μ disappearance parameters.

4.1.1 Table of Scientific Design Criteria

The two main NOνA goals translate into the scientific performance requirements summarized in Table 4.1. The requirements are developed in this chapter in the sections indicated in the table.

Design Parameter	Scientific Design Criterion	Section
Distance off-axis	11.5 to 12.0 km	4.2.1
Distance from Fermilab	As far from Fermilab as practically possible.	4.2.2
Experimental Sensitivity	Figure of merit greater than or equal to 18 *The Figure of Merit is defined as the number of ν_e signal events divided by the square root of the background for 36 x 10^{20} protons on the NuMI target equally divided between neutrino and anti-neutrino focusing at the oscillation values $\sin^2(2\theta_{13}) = 0.1$ and $\Delta m^2_{32} = 0.0024$ eV^2 without regard to matter and atmospheric-solar interference effects.*	4.3.1
Energy resolution for ν_e Charged Current events	Less than 8% at 2 GeV	4.4.1
Energy resolution for Quasi-Elastic ν_μ Charged Current events	Less than 4% at 2 GeV	4.4.1
Far Detector overburden	>10 radiation lengths	4.4.2
Near Detector	a) At least a 20 ton fiducial volume located about 1 kilometer from the NuMI target with sufficient transverse and longitudinal size for neutrino event containment. b) Segmentation in the fiducial volume identical to the Far Detector. c) Orientation identical to the Far Detector	4.5

Table 4.1: Summary of the scientific design criteria and the chapter sections in which they are established.

4.2 Siting Requirements

4.2.1 Transverse Siting

NOνA has multiple physics goals and each goal is optimized by a slightly different neutrino spectrum. The shape and central value of the neutrino energy spectrum is determined by the transverse location (i.e. the off-axis angle) of the Far Detector so the optimization of the neutrino spectrum is realized by choosing the optimum distance to place the detector off-axis. As shown in Figure 4.1, measurements of $\sin^2(2\theta_{13})$ and measurements of the mass hierarchy are optimized at slightly different off-axis locations. The measurement of $\sin^2(2\theta_{13})$ is optimized by maximizing the total neutrino rate, favoring a more on-axis location, while the hierarchy measurement is optimized by maximizing the ratio of *L/E*, favoring a location further from the beam axis.

Since the unique feature of NOνA is the ability to measure the mass hierarchy, we have optimized for a mass hierarchy measurement at a cost of having a slightly lower event rate for the $\sin^2(2\theta_{13})$ measurement. The requirement for transverse location is chosen to be between 11.5 and 12 km off-axis. This requirement can be stated independent of the baseline since the relevant physics parameter is the ratio of a neutrino's flight distance to its energy, *L*/*E*, and *E* approximately scales inversely with the off-axis distance for large distances.

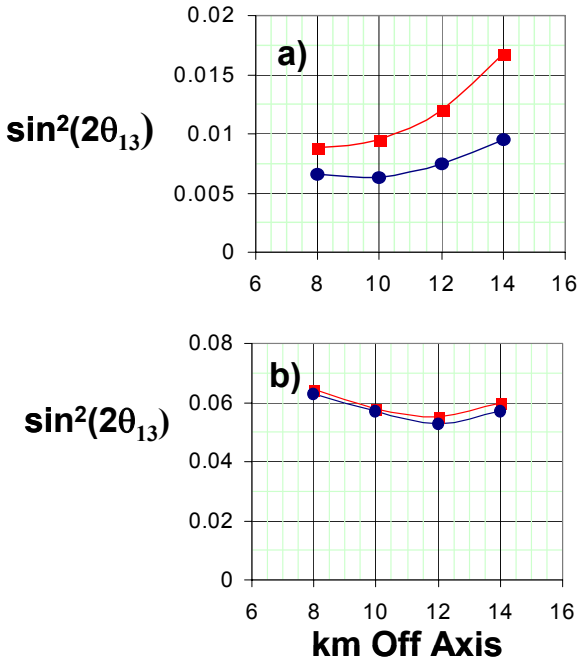

Fig. 4.1: a) Three standard deviation discovery limits for the observation of $\nu_\mu \rightarrow \nu_e$ oscillations versus the off-axis distance, and b) $\sin^2(2\theta_{13})$ versus the off-axis distance for the 95% confidence level resolution of the mass hierarchy. The upper red curve is for inverted mass hierarchy and the lower blue curve is for the normal mass hierarchy in both figures.

The curves in a) are for six years of neutrino running, while the curves in b) are for 3.6 years each of neutrino and antineutrino running. Both figures assume $\Delta m^2_{32} = 0.0025$ eV^2 and a 25 kiloton detector at 810 km.

The curves in a) assume a typical CP phase δ, while the curves in b) are for δ such that 25% of δ values give a lower $\sin^2(2\theta_{13})$ limit and 75% give a higher limit since in this case the typical δ gives a limit above the existing experimental limit. See reference [2] for additional details.

4.2.2 Longitudinal Siting

Equation 3.4 in Chapter 3 indicates how the matter effect modifies the oscillation probability observed in the experiment. The difference between the normal mass hierarchy (blue curves) and inverted mass hierarchy (red curves) in Figure 3.3 depends on the size of the matter effect. This is displayed in a slightly different form in Figure 4.2 below, which plots the neutrino oscillation probability versus the antineutrino oscillation probability for experiments operating at the oscillation maximum at different baselines *L*. A measurement of the mass hierarchy depends on the separation of the red and blue curves in Figure 4.2, and this is accomplished by inserting as much matter as possible in the path between the neutrino source and the detector.

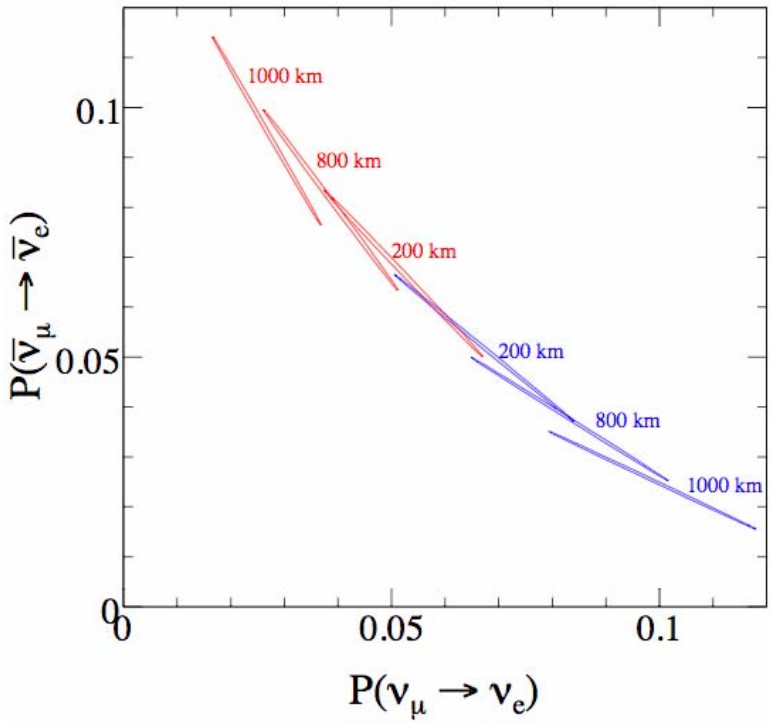

Fig. 4.2: The bi-probability curves for $\nu_\mu \rightarrow \nu_e$ oscillation for anti-neutrinos versus neutrinos, assuming a constant matter density of $\rho = 2.8$ g/cm^3. Curves are calculated assuming a normal mass hierarchy (blue) and an inverted mass hierarchy (red) with $\Delta m^2_{12} = 8\times10^{-5}$ eV^2, $|\Delta m^2_{13}|=2.5\times10^{-3}$ eV^2, $\theta_{12} = 35^o$, $\theta_{23}=45^o$ and $\theta_{13}=10^o$; the choice of the CP phase δ phase varies from 0 to 2π around each ellipse. The curves are computed for an experiment operating at the first oscillation maximum ($E = 2.54\ \Delta m^2_{13}$ [eV^2] L [km] / π) for several choices of baselines as indicated on the figure.

Since the experiment's ability to determine the mass ordering depends on the distance the neutrinos travel through the Earth, the NOνA Far Detector should be sited as far away from Fermilab as is practically possible. For a given detector mass, this longitudinal location requirement is modified somewhat by the solid angle of the detector as seen from Fermilab and by the inherent divergence of the off-axis beam. Modifications also occur because longer baselines with the same off-axis transverse distance have a higher energy neutrino beam and the interaction cross section for neutrinos is proportional to the beam energy. As an example, we have calculated the 95% confidence level for determining the mass ordering for detectors at 810 km and 775 km from Fermilab. In order to have the same sensitivity to the mass ordering, a

detector at 775 km would have to have 40% more mass than a detector at 810 km. It is difficult to make up for a shorter baseline with greater statistics.

Practical considerations of accessibility and community support limit the choice to Ash River, Minnesota as described in the NOνA Conceptual Design Report [1].

4.3 Experimental Sensitivity Requirements

The primary goal of the NOνA experiment is to measure $\nu_\mu \rightarrow \nu_e$ oscillations at the "atmospheric" oscillation length with a 90% C.L. sensitivity to a $\sin^2(2\theta_{13})$ value of ~ 0.01. This goal is approximately an order of magnitude greater sensitivity than can be achieved by the existing MINOS experiment [3] now operating in the NuMI beamline. This goal is also approximately the same sensitivity expected in the T2K experiment in Japan [4] that would be running in the same time frame as NOνA. Relative to T2K, NOνA has the unique advantage of a long baseline and is thus complementary to T2K.

4.3.1 Figure of Merit

There are five multiplicative factors that determine the sensitivity of the NOνA experiment to ν_e appearance: The beam power (or number of protons per year delivered to the NuMI target), the integrated data taking time (years) for the experiment, the mass of the NOνA detector, the detector's efficiency for identifying ν_e events, and the detector's ability to discriminate $\nu_\mu \rightarrow \nu_e$ oscillations from various backgrounds. The last two of these factors depend both on the detector design, such as its segmentation and light levels, and on the algorithms used to discriminate the signal from background.

The product of these factors can be expressed as a figure of merit (FoM), and its value is the basic scientific requirement for experimental sensitivity. The FoM is defined as the number of $\nu_\mu \rightarrow \nu_e$ signal events divided by the square root of the background for a three-year neutrino and a three-year anti-neutrino run with a 15 kt detector and 6 x 10^{20} protons on target per year for $\sin^2(2\theta_{13}) = 0.1$ and $\Delta m_{32}^2 = 0.0024$ eV^2, without regard to matter and atmospheric-solar interference effects. The choice of $\Delta m_{32}^2 = 0.0024$ eV^2 is driven by results from the MINOS experiment [5].

The current best limit on $\sin^2(2\theta_{13})$ at $\Delta m_{32}^2 = 0.0024$ eV^2 is set by the CHOOZ experiment which limits $\sin^2(2\theta_{13})<0.15$ at 90% C.L. (1.64 σ). NOνA requires a FoM of 11 to push one order of magnitude beyond this limit. In the next few years, searches for $\nu_\mu \rightarrow \nu_e$ oscillations by MINOS are expected to extend down to $\sin^2(2\theta_{13})<0.08$-$0.09$ at 90% C.L. To extend the search for $\nu_\mu \rightarrow \nu_e$ oscillations one order of magnitude beyond MINOS's reach requires a FoM of 18 for the NOνA experiment. This corresponds to a three standard deviation sensitivity to $\sin^2(2\theta_{13}) = 0.017$. Matter effects (whose sign depend on the mass hierarchy) and value of the CP violating phase δ modify the $\nu_\mu \rightarrow \nu_e$ oscillation probability and hence the sensitivity. Figure 3.4 in Chapter 3 shows the 3-sigma sensitivity of an 15 kt detector placed 12 km off axis at a baseline distance of 810 km from Fermilab as a function of δ and $\sin^2(2\theta_{13})$ for both mass hierarchies.

4.4 Far Detector Requirements

4.4.1 Neutrino Event Energy Resolutions

As discussed in Chapter 2, Section 2.2, one of the advantages of the off-axis site is that the narrow-band beam can be used to eliminate backgrounds. The rms width of the off-axis beam is about 25%, as can be seen in Fig. 2.4. With the limited statistics expected for the $\nu_\mu \rightarrow \nu_e$ oscillation signal, dividing this narrow energy range further does not increase the sensitivity appreciably. Therefore, the main use of good energy resolution is to prevent a widening of the

visible energy spectrum, which would increase the background. An energy resolution of one-third the beam width, or 8% is sufficient for this purpose.

Chapter 3, Section 3.4 discussed the need for excellent energy resolution for quasi-elastic ν_μ charged current events for the precise measurement of the dominant mode oscillation parameters, $\sin^2(2\theta_{23})$ and Δm^2_{32}. The required rms resolution is 4%.

4.4.2 Far Detector Hall Overburden Requirement

The physics requirement for the detector hall comes from the need to reduce cosmic ray backgrounds to a negligible level. The very low duty cycle of the NuMI beam aids greatly in cosmic ray rejection. We assume (see reference [2], Chapter 11) that the NuMI beam will run 1.2 $x10^7$ cycles per year and that the spill will be 10 μs per cycle, yielding a live time of only 120 seconds per year.

To fake a $\nu_\mu \rightarrow \nu_e$ signal event, a cosmic ray would need to appear to be a horizontal event from Fermilab within a 45^o cone, appear to have an electron-like track, and not leave any significant energy within 20 cm of the edges of the detector. Charged cosmic rays all fail the last requirement and thus are not a problem. Our simulation of the charged cosmic neutrino flux indicates that there would be less than one event simulating a signal event in a six-year run with no overburden over the detector.

Simulations of neutrons in cosmic rays also indicate NOνA should see only a fraction of an event from this source in a six-year run [2].

The major concern is the photon component of cosmic rays. These cosmic rays are strongly peaked towards the vertical as shown in Figure 4.3(a). Our acceptance for these events as ν_e interactions is limited to a 45^o cone around the horizontal in the direction of Fermilab, see Figure 4.3(b). The convolution of the two in our simulation of the photon flux with no overburden shielding the detector yields 1600 events in a six-year run with a 15 kt detector as shown in Figure 4.3(c).

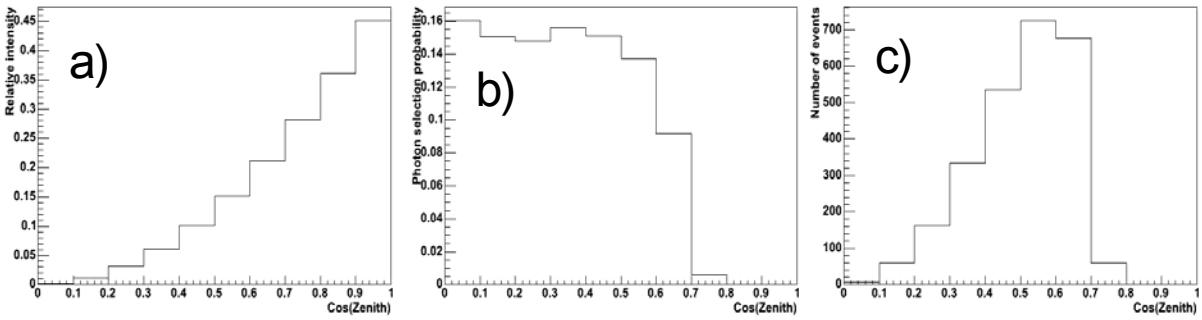

Fig 4.3: The photon component of cosmic rays. The incident cosmic rays are shown in (a) as a function of cos(Zenith). The NOνA selection probability for these events is shown in (b), and the convolution of production and selection yield the event distribution in (c).

To reduce these 1600 events to less than one event requires at least (9/7)log(1600) = 9 radiation lengths of material in the path of cosmic-ray photons directed at the detector surface. Additional radiation lengths beyond 9 are desirable to contain the resulting shower. Previously, we planned to use 20 radiation lengths to completely contain the electromagnetic showers started by cosmic ray photons. Simulations of the residual shower component that punch through indicate that 12 radiation lengths are adequate to attenuate the energies of the shower components such that they fall outside the signal energy window for electron neutrino appearance.

4.5 Near Detector Requirements

The NuMI beam is not a pure ν_μ beam and has a small inherent ν_e component which can simulate the $\nu_\mu \rightarrow \nu_e$ oscillation signal. In addition neutral current ν_μ events (events where there is no outgoing muon) can simulate the $\nu_\mu \rightarrow \nu_e$ oscillation signal. In order to measure these backgrounds to the oscillation signals, NOνA requires a Near Detector to measure neutrino interactions before they have had a chance to oscillate.

The primary Near Detector design requirement is that it should be as similar as possible to the Far Detector in material, segmentation, and orientation. This requirement ensures that the efficiencies for signal and background events are identical to the NOνA Far Detector. Other requirements are that the fiducial volume be large enough to have well-defined boundaries and that the Near Detector be large enough to fully contain events from the fiducial volume. A transverse cross section of 4 m^2 is sufficient to meet the first requirement. Simulations have shown that a 70 cm wide border around the fiducial volume in the transverse dimensions and 4 m in the longitudinal dimension provides sufficient of containment of ν_e charged current events.

The NOνA Near Detector will be placed approximately 1 km from the NuMI target and will be approximately 800 m from the typical pion decay vertex. Since the neutrino flux falls roughly as the inverse of the distance squared, the flux per unit mass in the Near Detector will be approximately one million times higher than in the Far Detector. Thus, the fiducial volume of the Near Detector can be quite small. A twenty-ton fiducial volume in the Near Detector would produce about 800 times more events there than in the fiducial volume of the Far Detector. The requirement on the fiducial volume of the Near Detector is that the number of background events to the $\nu_\mu \rightarrow \nu_e$ oscillation signal be large enough to perform systematic studies over a period of about a year. A twenty-ton fiducial volume would produce approximately 2000 beam ν_e events in one year, and this would be an adequate number for systematic studies.

4.6 Chapter 4 References

[1] NOνA Conceptual Design Report, March 31, 2006.

[2] The NOνA Collaboration, "Proposal to Build a 30 Kiloton Off-Axis Detector to Study $\nu_\mu \rightarrow \nu_e$ Oscillations in the NuMI Beamline," http://www-nova.fnal.gov/NOvA_Proposal/-Revised_NOvA_Proposal.html., Chapter 13.

[3] "Proposal for a Five Year Run Plan for MINOS, May 2003, NuMI Note 530.

[4] T2K Letter of Intent, January, 2003. http://neutrino.kek.jp/jhfnu/.

[5] J. Thomas, "Accelerator neutrino experiments", to appear in the proceedings of the XXIII International Symposium on Lepton and Photon Interactions, Aug. 13-18, 2007, Daegu, Korea. (http://chep.knu.ac.kr/lp07/index.html).

5 Overview of the NOνA Design

5.1 Introduction

This chapter contains an overview of the NOνA technical design. More detailed descriptions of the design are presented in Chapters 8 through 17.

5.2 The Neutrino Beam

Figure 5.1 shows the Fermilab accelerator complex and proton source for NOνA. The accelerator and NuMI upgrades for NOνA will provide about a factor of two increased beam power relative to the current output. This is accomplished by reconfiguring the Recycler into a proton storage device and by increasing the acceleration rate and repetition rate of the Main Injector (MI). The increased beam power only requires a 10% increase in the total beam intensity in the MI. Shielding and cooling modifications to the proton source and upgrades in the NuMI neutrino line are also required to handle the higher beam power. Many existing components in the accelerator complex are reconfigured for the NOνA upgrade and additional new components are required. Details on the NOνA accelerator and NuMI upgrades are found in Chapter 8.

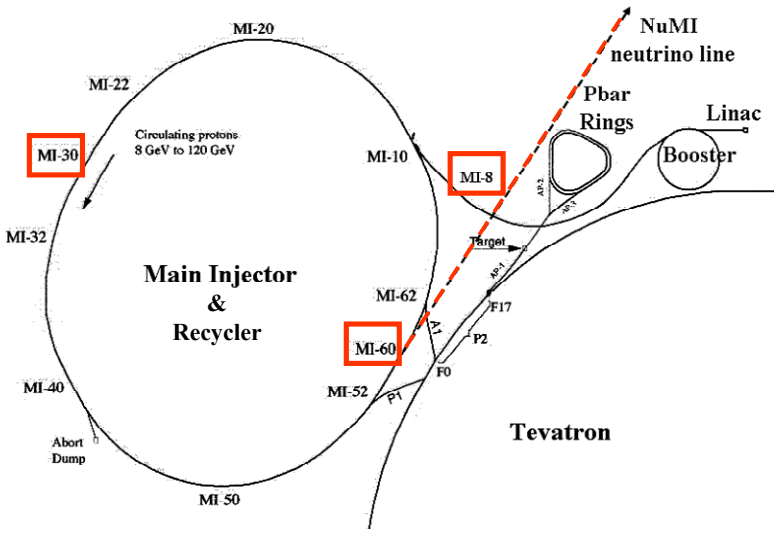

Fig. 5.1: Plan view layout of the Fermilab proton source consisting of the Linac, Booster, Recycler, Main Injector and NuMI neutrino line. The Recycler and Main Injector are in the same tunnel.

5.2.1 Recycler Upgrades

The Recycler is a permanent magnet machine designed for 8 GeV beam transport in the MI tunnel and currently serves as the main anti-proton storage ring for the Tevatron Collider program. When Tevatron Collider operations cease, the Recycler will be used as a proton pre-injector for the Main Injector (MI) for NOνA. The Recycler is the same size as the MI and is located in the same tunnel, making it possible to do a single turn fill which minimizes the proton injection time in the MI cycle and maximizes the protons on target. Figure 5.1 shows the layout of the Recycler, MI and NuMI beamline.

To convert from an anti-proton storage ring to a proton pre-injector, anti-proton specific devices will be removed from the Recycler. A new proton injection line will be built connecting MI-8 (from the Booster) into the Recycler, and a new extraction line from the Recycler to the MI will be built at MI-30. Figure 5.1 indicates the MI-8, MI-30 and MI-60 locations around the

Main Injector / Recycler tunnel. These beamlines and the abort system will require five new kicker systems. A new 53 MHz RF system is required using two new RF cavities with controls and power installed in the MI-60 service building. The Recycler instrumentation will be upgraded with new beam position monitors, new intensity measuring devices, and new dampers.

5.2.2 Main Injector Upgrades

For NOνA the Main Injector will be accelerating only 10% more proton intensity, but the beam power out of the MI will be much larger because the MI cycle time will be reduced from 2.2 seconds to 1.33 seconds. By using the Recycler Ring for stacking, the Main Injector cycle time is reduced to 1.5 seconds. To further decrease the Main Injector cycle to 1.33 seconds, the maximum acceleration rate must be increased from 204 GeV/sec to 240 GeV/sec. This faster ramp requires an upgrade to one of the quad power supplies. The MI also requires two extra RF stations to complement the existing 18 stations.

5.2.3 NuMI Beamline Upgrades

As part of NOνA, the target and focusing Horn 2 locations will be changed to the medium energy configuration described in Chapter 2. A new medium energy target is required. The second horn must move to a new location within the target chase area and horn stripline extension is needed to reach this position. Other parts of the NuMI beamline upgrade are mainly cooling modifications to handle the increase in beam power from 400 kW to 700 kW and power supply upgrades to allow operations at the faster cycle time.

5.3 The Far Detector Site and Detector Hall at Ash River, Minnesota

5.3.1 The Far Detector Site

The NOνA Far Detector will be located near Ash River, Minnesota. The site is 810.5 kilometers from Fermilab as shown in Figure 5.2. The Ash River site has the unique property of being the furthest site from Fermilab that is inside the United States and accessible by road.

Fig 5.2: Map of the central United States showing Fermilab, the NuMI beamline, and the NOνA Far Detector site at Ash River, Minnesota.

The Ash River area is located about 40 km southeast of International Falls, Minnesota on the Ash River Trail (St. Louis County Highway 129) near the entrance to Voyageurs National Park as shown in Figure 5.3. Ash River is about an hour drive from International Falls, about a 3 hour drive from Duluth, and about a 5 hour drive from Minneapolis.

The site is 11.8 kilometers west of the NuMI beamline. The on-axis NuMI beamline is itself about 4.2 kilometers above the surface at 810 km from Fermilab. The site is 15 km east of U.S. Highway 53 along the Ash River Trail road (St. Louis County 129). Both U.S. 53 and County 129 are maintained year-round.

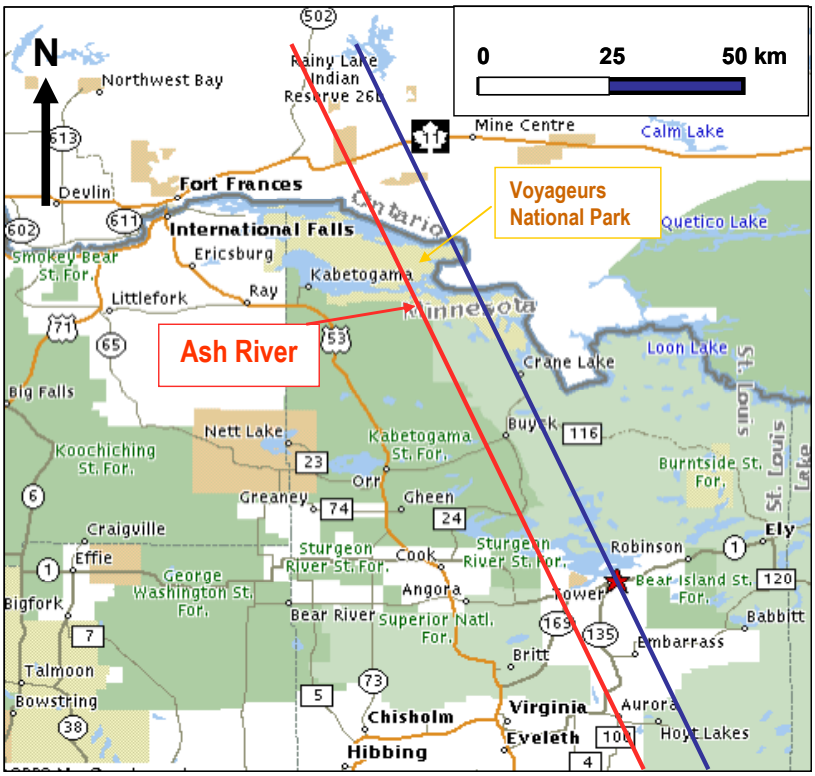

Fig. 5.3: Map showing the Far Detector site at Ash River. The NuMI beam centerline (blue) passes through the MINOS detector underground at Soudan (red star). The NOνA Ash River site is on the red line to the left (west) of the NuMI beam centerline, ~11.8 km (14.6 mradians) off-axis. Voyageurs National Park and the US-Canada border are just north of the site.

5.3.2 Cooperative Agreement

The University of Minnesota has been selected by the Department of Energy as the recipient of a Cooperative Agreement [1] to build and operate the NOνA Far Detector building and access road in collaboration with the NOνA Project headquartered at Fermilab. Details of the collaborative agreement among the DOE, Fermilab NOνA Project and the University of Minnesota are in the NOνA Project Management Plan [2].

The Ash River site is a 50 acre plot that will be acquired by the University of Minnesota. A detailed local topographic map of the site is shown in Figure 5.4. The NOνA site is located about 1.5 miles south of an entrance to Voyageur's National Park. but is not visible from the park due to intervening hills and trees.

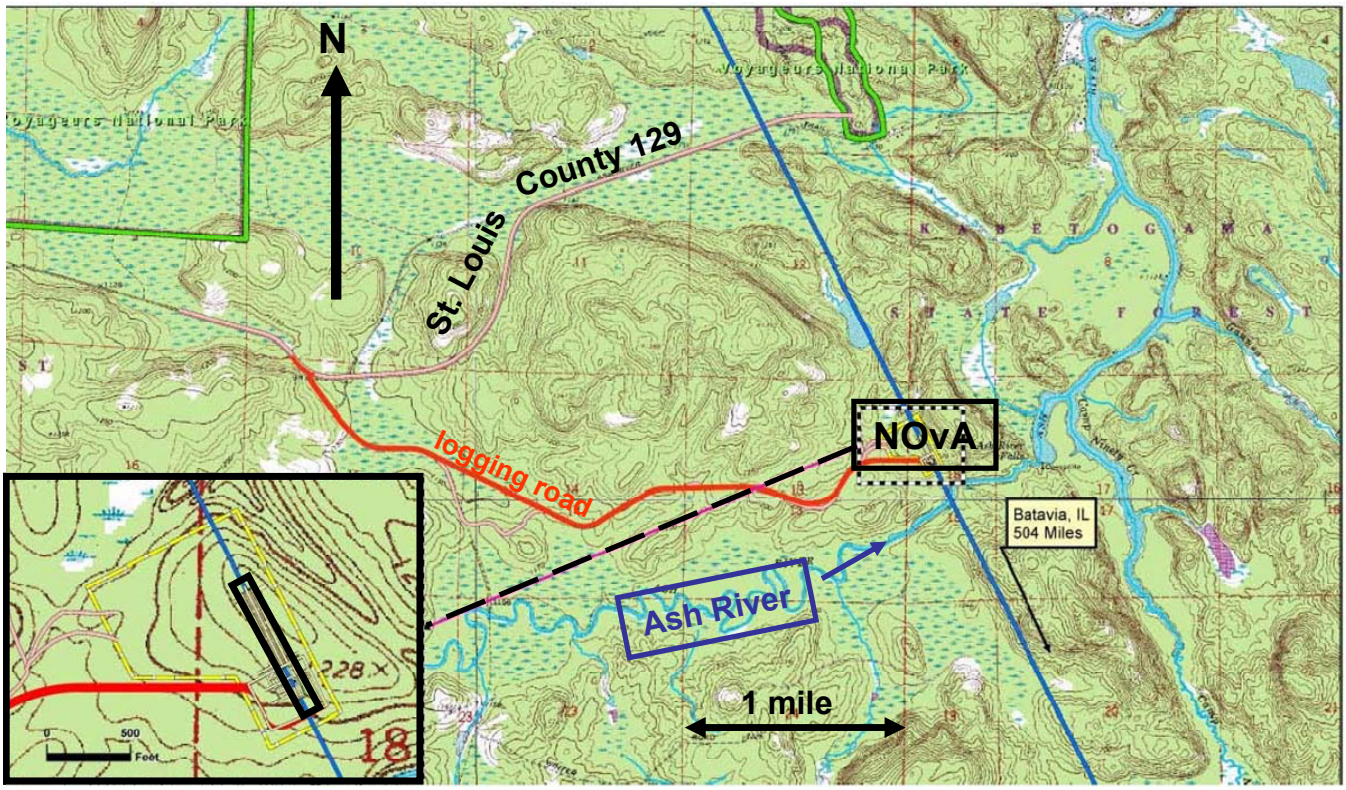

Fig. 5.4: Topographic map of the Ash River area. The NOvA site is in the rectangle at the end of the logging road (red) off St. Louis County Road 129. The inset in the lower left corner shows the site in more detail with the NOvA building sitting near the top of a hill at an altitude 1228 feet above sea level. The entrance road to the Ash River Visitor's Center in Voyageurs National Park is shown at the top right center of the map.

Access to the site is currently via an old clay base logging road off St. Louis County 129. The University of Minnesota will acquire an easement for this 3.6 mile long, 40 acre access road corridor. The access road passes through a wetlands area just as it leaves St. Louis County 129, and an Army Corps of Engineers permit will be required to allow construction of an all weather road like St. Louis County 129 to replace the existing logging road. A draft wetlands permit application has been prepared [3]. An advanced technical design of the access road is presented in Chapter 9.

5.3.3 Environmental Assessment

A NOvA Environmental Assessment (EA) [4] has been written which treats the environmental issues in detail. The Ash River portion of the NOvA EA depends on a State of Minnesota process in which an Environmental Assessment Worksheet (EAW) [5] has been submitted for review by the University of Minnesota.

5.3.4 NOvA Far Detector Hall at Ash River

The detector laboratory location at Ash River is in Section 18 of Township 68 North, Range 19 West, St. Louis County MN. This location is described in Table 5.1 and shown in Fig. 5.4. The site is located at an altitude of 1220 feet above sea level and is about 70 feet above the Ash River located to the south. Core borings at the site have determined [6] that the site has 5 – 15 feet of soil overburden and then is solid hard granite to a depth of at least 60 feet.

Description	Latitude	Longitude	Distance from Fermilab (km)	Transverse distance from the NuMI beamline (km)	Altitude (ft)	Angle to the NuMI beamline (mradians)
This calculation is for the center of the detector based on GPS data for the corners of the detector building.	48.37912	-92.83164	810.54	11.81	1211	14.57

Table 5.1: Parameters for the center of the NOνA detector at the Ash River site. The angle in the table is the full space angle relative to the NuMI beam.

A cross section through the Far Detector Hall as seen by the NuMI neutrino beam is shown in Figure 5.5. The below grade portion of the building is 350 feet long, 63 feet wide, 67 feet high, and is constructed approximately 40 feet below the existing grade in granite rock. The below grade portion of the building will provide 100% secondary containment for the liquid scintillator used in the detector. The roof of the building consists of 1.5 feet of cast-in-place concrete over 2.5 feet of precast concrete planks. This composite section provides support for 0.5 feet of loose barite (barium sulfate) roof ballast to reduce the background rate from electromagnetic cosmic rays. The sides of the building above ground are shielded with granite spoils from the excavation. Details of this conventional construction are found in Chapter 9.

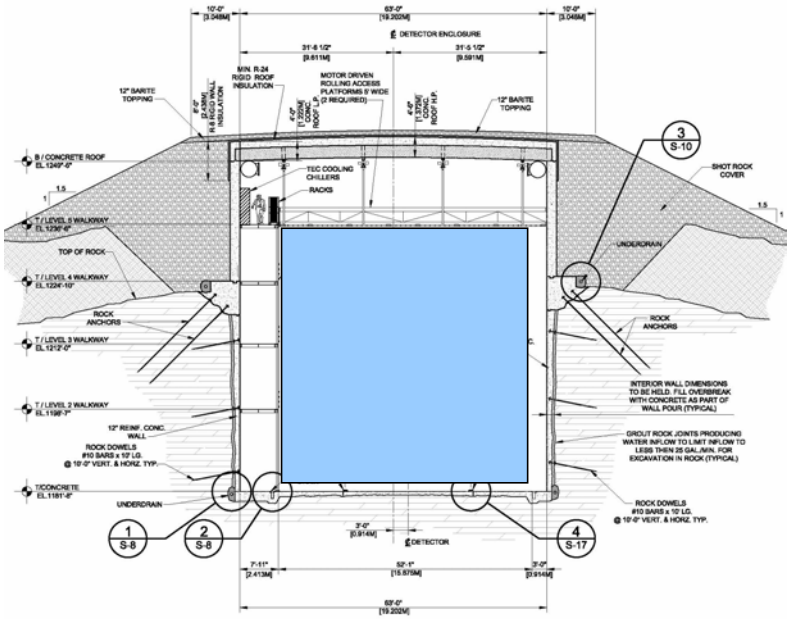

Fig 5.5: Neutrino beam view of the NOνA Far Detector Hall. The detector face is shaded blue. The detector is accessed via catwalks on one side and a rolling access platform suspended from the ceiling. The soil (light gray) has been removed at the detector site for excavation into the granite (block gray). The spoils from the excavation are loaded back on the sides of the detector to a minimum shield depth of 3m.

The plan view of the detector is shown in Figure 5.6. The detector sits in the south end of the building next to an assembly area also below grade. A loading dock and tanker truck delivery area (not shown) are at grade at the north end of the building. A longitudinal cross section through the building is shown in Figure 5.7 at the same scale as the plan view in Figure 5.6. This illustrates that the detector area is sized for an 18 kiloton detector, allowing later consideration of additional mass if the project can earn sufficient contingency.

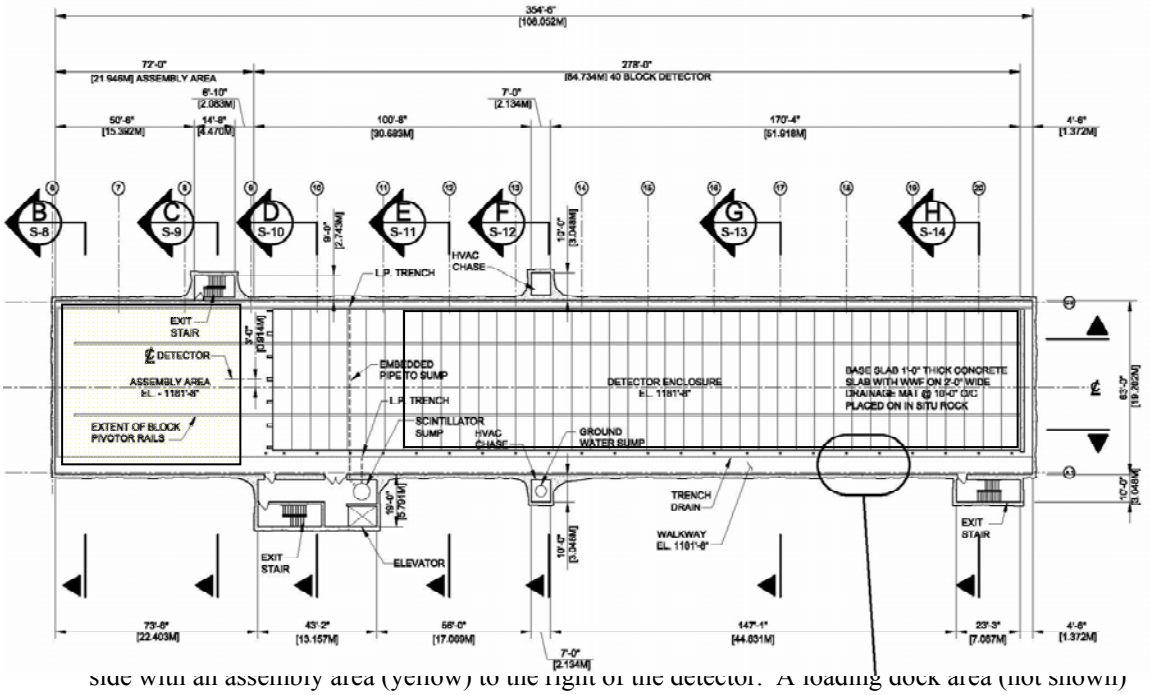

side with an assembly area (yellow) to the right of the detector. A loading dock area (not shown) is located to the left of the assembly area with recessed and drive-in truck bays. A scintillator tanker handling area (not shown) is further to the left of the loading dock.

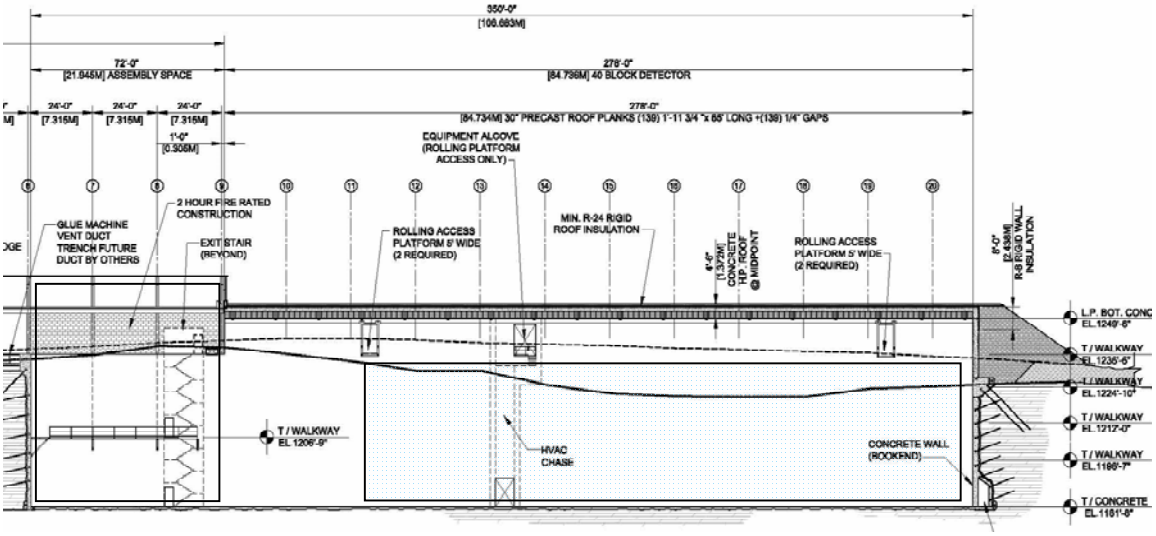

Fig 5.7: A longitudinal cross section through the building showing the detector and assembly areas below grade.

5.4 Near Detector Site and Detector Area at Fermilab

The NOνA Near Detector will be located in a new underground cavern off the existing MINOS access tunnel as shown in Figure 5.8. This new cavern requires a modest excavation of about 750 cubic yards of rock. Access to the area is via the existing MINOS shaft.

This Near Detector site will be located 1015 meters from the NuMI Target Hall and 105 meters below grade. The cavern is on a level grade and the NuMI neutrino beam enters the area from above at an angle of 58 milliradians (~3 degrees). At Ash River the beam enters the Far Detector from below at an angle of 58 milliradians. The cavern and Near Detector are located off-axis at the same angle of 14.6 milliradians as the Far Detector in Ash River as illustrated in Figure 5.9. Chapter 16 discusses the Near Detector cavern and Near Detector in detail.

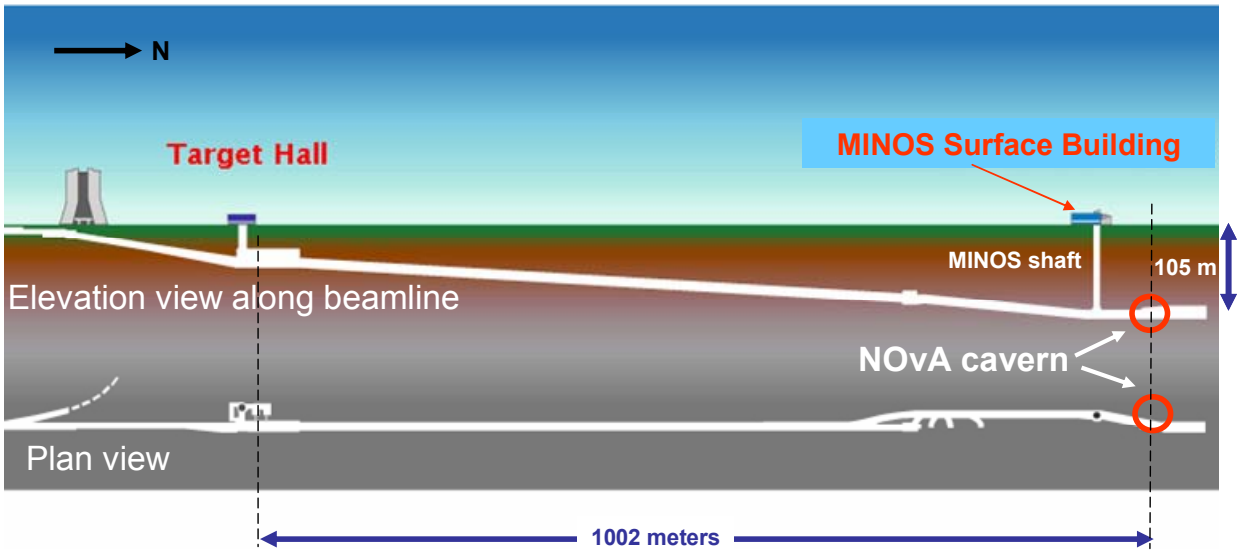

Fig. 5.8: Plan view and elevation (top) views of the NuMI beam line at Fermilab. The NOνA Near Detector will be located in the underground tunnel in the area labeled "NOνA cavern".

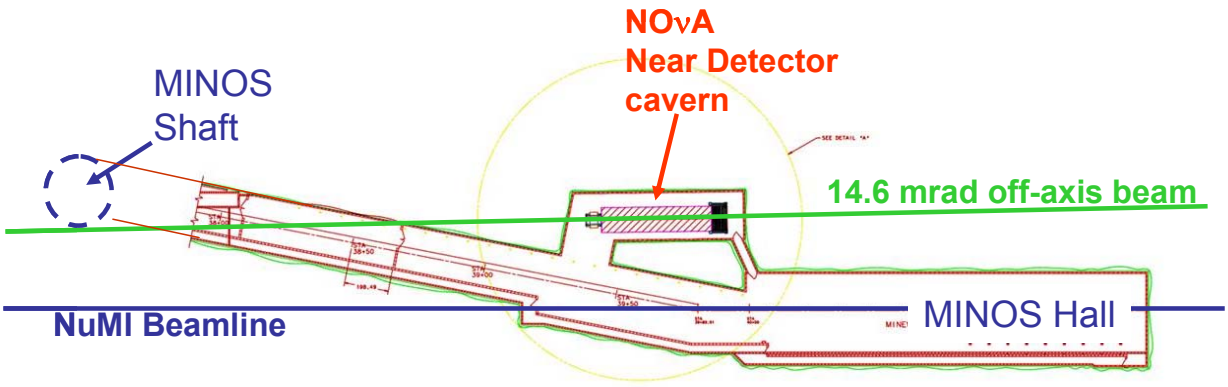

Fig. 5.9: A detailed plan view of the MINOS access tunnel from the vertical MINOS shaft to the MINOS hall. The new NOνA cavern is indicated.

5.5 Description of the NOνA Detectors

5.5.1 The Basic NOνA Detector Element

The basic unit of all the NOνA Detectors is a simple rectangular rigid PVC plastic cell containing liquid scintillator and a wavelength-shifting fiber. This is illustrated in Figure 5.10. Charged particles traverse the cell primarily along its depth (D) and scintillator light is produced in the liquid. The light bounces around in the rectangular cell of width W, depth D, and length L until it is captured by a wavelength-shifting fiber or absorbed by PVC or scintillator. The fiber is twice the length L of the cell and is looped at the bottom so the captured light is routed in two directions to the end (top in the illustration) of the cell. Effectively there are two fibers in the cell, each with a nearly perfect mirror at the bottom so that nearly four times the light of a single non-reflecting fiber is captured. At the top of the cell both ends of the looped fiber are directed to one pixel on an Avalanche Photodiode (APD) photodetector array and the light is converted to an electronic signal.

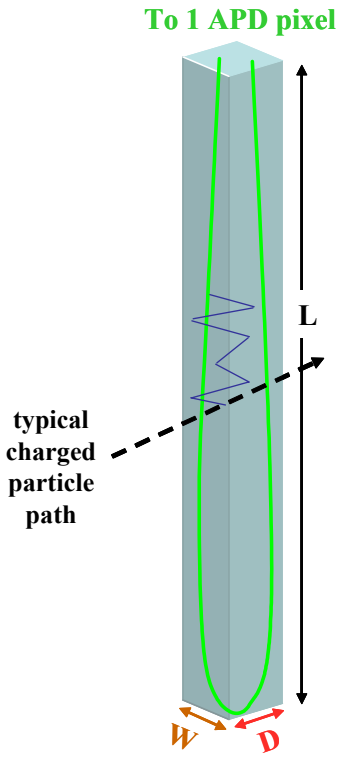

Figure 5.10: A PVC cell of dimensions (W, D, L) containing liquid scintillator and a wavelength-shifting fiber (green). A charged particle incident on the front face produces light (blue line) that bounces off the cell walls until absorbed by the fiber. The fiber routes the light to an APD.

The NOνA cell is made of a highly reflective titanium dioxide loaded rigid PVC cell with walls 2 to 4.5 mm thick. The cells have an interior width of 3.8 cm transverse to the beam direction, an interior depth of 5.9 cm along the beam direction, and an interior length of 15.5 meters. The cell width and depth satisfy the scientific requirements and the cell length is sized to fit on a standard domestic 53-foot semi trailer truck. To achieve the 15 kiloton mass stipulated by the scientific requirements, we repeat the cell structure 385,000 times.

5.5.2 Liquid Scintillator

Seventy percent (~ 10.5 kilotons) of the NOνA detector mass is the liquid scintillator held inside the NOνA cells. The 3.9 million gallons of liquid scintillator is composed primarily of mineral oil with 4.1% pseudocumene [1,2,4-Trimethybenzene] as the scintillant. The pseudocumene produces light with a spectrum peaked at 360 - 390 nanometers (nm). The liquid also contains chemical additives to shift the initial light to 400 - 450 nm matched to the wavelength-shifting fiber absorption spectrum. These additives are PPO [2,5-diphenyloxazole] and bis-MSB [1,4-di(methylstyryl)benzene]. An anti-static agent is added to the liquid at the level of 3 parts per million to prevent charge build-up during distribution to the cells. Blending of the scintillator components will take place at a toll blender in the Chicago area. Details of the NOνA liquid scintillator are discussed in Chapter 10.

Liquid scintillator mixtures like these are well known to have a ~ 20% decreased light output when exposed to oxygen, so the NOνA design requires only the lower oxygenated light level . Oxygen diffusion over time through the PVC walls is sufficient to produce the decreased light output effect. Since the scintillator light in a NOνA cell is captured locally by a wavelength-shifting fiber within about one meter path in the liquid, the attenuation length of the scintillator in NOνA is less of a performance driver than in previous experiments [7,8] where the light had to travel many meters through the liquid to the photodetector.

5.5.3 Wavelength-shifting Fiber

The NOνA detector contains about 13,000 kilometers of wavelength shifting fiber, with each 15.6 m long cell containing a loop of about 33.5 meters. The fiber captures the blue 400 – 450 nm light from the scintillator and wavelength shifts to green light in the range 490 - 550 nm. The fiber is 0.7 mm in diameter with a core of polystyrene mixed with 300 parts per million R27 dye as the wave-shifter.

The fiber is double clad with material of a lower refractive index than the core to facilitate total internal reflection of the shifted light along the fiber to the APD. The first cladding is a thin acrylic layer (PMMA or polymethylmethacrylate) and the second cladding is a fluor-acrylic, both claddings are about 3% of the fiber diameter. A similar fiber (but diameter of 1.2mm) was used in the MINOS detector [9].

As the internally reflected light travels down the 15.7 meter long fiber, it is attenuated by about a factor of ten with red light (520 – 550 nm) preferentially surviving. This property puts a premium on use of a photodetector with good quantum efficiency in the red and the APD is such a device. Chapter 11 contains more details on the fiber.

5.5.4 Rigid PVC Extrusions

The mass of the rigid PVC extrusions is ~ 4.5 kilotons or about 30 % of the mass of NOνA. Assembling 385,000 objects is achieved by using larger rigid PVC extrusions with 16 cells extruded together in a unit 0.635 meters wide as shown in Figure 5.11. Two different extrusions are required. The horizontal cells have exterior PVC walls 3 mm thick with 2 mm thick interior webs between cells. The vertical cells contain more PVC with 4.5 mm thick exterior walls and 3 mm thick interior webs. The extrusion thickness is 6.6 cm for both types, so the interior cells of the horizontals and verticals are slightly different in size. About 24,000 of the 16-cell extrusions are needed for the full detector.

The material properties of rigid PVC strongly influence the NOνA design. Unlike metals, plastics under stress can creep and perhaps creep to failure. The NOνA vertical cells build up an interior hydrostatic pressure of 19.2 psi at the bottom of the 15.7 meter column of scintillator (only 1.6 psi is seen at the "bottom" of a horizontal extrusion which is only 1.3 meters "tall"), so creep is a relevant concern. The NOνA extrusion design with the scalloped rounded corners

between cells is designed to minimize the stress and therefore minimize the creep. Chapter 12 has a more detailed discussion of the creep properties of the custom NOvA PVC formula.

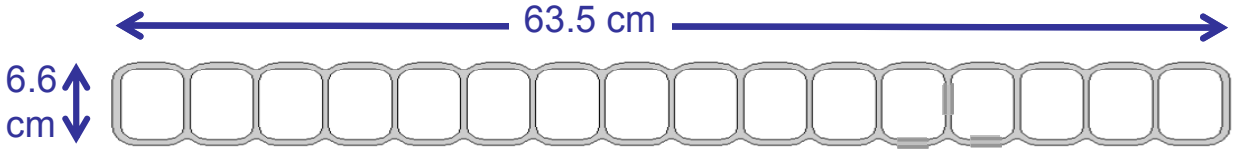

Fig. 5.11: Drawing of the NOvA rigid PVC extrusion.

The other crucial property of the PVC is its reflectivity for scintillator light of 400 – 450 nm. The light typically bounces off the PVC walls about 8 times before being captured by the fiber, so the surviving light at that point is proportional to the reflectivity raised to a power equal to the number of reflections, (reflectivity)^8. A 1% change in reflectivity translates into ~ 8% change in the amount of light seen by the fiber. Our baseline rigid PVC sample has demonstrated a reflectivity of ~ 90% at 430 nm using a PVC mixture loaded with 15% of the anatase form of titanium dioxide which boosts the reflectivity in the blue region. Additional details of NOvA PVC properties and NOvA extrusions are covered in Chapter 12.

5.5.5 Extrusion Modules

Two factories within the NOvA Collaboration construct leak-tight NOvA extrusion modules from the PVC and fiber. The first factory at Fermilab takes raw extrusion deliveries from the extruder and has the primary purpose of checking each extrusion for structural integrity. The extrusions are sorted to remove any variations in thickness which may arise during the extrusion process and additional sorting may take place to remove extrusions with excess "banana" along the length. The sorting will achieve a set of extrusions to form a single plane with a common thickness in the Far Detector at Ash River. Two sorted 16 cell objects are then attached with methyl methacrylate adhesive and the extrusion module is cut to an exact length.

The second factory is at the University of Minnesota is where the extrusions are threaded with wavelength shifting fiber loops as in Figure 5.10 and each fiber is tested for continuity after installation. The extrusion modules are capped at one end by a simple PVC end plate to contain the liquid scintillator and are capped at the other end by a more complicated fiber manifold which contains the liquid (in horizontal modules) and also routes the 64 fiber ends to 32 APD pixels. This is shown in Figure 5.12. As part of the assembly procedure, the 64 fiber ends are constrained into a block to match the APD pixel array, potted in epoxy, and faced off with a fly cutter.

The assembled extrusion modules with fiber manifolds and end caps are 15. 7 meters long, sized to fit inside a standard domestic 53-foot semi trailer truck. The end plates and fiber manifolds link the entire 32 cells into a common liquid volume. Thus the 1.3 meter by 15.7 meter extrusion module forms the primary containment vessel for the liquid scintillator. Each vertical extrusion module holds about 256 gallons of scintillator and each horizontal module holds about 278 gallons. As part of the construction process, each completed extrusion module is tested for leaks before being shipped to the Ash River site.

Chapter 13 contains more details on the extrusion module assembly.

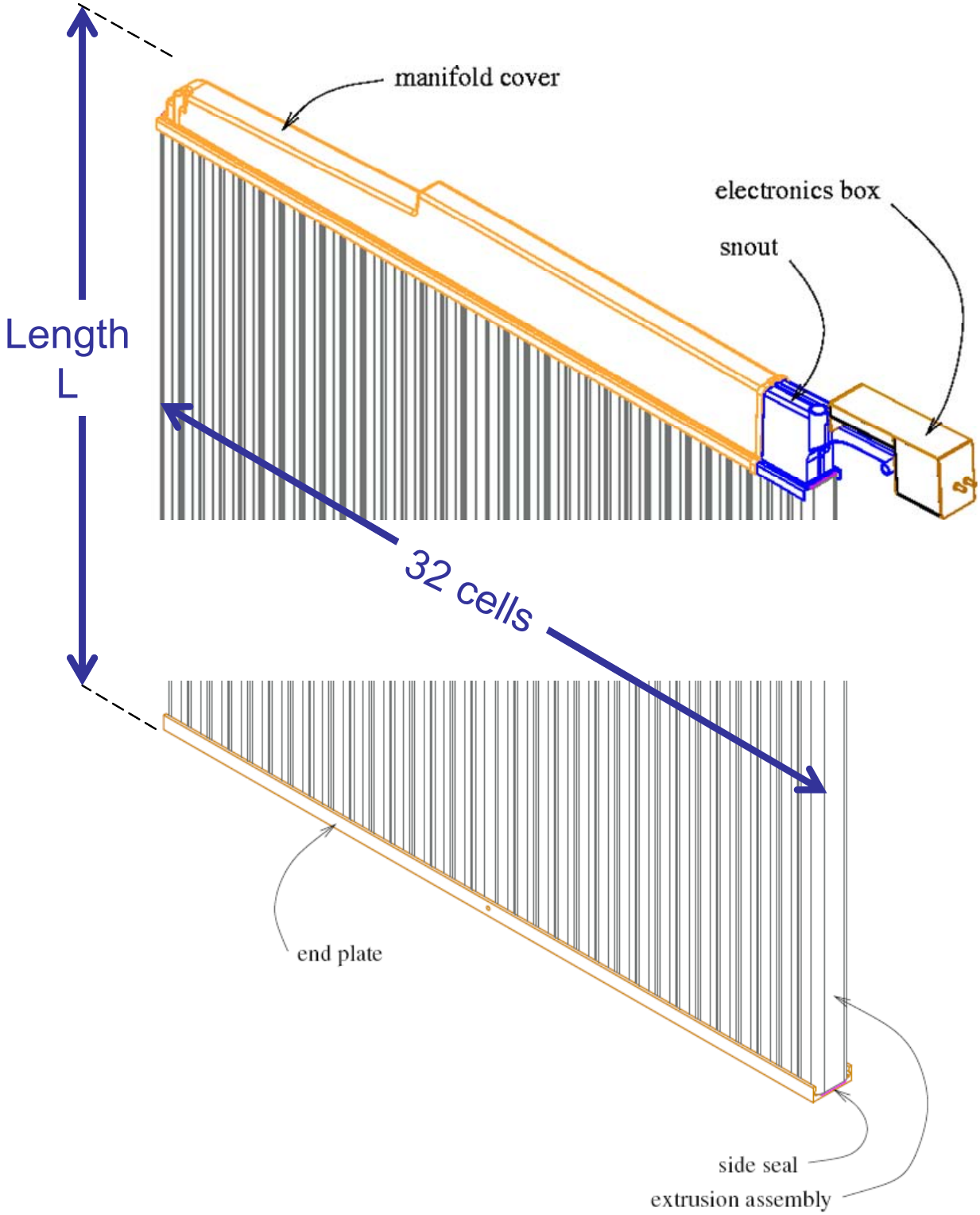

Fig. 5.12: A NOνA extrusion module constructed from two side by side 16 cell PVC extrusions and capped at both ends to contain the liquid scintillator. The manifold end also routes the 64 fiber ends to a cookie which couples to the avalanche photodiode array and associated electronics. The length L with the end plant and manifold is 15.7 meters for all the modules at the Far Detector site, but modules for the Near Detector are smaller.

5.5.6 Photodetector and Electronics

The NOνA photodetector is an Avalanche Photodiode (APD) manufactured by Hamamatsu and similar to the ones developed for use in the Compact Muon Solenoid (CMS) detector at the CERN Large Hadron Collider [10]. The APD has an 85 % quantum efficiency for the 520 – 550 nm light exiting the fiber. We operate the APDs at a gain of 100 using an applied voltage of about 375 volts. The thermal noise generated in the APD is reduced by cooling the devices to -15^{o}C using thermo-electric (TE) coolers. Heat from the hot side of the TE coolers is removed by a water cooling system in the Far Detector Hall. There are ~12,000 APDs on front-end boards in NOνA, one per extrusion module.

The signals from the APD are amplified by a special low noise pre-amp based on the Fermilab MASDA chip [11] and that pre-amp is combined in a new NOνA custom ASIC with 8:1 multiplexers, each running at 16 MHz. The signals are digitized by quad 40 MHz ADCs using the AD41240 from CMS. The multiplexing level on this ASIC can be switched to a 2:1 mode and this effectively speeds up the Near Detector electronics by a factor of four to cope with the higher intensity environment.

The front-end electronics will operate in continuous digitization mode and will not require any external trigger or NUMI timing gate. Data will be time stamped and compared to a NUMI timing signal in the DAQ system to determine if the event was in or out of spill. Data from the ADC is sent to an FPGA where multiple correlated sampling is used to remove low frequency noise. This processing also reduces the noise level and increases the time resolution.

Additional details on the APD and front-end electronics are in Chapter 14.

5.5.7 Data Acquisition System

The Data Acquisition System (DAQ) for NOνA is based on a standard Gigabit Ethernet network and commercial processor. The 14,000 front-end boards are connected in groups of 64 to 194 custom Data Concentrator board which then interfaces to the Ethernet network. The Ethernet network passes the data to a processing farm consisting of about 136 commercial PCs.

The NOνA front end electronics operates in un-triggered mode with data continuously being digitized, time-stamped, pedestal subtracted, and zero-suppressed. There is no spill trigger required at the front-end. The data must be buffered awaiting arrival of a spill trigger message. A spill signal is required to arrive within the buffering time so that the spill time can be correlated with the time-stamped data to determine if the hits occurred in or out of spill. There is no additional selection of in-spill data. All hits that occur in a 30 μs window centered on the 11 μs NuMI spill are recorded for further processing.

Randomly selected data for calibration and monitoring will be collected off-spill at a rate that is approximately 100 times higher than the in-spill rate. The overall data rate is driven by cosmic ray muons with approximately 200 hits per muon.

Chapter 15 contains details of the DAQ.

5.6 Assembly of NOνA Detectors

There are three NOνA detectors in the NOνA project: the Far Detector at Ash River, the Near Detector at Fermilab, and an Integration Prototype Near Detector (IPND) at Fermilab. The relative sizes of these detectors are illustrated in Figure 5.13.

All three detectors have an identical structure and are assembled in alternating layers of vertical and horizontal extrusions as shown in the inset to Figure 5.13. This layering organizes the detector into planes with 90^{o} stereo for tracking of particles produced in neutrino interactions originating in the PVC and scintillator mass. The assembled set of cells acts as a fully active or total absorption calorimeter since 70% of the mass is active liquid scintillator. Pulse height information is obtained from each cell and the total charged particle energy of a neutrino event is

formed from the sum of the pulse heights. The cellular structure makes the detector a tracking device as shown for a sample Monte Carlo generated event in Figure 5.14. This combination of calorimetry and tracking makes the NOνA detector capable of distinguishing signal neutrino events and of rejecting backgrounds to that signal as stipulated in the scientific design criteria of Chapter 4. Table 5.2 lists relevant parameters of the three detectors.

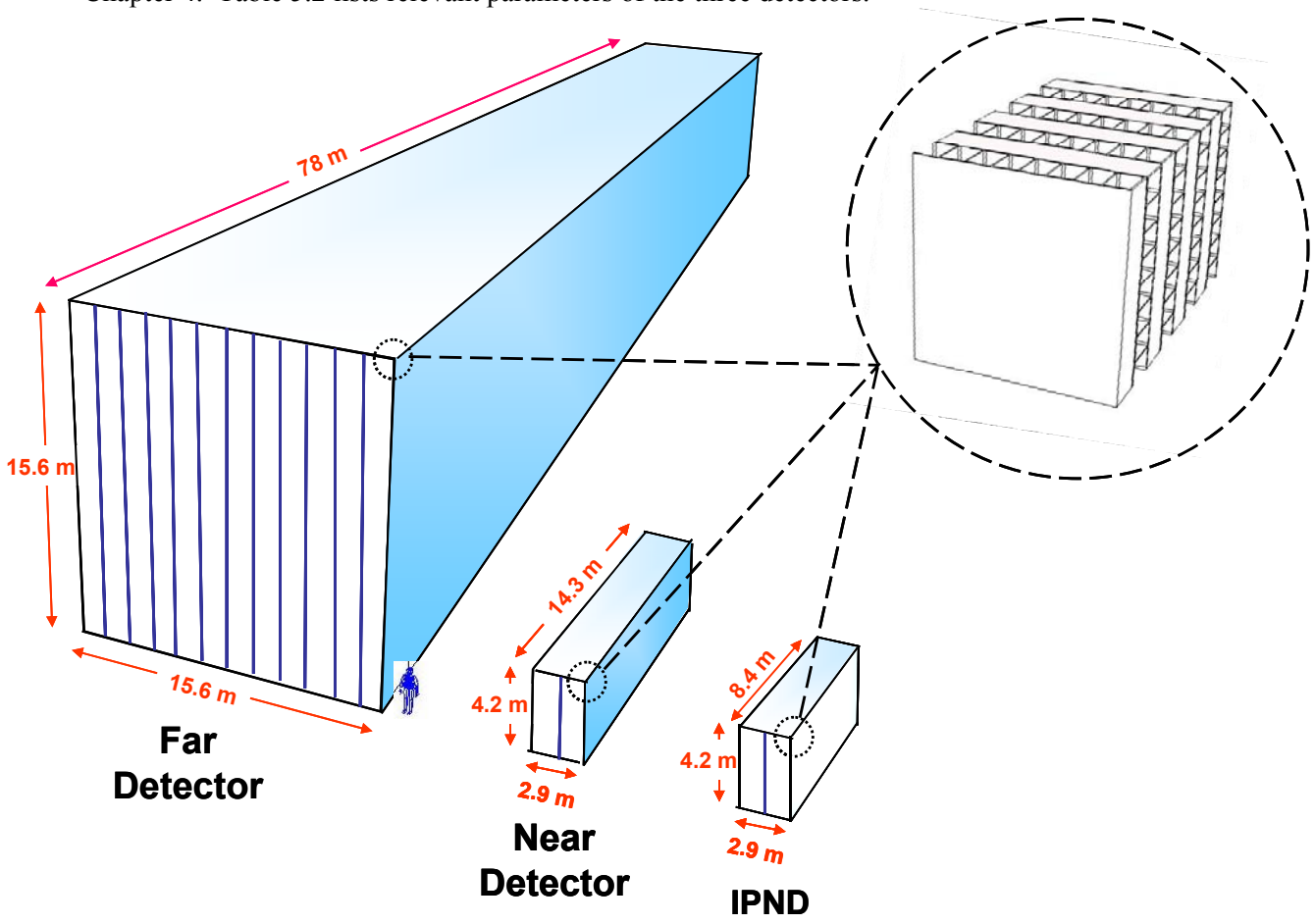

Fig. 5.13: The three NOνA detectors. The inset figure (dotted circle) shows that each detector has an identical alternating plane structure composed of vertical and horizontal cells like those shown in Figure 5.10.

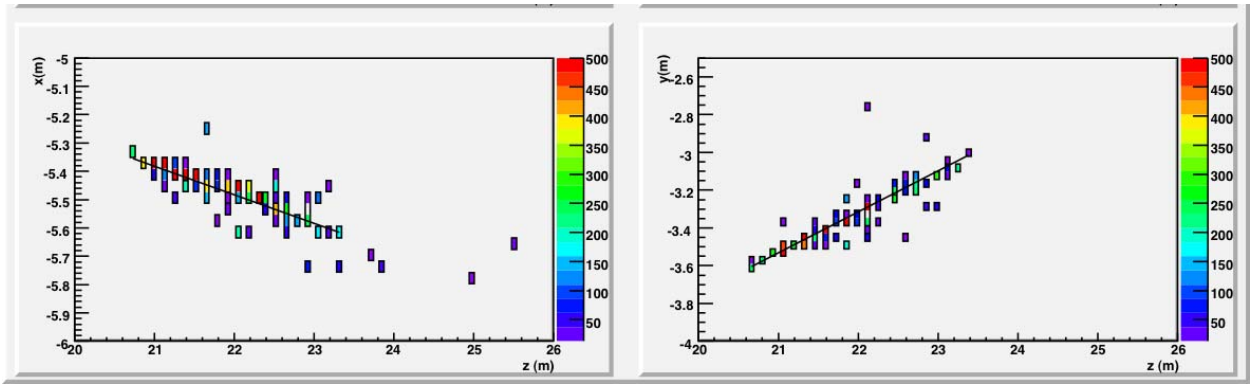

Fig 5.14: A simulated 2.2 GeV electron neutrino charged current event in the NOνA cell structure. The vertical cells are in the left diagram and the interleaved horizontal cells are in the right diagram. The color code indicates the relative pulse height in the cells.

	Integration Prototype Near Detector (IPND)	Near Detector	Far Detector
Mass (metric tons)	84 tons	222 tons	15,000 tons
Active Detector Size (width, height, length) in meters	(2.8 ,4.1, 8.4)	(2.8, 4.1, 14.3)	(15.6, 15.6, 66.9)
Liquid scintillator required (gallons)	18,700	30,000	3,210,000
Wavelength Shifting fiber required (kilometers)	75	113	13,000
Number of 32 cell extrusion modules required	310	496 (310 get re-used from the IPND)	12,036
Number of extrusion modules seen by the neutrino beam (horizontal by vertical)	3 by 2	3 by 2	12 by 12
Number of detector channels	9,892	15,904	385,152

Table 5.2: Parameters of the three NOνA detectors.

5.6.1 Integration Prototype Near Detector

An early prototype of the Near Detector will be assembled as part of the R&D effort for NOνA. This prototype is called the Integration Prototype Near Detector (IPND) and it serves as a venue to test all the parts of the NOνA detector together beginning in calendar 2008. This integration is the main goal of the IPND.

The IPND consists of planes that are 64 cells wide (2 extrusion modules) and 96 cells high (3 extrusion modules), arranged in alternating horizontal and vertical layers and in segments of 31 planes. The 31 planes within a block are attached to one another with methyl methacrylate adhesive. The IPND length is four blocks of 31 planes.

The plan is to operate the IPND in the MINOS Surface Building shown in Figure 5.8 and Figure 5.15. The MINOS Surface Building is about 107 mrad off-axis to the NuMI beam and at this location a neutrino beam composed of 85 - 90% ν_μ of energy ~ 2 GeV and 10 - 15% ν_e of energy ~ 1.3 GeV is available for studies with the prototype. The neutrino event rates per year for the MINOS surface building are shown in Figure 5.16 for Low Energy beam (see Chapter 2, Figure 2.1). The IPND has a fiducial mass of about 10 tons and the NuMI beam is expected to deliver about 3 x 10^{20} protons in a year during 2008 and 2009. About 2840 muon neutrino charged current events per year are expected in the energy range 1.6 – 2.4 GeV [12]. About 170 electron neutrino charged current events per year are expected in the energy range 0.5 – 2.0 GeV. In addition about 1100 neutral current events per year are expected in the energy range 1.6 – 2.4

GeV. The IPND is of adequate length to contain 1.3 GeV electron neutrino events, but the 2 GeV muons will exit the back of the detector, allowing only a tag that they were muon events and not electron events. While these samples are small, they should prove instructive to the NOνA simulation efforts.

Since the prototype detector is on the surface, the location also allows us to measure the unshielded cosmic ray backgrounds in the detector.

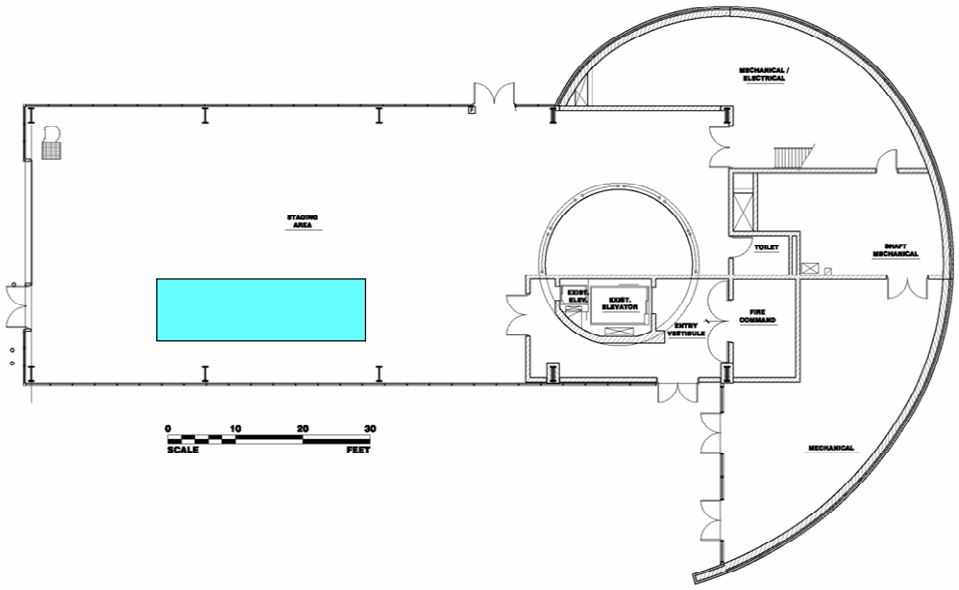

Fig. 5.15: Plan view of the NOνA IPND in the MINOS Surface Building.

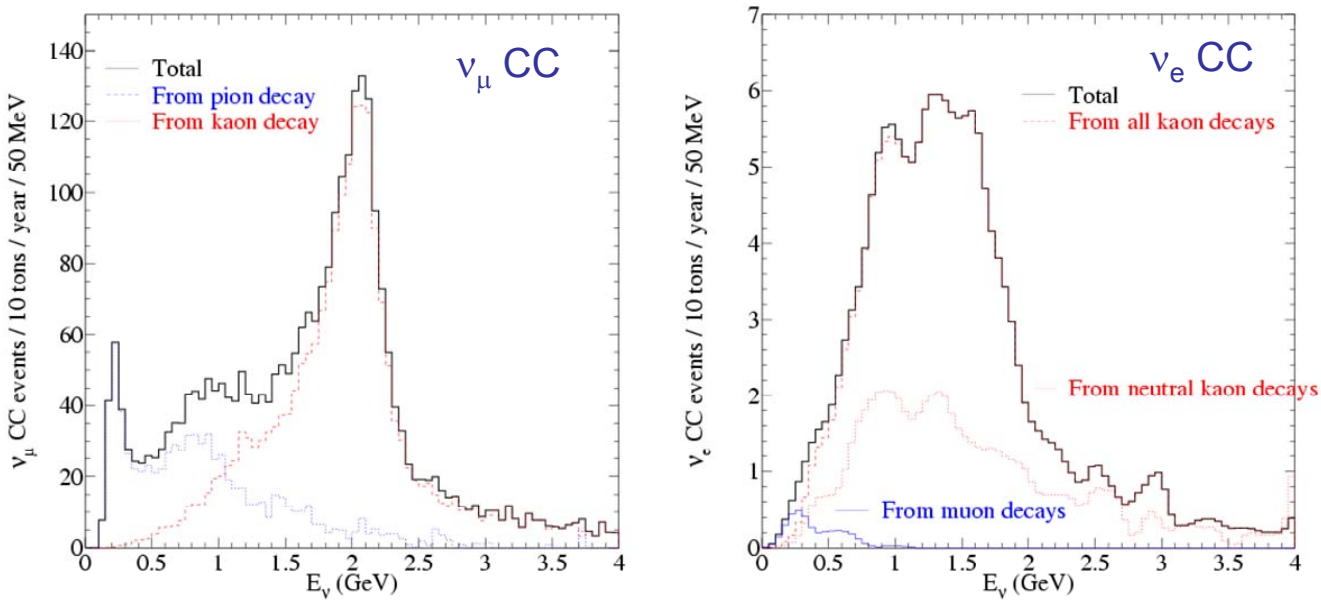

Fig. 5.16: ν_μ charged current (left) and ν_e charged current (right) event rates per year in the IPND at the MINOS surface building with the NuMI beam in Low Energy mode.

5.6.2 Near Detector

The Near Detector is an identical copy of the Far Detector except that the extrusion modules are shorter to accommodate the restrictions of the NuMI underground tunnel and MINOS access shaft described in Section 5.3. A diagram of the Near Detector is shown in Figure 5.17. The detector consists of planes that are 64 cells wide (2 extrusion modules) and 96 cells high (3 extrusion modules), arranged in alternating horizontal and vertical layers and in segments of 31 planes. There are 6 blocks of 31 planes and an additional set of ten planes interspersed with planes of steel to tag muons from ν_μ charged current events. Additional details are in Chapter 16.

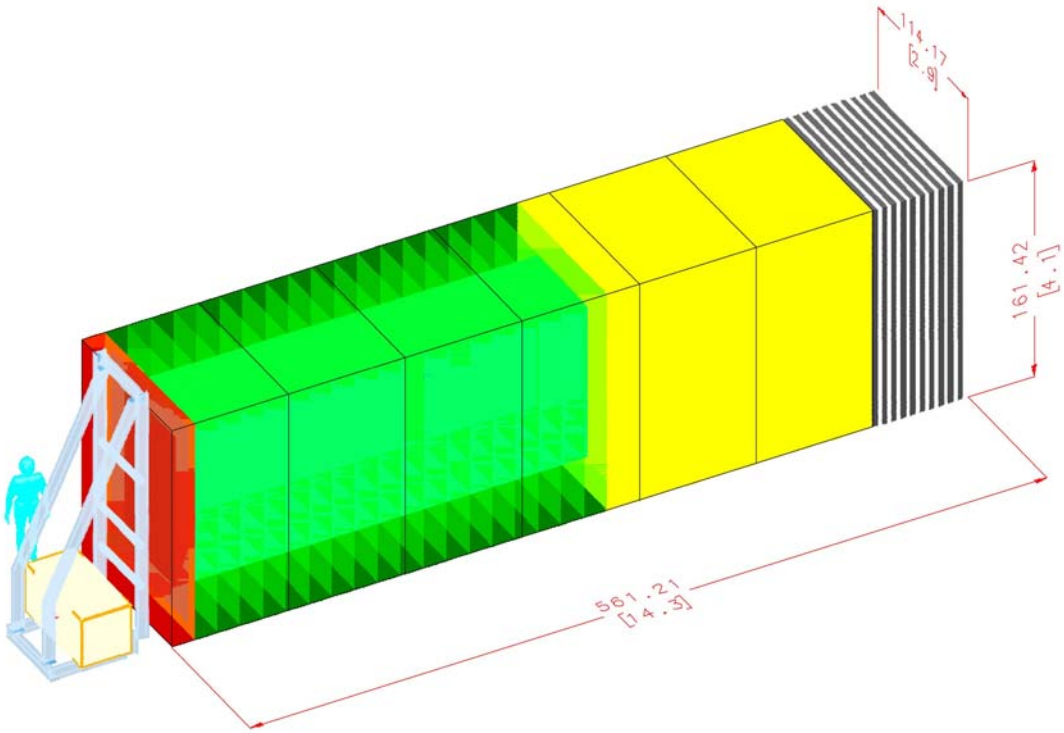

Fig. 5.17: The NOνA Near Detector constructed from 6 blocks of 31 planes plus a muon catcher. The beam comes from the lower left in this diagram. The upstream 6 planes form a veto region (red). The next 108 planes are the fiducial region (green) with transverse containment indicated. The fiducial volume is followed by a 72 plane shower containment region (yellow). All parts of these three sections are fully active liquid scintillator cells identical to the Far Detector and the colored areas just represent a logical assignment. Downstream of this active region is a 1.7 meter long muon catcher region of steel interspersed with 10 active planes of liquid scintillator (black and white).

5.6.3 Far Detector.

Twelve of the extrusion modules get placed side by side on a flat assembly table to form one plane of the NOνA detector. Thirty-one such planes are bonded together with methyl methacrylate adhesive (MMA) into a block to form the strong honeycomb-like structure shown in Figure 5.13. 120 metric tons of MMA are required for the full 15 kt detector, and this places requirements on the building ventilation system due to an OSHA 100 ppm limit (ACGIH TLV 50

ppm limit) [13] for MMA vapors in workspaces. MMA has been selected as the adhesive because it has the largest shear and peel strength of all the adhesives tested to date, and high strength is required for this five story tall PVC object.

A custom vacuum lifting fixture will be used to move the modules from incoming truck pallets to a custom glue machine for the MMA application and then onto the flat assembly table. The 31 plane blocks are constructed so that vertical planes of extrusion modules all have their readout fiber manifolds at the top of the detector. Horizontal planes of extrusions have all readouts on the west side (left of the beam) of the detector.

Each 31 plane block is 15.65 meters wide by 15.65 meters high by 2.05 meters thick. The PVC in a 31 plane block has a mass of about 139 metric tons. When filled with scintillator, the mass of a 31-plane block is about 460 metric tons. The empty 31-plane block is assembled in a horizontal position, moved down the Far Detector Hall to the previously constructed blocks, and then rotated 90 degrees into a standing position using the custom block pivoter machine illustrated in Figure 5.19.

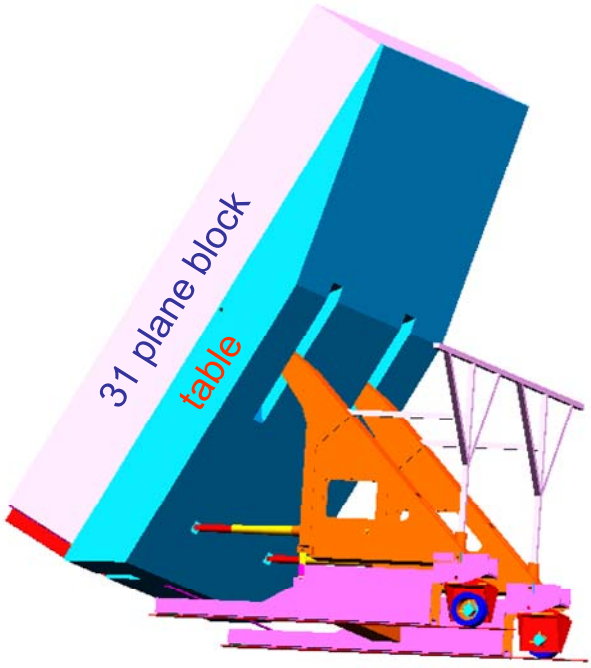

Fig. 5.19: The custom NOνA block pivoter. The table starts as a horizontal assembly table and is then used to tilt a 31-plane block into the vertical position.

Five of the 31-plane blocks get attached to one another to form a detector "Superblock". The 31 plane blocks are nominally touching, but we assume we might leave a gap as large as 2 – 3 mm (~100 mils) on parts of the adjacent surfaces. Between Superblocks we deliberately leave a larger gap of 2 cemtimeters, chosen to be a large enough gap that we can verify it from the outside of the structure. This 2 cm gap is made explicit at the top of the blocks via a 2 cm spacer. This gap serves as an expansion joint (like those in a concrete sidewalk) so that when the Superblock is filled with scintillator the stress in the PVC will be limited. The Superblock swells when filled as shown in Figure 5.20 with its largest thickness about 1 meter off the floor. If all the Superblocks touched, then filling the blocks would drive the PVC stresses to unacceptably high levels. The expansion gaps are designed to limit the stress build-up and therefore limit the PVC creep discussed in section 5.5.4.

A total of 6 Superblocks plus one smaller set of 3 blocks comprise the full 1003 planes in the NOνA Far Detector. The detector is built from south to north, starting against a strong bookend at the south end of the building. When all 33 blocks are in place, the block pivoter is braced to form a north bookend as shown in Figure 5.21.

The large NOνA PVC structure is unique and we have spent considerable time understanding the properties of rigid PVC and the properties of our structure. Calculations have been done via finite element analyses and confirmed with calculations and tests of small models. These details are presented in Chapter 17.

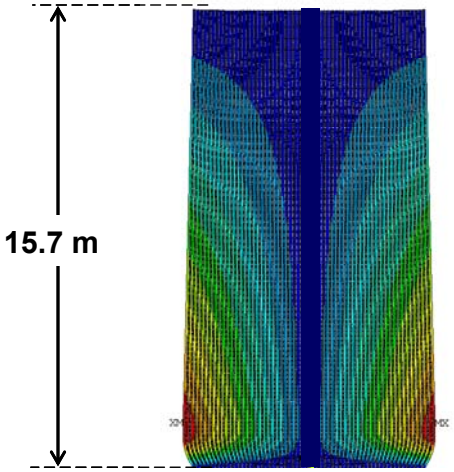

Fig 5.20: A NOνA Superblock of 155 planes showing the swelling that occurs near the bottom of the block when all the extrusions are filled with scintillator. The horizontal scale is exaggerated with the maximum (red) areas representing a horizontal increase of order 20 mm out of 10 meters.

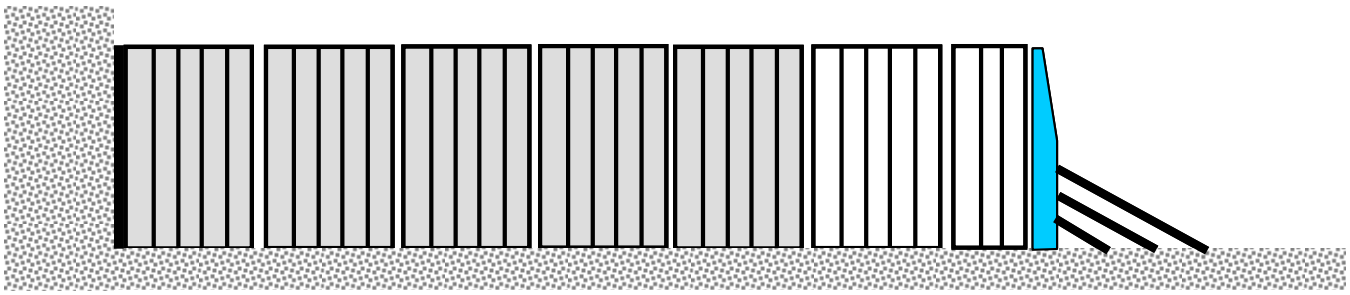

Fig 5.21: The full NOνA Far Detector composed of 6 Superblocks and a 3 block section. Expansion gaps are shown between the Superblocks. The detector is built from left to right starting against a strong bookend and assembly ends with the conversion of the block pivoter into another bookend at the right end. This figure shows 5 of the superblocks full of scintillator with 2 blocks yet to be filled.

Filling the blocks with liquid scintillator is a separate assembly operation and takes place after the blocks are attached to the full detector. To avoid a long serial schedule for completion of the detector, we fill the structure with scintillator almost in parallel with the PVC plane erection, following the empty PVC module assembly front by one Superblock (5 blocks) in a total 24 month schedule. The required scintillator fill rate of about 18 gallons per minute is accomplished with a custom metering machine which fills eight extrusion modules in parallel.

Outfitting of the detector with electronics follows the filling task with about a one month delay per block. Therefore the Far Detector becomes active linearly throughout the ~ 24 month assembly period.

5.7 Summary of Design Changes since the Conceptual Design Reports

The NOνA detector project and the Accelerator & NuMI upgrade project required for NOνA were merged into a single project with common contingency. Prior to January 2007 these were separate projects. In January the project also received target guidance from DOE for a TPC of $ 260 M. Most of the changes to NOνA since the two CDRs stem from value engineering studies done to keep the cost of the project within this cost envelope while preserving the scientific goals. This section outlines these changes so that the reader can compare the TDR to the CDRs.

5.7.1 Major Changes

The NOνA detector mass was reduced from 25kt to 15 kt. The loss of detected neutrino events was partially compensated by changing the planned five year data run of the detector to six years. Continuing work on the algorithms for neutrino event reconstruction also resulted in an increased detection efficiency of 26% compared to 24% in the CDR. This also partially compensated the reduced mass.

The small service buildings for the Accelerator & NuMI upgrade part of the project were removed from the project scope. These buildings are needed for the Fermilab program even if NOνA is not constructed. Similarly the number of kicker systems for NOνA was reduced from five to four by removing one kicker from the project scope. This kicker is required for gap clearing in the Main Injector during Collider and MINOS running and is needed even if NOνA is not constructed.

5.7.2 Accelerator and NuMI Upgrades

- The injection line design was changed to simplify installation and to minimize the number of powered elements near the Recycler Ring. The main design change in the extraction line was to move the injection point in the Main Injector. This allows use the same ceramic beam tube and magnet for this kicker as those planned for the Recycler extraction and abort kickers, thus eliminating a separate design for both the ceramic beam tube and the magnet.
- The design was changed to accept 81 Booster bunches per Booster batch instead of 82. This change loosens the kicker rise/fall time specifications from 38 nsec to 57 nsec with ~1% loss of protons to the NuMI target. Corresponding losses elsewhere in the accelerator complex have been studied and can be controlled.
- The kicker designs were further optimized and flattop bumper systems were removed.
- A simpler replacement device for the hole left after moving Horn 2 was devised.

5.7.3 Site and Buildings

- A larger site at Ash River has been stipulated for spoils piles during construction.
- The Far Detector Hall has been reduced to hold a maximum 18 kt detector instead of 30 kt.
- The loading dock in the Far Detector Hall was reduced by one 24 foot long bay.
- The orientation of the Far Detector hall was flipped (north / south ends interchanged) to keep liquid scintillator deliveries further away from the Ash River. This allows detector construction to proceed from south (Fermilab end) to north and simplifies commissioning of the detector.

- The Far Detector Hall roof design was changed from steel trusses supporting a granite spoils overburden to pre-tensioned concrete planks.
- The shielding overburden on the Far Detector Hall was enhanced with 6 inches of barite to reduce the number of electromagnetic cosmics entering the detector unseen.
- The side berm shielding on the north end of the building was removed when Monte Carlo studied indicated that the shield was only needed for events appearing to come from within 45 degrees of Fermilab. The NOνA reconstruction software can distinguish the incoming direction of events outside this 45 degree cone..
- A ventilation system for MMA vapors was added to the Far Detector Hall.
- The detector position within the Far Detector Hall was moved to one edge (east) of the building to reduce number of catwalks.
- The number of catwalks was further reduced by having each catwalk access three horizontal layers instead of just two layers.
- The Far Detector Hall loading dock level was changed to match the top catwalk level, providing ease in construction as most cable tray, cable, racks, power supplies and other infrastructure items are brought to the top of the detector from the loading dock.

5.7.4 Scintillator

- The scintillator quantity was reduced to the amount needed for 15 kt.
- The fluor (pseudocumene and waveshifters) content in the scintillator was reduced while preserving enough light to meet the scientific performance requirements.
- Scintillator blending will now take place at toll blender in the Chicago area instead of at a blending facility constructed on the Fermilab site. This allows larger batch sizes and a reduction in cost.

5.7.5 Fiber

- The fiber quantity was reduced to the amount needed for 15 kt.
- The fiber diameter was reduced from 0.8 mm to 0.7 mm to reduce cost and to reduce risk from the bending radius of the fiber at the end of each cell.

5.7.6 PVC Extrusions

- The PVC quantity was reduced to the amount needed for 15 kt.
- The reflective component of the PVC resin was changed from Rutile TiO_2 to Anatase TiO_2 to increase the reflectivity of the PVC extrusion cell walls. This increased the light collected by each cell by 15%.
- The 32 cell extrusions are now made by gluing two 16 cell objects side by side instead of having a single 32 cell object from a single expensive extrusion die.
- The extruder vendor now also serves as a buffer for output of extrusions before shipping to the Extrusion Module factory. This removes risk in the tightly coupled pipeline of PVC extrusions from extruder to factory to Ash River.

5.7.7 Extrusion Modules

- The number of module factories has been reduced from three to one. This allows a single set of factory tools to perform the entire job and avoids complicated shipping schemes from three factories to the Ash River site. Instead the one factory now has a warehouse space to buffer the output of the factory.

5.7.8 Electronics and DAQ

- The APD quantity was reduced to the amount needed for 15 kt.
- The multiplexing level for the Near Detector electronics was changed from 8:1 to 2:1 to effectively speed up the readout by a factor of four. This allows better Near Detector performance in the higher event occupancy environment at Near Detector site.

5.7.9 Near Detector Site and Assembly

- The Integration Prototype Near Detector (IPND) is now shortened to four blocks instead of six.
- However, all four blocks of the IPND are now re-used in the final Near Detector instead of three out of six.
- The Near Detector has been rotated to the proper off-axis angle in a new cavern off the MINOS access tunnel. This now satisfies a new scientific performance requirement which was developed after Monte Carlo studies of the Near Detector orientation. This also removes risk of compromising the secondary containment if the NOνA detector were sitting in a passageway used by others as in the CDR.

5.7.10 Far Detector

- The assembly adhesive has been changed to a Methyl Methacrylate adhesive for the PVC planes to increase the safety factor of the construct. This added cost since it put a more severe requirement on the Far Detector Hall ventilation system.
- The Block raiser is now a block Pivoter. Completed 31-plane blocks are rotated about a point near the center of mass of the table + empty block instead of being lifted from the floor.
- All the horizontal modules are now read out on the west side of the detector instead of interleaving alternating east and west readout in successive planes. This reduced the performance of the detector slightly, but allowed cost savings from the reduced number of catwalks required for detector access.
- The cosmic shield wall on the north end of the detector has been removed following Monte Carlo studies which show that cosmic ray induced events from the north cannot be mistaken for events originating from a neutrino beam from Fermilab (from the south).

5.8 Value Engineering Continues

The list of changes in Section 5.7 is the result of a continuous value engineering process done since the Conceptual Design Report. This value engineering will continue as we complete the final designs and test those designs with prototype structures and in the Integration Prototype Near Detector.

5.9 Chapter 5 References

[1] M. Marshak, principal investigator, Proposal for Collaborative Research and Development in Neutrino Physics submitted to the DOE, November 27, 2006.
[2] NOνA Project Management Plan, NOVA-doc-129. See Appendix A of this TDR.
[3] draft Storm Water Pollution Prevention Plan (SWPPP), NOVA-doc-1324.
[4] draft NOνA Environmental Assessment, NOVA-doc-2672 and NOVA-doc-1354.
[5] NOνA Environmental Assessment Worksheet, NOVA-doc-205.

[6] Steve Dixon, American Engineering Testing, Inc Report of Subsurface Boring and Piezometer Installation, NOvA Off-Axis Site, NOvA docdb note 162, November, 2005. See also NOvA docdb note 108, Preliminary Ash River Boring Logs, October, 2005.
[7] Some examples are: M. Ambrosio et al., the MACRO detector at Gran Sasso, NIM A 486 (2002) 663-707, D. Harris et al., Precision calibration of the NuTeV calorimeter, NIM A447 (2000) 373-415, L. Ahrens et al., A Massive, Fine-grained Detector for the Elastic Reaction Induced by Neutrinos in the GeV Energy Region (BNL-734), NIM A254 (1987) 515-528.
[8] M. Strait and D. Cronin-Hennessy, COSMOS ECAL 12 Year Aging Study, NOVA-doc-1957
[9] MINOS Technical Design Report, Fermilab, NuMI-L-337 (1998)
[10]K. Deiters et al., NIM A461 (2001) 574-576, NIM A453 (2000) 223-226, and NIM A442 (2000) 193-197.
[11] M. Maolinbay et al., NIM A485 (2002) 661-675, and T. Zimmerman, Fermilab Technical Note FERMILAB-TM-2063 (1998).
[12] M. Messier, NuMI Surface Building and Near Detector Fluxes, NOVA-doc-931.
[13] OSHA (Occupational Safety and Health Administration) and ACGIH (American Council of Governmental Industrial Hygienists) limits quoted in the Devcon Plastic Welder MSDS (Material Data Safety Sheet).

6 Performance of the NOνA Design

6.1 A Visual Overview of the NOνA Detector Performance

About one-third of the neutrino interactions at NOνA's 2 GeV neutrino beam energy are quasi-elastic, with just a nucleon and a lepton in the final state. A second third of 2 GeV neutrino interactions are resonant processes in which a Δ resonance is created which then decays to a proton + pion, or a neutron + pion. The final third of neutrino interactions at 2 GeV are deep inelastic scattering events where multiple pions are produced. Figure 6.1 illustrates this mix of the neutrino interaction as a function of the neutrino energy, based on a compilation from G. Zeller [1].

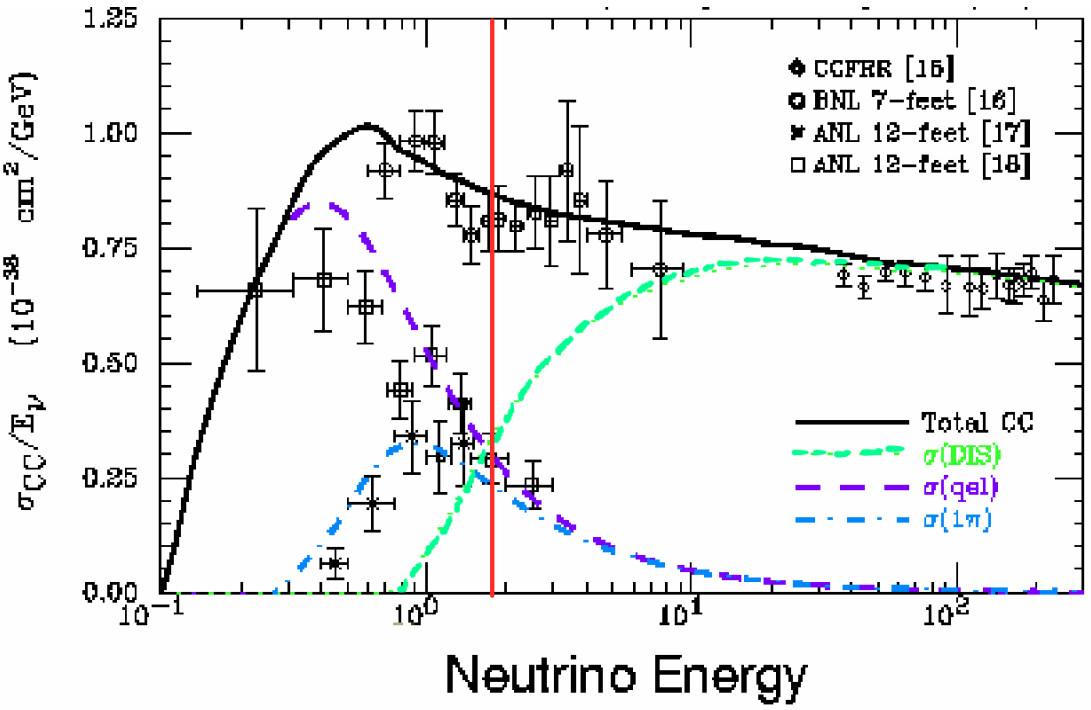

Fig. 6.1: A compilation of low energy charged current neutrino cross sections. The red line indicates the peak energy of NOνA events.

Some selected simulated NOνA events are shown in Figures 6.2 through 6.6 to illustrate properties of the detector. Figure 6.1 shows a simulated quasi-elastic ν_e charged current event and Figure 6.2 shows a simulated quasi-elastic ν_μ charged current event. Contrasting these two figures illustrates the NOνA detector's ability to distinguish electrons from muons. Electrons (Figure 6.2) tend to deposit more energy per plane and are more "fuzzy" in the transverse direction to the electron track, having more hits per plane of the detector. Muons (Figure 6.3) tend to leave much longer tracks than electrons, with typically a sharper transverse profile of one hit per plane. Figures 6.2 and 6.3 also illustrate the response of the NOνA detector to protons of energy 1 GeV or less. The protons do not travel far and deposit a large amount of energy in a short distance, typically ending with a large spike of deposited energy as highlighted in the inset of Figure 6.3.

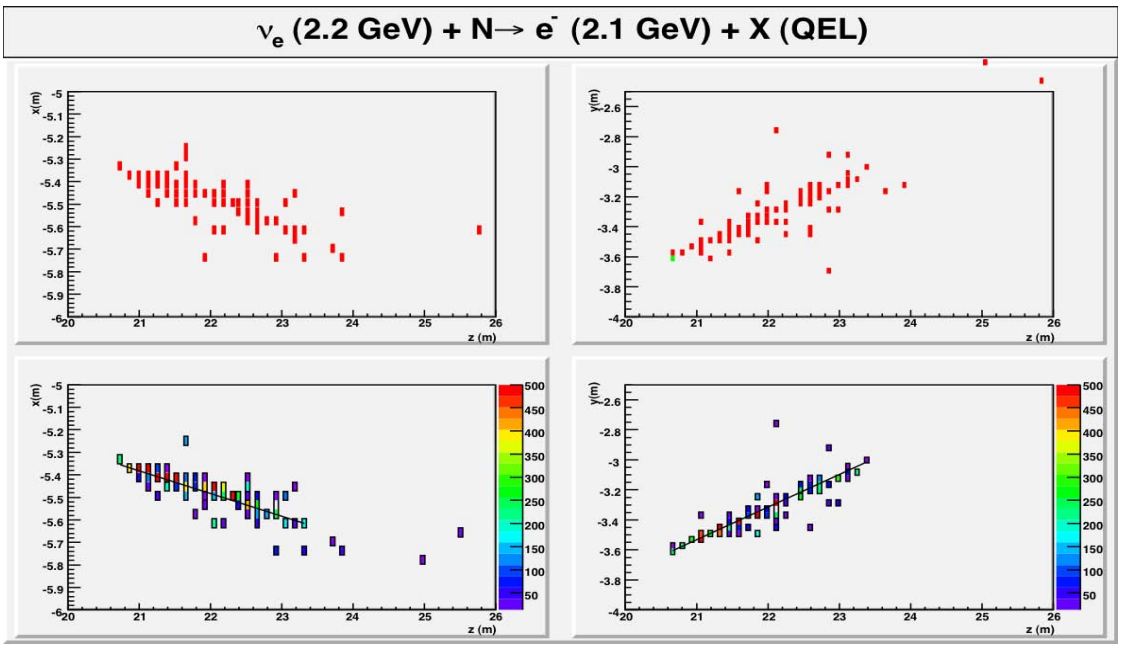

Fig. 6.2: A 2.2 GeV ν_e quasi elastic charged current event, ν_e A → p e^-. The top plots indicate the energy depositions in scintillator in the x-z (*left*) and y-z (*right*) views, color-coded by secondary particle: red for $e^{\pm}$ and γ, and a single green deposition from the recoil proton in the y-z view. The bottom plots show event as reconstructed, with pulseheight (ADC, ~5 counts/PE) indicated the color scale. The black lines indicate the reconstructed track in the two views.

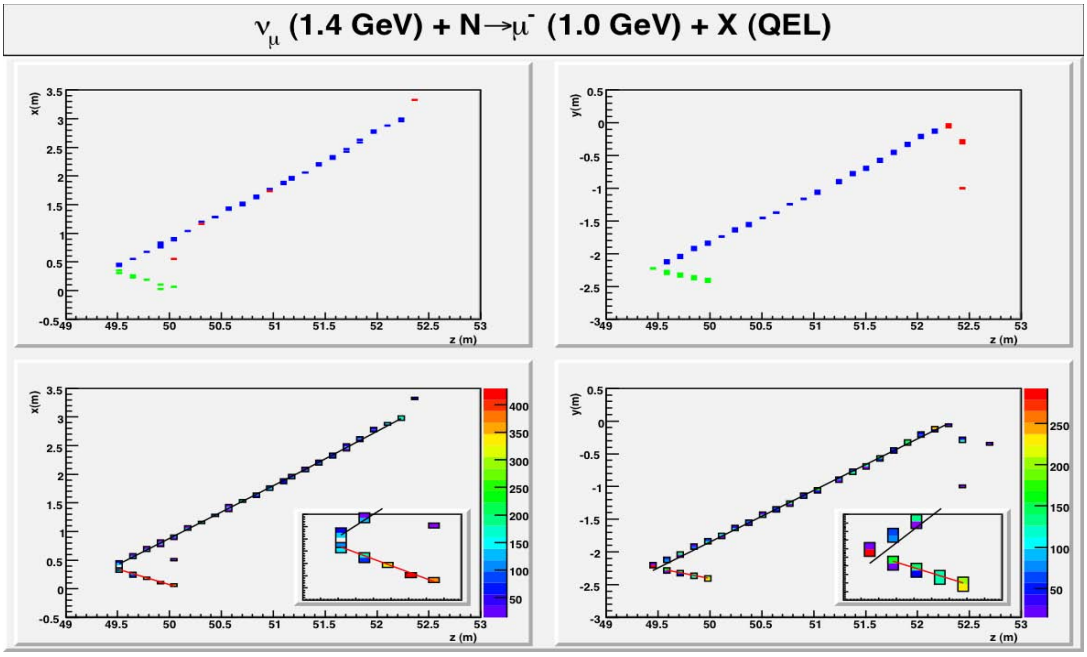

Fig. 6.3: A 1.4 GeV ν_μ quasi elastic charged current event, ν_μ A → p μ^-. The top plots indicate the energy depositions in scintillator in the x-z (*left*) and y-z (*right*) views, color-coded by secondary particle: red for $e^{\pm}$ and γ, blue for the muon, and green for the recoil proton. The bottom plots show event as reconstructed, with the color of the boxes indicated pulseheight in photoelectrons. The black and red lines indicate the reconstructed tracks. The inset is a close-up of the vertex, showing the higher pulseheight typical of hits on a proton track.

Figure 6.4 shows a resonant or single pion charged ν_e current event in NOνA. The typical pion has a low energy, but can be seen in the detector as a third track. Figure 6.5 shows a deep inelastic scattering ν_e charged current event in NOνA with several pions in addition to the outgoing electron. Such multiple pion events are harder to recognize as the 2 GeV of event energy gets divided into more and more parts, but the fuzzy electron can still be identified in many such events.

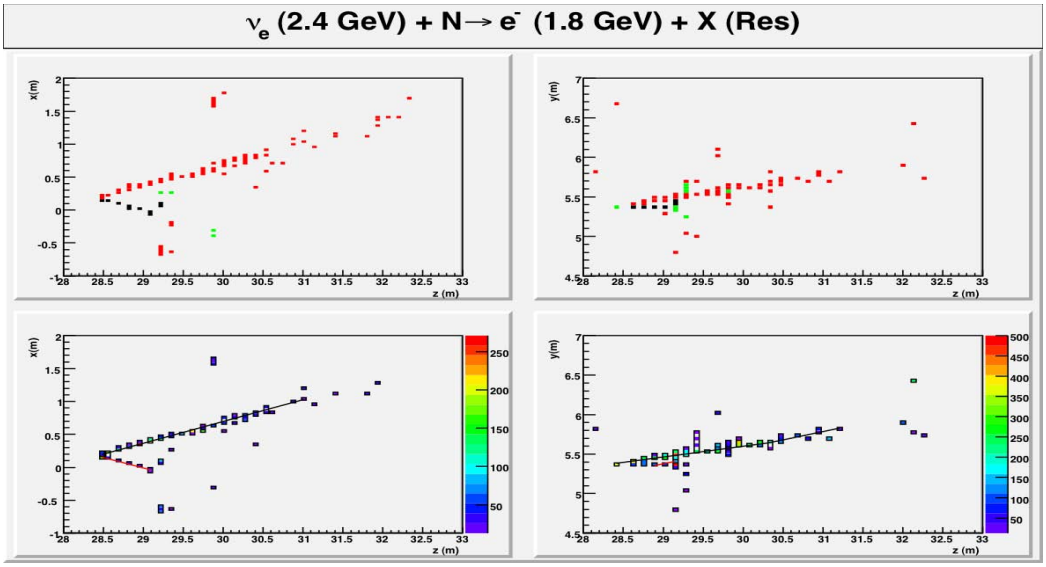

Fig. 6.4: A 2.4 GeV ν_e single pion charged current event, ν_e A → Δ^{++} (p π^+) e^-. The top plots indicate the energy depositions in scintillator in the x-z (*left*) and y-z (*right*) views, color-coded by secondary particle: black for p and π from the Δ^{++} decay, red for $e^{\pm}$ and γ, blue for the muon, and green for tertiary protons. The bottom plots show event as reconstructed, with the color scale indicating pulseheight. The black and red lines indicate the reconstructed tracks.

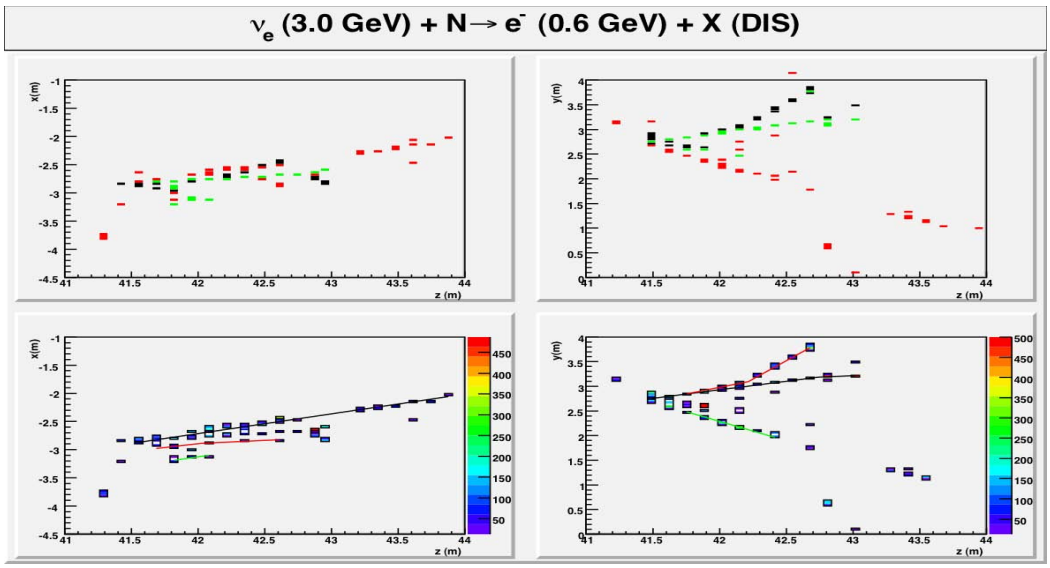

Fig. 6.5: A 3 GeV ν_e deep inelastic scattering charged current event, ν_e A → p e^- π^+ $\pi^-\pi^+$. The top plots indicate the energy depositions in scintillator in the x-z (*left*) and y-z (*right*) views, color-coded by secondary particle: black π, green for protons, red for $e^{\pm}$ and γ, blue for the muon. The bottom plots show event as reconstructed, with the color scale indicating pulseheight. The black, green, and red lines indicate the reconstructed tracks.

Neutral current (NC) events with a π^0 and the resulting electromagnetic showers in the final state are one of the largest sources of background for the NOνA experiment Typically, a higher energy neutrino interacts with the nucleus, and the outgoing neutrino takes good fraction of the incoming energy away and is unseen by the detector. The majority of such events are rejected by the identification in at least one view of separate electromagnetic showers from the two photons, and by the gap between the vertex and the first conversion of a π^0 decay photon. Figure 6.6 illustrates the exception for a 12.3 GeV NC event, where the reconstruction fails to resolve the two photons due to the overlap of the photons in one view and the short length of one of them in the other view. Furthermore, both photons converted close enough to the event vertex to prevent the resolution of the conversion gap.

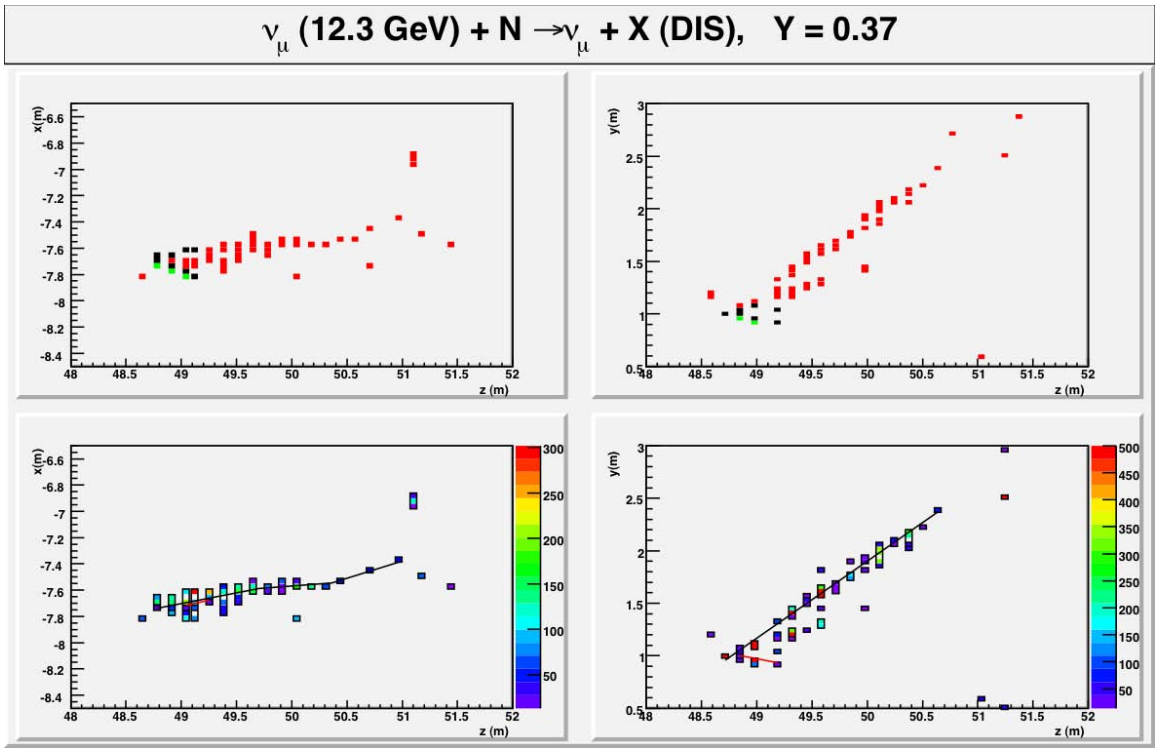

Fig. 6.6: A 12.3 GeV neutral current event, ν_μ A → ν_μ p $\pi^+\pi^-\pi^0$(1.21 GeV), π^0 → γ γ. The top plots indicate the energy depositions in scintillator in the x-z (*left*) and y-z (*right*) views, color-coded by secondary particle: black π, green for protons, and red for $e^\pm$ and γ. The bottom plots show event as reconstructed, with the color scale indicating pulseheight. The black and red lines indicate the reconstructed tracks.

6.2 NOνA Performance linked to Cell Light Output and Threshold Cut

6.2.1 Technical Requirement on the Threshold Cut.

The NOνA front-end electronics (described in Chapter 14) simply transmits all signals above a preset threshold to the data acquisition (DAQ) system (described in Chapter 15). There are two considerations with regard to the minimum allowable threshold. First, the data rate must be low enough to not overwhelm the DAQ system. Second, the noise must be sufficiently low so as to not affect the pattern recognition of the signal events.

The scale of the data to the DAQ system is set by the cosmic ray rate. We estimate the cosmic ray rate to be approximately 200 Hz with about 200 hits per per cosmic ray muon.. With 385,000 channels (for 15 kt, 12,036 modules) and 10 bytes per hit, this corresponds to a total hit rate of 40 MHz and aa data rate of about 0.5 GB/s. this is discussed in Chapter 15.

A conservative goal would be to limit the noise rate to one-third of the cosmic muon rate, or about 0.17 GB/s. The noise will be dominated by the amplifier noise, but a long tail of noise is seen due to excess noise of the APD amplification, shown in Figure 6.7. Taking the relevant time window to be 1μs, this requirement corresponds to a noise hit probability of 10^{-4}. From Figure 6.1, this gives a minimum threshold of 15 photoelectrons.

The largest events of relevance have a domain of interest approximately 2 m in width and 18 m in length. This corresponds to 15,000 cells, so a random noise probability of 10^{-4} would yield an average of 1.5 noise hits per event. This is clearly an acceptable level.

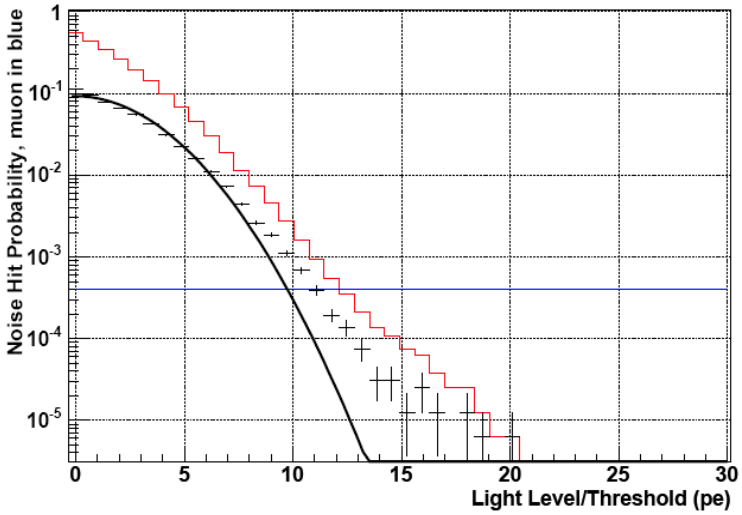

Fig 6.7: Noise hit probability versus the light threshold in photoelectrons. The top (red) histogram gives the integrated hit probability and the (blue) horizontal line is the expected hit probability from cosmic rays. The data points are shown as crosses and the best fit Gaussian, the amplifier noise, is the black line.

Figure 6.7 shows the noise hit probability for the amplifier in our test cell which had a mismatched capacitance to the APD. A new matched ASIC amplifier has been designed and produced, and that amplifier is much quieter with a noise level of ~ 150 electrons compared to the ~250 electrons RMS of the amplifier used to produce Figure 6.7. Our expectations for the threshold using the new ASIC amplifier at the same noise hit probability of 10^{-4} are a minimum threshold of 10 photoelectrons.

6.2.2 Required Light Level

Given a threshold of 10 - 15 photoelectrons, the next issue is what light level is required to give adequate pattern recognition. Our simulations do not show a strong dependence on the light output as indicated in the Table 6.1 from the NOvA CDR [1]. The table shows that if the mean signal is above the threshold by 25 to 30% there is no loss of sensitivity as measured by the figure of merit (FoM). This would indicate that for our expected noise contributions requiring a threshold of approximately 15 photoelectrons, the required mean light level is 20 photo electrons. Although we are wary of setting too low a light requirement which could compromise future efforts to improve our analysis algorithms, these simulations indicate that our scientific design criterion on the Figure of Merit (Chapter 4, Table 4.1) translates into a technical requirement for a minimum 20 photoelectrons from the far end of the cell with a photoelectron threshold set at 15.

Signal (pe)	10	15	20	25
Threshold (pe)				
10	0.95	1.00	1.02	1.00
15			1.00	
20			0.98	1.00

Table 6.1: Results of simulations showing the relative Figure of Merit for a given threshold and average light output in photoelectrons from a minimum ionizing particle transiting the far end of a NOνA cell.

6.3 Measured Performance of Multiple Cells

Our R&D efforts during 2005 - 2007 led to prototype lengths of extrusions with 15% Anatase titanium oxide loaded rigid PVC in a 16-cell wide arrangement. We have used this material to form a 4x3 array of NOνA cells of as shown in Figure 6.11. Several 33.4 meter lengths, 0.7 mm diameter, Kuraray, K27 (Y-11) fluor dye, S-type multiclad fiber have been inserted into the cells of this array. Fibers with 150, 250, and 200 ppm of K27 dye were used and these fibers were from Kuraray "Batch 1" as described in Chapter 12 The fibers in these test cells have a loop at the far end just like the NOνA design. The complete array of cells shown in Figure 6.11 were immersed in a bath filled with fully oxygenated liquid scintillator equivalent to Bicron BC-517P (see Chapter 10).

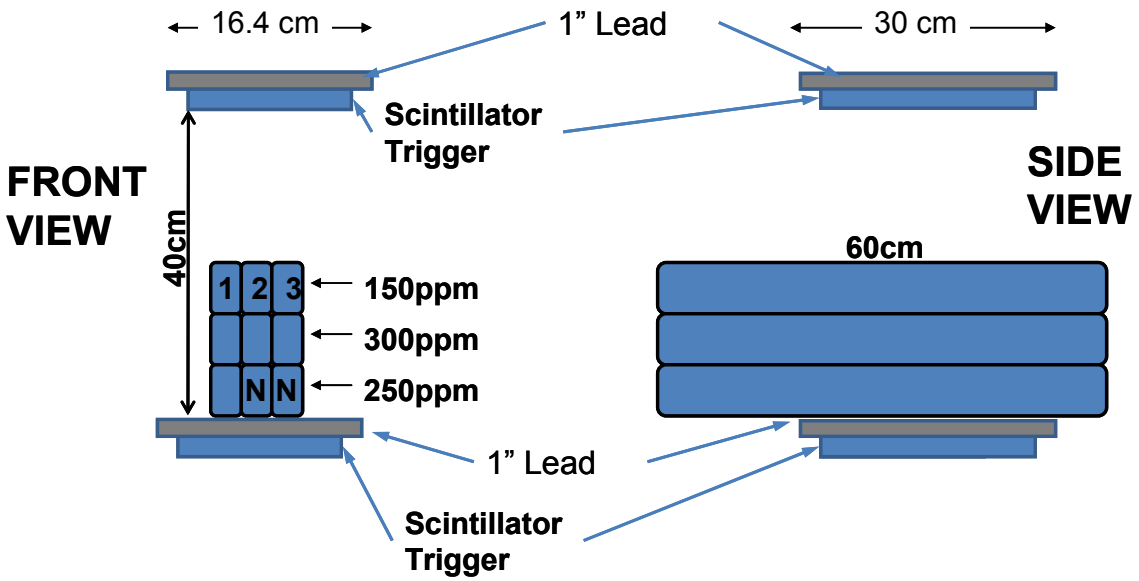

Fig. 6.11: Test cell array used to measure several cells. Ten of the twelve fibers were of Far Detector length and two ("N") were Near Detector length.

The fiber was connected to a prototype readout using a commercially available Hamamatsu APD array which has pixels of dimensions 1.6mm by 1.6mm. The APD was cooled to -15°C using a TE cooler and was operated at a gain of 100 as in the NOνA design. The APD was readout using the MASDA ASIC chip discussed in section 3.4.6 of the NOνA CDR [2]. This was

an existing version of the chip optimized for 70 picoFarad input capacitance rather than the APD's 10 pF, so the electronic noise in the system was 350 electrons.

A set of scintillator paddles were placed above and below the test cell and pulse heights were recorded from the test cell for cosmic ray muons crossing the 6.0 cm dimension of the test cell. This is the direction most tracks from neutrino events in NOνA will cross the cells. Cosmic tracks at angles to the cell were eliminated by vetoing on any events with observed pulse height in the adjacent cells.

We focus here on the cells with 300 ppm K27 concentration fiber following the optimization discussed in Chapter 12. The distribution of pulse heights observed are shown in Figure 6.12 a), b), and c) for the three 300 ppm cells.

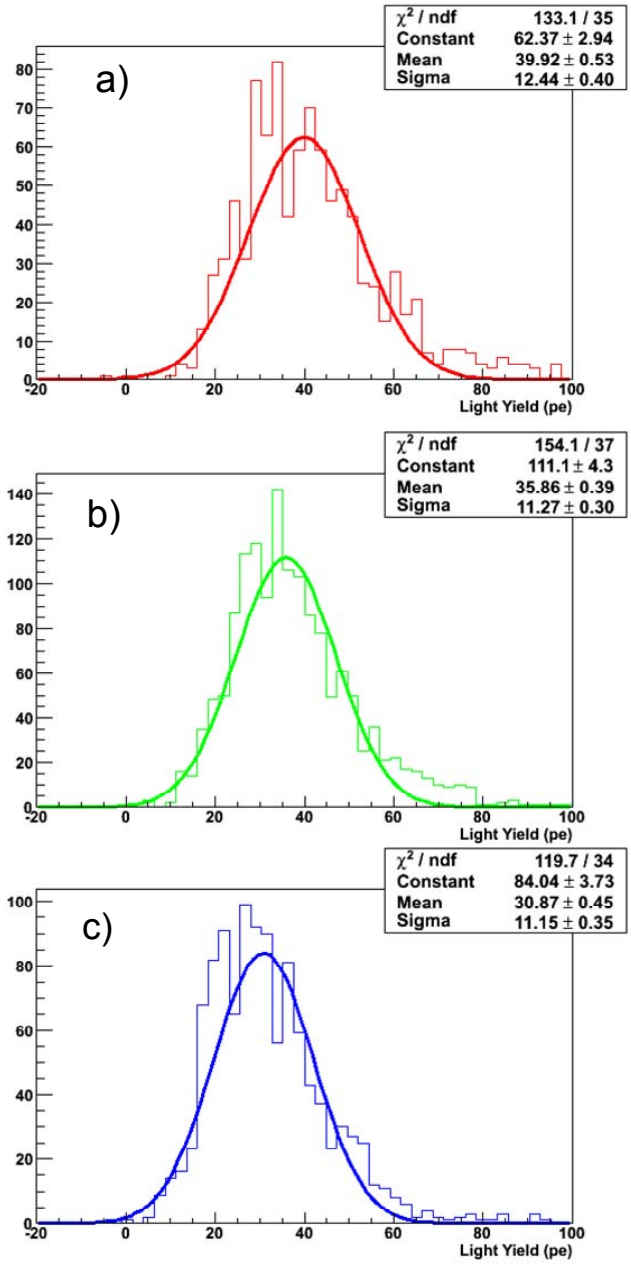

Fig. 6.12: Distribution of pulse heights in photoelectons from three NOνA cells with 300 ppm K27 0.7mm fiber and Bicron BC517P scintillator.

Figure 6.12 shows pulse height peaks in the range 31 – 40 photoelectrons. Photostatistics would imply the RMS widths in Figure 6.12 should be given by

$$\text{RMS width} = \text{Sqrt}\ [(N_{pe} * F) + (e_{RMS})^2\ ],$$

Where N_{pe} is the Mean of the distribution,
F is the excess noise factor = 2.5, and
E_{RMS} is the electronics RMS noise (~ 4 for this prototype).

So we expect widths of 10 – 11photoelectrons and see widths (sigma) of 11 – 12.5 photoelectrons.

The variation in means of the three distributions is presumably due to construction variations and that will be treated in the next section. Our conclusion from Figure 6.12 is that we have demonstrated a mean pulse height of ~ 35.5 photoelectrons from the far end of three standard NOνA cells.

6.4 NOνA Scientific Performance Requirement Translated into Design Criteria

Section 6.2 demonstrated that a minimum light level of 20 photoelectrons (p.e.) from the far end of a 15.7 m long NOνA cell is required to meet our scientific design criterion on the Figure of Merit (see Chapter 4). The test cells described in Section 6.3 indicate that our design results in ~ 35.5 p.e. from the far end of a cell, apparently meeting this criterion easily. Ideally all cells in the NOνA detectors would be identical and each would have this same performance. However, the multicell test described in Section 6.2 does not reflect the expected full range of variation since it used only one mixture of scintillator, only one run of PVC extrusions, only one small production run of fiber, and only one prototype APD. In reality we expect wider variations in these component parts that will result in a wider distribution of performance among the 385,000 separate cells.

Recognizing these construction variations, we have elected to set individual technical requirements on each component of the NOνA cell to ensure that all but a handful of cells in an event meet the 20 p.e. requirement. The individual requirements are somewhat arbitrary and are selected to allow for random variations in construction and systematic variations in the procured components. Some of these component requirements are based on cost considerations as we wish to preserve multiple vendors where possible. These criteria will be used as a starting point for additional technical design criteria developed for each component in Chapters 10 though 14.

6.4.1 Technical Design Criterion for the NOνA scintillator

We require the NOνA Scintillator to have a light output equivalent to 80% of the light observed at 1 meter in the commercially available scintillator Bicron BC517P. This criterion includes both light generation and light attenuation in the scintillator during its typical ~ 1 meter path through the scintillator before being absorbed by the fiber. The 80% criterion was arbitrarily chosen to allow a cost reduction in the fluor content of NOνA scintillator. An additional 4% (sigma) is allocated to cover our expected ability to mix the scintillator components to achieve a standard light output. This is discussed further in Chapter 10.

6.4.2 Technical Design Criterion for the NOνA Wavelength Shifting Fiber

Relative to the light seen in our tests of 0.7 mm diameter fiber with 300 ppm K27 waveshifter at 16 meters from the light source, we expect the NOνA fiber to have a random distribution with a standard deviation of 16% based on tests described in Chapter 11. Effects

from light absorption by the K27 dye, light attenuation along the fiber, and production variations in the fiber are included here. It is worth noting here that our test cells did not use the highest performance 300 ppm fiber we have obtained (see Chapter 10). The test cell fiber came from Kuraray "batch 1" which measured ~ 7% less light output than Kuraray "batch 2", but both batches had variations within the batch larger than this difference.

6.4.3 Technical Design Criterion for the NOνA PVC Extrusions

Nominally the light in the NOνA cell bounces off the PVC wall about 8 times before striking a fiber. Connecting PVC reflectivity to light output via the eighth power of the reflectivity indicates about a ± 1.5 % change in light output for the reflectivity variations of about 0.3 % observed in our PVC samples (see Chapter 11). We allow a 3% change in light output from the PVC reflectivity.

6.4.4 Technical Design Criterion for the NOνA Extrusion Modules

As discussed in Chapter 13, we do not control the fiber position inside the NOνA cells in our construction technique. At the looped end, the fiber is constrained to be in opposite corners to control the radius of curvature, but away from the loop the fiber is unconstrained. Simulations [3] indicate that there may be a loss of light if the fiber ends up against a wall or in the corners of the PVC. In studies [4] where the fibers have been forced into these reduced light positions predicted by simulations, we have been unable to measure any effect larger than about 4%. To cover these possible construction effects we assign a 5% random error to the light level due to fiber position in the cell.

6.4.5 Technical Design Criterion for the NOνA Avalanche Photodiodes and Electronics

We require the APDs to have a random variation of less than ± 5 %. This variation includes gain stability, pixel to pixel variations, and effects from alignment variations of the fibers to the pixels. This is discussed further in Chapter 14.

6.4.6 Aging Effects

We allow a 10% random degradation due to unknown aging effects in the NOνA cells. We do not expect any particular aging effects based on earlier detectors [5]ref CDR chapters where we discussed this], but are still engaged in accelerated and real time aging tests to see if any component acts on another over time.

6.4.7 Summary of Technical Design Criteria

Using the minimum requirements set in the previous six sections, our measured 35.5 photoelectron light level with BC-517P can be reduced by the one scintillator systematic effect to

(35.5 photoelectrons)*(0.8 for the scintillator minimum) = 28.4 photoelectrons

The random effects in the previous six sections are added in quadrature, resulting in an additional variation of

$$\sqrt{(0.04)^2 + (0.16)^2 + (0.03)^2 + (0.05)^2 + (0.05)^2 + (0.10)^2} = 20.6\ \%\ \text{(sigma)}$$

Our observed fluctuations in mean pulse height among the three test cells discussed in section 6.3 are consistent with this 20.6% sigma estimate.

The random effects variation of 20.6% implies the 1 sigma change in light on a 28.4 p.e. light level would be about 5.9 p.e., which is 1.4 sigma away from our desired minimum of 20 p.e. Assuming a Gaussian distribution, the area on the low side tail > 1.4 sigma below 20 p.e. would be about 8 % of the cells. Given a typical event track length of ~ 120 cells for a 2 GeV ν_μ CC event, this would mean about 5 of the 60 vertical cells in such an event would fail the 20 photoelectron requirement if the event occurred at the far bottom edge of the detector. Similarly 5 of the 60 horizontal cells would fail the 20 photoelectron requirement if the event occurred at the far east edge of the detector. This is acceptable, but we conclude that a mean light level of 28.4 photoelectrons from the far end of a NOνA cell is not excessive and instead insures the experiment against expected fluctuations in construction.

6.5 Quantitative Performance Analysis of the NOνA Far Detector

6.5.1 Simulation and Reconstruction Package

The NOνA Far Detector performance in the identification of signal and background for the $\nu_\mu \rightarrow \nu_e$ measurement has been studied using a detailed Monte Carlo simulation and reconstruction package. The simulation is a version of the highly developed GEANT-based package used by the MINOS collaboration, with appropriate changes to the detector geometry, composition, readout, and location. The reconstruction algorithm applies a Hough transform to the simulated digitizations to find track-like objects in each view. The objects are combined in the two views, and used to form a reconstructed event.

Neutrino oscillations are considered with the parameters of $\sin^2(2\theta_{13}) = 0.10$, $\sin^2(2\theta_{23}) = 1.0$, and $\Delta m_{32}^2 = 0.0024$ eV^2, without matter effects and without interference between solar and atmospheric scale transitions. The numbers of events described in this section are normalized to the expectation for a 15 kT detector with 18×10^{20} protons on target each for neutrino and anti-neutrino running.

Background events to the ν_e appearance charged current (CC) signal are divided into three classes: ν_μ CC, neutral current (NC), and intrinsic beam ν_e. Electron neutrino CC signal events have electrons that generate electromagnetic showers, while muons from ν_μ CC have clear straight track and are easily distinguished with the performance of NOνA Far Detector. Most of NC background events have more diffused patterns of hits at lower typically pulseheights, but occasionally have multiple electromagnetic showers induced from decay of π^0, and thus are a potential background to the ν_e CC signal. The intrinsic beam ν_e CC differ from the ν_e CC appearance signal only in energy spectrum, so despite their small overall contribution to the beam, they also contribute substantially to the total background.

Following a pre-selection based on total event length, total pulseheight, and the number of planes in the primary track, an Artificial Neural Network (ANN) technique is employed to discriminate ν_e CC appearance signal events from background. The ANN is trained with 19 variables characterizing reconstructed events. Generalizing from the specific examples in the preceding section, for example, the range of the primary reconstructed track shown in Figure 6.13 (a) tends to be longer for ν_μ CC and shorter for NC backgrounds than typical ν_e CC signals. Figure 6.13 (b) shows the distribution of charge/range (equivalent to dE/dx) of reconstructed tracks. The distribution for muon tracks in ν_μ CC background events is sharply peaked compared to that of the signal. The other variables utilize the number of reconstructed tracks, fraction of hits in the primary track, track profile of the primary and sub-tracks, etc. Figure 6.14 shows the discrimination of ν_e CC signal from the backgrounds in the ANN output parameter.

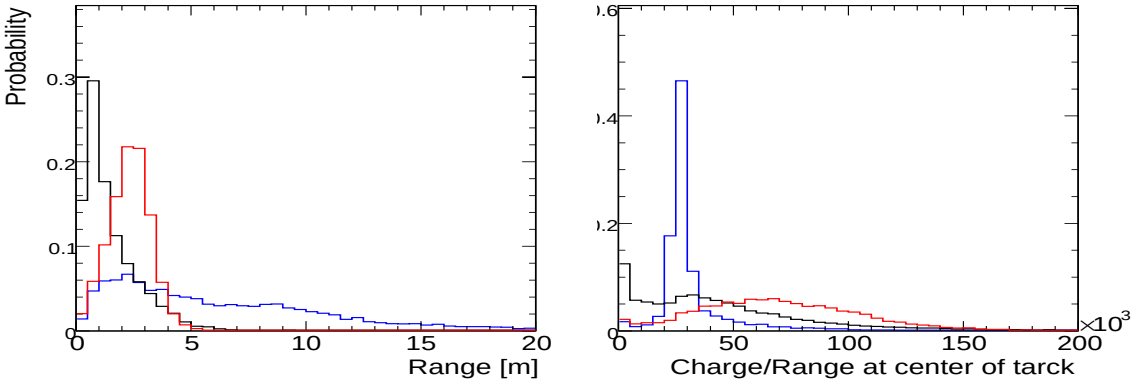

Fig. 6.13: Range (a) and charge/range (b) of reconstructed track in the NOνA Far Detector oriented parallel to the neutrino line of flight. The red histograms show the probability distribution for ν_e CC signal; blue and black histograms show ν_μ CC and NC background.

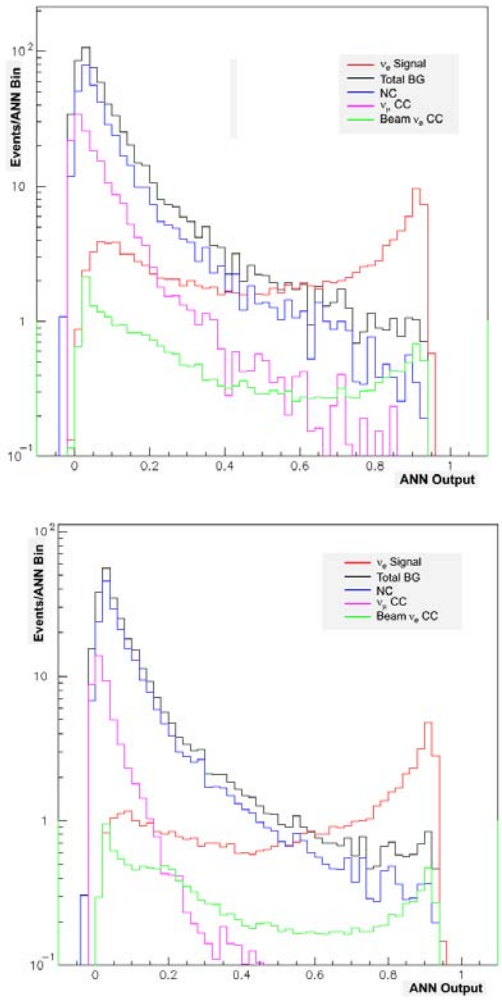

Fig. 6.14: Output parameter of ANN for ν_e CC for neutrino running (*top)* and anti-neutrino running (*bottom)*. The numbers of events are normalized to the expectations from 18 x 10^{20} protons on NuMI target with 15 kton NOνA Far Detector, assuming the oscillation parameters described in the text.

6.5.2 Figure of Merit

The Figure of Merit (FoM, see Chapter 4), defined as the number of signal events divided by the square root of the background, is calculated to evaluate the relative sensitivity of the reconstruction and selection algorithms. In the high statistics limit, a higher FoM corresponds to better sensitivity to $\sin^2(2\theta_{13})$. Figure 6.15 (6.16) shows the FoM as a function of the number of accepted signal events for neutrino (anti-neutrino) running.

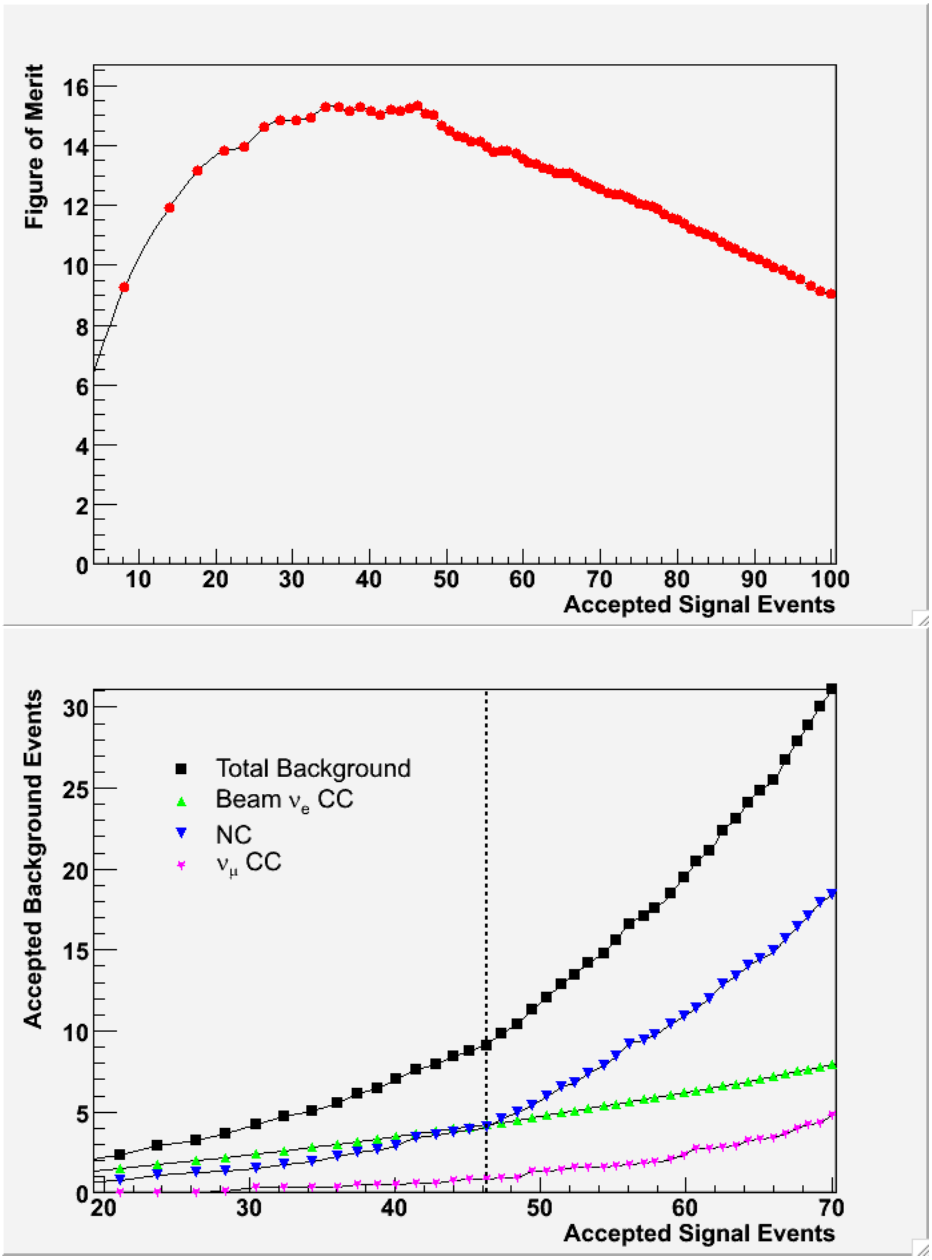

Fig. 6.15: The FoM (*top*) and the numbers of background events (*bottom*) vs. the number of accepted signal events passing the ANN selection parameter cut, in a $18\text{x}10^{20}$ POT neutrino-mode run with a 15kT detector and assuming the oscillation parameters given in the text. The dashed line in the bottom plot indicates the selection corresponding to the highest FOM. Note the different horizontal scales on the two plots.

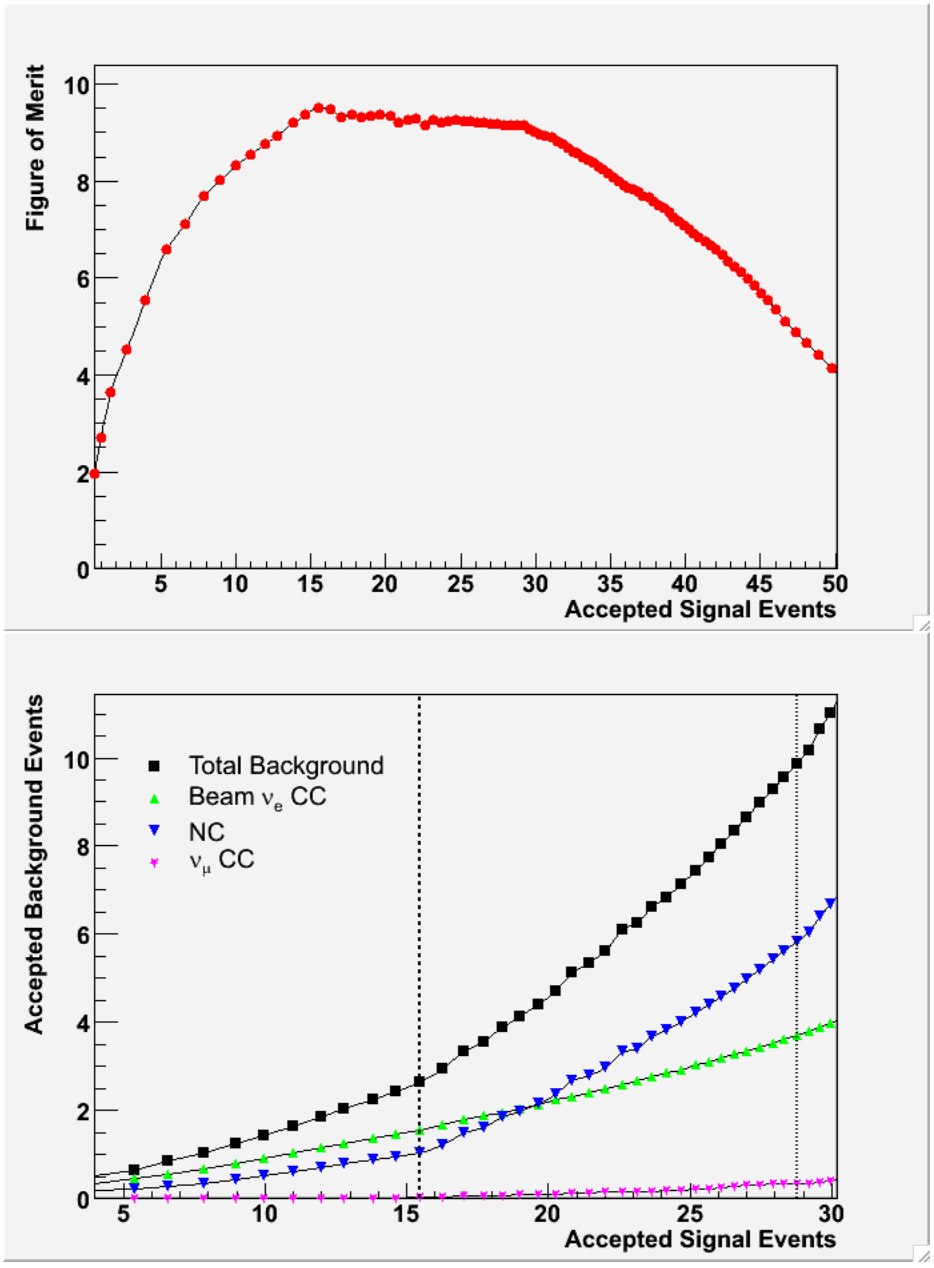

Fig. 6.16: The FoM (*top*) and the numbers of background events (*bottom*) vs. the number of accepted signal events passing the ANN selection parameter cut in 18×10^{20} POT anti-neutrino run with a 15kT detector and assuming the oscillation parameters given in the text. The dashed line in the bottom plot indicates the selection corresponding to the highest FOM; the dotted line indicates a selection with lower FOM but higher efficiency, resulting in optimal $\sin^2(2\theta_{13})$ reach. Note the different horizontal scales in the two plots.

The obtained FoM is effectively flat between 15 % and 25% (20% and 40%) signal efficiency for neutrino (anti-neutrino) running, and is almost independent on the cut value of ANN parameter in these ranges. The bottom half of Figures 6.15 and 6.16 show the number of each class of background events as a function of the accepted events. The maximum FoM obtained is 15.3 at an ANN cut value of 0.74 for neutrino running, and 9.5 at an ANN cut of 0.8 for anti-neutrino running, yielding a combined FoM of 18.0. However, due to the lower statistics of anti-neutrino running, the optimal sensitivity is achieved with higher efficiency and a reduced FoM of 9.2, corresponding to an ANN cut of 0.56. These selections yield 46.3 (28.8) ν_e and ν_e-bar CC appearance signal events. The total number of background events with the same criteria is 9.1 (9.8), as shown in Table 6.2. The number of signal events is proportional to $\sin^2(2\theta_{13})$, while the number of background events is essentially independent of $\sin^2(2\theta_{13})$. The overall efficiency for ν_e CC signal events from $\nu_\mu \rightarrow \nu_e$ oscillations is 26% (41%). The accepted fractions of signal and background are summarized in Tables 6.3 and 6.4.

	FoM	ANN Cut	ν_e signal	Total BG	ν_μ CC	NC	ν_e beam
Neutrino	15.3	0.74	46.3	9.1	0.8	4.1	4.2
Anti-Neutrino	9.5	0.80	15.5	2.7	0.05	1.0	1.6
Anti-Neutrino	9.2	0.56	28.8	9.8	0.3	5.8	3.7

Table 6.2: Event selection statistics for the selections maximizing the FoM for neutrino running, and the high-efficiency selection for anti-neutrino running.

	ν_e signal	ν_μ CC	NC	ν_e beam	Total BG
Reconstruction and Fiducial Cut	87.0%	78.1%	55.1%	89.3%	62.1%
Pre-selection	70.6%	18.9%	17.7%	44.0%	18.5%
ANN cut	29.9%	0.1%	0.3%	8.3%	0.4%
Total eff.	26.0%	0.1%	0.2%	7.4%	0.3%

Table 6.3: Efficiency of ν_e CC signal and background events for the optimal ANN cut of 0.74, for neutrino running. The efficiency of the ANN cut is relative to the number of events passing the preselection. The total efficiencies are cumulative.

	ν_e signal	ν_μ CC	NC	ν_e beam	Total BG
Reconstruction and Fiducial Cut	87.4%	76.7%	51.6%	89.8%	58.9%
Pre-selection	73.7%	0.3%	16.3%	70.9%	13.1%
ANN cut	46.8%	0.1%	0.8%	11.6%	0.9%
Total eff.	40.9%	0.1%	0.4%	10.5%	0.5%

Table 6.4: Efficiency of ν_e CC signal and background events for the optimal ANN cut of 0.56, for anti-neutrino running. The efficiency of the ANN cut is relative to the number of events passing the preselection. The total efficiencies are cumulative.

6.5.3 Detector Energy Resolution for Neutrino Events

The energy resolutions of the NOνA detector for electrons and muons are shown in Figures 6.17 and 6.18.

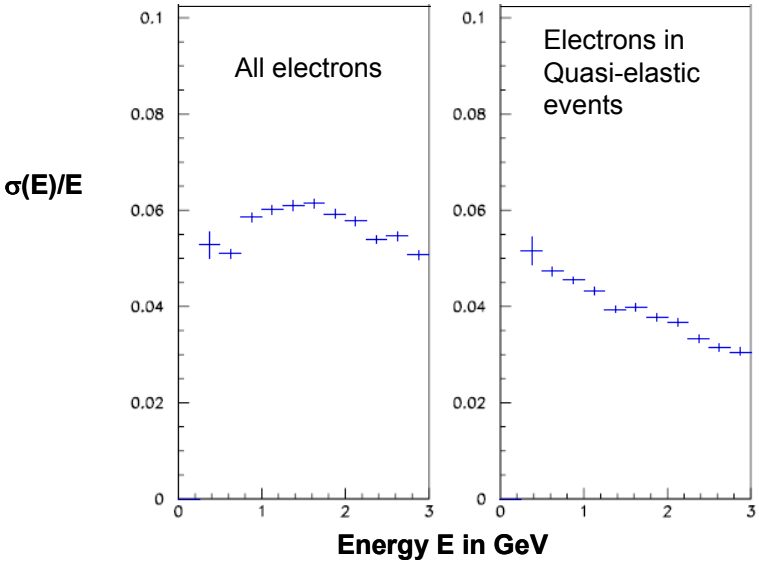

Fig. 6.17: σ(E)/E for electrons in NOνA. The left plot is for all ν_e events, while the right plot is for quasi –elastic events only.

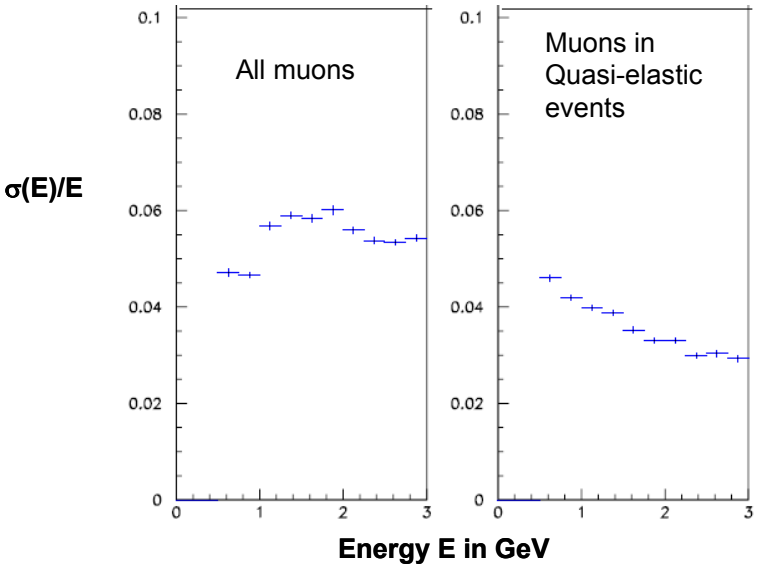

Fig. 6.18: σ(E)/E for muons in NOνA. The left plot is for all ν_μ events, while the right plot is for quasi-elastic events only.

The differences between all events and the quasi-elastic events reflect the mix of events as a function of energy shown in Figure 6.1. At about 0.5 GeV, the quasi-elastic events constitute 75% of all events so the left and right sides of Figures 6.17 and 6.18 agree at that energy. At 2 GeV, where most of the NOνA ν_e signal appears, the energy resolution σ(E)/E is about 6% for electrons. For 2 GeV muons, the energy resolution σ(E)/E is about 3.5% for quasi-elastic events.

6.6 Simulated Performance of the NOνA Near Detector

6.6.1 Location and Orientation

The NOνA Near Detector will be used to characterize backgrounds to the ν_e oscillation signal due to misidentified ν_μ CC and NC events, and the intrinsic beam ν_e content. It will also be used to characterize the unoscillated ν_μ flux for the high precision disappearance measurement. As shown below, the event rate in each 1 GeV energy bin in the near detector will correspond to statistical errors of 1% or better within 4 x 10^{20} protons on the NuMI target.

The Near detector will be situated approximately 200 feet downstream of the entry shaft to the MINOS access shaft as shown in Figures 5.8 and 5.9. The mean hadron decay position for ν_μ that interact in the fiducial volume of the near detector at this location is approximately 184 m from the target. The detector will be positioned transversely to the beam axis to maximize the similarity between the Near and Far detector spectra. It will also be oriented at an angle of 14.6 mrad with respect to the NuMI central beam axis direction in the horizontal plane to have a mean neutrino line of flight parallel to the detector horizontal axis, as in the Far Detector.

6.6.2 Comparison of Event Spectra between Near and Far Detectors.

The fiducial volume in the Near detector is defined accepting neutrinos interacting at least 40 cm away from the edges of the detector in the x (horizontal) and y (vertical) transverse directions. Along the detector axis, interactions are accepted in the range 0.53 m < z < 3.70 m for ν_μ charged current (CC) and neutral current (NC) events (9.2 tons), and 0.53 m < z < 8.5 m for ν_e CC events (21 tons).

The Monte Carlo truth neutrino energy spectrum for ν_μ CC events is shown in Figure 6.19 for the Near and Far detectors, normalized to a Near detector exposure of 4 x 10^{20} protons. The large difference in the shape of spectra between the two is due to the established θ_{23} oscillation effect.

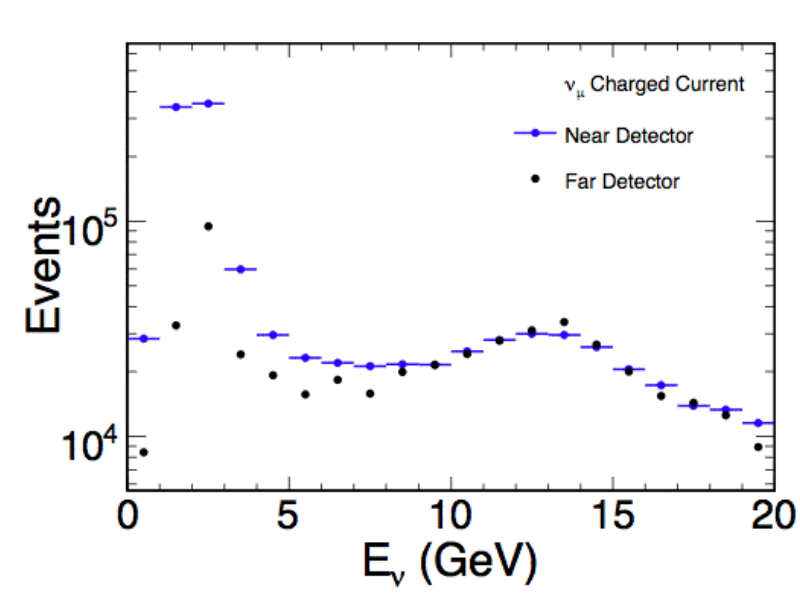

Fig. 6.19: The Monte Carlo (truth) neutrino energy spectrum in ν_μ CC events, for the Near and Far Detectors.

Figure 6.20 compares the ν_μ NC spectra in the two detectors. Since flavor oscillations are not manifest in the NC case, the differences in the two arise solely from the large variation among neutrino parent decay positions relative to the distance to the Near detector, compared to the effective point source of neutrinos for the Far detector. That is, the Near Detector sees a line source of neutrinos while the Far Detector sees a point source. However, since the mean decay angle for neutrinos traversing both detectors is the same, the spectra are very similar. This similarity will make the prediction of neutral current backgrounds in the Far detector based on observations in the Near less dependent on detailed modeling of the parent hadron beam and neutrino interactions. The Monte Carlo intrinsic beam ν_e CC spectra for the two detectors are shown in Figure 6.21.

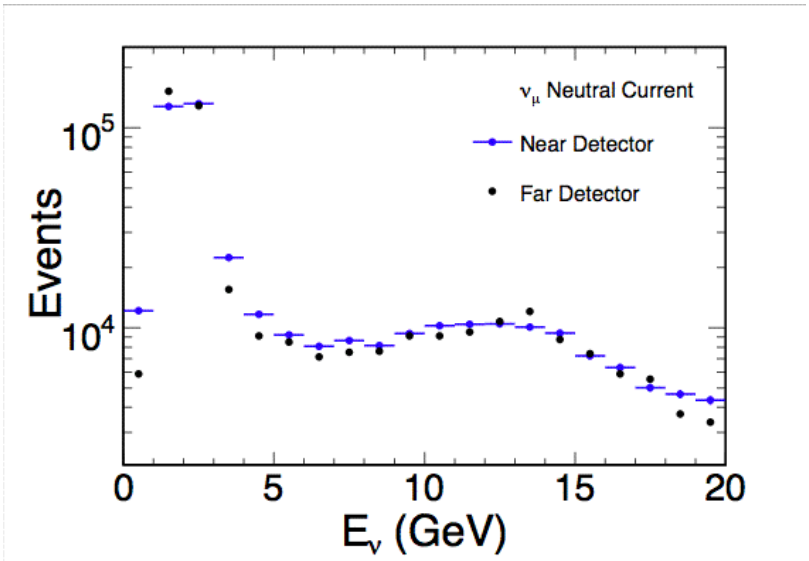

Figure 6.20: The Monte Carlo (truth) neutrino energy spectrum in ν_μ NC events in the Near and Far detectors.

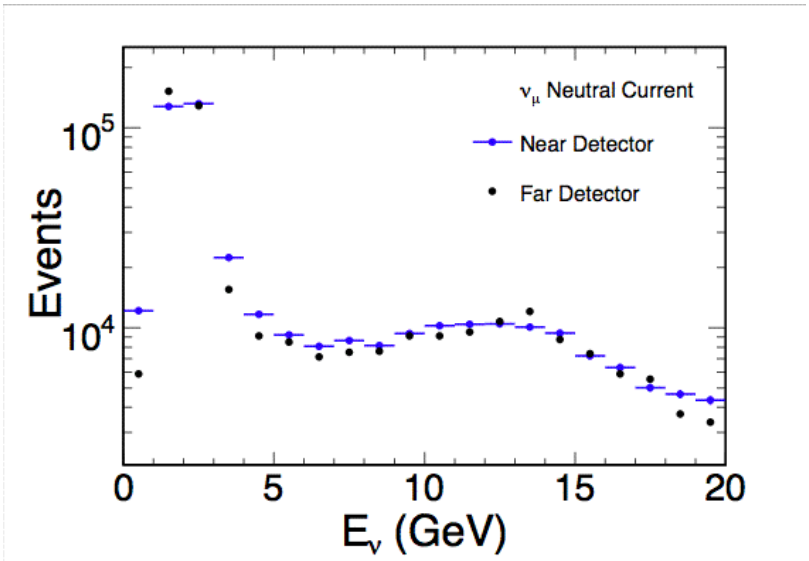

Figure 6.21: The Monte Carlo (truth) neutrino energy spectrum in ν_e CC events in the Near and Far detectors. The Far detector spectrum shown is without any ν_e appearance oscillation effect.

6.6.3 Near Detector Timing Requirements

Due to the proximity to the neutrino source, the Near Detector sits in a high event rate environment. In addition to neutrino interactions occurring in the detector, interactions occurring in the rock upstream and to the side of the detector contribute activity in the form of muons, neutrons, and other particles.

Preliminary Monte Carlo studies of the full rate of rock and detector interactions have been conducted for the Near detector in downstream cavern. In an average spill of 4x1013 protons on the NuMI target, about 25 interactions occurring in the rock and about 2 contained neutrino interactions contribute to the visible activity in the Near Detector. Given the topology of both classes of events, it is expected that events separated spatially by more than 2.5 m will usually be reconstructed correctly. At smaller distance separations, such as occurs in the single simulated spill of 4x1013 protons on target shown in Fig. 6.22, timing information from the front-end electronics will often be needed to correctly reconstruct the two events, as is the case in the spill shown.

Figures 6.23 and 6.24 show two time slices of activity in the same spill, assuming 1.5 μs double pulse separation. In this case, such separation is sufficient to correctly identify the two detector interactions contained in the spill, which occurred 1.76 μs apart. In general, however, the potential for improvements in proton intensity and other contingencies will make a finer timing separation desirable.

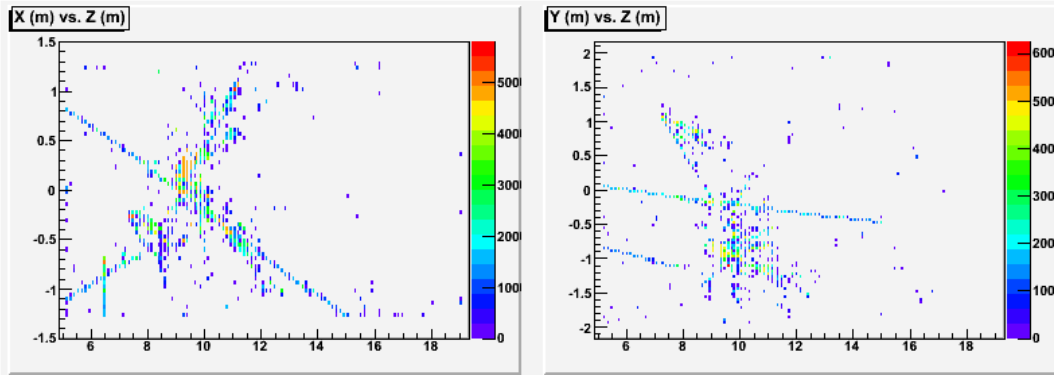

Figure 6.22: The ensemble of simulated digitizations in the X-Z and Y-Z views, from a single beam spill of 4×10^{13} protons on target. In these views, the front (upstream) end of the detector is at Z=5 m.

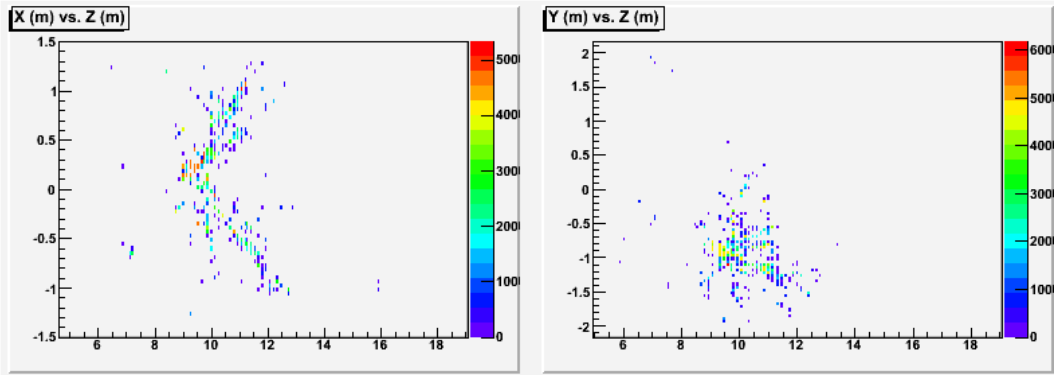

Figure 6.23: A 1.5 μs time slice from the spill shown in Fig. 6.20. Most of the remaining activity is from a single interaction in the detector: ν_μ (11.8 GeV) + N $\rightarrow$ μ + X (y=0.98).

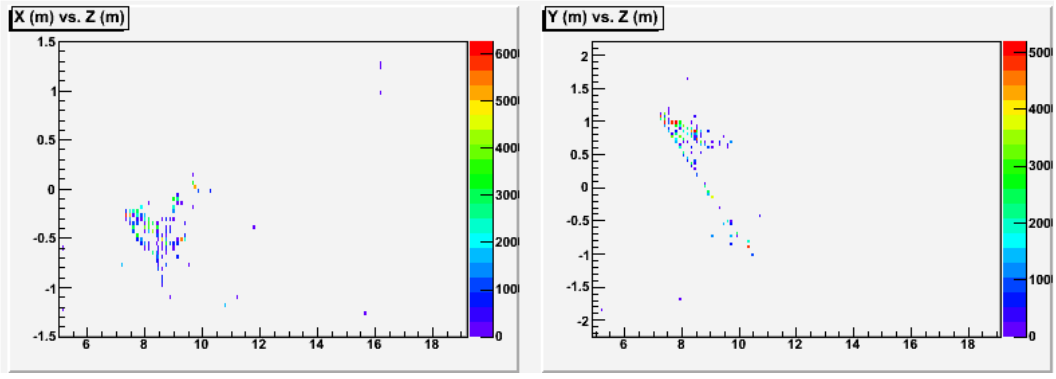

Figure 6.24: Another 1.5 μs time slice from the spill shown in Fig. 6.20. Most of the remaining activity is from a single interaction in the detector: ν_μ (8.9 GeV) + N $\rightarrow$ ν_μ + $3\pi^0$ (y=0.29).

6.7 Summary: NOνA Design Performance vs. Scientific Design Criteria

Table 6.3 compares the simulated performance of the selected NOνA design to the scientific design criteria discussed in Chapter 4. All the design criteria are met.

Design Parameter	Scientific Design Criterion	Performance of the NOνA Preliminary Design
Distance off-axis	11.5 to 12.0 km	11.77 km
Distance from Fermilab	As far from Fermilab as practically possible.	810 km, farthest possible site in the United States along the NuMI beamline
Experimental Sensitivity	Figure of merit greater than or equal to 18 *The Figure of Merit is defined as the number of ν_e signal events divided by the square root of the background for 36 x 10^{20} protons on the NuMI target equally divided between neutrino and anti-neutrino focusing at the oscillation values $\sin^2(2\theta_{13}) = 0.1$ and $\Delta m^2_{32} = 0.0024$ eV^2 without regard to matter and atmospheric-solar interference effects.*	FoM = 18
Energy resolution for ν_e Charged Current events	Less than 8% at 2 GeV	6% at 2 GeV
Energy resolution for Quasi-Elastic ν_μ Charged Current events	Less than 4% at 2 GeV	3.5% at 2 GeV
Far Detector overburden	> 10 radiation lengths	4 feet of concrete plus 0.5 feet of barite = about 14 radiation lengths
Near Detector	a) At least a 20 ton fiducial volume located about 1 kilometer from the NuMI target with sufficient transverse and longitudinal size for neutrino event containment. b) Segmentation in the fiducial volume identical to the Far Detector. c) Orientation identical to the Far Detector	a) 21 ton fiducial volume, located at 1.02 km from the NuMI target The transverse fiducial volume is 40 cm from all edges, and the longitudinal fiducial volume is followed by a 4.75 m containment region. b) identical construction in the fiducial volume c) Identical orientation.

Table 6.3: NOνA Design Parameters. The scientific Design Criteria and the performance of the preliminary NOνA design are given for each parameter.

6.8 Chapter 6 References

[1] G. Zeller, "Low-energy neutrino cross sections: comparison of various Monte Carlo predictions to experimental data", hep-ex/0312061, Proceedings of NuInt'02, Irvine CA, December 2002.
[2] NOνA Conceptual Design Report, Chapter 5, Section 5.3, March 31, 2006, NOVA-doc-536. The CDR is also available at http://www-nova.fnal.gov/.
[3] C. Howcroft, February 2007, NOVA=doc-1418. See also CDR [2], Chapter 12, Section 3.
[4] D. Cronin-Hennessy, August 2005, NOVA-doc-139.
[5] For examples, see the CDR [2], Chapter 10, Section 6.

7 WBS and Milestone Dictionary

The NOνA Work Breakdown Structure (WBS) defines the total set of items to be developed and produced in order to accomplish the scientific goals set out in Chapter 3. The breakdown at Level 2 is shown in Table 7.1.

WBS elements at Level 2		Task Name
R&D	**Construction**	
1.0	2.0	Accelerator and NuMI Upgrades
1.1	2.1	Site and Building
1.2	2.2	Liquid Scintillator
1.3	2.3	Wavelength Shifting Fiber
1.4	2.4	PVC Extrusions
1.5	2.5	PVC Modules
1.6	2.6	Electronics Production
1.7	2.7	Data Acquisition Systems
1.8	2.8	Near Detector Assembly
	2.9	Far Detector Assembly
1.9	2.10	Project Management

Table 7.1 NOνA Level 2 WBS tasks. 1.x are the R&D tasks and 2.x are the construction project tasks.

7.1 Construction WBS Dictionary at Levels 2 and 3

This section defines the WBS tasks for the NOνA Construction Project through Level 3. WBS 2.X is for the design and construction of the NOνA Near and Far Detectors and the Far Detector Hall.

WBS 2.0 <u>Accelerator and NuMI Upgrades</u>

This Level 2 element includes the procurement, QA, construction and installation of components necessary for accelerator improvements in the Main Injector and Recycler and as well as for upgrades to the beamline and target hall at the NuMI facility.

WBS 2.0.1 Recycler Upgrades

This summary task for the work to convert the Recycler Ring from an anti-proton storage ring to a proton pre-injector includes refurbishment of existing magnets, procurement and fabrication of new magnets, installation of injection and extraction lines, procurement, fabrication, and installation of a new 53 MHz RF system, and procurement, fabrication and installation of instrumentation upgrades.

WBS 2.0.2 Main Injector Upgrades

This summary task covers the upgrades for the Main Injector. These include procurement and installation of equipment for upgrades to the existing vertical quad bus, communication infrastructure for two new service buildings and the procurement, fabrication, installation of two new RF stations as well as modifications to associated cooling systems.

WBS 2.0.3 NuMI Upgrades

This summary task covers the procurement, fabrication and installation of equipment required for modification the NuMI Beamline to support 700kW operation for NOvA in the medium energy neutrino beam configuration. It includes the primary beam upgrades to support a shorter beam cycle time, upgrades to the cooling systems and electrical infrastructure to support the additional power needs. Also included are the medium energy target, baffle and carrier and an upgraded hadron monitor. Procurement, fabrication and installation of equipment in support of moving horn 2 and procurement, fabrication and assembly of the stripline, stripline block and chase temperature monitoring equipment are included.

WBS 2.0.4 Project Management

This summary task details the management and administrative resources required by WBS 2.0. It includes administrative costs such as travel, computers, training and labor for reviews. It includes labor for the L2 manager, deputy, L3 and L4 managers, project engineers and an ESH professional.

WBS 2.1 Site and Building

This level 2 summary element covers the design and construction of the Site Preparation Package and the Far Detector Building

WBS 2.1.1 Site Preparation Package

This WBS element contains the tasks necessary to build the access road, design and execute the site preparation work and perform wetlands mitigation in preparation for construction of the Far Detector Building.

WBS 2.1.2 Far Detector Building

This summary task includes the design, construction and outfitting of the Far Detector Building in Northern Minnesota. The Far Detector

Building includes the detector enclosure, Assembly area and service building. Utilities and safety systems are also included.

WBS 2.1.3 Site and Building Security
This WBS element includes the design, procurement and installation of security systems for the Far Detector site and building.

WBS 2.1.4 Management
This WBS includes the tasks required to support and manage WBS 2.1 activities including quality assurance, value engineering, risk management, ES&H, monitoring of vendor performance and schedule, preparation of reports and related activities.

WBS 2.2 Liquid Scintillator

This level 2 summary element covers the procurement, storage and QA of the components required to make liquid scintillator. Blending, storage, QA and shipping of the liquid scintillator to the Near and Far Detectors are also included.

WBS 2.2.1 Mineral Oil

This WBS element provides for vendor selection, procurement, transport and QA of the mineral oil required for the liquid scintillator.

WBS 2.2.2 Pseudocumene
This WBS element provides for vendor selection, procurement, transport and QA of the pseudocumene required for the liquid scintillator.

WBS 2.2.3 Waveshifters and Stadis 425
This WBS element provides for vendor selection, procurement and QA of waveshifters for the liquid scintillator as well as for procurement of the anti-static agent Stadis 425.

WBS 2.2.4 Blending
This WBS element provides for selection of a vendor to blend the liquid scintillator. This task includes blending and QA of the fluor concentrate, blending of the fluor concentrate with the mineral oil and QA of the final scintillator blend.

WBS 2.2.5 Transport
This WBS element provides for truck transport of the blended liquid scintillator from the blending facility to the Near and Far Detector sites.

WBS 2.2.6 Management
This WBS element includes the tasks required to support and manage WBS 2.2 activities including quality assurance, value engineering, risk management, monitoring of vendor performance and schedule, preparation of reports and other related activities.

WBS 2.3 Wavelength Shifting Fiber

This level 2 summary element covers the procurement, QA, storage and shipping of wavelength shifting fiber.

WBS 2.3.1 Procurement
This WBS element provides for vendor selection and procurement of WLS fiber as well as a QA, storage and shipping plan.

WBS 2.3.2 Production
This WBS element provides for design and production of fiber QA testing equipment as well as the development of procedures, documentation and reporting requirements. Delivery of fiber spools to the module factory on a schedule consistent with the factory schedule and available storage must also be organized and managed.

WBS 2.3.3 Management
This WBS element includes the tasks required to support and manage WBS 2.3 activities including quality assurance, value engineering, risk management, monitoring of vendor performance and schedule, preparation of reports and other related activities.

WBS 2.4 PVC Extrusions

This level 2 summary element covers vender selection, procurement and QA of the custom PVC resin as well as the selection of a vender to make the extrusions. Design and procurement of extrusion dies is included as well as pre-production runs to validate performance followed by full-scale extrusion production. QA and shipment of the PVC extrusions to the module factory is also included.

WBS 2.4.1 Procurement
This WBS element includes developing a list of vendors capable of producing the NOvA PVC compound and extruders capable of producing the NOvA profiles. Preparation of bid packages, evaluation of vendor proposals and selection of vendors is included.

WBS 2.4.2 Extrusion Pre-Production
This WBS element includes the fabrication of dies, tooling and other hardware needed for the pre-production and production of extrusions. Pre-production extrusions will be evaluated for adherence to mechanical tolerance, mechanical strength and reflectivity. Quality assurance methods for use in production as well as handling procedures will be finalized.

WBS 2.4.3 Extrusion Production
This WBS element provides for production of the extrusions as well as supervision and quality assurance monitoring of PVC extrusion production.

WBS 2.4.4 Production Quality Assurance and Extrusion Evaluation
This WBS element provides for the procurement and setup of hardware for performing QA on the PVC extrusions as well as the necessary manpower.

WBS 2.4.5 Shipping & Handling
This WBS element provides for the development of a shipping and handling plan for delivering extrusions to the module factory, for supervising trucking schedules and for managing the equipment necessary for shipping and handling.

WBS 2.4.6 Management
This WBS element includes the tasks required to support and manage WBS 2.4 activities including quality assurance, value engineering, risk management, monitoring of vendor performance and schedule, preparation of reports and other related activities.

WBS 2.5 PVC Modules

This level 2 summary element provides for assembly and QA of the PVC modules for both the Near and Far Detectors, design and construction of the machines required for module assembly, acquisition and setup of the factory space and shipping of the completed and tested modules to their respective detector sites.

WBS 2.5.1 End Seals
This WBS element includes the production of the fiber manifolds that cover and seal the readout end of a PVC module and route the WLS fibers to the photodetector interface, and the production of the bottom plates that seal the other end of the PVC modules.

WBS 2.5.2 Optical Connector Production
This WBS element includes the final design, procurement and QA of the hardware necessary to connect the WLS fibers from the PVC modules to the APD modules.

WBS 2.5.3 Module Production
This WBS element covers the set up and operation of the module factory where sets of 16-cell PVC extrusions are glued into 32-cell objects, WLS fibers are inserted into each cell, the end seals are glued to the ends of the extrusions and the WLS fibers are potted into the optical connector. QA of the completed modules as well as the procurement and construction of the various machines necessary to assemble and test the modules is also included along with transport of the completed modules to the Near and Far Detector sites.

WBS 2.5.4 Management

This WBS element includes the tasks required to support and manage WBS 2.5 activities including quality assurance, value engineering, risk management, monitoring of factory performance and schedule, preparation of reports and other related activities.

WBS 2.6 Electronics Production

This level 2 summary element includes procurement of the Avalanche Photo Diode (APD) optical sensors, the thermo-electric (TE) coolers for cooling the APDs, the custom ASIC that amplifies and multiplexes the APD signals, the ADC that digitizes the signals and the FPGAs that zero suppress and time-stamps the data. The low-voltage system for the TE coolers and the front-end electronics, the high voltage system for the APDs and a cooling system to remove the heat from the TE coolers are included as well as system design, board layout and assembly and component testing.

WBS 2.6.1 APD Module Production

This WBS element includes procurement and QA of the APD chips, the APD carrier boards, the TE coolers and the APD housing hardware. This task includes managing the flow of components for assembly and development and execution of the QA plan.

WBS 2.6.2 Readout-Front-End Board (FEB)

This WBS element provides for delivery of the specified system to receive signals from the APD modules, digitize them and deliver them to the Data Acquisition (DAQ) system. This task includes managing the flow of components for assembly and development and execution of the QA plan.

WBS 2.6.3 Readout Infrastructure

This WBS element includes design, production and installation of the infrastructure required to deliver power and cooling to operate the FEBs and APDs.

WBS 2.6.4 Management

This WBS element includes the tasks required to support and manage WBS 2.6 activities including quality assurance, value engineering, risk management, monitoring of performance and schedule, preparation of reports and other related activities.

WBS 2.7 Data Acquisition System

This level 2 summary element includes the hardware and software to record the data to archival storage and to control and monitor both the Near and Far Detectors. It includes the fiber, cable, switches and memory necessary to move and buffer the data, a PC farm for online filtering, local disk storage, a system for moving data to permanent storage at Fermilab, software and testing.

WBS 2.7.1 DAQ Software

This WBS element includes production and testing of software to run on buffering/triggering hardware for archival of data within selected time frames. Databases are also included in this WBS element.

WBS 2.7.2 DAQ Hardware

This WBS element includes the design, QA and installation of the hardware for receiving signals from FEB, buffering and archival, and delivery of clock/timing signals.

WBS 2.7.3 Integration

This WBS element includes the integration testing of DAQ and trigger electronics hardware and software.

WBS 2.7.4 Detector Control System

This WBS element includes the controls required to receive and archive monitoring data as needed.

WBS 2.7.5 Management

This WBS element includes the tasks required to support and manage WBS 2.7 activities including quality assurance, value engineering, risk management, monitoring of performance and schedule, preparation of reports and other related activities.

WBS 2.8 Near Detector Assembly

This WBS element provides for site preparation of the region to contain the Near Detector, mechanical assembly and installation of the detector itself, assembly and utilization of a liquid scintillator filling system extending from the MINOS service building to underground, and oversight of the outfitting of the detector. The site preparation consists of tasks necessary to reposition MINOS cabling and infrastructure, and to construct a new cavern at the appropriate off axis angle.

WBS 2.8.1 Near Detector Site Preparation

Complete the engineering design, procurement, fabrication and installation of the utilities and infrastructure required to install and operate the Near Detector in its underground tunnel location. These systems include excavation, lighting, HVAC, electrical power, fire protection, chilled water and liquid scintillator containment. This task covers the technical and ES&H reviews and approvals of equipment and assembly procedures.

WBS 2.8.2 Mechanical Construction and Installation

Complete the engineering design, procurement and fabrication of the Near Detector muon steel segment, the detector support structure and the systems for moving the detector subassemblies underground and to different positions along the MINOS access tunnel. This task includes

any shipping and moving costs and the final optimization, review and approval of equipment and assembly procedures.

WBS 2.8.3 Liquid Scintillator Filling Equipment

Complete the engineering design, procurement and fabrication of the Near Detector liquid scintillator supply system, the filling machine and the plumbing that connects these together and to the detector modules. Secondary containment of the liquid scintillator is included in this task as well as any shipping and moving costs and the final optimization, review and approval of equipment and assembly procedures.

WBS 2.8.4 Installation Coordination

This WBS element includes installing readout electronics, cabling, plumbing, filling with liquid scintillator, final component QA tests, detector alignment, the implementation of safety systems, the review and approval of equipment and installation procedures, and the documentation and initial commissioning of the assembled detector and its moving system.

WBS 2.8.5 Management

This WBS element includes the tasks required to support and manage WBS 2.8 activities including quality assurance, value engineering, risk management, schedule monitoring, preparation of reports and other related activities.

WBS 2.9 Far Detector Assembly

This task provides for the engineering design of the mechanical systems and tooling needed to install the NOvA Far Detector. Fabrication of the necessary tooling, installation and commissioning of the detector in the detector building in northern Minnesota is also included. This task requires close coordination with the WBS 2.1 (far site and buildings), WBS 2.2 (scintillator), WBS 2.5 (PVC modules), and WBS 2.6/2.7 (electronics and DAQ).

WBS 2.9.1 Mechanical Systems

This WBS element includes the engineering design, procurement and fabrication of the Far Detector support structure and machines for moving materials and equipment into and within the detector building. This task includes any shipping and moving costs and the final optimization, review and approval of associated equipment and assembly procedures.

WBS 2.9.2 Detector Infrastructure

This WBS element includes the infrastructure necessary to support detector construction. This includes installation of the electrical infrastructure necessary for the detector assembly and scintillator filling equipment and the design and fabrication of the North and South bookends

This WBS element includes the engineering design, procurement and fabrication of the block raiser, the 31-plane block assembly fixtures, the

adhesive dispensing system and the detector alignment systems. This task includes any shipping and moving costs and the final optimization, review and approval of associated equipment and assembly procedures.

WBS 2.9.3 Liquid Scintillator Filling Equipment

This WBS element includes the engineering design, procurement and fabrication of the Far Detector liquid scintillator transfer and filling equipment, the associated distribution controls, the plumbing that connects the transfer equipment to the filling machines and detector modules and the vapor recovery system. This task includes any shipping and moving costs and the final optimization, review and approval of equipment and assembly procedures.

WBS 2.9.4 Block Assembly and Installation

This WBS element includes the design and construction of the block pivoter, procurement and installation of the adhesive dispenser, design and procurement of the block pallets that form the base of each block, procurement of the adhesive required for block assembly and the scintillator expansion tanks required prior to filling the assembled blocks with liquid scintillator. This task also includes the assembly and erection of blocks, installation of readout electronics, cabling and plumbing, filling the blocks with liquid scintillator, final component QA tests, detector alignment, the implementation of safety systems, the review and approval of equipment and installation procedures, and the documentation and initial commissioning of the assembled detector.

WBS 2.9.5 Management

This WBS element includes the tasks required to support and manage WBS 2.9 activities including quality assurance, value engineering, risk management, schedule monitoring, preparation of reports and other related activities.

WBS 2.10 Project Management

This Level 2 summary element consists of reviews, reports, site visits, local supervision, running technical board meetings, standards preparation, tracking and analysis, schedule preparation tracking and analysis and change control. It also includes procurement of relevant software and computers, the cost of running the project office and the salaries of non-scientists working on the project. WBS 2.10 is broken down into L3 subsystems corresponding to fiscal years.

WBS 2.10.2 FY08 Project Management

WBS 2.10.3 FY09 Project Management

WBS 2.10.4 FY10 Project Management

WBS 2.10.5 FY11 Project Management

WBS 2.10.6 FY12 Project Management

WBS 2.10.7 FY13 Project Management

7.2 R&D and Operating WBS Dictionary at Levels 2 and 3

This section defines the WBS tasks for the NOνA R&D Project through Level 3. WBS 1.X is for the research and development of the NOνA Near and Far Detectors and the Far Detector Hall.

WBS 1.0 Accelerator and NuMI Planning, Engineering and Design

WBS 1.0.1 Recycler Upgrades
This summary task for the work to convert the Recycler Ring from an anti-proton storage ring to a proton pre-injector includes planning for removing anti-proton specific devices in the Recycler, design of new injection and extraction lines, design of new injection, extraction, and abort kickers, design of a new 53 MHz RF system, and engineering to upgrade the instrumentation.

WBS 1.0.2 Main Injector Upgrades
This summary task covers the modifications to low-level RF systems and associated machine timing modifications. It also includes planning for and removal of existing magnets and cavities no longer required. It also covers engineering for upgrades to existing LCW and RF cooling systems. Also included is the engineering and design for two extra MI RF stations.

WBS 1.0.3 NuMI Upgrades
This summary task covers the design and planning for modifications to NuMI Beamline to support 700kW NOvA operation in the medium energy neutrino beam configuration. It includes the primary beam upgrades to support a shorter beam cycle time, upgrades to the cooling systems and electrical infrastructure to support the additional power needs. Also included are the planning, engineering and design for a medium energy target, baffle and carrier and an upgraded hadron monitor. Planning for the movement of horn 2 to the medium energy position and the design of the stripline to connect to it in the new position are included.

WBS 1.0.4 Beam Physics
This summary task is to evaluate the efficacy the ANU project, to perform preparative beam physics measurements, calculations, and

simulations of the eventual ANU operation, and to establish and maintain a method of extrapolation to estimate future ANU proton production.

WBS 1.0.5 Management R&D Phase
This WBS details the management and administrative resources required for ANU R&D. It includes labor for the L2 manager, deputy manager, L3 and L4 managers, project engineers and an ES&H professional.

WBS 1.1 Site and Building

This Level 2 element covers the design, planning and value engineering for the far detector hall as well as the site evaluation and environmental assessment.

WBS 1.1.1 Site Conditions Investigation
This WBS element includes the investigations required to provide a comprehensive understanding of the conditions at the far detector site. This is a necessary prerequisite for designing the far detector hall.

WBS 1.1.2 Title 1 Preparation
This WBS element provides for preparation of Title 1 documents for the far detector hall.

WBS 1.1.3 Site Logistics
This WBS element consists of an investigation of the site support activities that will be necessary during the construction phase of the project.

WBS 1.1.4 Management R&D Phase
This WBS element includes the management required for planning, controlling and reporting efforts for WBS 1.1. This includes the identification and execution of value management task as well as appropriate external reviews.

WBS 1.2 Liquid Scintillator R&D

This level 2 summary element covers the development and documentation of the specifications for the liquid scintillator required for both the near and far detectors. This includes the studies, simulations and measurements required to define these requirements.

WBS 1.2.1 Requirements
This WBS element provides for development of a document detailing the experimental requirements for the liquid scintillator.

WBS 1.2.2 Scintillator Composition Studies
This WBS element provides for scintillator composition studies. These include studies of light yield, optimization of component concentrations, simulations and measurements of attenuation length.

WBS 1.2.3 Accelerated Aging Studies

This WBS task provides for accelerated studies of aging that results from the interaction of scintillator with various components and materials used in the detector.

WBS 1.2.4 Scintillator Production Method Studies
This WBS element provides for development of the plan for blending of liquid scintillator.

WBS 1.2.5 Development of QC Methods
This WBS element includes the tasks required to develop methods, procedures and plans for reliable and accurate QC testing procedures for the individual liquid scintillator components and the blended liquid scintillator.

WBS 1.2.6 Scintillator Transportation Studies
This WBS element includes the tasks required to develop methods, procedures and plans for delivering the liquid scintillator components to the blending site and for delivering the blended scintillator to the detector sites.

WBS 1.2.7 Blending Investigations
This WBS element includes the tasks required to develop, assess, and verify the ability of vendors to produce and QC liquid scintillator to meet our specifications.

WBS 1.2.8 Component Acquisition Investigations
This WBS element includes the tasks required to investigate the options available for acquiring the various components required to blend liquid scintillator.

WBS 1.2.9 Integration Prototype Detector Scintillator Production
This WBS element includes the tasks necessary to blend liquid scintillator at Fermilab for the integration prototype near detector.

WBS 1.2.10 Production Scintillator Specifications
This WBS element provides for development of the technical specifications documents for production quantities of liquid scintillator.

WBS 1.2.11 Management R&D Phase
This WBS includes the tasks required to support and manage WBS 1.2 activities including subproject activities and management for the liquid scintillator R&D phase.

WBS 1.3 Wavelength Shifting Fiber R&D

This level 2 summary element covers the development and documentation of the requirements for procurement, QA, storage and shipping of the wavelength shifting fiber.

WBS 1.3.1 Requirements

This WBS element provides for development of a document detailing the specifications for the wavelength shifting fiber.

WBS 1.3.2 Vendor Investigations
This WBS element includes the tasks required to develop, assess, and verify the ability of vendors to produce and QC wavelength shifting fiber to meet our specifications.

WBS 1.3.3 WLS Fiber Optimization Studies
This WBS task provides for studies of wavelength shifting fiber to optimize the performance for our specific application.

WBS 1.3.4 Development of QA Methods
This WBS element provides for development of the methods and procedures for QA testing of the wavelength shifting fiber.

WBS 1.3.5 Integration Prototype Detector Fiber Production
This WBS element provides for delivery and QA of fiber for the integration prototype near detector.

WBS 1.3.6 Production WLS Fiber Specification
This WBS element includes the tasks required to produce the technical specification documents for procurement of production quantities of wavelength shifting fiber.

WBS 1.3.7 Management R&D Phase
This WBS includes the tasks required to support and manage WBS 1.3 activities including subproject activities and management for the wavelength shifting fiber R&D phase.

WBS 1.4 PVC Extrusions R&D

This level 2 summary element includes studies of various PVC materials and their properties, production of prototype extrusions as well as the development and documentation of QA and shipping plans for the PVC extrusions.

WBS 1.4.1 Physical Properties Determination and Test Method Development
This WBS element includes measuring the optical and mechanical properties of various PVC compounds and extrusions.

WBS 1.4.2 Raw Materials
This WBS element includes the studies required to develop an appropriate custom PVC resin for prototype extrusion production.

WBS 1.4.3 Extrusions
This WBS element identifies venders capable of producing extrusions to meet the NOvA specifications and produces extrusions for the Integration Prototype Near Detector. The task will also develop methods for assuring the quality of extruded products.

WBS 1.4.4 Shipping & Handling
This WBS element includes tasks to develop a shipping and handling plan for delivery of extrusions.

WBS 1.4.5 Quality Assurance Hardware Modifications
This WBS element provides for the modification of prototype QA hardware to be used for QA of preproduction extrusions.

WBS 1.4.6 Management R&D Phase
This WBS includes the tasks required to support and manage WBS 1.4 activities including subproject activities and management for the PVC extrusion R&D phase.

WBS 1.5 PVC Modules R&D

This level 2 summary element provides for development and documentation of the procedures for assembly of the PVC modules and the design of the fiber manifolds, end seals and the various machines and fixtures necessary for module construction. Development of QA and shipping plans is also included.

WBS 1.5.1 Requirements
This WBS element provides for development of requirements documents for module assembly, manifolds and end seals. QA requirements for the completed modules are also included.

WBS 1.5.2 End Seal R&D
This WBS element includes the design and development of the manifolds and end seals as well as specification of QA procedures.

WBS 1.5.3 Photo Detector Interface R&D
This WBS element includes the design and development of the photodetector interface as well specification of QA procedures.

WBS 1.5.4 Module Factory R&D
This WBS element includes the development of assembly methods for the PVC modules as well as the design of machines, tooling and moving fixtures.

WBS 1.5.5 Quality Assurance and Quality Control Methods Development
This WBS task provides for the development of a QA plan for PVC module production. Construction of the required testing equipment is also included.

WBS 1.5.6 Module Shipping and Storage R&D
This WBS element provides for the development of a plan for shipping and handling of extrusion modules between the module factory and the Detector sites and for managing the equipment necessary for shipping and handling.

WBS 1.5.7 Integration Prototype Detector Modules

This WBS element provides for production of the PVC modules for the integration near detector prototype.

WBS 1.5.8 Initial Production Module Specifications
This WBS element provides for the development of the initial production module specifications.

WBS 1.5.9 Initial Factory Tooling Specifications
This WBS element provides for the development of the initial factory tooling specifications.

WBS 1.5.10 Management R&D Phase
This WBS includes the tasks required to support and manage WBS 1.5 activities including subproject activities and management for the PVC module R&D phase.

WBS 1.6 Electronics R&D

This level 2 summary element includes the design, development and testing of the front end electronics and infrastructure.

WBS 1.6.1 APD Modules
This WBS element includes development and procurement of prototype APD chips, APD carrier boards, TE coolers, optical connectors and the associated hardware that comprise the APD modules. Development of specifications for fiber alignment, power consumption, cooling and QA are also included. APD modules for the Integration Prototype Near Detector are included here.

WBS 1.6.2 Front End Board
This WBS element includes design of the front-end boards as well as the development of testing and installation procedures. Front-end boards for the Integration Prototype Near Detector are included here.

WBS 1.6.3 Power Distribution
This WBS element includes the design and specification of the low voltage, high voltage, cooling and power distribution for the NOνA electronics. Power distribution for the Integration Prototype Near Detector is included here.

WBS 1.6.4 Management R&D Phase
This WBS element includes the tasks required to support and manage WBS 1.6 management activities for the Electronics subproject during R&D phase.

WBS 1.6.5 Vertical Slice Tests
This WBS element provides for a small-scale test facility for evaluating various configurations of prototype PVC extrusions, liquid scintillator

and WLS fiber using cosmic ray muons, APDs and prototype versions of the front-end board.

WBS 1.7 DAQ System R&D

This level 2 summary element includes the development of specifications and design of the hardware and software necessary to acquire and record data to archival storage and to control and monitor both the Near and Far Detectors.

WBS 1.7.1 DAQ Software
This WBS element includes the development of specifications and the design of the DAQ software.

WBS 1.7.2 DAQ Hardware
This WBS element includes the development of specifications and the design of hardware for receiving signals from the FEBs, buffering and archival of data and distribution of clock/timing signals.

WBS 1.7.3 Integration
This WBS element includes the development of specifications and requirements for integration of the DAQ hardware and software.

WBS 1.7.4 Detector Control Systems
This WBS element includes the development of specifications and requirements for the detector control system.

WBS 1.7.5 Management R&D
This WBS element includes the tasks required to support and manage WBS 1.7 management activities for the DAQ System R&D phase.

WBS 1.7.5 Operate IPND
This WBS element accounts for the resources required to operate the IPND in the NuMI surface building.

WBS 1.8 Detector Assembly R&D

This level 2 summary includes R&D work to validate and optimize the mechanical designs and installation procedures for the NOvA Near and Far Detectors. This includes structural engineering calculations of the fully and partially assembled detectors, the mechanical design and prototyping of detector assembly mechanical systems and tooling, and the construction and testing of prototypes of both Near and Far Detectors.

WBS 1.8.1 Plane Assembly Adhesives R&D
This WBS element includes the tasks required to choose an adhesive that is suitable for bonding the extrusion modules together for the Far and Near detector.

WBS 1.8.2 Structural Design and Validation

This WBS element includes the tasks required to develop and optimize the structural design of the far detector.

WBS 1.8.3 Liquid Scintillator Filling and Handling R&D
This WBS element includes the tasks required to develop techniques and semi-automatic equipment for filling the Integration Prototype as well as the Near and Far detectors.

WBS 1.8.4 Near Detector Assembly R&D
This WBS element includes the tasks required to develop the procedures, equipment and assembly plan for the near detector. The task also includes the design of an assembly facility and associated procedures and equipment for assembling extrusion modules. Finally, this task will design the steel-plate muon-catcher segment of the near detector, along with associated support structures and assembly equipment.

WBS 1.8.5 Integration Prototype Near Detector
This WBS element includes the tasks required to design, fabricate and install the Integration Prototype Near Detector.

WBS 1.8.6 Far Detector Assembly Engineering
This WBS element includes the tasks required to specify and design the equipment needed to assemble and install the far detector.

WBS 1.8.7 Far Detector Installation Procedures
This WBS element includes the tasks required to develop the far detector installation procedures, schedules and labor requirements.

WBS 1.8.8 Far Detector Prototypes
This WBS element includes the tasks required to test and optimize the procedures and equipment designs developed in WBS 1.8. This task will lead to the final optimization of the designs for assembly tooling and materials handling equipment.

WBS 1.8.9 Management R&D Phase
This WBS element includes the tasks required to support and manage WBS 1.8 activities for the Detector Assembly R&D phase.

WBS 1.9 Project Management R&D
This Level 2 summary element provides for internal project reviews, report preparation, site visits, local supervision, standards preparation, tracking and analysis, schedule preparation tracking and analysis and change control. It also includes procurement of relevant software and computers, the cost of running the project office and the salaries of non-scientists working on the project.

7.3 Milestone Dictionary

The following table contains the milestone definitions for all NOνA milestones from Level 0 through Level 5. The milestones are ordered by WBS number. In many cases the definition is self explanatory and in others more explanation is required. In all cases it should be apparent what constitutes completion of the milestone.

WBS	Milestone	Milestone Definition
1.0.1.1.6.1	Recycler Ring (RR); All 3 ADC Magnets Found	Location of 3 ADC magnets in the Recycler Ring have been identified and documented.
1.0.1.1.6.2	RR; Lattice Designs Complete	Recycler Ring beamline design lattices completed and documented. This includes the 3d drawings to check for interferences.
1.0.1.1.6.3	RR; 53 MHz RF Design Review Complete	53 MHz RF design review complete and the committee report has been transmitted to the L2 manager.
1.0.1.1.6.4	RR; Decision on Vacuum Window Removal Finalized	The beam abort line contains a vacuum window. The decision is whether to eliminate the window and have the beam abort line vacuum integrated with the circulating beam vacuum, or to leave it as a separate vacuum system with its own vacuum pumping and instrumentation. This Milestone is complete when the L3 and L4 managers finalize the decision.
1.0.1.1.6.5	RR; Beamline Modifications Design Review Complete	A design review of the proposed beamline modifications in the Recycler Ring is complete and the committee report has been submitted to the L2 manager.
1.0.1.1.6.6	RR; Mirror Magnet Design Finalized	PDD Mirror magnet for the injection line design is complete and signed off by AD and the L2 manager.
1.0.1.2.7.1	RR; Injection & Gap Clearing Pulser Cables Finalized	Existing cables are measured for impedance vs. frequency to determine the pulse response for fall time and droop in voltage. The decision is whether to accept them for the new kicker system or buy new cables with a more desirable impedance. This Milestone is complete when the L4 manager makes this decision.
1.0.1.2.7.2	RR; External/MI Injection Pulser Cables Finalized	Existing cables are measured for impedance vs. frequency, to determine the pulse response for fall time and droop in voltage. The decision is whether to accept them for the new kicker system or buy new cables with a more desirable impedance. This Milestone is complete when the L4 manager makes the decision.
1.0.1.2.7.4	RR; Extraction MI Injection Kicker Prototype Pulser System Complete	After testing and iterating the design of the prototype pulser with a test magnet, the design is ready for procurement of production parts. This Milestone is complete when the L4 manager makes the decision to move forward on procurement based on successful prototyping.
1.0.1.2.7.5	RR; Injection Line Prototype Kicker Complete	This Milestone is complete when the L4 manager makes the decision to accept the kicker design for production and move forward on procurement of parts for two pre-production magnets based on successful prototyping.
1.0.1.2.7.6	RR; Ferrite Procurement or Re-design Finalized	This Milestone is complete when the L4 manager chooses the most acceptable of the ferrite designs for production in order to move forward on procurement .
1.0.1.4.3.1	RR; Shielding Assessment Complete	This milestone is defined as the point at which the RR shielding assessment issues for NOvA operation have been addressed in the MI Shielding Assessment.
1.0.2.1.6.1	Main Injector (MI); 2.5 MHz Cavities Removal Complete	The removal of the 6 coalescing cavities (2.5,5.0MHz) from MI is complete.
1.0.2.1.6.2	MI; Decommissioning of A1 Extraction Line Complete	The removal of the 3 Lambertson magnets and the 2 kickers used for the anti-proton extraction from the MI is complete.
1.0.2.1.6.3	MI; Machine Timing Complete	All the modifications to the MI and RR low level RF systems required for slip stacking in the RR are complete and documented.
1.0.2.2.4.1	MI; Cavity Pre-install Testing Complete	The testing of the two MI RF cavities is complete. This milestone is satisfied when the results of the testing have been transmitted to the L2 manager.
1.0.2.3.2.1	MI; Shielding Assessment Complete	This milestone is defined as the point at which the MI Shielding Assessment has been updated/appended for NOvA operation and is ready to start the Lab approval process.
1.0.3.1.5.1	NuMI; Charging PS Upgrade Design Complete	A review of the NuMI Charging PS Upgrade Design has been completed and a report on their findings.

1.0.3.1.5.2	NuMI; Profile Monitor Conceptual Design Review Complete	A review of the technical design for the NuMI Primary Beamline Profile Monitors has been completed and the committee report has been submitted to the L2 manager. The modifications to the Profile Monitor design have been determined and agreed to by the L3 and L4 managers.
1.0.3.1.5.3	NuMI; Profile Monitor Technical Design Review Complete	A review of the technical design for the NuMI Profile Monitors has been completed and the review committee has written a report on their findings and submitted it to the L2 manager.
1.0.3.2.5.1	NuMI; Target, Baffle & Carrier Initial Design Review Complete	A review of the conceptual designs for the NuMI Target, Baffle, & Carrier has been completed and the review committee has submitted a written report to the L2 manager.
1.0.3.2.5.3	NuMI; Final Design of Target Carrier Complete	This final design of the target carrier has been completed. The drawings for the carrier have been completed, and the procurement and fabrication of the carrier can begin.
1.0.3.2.5.9	NuMI; Hadron Monitor Initial Re-design Complete	An analysis of the Hadron Monitor performance under ANU operating conditions has been completed. The modifications to the Hadron Monitor design has been determined and agreed to by the L3 and L4 managers.
1.0.3.3.5.1	NuMI; Analyze Predicted Block Temperatures Effect on Chase Components Complete	This milestone is the completion of the finite element analysis (FEA) to calculate the amount of radiation heat transfer that takes place from the chase blocks to sensitive components (such as target, horn, & stripline assembly), with the results documented in a posted engineering note.
1.0.3.3.5.2	NuMI; Shielding Assessment Complete	A review of the technical design for the NuMI Primary Beamline Profile Monitors has been completed and the committee report has been submitted to the L2 manager. The modifications to the Profile Monitor design has been determined and agreed to by the L3 and L4 managers.
1.0.3.3.5.3	NuMI; Target Chase Cooling Design Complete	This milestone is the completion of the engineering analysis, design, and drafting of the Target Chase Air Cooling upgrades. It includes completion of the following tasks: 1) Design of new chiller cooling coils including modifications to the existing coil box, with a final drawing package that includes piping layout details, valve and instrumentation specifications, control wiring diagrams, and updating of the existing controls. After this milestone, the design is ready for review and procurement of parts.
1.0.3.3.5.11	NuMI; FEM 3-D Thermal Analysis Complete	This milestone is the completion of the 3-D thermal Finite Element Analysis (FEA) of the target chase region, with results documented in an engineering note.
1.0.4.4.1	Estimate Limits of Proton Plan Performance	Complete an analysis of the achieved Proton Plan performance and extrapolate its ultimate performance. In particular, several major items of the Proton Plan are evaluated in terms of the anticipated usage in ANU. This is an interim analysis that occurs after all the Proton Plan improvements have been implemented, but before all of their gains have been realized. Therefore, a certain amount of extrapolation may be necessary to evaluate them for ANU. This milestone is complete when a report is generated and posted that documents the Proton Plan performance and the ANU extrapolation.
1.0.4.4.2	Beam Physics Preparative Analysis Complete	All of the general beam physics studies for ANU are completed and documented. The preparative analyses are studies needed to facilitate commissioning and operation of ANU; they involve experimental characterization of the accelerators, optimization and detailing of the ANU stacking scheme, and simulation of intense beam dynamics. One or more reports are generated to document the studies.
1.1.1.1.7	Purchase order released for topographic study	The purchase order has been issued to conduct a topographic study of the Far Detector Hall site in Ash River Minnesota.
1.1.1.1.10	Topographic survey complete	The topographic survey of the Far Detector Hall site has been completed and the results documented by the L2 manager.
1.1.1.2.11	Subsurface investigation completed	This milestone is complete when the subsurface borings have been completed and the investigation report has been completed and transmitted to the L2 manager.

1.1.1.2.7	Purchase order released for subsurface borings.	The purchase order has been issued to perform subsurface borings at the Far Detector Hall site.
1.1.1.3.10	Wetland delineation completed	This milestone is complete when the wetland delineation report has been completed and delivered to the L2 manager.
1.1.1.3.7	Purchase order released for wetland delineation	The purchase order has been issued for wetland delineation at the Far Detector Hall site.
1.1.1.4.15	Environmental Assessment Worksheet (EAW) process completed	This milestone marks the point where the State of Minnesota Environmental Assessment Worksheet process is complete including publication, public comment and responses.
1.1.1.4.8	EAW revisions completed	This milestone is satisfied when revisions to the State of Minnesota Environmental Assessment Worksheet, required due to changes in the Project, have been completed and the final report has been received by the L2 manager.
1.1.2.1.21	Site preparation ACD completed	The advanced conceptual design of the Far Detector Hall site has been completed and the report has been received by the L2 manager.
1.1.2.2.7	PO Released for Building Design Modifications	The purchase order has been issued to incorporate building design modifications into the initial design of the Far Detector Hall.
1.1.2.2.11.5	Value engineering completed for Far Detector Hall.	This milestone marks the conclusion of the value engineering process for the design of the Far detector Hall. This includes investigation, review and documentation alternatives.
1.1.2.2.12.6	Document revisions completed.	This milestone marks the completion of revisions to design documents resulting from the building design modifications process.
1.1.2.2.13	Building design modifications completed	This milestone marks the completion of revisions to design documents resulting from the building design modifications process.
1.1.2.3	Title 1 preparation complete	This milestone is satisfied when the Title I design of the Far Detector Building is complete, value engineering has been completed and the documentation has been fully completed and reviewed.
1.1.4.1.1.7	Purchase order issued for initial independent cost estimate.	The purchase order has been issued for an initial independent estimate of the cost to prepare the site and construct the Far Detector Hall.
1.1.4.1.1.19	ICE review completed	The initial independent cost estimate has been reviewed and documented by the L2 manager.
1.1.4.1.2.4	Cost estimate update completed	An update to the initial independent cost estimate for the Far Detector Hall, capturing changes to the design since the initial estimate, is completed and the report has been received by the L2 manager.
1.1.4.1.3.1.5	Burns and McDonnell Cost Estimate Complete	This milestone is satisfied when Burns and McDonnell has completed their independent cost estimate for the Far Detector Hall and the report has been received by the L2 manager.
1.1.4.1.3.2.7	PO Release for J.E. Dunn North Central for cost estimate	The purchase order has been issued to J.E. Dunn for an independent cost estimate of the Far Detector Hall, site and road package.
1.1.4.1.3.2.14	JE Dunn North Central Cost Estimate Complete	This milestone is satisfied when J.E. Dunn has completed their independent cost estimate for the Far Detector Hall and the report has been received by the L2 manager.
1.1.4.1.3.3.7	PO Issued for Constructive Ideas cost estimate	The purchase order has been issued to Constructive Ideas for an independent cost estimate of the Far Detector Hall, site and road package.
1.1.4.1.3.3.14	Constructive Ideas cost estimate complete	This milestone is satisfied when Constructive Ideas has completed their independent cost estimate for the Far Detector Hall and the report has been received by the L2 manager.
1.1.4.2.7	Purchase order issued for secondary containment study.	The purchase order has been issued to commission a study of secondary containment options for liquid scintillator in the Far Detector Hall.
1.1.4.2.13	Secondary containment study completed	The study of options for secondary containment of liquid scintillator at the Far Detector Hall has been completed and the results documented by the L2 manager.

1.1.4.3.4	Overburden study completed	This milestone is complete when the study of options, methods and materials for an overburden covering the top and sides of the Far Detector Hall to attenuate cosmic rays has been completed and the report has been received by the L2 manager.
1.1.4.5.9	Risk management Assessment for the site and building complete.	This milestone is complete when the risk management assessment for WBS 1.1 and WBS 2.1 has been completed, the risks have been entered into the risk registry and the high risk items have been document in a risk assessment form that has been posted in the document database.
1.2.7.4	Baseline blending option selected	This milestone is satisfied once a decision is made and documents regarding the mode of blending the liquid scintillator. The options are to blend it ourselves at Fermilab or to contract with an outside firm, a toll blender, to do the work for us.
1.2.9.1.3	PO issued for ISO tanks	PO issued for ISO tanks for storage of mineral oil and scintillator blending for the IPND.
1.2.9.2.6	Prototype blending system facility completed	The blending system that will be used to blend liquid scintillator in ISO tanks at Fermilab for the IPND has been completed and is ready for blending.
1.2.9.3.4	Mineral oil PO issued	The purchase order for IPND mineral oil has been issued to the vendor.
1.2.9.3.6	Mineral oil batch 1 for IPND delivered	Delivery of 4,520 gal of Penreco oil and 4,520 gal of Renkert oil to Fermilab. This is the first round of mineral oil deliveries and it will be used to blend scintillator for the IPND.
1.2.9.3.9	Mineral oil batch 2 for IPND delivered	Delivery of 4,520 gal of Penreco oil and 4,520 gal of Renkert oil to Fermilab. This is the second round of deliveries and it will be used to blend scintillator for the IPND.
1.2.9.3.12	Mineral oil batch 3 for IPND delivered	Delivery of 4,000 gal of Renkert oil. This is the final round of deliveries for the IPND.
1.2.9.4.1.2	Pseudocumene PO issued	The purchase order for psuedocumene from Dixie Chemical for the IPND liquid scintillator has been issued to the vendor.
1.2.9.4.2.2	Pseudocumene PO issued	The purchase order for pseudocumene from China for the IPND liquid scintillator has been issued to the vendor.
1.2.9.5.2	Waveshifter PO issued	The purchase order for waveshifters for the IPND liquid scintillator has been issued to the vendor.
1.2.9.6.11	Prototype scintillator production completed	Blending of liquid scintillator scintillator at Fermilab for the IPND has been completed.
1.2.10.3	Liquid scintillator final specifications completed	The composition of liquid scintillator, optimized to result in the required light output for the lowest cost, has been determined and documented.
1.3.3.6	Baseline (IPND) WLS fiber diameter chosen	This milestone is satisfied when the nominal diameter of the fiber for use in the IPND has been selected and documented.
1.3.3.7	Baseline (IPND) WLS fiber dye concentration chosen	This milestone is satisfied when the nominal composition of the fiber for use in the IPND has been selected and documented.
1.3.5.5	IPND WLS fiber production completed	All fiber for use in the integration prototype near detector has been produced and delivered by the vendor.
1.3.6.5	Production WLS fiber diameter confirmed	The production fiber diameter and radial profile has been selected and documented.
1.3.6.6	Production WLS fiber composition confirmed	The production fiber composition, including waveshifter ppm, has been selected
1.4.2.1.2	Raw materials requirements document released	The document that defines the requirements for the raw material components that are used to formulate the custom PVC blend required for NOvA is complete and posted in the document database.
1.4.2.2.2.3	Prototype 16-cell PVC horizontal extrusion compound specified	Based on the results of our R&D program, the custom PVC blend that will be used to produce horizontal extrusions for the IPND is specified and documented.

1.4.2.2.2.4	Prototype 16-cell PVC vertical extrusion compound specified	Based on the results of our R&D program, the custom PVC blend that will be used to produce vertical extrusions for the IPND is specified and documented. This resin could be different than the resin used for the horizontal extrusions.
1.4.2.3.1.2	RFP issued for raw PVC resin	A request for proposals is issued to a list of qualified vendors to bid on a custom PVC resin to use to produce prototype extrusions using the 16-cell prototype die.
1.4.2.3.2.2	PO for raw PVC resin for 16-cell horizontal extrusions released	The purchase order for the custom PVC resin required for the IPND horizontal extrusions is issued to the vendor.
1.4.2.4.2.2	PO for raw PVC resin for 16-cell vertical extrusions released	The purchase order for the custom PVC resin required for the IPND vertical extrusions is issued to the vendor.
1.4.2.5.2	PO for raw PVC resin for 16-cell horizontal extrusions released	A purchase order for PVC resin for further horizontal die tuning iterations, if necessary, is issued to the vendor.
1.4.2.6.2	PO for raw PVC resin for 16-cell vertical extrusions released	A purchase order for additional PVC resin for further vertical die tuning iterations, if necessary, is issued to the vendor.
1.4.3.4.5.2	Purchase order released (16-cell horizontals)	The purchase order to fabricate a 16-cell die to produce prototype horizontal extrusions is issued to the vendor.
1.4.3.4.5.9	16-cell horizontal extrusion prototypes specifications completed	The extruding parameters for the Horizontal extrusions for the IPND are fully specified and documented.
1.4.3.4.5.11	16-cell horizontal extrusions for IPND completed	All Horizontal extrusions for IPND have been extruded and characterized.
1.4.3.5.2	Initial 16-cell vertical extrusion prototype specifications completed	Extrusion profile mechanical drawings are complete, documented and ready for submission to extruder.
1.4.3.5.4	PO for die inserts released (16-cell verticals)	A purchase order for "Inserts" to be placed into the prototype die in order to produce vertical extrusions with thicker walls is issued to the vendor.
1.4.3.5.10	16-cell vertical extrusion prototypes specifications completed	The extruding parameters for the vertical extrusions for the IPND are fully specified and documented.
1.4.3.5.12	16-cell vertical extrusions for IPND completed	All Vertical extrusions for IPND have been extruded and characterized.
1.5.2.1.1.7	Integration prototype manifold concept selected	The concept of how to make the manifold has been selected and documented. This includes a design of the parts that make the seal and route the fibers to the optical connector. The design may not be final.
1.5.2.1.1.14	Preproduction prototype manifold design (for IPND) completed	This milestone is satisfied when the solid models of the IPND manifold parts are complete and ready to go out for bid. The manifold parts include the cover, top and bottom snout halves, side and center seals, top and bottom fiber raceways, fiber cover, and fill tubes. This does not include the optical connector.
1.5.2.2.6	End plate integration prototype concept selected	The concept of how to make the end seal has been selected and documented. This includes a design of the parts that make this seal. The design may not be final.
1.5.2.2.13	Design of preproduction prototype bottom plate (for IPND) completed	The solid models of the IPND bottom plate parts are complete and ready to go out for bid. The bottom plate parts include the bottom plate and side and center seals.
1.5.2.3.3	IPND adhesive selected	The choice of adhesives to be used to join all parts of the modules that will be assembled in the IPND module factory have been specified and documented. This includes glue to band the manifold, end plate, and optical connector assemblies and to bond these parts to their mating assemblies. This also includes the adhesive to bond two 16-cell extrusions to form a 32-cell extrusion assembly.

1.5.2.3.5	RF welding go/no go decision made	A decision to use glue adhesives or an RF welding technology to bond the manifold, bottom plate, optical adaptor, and extrusion assemblies (two 16 cell extrusion to make a 32-cell extrusion) has been made and documented.
1.5.3.6	Integration prototype optical connector design concept selected	This milestone is satisfied when the features of the optical connector have been agreed upon by those responsible for parts that must interface with the device. A complete solid model need not exist at this point.
1.5.3.10	Design of preproduction prototype photodetector interface (for IPND) completed	The design of the prototype photodetector interface for the IPND is complete, documented and ready for fabrication.
1.5.4.2.7	Prototype extrusion fiber-stringing machine for IPND ready to operate	The fiber stringing machine is ready to be used by workers to string IPND modules.
1.5.4.2.10	Prototype fiber facing machine for IPND ready to operate	This milestone is satisfied when the fiber facing machine has been built and tested and is ready to face IPND modules.
1.5.4.2.12	Prototype gluing machine for IPND ready to operate	This milestone is satisfied when the gluing machine has been built and tested on sample modules and is ready to face IPND modules.
1.5.5.4	Pressure-testing hardware for IPND production ready to operate	The pressure testing hardware is ready to test for leaks in IPND modules. The tester has enough channels to simultaneously test the maximum number of modules to be assembled by the IPND factory in one day.
1.5.5.7	Fiber mapping and continuity hardware for IPND production ready to operate	The fiber testing hardware is ready to test for damaged fibers in the IPND modules.
1.5.7.3.7	IPND modules for first 8-plane segment completed	Completed is defined as assembled, tested, and shipped.
1.5.7.3.8	IPND module production 50% complete	Half of the IPND modules have been assembled, tested, and shipped.
1.5.7.3.9	IPND module production completed	All IPND modules have been assembled, tested, and shipped.
1.6.1.1.2.7	APD module first prototypes qualified	This milestone is satisfied when the first functioning APD prototypes are delivered.
1.6.1.1.3.7	APD modules second prototype completed	This milestone is satisfied when functional housing is delivered for the APDs.
1.6.1.2.8	QA/QC station ready	This milestone is satisfied when the automated test station for APDs is functional and ready to test first set of APDs.
1.6.1.6.1.1	APD module production for IPND started	This milestone is satisfied when production of the housing for the APDs for use with the IPND has started.
1.6.1.6.1.7	APD modules for 8-plane segment completed	This milestone is satisfied when the first 20 functioning APD modules are completed and available for use to outfit the 8-plane prototype.
1.6.1.6.1.9	APD modules for IPND completed	This milestone is completed when all 303 APD modules for the IPND have been constructed and tested.
1.6.2.3.12	FEB prototype II released to DAQ	This milestone is satisfied when a functional APD readout board (FEB) is delivered.
1.6.2.4.12	FEB prototype III released to DAQ	This milestone is satisfied when a functioning APD readout board (FEB) is delivered.
1.6.2.5.1	FEB modules for IPND started	This milestone is satisfied when production of the front end boards for the IPND has started.
1.6.2.5.13	FEB modules for IPND completed	This milestone is satisfied once all 303 FEB modules for the IPND have constructed and tested.
1.6.2.6.11	FEB prototype V for near detector released to DAQ	This milestone is satisfied when the first fast readout version of the APD readout boards (FEB) are produced and ready for testing.

1.6.3.5.8	IPND power distribution system online	This milestone is satisfied once the power distribution system for the IPND is functioning and can be operated by the Detector Control System.
1.7.1.10.1.5.3	Development database servers released for use	This milestone is satisfied when the online database is released for use.
1.7.1.11	DAQ software ready for IPND	This milestone is satisfied when all of the software required to take data with the IPND is completed and functioning.
1.7.1.2.4.8	Error handling system for first software release	This milestone is satisfied when the first version of the DAQ error handling system has been tested, documented and released for use with the DAQ.
1.7.1.3.4.8	Message passing system for software first release	This milestone is satisfied when the first version of the DAQ Message Passing System has been designed, evaluated, documented and released for use.
1.7.1.4.4.7	Run control system for software first release	This milestone is satisfied when the first version of the software for the Run Control System has been verified, documented and is released for use.
1.7.1.6.3.1.13	Event buffer farm core software for software first release	This milestone is satisfied when the first version of the Event Buffer Farm core software has been verified, documented and is released for use.
1.7.1.6.4.1.6	Event buffer farm server for software first release	This milestone is satisfied when the first version of the software for the Event Buffer Farm Server has been verified, documented and is released for use.
1.7.1.6.5.6	Trace kernel support for software first release	This milestone has been satisfied when the first version of Linux Kernel Support for Trace has been released for use with the DAQ.
1.7.1.8.3.6	Global trigger system for software first release	This milestone is satisfied when the software for the Global Trigger System has been verified, documented and is released for use.
1.7.1.8.4.8	Global trigger system for software second release	This milestone is satisfied when the second version of the Global Trigger System software has been verified, documented and is released for use.
1.7.2.1.1.3	Requirements approved for data concentrator	This milestone is satisfied when the requirements document for the Data Concentrator Module (DCM) has been documented and approved by the L2 manager.
1.7.2.1.2.2.3	Specifications approved for data concentrator	This milestone has been satisfied when the specifications for the Data Concentrator Module have been documented and approved by the L2 manager.
1.7.2.1.2.3.4	Schematic approved for data concentrator	This milestone is satisfied when DCM prototype schematics have reviewed and approved by the L2 manager.
1.7.2.1.2.8	Data concentrator design completed	This milestone is satisfied when the design for the Data Concentrator Module is complete, documented, and the simulations are complete.
1.7.2.1.3.3	PCB manufacturing approved	This milestone is satisfied when the requirements have been reviewed and documented for the PC boards for the prototype Data Concentrator Modules and the L2 manager has signed off on procurement of the prototype boards.
1.7.2.1.3.5	Prototype data concentrator PCBs and components received	This milestone is satisfied when the PC boards for the prototype Data Concentrator Modules have been received from the vendor.
1.7.2.1.4.4	DCM prototype completed	This milestone is satisfied when the prototype Data Concentrator Module is complete and ready for evaluation.
1.7.2.1.6.2	IPND data concentrator PCBs and components received	This milestone is satisfied when the boards and all necessary components for the IPND Data Concentrator Modules have been received.
1.7.2.1.8	IPND data concentrators ready for installation	This milestone is satisfied when the Data Concentrator Modules for the IPND have been fully tested and are ready for installation.
1.7.2.2.1.3	Requirements approved for Timing and Control System	This milestone is satisfied when the requirements for the Timing and Control System have been documented and approved by the L2 manager.
1.7.2.2.2.2.3	Specifications approved for Timing and Control System.	This milestone is satisfied when the specifications for the DAQ Timing and Control System have been evaluated, reviewed, documented and approved by the L2 manager.

1.7.2.2.2.3.4	Schematic approved for Timing and Control System.	This milestone is reached once the schematic for the circuit design of the Timing and Control System is approved by the L2 manager.
1.7.2.2.3.3	PCB manufacturing approved for Timing and Control System.	This milestone is satisfied once the requirements for the Timing and Control System PC boards have been documented and reviewed and the L2 manager confirms that the boards are ready for fabrication.
1.7.2.2.3.5	Prototype PCBs and components received for Timing and Control System.	This milestone is satisfied when the boards and all necessary components for the Timing and Control System have been received.
1.7.2.2.4.4	Control and Timing prototype tests completed	This milestone is satisfied when the tests of the prototype Control and Timing System have been completed and the results documented.
1.7.2.3.1.3	Networking requirements approved	This milestone is satisfied when the networking requirements for the DAQ have been documented, reviewed and approved by the L2 manager.
1.7.2.3.4	Evaluation components received for networking system.	This milestone is satisfied when all of the networking components have been received such that the network can be evaluated and the performance documented.
1.7.2.4.1.3	Control Room requirements approved	This milestone is satisfied when the document describing the Control room requirements has been approved by the L2 manager.
1.7.2.4.3	Evaluation components received for control room	This milestone is satisfied when all of the Control Room components have been received such that the system can be evaluated and the performance documented.
1.7.2.5.1.3	Requirements approved for buffer farm	This milestone is satisfied when the requirements document for Buffer Farm has been approved by the L2 manager.
1.7.2.5.3	Evaluation components received for buffer farm	This milestone is satisfied once the Buffer Farm components for evaluation have been received and evaluation may proceed.
1.7.2.6.1.3	Data storage requirements approved	This milestone is satisfied when the Data Storage requirements documentation has been approved by the L2 manager.
1.7.2.6.3	Evaluation components received for data storage system	This milestone has been reached when the components required for Data Storage evaluation have been received and evaluation may proceed.
1.7.2.7.1.3	Cabling Requirements approved	This milestone is achieved when the cabling requirements documentation is approved by the L2 manager.
1.7.2.7.3	Evaluation components received for cabling	This milestone is satisfied when the components required for cabling evaluation have been received and evaluation may proceed.
1.7.4.11	Detector control system released	This milestone is satisfied when the Detector Control System software is released.
1.8.1.6	Baseline plane assembly adhesive selected	This milestone is satisfied when an adhesive has been selected for use in assembling PVC modules into planes.
1.8.1.11	Final adhesive for plane assembly selected.	This milestone is satisfied when the selection of the final adhesive for use in assembling PVC modules into planes has been made and the decision documented.
1.8.2.2.4	Far detector structural concept selected	This milestone is completed when conceptual designs for the structure of assembled Far Detector blocks and the relationship between adjacent blocks have been documented.
1.8.2.10	Structural design validated	The Project Office will conduct an engineering design review of FEA simulations of the Far Detector mechanical structure. Benchmarking tests of the FEA on smaller-scale prototypes and cross-checks on the analysis, where possible, will also be included. This milestone is satisfied once the review process has been completed and documented.
1.8.3.3.4	Safety review of far detector scintillator handling techniques completed	This milestone is satisfied when a review of the handling techniques for liquid scintillator at the Far Detector site has been completed and the results documented.
1.8.3.3.7	FD filling machine design completed	This milestone is satisfied when the design of the prototype Far Detector filling machine has been completed and documented.
1.8.4.1.10	Conceptual design review of near detector mechanical systems	This milestone is satisfied once a design review for the Near Detector mechanical systems has been completed and documented.

	completed	
1.8.4.5	30% design of Near Detector design complete	This milestone is satisfied when the 30% design of the Near Detector has been completed and documented.
1.8.5.1.5	IPND requirements documents completed	This milestone is satisfied when the document that describes the requirements for the mechanical systems for the IPND is completed and approved by the L2 manager.
1.8.5.2.7	IPND systems review completed	This milestone is satisfied when a review of the mechanical systems for the IPND has been completed and documented.
1.8.5.2.12	IPND systems designs completed	This milestone is satisfied when the design of the IPND block structure, lifting and support fixturing and infrastructure in the MINOS Service Building has been completed and documented.
1.8.5.4.5	IPND block assembly facility completed	This milestone is satisfied when the facility for assembling IPND blocks is completed and a readiness review has been completed and documented.
1.8.5.5.7	IPND blocks completed	This milestone is satisfied when all of the IPND blocks have been assembled and are ready for installation in the IPND enclosure.
1.8.5.6.1.4	Notice to proceed - Phase 1 of IPND infrastructure in MSB	The IPND enclosure is built in two phases that are separated by the installation of the IPND detector. This milestone is satisfied when notice to proceed on the first phase of construction has been issued.
1.8.5.6.1.6	Notice to proceed - Phase 2 of IPND infrastructure in MSB	The IPND enclosure is built in two phases that are separated by the installation of the IPND detector. This milestone is satisfied when notice to proceed on the final phase of construction has been issued.
1.8.5.6.1.11	Infrastructure contract work completed	This milestone is satisfied when all of the infrastructure and secondary containment work for the IPND enclosure has been completed.
1.8.5.6.2.4	Notice to proceed - Phase 1 of IPND containment	The secondary containment for the IPND is built in two phases that are separated by the installation of the IPND detector. This milestone is satisfied when notice to proceed on the first phase of construction has been issued.
1.8.5.6.2.6	Notice to proceed - Phase 2 of IPND containment	The secondary containment for the IPND is built in two phases that are separated by the installation of the IPND detector. This milestone is satisfied when notice to proceed on the final phase of construction has been issued.
1.8.5.6.3.5	Beneficial occupancy of IPND enclosure	This milestone is satisfied once beneficial occupancy has been granted for the IPND enclosure.
1.8.5.7.7	IPND module filling completed	This milestone is satisfied when all of the IPND modules have been filled with liquid scintillator.
1.8.5.7.11	IPND ready to take data	This milestone is satisfied when the IPND modules are filled with scintillator and fully outfitted with electronics that connect to an operational DAQ system.
1.8.6.1.10	Mechanical systems CD-1 design completed	This milestone is satisfied when the conceptual design of the Far Detector mechanical systems, required for CD-1 approval, is completed, documented and approved by the L2 manager.
1.8.6.2.15	Assembly fixtures CD-1 design completed	This milestone is satisfied when the conceptual design of the assembly fixtures for the Far Detector, required for CD-1 approval, is completed, documented and approved by the L2 manager.
1.8.6.4	30% design of FD mechanical system and tooling complete	The 30% design for the Far Detector assembly fixtures and tooling has been completed, reviewed and documented.
1.8.7.6	Far detector installation procedures completed	This milestone is satisfied once the installation procedures for the Far Detector have been completed and documented.
1.8.7.7	FD installation procedure value engineering completed	This milestone is satisfied when the value engineering study for the Far Detector installation procedure has been completed and the results documented.
1.8.8.1.13	Full-scale block assembly prototype testing completed	This milestone is satisfied when the tests of the full-scale assembly prototype have been completed and documented.
1.8.8.2.6	Select site for block installation at FNAL	This milestone is completed when a site at Fermilab has been selected by the Project Manager for the full-height engineering prototype test.
1.8.8.2.17	Full-height engineering prototype testing started	This milestone has been satisfied once the full-height engineering prototype has been constructed, an operational readiness review has been completed and the prototype is ready to be filled with liquid.

1.8.8.2.18	Full-height engineering prototype testing completed	This milestone is satisfied when testing of the full-height engineering prototype has been completed and documented.
1.9.4.1	CD-0	DOE signs off on Critical Decision CD-0 – approval of mission need
1.9.4.2	CD-1	DOE signs off on Critical Decision CD-1
1.9.5.5	Cooperative-agreement institution determined	DOE identifies the institution that will enter into the cooperative agreement for the far detector site and building construction.
1.9.5.6	Acquisition strategy approved by DOE	The NOVA project acquisition strategy document is approved by the DOE
1.9.5.10	Cooperative-agreement in place	The cooperative agreement between DOE and the designated CA institution is signed by all parties.
1.9.5.15	Cooperative-agreement funds available	Initial funding based on the approved cooperative agreement is available for obligation by the cooperative agreement institution
1.9.5.20	Far detector site selected	The specific location of the far detector site is chosen.
1.9.5.25	Building conceptual design frozen (FESS)	FNAL Facilities Engineering Services Section freezes their initial conceptual design for the far detector site and building.
1.9.4.3	CD-2	DOE signs off on Critical Decision CD-2 – Baseline approval
2.0.1.1.5.1	Recycler Ring (RR); 53 MHz RF Ready for Beam	53 MHz cavities installed and power tested. Vacuum in the area has been reconstituted.
2.0.1.1.5.2	RR; Permanent Magnet Quads Refurbished & Mapped	38 permanent magnet quadrupoles will be removed from the tunnel, taken to TD, refurbished (to accommodate requested strength), and measured. This milestone marks the point where all magnets have gone through the process.
2.0.1.1.5.3	RR; Orders Placed for Copper for 53 MHz RF	Requisition issued to purchase copper to be used in the construction of the RR 53 MHz cavities.
2.0.1.1.5.4	RR; ADCW Magnet Refurbish Complete	The ADCW is a wide gap ADC magnet. All necessary magnets (3+1 hot spare) have had their gaps widened, been power tested, and mapped.
2.0.1.1.5.5	RR; LCW System Mods Complete	RR LCW Systems on line and operational
2.0.1.2.8.1	Gap Clearing / RR Injection Kicker Magnet Design Complete	After the final high voltage testing of one pre-production RR Injection magnet, the L4 manager decides to accept the design as final and go ahead with ordering parts for all production magnets.
2.0.1.2.8.2	RR; Extraction MI Injection Line Kicker Checkout/Test Complete	This Milestone is complete after the RR Extraction & MI Injection Line kicker magnets are installed with all cable and fluorinert piping, and tested with the pulser system, the checkout/test is complete and the kicker system is ready for beam.
2.0.1.2.8.3	RR; Beam Abort Kicker Checkout/Test Complete	This Milestone is complete after the RR Beam Abort Line kicker magnet is installed with all cable and fluorinert piping, and tested with the pulser system, the checkout/test is complete and the kicker system is ready for beam.
2.0.1.2.8.4	RR; Injection & Gap Clearing Magnets & Fluorinert Piping in Tunnel Checkout/Test Complete	This Milestone is complete after the RR Injection Line and Gap Clearing Line kicker magnets are installed with all cable and fluorinert piping, and tested with the pulser systems, the checkout/test is complete and the kicker systems are ready for beam.
2.0.1.2.8.5	RR; All Kicker Systems Ready for Beam	This Milestone is complete when all kicker systems are installed and tested and ready for beam. This includes the RR Injection, RR Gap Clearing, RR Extraction, MI Injection, and the RR Beam Abort kicker systems.
2.0.1.3.4.3	RR; DCCT Ready for Installation	DCCT in hand, inspected, calibrated, cleaned, and ready for installation.
2.0.1.3.4.5	RR; BPM System Procurement Complete	Purchased, received and inspected cables/connectors/transition boards for the RR BPM upgrade project.
2.0.1.3.4.6	RR; BPM Transition Boards Ready for Installation	All 216 BPM transition boards passed testing and are ready for installation.
2.0.2.1.4.1	Main Injector (MI); Vertical Quad Bus	The new transformer has been installed and tested, and the power supply modifications are complete.

	Upgrade Complete	
2.0.2.2.5.1	MI; RF Cavities Bus Bar Fabrication & Installation Complete	The bus bars for the 2 new RF stations have been fabricated and installed and tested.
2.0.2.2.5.2	MI; RF Cavities Fabrication of Ferrite Bias Supplies Complete	The fabrications of the two new bias supplies have been completed.
2.0.2.2.5.3	MI; RF Cavities Fabrication of Modulators Complete	The fabrications of the two new modulator supplies have been completed.
2.0.2.2.5.4	MI; RF Cavities (2) Installation & Testing Complete	The two MI RF cavities have been installed in the tunnel and testing without beam has been completed and the results documented.
2.0.2.2.5.5	MI; LCW System Mods Complete	MI LCW Systems on line and operational
2.0.3.1.5.1	NuMI; Charging PS Upgrades Testing Complete	The upgraded charging power supply for the NuMI extraction kicker has been assembled, tested, and approved for operational use.
2.0.3.1.5.2	NuMI; Primary Beamline Ready for Faster Cycle Time	The NuMI Primary Beamline has been tested and is capable of operating at a 1.33 second repetition rate. This includes the upgrade to the NuMI extraction kicker, the installation of the replacement quadrupole magnets, and the operation of the improved regulation of the dipole power supplies.
2.0.3.2.3.1	NuMI; Begin Baffle Procurement	The design of the target baffle has been completed with signed off drawings and a design review such that the procurement of the baffle can begin.
2.0.3.2.3.2	NuMI; Baffle Delivered	The baffle for the medium energy target has been delivered to Fermilab and has been inspected and accepted for installation into the target carrier
2.0.3.2.3.3	NuMI; ME Target/Carrier/Baffle Assembly Complete	The medium energy target, the baffle, and the target carrier have been assembled into a single unit that is ready for installation into the target chase.
2.0.3.2.3.4	NuMI; Target Carrier Delivered	The target carrier has been delivered to Fermilab, inspected, and approved.
2.0.3.2.3.7	NuMI; IHEP ME Target Accord Signed	An accord for the construction and delivery of a medium energy target has been written, approved, and signed by IHEP, Protvino and Fermilab.
2.0.3.2.3.8	Replacement Hadron Monitor Delivered	The replacement Hadron Monitor has been delivered to Fermilab, and has been inspected, and approved for installation.
2.0.3.3.4.1	NuMI; Shielding Blocks & Carriage Complete	This milestone defines the receipt of shielding & support components after fabrication from the vendor. These components are now ready for installation in the target hall. It includes fabrication completion and installation readiness of the following items: 1. Shielding blocks and 2. Carriage Assembly.
2.0.3.3.4.2	NuMI; Installation of Target Chase Cooling Complete	This milestone defines the completion of the Target Chase Cooling upgrades installation and successful testing & troubleshooting of all components with all systems online and operational.
2.0.3.3.4.3	NuMI; Stripline Assembly Complete	This milestone defines the completion of the Horn 2 stripline extension and stand components assembly. The stripline assembly is now ready for installation in the target hall.
2.0.3.4.4.2	NuMI; RAW Systems Mods Complete	NuMI RAW Systems on line and operational
2.0.3.4.4.3	NuMI; Cooling Water (Non-RAW) Mods Complete	NuMI Non-RAW Systems on line and operational
2.0.4.3.1	ANU Approval to Proceed with Project	This marks the date at which the original efforts on ANU were authorized to proceed (this was before ANU was incorporated into NOVA).
2.0.4.3.12	Start of ANU Accounting	This is the date at which accounting on the TPC began.

2.0.4.3.13	ANU Shielding Assessment Updates Complete	This milestone is defined as the point at which the MI and NuMI/MINOS Shielding Assessments have been updated/appended for NOvA operation and approved as defined in Fermilab Radiological Control Manual (FRCM) Chapter 8.
2.0.4.3.14	Ready for Shutdown to Install Accelerator Upgrades	All necessary preparation and planning work complete in order to begin the Accelerator Upgrades Shutdown.
2.0.4.3.15	MI Ring Modifications Ready for Beam Transport	All the NOvA Main Injector modifications have been completed and tested as appropriate and the machine is ready for beam transport.
2.0.4.3.16	RR; Modifications Ready for Beam Transport	This milestone is defined as the completion of the NOvA Recycler Ring modifications for beam transport. It includes the installation, testing, alignment, and vacuum certification of all the beamline elements (magnets, instrumentation, kickers) for injection into the Recycler from the MI8 line and extraction from the Recycler to the Main Injector.
2.0.4.3.17	Ready to Commission Upgrades with Medium Energy Neutrino Beam	Milestones for RR and MI ready for beam transport completed. The Target Hall has been reconfigured to the medium energy optics and the medium energy target has been installed in the target chase and tested. Horn 2 has been relocated to the medium energy position, connected to the extended stripline and tested. Also all NOvA upgrades for higher beam power down the NuMI line have been completed and tested as appropriate.
2.0.4.3.21	ANU Subproject Complete	The Ready to Commission Upgrades with Medium Energy Neutrino Beam milestone has been satisfied, all ANU cost accounts have been closed out and as-built documents have been completed.
2.0.4.4.1.2	Off Project: Gap Clearing Kicker System Ready for Installation	The gap clearing kicker system is ready for installation in the Recycler Ring.
2.0.4.4.1.3	Off-Project: Receive & Inspect ceramic beamtubes for RR Inj, Gap Clearing & MI Magnets	Ceramic beamtubes purchased off-project have been received at Fermilab, inspected, and accepted for use.
2.0.4.4.1.4	Off-Project:: MI-14 SB Construction Complete	Beneficial Occupancy is obtained for MI-14 allowing technical component installation to begin.
2.0.4.4.1.5	Off-Project:: MI-39 SB Construction Complete	Beneficial Occupancy is obtained for MI-39 allowing technical component installation to begin.
2.0.4.4.1.6	Off-Project:: MI-60 Anode Supply Room Construction Complete	Beneficial Occupancy is obtained for MI-60 APS Room allowing for the installation of technical components to begin.
2.0.4.4.2.8	Off-Project: NuMI Horn 1 Modules Installed in Chase Complete	The Horn 1 (ANU) has been attached to the Horn 1 Module, installed in the target chase. The stripline, water, and electrical connections have all been completed.
2.0.4.4.2.11	Off-Project: Work Cell & Equipment Ready for ANU Operation	The Work Cell and Equipment has been assembled in the target hall and is ready for use.
2.0.4.4.2.12	Off-Project:: RCRP Equipment & Procedures Ready for ANU Operations	The RCRP (Radioactive Component Repair/Removal Plan) has been completed and is ready for ANU operations.
2.0.4.4.2.13	Off-Project:: NuMI Modified Horn 1 Ready for Installation	The Horn 1 (ANU) has been assembled, tested on the test stand, and the magnetic field mapping has been completed.
2.0.4.4.2.39	Off-Project:: Radioactive Component Repairs/Removal Conceptual Design Review Complete	A review of the Radioactive Component Repair/Removal Conceptual Design has been completed and a report transmitted to the L2 manager.

2.0.4.4.2.40	Off Project: Profile Monitor Conceptual Design Complete	The Conceptual Design for the Profile Monitor has been completed
2.1.1.1.2	Issue RFP to A/E for Title 2 for Site Prep Package	This milestone is complete when a Request for Proposals has been issued to a list of A&E firms to bid on Title 2 design package for preparation of the Far Detector Hall site.
2.1.1.1.7	PO Released for Title 2 for Site Prep Package	The purchase order is issued to the A&E firm that wins the competitive bid to perform the Title 2 design for preparation of the Far Detector Hall site.
2.1.1.1.21	Site Prep Package Title 2 Complete	This milestone is complete when the Title 2 design of the Far Detector Hall site preparation package has been finished and the report transmitted to the L2 manager.
2.1.1.2.2	Wetland permit submitted	This milestone marks the point where the wetland permit has been submitted to the U.S. Army Corps of Engineers
2.1.1.2.6	Wetland Permit Issued	This milestone marks the point where a U.S. Army Corps of Engineer wetland permit is issued.
2.1.1.3.4	Issued RFP for Site Prep Package	This milestone is complete when a Request for Proposals has been issued to a list of construction firms to bid on the preparation work for the Far Detector Hall site.
2.1.1.3.7	Site preparation purchase order released	The purchase order is issued to the construction firm that wins the competitive bidding to execute the preparation work at the Far Detector Hall site.
2.1.1.4.1	Notice to proceed - far detector site preparation package	This milestone marks the point where construction on the Site Prep package may begin
2.1.1.4.7	Beneficial occupancy - far detector site preparation package	This milestone marks the point where the Site Prep package has been completed to a point where other subcontractors may begin to use the road
2.1.1.4.9	Final acceptance - far detector site preparation package	This milestone marks the point where all work is complete on the Site Preparation package.
2.1.2.1.2	Issue request for proposal to A/E	This milestone is complete when a Request for Proposals has been issued to a list of A&E firms to bid on Title 2 design package for the Far Detector Hall.
2.1.2.1.7	PO issued for Title 2 for Far Detector Building	The purchase order is issued to the A&E firm that wins the competitive bid to perform the Title 2 design of the Far Detector Hall.
2.1.2.1.21	Far Detector Building Title 2 Complete	This milestone is complete when the Title 2 design of the Far Detector Hall has been finished and the construction documents are transmitted to the L2 manager.
2.1.2.2.4	Issue RFP for Far Detector Building	This milestone is complete when a Request for Proposals has been issued to a list of construction firms to bid on the construction of the Far Detector Hall.
2.1.2.2.7	Purchase order released - far detector building	The purchase order has been issued to the construction firm that is awarded the contract to construct the Far Detector Hall.
2.1.2.3.1.1	Notice to proceed - DE/AA concrete	This milestone marks the point where construction on the Detector Enclosure and Assembly Area concrete work may begin
2.1.2.3.1.11	Detector enclosure/assembly area concrete completed	This milestone marks the point where all concrete work is completed on the detector enclosure and assembly area.
2.1.2.3.2.18	Outfitting completed	This milestone marks the point where all of the building outfitting, including walkways, secondary containment, electrical rough-ins, elevator, cranes, and movable access platforms, has been completed.
2.1.2.3.3	Beneficial occupancy - far detector building construction	This milestone marks the point where the Far Detector Building is essential complete and other subcontractors and NOvA Project personnel may begin to share the building.
2.1.2.3.5	Final acceptance - far detector building construction	This milestone marks the point where the Far Detector Building is complete.
2.2.1.4	Mineral oil PO issued	The purchase order for 3,082,145 gal of mineral oil is issued to the vendor.

2.2.1.5.1	Mineral oil production and delivery begins	The first delivery of mineral oil for liquid scintillator has been received by the toll blender. Deliveries will continue for 3 years.
2.2.1.5.5	Mineral oil production and delivery 25% completed	770,536 gal of mineral oil, corresponding to 25% of the total, has been received by the toll blender.
2.2.1.5.6	Mineral oil production and delivery 50% completed	1,541,073 gal of mineral oil, corresponding to 50% of the total, has been received at the toll blender.
2.2.1.5.7	Mineral oil production and delivery 75% completed	2,311,609 gal of mineral oil, corresponding to 75% of the total, has been delivered to the toll blender.
2.2.1.5.8	Mineral oil production and delivery completed	3,082,145 gal of mineral oil, corresponding to 100% of the total, has been received by the toll blender.
2.2.2.4	Pseudocumene PO issued	The purchase order for 128,439 gal of pseudocumene is issued to the vendor.
2.2.2.5.1	Pseudocumene production and delivery begins	The first delivery of pseudocumene for liquid scintillator has been received by the toll blender. Deliveries will continue over 3 years.
2.2.2.5.5	Pseudocumene production and delivery 25% completed	32,110 gal of pseudocumene, corresponding to 25% of the total, has been received by the toll blender.
2.2.2.5.6	Pseudocumene production and delivery 50% completed	64,220 gal of pseudocumene, corresponding to 50% of the total, has been delivered to the toll blender.
2.2.2.5.7	Pseudocumene production and delivery 75% completed	96,329 gal of pseudocumene, corresponding to 75% of the total, has been delivered to the toll blender.
2.2.2.5.8	Pseudocumene production and delivery completed	128,439 gal of pseudocumene, corresponding to 100% of the total, has been received by the toll blender.
2.2.3.4	Waveshifter PO issued	A purchase order for the 9,373 kg of PPO and 131 kg of bis-MSB required for production scintillator blending is issued to the vendor.
2.2.3.5.1	Waveshifter production and delivery begins	Waveshifter production begins and the first shipment is delivered to the toll blender. Periodic shipments will continue over two years.
2.2.3.5.4	Waveshifter production 15% completed	The first 15% of the waveshifters, corresponding to 1,406 kg of PPO and 19.7 kg of bis-MSB, have been delivered to the toll blender.
2.2.3.5.5	Waveshifter production completed	The full quantity of 9,373 kg of PPO and 131 kg of bis-MSB has been delivered to the toll blender.
2.2.4.1.4	Toll blending PO issued	A purchase order for blending the 3,210,584 gal of liquid scintillator required for the near and far detectors at a toll blender is issued to the vendor.
2.2.4.3.5	Scintillator blending begins	The first production batch of liquid scintillator has been blended at the toll blender and is ready for shipment.
2.2.4.3.6	Scintillator production for superblock 1 completed	The blending and QA/QC of 496,994 gal of liquid scintillator, corresponding to the volume required for the first Far Detector superblock, has been completed.
2.2.4.3.7	Scintillator production for superblock 2 completed	The blending and QA/QC of 993,998 gal of scintillator, corresponding to the volume required for the first two superblocks, has been completed.
2.2.4.3.8	Scintillator production for superblock 3 completed	The blending and QA/QC of 1,490,982 gal of scintillator, corresponding to the volume required for the first 3 superblocks, has been completed.
2.2.4.3.9	Scintillator production for superblock 4 completed	The blending and QA/QC of 1,987,976 gal of scintillator, corresponding to the volume required for the first 4 superblocks, has been completed.
2.2.4.3.10	Scintillator production for superblock 5 completed	The blending and QA/QC of 2,484,970 gal of scintillator, corresponding to the volume required for the first 5 superblocks, has been completed.
2.2.4.3.11	Scintillator production for superblock 6	The blending and QA/QC of 2,981,964 gal of scintillator, corresponding to the volume required for the first 6 superblocks, has

	completed	been completed.
2.2.4.3.12	Scintillator production for superblock 7 completed	The blending and QA/QC of 3,210,584 gal of scintillator, corresponding to the volume required for the first 7 superblocks, has been completed.
2.2.4.3.90	Scintillator production for 15 kt completed	The blending and QA/QC of liquid scintillator required for a 15 kt detector has been completed.
2.2.5.3.39	Scintillator delivery for first superblock completed	The 496,994 gal of scintillator required for superblock 1 has been shipped from the toll blender and received at the Far Detector site.
2.2.5.3.40	Scintillator delivery for all blocks completed	3,210,584 gal of scintillator, corresponding to 100% of the total, has been delivered to Ash River.
2.3.1.5	WLS fiber PO issued	The purchase order for the WLS fiber for the Near and Far detectors has been released to the vendor and fiber production can proceed.
2.3.2.1.6	WLS fiber production begins	This milestone is satisfied when the vendor informs us that fiber production for NOvA has started.
2.3.2.1.7	WLS fiber production 3% complete	450 km of fiber has been produced and delivered by the vendor.
2.3.2.1.8	WLS fiber production 35% complete	4,950 km of fiber has been produced and delivered by the vendor.
2.3.2.1.9	WLS fiber production 70% complete	9,450 km of fiber has been produced and delivered by the vendor.
2.3.2.1.14	WLS fiber for 15 kt detector produced and delivered	13,000 km of fiber has been produced and delivered by the vendor (15 kt detector).
2.4.1.1.5	Extrusion PO issued	A contract to fabricate Horizontal and Vertical dies and associated hardware and to extrude PVC according to NovA schedule is issued to the vendor.
2.4.1.2.5	Raw material Pos issued	A contract to produce a custom PVC resin on a time scale that is consistent with the NovA schedule is issued to the vendor.
2.4.2.1.4	First horizontal extrusions available for evaluation	The first horizontal test extrusions from the preproduction run are completed and available for evaluation.
2.4.2.1.13	Pre-production horizontal extrusions authorized	Tuning of the extruding process and the die geometry for horizontal extrusions is complete.
2.4.2.2.4	First vertical extrusions available for evaluation	The first vertical test extrusions from the preproduction run are completed and available for evaluation.
2.4.2.2.13	Pre-production vertical extrusions authorized	Tuning of the extruding process and the die geometry for vertical extrusions is complete
2.4.3.1.1.5	Near detector horizontal extrusions completed	The horizontal extrusions required for the Near Detector have been extruded, QA has been completed and the extrusions are ready to be shipped to the module factory.
2.4.3.1.2.5	Near detector vertical extrusions completed	The vertical extrusions required for the Near Detector have been extruded, QA has been completed and the extrusions are ready to be shipped to the module factory.
2.4.3.2.1.1.1	Production of horizontal extrusions authorized	After satisfying all of the preproduction requirements, the L2 manager authorizes the extrusion vendor to begin production of horizontal extrusions for the Far Detector.
2.4.3.2.1.2.1	Production of vertical extrusions authorized	After satisfying all of the preproduction requirements, the L2 manager authorizes the extrusion vendor to begin production of vertical extrusions for the Far Detector.
2.4.3.2.44.1	Far detector extrusion production started	After satisfying all of the preproduction requirements, the L2 manager authorizes the extrusion vendor to begin production of extrusions for the Far Detector.
2.4.3.2.44.2	Extrusions for superblock 1 produced	The vertical and horizontal extrusions required for superblock 1 have been extruded and QA has been completed and documented.
2.4.3.2.44.3	Extrusions for superblock 2 produced	The vertical and horizontal extrusions required for superblock 2 have been extruded and QA has been completed and documented.
2.4.3.2.44.4	Extrusions for superblock 3 produced	The vertical and horizontal extrusions required for superblock 3 have been extruded and QA has been completed and documented.

2.4.3.2.44.5	Extrusions for superblock 4 produced	The vertical and horizontal extrusions required for superblock 4 have been extruded and QA has been completed and documented.
2.4.3.2.44.6	Extrusions for superblock 5 produced	The vertical and horizontal extrusions required for superblock 5 have been extruded and QA has been completed and documented.
2.4.3.2.44.7	Extrusions for superblock 6 produced	The vertical and horizontal extrusions required for superblock 6 have been extruded and QA has been completed and documented.
2.4.3.2.44.8	Extrusions for superblock 7 produced	The vertical and horizontal extrusions required for superblock 7 have been extruded and QA has been completed and documented.
2.4.3.2.44.10	Far Detector extrusions for 15 kt completed	All vertical and horizontal extrusions required for a 15 kt Far Detector have been extruded and QA has been completed and documented.
2.5.1.1.5	Manifold production purchase orders released	Completed purchase orders have been issued to the vendor.
2.5.1.2.5	End plate and seals production purchase orders released	Completed purchase orders have been issued to the vendor.
2.5.2.5	Optical connector production purchase order released	Completed purchase orders have been issued to the vendor.
2.5.3.2.6.9	Factory infrastructure completed for block 1 module production	Enough factory machines, tooling, and material handling, procedures, and factory infrastructure outfitting is completed to begin assembling the first module.
2.5.3.2.6.10	Factory infrastructure completed for block 2 module production	Enough factory machines, tooling, and material handling, procedures, and factory infrastructure outfitting is completed to begin assembling the second block's worth of modules at a faster rate defined in the cost and schedule.
2.5.3.2.6.11	Factory infrastructure completed for block 3 (full rate) module production	Enough factory machines, tooling, and material handling, procedures, and factory infrastructure outfitting is completed to begin assembling modules at the full production rate.
2.5.3.3.2.45.44	Far detector module assembly started	Started is defined as the beginning of assembly of the first far detector module.
2.5.3.3.2.45.45	Far detector modules for superblock 1 completed	Completed is defined as all modules having been assembled and tested.
2.5.3.3.2.45.50	Far detector modules for superblock 2 completed	Completed is defined as all modules having been assembled and tested.
2.5.3.3.2.45.60	Far detector modules for superblock 3 completed	Completed is defined as all modules having been assembled and tested.
2.5.3.3.2.45.70	Far detector modules for superblock 4 completed	Completed is defined as all modules having been assembled and tested.
2.5.3.3.2.45.80	Far detector modules for superblock 5 completed	Completed is defined as all modules having been assembled and tested.
2.5.3.3.2.45.90	Far detector modules for superblock 6 completed	Completed is defined as all modules having been assembled and tested.
2.5.3.3.2.45.110	Far detector modules for superblock 7 completed	Completed is defined as all modules having been assembled and tested.
2.5.3.3.2.45.120	Far detector modules for 15 kt detector shipped	Modules for a 15 kt Far Detector have been assembled, tested and shipped to detector site.
2.5.3.3.3.2	Near detector module fabrication started	Started is defined as the beginning of assembly of the first near detector module.
2.5.3.3.3.6	All near detector modules completed	Completed is defined as all near detector modules having been assembled and tested.
2.6.1.1.1.2	POs released-manufactured parts	The purchase orders for the parts required for the APD housings have all been issued to the respective vendors.
2.6.1.1.2.2	PO released-TE coolers	The purchase order for the thermo-electric coolers has been released to the vendor.
2.6.1.1.4	APD housings completed and tested - superblock 1	This milestone is satisfied once the APD housings required for superblock 1 have been assembled and QA completed.
2.6.1.1.5	APD housings completed and tested - superblock 2	This milestone is satisfied once the APD housings required for the first 2 superblocks have been assembled and QA completed.
2.6.1.1.6	APD housings completed and tested - superblock 3	This milestone is satisfied once the APD housings required for first 3 superblocks have been assembled and QA completed.

2.6.1.1.7	APD housings completed and tested - superblock 4	This milestone is satisfied once the APD housings required for first 4 superblocks have been assembled and QA completed.
2.6.1.1.8	APD housings completed and tested - superblock 5	This milestone is satisfied once the APD housings required for first 5 superblocks have been assembled and QA completed.
2.6.1.1.9	APD housings completed and tested - superblock6	This milestone is satisfied once the APD housings required for first 6 superblocks have been assembled and QA completed.
2.6.1.1.10	APD housings completed and tested - superblock 7	This milestone is satisfied once the APD housings required 7or first 3 superblocks have been assembled and QA completed.
2.6.1.1.11	All APD housings completed and tested	This milestone is satisfied when all APD housings required for near and far detectors have been assembled and QA completed.
2.6.1.2.2	PO released-APDs	The purchase order for APD Array production is released to the vendor.
2.6.1.2.5.1	APDs for superblock 1 delivered	The APD arrays required for superblock 1 have been received from Hamamatsu.
2.6.1.2.5.2	APDs for superblock 2 delivered	The APD arrays required for the first 2 superblocks have been received from Hamamatsu.
2.6.1.2.5.3	APDs for superblock 3 delivered	The APD arrays for the first 3 superblocks have been received from Hamamatsu.
2.6.1.2.5.4	APDs for superblock 4 delivered	The APD arrays for the first 4 superblocks have been received from Hamamatsu.
2.6.1.2.5.5	APDs for superblock 5 delivered	The APD arrays for the first 5 superblocks have been received from Hamamatsu.
2.6.1.2.5.6	APDs for superblock 6 delivered	The APD arrays for the first 6 superblocks have been received from Hamamatsu.
2.6.1.2.5.7	APDs for superblock 7 delivered	The APD arrays for the first 7 superblocks have been received from Hamamatsu.
2.6.1.2.5.8	All APD arrays delivered	All of the APD arrays required for the near and far detectors have been received from Hamamatsu.
2.6.1.3.47	APD modules assembled and tested	All APD modules required for the near and far detectors have been assembled and tested.
2.6.1.4.47	All Far Detector APD modules shipped	All Far Detector APD modules shipped to far site
2.6.2.2.3	Front-end board fabrication and assembly completed	All of the front-end boards and front-end board assemblies required for the near and far detectors have been completed and tested.
2.6.2.3.1	FEB modules for near detector started	This milestone is satisfied once assembly of the front-end modules for the near detector has started.
2.6.2.3.5	FEB modules for near detector completed	This milestone is satisfied once the front-end modules required for the near detector have been completed and fully tested.
2.6.3.6.3	Cooling system hardware delivered	This milestone is satisfied once the complete set of cooling systems for the far detector have been delivered to the far detector site.
2.7.1.1.1.6	Error handling system for software second release	This milestone is satisfied when the second version of the DAQ error handling system has been tested, documented and released for use.
2.7.1.1.2.6	Error handling system for software third release	This milestone is satisfied when the third version of the DAQ error handling system has been tested, documented and released for use.
2.7.1.2.1.6	Message passing system for software second release	This milestone is satisfied when the second version of the DAQ Message Passing System has been designed, evaluated, documented and released for use.
2.7.1.3.1.10	Run control system for software second release	This milestone is satisfied when the second version of the software for the Run Control System has been verified, documented and is released for use.
2.7.1.3.2.6	Run control system fourth release	This milestone is satisfied when the fourth version of the DAQ Run Control system has been tested, documented and released for use.
2.7.1.4.1.6	Event buffer farm core software for software second release	This milestone is satisfied when the second version of the Event Buffer Farm core software has been verified, documented and is released for use.
2.7.1.4.2.6	Event buffer farm server for software second release	This milestone is satisfied when the second version of the Event Buffer Farm Server software has been verified, documented and is released for use.

2.7.1.4.3.6	Event buffer farm server for software third release	This milestone is satisfied when the third version of the Event Buffer Farm Server software has been verified, documented and is released for use.
2.7.1.5.8	Data logger server for software second release	This milestone is satisfied when the second version of the Data Logger Server software has been verified, documented and is released for use.
2.7.1.6.11	Data file transfer system for software second release	This milestone is satisfied when the second version of the Data File Transfer System has been tested, documented and released for use.
2.7.1.7.11	DAQ monitoring system for software second release	This milestone is satisfied when the second version of the DAQ monitoring software has been tested, documented and released for use.
2.7.1.8.14	Event monitoring system for software second release	This milestone is satisfied when the second version of the DAQ Event Monitoring System has been tested, documented and released for use.
2.7.1.9.14	Event display software for software second release	This milestone is satisfied when the second version of the Event Display software has been verified, documented and is released for use.
2.7.1.10.2.3	Release integration database servers for use	This milestone is satisfied when the online integration database has been released.
2.7.1.10.3.3	Release production database servers for use	This milestone is satisfied when the online database has been deployed on the production servers, is fully configured and released for use.
2.7.1.10.4.1.7	Deploy online calibration application in production environment	This milestone is satisfied when the online calibration software has been fully integrated, tested, documented and implemented in the production environment.
2.7.1.10.4.2.7	Deploy online run history application in production environment	This milestone is satisfied when the online run history application has been fully integrated, tested, documented and implemented in the production environment.
2.7.1.10.4.3.7	Deploy online monitoring application in production environment	This milestone is satisfied when the online monitoring system has been fully integrated, tested, documented and implemented in the production environment.
2.7.2.1.2.7	Release production hold	This milestone has been satisfied when evaluation of first production articles for the Data Concentrator Modules is complete and successful. This allows for production to resume.
2.7.2.1.2.8	Production data concentrators received	This milestone is satisfied when all of the Data Concentrator Modules required for the Near and Far detectors have been received.
2.7.2.2.2.2	Pre-production PCBs and components received for Timing and Control System	This milestone is satisfied when the PC boards and all necessary components for the pre-production version of the Timing and Control System have been received.
2.7.2.2.4	Production approved for Timing and Control System.	This milestone is satisfied when the pre-production components for the Timing and Control System have been fully tested and documented and the L2 manager has approved manufacture of the production components.
2.8.1.1.5	Administrative and safety signoffs on ear Detector (ND) excavation design	Excavation design is certified as buildable and safe. This milestone is satisfied when the Project Mechanical Engineer or his designee signs off.
2.8.1.3.4	Notice to Proceed on phase 1 of tunnel infrastructure contract	This milestone is satisfied once a contractor has been selected and they are ready to begin the first phase of the tunnel infrastructure work to move the MINOS utilities.
2.8.1.3.6	Notice to Proceed on phase 2 of tunnel infrastructure contract	This milestone is satisfied once the cavern excavation is complete and the contractor is ready to begin the second phase of the infrastructure work that includes safety systems, lighting and HVAC.
2.8.1.3.12	Infrastructure contract completed	This milestone is satisfied when the contractor has completed all of the Near Detector infrastructure work and only the FIRUS installation is still needed for beneficial occupancy.
2.8.1.4.4	Notice to Proceed – ND excavation	This milestone has been satisfied once the MINOS utilities have been moved, a contractor has been selected and they are ready to begin excavation of the Near Detector cavern.
2.8.1.4.7	ND Excavation contract completed	This milestone is satisfied when the cavern excavation has been completed.

2.8.1.7	Beneficial occupancy of new cavern	This milestone is satisfied when all cavern work has been completed and the cavern is ready for detector installation.
2.8.2.2.3	Muon catcher mechanical construction completed	This milestone is satisfied when the muon planes have been assembled, attached to the steel, moved underground and connected to the support structure.
2.8.2.3.1.2	Release of four blocks from IPND to ND	This milestone is satisfied when operation of the IPND is terminated and preparations may begin to prepare the blocks to be moved underground.
2.8.2.3.2.2.1	Modules for final two blocks available	The Near Detector consists of the four IPND blocks plus two additional blocks. This milestone is satisfied when the modules for the two additional blocks have been completed.
2.8.2.6	Muon catcher, all blocks and bookend in place	The Near detector mechanical construction is complete. The six blocks and the muon catcher are in place and captured between the two bookends. The detector is ready to be filled with liquid scintillator.
2.8.3.7	Shaft and Near Detector containment systems ready to accept scintillator	Both the Near Detector secondary containment and the secondary containment for the MINOS shaft are in place and ready to support scintillator filling.
2.8.4.6.1.2	Operational readiness approved for ND	This milestone is satisfied once Fermilab has performed an operational readiness review of the Near detector and given the OK to begin operations.
2.8.4.6.3	First cosmic ray tracks observed in near detector	The Near Detector, including the DAQ, is fully operational and cosmic rays are observed in the detector.
2.8.4.6.4	First NuMI beam events observed in near detector	The Near Detector, including the DAQ, is fully operational and neutrino events from the NuMI beam are observed in the detector.
2.8.4.6.5	Near detector completed and ready to operate	The Near Detector is fully complete, all approvals have been obtained and the detector is ready for continuous, un-manned operation.
2.9.1.1.3	Final design approved - module lifting fixture	Milestone achieved when the lifting fixture design is documented and approved for production by the L2 manager.
2.9.1.1.9	Module lifting fixtures completed	Milestone completed when the vacuum lifting fixtures are produced and are approved for use.
2.9.1.1.11	Module lifting fixtures ready for shipping	Milestone completed when the operation of the module lifting fixtures has been documented, operational readiness clearance has been granted and they have been disassembled and packed for shipping.
2.9.1.2.7	Adhesive dispenser completed	Milestone completed when the operation of the adhesive dispenser has been documented, operational readiness clearance has been granted.
2.9.1.2.9	Adhesive dispenser ready for shipping	Milestone achieved when the adhesive dispenser has been completed, tested, disassembled and packed for shipping.
2.9.1.3.8	Block safety constraint completed	Milestone achieved when the block safety beam has been constructed, documented and passed a readiness review.
2.9.1.3.10	Constraint beam ready for shipping	Milestone achieved when the block safety beam has been completed, tested, disassembled and packed for shipping.
2.9.1.4.3	Final design approved - block pivoter and pallet	Milestone achieved when the block pivoter design has been documented and approved by the L2 manager.
2.9.1.4.14	Block pivoter completed	Milestone achieved when the block pivoter has been built, tested
2.9.1.4.16	Block pivoter ready for shipping	Milestone achieved when the block pivoter has been constructed, documented, passed a readiness review, disassembled and packed for shipping to the Far Detector site.
2.9.1.5.4	Survey equipment ready for assembly	Milestone achieved when the survey equipment has been procured and all procedures for the assembly process have been approved.
2.9.2.2.21.3	Final design approved-south bookend	Milestone achieved when the south bookend has been designed, documented and approved for production by the L2 manager.
2.9.2.2.21.6	South bookend components ready for shipment	Milestone achieved when the components of the south bookend are ready to ship to the Ash River site.
2.9.2.2.22.3	Final design approved-north bookend	Milestone achieved when the design of the north bookend hardware has been documented and approved for production by the L2 manager.
2.9.3.1.3	Scintillator transfer facility final design approved	Milestone achieved when the transfer facility design is documented and approved for construction by the L2 manager.

2.9.3.6	Scintillator filling system completed	Milestone achieved when the scintillator filling equipment is completed and approved to deliver scintillator to detector modules.
2.9.4.1.7.6	Adhesive dispenser ready for operation	Milestone achieved when the adhesive dispenser is installed in the Far Detector Hall, passed a readiness review and is ready to be used on detector modules.
2.9.4.1.8.7	Block pivoter ready for operation	Milestone achieved when the block pivoter is installed in the Far Detector Hall, passed a readiness review and is ready for block construction to begin.
2.9.4.3.2	Ready for Far Detector plane assembly	Milestone achieved when the assembly equipment is ready for production and the assembly procedures are established and approved.
2.9.4.3.8	Super-block 1 assembled	Milestone achieved when this superblock has been assembled, installed, and is ready for final survey.
2.9.4.3.14	Super-block 2 assembled	Milestone achieved when this superblock has been assembled, installed, and is ready for final survey.
2.9.4.3.20	Super-block 3 assembled	Milestone achieved when this superblock has been assembled, installed, and is ready for final survey.
2.9.4.3.26	Super-block 4 assembled	Milestone achieved when this superblock has been assembled, installed, and is ready for final survey
2.9.4.3.32	Super-block 5 assembled	Milestone achieved when this superblock has been assembled, installed, and is ready for final survey
2.9.4.3.38	Super-block 6 assembled	Milestone achieved when this superblock has been assembled, installed, and is ready for final survey
2.9.4.3.44	Super-block 7 assembled	Milestone achieved when this superblock has been assembled, installed, and is ready for final survey
2.9.4.3.60	Block assembly and alignment completed	Milestone achieved when the final survey of all assembled and installed blocks has been completed.
2.9.4.4.7	Super-block 1 filled	Milestone achieved when this superblock has been filled with scintillator.
2.9.4.4.13	Super-block 2 filled	Milestone achieved when this superblock has been filled with scintillator.
2.9.4.4.19	Super-block 3 filled	Milestone achieved when this superblock has been filled with scintillator.
2.9.4.4.25	Super-block 4 filled	Milestone achieved when this superblock has been filled with scintillator.
2.9.4.4.31	Super-block 5 filled	Milestone achieved when this superblock has been filled with scintillator.
2.9.4.4.37	Super-block 6 filled	Milestone achieved when this superblock has been filled with scintillator.
2.9.4.4.43	Super-block 7 filled	Milestone achieved when this superblock has been filled with scintillator.
2.9.4.5.22	Superblock 1 outfitting completed	Milestone achieved when this superblock has all electronics infrastructure installed and operational.
2.9.4.5.25	Superblock 2 outfitting completed	Milestone achieved when this superblock has all electronics infrastructure installed
2.9.4.5.28	Superblock 3 outfitting completed	Milestone achieved when this superblock has all electronics infrastructure installed
2.9.4.5.31	Superblock 4 outfitting completed	Milestone achieved when this superblock has all electronics infrastructure installed
2.9.4.5.34	Superblock 5 outfitting completed	Milestone achieved when this superblock has all electronics infrastructure installed
2.9.4.5.37	Superblock 6 outfitting completed	Milestone achieved when this superblock has all electronics infrastructure installed
2.9.4.5.49	15kt installation completed	Milestone achieved when a detector mass of 15 kt is installed, filled with scintillator and outfitted with electronics infrastructure.
2.9.4.6.3	First cosmic ray tracks observed in Far Detector	Milestone achieved when the first cosmic ray events are observed in Superblock 1.
2.9.4.6.4	First NuMI neutrino events observed in Far Detector	Milestone achieved when the first neutrino events from the NuMI beam are detected and read out from Superblock 1.

2.10.10.1	2007 Shutdown Begun	This milestone defines the start of the FNAL 2007 accelerator shutdown as defined by laboratory management
2.10.10.2	2007 Shutdown Completed	This milestone defines the finish of the FNAL 2007 accelerator shutdown as defined by laboratory management.
2.10.10.3	2008 Shutdown Begun	This milestone defines the start of the FNAL 2008 accelerator shutdown as defined by laboratory management.
2.10.10.4	2008 Shutdown Completed	This milestone defines the finish of the FNAL 2008 accelerator shutdown as defined by laboratory management.
2.10.10.5	Accelerator Shutdown Begun	This milestone defines the start of the accelerator shutdown in FY2011 used to install the accelerator upgrades and start the NuMI upgrades as defined by NOvA management.
2.10.10.6	Accelerator Shutdown Completed	This milestone defines the end of the accelerator shutdown in FY2011 used to install the accelerator upgrades and start the NuMI upgrades as defined by NOvA management.
2.10.10.7	NuMI Upgrades Shutdown Begun	This milestone defines the start of the NuMI shutdown in FY2012 used to install the remainder of the NuMI upgrades and change to the medium energy neutrino beam configuration as defined by NOvA management.
2.10.10.8	NuMI Upgrades Shutdown Completed	This milestone defines the end of the NuMI shutdown in FY2012 used to install the remainder of the NuMI upgrades and change to the medium energy neutrino beam configuration as defined by NOvA management.
2.10.8.1	CD-3a	DOE signs off on Critical Decision CD-3a - construction start for long-lead items
2.10.8.2	CD-3b	DOE signs off on Critical Decision CD-3b - approval of construction start
2.10.8.3	CD-4	DOE signs off on Critical Decision CD-4 - Project complete
2.10.9.4	FY08 Funds Available	DOE funding for FY08 is available for obligation
2.10.9.5	CD-3a Funds Available	DOE makes CD-3a funding available for obligation
2.10.9.6	CD-3b Funds Available	DOE makes CD-3b (construction) funding available for obligation
2.10.9.7	FY09 Funds Available	DOE makesFY09 (construction) funding available for obligation
2.10.9.8	FY10 Funds Available	DOE makes FY10 (construction) funding available for obligation
2.10.9.9	FY11 Funds Available	DOE makes FY11 (construction) funding available for obligation
2.10.9.10	FY12 Funds Available	DOE makes FY12 (construction) funding available for obligation
2.10.9.11	FY13 Funds Available	DOE makes FY13 (construction) funding available for obligation
2.10.9.12	Decision point for more detector mass - waveshifter powders	Milestone to assess contingency usage to determine if more waveshifter powders should be purchased to build additional detector mass.
2.10.9.13	Decision point for more detector mass - WLS fiber	Milestone to assess contingency usage to determine if more WLS fiber should be purchased to build additional detector mass.
2.10.9.14	Decision point for more detector mass - APDs	Milestone to assess contingency usage to determine if more APDs should be purchased to build additional detector mass.
2.10.9.15	Decision point for more detector mass - extrusions, modules, mineral oil, pseudocumene	Milestone to assess contingency usage to determine if more components should be purchased to build additional detector mass.

8 Accelerator and NuMI Upgrades (ANU)

8.1 Introduction

8.1.1 Executive Summary

Proton Plan is the current campaign of upgrades to maximize delivery of protons to the NuMI beam line as well as to the 8 GeV Booster Neutrino Beam (BNB), which currently serves the MiniBooNE experiment. The goal of Proton Plan is to use a slip stacking technique to load protons into the Main Injector and ultimately deliver 320 kW of beam power to the NuMI beam line while still delivering protons for anti-proton production. The NOνA experiment requires a significant increase in beam power beyond this.

With the conclusion of the Collider program, several machines will become available to be used, in conjunction with the Booster and the Main Injector, to increase the beam power delivered to the NuMI facility. ANU, consisting of upgrades and modifications to existing accelerator and beamline systems, has been developed to increase the proton rate to the NuMI neutrino line. This chapter focuses on the upgrades necessary to reach 700 kW beam power (ANU subproject of NOνA), making use of the Recycler ring (currently an anti-proton storage ring) as a proton pre-injector to the Main Injector. This pre-injection removes the proton injection time from the Main Injector cycle time, and thereby enables the Main Injector to cycle as fast as allowed by magnets, power supplies and the RF system. ANU provides about a factor of 2 increase in beam power, with only 10% increase in total beam intensity in the Recycler and Main Injector, by making full use of the maximum acceleration rate of the Main Injector. Modifications to the proton source and upgrades in the NuMI neutrino line to handle the higher beam power are both addressed in this report.

Table 8.1 compares the present operating scenarios with multi-batch slip-stacking in the Main Injector for NuMI (Proton Plan) and with multi-batch slip-stacking in the Recycler (NOνA).

ANU achieves an 80% increase in proton throughput over Proton Plan by moving the injection and the slipping portion of the slip-stacking process from the Main Injector to the Recycler, and otherwise maintaining the production process of Proton Plan. The various upgrades will now be briefly discussed.

The Recycler will be converted from an anti-proton to a proton storage ring, starting with the decommissioning all anti-proton specific devices, such as stochastic cooling tanks and electron cooling. A new injection line from the MI-8 proton line directly into the Recycler and a transfer line from the Recycler into the Main Injector are needed. The plan is to slip-stack six on six Booster proton batches in the Recycler, for a total intensity of 5×10^{13} protons/cycle, and, at the time they line up, extract them to the Main Injector in a single turn, where they will be recaptured and accelerated. A 53 MHz RF system needs to be added in the Recycler for beam injection and slip-stacking.

The Main Injector will have the slipping process offloaded to the Recycler, but will have to cycle faster and more often. The Main Injector cycle time will be reduced from 2.2 s to 1.333 s. In order to accommodate the faster ramp, two additional RF stations need to be installed.

	Present operating conditions	Proton Plan Multi-batch slip-stacking in MI	NOνA Multi-batch slip-stacking in Recycler
Booster intensity (protons/batch)	$4.3\text{-}4.5\times10^{12}$	4.3×10^{12}	4.3×10^{12}
No. Booster batches	7	11	12
MI cycle time (s)	2.4	2.2	1.333
MI intensity (ppp)	3.3×10^{13}	4.5×10^{13}	4.9×10^{13}
To anti-proton source (ppp)	8.8×10^{12}	8.2×10^{12}	0
To NuMI (ppp)	2.45×10^{13}	3.7×10^{13}	4.9×10^{13}
NuMI beam power (kW)	192	320	700
Protons on Target per year to NuMI[1]	2×10^{20}	3×10^{20}	6×10^{20}

Table 8.1: Present and foreseen operating scenarios. The first two columns show NuMI intensities and beam power values for mixed-mode cycles in the Main Injector.

The ability of the NuMI neutrino line to accept a 75% increase in power, over its design value of 400 kW, mainly involves improvements to the primary proton line to handle the faster repetition rate, a new design for the target and upgrades to the cooling systems. The target and focusing horn configuration (neutrino beam optics) is also changed to meet the needs of the NOνA experiment. This means moving the target and the second horn to new locations within the target chase area in order to change the energy spectrum of the neutrinos to a higher energy (the medium energy configuration).

The implementation of the ANU subproject is planned to occur during two separate shutdown periods. The first shutdown period, of about 9 months in the fall of 2010, follows the completion of Collider Run II operations. During this shutdown the modifications to the accelerator complex will be completed and the NuMI beamline will begin preparation for the 700 kW phase, but without changing the neutrino beam focusing optics. This is planned to allow the MINERνA (Main Injector ν-A interactions) experiment [2] to operate for about one year in the low energy neutrino configuration, presently used by the MINOS experiment and to allow work to be completed for the NuMI upgrades. Since MINERνA requires the use of the existing low energy target, the NuMI beamline will be capable of only ~400 kW of beam power, but at the same time it will be possible to commission all the modifications to the accelerator complex. In Spring 2012 a second shorter shutdown is planned to switch from the low energy to the medium energy neutrino configuration. By then the NOνA experiment will have a good fraction of their detector available for data taking. The upgrades for NOνA have been designed for an annual integrated delivery of 6.0×10^{20} protons on target.

[1] See Reference [1]

The NOνA ANU subproject represents a technically feasible plan, which mainly relies on the reconfiguration of existing machines. By itself, these upgrades provide more than a 100% increase in beam power to the NuMI neutrino line over the present Proton Plan.

8.1.2 The Present Accelerator Complex

A sketch of the Fermilab accelerator complex is shown in Fig 8.1.

The Booster is effectively the proton horsepower of the complex. Fed by 400 MeV H^- ions from the Linac, it accelerates protons to 8 GeV of kinetic energy at 15 Hz rate. Booster batches (typically up to ~5×10^{12} protons) are transferred through the MI-8 line into the Main Injector (MI) or sent to the MiniBoone neutrino target.

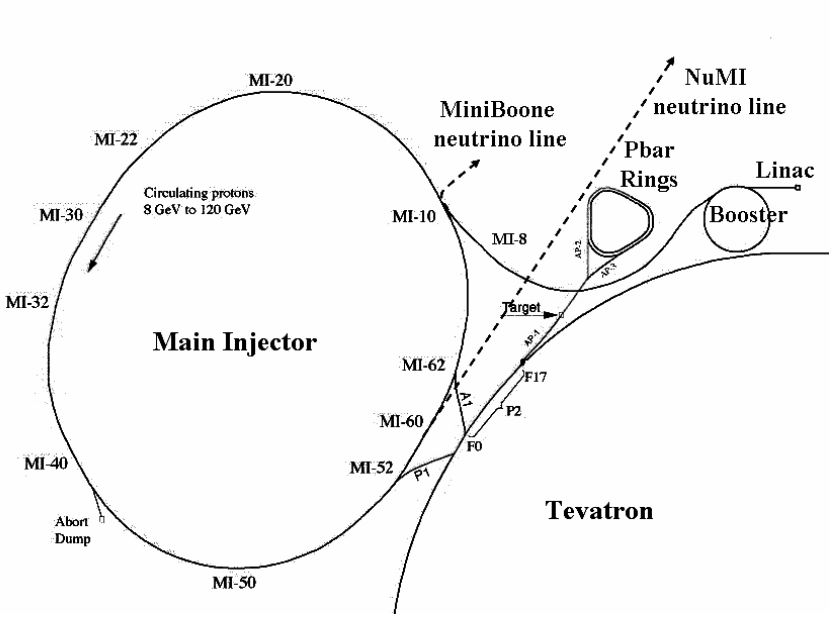

Fig 8.1: The Fermilab accelerator complex.

The Main injector is seven times the circumference of the Booster. Six Booster batches are required to fill up the machine, leaving one seventh of the circumference available for the rise-time of the extraction kicker. Table 8.2 summarizes the MI parameters.

Circumference (km)	3.319	Harmonic number	588
Injection momentum (GeV/c)	8.9	RF frequency at injection (MHz)	52.8
Extraction momentum (GeV/c)	120	RF frequency at extract. (MHz)	53.1
Transition gamma	21.8	Maximum RF voltage (MV)	4.3

Table 8.2: Parameters of the Main Injector.

The Main Injector is the central machine of the complex, equipped with a complex set of injection and extraction lines to connect to the other machines of the complex. It provides protons for anti-proton production, it has a dedicated extraction to the NuMI neutrino line and it is connected to the Tevatron for proton and anti-proton transfers.

An additional machine, the Recycler, is located in the Main Injector tunnel at a distance 57" above the MI ring and with the same basic cell geometry. The Recycler is a fixed 8 GeV kinetic

energy antiproton storage ring, which makes use of permanent gradient and quadrupole magnets for the ring lattice. Antiproton transfers in and out of the Recycler Ring take place through two transfer lines connecting the Recycler to the Main Injector. Fig 8.2 shows the Main Injector tunnel in the MI-60 region, where the NuMI extraction is located.

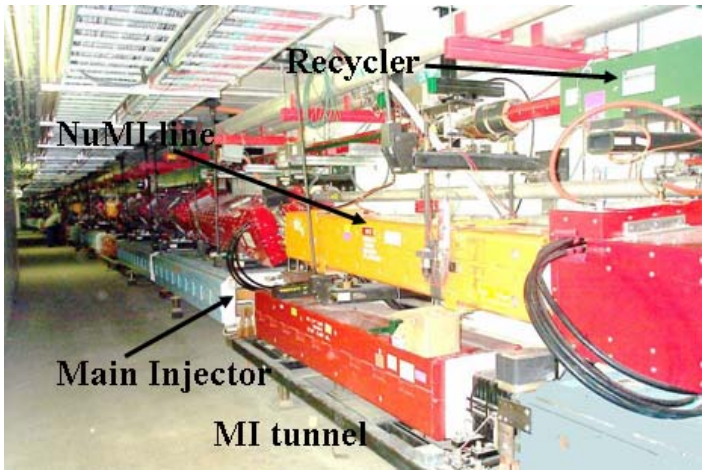

Fig 8.2: A photo of the Main Injector tunnel in the MI-60 region, showing the NuMI extraction line between the Main Injector at the bottom and the Recycler on top.

The NuMI Beamline line points from Fermilab to the MINOS detector installed in the Soudan mine, in Northern Minnesota, at a distance of 735 km from the neutrino target. A schematic of the NuMI line is shown in Fig 8.3.

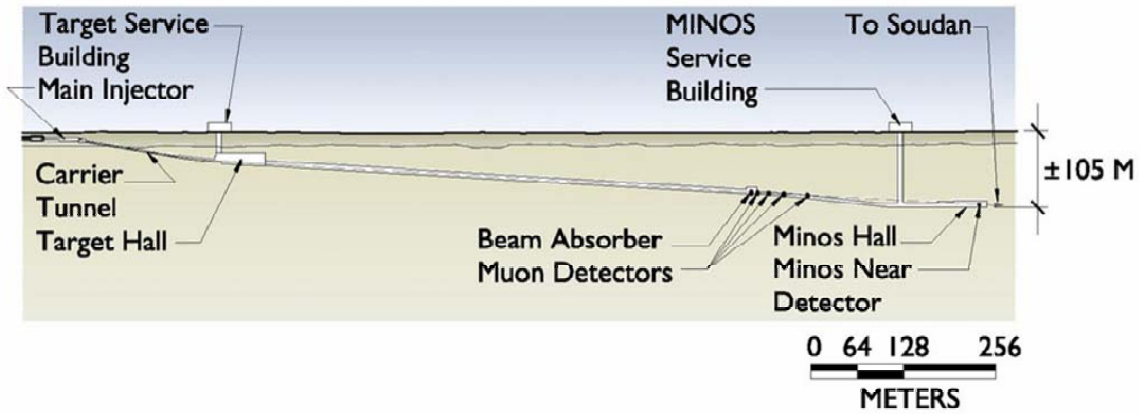

Fig 8.3: Schematic of the NuMI neutrino line. Protons are delivered from the Main Injector via the primary proton beamline through the carrier tunnel. The target and focusing horns are located in the target hall. The long section in the middle contains the decay pipe which is followed by the beam absorber, muon detectors, and near experimental hall.

The 120 GeV/c primary proton beam, single turn extracted from the Main Injector, is transported by a large acceptance primary proton line over a distance of 350 m, brought to a pitch angle of 58 mrad in order to point to the neutrino detector in the far location, and focused onto a

water-cooled graphite target. Design values of the NuMI line are 4×10^{13} protons/pulse (ppp) every 1.9 s, corresponding to a power of 0.4 MW.

The graphite target, of two interaction lengths, is followed by two water-cooled, parabolic aluminum horns, pulsed with up to 200 kA, providing a 1/r toroidal field that has a maximum of 30 kG. The focused particles are allowed to decay in a 675 m long decay pipe of 1 m radius, evacuated down to 0.4 Torr. A water-cooled aluminum beam absorber is positioned at the end of the decay pipe.

High rate ionization chambers are used to monitor the beam immediately upstream of the beam absorber (Hadron Monitor) and in three successive alcoves downstream of the absorber (Muon Monitors or detectors).

8.1.3 Proton Plan

The Proton Plan [3] is a campaign of upgrades to maximize delivery of protons to the NuMI beam line, which currently serves the MINOS experiment, as well as the 8 GeV Booster Neutrino Beam (BNB), which currently serves the MiniBooNE experiment. NOνA implicitly assumes that the Proton Plan has been completed and has been reasonably successful in achieving its goals.

The Proton Plan is concurrent with Run II (the second run of the Collider program). The current timeline has the final associated hardware improvements installed in the summer 2008 shutdown, and all benefits realized by mid 2009, at which point, it will be fully superseded by NOνA.

The goal of the Proton Plan is to use a slip stacking technique to load protons into the Main Injector and ultimately deliver approximately 320 kW of beam power to the NuMI beam line while still delivering protons (80kW) for antiproton production. By increasing the total proton output from the Booster, it is planned to continue delivering protons to the 8 GeV beam line (currently the MiniBooNE experiment) at a level of roughly $(1\sim2)\times10^{20}$ per year.

Broadly speaking, the Proton Plan elements fall into four categories:

1. Increasing the maximum Booster repetition rate from the 7.5 Hz to roughly 9 Hz
2. Increasing Booster efficiency so that more beam may be accelerated while keeping the total beam loss in the Booster tunnel at a constant level. Operationally, beam loss has been the limiting factor for Booster throughput, and will likely continue to be for some time.
3. A number of hardware and operational issues to implement slip stacked operation in the Main Injector
4. Some projects aimed at increased reliability and stability, particularly in the Linac.

8.2 Technical Design Criteria

Thermal expansion of the target chase and target hall components will affect the alignment of the target and horns. The NOνA experiment requires that alignment of the beam, target, and horns remain within a 1.5 mm tolerance [4]. Other design parameters for NOνA, together with the Proton Plan parameters, are shown in Table 8.3.

	Proton Plan	NOνA	
Booster			
Extracted Batch Intensity	4.3E+12	4.3E+12	protons
Average Pulse Rate	5.9	10.5	Hz
Average Beam Rate	5.0	9.0	Hz
Norm. Trans. Emittance at Extr.	15	15	π·mm·mrad @ 95%
Long. Emittance per Bunch at Extr.	0.08	0.08	eV·sec @ 95%
δp (After Bunch Rotation)	8	8	(±) MeV/c @ 95%
Recycler Ring			
Number of Injections		12	injections
Total Beam Injected		5.16E+13	protons
Injection Kinetic Energy		8	GeV
Injection RF Frequency		52.809	MHz
RF Frequency Difference		1260	Hz
Extraction RF Frequency		52.809	MHz
δp at Extraction		19	(±) MeV/c @ 95%
Main Injector			
Number of Injections	11	1	injections
Cycle Time	2.2	1.333	s
Beam Momentum at Extraction	120	120	GeV/c
Beam Intensity at Extraction	4.5E+13	4.9E+13	protons
Norm. Trans. Emittance at Extr.	20	18	π·mm·mrad @ 95%
Long. Emittance per Bunch at Extr.	0.4	0.4	eV·s @ 95%
δp/p at Extraction	8.E-04	8.E-04	(±) @ 95%
MI/RR Tunnel Losses			
8 GeV Beam Efficiency	95%	95%	
Controlled 8 GeV Loss to Abort	0.0%	1.9%	
Controlled 8 GeV Loss to Collimators	2.7%	1.8%	
Uncontrolled 8 GeV Losses	2.3%	1.3%	
Transition Losses (Upper Bound)	0.2%	0.2%	
Power Deposited in Abort	0	943	W
Power Deposited in Collimators	744	893	W
Distributed Uncontrolled Loss	0.23	0.27	W/m
NuMI			
Maximum Proportional Loss in Carrier Pipe	1.0E-05	5.7E-06	
Spot Size on Target	1.3	1.3	mm (RMS)
Max. Beam Intens. on NuMI Target	4.5E+13	4.9E+13	protons
Max. Beam Power on NuMI Target	392	705	kW
Protons per Hour	7.3E+16	1.3E+17	protons/hr.

Table 8.3: Summary of Design Parameters for Proton Plan & NOνA.

8.3 Recycler Ring Upgrades

8.3.1 Overview

The Recycler currently serves as the main anti-proton storage ring for the Tevatron Collider program. Through the use of stochastic and electron cooling, greater than 4 x 10^{12} anti-protons have been stored, with lifetime greater than 500 hours. The transverse acceptance is ~65 π mm mr (95% normalized emittance) and the momentum acceptance is ~1.5%. When Tevatron Collider operations cease, the Recycler will be used as a proton pre-injector for the Main Injector (MI) for NOνA. As the Recycler is the same size as the MI, it is possible to do a single turn fill (~11 μsec), minimizing the proton injection time in the MI cycle and maximizing the protons on target. Fig 8.4 shows the layout of the Recycler and the main areas where the work will occur.

To convert from an anti-proton storage ring to a proton pre-injector, filling the Main Injector every 1.3 seconds, it will be necessary to remove anti-proton specific devices in the Recycler, build new injection and extraction lines, build new injection, extraction, and abort kickers, build a new 53 MHz RF system, and upgrade the instrumentation. In the sections that follow, we will present the project components in detail. We plan for all of the conversion activities to take place during a single shutdown period after the Tevatron Collider program ends.

There are several anti-proton specific areas for beam cooling in the Recycler. The stochastic cooling pickup and kicker tanks in the RR10 and RR20 areas will be removed. The electron cooling section in RR30, which consists of the solenoidal cooling channel and electron injection and return lines, will also be removed.

The current R22 line (for pbar injection or proton extraction from the Recycler) and R32 line (for pbar extraction or proton injection into the Recycler) will not be adequate in the NOνA era. The original R22 line was designed to transport 40π pbar beams being recycled from the Tevatron. However, the measured acceptance of the R22 line is smaller than expected and the Lambertson is located in a dispersive region making this line unacceptable for extracting slipped stacked protons from the Recycler. The R32 line allows for proton injection through the MI, while we want direct injection from the Booster. These lines will be decommissioned and replaced with two new transport lines. The new injection line from the MI8 line into the Recycler will start at 848 and end with new injection kickers at RR104. A new extraction line in the RR30 straight section will start with a new extraction kicker at RR232 and end with new MI injection kickers at MI308.

To increase the beam current, we plan on utilizing slip stacking at 53 MHz in the Recycler. The existing Recycler RF system is a broadband 10 MHz system, designed to handle the anti-proton accumulation for the Tevatron Collider program. We will design, build, and install a new 53 MHz RF system for bucket to bucket injection from the Booster, slip stacking in the Recycler, and bucket to bucket extraction to the MI.

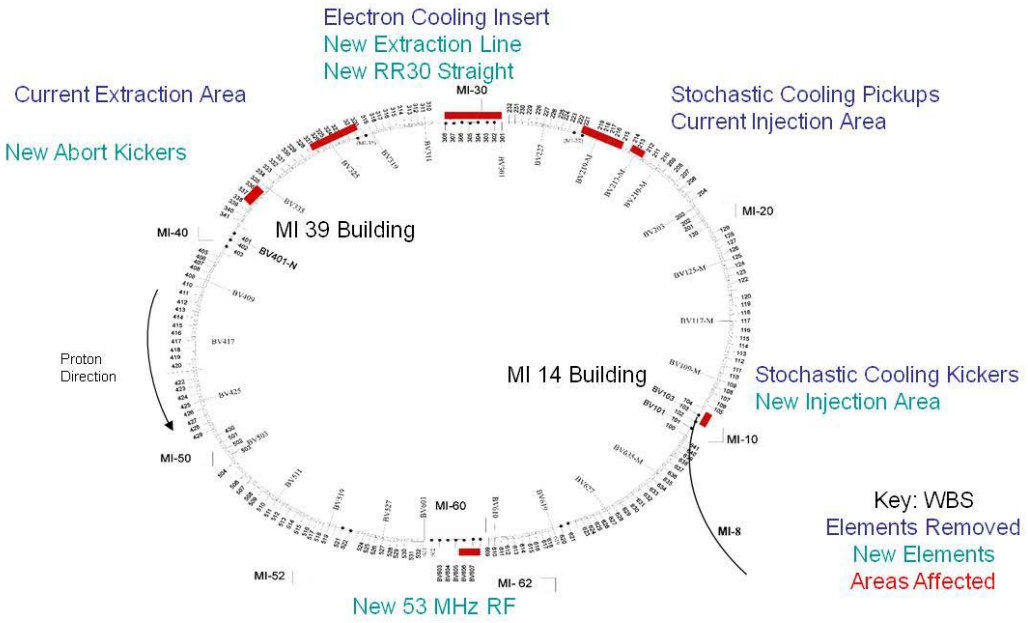

Fig 8.4: Recycler Upgrades Overview

We will upgrade the existing instrumentation to handle the increase in peak intensity (from 6e12 to 6e13) and the change in the RF structure. The Beam Position Monitor (BPM) systems will be upgraded to a 53 MHz system, using the recent MI BPM system upgrade as a model [5]. The damper systems will be upgraded to handle the intensity. We anticipate upgrades to the intensity monitors (a DC current transformer (DCCT) and beamline toroids) as well.

Cooling system modifications to the Recycler will affect three Low Conductivity Water (LCW) cooling systems: the Main Injector global LCW system, the RF (95 degree) LCW system and the Cavity (55 degree) LCW cooling systems located at MI-60. Work affecting these cooling systems is occurring in the Q-100 region (Injection Line), Q-300 region (Extraction Line), Q-400 region (Abort Line), and Q-600 region (RF Cavities). Work on cooling needs for the associated power supplies in the service buildings is occurring in MI-14, 30, 39, and 60 Service Buildings. It is currently assumed that the majority of the Main Injector Cooling Systems will have sufficient capacity for increased loads due to the Recycler modifications. However, there are extensive modifications planned in the Q-100 region, where a new Injection Line will be added.

8.3.2 Ring Modifications

8.3.2.1 Decommission Pbar Devices in the Tunnel

As the Recycler will no longer circulate anti-protons, we need to remove anti-proton specific devices from the ring for possible future use. These fall into two categories: (1) anti-proton cooling devices and (2) anti-proton transfer line devices.

8.3.2.1.1 Removal of Stochastic Cooling Tanks

The Recycler stochastic cooling system consists of pickup tanks in the RR 21 sector and the kicker tanks in the RR 10 sector. The tanks and all the support electronics will be removed from the tunnel and replaced with beam pipe (in the 21 sector) or the injection area devices (in the 10

sector). The removal is a well-understood task, which is anticipated to take 8 technicians 4 weeks to complete. It is one of the first tasks done during the conversion shutdown period.

8.3.2.1.2 Removal of ECool

The Recycler electron cooling system consists of a 6 MV Pelletron in the MI 31 service building, 4.3 MeV electron transfer lines, a 20 m cooling section populated by solenoids, and lattice matching sections for the cooling section. We wish to preserve the system for possible future use (at Fermilab or elsewhere).

In this task, we will remove and package the solenoids for future use, remove the sections of the transfer lines in the MI tunnel enclosure, and remove all Recycler components between 301 and 309 (the cooling insert) including the 38 permanent magnet quadrupoles. These magnets will be sent to Technical Division to be refurbished and used again in the rebuilt MI 30 straight section and the transfer lines (see Sections 8.3.2.2, "New Injection Line", and 8.3.2.3, "New Extraction Line and RR30 Straight Section").

As the cooling section solenoids and electron transfer lines were installed in a recent shutdown (Summer 2004), the removal is also a well-understood task. As the magnets will need to be refurbished and installed in other areas of the Recycler during the conversion shutdown, this task is one of the first ones scheduled.

8.3.2.1.3 R22 Line Removal

The R22 line is the anti-proton injection line from the Main Injector to the Recycler. We plan on removing the Lambertson magnets in the Main Injector (at MI Q222) and the Recycler (at Q214) and rebuilding the vacuum sections in both machines. We also anticipate removing instrumentation and trim magnets from the line for use in the new transfer lines. In the conversion shutdown, we do not plan on removing all the components and stands. As the instrumentation will be utilized again, this task is also to be done early in the shutdown.

8.3.2.1.4 R32 Line Removal

The R32 line is the anti-proton extraction line from the Recycler to the Main Injector. We plan on removing the Lambertson magnets in the Main Injector (at MI Q321) and the Recycler (at Q328) and rebuilding the vacuum sections in both machines. We plan on removing instrumentation and trim magnets from the line for use in the new transfer lines. In the conversion shutdown, we do not plan on removing all the components and stands. As the instrumentation will be utilized again, this task is also to be done early in the shutdown.

8.3.2.2 New Injection Line

We are designing a new injection line to take protons directly from the MI 8 line into the Recycler [6,7]. The MI 8 line transfers 8 GeV protons from the Booster to the Main Injector tunnel, where a horizontal switching magnet directs them into the Main Injector or to the MiniBoone target. We want to preserve the ability to inject into the Main Injector and transfer beam to the MiniBoone target, so we plan on installing a vertical switching magnet (upstream of the horizontal switching magnet) to direct protons into the Recycler.

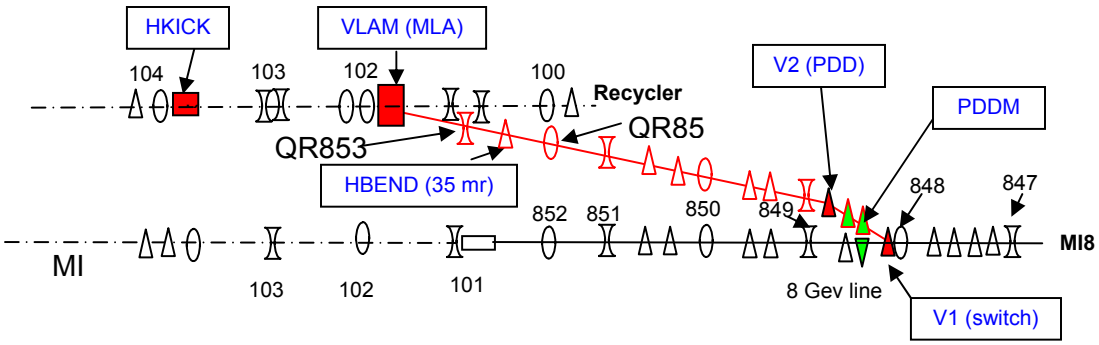

Fig 8.5: Diagram of new Recycler injection line

The solution uses three vertical bending centers and a horizontal kicker. A diagram of the transfer line is shown in Fig 8.5. The first vertical bend (V1 switch) bends up at about a 33 mrad angle to clear the downstream magnets. A vertical dipole (V2, rotated PDD, Fig 8.5) reduces the pitch from 33 mrad to about 14 mrad. These two bends act as a single extended bend center. This pitch is maintained until the third vertical bending center, the MLAW injection Lambertson (located just upstream of Q102A). The Lamberston bends the beam down to place it on the correct vertical closed orbit of the Recycler and cancels the vertical dispersion created by the switch magnet. The injection kicker (HKICK) applies a horizontal kick to put the injected beam onto the Recycler orbit. The injection/abort gap kicker design is discussed in detail later in this document. The required kick implies 5 kicker magnets and 1 tail bumper magnet.

8.3.2.2.1 Powered Elements

The injection line design contains only two large powered elements, the vertical switch magnet and the Lambertson. The vertical switch magnet, V1, is a modified ADC magnet [8]. The magnet aperture is widened from 1.5 to 2.12 inches. The magnet will be labeled ADCW. Preliminary design considerations verify that the required field is attainable.

The Lambertson (MLAW) and kicker geometry and strengths are found in Nova-doc-1495 [6]. In particular, the aperture of the field free region is increased by 5-6 mm which will increase the current requirements by 14%. This does not change the power supply specification. The Lambertson is also rolled by ~5º to generate the correct angle for closure. Additionally, apertures and beam sizes require an MI style beam pipe downstream of the Lambertson and through the Q102 quadrupoles.

There are five quad locations between the switch magnet and injection Lambertson. Powered dipole trims and two powered MQT type quad trims (with enough strength to adjust gradients by +/- 20%) are installed at each quad location.

8.3.2.2.2 Permanent Magnet Elements

The nominal Recycler straight section 20 inch quad RQMF/D was tuned to provide a gradient of 25 to 26 kG/m. Typical gradients in the MI8 matching section to either MI or Recycler are between 50 and 80 kG/m. For matching into the Recycler, each quad location has either two or three permanent magnet quads to keep the gradient within the tunable range of the permanent magnets. These quads will be recycled from the decommissioning of the RR30 straight section.

Utilization of the rolled PDD permanent magnet for V2 constrains the amplitude of the vertical switch magnet to be around 33 mrad. The elevation of the “upper” 8 GeV line at the downstream horizontal dipoles requires the use of mirror magnets. These mirror magnets

(PDDM) will be pure dipoles matching the aperture and field of the PDD. Currently, the separation between the beam centerlines of the upper and lower 8 GeV line at the first mirror magnet in the upper line is 4.324 inches. However, the mirror magnets are offset so that the beam centerline-to-steel dimension on the mirror side should be less than 3.45 inches.

8.3.2.2.3 Lattice and Matching

Retaining the ability to transport beam to the Main Injector, Recycler and MiniBoone will require modifications in the MI-8 line to successfully match the optical lattice functions of both synchrotrons. To get a unique solution, eight parameters must be supplied. To this end, the gradients at the locations 846 thru 853 are adjusted to match into the Recycler. The first electromagnet matching quad in the 8 GeV line is located at 847. This implies the addition of an electromagnet quad at the 846 location where there is currently a pair of gradient magnets. The required integrated gradient is less than 3 kG, which can easily be provided by the MQT trim quad. In addition, a trim quad will be added to the current 8 GeV line at the locations of Q847 and Q848, adjacent to the existing electromagnet quad. These can be utilized at 15 Hz for matching into the MI and or MiniBoone.

Type	Comment	Total	Modify	Construct	Recycle
	Permanent Magnets				
RQMx	Recycler style 20 in. permanent magnet quad	14	14	0	0
PDD_M	PDD mirror magnet, new design	3	0	3	0
PDD	PDD 8 Gev style double dipole, existing style	5	0	3	2*
PDD_R	PDD dipole design, reduced field	2	0	2	0
MGS	Recycler dispersion suppressor mirror magnet	0	0	0	0
	Powered Elements				
ADCW	Modified B1 style to open aperture	1	1	0	0
MLAW	MI style injection Lambertson, new, modified	1	0	1	0
ILA	MI style Lambertson, existing, move	0	0	0	0
	Trim Elements				
MQT	Old MR style quad trim	13	0	0	13
HDC	Old MR style horizontal corrector used in Recycler	2	0	0	2
VDC	Old MR style verticall corrector used in Recycler	2	0	0	2
MCH	LEP Horizontal corrector	2	0	0	2
MCV	LEP vertical corrector	2	0	0	2

Table 8.4: Magnet information for the injection line.

8.3.2.3 New Extraction Line and RR30 Straight Section

We are designing a new extraction line to take protons from the Recycler to the Main Injector, making use of the MI 30 straight section. The MI-30 straight section is a "D-D 8 half-cell" straight section, which starts at 301 and ends at 309--both horizontally defocusing locations. The MI lattice is a periodic FODO in the region. The Recycler lattice contains the symmetric electron-cooling insert between 305 and 307; the remainder of that Recycler straight section is roughly a FODO section, but is not periodic. The Recycler straight section between Q301 and 309 is replaced with the FODO lattice, as in the initial Recycler design. Fig 8.6(a) and Fig 8.6(b) give the beta functions of the two types of the lattice.

Note that the beta-functions in the SS30-FODO section still reach 80m in the horizontal plane. The beam pipe used in this section is either 3" round or 3.75"x1.75" elliptical and does not

represent an aperture restriction. However, the quadrupole strength requirement is ~15% more than the standard permanent magnet quadrupole strength in the Recycler. A solution is to add one more quadrupole per cell, requiring 25 quadruples in the RR-30 straight section.

The extraction line has been redesigned since the CDR to reduce required kicker strength by extending the whole line by a half-cell. The extraction line starts with an extraction kicker at 230 in the Recycler. A rolled, modified MI 8GeV injection Lambertson (MLAW) is located at 232 for the initial vertical bend. The next two vertical bends are located at 302 and 304 with the beamline following the same lattice structure of the Recycler until 306. The MI injection Lambertson is located at upstream of quad 306, which would put the beam on the MI vertical closed orbit. The kicker is now located 12 inches upstream of the Q308 quad coil.

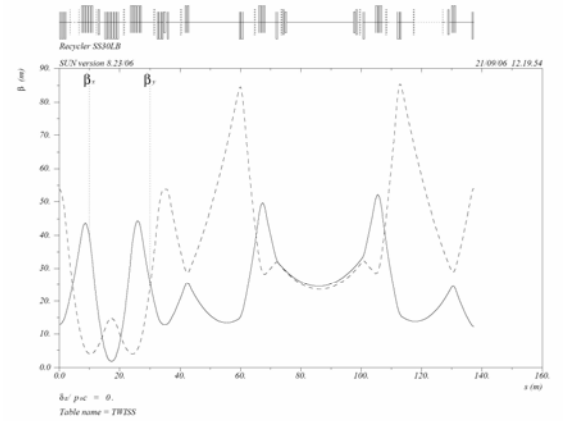

(a) SS30LB

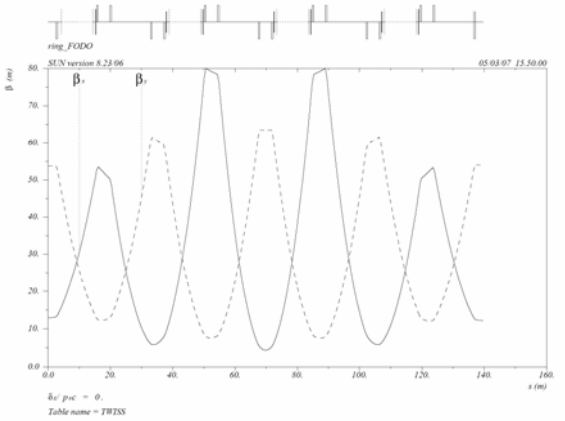

(b) SS30_FODO

Fig 8.6: Lattice functions of the RR-30 Straight Section.

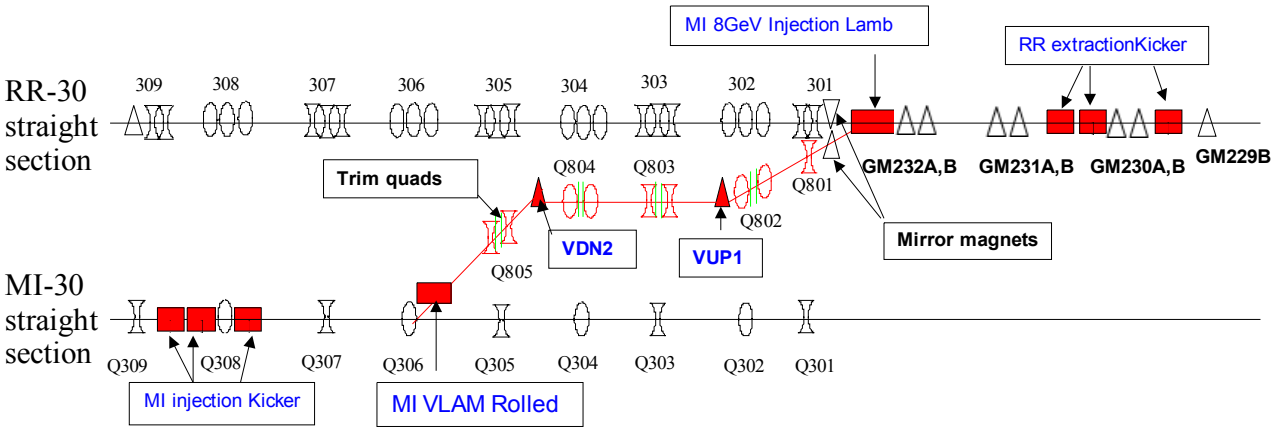

Fig 8.7: Cartoon of the extraction line from RR to MI and the RR 30 straight section.

Type	Comment	Total	Modify	Construct	Recycle
	Permanent Magnets				
RQMx	Recycler style 20 in. permanent magnet quad	9	9	0	0
PDDM	PDD mirror magnet, new design	0	0	0	0
PDD	PDD 8 Gev style double dipole, existing style	0	0	0	0
PDDW	PDD dipole design, reduced field	0	0	0	0
MGS	Recycler dispersion suppressor mirror magnet	1	0	0	1*
	Powered Elements				
ADCW	Modified B1 style to open aperture	2	2	0	0
MLAW	MI style injection Lambertson, new, modified	1	0	1	0
ILA	MI style Lambertson	1	0	0	1
	Trim Elements				
MQT	Old MR style quad trim	10	0	0	10
HDC	Old MR style horizontal corrector used in Recycler	2	0	0	2
VDC	Old MR style verticall corrector used in Recycler	3	0	0	3
MCH	LEP Horizontal corrector	0	0	0	0
MCV	LEP vertical corrector	0	0	0	0

Table 8.5: Extraction line magnetic elements. The columns represent the total number needed for the extraction line, the number that exist but need to be modified, the number to be constructed, and the number to be recycled.

Type	Comment	Total	Modify	Construct	Recycle
	Permanent Magnets				
RQMx	Recycler style 20 in. permanent magnet quad	25	25	0	0
PDDM	PDD mirror magnet, new design	0	0	0	0
PDD	PDD 8 Gev style double dipole, existing style	0	0	0	0
PDDW	PDD dipole design, reduced field	0	0	0	0
MGS	Recycler dispersion suppressor mirror magnet	1	0	0	1
ADCW	Modified B1 style to open aperture	0	0	0	0
MLAW	MI style injection Lambertson, new, modified	0	0	0	0
ILA	MI style Lambertson	0	0	0	0
	Trim Elements				
MQT	Old MR style quad trim	0	0	0	0
HDC	Old MR style horizontal corrector used in Recycler	4	0	0	4
VDC	Old MR style verticall corrector used in Recycler	4	0	0	4
MCH	LEP Horizontal corrector	0	0	0	0
MCV	LEP vertical corrector	0	0	0	0

Table 8.6: RR 30 straight section magnetic elements. The columns represent the total number needed for the extraction line, the number that exist but need to be modified, the number to be constructed, and the number to be recycled.

8.3.2.4 53 MHz RF System

The existing broadband RF system in the Recycler Ring will not be removed. For NOνA operation, a new 53 MHz RF system is required. This system includes RF cavities installed in the Recycler and a new low level RF system. For bucket-to-bucket transfers from the Booster and to the Main Injector, the required frequency is 52.809 MHz. For slip stacking, a tunable frequency range of ± 5 kHz and total voltage of 300 kV is necessary. Fast cavity tuning (for beam loading compensation) and higher mode dampers on the cavities are also required.

We propose to build 2 new RF cavities, to be installed in the 608 region of the Recycler. Controls, power, and other infrastructure support will be installed in the MI 60 service building. We plan on recycling the 53 MHz power amplifiers and modulators from the Tevatron RF systems.

8.3.2.4.1 Specifics of the design

The cavity is a λ/4 coaxial design with a 25" outer diameter made of OFHC copper with a step-up ratio of 6:1. The central frequency is 52.809 MHz with a Q of ~7000. By using fast garnet phase shifters developed for the Proton Driver [9], the cavity is tunable over a ± 10 kHz range. The shunt capacity is 140 kΩ, leading to 80 kW/cavity at 150 kV. R/Q is 20 Ω. The tetrode anode power dissipation with 1 A of DC beam current and no detuning is 130 kW, while the PA tubes are rated for 150 kW. Higher order mode dampers for the 3rd and 5th harmonic are included in the design. A cross sectional view of the cavity can be seen in Fig 8.8 and a 3D view in Fig 8.9.

To support direct injection from the Booster and proton slip stacking in the Recycler following the decommissioning of the Tevatron, a new Low Level RF system will be required to drive the new 53MHz cavities and provide synchronization for beam transfers. Further details are in Section 8.4, "Main Injector (MI) Upgrades".

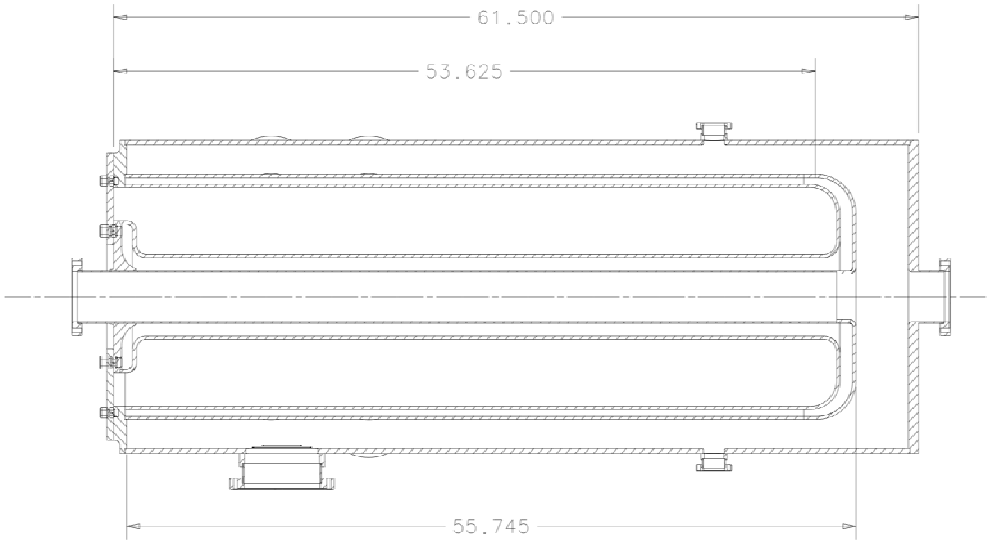

Fig 8.8: Cross sectional view of RF cavity.

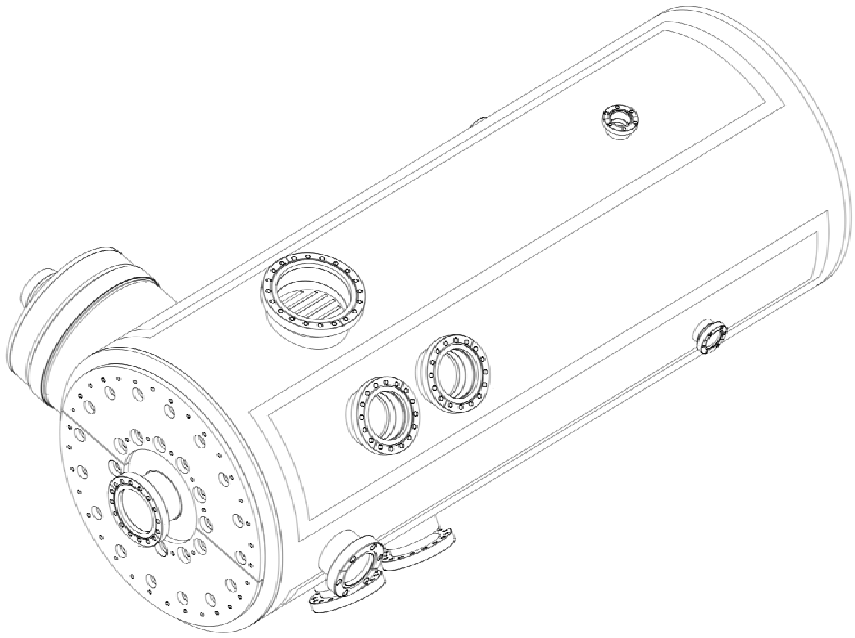

Fig 8.9: 3D view of RF cavity

8.3.2.5 Instrumentation

Instrumentation needs for the Recycler Ring can be broken down into three types of systems:

- Position (orbit) measurements: BPMs and multiwires
- Intensity measurements: DCCT and toroids
- Dampers

All of these systems need significant upgrades for the NOνA era.

8.3.2.5.1 BPMs

The current Recycler Ring BPM system uses resonant pickups and electronics at 2.5 MHz. We will upgrade to a 53 MHz system, modeled on the Main Injector BPM system [5]. A detailed specifications document is available [10]. While the pickups work well at this frequency, the signal cables from the tunnel to the service buildings do not. We need to pull new cables and purchase the associated transition boards for each BPM (216 in total) and reuse the existing EchoTek digitizers.

Signal to noise ratio is an important element of the performance of the system. The new BPM system will have no active elements in the tunnel, so the noise figure of the system will be dominated by the cable going from the BPM pickups to the upstairs electronics. We know from

the MI experience that a Heliax type cable performs acceptably, even in the noisy environment of MI 60 (near the MI RF cavities).

We are considering 3 different heliax cables, differing in diameter. They are:

1. Andrew LDF1-50 (1/4 in. foam dielectric)
2. Andrew LDF2-50 (3/8 in. foam dielectric)
3. Andrew LDF4-50A (1/2 in. foam dielectric)

Table 8.7 contains a summary of cable information, including cost, for these three cables.

	Cost ($/foot) (for quantities of 100,000 ft)	Attenuation at 50 MHz (dB/100ft)	Best Case Attenuation	Worst Case Attenuation
LDF1-50	$0.66	0.953	1.43 dB	12.4 dB
LDF2-50		0.736	1.10 dB	9.6 dB
LDF4-50A	$1.29	0.479	0.72 dB	6.25 dB

Table 8.7: Summary of cable information. The best case attenuation is for the shortest cable run (150 ft). The worst case attenuation is for the longest cable run (1304 ft).

The total length required for all the BPM pickups, including transfer lines, is 275,142 ft, with a longest cable run of 1304 ft and a shortest cable run of 104 ft. We have performed the calculation of signal strength for 1e10 protons at 8 GeV in a 19 nanosecond Gaussian bunch. In this situation, a signal attenuation of 12 dB (the worst case in Table 8.7) is acceptable. Considering just signal strength, we believe we can use the LDF1-50 cable throughout the ring.

As stated above, the MI 60 region in the tunnel is the location of the MI RF cavities, so there are significant sources of 53 MHz noise. The larger diameter cable (LDF4-50A ½ in. diameter heliax) does have better noise rejection. The MI BPM system uses a similar ½ in heliax cable in this region of the tunnel. Based on recommendations from the Main Injector BPM project personnel, we will use the larger diameter cable for this region ($1/6^{th}$ of the ring) and the LDF1-50 ¼ in. diameter cable elsewhere.

With this amount of additional cable, we have investigated penetrations and cable tray space. We will need to make use of the service building kicker room penetrations, which are available at each service building.

For position measurements in the transfer lines, we will have both BPMs and multiwires. We will be moving the physical BPMs and multiwires from the current transfer lines to the new transfer lines and pull new cables for both types of instrument.

8.3.2.5.2 Intensity measurements

We will install a new DCCT for the Recycler Ring. We are currently investigating with the Instrumentation Department the choice between a commercial product (the Recycler currently has a Bergoz DCCT) or an in house design (like the Main Injector DCCT). In the RLS, we have costed for the purchase and installation of a commercial DCCT. It is estimated that an in house design will be similar in cost. For the transfer lines, we will move existing Pearson toroids.

8.3.2.5.3 Dampers

We anticipate that we will need both longitudinal and transverse dampers at the intensity of 6e13 protons. For the longitudinal system, we believe that the current pickups, kickers, and power amplifiers are adequate for our needs. For the transverse systems, the pickups and kickers are adequate but we will need to purchase 5 additional power amplifiers. This is what is included in the resource loaded schedule.

8.3.3 Kicker Systems

8.3.3.1 Overview

There are five new kicker systems for this project (see Table 8.8). A new pulser and magnet design are required to inject protons into the Recycler Ring (RR). Another new kicker system is required to remove unwanted beam in the injection gap just before injection. This Gap Clearing System will first be installed in the Main Injector for the remainder of the Collider Run and then moved to the RR as part of the ANU Project. Next, a new pulser and new magnets are required to extract the entire Recycler beam to the Main Injector. Another new pulser and new magnets are required at the other end of that transfer line to inject the beam. Finally, a new pulser and new magnet are required for aborting beam in Recycler. The first two systems are similar and will share the same design. The last three are also similar and will share the same pulser design and an updated magnet design. The two different types of systems will be described in general with a specific table to show differences.

System Name	Location	Total Field (G•m)	Field Rise Time (ns)	Field Flattop (ns)	Flattop Stability	Field Fall Time (ns)	Post Kick Stability
Recycler Injection	RR104	360	57 (3 bkt)	1534 (81 bkt)	±3%	57	±3%
Recycler Gap Clearing	RR400	350	57	1534	±4%	57	±3%
Recycler Abort	RR400	320	1650 (86 bkt)	9510 (502 bkt)	±4%	n/a	n/a
Recycler Extraction	RR232	510	1650	9510	±3%	n/a	n/a
MI Injection	MI309	370	1650	9510	±3%	1650	±3%

Table 8.8: Kicker Specifications from NOvA Document #1596

The first system, Recycler Injection, in Table 8.8 has a fast rise and fall time to cleanly inject an incoming bunch train of protons. The rise time is required to be no more than 3 RF buckets to allow for loading beam from Booster into the Recycler. The flattop has to be no less than 81 RF buckets (1 batch), which is the pulse train length from Booster. The fall time has to be no more than 3 RF buckers so that on the last 6 injections of the slip stacked beam, the existing, circulating beam will not be kicked. This system operates at the Booster repetition rate of 15 Hz, but in a train of 12 injections over a minimum of 1.33 seconds. It must also be thermally stable over time and different Recycler operating modes.

The function of the next system, gap clearing, is to clean beam out of the injection gap which arises from losses in the slip stacking process. This unwanted beam is kicked into the abort line just before the next injection into the Recycler, so it operates in unison with the Recycler Injection kicker. Without this gap clearing kicker, some beam will be kicked into magnets downstream of the Recycler Injection kicker when the next batch is injected. Larger variation on the flattop is allowed because the beam is being dumped, but the tail must remain low to avoid kicking the circulating beam.

The specifications for these two systems require a new kicker magnet design and modification of an existing kicker power supply design. Building prototypes to prove the performance of these systems is mandatory and is planned. This necessary step increases the time before a finished system is ready to install.

The next three systems in Table 8.8 (RR abort, RR extraction, and MI injection) all have a rise time associated with the abort gap in each machine, which is approximately 1/7 of the circumference. The flat top for all has to be long enough to fully extract 6 batches. Only the MI injection kicker has a fall time constraint to avoid kicking the leading bunches of the beam as they come around after injection.

For these three systems, we can make use of an existing kicker magnet design (the current RR extraction kicker). Because of time and personnel constraints during the shutdown, existing magnets will not be removed, refurbished and re-installed, instead new magnets are required to be built. A few modifications to update and improve the design will be done. A prototype magnet with these changes will also be built to verify performance. The shape of the falling edge and post flattop are especially important. A new power supply to meet the specifications for all three of these kicker systems needs to be built. This will be based on an existing power supply so only minor changes will be made. A new charging supply is required to be prototyped for this system however.

Finally, almost all of the existing kicker magnets in the Fermilab complex are built using a ceramic chamber to provide the required level of vacuum. This chamber is installed between the magnetic material and the proton beam, which has several tradeoffs. The magnet itself does not need to be vacuum certified. This greatly simplifies the constraints on materials to 1) provide high voltage insulation, 2) to provide high voltage capacitance and 3) for the magnetic material itself. The ceramic chamber itself can also be used to support beam current return paths to lower the transverse and longitudinal impedance of the magnet. The tradeoff is that a vacuum tight ceramic chamber must be made. Like the development of a new magnet, long lead times are required and prototyping at various stages is required. For this reason, an existing chamber design and end flange design have been chosen. This decision has made the magnet aperture larger than beam physics requirements for the Recycler kickers. Details on all the kicker systems follow.

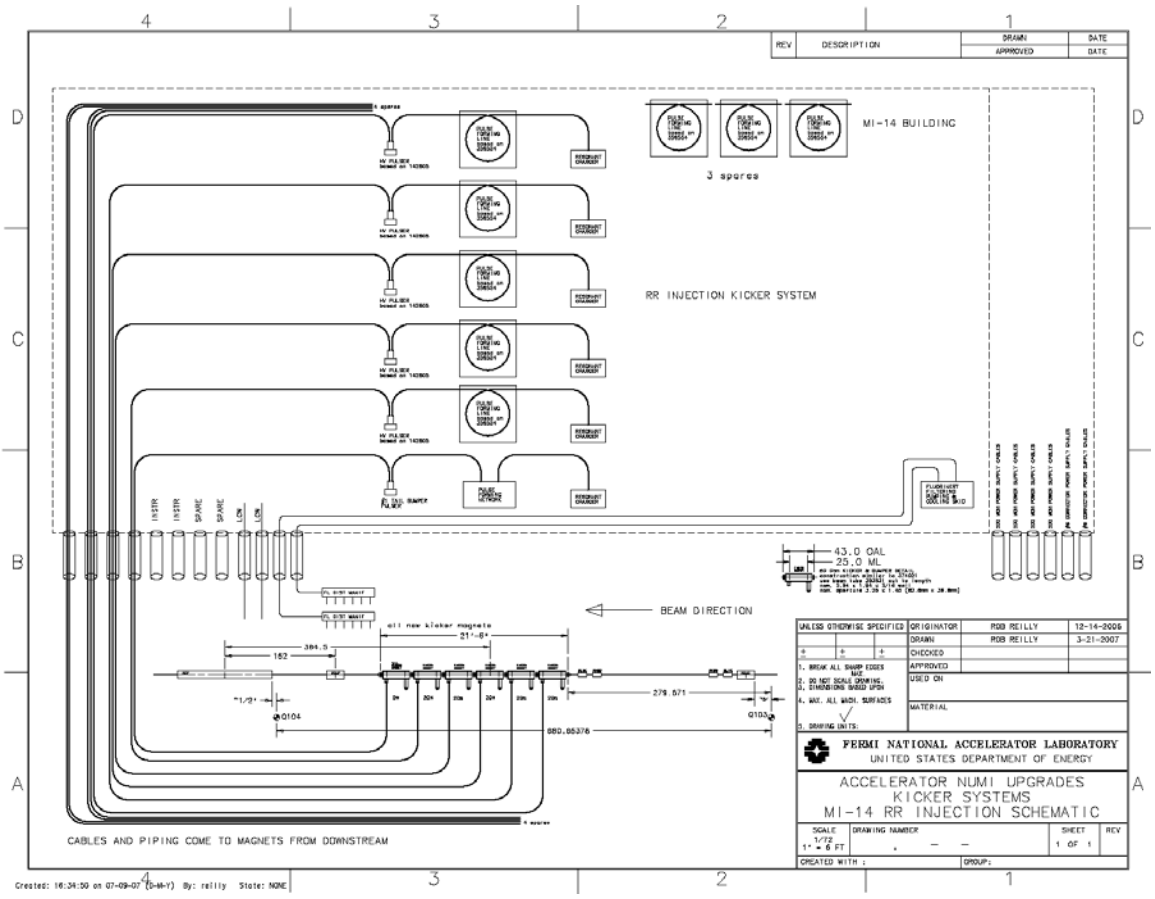

Fig 8.10: Proposed layout of RR injection kicker. Schematic includes location of magnets in the tunnel, cabling, penetrations used, and fluorinert cooling.

8.3.3.1.1 Recycler Injection and Gap Clearing Systems

A new and faster injection kicker system is needed to perform 12 batch slip stacking in the Recycler. The existing Main Injector Injection kicker design is capable of slip stacking 11 batches but studies have shown that several bunches were kicked out of the MI because of the kicker tail. The specifications required to perform the 12 batch injection are shown in Table 8.9 along with the measurements for other existing fast kickers. The new Recycler Injection kicker has approximately the same beam aperture as the existing MI Injection kicker, however the direction of the field is vertical instead of horizontal.

The Recycler injector kicker system will be built on the model of these previous fast kicker magnets. It will have a magnetic aperture of 53 mm x 107 mm (to meet the beam aperture of 33 mm x 81 mm) [11], a fill time of 34 ns, a pulser voltage rise time (1% to 99%) of a little less than 23 ns and a Z_0 of 50 ohms. With these design parameters, the magnetic length is limited to 0.7 meters with a physical length per magnet of 1.1m. This magnet will have a nominal B field of 113 Gauss with a nominal current of 450 and a maximum current of 550 A. In order to get the required 360 G•m, we will need a magnetic length of more than 3.2 m and thus we propose a 5 magnet and pulser system to give substantial tuning range for the main deflection. The additional margin in integrated field may be reduced after the prototype magnet has been built. Reducing the magnetic length may be required to meet the magnetic field rise time specification.

The magnets for the kicker are transmission line style and are terminated with slightly less than the characteristic impedance to give a flat pulse shape. Because the system will be running at a variety of average repetition rates, the affect of average power on the termination resistor value has to be less than ~2%. This has been done successfully on two previous systems including recently the MI Injection kicker. An electrically insulating oil, Fluorinert®, is temperature regulated and pumped through these resistors.

This system is expected to need a "bumper" system to cancel the tail and allow the system to meet the fall time requirement to the 3% level. The bumper system will have a prototyping stage for the power supply. It will use the same magnet as the main kick however the orientation will be reversed so that the kick direction can be made to cancel. The requirements for the bumper power supply are generally known from existing measurements. This power supply is required to reduce the amount of field variation to the 3% level and is especially needed to meet the fall time requirements.

The fall time corrector is necessary to reduce the tail to the ~3% level in the required 57 ns. The same style magnet will be used with these bumper power supplies and installed with the main magnets because the peak current of the tail bumper is roughly the same as the main power supply. The bumper magnets will need to be installed upside down to provide a canceling field for the same polarity of charging and pulser supply. There are subtle polarity issues on the thyratron switch, which is used for the main pulse and bumper pulse, which cause a change in waveform with a different polarity. A proposed layout, including cabling, penetrations from the MI 14 service building, and cooling piping is shown in

Fig 8.10

8.3.3.1.2 Magnet Design

Several fast kicker magnets have been built over the years. Existing designs and their rough capabilities are shown in Table 8.9. The MI injection kicker magnet design is over 10 years old and Booster kicker magnet is over 20 years old. Some improvements can be applied to these to improve response. The Tev injection kicker magnet has most of the improvements incorporated into it.

Magnet Type	Electrical Impedance (Ohm)	Total Inductance (nH)	Propagation Time	Field Rise (ns)	Nominal Field (mT)	Magnetic Height x Width (cm)	Magnetic Length (m)
Booster Kicker	50 Ohm	1250 nH	27 ns	~ 35ns	10	7.3 cm x 7.0 cm	1.08 m
MI Injection	25 Ohm	710 nH	28 ns	~ 50 ns	6.8	11.1 cm x 6.3 cm	0.79 m
Tev Injection	12.5 Ohm	860 nH	70 ns	84 ns	52	4.8 cm x 7.4 cm	0.86 m
NEW RR Injection	50 Ohm	1600 nH	34 ns	57 ns	11.3	5.1 cm x 11.0 cm	0.64 m

Table 8.9: Comparing Existing Kicker Magnet Parameters to New Design. Note that the Tev Injection kicker magnet is driven by a positive and negative power supply to further decrease the field rise time. This should not be necessary for this application.

The Recycler Injection magnet will need distributed capacitance. The same potting material that is required for insulating the high voltage bus will be used for making the high voltage capacitors. This has been done in both the Booster and MI kickers with success, but the capacitance required here is about twice as much per unit length. Simulation of the magnet

parameters is being done. A prototype design of the magnet will be built and then the propagation time and impedance will be measured. The prototype will also be pulsed at maximum voltage to determine if there are any major issues.

The magnet design for the gap clearing kicker will be an exact duplicate of the Recycler Injection magnet. The first production magnets will be installed in the Main Injector for gap clearing in the current Collider Run. After the end of the Collider Run, these magnets will be moved from the MI and installed in the Recycler at the same lattice location. The magnetic requirements are exactly the same so no further prototyping will be required and the spares can be shared between systems.

8.3.3.1.3 Main Pulser Design

A fast pulser design was done several years ago for the Tevatron injection kickers (see Fig 8.11)

Originally the pulser was designed to drive a 12.5 Ohm load, but it has been tested with a 25 Ohm and 50 Ohm load. The rise time at higher resistance (lower current) is faster and may be fast enough to meet the requirements for NOνA. Additional work is being done to further reduce the rise time by using saturating magnet materials (ferrite) in order to have a safety margin in the rise time. This shows good promise (Fig 8.12). The ferrite can be seen to reduce the rise time to about 8ns. More work and prototyping are required to determine the source of the overshoot. A little overshoot is in fact helpful in reducing the field rise time, but it must be damped fast enough The mechanical design of the pulser also needs some changes to incorporate the ferrite material in a reliable manner. The pulser has not been able to be pulsed at the 15 Hz repetition rate due to lack of a load cooling system but one is being built for prototype use.

One other design decision to be done is the cable type for the pulse forming line. Two variations are available, both with the required voltage and impedance. The newer style cable has 2/3 the loss factor. This may be critical in meeting the fall time requirement as the dispersive losses in the cable lead to a longer fall time than rise time and even a slightly faster fall time may ease the requirement of the bumper pulser. Testing of the new cable for fall time has begun but the result is difficult to separate from pulser rise time. The cable will need to be tested again when most of the changes to the prototype pulser have been completed.

The pulsers for the Gap Clearing system will also be identical to the Recycler Injection kicker. The slightly higher flattop ripple allowed does not impact the design of the pulser and bumper. The post flattop amplitude remains the same as the Recycler Injection system so the bumper is still required.

8.3.3.1.4 Bumper Pulser Design

The tail correcting bumper will consist of the same pulser and controls as the main pulser, however a pulse forming network (PFN) will be used in place of the pulse forming line (PFL, cable). The tail falls to ~ 20% of the main pulse after 25 ns. Because there are five main magnets and pulsers to get the total kick, the bumper corrector has to supply ~ 100% of the single main pulser current. The tail correcting bumper needs to have the same peak voltage and current as the main pulser and so will have the same switch and controls. The initial fall can be approximated by several RC sections to match the fall time of the pulse forming network for the tail correcting bumper.

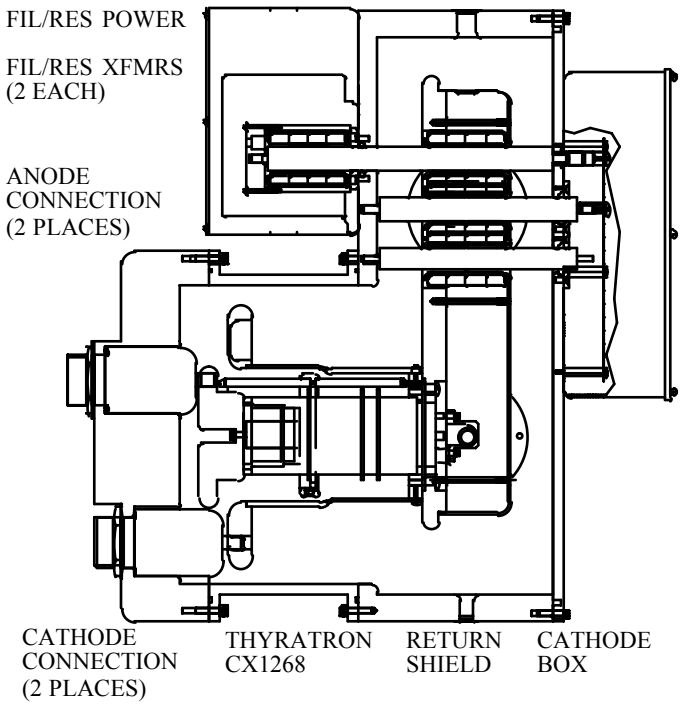

Fig 8.11: Tevatron Injection Kicker Fast Pulser

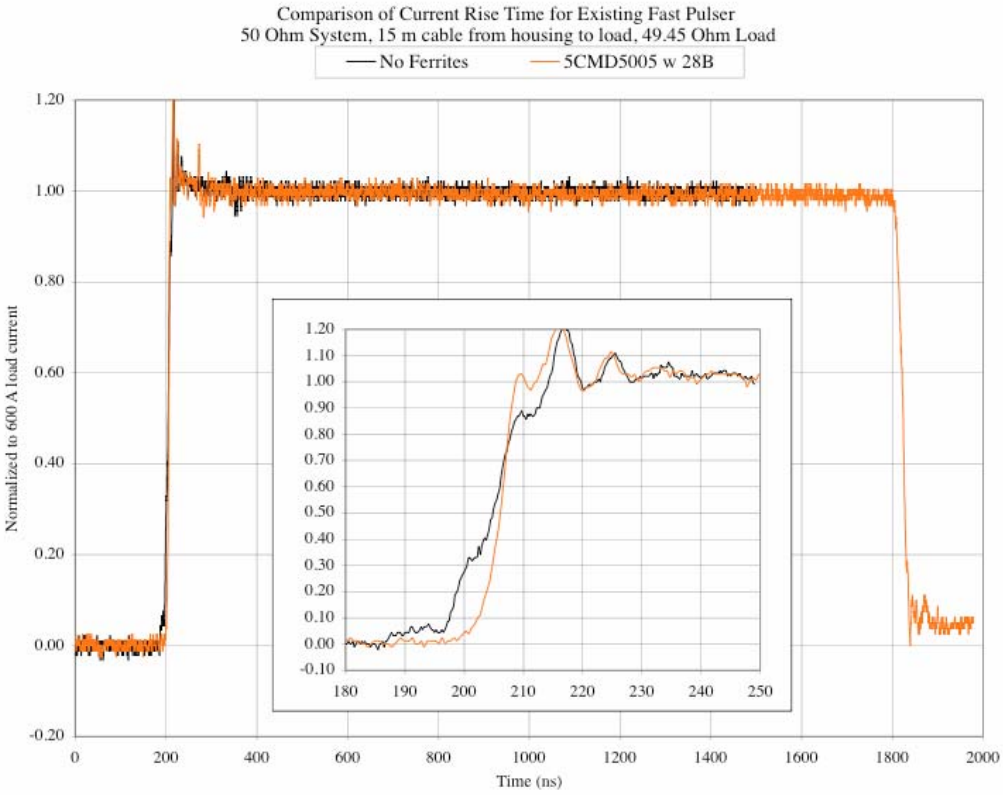

Fig 8.12: Measured Pulse Response of Prototype Pulser. The black trace is a measurement without the ferrite compensation; the orange trace is a measurement with the ferrite compensation. Note the improved rise time in the second case.

8.3.3.1.5 RR Abort, RR Extraction and MI Injection Kicker Systems

These three kicker systems will require a long pulse (~9.5usec) with a fairly long rise time (~1.6usec). We propose updating the design of the existing 25 ohm Recycler transmission line magnets currently in use for the transfer lines with a 1.6 μsec flat top. Each magnet has an insertion length of 1.8 meters (70 inches) and a magnetic length of 1.4 meters (54 inches). The magnet aperture of the new kicker magnets is again 53 mm x 107 mm to meet the beam aperture of 33 mm x 81 mm.

The power supply for these three kickers requires a fairly long pulse and so a pulse forming network is usually used. The existing NuMI kicker uses a PFN to provide a 5000 A pulse into a pair of 10 Ohm magnets in parallel. Because only 1000 A are required for these kickers, it is actually more cost effective to use a long pulse forming line. Six spools of cable will be spliced end to end to provide the required pulse length, and six other spools are required in parallel to provide the correct impedance. An important technical reason for using the cable is that the falling edge for a cable is monotonic and somewhat faster than for a matched PFN. This is important for the MI injection kicker.

The magnets for these kicker systems will not have the load termination installed on them. The termination will be in the same service building as the power supply. This is possible because of the fairly fast field rise time of the magnets used in comparison to the requirement. Because the Recycler extraction has a much larger total field, two magnets will be wired in series.

A tail bumper will be needed for the MI injection kicker and thus is planned and costed in the schedule. The tail bumper will use the same concept as the Recycler Injection system; however the pulser will need to have different component values for the PFN. The system is shown in Fig 8.13.

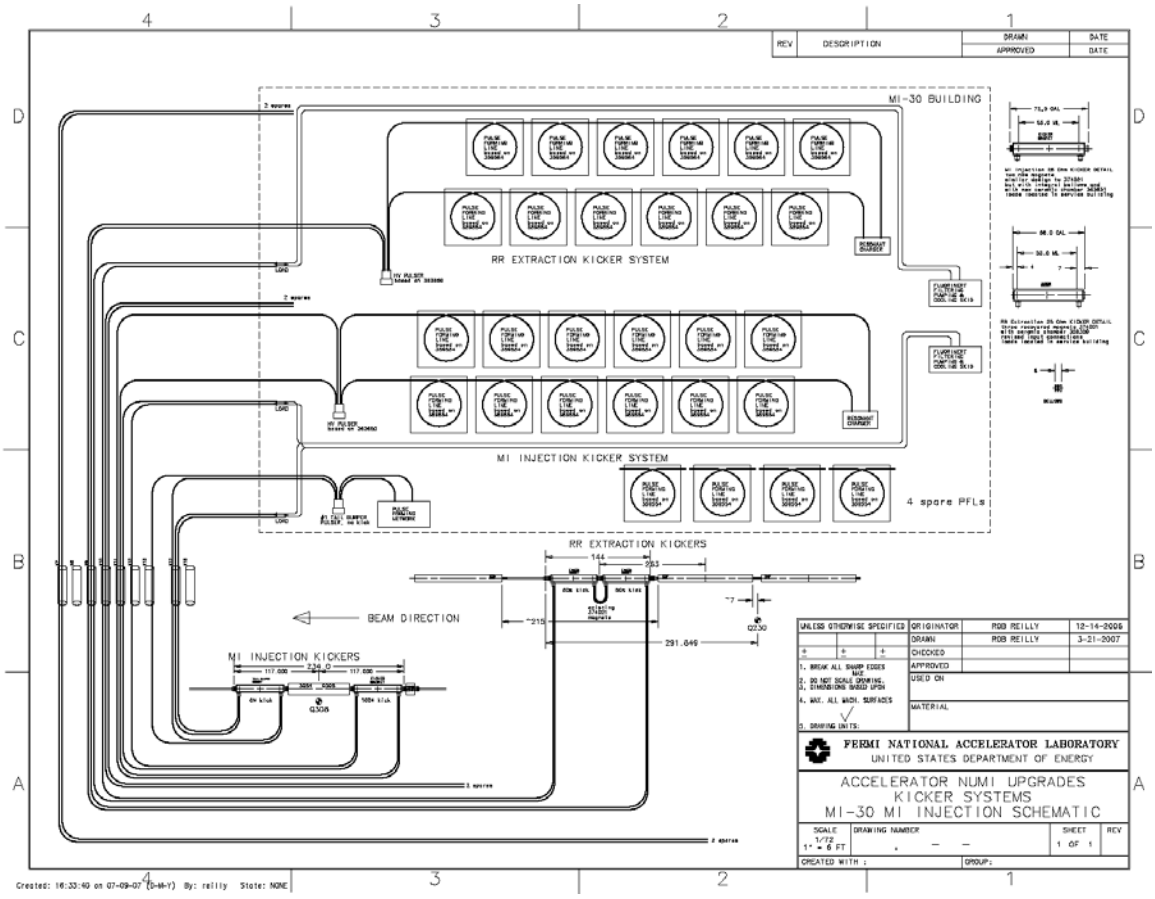

Fig 8.13: Proposed layout of MI 30 injection kicker. Schematic includes location of magnets in the tunnel, cabling, penetrations used, and Fluorinert cooling

All of the kicker systems will need active cooling. Existing Main Injector kickers use an active Fluorinert® cooling for load temperature control. We will make use of these existing designs for the new kicker systems.

8.3.3.1.6 Main Pulser Supply

The main pulser for these systems will consist of controls, a charging supply, a thyratron enclosure and a pulse forming line. The controls will be the same across all kicker systems. A new charging supply will be required. The design has the pulse forming line resonantly charged about 2 msec before the kicker is fired to transfer beam. A new charging system will be prototyped for this application. Resonant charging is used to limit the possibility of the thyratron switch self triggering. It also allows the use of a combination of a readily available commercial charging supply and transformer for improved reliability and overall cost.

The pulse forming line will consist of an improved RG-220 cable made to Fermi specifications. This cable has been used reliably for many years at these voltage levels.

The cable is only available in continuous lengths of up to about 200 m. A total length of approximately 1000 m is required to get the full pulse length. Two of these lengths are then connected in parallel to get the nominal current at the voltage where the cable and switch will operate reliably. The splice required for this is based on existing commercial connector design. Prototypes have been ordered and are being tested.

The switch enclosure will be very similar to the Recycler Injection and Gap Clearing kicker. Minor changes will be done so that a larger voltage and current thyratron can be used. Pulse sharpening will not be needed for this pulser.

8.3.4 Cooling System Modifications

Modifications to the Recycler will affect three Low Conductivity Water (LCW) cooling systems: the Main Injector global LCW system, the RF (95 degree) LCW system and the Cavity (55 degree) LCW cooling systems located at MI-60. Work affecting these cooling systems is occurring in the Q-100 region (Injection Line), Q-300 region (Extraction Line), Q-400 region (Abort Line), and Q-600 region (RF Cavities). Work on cooling needs for the associated power supplies in the service buildings is occurring in MI-14, 30, 39, and 60 Service Buildings.

It is currently assumed that the majority of the Main Injector Cooling Systems will have sufficient capacity for increased loads due to the Recycler modifications. However, there are extensive modifications planned in the Q-100 region, where a new Injection Line will be added. This is an area already running at capacity, both for heat load and pressure & flow capabilities. Additional loads may push the need for the installation of an LCW Pump Room at MI-8 (originally planned for the MI installation, but never installed). This would add about 600 kW of cooling capacity and 450gpm of flow. Therefore, this estimate also covers studying this solution, and the impact of such on the overall operation of the Recycler Cooling Systems.

Additionally, all added heat loads eventually reach the cooling ponds. Studies conducted in the Fall of 2006 [12] suggest that current pond capacities are sufficient for the estimated heat loads. However, the ponds will see an increase in operating temperatures of around 1°F. Further work is required to identify and verify all additional heat load changes with the expected 700 kW operation conditions, compare with current operational conditions, and repeat modeling of the resulting pond water temperatures.

Details on all these system upgrades follow.

8.3.4.1 Injection Line

This work consists of the relocation and reconnection of pipe and bus for magnets in the Q-100 area. In addition, lines are installed from the Q100 tunnel area into the MI-14 service building, where the connections to new Fluorinert® skids and power supplies will be made.

8.3.4.2 Extraction Line

This work consists of the relocation and reconnection of pipe and bus for magnets in the Q-300 area. Additional lines are installed in the MI-30 service building, where connections to new Fluorinert® skids and power supplies are made.

8.3.4.3 Abort Line

This work consists of the relocation and reconnection of pipe and bus for magnets in the Q-400 area. In addition, lines are installed from the Q-400 tunnel area into the MI-39 service building, where connections to new Fluorinert® skids and power supplies are made.

8.3.4.4 RF Cavities

This work consists of the relocation and reconnection of LCW lines to magnets and cavities in the Q600 through Q609 region, as well as the installation of additional pipe drops for the new cavities. Likewise, there will be additional pipe drops installed in the MI-60 gallery to supply LCW to new power supplies. This work will be performed on both the RF (95°F) and Cavity (55°F) LCW Systems, which have the main components located in the MI-60 Pump Room.

Both the Main Injector and Recycler lines are adding RF cavities in the region. At this time it is thought that the capacity of both the 95°F and 55°F systems is adequate for all additional RF cavities. This will be verified as part of the engineering design process.

8.3.4.5 MI-8 Pump Room

Such a pump room was initially planned with the construction of the Main Injector. Because of this, the building floor space already exists for the installation of this pumping facility, as does the piping to the MI-8 beam line LCW headers, pond water lines to PV-9 and Pond H, and substantial basic electrical service to the room. Also, 100 Hp LCW pumps were procured as part of the MI build package, and are sitting as spares, ready for use.

It must be emphasized that at this time, it is not known whether or not the addition of this pump room is fully justified and required. Such determination will be made in the design reviews for the Recycler and Main Injector upgrades.

For the installation of the MI-8 Pump Room, the majority of component costs and installation efforts are fairly well known, hence the use of low contingencies on many tasks. The very notable exception to this is the Pond Water system to and from the MI-8 heat exchanger. Pond Pump Vault PV-9 was originally planned for this use, but has since been redirected and outfitted for supplying pond water to MI-62. It appears these lines may be already functioning at full capacity. The extent of the ability to adapt or upgrade PV-9 to also feed Pond Water to MI-8 is not known at this time, and will require engineering work, covered in the OPC BOE. This leads to 3 distinct scenarios:

1) we have to add larger pumps,
2) we need larger pumps plus either larger or new pond-to-vault lines, or
3) we need an entirely new vault, with new lines and pumps.

Further engineering is required to determine correct needs. To address this task with a reasonable accuracy, we have costed Scenario 2 and 100% contingency is used for both M&S and labor for PV-9 modifications.

8.3.5 Changes in the Recycler Upgrades Design since the CDR

We have made changes since the CDR in the following areas:

- Transfer lines
- Kicker specs
- BPM cable choice

The design changes have been driven by the desire to simplify the construction, installation, and operation of the Recycler Ring, thus applying value engineering and risk management.

8.3.5.1 Changes in transfer line design

We have made changes to both the injection and extraction line design. The main design change in the injection line is to move from a design with a series of 4 vertical bends to a design with 2 vertical bends. The change was driven by two considerations, (1) to simplify installation

and (2) to minimize the number of powered elements near the Recycler Ring. The design presented in the CDR had 4 large powered dipoles (the ADCW listed in Table 8.4), one as the switcher magnet in MI8, two in the mid point of the line, and one near the injection area of the Recycler. By changing to two vertical bends, one being the switcher magnet and the second a permanent magnet dipole, we no longer have to support these multi-ton magnets between the floor and the ceiling (for the two in the mid point) or near the ceiling (for the one near the injection area), thus making the installation of the line simpler. In addition, we do not have the possible field effects of having a large ramped dipole magnet near the Recycler.

The main design change in the Extraction line is to move the injection point in the MI one half cell from the 309 location to the 308 location (with a corresponding move in the extraction point in the Recycler). This location is better for both aperture and phase advance reasons. With the MI injection kicker at 308, we can use the same ceramic beam tube and magnet for this kicker as we are using for the Recycler extraction and abort kickers, thus eliminating a separate design for both the ceramic beam tube and the magnet.

8.3.5.2 Changes in Kicker specifications

We have decided to accept 81 Booster bunches per Booster batch instead of 82. This change loosens the kicker rise/fall time specifications from 38 nsec to 57 nsec with ~1% loss of protons to the NuMI target. The change the MI injection location (discussed in Section 8.3.2.3 and Section 8.3.5.1) results in a change to the required aperture and integrated gradient.

Based on measurements on the MI 10 Injection Kicker, the kicker specifications were relaxed to 3% (from 1%) for flattop stability and post kick stability for the systems with the tighter requirements. Due to this change, the coarse bumper (flattop bumper) system can be removed from the project and still meet the $\pm$ 3% specs. This thus means that the RR Extraction system has no bumpers and the MI Injection, RR Injection and the Gap Clearing Systems all only have tail bumper systems.

The kicker systems will be able to meet $\pm$ 3%, and the damper system will simply improve upon this. However, this will mean that the tail bumper will not be able to be a hot spare, as it will be installed "upside down". However, with a several hour shutdown, it could be reconfigured and used as a spare if necessary.

8.3.5.3 Changes in BPM cable choice

We have completed the Recycler BPM specification, which allowed a detailed cable specification to be written. We have narrowed down the cable choice based on these specifications and received new pricing information.

8.3.6 Remaining Design Work for the Recycler Upgrades

There is significant design work to do on the Recycler Ring modifications and kicker systems tasks. Most of what has been presented in previous sections represents the physics and preliminary designs for the different aspects of the project.

For the Recycler Ring modifications, we need to continue and complete the detailed engineering design work for the injection line, extraction line, and RR30 straight installations. The work spans the range from individual stand designs for magnets to the installation plan for each beamline. These design tasks are included in the project schedule, e.g., the installation planning tasks are a series of tasks in WBS 2.0.1.1.1.14, including resources and M&S costs. There is a similar set of work for the 53 MHz RF system.

The kicker systems have an extensive R&D and prototyping program that has already begun. The R&D work includes the magnet design, the primary and bumper power supply design, and

the Fluorinert® cooling system design. In addition, there is detailed installation design in the accelerator enclosures.

Changes to the water cooling systems are still at the conceptual level. Further work is required to verify and identify the total heat loads with the 700 kW operating conditions, to compare with current operating conditions, and to model the cooling pond water temperatures.

8.4 Main Injector (MI) Upgrades

8.4.1 Overview

For NOνA the Main Injector will be accelerating only 10% more proton intensity as in the Proton Plan (4.9E13 ppp instead of 4.5E13 ppp). The beam power out of Main Injector is much larger (705 KW instead of 392 KW) mainly because the cycle time is reduced from 2.2 sec to 1.33 sec. By using the Recycler Ring for stacking, the Main Injector cycle time is reduced to 1.5 sec increasing the beam power from 392 KW to 628 KW (a factor of 1.47 because of the cycle reduction and a factor of 1.09 because of the intensity increase). To further decrease the Main Injector to 1.33 sec and thus increasing the power to 705 KW we will need to increase the maximum acceleration rate from 204 GeV/sec to 240 GeV/sec. In order to accommodate the faster ramp, one of the quad power supplies needs to be upgraded and two extra RF stations need to be added.

8.4.2 Modifications

In order to reduce the Main Injector 120 GeV cycle time to 1.33 sec, the maximum acceleration rate has to be increased from 205 GeV/sec to 240 GeV/sec. The current 120 GeV ramp used for the mixed mode Slip stacking and NuMI along with the NOνA era proposed ramp is shown in Fig 8.14. The current Main Injector 120 GeV ramp has a 488 msec dwell at injection in order to accommodate the slip stacking for pbar stacking and five injections for NuMI. This dwell time is reduced to 80 msec for NOνA since we only have one injection per cycle from Recycler.

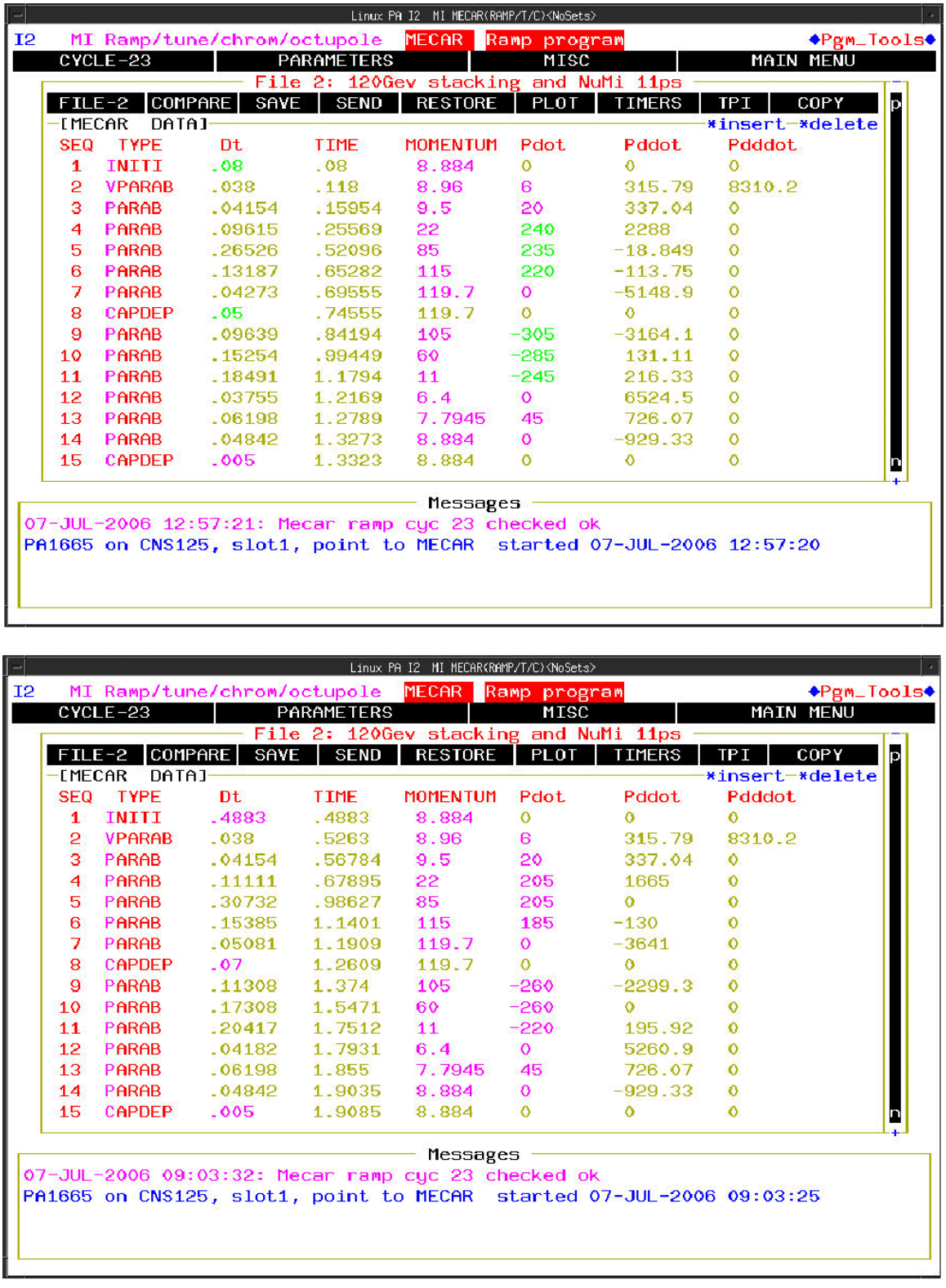

Fig 8.14: Current 120 GeV Main Injector ramp (bottom) and NOνA ramp (top).

The voltages and currents for the Main Injector Bend and the two Quad Buses during the NOνA ramp are shown in Fig 8.15. The max voltage available in the main bending bus is 11.8 KV, while the voltage available for the horizontal and vertical quad busses is 3.2 and 2.8 KV respectively.

As can be seen from Fig 8.15, during the NOνA ramp we are going to exceed the maximum available voltage of the defocusing (vertical) bus. For this we propose to increase the available voltage at the defocusing bus by replacing one of the transformers with a higher voltage one and modifying the corresponding supply. These changes will make the available voltage from the defocusing bus equal to the focusing one.

The RMS current for the Main Injector dipoles and quads for the NOνA ramp has been calculated to be 4000 A and 1600 A respectively. These numbers are lower than the values of 5000 A and 2000 A that the Main Injector water-cooling system was designed to handle. For comparison the RMS current values for the present Main Injector $23 ramp are 3550 A and 1425 A.

The Low level RF (LLRF) is responsible for controlling the frequency(s) and phase of the RF that is applied to the beam. It accomplishes this control through physics models and feedback loops using phase and radial position detectors. The LLRF systems are also responsible for controlling beam transfers between accelerators and providing beam markers to the beam sync clock system which can be used to identify a specific bucket in the machine. Some of the services that the LLRF system provides are: paraphrase control, counter phasing, cogging, injection phase and bucket alignment, transition phase jump, and bunch rotation.

In comparison to the LLRF system, the high level RF system (HLRF) receives the RF signal from the LLRF system and is also responsible for applying the requested RF voltage to the beam. To accomplish this control, the HLRF system has a collection of curves that include: anode program for voltage, bias program for cavity tuning, and several gain curves to keep the stations linear. There are also feedback compensation that works on beam loading and anode program variations.

To slip stack protons in the Recycler Ring, a two RF group controller is needed that will interface with Booster for transfers into the machine and the Main Injector for extraction. Automated frequency and phase control are needed for each RF group. Transfer enable and revolution markers must be provided to the control system to synchronize kickers and instrumentation. In addition, beam and system diagnostics need to be available to the operators and studiers. The present Main Injector Low Level RF (LLRF) system provides all the same required functionality and we propose that a duplicate MI system be modified for the RR. The present Main Injector system can be modified to interface with the new RR system with minor modifications.

While the custom hardware for the new LLRF would be quite expensive to build from scratch, we plan to decommission the present RR and TeV LLRF system before proton stacking in the RR begins. Then the plan is to salvage the bulk of the required hardware to build both new operational and development crates. New custom cables and cable pulls will be needed. While a great deal of software will be reused, there will be a fair amount of software modification, testing and commissioning work to be done. The RR LLRF system is included in the MI Modifications WBS since it will be managed by this team. The Recycler HLRF will be managed by the recycler team and is described in Section 8.3.2.4.

Two new service buildings will be needed to house the kicker and beamline supplies named MI-14 and MI-39. Before those buildings can be used operationally the communications

infrastructure needs to be build. This includes racks, controls hardware and communications cable. This work is included in this WBS.

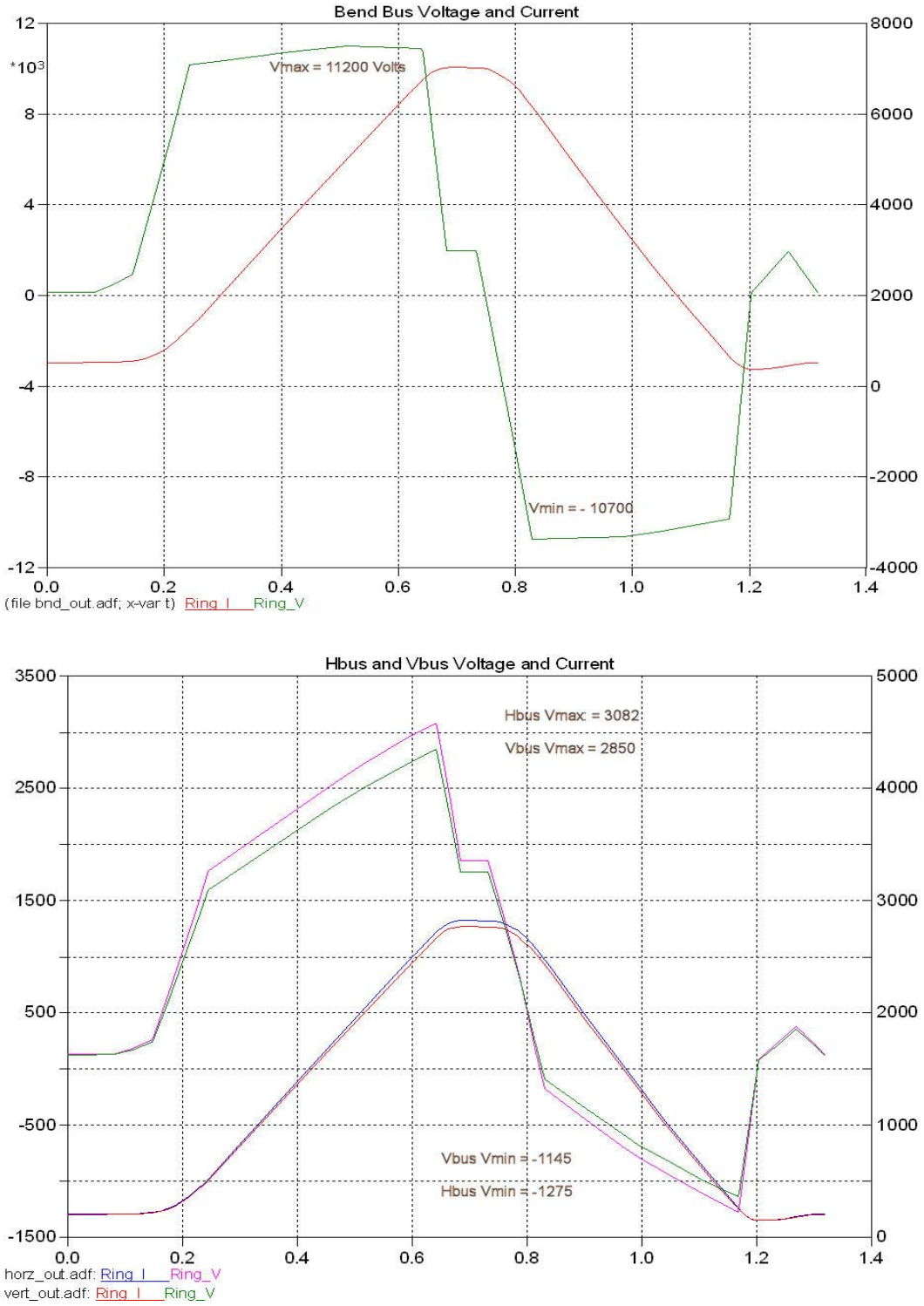

Fig 8.15: Voltages and currents for the bend bus (top) and the two quad busses (bottom) during the NOνA ramp.

The A1 line used for Pbar transfers from Main Injector to the Tevatron will not be used and needs to be decommissioned. In addition the three Lambertson magnets and the kicker used for the Pbar extraction in the Main Injector ring need to be removed since they represent aperture restrictions and are large sources of impedance. This work is included in this WBS.

8.4.3 RF Cavities

The current Main Injector RF system consists of 18 stations (RF cavities, power amplifiers, power supplies and ancillary systems) providing a maximum acceleration voltage of 235 KV and 175 KW per station. It has enough power to accelerate up to 5.5E13 protons with 240 GeV/sec.

The moving bucket area available after transition is a function of the acceleration rate and the maximum RF voltage available. For a fixed RF voltage and acceleration rate, the bucket area has a minimum at $\sqrt{3}$ times the transition energy. In the Main Injector we have found that we need a moving bucket area after transition of at least 1.8 eV-sec with slipped stacked beam in order to avoid beam losses. From Fig 8.16 we can see that with 18 RF stations we cannot produce a sufficiently large enough bucket area to efficiently accelerate slipped stacked beam faster than 240 GeV/sec. Since we have a total of three spare cavities we propose to install two extra cavities in Main Injector in order to have enough extra voltage for running with 240 GeV/sec reliably (even with a station down). A picture of an MI RF cavity is shown in Fig 8.17. The two cavities are going to be installed at the "phantom" locations 4A and 14A. Most of the utilities that we need are available and the penetrations exist in these locations. In the location 4A two barrier cavities are currently installed that will need to be removed, while in the location 14A we have the second harmonic (h=1176) cavity used for proton coalescing which will no longer be needed after the end of the collider program (Fig 8.18). In installing cavities at 4A and 14A, the cavities at 4 and 15 will need to be moved slightly to allow for this installation.

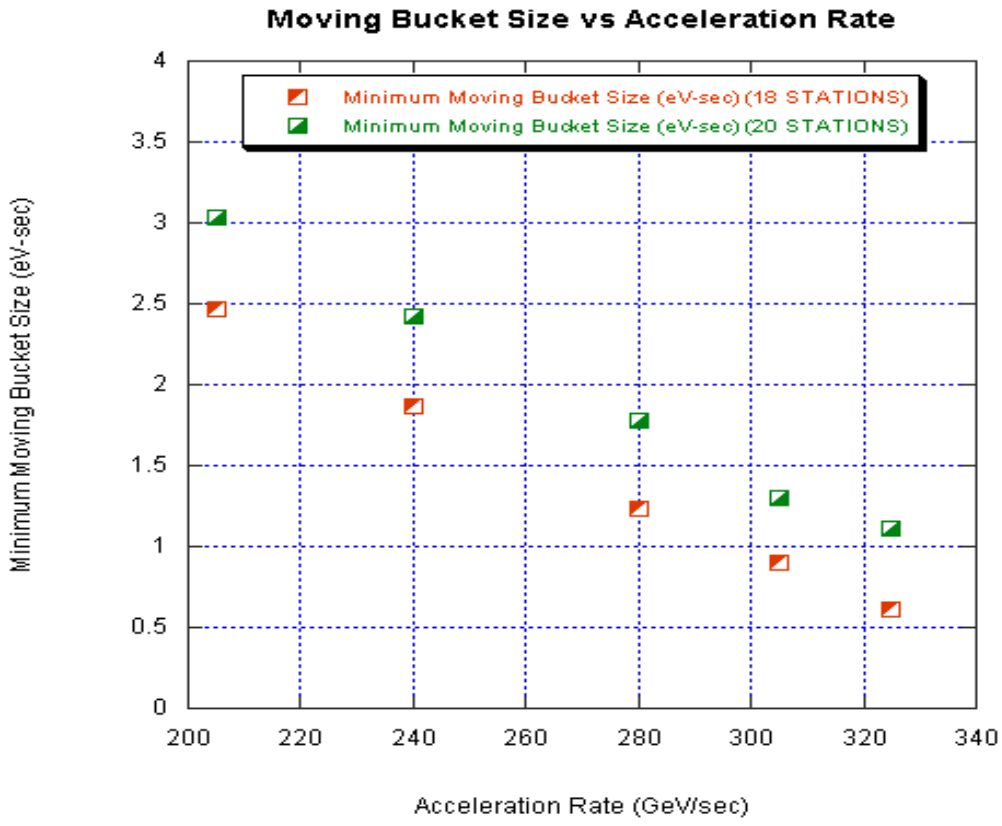

Fig 8.16: Minimum moving bucket area as a function of acceleration rate for 18, 20 RF stations.

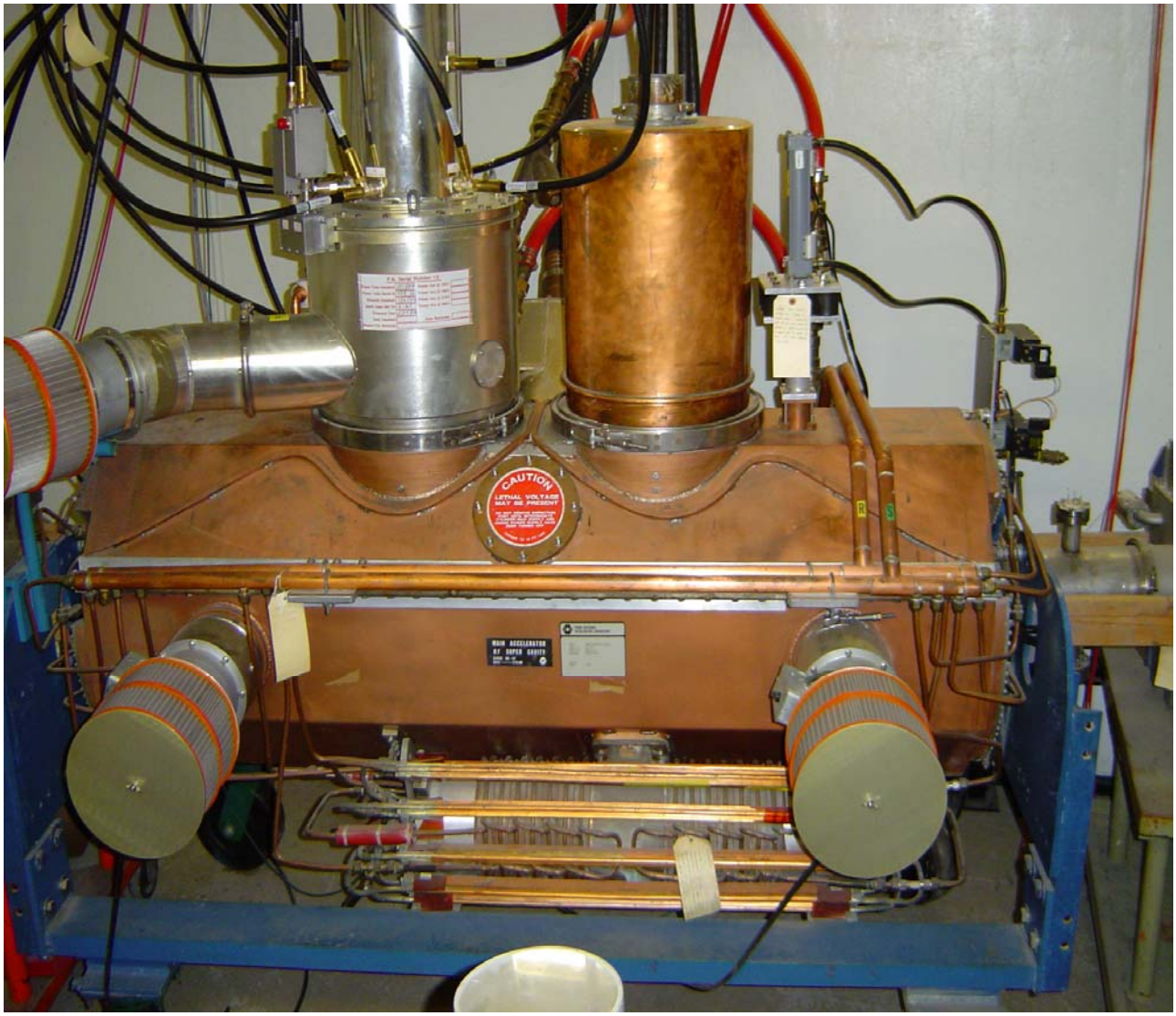

Fig 8.17: Picture of a MI RF Cavity. In front and under the cavity one of the cavity tuners can be seen. On the top of the cavity one can see the places of the two possible power tubes. Currently only one power tube is installed in each cavity (top left).

Fig 8.18: Pictures of the phantom locations where the two extra RF cavities will be installed. The location 4A is shown on top while the location 14A is shown in the bottom.

Two new modulators and two bias supplies will need to be fabricated. Those modulators and bias supplies are the same as the existing MI supplies. A picture of those supplies is shown in Fig 8.19.

Fig 8.19: Pictures of the series tube modulator supply (left) and the bias supply (right).

The spare cavities do not include the power amplifier tubes which need to be purchased and the whole assembly that houses the tube and attaches to the cavity needs to be manufactured. A picture of the power tube assembly is shown in Fig 8.20. The power amplifiers are driven by 8KW solid state drivers that are located upstairs in the gallery. Two extra solid state drivers will be needed for the two extra RF stations. The solid state amplifiers needed (eight 1KW modules for each station) will be recycled from the Tevatron but we will need to purchase the DC power supplies and the racks. A picture of a solid driver amplifier rack is shown in Fig 8.21.

Fig 8.20: Picture of the power tube assembly. We can see the matching section on top and the copper cooling lines. The power tube is located at the bottom of the assembly.

Fig 8.21: Pictures of a rack housing the solid state driver for an MI rf station.

The most challenging part of this job is the manufacturing and installation of the bus bars for the cavity tuners. Those bus bars are used to connect the bias supplies from the equipment gallery to the cavity tuners which are located next to the RF cavities in the tunnel. .The total length of the existing bus bars is 502" and, originally, they were comprised of two pieces welded together. The bus bars of the existing 18 RF stations were installed by using a support and installation fixture at the early stages of the MI-60 RF service building construction when there was no roof (Fig 8.22). In the present plan we will clamp together three 14' (168") pieces. This way we can install the whole bus bar through the penetrations without having to take part of the building's roof off. A picture of the proposed clamp assembly for the bus bars is shown in Fig 8.23.

Fig 8.22: Pictures of the original bus bar installation during the construction of the MI-60 building. In the top picture the whole bus bar can be seen hanging from the crane with a support, while in the bottom picture we can see the bus bar inside its fixture for installation.

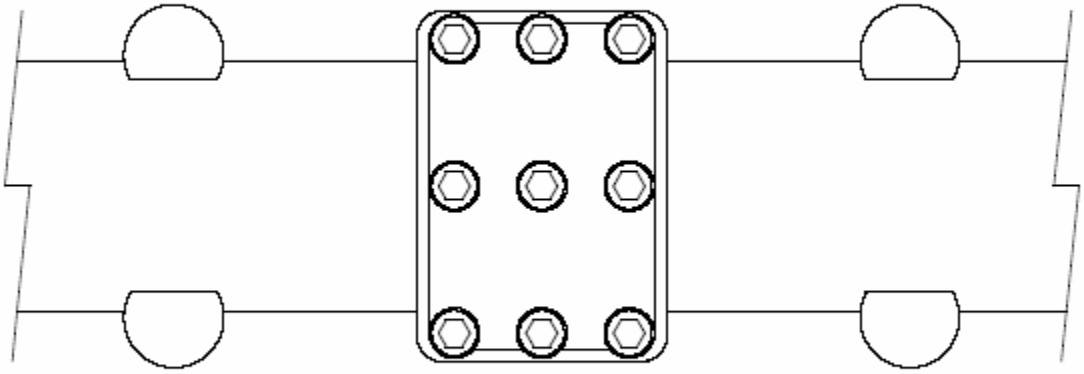

Fig 8.23: Drawing of the proposed clamp assembly for the MI bus bars.

8.4.4 Cooling system modifications

Cooling system modifications are required by the MI, RR, and NuMI. While modifications to RR and NuMI cooling systems are quite extensive, they are rather small in scope for the MI.

Cooling system modification considerations resulting from MI upgrades are primarily limited to two areas. The first is the increased heat load to the entire MI LCW system in general, due to changes in the MI cycling specifications. The second is the addition of kickers in the Q-600 region.

In general, the MI LCW system will see a global increase in heat load of around 25%. Hydraulically, the current systems can supply the required flows and pressures, since little of the MI equipment changes. Thermodynamically, this poses questions for the capacities of the Cooling Ponds. Pond Water Modeling already performed suggests that, when normalized for our operational conditions, a global heat load increase of 25% will result in a pond water rise of approximately 1°F [12].

The additional Kickers will require cooling water. The current RF (95°F) and Cavity (55°F) LCW Systems housed in the MI-60 Pump Room were initially built with sufficient capacity that they should easily accommodate these additional Kickers, both hydraulically and thermodynamically.

MI, RR, and NuMI cooling systems are all interrelated. Therefore, all Cooling Systems will go through Conceptual Design Reviews to assure good engineering practices are maintained, and any conflicting needs are addressed. Furthermore, capabilities for heat removal the Cooling Ponds will be further verified.

8.4.5 Changes in the MI Upgrades Design since the CDR.

The main change since the CDR is the optimization in the position of the MI collimators needed for the Proton Plan and NOνA. The final positions of those collimators that are scheduled to be installed the summer of 07 for Proton Plan are such that they do not interfere with the NOνA injection line from the Recycler to Main Injector. As a result no collimator moves need to be included in the MI Upgrades required for NOνA.

We have also a design for the manufacturing of the bus bars for the cavity tuners that greatly simplifies the installation and does not require the use of an external crane and removal of parts of the roof from the MI-60 building.

8.4.6 Remaining Design work for the MI Upgrades

The design of the bus bars for the two extra RF stations is expected to be finalized the summer of 07. The design of the RR low level RF system remains to be finalized. To the first order this design is expected to be very similar to the existing MI low level RF system since the expected functionality is the same. Even if the MI water cooling system was designed to handle the increase in heat load the realistic capacities of the cooling ponds need to be re-evaluated.

8.5 Radiation Safety for the Recycler and Main Injector

8.5.1 Overview

In this chapter, the radiological considerations for operation of the Recycler and Main Injector for NOνA are considered. The scope of the review includes the 8 GeV Transfer Line, the Recycler Ring, and the Main Injector. (The radiological concerns for the NuMI beamline are addressed separately in Section 8.6.6.) The analysis contained in this section is based on current requirements of the Fermilab Radiological Controls Manual. This section is considered preliminary; analysis and proposed solutions have not yet been fully reviewed or approved by laboratory safety professionals.

The radiological considerations for all of the above accelerators and beam lines have been considered extensively and are documented in shielding assessments conducted by the Accelerator Division and reviewed and approved by the ES&H Section. In all cases, the shielding assessment for each accelerator and each beam transfer line is used as a starting point in the evaluation which is to follow. Other measurements and verification data available are used where applicable.

The posting and entry control requirements for access to areas outside of beam enclosures where prompt radiation exposure may exist for normal and accident conditions are given in the Fermilab Radiological Controls Manual and are repeated here in Table 8.10 and Table 8.11, respectively. In some instances such as at a beam absorber or target hall, the normal condition may dominate or be equivalent to the worst case condition.

Dose Rate (DR) Under Normal Operating Conditions	Controls
DR < 0.05 mrem/hr	No precautions needed.
0.05 ≤ DR < 0.25 mrem/hr	Signs (CAUTION -- Controlled Area). No occupancy limits imposed.
0.25 ≤ DR < 5 mrem/hr	Signs (CAUTION -- Controlled Area) and minimal occupancy.
5 ≤ DR < 100 mrem/hr	Signs (CAUTION -- Radiation Area) and rigid barriers (at least 4' high) with locked gates. For beam-on radiation, access restricted to authorized personnel.
100 ≤ DR < 500 mrem/hr	Signs (DANGER -- High Radiation Area) and 8 ft. high rigid barriers with interlocked gates or doors and visible flashing lights warning of the hazard. Rigid barriers with no gates or doors are a permitted alternate. No beam-on access permitted.
DR≥ 500 mrem/hr	Prior approval of SRSO required with control measures specified on a case-by-case basis.

Table 8.10: Control of Accelerator/Beamline Areas for Prompt Radiation Under Normal Operating Conditions

Maximum Dose Equivalent (D) Expected in 1 hour	Controls
D < 1 mrem	No precautions needed.
1 ≤ D < 5 mrem	Signs (CAUTION -- Controlled Area). No occupancy limits imposed.
5 ≤ D < 100 mrem	Signs (CAUTION -- Radiation Area) and minimal occupancy. The Area RSO has the option of imposing additional controls in accordance with the guidance of Article 231 to ensure personnel entry control is maintained.
100 ≤ D < 500 mrem	Signs (DANGER -- High Radiation Area) and rigid barriers (at least 4' high) with locked gates. For beam-on radiation, access restricted to authorized personnel.
500 ≤ D < 1000 mrem	Signs (DANGER -- High Radiation Area) and 8 ft. high rigid barriers with interlocked gates or doors and visible flashing lights warning of the hazard. Rigid barriers with no gates or doors are a permitted alternate. No beam-on access permitted.
D ≥ 1000 mrem	Prior approval of SRSO required with control measures specified on a case-by-case basis.

Table 8.11: Control of Accelerator/Beamline Areas for Prompt Radiation Under Accident Conditions

The NOνA goal is to operate the NuMI target hall at 700 KW beam power or about 1.3E17 protons per hour. To accommodate such operation, the Accelerator Division Beam Permit must be considered. For the RR and the MI, the Beam Permit used by the Operations Department is set equal to the DOE approved Beam Safety Envelope. Additionally the AD ES&H Department has established an Operating Intensity Limit which is approximately 90% of the Beam Permit. The AD Operations Department imposes a Warning limit on the Operating Intensity Limit. The Warning Limit is the de facto upper level of beam intensity at which beam is operated. In the most conservative of cases, the net effect on the Beam Permit is that operations are conducted at

about 80% of the Beam Permit. In evaluating the Accelerator complex then, it is necessary to consider the radiological implications of operating 120 GeV accelerators and beam transfer lines at 700KW/0.8 or 875 KW.

The beam intensity necessary to be evaluated for all accelerators and beam transfer lines for NOνA operation is thus 1.64E17 protons per hour. There is no consideration of additional beam power for other programs in this review. However, excess capacity is identified where it exists.

Note that there are a fair number of Radiation Safety Systems used in the present configuration of the Accelerator complex. The arrangement of these systems is designed to meet present operational requirements. The Radiation Safety Systems will need to be reviewed and may need to be reconfigured for NOνA. The configuration of the Radiation Safety Systems will require reevaluation, based upon the new programmatic goals and anticipated operating scenarios. Only minor changes are envisioned relating to radiation safety as sufficient earth shielding should be present over the MI 8 Line, Recycler and Main Injector. The MI shielding assessment will need to be updated for NOνA operation and labyrinths, penetrations, etc. will need to be revisited.

8.5.2 Machine Shielding Assessments

8.5.2.1 MI 8 Line

The MI 8 line shielding was evaluated as part of the 1998 MI shielding assessment [13]. The present Beam Permit limit for the MI8 line is 1.35E17 protons per hour. The limit for the MI8 line was set to meet programmatic goals of the time. The MI8 line was assessed beginning at cell body 803 through the injection region at MI 10. The MI 8 line shielding is equivalent to at least 24.5 feet throughout the entire length. The magnet to ceiling height in the MI 8 line is about 3 feet through the sections 803 to 810 and about 6 feet for the remainder of the line.

Table 8.12 shows the required amount of shielding considering the line for unlimited occupancy. Thus the MI 8 line is adequately shielded for 700 KW (NOνA).

energy	intensity	cycle time (sec)	component to ceiling distance
8	1.64E+17	3600	3
		Required shielding	23.3

Table 8.12: Shielding requirement for MI 8 line for 700 KW NOνA operations.

The Main Injector shielding assessment will need to be revised to allow sufficient 8 GeV beam intensity to support 700 KW NOνA operations. The nature of the revision work would be to apply the present shielding scaling methodology for analysis of 8 GeV shielding. It should be possible to establish a Beam Permit of up to 1.64×10^{17} protons per hour based upon the existing 24.5 feet of shielding over the MI8 line. Exit stairwells, labyrinths, drop hatches, and penetrations would also need to be re-examined to determine the whether any of them are more limiting than the earth berm shielding. The actual upper limit of the Beam Permit could be set based upon the most limiting feature of the MI8 line.

8.5.2.2 Recycler Ring

The Recycler Ring shielding assessment was originally conducted within the MI shielding assessment in 1998 [13]. The present intensity limit for the Recycler Ring is 1.2E16 protons per hour, so shielding assessment updates are required before NOνA operation can take place.

Table 8.13 shows the required shielding for a minimally-occupied, controlled area, the category under which the MI shielding was re-evaluated during an October 2004 shielding assessment [14].

energy	intensity	cycle time (sec)	component to ceiling distance
8	1.64E+17	3600	1
		Required shielding	23.9

Table 8.13: MI shielding requirement for Recycler Ring operation to support 700 KW NOνA operations for a minimally-occupied, controlled area

The shielding design requirement for the Main Injector was 24.5 feet; however, the as-built condition achieved was typically 26 feet. The Recycler Ring shielding should be sufficient if the MI shielding is evaluated as minimally-occupied, controlled area. Exit stairwells, labyrinths, drop hatches, and penetrations would also need to be re-examined to determine the whether any of them are more limiting than the earth berm shielding.

8.5.2.3 Main Injector

The Main Injector shielding assessment was reviewed and appended in October 2004 [14] in order to provide the incremental increase in beam power to support the NuMI project. In the October 2004 assessment, the MI shielding berm was evaluated primarily as a minimally-occupied, controlled area. A Safety Assessment of the MI berm included with the latest assessment concludes that Controlled Area posting is not required for minimally-occupied, controlled areas in accordance with the requirements of Article 236 of the FRCM [15]. Some regions of the MI have been posted as Controlled Areas as delineated in Article 236 of the FRCM.

There was some built-in conservatism identified in the 1998 Shielding Assessment, which has, to date, not been considered for the Main Injector. While the magnet to tunnel ceiling distance in the MI beam enclosure is typically 5.5 feet, the shielding was evaluated for a magnet to tunnel ceiling distance of 3 feet. The shielding requirement for 120 GeV operations at 700 KW (NOνA) considering the actual magnet to tunnel ceiling distance and unlimited occupancy requirements, is shown in Table 8.14.

energy	intensity	cycle time (sec)	component to ceiling distance
120	1.64E+17	3600	5.5
		Required shielding	24.4

Table 8.14: MI shielding requirement for 700 KW operations (NOνA)

The Main Injector shielding design was for a minimum of 24.5 feet. The typical as built shielding thickness achieved was 26 feet. From the forgoing, one may conclude that the shielding is sufficient for 700 KW operation of the Main Injector for NOνA.

The existing Main Injector shielding assessment (October 2004) will need to be revised for NOνA operation. Exit stairwells, labyrinths, drop hatches, and penetrations would also need to be re-examined, although no issues are foreseen.

8.5.3 Surface Water, Ground Water, Air Activation, and Residual Activation

The activation of surface water, ground water, and air are considered in this section. In general, the activation of air and water associated with the Accelerator complex is well understood. The levels of activation of air and water under present conditions, while measurable, do not approach any State or Federal limits. The levels of water and air activation can be expected to increase by the ratio of the beam power increase required for NOνA. The anticipated levels of water and air activation for NOνA should not pose any restrictions on operation of the Accelerator complex. The specific conditions are discussed below.

Residual activation of beam line components is an important consideration for a number of reasons. In general, as beam power increases the radiation dose to workers can be expected to increase. In addition, higher levels of activation can lead to reduced lifetime of accelerator components. The efforts to reduce residual activation are discussed in the following sections.

8.5.3.1 MI 8 Line

Groundwater was extensively reviewed for the MI project. Residual activation routinely found in the MI8 line is historically quite low. Ground water activation does not pose a limitation on NOνA operation.

Surface Water is routinely monitored in MI 8 Line sumps. Periodic sump sample results from MI8 line routinely show less than detectable radioactivity. Surface water resulting from operation of the MI 8 Line does not pose a limitation on NOνA operation

MI8 Line air activation in the MI8 Line has been monitored by the AD ES&H department. No significant activity has been detected. Air activation in the MI8 Line should not pose a limitation on NOνA operation.

Residual activity in the MI 8 Line has historically been quite low, residual activity levels in the MI 8 line (except at Booster extraction and MI injection) are quite low

Residual activation due to MI 8 line operation does not pose a limitation on NOνA operation.

A new beam collimation system has been designed and built for the MI8 line [16]. Radiological concerns for the collimation system have been addressed. Operation of the new collimation system in the MI 8 Line will not pose a limitation on NOνA operations.

8.5.3.2 Main Injector and Recycler Ring

Ground water was extensively reviewed during the Main Injector shielding assessment. Ground water activation does not pose a limitation on NOνA

Surface water is routinely monitored at 17 sump locations around the Main Injector. Tritium levels found in the sump water are typically less than the detection limit of 1 pCi/ml. Recently, a small number of samples have been found with 1 to 3 pCi/ml. Beginning in 2005, Main Injector sump discharges are being directed to controlled retention ponds and routinely monitored and managed. Main Injector surface water activation does not pose a limitation on NOνA operation.

Air activation has been monitored in the Main Injector by the AD ES&H Department. Beam losses are distributed around the Main Injector and no significant sources of air activation have been identified. Control of beam losses in the Recycler Ring and the Main Injector is the primary method available to control air activation. Air activation due to operation of the Recycler Ring and the Main Injector should not pose a limitation on NOνA operation.

Residual activation in the Main Injector is actively managed by Main Injector Department personnel. Loss points are determined in radiation surveys by department personnel. Orbit

corrections or optics corrections are applied. Follow up radiation surveys are made and improvements in Main Injector residual activation levels have lead to dramatic reductions in residual activation in spite of increasing Main Injector beam power. Nevertheless radiation levels in those parts of the tunnel where work is scheduled, remain a concern. In order to effectively manage this issue the project will monitor the activation levels at these areas and will take measures to mitigate the problem. The measures chosen will depend on the anticipated activation levels and will include the following; designing the construction work flow and methodology so as to minimize the time required inside the tunnel, using lead blankets to protect workers from activated beamline elements, and if necessary removing activated elements from the tunnel during the construction work.

8.6 NuMI Upgrades

8.6.1 Overview

To meet its physics goals the NOνA experiment requires 6×10^{20} protons on target per year from the NuMI facility. As explained earlier, this proton delivery rate is accomplished with modifications to the Recycler Ring and upgrades to the Fermilab accelerator complex. For the NuMI facility this implies a faster cycle time of 1.33 seconds and modest increase in the protons per pulse on the target. The beam parameters for the original NuMI beamline design and for the NOνA/ANU upgrades are summarized in Table 8.15 which also includes beam parameters for the highest beam power and intensity achieved operationally as of August 2007. To handle the increase in beam power, up to 700 kW, the existing NuMI beamline requires upgrades beyond the original design capability of 400 kW

	Highest Power Operations*	Highest Intensity Operations†	NuMI Design	NOνA/ANU
Beam power to NuMI (kW)	315		400	700
MI intensity (ppp)	3.3×10^{13}	4.1×10^{13}	4.0×10^{13}	4.9×10^{13}
MI cycle time (seconds)	2		1.9	1.33
Spot size on target (mm RMS)	1.0	1.2	1.0 – 1.2	1.3
Protons/hr	5.9×10^{16}		7.3×10^{16}	13×10^{16}

Table 8.15: Comparison of the NuMI beam parameters during operations, for the original NuMI design and for the NOνA/ANU upgrades. (*The highest power was achieved on December 27, 2006 during an operations period without pbar stacking. †The highest intensity was achieved on February 22, 2007 during 11-batch slip stacking studies.)

The essential nature of the neutrino production process (see [17] for instance) is unchanged for the NuMI upgrades. The first step in the production of neutrinos is directing a beam of protons from Fermilab's Main Injector onto a production target. Interactions of the proton beam in the target produce mesons (mainly pions and kaons), which are focused toward the beam axis by two magnetic horns. The mesons then decay into muons and neutrinos during their flight through a long decay tunnel. A hadron absorber downstream of the decay tunnel removes the remaining

protons and mesons from the beam. The muons are absorbed by the subsequent earth shield, while the neutrinos continue through to an experimental hall at Fermilab and onwards toward "far" detectors. A view of the NuMI tunnel is shown in Fig 8.24 and a schematic of the neutrino production process is shown Fig 8.25. More detail can be found in the NuMI Technical Design Handbook [19].

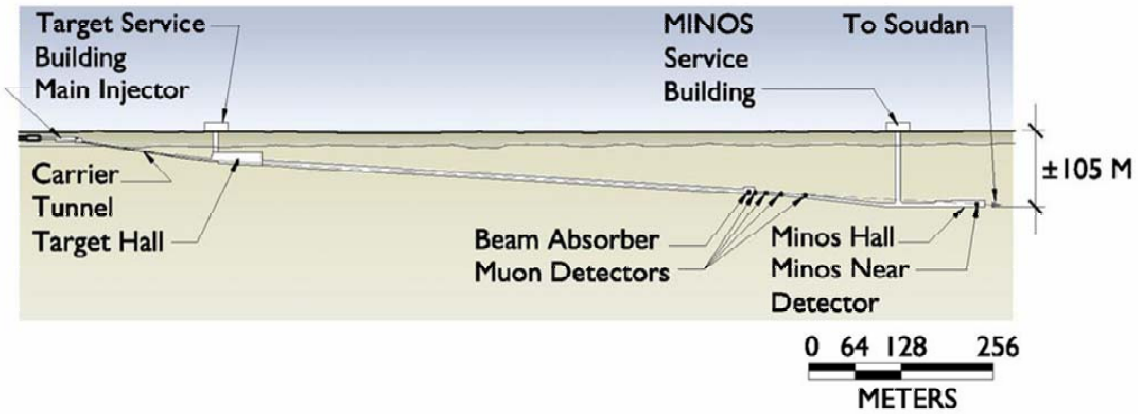

Fig 8.24: The NuMI beamline tunnel. Protons are delivered to the target hall from the Main Injector via the primary beamline and through the carrier tunnel. The target and focusing horns are located in the target hall. The long section in the middle contains the decay pipe which is followed by the beam absorber, muon detectors, and experimental hall.

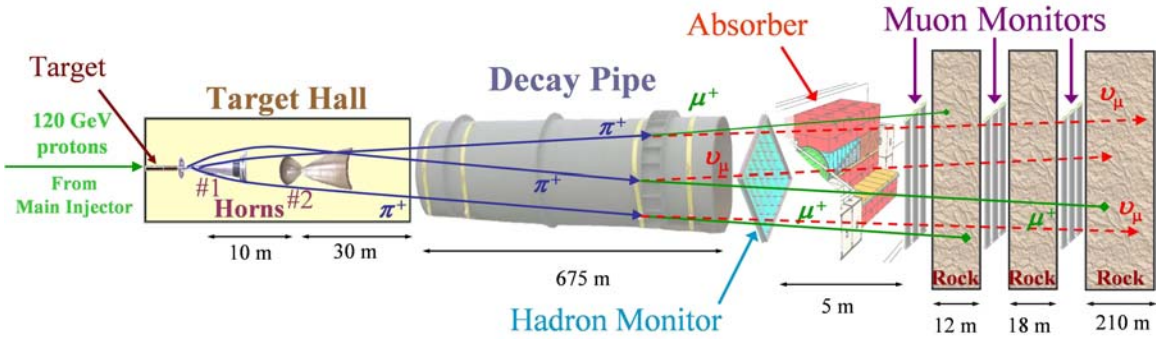

Fig 8.25: A schematic of the neutrino production process in the NuMI beamline.

NuMI uses pulsed magnetic horns with parabolic shaped inner conductors to focus the pions. The horns produce magnetic fields that act to first order as lenses, where the focal length is proportional to the pion momentum. Thus the relative position of the target and the first horn determines the momentum selection of the pions. Pions that were well focused by the first horn pass unaffected through a central aperture in the second horn. Pions that were not well focused by the first horn move to a larger radius and are focused by the second horn, extending the momentum range of the system.

To fully optimize the neutrino beam energy spectrum it is necessary to optimize the locations of the target and the horns. In the original NuMI design three different target and horn placements were chosen to give low (LE), medium (ME), and high energy (HE) neutrino beams. The

resulting neutrino energy spectra in these three cases are shown in Fig 8.26. Plotted are the spectra of the neutrino energy at a location along the axis of the neutrino beam. One such location is the MINOS far detector. For the NOνA experiment the neutrino energy spectrum is different because the NOνA far detector is located off-axis. In this case the energy spectrum depends on the off-axis angle as shown in Fig 8.27. The NOνA experiment is located 14 mrad off-axis and will operate with the NuMI beamline in the ME configuration. The narrowness of the energy spectrum at the far detector is important for the NOνA experiment because it improves the background rejection.

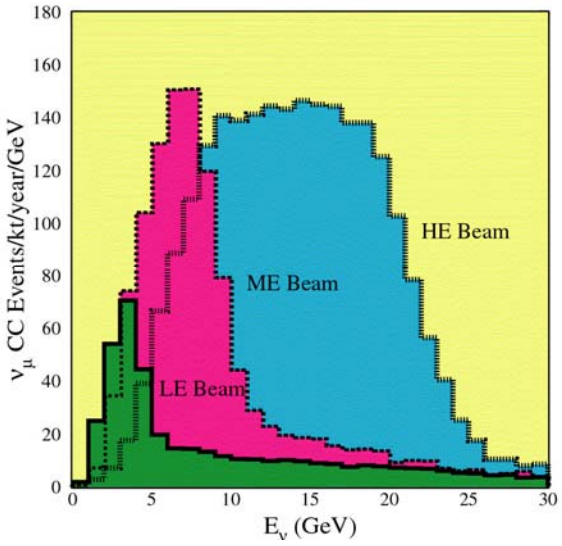

Fig 8.26: Expected energy spectra of charged-current (CC) events at the MINOS far detector (located on the axis of the neutrino beam) for low (LE), medium (ME) and high (HE) energy beam configurations.

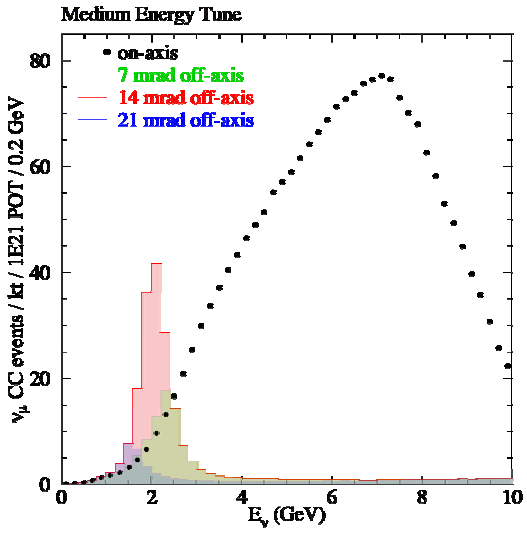

Fig 8.27: The expected energy spectra of charged-current (CC) events at the NOνA far detector with NuMI in the medium energy configuration. Shown are the spectra for different off-axis angles of the NOνA far detector.

As part of the NuMI upgrades, the target and focusing horn locations will be changed to meet the needs of the NOνA experiment. This means moving the target and the second horn to new locations within the target chase area in order to change the energy spectrum of the neutrinos. Simulations have been performed to confirm that the location of the target in the ME configurations is optimal for the NOνA experiment [18]. A description of the different configurations is given in [19].

Other parts of the NuMI upgrade are modifications to handle the increase in beam power from 400 kW to 700 kW and to allow operations at the faster cycle time.

In the following sections the designs are presented for each of the NuMI beamline systems requiring upgrades for the NOνA ANU subproject. Here we summarize the scope of the upgrade by listing the major changes needed:

- Replace five of the primary beamline quadrupole magnets with magnets from the A1 transfer line which are designed to handle the higher heat load of a faster cycle time.
- Replace the existing target and baffle with a new design capable of handling the higher beam power.
- Reconfigure the target chase from the low energy to the medium energy neutrino configuration. This involves repositioning Horn 2, reconfiguring the shielding, and extending the Horn 2 stripline.
- Add capacity to the target chase cooling system to maintain a reasonable temperature of the target pile.
- Upgrade the cooling water systems including the RadioActive Water (RAW) systems for the target, horns, decay pipe, and hadron absorber.
- Update the beam permit system inputs to help prevent accident conditions which can damage beamline components.

Two separate shutdown periods are planned for the installation of the upgrades. The first shutdown period follows the completion of Collier Run II operations. During this shutdown the NuMI beamline begins preparation for the 700 kW operations and accomplishes the following tasks:

- Upgrade the target chase cooling system
- Upgrade the capacity of the RAW systems
- Replace the quadrupole magnets in the primary beamline
- Extend the Horn 2 stripline
- Modify the target chase shielding in preparation for the future Horn 2 relocation.

It is expected that the MINERνA experiment will operate for about 2 years with NuMI in the low energy configuration. Because this requires the use of the existing target, the NuMI beamline will be limited to a maximum beam power of 400 kW during this time. Upon completion of the MINERνA operations a second shutdown is planned to switch from the low energy to the medium energy configuration and to replace the target with a higher power design. After the second shutdown, the NuMI facility will be capable of operating at a beam power of 700 kW.

The second shutdown involves the following tasks:

- Replace the target with the medium energy target design
- Replace the Horn 1 with the new design
- Relocating Horn 2 from the low to the medium energy position

8.6.2 Primary Proton Beam

The current 400 kW design NuMI beam has the capability to extract up to 6 Booster batches from the Main Injector at a cycle time of 1.87 sec. Both the extraction system and the primary beam transport are conservative designs, with robust operation for NuMI demonstrated and operational beam loss levels consistently 1-2 orders of magnitude below the relatively severe NuMI design criteria of 1×10^{-5} fractional beam loss. If the next level upgrades for beam intensity capability, involving slip-stacking of multiple batches to NuMI, can maintain the level of beam control achieved for NuMI, a significant window for higher per pulse beam intensity is available. The most significant modification of the NuMI primary beam-line for ANU involves acquiring the capability for faster cycle repetition rates. More detail can be found in [20].

8.6.2.1 Extraction Kicker

Only limited modifications to the NuMI extraction kicker system are needed. No modification of the kicker magnet is needed since the bunch spacing and beam energy do not change for the NuMI upgrade. The existing NuMI extraction kicker is designed for a 9.6 μs flattop and operates at 50 kV. The shorter Main Injector cycle time reduces the available time for power supply charging from 1.1 to 0.7 sec and this leads to the requirement for a new extraction kicker charging power supply.

An upgraded fluorinert pump is also required for the existing kicker system water heat exchanger to handle the additional heat load caused by the increased repetition rate.

8.6.2.2 QQM 3Q120 Quadrupole Magnets

The most significant upgrade to the NuMI primary beamline is the replacement of the highest current 3Q120 quadrupole magnets. For NuMI these quadrupole magnets were refurbished from existing fixed target beam system inventories, but a number of internal cooling leaks were found during this process in some of the tested magnets. The available laboratory supply of 3Q120 magnets was exhausted to successfully refurbish the 19 ones needed for NuMI, along with two spares.

For these 25 to 30 year old magnets, a concern is that the water-cooling of the coil packs is inefficient since there is no direct cooling for the coils themselves. To provide some safety margin, cooling for the highest current NuMI quadrupoles was augmented with external cooling plates as shown in Fig 8.28.

Fig 8.28: NuMI 3Q120 with External Cooling Plates

Although there have been no failures of installed NuMI quadrupoles to date, the Technical Division [21] recommends replacing the NuMI quadrupoles with the highest operating currents (those operating at greater than 70 amps) for cycle times below 1.87 seconds. The newer design QQB magnets have direct water cooled coils and are more suitable for use after the NuMI upgrades. Since the A1 line, which transfers pbars from the Main Injector to the Tevatron, will not be used after the finish of collider operations, the existing QQB magnets in this line will be removed and used for the NuMI upgrades. The QQB design has internal coil cooling, fewer turns and higher current for the same field. The QQB magnets are projected to be much more robust. Specification differences between QQM and QQB quadrupole magnets are shown in Table 8.16.

	QQM	QQB	Units
Turns per pole	118	28	
Resistance	1.6	0.16	Ohm
Inductance @ 100 Hz	1.4	0.082	H
Water flow @ 100 psi (not including supplemental plates)	17	5.7	GPM
Core width	17	17	Inches
Core height	15	15	Inches
Steel length	120	120	Inches
Flange-to-flange length	132.0	132.0	Inches
Core to lead end flange	5.0	6.5	Inches
Core to bellows end flange	7.0	5.5	Inches
Assembly drawing	ME-388120 Link to TIF	ME-331805 Link to TIF	

Table 8.16: QQM quadrupole magnet versus QQB quadrupole magnet specifications.

Hence, the plan is:

- Remove six of the QQB design 3Q120 magnets from the A1 line at the conclusion of collider operations. (The 3Q120 nomenclature refers to the 3 inch aperture of the quadrupole and the 120 inch length of the magnet.)

- Replace the five quadrupole magnets in the NuMI beam-line with the highest operating current with the QQB design magnets. The five quads and their currents are:

    - Q111 (78 Amps)
    - Q112 (83 Amps)
    - Q113 (83 Amps)
    - Q114 (78 Amps)
    - Q120 (71 Amps)

The QQB design magnets can be installed in the primary beamline using the existing magnet stands since the QQB magnets have the same external dimensions as the existing QQM magnets.

New 75 kW, higher current power supplies are required to utilize the more robust QQB quadrupoles for NuMI, as well as higher current capability cables between power supplies and magnets. These supplies will be vendor built to Fermilab design specifications. Several identical units are currently in operation in the accelerator complex.

8.6.2.3 Large Power Supply Modifications

Relatively minor changes are needed to the existing large dipole power supply setup to enable the faster cycle time for NOνA. These are summarized in Table 8.17.

I:LAM60	**Tap change** from 50 to 100 volts. RMS current from 474 A to 434A
I:LAM61	**No change.** Increase RMS current from 931A to 1073A
E:V100	**Tap change** from 50 to 100 volts. RMS current from 1426A to 1226A
E:HV101	**No change.** Increase RMS current from 814A to 932A
E:V118	**Use full voltage.** Increase RMS current from 2270A to 2292 A

Table 8.17: Large power supply changes for 1.33 second cycle time.

With the increase in beam power for NOνA, there also is increased danger to beam system components from large accidental beam loss, even with a single bad pulse. Currently the Beam Permit System robustly precludes a 2nd bad beam pulse, but only monitors power supply currents at a level of 0.5 to 1.0%. This leaves a significant window where a power supply regulation problem could be missed at a level which could produce component damage from miss-steered beam.

The planned solution for this is to implement new BμLB regulation systems for the six major dipole power supplies. This upgrade will provide a precision power supply readout capability of accuracy 0.01% to the permit system, as well as additional feedback control for enhanced power supply regulation.

8.6.2.4 Upgraded Primary Transport Profile Monitors

An operational requirement [22] for the NuMI primary beam is to maintain fractional beam loss at a level of less than 1×10^{-5}. The existing primary transport profile monitors are built with extremely thin 5 μm Ti foils spaced at 1 mm pitch, to have a minimum amount of material (~ 4×10^{-6} interaction lengths) exposed to the beam. These are generally not used during NuMI operations due to a 10-20 second required insertion time during which beam loss is an order of magnitude greater and generates beam permit trips. This is not a problem for the pre-target profile monitor at the downstream end of the primary beam, which can and does remain in the beam at all times since it is just upstream of the target pile.

For the other beam transport monitors, the plan is to implement the thin Ti foils with an existing design fast acting (< 1 sec) mechanical drive and vacuum system. These systems will also be built such that excess material is not exposed to the beam during monitor insertion. Of the ten units needed, a total of five of the mechanical systems already exist for NuMI. Five new mechanical systems will be constructed, as well as new Ti foil packages for the ten units.

As this is an upgrade which should provide a considerable improvement for profile monitor use in Fermilab high intensity beams, the foil package prototype development is not part of the NOνA project.

8.6.3 Target Hall Technical Components

A layout of the NuMI Target Hall including the technical components is shown in Fig 8.29 and Fig 8.30. The technical components are used to produce and focus pions and kaons, and to

monitor the proton and pion/kaon beam. Specifically, the components needing modifications for the NuMI upgrade are the:

- Baffle
- Target
- Carrier for the Target and Baffle
- Hadron Monitor
- Beam Abort Input for Hadron Monitor

Only minor modifications are needed to the magnetic focusing horns in order to handle the increased energy deposition in the horns at the higher beam power. The horns have a finite lifetime of about 1-2 years before they need replacement. Therefore the modifications to the horn design can be accomplished during the usual production cycle for fabricating replacement and spare horns.

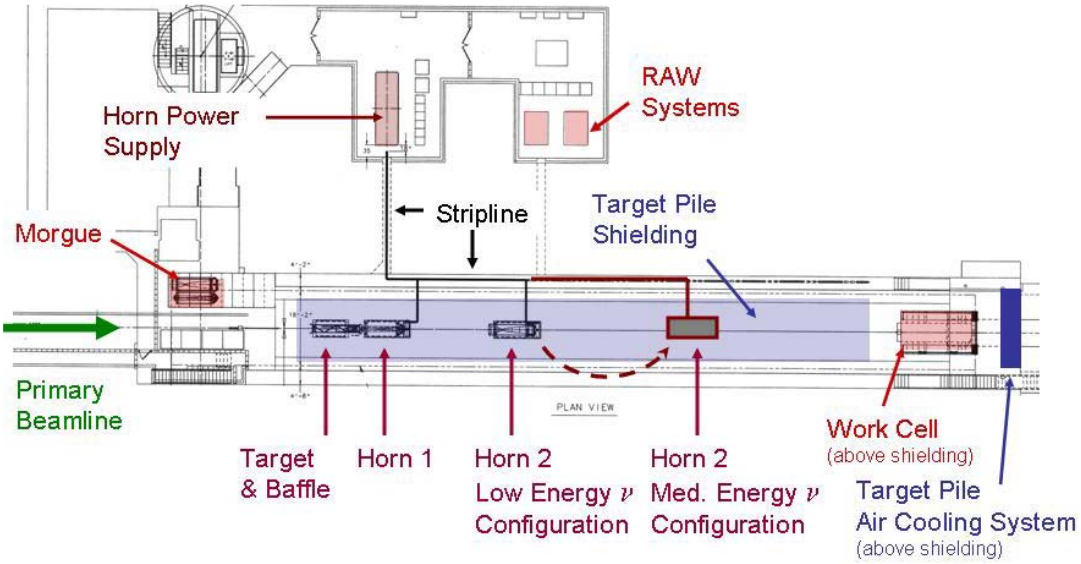

Fig 8.29: Plan view of the NuMI Target Hall. Note that the Horn 2 location depends on the neutrino energy configuration.

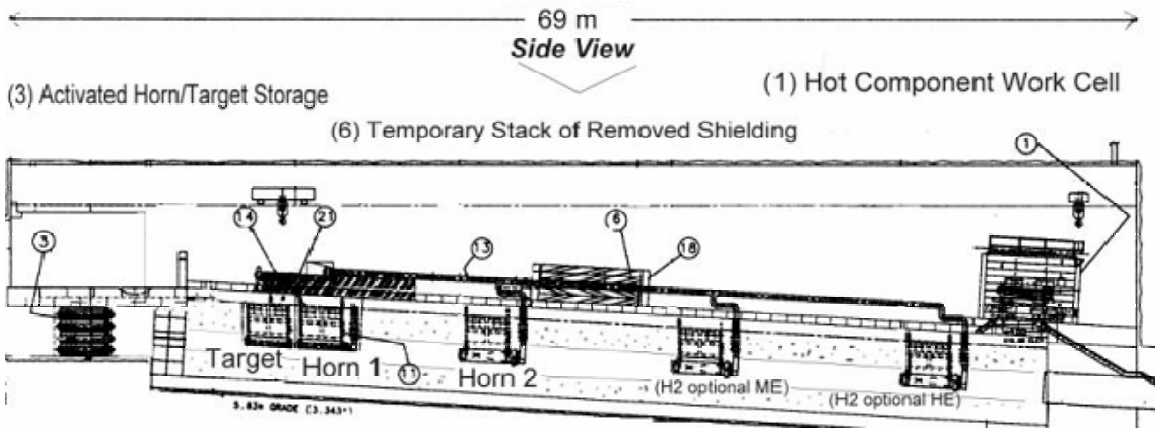

Fig 8.30: Elevation view of the NuMI target hall. Note the three possible locations for Horn 2 corresponding to the Low, Medium, and High Energy neutrino spectrums shown in Fig 8.26.

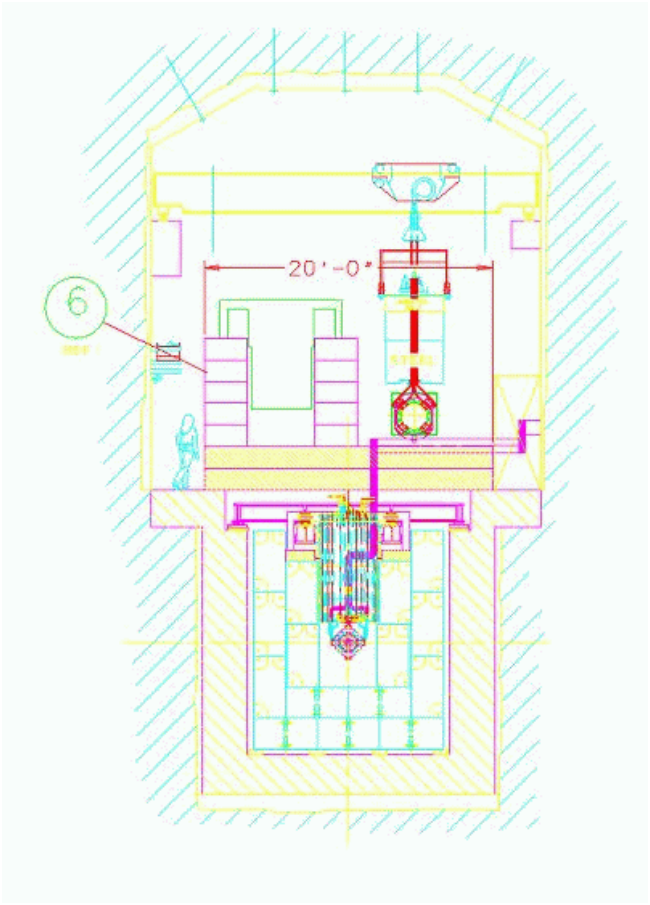

Fig 8.31: Cross sectional view of the NuMI target hall, showing a temporary stack of removed shielding, and a module plus horn being transported.

8.6.3.1 Target Baffle

In the NuMI baseline design a 1.5 m long baffle 68 cm upstream of the target fin protects the neck of the horn and the target cooling hardware from miss-steered beam pulses. The baffle moves along with the target from Low Energy (LE) to High Energy (HE) locations.

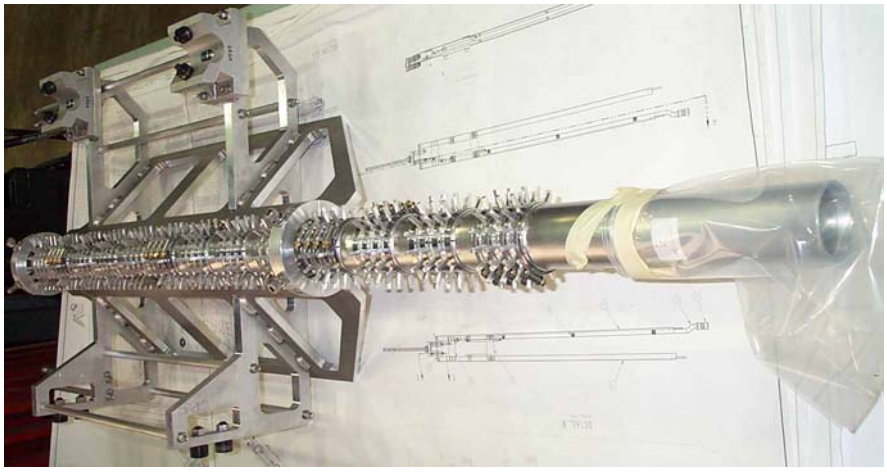

Fig 8.32: NuMI target pile baffle

The NOνA beam intensity of 4.9×10^{13} protons/spill is 22% higher than the NuMI baseline design. In the base design, excluding high-cycle fatigue (which the baffle should not be subject to) the stress safety factor of the baffle in accident conditions is 4.5 [23]. With this margin on the safety factor the baffle design is well inside the safety factor and the baffle will survive the shock of accident conditions in NOνA running.

The baffle serves to protect the horn neck and the target cooling system. The heating (and thus induced stress) of various components is shown in [19] as a function of the baffle location; moving the baffle upstream reduces the stress. For the NOνA project, the move of the target to the ME location naturally moves the baffle further from the horn neck, compensating for the higher intensity per spill. The protection of components of the new target will have to be evaluated, but based on the safety factors for the old components, is likely to be OK without modification of the baffle. If desirable, the baffle can be moved another 1 m upstream of the target (to its current location for the HE beam), increasing the stress safety factor.

The D.C. beam power in the upgrade is 75% higher than the NuMI baseline design. The baffle is air-cooled with pin radiators, and the temperature rise is used to monitor the amount of beam scraping. Calibration with real beam shows the original safety factor would cover the increased temperature but there is room for more pin radiators on the baffle which will be added.

SLG grade R7650 graphite was used in the baffle rather than the POCO ZXF-5Q used in the calculations in [23], but R7650 has a better combination of yield strength, heat capacity, coefficient of thermal expansion and Young's modulus.

8.6.3.2 Medium Energy Target

The NOνA experiment requires a medium energy neutrino configuration as discussed in Section 8.5.1. In this configuration the optimal location for the target begins 135 cm upstream of Horn 1 and extends to 15 cm upstream of Horn 1. As part of the NuMI project, the Institute for High Energy Physics (IHEP), Protvino, Russia had already completed a preliminary design of a target for use in this configuration. A general view of the target design is shown in Fig 8.33. The medium energy (ME) target design is described in IHEP reports and drawings [24, 25].

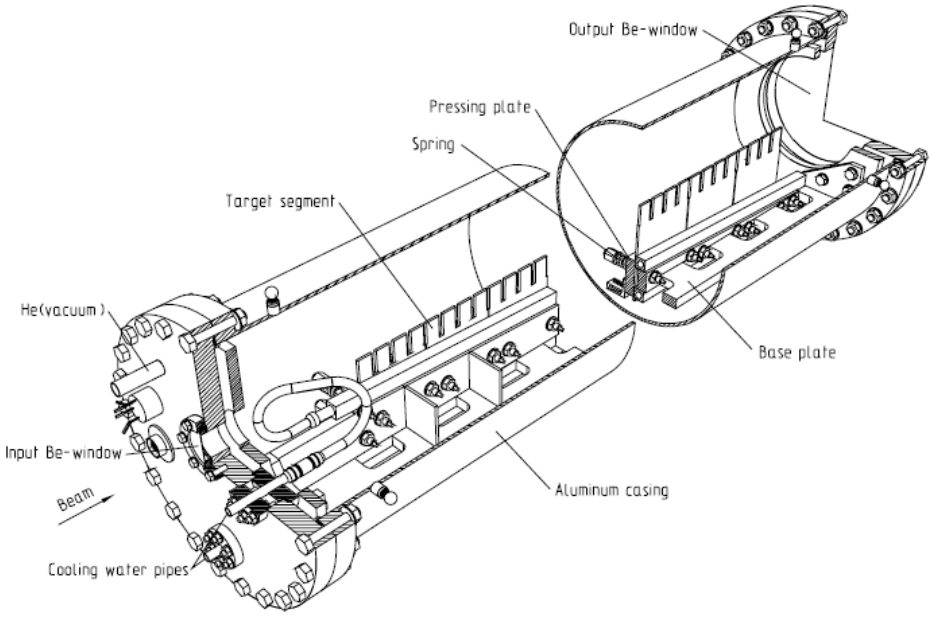

Fig 8.33: General view of the Medium Energy Target

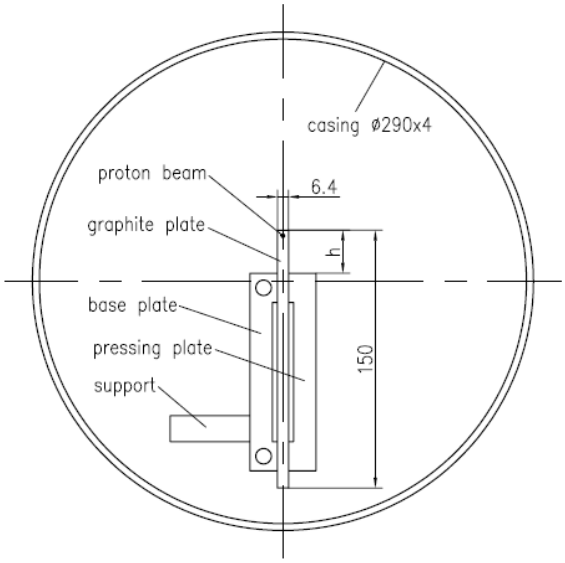

Fig 8.34: Cross section of the Medium Energy Target

Views of the ME target design are shown in Fig 8.33 and Fig 8.34. The incident protons travel through the upper portion of twelve 6.4 mm thick and 100 mm long graphite plates. The bottoms of the graphite fins are clamped by a base plate that contains water-cooling channels. Two springs per target plate provide ~2 atmospheres of pressure. The distance from the fin tip to the cooling channel is minimized at the upstream end where beam heating is maximal. To prevent absorption of secondaries contributing to the neutrino flux, the fin extension increases continuously along the target length. The base and pressing plates are made of an aluminum alloy and anodized with 30 μm thick alumina. To decrease quasi-static thermal stresses, cuts are machined in the upper part of each graphite plate forming four 22 mm long, 30 mm high segments (or teeth). Note that the casing diameter for the medium energy target is wider than the inner conductor of Horn 1 and therefore operations in the low energy configuration are precluded with the ME target design.

The longitudinal position of the ME target will remain fixed and will not be remotely moveable. Remote motion capability in the transverse plane is still provided by the target module in order to perform target and horn scans. To perform these horn scans the design of the target carrier and motion apparatus must provide enough travel to completely remove the target and aluminum casing from the beam path.

IHEP has performed preliminary calculations of stress and temperature in the ME target with a 6.4 mm wide graphite target. The calculations were made as a function of beam spot size from 1.0 to 1.5 mm rms for up to 5.5×10^{13} protons per pulse every 1.3 seconds corresponding to a primary beam power of 780 kW. The preliminary results show that the target design is capable of withstanding the higher beam power provided that the transverse size of the proton beam is 1.3 mm rms or larger in both transverse planes [26].

Further analysis and design of the IHEP medium energy target is required to add water cooling to the outer casing and to understand the cooling of the windows at the entrance and exit of the target.

8.6.3.3 Target Carrier

The target carrier hangs below the target module and is used to support the target and baffle. A picture of the target carrier used for MINOS operations is shown in Fig 8.35. In the present design the target carrier also provides remote longitudinal motion capability of the target and baffle within the target carrier. For the ME target needed for the NOvA experiment, longitudinal motion is not required and will not be provided with the new target carrier design. Since the ME target casing has a larger diameter than the low energy target some modifications to the target carrier will be necessary.

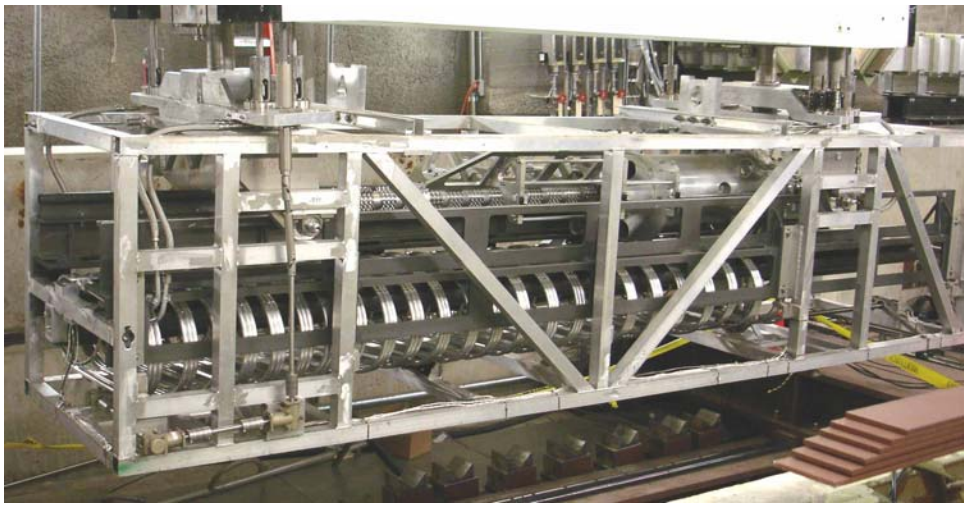

Fig 8.35: Photo of the target carrier used during operations for the MINOS experiment.

8.6.3.4 Hadron Monitor

The purpose of the hadron monitor is to measure the intensity and transverse widths of the remnant hadron beam at the end of the decay pipe just upstream of the hadron absorber. The location of the hadron monitor with respect to the NuMI beamline is shown in Fig 8.36. A photograph of the present Hadron Monitor is shown in Fig 8.37.

The present Hadron Monitor [27] will not be able to handle the increased beam intensity during operations for the NOvA experiment. The University of Texas – Austin designed and built the first hadron monitor and will design and build a new hadron monitor to handle the increased beam power.

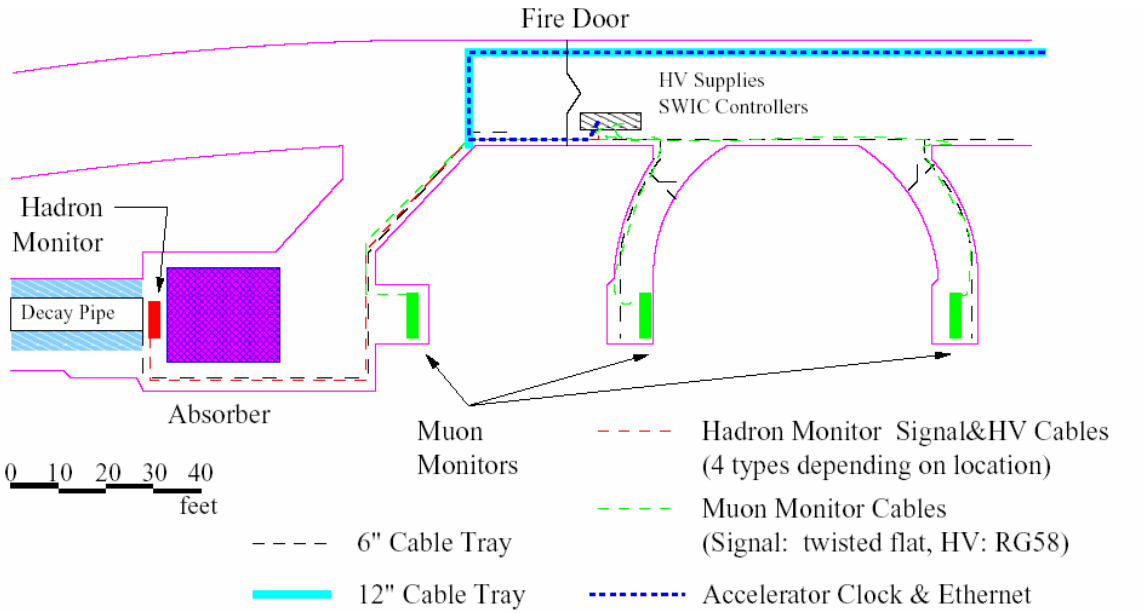

Fig 8.36: Plan view of the downstream end of the NuMI beam line, indicating the decay pipe, beam absorber, and the Hadron Monitor upstream of the absorber.

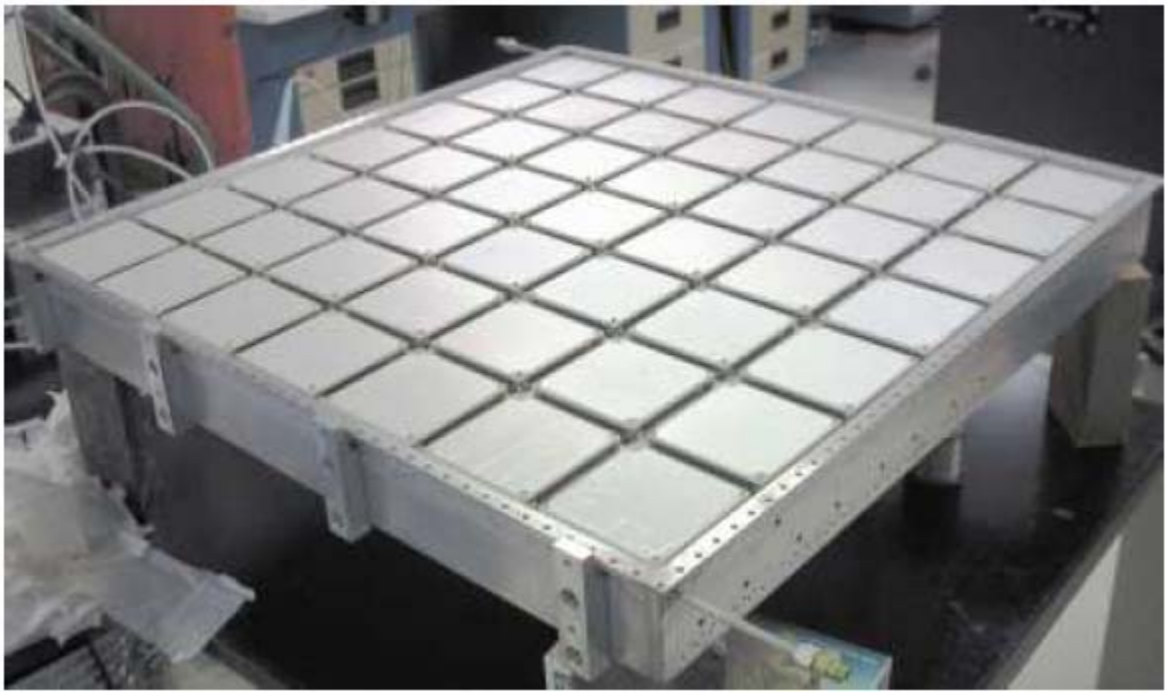

Fig 8.37: Photograph of the first Hadron Monitor prior to installation in the NuMI beam line. A total of 49 ionization chambers reside inside the thin aluminium gas vessel. Each ionization chamber consists of parallel ceramic plates with silver electrodes.

8.6.3.5 Hadron Monitor Beam Abort

Protection of the NuMI Target Hall equipment from errant beam pulses is necessary in operations for the MINOS and NOvA experiments. Equipment monitoring and beam diagnostics are already used as part of a beam permit system for NuMI. The increased beam intensity for the NOvA experiment increases the possibility of equipment damage. To mitigate this risk, the Hadron Monitor will be incorporated into the beam permit system. Intensity and beam size thresholds on the Hadron Monitor can be used to not permit beam operations on the next pulse in the event of an errant beam pulse. Tasks looking into using the Hadron Monitor in the beam permit system are in the resource loaded schedule.

8.6.4 Target Hall Infrastructure

The Target Hall Infrastructure covers the support systems for the technical components (target and horns), shielding of the target hall from radiation, and cooling of the target pile and support systems within the target chase. Also included are space issues in the target hall for the different shutdown activities planned, with particular emphasis on the Horn 2 move to the medium energy position which will require significant shielding reconfiguration. Available space is very limited for moving and staging various shielding/technical components so early planning is crucial. The cooling of the target pile and support systems covers upgrades to the chase air cooling system and enhancements to the Horn 1 stripline block cooling.

8.6.4.1 Target Hall Operations Space Planning

Several shutdown activities are planned in the target hall, but space is very limited and careful planning is needed ahead of time to effectively carry out these tasks. A list of the major target hall activities is given below. Some of the activities are not part of ANU and will be done as part of NuMI operations and upgrades. These activities are marked as off-project. Since the off-project activities will occur in conjunction with ANU, an overall plan must be developed.

- Horn 2 move to the medium energy position (includes evaluating R-Block, T-block and blue block staging options, stripline extension, etc.).
- Target & Horn change outs, upgrades and repairs. (Off-project)
- Radioactive component repair/removal (work cell activities, remote tooling & manipulators setup, additional shielding, etc.). (Off-project)

Fig 8.38 and Fig 8.39 show a longitudinal cross section of the target hall shielding together with the proposed new Horn 2 location. Fig 8.40 shows a picture of the NuMI Target Hall looking downstream during a recent target repair job. In Fig 8.40 concrete R-blocks have been removed and staged at the downstream end near the work cell (red shield door), T-block are staged just upstream of that. It can be seen that space is very limited especially when it will come to staging several more shielding blocks which will be required during the Horn 2 relocation. Some creative stacking arrangements will have to be developed for effective and safe staging of these blocks.

Concrete “R” blocks placed on top of the target vault (to seal the target pile and provide shielding) are also used for shielding and storage of the T-blocks and blue blocks as shown. Since the new horn location falls beneath the existing T-block and Blue-block storage space, a completely new shielding storage scheme will have to be developed. This will also have to take into account the addition of a new (temporary) work area just upstream of the work cell to be used for conducting radioactive component repairs using remote tooling (The radioactive component repairs using remote tooling is an off project activity). A preliminary layout of this proposed new shielding configuration is shown in Fig 8.41. This will require more shielding

blocks, and more concrete blocks will also be required to extend the existing battlement (vertical R-blocks that run parallel to the length of stripline) further downstream. Therefore, it is important that a detailed study of the available space be conducted that aims to develop a comprehensive new layout plan for the various target hall activities. As a result, new equipment (mostly in the form of structural supports) might be designed to help with the transport and staging of shielding blocks during shutdown activities, in a way that optimizes use of the target hall space. The cost of this equipment is included in the resource loaded schedule.

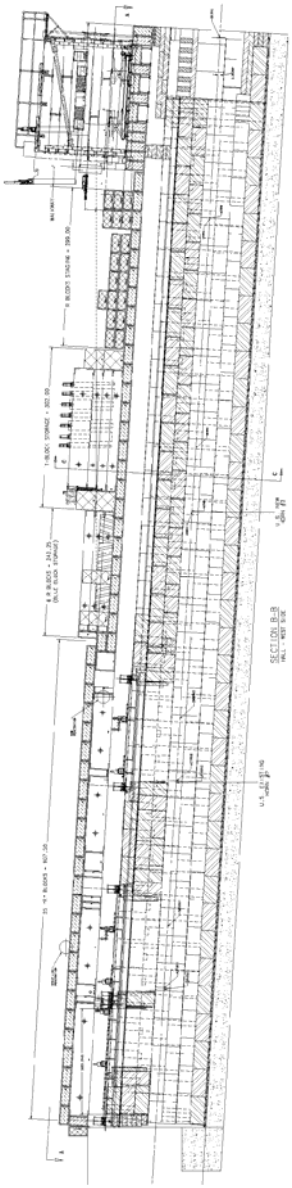

Fig 8.38: A Longitudinal cross section of the NuMI Target Hall showing shielding layout.

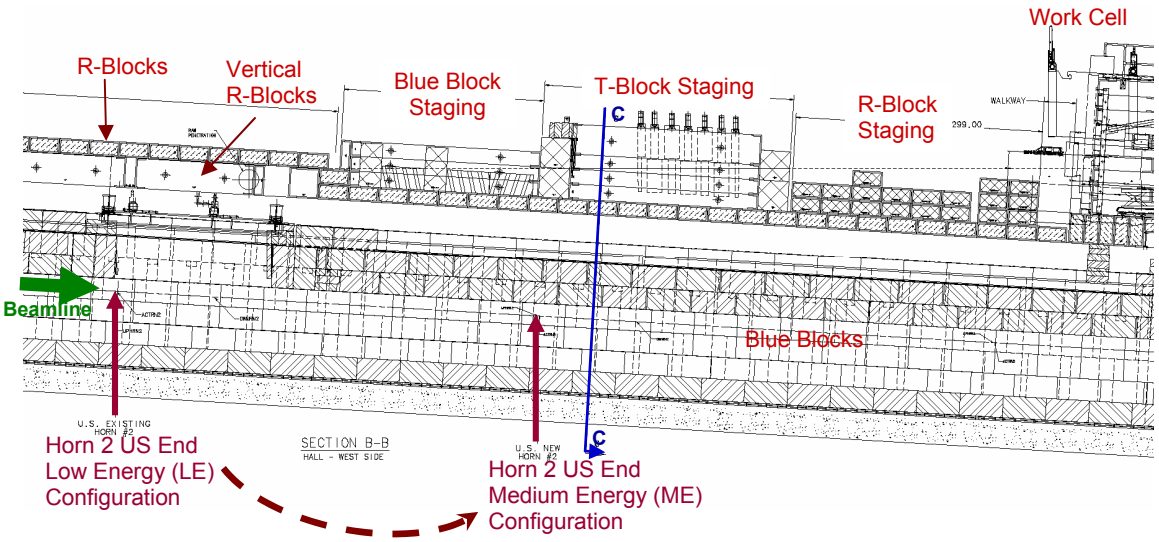

Fig 8.39: Close up of NuMI Target Hall longitudinal cross section showing existing Horn 2 location and proposed new medium energy position approximately 13 meters further downstream. As can be seen, the shielding block staging areas will have to be re-located to accommodate Horn 2.

Fig 8.40: NuMI Target Hall looking downstream during a recent target repair job.

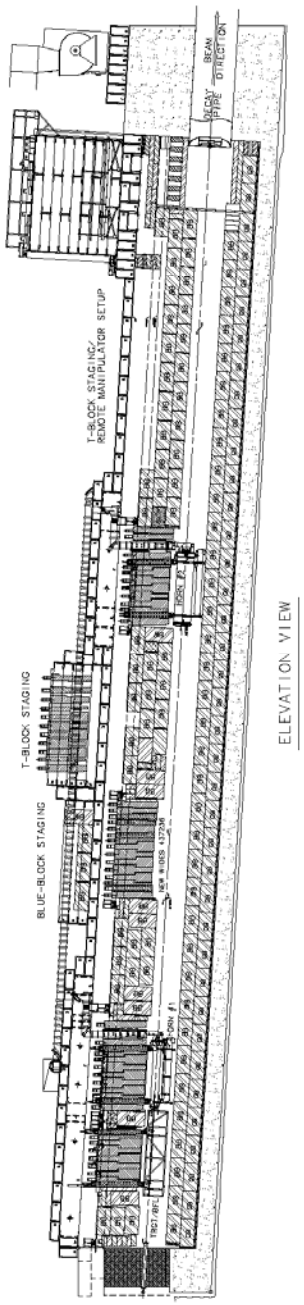

Fig 8.41: A Longitudinal cross section of the NuMI Target Hall showing proposed shielding layout for NOvA (i.e. after Horn 2 relocation).

8.6.4.2 Horn 2 Relocation to Medium Energy Position

To switch from the low energy to the medium energy neutrino spectrum, Horn 2 will need to be relocated approximately 13m further downstream [28] from its current position in the target chase, as shown in Fig 8.38 and Fig 8.39. This will require extension of the existing stripline and significant reconfiguration of the existing shielding layout.

8.6.4.2.1 Stripline Extension

The stripline is the electrical connection between the 240 kA pulse power supply and the horns. The original NuMI design concept was to have Horn 2 capable of being moved into three discrete locations and provisions were made to extend the existing stripline in the future for the new horn locations. However, no stripline extensions were built so new ones are needed for the NOνA Project. Fig 8.30 shows the stripline running along the wall and the connections needed for the various horn 2 locations. Fig 8.40 shows the existing stripline along the left wall, enclosed in plastic, and the connection to horn 2 (about ½ way down on the left in the photo), under the R-blocks, but now visible due to the R-Blocks being removed.

The stripline consists of 8 layers of high conductivity 6101-T61 aluminum bus bars which are 12 inches wide by 0.375 inches thick. The bus bars are held together by aluminum clamps with fiberglass insulators in low radiation areas. The walkway stripline assembly is mounted to steel C-channels supported by steel stands. The walkway stripline extension will be pre-assembled in a building and then installed in the target hall. On the downstream end of the existing walkway stripline in the target hall there are silver plated contacts that currently have four shunts plugged into them. The shunts will be moved to the end of the new extension (10 meters downstream) and the new stripline extension will plug into the end of the existing stripline. The two existing stripline assemblies (chase and module stripline sections connecting to Horn 2), under the R-blocks will be reused at the new Horn 2 location.

The horn power supply is a 0.225 F capacitor bank that operates up to about 1 kV and the power supply output is presently set to 200 kA at 680 V. The two focusing horns, each a single turn air core magnet, are constructed in a co-axial configuration. The addition of 10 meters of stripline will increase the inductance of the system by 160 nH. The power supply voltage will have to be increased to 787 V to maintain the 200 kA output. Even though there is an increase in power supply output, the electrical heating of the stripline will increase only slightly due to 10 extra meters of stripline.

8.6.4.2.2 Shielding Reconfiguration

The target hall shielding is made up almost entirely of steel “blue blocks” stacked as shown in Fig 8.42. At the horn locations, the center three rows of blue blocks are replaced with the horn modules together with associated shielding blocks (T-blocks, end blocks and stripline block.) A drawing of the Horn 2 module is shown in Fig 8.43. A photograph of the Horn 2 module assembled on a test stand at MI-65 is shown in Fig 8.44.

At the new location for Horn 2 in the shielding pile, the center set (of approximately 12) blue blocks will need to be removed to make space for the Horn 2 module. Also needed are 6 additional vertical R-blocks to extend the existing battlement (vertical R-blocks that run parallel to the length of stripline) for the Horn 2 relocation. These additional R-blocks are used to raise the level of the R-block shielding covering the chase and thereby create a vertical space for the stripline extension when Horn 2 is relocated downstream. (The vertical R-blocks can be seen in Fig 8.39.)

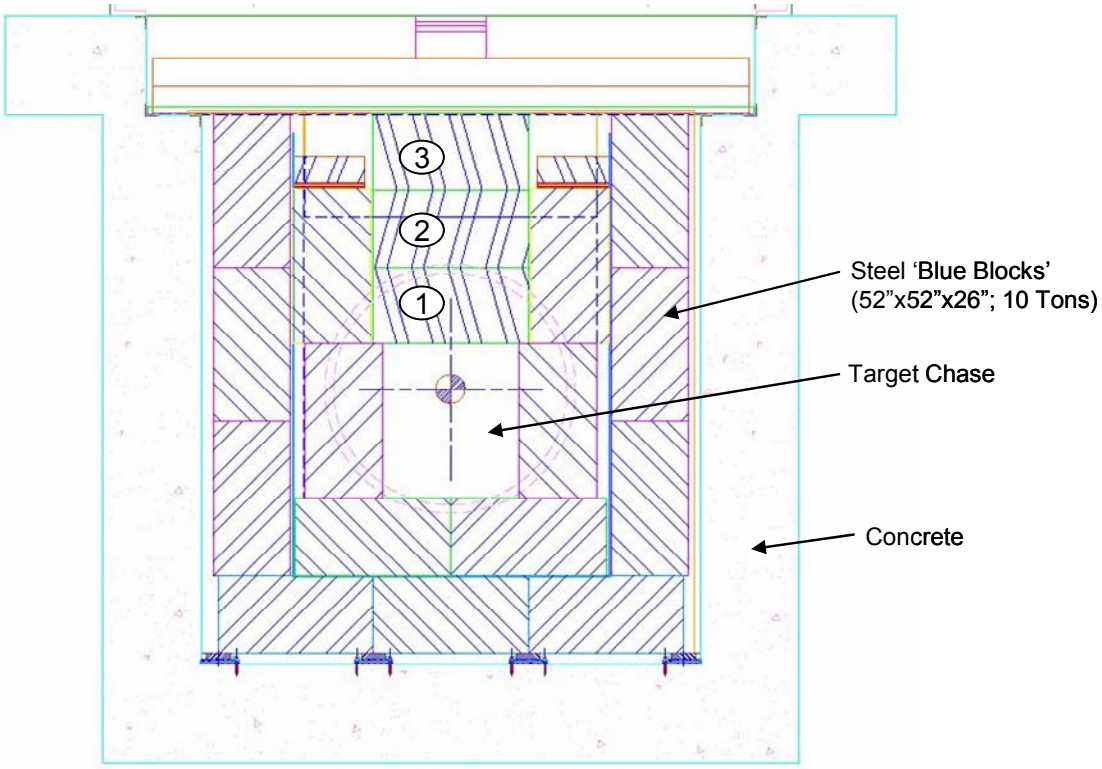

Fig 8.42: Typical NuMI Target Hall shielding cross section. At the new Horn 2 position, only the center row of blue blocks (marked 1, 2, & 3) will have to be removed.

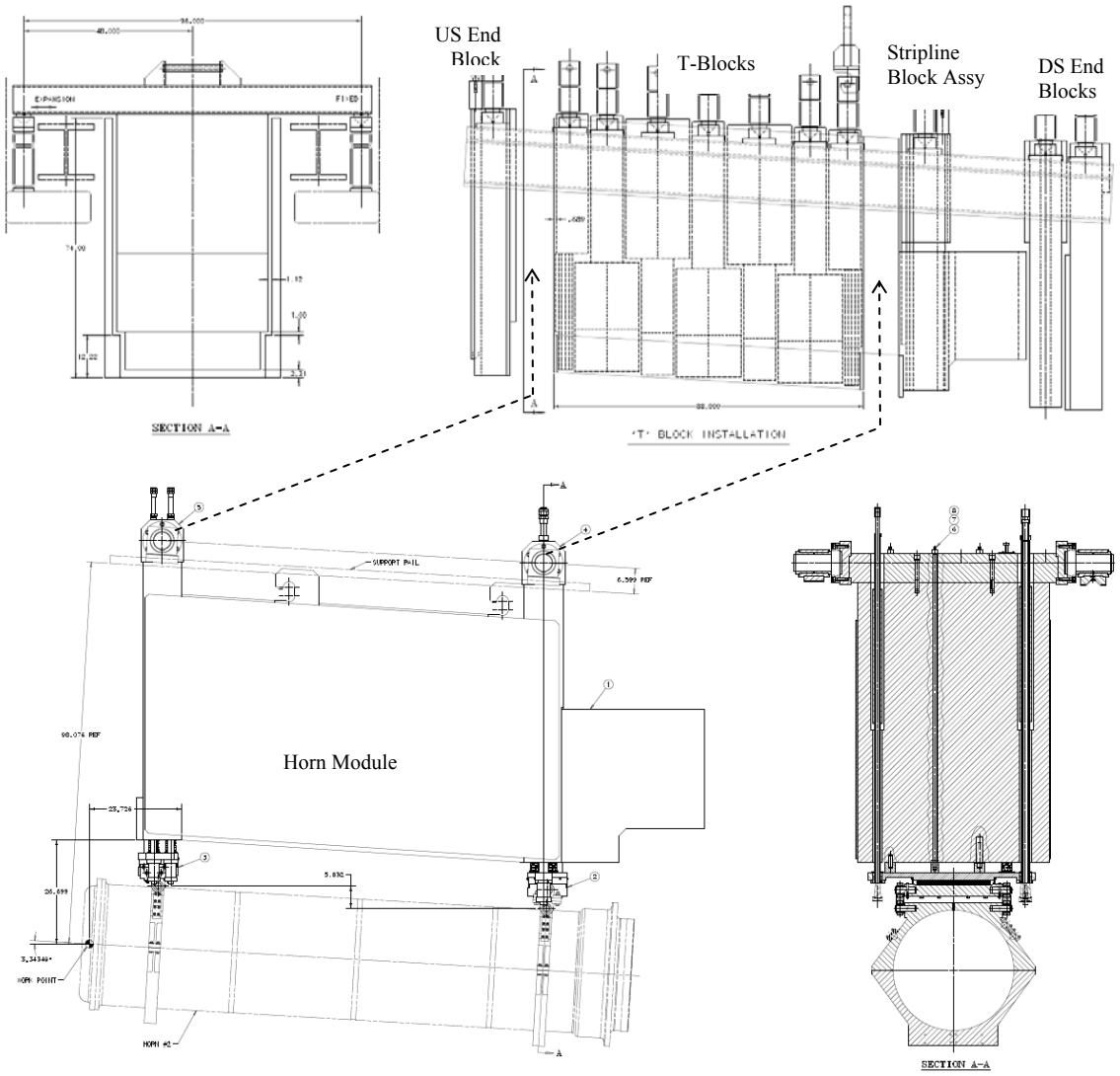

Fig 8.43: NuMI Horn module and shielding blocks (T-blocks, end blocks, & stripline block) that will be moved to the ME position together with Horn 2.

Fig 8.44: Horn 2 attached to module in the MI-65 service building.

To greatly simplify moving Horn 2 to its new location, a new set of shielding T-blocks and support tube will be built as shown in the drawings in Fig 8.45. This shielding scheme will be installed in the vacant LE location after Horn 2 is moved. (Re-using the extracted blue blocks from ME is not a viable option due to the difficulty in remote stacking radioactive blue blocks). The new shielding blocks are similar to the existing T-block design (Fig 8.43), with the major difference being wider (and heavier) T-blocks at the center to fill the space left by the module walls. Due to this increased weight, the concrete R-blocks were re-analyzed [32] and found to be

structurally adequate to support the additional load of the T-blocks during staging as shown in Fig 8.41.

This new shielding scheme will eliminate the need for the module assembly altogether and can be installed in either the low energy or medium energy location and essentially acts as a shielding “plug”. Therefore, work could begin on its installation during the first shutdown in the schedule after the completion of Collider Run II operations. During this shutdown, the ME blue blocks can be extracted and the new shielding T-blocks installed in their place. Finally, it is anticipated that some additional custom filler blocks will be needed to match the new interface condition after removal of blue blocks and installation of the new T-blocks.

Once Horn 2 is ready to be moved, it will simply require swapping of the assemblies, Fig 8.43 and Fig 8.45, at the LE and ME locations. It should also be noted that a new Horn 2 carriage and T-Block support tube weldment will have to be built and surveyed into position. Another advantage of having two interchangeable assemblies is that it will allow Horn 2 to be easily moved back to the low energy position if the need arises in the future.

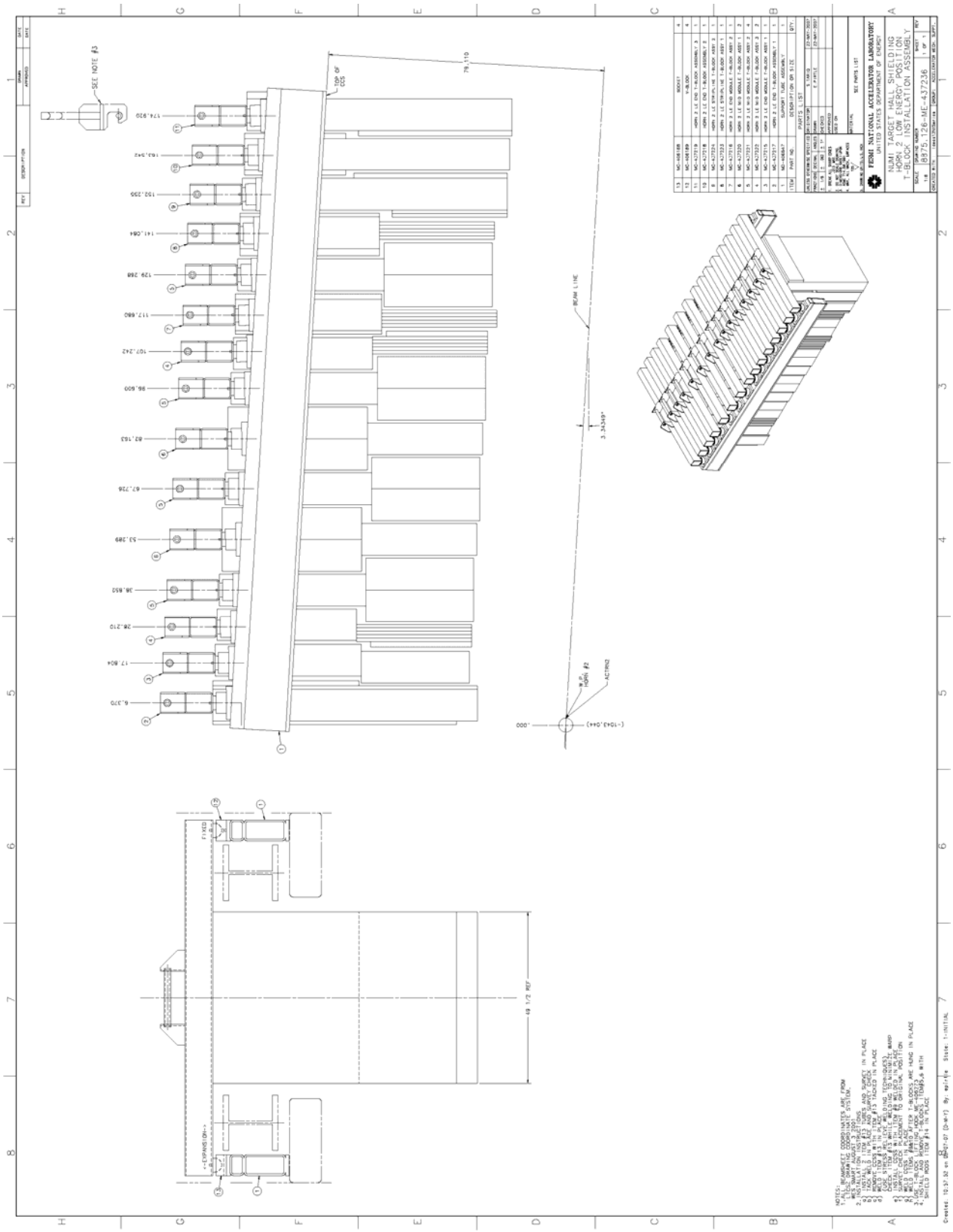

Fig 8.45: Revised shielding T-block design pattern and support tube assembly to be installed at the LE location.

Fig 8.46: Horn 1 connected to transmission line in the MI8 service building.

The resource loaded schedule assumes the use of new shielding T-blocks as described above, with most of the steel being purchased from the outside which is the most expensive option. A cost saving alternative also being studied is to utilize steel available onsite at minimal cost (mostly radioactive shielding steel left over from previous experiments) plus maximizing the use of continuous cast salvage steel which is significantly cheaper than regular HR plate. Recycling radioactive steel from onsite prevents creating any new future radioactive waste. This latter option, if viable, could lead to significant cost savings in both the short and long term.

During the Horn 2 move, a number of surplus blue-blocks will be taken out from the new location. These could then either be completely removed from the target hall (the ideal scenario) or stored in some fashion within the available target hall space. A detail radiation survey needs to be first conducted to measure the residual dose rates. If dose rates are reasonable, a coffin can be designed to safely remove and transfer some of the blue blocks to an external storage site (weight and size of the coffin being the limiting factor), and this is covered by the Radioactive Component Repair/Removal off project task. The morgue could also be used as a temporary storage for hot blocks but this should only be considered a short-term solution. As shown in Fig 8.41, some of the blocks could be stacked on top of the existing two layers of blue blocks assuming there is no interference with equipment. These options will all be part of the detail study on available space issues in the target hall. The resource loaded schedule assumes we will remove and re-use/store most of the blue blocks within the available target hall space, with the possibility of loading some of the blocks on a coffin/hearse assembly ready for transport up-shaft.

If residual dose rates are high on some of the blocks, which will most likely be the case with the target chase blocks, then remote handling will be required. The existing remote handling lifting fixture and camera system are not adequate to do this task effectively. An assessment of

the remote lifting system will have to be made resulting in upgrades to the fixture and camera system. These upgrades are included in the resource loaded schedule.

8.6.4.3 Target Chase

Additional cooling of the target chase is needed due to the large amount of beam energy deposited. With the 700 kW of beam power anticipated for NOνA, approximately 280 kW is deposited in the target pile. Maintaining a reasonable temperature in the target chase is important for several reasons:

- Thermal expansion of the target chase and target hall components will affect the alignment of the target and horns. The NOνA experiment requires that alignment of the beam, target, and horns remain within a 1.5 mm tolerance [28].

- The target pile consists of stacked steel blocks (referred to as "Blue Blocks"), which are painted to reduce corrosion. Burning and smoldering of the paint can be a problem if the target pile becomes too hot.

- Higher temperatures and radiant heating from the target pile can add to the heat load of target, horns, and striplines (see section on Radiant Heat Loads). This can lead to unacceptable temperatures of the target hall components.

Testing of the paint samples is planned to determine the maximum allowable temperature requirements in the target chase. Further analysis is also planned to determine the maximum acceptable operating temperatures for the target hall components.

8.6.4.3.1 Target Chase Cooling

A preliminary estimation of the expected target chase temperatures has been performed. The beam energy deposition values used in this analysis are scaled up from the NuMI values by multiplying them by 1.75 (the ratio of 700 kW to 400 kW). The preliminary estimate for NOνA target pile shielding temperatures is shown in Fig 8.47. The highest shielding temperature is 115 °C at the peak beam heating location just downstream of the Horn 1 location. The estimate has been made using the refined 2-D NuMI target pile finite element model (FEM).

The original NuMI target pile FEM was refined by incorporating the actual average heat transfer rate from two Duratek shielding blocks in the inner chase wall. The average rate was experimentally determined by monitoring the temperature of the two Duratek blocks as they cooled down with no beam heating and with the target pile fan on. Both of the Duratek blocks are at the location of the theoretical peak of beam heating. The blocks are on opposite sides of the chase directly across from each other and just downstream of Horn 1. Each of these blocks has a thermocouple welded to it that was used to monitor block temperature during the test. The light blue colored block in Fig 8.47 has the one with the thermocouple welded to it on that same side of the chase.

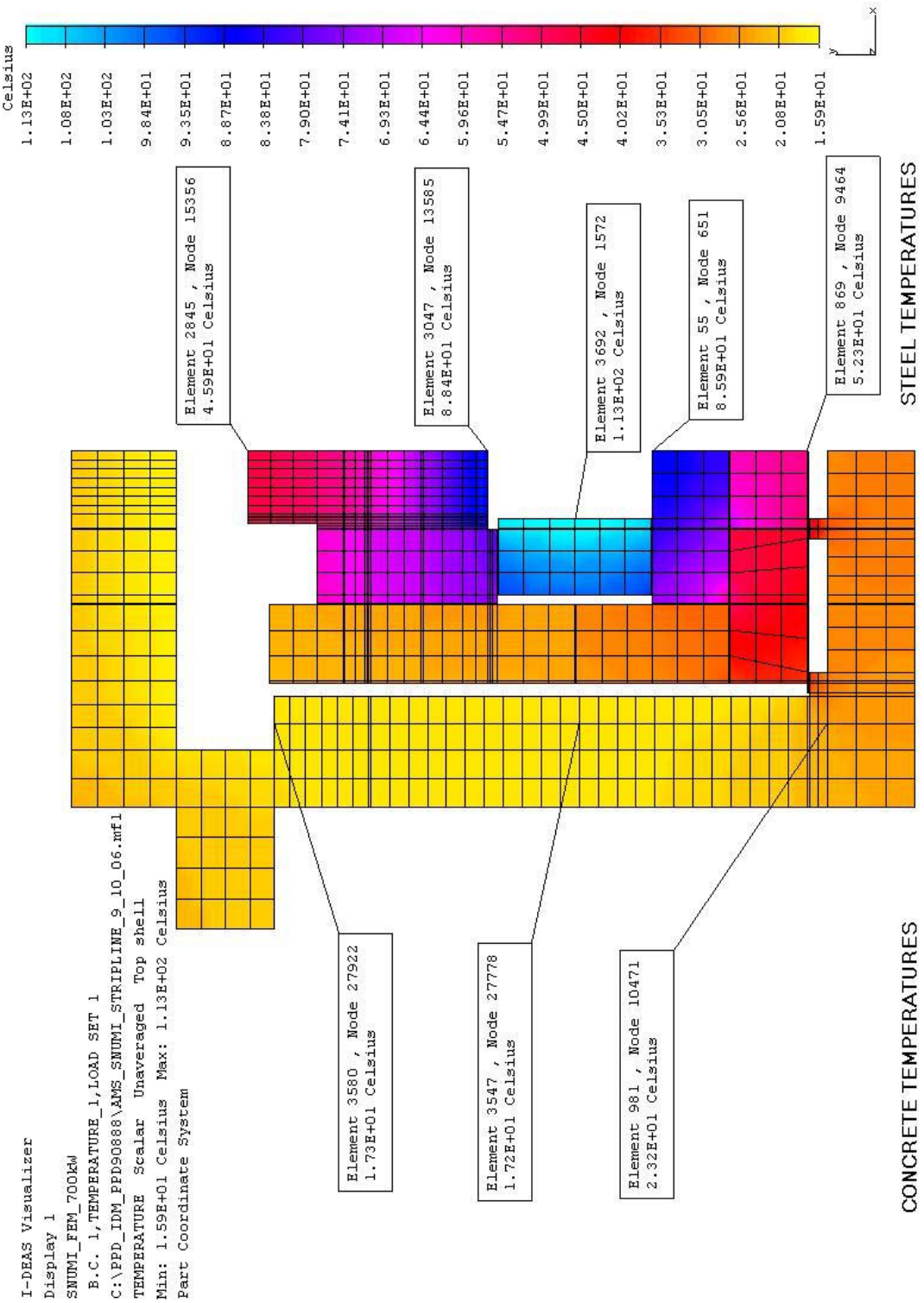

Fig 8.47: Estimated target pile peak temperatures at 700 kW of beam power.

Concrete temperatures estimated using the 2-D NuMI FEM are slightly higher than expected because the model assumes that the concrete liner is insulated at its outermost boundary where it contacts water-bearing rock instead of being modeled as a semi-infinite solid. A MARS simulation of the complete target chase region (including technical components) at 700 kW beam power has been performed to obtain updated energy deposition numbers shown in Table 8.18. This data will then be used in a new comprehensive 3-D FEM of the target chase region and will provide more accurate temperature data. Preliminary results from this FEM study can be found in [30].

Table 8.18 gives a breakdown of the NOvA heat loads in the target chase [31]. The target pile heat load of 260 kW was based on MARS and includes an 18% safety factor. The total heat load for the target chase is thus estimated at 458 kW. The NuMI operational upgrade during the 2007 summer shutdown (as part of the tritium mitigation plan) will install 4 new surface chiller units (and a new dehumidification system) with a capacity of 160 kW each to replace the existing chiller unit downstairs. This upgrade will meet NOvA requirements by running three of the four chiller units for a combined total capacity of 480 kW to cover the 458 kW NOvA heat load. The fourth unit can then be kept as an on-line spare and made quickly operational if one of the other three were to fail. This adequately addresses the operational and reliability concerns for NOvA. The remaining scope for the chase cooling upgrade is to evaluate the existing chiller cooling coil design and address the option of adding more heat exchanger coils to increase capacity of the air cooling system. This heat exchanger upgrade will involve modifying the existing coil box to accommodate the new coils and laying out piping to connect the new coils to the existing coolant loop. This upgrade will include specifying valves and instrumentation, making control wiring diagrams, and updating the existing controls (PLC and ACNET). This heat exchanger upgrade is included in the resource loaded schedule.

Description	Load (kW)	Comments
Target Pile (710kW beam)	260	from MARS + 18% SF
Stripline	7	
Fan	50	
Chilled water pump	20	
Dehumidify 14kg/hr water*	11	
Dehumidifiers	110	2 units, 55kW ea
Total load to chiller:	**458**	

*Air leak ~600cfm

Table 8.18: NuMI Target Hall Chiller Heat Loads for 710kW beam power.

In summary, from this preliminary estimate we should be able to meet the alignment tolerance [28] of Horn 1 based on the latest estimates of the motion of Horn 1 due to thermal effects [32, 33]. A detailed analysis of the target chase region (using 3-D FEM) is currently underway to calculate more accurate temperature and alignment data. The NuMI chiller/dehumidification upgrade this summer will accommodate NOvA's increased heat load, and the only upgrade required for the existing cooling system will be the addition of new heat exchanger cooling coils. Finally, a further study of the paint characteristics and target hall components will be conducted to determine if the temperatures will be acceptable.

8.6.4.3.2 Radiant Heat Loads

As discussed in the previous section, the Duratek shielding blocks at the inner chase wall are predicted to reach very high temperatures due to the increased beam power, especially downstream of Horn 1 (113ºC). Thermal radiation between the hot wall surfaces and sensitive chase components (such as horns, target, and stripline) is of concern. The comprehensive 3-D finite element analysis (FEA) model will be used to compute the amount of heat transfer (primarily radiation heat transfer) from the shielding blocks to the chase components. This additional heat input will be included in the thermal analyses for these components to determine whether radiation heat shields will be needed. The cost for these heat shields will be covered under the Horn 1 off-project task. Additional chase temperature monitoring equipment will also be installed at critical locations, such as on chase walls and module bottoms, to better monitor temperatures of these areas during operation. The cost of this monitoring equipment is included in the resource loaded schedule.

8.6.4.3.3 Horn 1 Stripline Block

The section of NuMI Horn 1 stripline (aluminum 6101-T61) which delivers pulsed current from the top of the Horn 1 module to the downstream end of the Horn conductors is heated from two sources: joule heating from the current pulse and beam heating from the interaction with secondaries from the upstream target. One upper portion of this stripline is encased in steel shielding called the stripline block (basically part of the Horn 1 shielding module). The path of the stripline through the block is actually a dog-leg to reduce straight line holes through the shielding and is called a labyrinth (see Fig 8.48). The lower portion of this stripline flares out to attach (through bolted connections) to the conductors of Horn 1 and is part of the Horn 1 assembly (see Fig 8.49). The two portions, upper and lower, are connected via a remotely operated clamp mounted on the bottom of the stripline block.

Cooling to the stripline is achieved via 4 heat transfer paths, depending upon location: 1) forced air convection through the stripline block labyrinth channel (about 14 scfm from “short-circuit” in the chase air circuit), 2) forced air conduction of the Horn stripline that is exposed to chase airflow, 3) natural air convection of the Horn stripline that is “hidden” downstream of the Horn and not exposed to chase airflow, and 4) conduction along the stripline (in the same “hidden” area as 3) to the Horn 1 body (water cooled).

Future operations with 700 kW beam on target increases the beam heating source by a factor of roughly 1.75. Concerns that the increased heating will raise the temperature of the stripline above acceptable limits need to be addressed. This will require upgrades and enhancements to the chase stripline assembly cooling.

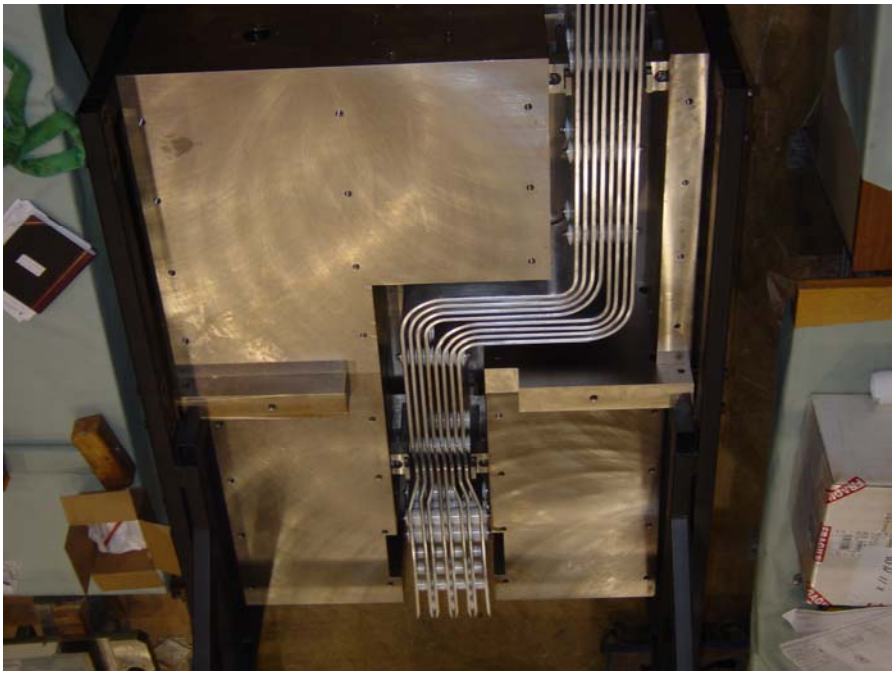

Fig 8.48: Stripline Block Assembly showing labyrinth with the cover removed.

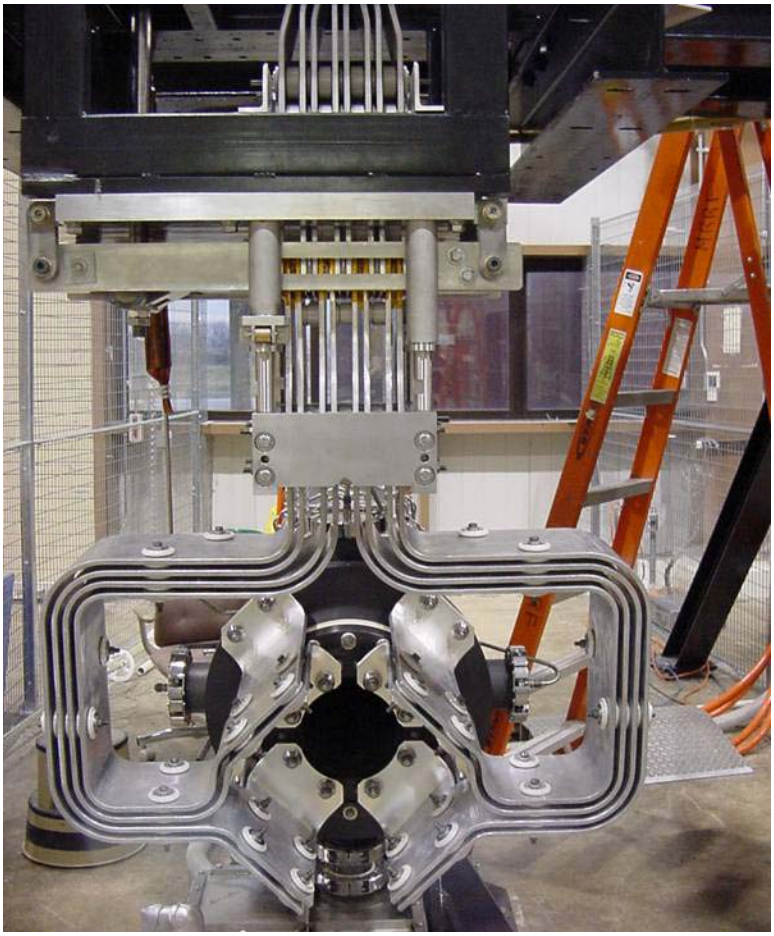

Fig 8.49: Photo of Horn 1 Stripline going up into the remote clamp on the test stand

An FEA of the stripline with the original NuMI design conditions (400 kW beam power) predicted a peak temperature of 100 ˚C in the stripline flag area (stripline segment that is bolted onto the Horn 1 nearest the beam centerline). This FEA was repeated for the ANU beam conditions (700 kW) and the peak temperature in the stripline flag rose to 166 ˚C (Fig 8.50). However, the joule heating estimate used in this FEA was overly conservative and high by a factor of 2, so further analysis is needed. Fig 8.51 shows structural FEA results for 400 kW NuMI conditions. The highest stresses are about 13 ksi in the region near the bolted connections to the horn conductors and are estimated to be 16.25ksi for the 700kW condition. Further details on stripline cooling concerns can be found in reference [34].

For ANU beam conditions, a more detailed and comprehensive thermal and structural FEA will be performed using the latest estimations of heat loads and cooling capacities to more accurately predict temperatures and stresses. This will be in conjunction with R&D to measure air velocities and convection heat transfer coefficients around a mock-up of the Horn 1 downstream chase area (using spare stripline components), which will help determine the level of forced air cooling required (if any). This work is currently underway and Fig 8.52 shows the test set-up at MI-8. The cost for this testing is included in the resource loaded schedule. The schedule also assumes that forced air cooling will be required, and the cost for the design, procurement, and assembly of a new cooling system on the stripline block has been included.

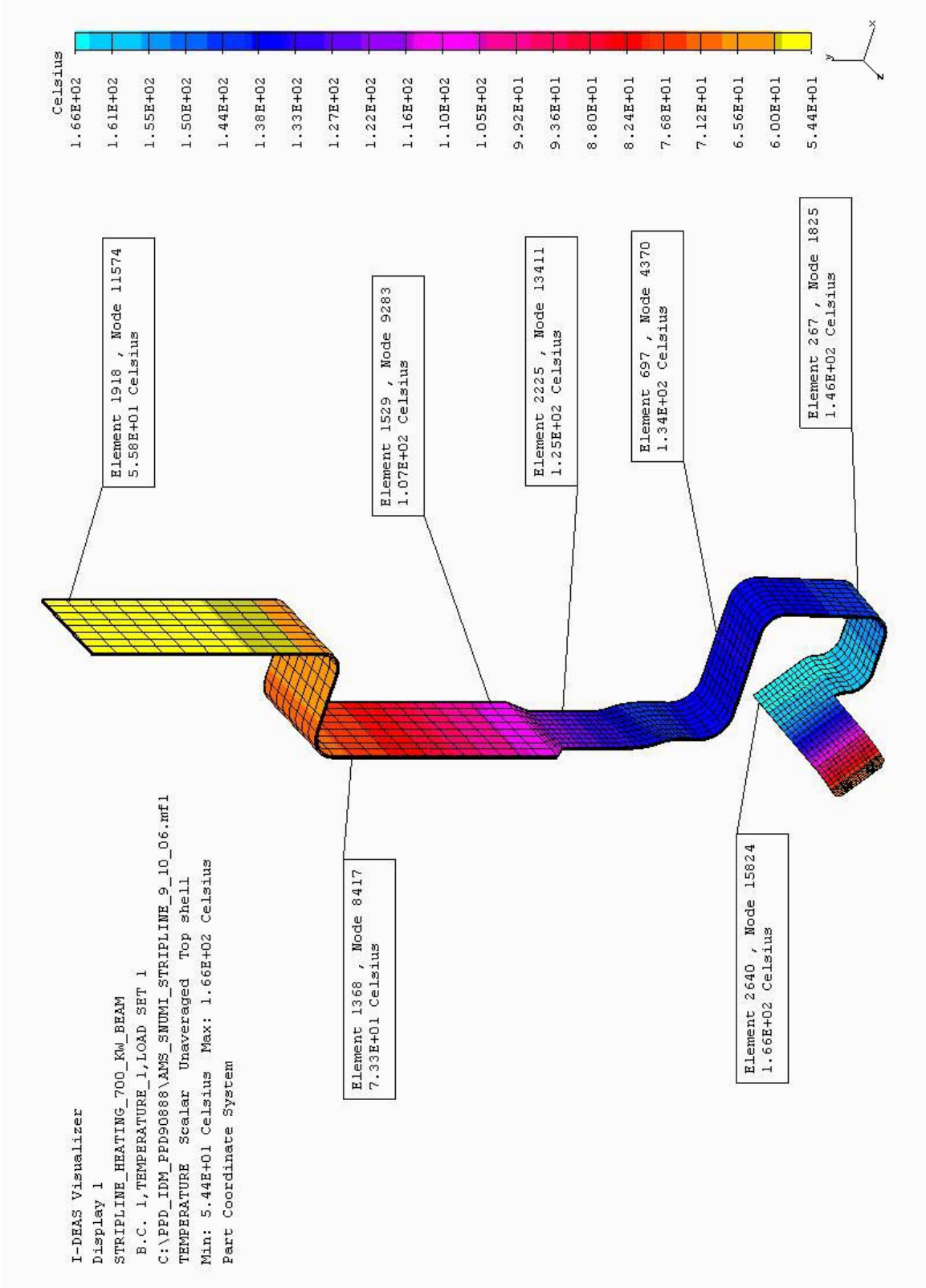

Fig 8.50 : Preliminary estimate for ANU Horn 1 stripline temperatures using NuMI FEM.
Note: Temperature distribution is over-predicted in figure (see text).

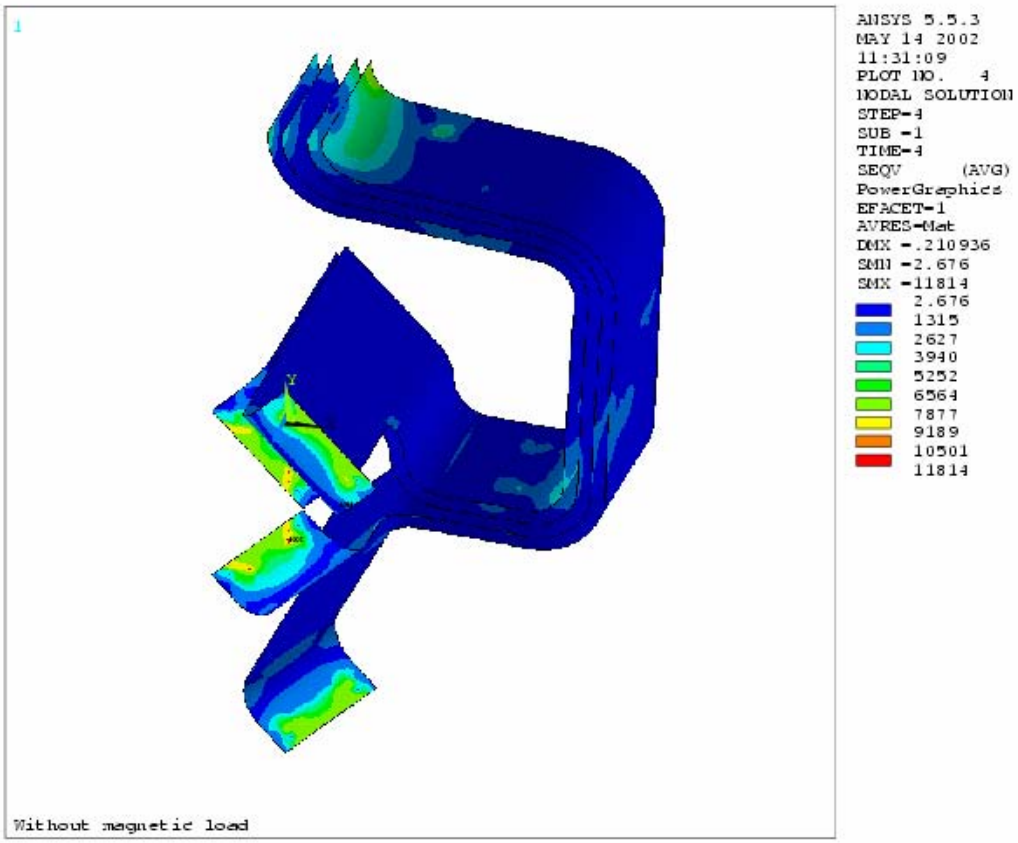

Fig 8.51: Equivalent stress (psi) in Horn 1 stripline for NuMI (400 kW beam) case without magnetic loading (includes alignment offset and thermal expansion).

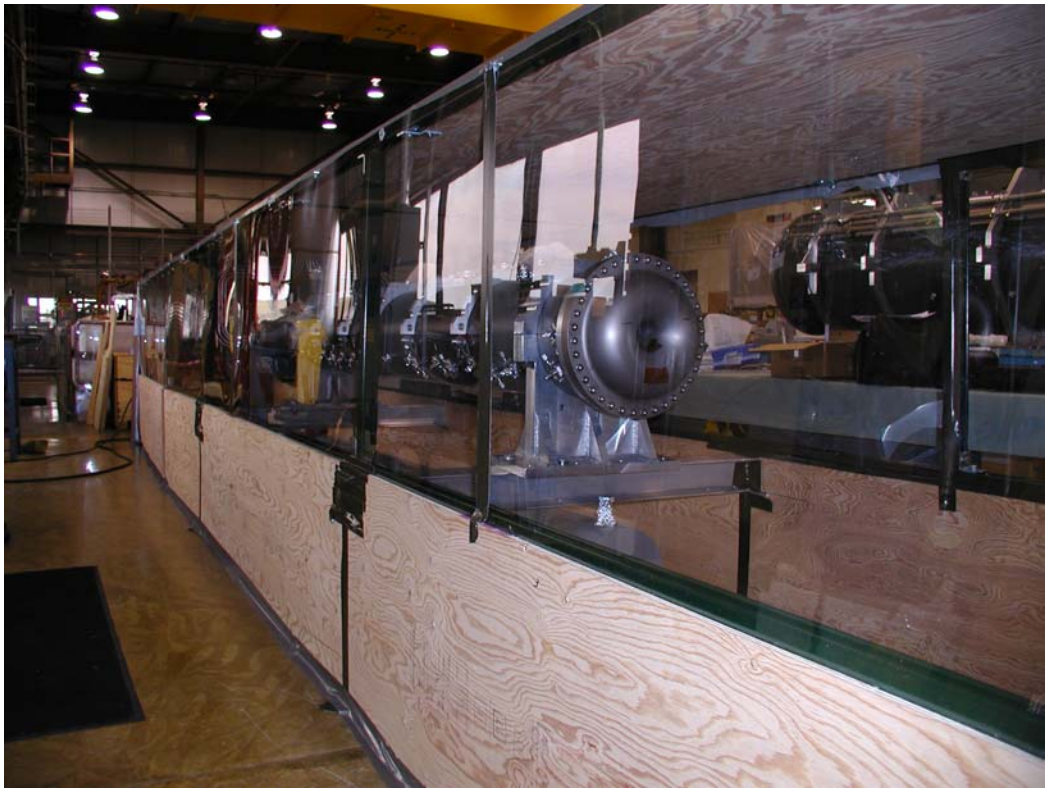

Fig 8.52: Wind tunnel mock-up at MI-8 of the Horn 1 chase area (using spare horn and stripline components) to study air velocities and cooling characteristics of stripline components.

8.6.5 Decay Pipe, Hadron Absorber, and Utilities

8.6.5.1 Decay Pipe and Hadron Absorber

The NuMI decay pipe consists of a 2 m diameter A36 steel pipe, 0.375 inches thick, 670 m long, encased in a cylindrical shell of concrete varying in diameter from 4.6 to 6.3 meters. In use, the steel pipe is evacuated. The decay pipe is cooled by twelve tubes, evenly spaced azimuthally, and running parallel to the steel pipe, but attached directly to the pipe only at the stiffening rings, which are spaced ten feet apart. The tubes comprise six distinct circuits. Six tubes bring chilled water from the downstream to the upstream end, where it is re-chilled and returned (see Fig 8.53 and Fig 8.54). The design flow rate of each circuit is 4.5 gallons per minute, for a total system flow of 28 gallons per minute. The water temperature leaving the chiller is 25 °C. The decay pipe and cooling has been analyzed at the higher heat loads expected during NOνA operations. Sufficient cooling can be supplied with a doubling of the flow rate in the decay pipe cooling pipes [35].

The upstream NuMI decay pipe window is a 72 inch diameter closure consisting of a 1 m diameter, 1/16 inch thick aluminum central portion, transitioning to a 3/8 inch thick steel head at the larger diameters (Fig 8.53). This transition is achieved with an explosion-welded aluminum-to-steel flange. This structure is not actively cooled. The heating and stresses in the central portion were investigated using an axisymmetric finite element model with approximately 800 four-node elements. A thermal version of the model was used to calculate the temperature profile in the head; a structural version of the model then read the temperature profile to calculate

stresses. The rules for the allowable stresses were taken from the ASME Boiler and Pressure Vessel Code, Section VIII, Div. 2, Appendix 4. The loading to the thin window is due to vacuum and the cyclic thermal stresses resulting from beam energy deposition. The NuMI decay pipe window is capable of withstanding the higher beam power operations for the NOνA experiment as documented in [35].

The NuMI hadron beam absorber core consists of nine water-cooled aluminum modules, 1.32 x 1.32 x 0.31 meters in size. The (present) NuMI design criteria require that the absorber operate for one hour (approximately 1800 pulses) under the fault condition. The fault condition is defined as an improperly steered primary beam that misses the target and clears the protection baffle and thus is a much focused beam. Under normal operating conditions only about 18% of the 120 GeV primary protons strike the absorber, and the rms radial size of the beam is 20 cm compared to 5 cm in the fault condition. The fault condition is the critical operating condition for the absorber system [35]. To prevent multiple fault condition pulses, the hadron monitor will be used to monitor the NuMI beam. The hadron monitor will also be incorporated into the Beam Permit System and automatically stop beam operations should an errant beam pulse be detected.

Analyses of the mechanical integrity of the decay pipe, decay pipe window, and hadron absorber have been completed under NOνA/ANU operating conditions. In summary, these systems are capable of handling operations of the NuMI beamline with 700 kW of beam power and no modification to these NuMI beamline elements are required. A description of the analyses can be found in [36].

Fig 8.53: Decay Pipe Upstream Window (with decay pipe cooling pipes shown).

Fig 8.54: Decay Pipe Downstream Window (with decay pipe cooling pipes shown) and Absorber Hall (Hadron Absorber not installed) – emergency egress passageway on left.

Fig 8.55: Hadron Absorber Installed

8.6.5.2 Basic NuMI Cooling Systems Layout

The NuMI cooling systems consist of numerous Radioactive Water (RAW) and Non RAW skids in several locations. The following three diagrams are maps showing the general location and layout of the various systems. Beginning upstream, where the NuMI beamline originates, a Low Conductivity Water (LCW) system is housed at MI-62 (Fig 8.56). This feeds cooling water to the NuMI Extraction Line from the Main Injector Enclosure through to the Target Hall, where it cools the Target RAW skid. It also supplies some cooling for power supplies upstairs at MI-65.

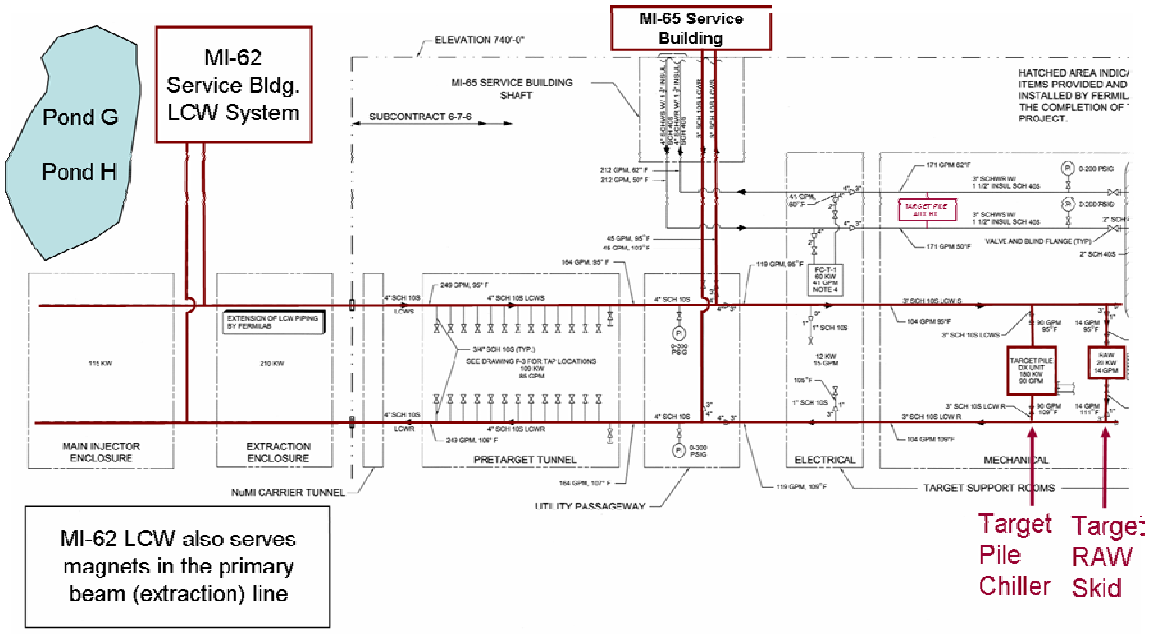

Fig 8.56: LCW System from MI-62 to the NuMI Extraction Line

In the Target Hall, there are also several RAW Systems to cool the Target, as well as both Horn 1 and Horn 2 (Fig 8.57). Also, there is a RAW System which cools the Decay Pipe, and which has a heat exchanger and expansion tank located on the Upstream (US) end at the Target Hall, and a second heat exchanger and circulation pumps located at the Downstream (DS) end at the Absorber Hall (Fig 8.57 and Fig 8.58). Lastly, in the Absorber Hall are the RAW and Intermediate Systems for the Absorber (Fig 8.58).

Outside of the local systems mentioned above, two systems bring water from external sources. The first is Industrial Chilled Water, ICW, which is 55 degree unpolished cold water from CUB, which supplied additional cooling capacity at MI-65. Second is the ground water, which is reclaimed from the MINOS sump, and used to cool the systems in the Absorber Hall and MINOS Hall before being pumped on to CUB for use there.

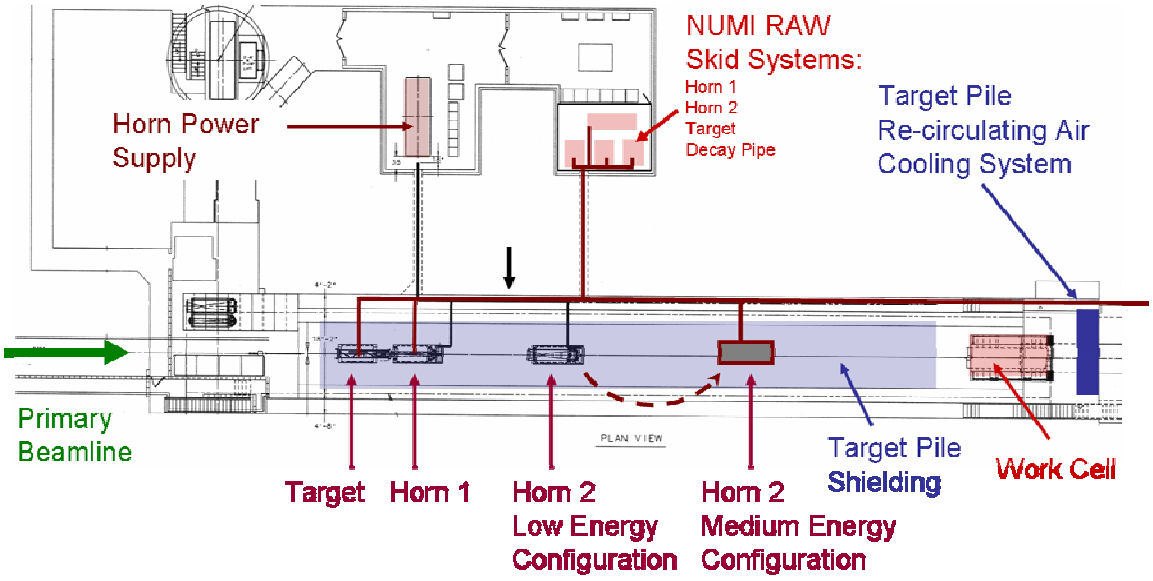

Fig 8.57: Horn, Target, and US Decay Pipe RAW Systems in the Target Hall

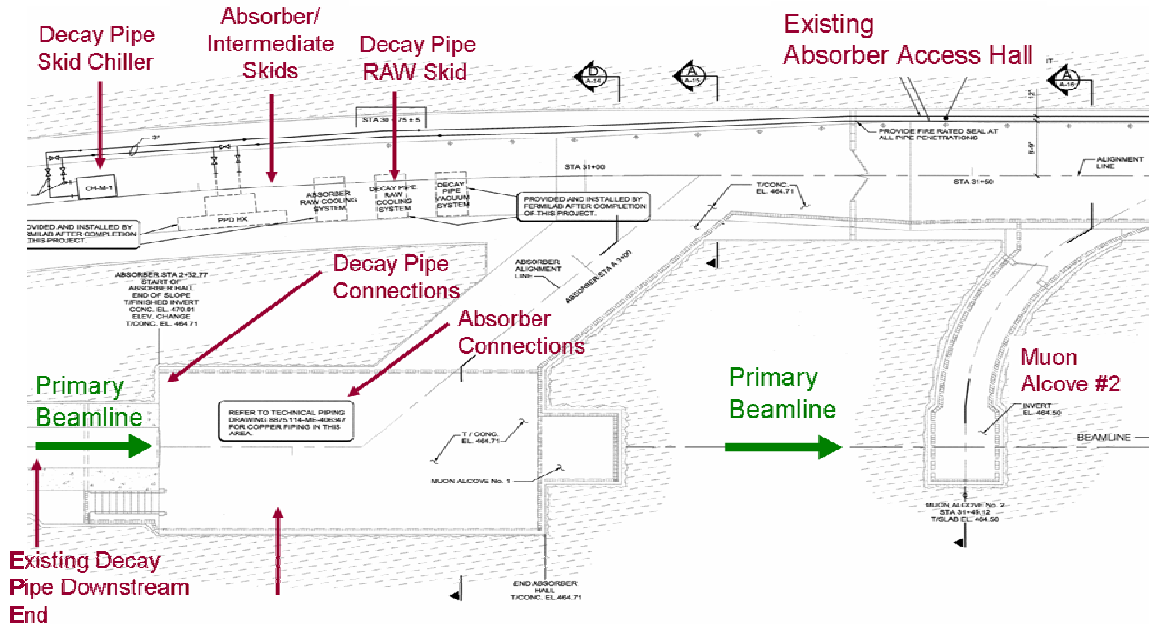

Fig 8.58: Downstream Decay Pipe and Absorber Cooling Systems in the Absorber Hall

8.6.5.3 NuMI RAW Systems

NuMI uses 6 RAW skids and 1 intermediate RAW skid to cool the target, horns, decay pipe, and hadron absorber. At this time, the skids appearing to require upgrades for capacity or performance are the Horn 1 and 2 skids, and the Hadron Absorber RAW and Intermediate skids. In any case there are plans to upgrade the instrumentation of the RAW skids to include remote

readback of the temperature and flow measurements. Preliminary estimates of the necessary upgrades follow.

8.6.5.3.1 Target Raw System

Initial calculations suggest that the target RAW skid will be sufficient for NOvA, but final determination awaits a report from IHEP on the heat load of the medium energy target design. The need for upgrading the pumps and heat exchanger is not likely at this time, and such costs are not included in the project. The skid will be upgraded with modern instrumentation and controls.

8.6.5.3.2 Horn 1 and 2 RAW System

It is likely that the Horn 1 skid will need an upgrade to handle the higher heat load for NOvA. In addition to circulating the cooling water, the pump on the RAW skid also powers the ejector pump which removes water from the collection tank below Horn 1. Presently the ejector pump is barely adequate for the purpose of removing water from the holding tank. Therefore, the Horn 1 RAW system will be equipped with a larger water pump and the ejector pump for Horn 1 may be redesigned as well. This may be due to either pump capacities or piping sizes which restrict the pump capacities.

Initial calculations suggest that the Horn 2 RAW skid will be sufficient for NOvA. However, ejector pump performance will be reviewed to ensure similar issues do not exist with Horn 2. Project costs include both pumps and heat exchangers for both Horn 1 and 2 RAW systems. Both Horn 1 and 2 skids will be upgraded with modern instrumentation and controls.

8.6.5.3.3 Horn 1 and 2 RAW Piping

Horn 1 RAW system modifications that may require changes to the ejector piping are included in the Horn 1 estimate. Similarly, possible piping changes for the Horn 2 ejector pump are included in the Horn 2 estimate. Although it is not precisely known at this time which components need addressed, or to what extent, it is thought that the estimate is sufficiently conservative to address the performance issues suitably.

At this time, there are no plans to shift the location of Horn 1. Therefore, there are no associated piping costs.

During the shutdown for installing Horn 2 into the Medium Energy position, Horn 2 piping will need modifications. The piping for the RAW system will need to be extended from the Horn 2 low energy location to the Horn 2 medium energy location.

8.6.5.3.4 Decay Pipe RAW

At this time, the need for upgrading the pumps and heat exchangers for the Decay Pipe Systems is not clear. It appears that the current Decay Pipe RAW Systems are performing more than adequately. This may be due largely to the inability to model the system correctly. Originally, a worst-case scenario was used, one in which no heat loss to the surrounding rockbed was assumed. In reality, this transfer does occur, and apparently accounts for a significant level of cooling. At this time, Decay Pipe Upstream RAW Skid does not need to operate near capacity, and the chiller installed for the Decay Pipe Downstream RAW Skid is not even used. Therefore, sufficient capacity should be already available.

Decay Pipe RAW (Upstream Skid): An upgrade is planned for the Decay Pipe RAW skid that is located in the RAW room in order to handle the higher heat load for NOvA. The skid will be upgraded with modern instrumentation and controls.

Decay Pipe RAW (Downstream Skid): The skid will be upgraded with modern instrumentation and controls.

8.6.5.3.5 Hadron Absorber RAW and Intermediate

The absorber raw system will need upgrading to handle the higher heat load. In addition, there is an **Intermediate RAW System** inserted between the Absorber RAW system and the NuMI sump water cooling. This provides an extra measure of protection by isolating the absorber RAW water from the sump water. This system will also be upgraded with new pumps and heat exchangers for both, plus planned upgrades in instrumentation.

8.6.5.4 NuMI Cooling Water (Non-RAW)

There are three primary water-cooling systems used for NuMI. These cooling systems serve power supplies in the Main Injector and Primary Beamline areas, the RAW water systems in the target hall, the target hall air-cooling system, and decay pipe and absorber RAW systems.

Of the three water-cooling systems, only the heat exchanger on the MI-65 Secondary Chilled Water (SCHW) system needs upgrading before running NuMI at 700 kW. This was addressed during the Summer 2007 Shutdown, at which time an entirely new Target Pile air-handling system was installed.

8.6.5.4.1 MI-62 Low Conductivity Water (LCW) System

Currently this system serves heat loads in the Main Injector, extraction enclosure, pre-target area, power supplies in the below grade power supply room and in MI65, and the target area RAW skid. Refer to Table 8.19 for a summary of these heat loads. Some heat loads do increase, but these are offset by the removal of the Target Pile heat loads, which will be supplied by a separate chiller. Net heat loads will be slightly less than current demands. Therefore, modifications to this system for the NOνA 700 kW upgrade are considered to be minimal, consisting of additional instrumentation.

Systems Served by MI-62 LCW (Pond-H)	**Estimated Heat Loads (kW) NuMI (400 kW beam power)**	**Estimated Heat Loads (kW) NOνA (700 kW beam power)**
MI-62 LCW Pump	51	51
MI-62 Power Supplies	13	13
MI-NuMI Extraction Stub	453	471
Pre-Target Enclosure	189	196
MI-65 Target Service Bldg	33	40
Horn Power Supplies	12	18
Target Pile Chiller Coil	180	0
Target RAW	20	20
Total	**951**	**809**

Table 8.19: Systems served by the MI-62 LCW system. The capacity of the LCW system is 1.2 MW.

The existing Main Injector cooling pond that provides heat rejection for the LCW system is Pond H. It is approximately 1.1 acres and was initially designed to serve a 550 kW heat load through pump vault PV9. PV9 was modified during the NuMI construction project and has flow characteristics of 820 gpm with 90 ºF Cooling Pond Water Supply (CPWS) and 100 ºF Cooling Pond Water Return (CPWR). PV9 flow is routed to buildings MI62, MI65 and MI8. There currently are no connected loads in MI65 or MI8.

It is noted that the extra load will increase the temperature of Pond-H by about 1 degree. Pond-H is already somewhat problematic during summer months and can reach temperatures above the desired 95 degrees of the LCW system. Further analysis of Pond-H heating is continuing and more results can be found in [37, 12]. As a summary, cooling pond thermodynamics were modeled by a method that first benchmarked them to the actual performance we operate at and witness, and then modeled with a global heat load increase of 25%.

8.6.5.4.2 NuMI Sump Water Cooling System

In the MINOS Hall (underground cavern), heat is rejected to the sump water collected from tunnel inflow. The current inflow, measured in Oct 2006, is 165 gpm which is less than the initial flow of 235 gpm at occupancy in March 2004. Electronics equipment in the MINOS detector hall rejects heat to the 165-gpm sump water system through an LCW system and to air through fan coil units located in the hall. A portion of this flow, approximately 75 gpm, is then pumped to the Absorber area where the sump water is routed through an intermediate RAW skid for the hadron absorber and the decay pipe chiller in series. Refer to Table 8.20 for a summary of these heat loads. The intermediate Absorber RAW system was designed with a capacity of 210 kW and will not need to be upgraded. However, costs for pump and piping upgrades are included as a precautionary measure. Upgrades to the Absorber and Decay Pipe heat exchangers, which transfer heat to the Sump Water system, are covered in their respective sections.

This water is available for use by the NuMI facility after the NOνA upgrades and (if necessary) additional cooling for the MINERνA detector, the MINOS near detector, or the NOνA near detector will be supplied by an additional cooling system that is not included in the scope of the NuMI upgrades.

Systems Served by MI-62 LCW (Pond-H)	**Estimated Heat Loads NuMI (kW) (400 kW beam power)**	**Estimated Heat Loads NOνA/ANU (kW) (700kW beam power)**
Decay Pipe RAW	82	116
Intermediate Absorber RAW	60	105
Total	**145**	**220**

Table 8.20: Heat Loads for systems served by NuMI tunnel sump water.

8.6.5.4.3 MI-65 Secondary Chilled Water (SCHW) System

The current configuration of the secondary chilled water (SCHW) system consists of primary and standby 7-1/2HP pumps, a heat exchanger (HX) located on the mechanical mezzanine of the MI65 service building, and 4” piping that traverses down the shaft and to the below grade service

rooms. Heat loads rejected to this system include the power supply room fan coil unit, the decay pipe cooling RAW skid, Horn 1 RAW skid, and Horn 2 RAW skid. Refer to Table 8.21 for a summary of these heat loads.

Currently, the Target Pile Chiller and Fan Coil Unit are being upgraded off project to be supplied with their own chiller at MI-65, so these loads will be removed. Therefore, included are costs for instrumentation upgrades only.

Heat from the heat exchanger is rejected to the Industrial Chilled Water, ICW, supplied from the Central Utility Building (CUB). The current SCHW pump has a flow and head capacity of 212 gpm at 60 fthd. The heat exchanger was designed with the following parameters: CUB chilled water ewt 45 ºF/lwt 55 ºF at 215 gpm; SCHW ewt 60 ºF/lwt 50 ºF at 212 gpm with a 310 kw capacity. At this time, no additional capacity requirements are expected for the CUB ICW. However, upgrades to the instrumentation are planned, and costs are listed as such.

Systems Served by MI-65 SCHW	**System Design Capacity (kW)**	**NOνA/ANU (700 kW) Heat Load (Estimated kW)**	**Comments**
Horn 1 RAW	72	90	
Horn 2 RAW	72	55	Horn 2 heat load may be higher in the ME location.
Decay Pipe RAW (Upper)	80	138	Scaled from MARS simulations of NuMI Design (400kW)
Fan Coil Unit	60	0	Cools the NuMI power supply and RAW rooms
Target Pile Chiller Heat Exchanger	28	0	No Change for NOνA Upgrade
New Target Pile Air Handling Unit	N/A	0	New for NOνA Upgrade
Total	**312**	**238**	

Table 8.21: Systems served by the MI-65 Secondary Chilled Water. The total estimated heat load of 440 kW is greater than the current capacity of 310 kW.

This system will be modified to provide additional cooling as required by NOνA. The above described pumps and heat exchanger will be replaced or modified to meet the new heat load requirements. Piping will be routed to the target hall through the utility passageway above the labyrinth.

8.6.5.5 NuMI Electrical Infrastructure

Increases in the capacities of the RAW water systems may require increases in the capacity of the electrical utilities serving the NuMI Target Hall. The scope of this task is limited to addressing electrical service modifications needed to handle the upgraded water systems. It is anticipated that the service supplied to the locations is substantive enough for skid upgrades, and that electrical modifications will be mainly for circuit breakers, contacts, and minor associated wiring, for only the skids that receive significant upgrades.

It is currently assumed that all systems receiving pump and other extensive upgrades will require electrical service upgrades. However, this may not be the case, as present system equipment may be sufficient. For example, a system with a 3 Hp pump, being upgraded to a 5 Hp pump, may already have breakers and contacts sufficient for the new load. All upgraded systems will be looked at, to verify the appropriateness of currently installed hardware, and, if required, determination of proper upgrades.

8.6.6 NuMI Radiological Safety Issues

8.6.6.1 Overview

Safety issues are an important consideration for NovA. Fermilab is committed to maintaining a safe work place, minimizing worker exposure to radioactive material, and protecting the environment. Radiological concerns are of particular concern for the NuMI beamline given the intensity of protons directed on the target. The NovA upgrades will be installed during shutdowns occurring after the NuMI beamline has been operational for several years. At this time residual radiation does rates in the target hall will be significant and advance preparations are necessary to perform the installation work safely and with exposure to radiation as low as reasonable possible.

The NuMI/MINOS Shielding Assessment [38] has recently been updated to 500 kW operation. It will need to be updated again for NovA operation at 700 kW. In order to run at 700 kW, the shielding assessment needs to address ~850 kW operation for a safety margin of ~20% over the 700 kW operation. Potential environmental impacts include radioactive air emissions, groundwater protection, prompt radiation doses, and tritium production. These issues are discussed in some detail in the following sections. More details on the radiological releases for the NuMI facility can be found in FERMILAB-TM-2375.

8.6.6.2 Earth shielding assessment:

The NUMI extraction line would require 23.8 ft. of earth shielding for NOvA operation at 850 kW beam power (based on a safety margin of ~20% over the 700kW operational level) if the berm is categorized as minimal occupancy. The nominal shielding for the NUMI extraction line is 24.5 feet and because of the 3 degrees down slope of the carrier pipe, there is sufficient earth shielding for the rest of this beam line [14,39].

8.6.6.3 Groundwater and surface water:

Activation levels of ground water from beam line operations would remain below applicable regulatory limits [40]. The result in Table 8.22 indicates the concentrations of radionuclides immediately outside the NuMI tunnel. These concentrations will be significantly reduced due to the further mixing with the NuMI tunnel inflow water [41, 42, 43, 44, 45].

Type of Operations	Estimated Maximum Tritium Level	Estimated Maximum ^{22}Na Level
NuMI/NOvA at 850 kW	4 pCi/ml	0.4 pCi/ml
Groundwater Regulatory Limits	20 pCi/ml	0.4 pCi/ml

Table 8.22: Estimated radionuclide concentrations in the water immediately inside the NuMI tunnel that would be expected during the running of the NuMI facility under NOvA operating conditions at 850 kW of beam power.

The design of the NuMI tunnel ensures that groundwater in its vicinity continuously flows into the tunnel, where it is collected and continuously pumped through the industrial chilled water system eventually ends up in the surface cooling ponds. The cooling ponds are underlain with naturally occurring clay, therefore preventing direct contact of radionuclides such as tritium or ^{22}Na produced during the MINOS and NOνA experiments with surface water [46].

The estimates for the pond water concentration would be conservative because they assume drought conditions. In drought conditions the volume of water in the Fermilab pond system would be reduced resulting in a higher concentration of radionuclides. Estimates of the tritium and ^{22}Na concentration that would result from running NuMI under the NOνA operating conditions are summarized in Table 8.23. All of these concentrations are predicted to be well below the regulatory limit for surface water.

Phase	Tritium Levels (NuMI Sump Water)	Tritium Levels (Pond Water)	^{22}Na Levels (NuMI Sump Water)	^{22}Na Levels (Pond Water)
NuMI/NOνA	57 - 114 pCi/ml	14 - 28 pCi/ml	< 0.7 pCi/ml	< 0.2 pCi/ml
DOE Surface Water Regulatory Limits	2,000 pCi/ml	2,000 pCi/ml	10 pCi/ml	10 pCi/ml

Table 8.23: Estimated concentrations of tritium and ^{22}Na in the NuMI sump and Fermilab ponds during NuMI operations for the MINOS experiment and for the NOνA experiment at 850 kW of beam power.

8.6.6.4 Air emissions:

Tritium and other short lived radionuclides are also produced as a normal by-product of NuMI operations. The airborne radionuclides produced in the NuMI facility are released into the atmosphere through vent stacks to the surface of the Fermilab site. Environmental emissions are limited by minimizing the ventilation of the tunnels during beam operations. Ventilation is maximized for personnel access, however, by allowing sufficient time for decay after beam shutdown, and before accessing thus air emissions are still limited. Air from the ventilation stacks is monitored for radionuclide emissions.

The total activity released from NuMI stacks in 2006, the extrapolated quantities to NOνA beam powers, and the estimated maximum dose rate at the site boundary from these releases is summarized in Table 8.24. This dose rate at the site boundary is assessed for a hypothetical member of the public who would spend the entire year at the location of maximum exposure at the Fermilab site boundary. Total releases are reported annually to the IEPA and the U.S. Environmental Protection Agency (EPA) in accordance with conditions of the relevant NESHAP permit [47].

The operations of the NuMI facility for the MINOS experiment have not caused Fermilab to approach the regulatory limits for total activity releases or for the dose limit at the site boundary [48, 49].

	2006 measurements Ci/yr	Scaled to NOvA beam power Ci/yr
EAV1	22.0	77.0
EAV2	8.7	30.5
EAV3	2.9	10.2
SR3	2.7	9.5
Total(Ci)	36	127
DE (μrem)	28	97

Table 8.24: Estimated maximum release of radionuclide air emissions and estimated maximum dose at the Fermilab site boundary during operations of NOνA at 850 kW of beam power.

With no further mitigation, total emissions at the site boundary produce 0.097 mrem/yr, which is less than the EPA limit. EAV1 is the largest contributor to the total NuMI emissions. The EAV1 source can be reduced significantly with out any significant affects on the experiment by reducing the flow rate or using a different exhaust location to allow longer decay times for the radioisotopes.

8.1.1.1.1.1 Primary radio-active water (RAW) systems:

Primary cooling water for the target, horns, decay pipe and the absorber become radioactive. ^{3}H and ^{7}Be are the relevant radioisotopes. Usually in a few hours all the other radioisotopes have decayed away. Most of the ^{7}Be is trapped in the de-ionization bottles. Table 8.25 shows the estimated annual amount of radioactive isotopes ^{7}Be and ^{3}H produced in the cooling water [50]. RAW tanks are sampled frequently [51]. RAW systems concentration levels, the neutrino program schedule, operational impact to other parts of the accelerator complex, and ALARA principles are all considered in determining the appropriate schedule for water replacement.

At 850 kW	^{3}H (Ci)	^{7}Be (Ci)	Volume (Gallons)
Target	0.1	1.0	30
Horn1	4.5	22.5	115
Horn2	1.1	6.7	100
Decay Pipe	0.0	0.1	725
Hadron Absorber	0.0	0.1	135
Total	5.7	30.4	1105.0

Table 8.25: Estimated maximum production of long lived radionuclide in the radioactive water systems during operations NOνA at 850 kW of beam power.

8.6.6.5 Residual radioactivity and the work cell upgrade:

The original NuMI Target Hall Work Cell (Fig 8.59 and Fig 8.60) and associated Waste Stream Plan were developed with 2 key concepts in mind. The first was that components

(Target/Baffle, Horn 1 & Horn 2 [52]) would not be repaired in the Work Cell, but only replaced. The second was that failed, radioactive components would be long term stored in a shielded pit, called "the Morgue" (Fig 8.61 and Fig 8.62) with no plans for radioactive component removal up-shaft for disposal. Practical lessons learned from 2 years of operational experience of NuMI and the proposed upgrades for NOνA have altered those fundamental concepts and require re-designing the Work Cell and Waste Stream Plan. These changes need to be implemented for NuMI operation, regardless of NOνA, thus they are off project operational upgrades. Residual dose rates have been predicted for the various stages of the NOνA Project [53]. They are shown in Table 8.26. The last row of Table 8.26 shows the predicted residual activity of NuMI beam devices after three years 850 kW beam operations.

Time	Protons on Target	Power (kW)	Scale Factor	Target (**R/hr**)	Target module/carrier (mrem/hr)	Horn 1 (**R/hr**)	Above Horn 1 Module, by "ears" (mrem/hr)	Horn 1 T-Blocks Top (mrem/hr)	Horn 2 (**R/hr**)
MARS predicted	1.40E+20	400				160	4	4	
Spring 2006 shutdown	1.40E+20	250	1	1.20	50 to 150	80	200	75	5 to 8
At time of first NOνA shutdown	9.00E+20	250-400	1.2 to 2	2.40	100 to 300	120	300	110	8 to 12
At time of second NOνA shutdown	1.20E+21	400	1.7	2.64	170	136	340	127.5	11.05
Running NOνA for three years	6E20/yr	850	4.9	**6**	486	**389**	971	364	**32**

Table 8.26: Summary of the predicted residual dose rates, after one day of cool down, of the beam devices after three years of NOνA beam operations at 850 kW.

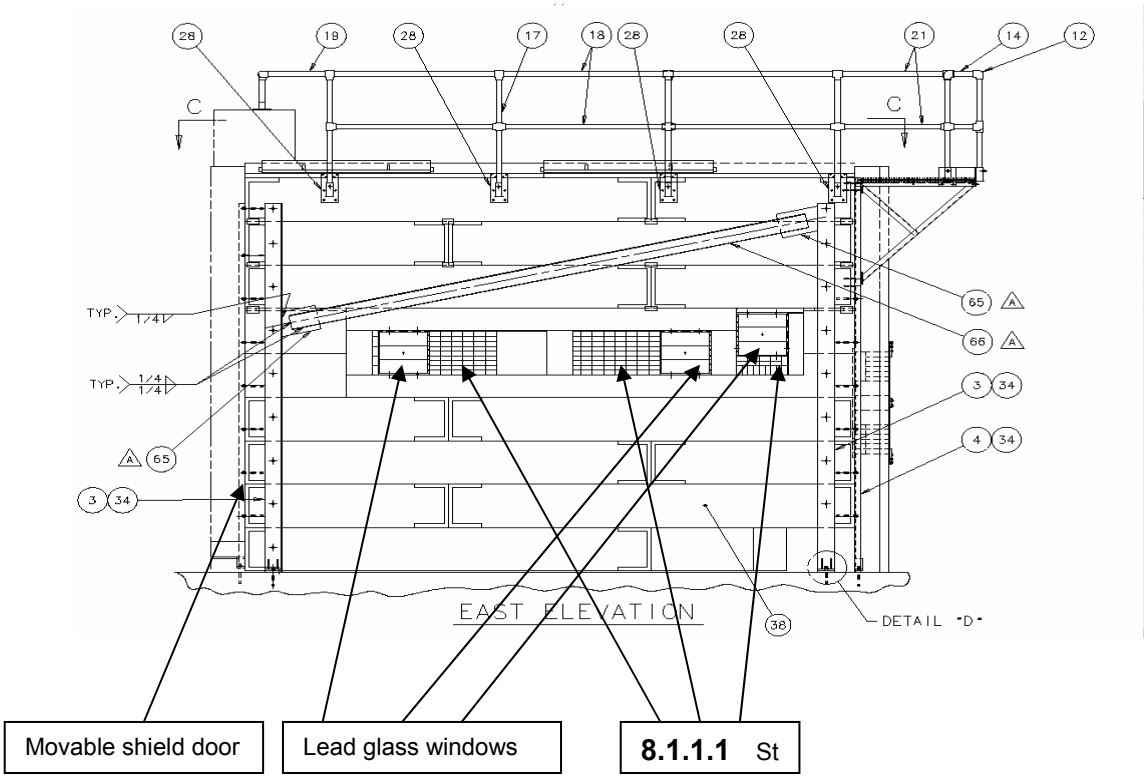

Fig 8.59: East Elevation view of existing Work Cell.

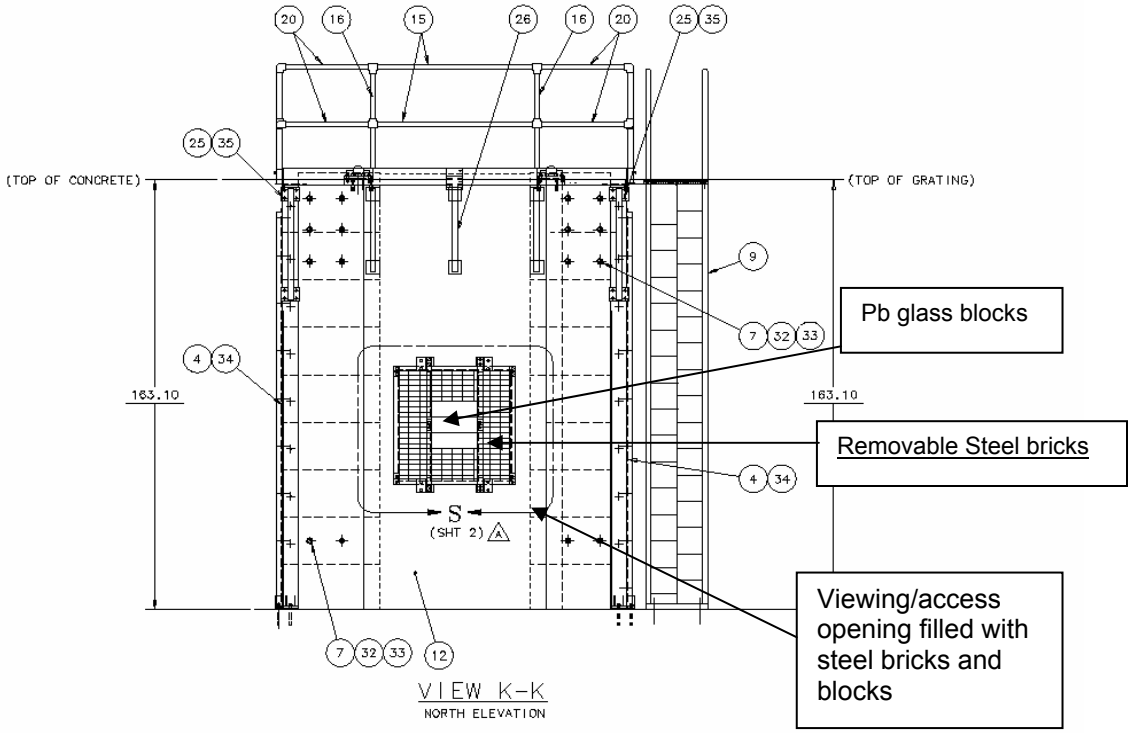

Fig 8.60: North Elevation view of existing Work Cell

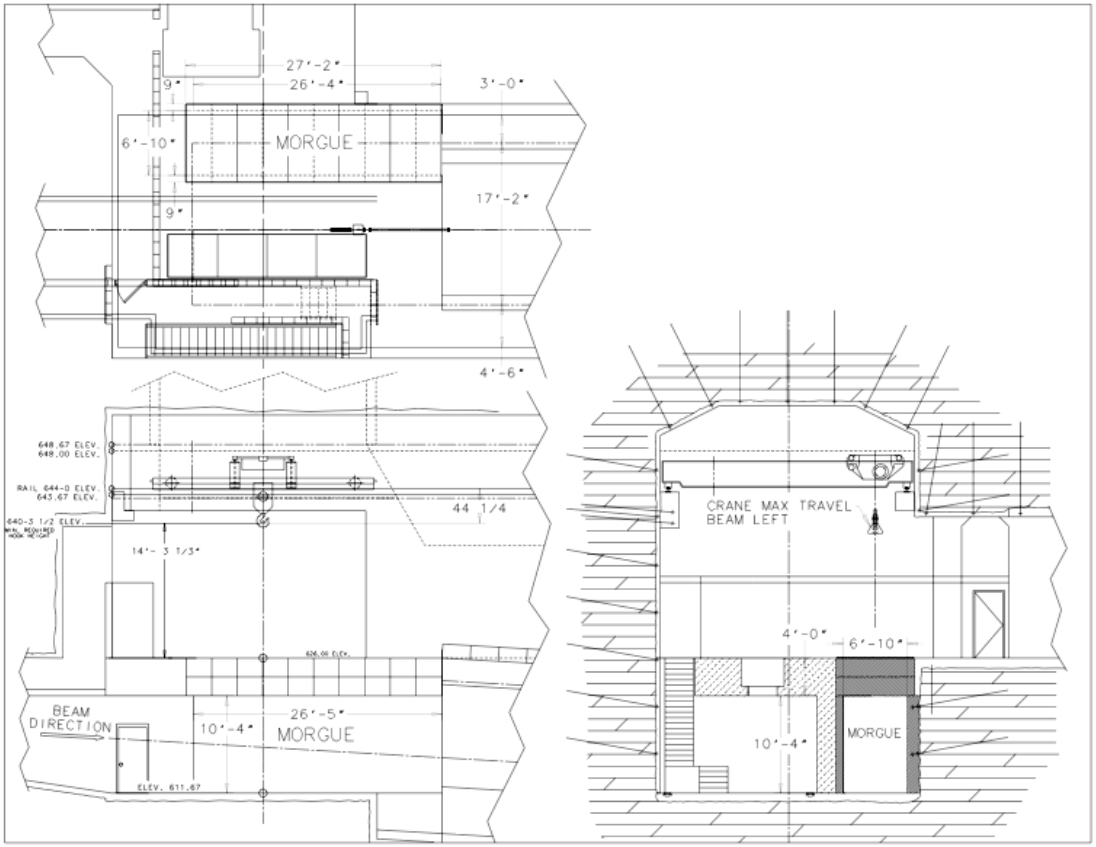

Fig 8.61: Plan and elevation views of existing Morgue area.

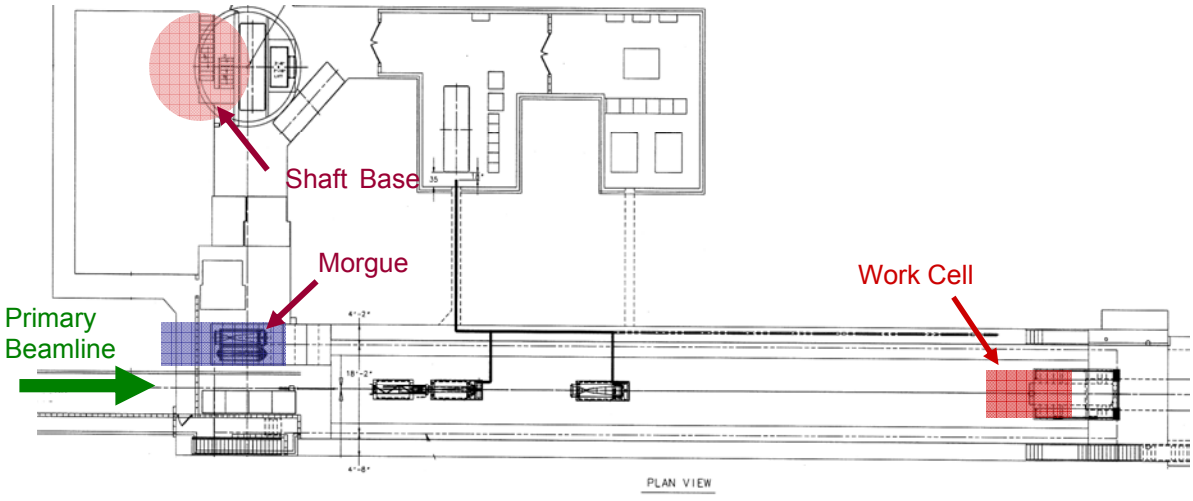

Fig 8.62: Plan view of Target Hall showing relative locations of Morgue, Work Cell, and MI-65 shaft base.

The design concept for the Work Cell upgrade is to design and fabricate a (possibly reconfigurable) set of shielding walls that can be assembled to form a shielding extension to the current Work Cell. The Work Cell upgrade will include at least one set of tele-manipulators and a

lead glass window unit to allow remote repair activities without excessive dose to workers. If space constraints do not allow the shielding extension to remain in an erected configuration, then the shielding extension and tele-manipulator station will need to be designed for easy erection and disassembly to keep access times for repairs short. It may also need to be designed to allow storage in the limited space of the Target Hall when not in use. Thus it is envisioned that a modular design will be pursued such that the shielding extension can be custom configured to place the manipulators at the proper location for the repair work at hand while providing adequate shielding for workers.

With operations at the NuMI Target Hall for NOνA now projected to extend beyond 2012, capacity of the Morgue is inadequate for storage of radioactive components. It is conceivable that NOνA components could require storage at a rate of 2 components per year, on average. In addition, component modules, previously not considered replaceable, may need to be replaced during the NOνA era. The Radioactive Component Removal Plan must be developed to include short-term storage of components and possibly modules in the Morgue, removal of those components up-shaft, and subsequent long-term storage.

8.6.6.6 Prompt radiation:

There are several labyrinths and penetrations in the NuMI tunnels and halls for personnel access, connection to equipment, air inlets and exhausts, survey risers and an air-cooling labyrinth [38]. Prompt radiation from the penetrations and labyrinths are estimated by calculations and extrapolation from measurements during the operation of NuMI [54,55]. The results of the radiation attenuation calculations for these labyrinths and penetrations are given in the Table 8.27 and the discussed below. Dose rates due to losses under normal and accident conditions are given. An accident is defined as five sequential full intensity proton pulses. Normal losses depend on the location. Near the target and baffles it is full beam loss during an hour and 0.01% of the full beam at other locations.

Region	Normal Loss		Accidental Loss	
	Exit Dose Rate (mrem/hr)	Comment	Exit Dose Rate (mrem/hr)	Comment
Survey Riser SR-1	7.3	existing plug is ok	192	Existing plug is enough
Air Vent EAV-1	0.001	OK (loss rate 1E-4)	0.001	OK
Survey Riser SR-2	0.45	existing plug is ok	11.8	Existing plug is enough
Target Hall labyrinth	0.009	OK	0.2	OK
Target Hall Equipment Door	1.6	Post as Controlled Area Min. Occup.		
Stripline Penetration	290	Existing shielding ok	Current shielding is sufficient	
RAW Penetration	0.13	Pipes will fill voids		
Survey Riser SR-3	0.007	OK		
Vent EAV-2	0.002	OK		
Vent EAV-3	0.001	OK		
Absorber Labyrinth	1.1	Post as Controlled Area Min. Occup.		
Bypass tunnel (muons)	1.7	Post as Controlled Area Min. Occup.		
Muon Alcove 2	0.4	Door posted and interlocked		
Muon Alcove 3	0.024	Door posted and interlocked		
Muon Alcove 4	0.001	Door posted and interlocked		

Table 8.27: Dose rates at the exit and mitigation where needed for the NuMI labyrinths and penetrations during 850 kW operations.

As the table shows the horn strip line penetration was a concern. The section of the penetration between the horn and the top of the module is not considered here, since the target hall is not accessible during the beam operation. Only the section of penetration between the target hall and the power supply room is needed to calculate the dose to personnel in the power supply room. The source term is calculated at the entrance to this penetration using MARS [56]. The neutron spectrum at the entrance to this penetration is mainly composed of neutrons of energy less than 1 MeV. Polyethylene, which is an effective absorber of these neutrons, was effectively used to shield this penetration. The dose rates in the power supply room are less than 0.25 mrem/hr.

Because of the muons and the radiation leaking out of the Hadron Absorber labyrinth and Muon Alcove 2, the bypass tunnel starting at Muon Alcove 4 will most likely need to be posted as radiation area for the 850 kW beam operations.

8.6.6.7 Summary

The NuMI/MINOS Shielding Assessment will need to be updated to address NOνA operation. No upgrades, other than posting changes, are anticipated to be necessary. Planned off project operational upgrades to radioactive component removal, repair and storage will facilitate component replacement for NOνA operations.

8.6.7 Changes in the NuMI Upgrades Design since the CDR

A number of changes have been made to the scope of the NuMI upgrades since the writing of the CDR for the NuMI Upgrades [36].

There is no longer a need to build six new quadrupole magnets for the primary beamline. Enough magnets exist in the A1 beamline that can be removed and transferred to the primary beamline. The A1 beamline is used to transfer antiprotons from the Main Injector to the Tevatron and will not be needed upon the completion of Collider Operations.

Further analysis of the ME target has been performed by IHEP. The study reached the conclusion that the instantaneous pressure rise in the water cooling channels will not pose a problem. Therefore a bubbler system to protect the target water cooling lines from thermal shock is not necessary and has been removed from the scope of the project.

Only minor modifications to the Horn 1 are needed in order to handle the increase in the beam power from 400 kW to 700 kW. Essential the only change needed is to reduce the thickness of the outer conductor. Since the horns are consumable with a lifetime of ~1-2 years, the necessary modifications to the horns can be made during the normal spares/replacement production cycle. This task is thus off project.

A complete redesign and construction of a new Horn 1 module is not necessary. The present Horn 1 module is capable of handling the higher energy deposition. Modifications to the stripline block will still be needed, but these can be done independently of the Horn 1 module. Thus the horn 1 module is not longer on project.

Upgrades to the target chase chiller are expected as part of the continuing operational improvements of the NuMI beamline. The upgrades are presently in the design stage and expected to be complete by the fall of 2007. The upgrades are consistent with the ANU project but will not completely cover the cost of future upgrades needed to operate at the higher power. The completion of this work will allow a reduction in the cost and scope of the target chase cooling upgrade, but the magnitude will not be determined until the operational improvements are completed.

8.6.8 Remaining Design Work for the NuMI Upgrades

Further analysis and design of the IHEP medium energy target is required to add water cooling to the outer casing and to understand the cooling of the windows at the entrance and exit of the target.

Modifications to the target carrier are necessary to handle the larger diameter of the ME target that will be used for the NOvA experiment. The design and engineering work for these modifications are needed before proceeding with the construction

The University of Texas – Austin designed and built the first hadron monitor that is now in use for the NuMI beamline. With the increased beam power the hadron monitor may need modifications. The necessity or extent of the modifications has not been determined yet, but the project does include a task to review the existing design.

It is important that a detailed study of the available space in the Target Hall be conducted that aims to develop a comprehensive new layout plan for the various target hall activities. As a result, new equipment (mostly in the form of structural supports) will be designed to help with the transport and staging of shielding blocks during shutdown activities, in a way that optimizes use of the target hall space.

As discussed in earlier sections, the Duratek shielding blocks at the inner chase wall are predicted to reach very high temperatures (113ºC) due to the increased beam power, especially

downstream of Horn 1. Thermal radiation between the hot wall surfaces and sensitive chase components (such as horns, target, and stripline) is of concern. The comprehensive 3-D finite element analysis (FEA) model will be used to compute the amount of heat transfer (primarily radiation heat transfer) from the shielding blocks to the chase components. This additional heat input will be included in the thermal analyses for these components to determine whether radiation heat shields will be needed.

A more comprehensive thermal and structural FEA of the horn 1 stripline is needed to more accurately predict temperatures and stresses under the 700kW condition. In summary, by making relatively minor changes to Horn 1's water cooling components, preliminary studies indicate that the Horn 1 stripline and stripline block will survive the 700 kW beam power scenario [34]. More detailed and sophisticated FEA plus air velocity measurements need to be performed to confirm this preliminary conclusion

A final determination of the heat loads in each of the RAW systems is needed before proceeding with the detailed design of the RAW system modifications.

8.7 Beam Physics

8.7.1 Overview

The Accelerator and NuMI Upgrades (ANU) activity achieves an 80% increase in proton throughput over the Proton Plan[2] [57] by moving the slipping portion of the injection and slip-stacking processes from the Main Injector to the Recycler, otherwise maintaining the production process of the Proton Plan. For the Booster, the additional issue will be the need to increase throughput by 80% through an increased rate of pulses (the rate planned to be achieved by the Proton Plan). The Main Injector will have the slipping process offloaded to the Recycler, but will have to cycle faster and more often. The Recycler was not built to store high-intensity proton beams, but the similarity of its lattice and aperture with the Main Injector make it capable of doing so; the beam dynamics within the Recycler will be similar to those in the Main Injector.

This overview summarizes the beam physics issues associated with implementing the ANU design and achieving the planned beam power. The following sections detail the beam physics efforts as part of the NOvA ANU subproject. The Beam Physics efforts are organized into three sections:

- **ANU Demands on the Proton Plan** analyzes the dependencies of the ANU design on the Proton Plan design. Implementing ANU relies on the sustained operation of existing machines, as well as improvements that are to be achieved through the Proton Plan.
- **Machine and Process Analysis** is a collection of theoretical, experimental, and simulation studies on existing machines and the planned ANU processes. The results will be documented and used as reference for commissioning and operation with the ANU schemes.
- **Proton Projections** produces a method for realistic predictions of future ANU performance. This primarily includes designing a set of reasonably measurable performance metrics for the accelerator and NuMI complex. These metrics will be measured during the ANU project and used to produce updated projections.

[2] The Proton Plan Design Handbook is found on its webpage: http://www-accel-proj.fnal.gov/internal/Proton_Plan/index.shtml. A public site viewable outside Fermilab is: http://www-accel-proj.fnal.gov/Proton_Plan/index.shtml.

8.7.1.1 The ANU Beam Cycle

The ANU Recycler cycle involves stacking 12 batches of 8 GeV booster beam in the Recycler, accelerating the beam in the Main Injector, and extracting the beam to NuMI. An approximate timeline is shown in Fig 8.63 and is described in this section.

The Linac and Booster will accelerate beam on 12 successive cycles spaced at 15 Hz (67 ms). Such operation is presently typical for the Proton Source. The Linac beam will provide its typical beam: debunched 200 MHz bunches at 400 MeV and intensity of ~ 10^9 H^- ions per bunch, with ~ 20 μs pulse length.

The Booster will accumulate the Linac beam and accelerate it to 8 GeV. The extracted beam will be bunched at 53 MHz and have an intensity of 4-5×10^{12} protons per batch (~81 bunches). On every Booster cycle, the Booster must rebunch the beam from the Linac and accelerate it through transition; beam loss is experienced early in the cycle after debunching and at transition. The extracted beam will use the MI-8 collimators (installed as part of the Proton Plan) to reduce the tails of the transverse and momentum distributions.

Each Booster batch will be injected to a particular location on the Recycler azimuth with respect to the beam already circulating[3]; the batches are injected every 1/15 s. The first six batches are injected such that they lie adjacent to each other, within the limitations set by the injection kicker[4]. The Recycler 53 MHz RF will be active to keep the beam bunched, using about 100 kV; whether one or two frequencies will have voltage will depend on the optimized details of slip-stacking. After the sixth injection, the six revolving batches must be accelerated or decelerated to a different orbit. The Recycler, being seven times the circumference of the Booster, would then have one additional slot for further injections[5]. Beam is then injected six more times into that gap; the momentum difference induces slipping which moves the newly injected beam out of the gap in the time between injections. Two RF frequencies will be used to keep each of the beams bunched. After the final batch is injected the beams slip again for 1/15 s, reestablishing the gap for extraction. A kicker system pulses before each injection and extraction to clear beam from the needed gap, sending it to the abort instead; this system is necessary to prevent injection losses from exceeding acceptable levels.

The Recycler beam is extracted in a single-turn into stationary 53 MHz RF buckets in the Main Injector, for a total intensity of ~5×10^{13} protons. For twelve batches being merged into six, the Main Injector will have charge in about 500 of its 588 buckets. The buckets are sized to each contain two slip-stacked bunches[6] using about 1 MV/turn among the 20 cavities. The beam is accelerated and collimated as in the Proton Plan, except that the ramp rate of the magnets will be increased to 240 GeV/s (from 205), and an additional two RF cavities will increase the ring voltage by 11%. Extraction will occur in a single turn, sending the entire beam to the NuMI beamline; this extraction is presently in place for NuMI operation.

The NuMI primary line optics will remain the same as the original design, except that the final focus may be changed to enlarge the beam size on target for survivability[7]. However, the

[3] The first batch is not sent to a particular location as there is no beam already circulating in the Recycler.

[4] We expect that there will be three vacant buckets between 81-bunch batches.

[5] This assumes that the injection kicker has sufficiently short rise and fall times to fit in the seventh batch, as designed. If the kicker is not fast enough, a double-length slot must be made by injecting only five batches before slipping, reducing the total beam power to NuMI by 8%.

[6] The two bunches are initially separated by momentum, but not azimuth.

[7] The present spot size is typically 0.8-1.2 mm RMS in both transverse directions. The larger beam sizes are correlated with higher intensities. The design of the primary beamline allows the spot size to be tuned by a simple adjustment of the last few quadrupole magnets.

line will need to operate at an increased rate from its design, forcing some changes in magnets and power supplies. Target hall components will have to deal with greater average power deposition, though the intensity per pulse will be the same as in the Proton Plan.

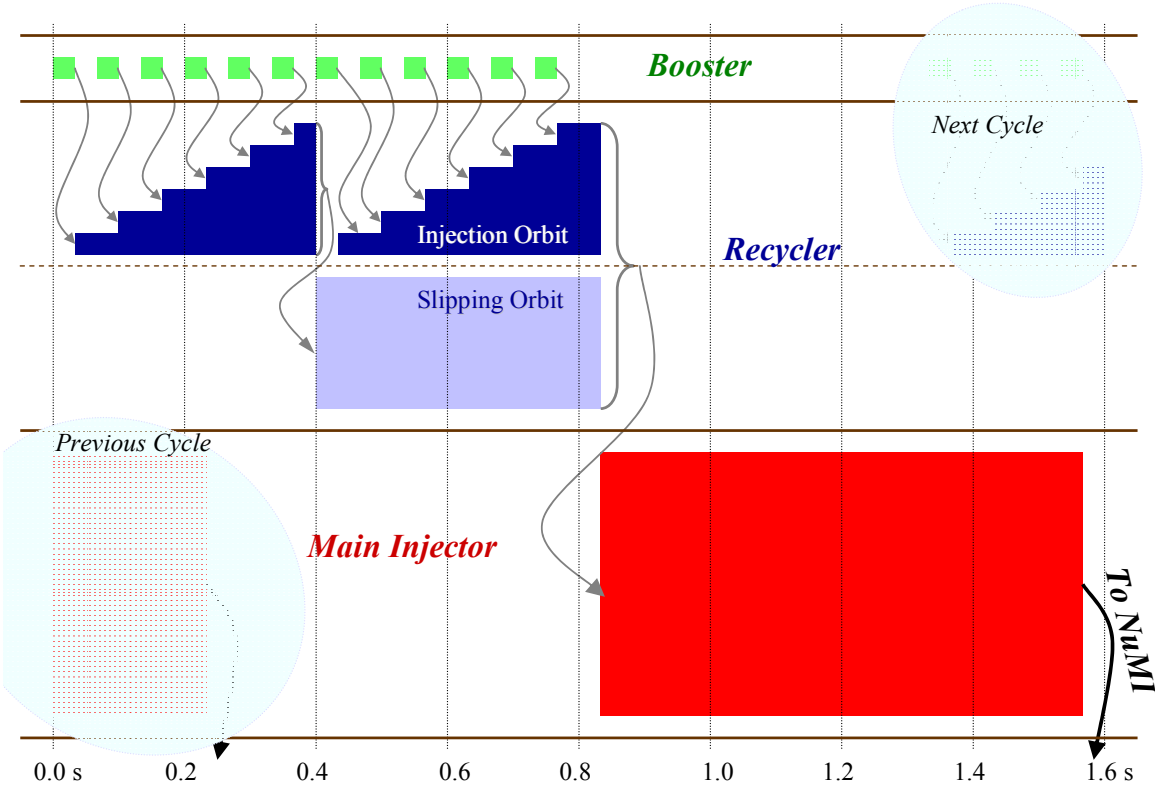

Fig 8.63: A diagram of the timeline for the slip-stacking process. The vertical height of each bar is proportional to the amount of beam. The zero is set arbitrarily at the time of first injection from the Booster; an operational timeline will likely start earlier.

8.7.1.2 Slip Stacking

Slip stacking is a set of RF manipulations which merges two sets of bunched beam into one, doubling the bunch intensity (or conversely halving the azimuth used for the two beams). The distinguishing component of slip stacking is the use of two RF systems with slightly different frequencies; the RF is used to keep two separate bunch trains bunched, while being at different energy from each other and thus having different revolution frequencies. The RF voltages are just high enough to keep the beams bunched, but low enough to allow the two beams to slip past each other. When the two are coincident in azimuth (separated in energy), a significantly more powerful RF system is turned on. The third system operates at the mean of the two initial frequencies and is powerful enough to keep beam contained in its large amplitude RF buckets, preventing further slippage. Compared to other stacking procedures, the advantage of slip stacking is that it occurs quickly, because it does not require debunching, rebunching, or other slow processes.

The procedure of slip stacking was first developed and demonstrated at CERN [60], but the gains were not sufficient to offset the increased losses in the CERN PS or SPS; so slip stacking was never used in regular operation at CERN. At Fermilab, slip stacking was proposed in the

Main Injector as part of the Run II luminosity upgrades[8] [58], where it would improve antiproton production rates by increasing the number of protons delivered to the antiproton target. A scheme was developed through which the Main Injector could support slip stacking for antiproton production, while also providing (unstacked) beam to NuMI. This mode of operation has been in place since 2004 [59] and typically provides batch intensities of 8×10^{12} protons, concurrent with an additional 22×10^{12} of unstacked beam for neutrino production.

Slip stacking, as operational in the Main Injector, combines two Booster batches into one for antiproton production. Typically, an additional five batches are injected after the initial two, but are not slipped – these do not directly affect the slipping process. To accommodate slipping, two RF systems change between four different RF frequencies: $\{f_0 - \Delta f, f_0 - \Delta f/2, f_0, f_0 + \Delta f/2\}$. f_0 = 52.8114 MHz is the Main Injector injection frequency; $\Delta f \approx$ 1400 Hz is the frequency separation between the beams at injection and capture.

As shown in Fig 8.64, the beam is injected into the first RF's buckets at f_0, and then decelerated to $f_0 - \Delta f$. 1/15 s after the first injection, the second batch is injected into the second RF at f_0. In a sequence that maintains a minimum frequency difference[9], the frequencies of the two beams are adjusted so that they finish at $f_0 \pm \Delta f/2$ and the time integral of Δf between the second injection and capture must equal the azimuthal separation of the batches at the second injection. In the sequence shown in Fig 8.64 the frequency difference is modulated, reaching a maximum near 2 kHz, leading to an integral of around 130 buckets. The batch length is only 84 buckets; the greater initial separation minimizes interference of the injection with beam leeched from the first batch due to the two RF frequencies. Some of the freedoms in choosing the above parameters are reduced when slipping more than two batches, as in the Proton Plan and ANU.

[8] The Run II project homepage is http://www-ad.fnal.gov/run2upgrade/. Slip stacking was an addition to the original Run II designs.

[9] A minimal criterion for stability is that $\alpha = \Delta f / f_s \geq 4$, where f_s is the synchrotron frequency of the beam under the influence of a single RF system. For a typical voltage of 100 kV/turn f_s =280 Hz, and scales with the square root of voltage. For details, see. Boussard and Mizumachi [60] or the F. E. Mills reference [61].

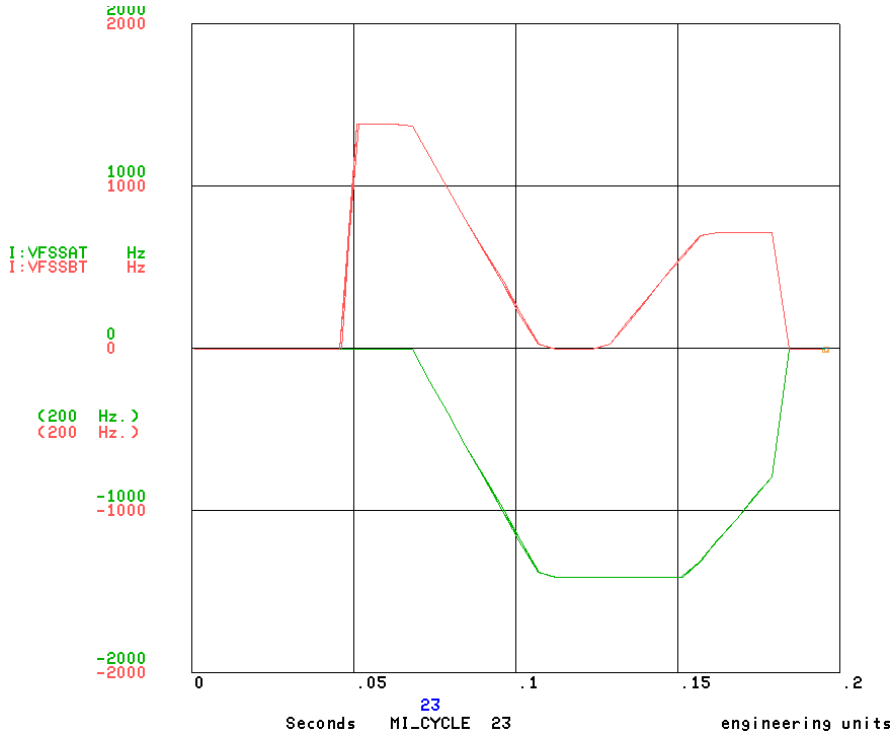

Fig 8.64: Operational frequency curves for two-batch slip stacking. Beam is injected on the central frequency (0 Hz) at ~ 0.06 and 0.12 s. The frequencies of the two beams are adjusted (also changing the energy) until they slip fully and bracket the central frequency, at which time they are captured (0.18 s).

The Proton Plan is extending slip stacking to NuMI by injecting 11 batches of beam into the Main Injector: two for antiproton production and nine for neutrino production. These batches will be injected in groups of 5 and 6, and then slipped together. The procedure is conceptually similar to two-batch stacking and is illustrated in Fig 8.65 and Fig 8.66. The obvious difference in the procedure is that more injections take place (5 on the first RF, 6 on the second) and the process takes longer. Additionally, the frequency difference is constrained to be the spacing between batches, which is nominally 84 buckets. So, $\Delta f = 84 \times 15 = 1260$ Hz and cannot be significantly modulated. This constraint limits the voltage that can be applied to the two RFs and will also apply for ANU.

To produce the two azimuthally separated bunch trains for antiproton and neutrino production (as shown in Fig 8.65), only 11 batches can be injected into the Main Injector, while it could in principle hold 12 and preserve a single abort gap. This is shown in sequence 6 of Fig 8.65, where the last batch is displaced an additional 42 buckets. Allowing for the slippage of the additional gap requires an additional $1/30^{th}$ second. Additionally, the fall time of the 8 GeV injection kicker is slow enough that several bunches of beam are kicked out of the machine. A similar loss will occur if 12-batch injection is attempted for NuMI. To control this loss ANU will have faster injection kickers.

The Proton Plan has achieved 11-batch slip stacking in the Main Injector with very good efficiency (96%) at moderate intensity (3.8×10^{13}), and moderate efficiency (92%) at high intensity (4.5×10^{13}). Advances and experience in the Proton Plan is expected to improve the efficiency and intensity. The losses will also be controlled by a collimator system in the Proton

Plan. After the above improvements, 11-batch operation will be the standard mode of operation (presently expected late 2007).

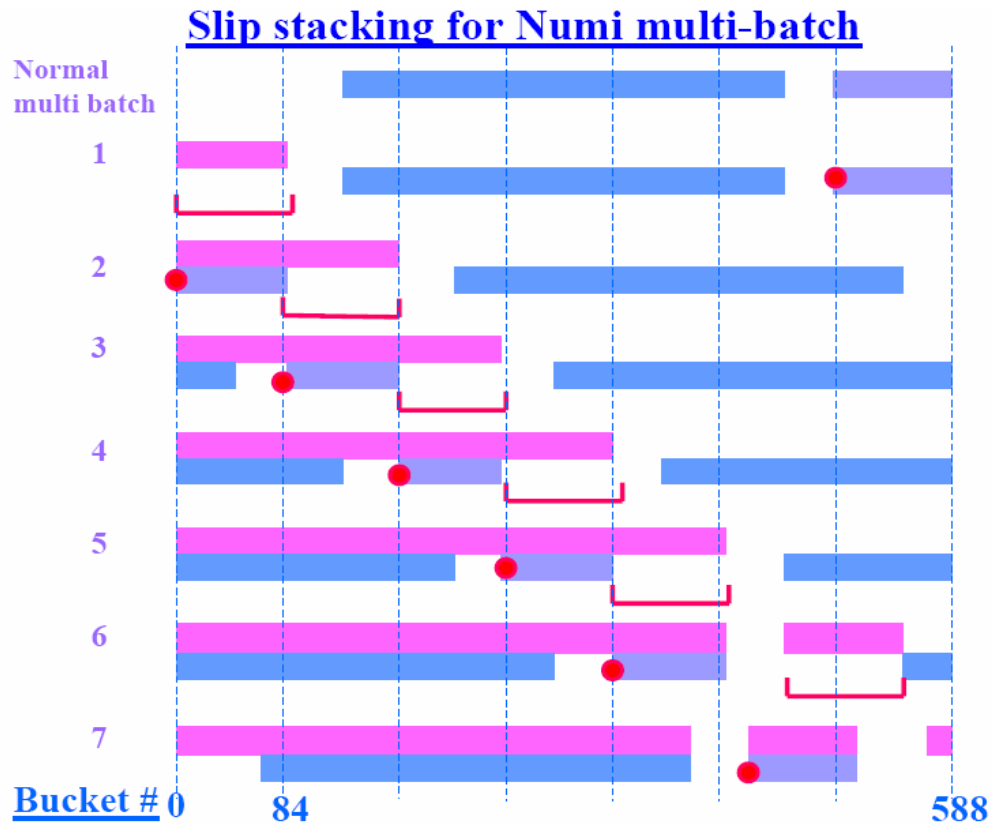

Fig 8.65: Illustration of batch positions at various times throughout the slipping process of the Proton Plan. The blue bars show the position of beam on a slipping orbit, i.e. slipping relative to injected beam. Sequences 1-6 indicate the last 6 injections, each injection indicated by a red bracket. Sequence 7 shows the position of the beams at the time of recapture.

There are several disadvantages or issues related to slip stacking in the Main Injector. The process always dilutes longitudinal emittance, even under ideal circumstances. The dilution occurs because the bunches must be separated in energy, but combined into a single bucket. The interior area is then filled by filamentation. The total longitudinal phase space is increased by at least 50% (over the sum of the initial two). Furthermore, longitudinal emittance is minimized by maintaining a lower RF capture voltage, but that leads to slippage of the uncaptured tails, which contribute to losses elsewhere. In typical operation, the longitudinal emittance of slipped beam is ~ 80% greater than the combined emittances of the original beams.

Another issue is that the RF manipulations make use of a large portion of the momentum aperture. The beam centroids are moved from $f_0 - \Delta f$ to $f_0 + \Delta f / 2$. Additionally, the momentum distribution of the beam contributes. The total used aperture is then[10]:

[10] Here, δp = 8 MeV/c is the momentum width of the incoming Booster beam; p = 8.89 GeV/c is the momentum of the Booster beam; and η = -0.0087 is the slip factor of the Recycler.

$3\Delta f/2 + 2f_0|\eta|\delta p/p$, which is 2700 Hz or 52 MeV/c. While this usage is large, the Main Injector and Recycler apertures are adequate.

Beam loading in the Main Injector RF cavities has long been recognized as a possible limitation to slip stacking performance [62]. The induced transient voltages on the main RF cavities could only be controlled through an aggressive system of beam loading compensation using both feedback and feedforward loops [63]. Even when compensation allows acceleration of beam to the production target, there are always increased losses with beam current. The dominant effect is that beam is not properly contained within the slipping buckets [64]. Those particles are then moved to higher amplitude along the separatrices. If the particles are not immediately lost they can then slip to an empty area of the ring and be lost at injection, extraction, or during acceleration. ANU will have to mitigate these losses through several methods described below.

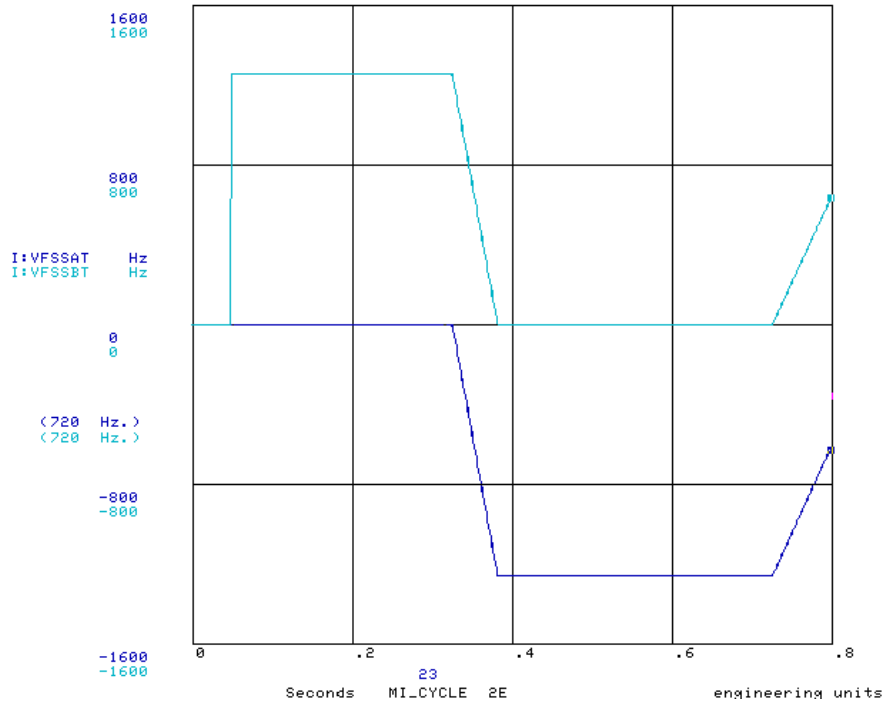

Fig 8.66: Study frequency curve for the 11-batch slip stacking of the Proton Plan. Beam is injected on the central frequency (0 Hz) 11 times between 0.06 and 0.66 s. The frequencies of the two beams are adjusted (also changing the energy) until they slip fully and bracket the central frequency, at which time they are captured (0.8 s).

The ANU implementation of slip stacking in the Recycler will be entirely derived from the Main Injector experience with Run II and the Proton Plan [64]. The Recycler's circumference and gross lattice characteristics will be identical to the Main Injector's[11]. The RF used to keep the beam bunched while slipping is a moderate voltage of ~ 100 kV. As the Recycler will not be called upon to accelerate beam, it can have significantly fewer RF cavities, each designed with smaller geometric factor[12]: R_s/Q. The reduction of shunt impedance and number of cavities will

[11] The Recycler presently has a modified lattice in the area where electron cooling takes place

[12] The geometric factor is the ratio of the cavity's shunt impedance to its quality factor. This ratio describes how much reactive power from the beam is stored in the cavity; power which can disrupt later bunches. The change in reactive power must be compensated by the RF system.

significantly improve the beam-loading situation. Additionally, a compensation system similar to the Main Injector's can be implemented.

The frequency scheme can also be optimized in the Recycler to reduce the number of acceleration/deceleration cycles and use less of the momentum aperture. A potential frequency schedule is shown in Fig 8.67. The first six batches are injected at a momentum corresponding to a frequency higher than the central by half the separation. The separation frequency is fixed, as in the Proton Plan, to 1260 Hz. Those batches are then decelerated to an orbit below the central frequency by half the separation[13]. The other six batches are injected on the second RF. The beam can be extracted as a whole to the Main Injector without any further acceleration or deceleration.

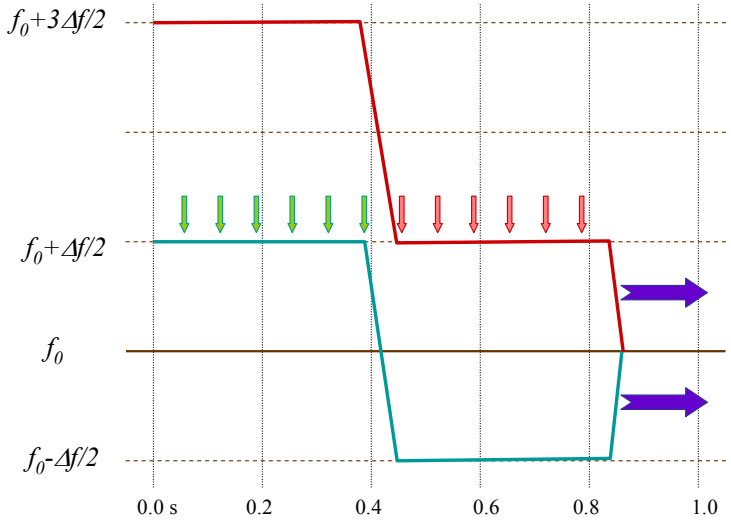

Fig 8.67: Proposed frequency scheme for Recycler slip stacking. Beam is injected six times above the central frequency by half the separation frequency. That beam is decelerated to below the central frequency to a slipping orbit and six more injections take place on the injection orbit. The beams are extracted in a single turn when they overlap in azimuth, one Booster tick after the last injection.

Slip stacking is expected to operate well in the Recycler for ANU, but it cannot be tested until actually installed. The risks associated with slip stacking are that the loss levels will not be reduced sufficiently by the advances of the Proton Plan, the move to the Recycler, and other ANU mitigation schemes. In such a case, the Recycler can still be used to increase the proton throughput of the complex. At the conclusion of the Proton Plan, the Booster is expected to be able to deliver batches of 20-30% greater intensity than those useful for slip stacking[14]. These batches could be boxcar stacked in the Recycler[15], leading to 20-30% production gains. Additionally, the proposed scheme of batch compression using barrier buckets [65] might be

[13] Batches cannot be injected at different frequencies because the transfer line may not be able to handle the momentum difference, and because different frequencies are not compatible with the notch cogging system in the Booster.

[14] These larger batches from the Booster are possible by filling a larger longitudinal emittance than useable for slip-stacking.

[15] The bunches in the Booster would require bunch rotation to fit inside the 300 kV buckets capable at this stage of the upgrades; the amount of rotation necessary would be less than that for slip stacking. If an additional two RF cavities are installed, so that 600 kV are available, then bunch rotation would not be needed at all.

possible in the Recycler as long as the LLRF system remains intact[16]. Batch compression has not been used operationally, as slip stacking has, but it has similar or greater potential for increasing proton throughputs. These two contingencies provide greater certainty that the ANU Recycler upgrades will improve proton throughput.

8.7.1.3 Booster

The Booster will be called upon to deliver 12 successive batches of 4.3×10^{12} protons every 1.33 s for the ANU program. The Proton Plan goals include being able to deliver equivalent batches to the Main Injector for slip-stacking by 2009. Compared to the Proton Plan, ANU will use 80% more protons from the Booster for the Main Injector; however, the Proton Plan will have an additional number of protons for the 8 GeV neutrino program which can be redirected to ANU.

The critical factors in the Booster that are most likely to affect ANU are loss control and longitudinal emittance conservation. The Booster proton throughput is limited by proton losses; the Proton Plan is designed to reduce these losses, but the necessary proton rate for ANU has not yet been demonstrated operationally. The momentum spread of the beam from the Booster is a primary factor in slip stacking efficiency. The momentum spread of ± 8 MeV/c (at 95%) is achieved by constraining the longitudinal emittance to no more than 0.08 eV·s and a bunch rotation. The Booster's transverse emittance is set by the injection and early capture process. A 95% normalized emittance of 15 π mm·mrad is typically achieved in each plane and adequate for operation.

While the devices in the Booster may be able to operate at 9 or 15 Hz, beam can only be accelerated if losses are sufficiently controlled. The Proton Plan improvements are designed to decrease and control losses such that throughput can be improved. At the conclusion of the Proton Plan, the Booster is estimated to provide 18.9×10^{16} protons/hour, with a fallback number of 13.0×10^{16}. Those estimates make assumptions about the users of the protons with regard to cogging which is estimated to incur 20% greater loss; adjusting to ANU uses the limits would be 17.2×10^{16} and 12.7×10^{16}. The anticipated ANU usage is 13×10^{16} protons/hour, which is slightly above the fallback and well below the design capability. The ANU proton consumption from the Booster will be achievable if the Proton Plan at least achieves its fallback goals.

8.7.1.4 Recycler

The Recycler is a permanent magnet 8 GeV storage ring with the same circumference as the Main Injector (7x that of the Booster), and similar gross lattice features of beta functions, tunes, dispersion, and momentum compaction. The Recycler is presently used to store and cool antiprotons for Run II. When suitably modified for ANU, it will accept twelve batches of Booster beam, merge them into a length of six batches through slip stacking, and transfer them to the Main Injector in a single turn.

The Recycler will use the same scheme as the Main Injector for slip stacking, so it will require similar control of beam loading distortion [63]. However, such control will be substantially simpler in the Recycler as it will only have two 53 MHz cavities, instead of the MI's 18 or 20. Additionally, the new cavities for the Recycler are being designed to have smaller R_s/Q by a factor of five. Nevertheless, a beam loading compensation system is expected to be necessary [59]; duplicating the features of the MI system will be adequate.

[16] Batch compression involves debunching, compression, and rebunching into 53 MHz. 300 kV is inadequate for a complete rebunching, so either time must be spent in the Main Injector for bunching, or two more RF cavities must be installed in the Recycler.

The transverse instability arising from the resistive wall effect is suppressed in the Main Injector through the use of negative chromaticity at injection and a bunch-by-bunch damping system [66]. The damping system is necessary to keep the chromaticity to reasonably small values. Instabilities are typically seeded by injection errors [67]. The Recycler beam pipe is smaller than the Main Injector's, leading to a comparable, but somewhat larger resistive wall effect. The growth rate of oscillations should be no more than 50% greater in the Recycler than Main Injector. The transverse dampers in the Main Injector presently have a 500% gain margin; though at the Proton Plan intensities this margin may be reduced[17]. A similarly designed system for the Recycler will accommodate the transverse instability.

Explicit longitudinal damping is not performed in the Main Injector for slipping beam[18], and is assumed to not be necessary in the Proton Plan. Damping is implicitly performed through beam loading compensation in the Main Injector, which will also be present in the Recycler.

No widespread formation of electron clouds is expected in the Recycler for ANU. In the Main Injector only minimal and local electron activity has been observed for bunched beam. No electrons have been observed for slipping beam and no associated beam instabilities have been observed. The Recycler parameters will be substantially similar to the Main Injector. The electric field will be slightly higher at the beam pipe due to the smaller cross section, but the distance available for acceleration will also be smaller.

The space charge tune shifts experienced in the Recycler will be greater than those presently experienced for antiprotons. However, the marginal loss of lifetime will not be relevant for a beam that persists in the Recycler for less than one second, compared to tens of hours for antiprotons.

8.7.1.5 Beam Cleaning

The ANU design includes an additional abort kicker in the Recycler that will ensure that the azimuthal gap used for injection is clear of beam prior to injection. The beam cleaning will substantially reduce the uncontrolled loss that would otherwise heavily irradiate the injection region.

The process of slip stacking in the Main Injector is known to have an inefficiency of about 5% in ideal circumstances with high-intensity beam. However, the 5% of the beam is not immediately lost; instead it escapes from the slipping buckets and transits around the azimuth. The beam is then typically lost in two ways: further injections displace the escaped beam into a series of magnets, producing a local area of high irradiation; if not displaced, the beam will fail to be accelerated once the main ramp begins and be lost longitudinally. Additionally, some portion is captured into the main RF's accelerating buckets; that portion of the beam is not typically lost, but does produce larger tails in the longitudinal distribution.

The losses from accelerating the beam will not occur inside the Recycler, only the large injection loss. From experience in the Main Injector, we can predict that the injection loss would be on the order of 1000 W for ANU. Even spread over a larger area of up to 100 m with bumps

[17] From intensity scaling exercises the margin of 300% would be expected. The margin may ultimately be greater due to the longer bunch length of the beam injected for slip stacking. However, the details of how to damp injection oscillations in the Main Injector for Proton Plan have yet to be worked out. The immediate slipping of the beams complicates the procedure, potentially leading to a reduced damping efficiency. The possibility of using a narrow-band damping system for the dominant mode may alleviate the complication.

[18] Longitudinal damping is performed for captured beam and other types of acceleration, leading to a reduction in longitudinal emittance. In ANU such beam conditions will still be limited to the Main Injector, not the Recycler.

(as is currently done in the Main Injector), the loss would lead to large radioactivation and potential component failure.

Instead of suffering the injection loss, the ANU design includes an additional kicker system, identical in kick to the injection kicker, but designed to extract circulating beam to the abort. This kicker would pulse immediately before injections (and the final extraction) to remove all beam from the injection and extraction gaps. Considering the rise and fall times involved, the beam cleaning system could reduce the injection losses by 95%.

8.7.1.6 Main Injector

The Main Injector will operate almost identically in ANU as in the Proton Plan; the differences being that the slipping process will no longer occur in the MI, and that the ramp rate will be increased to reduce the cycle time. The improvements made in the Proton Plan will be necessary to run the Main Injector with reasonable losses.

Removal of the slipping process from the Main Injector to the Recycler reduces the low-voltage requirements on the MI RF system. Cavities will no longer need to provide zero voltage and will no longer have to deal with the detailed transients of slip stacking. Nevertheless, the cavities will sustain a large DC beam loading and still have the transient of the abort gap. The Proton Plan beam-loading compensation will be adequate for these loadings.

A set of collimators will be installed in the Main Injector for the Proton Plan to intercept the beam that fails to accelerate, and to provide a limiting aperture [68]. These collimators are necessary for ANU to intercept the same type of loss.

8.7.2 ANU Demands on Proton Plan

As described above, the ANU designs are upgrades to the existing Fermilab accelerator complex. That complex is the sum of already operating machines and the Proton Plan upgrades presently being performed. To assure that ANU operations meet expectations, the project will monitor the progress of key Proton Plan upgrades and determine whether their performance is adequate for ANU.

Several items have been identified as meriting particular attention:

- Booster performance in terms of proton delivery rate, protons per pulse, and longitudinal emittance are to be improved by the Proton Plan. ANU relies on each of these improvements. The major outstanding upgrade in the Booster is the complete replacement of its corrector magnet systems. This major upgrade is scheduled to be installed by the end of the 2008 shutdown, and to be commissioned thereafter. The time between corrector commissioning and ANU installation may be short; however, we are fortunate in that the Booster is already close to the proton needs of ANU.
- The MI-8 collimators need to remove large amplitude (transverse and longitudinal) particles in the transfer between the Booster and Main Injector. Removing these protons reduces losses in the Main Injector. These collimators are installed and undergoing commissioning. Their impact is part of several activities needed to decrease losses in the Main Injector.
- 11-batch slip stacking in the Main Injector must perform at the necessary intensity and efficiency. The Recycler implementation may be marginally improved from the Proton Plan scheme, but the process must still be proved by the Proton Plan. The 11-batch scheme has been partially demonstrated in the Main Injector and awaits further tuning and installation of the collimators. Once operational, the long-term prospects for intensity and efficiency will be established.

- Collimators are being planned in the Main Injector that will control a substantial portion of the Proton Plan losses in the Main Injector. The collimators are to be installed in the 2007 shutdown and commissioned thereafter. For the Proton Plan, the collimators will intercept beam loss occurring at the extended period at 8 GeV and the loss occurring at acceleration from uncaptured beam. In ANU the collimators must also intercept the acceleration loss. Once 11-batch slip stacking and the collimators are implemented the utility of the collimators for ANU can be well estimated.

The above items will be analyzed, once commissioned, to assure that they will meet the needs of ANU. Quantitative results of efficiencies and other metrics will be documented and used as inputs to estimations of ANU proton production and efficiencies. The ANU tasks will also serve notification if any of the needed upgrades fall short of the needed improvements.

8.7.3 Machine and Process Analysis

The ANU stacking and acceleration schemes are derived and extrapolated from those already in place at Fermilab. Nevertheless, commissioning and operation of the upgrades will need extensive documentation of the machines and beam physics analyses of the involved processes. This set of tasks will perform measurements, simulations, and calculations pertaining to each of the machines in their new roles in ANU. We assume that substantial analyses of the machines and processes occurs outside of the project, but focused more on the machines' roles in present operations (Run II, NuMI, and the Booster Neutrino Beam) and the Proton Plan. The items that have been identified as needing further analysis and documentation for ANU are:

- Beam simulations and calculations of the slip stacking process in the Recycler, and optimization for ANU. These will be mostly longitudinal analyses of the process, focused on minimizing the beam lost outside of the RF buckets.
- Beam dynamics simulations in the Recycler and MI. Beams of the ANU intensities and characteristics need to be studied theoretically for collective effects. These analyses will be used to estimate loss patterns in the Recycler from those in the Main Injector.
- Further measurements in the Main Injector to study loss mechanisms and transition crossing during acceleration. Of particular interest will be locating areas of impedance.
- Once the Proton Plan has commissioned 11-batch slip stacking and the Main Injector collimators, ANU will measure the spatial loss pattern in the Main Injector. This will be correlated with radioactivation data and the Recycler simulations to estimate the loss pattern in the Recycler for the ANU 12-batch slip stacking.
- Some ANU–relevant beam measurements in the Recycler can take place in its present configuration. These measurements will be limited as the Recycler does not have the ability to maintain the 53 MHz bunching of beam.
- Formation of the electron cloud can be measured directly through the use of a dedicated electron counter. Such a device exists in the Main Injector, but needs to be installed in the Recycler in such a way that does not impact its role as an antiproton storage machine. The electron cloud is not expected to significantly impact the ANU beam, but must be monitored to ensure its low impact.
- The electron cloud needs to be simulated and analyzed for the ANU beam. The cloud does form in the Main Injector during high intensity operation, but does not negatively impact the beam. Simulation will be developed to form a model of the electron cloud that conforms to observations, and can be extrapolated to ANU operations.

- The new ANU transfer lines are short lines, designed to well match the Recycler and Main Injector lattices. These lattices need to be documented and have tuning protocols developed.
- The ANU beam cleaning system is an important part of loss control in the project. Once the ANU 12-batch cycle is analyzed in terms of anticipated losses and the kickers have predicted waveforms, the beam cleaning system can be analyzed in terms of how much of the losses will be directed to the Main Injector abort.

The above analyses will be performed and combined into an ANU Beam Physics Source Book. The Source Book will be used for future reference in commissioning and operating the ANU beam.

8.7.4 Proton Projections

Realistic and accurate projections of the number of protons delivered through the ANU schemes are required for estimating the eventual measurement precision achieved by the NOvA experiment. ANU wishes to provide realistic long-term estimations of the number of protons that the experiment can expect. These estimations depend on how intense and efficient the ANU beam eventually is, and the amount of time that beam can be delivered to the NuMI target. ANU will maintain estimates of both of the above factors, anticipating that they will evolve with further knowledge of how the present accelerator complex performs.

The accelerator division and NuMI operations personnel keep track of a large amount of information about performance of the current complex. ANU will develop a set of performance metrics that are derived from the present measurements, and can be extrapolated to the ANU beam, producing justified projections of proton performance.

8.7.5 Changes in the Beam Physics Design Since the CDR

Since the CDR was written, the Main Injector department has achieved 11-batch slip stacking for the Proton Plan. This achievement proves, in principle, that 11-batch slip stacking is possible and increases the likelihood that the ANU stacking scheme will be successful as designed.

8.7.6 Remaining Design Work for Beam Physics

No design work remains for beam physics. Substantial additions to the Proton Plan or modifications of the ANU designs would require additional validation within ANU – Beam Physics (none are presently envisioned).

8.8 ES&H and Quality Assurance

NOvA has a Quality Assurance Plan (QAP) [69] and an Integrated Safety Management Plan (ISM) [70]. The ANU subproject implements and continues to implement both these plans. Design reviews are carried out before all procurements that have risk associated with them either from a cost, schedule, technical or ES&H viewpoint. These reviews are in the resource loaded schedule. A table of elements that will be used by the ANU subproject, the basis of their design and comments on other risk elements is used by the project to determine which elements need design reviews [71]. This table and management input is used to determine how detailed and extensive the review and review committee is for the review.

Many different types of reviews will occur within the ANU subproject. “Internal” Design Reviews for the new designs or major modifications to existing designs of technical components often included ES&H Personnel. Other reviews occur within the department in which the item is designed. Each department, whether in AD or TD or elsewhere, has its own internal design

review guidelines. Often these reviews included detailed checking of calculations and/or Engineering Notes. The third type of review is performed by the NOνA ESH/QA Review committee. These vary in detail, depending on the item being reviewed. These reviews always cover the ESH issues. The NOνA ES&H/QA review committee is in the process of being formed to look at ES&H and QA issues related to design, construction, installation and operation. This committee will be composed of people with expertise in mechanical, electrical, structural, radiation and conventional safety.

Inspection and acceptance testing, quality improvement, prototypes for high risk items are all used for improving quality and safety during all phases of the project.

8.9 Risks

Risks are managed as described in the NOνA Risk Management Plan [72]. Risks are mitigated through the processes described in Section 8.9 and as described in the NOνA Risk Management Plan. Details on risks and risk management for the ANU subproject are entered into a risk registry using WelcomRisk©. They are then ranked and for those that rank high, a NOνA Risk Form is filled out. Nearly 100 risks associated with ANU have been entered into the WelcomRisk© risk registry. Mitigations are listed along with the risks. The high risk items have been entered into the NOνA High Risk Registry (see NOνA docdb #1323) and have had detailed Risk Forms filled out for them.

All ANU risks are listed by number, score and tolerance in NOνA docdb #1983. Several risks on the same topic in the WelcomRisk© risk registry are entered into one form for the above NOνA High Risk forms.

8.10 Value Management

Value management is an integral part of the planning, design, construction and installation process. Many items are re-cycled or refurbished (many different kinds of magnets, TeV LLRF system, software, etc.) for ANU. This saves money in all phases of the project and leads to the use of known, reliable systems. This also saves in decommissioning costs where these items would have to be disposed of in some manner, with some being radioactive.

Within the 9 months, the injection line design has changed to simplify installation and to minimize the number of powered elements near the Recycler Ring. The main design change in the extraction line was to move the injection point in the MI. This allows us to use the same ceramic beam tube and magnet for this kicker as we are using for the Recycler extraction and abort kickers, thus eliminating a separate design for both the ceramic beam tube and the magnet. We have decided to accept 81 Booster bunches per Booster batch instead of 82. This change loosens the kicker rise/fall time specifications from 38 nsec to 57 nsec with ~1% loss of protons to the NuMI target.

The position of the MI collimators needed for the Proton Plan and NOνA has been finalized such that they do not interfere with the NOνA injection line from the Recycler to Main Injector. As a result no collimator moves need to be included in the MI Upgrades required for NOνA. We also have a design for the manufacturing of the bus bars for the cavity tuners that greatly simplifies the installation and does not require the use of an external crane and removal of parts of the roof from the MI-60 building.

To greatly simplify moving Horn 2 to the medium energy neutrino beam location, a new "dummy" horn module will be built identical in dimension to the existing design, but without all the associated penetrations, drive system, or horn support system. This "dummy" module assembly will essentially act as a shielding plug and work could begin on its installation during

the first shutdown after the completion of Collider Run II operations. Another advantage of having two module assemblies is that it will allow Horn 2 to be easily moved back to the low energy position if the need arises in the future.

There are many other examples of Value Management on the ANU subproject. Many are described in the text within the subchapters of this section.

8.11 Chapter 8 References

1. "Proton Projections", R. Zwaska, NOVA-doc-1698, (2007).
2. The MinervA Collaboration, D. Drakoulakos et al., 'Proposal to perform a high-statistics neutrino scattering experiment using a fine-grained detector in the NuMI beam'.
3. The Proton Plan web page is http://www-accel-proj.fnal.gov/Proton_Plan/index.shtml.
4. "NOvA Beam Requirements", M. Messier, NOVA-doc-1632, (2007).
5. See the documents associated with MI BPM requirements in the BeamsDoc Database, event id = 29 (https://beamdocs.fnal.gov/AD-private/DocDB/ListBy?eventid=29&mode=conference).
6. "Recycler Injection Kicker Configuration in the Nova Era", D.E. Johnson ,NOVA-doc-1495, (2007)
7. "Recycler Injection Line Options for the Nova Project", D.E. Johnson, NOVA-doc-1501 (2007)
8. Web page "ANU Magnet Naming Cheat Sheet" helps to explain magnet names.
9. "The Proton Driver Design Study", Fermilab-TM-2136, December 2000.
10. "Recycler BPM Requirements for Nova ANU", P. Derwent, M.J. Hu, NOVA-doc-1799 (2007)
11. "Main Injector and Recycler Kicker Apertures for the Nova Project ", D.E. Johnson, NOVA-doc-1843 (2007)
12. "MI Pond Water Modeling for ANU Increased Heat Loads", Stephen F Krstulovich, NOvA-doc-1895.
13. Main Injector Shielding Assessment 1998
14. Main Injector Shielding Assessment, October 2004
15. Fermilab Radiological Control Manual
16. MI8 Beamline Collimation Design, B.C. Brown, Beams-doc-1977, 9/30/2005
17. "Accelerator-based Neutrino Beams", Sacha E. Kopp, Submitted to Phys.Rept., http://arxiv.org/PS_cache/physics/pdf/0609/0609129.pdf
18. "Optimization of Target and Horn Locations for NOvA", M. Messier, NOVA-doc-2606, (2007).
19. "The NuMI Technical Design Handbook", www-numi.fnal.gov/numwork/tdh/tdh_index.html
20. "NuMI Primary Beam Upgrade for SNuMI", Sam Childress, NOvA-doc-1571
21. Conversation with D. Harding from Technical Division
22. "MARS Simulations of the NuMI Primary Beamline", Sergei Striganov, NuMI-NOTE-SIM-1022, 17 May 2004.
23. "Technical Design of the Target Pile Protection Baffle," S.Filippov et al., NuMI-B-1092, April 30, 2002.
24. The medium energy target is documented in NuMI-B-675, IHEP report, "Dynamic Stress Calculations for ME and LE Targets and Results of Prototyping for the LE Target." August 10, 2000. See also Beams-doc-676.
25. See drawing 7538-00-00-00.dwg for the ME target. (/afs/fnal.gov/files/home/room2/garkusha/ME_target). In this drawing there are 14 graphite plates and the drawing has not been updated to reflect the change to 12 graphite plates. In this drawing there is also a special graphite plate at the downstream end for vertical alignment. The drawing has not been updated with this piece removed.

26. “Design Study of the NuMI Medium Energy Target for Higher Power Beams”, V. Garkusha, A. Ryabov, T. Ryabova, F. Novoskoltsev, V. Zarucheisky, State Research Center of Russia Institute for High Energy Physics, November 27, 2006, NOvA-doc-619.
27. “Ion Chamber Arrays for the NuMI Beam at Fermilab”, D. Indurthy, *et al.*, Particle Accelerator Conference (PAC 05), Knoxville, Tennessee, 16-20 May 2005. (Also, FERMILAB-CONF-05-108-AD.)
28. M. Messier, “NOvA Beam Requirements”, NOvA-doc-1632.
29. S. Tariq, E. Chi, “Brief Analysis of the “R” Shielding Block for the New Loading Case”, NOVA-doc-2621.
30. Z. Tang, “Target Chase Shielding Thermal FEA documents”, NOvA-doc-2620.
31. S. Tariq, “Notes on meeting to scope Target Chase Cooling Upgrades”, NOvA-doc-2416.
32. Salman Tariq, “Horn 1 Vertical motion in 700 kW operation”, NOvA-doc-1572
33. Salman Tariq, “Horn 1 Horizontal motion in 700 kW operation”, NOvA-doc-1586
34. P. Hurh, “Summary of Horn 1 Stripline/Stripline Block Cooling Concerns”, NOvA-doc-1787.
35. Bob Wands, “Qualifying the NuMI Decay Pipe and Hadron Absorber for SNuMI Loads”, NOvA-doc-1622.
36. “Conceptual Design Report: Proton Plan 2”, NOvA-doc-1375, November 9, 2006.
37. K.E. Williams, “MI LCW and Pond Water Temperature Studies”, NOvA-doc-1573.
38. NuMI Shielding Assessment, October 2004.
39. NuMI Safety Assessment Document 11/1/2004.
40. N. Grossman, G. Rameika, “Methodology for Determining Radionuclide Concentration in Groundwater in the Vicinity of Accelerator and Beamline Enclosures”, NuMI Note 970, July 2004.
41. F. Breen, “Evaluation of Boundary Conditions for the Two Dimensional Groundwater Model Simulations, Technical Memorandum, June 12, 1999.
42. Earth Tech Draft Groundwater Modeling Report, dated, May, 1999”.
43. NuMI Tunnel Modeling Project Report, August 1999.
44. Earth Tech, Inc., “Two Dimensional Groundwater Flow Model, Results Estimated Inflow to NuMI Tunnel”, May 1999.
45. Breen GeoScience Inc., “NuMI 3D Groundwater Model Update”, August 2004.
46. D. Cossairt, “A Model for Calculating Radionuclide Concentrations in Fermilab Cooling Ponds”, June 2006.
47. Illinois Environmental Protection Agency, Lifetime Operating Permit - National Emissions Standards for Hazardous Air Pollutants (NESHAP), Issued March 2, 2006, and application number 79070012, dated March 1, 1991.
48. Fermilab Annual Environmental Report
http://www-esh.fnal.gov/pls/default/esh_home_page.page?this_page=12831
49. Title 40, Code of Federal Regulations, Part 61, Subpart H, “National Emission Standards for Emissions of Radionuclides Other Than Radon From Department of Energy Facilities”.
50. K. Vaziri, “SNuMI beamline radiological safety”, NOvA-docdb-1635, 2007.
51. “Beams Division Routine Monitoring Program”, BDDP-SH-1003, Rev 0.
52. See NuMI TDR Chapter 4.2.10 for details.
53. N. Grossman, “Residuals Estimates for SNuMI”, NOvA-docdb-1580.
54. D. Harris and N. Grossman, “Radiation Dose Estimates for the Monitoring System”, NUMI-NOTE-BEAM-845, 7/8/2002.
55. N. Grossman and D. Harris “NuMI Muon Rates” March 2004, -updated July 2004. NuMI Note 1025.
56. N.V. Mokhov, "The MARS Code System User's Guide", Fermilab-FN-628 (1995); N.V. Mokhov, O.E. Krivosheev, "MARS Code Status", Proc. Monte Carlo 2000 Conf., p. 943, Lisbon, October 23-26, 2000; Fermilab-Conf-00/181 (2000); N.V. Mokhov, "Status of MARS Code", Fermilab-Conf-03/053 (2003).

57. The Proton Plan Design Handbook is found on its webpage: http://www-accel-proj.fnal.gov/internal/Proton_Plan/index.shtml. A public site viewable outside Fermilab is: http://www-accel-proj.fnal.gov/Proton_Plan/index.shtml
58. The Run II project homepage is http://www-ad.fnal.gov/run2upgrade/. Slip stacking was an addition to the original Run II designs.
59. K. Seiya *et al.*, "Status of Slip Stacking at Fermilab Main Injector" PAC 2005, MOPA004; FERMILAB-CONF-05-110-AD.
60. B. Boussard and Y. Mizumachi, "Production of Beams with High Line-Density by Azimuthal Combination of Bunches in a Synchrotron", IEEE Trans. Nucl. Sci., NS-26. No.3, June 1979, pp. 3623-5.
61. F. E. Mills, BNL Internal Report AADD 176, 1971.
62. S. Shukla *et al.*, "Slip Stacking in the Fermilab Main Injector", 1996 DPF / DPB Summer Study on New Directions for High-Energy Physics, eConf C960625:Acc015, 1996.
63. J. Dey and I. Kourbanis, "53 MHz Beam Loading Compensation for Slip Stacking in the Fermilab Main Injector", PAC 2005, TPPT027, FERMILAB-CONF-05-175-AD.
64. K. Seiya and I. Kourbanis, "Slip Stacking in MI", FNAL-Beams-doc-2179, 2006.
65. G. W. Foster *et al.* "Beam Manipulation and Compression Using Broadband RF Systems in the Fermilab Main Injector and Recycler" EPAC 2004, TUPLT149, p. 1479.
66. P. Adamson et al., "Operational Performance of a Bunch by Bunch Digital Damper in the Fermilab Main Injector", PAC 2005, MPPP015, FERMILAB-CONF-05-145-AD.
67. V. Balbekov, "Recycler Transverse Instability in Context of the Proton Plan (Rigid Modes Instability at Dominating Space Charge)", internal Recycler note, 2006.
68. B. Brown *et al.*, "Beam collimation in the Main Injector at Slip-Stacking Injection", FNAL-Beams-doc-2330, 2006.
69. NOvA Quality Assurance Plan (QAP), NOvA-docdb 1353
70. Integrated Safety Management Plan (ISM), NOvA-docdb 1925
71. ANU Design Review Table, NOvA-docdb-2052
72.NOνA Risk Management Plan, NOvA-docdb-185

9 Ash River Site and Far Detector Hall

9.1 Introduction

This chapter describes the Ash River site and the Far Detector Building at the Ash River site. The access road to the Ash River site is described at an advanced technical design level.

9.2 Details of the Ash River Site

9.2.1 Technical Design Criteria

The project site must provide adequate space and infrastructure for the construction of the Far Detector Building, assembly of the Far Detector and normal operations for the life of the project.

The Ash River Site is located approximately 3.5 miles from the Ash River Trail (St. Louis County Road 129) by way of an existing logging road. This existing access will be improved to provide all weather access to the project site.

Construction of a facility the size of the Far Detector Building requires significant contractor staging and segregated stockpiling areas. The stockpiled material will be segregated into topsoil, suitable fill material and rock areas. Each stockpile will require sediment and erosion control devices as well as adequate access. The size of the contractor staging area must accommodate not only the normal construction materials, but given the remote location, also those materials and supplies not readily available in the vicinity of the project site. The size of the Ash River Site will provide space for the anticipated stockpiles and staging areas.

The Ash River Site is within the watershed of the Ash River, a designated trout stream. The project site has been sized to allow the Far Detector Building to be located over 1,160 feet away from the river to minimize the impact of construction, assembly and operation of the facility. In addition, the preliminary Storm Water Pollution Prevention Plan (SWPPP) includes site features to minimize the transmission of sediment and storm water in the areas adjacent to the river.

A water well capable of providing 50 gallons per minute at the Ash River Site will provide potable water for both domestic uses and fire protection functions.

Electrical infrastructure with a capacity of approximately 2 megawatts is needed to support the building construction, detector assembly and normal operations of the facility is located along the Ash River Trail.

A fiber optic data network capable of DS-3 access level is required for normal operations of the detector.

Telephone communication for normal business service is required for construction of the building, detector assembly and normal operations of the facility.

9.2.2 Overview of the Ash River Site

The Ash River site is 810 km from Fermilab and offers the longest possible baseline along the NuMI beam within the United States. Figure 9.1 is a relief map of the general area around the selected site with an inset map showing how this area is located in the State of Minnesota. Voyageurs National Park dominates the northern half of Figure 9.1. U.S. 53 runs north-south on the western edge and the city of International Falls is off the map towards the northwest. The red line from the Ash River Trail to the Project Site is an existing logging road which must be upgraded for truck traffic as part of the project.

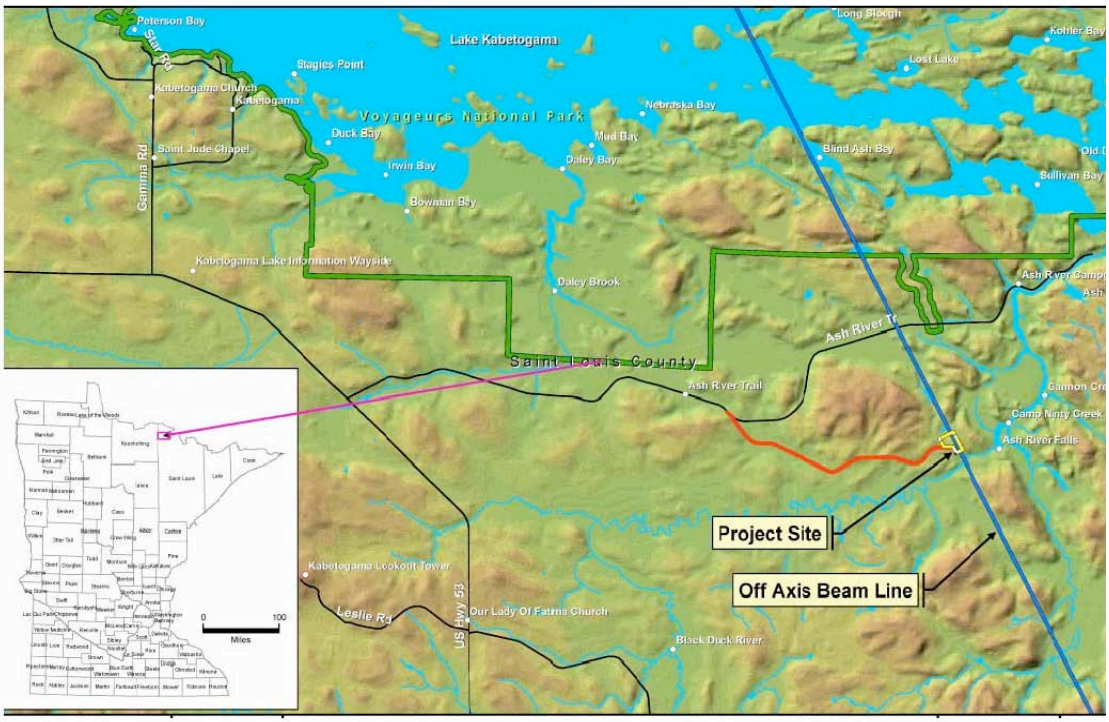

Fig 9.1: Shaded relief map of the Ash River site. The inset black and white figure indicates the site position within the State of Minnesota. North is to the top of the page in this figure.

The project will require approximately 89 acres for the Far Detector Building and another 19 acres for the upgraded access road tentatively called “Bright Star Road”.

Access to the project site will be provided through improvement of an existing logging road from the Ash River Trail (St. Louis County Road 129). The existing unpaved logging road is approximately 15 feet wide and approximately three and one half miles in length to the site of the detector. The road will be improved to a two-lane, paved roadway to provide access for construction traffic that will carry materials for construction of the facility and as well as trucks deliveries required for the assembly of the detector. The entrance will be improved to allow trucks entering the site to slow and turn onto the Brightstar Road while minimizing the impact on other traffic along Ash River Trail (St. Louis County Road 129).

Fig.9.2: Photo Looking East along existing access road taken in November 2006.

The proposed site work includes extension of existing electric and communication utilities and installation of domestic water well and septic as related work. Electric utilities and fiberoptic

will be extended from Ash River Trail along the improved access road. Improvements to the existing transmission system serving the site will also be required. These improvements will include only upgrades to existing transmission lines to increase capacity. No new lines will be constructed.

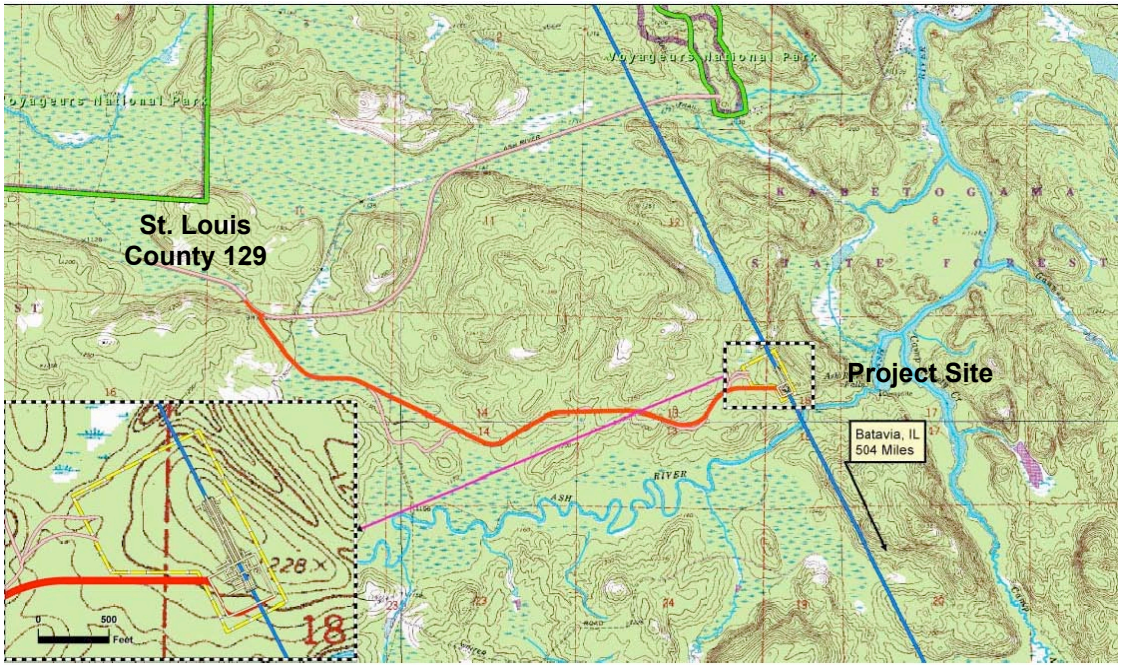

Fig. 9.3: Site Plan showing soil borings and topographic information along the Bright Star access road and at the Far Detector Building site.

Figure 9.3 is a US Geological Survey 7.5 minute, 1:24,000 scale map showing the topology of the Ash River area. The inset figure shows that the selected site is on a hilltop, roughly 70 feet above the level of the Ash River. The red line on Figure 9.3 is the access road to the site with details showing how it deviates from the logging road to provide for anticipated truck traffic to the site. The blue diagonal line indicates the 11.8 kilometer distance to the center of the existing NuMI beamline.

Figure 9.4 is an aerial photograph of the area with map details overlaid. In particular, the type of vegetation is identified, and the 100 year floodplain of the Ash River is marked. The inset figure shows the required setback from the 100 year floodplain just touches the Project Site in the southeast corner. This figure also shows how the access road crosses through an area of wetlands (bog) that will require mitigation through purchase of the required compensatory area in a wetlands bank. The road will require permits from the US Army Corps of Engineers under Section 404 of the Clean Water Act and from St. Louis County under the requirements of the Wetland Conservation Act of Minnesota. None of the impacted area is designated as a Protected Water or Wetland by the Minnesota Department of Natural Resources.

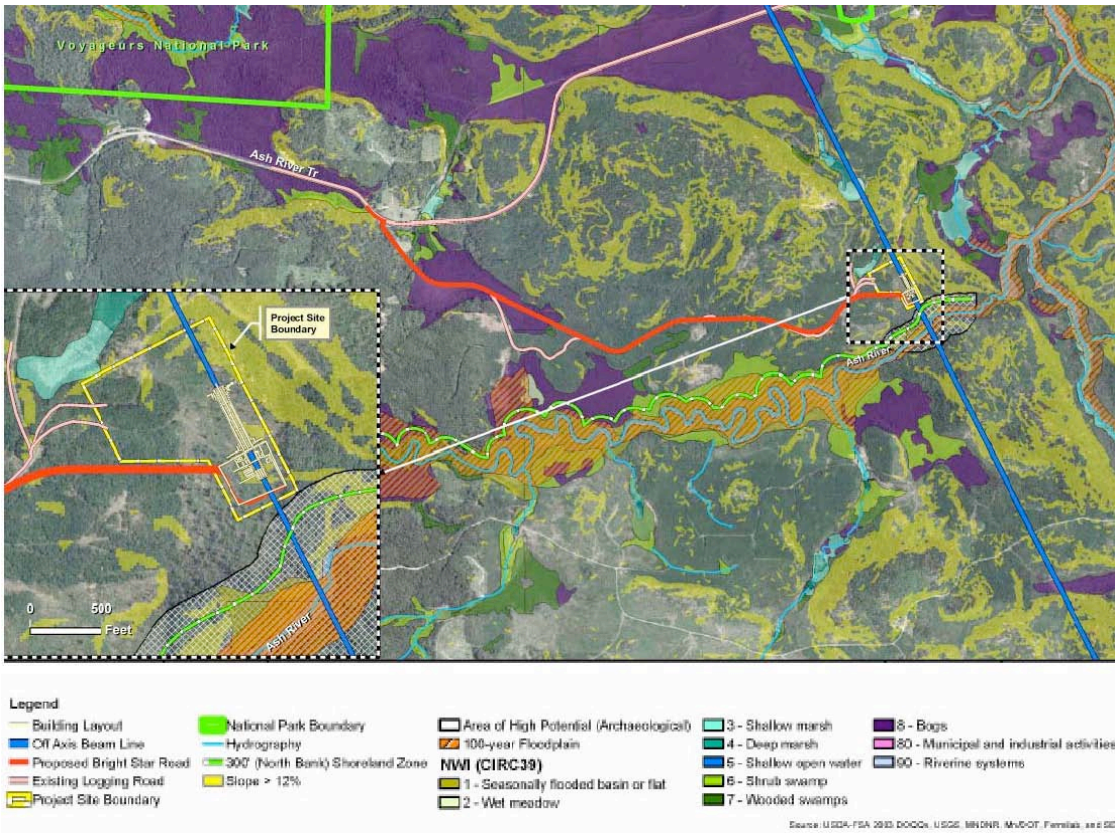

Fig. 9.4: A detailed map of the Ash River site shows wetlands, required wetlands setback lines, and other land characteristics in the area. The yellow shading in the forested areas indicates places with a > 12% slope.

Figure 9.5 is an aerial photograph that depicts the proposed project site boundaries along with the topsoil, clay and rock stockpiles as well as the subcontractor staging area. Also indicated on the figure are the one foot topographic contours showing the existing ground features. The proposed building site is approximately 70 feet above the elevation of the Ash River.

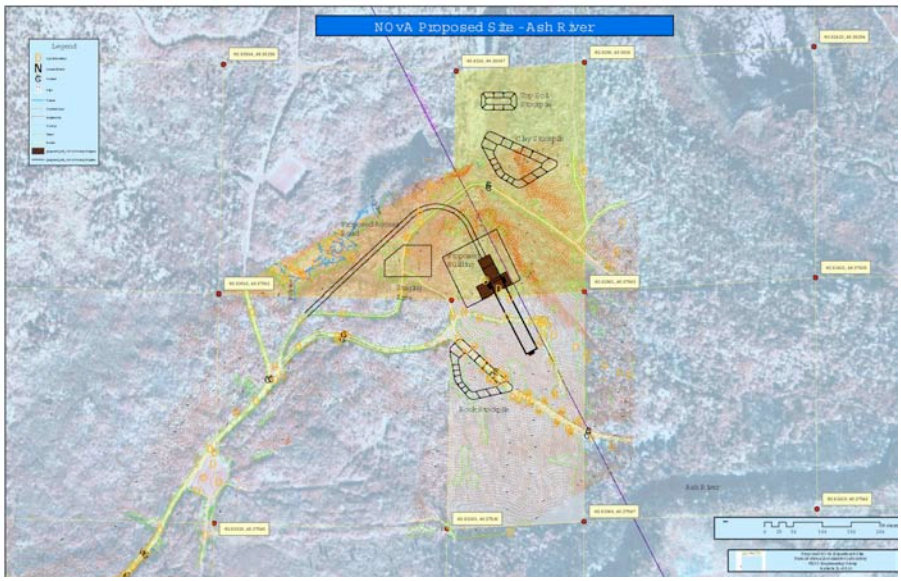

Fig. 9.5: Aerial Photo of the Far Detector Building Site.

Figure 9.6 shows the core samples from a typical core drillings done on the project site in the fall of 2006. In general, the surface deposits are approximately 7 feet deep and include soil over a layer of clay. Below the surface soils is a layer (at least 65 feet thick) of hard granite bedrock down to the proposed bottom of the NOvA excavation for the Far Detector. A packer test, used to determine hydraulic conductivity in the material, was done at several of the borings at a depth of 36 – 41 feet below the surface. No pressure loss was observed, indicating that the granite is not very fractured within the tested zone.

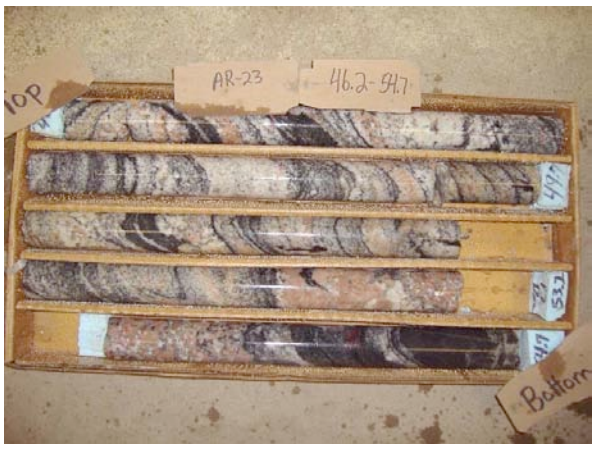

Fig. 9.6: Photos of typical core samples taken in fall of 2006.

9.2.3 Nearby Roads, Power, Data Communications

Highway US 53 does not have road restrictions in any season. The normal limits are 10 tons per axle (see Figure 9.7 below). The Ash River Trail (St. Louis County Road 129) between US 53 and the NOνA site access road does have road restrictions during the spring thaw, limiting trucks to 9 tons per axle for a 60 day period, March 15 – May 15 each year. Recent discussions with St. Louis County personnel indicate that the County is in the process of re-classifying the Ash River Trail as a 10 ton per axle highway. In northern Minnesota it is common to use trucks with an extra axle during restricted seasons. For example, the chassis trailers discussed in Chapter 10 for scintillator transport come in 2 and 3 axle versions, so the delivery of liquid scintillator to the site should not be interrupted except during actual severe storm conditions.

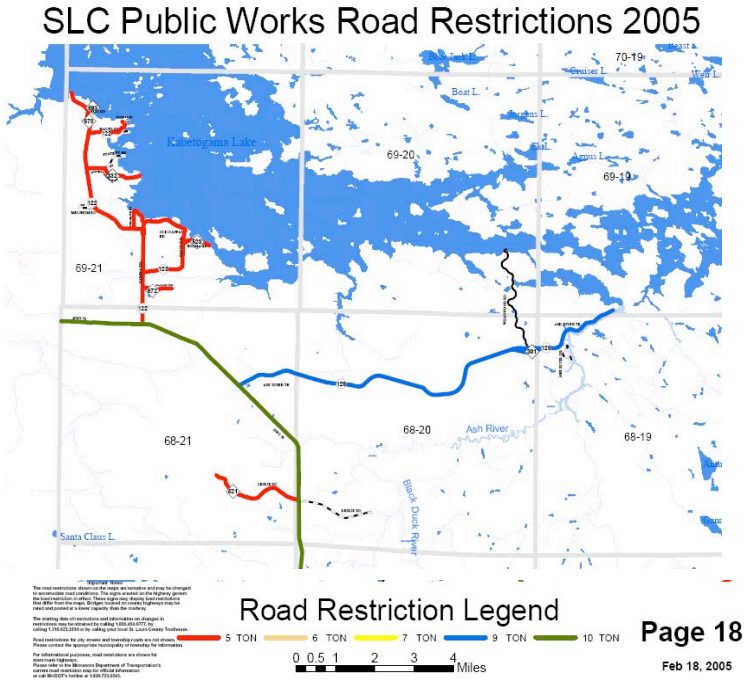

Fig. 9.7: St. Louis County Public Works Road Restrictions published for 2005.

There is limited power available along the Ash River Trail. Currently only 300 kVa is available versus the estimated need of 1,500 – 2,000 kVa. The area is served by North Star Electric, a part of the MinnKota Power, with about 6,000 customers in this part of Minnesota. North Star Electric Cooperative has provided an estimate [1] to upgrade the electrical service to the site from the Kabetogoma Substation some 35 miles from the Bright Star access road turn-off from St.Louis County 129. Figure 9.8, below, indicates the existing sources of power in the vicinity of the project site.

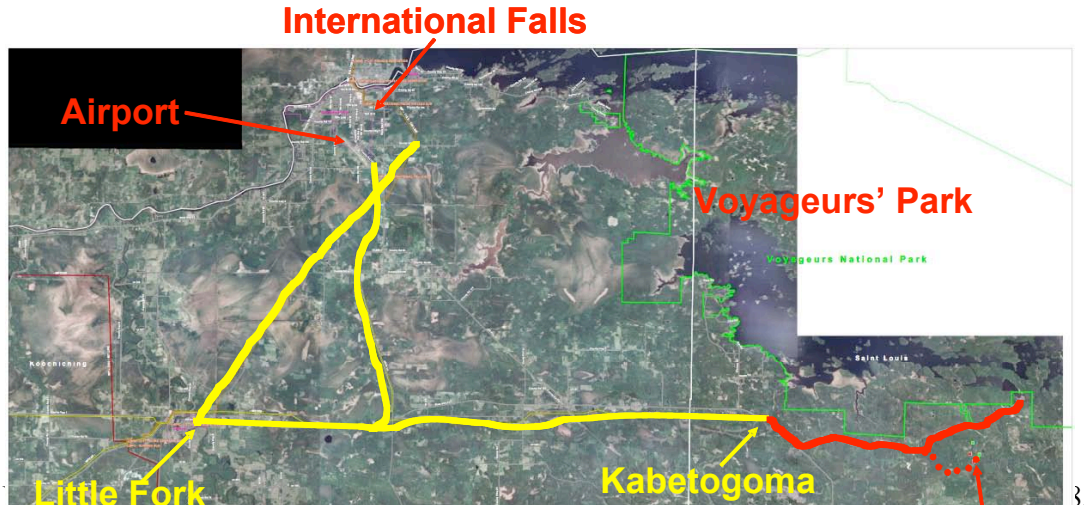

3, 2007

Fig. 9.8: Power distribution lines in the Ash River area.

The power in the project area is fed from the Kabetogoma substation via overhead pole lines. This area is served from a single direction with no secondary source in the event of a disruption. The NOvA site will include on-site capability for emergency power for critical systems from a backup generator powered by propane.

The project will connect to the existing electrical pole line along the Ash River Trail (St. Louis 129) at the intersection of the new Bright Star Road. The new electrical infrastructure will be routed parallel to the new access road in a designated underground utility corridor to the Far Detector Site.

Telephone and data communications in the Ash River area are provided by the Blackduck Telephone company, a small company with two (2) telephone exchanges and less than ten (10) employees. An existing underground fiber optic line and telephone line is located along the Ash River Trail (St. Louis 129) and serves the town of Ash River, Minnesota. The project will connect to the telephone and data lines at the intersection of the new Bright Star Road and Ash River Trail. Blackduck Telephone has provided an estimate for this work. [2].The new infrastructure will be routed parallel to the new access road in a designated underground utility corridor to the Far Detector Site.

9.2.4 Proximity to Voyageurs National Park

The Far Detector site is located approximately 2 miles southeast of the entry to the Ash River Trail entry to Voyageurs National Park. The design of the NOvA project incorporates features and considerations to minimize the impact on the adjacent properties in order to provide good environmental stewardship and become a respected, long term member of the Ash River community.

As part of this approach, the design includes consideration of the concerns of interested stakeholders gathered during community outreach meetings including representatives of Voyageurs National Park [3]. These concerns include project siting, noise and light pollution.

Several strategies were employed to minimize the visual impact of the facility. The first of these involved utilizing the existing logging road corridor for access to the site. This route, while approximately three times longer than a direct access from the Ash River Trail, respects the existing entry to Voyageurs National Park and provides an uninterrupted buffer between the project site and the road.

In April 2005 [4] the road alignment was discussed during a meeting included representatives from the Minnesota Department of Natural Resources (DNR) , Voyageurs National Park, Forest Capital Partners as well a the University of Minnesota. Of importance to the road alignment are notes indicating that the DNR did not prefer a route that created additional corridors that could restrict wildlife crossing. A list of attendees is included with the meeting notes is attached.

In April 2006 [5] another meeting concerning the road alignment was held. This meeting was held to discuss possible alternate road alignments for the access road. Attendees included

representatives from the Minnesota Department of Natural Resources (DNR) , Voyageurs National Park, Forest Capital Partners (FCP) as well a the University of Minnesota. The FCP representative and the DNR representative recommended utilizing the existing road alignment to minimize the overall impact on the area.

Based on input from the significant stakeholders, the project team opted to accept the recommendation to follow the existing road alignment as closely as possible. During the subsequent design phases, each deviation from the existing alignment was reviewed in order to minimize the overall impact on adjacent properties while developing a design that met the criteria for road construction in St. Louis County. The variations from the existing alignment were generally based on traffic safety concerns.

In February 2007 [6] the road alignment was presented during a meeting of local stakeholders. Attendees included representatives from the Minnesota Department of Natural Resources (DNR) , St. Louis County, Forest Capital Partners (FCP) as well a the University of Minnesota. The stakeholders recommended, and the design team concurred, that the right of way access should be limited to sixty six (66) feet in lieu of the preferred one hundred (100) foot corridor in order to minimize the impact on the adjacent properties and land features.

Subsequent design refinement included investigating three modifications to further minimize impacts.

1. Refinement #1 included reducing the width of the side slopes from 4:1 to 3:1 along much of the length of the access road. This refined was incorporated into the design.
2. Refinement #2 investigated a 2:1 slope for those portions of the road through the identified wetlands. This option was rejected for safety reasons. The 2:1 slope would have required a guardrail along the shoulders of the road. It was felt that the snow plowing during winter conditions would have resulted in a narrower lane width due to the potential for the guardrail to restrict the movement of snow. This condition, especially through the wetland, was deemed to create an unacceptable condition.
3. Refinement #3 investigated a reduce road width. The conceptual design included a 31 foot wide road width (24 feet of pavement with 3 foot paved shoulders over 31 foot wide gravel base). After review, the width of the access road was reduced to 28 feet (22 feet of pavement over 28 feet of gravel base). This refinement was incorporated into the design.

Another strategy to minimize the visual impact was accomplished at the project site. Instead of constructing the Far Detector Building on top of a hill, the design will incorporate a scheme where the majority of the detector will be located below grade with approximately 40 feet of the building above grade.

The siting also includes selection of a building location in the center of the site with significant grade changes to the north. These hills, when restored, will provide a visual buffer between the building and the property to the north. By acquiring the additional land, the project can ensure that this buffer remains in place.

Fig. 9.9: Photo Looking North from Project Site taken in November 2006.

Consideration of the Ash River, a Minnesota designated trout stream, to the south was included in the design of the building orientation. This resulted in locating the truck traffic to the north end of the building, away from the Ash River.

Fig. 9.10: Photo Looking South from Project Site taken in November 2006.

The design also included noise considerations. The majority of the noise is expected to occur during construction of the new Bright Star Road and Far Detector Building over a period of approximately two years. Of this time, the rock excavation is expected to last 3-4 months. In order to help mitigate the noise concerns, the noisiest construction activities will be restricted to between 0700 and 1900 hours.

The current traffic level on the Ash River Trail has been measured at 310 vehicles per day and the NOνA plan would add about approximately 90 trips to that total, a 33% increase.

Light pollution was discussed as another concern. The NOvA project intends to balance the safety and security concerns with the light impact on the surrounding areas. The lighting will be designed to not exceed 80% of the lighting power densities for exterior areas as defined in ASHRAE/IESNA Standard 90.1-2004, Exterior Lighting Section. The project site will be defined as LZ-1 –Dark (Park and Rural Settings) per IESNA RP-33. This standard specifies that all site and building mounted luminaries produce a maximum initial illuminance value no greater than 0.01 horizontal and vertical footcandles at the site boundary.

9.2.5 Site Design Changes since the Conceptual Design Report

The site design changes since the Conceptual Design Report include increasing the amount of land required for the project. This increase is due to the better understanding of the site conditions, stockpile areas, contractor staging areas as well as physics driven adjustments.

The increase in the land area required an updating of the Environmental Assessment Worksheet (EAW) for the project site and access road. The field work for this updating was completed in the summer of 2006 and the updated EAW was completed by Short Elliot Hendrickson in May 2007. This work was accomplished to mitigate an identified risk associated with schedule delays [7].

In support of the EAW updating and to prepare a U.S. Army Corps of Engineers Wetland permit, a detailed delineation of the wetlands was accomplished by Short Elliot Hendrickson in the summer of 2006. The development of the permit application was prepared and submitted for review in April 2007 [8].

In December 2006, a Storm Water Pollution Prevention Plan (SWPPP) was prepared by Burns and McDonnell as part of the development of the Site Preparation package. This living document contains the information needed to comply with applicable ordinances, codes and regulations concerning storm water management. This work was accomplished to address environmental safety and health concerns during construction [9].

A detailed topographic survey of the access road and project site was completed by Hanson Professional Services in the spring of 2006. This survey documented the ground features to produce a one foot contours. This work was accomplished to mitigate an identified risk associated with unknown topographic conditions [10]

The project team has identified cost and schedule risks associated with unknown subsurface conditions [11]. As mitigation, a comprehensive subsurface investigation program of the access road route and project site was completed by Short Elliot Hendrickson in the fall of 2006 to better characterize the site conditions. The goal of the subsurface exploration program was to further define soils, bedrock, and groundwater conditions for the project for the purpose of developing preliminary plans for the access road and building site. In addition to the subsurface exploration program included the development of recommendations related to road, utility and building construction. The subsurface exploration program consisted of several components, all designed to obtain information necessary for the design and construction of project facilities. The components consist of a drilling and testing program, geophysical investigation, and groundwater study.

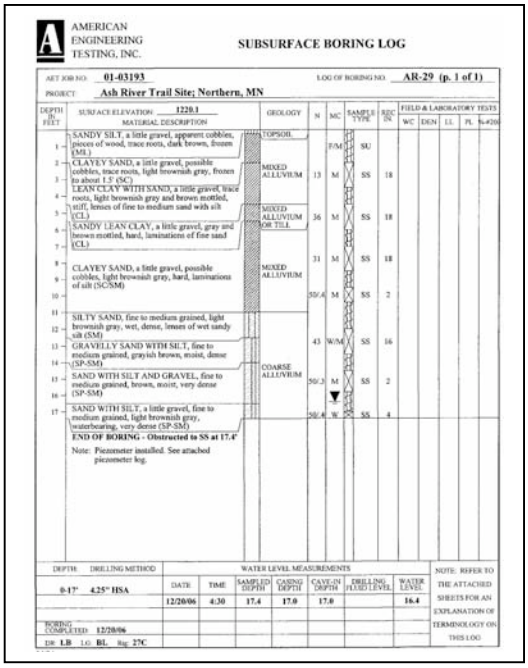
AMERICAN ENGINEERING TESTING, INC.

SUBSURFACE BORING LOG

AET JOB NO: 01-03193 LOG OF BORING NO. AR-29 (p. 1 of 1)

PROJECT: Ash River Trail Site; Northern, MN

SURFACE ELEVATION: 1220.1

DEPTH IN FEET	MATERIAL DESCRIPTION	GEOLOGY	N	MC	SAMPLE TYPE	REC IN	FIELD & LABORATORY TESTS: WC	DEN	LL	PL	%#200
1	SANDY SILT, a little gravel, apparent cobbles, pieces of wood, trace roots, dark brown, frozen (ML)	TOPSOIL		F/M	SU						
2-4	CLAYEY SAND, a little gravel, possible cobbles, trace roots, light brownish gray, frozen to about 1.5' (SC)	MIXED ALLUVIUM	13	M	SS	18					
4-5	LEAN CLAY WITH SAND, a little gravel, trace roots, light brownish gray and brown mottled, stiff, lenses of fine to medium sand with silt (CL)	MIXED ALLUVIUM OR TILL	36	M	SS	18					
6-7	SANDY LEAN CLAY, a little gravel, gray and brown mottled, hard, laminations of fine sand (CL)										
8-10	CLAYEY SAND, a little gravel, possible cobbles, light brownish gray, hard, laminations of silt (SC/SM)	MIXED ALLUVIUM	31	M	SS	18					
10			50/4	M	SS	2					
12-14	SILTY SAND, fine to medium grained, light brownish gray, wet, dense, lenses of wet sandy silt (SM)	COARSE ALLUVIUM	43	W/M	SS	16					
14-16	GRAVELLY SAND WITH SILT, fine to medium grained, grayish brown, moist, dense (SP-SM)										
16	SAND WITH SILT AND GRAVEL, fine to medium grained, brown, moist, very dense (SP-SM)		50/3	M	SS	2					
17	SAND WITH SILT, a little gravel, fine to medium grained, light brownish gray, waterbearing, very dense (SP-SM)		50/4	W	SS	4					

END OF BORING - Obstructed to SS at 17.4'

Note: Piezometer installed. See attached piezometer log.

DEPTH	DRILLING METHOD
0-17'	4.25" HSA

WATER LEVEL MEASUREMENTS

DATE	TIME	SAMPLED DEPTH	CASING DEPTH	CAVE-IN DEPTH	DRILLING FLUID LEVEL	WATER LEVEL
12/20/06	4:30	17.4	17.0	17.0		16.4

BORING COMPLETED: 12/20/06

DR: LB LG: BL Rig: 27C

NOTE: REFER TO THE ATTACHED SHEETS FOR AN EXPLANATION OF TERMINOLOGY ON THIS LOG

Fig. 9.11: Typical Boring Log

The drilling and testing component included twenty one (21) soil borings along the access road and six (6) borings at the building site. The drilling and testing field work component included the packer tests at two (2) borings. A packer test isolates specific regions of the bedrock borehole with inflatable bladders (or packers) so that water levels can be determined. This test is useful in characterizing the amount of water inflow. A further description of the testing methods and results can be found in the completed report [12].

The drilling and testing component also included the installation of piezometer in the boreholes in the vicinity of the building. Piezometers are used to measure the level of water in the boreholes. In addition to single piezometers, three (3) boreholes received nested piezometers to better characterize the water levels. A further description of the testing methods and results can be found in the final report [12].

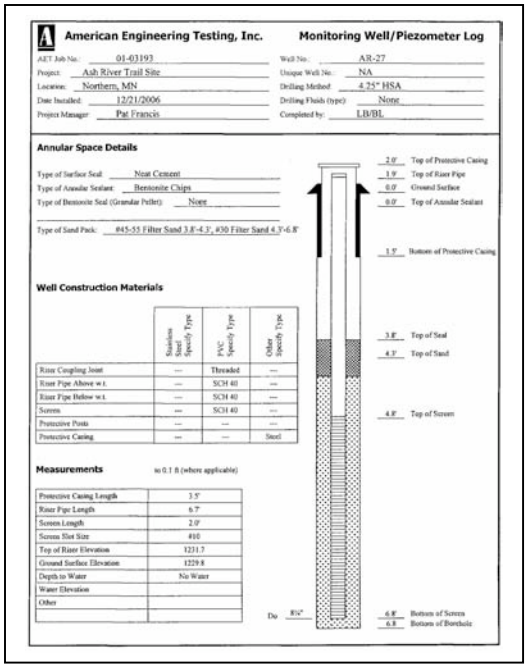
American Engineering Testing, Inc. Monitoring Well/Piezometer Log

AET Job No.: 01-03193 Well No.: AR-27

Project: Ash River Trail Site Unique Well No.: NA

Location: Northern, MN Drilling Method: 4.25" HSA

Date Installed: 12/21/2006 Drilling Fluids (type): None

Project Manager: Pat Francis Completed by: LB/BL

Annular Space Details

Type of Surface Seal: Neat Cement

Type of Annular Sealant: Bentonite Chips

Type of Bentonite Seal (Granular Pellet): None

Type of Sand Pack: #45-55 Filter Sand 3.8'-4.3', #30 Filter Sand 4.3'-6.8'

2.0' Top of Protective Casing
1.9' Top of Riser Pipe
0.0' Ground Surface
0.0' Top of Annular Sealant
1.5' Bottom of Protective Casing
3.8' Top of Seal
4.3' Top of Sand
4.8' Top of Screen
6.8' Bottom of Screen
6.8 Bottom of Borehole

Well Construction Materials

	Stainless Steel Specify Type	PVC Specify Type	Other Specify Type
Riser Coupling Joint	---	Threaded	---
Riser Pipe Above w.l.	---	SCH 40	---
Riser Pipe Below w.l.	---	SCH 40	---
Screen	---	SCH 40	---
Protective Posts	---	---	---
Protective Casing	---	---	Steel

Measurements to 0.1 ft (where applicable)

Protective Casing Length	3.5'
Riser Pipe Length	6.7'
Screen Length	2.0'
Screen Slot Size	#10
Top of Riser Elevation	1231.7
Ground Surface Elevation	1229.8
Depth to Water	No Water
Water Elevation	
Other	

Do 8¼"

Fig. 9.12: Typical Piezometer Log

Laboratory testing of the boring samples included Sieve analysis, hydrometer, moisture content, Atterberg Limits, R-value, Standard Proctor and consolidation tests were performed on soil samples selected by SEH. The results of the tests are included in the boring logs and data sheets.

The geophysical component of the investigation included two (2) major components. The first was a 3D Earth Resistivity Survey. This survey at the building site was undertaken to document the depth and characteristics of the solid overburden and underlying rock. This type of survey uses the electrical properties of the subsurface materials to characterize the resistivity and thus the structure.

The survey collected subsurface data from a 68,750 square foot area in the vicinity of the building site to determine the depth and condition of the overburden and bedrock. The survey included six (6) resistivity profiles collected at the site within a rectangular-shaped survey area. The 3D earth resistivity survey consisted of six (6), 550 ft lines with a 25 ft line separation.

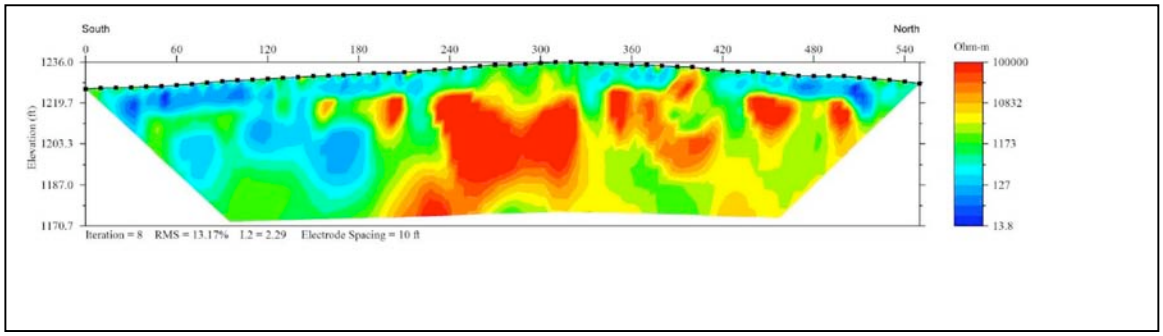

Fig. 9.13: Data collected from earth resistivity survey

In addition to the 3D Earth Resistivity Survey, shear wave seismic refraction survey was also performed. Seismic refraction surveys are used to identify the depths to various layer boundaries or to the bedrock surface. At this site, the survey consisted of two (2) crossing lines, each 220 ft in length. The lines were located in the southeast portion of the site between earth resistivity lines. Each line was comprised of twelve (12) seismic sensors (geophones) separated by 20 ft.

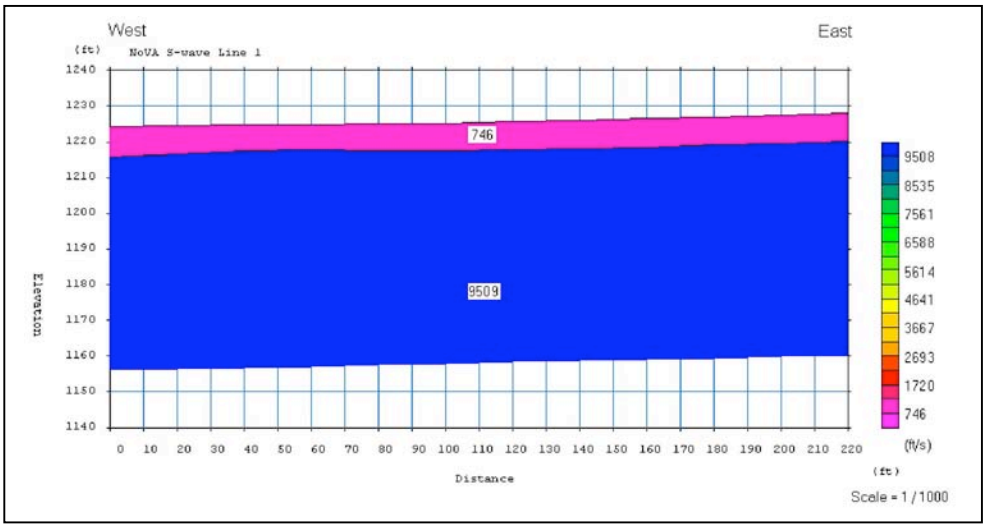

Fig. 9.14: Data collected from seismic refraction survey

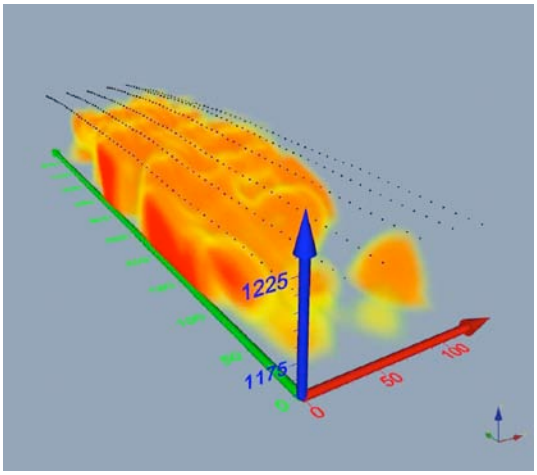

Figure 9.15: Seismic Refraction Visualization

The information collected from the earth resistivity survey and the seismic refraction survey was combined to provide a visualization of the subsurface features. Figure 9.15 at the left is one view of the visualization

The subsurface characterization program provided additional information of the subsurface conditions and reduced the unknowns. In addition, the subsurface investigation provided the basis for the design of the access road pavement, embankment, utility installation as well as foundation design, frost protection criteria and allowable bearing capacity [13].

No issues were noted during the site investigation activities since the Conceptual Design Report that would impact the EAW from being accepted by the Minnesota Environmental Quality Board as sufficient documentation for a determination that a full Minnesota Environmental Impact Statement will not be required. The Ash River EAW is available [14]. In July 2007, the University of Minnesota Board of Regents agreed to serve as the Responsible Government Unit submitting the EAW. The EAW will be published in the Minnesota Environmental Quality Board's Monitor in September 2007 which will start the thirty (30) day public comment period.

Following the example of the MINOS project done by DOE / Fermilab in the Soudan Mine, the State of Minnesota EAW will be accepted by the DOE as part of the federal Environmental Assessment for the Minnesota portion of the project.

No issues were noted during the delineation of the wetland or preparation of the Wetland Permit Application that would prevent the project from proceeding. It is expected that the University of Minnesota would serve as the submitting entity.

9.3 Advanced Technical Design of the Site Preparation Package.

9.3.1 Technical Design Criteria

The Site Preparation bid package consists of the work required to construct the access road and prepare the site for subsequent construction work including clearing and grubbing, rock excavation, establishing topsoil, clay and rock stockpile areas and creating a contractors staging area.

The Bright Star access road has been designed to serve as the primary means of access to the Ash River Site for construction, detector assembly and operations. The type and traffic volume dictate that the roadway be designed as an all weather road similar in construction to the Ash River Trail (St. Louis County Road 129). Listed below is the design criteria used in developing the roadway plan and profile

Design Criteria	AASHTO , Geometric Design of Highways and Streets, 2004	MnDOT Road Design Manual	Proposed Criteria
Functional Class	Local Rural	Collector Rural	Local Rural
Terrain	Rolling	Rolling	Rolling
Projected ADT	400-1500 veh/day	400-1500 veh/day	400-1500 veh/day
Design Speed	45 mph	45 mph	45 mph
Design Vehicle			
Stopping Sight Distance	360 ft	ft	360 ft
Stopping Sight Distance - eye height	3.5 ft		3.5 ft
Stopping Sight Distance - object height	2.0 ft		2.0 ft
Passing Sight Distance - eye height	3.5 ft		3.5 ft
Passing Sight Distance - object height	3.5 ft		3.5 ft
Stopping Sight Rate of Vertical Curvature (Crest)	61 ft	ft	61 ft
Stopping Sight Rate of Vertical Curvature (Sag)	79 ft	ft	79 ft
Passing Sight Distance	1625 ft		1625 ft
Passing Sight Rate of Vertical Curvature (Crest)	943 ft		943 ft
Minimum Longitudinal Grade		0.5%	0.5%
Maximum Longitudinal Grade	10%	8%-10%	10%
Cross Slope	2.00%	2.00%	2.00%
Maximum Superelevation	8%	6%	6%
Minimum Superelevation Runoff	192 ft		
Minimum Length of Tangent Runout	48 ft		
Minimum Radii - Horizontal Curve	587 ft		643 ft
Lane Width	10 ft	10 ft - 12 ft	12 ft
Shoulder Width	5 ft	5 ft	6 ft
Shoulder Cross Slope			4%
Foreslopes	1V:2H	1V:3H or 4H	1V:4H
Backslopes	Max. for slope stability	1V:3H	1V:3H
Clear Zone	7-10ft		7ft
Max. Longitudinal Grade Change			6%
Roadway Lighting			N/A
Pavement Marking			
Culverts			CMP w/PCC headwalls or CMP FES
Design Storm			25 yr.
		Minnesota Stormwater Manual	
Recharge		infiltration of up to 2-year, 24 hour storm	infiltration of up to 2-year, 24 hour storm
Water Quality		Rule 2 for Special Waters: 1.0"*IC*1/12	Rule 2 for Special Waters: 1.0"*IC*1/12
Channel Protection		12-hour ext. det. of 1-year 24 hour storm	12-hour ext. det. of 1-year 24 hour storm
Overbank Flood Protection		10-year post to pre-development runoff	10-year post to pre-development runoff
Extreme Storm Protection		100-year post to pre-development runoff	100-year post to pre-development runoff

Design Criteria Table 12/2/2006

Figure 9.16: Design Criteria for Access Road

9.3.2 Site Preparation Overview

The Site Preparation bid package consists of the work required to construct the access road and prepare the site for subsequent construction work including clearing and grubbing, rock excavation, establishing topsoil, clay and rock stockpile areas and creating a contractors staging area.

The access road portion of the work consists of a new road from St. Louis County 129 to the Ash River Site. The road generally follows the route of the existing logging trail but has been re-aligned to accommodate the anticipated 53-foot trailer truck traffic.

The road right of way will include an underground utility corridor to bring power and communication lines to the site. The Ash River site requires a power upgrade and the local electrical cooperative will upgrade the electric service to the site by replacing an existing transformer at the Kabetogama substation, replacing existing insulators and step down transformers along the route as well as installing a new transformer and related accessories at the project site. The project bears the cost for this electrical work.

9.3.3 Site Preparation Details

The Bright Star access road portion of the site preparation work is based on design criteria obtained from Association of State Highway and Transportation Officials (AASHTO) and the Minnesota Department of Transportation (MDOT). In addition, the existing site features and intended use of the road were incorporated into the design. Shown below in figure 9.17 is a representative sample of the completed documents. The complete set of the drawings and specs is available [15].

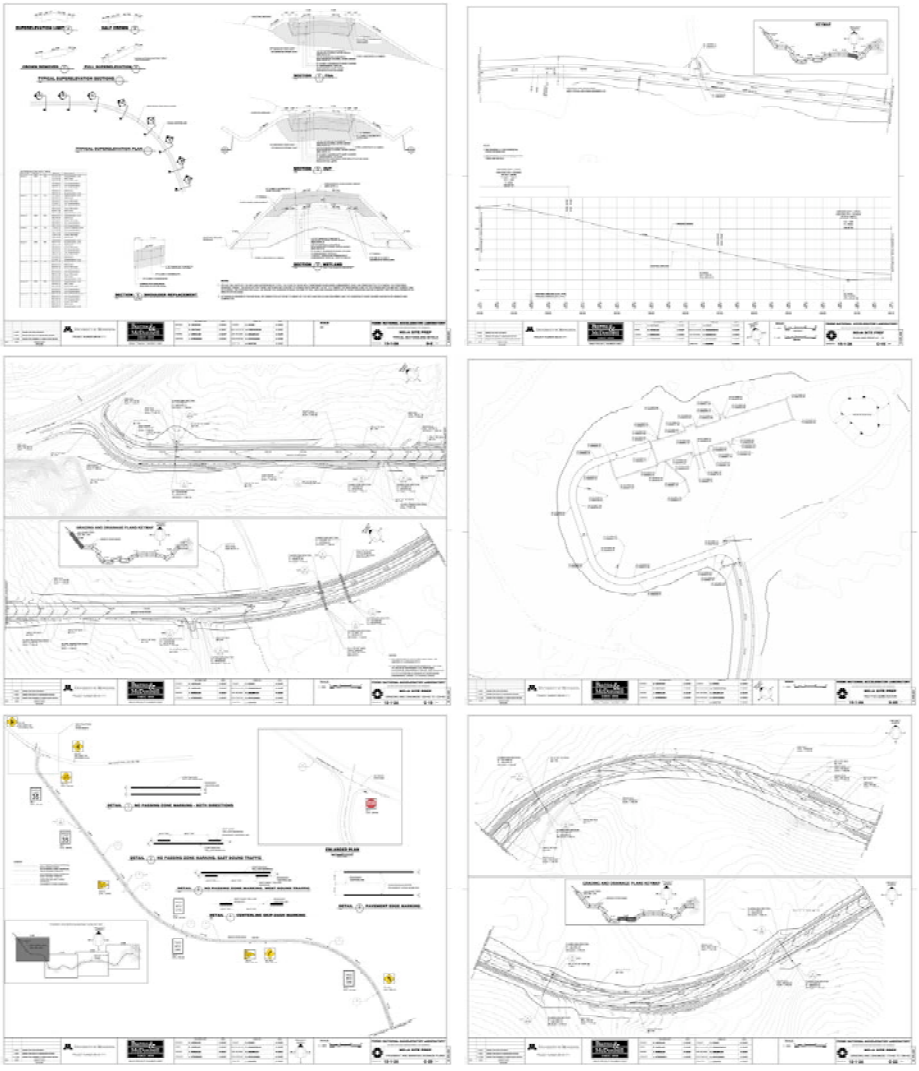

Figure 9.17: Representative Sample of Site Prep Documents

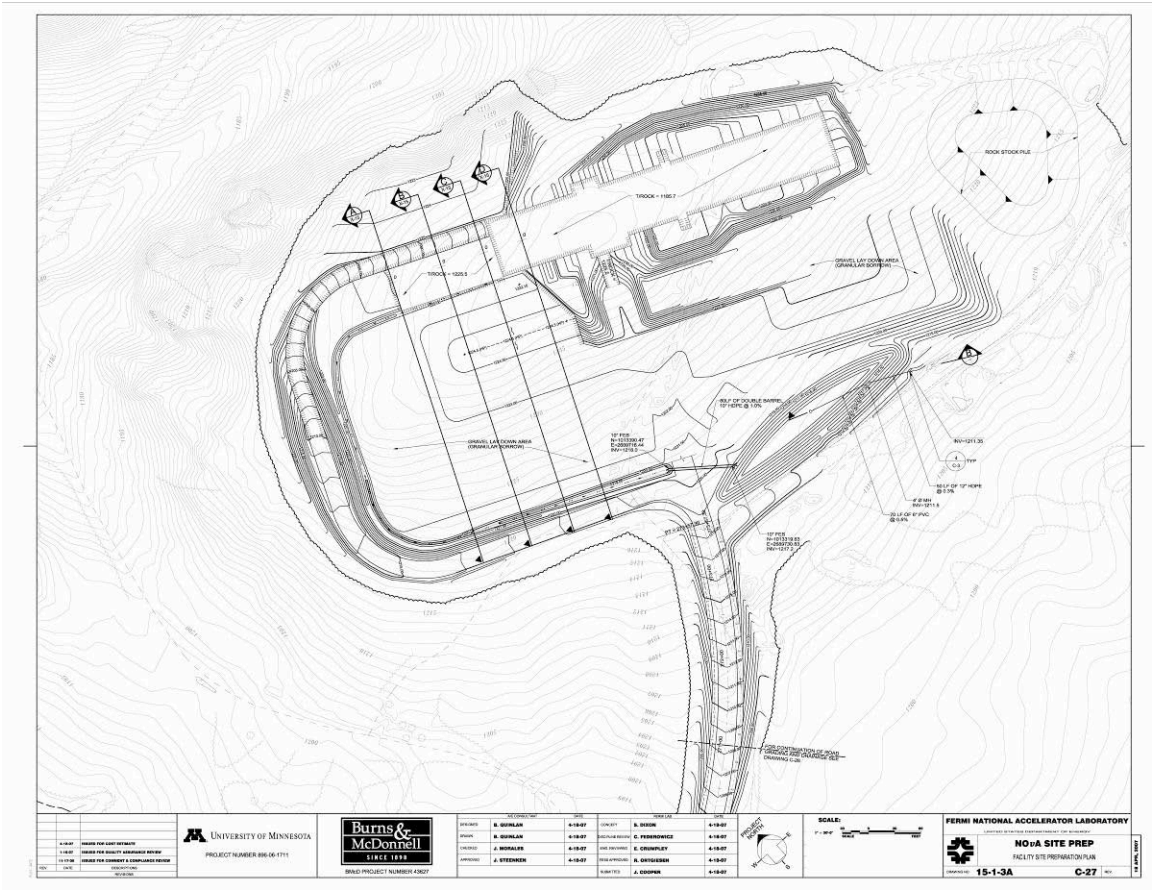

Figure 9.18: Far Detector Building site excavation

In addition to the construction of the Bright Star access road, the Site Preparation package contains the work required to prepare the project site for the construction of the Far Detector Building. This includes general clearing and grubbing of the facility site, stockpile areas and subcontractor staging areas as well as rock excavation at the Far Detector Building site. Figure 9.18 below depicts the rock excavation plan at the Far Detector Building site.

9.3.3 Design changes in the Site Preparation Package since the Conceptual Design Report

The design of the Site Preparation Package has been revised to incorporate information obtained from the site investigation work accomplished in the summer and fall of 2006. This has resulted in an increase in the project site to accommodate anticipated stockpile and staging areas. In addition, the access road alignment has been optimized to accommodate the required truck traffic and site features.

Representatives of the University of Minnesota were involved in the advanced technical design of the Site Preparation package. This coordination included telephone conversations and presentations in the offices of the Building Code Division of the University of Minnesota [16]. The input from the University of Minnesota is considered vital to the continuity of the design throughout the subsequent phases of the project since the university will coordinate the work as part of their Cooperative Agreement responsibilities.

In April 2006, members of the project team met with representatives of the Forest Capital Partners, Minnesota Department of Natural Resources and Voyageurs National Park to discuss alternate access road routes that would lessen the impact on surrounding stakeholders [17]. The consensus was that the new access road should follow the existing road as close as possible to avoid unduly impacting the adjacent land.

In the spring of 2006, the firm of Burns and McDonnell was retained to complete an independent cost and schedule review of the CDR design. This study indicated that the estimated cost of the site and building were greater than the in-house estimate completed for the CDR. The project team reconciled the two estimates and undertook a value management exercise to manage the estimated costs. The schedule component of the review indicated that a two year construction period was reasonable.

A detailed topographic survey of the access road and project site was completed by Hanson Professional Services in the spring of 2006. This survey documented the ground features to produce one foot contours.

Changes in the access road routing and building location required an updating of the Environmental Assessment Worksheet (EAW) for the project site and access road. The field work for this updating was completed in the summer of 2006 and the updated EAW was completed by Short Elliot Hendrickson in May 2007.

In the summer of 2006, the firm of Short Elliot and Hendrickson was retained to delineate and document the wetlands along the access road and project site. This was used as input for road routing and building siting in addition for use in developing the required mitigation in support of the EAW updating and to prepare a U.S. Army Corps of Engineers Wetland permit.

In order to provide a better understanding of the subsurface conditions along the access road and project site, the firm of Short Elliot and Hendrickson was retained in the summer of 2006 to perform a subsurface investigation. This investigation included a comprehensive program of field work of soil borings, rock borings, pump test and packer tests as well as lab work required to analysis and document the conditions. In addition, a 3D resistivity survey was completed of the area around the Far Detector Building site for the purpose of mapping bedrock fracture zones.

As part of the internal quality assurance procedure, the Site Preparation Package underwent two (2) formal reviews. These reviews focused on the appropriateness of the proposed systems, impacts on existing systems and operations, specific technical requirements to be incorporated into the design and compliance with best and required practices of authority having jurisdiction. The first of these reviews was completed in November 2006 was titled “Comment and Compliance Review” and included representatives of the various project WBS groups as well as the University of Minnesota code officials as was based on a design that was 40% complete. The second review, in January 2007, was a “Quality Assurance Review” and was sent to the same review team as the earlier review [18].

9.3.4 Work Remaining to Complete the Site Preparation Package.

The design of the Site Preparation Package is approximately 95% complete. Final adjustments to road alignment based on feedback from the EAW and wetland permitting process could impact the current design. In addition, slight adjustments to the building location based on bedrock topography may require modifications.

Prior to beginning construction, the road permitting process with the Corps of Engineers will need to be completed. In addition, EAW will need to be submitted to the Minnesota Environmental Quality Board and proceed through the public comments phase in parallel with the federal EA. Finally, the project will need DOE approval and a FONSI for the Minnesota work.

9.4 Design of the Far Detector Building at Ash River

9.4.1 Technical Design Criteria

The technical design criteria for the Far Detector Building (FDB) have been developed based on physics-driven requirements for the detector assembly and operation.

Listed below are the requirements for key components of the building. Where available, a reference to a NOvA note is included

- Support Functions Requirements - NOvA-doc-1192
- Loading Dock Requirements – NOvA-doc-1159
- Assembly Area Requirements – NOvA-doc-1159
- Moveable Access Platform Requirements – NOvA-doc-1155
- Detector Electronic Requirements – NOvA-doc-919
- Computer Requirements – NOvA –doc-1141
- Scintillator Transfer Station – Space for four (4) trucks under canopy and parking for an additional (2) trailers.
- Parking for 8-10 vehicles during normal operations – NOvA-doc-1192
- Scintillator Containment – 100% containment.
- Backup Electrical Power – Critical systems only.
- Structural Systems
  Design Loads shall be as listed below and in accordance with the Fermilab Engineering Standards Manual:
  - Floors shall be designed to support a concentrated load of 2000 lbs. applied to an area 2'-6" x 2'-6".
  - 150 psf or weight of actual equipment.
  - Live Load Reduction: No live load reductions are permitted for roof or mechanical equipment areas.
  - Handrails and Guardrails: Top rail = 50 plf or 200 lb. concentrated load (applied any direction – not simultaneous) infill area = 50 lbs. on an area 1'-0" x 1'-0" (the above loads are not superimposed)
- Mechanical Systems: The HVAC systems will conform to ASHRAE 90.1, ASHRAE 62 and applicable NFPA requirements and applicable sections of the Fermilab Engineering Standards Manual Mechanical systems and controls will be further investigated during subsequent phases in accordance with ASHRAE 90.1 and Federal Life Cycle costing analysis.
- Plumbing: All plumbing work to be installed in accordance with State of Minnesota and St. Louis County Plumbing Codes, ordinances and regulations.
- Electrical Systems: Electrical system design will comply with applicable sections of National Electric Code and applicable sections of the Fermilab Engineering Standards Manual.
  - Primary Supply 480/277 V, 3 phase, 4 wire
  - Secondary Supply Power Distribution: 120/208 V, 3 phase, 4 wire
  - Lighting: 277 V
  - Illumination Levels:
    Mechanical Spaces: 30 fc.
    Computer Room and Office Areas: 50 fc.
    Loading Dock: 30 fc general lighting supplemented by task lighting
    Assembly Area: 30 fc general lighting supplemented by task lighting
    Detector Enclosure: 30 fc general lighting .
    Interior Emergency Lighting: 5 fc.

- Fire Protection Systems: Fire Alarm/Fire Suppression systems shall be designed in accordance with the applicable sections of the Fermilab Engineering Standards Manual.
    - Fire alarm systems shall be designed with a minimum standby power (battery) capacity. These batteries shall be capable of maintaining the entire system in a non-alarm condition for 24 hours, in addition to 15 minutes in full load alarm condition. The most commonly used NFPA standards relative to fire alarm systems are: 70, 72, 90A, and 318.
    - Water mist fire suppression systems will be installed throughout the Detector Enclosure, Assembly Area, Loading Dock and other areas that will contain scintillator. These systems will be designed in accordance with NFPA 11, NFPA 13 and NFPA 16.
    - Areas of the facility that will not contain scintillator will include automatic sprinkler systems designed and installed in accordance with NFPA 13.
    - Exit stairways will contain a dry standpipe system in accordance with NFPA 14.
- Sustainable Building Design: Sustainability is broadly defined as the design and implementation of projects to simultaneously minimize their adverse environmental impacts, maximize occupants' health and well-being, and improve bottom line economic performance. The concept of sustainability is a desirable approach to development that recognizes that resources are limited, and that there is a responsibility of the present generation to preserve resources for future ones. The United States Green Building Council (USGBC) has developed the Leadership in Energy and Environmental Design (LEED) standard to provide guidance for builders who wish to incorporate sustainable elements into their projects. LEED for new construction is a set of specific and quantifiable measures, each of which confers a credit towards certification of a project as a "LEED-certified" building. While this project is not intended to become a certified building, the project processes and each project element will be evaluated during design to reduce their impact on natural resources without sacrificing program objectives. The project design will incorporate maintainability, aesthetics, environmental justice and program requirements to deliver a well-balanced project [19].
- A project of this scale has the potential to include an overlap of systems and construction. In order to delineate the specific area of a responsibility for each WBS section, a responsibility matrix has been developed that describes the system and the area of responsibility for each WBS [20].

9.4.2 Overburden Design

The overriding design requirement for the Far Detector Building is the cosmic overburden [21]. The overburden is defined as the ability of the material to shield the detector components from cosmic rays. Several methods of achieving the overburden have been investigated and the current design has been optimized to balance the amount of material with the shielding capacity. A shield of about 14 radiation lengths is realized in this design [21].

The overburden design is based on a system maximizing standard construction methods while minimizing exotic materials or techniques. To this end, the design is based on a combination of precast concrete, cast-in-place concrete and a small amount of loose barite material. Barite, in the form of barium sulfate, has been selected since it provides an increased shielding benefit over concrete or granite shot rock. The combination concrete/barite roof system described below has been designed to provide an equivalent of 9.86 feet of earth shielding.

From a constructability point of view, the critical shielding location is the roof of the Detector Enclosure. The long span and the weight of the overburden material have driven the structural solution for this area. The roof is designed as a composite structural member consisting

of a 2.5 feet precast concrete plank that spans the width of the Detector Enclosure capped with a 1.5 feet depth of cast-in-place concrete. Once cured, this composite structural member will be topped with insulation, roof membrane and 0.5 feet of loose barite roof ballast. The precast plank will serve as the finished ceiling of the Detector Enclosure as well as the formwork for the cast-in-place concrete. Figure 9.19 below depicts the typical roof construction detail.

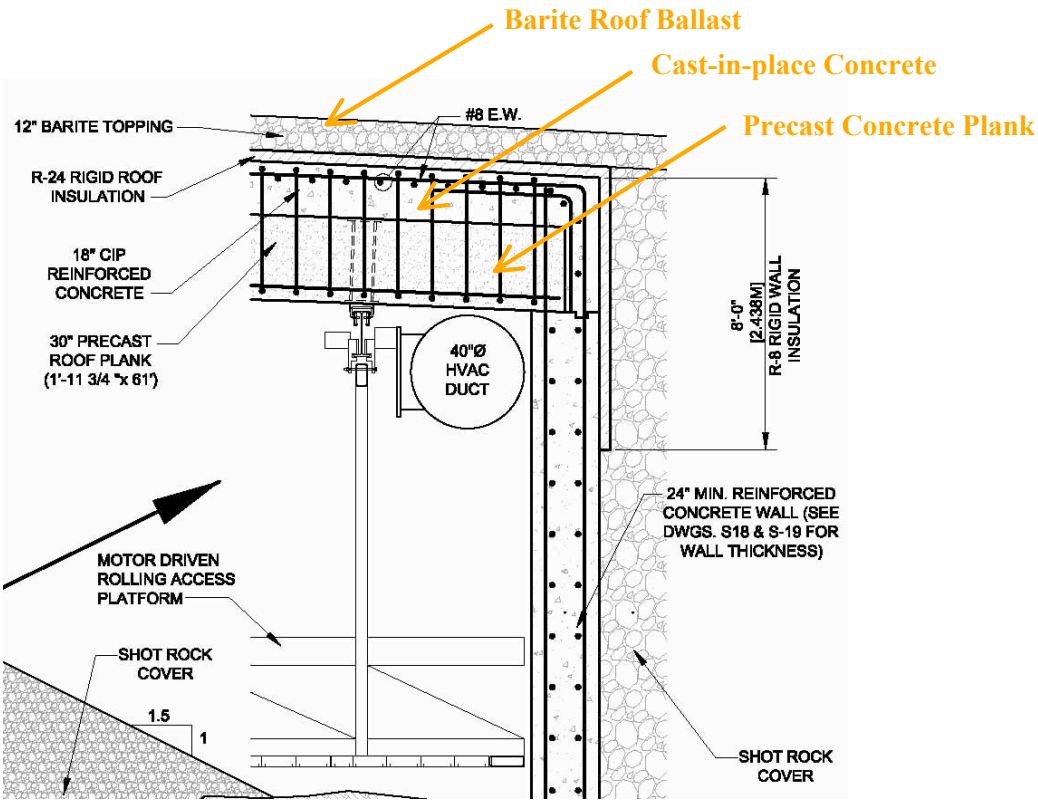

Fig. 9.19: Detail at Detector Enclosure Wall/Roof Interface showing roof construction

Those portions of the Detector Enclosure walls that extend above grade will be constructed of normal weight cast-in-place concrete and backfilled with loose granite shot rock as depicted in figure 9.20 at right. This approach utilizes conventional construction techniques and incorporates excavated material. The granite shot rock will be installed at a slope to minimize the amount of material used while providing a maintainable slope. The loose barite ballast will extend from the roof to cover the upper level of the berm.

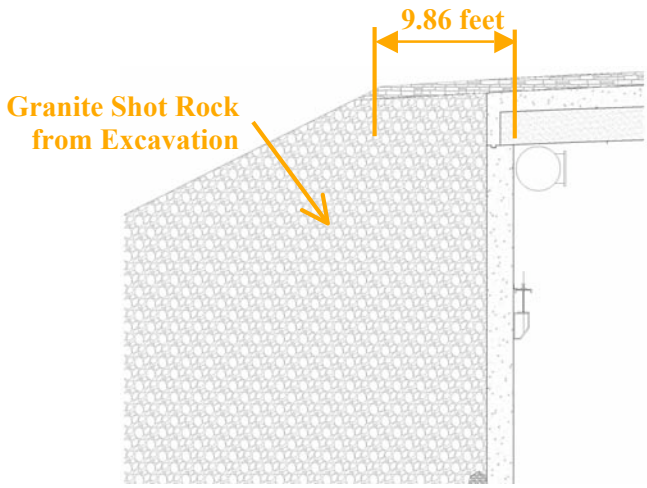

Fig. 9.20: Detail at Detector Enclosure Wall showing shielding thickness

9.4.3 Below Grade Areas

The below grade areas of the Far Detector Building consist of the Detector Enclosure and adjacent Assembly Area. The two areas combined are a single cast-in-place concrete enclosure 113.8 meters long, 20.4 meters wide and 21.4 meters high (373.25 feet long, 63 feet wide and 71 feet high) shown in Figures 9.21 and 9.22.

.

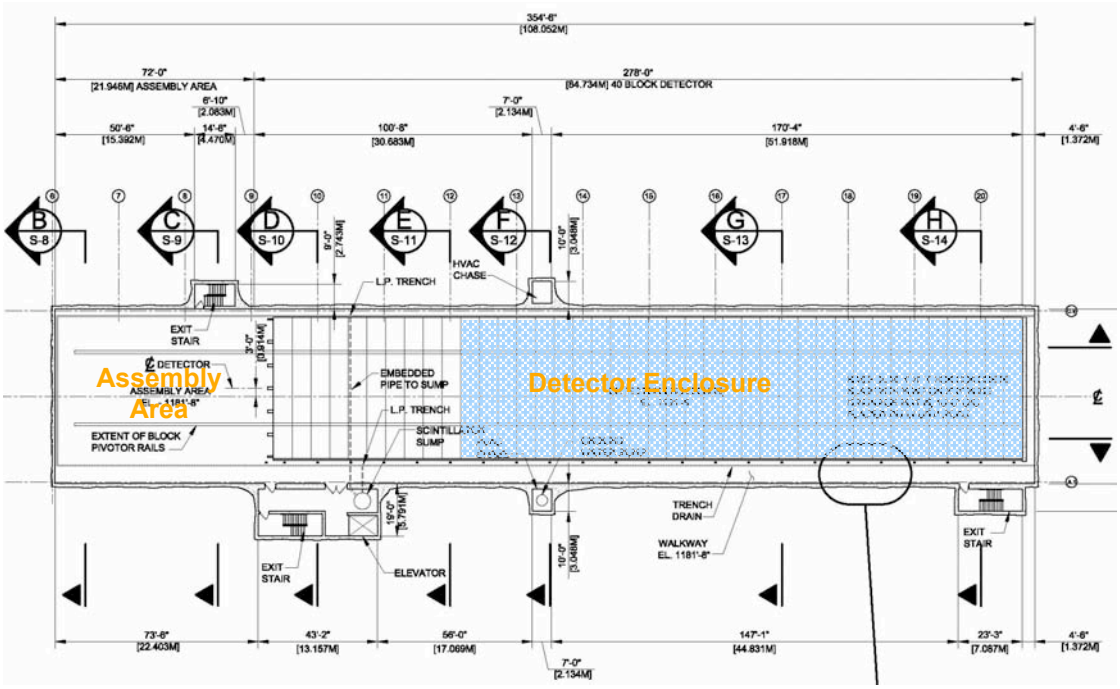

Fig. 9.21: Plan view showing relationship of the Assembly Area (at left) and the Detector Enclosure (at right) with the Far Detector indicated in blue.

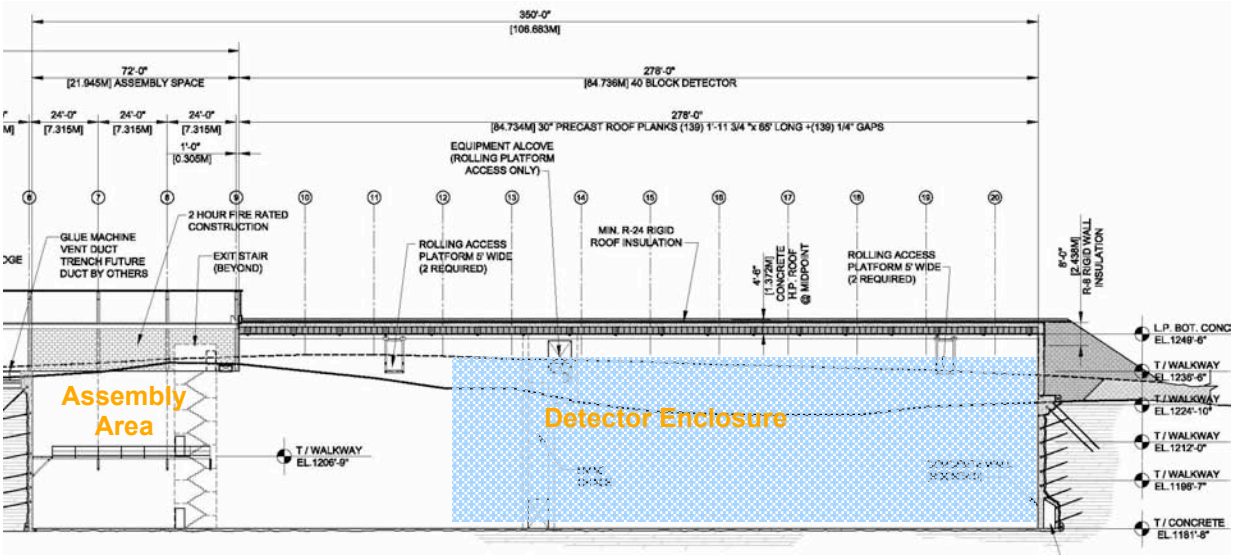

Fig. 9.22: Longitudinal section showing relationship of the Assembly Area (at left) and the Detector Enclosure (at right) with the Far Detector indicated in blue.

The Detector Enclosure (90 meters long, 20.4 meters wide and 21.6 meters high) will house the completed Far Detector, provide access to the top and sides and support installation and operation of the detector components. The Detector Enclosure is sized to accommodate up to a 20 kiloton detector.

The Assembly Area (20.1 meters long, 20.4 meters wide and 21.6 meters high) will provide space for the equipment and devices required to assemble the detector. This includes the block assembly device and associated access equipment.

One goal of the project is to provide for 100% secondary containment of the scintillator in the event of a catastrophic loss of the detector. In order to accomplish this project goal, the firm of Burns and McDonnell was retained to investigate possible alternates to providing secondary containment for the detector [22]. The concepts contained in the report were incorporated into the design.

The primary containment for the scintillator is the PVC cells of the detector. The walls and floor of the Detector Enclosure and Assembly Area will provided the secondary containment. These surfaces have been designed to contain 100% of the liquid scintillator as well as the fire protection foam that would be used in the event that a full release of water occurred during a complete release of the scintillator. The surfaces will be coated with a sealant to provide a non-porous surface. The walls and portions of the floors will be left exposed to view for inspection purposes. The bottom of the detector will be separated from the concrete floor by the steel "pallet" so that the detector will not be in direct contact with the floor. This separation will prevent scintillator from being forced into the concrete surface. Any scintillator that escapes the primary containment of the detector will be atmospheric pressure and will not be forced into the concrete surface. A trench drain will be embedded in the floor of the Detector Enclosure that will allow for the collection of spilled scintillator. These drains will be sloped to allow any spilled scintillator to be routed to a scintillator collection basin.. The scintillator collection basin will be isolated from the groundwater sumps and will be monitored for fluid levels. No automatic discharge from the scintillator collection basin will be provided in order to prevent unintended release of scintillator to the environment.

The floor of the Assembly Area and Detector Enclosure will accommodate the steel "pallet" used as the base of the detector. These pallets will separate the block from the concrete floor and serve as the "witness zone" for the space beneath the detector as a component of the secondary containment system.

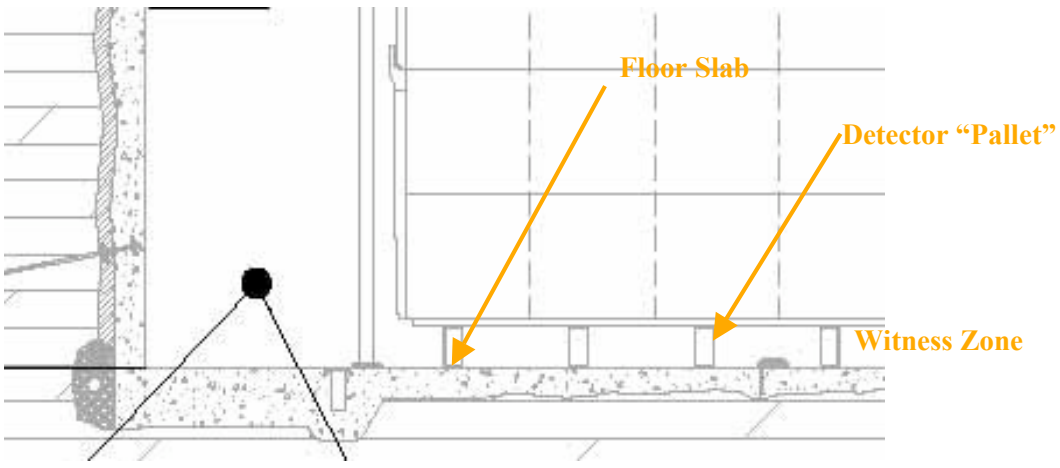

Fig. 9.23: Detail at Detector Enclosure floor slab

The Detector Enclosure and Assembly Area are serviced by three (3) code compliant exit stairs that provide two (2) means egress for each level of the below grade enclosures. These stairs also serve the Detector Enclosure access walkway system. One (1) standard sized elevator, located on the west side of the building will provide vertical access to all levels of the walkways.

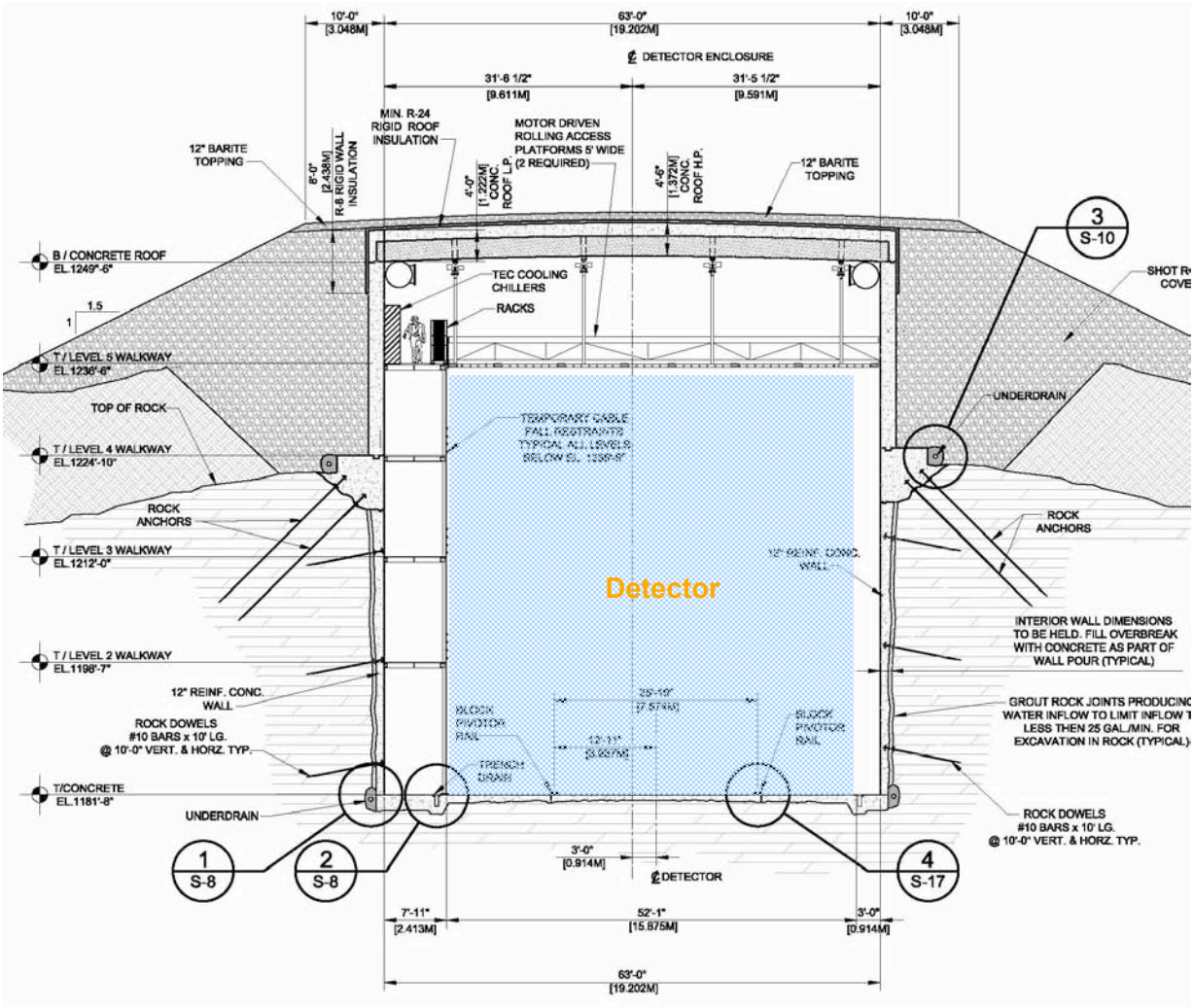

Fig. 9.24: Typical Cross Section of the Detector Enclosure

Figure 9.24 shows a typical cross section view of the Detector Enclosure. The below grade areas will be excavated to approximately 12 meters (40 feet) below grade to accommodate existing terrain as well as provide a below grade containment volume sized to contain the 100% of the liquid scintillator and a full discharge of the fire suppression system. The material removed during excavation activities will be stockpiled on site and used, as appropriate, as backfill and for site improvements

The Assembly Area is sized to support the block assembly device and related components for the assembly of the detector. The Assembly Area is adjacent to the at-grade Service Building and is served by a 10 ton capacity overhead bridge crane. The NOvA detector is assembled from right to left in Figures 9.21 and 9.22, and the Assembly Area is sized to accommodate the apparatus required to assemble the detector. This equipment includes a block assembly device, adhesive dispenser and related support devices described in Chapter 17. This assembly apparatus requires approximately 66 feet (20 meters) of floor space north of the detector face being assembled.

A subsurface investigation [1] has indicated that the top of that the site has 5 – 15 feet of soil overburden on top of granite to a depth of at least 60 feet. Based on these conditions, the walls of the Detector Enclosure and Assembly Area have been designed to be cast-in-place concrete tied to the rock below. This system provides a uniform surface suitable for treatment and use as a secondary containment for the liquid scintillator.

The roof of the Detector Enclosure is designed as a composite structural member consisting of a 2.5 feet precast concrete plank that spans the width of the Detector Enclosure capped with a 1.5 feet depth of cast-in-place concrete. Once cured, this composite structural member will be topped with insulation, roof membrane and 0.5 feet of loose barite roof ballast. The precast plank will serve as the finished ceiling of the Detector Enclosure as well as the formwork for the cast-in-place concrete.

The above grade portion of the Assembly Area is designed as a pre-engineered portion of the adjacent at-grade Service Building.

The Assembly Area requires strict environmental control. The requirements are a range of temperature that is +/- 5 degrees Fahrenheit for a 20% delta relative humidity range or no variance in space temperature at 35% delta relative humidity range. The design assumes a summer temperature set point of 70 degrees +/- 5 degrees Fahrenheit at 50% relative humidity and a winter temperature set point of 70 degrees +/- 5 degrees Fahrenheit at 15% relative humidity. In addition, the adhesive used to assemble the detector requires a unit capable of providing conditioned 100% outside air.

The Detector Enclosure requires a stable environment for the normal operation of the detector. The design assumes a summer temperature set point of 72 degrees +/- 5 degrees Fahrenheit at a relative humidity compatible with a 50 degree Fahrenheit dewpoint and a winter temperature set point of 72 degrees +/- 5 degrees Fahrenheit at 15% minimum relative humidity.

The heating, ventilation and air conditioning (HVAC) systems in the Assembly Area and Detector Enclosure will conform to ASHRAE 90.1, ASHRAE 62 and applicable NFPA requirements and applicable sections of the local codes and ordinances.

Since a portion of the detector will be operational while the remaining detector is being assembled, a temporary wall will be installed to isolate the two conditioned spaces. This wall will be removed during the final stages of detector assembly and reinstalled during gluing operations.

The mechanical systems in the Detector Enclosure and Assembly Area have been designed to support the installation and operation of the detector. The HVAC systems will conform to ASHRAE 90.1, ASHRAE 62 and applicable NFPA requirements and applicable sections of the local codes and ordinances.

The Detector Enclosure will be provided with an automatic water mist fire suppression system installed in accordance with NFPA 11, NFPA 13 and NFPA 16 Fire Alarm systems will be installed in accordance with NFPA 72 To prevent accidental discharge, the activation of the suppression system will occur in a two step process. The first step includes an air sampling system that upon signal of smoke detection will signal an alarm and notify emergency personnel. The second step includes a line type heat detection system that upon heat will signal an alarm, notify emergency personnel, shunt trip the HVAC equipment serving the spaces and activate the fire suppression system. The system has been designed to provide an application rate of per

minute per square feet over the detector for a discharge time of 15 minutes. The depth of the below grade areas provide a containment volume sized to hold 100% of the NOvA detector liquid scintillator plus a full discharge of the fire suppression system.

Electrical service to the Detector Enclosure and Assembly Area will provide general house power and lighting for the installation and operation of the detector as well as power for the detector components.

Code required emergency lighting and exit lighting will be provided in the enclosure.

9.4.4 Access to the Detector

Access to the sides of the detector is provided by means of a steel framed access system that runs the length of west side of the detector. The design includes four (4) levels of access walkways along the side of the detector. Each level of the system will be accessible from the exit stairs as well as the elevator located on the west side of the Detector Enclosure Figure 9.25 indicates a typical column bay at the catwalk level with the service platform adjacent to detector.

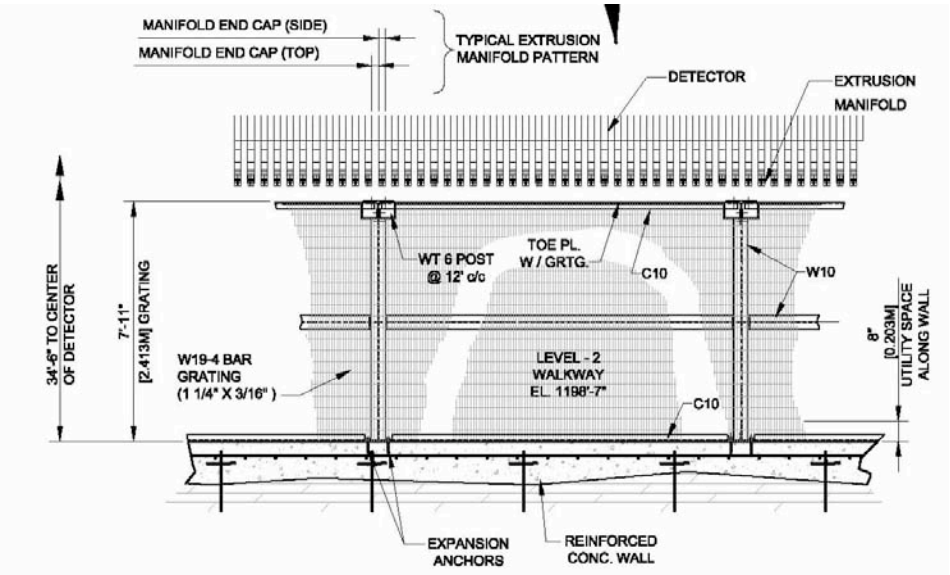

Fig. 9.25: Typical Catwalk bay

Access to the top of the detector is provided by means of two (2) moveable access platforms (MAP) that will span the width of the detector. Access to the MAPs will be from the upper access walkway level. These platforms will serve for the installation of the detector components as well as normal operation of the detector. These platforms, similar in construction to window washing scaffolds will be designed to support up to 1,000 pounds of personnel and equipment [23]. Access to the moveable access platforms will be by way of gated openings in the handrail along the inner edges of the upper catwalks. These openings will be spaced at approximately 50 feet (15.25 meters).

The uppermost access walkway (elevation 1236'-6") will provide space for the majority of equipment used to support detector operations. This equipment includes electronic racks, chillers, data connections as well as associated piping and cable trays.

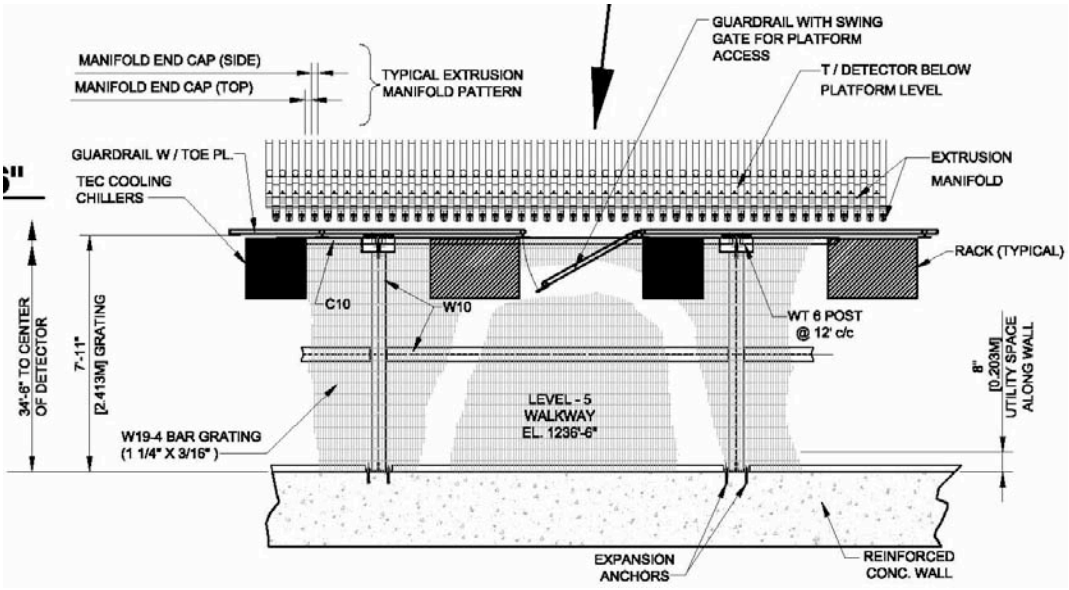

Fig. 9.26: Typical Upper Level Access Walkway Bay

9.4.5 Detector Enclosure Support Spaces

Adjacent to the Detector Enclosure are the support spaces requiring close proximity to the detector components. These spaces include the Control Room, Computer Room and Electrical Equipment Room. These spaces are constructed of cast-in-place concrete and contained within the shielding overburden.

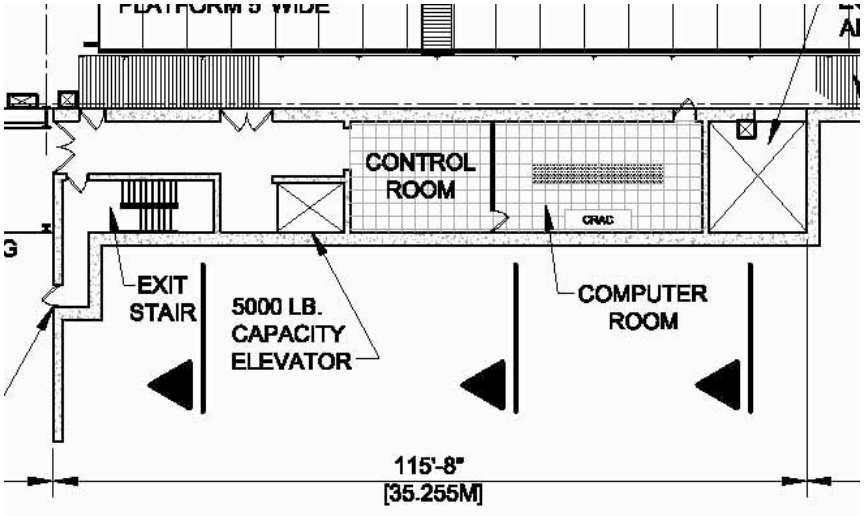

Figure 9.27: Floor Plan of Computer Room and Control Room

The Computer Room (32’ long by 15’ wide) will provide space for six (6) computer racks of up to 8 kW each and related equipment. For the purposes of this TDR the following computing node criteria was used for developing the space:

- A computing node has an electrical draw of 2.4 amps per node at 120 volts;
- A typical rack will hold up to 40 nodes, but will not exceed 8 kW/Rack;
- A typical rack requires five (5) 30 amp electrical circuits;
- One (1) 120v convenience outlet is required for each rack;
- A typical rack requires a floor area of 2’x3’-0”;
- The operating temperature of the computing rooms is 70 degrees Fahrenheit (+/- 5 degrees);
- 40%-45% relative humidity is required;
- Standard filtration is acceptable
- Uninterruptible Power Supplies (UPS) for a total 10 kW will be needed in the Computer Room;

The above requirement describes the current computing technology used in recent computing facilities at Fermilab. As the technology continues to evolve different computer configurations and power factors will likely be employed to respond to the physic requirements. While the Computer Room will be provided with the power and cooling infrastructure to serve the known requirements, it will be possible to reconfigure the space to meet the future needs as long as the upper limits of electrical power and cooling capacity are not exceeded.

The anticipated computing Uninterruptible Power Supply (UPS) load for the Computer Room is 10 kW. A 15 kVA/12 kW system will provide approximately 10 minutes of battery backup for the computing equipment. This will allow an orderly shutdown of the computer equipment in the event of an unscheduled power disruption. The UPS system including batteries will be located in the Electrical Equipment Room.

The cooling for the Computer Room will be accomplished through a Computer Room Air Conditioning (CRAC) Unit discharging into a common below-floor plenum. The system will utilize high volume airflow tiles to create a “cold aisle” on one side of the computer racks. A corresponding “hot aisle” on the opposite side of the computer racks will collect the hot air and route it to the ceiling for return to the CRAC units. This arrangement will allow for reconfiguration of the computers if needed. The volume of air moved in this scenario requires a 2’-0 high raised access floor. Computer Site Engineering notes this system as a best practice for providing reliable cooling for server farms [24].

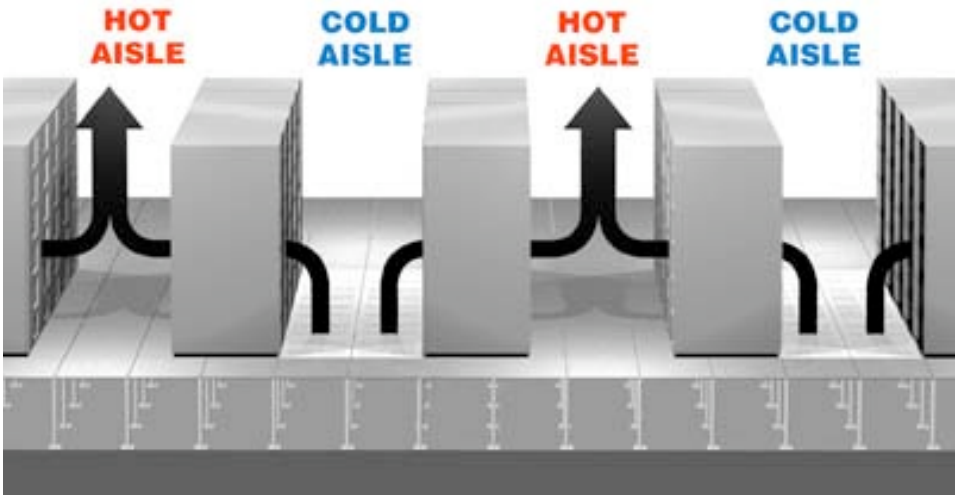

Figure 9.28 : Computer Room Cooling Strategy

One (1) 30 Ton CRAC unit will be installed in the Computer Room. The unit will be air-cooled, downflow, compressorized systems. This will provide cooling for approximately 78 kW of heat load. The unit will discharge the cooled air beneath the raised access floor for distribution throughout the room. Return heated air will be taken from the ceiling space. The matching remote air-cooled condenser unit will be located west of the building on a cast-in-place concrete slab to facilitate maintenance. The CRAC unit will be monitored by a Liebert SiteLink system.

The Computer Room will have a raised access floor system with a 2'-0" clear height to provide plenum space. This floor system will be at the same elevation as the adjacent floor areas to eliminate ramping for access to the space. The roof structure will remain exposed. This will provide a 12'-8" floor-to-ceiling height.

The raised access floor in the Computer Room will have under floor fire detection system. Sprinklers will be installed beneath the roof structure to protect the room.

Adjacent to the Computer Room will be the Control Room. The Control Room (27' long by 15' wide) will provide space for monitoring and operation of the detector. Space for four workstations and a conference table have been provided. The Control Room will be similar in construction type to the Computer Room and has been designed to allow for expansion of the Computer Room should the need arise.

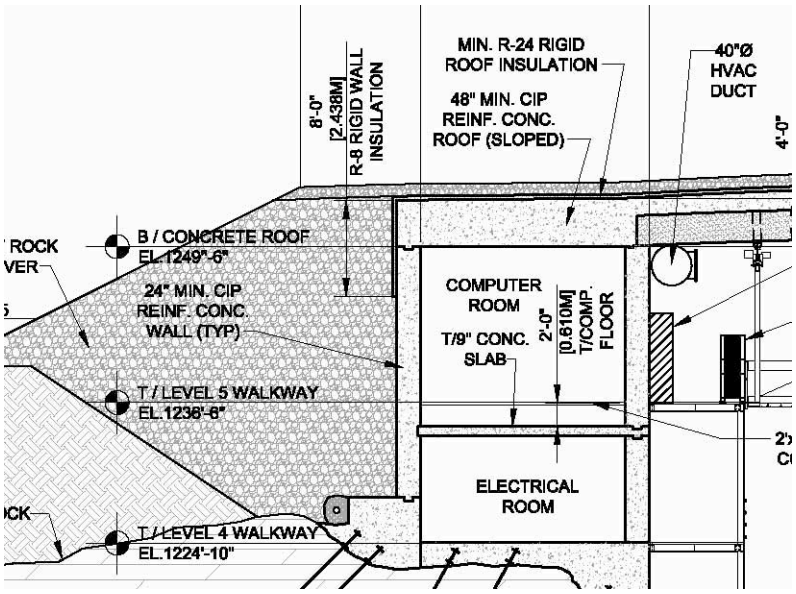

Figure 9.29: Section showing relation of Computer Room and Electrical Equipment Room to Detector Enclosure

The Computer Room and Control Room are located off the 1236'-6"Level access walkway with access to the exit stair and elevator. This will allow ease of access to the detector components located on the 1236'-6" walkway and reduce cable lengths for the experimental equipment.

Beneath the Computer Room/Control Room is the Electrical Equipment Room. The Electrical Equipment Room (72' long by 16' wide) will house the switchgear required for incoming electrical service, transfer switches, and related equipment. The Electrical Equipment Room will incorporate space for incoming telephone/data communication service equipment. This equipment will consist of space adequate for two (2) computer racks and

associated equipment and has been sized based on input from the local telecommunication company [25].

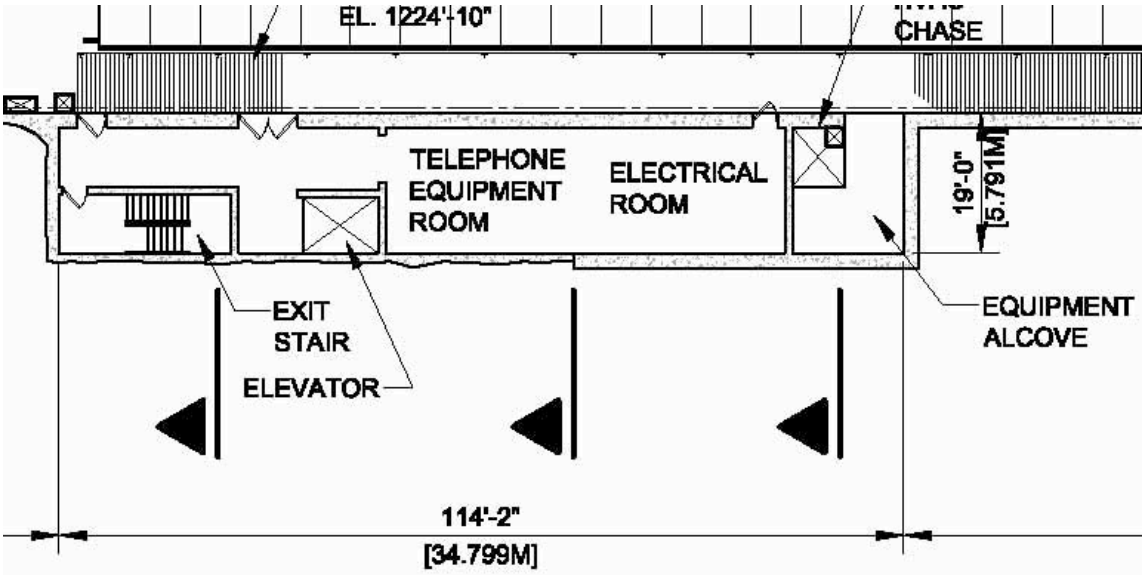

Figure 9.30: Floor Plan of Electrical Equipment Room at Grade

The design includes the provision for standby and emergency generators for the critical systems in the building. The design includes two (2) 125 kvA emergency generators. One generator will provide emergency power for life safety systems while the other will power elevators, sump pumps and building heating. These generators will be housed in Generator Rooms adjacent to the at-grade entry to the Detector Enclosure. These generators will use propane as a fuel source. The power will be brought into the Electrical Equipment Room via a new concrete encased power duct bank. The duct bank will be routed to reduce the future impact on utilities.

At Grade Areas

The at grade portion of the facility consists of a Service Building (121'-6"long by 71'-0" wide) that houses support spaces required to deliver, assemble and operate the Far Detector. Figure 9.31 below indicates the floor plan of the Service Building.

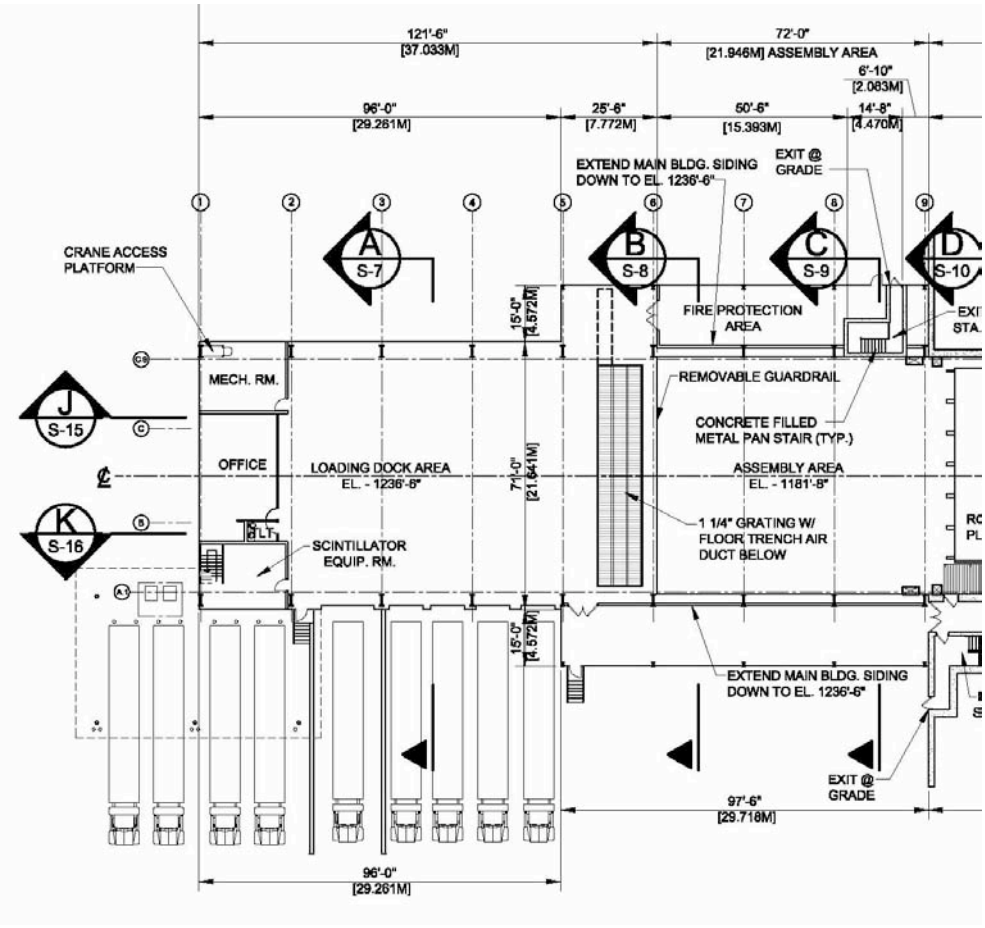

Figure 9.31: Service Building Floor Plan

The Service Building spaces can be broken down into five (5) main areas as described below.

The Loading Dock Area has been designed to accommodate deliveries of detector components, liquid scintillator and related materials. The Loading Dock Area will have four (4) dock locations for recessed loading dock along the west side and one (1) dock at-grade to allow trailers to be located inside the building and underneath the coverage of the overhead cranes. The requirements for the Loading Dock Area have been taken from technical requirements provided by the WBS 2.9 group [26]. The design solution includes a floor level of the Service Building that is four (4) feet above grade to accommodate trailer beds without a recessed dock system. These overhead door locations will be equipped with dock levelers and weather seals. The one (1) loading dock station that requires that the trailer be located inside the building will be equipped with a ramp so that a trailer can be backed into the Loading Dock and underneath crane coverage.

Adjacent to the Loading Dock Area is the Scintillator Equipment Room. This room is based on the requirements from the WBS 2.9 group [27] and includes space for pumps, inspection testing equipment, piping and related scintillator distribution equipment. Located exterior and adjacent to the Scintillator Equipment Room is a concrete pad designed for heating and cooling equipment for the scintillator. West of the Scintillator Equipment Room is a Scintillator Unloading Area sized to handle four (4) tanker trailers. The trailers will be located within a concrete containment area similar in construction to those found at gasoline fueling stations. Spills will be routed to a collection basin for removal. A canopy will cover the rear half of the trailers. A walkway system on top of the canopy will allow for access to the vent piping that will be connected to the trailers.

An Office area will provide space for support of detector assembly as well as normal facility operations. This space is sized for two (2) semi-private offices and five (5) visitor offices will be provided along with a small lunchroom and adjacent toilet facility. It is recognized that the initial arrangement will likely be configured for use during detector assembly (lunch tables, lockers, etc.) and be reconfigured for normal operations at some later date.

A Mechanical Room will house water service equipment including pumps, pressure tanks, conditioning equipment and related pumps and piping. This room will include space for building automation functions. A Janitor's Closet will also be located in the Mechanical Room.

At the east side of the Service Building, adjacent to the Assembly Area will be the Fire Protection Area. The Fire Protection Area will house the diesel fire pump, valving, water storage tanks and related equipment for the fire suppression system for the building. This space will be located in a one-store wing of the Service Building to take advantage of the central location in the building as well as the at-grade elevation.

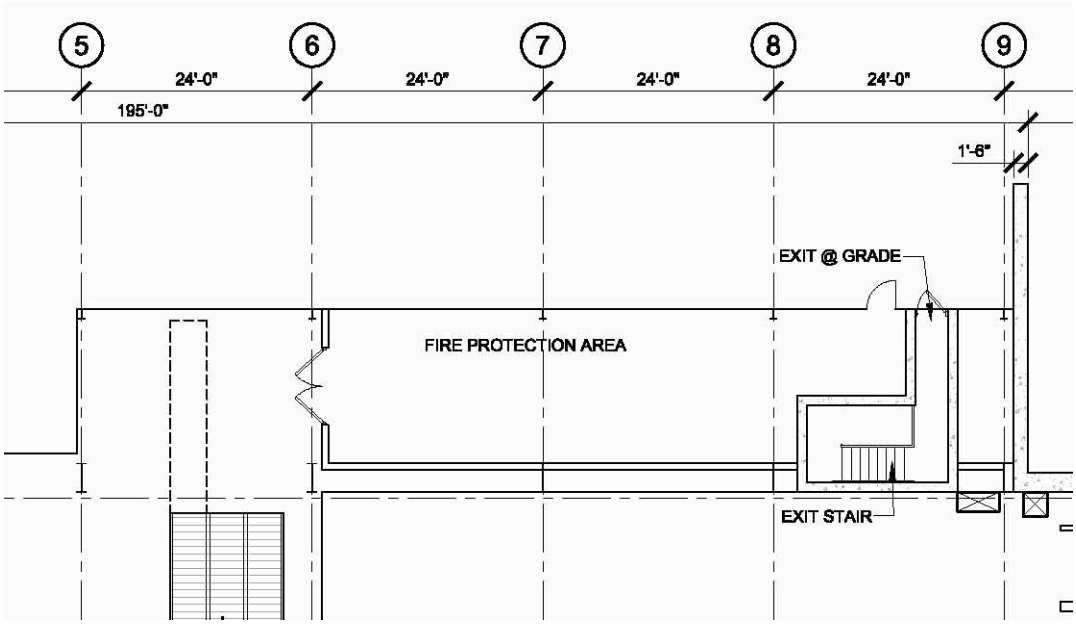

Figure 9.32: Plan at Service Building indicating location of the Fire Protection Area.

The Service Building will contain two (2) overhead bridge cranes. One bridge crane will be sized at 10 tons and will be used primarily for module handling. The second bridge crane will be sized at 10 tons and will be used for transport of the block assembly device components in addition to the module handling. Both cranes will be supported by the Service Building structure.

The Service Building shell will consist of a pre-engineered steel building based on manufacturer's standard components. This includes prefinished metal siding and roofing materials, vinyl faced batt insulation, doors and windows. Figure 9.33 below depicts the west elevation of the Service Building.

Figure 9.33: West Service Building Elevation

The Loading Dock Area of the Service Building requires strict environmental control. The requirements are a range of temperature that is +/- 5 degrees Fahrenheit for a 20% delta relative humidity range or no variance in space temperature at 35% delta relative humidity range. The design assumes a summer temperature set point of 70 degrees +/- 5 degrees Fahrenheit at 50% relative humidity and a winter temperature set point of 70 degrees +/- 5 degrees Fahrenheit at 15% relative humidity. In addition, the adhesive used to assemble the detector requires a unit capable of providing conditioned 100% outside air.

The HVAC systems in the Service Building will conform to ASHRAE 90.1, ASHRAE 62 and applicable NFPA requirements and applicable sections of the local codes and ordinances.

The Office area of the Service Building will be conditioned to provide a 75 degrees +/- 5 degrees Fahrenheit at 55% relative humidity and a winter temperature set point of 68 degrees +/- 5 degrees Fahrenheit with no relative humidity requirement. The outdoor air requirements are based on a normal operational occupancy of 10 people and are based on ASHRAE 62.

The Service Building will be provided with an automatic sprinkler system installed in accordance with NFPA 13. Fire Alarm systems will be installed in accordance with NFPA 72.

Electrical service to the Service Building and adjacent support spaces will provide general house power and lighting for the installation and operation of the detector as well as power for the overhead cranes.

Code required emergency lighting and exit lighting will be provided in the Service Building.

Parking will be provided for 10 vehicles during assembly of the detector. During normal operations 8 parking spaces are required. These parking spaces will be located along the west side of the building.

9.4.7 Other Design Features

Since the Detector Enclosure and Assembly Area will be located below grade, ground water control has been included in the design. The retaining wall will include provisions for damp proofing to be applied to the exterior face of the walls. Drainage strips ("dimple mats") will be located along the excavated rock face prior to placement of concrete for those walls in rock. These strips will divert accumulations of ground water to an underdrain system that encircles the Assembly Area and Detector Enclosure. Water from these underdrains in the rock

will be routed to a sealed ground water sump basin where it will be discharged to the surface away from the enclosure. For those underdrains located at the rock/soil interface it is anticipated that the drains will be extended to daylight in order to provide a drainage system that does not rely on mechanical means to remove the groundwater.

The Detector Enclosure and Assembly Area will serve as secondary containment in the event of an unintended spill of scintillator. The volume has been sized to contain a 100% spill of the scintillator and a full discharge of the fire suppression system. The interior walls and floor of these spaces will be sealed. A separate collection basin will be installed for the interior portion of the Detector Enclosure and Assembly Area. This basin along with a perimeter trench drain will serve as the collection system for unexpected scintillator leaks from the detector. In addition, the space beneath the detector will be used as a collection system, in effect making the space a "witness zone" for the area beneath the detector. The collection basin will be outfitted with alarms that signal the presence of scintillator. No automated means of emptying the basins will be installed in order to prevent an unintended discharge of scintillator into the environment.

9.4.8 Design Changes in the Far Detector Building since the Conceptual Design Report

The design of the Far Detector Building has been revised significantly since the CDR was completed. These changes reflect the state of the knowledge of the site and physics driven requirements. In general, each component was investigated for possible reduction in size, scope and cost.

The most significant change in the design since the CDR stage was the decision to reduce the maximum size of the detector to 18 kilotons. This resulted in a shorter Detector Enclosure. In addition, the support functions previously housed in a Loading Dock building and Service Building were consolidated into one simple Service Building design.

In support of the EAW updating and to prepare a U.S. Army Corps of Engineers Wetland permit, a detailed delineation of the wetlands was accomplished by Short Elliot Hendrickson in the summer of 2006. The development of the permit application was prepared and submitted for review in April 2007.

In December 2006, a Storm Water Pollution Prevention Plan (SWPPP) was prepared by Burns and McDonnell as part of the development of the Site Preparation package. This living document contains the information needed to comply with applicable ordinances, codes and regulations concerning storm water management. This work was accomplished to address environmental safety and health concerns during construction.

A detailed topographic survey of the access road and project site was completed by Hanson Professional Services in the spring of 2006. This survey documented the ground features to produce one foot contours. This work was accomplished to mitigate an identified risk associated with unknown topographic conditions as documented in NOVA-doc-1457.

In the spring of 2006, the firm of Burns and McDonnell was retained to complete an independent cost and schedule review of the CDR design. This study indicated that the estimated cost of the site and building were greater than the in-house estimate completed for the CDR. The project team reconciled the two estimates and undertook a value management exercise to control the costs. The schedule component of the review indicated that a two year construction period was reasonable.

In order to provide a better understanding of the subsurface conditions along the access road and project site, the firm of Short Elliot and Hendrickson was retained in the summer of 2006 to perform a subsurface investigation. This investigation included a comprehensive program of field work of soil borings, rock borings, pump test and packer tests as well as lab work required analysis and document the conditions. In addition, a 3D resistivity survey was

completed of the area around the Far Detector Building site for the purpose of mapping bedrock fracture zones.

The orientation and location of the building was changed to accommodate site conditions. The CDR design incorporated the Loading Dock and Service Building functions at the south end of the building. The current design has placed these functions at the north end of the building in response to recommendations in the Environmental Assessment Worksheet to provide at least a 1,000 foot buffer between the development footprint and the Ash River to the south.

The cosmic ray shielding strategy is the most significant change to the Detector Enclosure Design. The use of conventional precast concrete planks and cast-in-place concrete resulted in a minimization of the use of barite material.

As a result of the Burns and McDonnell Secondary Containment study and input from the design of the block raiser, the floor of the Assembly Area and Detector Enclosure has been designed as a "witness zone" to verify the viability of the secondary containment method.

Additional research on fire suppression systems indicated that a water mist fire suppression system would allow for a reduction in the quantity of water required for the system. Selection of an alternate method allowed the on-site water storage to be reduced from 500,000 gallons to 2,000 gallons.

9.4.9 Work Remaining to Complete the Far Detector Building Design

The overall design of the Far Detector Building is approximately 45% complete with the concrete design work approaching 55% complete. The work remaining generally includes completing the construction documents to a point where they are ready for competitive bidding. This effort will include continued optimization of the building components in order to achieve the best value solution.

As the design is developed, all aspects of the project will be periodically reviewed with regard to Quality Assurance issues from Conceptual Design through Title III completion. This review process will be completed in accordance with the applicable portions of the Fermilab policies. The following elements will be included in the design and construction effort:

- An identification of staff assigned to this project with clear definition of responsibility levels and limit of authority as well as delineated lines of communication for exchange of information;
- Requirements for control of design criteria and criteria changes and recording of standards and codes used in the development of the criteria;
- Periodic review of design process, drawings and specification to insure compliance with accepted design criteria;
- Identification of underground utilities and facility interface points prior to the commencement of any construction in affected areas;
- Conformance to procedures regarding project updating and compliance with the approved construction schedule;
- Conformance to procedures regarding the review and approval of shop drawings, samples test results and other required submittals;
- Conformance to procedures for site inspection by project personnel to record construction progress and adherence to the approved contract documents;
- Verification of project completion, satisfactory system start-up and final project acceptance.

While the design of the conventional facilities has progressed to a point where a cost and schedule range can be estimated, the design requires iteration with the other Level 2 tasks to

respond to an evolving detector design. This process will continue throughout the Title 2 design phase.

The conventional facilities are seen as a significant cost and schedule driver for the project. Increased costs and/or schedule slippage has the potential to negatively impact the overall project. Prior to commencing the design portion of the Title 1 effort, the design firm completed a cost and schedule review of the revised design. This cost estimate/schedule served as the touchstone throughout the Title 1 phase. Changes and modifications to the design that impact the cost and/or schedule were tracked and evaluated prior to being incorporated into the design. The goal of this effort was to raise the awareness of the importance of the cost and schedule. As part of the Title 2 Design Process this tracking will continue.

The project team will continue to evaluate the site and building for incorporation of appropriate safeguard and securities measures. The assembled detector will be located within the concrete encased Detector Enclosure and be relatively secure, but the Loading Dock and truck dock areas are a point of vulnerability. Security measures like berms, fencing, gates, and card readers on doors are being considered.

While several value management design changes have been incorporated into the design since the CDR, the project team is committed to investigating additional value analysis possibilities. These include a "cut and fill" study to balance the amount of excavated material with the volume of the overburden, and a detector enclosure length study that will examine the implications of the depth of the detector enclosure. In addition, the mechanical systems are being investigated to determine a cost effective solution that provides the best life-cycle solution.

9.5 Chapter 9 References

[1] See NOVA-doc-1881 for the Basis of Estimate for the Northstar Electric electrical service upgrade

[2] See NOVA-doc-1914 for the Basis of Estimate for the data and communication service upgrade to the project site from Blackduck Telephone Company.

[3] Bill Miller and Marvin Marshak, NOVA-doc-384, May 2005

[4] NOVA-doc-168 contains the minutes from an informal meeting with the Minnesota Department of Natural Resources in April 2005.

[5] NOVA-doc-830 contains the minutes from a meeting to discuss road alignment issues in April 2006.

[6] NOVA-doc-1424 contains meeting minutes of a presentation to stakeholders in Orr, Minnesota in February 2007.

[7] For a complete Environmental Assessment Worksheet see NOVA-doc-205. The Cultural Resources Assessment done in conjunction with the Environmental Assessment Worksheet can be found in NOVA-doc-1834.

[8] The wetland delineation and permit application can be found in NOVA-doc1892.

[9] The Stormwater Pollution Prevention Plan can be found in NOVA-doc-1324.

[10] The topographic survey information from Hanson Professional Services can be found in NOVA-doc-1450.

[11] NOVA-doc-1458 contains the risk assessment and mitigation methods for the subsurface conditions at the Ash River Site.

[12] The Short Elliot Hendrickson Geotechnical Engineering Report is located in NOVA-doc-1225.

[13] The Geophysical Investigation Report is located in NOVA-doc-1225.

[14] For a complete Environmental Assessment Worksheet see NOVA-doc-205.

[15] The Site Preparation documents prepared by Burns and McDonnell can be found in NOVA-doc1207.

[16] The trip report from the April 2006 meeting can be found in NOVA-doc-830.

[17] The preliminary Leadership in Environmental Engineering Design (LEED) checklist was completed by the project team in December 2006 and can be found in NOVA-doc-1318.

[18] The WBS Responsibility Matrix that delineates the interfaces and responsibilities for the WBS groups can be found in NOVA-doc-1170.

[19] The presentation for the University of Minnesota in December 2005 can be found in NOVA-doc-390. The presentation held in December 2006 can be found in NOVA-doc-1289.

[20] The review information for the Comment and Compliance Review held in November 2006 can be found in NOVA-doc-1207-v4. The review information for the Quality Assurance Review held in January 2007 can be found in NOVA-doc-1207-v7.

[21] NOVA-doc-1094 contains the risk description and cosmic ray overburden requirements that were used as the basis of design. NOVA-doc-1409 contains additional information.

[22] Two documents concerning secondary containment are available in the document database. NOVA-doc-1460 contains the risk assessment form for the secondary containment. NOVA-doc-1021 contains the report of secondary containment methods produced by Burns and McDonnell in September 2006.

[23] The requirements for the moveable access platforms are taken from NOVA-doc-1155 produced by WBS 2.9.

[24] NOVA-doc-1974 contains the Best Practices paper by ComputerSite Engineering titled "Alternating Cold and Hot Aisles Provides More Reliable Cooling for Server Farms".

[25] The trip report for the February 2007 meeting in Orr, Minnesota can be found in NOVA-doc-1424.

[26] The Loading Dock requirements developed by WBS 2.9 can be found in NOVA-doc-1433.
[27] The requirements for the Scintillator Transfer Facility can be found in NOVA-doc-1921.

10 Liquid Scintillator

10.1 Introduction

This chapter describes the details of the liquid scintillator, the active detector medium for the NOνA experiment. In this chapter we demonstrate that the composition and technical specifications for the scintillator have been determined, suppliers for the components have been identified, QC methods to test that the components and the blended scintillator meet technical specifications have been developed, a model for blending the scintillator components has been established, and a transportation model for delivery of the scintillator to the NOνA detector in Ash River is understood.

10.1.1 Liquid Scintillator Composition and Light Spectrum

Liquid scintillator is typically made up of four components: a primary scintillant that produces light in the UV when ionizing particles traverse it, waveshifters that downshift the UV photons to longer wavelength to facilitate absorption by the wavelength shifting (WLS) fibers, and a solvent to blend the components into a stable solution. The light production mechanism is shown below in Figure 10.1 with data from [1]. Pseudocumene [1,2,4-Trimethylbenzene], a benzene derivative with many uses in the plastics and paint industries, is the primary scintillant. Pseudocumene is excited by traversing ionizing particles and the photons that are given off as it de-excites are in the UV, as shown in Figure 10.1(a). Figures 10.1(b) and 10.1(c) show how PPO [2,5-diphenyloxazole] and bis-MSB [1,4-di(methylstyryl)benzene] shift the UV photons from the pseudocumene to the wavelength region where they can be absorbed by the dyes in the WLS fiber.

The normalized output spectrum of two commercial scintillator families is shown in Figure 10.2. The BC517 family is manufactured by Saint-Gobain (Bicron); the EJ-321 family is manufactured by Eljen Technologies. The NOνA baseline scintillator was engineered to have properties similar to the commercial liquid scintillator BC517P.

BC-517P [2] is made up of approximately 5% pseudocumene by weight as the primary scintillant in a 95% mineral oil base with small amounts of UV waveshifters and small amounts of anti-oxidants. Most of these components have been known since the 1950s [1]. These scintillators have a moderate light output, 28% of anthracene when fresh and 21% of anthracene when fully oxygenated [2,3]. The advantages of this mixture include stability, low cost, availability in large quantities, low toxicity, high flashpoint and low potential as an environmental hazard. Previous work has shown that this scintillator attacks neither wavelength shifting fiber nor PVC over lifetimes exceeding this experiment (see Chapter 11, Section 11.4).

To study the performance of liquid scintillator in the NOνA detector, a Monte Carlo program was written that simulates a prototype NOνA PVC extrusion cell with a loop of WLS fiber running through it. In this simulation, the composition and concentration of the TiO_2 in the PVC and the diameter of the fiber could be varied. Figure 10.3 shows a Monte Carlo calculation of the output spectrum of the NOνA baseline liquid scintillator in a prototype NOνA PVC cell in which the plastic is loaded with 18% anatase TiO_2 and the light is collected by a 0.7mm WLS fiber. This figure shows the output spectrum of the photons that are captured by the fiber and transmitted to the photodetector. For the baseline scintillator, the output spectrum peaks in the wavelength range 410 – 440 nm.

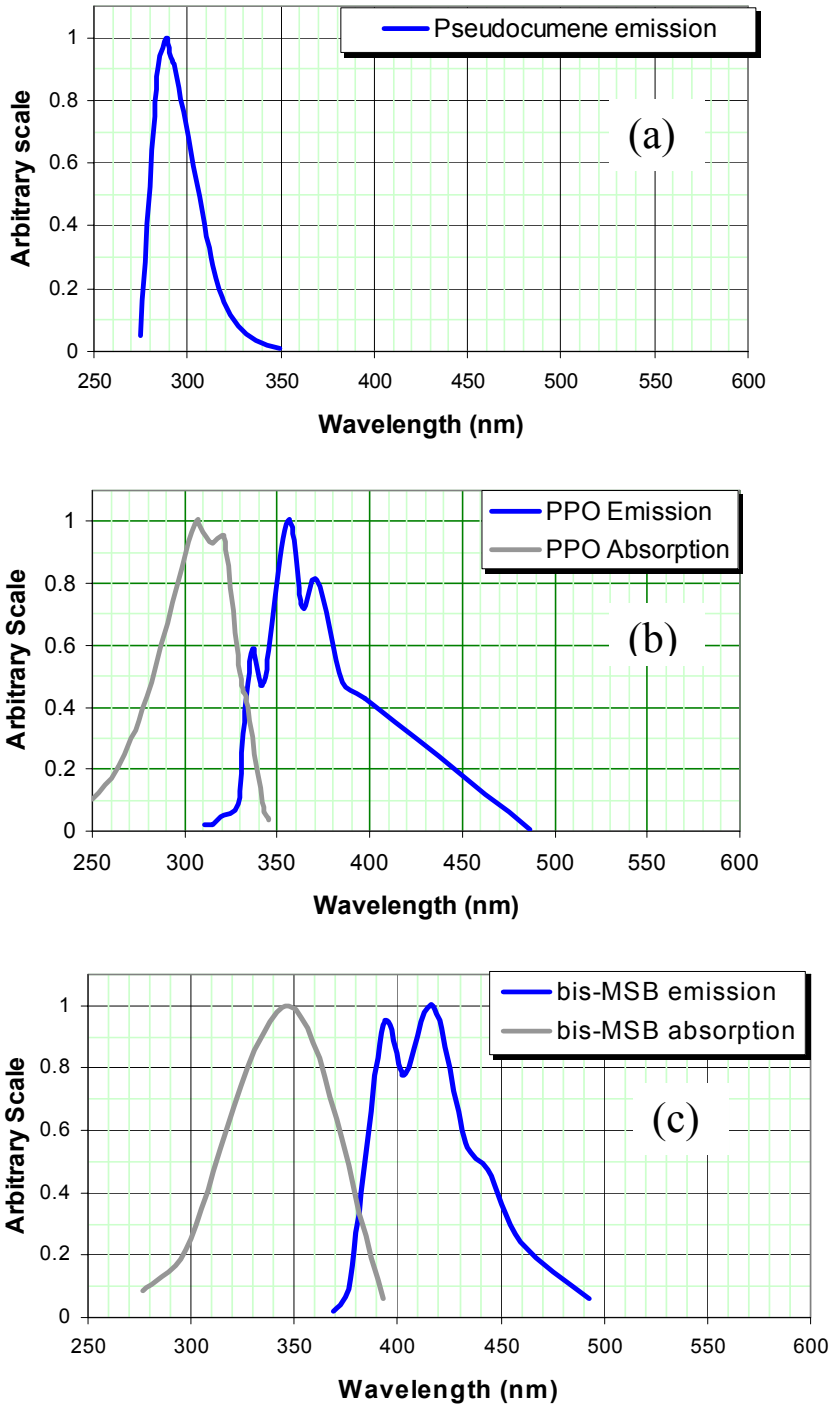

Fig. 10.1: Light production by liquid scintillator. The emission spectrum of the primary scintillant psueudocmene when traversed by an ionizing particle is shown in (a); the absorption and emission spectrum of the first waveshifter PPO is shown in (b); the absorption and emission spectrum of the second waveshifter bis-MSB is shown in (c).

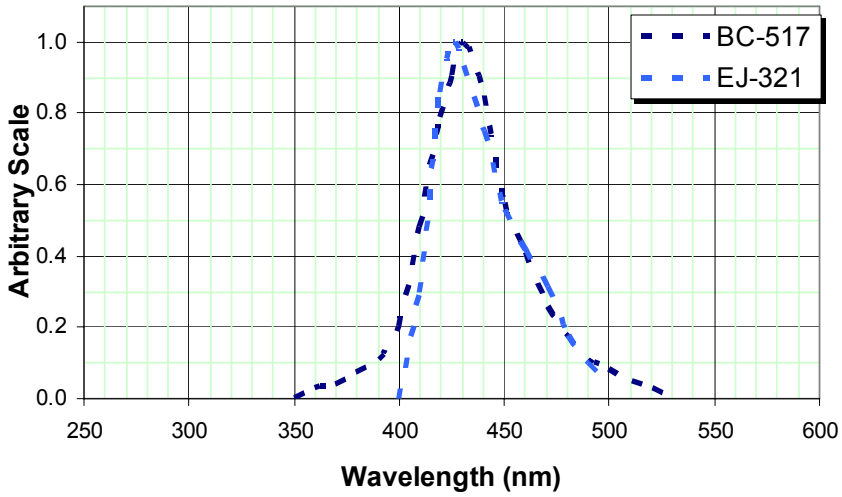

Fig. 10.2: The output spectrum of two commercial scintillators, Saint-Gobain (Bicron) BC-517 and Eljen Technologies EJ-321.

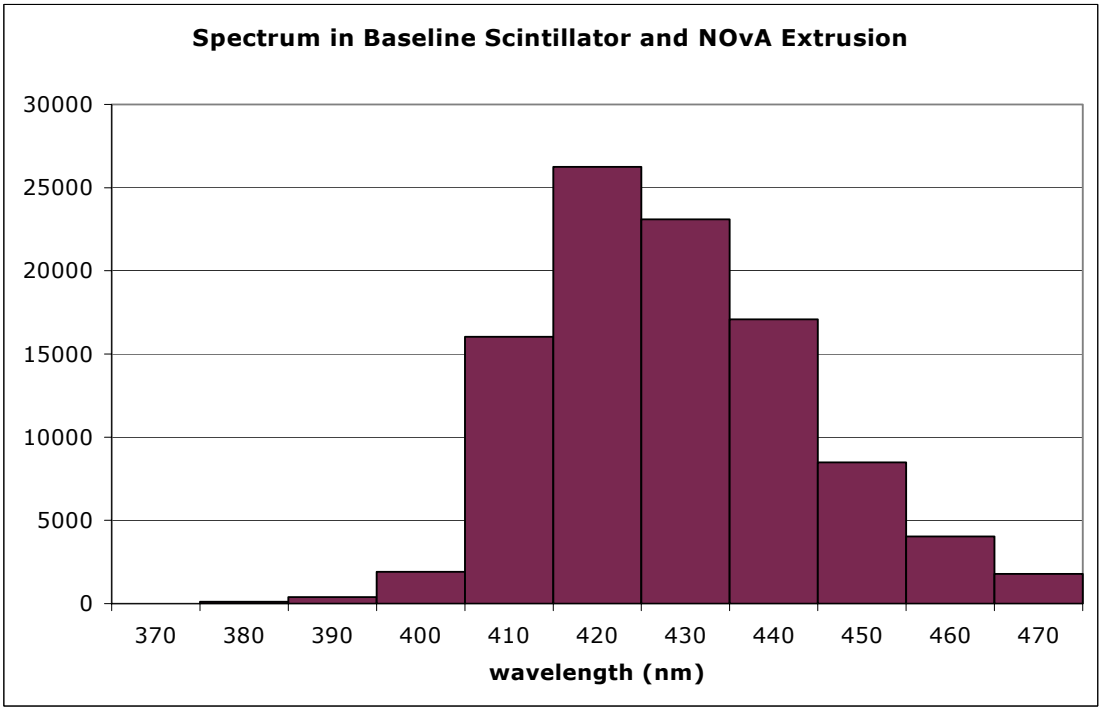

Fig. 10.3: A Monte Carlo calculation of the spectrum of photons absorbed by the fiber for the baseline NOνA liquid scintillator in a prototype NOνA PVC cell in which the plastic is loaded with anatase TiO_2 and the light is collected by a 0.7mm WLS fiber.

Unlike previous experiments that require photons to travel long distances to the photodetector, the NOνA design requires a scintillator with only a modest attenuation length for the relevant wavelengths of scintillator light. This requirement can be demonstrated by Monte Carlo simulations that compute the mean distance traveled by a photon before its absorption by the WLS fiber. Figure 10.4 shows the results of such a simulation for the prototype NOνA PVC extrusion loaded with anatase TiO2, and 0.7mm WLS fiber running through it. The figure shows that the mean distance traveled by a photon before absorption is only about 0.5 m, although there are tails extending out to much longer path lengths. In other high energy physics experiments, photons more typically must travel tens of meters before detection.

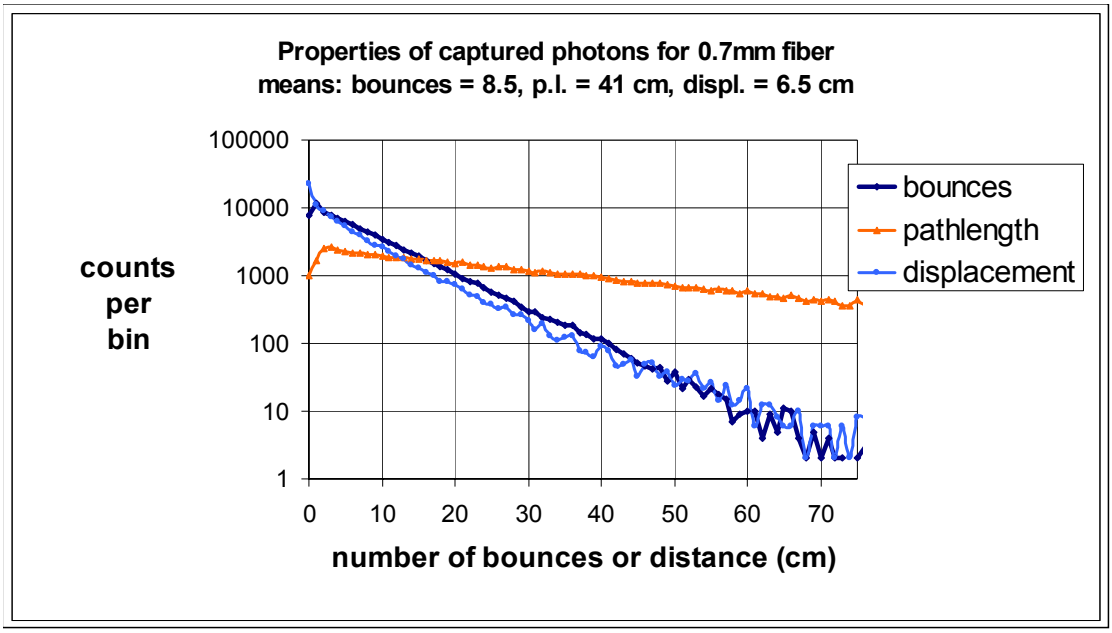

Figure 10.4. Distributions of the number of bounces seen by a photon before capture, the path length (p.l.) traveled before capture, and the displacement relative to its starting position computed by Monte Carlo. The Monte Carlo simulation uses the properties of baseline scintillator, a prototype NOνA PVC extrusion cell, and 0.7 mm WLS fiber.

10.2 Technical Design Requirements for the NOνA Liquid Scintillator

As discussed in Chapter 6, based on our current understanding of the performance of the PVC, WLS fiber and APDs, the technical performance specification can be achieved using liquid scintillator with a light output equivalent to 80% of Saint-Goban (Bicron) BC-517P [2]. The Technical Design Requirement on the light yield for the NOνA Liquid Scintillator is therefore 80% of the light yield of BC-517P.

The Technical Design Requirement on the attenuation length for the NOνA Liquid Scintillator was determined by the following considerations. R&D studies at Indiana University over several years have shown that liquid scintillator blended with 75% of the fluor concentration found in BC-517P is adequate to yield a light output equivalent 80% of BC-517P if the solvent for the fluors, mineral oil, has a long enough attenuation length. We therefore set about testing the light output of scintillators loaded with 75% of the fluors in BC-517P and blended with mineral oils having a broad range of attenuation lengths. Figure

10.5 shows the results of these studies. The methods used to measure light output and attenuation length are described in later sections of this chapter.

From Figure 10.5, we determined that mineral oil with an attenuation length of ≥ 5m when blended with 75% of the fluors in BC-517P meets the Technical Design Requirement on NOνA Liquid Scintillator light yield. We therefore adopt 5 m as the Technical Design Requirement on NOνA mineral oil.

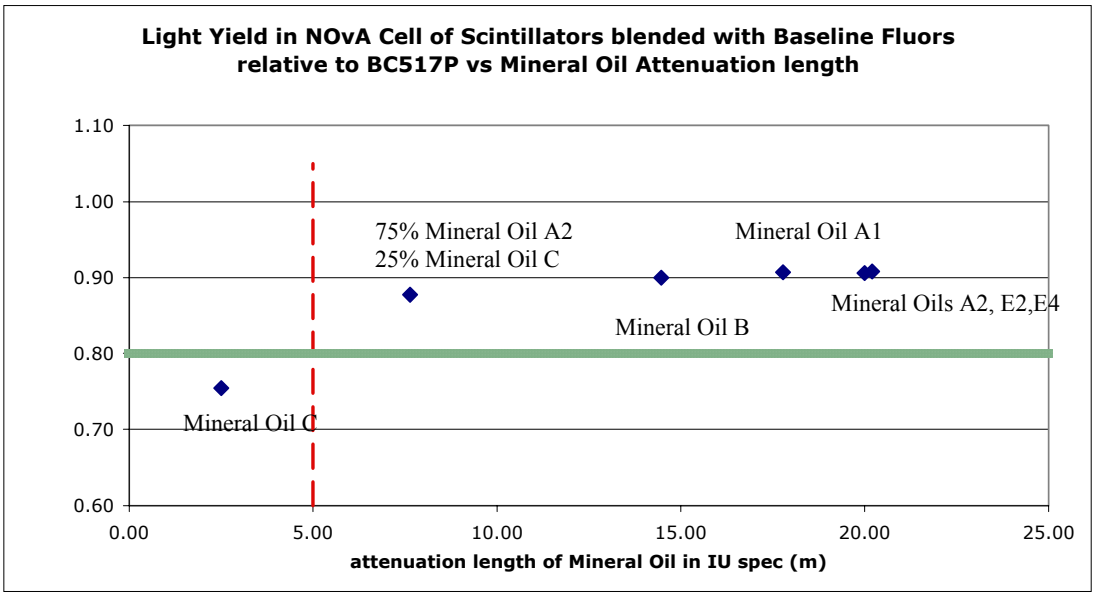

Fig. 10.5: Liquid scintillators blended with 75% of the fluors found in BC-517P and mineral oil solvents of varying attenuation lengths. The dashed line indicates the 5m Technical Design Requirement on the attenuation length of mineral oil.

Liquid scintillator is extremely non-conductive. Non-conductive fluids develop a net charge through the triboelectric effect during flow, which can under certain circumstances lead to spark discharge between the liquid and container or between non-bonded plumbing components. To mitigate potential sparking problems, the baseline scintillator has as an added component the anti-static agent Stadis-425 [4], which brings the scintillator conductivity up to safe levels. The technical requirement for conductivity has been taken from the recommendations given by the National Fire Protection Association (NFPA) [4]. NFPA safe practices dictate that the scintillator be made "semi-conducting", which is defined as "possessing a conductivity at least 100 picosiemens/meter".

The Technical Design Requirements for the NOνA Liquid Scintillator (NLS) are given in Table 10.1.

Scintillator Property	**Technical Design Requirements**
Liquid Scintillator Light Yield	NOνA Light Yield / Light Yield (BC-517P) ≥ 0.80
Attenuation Length of Mineral Oil Solvent	AttenuationLength ≥ 5 m @ 420 nm
Conductivity	≥ 100 picosiemens/meter

Table 10.1. Technical Design Requirements for the NOνA Liquid Scintillator (NLS)

10.3 Scintillator Composition

The NOνA detector liquid scintillator volume is 3,210,584 gallons. The components of the scintillator are given in Table 10.2 The anti-oxidant agent tocopherol (Vitamin E) is added in order to minimize the degradation in light due to oxygenation.

component	purpose	mass fraction	volume (gal)	tot mass (kg)
mineral oil	solvent	95.8%	3,082,145	9,917,109
pseudocumene	scintillant	4.1%	128,439	425,908
PPO	waveshifter #1	0.091%		9,373
bis-MSB	waveshifter #2	0.0013%		131
Stadis-425	antistatic agent	0.0003%		46.6
tocopherol (Vit.E)	antioxidant	0.0010%		104
Total		**100.0%**	**3,210,584**	**10,352,551**

Table 10.2. The composition of NOνA Liquid Scintillator

The component masses given in Table 10.2 are based on the nominal component densities given in the MSDS sheets.

During the R&D studies at Indiana University, many batches of liquid scintillator with the composition given in Table 10.2 were blended and tested. Of particular concern in these studies was the effect of various mineral oils on the liquid scintillator performance, mainly because liquid scintillator is mostly mineral oil. Below we describe the effects of several technical grade mineral oils purchased from multiple producers. These oils have been labeled A through E. Mineral oil from producer A has been adopted as the "Baseline Mineral Oil". Three different shipments of this baseline mineral oil were studied and these oils have been labeled A1, A2, and A3. We also tested six different grades of mineral oil from producer E and these have been labeled E1-E6. Finally, we tested several blends of mineral oils made up of Mineral Oil A and Mineral Oil C. Our tests include both studies of the properties of the mineral oils themselves and the scintillators blended from them.

Pseudocumene for these studies was obtained from two suppliers and these have been labeled Pseudocumene A and Pseudocumene B. Both pseudocumenes have the same purity and chemical composition as measured at Indiana University using Gas Chromatography Mass spectroscopy (GCMS).

There is a sole US supplier for the waveshifters, Curtiss Laboratories in Pennsylvania. This company has worked successfully with other high energy physics experiments (MINOS, MINERνA) .

In this chapter scintillators blended with the fluor composition (pseudocumene + PPO + bis-MSB) given in Table 10.2 are called "Baseline Scintillator"; the fluor concentration is called "Baseline Fluors".

10.3.1 Light Yield of NOνA Liquid Scintillator

Light yield tests were made in the Indiana University "NOνA cell". This is a 60 cm NOνA PVC cell that has walls loaded with 15% anatase TiO_2. The cell has two 0.8 mm diameter, 1.2 m long WLS fibers that are read out with a green extended phototube. NOνA cell measurements are made with cosmic ray muons.

The light yield of Mineral Oil A2 + Baseline Fluors is shown in Figure 10.6. As expected from Figure 10.5, these measurements demonstrate that the scintillator blended with Baseline Mineral Oil + Baseline Fluors meets the technical design requirement for light yield given in Table 10.1.

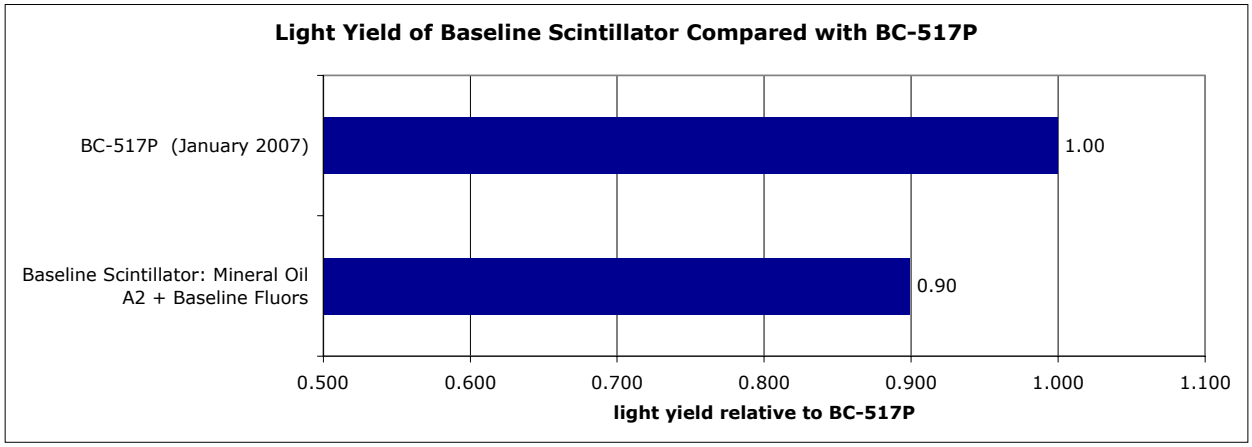

Fig. 10.6: Light yield of Mineral Oil A2 + Baseline Fluors compared with the light yield of commercial BC-517P in the NOνA cell. The measurements for BC-517P were made with scintillator received from Bicron in January 2007.

10.3.2 Conductivity

Conductivity measurements were made with a "Digital Conductivity Meter" (EMC Electronics Corp., Venice, FL). See Section 10.4.3 for a discussion of how the conductivity is measured. The conductivity of Mineral Oil A + Baseline Fluors is shown in Figure 10.7 as a function of Stadis-425 concentration.

The addition of 2 ppm of the anti-static agent Stadis-425 makes the scintillator semi-conducting. We choose 3ppm (instead of 2 ppm) because in large scale production, we want to guarantee that small errors in measuring out small quantities of Stadis-425 do not compromise the anti-static technical requirement in Table 10.1 for a large batch of scintillator. The addition of 3 ppM of Stadis-425 does not affect the light yield of the scintillator when measured in a NOνA cell as shown in Figure 10.8.

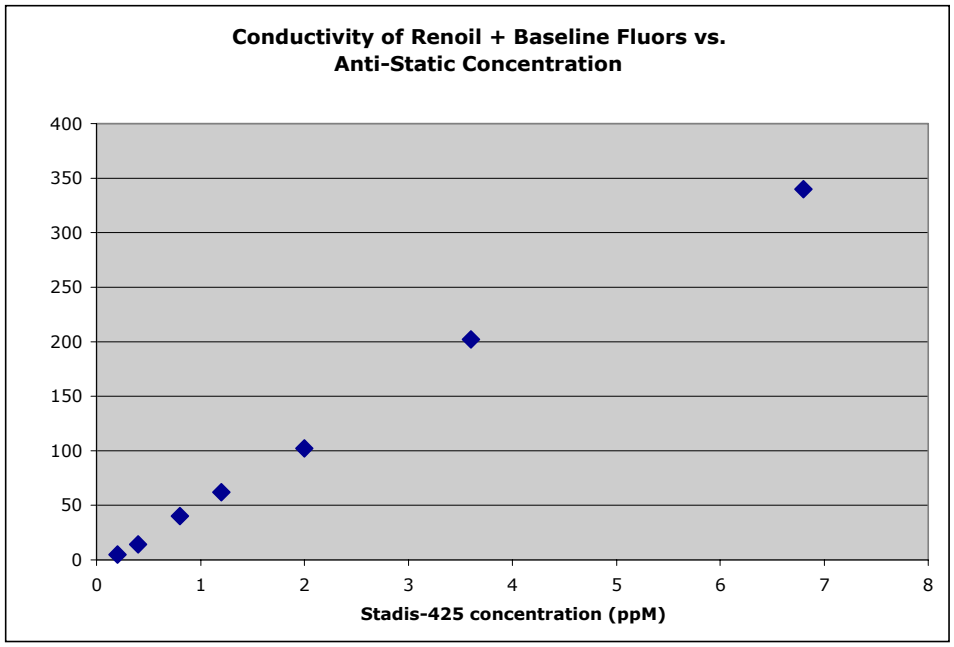

Figure 10.7. Conductivity of Mineral Oil A + Baseline Fluors as a function of the concentration of the anti-static agent Stadis-425 measured with the Digital Conductivity meter.

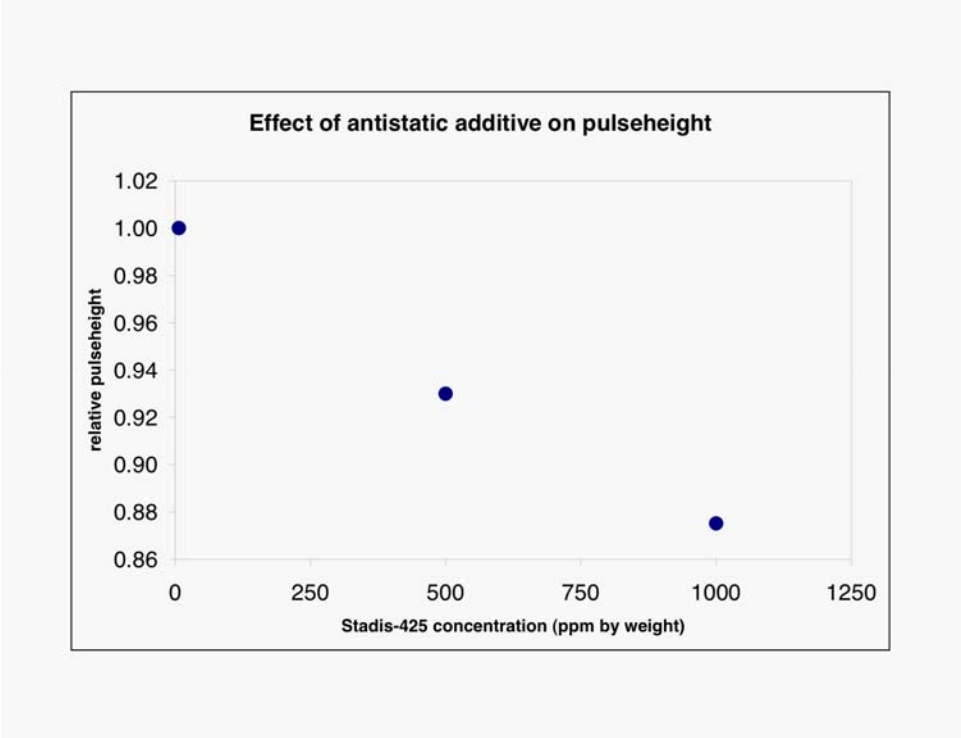

Figure 10.8. The effect of anti-static agent Stadis-425 on the light yield of baseline liquid scintillator. At the level recommended by the NFPA, 3ppM, there is no adverse effect on the light yield.

10.3.3 Anti-Oxidant

The anti-oxidant requirement for the scintillator was set by the Vitamin E concentration in the liquid scintillator used in the MACRO experiment [5].

10.3.4 Technical Specifications for Mineral Oil

The NOνA liquid scintillator constitutes 69% of the NOνA detector mass and is itself 96% mineral oil by weight. The mineral oil is inert and acts as a solvent for the scintillant and waveshifters. The primary performance feature of the mineral oil for NOνA is its attenuation length for light near 420 nm (see Figure 10.3). Mineral oil is a cost driver and the attenuation length of different grades and qualities of mineral oil must be compared to the costs of those different grades.

Experiments like MiniBooNE and MACRO used large quantities of mineral oil and mineral oil based liquid scintillator, respectively. But these experiments required mineral oil with very long attenuation lengths because of their detector technologies and geometries employed. The NOνA geometry is very different from those detectors since the light is collected locally by the wave shifting fiber. Since typical light path lengths in the NOνA scintillator are approximately 1 meter (Figure 10.4), long attenuation lengths are not required. This allows NOνA to relax the mineral oil requirements.

The most highly refined mineral oils are classified as food grade and meet the FDA requirements for consumption by humans. US Pharmacopoeia (USP) mineral oil is considered a heavy food grade mineral oil and has a large viscosity. National Formulary(NF) mineral oil is considered light food grade mineral oil and has a smaller viscosity. Higher viscosity means higher price. The step from USP to NF is about a 5 - 15% reduction in price. MiniBooNE used an NF mineral oil for their detector since an attenuation length of 20 meters was required.

Technical grade mineral oils are the next grade down from food grade. Technical grade mineral oils are not as highly refined as food grade mineral oils, but are approved by the FDA for indirect food contact and are typically used as lubricants for food processing machinery. The cost of technical grade mineral oil is less than NF mineral oils by about another 10 - 40%, depending on the viscosity.

The petroleum industry is not familiar with attenuation length as a specification and instead uses the Saybolt scale to characterize the color range of petroleum products including aviation fuels, kerosene, white mineral oils, hydrocarbon solvents and petroleum waxes. The Saybolt color index scale runs from -16 (darkest) to +30 (lightest) and, unfortunately, attenuation lengths above a few meters all lie at +30 on this scale. NOνA has blended scintillators using Saybolt +28 Technical Grade Mineral Oil and found these scintillator to be unacceptable for the experiment. Consequently, NOνA requires the development of a reliable and efficient method for determining the transmission properties of mineral oil in a way that does not demand a detailed understanding of attenuation length by the mineral oil producers.

Mineral oils are derived from petroleum feedstocks called Paraffinic Group II Base Oils. The American Petroleum Institute has defined the broad Base Oil group categories to create guidelines for licensing engine oils. All the groups cover a wide range of viscosities, but solvent-refined base oils typically fall into Group I , while hydroprocessed base oils fall into Group II. Hydroprocessing [6] is a way of adding hydrogen to the base oil at elevated temperatures in the presence of a catalyst to stabilize the most reactive components in the oil, improve the color, and increase the working life of the oil. Several hydroprocessing steps have been introduced in recent years to advance this industry: Hydrocracking was introduced in 1969 and adds hydrogen at high temperatures and pressures to crack feedstock molecules into smaller molecules. Catalytic dewaxing was added in 1984 and catalytically removes

n-paraffins and other molecules with waxy side chains by cracking into smaller molecules. In 1993 hydroisomerization was added to this string of processing steps to reshape the n-pariffins and other molecules with waxy side chains into desirable compounds instead of cracking them completely away. This third step has resulted in distinctive Paraffinic Group II base oils which typically have no color.

An increasing fraction of the base oil manufacturers use this full range of technology, but as recently as 2003 less than half used the full three step package. This technology is proprietary and several competing ones now exist, each using different catalysts and different temperatures and pressures for the various steps. NOνA has obtained identically classified (and similarly priced) mineral oils with attenuation lengths for 420 nm light in the range 2m to 10m. While our current state of knowledge is incomplete, we suspect that the range is due to the technologies being applied.

From our R&D studies, it is clear that a Technical Grade (cheaper) oil can be found that will meet NOνA's needs.

The technical design requirements for the NOνA mineral oil are given in Table 10.3. These requirements can be met by Technical Grade mineral oils.

	Technical Design Requirement
attenuation length @420 nm	$\geq$ 5 m
specific gravity @ 60/60F	0.850 < specific gravity < 0.865
viscosity @ 40 C	< 15 cSt
anti-oxidants	10 ppM
Water	< 30 ppM

Table 10.3. Technical Requirements on the NOνA Mineral Oil

The attenuation length requirement for the NOνA mineral oil @420 nm was discussed in Section 10.2 and shown on Figure 10.. The data for Figure 10.5 were obtained by blending the baseline fluor mix (c.f., Table 10.2) with mineral oils of differing attenuation lengths. The attenuation lengths of the mineral oils and blended scintillators were measured in the "Indiana University Spectrophotometer" (IU Spec) [5]. The narrow band measurements were made by passing the scintillator light through narrow band interference filters before reaching the PMT.

Figure 10.9 shows the attenuation lengths at 420 nm of the mineral oils used in the IU R&D studies. Scintillators were blended with several of the mineral oils shown in Figure 10.9 and Baseline Fluors. These scintillators were tested for light yield in the NOνA cell and the results of these tests are shown in Figure 10.10. These are the data used in Figure 10.5. The attenuation lengths of these blended scintillators were measured in the IU Spec and the results are shown in Figure 10.11.

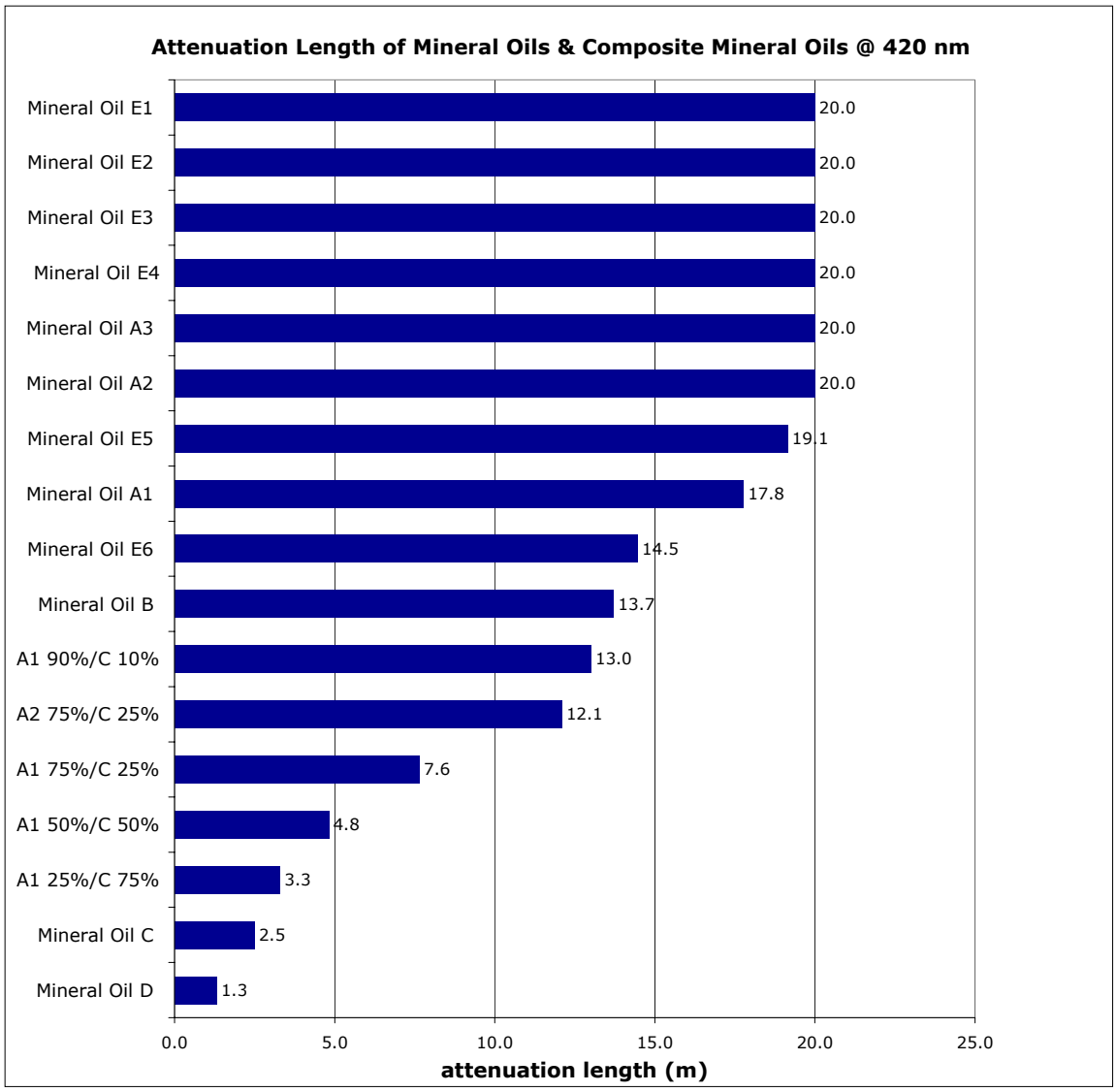

Fig. 10.9: Attenuation of mineral oils at 420 nm as measured in the IU Spec. Since the IU Spec does not accurately measure attenuation lengths > 20m, all measured attenuation lengths > 20m are shown as 20m.

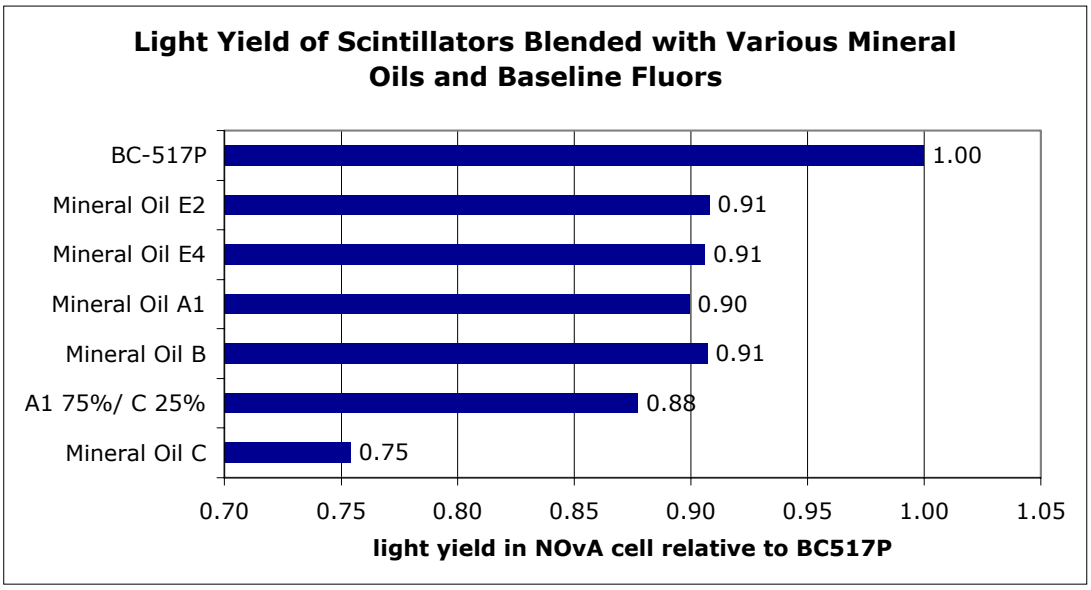

Fig. 10.10: Light yield of the scintillators blended with mineral oils shown in Figure 10.9 and Baseline Fluors. The light yield measurements were made in the NOνA cell.

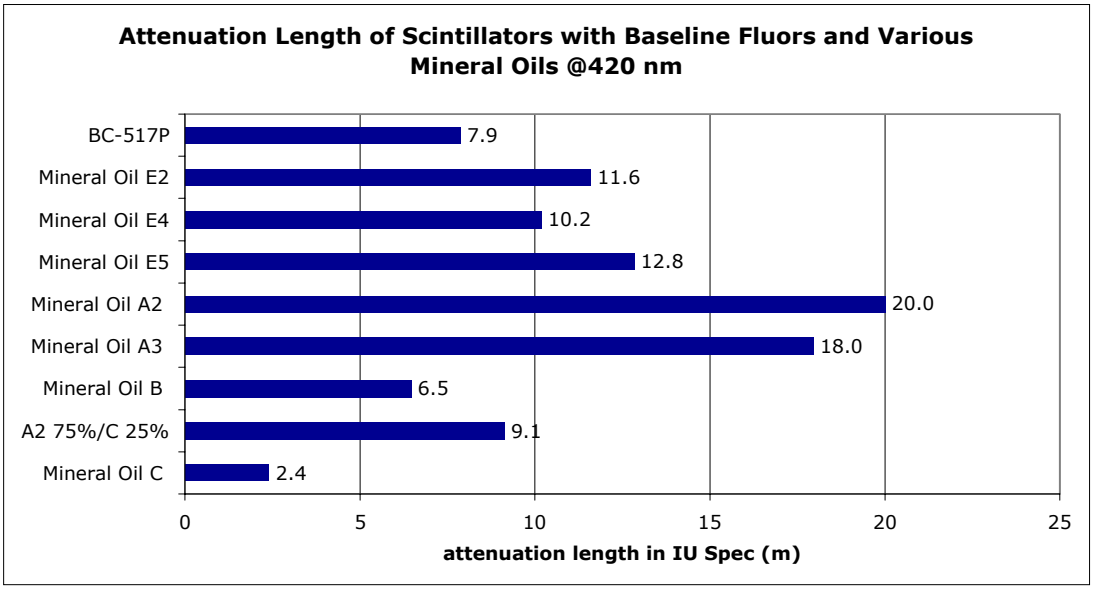

Fig. 10.11: Attenuation length of scintillators blended with mineral oils shown in Figure 10.9 and Baseline Fluors.

Additional mineral oil Technical Requirements:

- specific gravity – a narrow range of density distributes the scintillator uniformly throughout the detector, which in turn leads to a better understanding of fiducial mass. Producers routinely manufacture mineral oil to this standard.
- viscosity – higher viscosity mineral oil is more expensive and high viscosity mineral oil does not add value to this detector since it can be more difficult to pump.
- anti-oxidant – the anti-oxidant requirement for the scintillator was set by the Vitamin E concentration in the liquid scintillator used in the MACRO experiment [5]. Antioxidants are common additives in mineral oil and mineral-oil based liquid scintillators. They are used to stop the slow degradation occurring in long hydrocarbon chains and the radicals formed in this process react with oxygen dissolved in the liquid. The resulting product becomes discolored (yellowing) and is therefore detrimental to the transmittance of the liquid scintillator at 420 nm. The antioxidant essentially acts as a radical scavenger.
- water – technical specification taken from MiniBoone; industry standard; water settles out but takes up detector mass

10.3.5 Technical Specifications for Pseudocumene

Table 10.4 lists the technical specifications for the Pseudocumene.

	Technical Design Requirement
Purity	≥ 98%
specific gravity @ 60/60F	0.875 < specific gravity < 0.882
Clarity	< +25 Color Units measured on Pt-Co scale
Total Sulfur content	< 2.0 ppM

Table 10.4. Technical Requirements on the NOνA Pseudocumene

Source of the requirements in Table 10.4:

- purity – this requirement is the industry standard for pseudocumene production. When delivered to the toll blender, samples of pseudocumene are drawn and then sent to Indiana University where their purity will be measured using GCMS by the Indiana University Chemistry Department.
- specific gravity – this requirement is the industry standard for specific gravity.
- clarity – this requirement is the industry standard for clarity, as measured on the Pt-Co scale. The Pt-Co scale is measured by the Lovibond Tintometer;
- sulfur content – The Certificate of Analysis from the vendors lists the sulfur content in the pseudocumene. The presence of sulfur in the original distillate (fraction) is fairly common. NOνA plans to monitor the sulfur level reported by the manufacturer since it may potentially lead to light yield quenching and acidity variations.

Pseudocumene has been obtained from two suppliers. A GCMS analysis of the pseudocumene from the two suppliers shows that they both meet the Technical Design Requirements for purity. Figure 10.12 shows that scintillators blended with pseudocumene from the two suppliers meet the Technical Requirement on light yield. In this figure, the scintillators were blended with 100% of the fluor concentration found in BC-517P.

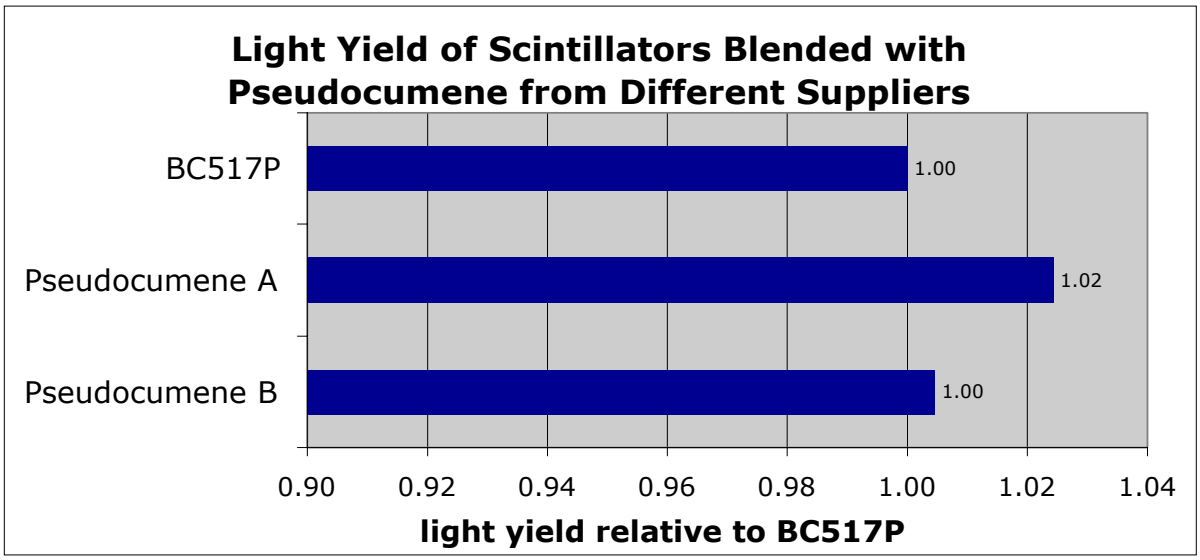

Fig. 10.12: Light yield of the scintillators blended with pseudocumene from two suppliers as measured in the NOνA cell. The scintillators blended with Mineral Oil A1 and 100% of the fluors found in BC-517P.

10.3.6 Technical Specifications for Scintillator Waveshifters

The technical specifications for the wavelength shifters have been presented to the vendors and are listed in Table 10.5. The Certificate of Analysis prepared by the manufacturer, Curtiss Laboratories, will include the results of these tests with the exception of the transmittance in toluene (1 g wavelength shifter in 100 mL toluene, measured in optical cells with 1-cm and 10-cm path lengths) which will be performed at Fermilab. The manufacturer will carry out a parallel test as a check. The NOνA experiment will repeat the check for melting point, appearance and odor at Fermilab. We will also perform new tests using ultraviolet (UV), Infrared (IR) and nuclear magnetic resonance (NMR) to better define potential impurities. Most of the impurities in the wavelength shifters are related to unreacted materials and solvents. The wavshifters are susceptible to the presence of impurities so that testing must ensure that the wavelength shifters used are over 99.6% pure. PPO was used as the primary wavelength shifter in the MINOS experiment and the manufacturer met the same technical specifications over a two year delivery schedule.

	Technical Design Requirement	
	PPO	bis-MSB
Melting point	71-73 °C	179-181 °C
Appearance	white powder	light yellow powder
Odor	Odorless	Odorless
Loss in drying	≤ 0.2%	≤ 0.2%
Residue	none	none
Purity	≥ 99.6%	≥ 99.6%
Tansmittance in Toluene	≥ 85% @ 370 nm	≥ 90% @ 420 nm

Table 10.5. Technical Requirements on the NOνA Waveshifters

10.4 Quality Assurance and Quality Control

The liquid scintillator is the heart of the NOνA experiment. In combination with the wavelength shifting fiber and PVC cells, the scintillator is crucial to the performance of the detector. We must be sure that the scintillator is free of impurities and properly blended. Quality Control (QC) and Quality Assurance (QA) are fundamental to the successful construction of this detector.

The problem with petroleum based products like mineral oil and pseudocumene is that they come out of oil fields from a variety of wells, so the base material is variable. In addition, mineral oil and pseudocumene are often distilled by many successive vendors via proprietary processes in a long supply chain. These products are blended by the vendors to meet specifications having little to do with our applications in high energy physics.

10.4.1 QA/QC Measurements of Attenuation Length using a Tintometer

NOνA needs a reliable and efficient method of measuring the attenuation length of mineral oil and blended scintillator. Currently, production plans call for monitoring the mineral oil attenuation length before shipping at the producer, on arrival at the toll blender, and before it is blended into scintillator. Once blended, the scintillator attenuation length will be monitored to assure that the blended scintillator meets the Technical Design Requirements.

Given the large volume of mineral oil required by NOνA and the necessity for a reliable and efficient method of measurement, our work has focused on the Lovibond PFX880 Tintometer shown in Figure 10.14 as the attenuation QC/QA device. The Lovibond tintometer makes transmission measurements from 400-700nm through a 6" glass cell. As will be shown below, the transmission measurements at 420 nm correlate well with the attenuation length at 420 nm in the range of interest to NOνA. Equally important, tintometer measurements on an individual sample take less than a minute to make.

Fig. 10.14: The Lovibond PFX880 Tintometer in the Indiana University lab. In the foreground are 6" optical glass cells.

10.4.2 QA Attenuation Length of Incoming Mineral Oil

In the production plan for the NOνA Liquid Scintillator, there are three stages at which the attenuation length of the mineral oil is tested: (1) at the production facility before shipping to guard against shipping the mineral oil from the producer that will be rejected at the blender, (2) at the blender to guard against accepting mineral oil that does not meet the technical requirements, and (3) at the blending tank, before adding the pseudocumene and waveshifters. These attenuation length measurements will be made with the tintometer and the results will be kept in the NOνA database.

Figure 10.5 shows that scintillators blended with the mineral oil having an attenuation length ≥ 5 m meet the Technical Design Requirements. In Figure 10.15 we plot the attenuation lengths of several of the mineral oils shown in Figure 10.9 vs. their transmission at 420 nm as measured in the tintometer. There is a clear separation (dashed line) between oils that have an acceptable attenuation length and those with an unacceptable attenuation length when measured in the tintometer. Figure 10.15 demonstrates that the tintometer is capable of making the QC mineral oil measurements required by the NOνA Liquid Scintillator production plan. In addition, QC procedures based on the tintometer are quick and cost effective.

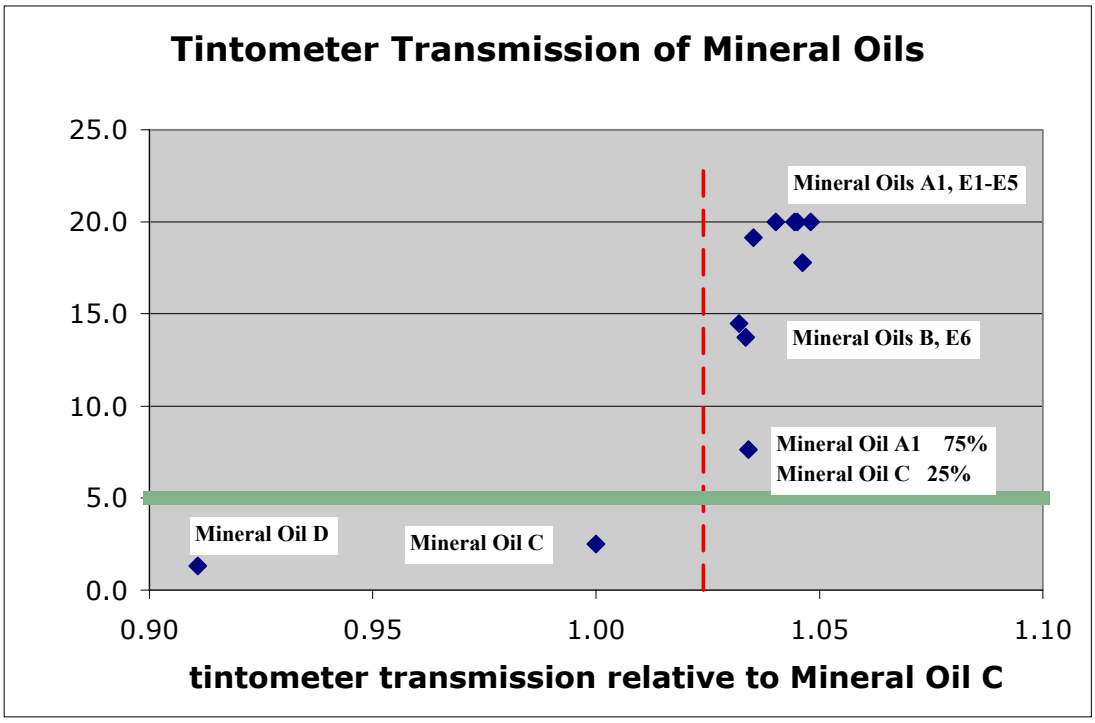

Fig. 10.15: The attenuation length (meters) of several of the mineral oils in Figure 10.9 as measured in the IU Spec vs. transmission measurements in the tintometer at 420 nm. The dashed line represents the approximate acceptance criterion for the attenuation length of mineral oil.

10.4.3 Alternative Method to QA/QC Mineral Oil Attenuation Length

In parallel with the proposed QA/QC methods that use the tintometer, NOνA is developing a fully automated instrument that makes an absolute measurement of attenuation length, without the use of reference standards, for both mineral oil and liquid scintillator. A prototype of this device, incorporating some features of the existing IU Spec is being evaluated to optimize measurement time, readout electronics performance, fluid column length and attenuation length resolution.

10.4.4 QC Attenuation Length of Outgoing Blended Scintillator

In the production plan for the NOνA Liquid Scintillator, there are two stages at which the attenuation length of the scintillator is tested: (1) at the blending facility before being shipped to Ash River and (2) at Ash River before being unloaded into the detector. The results of these tests will be kept in the NOνA database. For these QC measurements we again plan to use tintometer transmission measurements at 420 nm. In Figure 10.16 we plot the attenuation lengths of several of the blended scintillators shown in Figure 10.11 vs. their transmission at 420 nm as measured in the tintometer. Again there is a clear separation (dashed line) between oils that have an acceptable attenuation length and those with an unacceptable attenuation length when measured in the tintometer. As for mineral oil, we adopt the tintometer as the efficient and cost effective QC measurement apparatus to qualify the attenuation length of NOνA Liquid Scintillator.

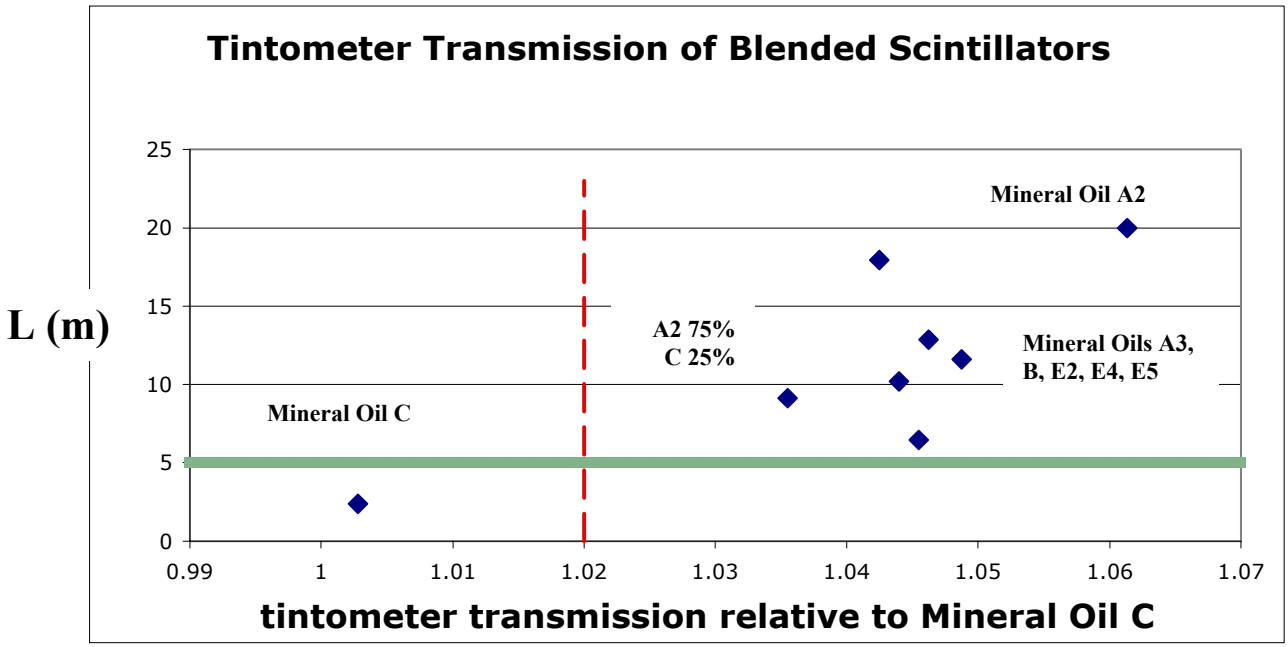

Figure 10.16. The attenuation length L (meters) of several of the scintillators in Figure 10.11 as measured in the IU Spec vs. transmission measurements in the tintometer at 420 nm. The dashed line represents the approximate acceptance criterion.

10.4.5 QA Incoming Pseudocumene

Samples of all incoming batches of pseudocumene will be drawn and shipped to Indiana University where they will be analyzed by gas chromatography-mass spectroscopy

(GCMS) to determine for compliance with the Technical Requirements on composition, purity and sulfur content in Table 10.4.

In addition, the pseudocumene will be tested with the tintometer for compliance with the Technical Requirement on clarity in Table 10.4. In the production plan for the NOνA Liquid Scintillator, there are two stages at which the clarity of the pseudocumene is tested: (1) at the blender to guard against accepting pseudocumene that does not meet the technical requirements and (2) at the blending tank before being blended with the waveshifters. The results of these tests will be kept in the NOνA database.

10.4.6 QA Incoming Waveshifters

The vendor will send a sample of each wavelength shifter (PPO and bis-MSB) from each batch manufactured to Fermilab. The vendor will provide a Certificate of Analysis for each lot. A series of tests will be performed at Fermilab. These tests will aim to verify some of the parameters measured by the manufacturer such as melting point, appearance and odor; and to check the spectral characteristics of each component such as UV transmittance under specific conditions, infrared (IR) and nuclear magnetic resonance (NMR) data. These tests can be completed in 1-2 days. The vendor will then be notified to proceed with the shipment to the location where the blending of the wavelength shifters and pseudocumene will take place. A similar procedure was used for the wavelength shifters used in the MINOS experiment. The results of these tests will be kept in the NOνA database.

10.4.7 QC Outgoing Scintillator Composition with an Alpha Source Test

A 1 μCi Am-241 α-source will be used to measure the light yield of liquid scintillator. Light yield in the "α-test" is correlated with scintillator composition. In the production plan for the NLS, there are two stages at which the light yield of the scintillator is tested: (1) at the blending facility before being shipped to Ash River and (2) at Ash River before being unloaded into the detector. The results of these tests will be kept in the NOνA database.

The test is performed as follows: A 7.5 cm diameter photomultiplier (PMT) is mounted vertically (window up) in a darkbox. Two commerical filters are placed on the PMT to block all but the useful spectrum wavelengths. Uniform size/shape bottles (inner volume ~3 cm diameter X ~8 cm high) are filled approximately half full with scintillator. One bottle contains a standard scintillator (BC-517P) and a second bottle contains the sample whose relative light output is to be determined. A special bottle lid has been manufactured that was fitted with a 1 μCi Am-241 α-source attached and this is placed on the bottle (standard or sample) to be measured. The bottle is placed on the PMT and the light detected by the PMT is recorded. The procedure requires that for each sample measurement, a standard measurement is made before and after to track drift.

The PMT output is then fed through an electronics chain: charge sensing preamplifier, linear (voltage) shaping amplifier, and MultiChannel Analyzer (MCA). The MCA spectrum shows a clear peak for the α energy deposited in the scintillator. Determining the peak (with peak-fitting software) gives a measurement of the light output. A direct comparison (ratio) of peak locations of standard and sample indicates the relative light yield of the sample.

Because the range of alphas in liquid scintillator is very short (order of 50-60 um), the α-source must be cleaned in soap and water, rinsed, and dried between measurements. The high voltage driving the PMT must also be kept within a very tight range (+- 0.5 V for a ~1000 V divider voltage) in order to minimize drift. For the above setup, the event rate is sufficient to collect a spectrum in 90 sec.

We have studied the results of the α-test during the R&D period and find that the light output measured is primarily correlated with the composition of liquid scintillator. To test this hypothesis further, we tested two samples of BC517P purchased from Bicron, one

purchased in 2005 and another purchased in 2007, in which the composition is advertised to be equivalent. The chemical analysis of these two commercial scintillators in Table 10.6 shows that the two scintillators have virtually the same composition.

	"2005" BC517P	**"2007" BC517P**
component	**mass fraction**	**mass fraction**
mineral oil	94.4%	94.7%
pseudocumene	5.5%	5.2%
PPO	0.12%	0.12%
bis-MSB	0.0016%	0.0014%

Table 10.6. Composition of Two Batches of Commercial BC517P

On the other hand, as shown in Figure 10.17, the attenuation length of these two scintillators differ significantly.

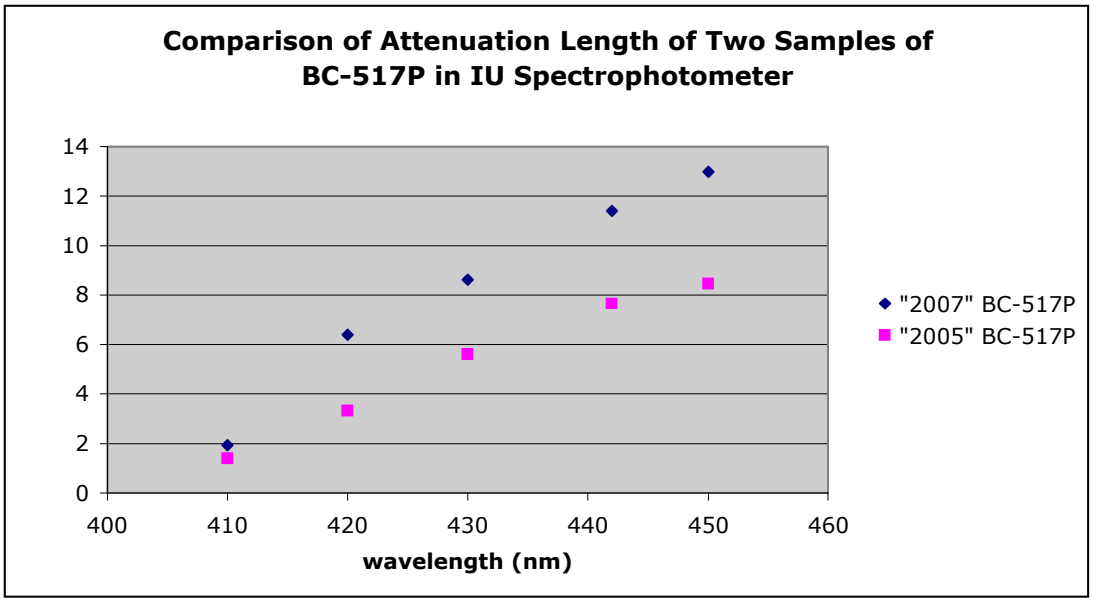

Fig. 10.17: Attenuation length of the two BC517P as measured in the IU Spec.

The α-test, if it is primarily a measure of composition, should give similar results for both scintillators. Figure 10.18 shows this expectation is met. These results are consistent with the α-test being primarily a measure of composition.

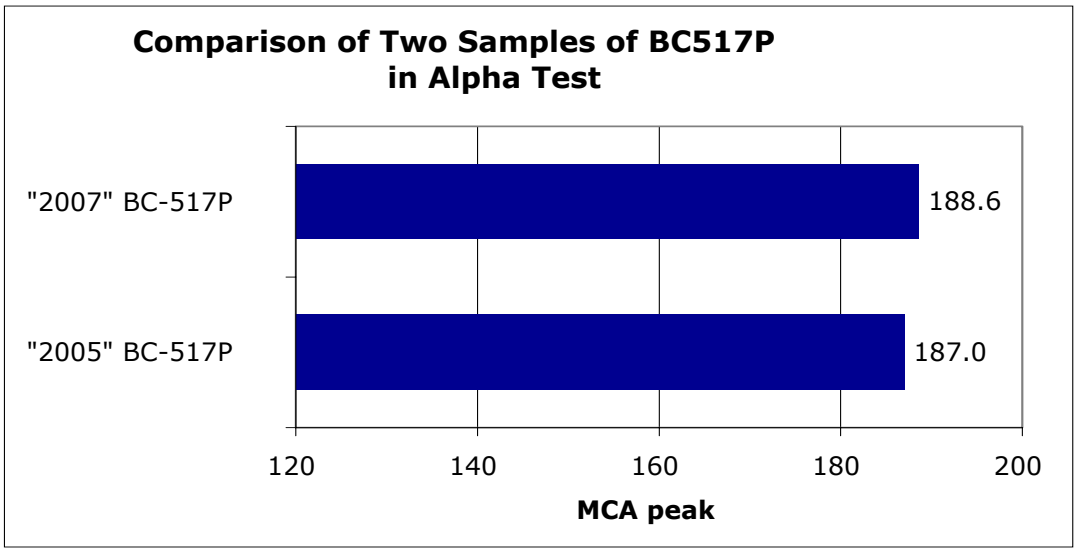

Fig. 10.18: α-test of the two BC517P scintillators produced at different times.

Finally, in Figure 10.19, we show the light yield of the two BC517P scintillators in the NOνA cell. Not surprisingly, scintillators with similar compositions but differing attenuation lengths will have different light yields in the detector.

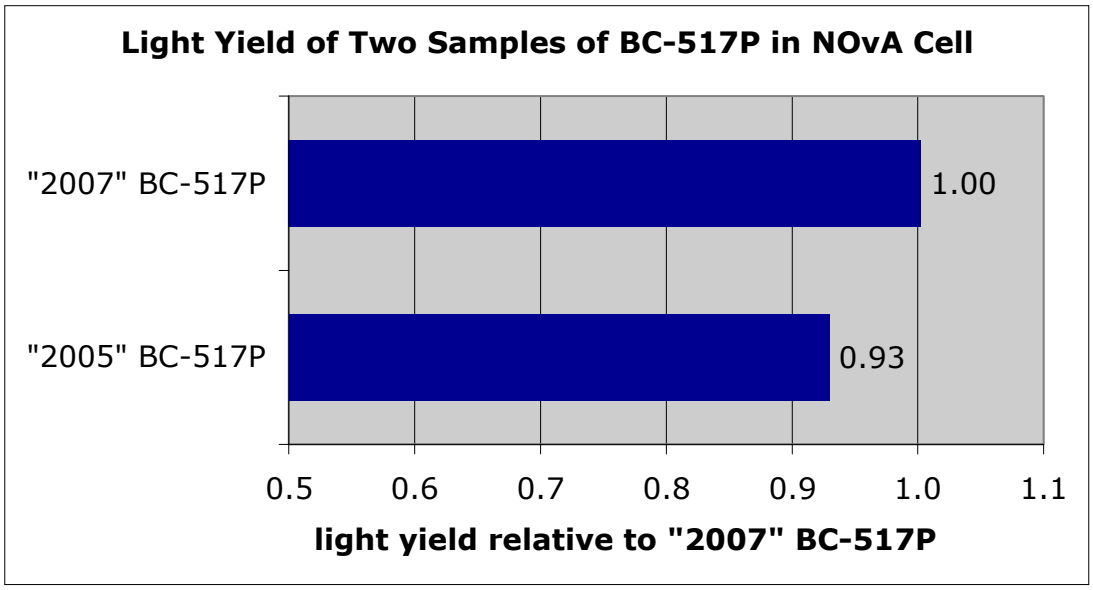

Fig. 10.19: Light yield of the two BC517P scintillators as measured in the NOνA cell.

As a second test of the α-test, we blended 4 scintillators with 100% of the fluors found in BC-517P and mineral oils with different attenuation lengths, and then compared these scintillators in the α-test. The attenuation lengths of these scintillators are shown in Figure 10.20. The differences in the attenuation length are clear.

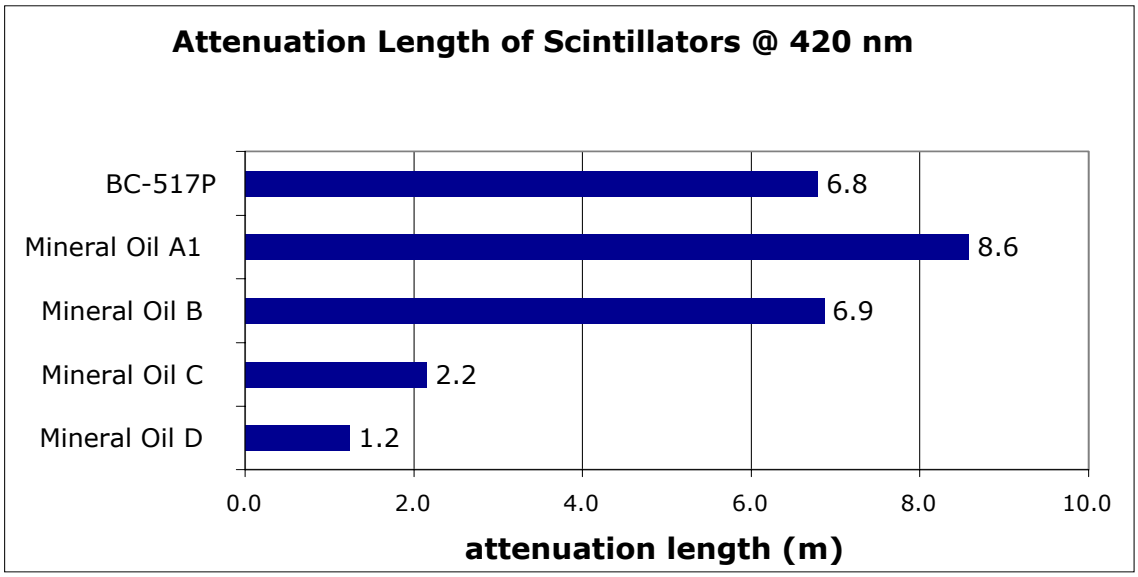

Fig. 10.20: Attenuation length of scintillators as measured in the IU Spec blended with the fluor concentration found in BC-517P and mineral oils with different attenuation lengths.

The results of the α-test for these scintillators are shown in Figure 10.21. This figure clearly shows that scintillators blended with mineral oils of very different attenuation lengths but with similar fluor concentrations give very similar results in the α-test. This test too demonstrates that the α-test is primarily a measure of composition.

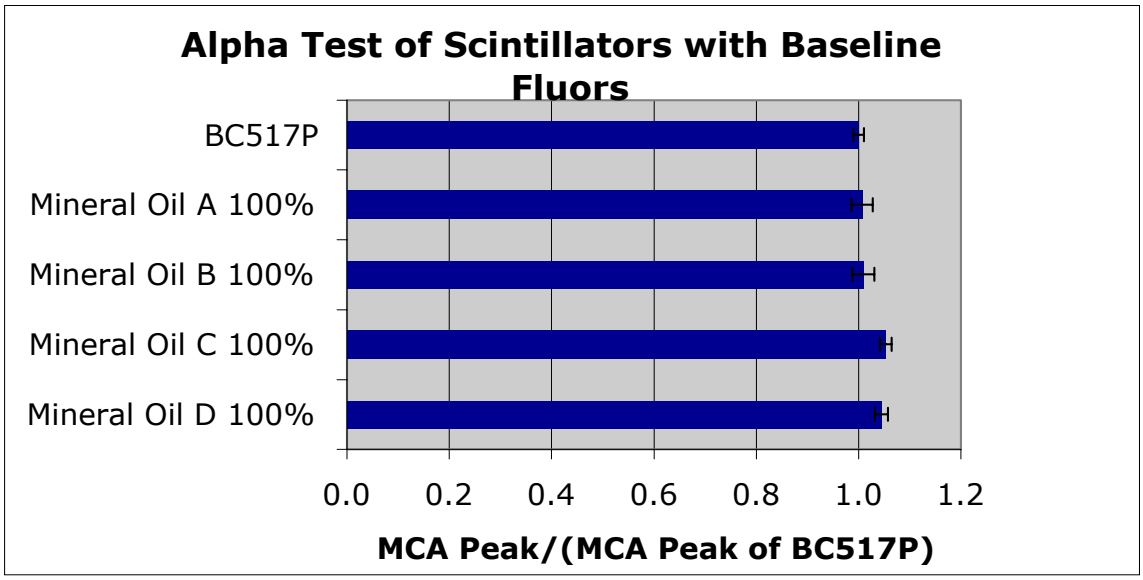

Fig. 10.21: α-test of the scintillators shown in Figure 10.19.

10.4.7.1. Precision of α-Test determination of composition

We next tested the precision to which we could measure the fluor concentration with the α-test. We blended scintillators with differing concentrations of fluors and Mineral Oil A1, and compared these scintillators with BC517P in the α-test. The results of these tests are shown in Figure 10.22. This figure shows that we can reliably detect a 3% difference in the concentration of Baseline Fluors.

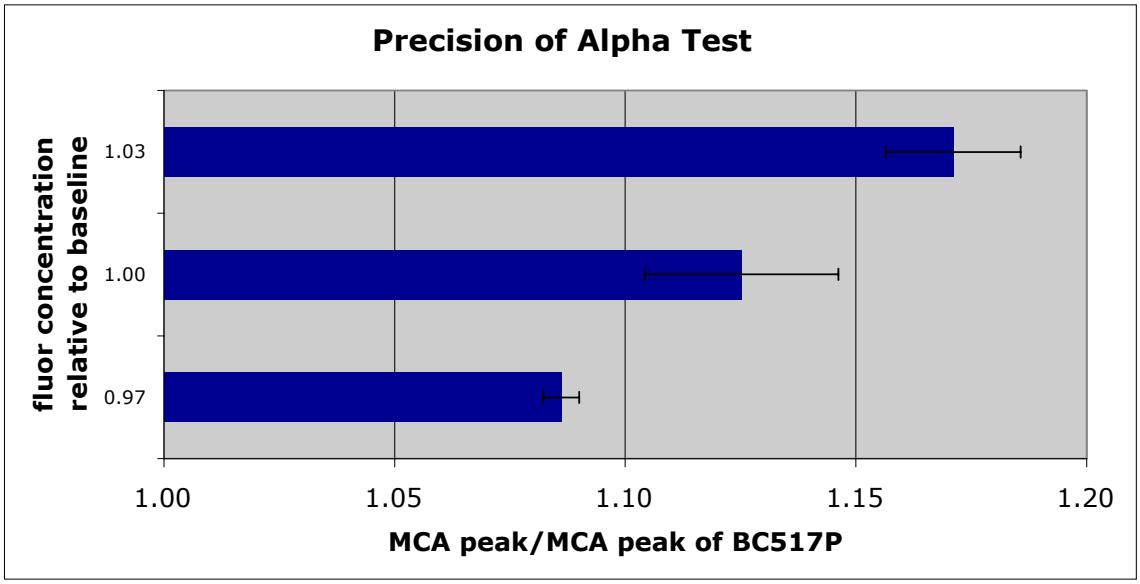

Fig. 10.22: The α-test results of the three scintillators blended with Mineral Oil A1 and differing concentrations of fluors. The error bars are statistical and reflect repeated measurements..

10.4.7.2. Radiation Safety

The α-test described above uses a 1 μCi Am-241source. These sources will be used both at the toll blender site and the Ash River site. NOνA must therefore comply with the radiation safety regulations at both locations.

Illinois is an "Agreement State", which means that Illinois has entered into an agreement with the US Nuclear Regulatory Commission, whereby the NRC has relinquished to Illinois the regulatory authority over the small quantities of nuclear materials used in the α-test. NOνA consequently is required to apply to Illinois for a license to procure, possess and use the radioactive source. After discussing this issue with officials at the Illinois Emergency Management Agency, Division of Nuclear Safety, NOνA needs only an R&D license because of the small quantity of radioactive material for the project and its research use.

The Ash River laboratory is part of the University of Minnesota and is obligated to follow the University radiation safety rules. The application and rules for "Possession and Use of Radioactive Materials" can be found at http://www.dehs.umn.edu/rpd/.

10.4.8 QC Conductivity

NOνA needs a reliable and efficient method of measuring the conductivity of blended scintillator to be confident that the scintillator conductivity is at safe levels. Currently production plans call for measurement of the conductivity before shipping at the producer. The results of these tests will be kept in the NOνA database.

Given the large volume of mineral oil required by NOνA and the necessity for a reliable and efficient method of measurement, our work has focused on the Emcee Electronics Model 1152 Digital Conductivity Meter shown in Figure 10.23. This device is a reliable and inexpensive instrument for measuring conductivity. It reads conductivity in picosiemens/meter. The meter uses a probe consisting of two concentric steel electrodes. The probe is shown in Figure 10.24. When the probe is immersed in oil, a fixed voltage is applied to the electrodes. The unit generates a current which is amplified and displayed on the meter.

The conductivity measurements shown in Figure 10.7 were made with an Emcee Conductivity Meter using the following procedure: A volumetric flask was filled with 1 liter of Mineral Oil A1 + Baseline Fluors without Stadis-425 and the contents transferred to an open mouth stainless steel container. The meter was calibrated using the standard test procedure. The conductivity meter ground lead was clipped to the edge of the stainless steel can and the meter probe inserted to the specified depth of 2.75″. Measured amounts of Stadis-425 were added and the mixture was stirred for 1 minute with a teflon paddle. The mixture was then allowed to stand for 5 minutes before the mixture was tested.

Fig. 10.23: The Emcee Electronics Model 1152 Digital Conductivity Meter

Fig. 10.24: Probe for the Emcee Electronics Model 1152 Digital Conductivity Meter

10.5 Scintillator Production

10.5.1 Production Model

The NOvA liquid scintillator will be blended at a commercial toll blending facility in the greater Chicagoland area. The production model is shown in Figure 10.25. Components are purchased by Fermilab and delivered to the blending facility by the most cost-efficient method: the mineral oil by rail or barge, the pseudocumene by rail or tanker truck, and premeasured waveshifter packages by common carrier. Blended liquid scintillator is delivered to Ash River by tanker trailers dedicated to the NOvA experiment.

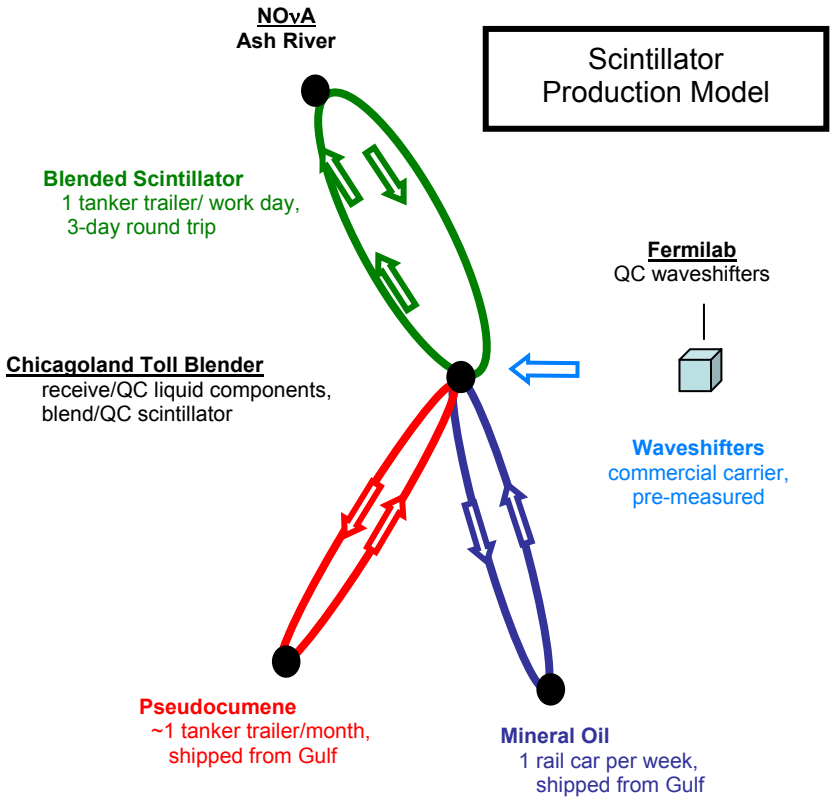

Fig. 10.25: Scintillator Production Model as described in the text.

10.5.2 Toll Blender Operations

The NOvA liquid scintillator will be blended at a commercial toll blending facility in the greater Chicago area. The blending model is shown schematically in Figure 10.26. In this model the components are purchased by Fermilab and delivered to the blending facility by the most cost-efficient method. At this facility, all the tanks used in the NOvA liquid scintillator blending will be stainless steel or epoxy-lined. It should be noted that MiniBooNE stores 250,000 gallons of very high quality mineral oil in an epoxy-lined tank "and has noticed no degradation after many years". These tanks can be heated. In addition, all transfer lines, hoses, and pumps used in the blending will be dedicated to NOvA liquid scintillator blending and locked off between deliveries for all the process steps. The lines and pumps will be insulated and fitted with filters.

The toll blender will offload the mineral oil into a storage tank with capacity in the range of 650,000 gallons. The specific gravity, kinematic viscosity, and anti-oxidant content as certified by an independent testing laboratory, with documentation supplied by the producer, will be checked against the Technical Requirements in Table 10.3 for compliance and the data added to a database. An on-site Fermilab technician will test the mineral oil for compliance with the attenuation length Technical Requirement on the NOνA Mineral Oil in Table 10.3 with the Lovibond tintometer. The attenuation length data will be added to the database.

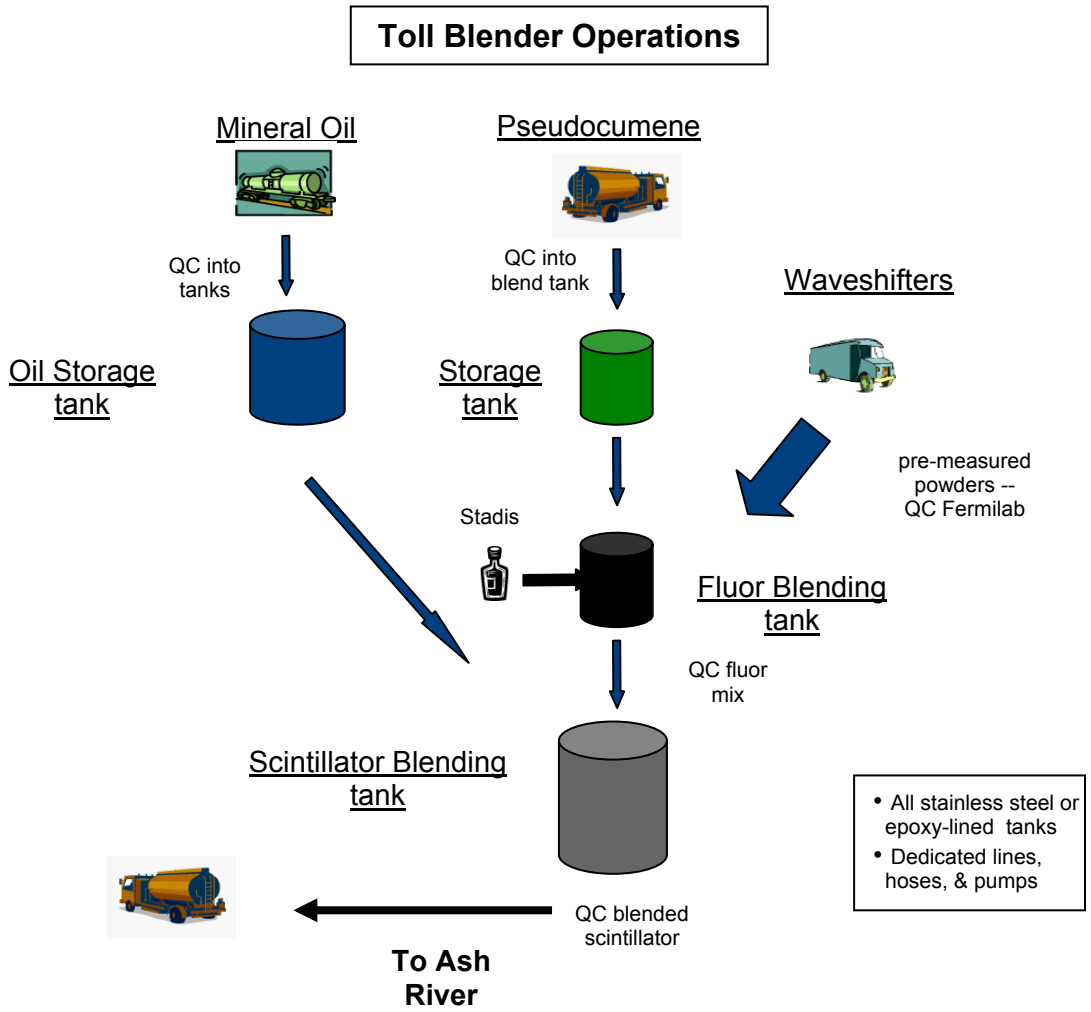

Fig. 10.26: Toll Blender Operations for the production of liquid scintillator.

Pseudocumene will be delivered to the blending facility by rail car. The kinematic viscosity as certified by an independent testing laboratory with documentation supplied by the producer will be checked against the Technical Requirement in Table 10.4 for compliance, and the data added to a database. A sample of pseudocumene will also be tested for compliance with the Technical Requirement on clarity in Table 10.4 with the Lovibond Tintometer and the data added to the database. As a final QA step before it is offloaded, a sample of the pseudocumene will be drawn and shipped to Indiana University where it will be analyzed by gas chromatography-mass spectroscopy (GCMS) to determine its composition and its compliance with the Technical Requirements on purity and sulfur content in Table

10.4. These data will also be added into the database. The pseudocumene will then be offloaded into a tank that holds of order 30,000 gallons.

Waveshifters will be delivered by commercial carrier in pre-measured packages to the Toll Blender. Before being shipped, samples of the wave shifters from each batch will be sent to Fermilab where the QA analysis will be done, as described in §10.3.1.2. Once the QA analysis establishes compliance with Technical Requirements, these packages will be transported to the blending facility where they will be combined with the pseudocumene in the Fluor Blending tank of order 30,000 gallons. The anti-static agent Stadis-425 will also be added at this step.

The blending will be done by mixing nozzles in the tank which draw from a bottom sump. After blending, a sample of the fluor mix will be drawn, mixed with mineral oil, and tested for compliance with the light yield, attenuation length, and conductivity Technical Requirements. These tests qualify the Fluor Mix. Blending in smaller batches will minimize the losses from any blending error.

The Fluor Mix is then combined with mineral oil in the Scintillator Blending tank of order 50,000 gallons. The fluids will be metered into the Scintillator Blending tank with PLCs. The blending will be done with mixing nozzles that can draw from the top or bottom of the tank. Once blended, the scintillator will be tested for compliance with the Technical on attenuation length, light yield, and conductivity. Once certified, the blended scintillator will await shipping to Ash River by tanker trrailer. The Storage tank will allow time to diagnose and correct any off-specification blends.

The baseline plan is to transport liquid scintillator by tanker trailer. The tolerances on the composition of the liquid scintillator blended from qualified components per standard 6,341 gallon tanker trailer are given in Table 10.7.

component	weight/mass per 6,341 gal	tolerance	weight/mass tolerance per 6,341 gal
mineral oil	**8,884 lbs**	**1%**	**88.8 lbs**
pseudocumene	**382 lbs**	**1%**	**3.8 lbs**
PPO	**18.5 kg**	**1%**	**185 gm**
bis-MSB	**260 gm**	**1%**	**2.6 gm**
Stadis-425	**61 gm**	**10%**	**6 gm**

Table 10.7. Blending Tolerances for 7,000 gal Tanker Trailers

10.5.3 Liquid Scintillator Delivery

The details of the NOνA liquid scintillator logistics plan are driven by the requirements on the scintillator delivery rate and the time it takes a driver to make the round trip Chicago (toll blender) – Ash River – Chicago.

The NOνA detector is made up of a large volume of liquid scintillator and this scintillator needs to be delivered at approximately the same rate as the detector is being filled in order to minimize infrastructure costs. Since this requirement closely links the delivery schedule to the detector construction schedule, the detector mass, and the funding profile, and these are not yet definite, the delivery schedule needs to remain flexible.

There are several additional constraints on the logistics of delivering scintillator. The Ash River site will only be able to take deliveries during a normal Monday through Friday work week, and there can be no assurance that the toll blender selected would not have similar restrictions. Consequently, tanker trailer deliveries and returns must be scheduled so

that drivers do not make drop-offs or pick-ups on weekends (which translates into no weekend driving). In addition, to minimize driver down time, deliveries at Ash River need to be scheduled so that there is an empty tanker trailer available for the return trip immediately upon the delivery of a full tanker.

NOνA requires 3,210,584 gallons of liquid scintillator to be delivered over a period of 21 months. With the constraints described above, this schedule leads to an average delivery of 8,170 gallons per M-F work day. (At this early stage, no account need be taken yet for holidays.) Assuming standard 7,000 gallon tanker trailers, this schedule requires approximately 6 deliveries of liquid scintillator per M-F work week.

FThe distance from Fermilab to Ash River is about 600 miles. Driving at the speed limit, the driving time is about 10 hours. Since truckers must enter all driving times in their log books by law, show 1/2 hour of truck inspection per day, and take a 1/2 hr lunch break, the round trip takes 22 hours. Assuming an hour for the pick-up or drop-off time, the round trip takes 26 hours. After adding in time for traffic and weather delays, a round trip driving time of 3 days is reasonable and conservative.

Tables 10.8 and 10.9 show a logistics plan that meets the requirements for liquid scintillator delivery. There is a natural two week cadence for deliveries. Table 10.8 shows the two week cadence for a given tanker trailer.. A tanker trailer leaves the toll blender in Chicagoland in the morning and arrives at midday of the following day. The driver then picks up an empty tanker trailer in the afternoon and drives back to the toll blender, arriving at the end of the third day. This schedule enables a driver to stay clear of weekend pick-ups and deliveries.

day		**activity**	**duration**
			(days)
1	**prep/Chicago**	inspect truck, QC scintillator, load truck	1
2	**out**	travel	1
3 (AM)	**out**	travel	0.5
3 (PM),4,5,6,	**idle/Ash River**	unload truck,	5
7,8 (AM)	**idle/Ash River**	QC scintillator	
8 (PM)	**return**	travel	0.5
9	**return**	travel	1
10	**idle/Chicago**		1

Table 10.8. Two Week Tanker Truck Schedule for Delivery of NOνA Liquid Scintillator.

Table 10.9 shows the logistics plan that delivers 6 tanker trailers to Ash River/M-F work week. It operates on a two week cadence and requires 12 tanker trailers. The schedule runs from Friday-Thursday because drivers are on the road Monday-Wednesday or Wednesday-Friday, thus requiring no weekend pick ups or drop offs. Drivers end up where they began, as required.

The schedule shown in Table 10.9 is flexible and can be simply modified to adjust to needed increases or decreases in the quantities of scintillator delivered. There are two ways that we can vary the quantity of scintillator transported. First, we can vary the size of the tankers with the same schedule. The delivery schedule in Table 10.9 is based on 6,341-gallon tanker trailers. Other standard size tanker trailers have 7,000-gallon capacity and 7,500

gallon capacity. Second, the schedule in Table 10.9 can be modified to accommodate required increases or decreases in delivered scintillator. This schedule should be considered as an example. It is quite simple to alter the schedule by multiples of two tanker trailers.

	Friday	Monday	Tuesday	Wednesday	Thursday
			week 1		
prep	1,2,3		4,5,6		
out		1,2,3		4,5,6	
out			1,2,3		4,5,6
Ash River	7,8,9, 10,11,12	7,8,9, 10,11,12	1(PM),2(PM),3(PM) 7(AM),8(AM),9(AM) 10,11,12	1,2,3, 10,11,12	1,2,3, 4(PM),5(PM),6(PM) 10(AM),11(AM),12(AM)
return			7,8,9		10,11,12
return	4,5,6			7,8,9	
idle		4,5,6			7,8,9
			week 2		
prep	7,8,9		10,11,12		
out		7,8,9		10,11,12	
out			7,8,9		10,11,12
Ash River	1,2,3, 4,5,6	1,2,3, 4,5,6	1(AM),2(AM),3(AM), 4,5,6, 7(PM),8(PM),9(PM)	4,5,6, 7,8,9	4(AM),5(AM),6(AM) 7,8,9, 10(PM),11(PM),12(PM)
return			1,2,3		4,5,6
return	10,11,12			1,2,3	
idle		10,11,12			1,2,3

Table 10.9. Delivery Schedule for 12 Tanker Trailers every 2 weeks

10.6 Design Changes since the Conceptual Design Report

There have been several changes since the Conceptual Design Report.

The fluor concentration has been reduced from 100% to 75% of Bicron BC-517P. this produces a scintillator with 75% of the light output of BC-517P as required in Chapter 6.

Blending liquid scintillator is planned to take place at a commercial toll blending facility. In the Conceptual Design Report, scintillator blending was to be done at Fermilab.

The importance of making liquid scintillator semiconducting has been recognized since the Conceptual Design Report and the baseline composition of the liquid scintillator now includes the addition of Stadis-425.

We have shown that the Lovibond tintometer is a commercial device that can make rapid and consistent measurements of the transmission of mineral oil, pseudocumene, and blended liquid scintillator. The Lovibond tintometer has been adopted as the baseline measurement device for monitoring transmission of mineral oil at the producer and the toll blender, and the blended liquid scintillator at the toll blender and Ash River.

10.7 Work Remaining to Complete the Scintillator Design

There are two issues that need to be addressed with the Integration Prototype Near Detector (IPND). These issues concern production in quantity and so are not easily studied in the lab.

The first issue has to do with scintillator composition in large quantities. So far we have been blending scintillator in small batches of approximately 1-10 gallons each. For the IPND, we will be blending four batches of approximately 5,000 gallons. Two of these batches will be produced in the fall of 2007 and the second two will be produced in spring 2008. Among the issues that will be studied during these production runs will be the mixing time required to fully blend liquid scintillator in quantity and procedures for QC/QA testing during production. Since the four batches of scintillator will be blended with combinations of Mineral Oils A3 and C and Pseudocumene from producers A and B, we will be able to quantify the light yield of scintillators blended from components from multiple vendors delivered at multiple times over the next year.

The second issue concerns the blending tanks and transportation tanks. In the IPND we are using ISO tankers cleaned to chemical grade cleanliness and then cleaned once again to food grade cleanliness. The current plan calls for the tanker trailers used in transporting liquid scintillator to Ash River to be cleaned this way. The IPND will therefore provide valuable information in evaluating this cleanliness standard. Since we will be blending four batches of scintillator, we will also be able to examine the cleanliness of the blending tank after it has been used several times.

One last issue concerns the Toll Blenders in the Chicago area. We plan visits to these facilities in order to understand their capabilities. These visits will form the basis of a full RFP to select a vendor.

10.8 Chapter 10 References

[1] For example, see Birks et al., *Brit. J. Appl. Phys*, **14**, 141 (1963) for the absorption and emission spectra of PPO and POPOP. There are references in this paper to work by Kallman and others from the early 1950s. See also H. Rheinberger, "Liquid Scintillation Counters, 1950-1970", Max Planck Institute for the History of Science, 1999.

[2] Mineral Oil Based Liquid Scintillators, www.bicron.com

[3] Mineral Oil Based Liquid Scintillators, www.eljentechnology.com/index.html

[4] NFPA 77, "Recommended Practice on Static Electricity", 2000 ed.

[5] The MACRO Collaboration. *Nucl.Instrum.Meth*., **A486,** 665 (2002).

[6] See Kramer, Lok, and Krug, "The Evolution of Base Oil Technology", in "Turbine Lubrication in the 21st Century", edited by Herguth and Warne, American Society for Testing and Materials, ASTM STP#1407, 2001. See also Kramer et al., Machinery Lubrication Magazine, May 2003.

[7] J.P. Petrakis, *et al. Nucl.Instrum.Meth*., **A238,** 256 (1988).

11 Wavelength Shifting Fiber

11.1 Introduction

Plastic wavelength shifting (WLS) fibers provide an efficient method for collecting light generated in the long liquid scintillator filled cells of the detector. The violet light (~425nm) emitted by the scintillator is absorbed by a fluorescent dye in the WLS fiber. The blue-green (450 – 650 nm) light emitted by the dye is partially trapped within the fiber by total internal reflection. Once trapped much of the short wavelength light (< 520 nm) is attenuated while traveling through a full length of WLS fiber, however, the longer wavelengths are only weakly attenuated. This light coupled with the high quantum efficiency of avalanche photodiodes at long wavelengths yields a strong signal for minimum ionizing particles traversing anywhere along the length of a cell. To instrument the 15 kT NOνA detector, 13,000 kilometers of fiber are required.

11.2 Technical Design Criteria

NOνA scientific performance requirements (see Chapter 4) can be met with a mean signal of at least 20 photoelectrons for minimum ionizing particles through the far end of the 15.5 m long NOνA cell. The combined effects of the Scintillator, PVC cell walls, and the Wavelength Shifting Fiber determine the amount of light reaching the APD (See Chapter 5). For the WLS fiber this translates into two technical design criteria:

1) Capture fraction for the scintillation light, and
2) An effective attenuation length for light transmitted through ~16 meters of fiber.

A large fiber diameter will maximize the capture fraction, however, the diameter is limited by the need to fit a loop of fiber safely into the cell cross section. A high concentration of K27 fluorescent dye in the fiber will improve the capture fraction but worsen the attenuation length for short wavelength light. Required therefore, is an experimental optimization dependent on the details of the cell shape, wall reflectivity, the number and diameter of the fibers, and the photodetector quantum efficiency (see chapter 6).

The WLS fiber also must survive emersion in liquid scintillator for the 20-year lifetime of the experiment.

11.3 The NOνA Wavelength Shifting Fiber

11.3.1 Overview

To maximize light collection and transmission at a reasonable cost and to satisfy the experiment's mechanical constraints, NOνA will use loop of a 0.7 mm diameter fiber inside of each PVC extrusion cell. The looped fiber design, as shown in Figure 11.1, effectively provides two fibers with a no cost 95% reflective mirror about 16 meters from the photodetector. From the far end of each cell, where light collection is most important the looped fiber can yield more light by nearly a factor of four when compared to a single fiber with a nonreflecting end. Because two fibers in the same cell will partially shadow each other, the overall improvement factor is only ~3.7.

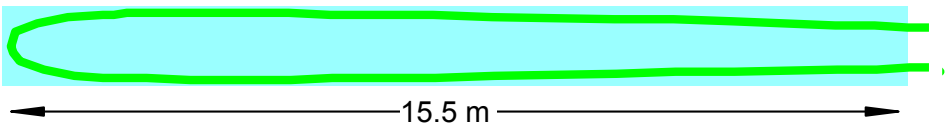

Fig. 11.1: A single NOνA cell with a looped WLS fiber, shown in green

Suitable multi-clad WLS fiber is available from Kuraray [1], the same vendor (Kuraray) and type of fiber (multiclad) used for optical readout of most large area scintillation counters. The fiber core material is polystyrene (refractive index n=1.59) followed by an acrylic inner cladding (n=1.49) and a fluorinated-polymer outer cladding (n=1.42). The second cladding increases the acceptance angle for total internal reflection, improves the transmission of the fiber, and provides protection for the inner layer of cladding and the fiber core. The thickness of each cladding layer is 3% of the fiber diameter reducing the diameter of the core to 88% of the outer diameter. Variations in the WLS fiber diameter or cladding thickness are carefully controlled by Kuraray to minimize attenuation variations and to maintain compatibility with precision connectors.

The absorption spectrum of the commonly chosen K27 fluorescent dye is well matched to the emission spectrum of liquid scintillators. A typical concentration of the K27 fluorescent dye is 200 parts per million (ppm), however, the NOvA fibers are atypical. The fibers are unusually long and thin. Also, the avalanche photodiodes used in the readout have high quantum efficiency at long wavelengths. These characteristics of the readout are sufficiently different from previous applications that a thorough survey of the available dye concentrations was performed. This is discussed in section 11.4 of this chapter.

11.3.2 NOvA fiber diameter

The NOvA baseline fiber has an outer diameter of 0.70 mm, the smallest fiber diameter that is practical to handle during module construction. We use the most flexible fiber (called S-type) to facilitate the U-bend at the far end of a cell and the right angle bend toward the APD. Data provided by Kuraray indicates that S-type fiber of 1mm diameter will suffer core damage with a bend diameter smaller than 40 mm, or 40 times the fiber diameter. Kuraray conservatively recommends a bend diameter of 100 times the fiber diameter. The smallest U-bend diameter, 60 mm or 85 times the fiber diameter, occurs in the thicker walled vertical modules, but Kuraray has indicated [2] that this bend should be safe for the fiber core. Although Non-S fiber exhibits much longer attenuation lengths, for this fiber Kuraray recommends a bend diameter greater than 200 times the fiber diameter, which rules out Non-S fiber.

11.3.3 Fiber Survival in Liquid Scintillator

The WLS must survive in liquid scintillator for the length of the experiment. Kuraray has verified [2] that the two claddings are insoluble in pseudocumene and therefore provide a double barrier against scintillator penetration to the sensitive fiber core. Previous aging tests on single clad fibers [3,4] and double clad fibers [4-7] have shown that WLS fiber are unaffected by room temperature scintillator for at least 10 years, and for an equivalent of >15 years in accelerated aging tests in heated scintillator. To provide another measure of safety, an increase in the thickness of the inner acrylic layer has been suggested [8]. We are investigating this option with Kuraray, however, they have no experience with this product. Consequently, they require an R&D period to engineer the pre-form and search for hidden problems.

Since the NOvA fiber will have a U-bend of 60 mm diameter in the scintillator, the continuity of the cladding layers protecting the fiber core from the liquid scintillator in this condition was tested. A 0.8 mm fiber coiled 10 times at a diameter of 60 mm, was immersed in a liquid scintillator containing 50% pseudocumene at a temperature of 42 C for 14 days with no measurable degradation in light transmission [9]. Another series of tests on a larger sample of fiber with various diameters, curvatures of 3 and 6 cm, and at a range of temperatures is being performed. In results representing 2 months of exposure, all of the S-type fibers are still active. Aging tests will continue throughout the project. Another study [10] immersed the fiber end directly into scintillator samples and periodically measured the length of fiber core that had dissolved. Below a concentration of 25% pseudocumene, no loss of core material could be seen over a period of 120 days. Also, fiber ends with exposed cores that had been sitting in vials

containing 16% pseudocumene scintillator for 10 years showed a typical 0.5 mm of dissolved core. For comparison, NOvA uses scintillator with a 4% concentration with the core of the fiber protected by two layers of cladding.

11.4 Dye Concentration in NOνA Fiber

With the major characteristics of the WLS fiber determined by other considerations, only the dye concentration remained as an adjustable parameter. For concentrations < 1000 ppm the dye does not significantly affect the cost of the fiber.

Fiber optimization involves finding the dye concentration that achieves the largest APD signal for scintillation light generated at the far end of a cell. Due to an imperfect cell reflectivity (~ 93%) it is important that the scintillation light be absorbed by a fiber after a small number of reflections. For example, increasing the dye concentration from 150 to 300 ppm in the fiber core reduces the absorption length from 0.4 mm to 0.2 mm for scintillation light. For light intercepting the core of the 0.7 mm diameter fiber, this increase in dye concentration yields an average absorption probability that increases from 68% to 88%. In a simple model of a looped 0.7 mm diameter fiber in a 93% reflective cell, this increased dye concentration results in a scintillation light capture efficiency that increases by 25%, from 0.24 to 0.30. However, a stronger attenuation caused by the increased dye concentration might reduce the amount of light reaching the photodetector.

Due to the overlap of the absorption spectrum and the emission spectrum of the dye [1], as shown in Figure 11.2, the light emitted below 500 nm is severely attenuated. The intensity at wavelengths < 490 nm, including the first emission peak of the K27 dye at 475 nm, has been completely absorbed after passing through less than 0.5 m of fiber. The result is a spectrum shifting toward longer wavelengths after passing through typical lengths of fiber, as shown in Figure 11.3. The intensity at number of fixed wavelengths > 520 nm, shown in Fig. 11.4, are adequately parameterized by single exponentials. The integrated intensity, a sum of exponentials, cannot be described by such a simple function.

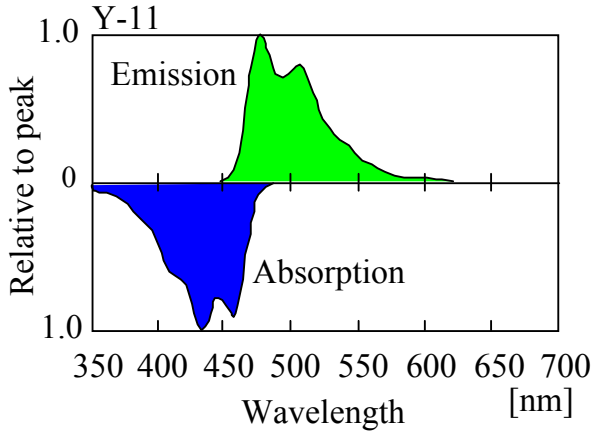

Fig. 11.2 Absorption and emission spectra of the K27 dye (Kuraray Y11 fiber) dissolved in styrene monomer.

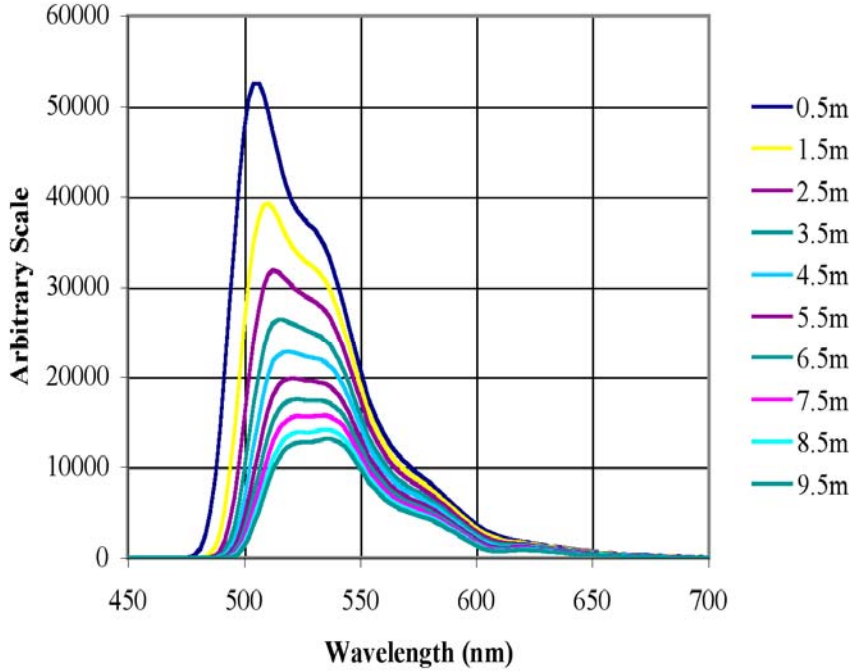

Fig. 11.3: Spectrum of light exiting a 0.7 mm WLS fiber doped with 150 ppm of the K27 dye stimulated at distances from 0.5 to 9.5 meters.

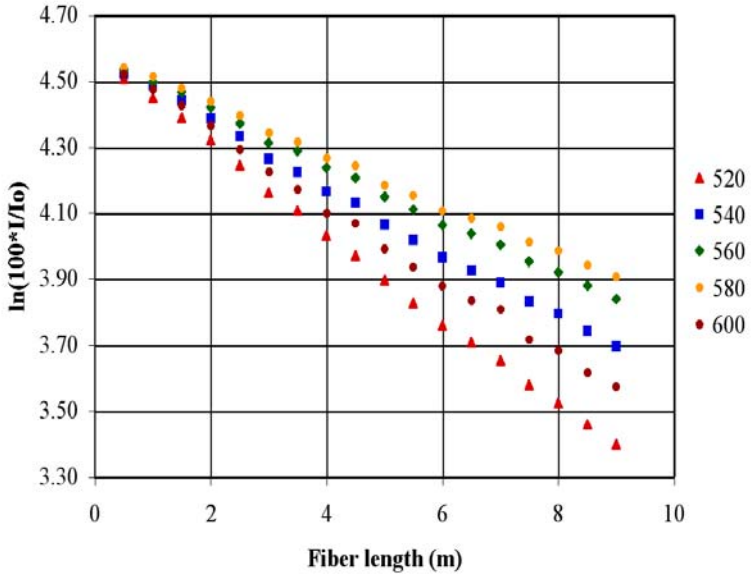

Fig. 11.4: log(Intensity) vs. distance at fixed wavelengths for light exiting a 0.7 mm WLS fiber doped with 150 ppm of the K27 dye stimulated at distances from 0.5 to 9.5 m.

With a typical dye concentration the attenuation of light at long wavelengths (> 550 nm) is determined primarily by the optical properties of the polystyrene core rather than by the dye. An increased dye concentration, therefore, does not lead to a comparable increase in the absorption of the longer wavelength light.

11.4.1 Studies of Kuraray Fibers (Batch1)

In our initial study we obtained fibers in 3 diameters (0.6, 0.7 and 0.8 mm) and 3 dye concentrations (150, 250 and 300 ppm) and a few other samples. We obtained attenuation length vs. wavelength data for each of these fibers. At 580 nm, the attenuation length can exceed 18 m, as shown in Fig. 11.5; only slightly shorter than the ~22 m attenuation length that Kuraray quotes for S–type fiber with an un-doped polystyrene core at this wavelength. The sharp drop in the attenuation length to ~7 m at 610 nm is due to an absorption resonance observed in all fibers with a polystyrene core.

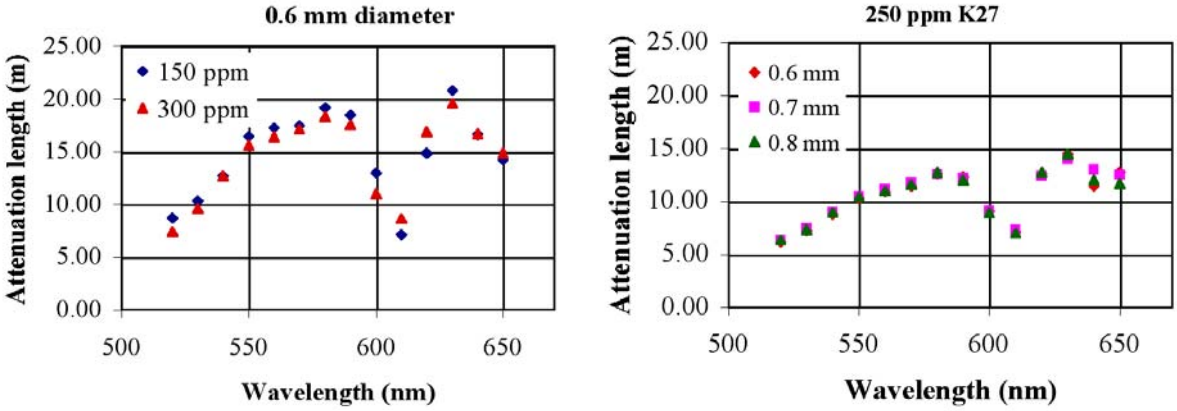

Fig. 11.5 Attenuation lengths derived from fits to the light intensity exiting a fiber illuminated at distances between 4 and 9 m: 0.6 mm diameter fibers with K27 dye concentrations of 150 and 300 ppm (left), and various diameters for a dye concentration of 250 ppm (right).

If determined primarily by the dye concentration, the attenuation length would be inversely proportional to the dye concentration and a reduction of 50% would have been expected for an increase of a factor of two in dye concentration. However, a doubling of the dye concentration from 150 to 300 ppm has reduced the attenuation length only slightly, ~5%, uniformly across the wavelength range. An upward fluctuation in the properties of the particular 300 ppm fiber samples could explain this measurement. Also, we have measured at 580 nm attenuation lengths approaching 20 m in fibers with diameters between 0.6 and 0.8 mm with no discernable diameter dependence. Therefore, the core-cladding interface in fibers with diameters in this range can be of sufficient quality that attenuation due internal reflections does not compete with the core polystyrene attenuation.

It was surprising to find, as shown in the second plot in Figure 11.5, that all fibers with a dye concentration of 250 ppm had an attenuation length of about 12 m at 580 nm. For light traveling from the far end of the NOvA cell, 36% less light is seen at this wavelength than with the two other dye concentrations. All fiber diameters with the same dye concentration were produced sequentially from the same pre-form. This suggests a problem with the 250 ppm pre-form, but a further investigation lead away from that conclusion.

We obtained Kuraray's spectrographic Quality Control (QC) measurements [2] for two samples of each fiber diameter and dye concentration in the production of this R&D fiber. These measurements exhibit the short attenuation lengths for the 250 ppm dye concentration we had observed. Also, their data shows two fiber samples with a 0.6 mm diameter fiber and a 150 ppm dye concentration that had attenuation lengths at 580 nm that differed by 20% from an average of 17.5 m. Kuraray reported that they could not find any anomalies in their pre-form production or in the drawing parameters that would explain any of the variations seen in attenuation length. Independently, we had the K27 content in the fibers analyzed [10] by liquid chromatography at

Indiana University and found that the dye concentrations were consistent with the quoted values, with no indications of impurities.

Under the assumption that the attenuation length is diameter independent (consistent with our observations in the range 0.6 – 0.8 mm), the six measurements by Kuraray of attenuation at each dye concentration could be used to determine their variation. If attenuation length variations are induced in the drawing process, they should depend only on wavelength. Therefore, we determined the average attenuation length and the fractional variation at the seven wavelengths in the range 520 – 580 nm that Kuraray provided, as shown in Fig. 11.6. The averages at each wavelength are not independent but show a general trend of increasing attenuation length and fractional variation as the wavelength increases.

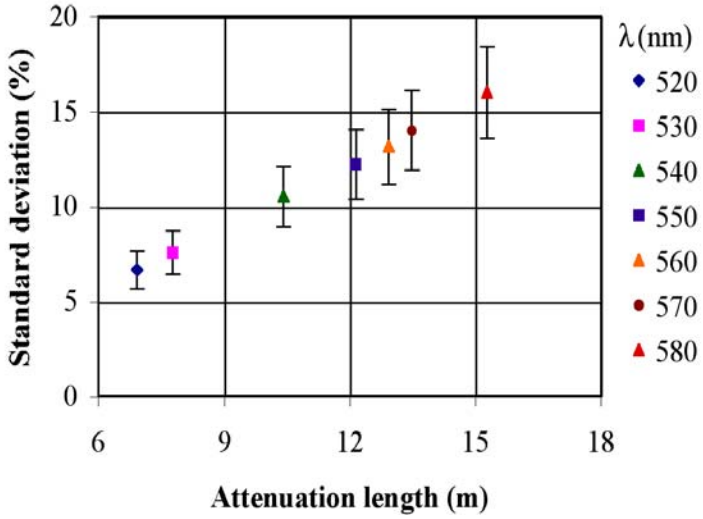

Fig. 11.6: Variation (%) in the attenuation length as determined from Kuraray QC data for six fiber samples with each dye concentration.

The experience of the MINOS collaboration [11] is that their batch-to-batch variations in attenuation were about 8% at an average detected wavelength that we estimate to be about 530 nm. At this wavelength the current samples show a similar variation (Fig 11.6). The light from the far end of the NOvA cell detected by the APD will have an average wavelength of about 550 nm, so that 12 m attenuation length with a variation of about 12% can be expected, and variations of 15-20% from the average would be fairly common at 580 nm.

As discussed in Chapter 6, variations in the fiber will impact the overall NOvA light output. In this chapter we show that the technical design criterion of 16% variation (std. dev.) set in Ch 6 is satisfied by a 12 % variation (std. dev.) in attenuation length for the fiber. The long attenuation length of the 150 and 300 ppm doped fibers above are likely examples.

11.4.2 Studies of Kuraray Fiber (Batch 2)

In additional samples of 0.7 mm diameter fiber ordered from Kuraray the attenuation length variations are similar to those seen in the first batch. It appears that Kuraray has not been able to improve the control the variations in the attenuation length at long wavelengths. Therefore, we will assume that the variations in the production fiber will be about the same as those seen here.

To perform the fiber optimization, we constructed a test cell with an approximate NOvA cross section (4 cm x 6 cm), assembled from sections of white PVC produced in an early extrusion test and placed it in a dark box, as shown in Fig. 11.7. This simulation does not entirely reproduce the environment of the fibers in the NOvA liquid scintillator filled cells. However,

given the broad maximum in the light yield vs. dye concentration that can be expected, these tests incorporate all the important features of light collection and transmission in the NOvA cell.

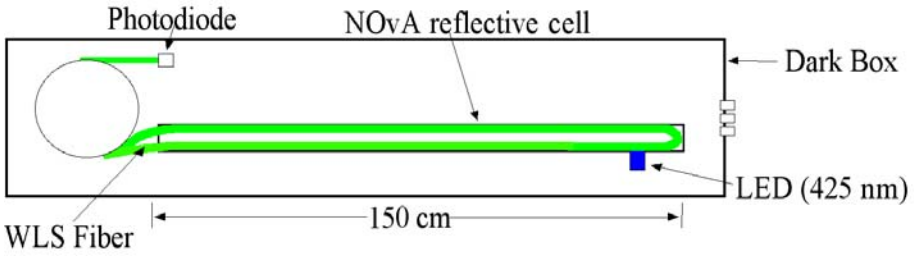

Fig. 11.7: Station to test WLS fibers in a simulated NOvA cell illuminated by an LED.

A blue LED with an emission spectrum similar to that of liquid scintillator illuminated the cell, and a photodiode with the same quantum efficiency characteristics as an APD measured the light amplitude. The LED was located 15 cm from the end of the cell and its light collimated to a spot on the cell wall to insure a diffuse illumination of the cell. Five small spools, each holding a WLS fiber loop 16 m long, were prepared in each of the six dye concentrations. The free ends of the fiber loop were glued into a plastic ferrule and polished. The polished ends were lead to the photodiode while the U-bend in the loop was guided around a semi-circular section of clear plastic at the end of the cell. The loop legs were held near the walls by clips.

The maximum photodiode current in the simulator was seen with the fiber with a dye concentration of 300 ppm. Four of the six fibers had a light yield that ranged from 5 to 15% lower than the maximum, as shown in Fig. 11.8. However, the fiber with a dye concentration 500 ppm yielded <50% of the maximum light output. This is another example of light yield variations that are not associated with dye concentration.

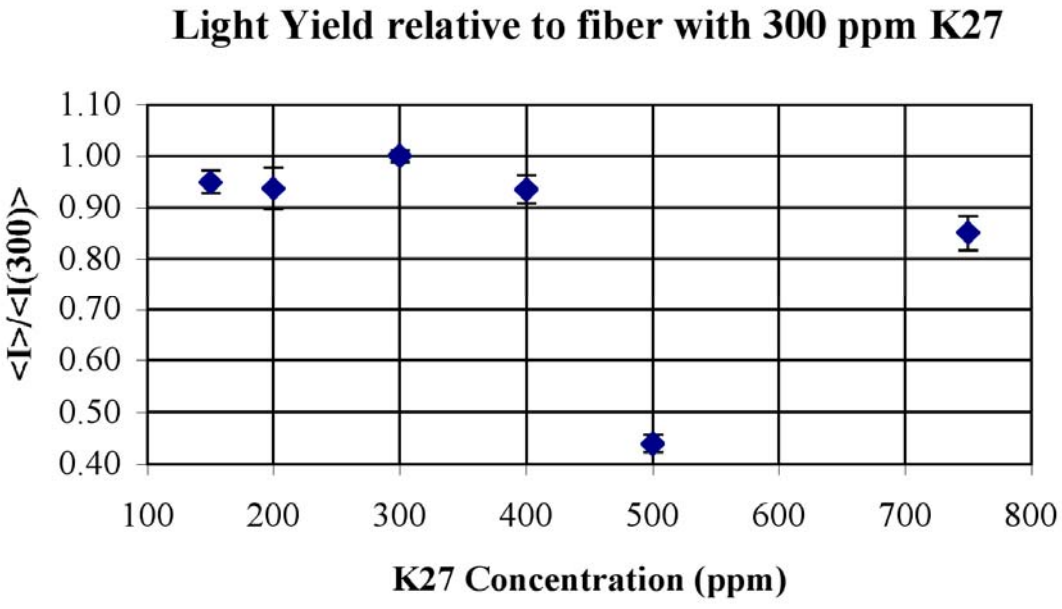

Fig 11.8: Using the NOvA test cell described in the text, the average photodiode current for five full-length fiber loops in each dye concentration relative to the fiber with a dye concentration of 300 ppm giving the maximum light yield.

In both batches of fiber the 300 ppm dye concentration yielded the highest photodiode current and this is the reasonable choice for the experiment. However, we must assume that the variations we have seen in the light output of the fibers will continue to be found in the delivered fiber. Therefore, the average photoelectron yield must be sufficiently high to allow for reasonable fluctuations in the fiber quality.

11.4.3 Studies with APDs

Fibers from Batch 1 were tested with cosmic ray muons in scintillator-filled cells with fibers readout by an APD, as discussed in Section 6.3. These results show that the light yield for the 250 ppm doped fiber was lower than would be expected compared to the 150 and 300 ppm doped fibers, consistent with the scanning and cell simulator measurements discussed above. Therefore, the QA procedure, measuring the attenuation length vs. wavelength of the supplied fiber, discussed in the next section, is a good predictor of the light yield.

11.4.4 Summary of Observed Fluctuations

The light from the far end of the fiber loop must travel an average distance d = 16m, to reach the APD. Our measurements indicate that this light has an average attenuation length $L \sim$ 12m. Therefore, of the light generated at the far end of the loop, about 26% (exp[–16/12]) reaches the APD. As discussed in this chapter, there are variations in the attenuation length of $\sigma_A = 12\%$. These variations result in a variation of the light reaching the APD, $\sigma = (d/L)\,\sigma_A = 16\%$, which meets the requirement for light output of the fiber as specified in Chapter 6.

11.5 Measurement Methods for NOνA Fiber Technical Criteria

11.5.1 Quality Assurance Instruments developed for Fiber Tests

In the Quality Assurance (QA) process the diameter, attenuation length vs. wavelength, and normalized light yield will be measured over a fiber length of up to 30 m at the beginning of every spool, each spool containing ~3200 m of fiber. The measurements will not require that fiber be cut from the spool, so that the tested fiber can be rewound onto the spool for later use in module production. In the attenuation length measurements made to date, samples that yielded significantly lower values than previous measurements or there were indications that the fiber had been damaged in handling, were eliminated. While the selected trials correlated well with the light yield measurements made in a simulated NOνA cell and with Kuraray Quality Control measurements, by constructing new equipment as planned, the handling of fiber will be minimized, the reliability of the attenuation length measurements will be improved, and light yield normalization will be maintained over the full production.

The attenuation length vs. wavelength measurements are made with an excellent and inexpensive digital spectrometer obtained from Ocean Optics Corporation. The entrance slit is 0.25 mm wide which allows for quick measurements, however, the light cone exiting a fiber has a large half angle (45°), and the intensity is not uniform over the fiber cross section. To keep the light levels high, the fiber cannot be located far from the slit to approximate a point source. Effects seen in the initial measurements indicate that a better mounting scheme will be needed to insure that the fiber has a repeatable position and is axially aligned.

To make a light yield measurement the preparation of the fiber face must be carefully executed and it is essential to avoid contamination of the fiber face or the spectrometer optics with dust or fiber polishing detritus; most fibers carry a static charge causing them to attract small dust particles and cladding flakes. Before polishing, fast curing glue is used to secure the fiber into a hard plastic and close fitting ferrule. A machine for diamond polishing of fibers, designed for this purpose by Fermilab engineer Carl Lindenmeyer is used to face-off the fiber and ferrule. This single-fiber polishing machine has been used in preparing fibers for a number of

experiments, including CDF and ATLAS. The hard surface of the ferrule will insure an accurate positioning of the fiber at the spectrometer entrance.

There are two common techniques for measurement of fiber light yields and attenuation lengths: a string of LED light sources lit sequentially at fixed distances along the fiber, as employed by the MINOS collaboration, or a single LED light source (or a radioactive source and scintillator) translated to known locations over the fiber, as employed by the CDF and ATLAS collaborations. The two techniques have a common set of trade-offs.

Multiple light source systems have no moving parts and produce results quickly, however, the individual sources must be checked often to avoid drifts in the normalization and relative calibration. Scanning on the other hand, takes time and requires maintenance of an electro-mechanical device, however, the relative normalization along the fiber is constant, with the single light source monitored by a photodiode and requiring only periodic recalibration. Both systems require the development of an automated procedure to prepare a length of fiber for measurement with the minimum amount of handling. Over the 4 years of absolute light yield and attenuation length measurements, the calibration ease of a single light source scanning system, we feel outweighs the slower speed and scanner maintenance requirements.

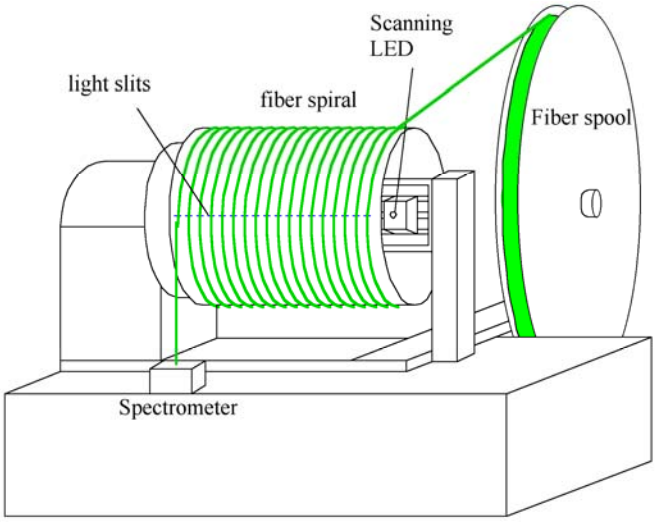

Fig. 11.9. Drawing of the fiber scanning machine to be used in the Quality Assurance procedures. Spectrometer is mounted on the drum and uses slip ring electrical connections.

The mechanics of the scanner, shown in Fig. 11.9, enables unrolling of ~30 m of fiber from a spool at a constant but low tension onto a 15.9 cm radius drum and into a helical groove on its surface locating the fiber over the illumination holes. The fiber is feed into the groove using a modified lathe that has the appropriate gearing for very coarse screw threads (2 threads per inch). The fiber spool is mounted on a stage that moves 1.27 cm along the drum axis for each rotation of the drum. Torque motors maintain a safe tension on the fiber spool at all times. Before winding, the polished end of the fiber is inserted and clamped into the spectrometer. Once the 30 m long spiral has been completely wound, the drum is locked in place. At this point the measurement room is darkened and a blue LED light source is stepped down the inside of the drum, illuminating one hole in the drum and one fiber location at a time. The light pattern will be adjusted to minimize the sensitivity to the exact positioning of the LED. If necessary, the spectrometer gate can be adjusted to maximize the statistical significance at each point. Scanning, readout of the spectrometer, and database entry are performed by a single PC.

The light intensity will be monitored by two independent photodiodes mounted on the LED scanning head. In addition, a few spools containing fiber standards will be maintained and used

occasionally to cross check the normalization. The LED power-supply has two options for control: maintain a constant LED current, or adjust the LED current to maintain a constant photodiode signal. As we gain experience with the LED and photodiodes we will choose the control function that is most reliable.

Kuraray provides a series of fiber tests, however, we intend to make an equivalent scanning machine available to them. We expect that they will then test for out-of-specification fiber before shipment.

11.5.2 Fiber Transportation and QA Testing Plan

The testing of fiber in our R&D to optimize the dye concentration has provided the data necessary to choose the Quality Assurance procedures and provided data on the variations in the attenuation length at long wavelengths, the critical parameter in maintaining an optimum signal from the fibers. The contract with Kuraray for the production fiber will contain acceptance criteria balancing their production realities and the requirements of the experiment. These criteria will be based on Kuraray's Quality Control data and NOvA Quality Assurance data taken during the R&D period.

The WLS Fiber QA plan has all fiber delivered to the High Energy Physics Laboratory at Michigan State University's Biological and Physical Science (BPS) Building. The laboratory has a high bay area, 60' x 20', equipped with a crane, and a roll up door allowing ground level truck entry. Adjacent to the high bay area are 3 secure laboratories, each 15' x 20', and a chemical, paint and plastics processing room with an exhaust hood. The laboratory is large enough to accommodate areas for the following tasks in the QA process:

1) receive the monthly shipments of fiber spools in crates,
2) unpack the spools from the crates, check fiber diameter and prepare end for QA testing,
3) perform the QA measurements on each spool of fiber and analyze the data,
4) repackage fiber spools in the crates,
5) prepare crates for transportation to a subbasement storage location, and
6) transmit QA data to a central database.
7) Four times per year, ship fiber crates to the module factory, once it is in operation.

Approximately 120 spools, each carrying about 3200 m of 0.7 mm diameter fiber, will be delivered to MSU monthly for ~3.5 years during the NOvA construction project. The long procurement from a single vendor will require that nearly all the fiber is received and QA tested before the module factories are ready to begin full production. The fiber is supplied in sturdy pine crates, 2 m long, 1 m wide and 0.67 m high, containing 16 spools of fiber, and weighing about 150 kg. In three years of production, 253 crates will need storage. Stacking 3 crates one on top of the other, the storage area needed will peak at ~1,500 sq. ft. in the 31st month of production when shipment of fiber to the module factories begins. A storage space has been secured in the subbasement of the BPS building that is temperature controlled and has full fire protection via sprinklers. Though water will not hurt the fibers, the spools are cardboard. Storing the crates well off the floor and covering them with a waterproof material should prevent any damage to the spools. A single fiber of ~16 m will be cut from one spool of each delivery and stored in a separate box nearby the other crates. It will be periodically tested to monitor the light yield of the fiber while in storage.

The QA team consists of the Level 2 and Level 3 Managers to supervise a Senior Technician and a Student Technician. The team must perform the tasks 1 – 7 noted above. The monthly tasks 1,2,5 and 6, should occupy two people for about one week (5 days). Tasks 3 and 4 involve the daily operation of testing 8 spools of fiber including the analysis of the data and entries into the local database. We are reasonably certain that the testing of a spool, including a

preliminary data check and local database entries can be made in less than one hour, including 15 minutes of contingency, e.g., dealing with out-of-specification fiber or spurious test data. A total of 3 weeks (15 days) or less is needed to process the 120 spools, with holiday and vacation breaks made up by management personnel or by employing additional Student Technician labor.

On a spool found to have substandard fiber, the Quality Assurance testing will be repeated after removing ~100 m of fiber from the spool. Also, the previous spool of fiber in the production sequence can have its fiber transferred to an empty spool to access the fiber produced immediately before the substandard fiber. In this way the region of substandard fiber at the beginning and end of a spool will be bracketed. Spools with indications that substandard fiber continues beyond the tested point at the beginning or end of a spool will be segregated and perhaps returned to Kuraray for credit and analysis.

11.6 Changes in the Fiber design since the CDR

At the time of the Conceptual Design Report, the proposed fiber diameter was 0.8 mm with a K27 dye concentration of 200 ppm, a concentration typical of the previous fiber applications. In testing we have found that the requirement of a mean number of 20 photoelectrons for minimum ionizing particles through the far end of a NOvA cell could be met with a fiber of 0.7 mm diameter at a considerable cost savings. Furthermore, the smaller diameter provides a greater safety margin between the curvature of the fiber at the bottom of the loop, and the point at which the fiber is damaged. Difficulties in handling fibers with a diameter smaller than 0.7 mm prevent any additional cost savings. However, we have found during R&D that improvements in the photoelectron yield can be obtained by optimizing the dye concentration at values of ~300 ppm.

11.7 Work Remaining to Complete the Fiber Design

The QA procedures will be given a good workout with about 75 km of fiber required for the Integration Prototype Near Detector (IPND). This IPND effort will provide a step towards the QA required for 13,000 km of fiber expected during a 3.5year period of NOνA fiber production. The IPND fiber represents about 3 days of module production for the Far Detector.

Long term fiber survival tests will continue throughout the project.

11.8 Chapter 11 References

[1] Kuraray Scintillation Materials, Kuraray Co., Ltd., Methacrylic Resin Division, contact psf@kurary.co.jp. The Kuraray fiber catalog can be found in docdb note # 2665

[2] O. Shinji, Chief Scientist at Kuraray, private communication

[3] K. G. Young et al., Radiat. Phys. Chem. **41** 215 (1993)

[4] D. Koolbeck and K. Ruddick, a re-analysis of the ref [2] data, NOvA docdb note # 389, August 2005.

[5] P. Border et al., Nucl. Instrtum. Methods **A463**, page 194 (2001).

[6] L. Benussi et al., Nucl. Instrtum. Methods **A488**, page 503 (2001)

[7] D. Cronin-Hennesy, NOνA docdb note # 139, December 2005.

[8] A. Bross and A. Pla-Dalmau, private communication.

[9] Stuart Mufson and Mark Messier, private communication.

[10] Matt Strait, NovA docdb note # 2014.

[11] Jon Karty, private communication

[12] Leon Mualem, NOvA docdb note # 24, August 2005.

12 PVC Extrusions

12.1 Introduction

Rigid PVC extrusions are the basic building blocks of the NO_A detectors. They are the structural elements, the reflectors of scintillation light and the primary containment vessels for liquid scintillator. The mass of PVC used to make the far detector is 4.5 kilotons, which is 30% of the total far detector mass. Extrusions have a cellular structure, with 16 isolated cells per extrusion. Furthermore, there are two types of PVC extrusions differing in thickness but not in outer dimensions: thick-wall extrusions are oriented vertically and bear the weight of the detector (refer to Chapter 17); thin-wall extrusions are oriented horizontally.

All far detector extrusions are 15.494 m long, Extrusions destined for the near detector are 2.63 m long (horizontal extrusions) and 3.94 m long (vertical extrusions) Detector modules are made by joining two PVC extrusions at the sides, as described in Chapter 13. An example of two prototype 16-cell extrusions, 15.5 m long, placed side-by-side, is shown in Fig. 12.1.

This chapter is organized in the following way: After stating the technical design criteria, we present details of the production of PVC extrusions, including the PVC resin composition. Quality control methods are described and dimensional measurements of prototype extrusions are presented. Reflective properties of NOνA PVC and the relationship to light yield are discussed in the next section, followed by a detailed description of the mechanical properties of NOνA PVC, which includes a variety of tests and models used to predict creep in PVC. Shipping and handling techniques are outlined next, followed by a summary of the changes in design since the CDR and the work remaining to complete the PVC Extrusion Design.

Fig. 12.1: Two 53 foot NOνA prototype PVC extrusions from an early R&D production illustrate the straightness of the extruding process. These 16 cell extrusions are not attached to each other.

12.2 Technical Design Criteria

The major technical design criteria for NOνA PVC extrusions are: (1) they must be sufficiently reflective to produce the required light yield, (2) they must be sufficiently strong to form a self-supporting NOνA detector structure, filled with liquid scintillator, over the lifetime of the experiment and (3) their shape must be within the specified tolerances for assembly of modules and detector blocks.

12.2.1 Light Yield and Reflectivity

NOνA readout electronics requires, at minimum, a 20 photoelectron signal in response to minimum ionizing radiation at the far-end of a 15.5 m NOνA cell as discussed in Chapter 6. The signal strength is due to the APD quantum efficiency and the light yield in response to ionizing radiation. The light yield, in turn, is due to a combination of the PVC reflectivity, the scintillator and wavelength-shifting fiber responses. Because the spectral shape of scintillation light is broad, NOνA PVC material must be highly reflective over a range of wavelengths matching the product of the scintillator emission spectrum and the WLS absorption spectrum.

NOνA PVC is designed to be highly reflective by adding substantially more titanium dioxide (TiO_2) to the PVC resin than is normally used in commercial applications. This can yield reflectivity values as high as 92% at 430 nm, near the peak of the scintillator emission spectrum. However, in order for any PVC compound to be extruded, a number of processing ingredients must be added to the mix. Great care must be taken to ensure that these ingredients have a negligible effect on the reflectivity of the extruded material. Reflectivity and light yield of NOνA rigid PVC is discussed in more detail in section 12.5.

TiO_2 is available commercially in two crystalline types: rutile and anatase. Rutile is generally used throughout the PVC industry but anatase is not. PVC with anatase is said to be more difficult to extrude and the extrusions don't hold up well outdoors, exposed to sunshine and rain. However, anatase offers an advantage to NOνA because it extends the high reflectivity of PVC by ~30 nm to wavelengths below 400 nm. This extended range is enough to overlap most of the short-wavelength tail of the scintillator emission spectrum. Direct comparisons of NOνA extruded PVC detector cells, filled with liquid scintillator and instrumented with WLS fibers, showed 15% more light yield for extrusions made with anatase as compared to extrusions made with rutile.

Since the NOνA experiment will not be subjected to harsh outdoor conditions, we have decided to use the anatase form of TiO_2. Mechanical strength tests and light yield tests show no adverse effects due to the use of anatase when exposed to liquid scintillator. Therefore the technical requirement for reflectivity assumes the use of anatase as the reflective ingredient in the PVC mixture. More details are presented in section 12.3.1.

The NOνA technical design requirement for reflectivity within all of the 16 cells in an extrusion is based on light yield tests described in section 12.5.2. It is required that the reflectivity is a monotonically increasing function of the wavelength (refer to Fig. 12.21) and that the value of the reflectivity is at least 78% at a wavelength of 400 nm and at least 90% at a wavelength of 430 nm.

12.2.2 Strength

The second technical criterion concerns the material strength of PVC. Because the extrusions are used as the structural members in the NOνA design (see Chapter 17), NOνA PVC must meet minimum strength requirements determined by the structural demands. Strength requirements are normally defined by the material's yield and ultimate stress. In the case of PVC as used in this structure, the dominant mechanical property is that of creep. In order to minimize

creep, the stresses are kept below 700 psi. This is well below the yield and ultimate stresses of PVC which are typically > 4000psi and > 6000 psi, respectively. Additionally the PVC must have sufficient impact strength and exposure to the liquid scintillator should not lower any of these values significantly. Strength of PVC is discussed at length in Section 12.6.

For structural reasons, extrusions come in two types: one with 3 .3 mm exterior walls and 2.3 mm interior webs for horizontal cells, and a thicker version with 4.8 mm exterior walls and 3.3 mm interior webs for the vertical cells. This difference is required because the horizontal extrusions filled with scintillator are supported by vertical extrusions that transmit the load to the floor (See Chapter 17). The exterior sizes of horizontal and vertical extrusion are identical for assembly purposes. Therefore the interior cells sizes of vertical extrusions are slightly smaller than the horizontal interior cell sizes.

The NOνA technical design for PVC strength requires a tensile strength of 6,000 psi and a creep modulus (after 20 years) of at least 75,000 psi. The creep modulus characterizes the "plastic" nature of the PVC and is discussed in Section 12.6. The strength properties of rigid PVC are not strongly influenced by our optimization of the PVC formulation to attain high reflectivity.

12.2.3 Shape

The third technical design criterion requires that PVC shape must be within specified tolerances to facilitate assembly of modules and detector. This puts constraints on thickness, flatness and straightness of the extrusion's outside edges (bond two 16-cell extrusions to make one 32-cell module), the extrusion's profile (manifold and bottom plate must mate to two extrusions properly), and the extrusion's flatness (upper and lower extrusion surfaces must attach in the process of block assembly).

The shape of vertical and horizontal extrusions must meet the design profiles, within tolerances stated, as shown in the engineering drawings on the next two pages. The dimensions for horizontal and vertical extrusions are shown below in Figures 12.2 and 12.3. Extrusion thickness is determined by the structural considerations presented in Ch. 17. The outside walls of horizontal extrusions are 3.3 (+ 0.7/-0.3) mm thick and the inner walls, called webs, are 2.3 (+0.7/- 0.3) mm thick. The outside wall of vertical extrusions outside walls are 4.8 (+0.7/-0 .3) mm thick and the webs are 3.3 (+07/- 0.3) mm thick.

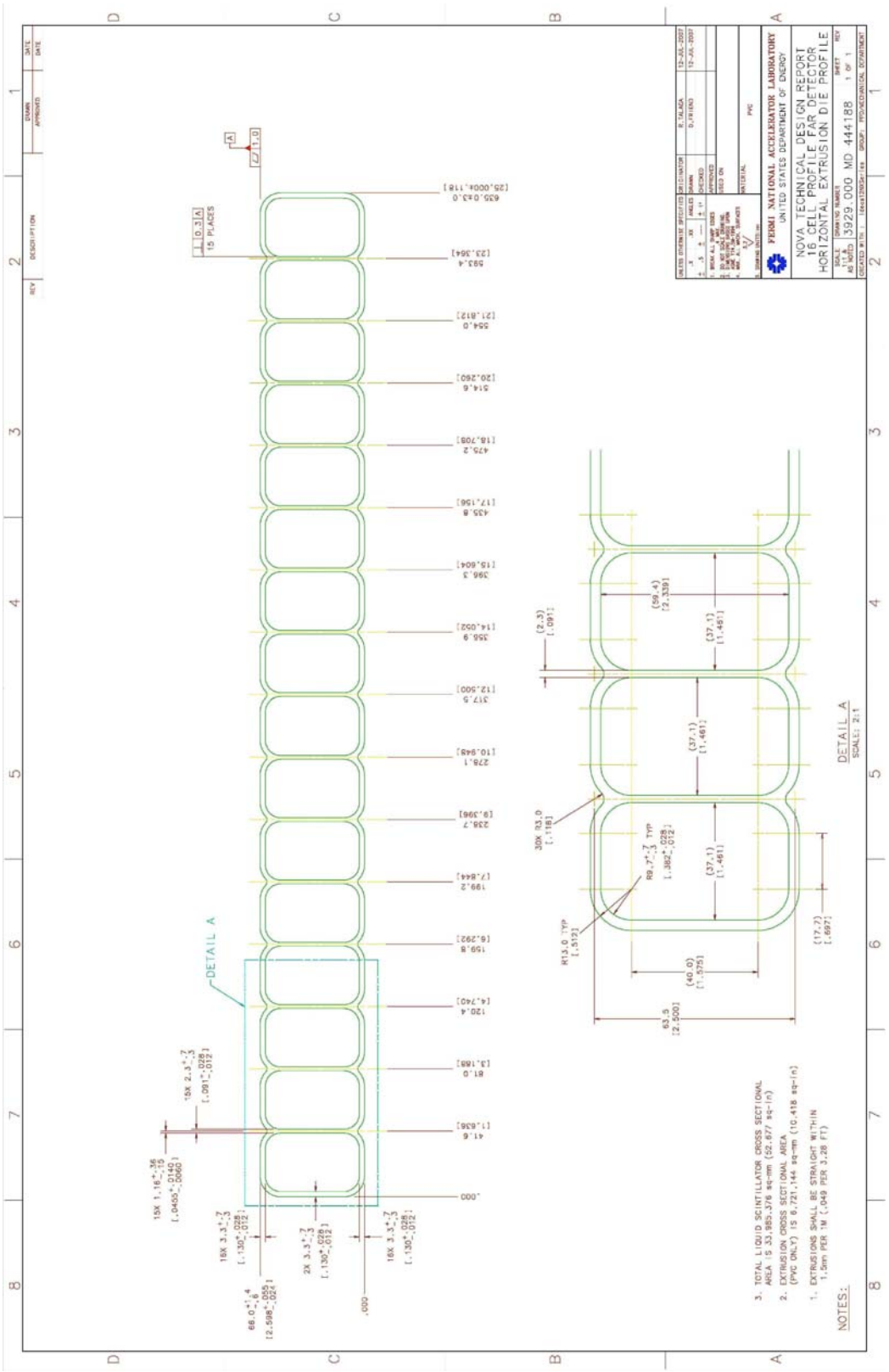

Fig. 12.2: Drawing of the NOνA thin-walled extrusion for horizontal modules.

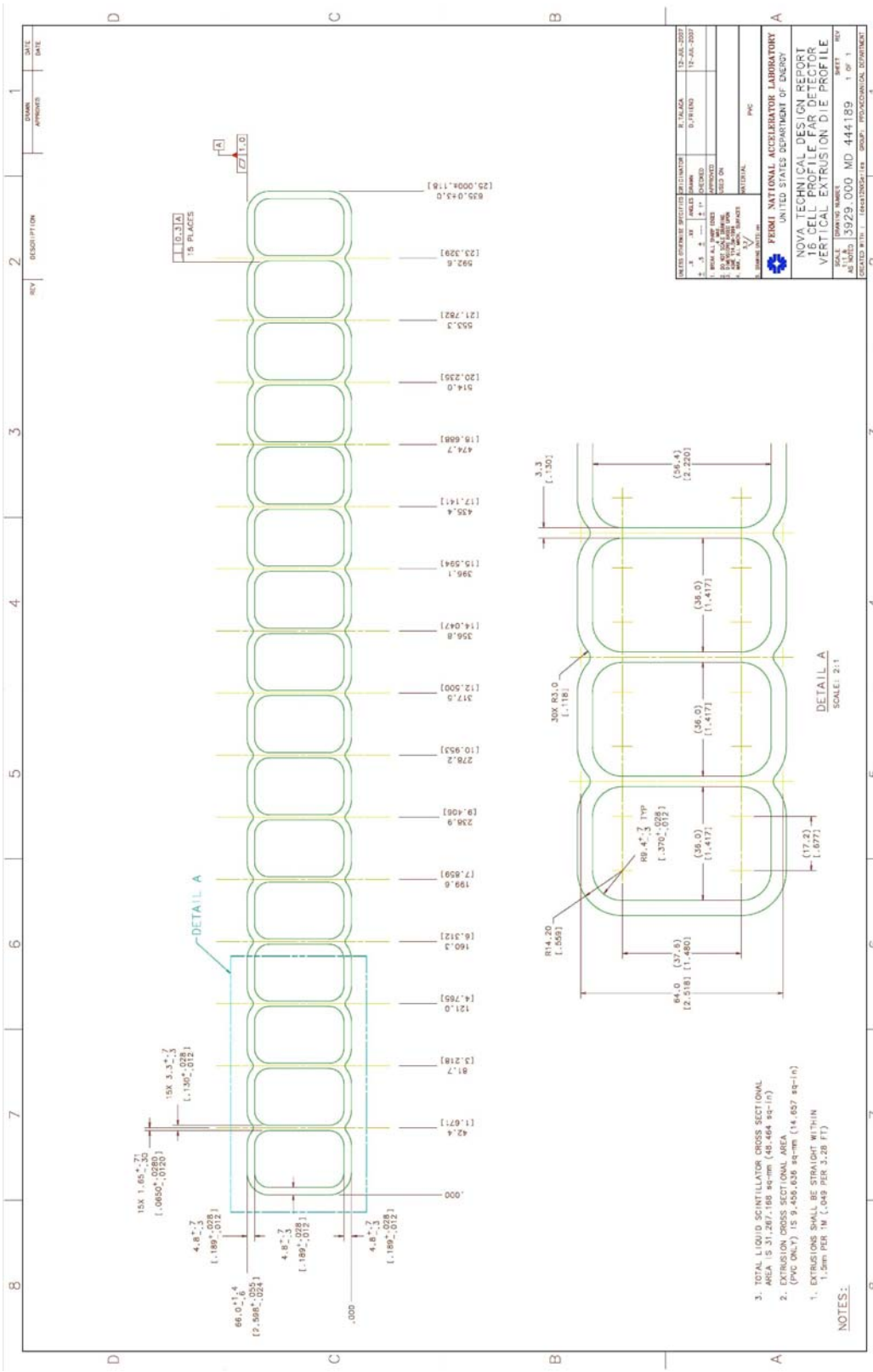

Fig. 12.3: Drawing of the NOvA thick-walled extrusion for vertical modules.

12.3 PVC Resin and the Extruding Process

Production of extrusions is a two-step process. The first step is to mix PVC polymer with titanium dioxide and a number of processing aids to produce a NOνA specific resin called N-27. This is performed by a commercial compounding firm. The second step is to produce rigid PVC extrusions at an extruding company. There, the resin (in powder form) is inserted into an extruding machine where it is melted and pushed through a NO_A-designed die. After exiting the die, extruded PVC enters water-cooled sizing tools that helps maintain the shape (by vacuum suction) as the extrusion is cooled. After the extrusion exits the sizing tools it enters water tanks to remove residual heat, ensuring the extrusion to be at room temperature upon exit.
After the extruded PVC is cut to length it is labeled, measured and placed in one of four sorting stacks, depending on the height of the extruded profile (refer to section 12.4.2). Once a stack of extrusions is full, it is packaged for shipment.

12.3.1 PVC Resin Composition

Selection of the quantity and type of TiO_2, the processing aids and the PVC polymer was made after almost two years of R&D, which included consultation with James Summers, an expert on PVC production, and close interaction with two commercial compounding companies, an independent plastics laboratory, and two commercial extruding companies and their production staffs. The ultimate goal of the R&D was to produce a formulation that, when extruded, produces PVC extrusions with excellent reflectivity, mechanical strength and geometrical shape.

PVC will not extrude without addition of processing aids to the polymer, which typically number anywhere between 5 and 10 ingredients. In the extruding process, the PVC resin is subjected to pressures up to 4,000 psi and temperatures of nearly 400 degrees F for a significant period of time. The processing aids (stabilizers and lubricants) are added to the PVC polymer and the TiO_2 to keep molten resin flowing through the die without sticking, burning or otherwise decomposing. Care must be taken to ensure that processing aids do not have adverse effects on the reflectivity or strength of the extruded product.

The reflectivity requirement of NOνA posed a challenge in the selection of specific processing aids, the type of PVC polymer and the type and brand of TiO_2. Extensive laboratory R&D was performed on over two dozen formulations with particular attention paid to reflectivity; those with satisfactory results were extruded and their extrudability, mechanical properties and reflectivity were evaluated.

In addition to selecting the resin formulation, the mixing method was also optimized. This is the order in which ingredients are mixed with the polymer, the length of time and the temperature of the mixture.

Commercially available PVC resins are proprietary and their reflectivity properties are not optimized for NOνA. In order to control all of the ingredients and, in some cases, the brand names of ingredients, we have developed a resin formulation that meets NOνA requirements for reflectivity, strength and extrudability. This resin is called NO_A-27, or N-27. The ingredients in the N-27 resin are PVC, tin stabilizer, TiO_2, calcium stearate, paraffin wax, oxidized polyethylene and glycerol monostearate. They are listed in Table 12.1, along with the commercial brand names and the relative proportion by weight: parts per hundred. The PVC and other ingredients were specifically selected to optimize reflectivity. The net result is a rigid PVC compound with 14.7% anatase TiO_2 by weight.

N-27 PVC Resin

Ingredient	Commercial Brand Name	Parts per Hundred	per cent
PVC	Shintech SE950EG (high reflectivity)	**100**	**77.5%**
Tin stabilizer	Rohm & Haas Advastab TM-181 20% monomethyl tin	**2.5**	**1.9%**
Titanium dioxide anatase	Kronos 1000 anatase titanium dioxide	**19**	**14.7%**
Calcium stearate	Ferro 15F calcium stearate	**0.8**	**0.6%**
Paraffin wax	Ferro 165 paraffin wax	**1.1**	**0.9%**
Oxidized polyethylene	Ferro Petrac 215 oxidized polyethylene	**0.2**	**0.2%**
Glycerol monostearate	Rohm & Haas F1005 glycerol monostearate	**0.3**	**0.2%**
Acrylic impact modifier	Arkema Durastrength 200 Acrylic impact modifier	**4**	**3.1%**
Processing aid	Rohm & Haas Paraloid K120N processing aid	**1**	**0.8%**
	Total	**129**	**100%**

Table 12.1: Composition of N-27 rigid PVC compound.

Selection of the N-27 formulation was made after testing a number of PVC resins, both proprietary and those developed by NOνA. The criteria for selection are: (1) there should be no significant build-up or sticking of the resin to the NOνA 16-cell die over a period of at least two days of continuous production, (2) the resin produces a complete extrusion with proper welding of all interior webs to the outside walls and (3) the extrusion produces the highest light yield in response to ionizing radiation when it is filled with liquid scintillator and equipped with a fiber (as explained in section 12.5.2). N-27 met these requirements and had the fewest additives of any of the candidates.

N-27 resin produces an extrusion with density equal to 1.49 gm/cc. Given this density and the nominal profile dimensions shown in Figs. 12.2 and 12.3, the thin-wall horizontal extrusions weigh 10.0 kg/m and the thick-wall vertical extrusions weigh 14.1 kg/m.

12.3.2 *Extruding the PVC Resin*

The extruding process utilizes a number of custom-made tools and commercial components arranged in a sequential order. This "extrusion line" begins with the extruding machine, a high-capacity twin-screw extruder. This is followed by a die, sizing tools, cooling tanks, a "puller" and a traveling saw. The die, sizing tools and cooling tanks are custom-made for NOνA. The extruder, puller and traveling saw are commercial products, as is the movable table that supports the sizing tool and cooling tank. A photo of the extruding line used for production of NOνA

prototype extrusions is shown in Figure 12.4. Additional photos of the individual components in the extruding line are shown in Figures 12.5 through 12.9.

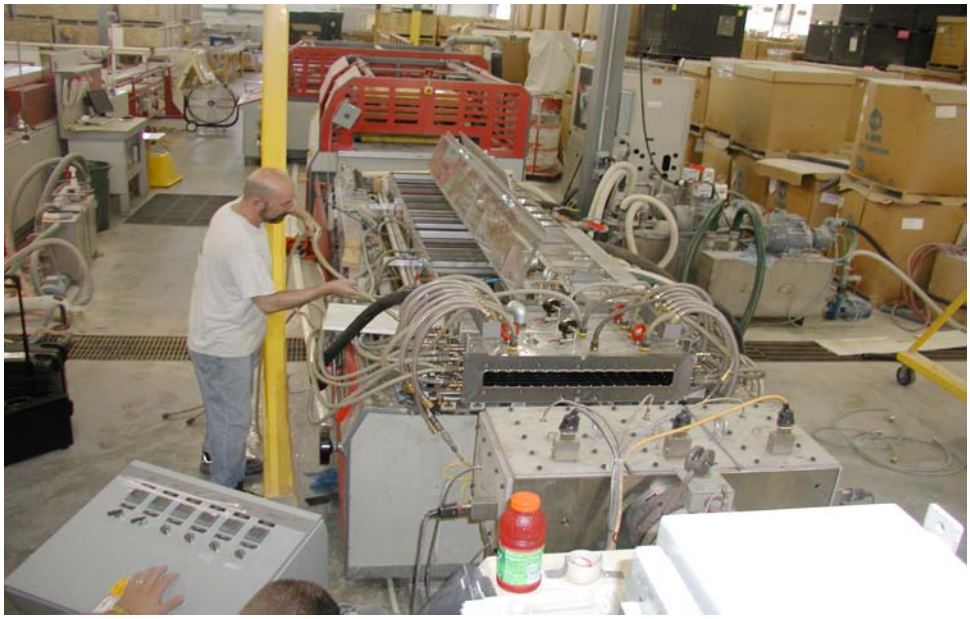

Fig. 12.4: Extruding line for NOvA prototype production. A partial view of the extruding machine is at the bottom right of the picture with the prototype 16-cell die just beyond it. The wide opening beyond the die is the entrance to the vacuum sizing tool, which is followed by the water cooling tank. The smaller red object downstream of the cooling tank houses the extrusion puller and the larger red object at the very top of the picture houses the cutting station.

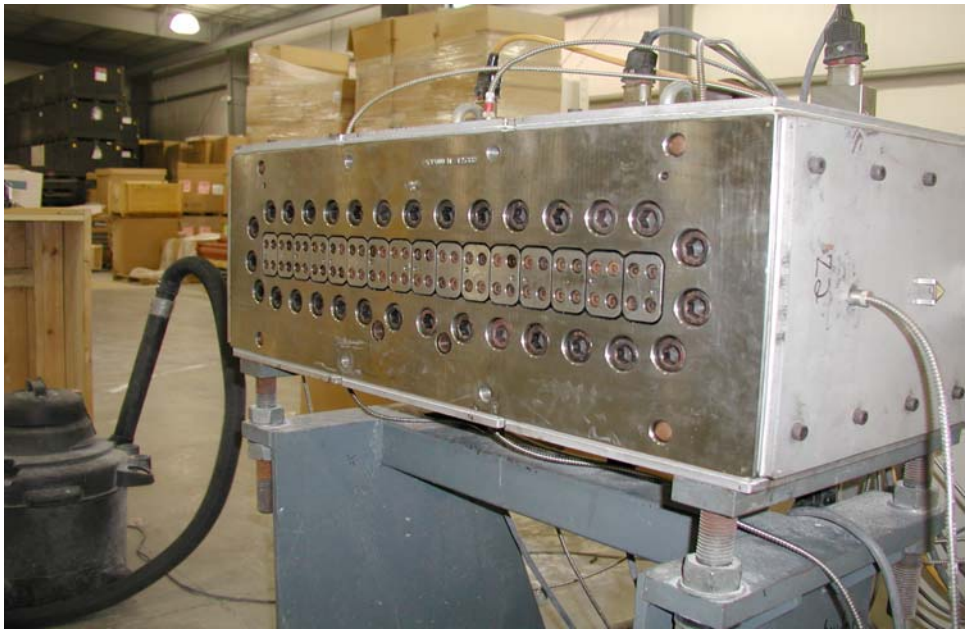

Fig. 12.5: The custom NOvA prototype 16-cell die. PVC resin moves right to left and exits the die through the scalloped profile shown in this view.

Fig. 12.6: The custom NOvA vacuum sizing tool. During production, this tool is in close proximity to the exit face of the die. As the molten PVC exits the die the water-cooled sizing tool keeps extrusion shape from collapsing by sucking the outside walls of the extrusion against the walls of the sizing tool .

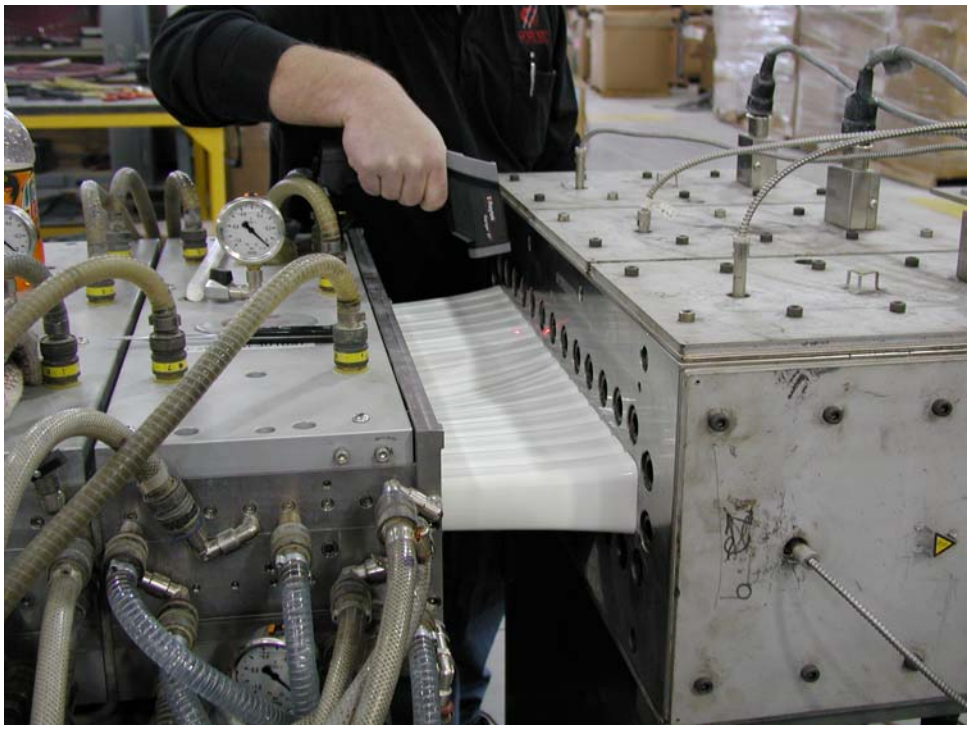

Fig. 12.7: PVC exits the die (on the right) and moves toward the vacuum sizing tool at startup. PVC melt temperature is measured just outside the die. After this inspection, the sizing tool is moved up against the die and vacuum suction is initiated.

13 PVC Modules

13.1 Overview

The fundamental building block for the NOνA Far and Near Detectors is the PVC module. A PVC module consists of a 32-cell PVC extrusion assembly, an end-plate, and a fiber manifold. The 32-cells each contain a looped wavelength-shifting fiber, described in Chapter 11, that is routed through the fiber manifold and terminates in an optical connector mounted on the fiber manifold. Approximately 13,000 such modules are required for the NOνA Far Detector.

13.2 Technical Design Criteria

The overall length of the completed modules, including the manifold, end-plate and packing material must be less than 53 feet in order to fit on a truck for shipping. The PVC modules will ultimately be filled with liquid scintillator and must be leak-free. The modules also hold wavelength-shifting fiber that must be controlled so that its bend radius is not significantly less than the manufacturer's specifications. Each of the fiber ends must be precisely routed to one of the pixels on the APD photodetector.

13.3 NOνA Modules

NOνA modules consist of two 16-cell PVC extrusions described in Chapter 12 glued together to make a 32-cell extrusion assembly. A looped wavelength-shifting fiber is then inserted down the length of each cell.

The module assembly is shown in Figure 13.1. The end of the extrusion assembly with the loop is sealed with a PVC end-plate. At the other end of the extrusion assembly the two fiber ends per cell are routed through a PVC manifold to an optical connector. The manifold assembly is also sealed giving a module assembly that is a leak-tight container for liquid scintillator.

13.3.1 32-Cell Extrusion Assembly

The 16-cell extrusions will be measured and selected so that they match in thickness and cut to the appropriate length at the extruder as described in section 12.x. These extrusions will be stored at the extruder and shipped to the module assembly factory for just-in-time module construction. At the module factory, two matched extrusions are glued together to make an extrusion assembly.

13.3.2 End-plate and End Seals

The end-plate is extruded from the same PVC as the 16-cell extrusions. It is formed such that it has a raised wall that covers the outside edge of the extrusion assembly, a channel through which liquid scintillator flows, and a ledge on each side of that channel on which the extrusion assembly sits. The end-plate is glued across the end of the extrusion assembly, as shown in Figure 13.2. The length of the end-plate is equal to the minimum width of the extrusion assembly. The side seals are glued such that they provide a leak-tight seal at each side of the extrusion assembly. The side seals are designed to take up the tolerance of the width of the 32-cell extrusion assembly so that there is a liquid seal with no part of the end closure extending beyond the end of the extrusion assembly. The center seal assures that there is a leak-tight joint between the two 16-cell extrusions that comprise the extrusion assembly. Figure 13.3 shows a close-up view of the end-

plate and one side seal. Figure 13.4 shows how the side seals adjust the closure end assembly to take up the tolerance of the extrusion width dimension.

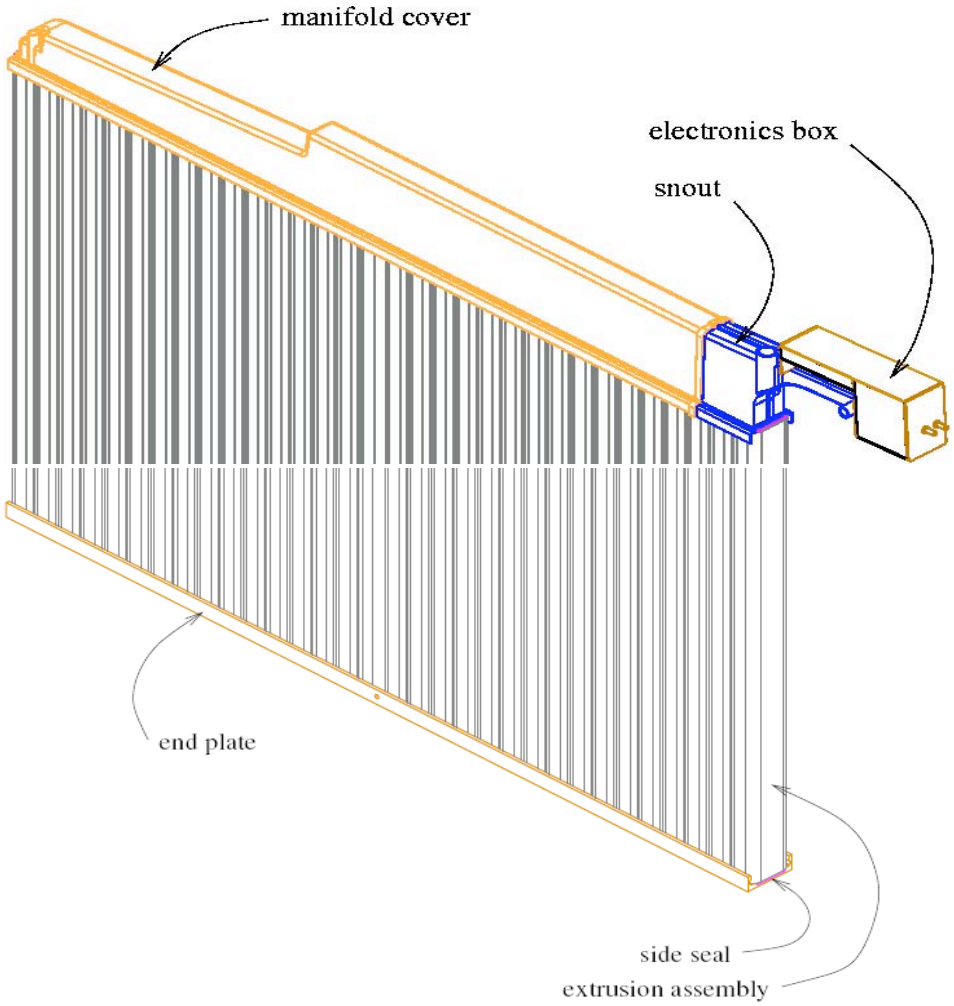

Fig. 13.1: PVC module assembly showing the end-plate at the bottom and the fiber manifold at the top. Both vertical and horizontal modules have the same configuration.

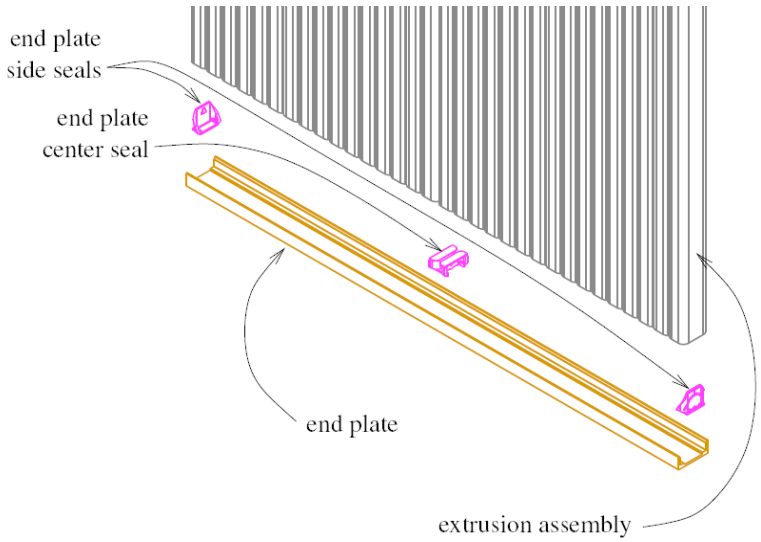

Fig. 13.2 Exploded view of the end-plate as it attaches to the extrusion assembly.

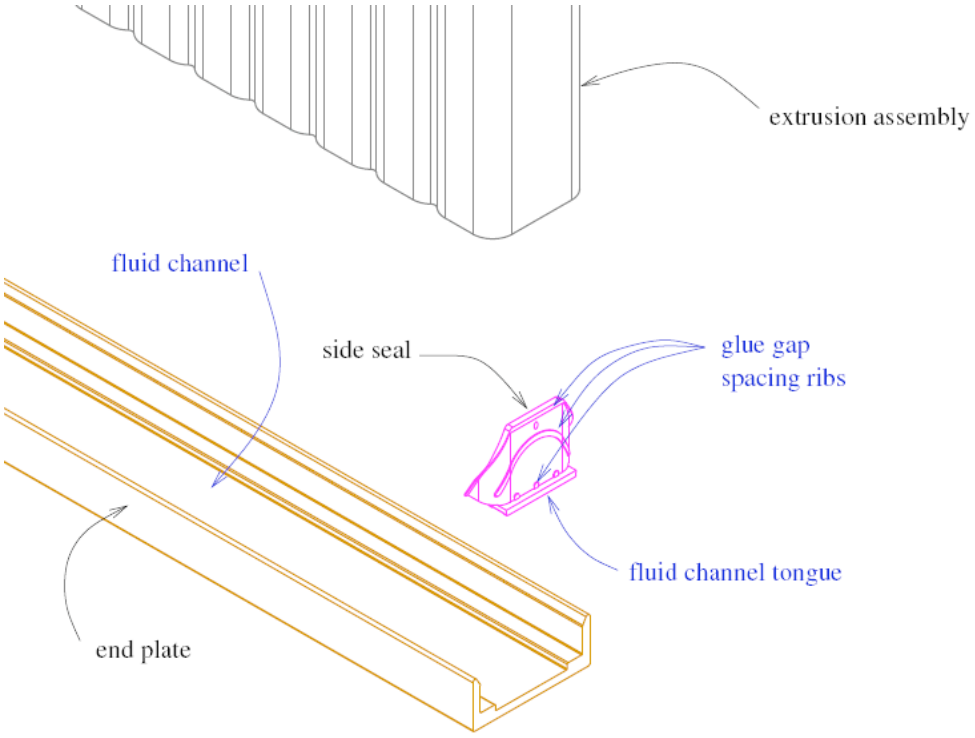

Fig. 13.3: Exploded view of an end-plate assembly in the region of a side seal. The side seal enables sealing the last cell in an extrusion without extending the end-plate past the edge of an extrusion assembly.

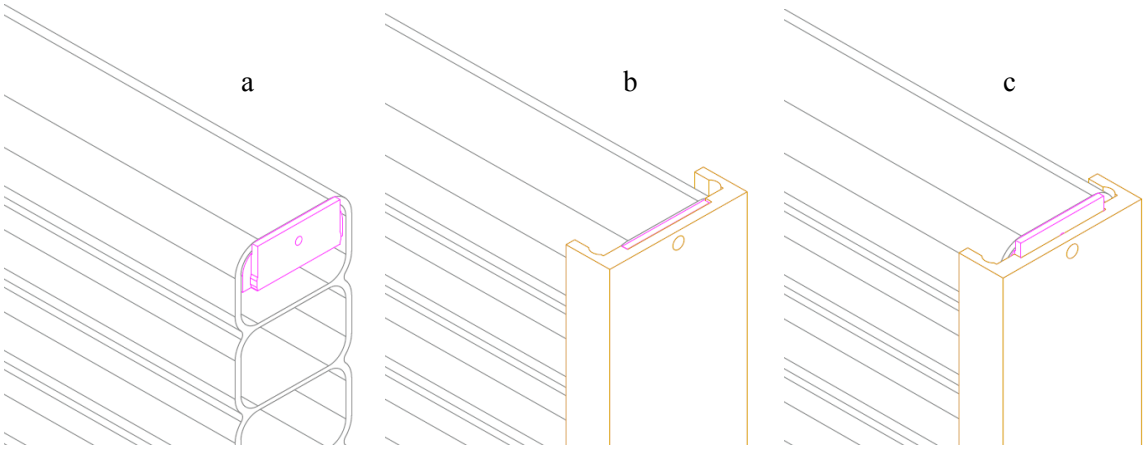

Fig. 13.4: Side seal function. (a) shows a side seal installed in the first or last cell of the extrusion assembly so that it is flush with the edge. (b) shows the relationship of the end-plate, side seal, and extrusion assembly edge if the extrusion assembly is its minimum acceptable width. Here the side seal, the end-plate, and the edge of the extrusion assembly are flush. (c) shows the relationship of the end-plate, side seal, and extrusion assembly edge if the extrusion assembly is its maximum acceptable width. Here the side seal and the edge of the extrusion assembly are flush. Even though the end-plate does not extend for the entire width of the extrusion assembly, the side seal still provides an ample seal surface with the end-plate.

The side seals and center seal are injection-molded parts made from PVC. Side seals and center seals are glued to the extrusion assembly and end-plate using epoxy glue that is chemically inert with liquid scintillator. Our tests show this glue fails in the cleavage-peel mode at a pressure of about 380 KPa (55 psi), about 3 times the maximum hydrostatic pressure at the bottom of the vertical modules. As an added safety factor, fiberglass webbing is glued around the edges of the module assembly using an extremely strong methacrylate adhesive which eliminates this cleavage-peel failure of the side seal up to the strength of the PVC extrusion, about 830 KPa (120 psi).

The procedure for attaching the end-plate consists of four stages of gluing with two different types of glue, epoxy adhesive (3M2216 no-sag), which has been shown to be chemically inert to liquid scintillator, and methacrylate adhesive (Devcon Plastic Welder) which forms joints stronger than the PVC extrusion. The 3M2216 is used for any surfaces in contact with liquid scintillator. All surfaces to be glued with the 3M2216 epoxy are abraded to increase glue strength. First the side seals (cells 1 and 32) and center seals (cells 17 and 18) are glued into the extrusion assembly as shown in Figure 13.2 using 3M2216. The structure of these injection-molded parts, shown in Figure 13.3, assures that they are aligned with the extrusion cell and have the proper gap for maximum glue strength. This structure also assures that the glue injected into each part gives a reliable seal. The next step is to attach the end-plate which is done after the end seal glue has cured and the wavelength-shifting fibers are strung through each cell. A layer of glue (3M2216) between the end-plate and the end of the extrusion assembly forms a butt joint that acts as a seal for the liquid scintillator. The end seals, already glued in place, align the end-plate to the extrusion assembly. After overnight pressure testing to verify that the chemically inert glue has no leaks, the structural adhesive (Devcon Plastic Welder) is injected into the space between the outside of the extrusion assembly and the wall of the end-plate. The placement of the two glues is shown in Figure 13.5. Finally a 10 cm long strip of fiberglass reinforcement netting is glued to each edge of the extrusion assembly at the end of the end-plate to give additional strength against the possibility of cleavage-peel at the side seals.

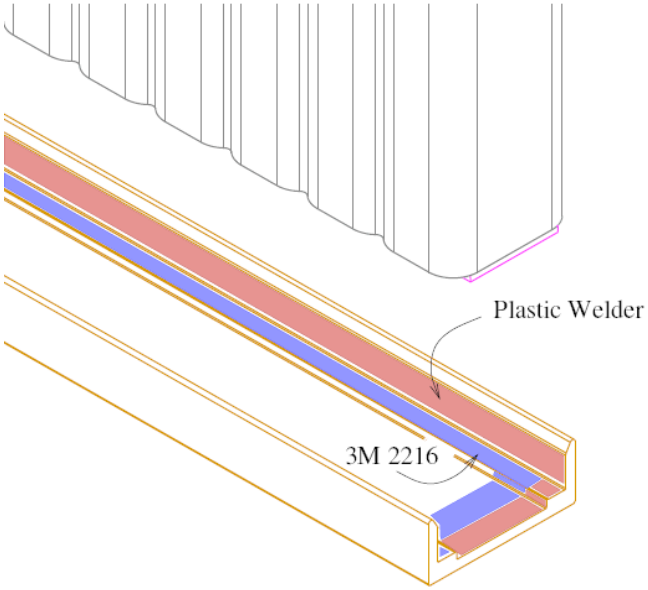

Fig. 13.5: End-plate assembly showing the position of the two different glue joints.

13.3.3 Fiber Manifold

All parts of the fiber manifolds are made from black injection-molded plastic. The manifold cover and snout are glued to the top of the PVC extrusion assembly in the same manner as the end-plate described previously. The manifold has several functions: it must route the optical fibers in each of the manifold cells to an optical connector, it must protect the optical fibers from over-bending, it must shield the optical fibers from cosmic ray events in the manifold, it must provide the interface for the APD electronics module, it must hermetically seal the back of the optical connector, and it must provide the liquid scintillator fill interface. Nearly identical fiber manifolds are used on both the vertical and horizontal modules. Two side-by-side vertical extrusion modules with their fiber manifolds are shown in Figure 13.6. An exploded view of the parts of the manifold assembly is shown in Figure 13.7. The vertical extrusion manifolds have room for thermal expansion of the liquid scintillator. The horizontal extrusions have external overflow containers described in the detector installation Section xx.xx.

Figure 13.8 shows how the fibers are routed by the manifold to the optical connector. A manifold raceway assures that the bend radius of the fiber does not exceed the manufacturer's specification. The raceway also optically isolates each fiber to reduce the unwanted detection of cosmic rays that pass through the scintillator in the manifolds.

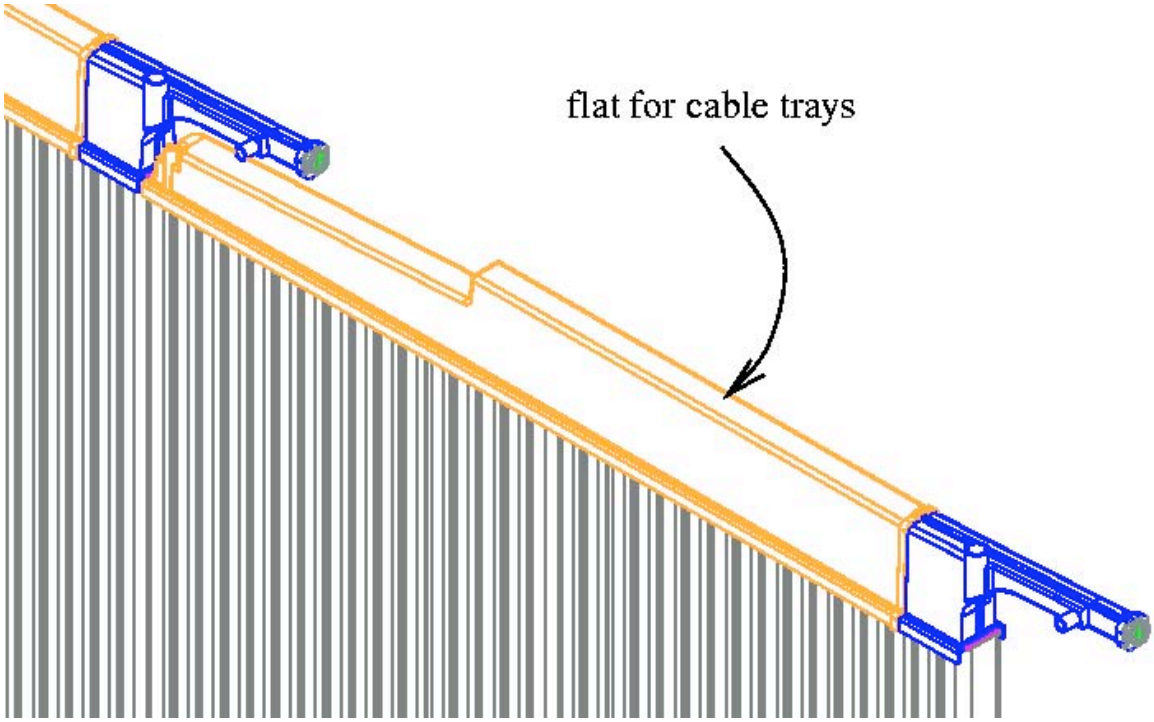

Fig. 13.6: Nesting of two adjacent manifolds. The top of the manifold cover will support cable trays for the electronics.

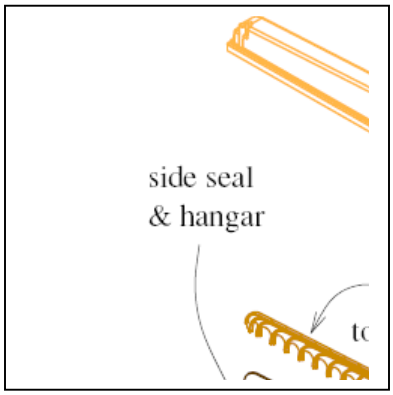

Fig. 13.7: Exploded view of manifold assembly.

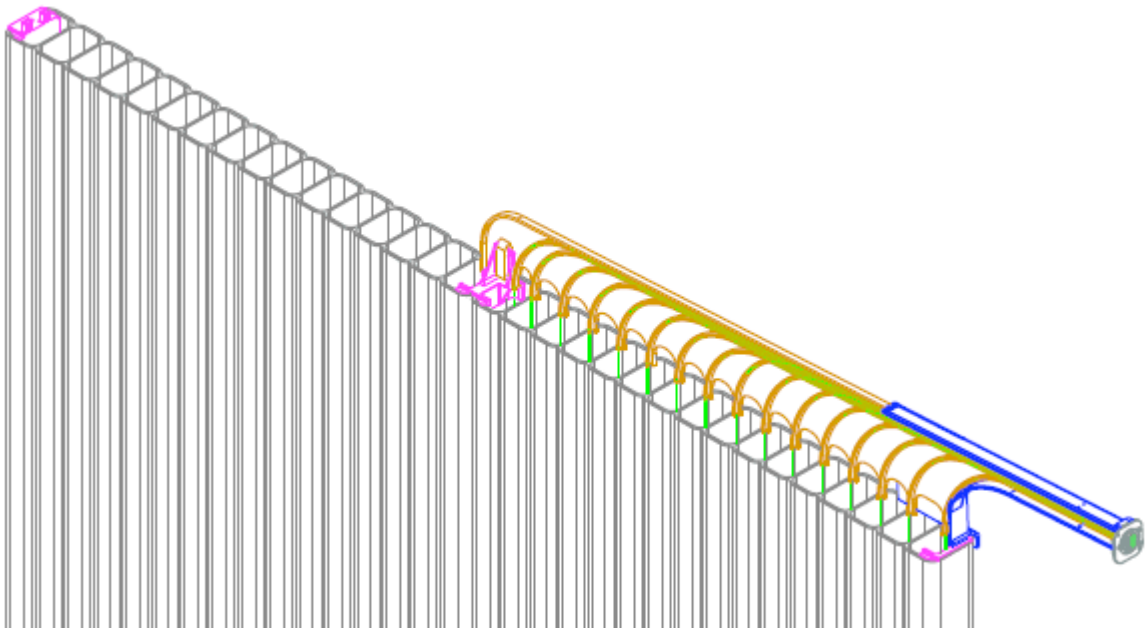

Fig. 13.8: Fiber routing to the optical connector for the first 16-cells. There are two fiber ends per cell routed to the optical connector.

The snout is the most complex part of the manifold assembly since it has to satisfy the most constraints. Physically the snout must fit over the manifold of the adjacent module to allow for close packing of the extrusions as shown in Figure 13.9. Since it defines the length of a module, its length must be minimized to achieve the largest possible active volume that fits within a standard 53 ft truck length. It must also be sturdy enough to carry the APD photodetector and its associated electronics and cooling system. It routes the wavelength-shifting fiber to the optical detector in a manner that facilitates efficient stringing. It also incorporates a seal between the cold optical connector and the liquid scintillator to prevent the possibility of pseudocumene vapor condensation on the fibers. The fiber routing and vapor seal are shown in Figure 13.10. Finally, the snout provides the fill and vent ports that allow the module to be filled with liquid scintillator and a tube to distribute the liquid scintillator flow down the sides of the cells, as shown in Figure 13.11. The fill port is positioned above the first cell when the module is installed in the horizontal position so that the fill nozzle can be removed without draining oil from the extrusion. The fill port is also connected to an expansion tank for the horizontal modules. The vent port is 155 mm from the fill port on the horizontal modules and above the level of the first cell.

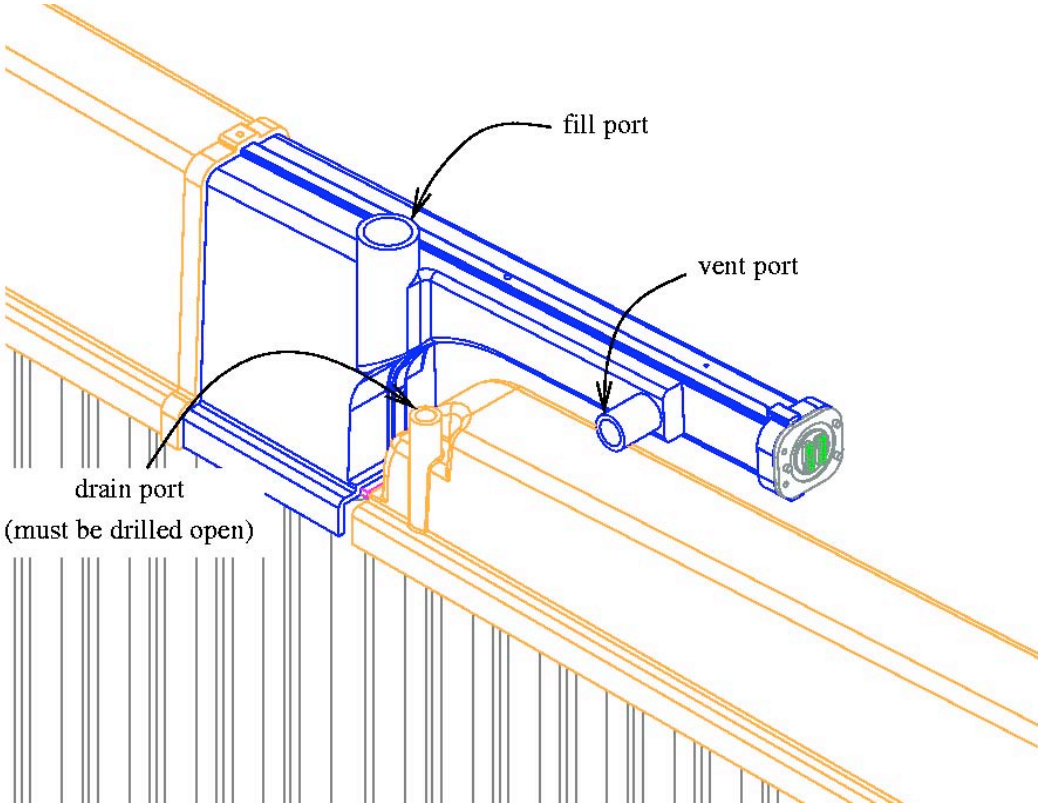

Fig. 13.9: The manifold snout fitting over the adjacent manifold. Also shown is the fill port on top of the snout and the vent port on the side.

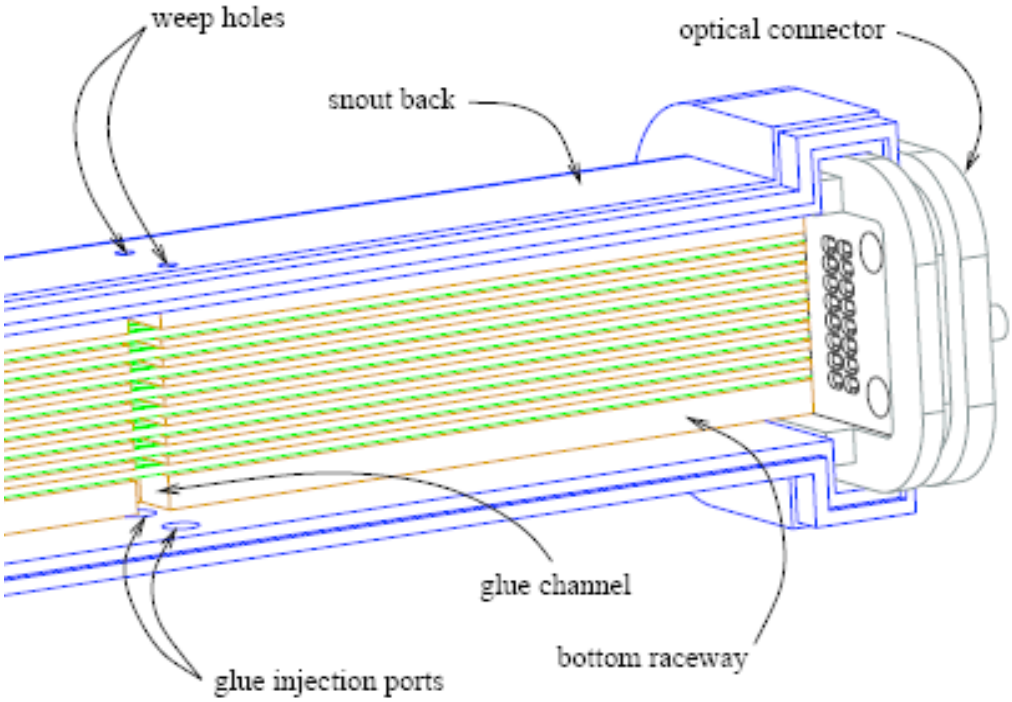

Fig. 13.10: Cutaway of the manifold snout showing the fiber routing to the optical connector and the vapor seal.

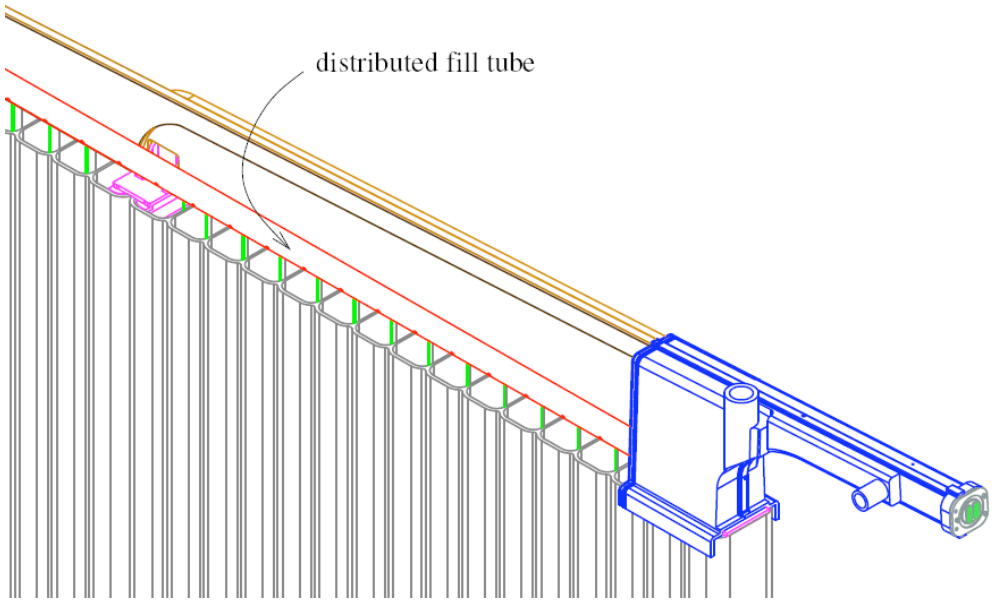

Figure 13.11: A cutaway of the manifold showing the snout with the fill and vent ports. The tube to distribute the liquid scintillator to the 32-cells of the extrusion assembly is also shown.

The manifold is glued to the extrusion assembly in much the same manner as the end-plate assembly. However, its parts, shown in Figure 13.7, are assembled to facilitate threading of the fiber into the optical connector. Before any of the wavelength-shifting fibers are strung through the cells, the side seals and center seal are glued into place, and the raceway closest to the snout is snapped into place. Then the side seals, center seal, back of the snout assembly, and optical connector are glued into place. The side and center seals are similar to those used for the end-plate assembly, except that they have features that support the fiber raceways. Figure 13.8 shows this part of the assembly with the first 16 fibers in place. A close-up of the snout at that stage is shown in Figure 13.12. A second raceway is then attached to the side seal and first raceway so that it covers the first raceway and the next 16 fibers are strung. After all the fibers have been strung through the cells and threaded through the raceways into the optical connector, the fiber cover, scintillator distribution tube, front of the snout, and manifold cover are glued into place. Figure 13.13 shows the glue joint between the snout and the manifold cover.

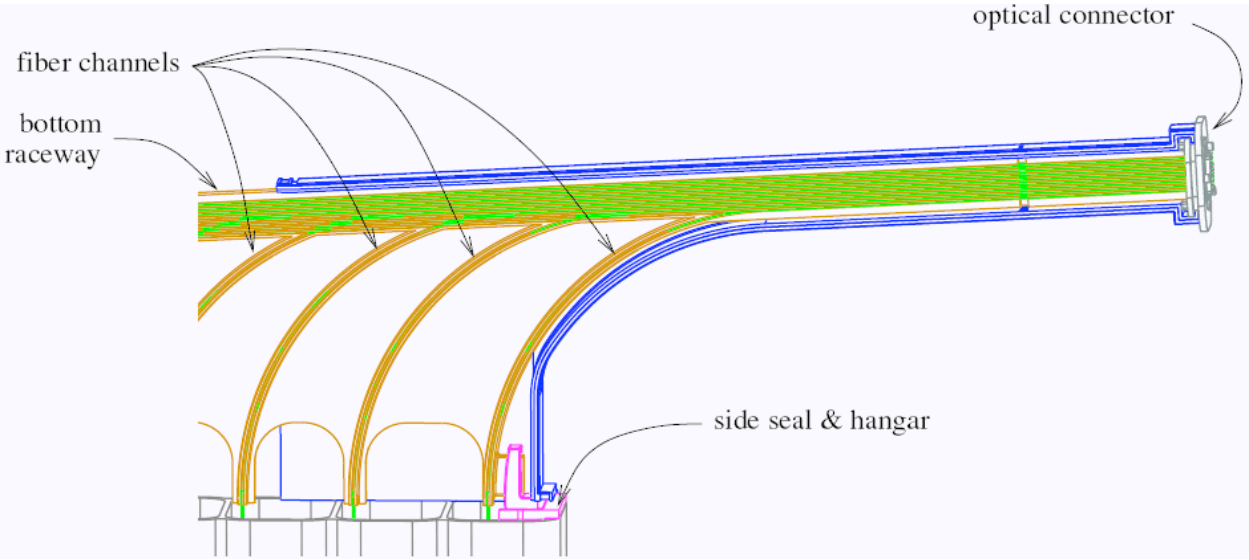

Fig. 13.12: Close-up showing the snout assembly after stringing half of the wavelength-shifting fibers.

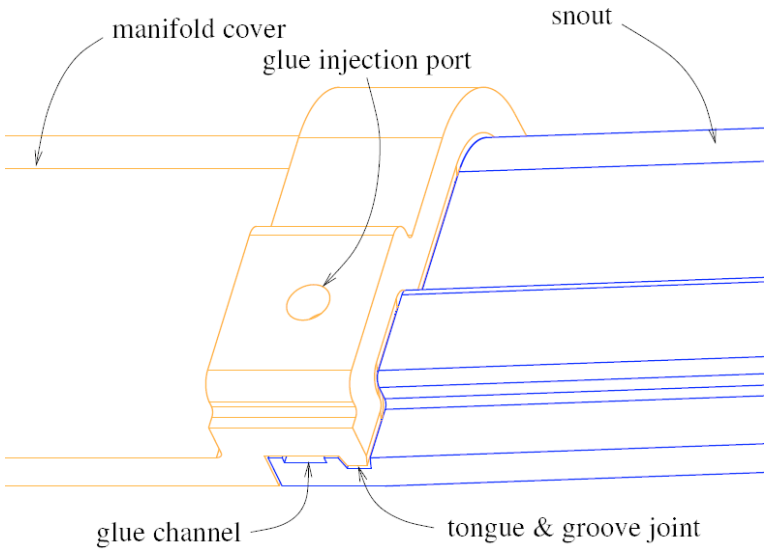

Fig. 13.13: Close-up of glue joint between the snout and the manifold cover. The manifold cover is slipped over the snout and then glue is injected into the tongue-and-groove joint.

13.3.4 Fiber Stringing

The fiber stringing machine is designed to insert fiber loops down the cells of the modules without damaging them. The machine consists of two major components: the fiber spooling apparatus, shown in Figure 13.14, and the far end vacuum adapter, shown in Figure 13.15. There are also fiber-puller assemblies for each cell that are used to draw the fiber loops down the module, shown in Figure 13.16.

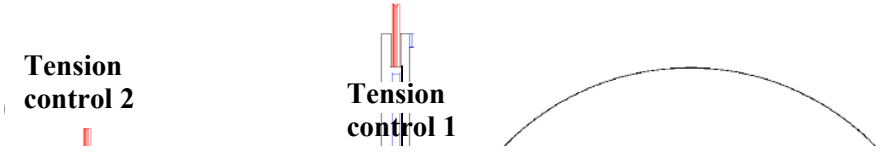

Fig. 13.14: Fiber spooling machine.

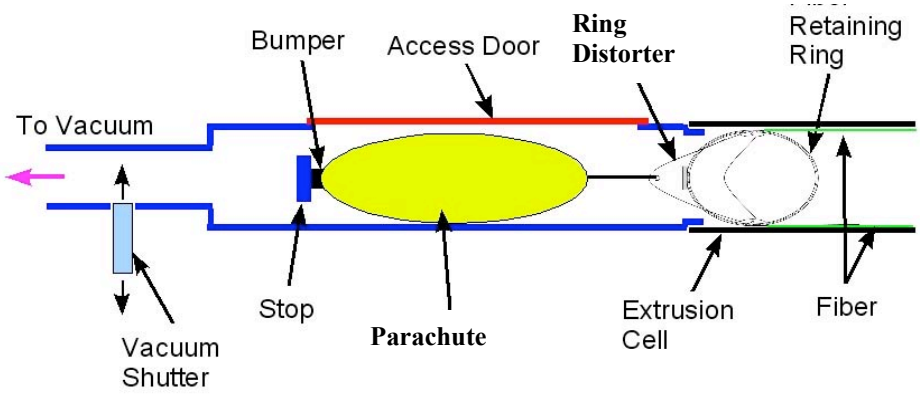

Fig. 13.15: The vacuum adapter showing the side view showing a single cell. The vacuum adapter (blue and red) is attached to the extrusion (black). The parachute hits the stop in the vacuum adapter. After all 32-cells are strung, the parachutes and distorters are removed through the access door located on top of the vacuum adapter.

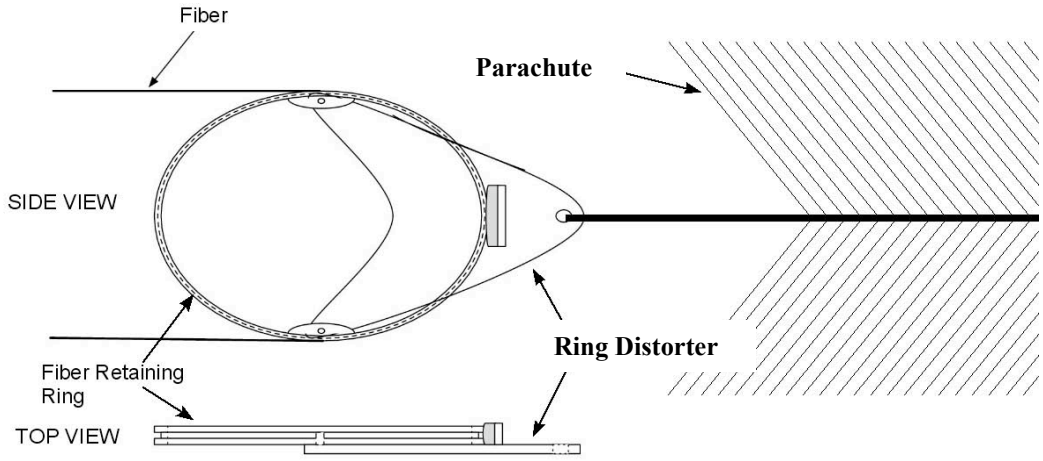

Fig. 13.16: Fiber-puller assembly.

13.3.4.1 Fiber Stringing Operation

To begin the fiber stringing operation, the fiber spooler is positioned so that the operator initially aligns it to one side of the manifold end of the module. The vacuum adapter is attached to the other end of the extrusion. A microprocessor in the spooling machine controls the position of the machine and the length of the fiber depending on which cell is being strung. The machine controls the tension on the fiber while the vacuum rapidly draws it down the channel. When the fiber nears the end of its travel, the machine automatically cuts it to the proper length for that cell. The operation of this machine is described in more detail in the next section.

The vacuum adapter seals the edges of the extrusion assembly with a soft gasket so that all 32-cells have access to the vacuum. The adapter has a solenoid gate that isolates all cells except the one being strung from the vacuum. The gate is operated electronically from the microprocessor of the stringing machine.

Once the machine positions itself at the appropriate cell, the operator threads the fiber though the pulleys and clamps the end in the secondary spool. A button on the touch screen is pressed to begin spooling up half of the loop. After the spooling is complete, the operator attaches a fiber-puller assembly, consisting of a fiber retaining ring, a retaining ring distorter, and a parachute. The fiber retaining ring is deformed into an oval when placed in the distorter to allow it to fit through the obstructions at the manifold ends of the cells. The configuration of this puller assembly is shown in Figure 13.16. The operator places the parachute in the cell and vacuum draws the assembly down to the far end of the extrusion. The spooler apparatus moves to the next cell and the vacuum adapter automatically switches the solenoid gate. After all thirty-two cells are strung, the vacuum adapter is removed and the fiber-puller assemblies are removed from the retaining rings, leaving the rings in the cells. The retaining rings expand and fit tightly to prevent the fiber from creeping up the cell during shipping.

13.3.4.2 Fiber Spooling Machine

The primary motivation of this design is the large number of repeated actions at both high speed and high acceleration during which the fiber must be maintained at a safe tension. This is accomplished with the semi-automatic machine described below.

The primary components of the stringing machine, some of which are shown in Figure 13.14, are as follows:

- Main spool: the 1 meter diameter fiber spool delivered by the fiber manufacturer. It is controlled by a servo motor.
- Secondary spool: the 1 m circumference metal spool that stores half of the cell's fiber. It is controlled by a servo motor.
- Tension control: The two tension control fiber loops operated such that, if the tension deviates from the desired value, the size of the loop changes. The size of each loop is determined by a wheel mounted to a track. The wheel is pulled upwards by a spring and is attached to a spring potentiometer to measure its position.
- Cutter encoder: an encoder on the wheel immediately before the cutter which senses how much fiber has passed this point.
- Puller: The fiber-puller assembly that is sucked down the cell.
- PLC: Programmable Logic Controller, a specialized computer that controls the various electro-mechanical actuators and sensors including the two servo motors.
- Servo drive: electronics that controls the servo motors. It has preset speeds and acceleration profiles and receives signals from the PLC.
- Motor modes:
    - Tension mode: the PLC can read the position of the tension control wheels and control the speed of the corresponding spool to keep the tension at the desired value.
    - Position mode: the servo can direct a spool to turn a specified number of times and then stop.
    - Velocity mode: the servo can direct a spool to turn at a constant rate. This is used in two ways:
        - Jog: during setup, the operator can move either spool forwards or backwards at a fixed low speed. This is primarily when a new main spool is being started or for error recovery.
        - Secondary spool alignment: returns the secondary spool to its home position after fiber release or when an error is detected.
    - Stopped: keeps the motors stationary when the PLC is neither controlling the speed nor position of a spool.
- Touch screen: The touch screen is the operator interface to the PLC that allows commands to be issued and the machine status to be monitored. The possible controls are selected by the PLC depending on the state of the system.

At the beginning of a normal stringing cycle, the fiber already goes through Tension Controller 1 and is held clamped at the cutter, as shown in Figure 13.17. The fiber is held in tension through the combined actions of the spring loaded tension controller and a servo motor on the main spool, as shown in Figure 13.18. The tension is controlled through a closed loop feedback algorithm programmed within the PLC. This loop maintains the tension control wheel at a desired position (obtained through a displacement sensor) by controlling the velocity of the servo that drives the main fiber spool. The tension is maintained to prevent the fiber from uncoiling and is selected to be at a safe value for the fiber. The spooling machine is mounted to a track that allows it to traverse perpendicular to the extrusion and line up with each cell. This slide includes a sensor so that the machine automatically determines the cell to be strung. Since the fiber length varies by cell because of the differing path length through the module manifold, the machine automatically spools the correct amount of fiber without operator intervention.

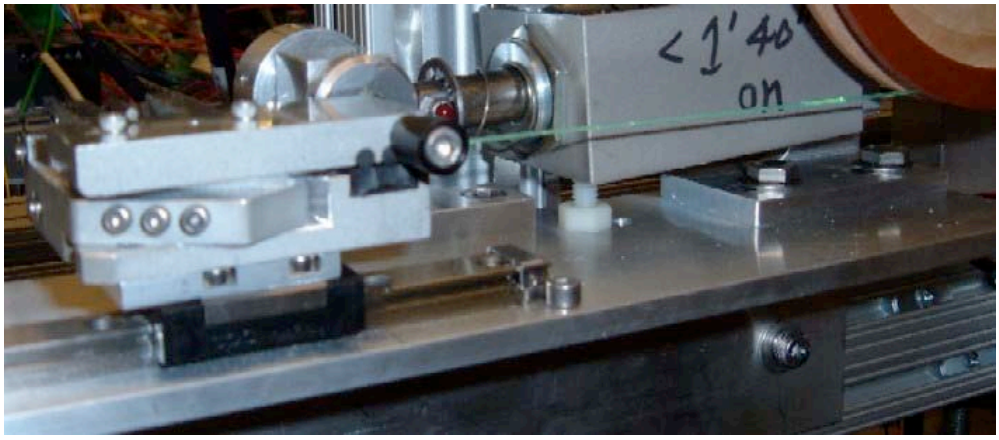

Fig. 13.17: Cutter/clamping mechanism

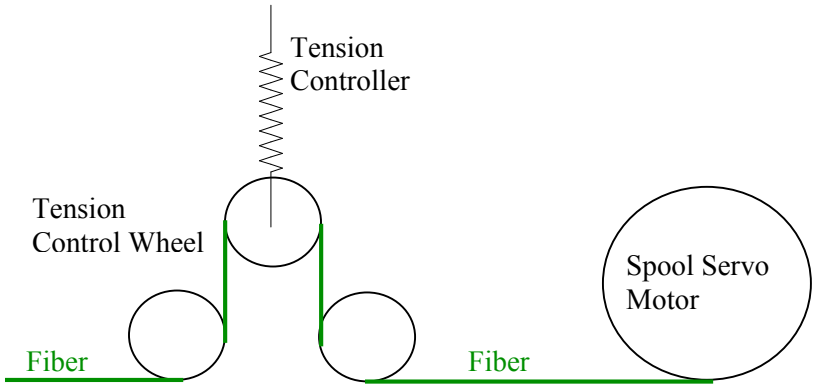

Fig. 13.18: Fiber tension control.

To begin, the operator releases the clamped fiber from the cutter and threads it through the guide rollers and Tension Controller 2, clamping it to the Secondary Spool. The operator then presses the touch screen and the secondary spool turns to accumulate the amount of fiber needed for the present cell. A digital encoder attached to the shaft of the secondary spool ensures that the correct amount of fiber is spooled. At this point, Tension Controller 2 is not activated and its tension control wheel is locked in place so that a precise length of fiber can be measured out.

Next, the operator attaches the fiber-puller assembly to the fiber and activates Tension Controller 2, which also activates the vacuum. The two tension controllers are necessary because the fiber-puller assembly fixes the fiber at its midpoint, creating two independent fibers that each require tension control during the stringing process. The operator then pulls the fiber-puller assembly to the near end of the extrusion and the fiber is drawn down the length of the extrusion. During the travel down the extrusion, the fiber length is measured by an encoder attached to a guide roller located just before the cutter. This allows the fiber coming off the main spool to be automatically cut to the correct length on the fly. Safely cutting the fiber on the fly is accomplished by installing the cutter mechanism on a slide activated by a solenoid. At the cutting point, the solenoid fires so that the cutter and clamp move with the fiber for a short distance. Thus the cut occurs at a small relative velocity between the fiber and the cutter. The cutter/clamp mechanism also clamps the fiber so that the fiber is ready for the next cycle and still in tension. The second half of the fiber loop, having been pre-measured in the spooling process,

simply comes free of the secondary spool at the end of its travel using a Geneva mechanism to release that clamp.

During the entire stringing process, the PLC checks for various faults and takes automatic corrective actions. A more flow chart of the machine operation is found in Figure 13.19

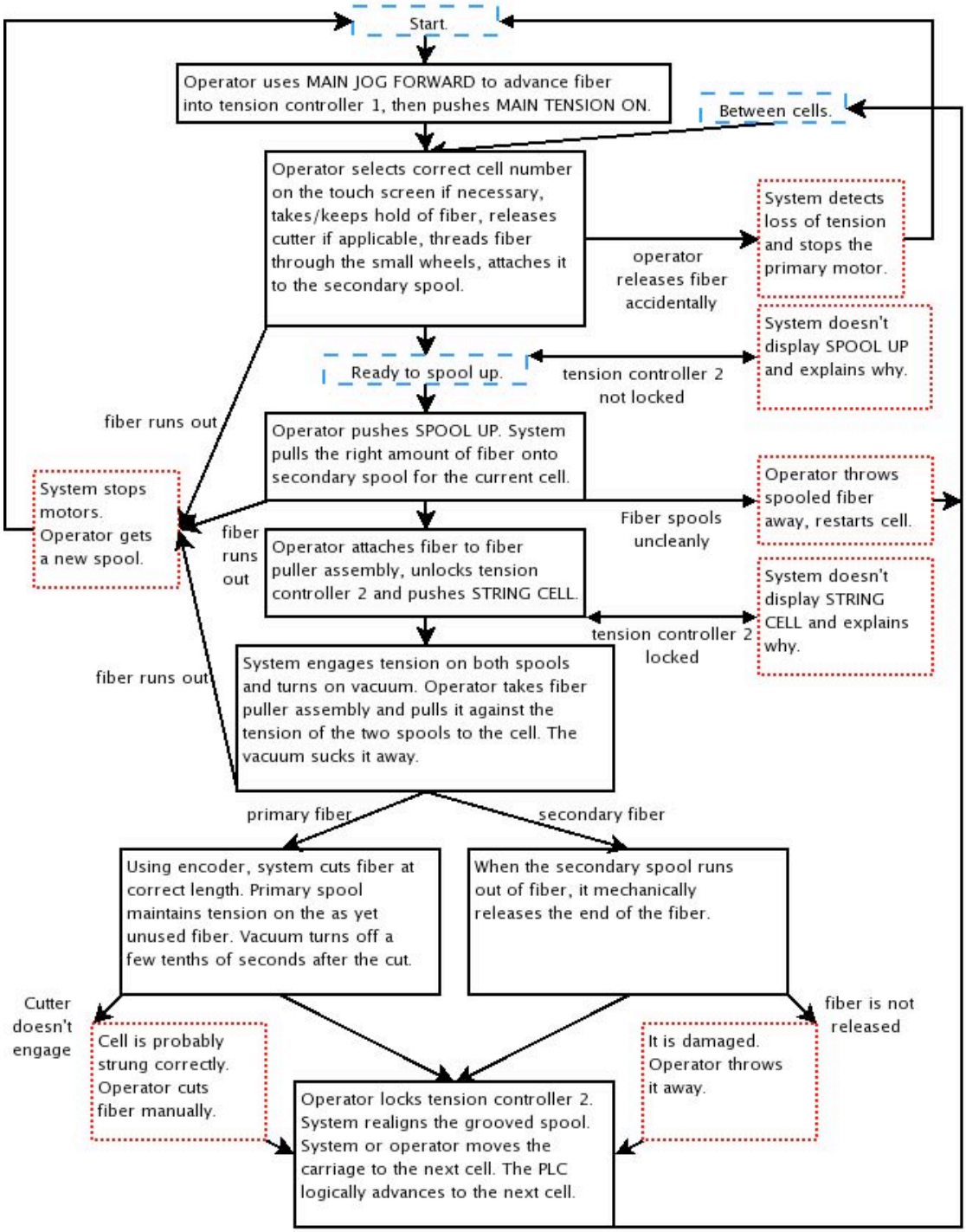

Figure 13.19: Flow chart of operation of the stringing machine. Solid black boxes are correct actions. Dashed blue boxes are system states. Dotted red boxes are error handling. Words in all caps are the names of buttons on the touch screen.

13.3.5 Optical Connector

The optical connector is an injection-molded part made of Delrin that serves as the interface between the wavelength-shifting fibers and the APD photodetector. It aligns the 64 fiber ends from the 32 module cells with the 32 pixels of the APD such that the fibers do not physically contact the APD surface. It must seal the face of the APD to prevent any condensation from the air and seal the manifold snout. The optical connector is mounted on the manifold module snout, shown in Figure 13.20, using a tongue and groove joint. This tongue-and-groove construction provides a rigid mechanical connection between the optical connector and the snout. In addition, it provides a light barrier and an environmental seal. Glue is inserted in the tongue-and-groove joint upon assembly.

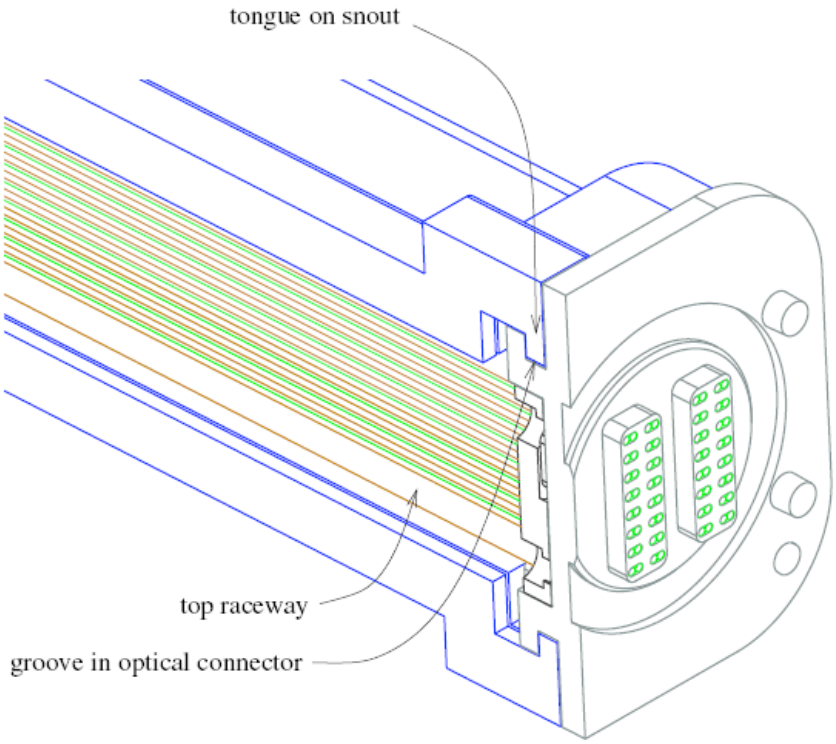

Fig. 13.20: Optical connector mounted on the manifold snout. Portions of the optical connector and the snout have been cut away to reveal the tongue-and-groove joint between the two components.

The optical connector has 32 oblong slots that each hold the two fiber ends from a single module cell. These slots are arranged in four rows of 8 to correspond to the APD pixel pattern. Each set of two rows is in one of the two raised bosses that fit through slots in the APD carrier board. Two dowel pins are used to provide precise *x_y* alignment. In addition, the connector precisely controls the gap between the ends of the fibers and the face of the APD. This is accomplished by flycutting three spacer pins at the same time as the fiber bosses. All three spacer pins press against a reference surface in the electronics module to set the gap. This flycutting also provides an optical finish to the surface of the fiber ends. Figure 13.21 shows the face of the optical connector that is the interface to the APD. The optical connector seals the volume between the fiber bosses and the APD surface using a variant of an O-ring with an X-shaped cross-section called a quad ring. A quad ring groove contains the quad ring which is designed to allow flycutting the optical connector as many as four times, if necessary, to obtain the desired surface quality.

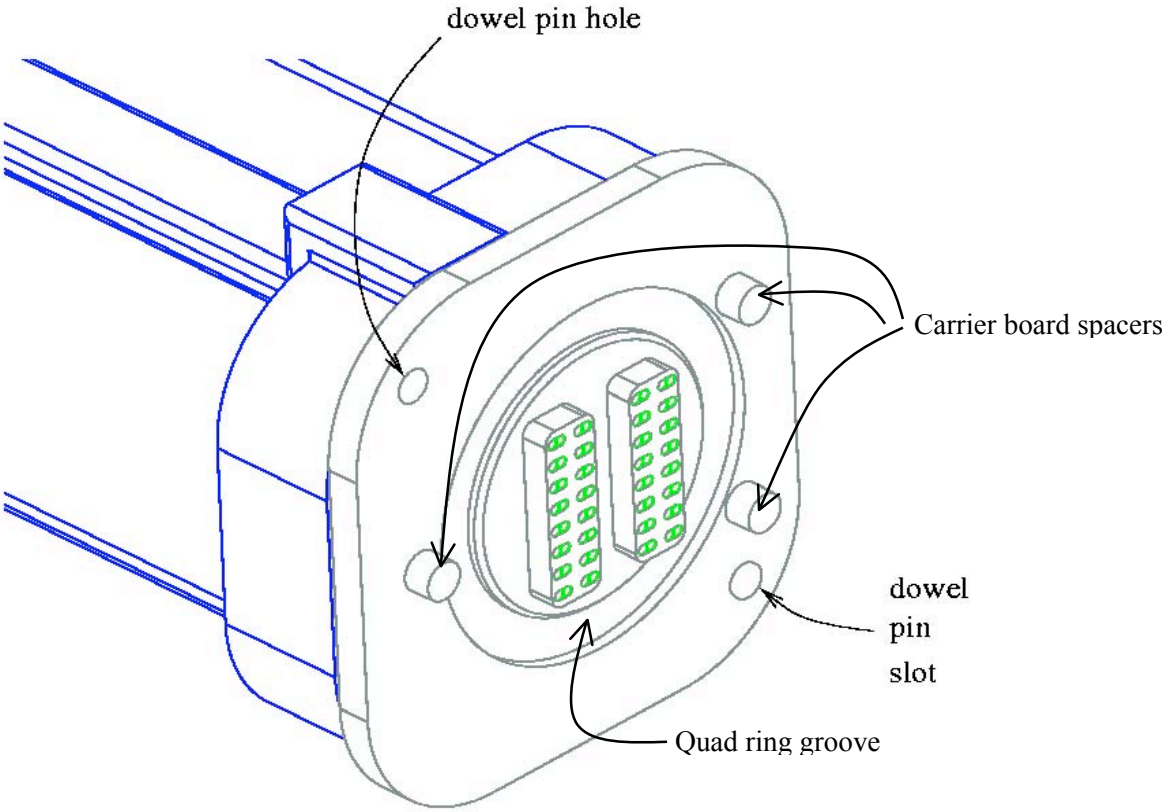

Fig. 13.21: The side of the optical connector that is the interface to the APD highlighting the alignment features.

The optical connector is constructed from two injection-molded parts, shown in Figure 13.22. The two parts are ultrasonically welded together by the manufacturer of the parts. The two-piece construction facilitates the potting of the fiber ends to provide a seal and to hold them rigidly for flycutting. As shown in Fig. 13.22, channels route glue to pockets which surround the fibers between the front and back parts. The channels are fed by glue injection ports on the back of the connector, Fig. 13.23. These ports are positioned above the fiber raceways when the modules are placed on the assembly table, so they remain accessible after fiber threading is completed.

Figure 13.24 shows a prototype connector after fiber threading has been completed and the potting glue has been injected. Note that the glue has surrounded every fiber at the point of protrusion from the connector. This figure also shows the same connector following flycutting.

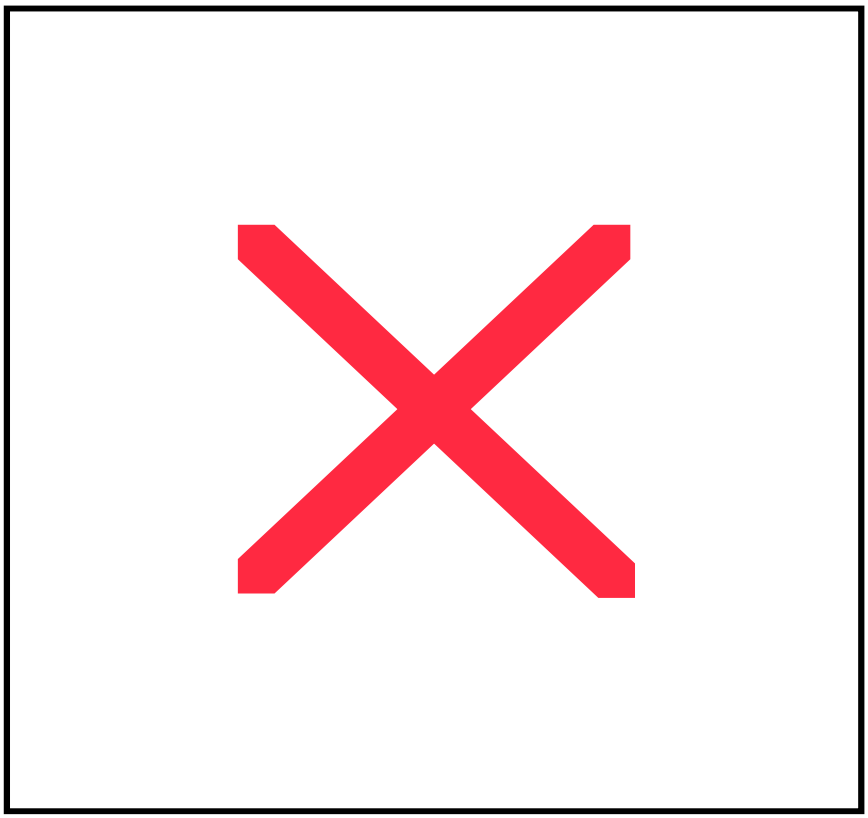

Fig. 13.22: Exploded view of an optical connector.

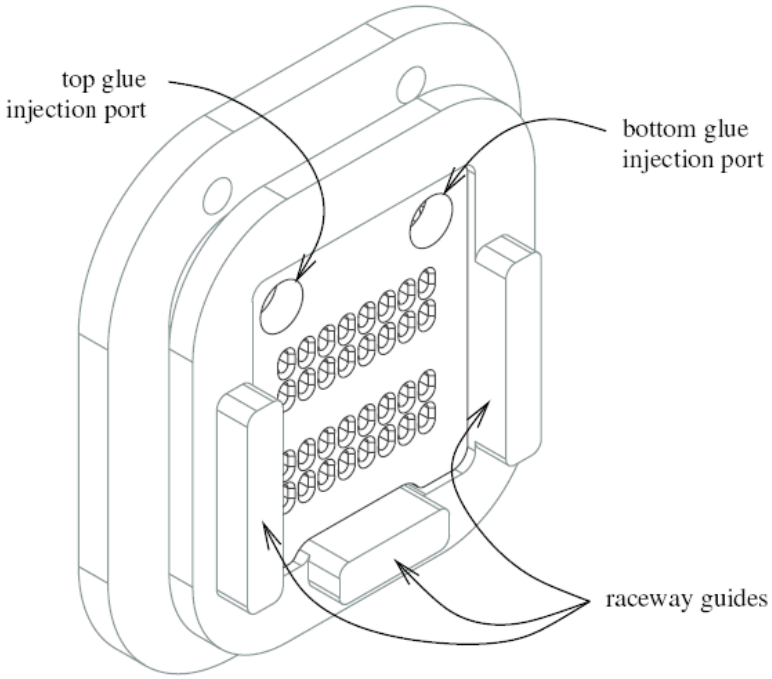

Fig. 13.23: Side of the optical connector that receives fibers in the snout.

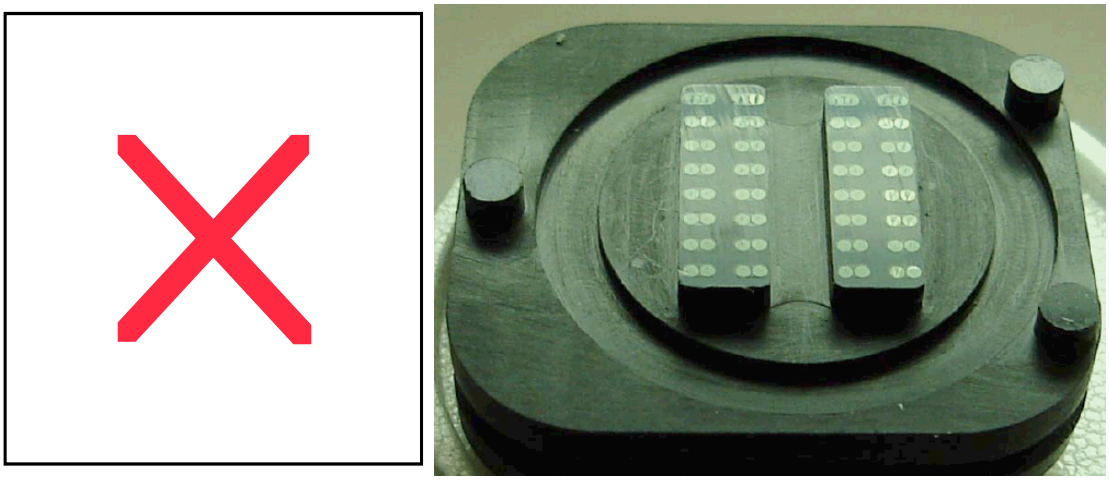

Fig. 13.24: A prototype optical connector with wavelength-shifting fibers potted with glue both before and after flycutting.

13.4 PVC Module Factory

13.4.1 Introduction

The module assembly factory is located at the University of Minnesota. There the 16-cell PVC extrusions are glued together to make 32-cell module assemblies, wavelength-shifting fibers are inserted, the module sealed, tested, and shipped to the far or near detector site as appropriate. The module assembly factory will be able to produce 30 modules per day at peak production. The procedures used in the factory are given below.

13.4.2 Module Assembly Factory

The module assembly factory receives a truckload of 60 horizontal or vertical extrusions each day. Each truckload has been matched for thickness at the extrusion manufacturer. The module factory glues together pairs of extrusions and trims them to size to make 32-cell extrusion assemblies. The factory then strings the extrusion assemblies with wavelength-shifting fiber in each cell, threads the fiber through the manifold and into the optical connector, seals the cells and the optical connector, flycuts the fibers in the optical connector, verifies that the fibers are routed to the correct optical connector pixel and that no fibers are damaged, verifies that the modules are leak-tight, packages the finished modules, and ships the package of 24 modules to the detector site for installation. Six such shipments will occur per week. Extrusions will be unloaded from a truck and finished modules will be loaded to a truck using the same air caster system used at the extruder and at the far detector. Stacks of modules will also be moved within the factory using this air caster system. All glue joints that contact the liquid scintillator use a chemically inert epoxy adhesive (3M2216). When additional structural strength is needed, a methacrylate adhesive (e.g. Devcon Plastic Welder) is used. When both glues are used on a joint, the chemically inert adhesive is used in a butt joint as a gasket to seal the liquid scintillator from the structural adhesive. The factory layout, based on a currently available building, is shown in Figure 13.25. A scale model of the building and a photograph of the building are shown in Figures 13.26 and 13.27.

An overview of the assembly of a module is given below with the steps in logical, but not time order. The details are described later. Because of the time needed for the chemically inert epoxy to cure and the time needed to leak check the modules, the process to produce a module takes four calendar days. The throughput of the factory is 30 modules per day at its peak output. At each stage of the assembly, the extrusion bar code is read into the database and its status is entered.

1. Unload a stack of 60 16-cell extrusions from the truck. An air caster system will be used to move the load off the truck and into one of the two receiving spaces in the factory. One crane bay will be used to receive and process vertical extrusions, the other for horizontal extrusions.
2. Inspect extrusions for possible shipping damage.
3. Use a floor-mounted crane to lift pairs of extrusions to gluing tables, glue the pairs together to make an extrusion assembly, trim them to length, and abrade their surfaces for gluing.
4. Use the floor-mounted crane to lift extrusion assemblies to a gluing rack. Three inch spacers are placed between the modules to allow access for gluing of the module parts to the ends of the extrusion. Repeat to fill 4 gluing racks for a total of 30 extrusion assemblies.
5. The side and center seals for each end of the module are glued into place.
6. The fiber raceway assembly near the snout is attached to the center and side seals and manifold snout back half.
7. The manifold snout back half is glued in a butt joint to the extrusion assembly using the chemically inert epoxy adhesive (3M2216). The optical connector has previously been glued into the snout half in a preassembly operation.
8. The glue is allowed to cure overnight.
9. Each of 30 extrusion assemblies that have already cured overnight is craned from a gluing stack onto a rolling table. The table is rolled to workstation part of the factory for fiber stringing, threading, and additional gluing.
10. The stringing machine is positioned at the first cell. Six stringing machines are used in parallel to process 5 modules each.
11. A shield tray is placed over the raceway to protect and support the fibers as they are strung.
12. A vacuum fitting covering all 32-cells is attached to the opposite end of the extrusion from the stringing machine.
13. Fibers are strung down the eight cells closest to the snout using the fiber stringing machine.
14. The first eight fibers are threaded through the raceway and snout while the next 8 cells are strung.
15. The last two steps are repeated for the remaining 24 fibers.
16. The vacuum fitting is removed.
17. The parachutes used to pull the fiber down the cells are removed.
18. The optical adapter is potted with 3M2216 epoxy to seal the fibers in place.
19. The end-plate is glued in a butt joint to the extrusion with the chemically inert glue.
20. The fibers in the snout are sealed with 3M2216 epoxy by injecting glue into the snout sealing port.
21. The snout top half is glued in a butt joint to the extrusion using 3M2216 epoxy.
22. The fill distribution tube is attached to the fill port on the snout.
23. The manifold cover is glued in a butt joint to the extrusion using 3M2216 epoxy.
24. The joints in the manifold covers are injected with 3M2216 epoxy.
25. All joints using the 3M2216 epoxy are allowed to cure overnight.
26. The module is rolled under the crane bay at pressure testing area 1.
27. All modules are leak tested for eight hours at a pressure of 10 psi. If leaks are found, the module is removed and, if possible, repaired.
28. Each module is craned to a rolling table.

29. Structural adhesive is injected between the sides of the end-plate and the extrusion for modules for which the butt joint has already cured for a day.
30. Fiberglass mesh is glued to the extrusion edge to reinforce the end-plate side seals.
31. Edge stiffeners are glued to the bottom outside edge for the 2 outside vertical modules in a plane.
32. Structural adhesive is injected between the sides of the manifold cover and the extrusion on modules for which the joint has already cured overnight.
33. Structural adhesive is injected between the sides of the snout and the extrusion for which the joint has already cured for a day.
34. The structural adhesive is allowed to cure for 12 minutes.
35. The optical adapter given an optical finish using the flycutting machine.
36. The module is checked for damaged fibers using the continuity tester.
37. The module is rolled under the crane bay at testing area 2.
38. Shipping spacers are placed on top of the previous module and the module is craned onto the top of the shipping stack.
39. The module is tested for leaks using the leak tester. If leaks are found, the module is removed and, if possible, repaired.
40. The bar code for the module is read and its database entry updated.
41. Modules are packed for shipping and loaded onto the truck using the loading air caster system.

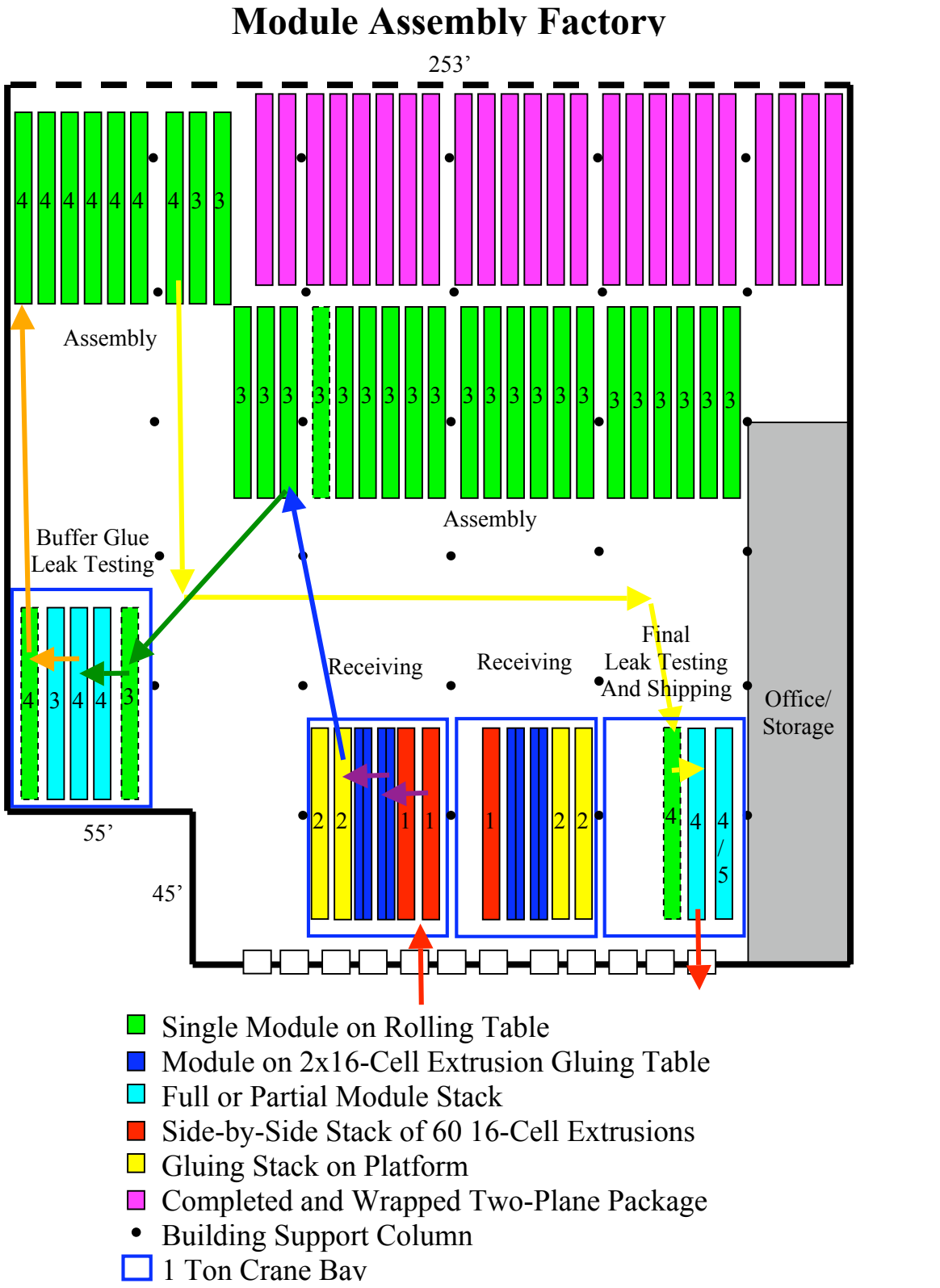

Fig. 13.25: Layout of the module assembly factory as it fits into a currently available space. The numbers show the number of days that the module has been in the assembly stream. Moves of modules within the factory over 5 days are given by the arrows. The unnumbered pink space is for storage of extrusions and finished modules.

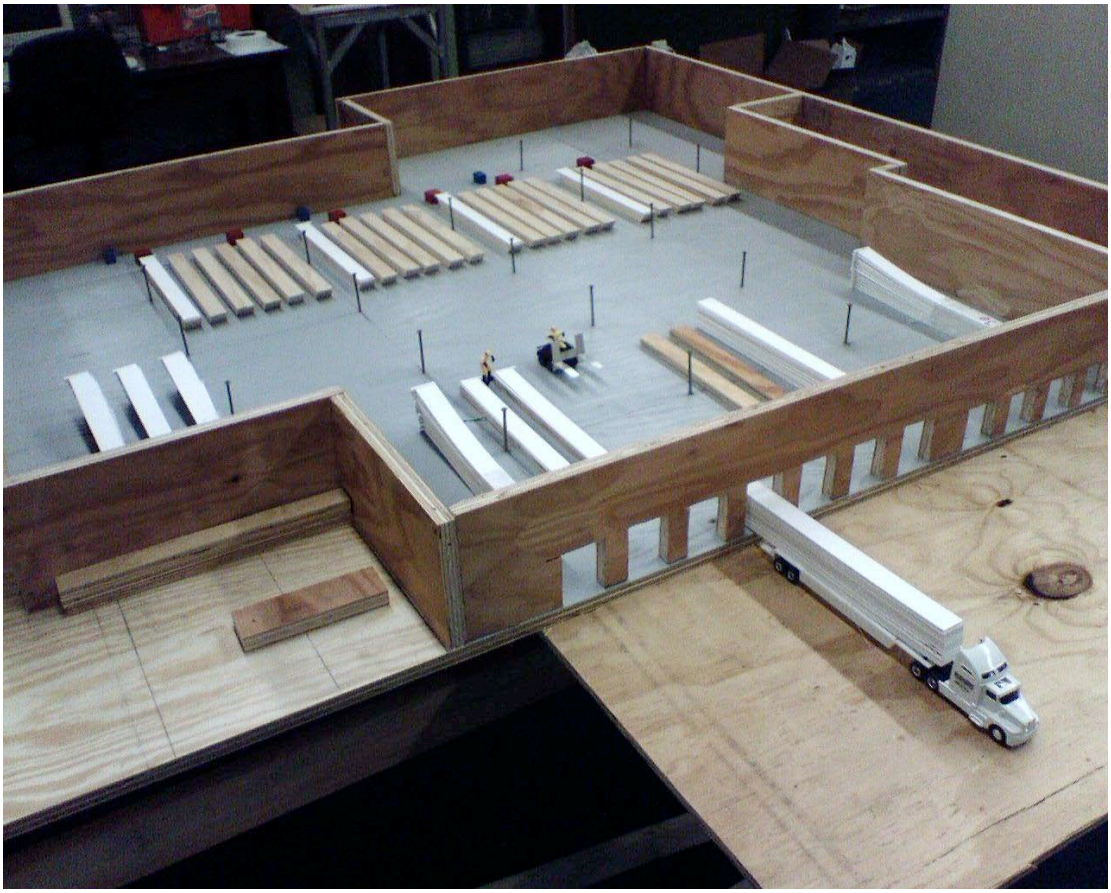

Fig. 13.26: A scale model of a factory space that is currently available. This model was used to develop some of the procedures in this document. The loading and unloading assembly area is near the loading docks as shown. The assembly area where individual modules are assembled is also shown. The long rectangles represent the modules.

Fig. 13.27: Picture of currently available warehouse space used as a template to design the module assembly layout. This space is typical of many such spaces near the University of Minnesota campus.

13.4.3 Quality Assurance at Module Factory

While producing modules, three crucial aspects of the detector will be continuously monitored: possible fiber damage, possible leaks, and glue quality. These quality assurance procedures are described in the next sections.

13.4.3.1 Quality Assurance of Fibers at Module Factory

The quality assurance procedures for the wavelength-shifting fiber are designed to determine that the fiber was not damaged while in transit to the factory, to assure that the fiber was not damaged during module construction, to check that all fibers were routed to the correct APD pixel, and to discover if any fiber damage occurred during shipping to the detector site.

Fiber arrives at the module assembly factory on 1 meter diameter spools (approximately 2 km of fiber on each spool). This fiber has already been tested to assure that it meets the required specifications and to check for shipping damage during shipping from the manufacturer. At the module assembly, a 10 meter sample from each spool will be tested for shipping damage. To do this, an attenuation measurement will be performed by looping the fiber around an aluminum cylinder with a machined groove (Figure 13.28). The fiber is illuminated at 20 locations in sequence by blue LED's. We obtain 20 amplitude measurements at 0.5 meter intervals along the 10 meter length. These data provide an attenuation measurement that will be compared to the previously measured performance of fiber from that spool.

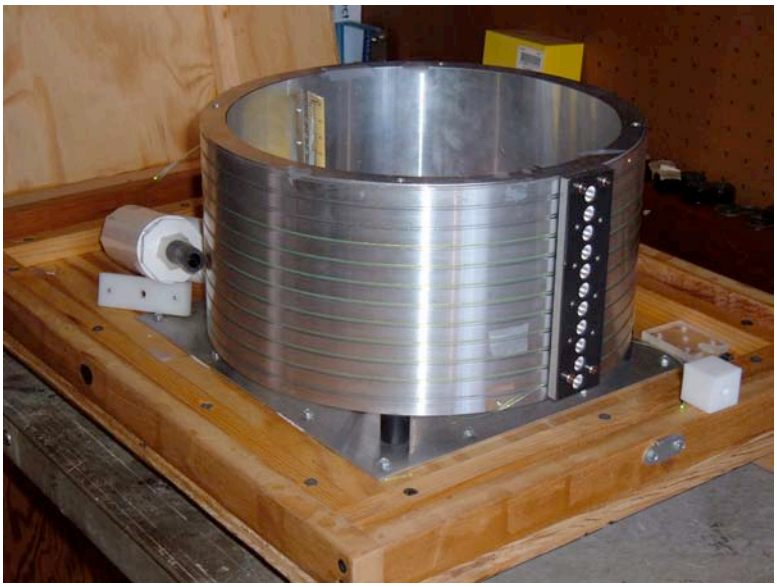

Fig. 13.28: Picture of light attenuation device.

When fiber is strung through a cell, its spool is recorded by scanning its bar code. When the module is completed, each fiber is compared to that data to check for fiber damage. This procedure removes any lot-dependent variation in the post-fabrication attenuation checkout. This test is performed by injecting light from a blue LED into one end of the fiber loop through the optical connector and measuring the amplitude at the other end with a photodiode. This will be a DC light amplitude measurement during which the LED is illuminated for about 1 sec while a voltage measurement is performed on the photodiode circuit (Figure 13.29). The reproducibility of attenuation measurements on fiber is at the 3% level (Figure 13.30).

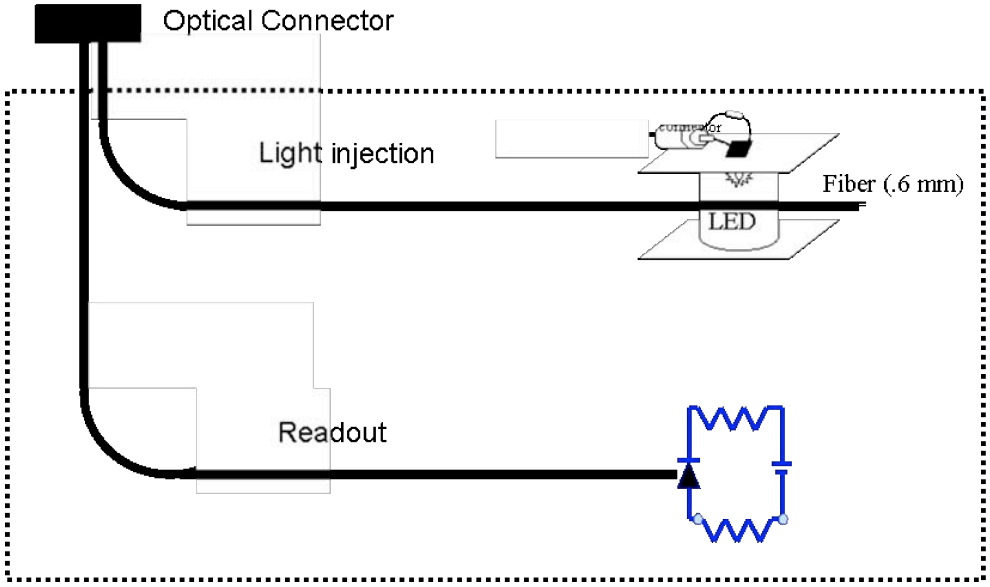

Fig. 13.29: Diagram of the light continuity machine showing integrating sphere for light injection (LED) and photodiode readout circuit. The voltage measured across the lower resistor indicates the light output.

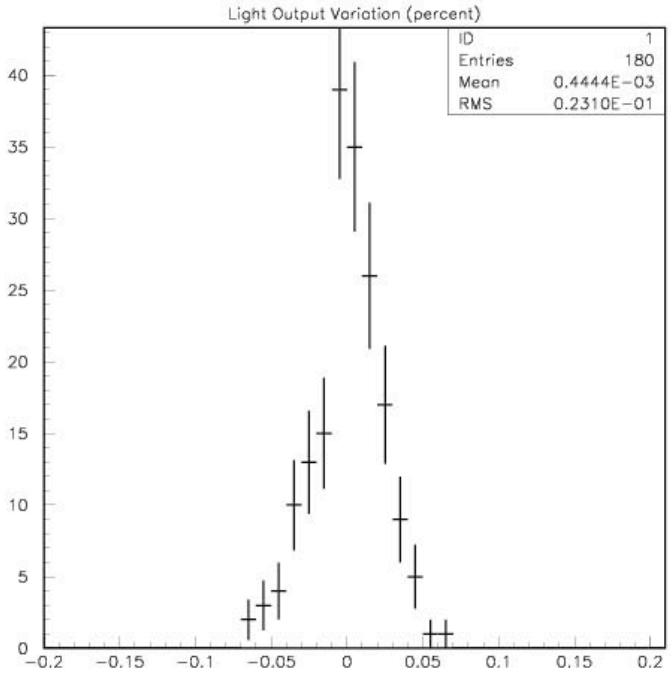

Fig. 13.30: Light output measurement variation for repeated measurements on a single undamaged fiber.

In order to simulate possible fiber damage, we have bent fiber beyond its recommended minimum bend radius, remeasured its light output, and compared the results to pre-calibration

data. Only a small (<1%) light loss was observed while the fiber was bent significantly beyond its minimum recommended bend radius and this was recovered upon relaxation of the fiber. When the fiber is damaged by a very sharp bend, it shows a light loss that is large compared to the measurement precision (Figure 13.31) that does not recover even if it is straightened. There are also irregularities (slight bulges in the fiber) intrinsic to the manufacturing process but. their occurrence is low. The light loss associated with these is significantly less than that from fiber damage.

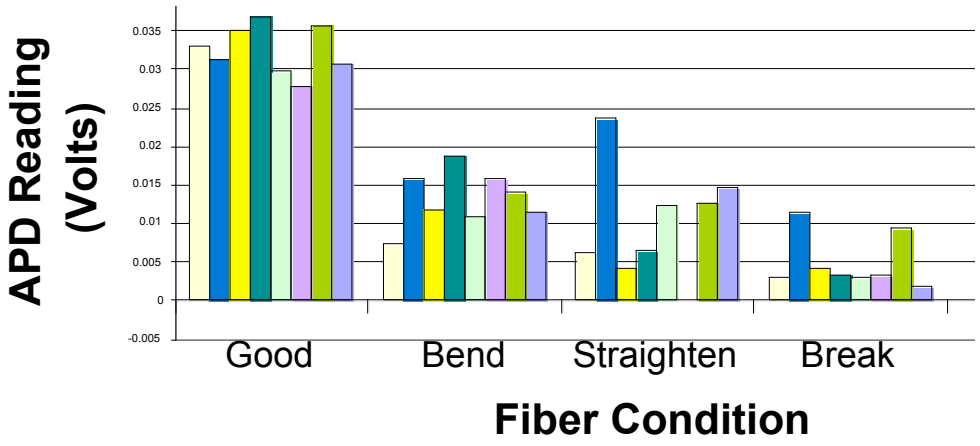

Fig. 13.31: Light output for 8 fibers when damaged. Each color is a different fiber. The histogram compares the light output from the undamaged fiber (good), fiber with a very sharp bend (bend), fiber that is straightened after it is sharply bent (straighten), and fiber which is bent until it is cracked (break).

Upon completion of the fiber continuity checkout, the data for each cell will be recorded in a database which can be used as the initial cell calibration. The fiber continuity test is repeated at the detector site with an identical device to check for damage in shipping.

13.4.3.2 Quality Assurance of Modules against Leaks at Module Factory

Since the modules must hold the liquid scintillator without leaking, every assembled module will be tested to assure no leaks occur. This QA leak test will be performed twice, once when all of the module parts have been glued with the 3M2216 epoxy and once when the module assembly is complete, before it is shipped to the detector site. The leak test will also be performed prior to installation at the detector site. Tests, described below, show that leaks that occur from assembly flaws are large enough to be detected using a the bubble-bottle arrangement shown in Figure 13.32. This technique measures air flow through the modules pressurized to 10 psi before the modules are reinforce with structural glue and again at 20 psi once the modules are complete. 20 psi is slightly above the operating pressure. Leaks below the level of sensitivity of this device have not been detected in more sensitive florescent dye tests. This allows us to estimate the leak rate of the detector for modules that pass the QA procedure.

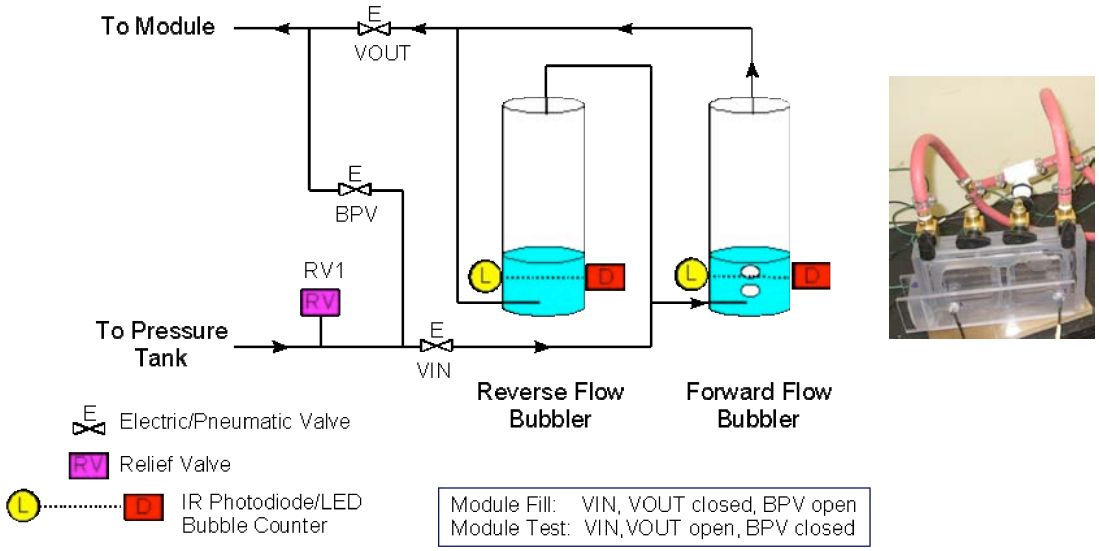

Fig. 13.32: A bubbling apparatus designed to check completed modules for leaks. Also shown is a picture of the bubble-bottle.

The frequency of occurrence of very small leaks, less than 9 μm, in glues joint was investigated using short samples of the extrusion modules which were filled with water containing a fluorescent dye and pressurized with compressed air, a standard industry test to reveal very small leaks. Two sets of these modules were tested. Those sealed with only the 3M2216 epoxy were tested at 10 psi, while those sealed with both glues were tested at 20 psi. The joints of these test modules are examined periodically under ultraviolet light to look for evidence of the fluorescence as shown in Figure 13.33. Fluorescence down to an integrated single leak volume of 0.02 cubic centimeters of water can be detected by a trained observer, as shown in Figure 13.34.

Fig. 13.33: Inspecting the test joints for the fluorescence that would indicate a leak

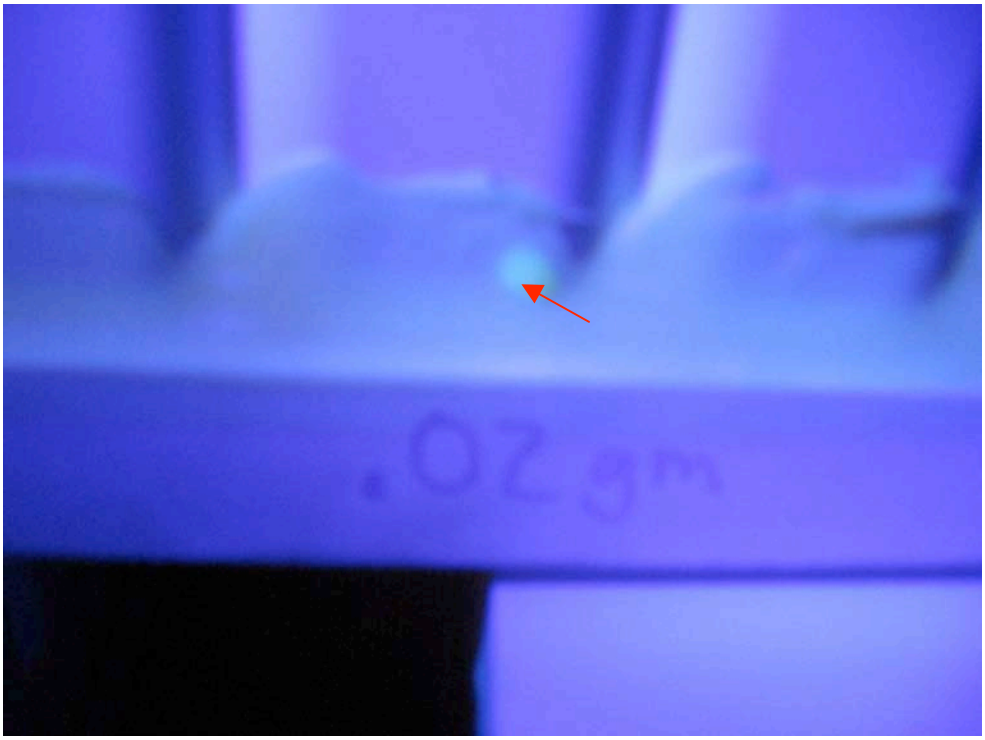

Fig. 13.34: The bright spot (indicated by the red arrow) shows 0.02 cc's of water with fluorescent dye placed at the glue joint of a test module. This is the smallest leak that can be consistently detected with this technique.

Thus far no leaks have been observed for 57 sixteen cell test modules for an average time of 217 days. Each of these 57 modules represent one half of the liquid seal length of a vertical module and one quarter that of a horizontal module which has both ends exposed to the liquid. Assuming that leaks flow at a constant rate, this gives a leak rate that is below 0.02 grams for 1.2×10^4 test module days. The detector has approximately 6000 vertical modules and 6000 horizontal modules. Assuming that the leak probability is proportional to the glue joint length, this test predicts a leak rate of less than 1.2×10^{-3} cc/vertical module/year and 2.3×10^{-3} cc/horizontal module/year. For the entire detector the leak rate has an upper limit of 0.02 liters/year, a negligible amount. A similar test of only the inner seal at a pressure of 10 psi finds no leaks in 75 modules for an average time of 40 days. This gives an upper limit leak rate for the chemically inert glue seal of 0.02 grams/3×10^3 test module days. This gives an upper limit of the scintillator coming in contact with the structural glue of 0.05 cc over 10 years at each seal. These leak tests are continuing.

During the initial testing of glue joints for the test modules, 12 leaks were observed from a loss of pressure using a 1% accurate pressure gauge. Nine of the 12 leaks were very large, with at least a 2 psi drop in 12 hours. The smallest leak found had a pressure loss of 2 psi in two days. All leaks were located using the standard soap bubble technique and repaired. The repaired modules were included in the sample of 57 in which no leaks have been observed using the fluorescent dye technique. This small sample of leaks gives information about the necessary precision of the leak QA procedure. A calibrated 6 micron hole in one of the test modules under the same conditions of 10 psi pressure gave a pressure drop of 0.5 psi in 22 hours or about half the rate of our smallest detected leak. Since the leak rate is proportional to the square of the hole diameter, this is equivalent to a 9 micron hole. Thus, if our QA can detect leaks below the 9

micron level, the probability of having any leak is small and an estimate of the upper limit for leaks of less than liter/yr.

To determine the sensitivity of the bubble-bottle technique, two 32-cell full length extrusion assemblies were tested. One had no leak and one was given a calibrated 9 micron leak. Figure 13.35 gives the integrated number of bubbles as a function of time for both modules pressurized to 20 psi. During the initial time the cells in the module are expanding under pressure causing the volume to change. The integrated bubble count in 8 hours after the initial turn on was approximately 230 bubbles in the module with the 9 micron leak but 0 in the module with no leak, The integrated bubble count for the module with the leak continues to rise while the module with no leak stays flat . Over the entire time scale both the atmospheric pressure and the factory temperature change sufficiently to cause fluctuations in the bubble count. Nevertheless there is a large qualitative difference in response between a module with a leak larger than 9 microns and one with no leaks. The bubble-bottle QA method has sufficient precision to detect the types of leaks that occur from assembly flaws. The current plan has each of the QA leak tests integrated over approximately 12 hours.

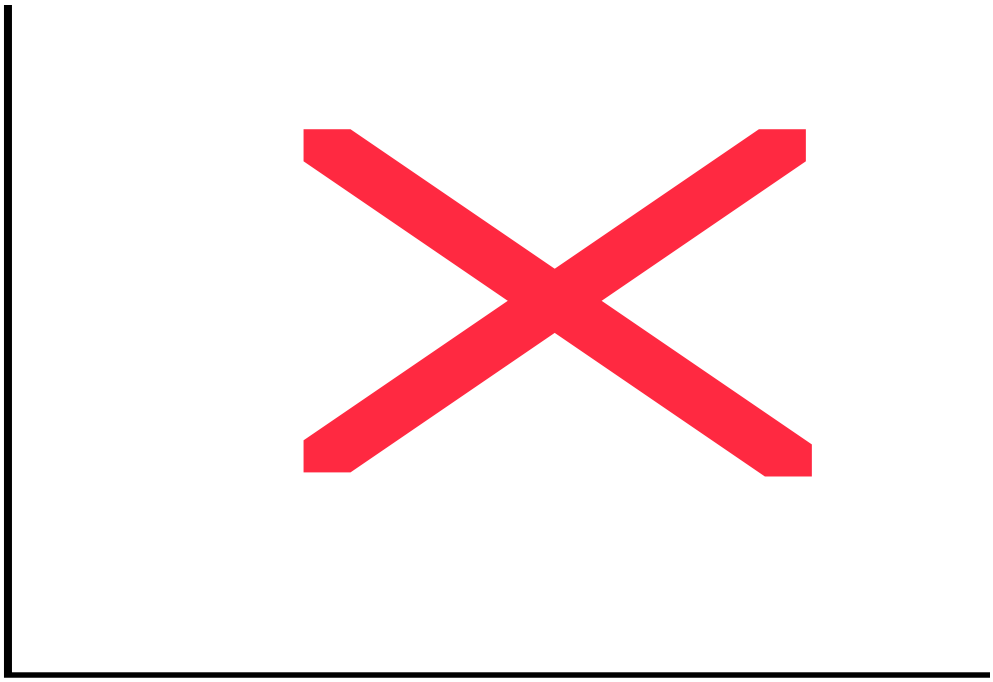

Fig. 13.35: Integrated number of bubbles as a function of time for a full length 32-cell module with no detectable leak (red) and one with a calibrated 9μm leak (blue). Both modules were tested at 20 psi.

13.4.3.3 Quality Assurance of Glue at Module Factory

During module construction, samples of the glue used in each joint will be saved. That glue will be examined after its fixture time has elapsed (15 minutes for the Devcon Plastic Welder structural adhesive and 12 hours for the 3M2216 chemically inert epoxy) to assure that it has been mixed properly and has cured according to specifications. Each sample will also be tested after its full cure time has elapsed, 1 day for the Plastic Welder and 7 days for the 3M2216 epoxy. In addition each batch of glue (typically a 55-gallon drum) will be tested for its adhesive strength with the PVC used in the modules in tension, shear, and cleavage-peel, as shown in Figure 13.36. These tests will also allow each glue joint to fully cure before force is applied. These tests will be compared to the current results given in Figure 13.37.

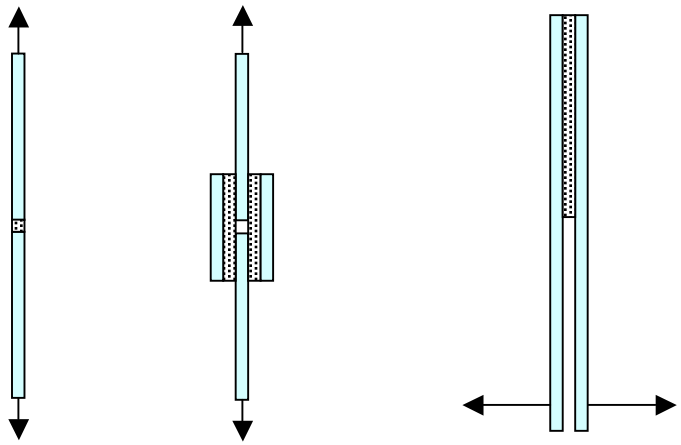

Figure 13.36: Stress configurations to test on the strength of glue joints. PVC is light blue and glue is the black dotted volume. The arrows show the directions of the applied forces: (a) the glue joint in tension, (b) in shear, and (c) in cleavage-peel.

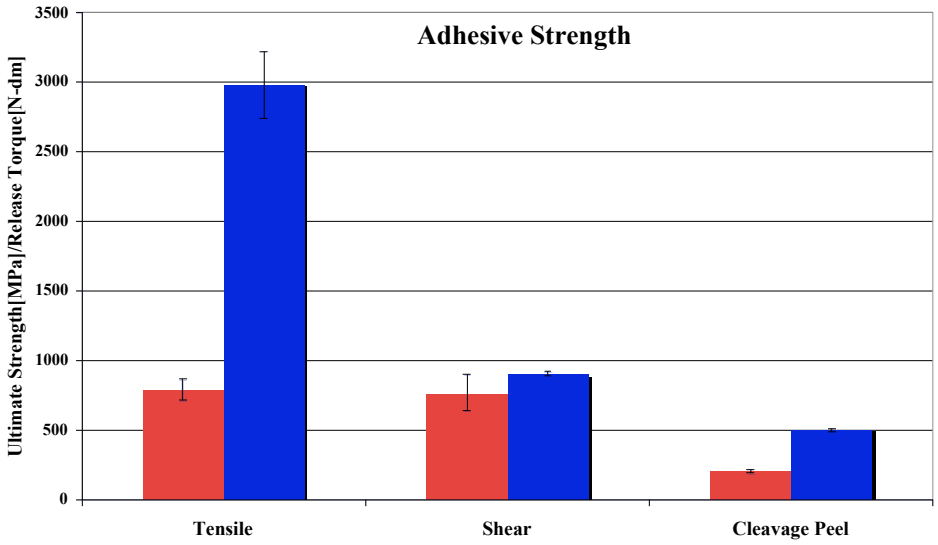

Fig. 13.37: The adhesive strength of 3M2216 gray (the chemically inert epoxy) in red and Devcon Plastic Welder (the structural adhesive) in blue, the glues used in the construction of extrusion modules. The 3M2216 is tested with a roughened PVC surface. Tension and shear are given in MPa and cleavage-peel is in N-dm.

Prototype modules were pressure tested to destruction and the structural failures examined. Joints with 3M 2216 alone failed at 380 KPa or higher. The maximum pressure in actual service is 130 KPa. Therefore, modules made with 3M 2216 alone would be expected to have a factor of safety of approximately 3. The failure of the 3M 2216 joints was due to cleavage-peel at the side seals. In actual module construction, all 3M 2216 joints will be reinforced with Plastic Welder.

Joints in full-sized modules sealed with the designed gluing technique using both 3M2216 and Plastic Welder were able to withstand pressures of 1 MPa, the strength of the PVC, without failure. Figure 13.37 shows that the cleavage-peel strength of Plastic Welder is more than double

that of 3M 2216. Since the actual modules utilize Plastic Welder as the structural adhesive, this gives a safety factor of approximately 6 for the glue joints.

Due to tolerances in the extrusions, gaps may develop in adhesive joints at the end-plate and manifold. The module parts are designed to produce gaps no smaller than 0.5 mm or larger than 4 mm. Therefore, the strength of the module adhesives were tested for ranges of gaps from 0.5 mm to 4 mm. The results show that the adhesive strength provided by the combination of glues is adequate over the entire range of gaps expected in NOvA modules. In the worst case, the shear strength of 3M 2216 epoxy drops approximately linearly with gap thickness. Its strength at 4 mm thickness is approximately 50% of its strength at 0.5 mm thickness. Plastic Welder strength drops about 20% as the gap increases to 4 mm. As the factor of safety for the adhesives is approximately 6, the reduction in shear strength for larger gaps does not threaten module integrity. This range of gaps does not affect the tensile strength or the cleavage-peel strength of the Plastic Welder.

Tests were also performed to determine the effect of the scintillator used in this detector on the glue joints. Specimens of the variety illustrated in Figure 13.37 were soaked in scintillator and tested after 2 days, 7 days, 21 days, and 65 days. Glue thicknesses were 0.5 mm for shear and cleavage-peel and 1 mm for tension. The temperature was elevated to 49° C during soaking to accelerated aging. For example, 65 days at 49° C approximates aging for 1-2 years at room temperature. For 3M2216, the glue strength appears not to be affected by the scinitillator. The specimens soaked in scintillator behave similarly to those soaked in plain mineral oil. For Plastic Welder, the results are similar for shear or tensile strength. However, there may be a small decrease in cleavage-peel strength, which is not statistically significant at this time. It should be noted that the Plastic Welder is isolated from the scintillator in the detector by the 3M2216. These lifetime tests are continuing.

13.4.4 Module Assembly Factory Procedure and Rate

This factory receives extrusions from the extruder as they are needed to match the rate of detector assembly. To assure smooth operations, the factory will be able to store up to 1 week of extrusions and 2 weeks of finished modules as a buffer against shipping disruptions. An additional 1 week of flexible storage is available to add to either the input or output buffer as necessary. The production, inspection, and storage tasks for the extrusions are asynchronous from the module assembly, packaging, and shipping to the detector sites. The output rate of the factory is matched to the peak detector installation rate of about 28 modules per day, which results in six truckloads per week to the far detector site.

The module production process is primarily determined by the most time consuming processes in the assembly, the stringing of the fiber down each of the 32-cells, and the threading of the fiber through the manifold into the optical connector. Our time-and-motion studies have determined that these two processes take about 75 minutes. Each module will take 5.1 person hours to assemble. This estimate is based on time-and-motion measurements for actions that make up 68% of the time. The major assembly actions and their times are given below in rounded-up person minutes:

Gluing operations	96 minutes (79% time-and-motion measurement)
Moving modules	82 minutes (36% time-and-motion measurement)
Stringing fibers	45 minutes (74% time-and-motion measurement)
Threading fibers	30 minutes (time-and-motion measurement)
Flycutting	15 minutes (time-and-motion measurement)
Packaging and loading truck	10 minutes = 240 minutes/24 modules (estimate)

QA fiber mapping	6 minutes (time-and-motion measurement)
Unloading truck	6 minutes = 144 minutes/30 modules (estimate)
QA leak testing	3 minutes (30% time-and-motion measurement)

The module factory is organized around 3 assembly areas, as shown in Figure 13.25. The shipping and receiving area has crane coverage and is near a loading dock with at least 3 bays. In addition to receiving extrusion assemblies at the beginning of the process and shipping the finished modules at the end of the process, this area is used to distribute the extrusion assemblies to gluing racks and then to individual work tables at the beginning of the assembly process. It also combines the finished modules into stacks for testing and packaging at the end. The second area consists of rolling work tables of individual modules for stringing the fiber down the cells, threading the fiber through the manifolds, gluing the manifolds and end-plates to the extrusions, and creating an optical surface on the fibers in the optical connector. The third area is used for leak testing the 3M2216 epoxy seals of the modules.

The factory will function for approximately 13 hours/day for 5 days/week and produce up to 30 modules/day. There is a great deal of flexibility in this schedule, which is well suited to the student labor to be employed.

A given module takes 5 days to emerge fully assembled, tested, and packaged in a stack of 24 modules ready for shipping to the detector site. This allows for two overnight times in the assembly where the 3M2216 epoxy is allowed sufficient time to cure and two overnight leak tests. The following sections will follow a set of 30 modules through these five days through the factory.

13.4.4.1 Module Factory Flow Day 1

The flow of modules through the factory on their first day is illustrated by the purple arrow in Figure 13.25. A typically day would have three stacks of 60 raw extrusions left over from the previous day and one stack of 60 delivered that day. The rectangles are the length of an assembled module. The areas outlined in blue have crane coverage.

Individual extrusions are lifted by the free-standing crane, such as that shown in Figure 13.38, and put onto assembly tables used to glue two of the 16-cell extrusions to make a 32-cell extrusion assembly. These assemblies are then trimmed to a common length and abraded on their ends to prepare them for gluing. An assembly table, shown in Figure 13.39, is 16 m long and 2 m wide. The width of the table top is divided in half so that it can swing from a horizontal to a vertical orientation. This allows the glue to be applied horizontally along the edge of one of the extrusions. Then the table top on which this extrusion is attached is swung up so that the two extrusions can be pushed together. The table has fittings to align the two extrusions to better than 0.3 mm and hold them in place. It also has clamps to push the extrusions together and hold them while the structural adhesive cures sufficiently. Four assembly tables are used in parallel.

Fig. 13.38: Commercially available free-standing crane of the type to be used in the module assembly.

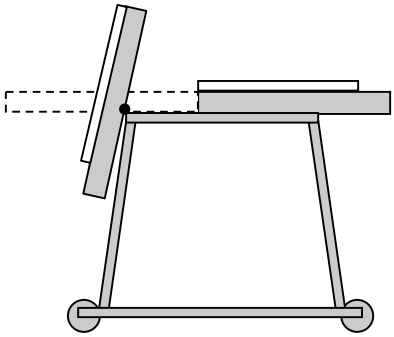

Fig. 13.39: Table used to glue two 16-cell extrusions into a 32-cell extrusion assembly. The 2 extrusions are shown in white on the drawing.

The extrusion assemblies are then craned to racks that each hold 8 extrusion assemblies. A gluing rack is shown in Figure 13.40. The side and center seals are glued into cells 1, 32, 16, and 17 on both ends of the extrusion. The bottom fiber raceway and the lower part of the manifold snout are also glued to the manifold end of the extrusion. These operations are shown in detail in Figures 13.41 – 13.43. This glue is the 3M2216 epoxy. These extrusions then sit overnight for the glue to cure. A detailed breakdown of the labor required for these 30 modules on their first day in the factory is given in Tables 13.1 – 13.7.

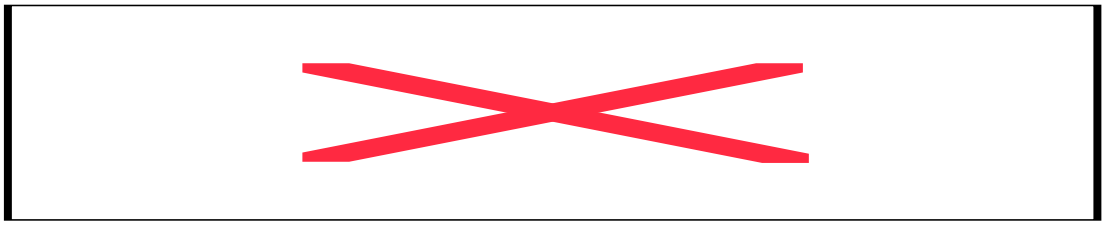

Table 13.1: Manifold preassembly labor. This can be done anytime before the parts are needed.

	Min/Module	People	
Move air caster halves into truck & connect to pallets	0.5	3	Estimate
Float load on aircasters	0.3	3	Estimate
Pull load off truck into receiving area	0.7	3	Estimate
Lower load off aircasters	0.2	3	Estimate
Total Time/ Module	**1.7**		
Total Labor/ Module	**5.1**		

Table 13.2: Labor to unload 60 raw 16-cell extrusions from the truck. Time for the operation is estimated to be 51 minutes for 3 people to unload 60 extrusions. Note that a module is built from 2 extrusions.

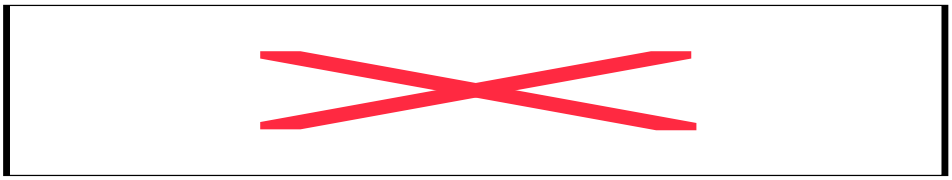

Table 13.3: Labor to distribute the extrusions from the incoming stacks to the extrusion assembly tables. Two cranes are used at the same time.

	Min/Module	People	
Lower one side of gluing table	0.5	1	Measured
Apply structural adhesive to edge of tilted extrusion	7	1	Measured
Raise the side of gluing table, latching it in the flat position	0.5	1	Measured
Clamp modules together	0.5	1	Measured
Allow glue to cure	15	0	
Total Time/ Module	**23.5**		
Total Labor/ Module	**8.5**		

Table13.4: Labor to glue 2 extrusions to make one extrusion assembly. Four assembly tables are used at the same time.

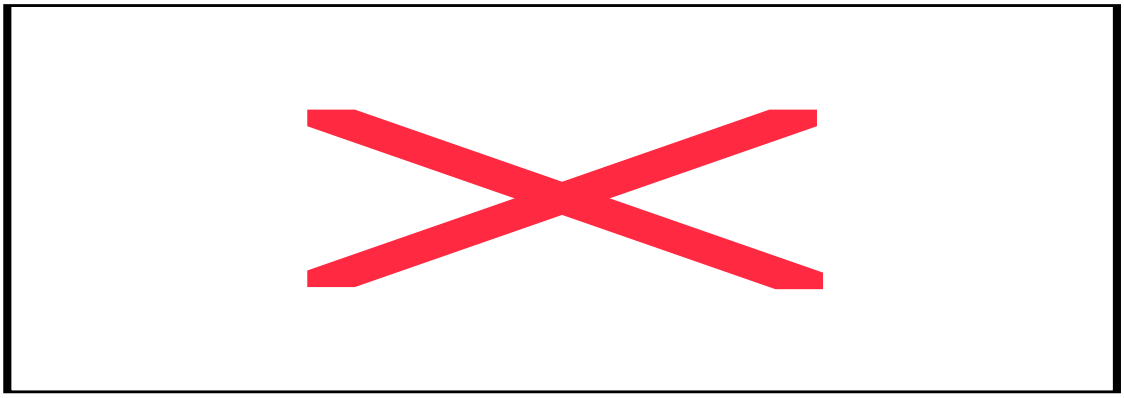

Table13.5: Assembly steps to trim and abrade the extrusion assembly. Four assembly tables are used at the same time.

	Min/Module	People	
Move 30 modules from stacks onto 4 gluing platforms.	4	2	Estimate
Total Time/ Module	**4**		
Total Labor/ Module	**8.0**		

Table 13.6: Labor to distribute the extrusions from the incoming stacks to the gluing platforms.

	Min/Module	People	
Place side seals & center seals in cells.	11	1	Measured
Snap the lower fiber raceway into the center & side seals.	1	1	Measured
Inject glue into the seals to make a leak-tight joint	2	1	Measured
Clean up runoff glue	1	1	Measured
Glue the manifold snout lower half to the extrusion assembly.	4	1	Measured
Glue cures overnight.	0	0	
Total Time/ Module	**19.0**		
Total Labor/ Module	**19.0**		

Table 13.7: Assembly steps for the side and center seals, the lower fiber raceway, and snout lower half.

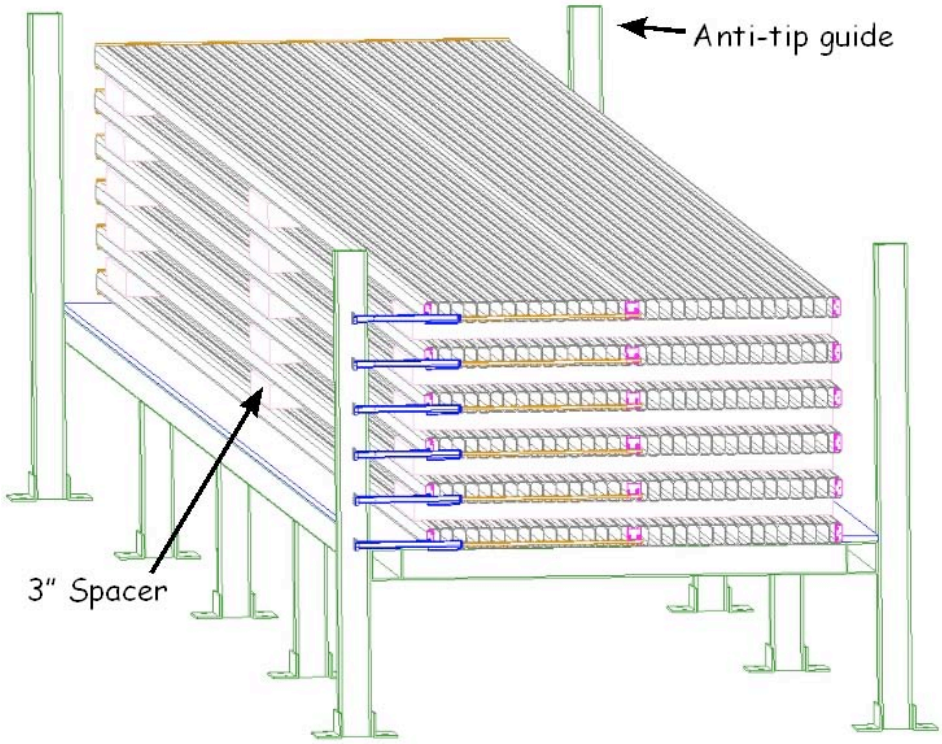

Fig. 13.40: Gluing rack for 8 modules. The center and side seals are glued into each end, as is the lower fiber raceway and the lower half of the manifold snout assembly.

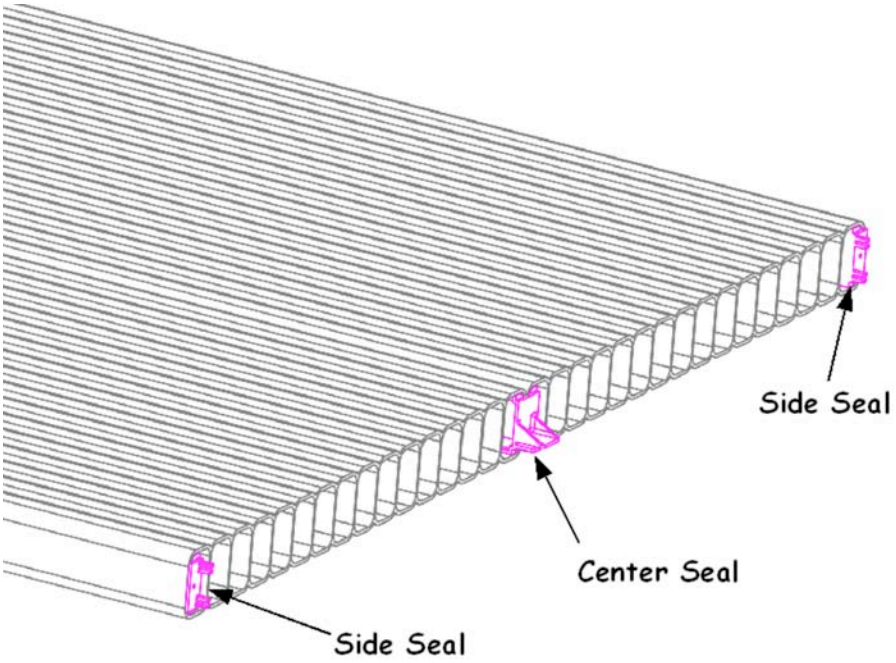

Fig. 13.41: Assembly of side and center seals in the extrusion.

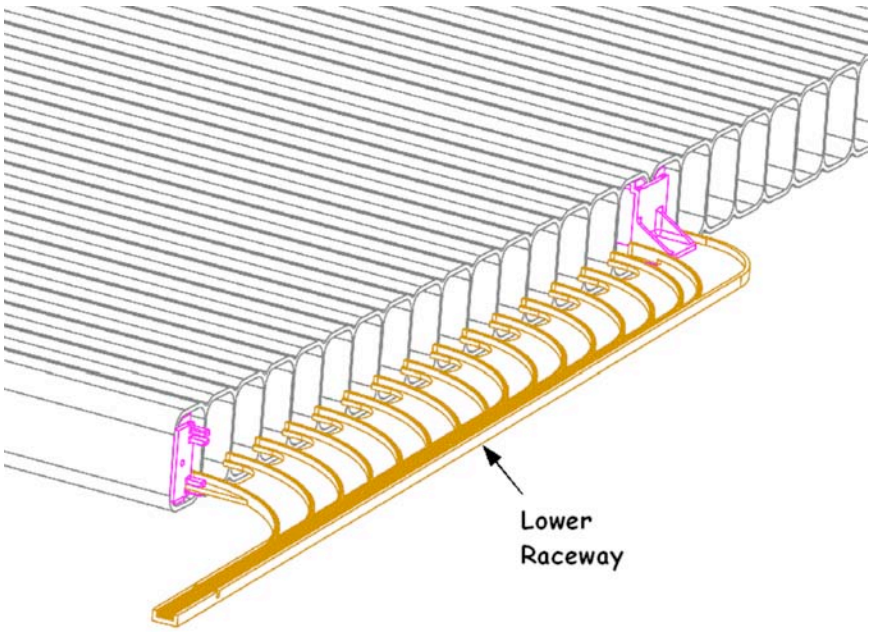

Fig. 13.42: Attachment of the lower fiber raceway to the module. This part snaps onto the center and side seals and references the center of the extrusion assembly through its connection to the center seal.

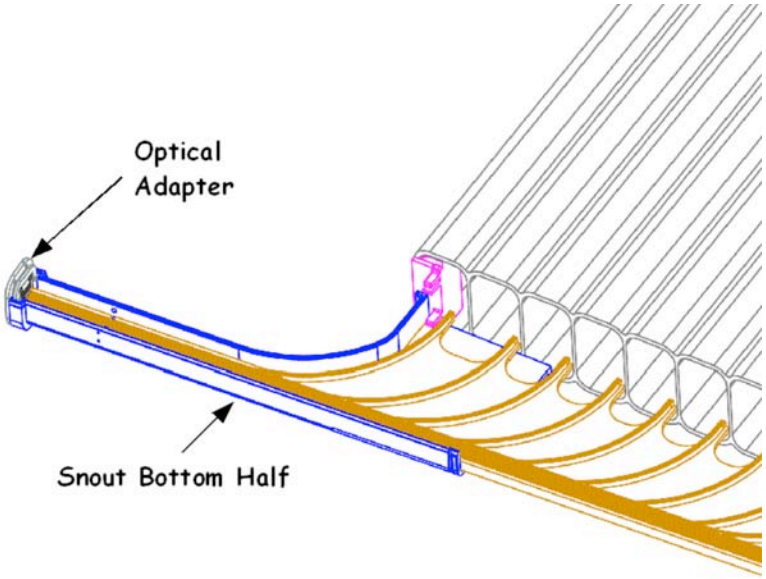

Fig. 13.43: Placement of the snout lower half on the module. The lower fiber raceway locates this part relative to the center of the extrusion assembly. The optical adapter has been preassembled on the snout lower half.

13.4.4.2 Module Factory Flow Day 2

The flow of modules through the factory on their second day is illustrated by the blue arrow in Figure 13.25. The 30 extrusions that have cured on the 4 gluing racks overnight are now each craned on to a rolling table and that table is rolled to the worktable area. These modules replace those which are in their third day of assembly and have been brought to the crane coverage area for pressure testing of the inner glue seal, as shown by the green arrow in Figure 13.25.

In the work table area, the modules will have fibers strung into each cell, the fibers threaded through the manifold into the optical connector, the fibers glued into the optical connector, and the end-plate and manifold glued into place. Six separate crews string and thread the modules using six stringing machines. The fiber stringing proceeds in groups of 8 cells. Once 8 cells are strung by one person, a second person threads these fibers through the raceway and into the optical connector. Meanwhile the first person strings the next 8 cells. A third person on each crew detaches the vacuum adapter and fiber-puller assembly and glues the end-plate and manifold parts. These operations are shown in detail in Figures 13.44 – 13.54. The optical connector has been described in section 13.3.5. The glue used during this day is the 3M2216 epoxy. These extrusions then sit overnight for the glue to cure.

As in day 1, most of the assembly is done by human hands. However, stringing the looped fiber rapidly down an extrusion cell without putting undue stress on the fiber requires the semi-automated machine described in section 13.3.4. A semi-automated glue dispenser assures the correct epoxy mixing and flow rate. A detailed breakdown of the labor required for these 30 modules on their second day in the factory is given in Tables 13.8 – 13.12.

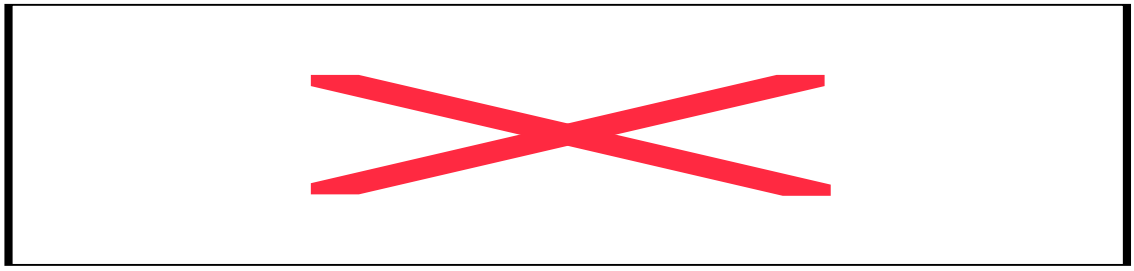

Table 13.8: Distribution of the extrusions from the gluing platforms to the work tables. The factory has 30 work tables operating at the same time.

	Min/Module	People	
Position stringing machine at extrusion.	2	1	Estimate
Place shield tray over raceway of first eight cells	0.25	1	Estimate
Attach vacuum connector to other end of the extrusion	1	1	Estimate
Mount new spool of fiber on stringing machine if necessary	2	1	Estimate
String fiber for 1 cell: enter cell number, thread correct fiber length onto doubling wheel, attach retaining ring and parachute to fiber, pull parachute to cell, activate vacuum, cut fiber to correct length when strung.	1	1	Measured
String fiber for next 7 cells.	7	1	Measured
String fiber for next 3 sets of 8 cells	24	1	Measured
Remove vacuum fitting and parachutes for the module	6	1	Estimate
Total Time/Module	**43.3**		
Total Labor/ Module	**43.3**		

Table 13.9.: Stringing of fibers through the module cells. Six stringing machines are operating at the same time.

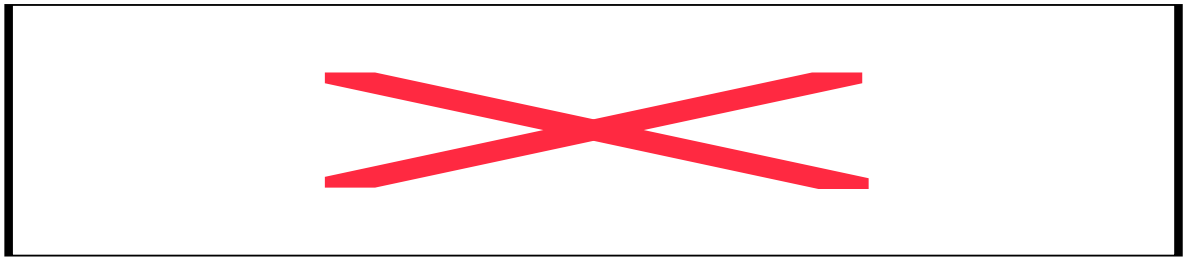

Table 13.10: Threading of fibers through fiber raceway and manifold snout into the optical connector. Threading is occurring at 6 work tables at the same time.

	Min/Module	People	
Glue end plate to the extrusion with butt joint	11	1	Measured
Glue upper half of snout to extrusion, butt joint	2	1	Measured
Attach fill distribution tube.	3	1	Estimate
Glue mannifold cover to extrusion, butt joint	11	1	Measured
Inject manifold cover/snout joint with glue	4	1	Estimate
Glue cures overnight	0	0	
Total Time/Module	**31.0**		
Total Labor/Module	**31.0**		

Table 13.11: Gluing of end-plate and manifold parts with 3M2216 epoxy.

Table 13.12: Gluing of fibers into the optical connector with 3M2216 epoxy.

Fig. 13.44: Rolling a work table with an extrusion assembly.

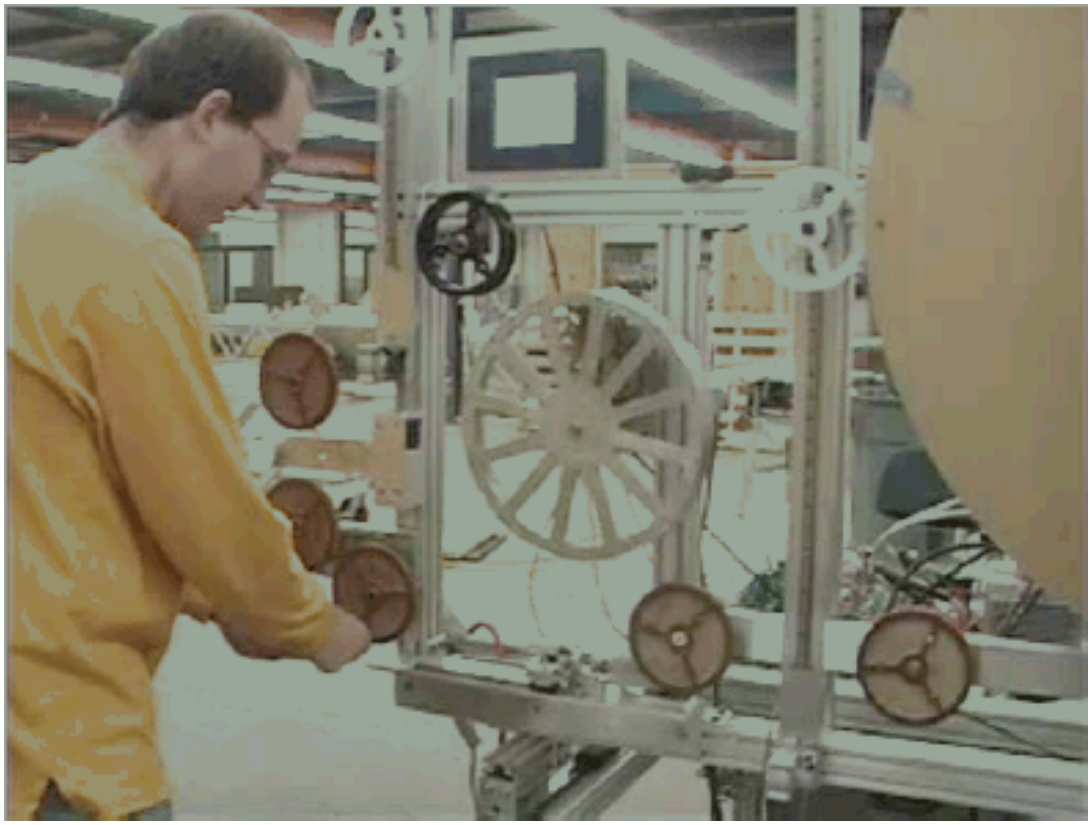

Fig. 13.45: Stringing machine operator preparing a fiber.

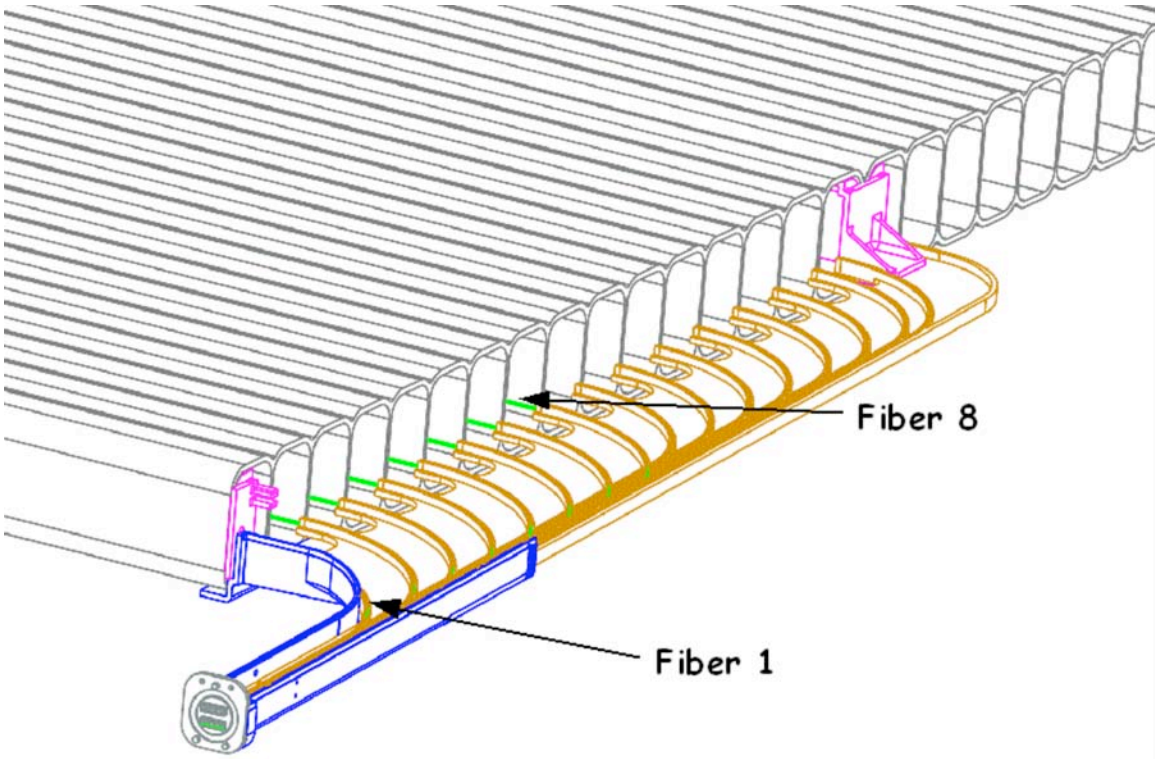

Fig. 13.46: Fibers 1-8 are strung down the cells and threaded through the lower raceway and snout.

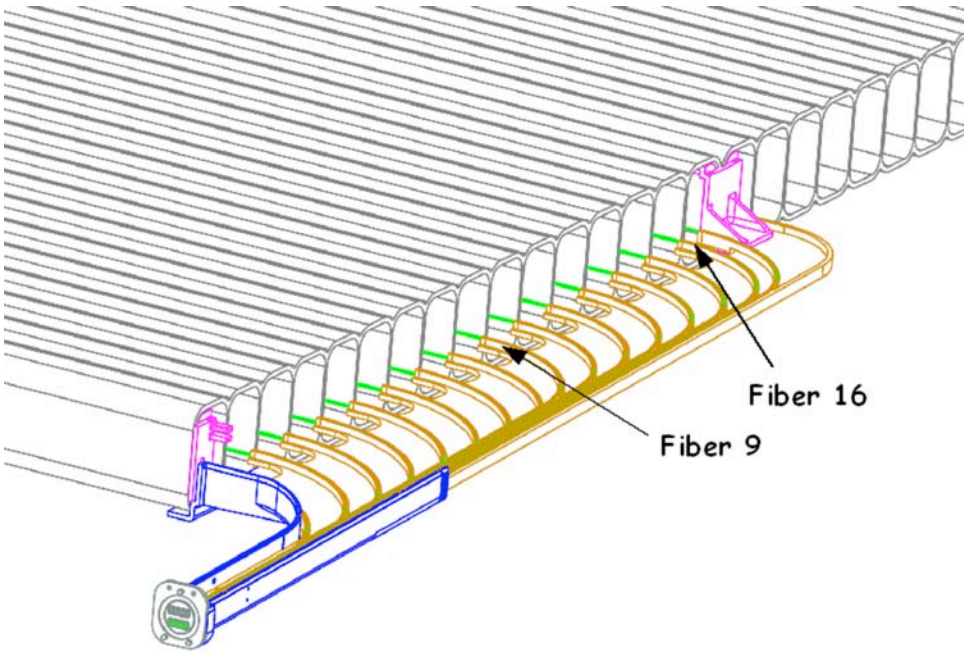

Fig. 13.47: Fibers 9 -16 are strung down the cells and threaded through the raceway and snout.

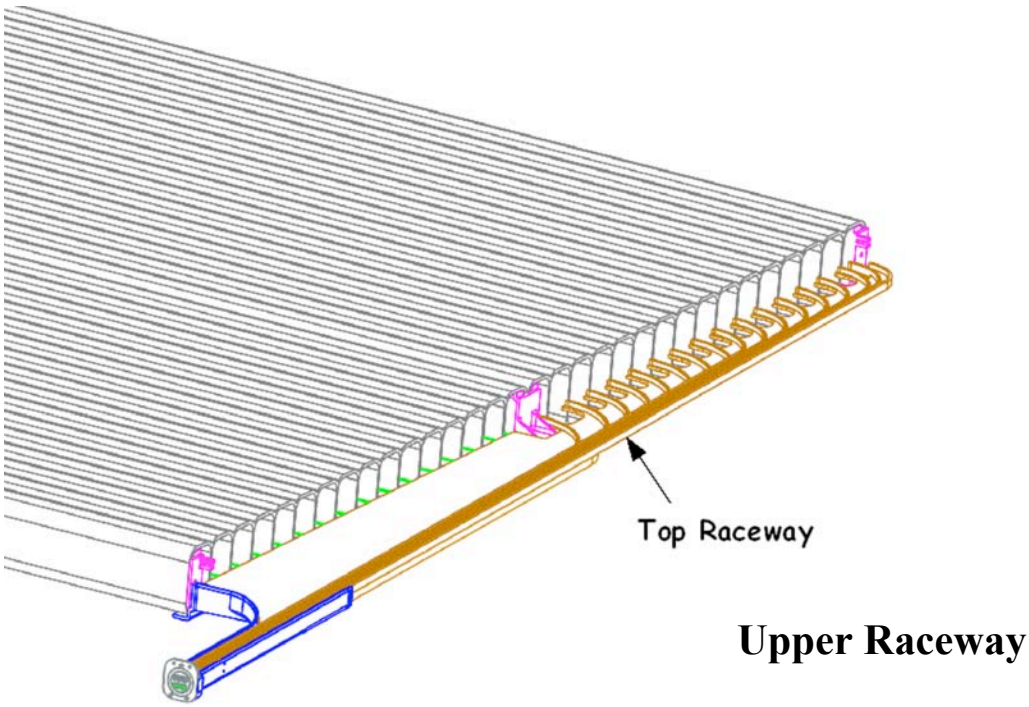

Fig. 13.48: The upper raceway is snapped in place over fibers 1-16 covering the lower raceway.

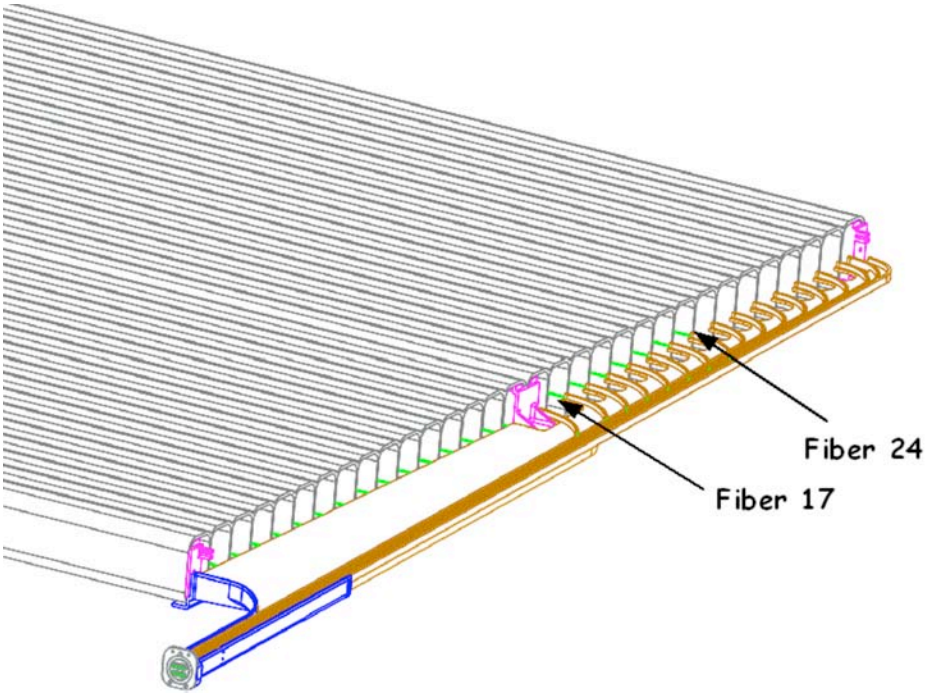

Fig. 13.49: Fibers 17-24 are strung down the cells and threaded through the upper raceway and snout.

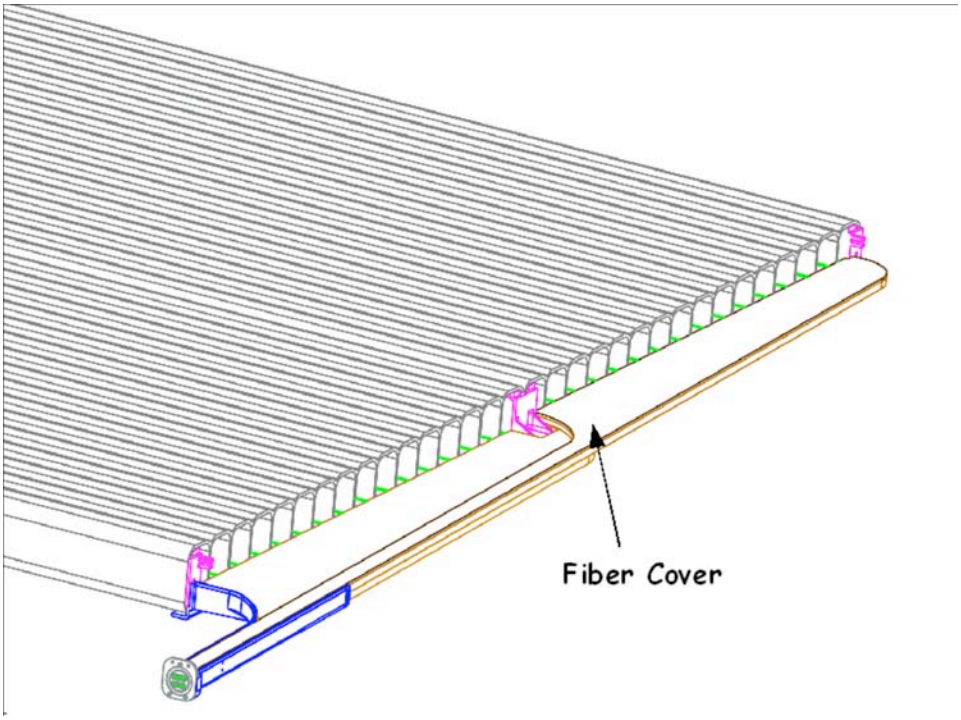

Fig. 13.50: Fiber cover is snapped in place over fibers 17-32 after the last 8 are strung.

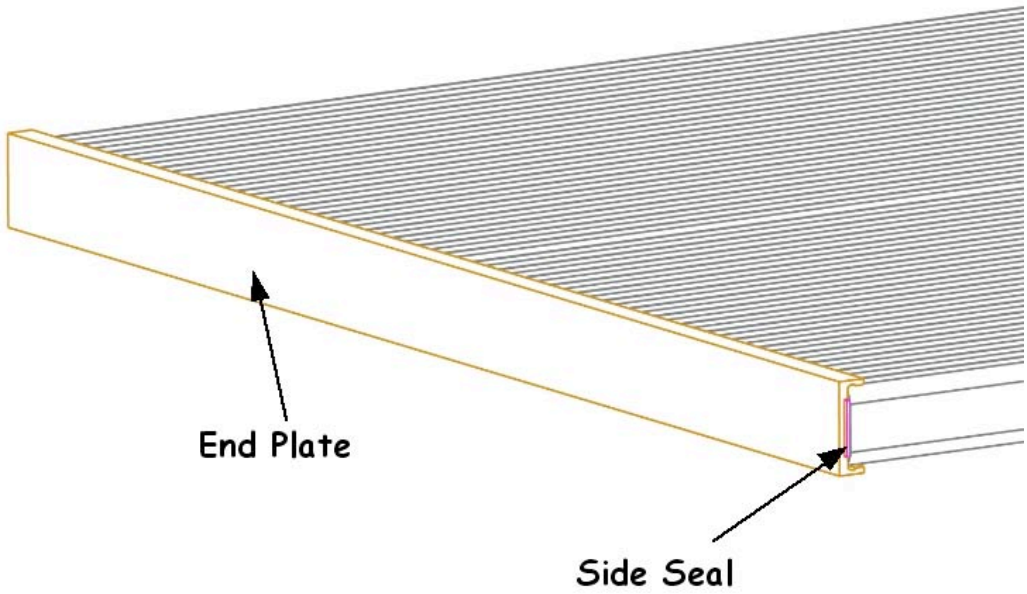

Fig. 13.51. End-plate is glued to the extrusion.

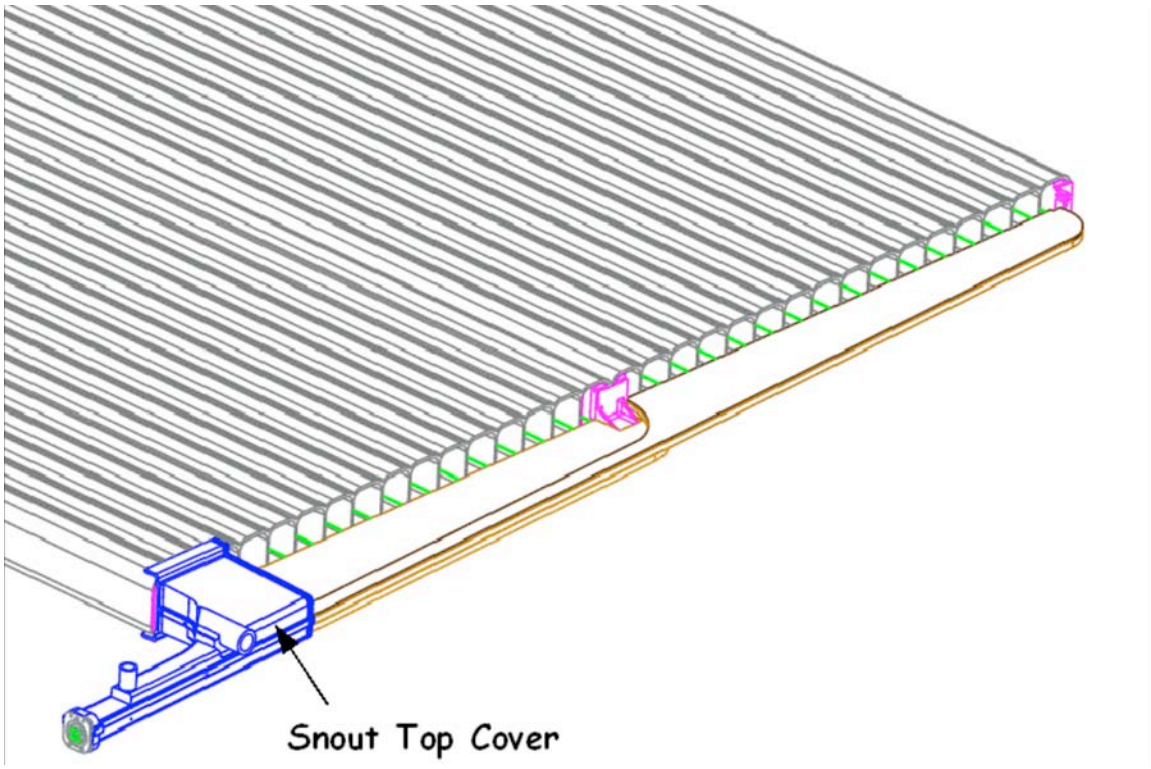

Fig. 13.52.: Glue snout top cover to the module.

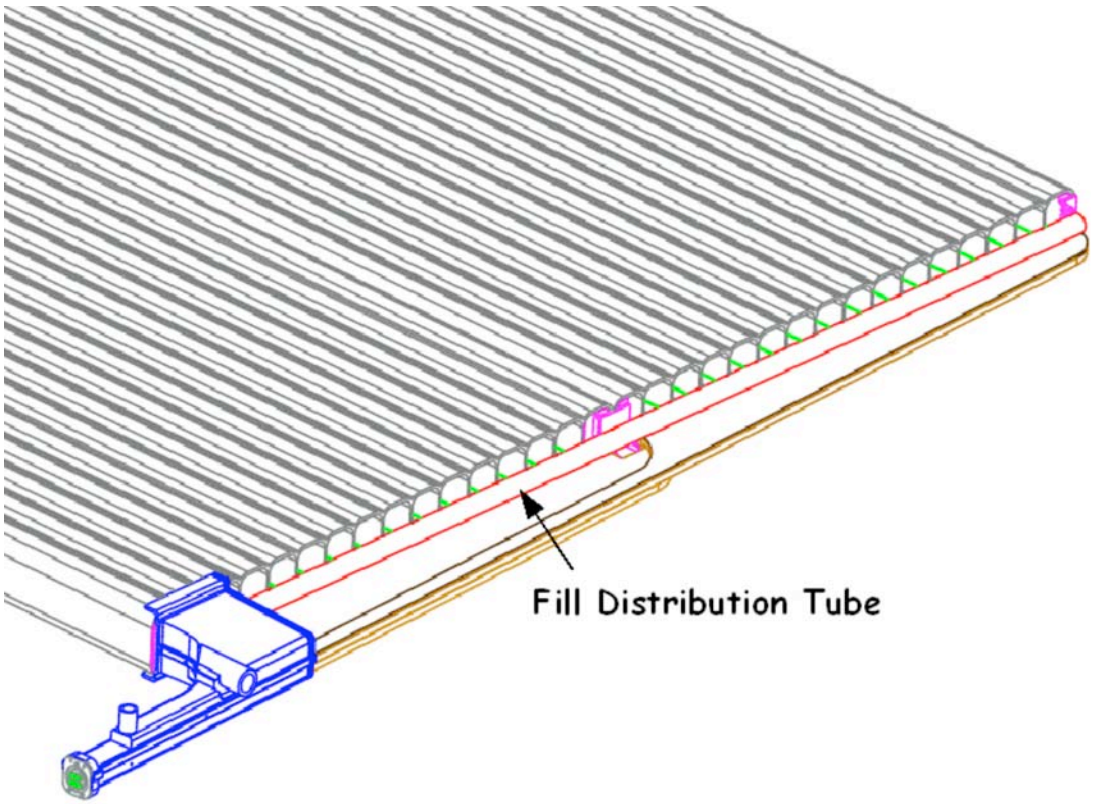

Fig. 13.53: Attach the fill distribution tube to the module.

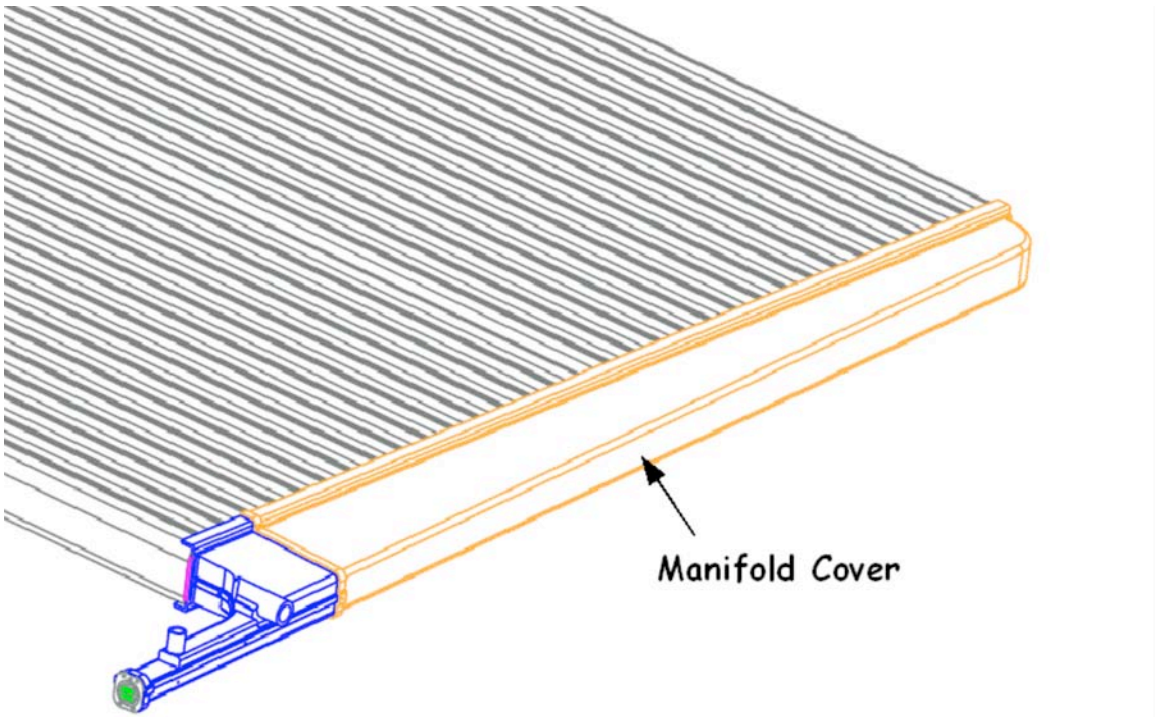

Fig. 13.54.: Glue manifold cover to the extrusion and snout.

13.4.4.3 Module Factory Flow Day 3

The chemically inert epoxy has cured overnight. The modules are now moved to the leak test area and attached to the testing machine. This leak test will last for approximately 12 hours. A detailed breakdown of the labor required for these 30 modules on their fourth day in the factory is given in Tables 13.13 and 13.14.

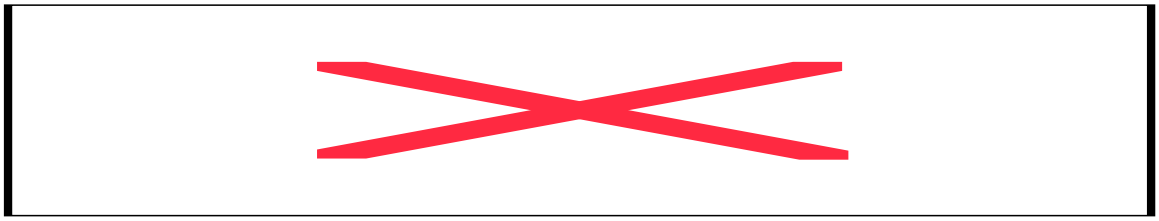

Table 13.13: Transfer of the modules to the leak testing stack.

	Min/Module	People	
Leak tester is connected to all modules in the stack and scan each bar code	0.5	1	Estimate
Place safety shield around the module stack	0.2	1	Estimate
Presurize modules to 10 PSI and begin test.	0.3	1	Measured
Run automated leak test overnight		0	
Total Time/Module	**1.0**		
Total Labor/Module	**1.0**		

Table 13.14: Setting up and executing the inner seal leak test. 30 modules are leak tested at the same time.

13.4.4.4 Module Factory Flow Day 4

The flow of modules through the factory on their fourth day is illustrated by the orange and yellow arrow in Figure 13.25. The 30 extrusions have had their inner seal leak tested. Now all of the external parts of the glue joints of both the manifold and the end-plate are reinforced with structural adhesive. As soon as the structural adhesive has cured enough for handling, the optical connectors are flycut and the fibers are tested for optical transmission. Any module with a damaged fiber will be rejected, a situation we expect to occur very infrequently. Rejected modules are replaced with good ones from storage. Following this testing, the modules are rolled to the crane area and assembled into a shipping stack of 24 modules. Six modules are used to build the next shipping stack. When the day's stack is completed, it is leak tested at 20 psi for approximately 12 hours.

A detailed breakdown of the labor required for these 30 modules on their fourth day in the factory is given in Tables 13.15 – 13.21. Flycutting is shown in Figure 13.55.

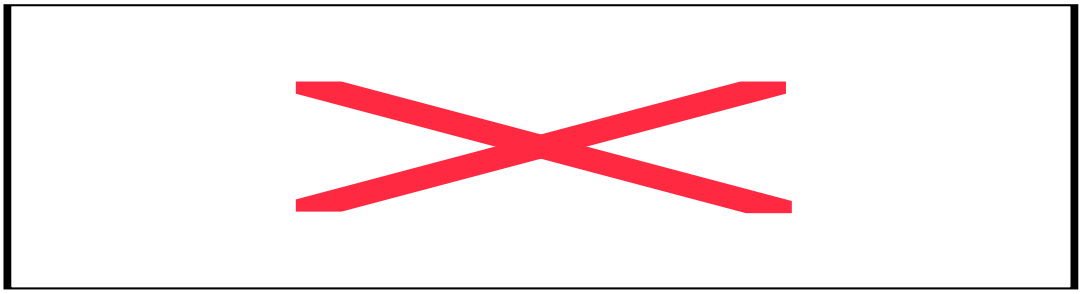

Table 13.15: Modules are disconnected from the inner seal leak test.

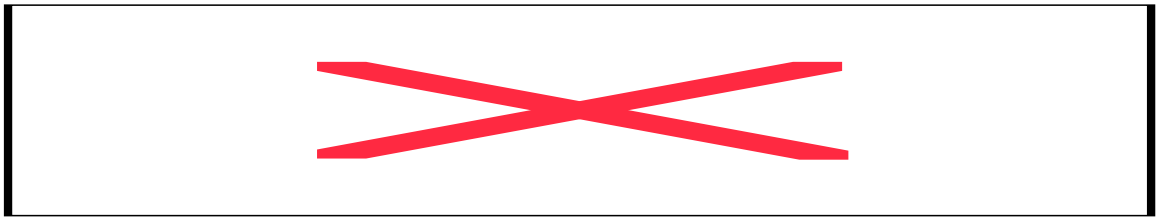

Table 13.16: Transfer of the modules from the leak testing stack to work tables.

	Min/Module	People	
Glue end plate and add fiberglass mesh reinforcement	6.5	1	Measured
Glue mannifold cover to extrusion	6.5	1	Measured
Glue manifold cover/snout joint	3	1	Measured
Glue edge stiffeners (2 edges/vertical plane)	0.33	1	Estimate
Structural adhesive cures	12	0	
Total Time/Module	**28.3**		
Total Labor/Module	**16.3**		

Table 13. 17: Add structural glue to strengthen joints. Edge stiffeners are only glued on 2 edges out of every 24 modules (vertical planes only).

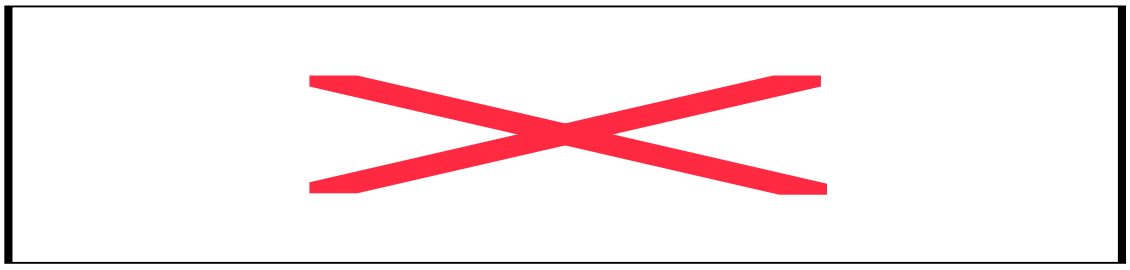

Table 13.18: Flycut the optical connector.

	Min/Module	People	
Connect fiber tester to optical connector and scan bar code	5	1	Measured
Start the fiber test program	0.5	1	Measured
Fiber tester program runs	0.2	1	Measured
Total Time/Module	**5.7**		
Total Labor/Module	**5.7**		

Table 13.19: Test for fiber damage.

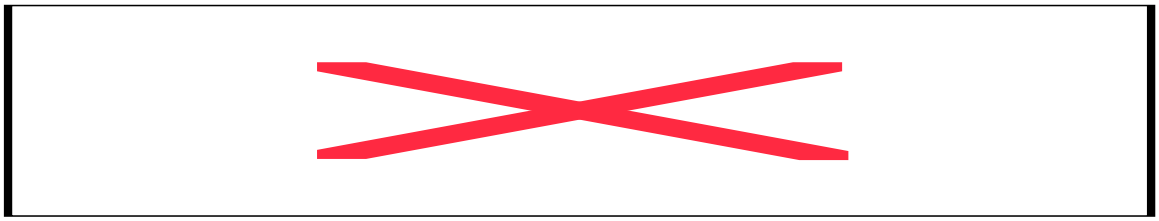

Table 13.20: Transfer of the modules to the shipping stack.

	Min/Module	People	
Leak tester is connected to all modules in the stack and scan each bar code	0.5	1	Estimate
Place safety shield around the module stack	0.2	1	Estimate
Presurize modules to 20 PSI and begin test.	0.3	1	Measured
Run automated leak test overnight		0	
Total Time/Module	**1.0**		
Total Labor/Module	**1.0**		

Table 13.21: Setting up and executing the final leak test. 30 modules are leak tested at the same time.

Fig. 13.55. Flycutting an optical connector.

13.4.4.5 Module Factory Flow Day 5

When the overnight leak testing is completed, the results are checked to make sure there are no leaks. This procedure is given in section 13.4.3.2. In the rare instance that a leak is found, the module with the leak is removed from the stack and replaced with a good one from storage. A stack of 24 modules is then packaged for shipping and loaded on a truck. The additional 6 modules begin the next shipping stack.

A detailed breakdown of the labor required for these 30 modules on their fifth day in the factory, assuming no leaks are found, is given in Tables 13.22 and 13.23.

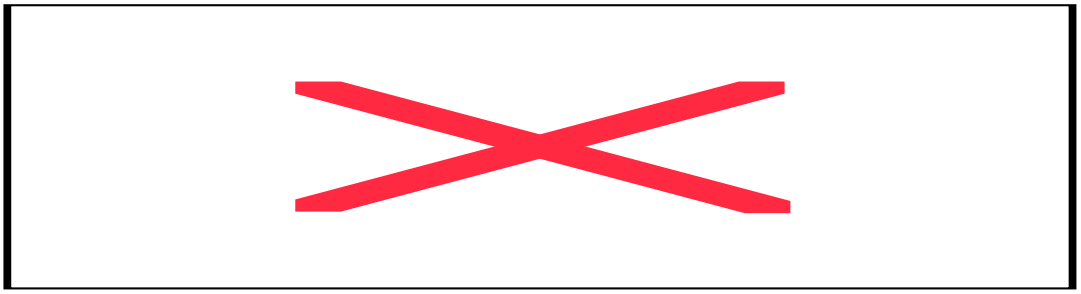

Table 13.22: Disconnecting the modules from the final leak test.

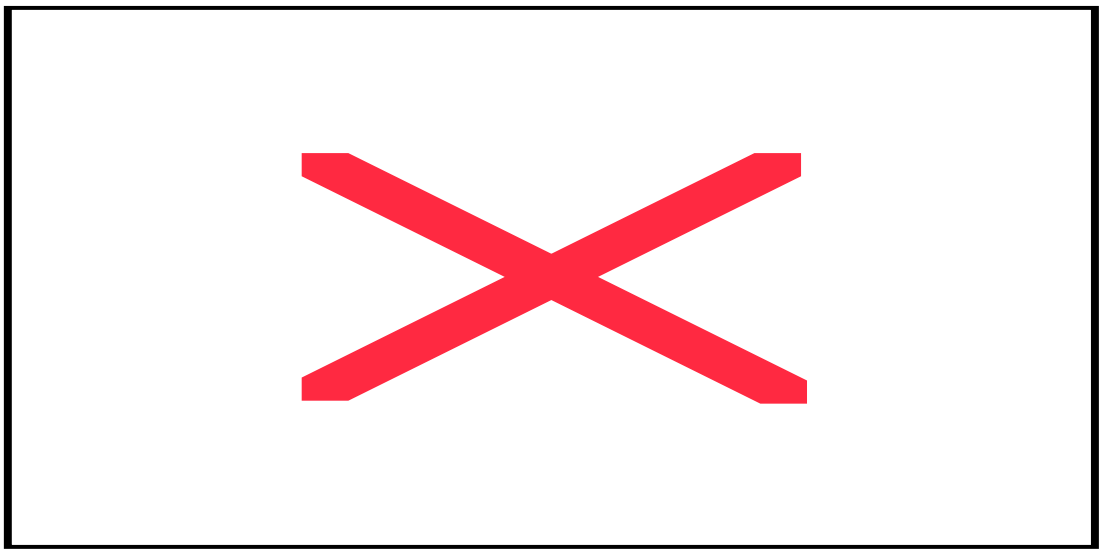

Table 13.23: Packaging and loading of completed modules.

13.5 Changes in the Module and Factory Designs Since the CDR

The primary change since the CDR is a revision of the factory model. In the CDR there were 3 factories that all did the same assembly tasks. There is now 1 factory that receives 16-cell extrusions and produces 32-cell detector modules.

Other minor changes involve improvements in the engineering of the parts that make up the modules. These changes are motivated by the cost improvements gained by injection molding and the impact of time-and-motion studies on the design. The factory also conducts an additional leak test that tests only the inner seal before applying structural glue and performing the final leak test at a higher pressure.

13.6 Work Remaining to Complete the Module and Factory Designs

Production of the integration prototype and purchase of a floor-mounted crane for time-and-motion studies may cause some factory procedure and module design modifications to optimize the cost.

Testing of modules under severe stress and further aging continues to determine if any modification is needed to either handling or gluing procedures.

Value engineering on both the module design and the factory procedures continues in order to investigate ways of reducing cost or increasing performance.

14 Photodetector and Electronics

14.1 Introduction

The NOνA photodetector is an avalanche photodiode (APD) operated at a gain of 100, cooled to -15˚C by a thermoelectric cooler (TEC), and readout via a Front-End Board (FEB). The FEB has a low noise, <200e^- custom ASIC amplifier matched to the APD. Over 12,000 APD / TEC / FEB assemblies are required for the NOνA Far Detector.

14.2 Technical Design Criteria

The readout of the NOνA Far Detector has two distinct tasks: (1) read out events caused by neutrinos from the NuMI beamline at Fermilab and (2) operate between spills to collect cosmic ray events for calibration and monitoring. The readout will operate in a triggerless mode to accomplish both tasks seamlessly.

The NOνA Near Detector uses similar electronics but must satisfy different constraints. The mean signal from the far end is approximately 4 times greater for the shorter modules, and there will be multiple neutrino induced events in the detector during the NuMI spill. A modified version of the basic Far Detector design that samples each channel more frequently is required.

A time-stamp generated from the kicker fire, signal $74, from the NuMI beam line will be used to determine which events occur during the 11.1 μs single turn extraction of the Main Injector protons onto the NuMI target. The actual length of time the protons will hit the target will be 6/7 of this, or 9.5μs.

14.3 Avalanche Photodiodes (APDs)

The photodetector for NOνA is an avalanche photodiode (APD), shown in Figure 14.1. The APDs are packaged in arrays of 32 pixels and mounted on a carrier board substrate using flip-chip mounting. This device has been custom made for NOνA to optimize the fit of two fiber ends on a single pixel. The 32 pixels map directly onto the 32 cells of a single PVC extrusion module. Table 14.1 summarizes the key parameters for the NOνA APDs.

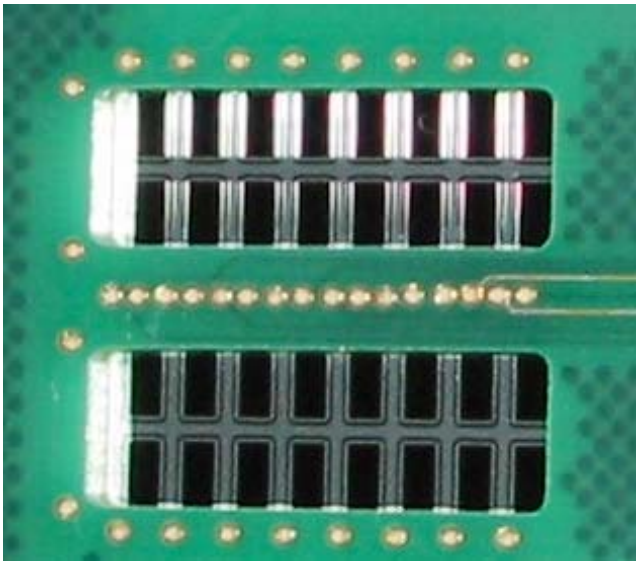

Fig. 14.1: Prototype NOνA APD mounted on carrier board.

Manufacturer	Hamamatsu
Pixel Active Area	1.95 mm _ 1.0 mm
Pixel Pitch	2.65 mm
Array Size	32 pixels
Die Size	15.34mm _ 13.64mm
Quantum Efficiency (>525 nm)	85%
Pixel Capacitance	10 pF
Bulk Dark Current (I_B) at 25 C	<50pA
Bulk Dark Current (I_B) at -15 C	<2.5 pA
Peak Sensitivity	600 nm
Operating Voltage	375 ± 50 volts
Gain at Operating Voltage	100
Operating Temperature (with Thermo-Electric Cooler)	-15°C
Expected Signal-to-Noise Ratio (Muon at Far End of Cell)	10:1
APD channels per plane	384
APD arrays per plane	12
Total number of planes	1003
Total Number of APD arrays	12,036
APD pixels total	385,152

Table 14.1: Avalanche Photodiode parameters.

The general structure of an APD is shown in Figure 14.2. Light is absorbed in the collection region, electron-hole pairs are generated and, under the influence of the applied electric field, electrons propagate to the p-n junction. At the junction, the electric field is sufficiently high that avalanche multiplication of the electrons occurs. The multiplication of the current is determined by the electric field at the junction and by the mean-free-path of electrons between ionizing collisions, which depends on both the accelerating field and on the temperature. This temperature dependence occurs because the probability of electron-phonon scattering, which competes with the avalanche multiplication process, increases with temperature.

One of the operational characteristics of APDs, and, in fact, all silicon devices, is the thermal generation of electron-hole pairs which mimic the signal. Since the current from the positive carriers is amplified about fifty times less than the negative carrier current at the junction, only the current from electrons generated in the photo-conversion region (I_B), or the bulk current, needs to be considered in the noise current estimation. As it is a thermally generated current, it can be reduced by lowering the operating temperature of the APD. We will operate the APDs in the NOνA detector at -15° C to keep the noise contribution from I_B small in comparison to the front-end noise. This choice is based on measurements obtained with prototype readouts.

The amplification mechanism in the APD is itself subject to noise, characterized by the excess noise factor F, with such factors as device non-uniformities and the ratio of the positive to negative impact ionization coefficients contributing. This factor is well modeled and has been included in our signal to noise calculations.

APDs have two substantial advantages over other photodetectors: high quantum efficiency, and uniform spectral quantum efficiency. The high APD quantum efficiency enables the use of very long scintillator modules, thus significantly reducing the electronics channel count. In the wavelength region relevant to the output of the wavelength shifting (WLS) fibers, 500 to 550 nm, the APD quantum efficiency is 85%. See Figure 14.3.

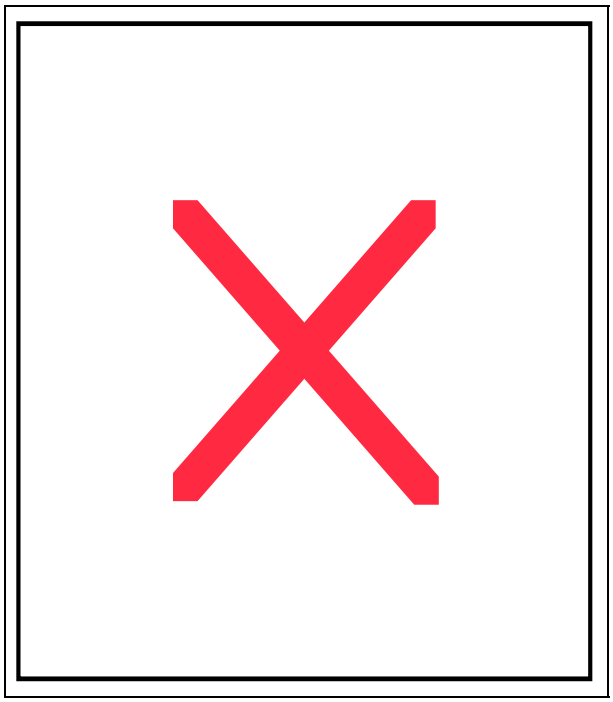

Fig. 14.2: The basic structure of a blue/green sensitive APD. Light crosses the anti-reflection coating at the surface and is absorbed in the collection region. Photoelectrons drift in the electric field to the junction where they undergo avalanche multiplication.

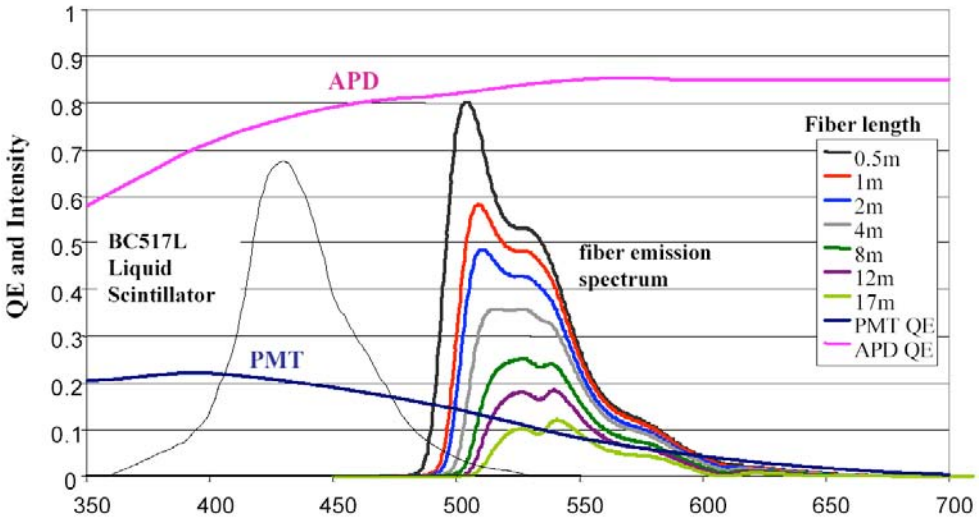

Fig. 14.3: WLS fiber emission spectra measured at lengths of 0.5, 1, 2, 4, 8, 16 m, respectively illustrating the shift of the average detected wavelength as fiber length increases. Also shown are the quantum efficiencies of APDs and PMTs (bialkali photocathode).

Hamamatsu is the only known vendor for APD pixel arrays. Hamamatsu markets a 32-pixel packaged APD with a pixel size of 1.6 mm by 1.6 mm. To maximize light output, NOvA utilizes a looped or U-shaped WLS fiber. Both ends of the looped fiber terminate on the same APD pixel. To comfortably accommodate both fiber ends, Hamamatsu has modified the pixel size and shape to match our requirements. Prototypes of the modified APDs have been provided bump bonded to an APD carrier circuit board. These devices are being tested as part of our

qualification process for the final design. Results of qualification tests for gain and bulk dark current (dark current divided by gain) are shown in Figures 14.4 and 14.5. These channels performed well.

For initial evaluation we also purchased a number of Hamamatsu S8550, packaged APD arrays. The dark currents were consistent with expectations, and the gains were uniform from pixel to pixel on the same chip and within individual pixels. The measured pixel separation for one of the sample arrays is shown in Figure 14.6. The fall-off on the pixel edges reflects the finite spot size used to illuminate the APD pixels.

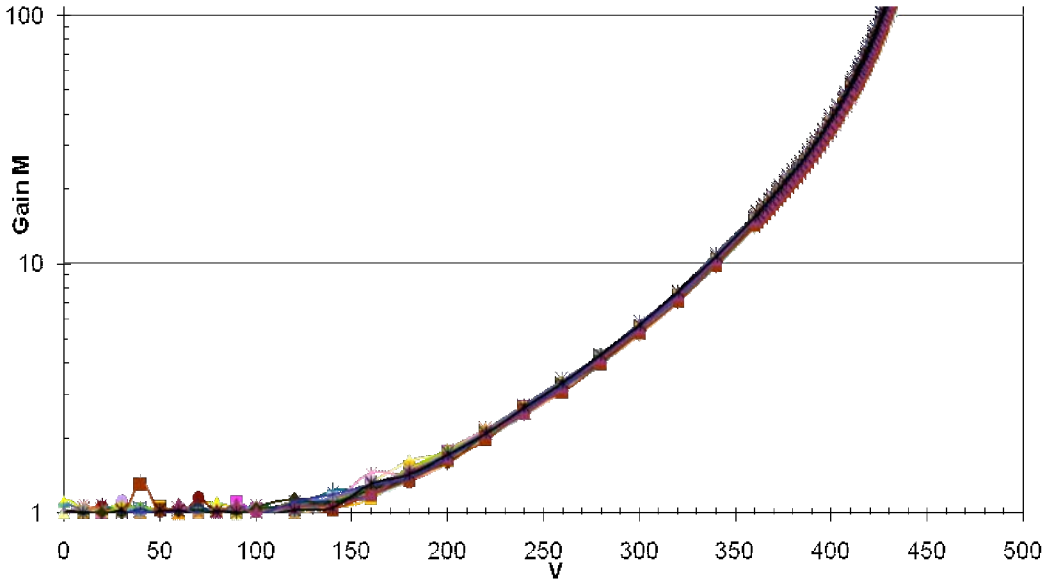

Fig. 14.4: Gain vs. applied voltage at Room Temp for 32 channels of a Hamamatsu NOvA prototype APD array.

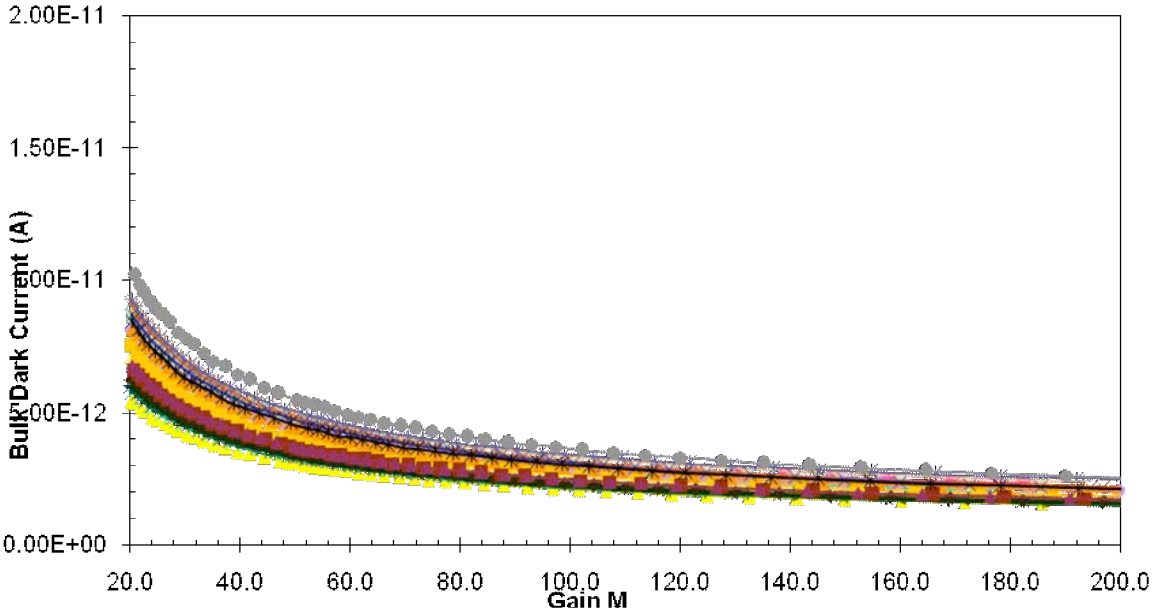

Fig. 14.5: Bulk Dark Current vs. gain for 32 channels of a prototype APD array measured at room temperature. Cooling to -15C will decrease the current by a factor of at least 20.

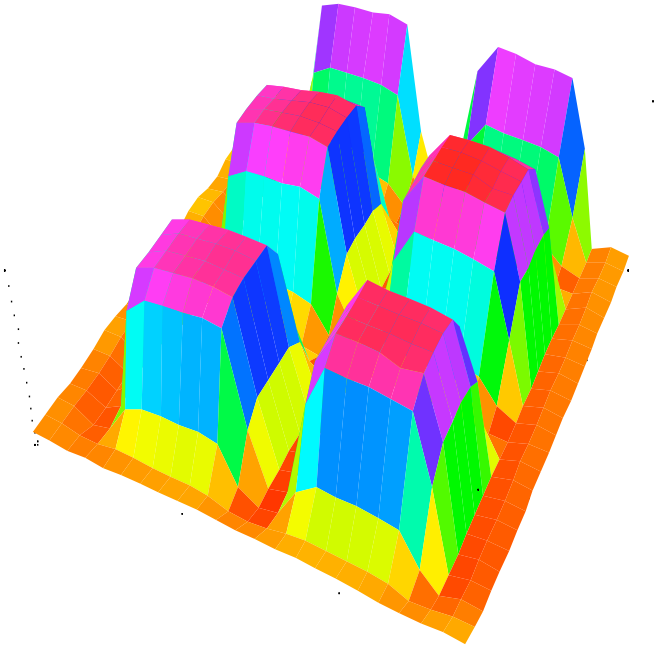

Fig. 14.6: Fine point scan across part of a Hamamatsu S8550 APD array. The fall-off on the pixel edges reflects the finite spot size used to illuminate the APD pixels.

One of the attractive features of APDs is that once they have been calibrated, the gain can be easily determined from the applied bias voltage and the operating temperature. In the NOvA detector, we will maintain the operating bias to a precision of 0.2 Volts and control the temperature to 0.5° C and thus hold the gain stability to about 3%, consistent with the pixel-to-pixel variation. The absolute calibration of temperature and voltage are not critical for the

experiment, only the gain. The NOvA APDs will typically operate between 350V - 450V at a standing current of approximately 1 nA per 32-channel APD array. The high voltage system is described in Section 14.10.

14.4 Carrier Boards

The APD arrays will be mounted on a separate APD carrier board that is environmentally isolated from the other electronic components to minimize the thermal load. The mounting will be done with flip-chip technology, so the active area of the APD will face rectangular slots cut out of the PC board where the fibers will terminate. The back of the APD is protected and stiffened by a ceramic backer as shown in Figure 14.7. The flip-chip method provides an accurate means of aligning the APD to the PC board to which the fiber connector will also be aligned. The fiber connector must accurately align the fibers both longitudinally and transversely to the APD pixels.

One of the operating requirements for the APDs is that they be kept dry. Dew-point concerns associated with the low operating temperature of the TE coolers have led us to a design where the APD and TE cooler are enclosed in a sealed environment, kept dry with silica gel as in computer disk drives.

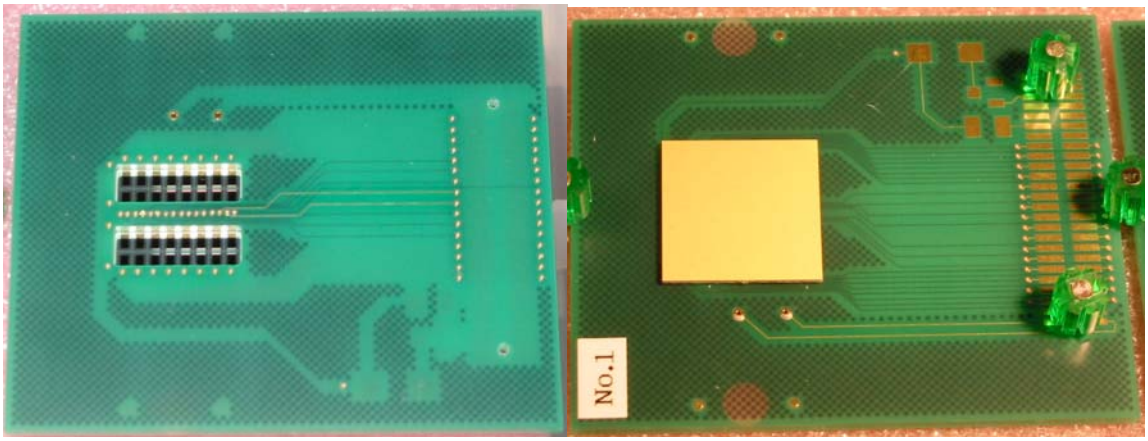

Fig. 14.7: Front and back views of an APD array mounted to a carrier board.

14.5 APD Module

The APD arrays mounted on the carrier will be integrated into a housing, and the device will be called the APD Module. The requirements on the mechanical housing for the APD arrays and associated systems required to operate the APD's are enumerated. This includes the requirements on the (1) structural, (2) thermal, (3) environmental, (4) optical and (5) electrical couplings/interfaces that must be provided by the APD module system.

The APD module provides an optical interface between a single 32-cell scintillator detector module and a 32-channel Avalanche Photodiode array, which is used to convert the optical signals from the detector module to electronic signals. The APD module thus also provides an interface to the Front End Board (FEB).

In addition to the interfaces mentioned above, the APD module must provide the means to operate the APD array in a robust and problem-free manner. A stable bias voltage must be supplied. Control and readback of APD array temperature must be provided. Exposure to light and moisture must be avoided during operation of the APD module. Ease of assembly and disassembly must be considered.

Consequently, the APD module currently consists of the following components: (a) a 32-channel APD array, (b) a "carrier" printed circuit board on which the APD array is mounted, (c) a thermoelectric cooler (TEC), (d) a heat sink for removal of heat from the TEC, and (e) an enclosure. These components are shown in Figure 14.8..

14.5.1 APD Module Testing

The APD housing will be tested after production for water tightness. The assembled module with the APD array will be tested at a separate time. An automated testing apparatus is being developed to perform this function efficiently, 12 modules at a time. The individual pixels of the APD arrays will be tested for dark current that is out of spec, high or low, and gain as a function of voltage. These measurements will be performed at room temperature for comparison to the manufacturer tests and at operating temperature of -15C. This will test the operation of the TEC devices as well as the APD. The test will determine the operating voltage required to operate each array at a gain of 100 at the operating temperature of -15C. The results of the first test will determine the required setting of the voltage adjustment potentiometer on each carrier board. The board will be set to the correct value, and retested to confirm the proper gain is achieved.

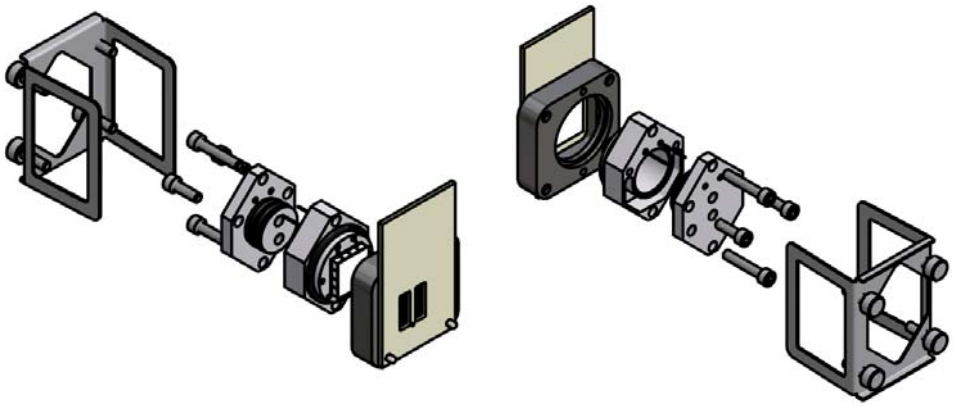

Fig. 14.8: APD Module design which isolates the APD from the environment and provides cooling via the TEC

14.6 APD Cooling

14.6.1 Thermoelectric Coolers

A single-stage TE cooler will cool each APD array. The APD module has been tested with a TEC from TE Technology, TE-31-1.0-1.3, with specifications given in Table 14.2. This has a maximum cooling capacity of 8.4W, and size to match the APD array. Measurements with a prototype APD module have shown a TE cooler electrical power requirement of 2.1W, and heat removal of less than 2W to maintain an APD temperature of -15ºC. The TE cooler and power supplies have additional headroom of 3.2W and 5W respectively. The system should quickly and easily reach operating temperature. The TE cooler must not apply significant mechanical stress to the APD array, so we deploy a deformable, thermally conducting crush pad between the TE cooler and the APD array. The thermal power generated in the APD array itself is ~2 μW, so the thermal load will come from other components through the mechanical and electrical interconnects. The TE cooler will generate approximately 3W of heat for each 32 channel APD array.

Given the industry standard reliability of a TEC of 200,000 hours MTBF, or 22.3 years, we expect a 4%/year failure rate of the TE coolers. The APD module is designed to allow replacement of the TEC without complete removal from the detector module.

Part Number	Qmax (W)	Imax (A)	Vmax (V)	dTMax (C)	Width (mm)	Length (mm)	Height (mm)
TE-31-1.0-1.3	8.4	3.6	3.8	69	14.8	14.8	3.6

Table 14.2 Specification for TEC tested with the APD module.

14.6.2 Water Cooling System

Liquid cooling is a reliable and effective means of removing the heat from the TE coolers. The high heat capacity of water facilitates the removal of the required heat without requiring large temperature differences. We will use a chilled water system that provides approximately 2mL/s of 15°C water to remove the heat from each TE cooler. The water will be supplied by cooling loops covering a pair of blocks. Each loop will service 744 TE coolers. Commercially produced compact process water chillers with a capacity of 7kW and capabilities similar to Neslab HX-300 will be installed at the head end of each loop on the highest catwalk level. The chillers will reject heat directly to air. Each chiller is capable of maintaining its water output temperature within +/- 0.1 deg C of a setpoint. A block diagram of a cooling loop is shown in Figures 14.9 and 14.10. Water is distributed to the cooling elements via a supply and return manifold system. The system is arranged with reverse return flow to help naturally balance the flow through each element. A monitoring station in each loop housing control and monitoring equipment provides an interface to the Detector Control System. There are 17 complete cooling loops for the entire detector. The 17 chillers and monitoring stations are located approximately every 14 feet along the length of the detector.

Distribution manifolds supply water to the 24 service(hose) manifold sections, 12 on the side and 12 on the top of the detector. The supply and return service manifolds in each location will be identical. The general features of a manifold are shown in Figure 14.11. Each service manifold provides 32 hose connections with valved quick disconnect connectors at their ends. The service manifolds are installed as two sections that correspond to a pair of 31 plane blocks. This matches the readout electronics commissioning as well.

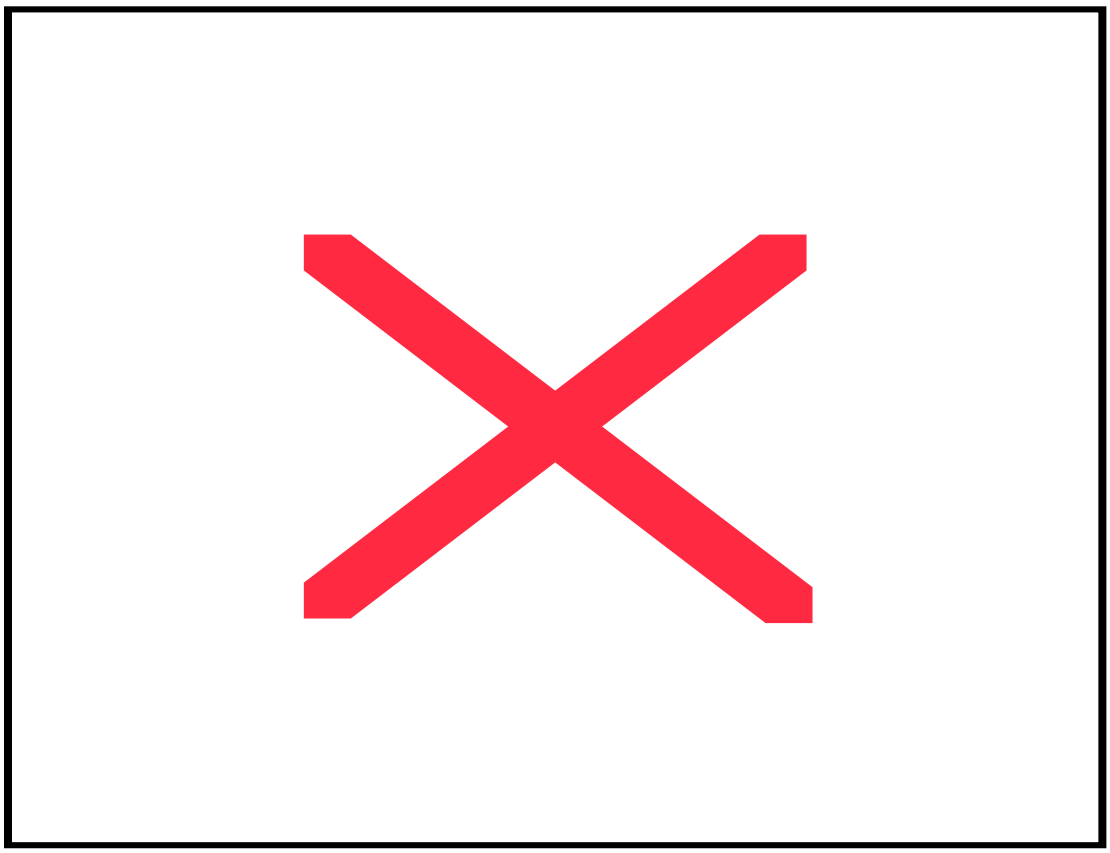

Fig. 14.9.: Schematic of single water cooling loop.

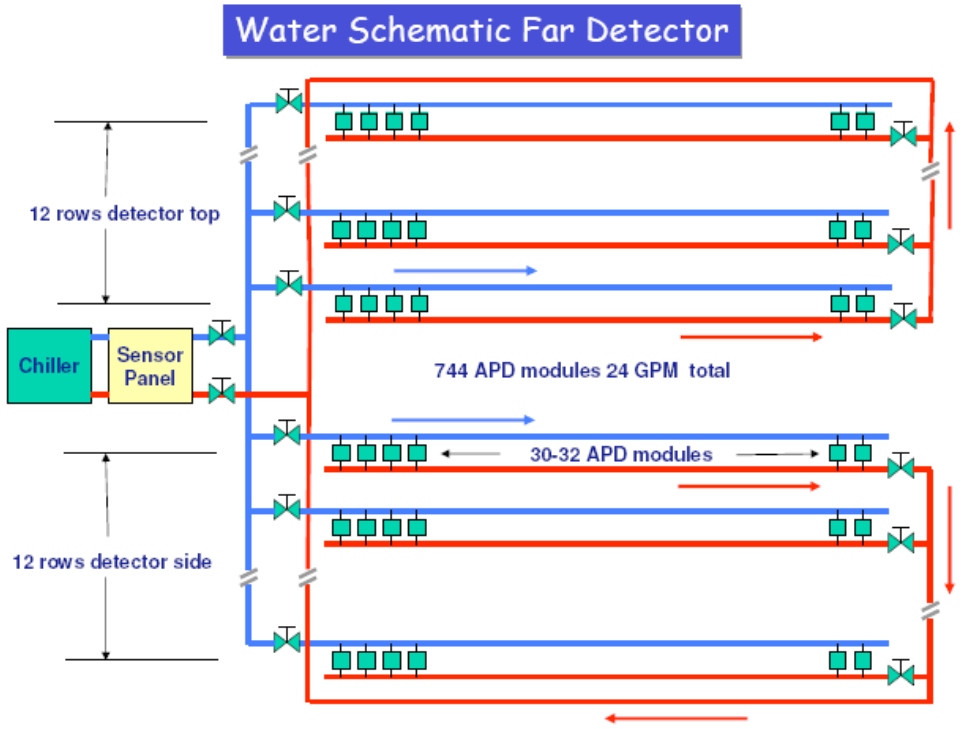

Fig. 14.10: Water cooling schematic.

15 Data Acquisition System

15.1 Introduction

The primary task for the readout and data acquisition system (DAQ) is to concentrate the data from the large number of APD channels into a single stream that can be analyzed and archived. The DAQ also provides for an intermediate buffering location where the data can be held until it is determined that the data should be recorded or rejected. Online trigger processors will be used to analyze the data stream to correlate data with similar time stamps and to look for clusters of hits indicating an interesting event. Additional functionality for dealing with flow control, monitoring, system operations and alarms is also included.

15.2 Technical Design Criteria

The NOνA front end electronics (described in Chapter 14) operates in un-triggered mode with data continuously being digitized, time-stamped, pedestal subtracted and zero-suppressed. There is no spill trigger required at the front-end. The data must be buffered for up to 20 seconds awaiting arrival of a spill trigger message. While the data is in the cache it can be searched for data satisfying a software trigger condition, and analyzed for calibration and monitoring purposes. A spill signal is required to arrive within the buffering time so that the spill time can be correlated with the time-stamped data to determine if the hits occurred in or out of spill. There is no additional selection of in-spill data. All hits that occur in a 30 μs window centered on the 11 μs spill are recorded for further processing. The data selected in this manner corresponds to approximately 190 GB per year.

Randomly selected data for calibration and monitoring will be collected off-spill at a rate that is approximately 100 times higher than the in-spill rate. This corresponds to about 18 TB/yr of raw data. The overall data rate is driven by cosmic ray muons that occur at a rate of approximately 200 kHz with a modest overburden. Monte Carlo simulations predict approximately 200 hits per cosmic ray muon. This corresponds to a total hit rate of 40 MHz and a total data rate of about 0.5 GB/s. Table 15.1 summarizes the channel count and rates in the NOνA Far Detector and in the Near Detector where the rate is much lower at the underground location.

	Far Detector	**Near Detector**
Front end boxes	12,036	497
Front end boxes per plane	12	2.5
APD channels per box	32	32
Total channels	385,152	15,904
Average Noise hit rate per channel	< 30 Hz	< 30 Hz
Total Noise hit rate	<12 MHz	500 kHz
Bytes per hit (channel ID, TDC, ADC, status)	10	10
Muon rate	200 kHz	5 Hz
Average Hit channels/muon	200 (multiple hits/plane)	50
Muon Hit Rate	40 MHz	250 Hz
Total hit rate	52 MHz	500 kHz
Average hits rate per channel	100 Hz	50 per hour
Digitizing rate	2 MHz	8 MHz
Total data rate	0.4 GB/s	5 MB/s
Average occupancy	2.5×10^{-4}	3×10^{-5}

Table 15.1 Channel count and rates in the NOνA Detectors.

15.3 System Architecture

NOνA has only one type of detector and one type of readout, making the NOνA DAQ conceptually simple compared to typical high energy physics experiments. The near detector is slightly different, in that the electronics will be required to accommodate the high burst rate of hits during a spill. However, the detector modules will be significantly smaller, and the detector will be located underground, so that the average data rate is much lower for the near detector. This means that the DAQ components can be the same and still accommodate the high hit rate during a spill.

The front-end electronics are described in detail in Chapter 14. In summary, the front-end boards digitize signals from the APD arrays. The digitized data are then input into a Field Programmable Gate Array (FPGA) that applies zero suppression, timestamps and buffers the data before serialization and transmission to the DAQ. The FPGA also provides control and monitoring of the front end electronics and APDs and the external interface to the DAQ using a custom protocol over inexpensive CAT5 cabling.

The DAQ system is composed of four main components, a timing and command distribution system, an array of Data Concentrator Modules (DCM), a Gbit Ethernet network, and a buffer farm. Timing synchronization and command packets for the data concentrator modules come from the timing and command system consisting of one Master Timer Unit and ten Timing Distribution Units that act as a separate network backbone for these signals. Digitized data from up to 64 front end boards are routed through CAT5 cables to a custom DCM. The DCMs send data to the buffer farm, and eventual storage over the Gbit Ethernet network. The buffer farm and DCMs are under the control of a Run Control Computer.

15.4 Timing and Command Distribution System

The Global Timing and Command Distribution system provides a timing infrastructure and distributes commands from the run control computer to the DAQ and the detector. Timing information and actions are carried by special timing packets on high speed serial links. Timing packets have deterministic timing and the system is self-compensating for propagation delays. This means that any action initiated by timing commands to all DCMs are coherent across the detector with an accuracy of better than one 163.84 MHz clock cycle. The Master Timer Unit (MTU) contains a Common View Global Positioning System (GPS) trained clock oscillator with a time-stamp counter and generates timing command packets at a fixed repetition rate which are distributed in a serial loop as shown in Fig. 15.1. The bidirectional high speed links facilitate compensation for the propagation time of the system as described below. All non-timing controls command packets to the system, usually reads & writes, are queued and interlaced between the timing packets at a lower priority.

The nine Timing Distribution Units (TDU) make up the timing backbone of the detector with the Master Timing Unit (MTU)at the near end as shown in Fig. 15.1. The self compensation of the TDU backbone is based on the round trip time-of-flight (TOF) of a timing command through each TDU to the far end of the cable loop and back. The reference point for all of the timing is the far endpoint of the backbone loop as shown in Fig. 15.2. The measurement is made in each TDU independently and the TOF count is related to the TDU position along the backbone. The TOF count starts on the first arrival of the timing packet and ends on the arrival of the return packet as in Fig. 15.3. This time-of-flight measurement is divided by two to give the specific TOF for each TDU across the entire backbone. A synchronization trigger output is generated by each TDU after receiving a new timing command by counting down the TOF/2 measured from the previous timing command. All TDUs perform the same timing measurement which allows each TDU to delay the trigger signal to be synchronized to the far end of the backbone. This calibrates the propagation delay out of the TDU system. The cables between TDUs can be any length without affecting the timing synchronization. The synchronized trigger

signal generated at all TDUs, causes the timing command to be issued on all of the DCM links along the backbone simultaneously. The MTU can also synchronize to the far end reference point in the same way and compensate the GPS clock time for the cable propagation.

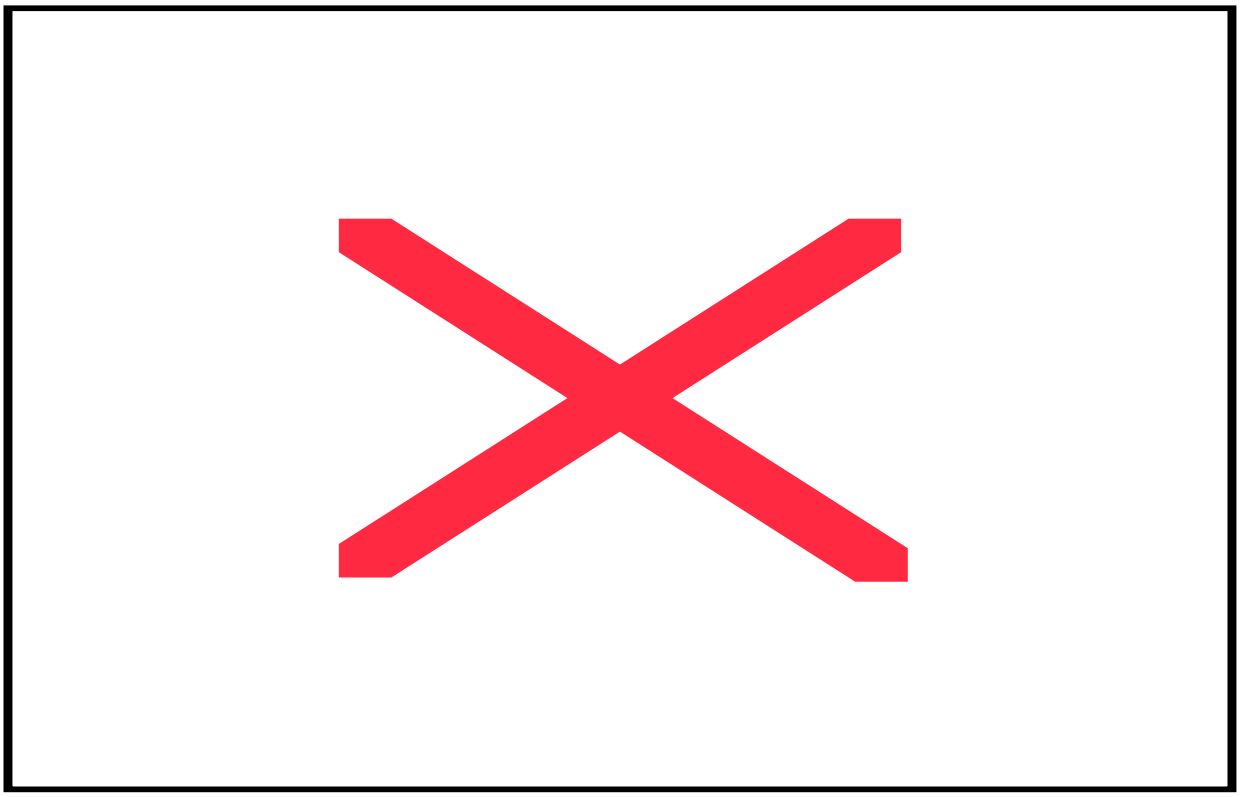

Fig. 15.1: Diagram of Global and Local Timing Distribution System

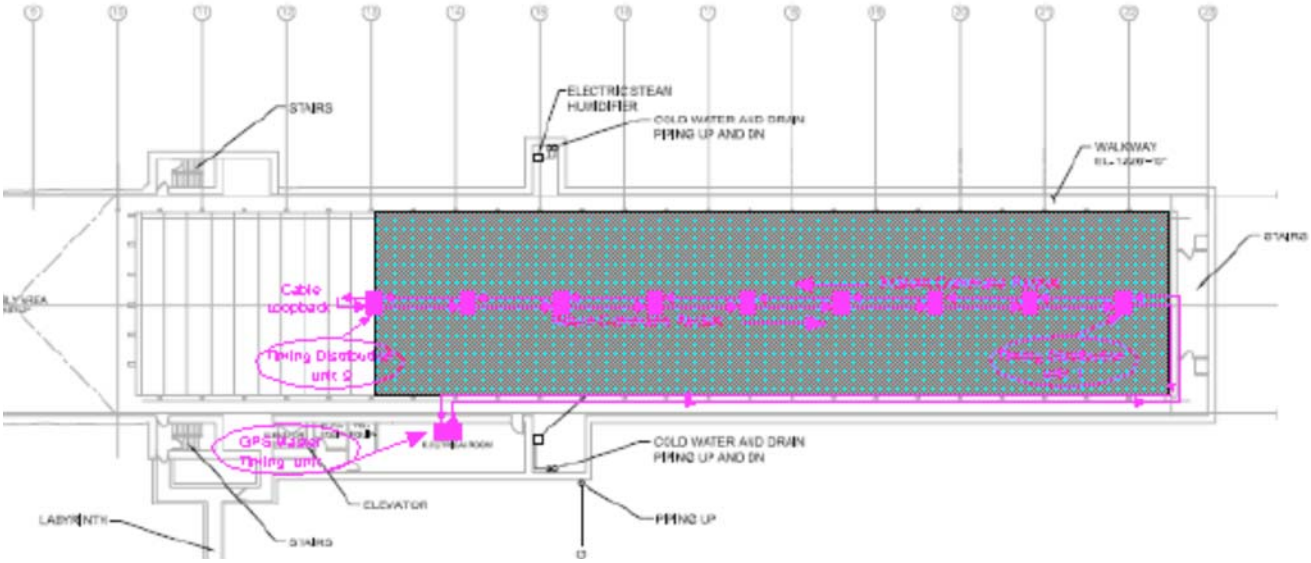

Fig. 15.2: NOvA detector cabling for timing and command distribution system (18kton detector shown. System typical of smaller or larger detector)

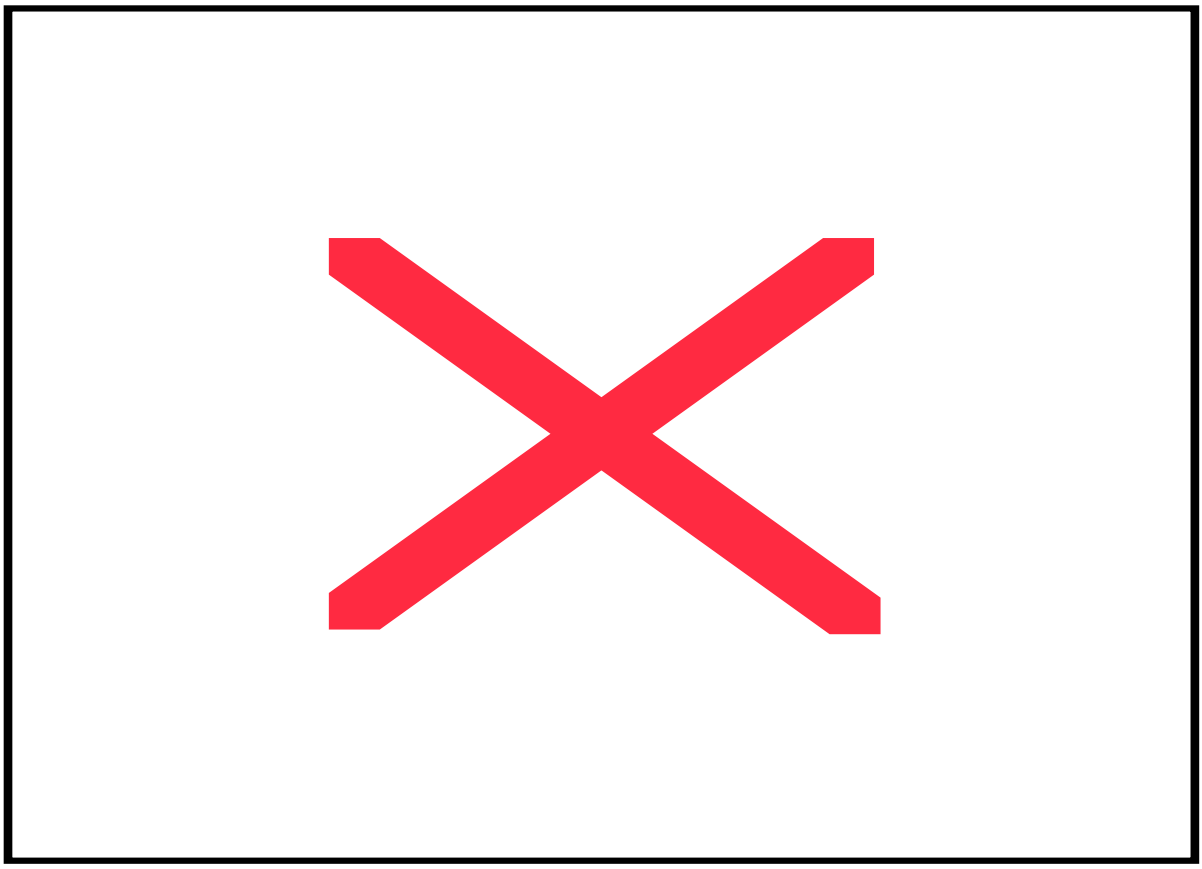

Fig. 15.3: Command Time-of-Flight and Synchronized Trigger at TDBs

Compensation of the propagation delay on each of the TDU to DCM links is performed similarly to the TOF/2 measurement of the detector backbone except there are multiple loops so the longest TOF/2 needs to be determined and distributed such that it is used in all of the timing calculations. Rather than determining the longest TOF/2 and broadcasting it, an alternative method is to predetermine a delay parameter that is slightly greater than the longest actual measurement of all of the DCM links. The actual measured TDU to DCM round trip TOF is subtracted from this delay parameter in the timing calculation for each DCM port. Long cables will have short added delays and short cables will have long added delays such that all the DCMs receive timing signals at the same time. The TDU still compensates for cable lengths differences but the reference point is artificially longer than the longest link cable. An advantage to this method is that communicating the TOF parameters between TDBs about the TDU to DCM links is unnecessary and the single predetermined delay is simply hard coded in the firmware.

15.5 Data Concentrator Module (DCM)

The NOvA Data Concentrator block diagram is shown in Fig. 15.4. The main functions of the Data Concentrator boards are to collect serial data from up to 64 Front-End Boards (FEBs), combine and packetize this data for transmission over Gigabit Ethernet to Buffer Nodes, and finally to fan out timing and control information from the timing system to the FEBs.

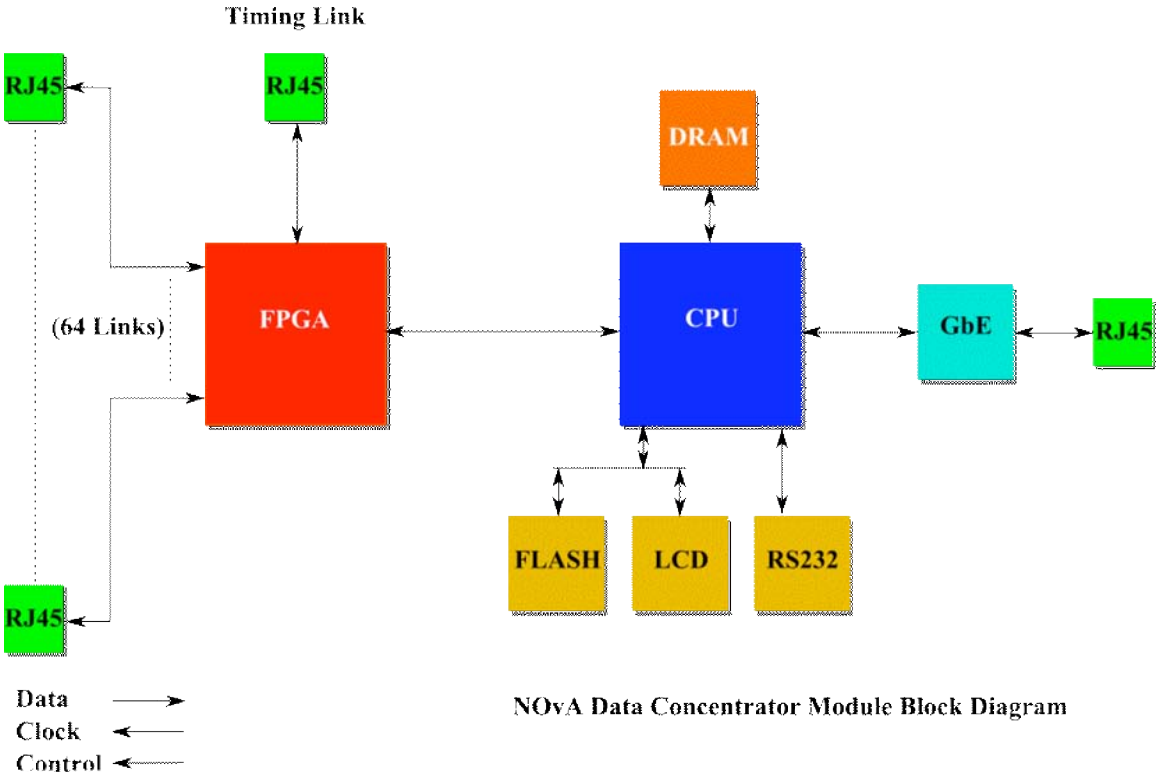

Fig. 15.4: Block Diagram of Data Concentrator

The DCM mainly consists of a midsized FPGA, an embedded Power PC processor running embedded Linux, and numerous connectors, as shown in the prototype design in Figure 15.5. On power-up, the processor runs a bootloader from onboard flash memory. The bootloader initializes the Gigabit Ethernet port and connects to a boot server to download its embedded Linux image. Once Linux is booted, a connection to the server is once again established so that the FPGA firmware, DAQ application software, and DCM configuration data can be downloaded. The processor then configures the FPGA and starts the DAQ application code. Among the DCM configuration data is the buffer node destination table. This table contains a list of available destination buffer nodes and the timeslices each node is assigned to. Other configuration information will include configuration data for FEBs, as well as any other configuration data necessary for operation.

DCMs connect to FEBs with CAT5 cables through RJ-45 jacks. Of the four pars of wires in an FEB to DCM cable, one is used for serial data transmission from the FEB to the DCM, one is used for system clock transmission from the DCM to the FEB, one is used for serial Command transmission from the DCM to the FEB, and the fourth is used for transmission of a sync pulse from the DCM to the FEB. Data from the FEB consists of a header and hit information for a given timeslice. The FPGA on the DCM combines the hit information for all 64 FEBs in each timeslice into a data block. The data is then read from the FPGA by the embedded Power PC processor. Application code running on the processor packetizes the data into Ethernet packets and transmits these packets to a buffer node through its Gigabit Ethernet port.

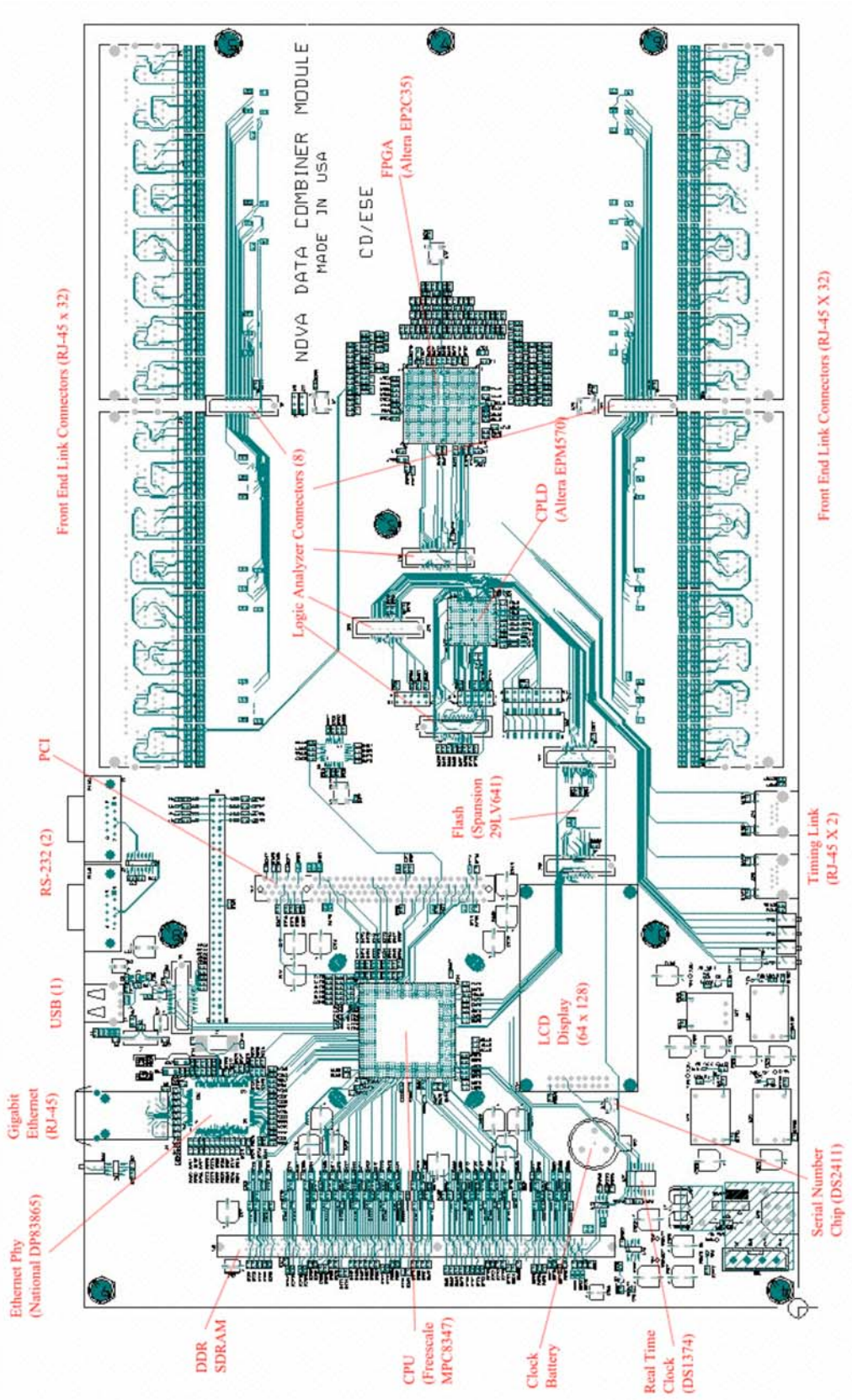

Fig. 15.5: Layout of Prototype Data Concentrator Module

DCMs are connected to the buffer nodes through a Gigabit Ethernet switch array. To make the most effective use of network bandwidth through the switch array, DCMs are each programmed to transmit data to different buffer nodes in a round robin rotation, with each DCM starting with a different buffer node. Timing information from the timing system is used to divide time into slices such that data packets are transmitted to a different buffer node in each slice. In this way, DCMs stay synchronized in their rotation, and no two DCMs ever transmit to the same buffer node at once. Buffer nodes are receiving data from only one DCM at a time, and all buffer nodes are receiving data on all time slices. Because there are more DCMs than buffer nodes, each DCM will have null time slices where it will be idle part of the time. This ensures that collisions on the network are minimized. The buffer nodes collect data from all DCMs for different events. Event data files are stored locally until they can be copied to Fermilab for permanent storage.

The DCM also connects to the timing system with a CAT5 cable. Clock, Command, and Sync information are encoded in a serial bitstream on one of the pairs of wires in the timing system connection and transmitted to the DCM. A second pair of wires on the cable is used to transmit clock information back to the timing system to allow a round-trip time measurement to occur. Once the timing system measures the round-trip delay time to each DCM, it can insert delays as necessary to synchronize all DCMs. Clock, Command, and Sync are decoded by the DCM and transmitted to each FEB.

15.6 Gigabit Ethernet links and Data Buffer Processor Farm

The buffer farm nodes serve as a large data caching system for the detector with search capabilities. The buffer size must be large enough to hold 20 seconds of data at the design rate for the system (twice the nominal rate). The data is buffered in these nodes until a trigger is received from the global trigger system. This trigger is a time window (GPS based), and the buffer nodes use the time window to search for all data within that frame of time and route it to a logging process. All data for one time frame will be buffered in the same buffer node. The buffer node will need to aggregate the data from each of the DCMs for the time frame and insure data from all DCMs is seen. This is a form of event building where data for a large time frame is built as a single event. For any frame seen by a buffer node, data must be received from each DCM. This provides a system integrity check and also allows more performant searching when a trigger is received.

While all the data from a given time frame will be contained in one farm node, an actual 30μs trigger, which defines an event, may span these large time frame boundaries and thus be split across two farm nodes. Each farm node will need to determine if it has any data for the trigger window in its memory buffer and send it to the logging process. It might also be sent to an event monitor server which could cache events for event displays. Any problems sending would raise an error. In addition to buffering the data, the data may need to be made available to a processor framework while waiting for a trigger.

The buffer farm nodes will be connected to the Data Combiner Modules through a set of interconnected Gigabit Ethernet switches. The switches are interconnected to allow a connection from every DCM to every buffer farm node over a Gigabit interface. The physical layout of the cabling on the detector is shown in Figure 15.6, while the connection to the buffer farm and control room is shown in Figure 15.7.

To determine the number of switches, it is assumed that full bandwidth through the switch is needed, and we want complete flexibility for data routing, in that any DCM can talk to any buffer node. That means each switch module needs as many inputs as outputs on each switch module on the side of the switch with the fewest modules, and a three stage switch is needed. There are six DCMs and approximately 4.2 Buffer Nodes needed per block. A 15kton detector (32.3 blocks) then requires 194 DCMs and 136 Buffer Nodes. The buffer node side of the switch then determines the maximum data rate through the switch. For full bandwidth through a 48 port switch module 24 ports are used as inputs and 24 are used as outputs. Since 136 / 24 ~ 6, there

will be six output switch modules with some empty ports. An even number of switch modules is desirable to ensure even bandwidth distribution across the switch modules. The intermediate switch stage connects directly to the output stage, so there needs to be six switch modules here also. The input switch stage needs enough ports to connect 194 DCMs to 136 intermediate switch ports. A total of 330 ports are needed to connect the 194 DCM inputs and 136 buffer farm outputs. The minimum number of 48 port switches that could to this is nine. Connecting these nine switches to six intermediate switches does not map very well with regard to the number of links per intermediate switch connecting to input switches. Some would have three and some would have two connections. This could cause problems with the time-slicing algorithm, which prevents collisions and blocking. Using seven output switches works much better. This allows as many as 168 intermediate connections and a non-blocking switch array is assured. There will be 9 layer 1 switches, 7 layer 2 switches, and 7 layer three switches for a total of 23 48-port switch modules required.

More switches are needed for the control network. All of the buffer nodes need to connect to run control through the control network. Four 48 port switches would have enough ports to connect to the buffer nodes, but the switches need to connect to each other and to the run control machines, so this will take about five more switches, bringing the total to 32.

16 Near Detector Site and Assembly

16.1 Introduction

The NOνA Near Detector will be located underground on the Fermilab site, in a new cavern adjacent to the MINOS access tunnel, downstream of the MINOS shaft. Chapter 4 discusses the rationale and requirements of the Near Detector. The purpose of this chapter is to show where it will be placed, tell how its location was chosen and indicate the details involved in assembling this detector there. Most aspects of the design of the Near Detector – PVC extrusions, modules, planes, blocks, fiber readout – were developed for the Far Detector. They are used for the Near Detector so that it will be as similar as possible to the Far Detector. Other chapters of this TDR go into considerable detail as to the particulars of this design.

Figure 16.1 is a schematic view of the planned detector. There is an active detector part, similar to the Far Detector and broken logically into veto, fiducial and shower containment regions, followed by a steel and liquid scintillator muon catcher. The upstream end, without steel, is held firmly in place by a "bookend."

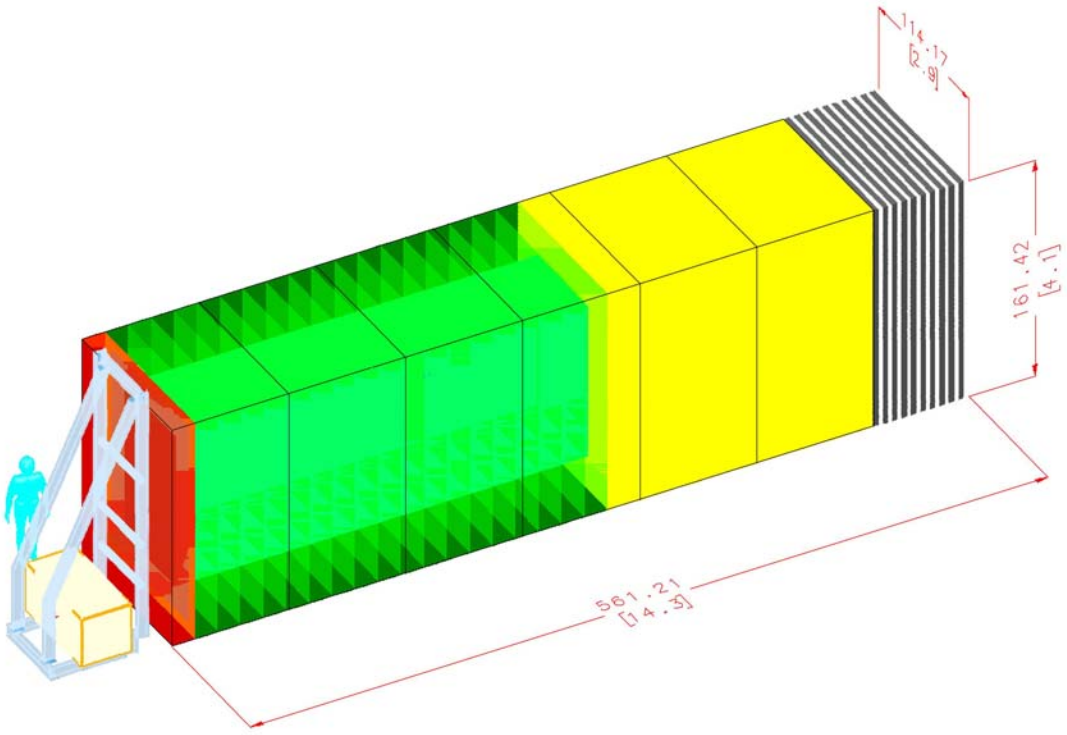

Fig. 16.1: View of the Near Detector indicating its various sections. The veto (red), fiducial (green, with actual fiducial volume highlighted) and shower containment (yellow) regions represent only a logical breakdown; all are constructed in the same manner, with six physical blocks indicated. The muon catcher region is ten planes of 0.1 m thick steel each with a plane of liquid scintillator attached (four planes in the most downstream case). The upstream bookend provides support and holds the detector in place.

16.2 The Near Detector Site

16.2.1 Technical Siting Criteria

The plan view shown in Figure 16.2, upper pane, indicates the path of the NuMI access tunnel from the MINOS shaft downstream to the MINOS near detector. It is seen that this location is appropriate for the placement of an off-axis detector, and calculations show that the off-axis angle of the Far Detector can be matched by that of a Near Detector in this region. However, seen from an off-axis position so close longitudinally to the decay region, the neutrinos come from a line source, unlike the effective point source of the Far Detector. The decision has been made to have the correct off-axis angle for the part of the decay region from which comes the highest flux of muon neutrinos. Note that this decision is not a trivial one. In particular the electron neutrinos come from a different part of the decay region and thus have an effectively different off-axis angle. The detector axis is similarly aligned so that the neutrinos at the appropriate off axis angle enter perpendicular to the face. Given the angle of the tunnel, it is not possible to achieve this condition without some excavation. Earlier attempts to design a smaller excavation, with most of the detector angled across the tunnel, met with serious logistical problems and were abandoned.

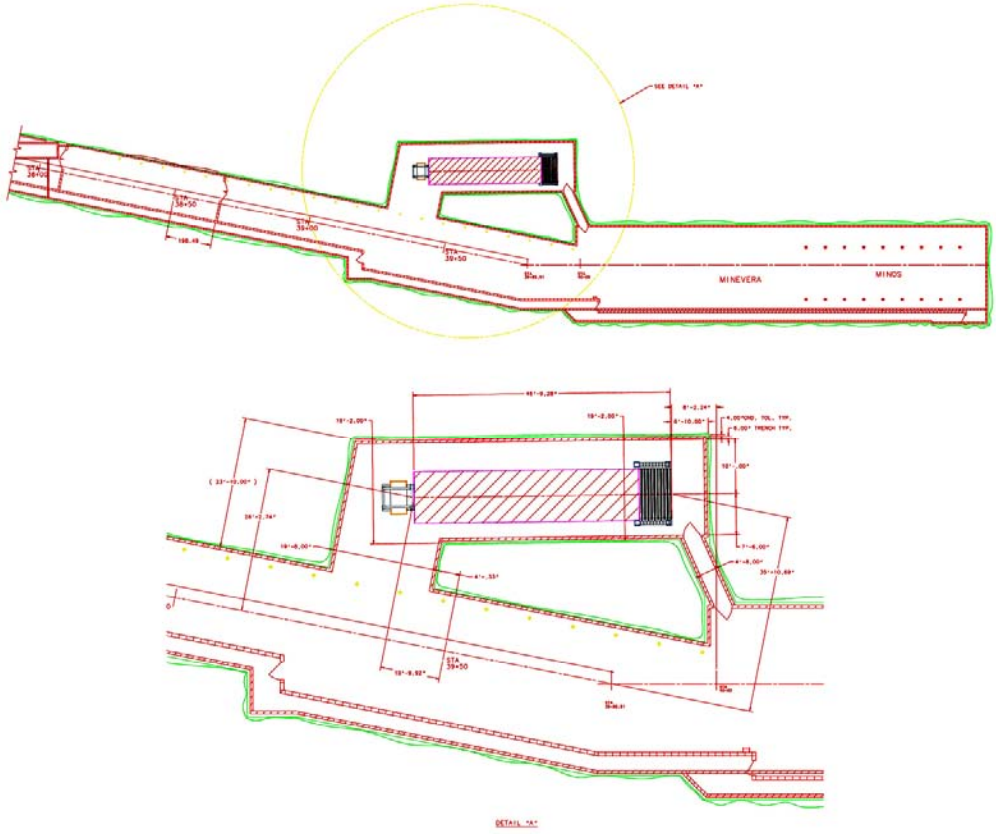

Fig. 16.2: Plan view of the downstream MINOS access tunnel with the NOνA Near Detector indicated. The top pane shows the tunnel from the shaft area at the left to the MINOS near detector at the right. The lower pane is an expanded view of the new cavern to be excavated. The green highlighting indicates the rock surfaces after the excavation is complete. The passageway below and to the right of the detector is a required safety egress from the cavern. North is to the right in this figure.

As is noted in Figure 16.2, the cavern is constructed so that the lower (east) wall is quite close to the detector. All horizontal modules of the detector will have readouts on the opposite (west) side, and sufficient clearance is provided there for installation and maintenance. Similarly all vertical planes will have their module snouts facing west. This orientation, as opposed to the opposite, is chosen so that the detector can be placed as required by the physics while maximizing the size of the rock pillar between the existing tunnel and the new cavern. A preliminary opinion of Fermilab's underground construction expert is that this excavation is safe and constructible for the cost quoted. A more detailed discussion of the excavation process is given in [1].

The detector requires a certain amount of infrastructure. In particular the readout electronics will require two standard relay racks and the cooling system will require a water facility 8 feet long by 4 feet wide by 8 feet high. These fit easily in the access tunnel upstream and downstream of the new cavern. If more power is required it can easily be supplied through the shaft area. If water is required it can be taken from the nearby sump, as is done for MINOS.

Figure 16.3 is a picture of the MINOS tunnel with the area to be excavated highlighted. The piping and cabling seen are infrastructure for the MINOS near detector. This will have to be rerouted for the excavation to proceed.

Fig. 16.3. View looking downstream in the MINOS tunnel at the location proposed for the Near Detector cavern. The infrastructure along the wall will have to be rerouted.

16.2.2 MINOS Shaft Area

Shown in Figure 16.4 is one view of the MINOS access shaft indicating how the MINOS near detector segments were brought underground. Figure 16.5 is a plan view of the shaft cross section showing a NOvA Near Detector block similarly being lowered. A 31 plane block in its transport cradle (see below) is seen to fit in the open shaft area even when the space occupied by tunnel infrastructure is taken into account. The steel for the muon catcher will be lowered in a manner similar to the MINOS planes, in particular one plane at a time.

Fig. 16.4: View from the bottom of the vertical D-shaped MINOS shaft as a MINOS near detector plane comes down the shaft. The MINOS module shown is ~4.5 m wide by ~3.5 m high by ~0.2 m thick (including the red strong-back frame).

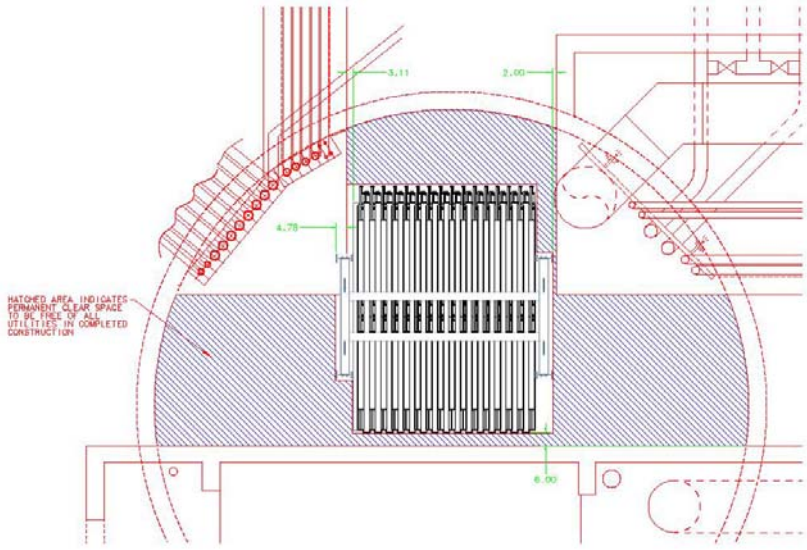

Fig. 16.5: Plan view of the MINOS shaft indicating the space occupied by a 31 plane NOνA Near Detector block.

16.2.3 Design Changes in the Near Detector Site since the CDR

In the CDR a large region of the tunnel was considered appropriate for the detector. It was also being actively considered that the Near Detector would be moved to different areas to see neutrinos of different energies. There was no excavation. It is now considered that since the decay region of NuMI is a line source as seen from the Near Detector, neutrinos of a range of energies and angles are all seen at any single location. Also, in the CDR the neutrinos did not enter the detector normal to its face, leading to a serious difference between Near and Far Detectors.

16.2.4 Work Remaining to Complete the Near Detector Site Design

A consulting engineer will be employed to study the rock properties in and near the proposed cavern location. Minor location changes which do not compromise the ND physics potential can still be considered.

16.3 Near Detector Design

16.3.1 Technical Design Criteria for the Near Detector

The physical design of the Near Detector is constrained by three requirements. The first is that it should be as similar as possible to the Far Detector in material and segmentation. This requirement ensures that the Near and Far efficiencies for signal and background events are essentially the same. Ideally, this will allow us to understand both the ν_e charged current and the ν neutral current beam spectra seen in the Near Detector as a measure of the expected backgrounds to $\nu_\mu \rightarrow \nu_e$ oscillation signals in the Far Detector. In practice there are three unavoidable differences. The first is that the Near Detector sees the decay region as a line source as was noted above. The second is that the Near Detector is smaller and thus has wavelength shifting fibers much shorter than those in the Far Detector. The third is that there are multiple events per NuMI spill so that the electronics must be different (this is discussed in Chapter 14, Section 13.8).

The second requirement is that there must be a fiducial volume of order 20 tons, which sets a minimum size, while the third is that the pieces from which the detector is constructed must fit down the MINOS access shaft. This last sets a practical maximum size for the detector transverse dimension and is shown to be satisfied as is seen above.

16.3.2 Near Detector Overview

The Near Detector uses the same technology as the NOνA Far Detector and satisfies the space constraints described above. It is 2.8 m wide, 4.1 m high and 14.5 m long. The first 12.5 meters is composed of similar extrusion cells to those in the Far Detector. The transverse size is of course scaled down from that of the Far Detector, but the longitudinal and transverse segmentations are the same as in that case. As noted, the detector is split into four logical parts: an upstream veto region, a fiducial event region, a shower containment region and the steel/scintillator muon catcher as is shown in Figure 16.1. The 4.85 m long shower containment length is chosen to fully contain electron showers from charged current ν_e interactions of a few GeV. The active detector sections are followed by a muon catcher composed of 1.0 meters of steel interspersed with ten planes of liquid scintillator cells (with three extra planes at the downstream end). There are ten steel plates each 4.1 x 2.9 x 0.1 m^3 with a mass of 8.2 metric tons. The length of the muon catcher is chosen so that it plus the shower containment region will stop muons from few GeV charged current ν_μ interactions. The parameters of the detector are summarized in Table 16.1 and presented in more detail in [2].

Parameter	ParameterValue
Total mass	215 metric tons
Active detector mass	125 metric tons
Extrusion cells, liquid scintillator, waveshifting fiber, APD readout	Identical to the NOνA Far Detector except for size
Number of channels	15,904
Total Liquid Scintillator	29,616 gallons
Detector PVC width Full width PVC height Full height Length	(3 upstream blocks differ slightly from 3 downstream) 2.553 m, 64 cells and 2.633 m, 64 cells 2.83 m, 2.91 m 3.829 m, 96 cells and 3.949 m, 96 cells 4.11 m, 4.23 m 14.5 m
Total active planes	199 planes, 99 horizontal & 100 vertical
Basic block in the active section # planes, Thickness 31 plane block Empty mass of block Full mass of block	 31 planes 2.09 m A blocks (ups 5.83, dns 6.08) B blocks (ups 5.77, dns 6.02) metric tons ~19.51 metric tons
Veto region, # of active planes	6 planes
Fiducial region, # of active planes Width (m) Height (m)	108 planes 1.17 m (approx 70 cm wide picture frame 2.45 m around fidvol)
Fiducial mass	~20 metric tons
Shower containment region, # of active planes	 72 planes
Muon catcher Steel (m/section, # of sections) # of active planes	 0.1 m, 10 sections 13 planes, 6 vert & 7 hor
Muon catcher mass Steel Scintillator planes	 81.6 metric tons 8.5 metric tons

Table 16.1: Near Detector Parameters

16.3.3 Assembly Process for the Near Detector

Altogether there will be 199 planes of PVC with liquid scintillator, 99 planes with horizontal cells and 100 with vertical cells. The total mass of the detector (excluding the steel) is 215 tons with 125 tons active. The fiducial mass is ~ 20 tons.

The detector will be constructed in 31 plane blocks for uniformity with the Far Detector. With an odd number of planes per block, there are two possible configurations, called A when the first and last planes are vertical and B when they are horizontal. The block configuration starting from the upstream end is to be ABABAA, mimicking the Far Detector superblock arrangement. The blocks will be constructed at Argonne National Laboratory using a considerably scaled down version of the procedure envisioned for the Far Detector. Part of the cradle, which will later be used to transport the block, will be used to support it during construction. Blocks are constructed in a horizontal orientation, with successive planes stacked upon each other as is shown in parts (b) and (c) of the figure. The modules are stacked against the steel baseplate of the cradle. There will be "module stops" attached to one side to assure alignment. The first step for each module is that Devcon adhesive is applied to the top by an appropriate dispenser. Next the module is

flipped about its long axis by hand so that the glue side is on the bottom. It is then moved by a vacuum lifting fixture to its designated location in the currently active plane. When a block is completed it is rotated to its final upright position. This process is much simpler than the corresponding one for the Far Detector. The assembly part of the cradle is hinged on one end, as seen in Figure 16.6b, and with an empty (of scintillator) weight of only ~5.5 metric tons, the block is easily rotated by a crane, as shown.

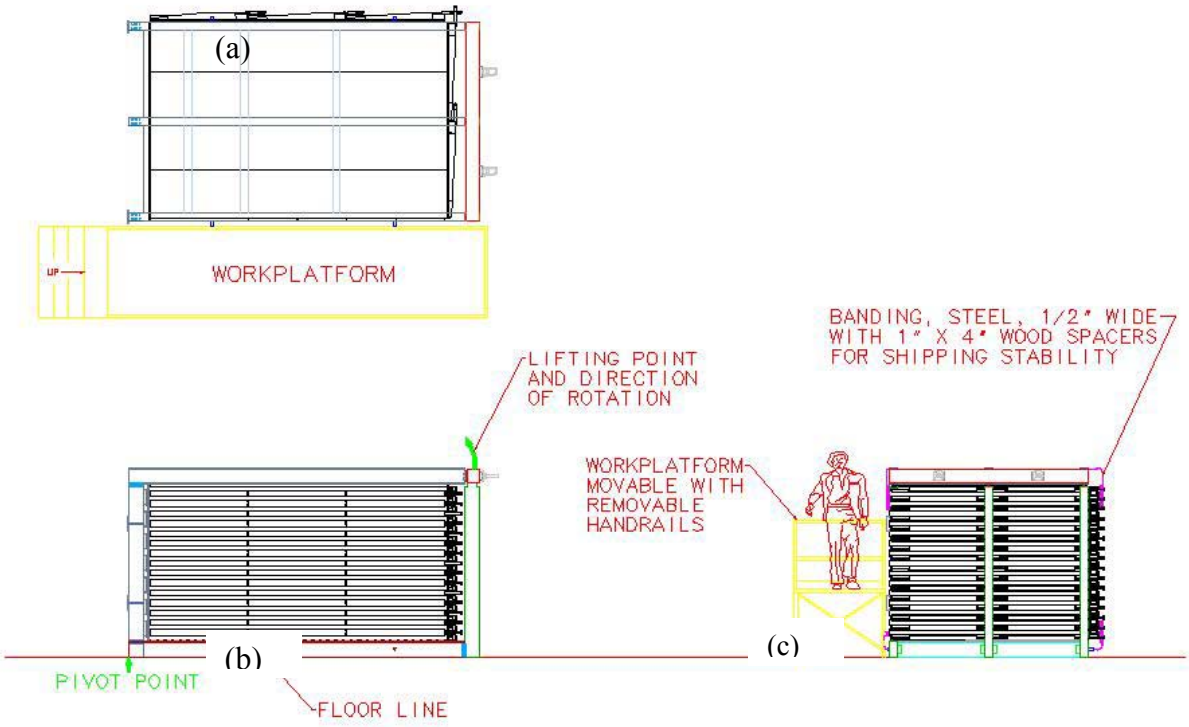

Fig. 16.6. The Near Detector assembly form, later to become part of the support cradle. Part (a) is a plan view of the empty form. Part (b) is an elevation view of the form holding a completed block. The hinge point for rotating the block to upright is indicated. Part (c) is a transverse cut of the completed block. The work platform height is adjustable so that the workers move higher as planes are added.

When a block is completed, the remainder of the cradle is constructed around it. Figure 16.7a shows an empty cradle including the baseplate while 16.7b shows a loaded one transporting a block. The cradle is used to transport the block to the Fermilab MINOS Service Building and then to lower it down the MINOS shaft, as was indicated in Figure 16.5. The detector blocks will be on wheels which are part of the cradle assemblies, and will easily be positioned in the ND cavern. As the detector is constructed, the sides and top of the cradle are removed while the bottom, lifted off the wheels, remains. In practice, three of the ND blocks will first be used as part

of the IPND in the MINOS service building, and will be drained of scintillator and lowered to the ND cavern when the IPND is decommissioned.

The muon catcher part of the detector resembles MINOS and is assembled similarly. Each active detector plane (4 planes in the most downstream case) will be attached to its corresponding steel plate by several strong clips welded to the plate. The steel planes will in turn be supported "hanging file folder style" from a steel support. The steel will have protrusions on the sides ("ears") by which each is hung from the support structure. A conceptual diagram showing the plates and support structure is shown in Figure 16.8.

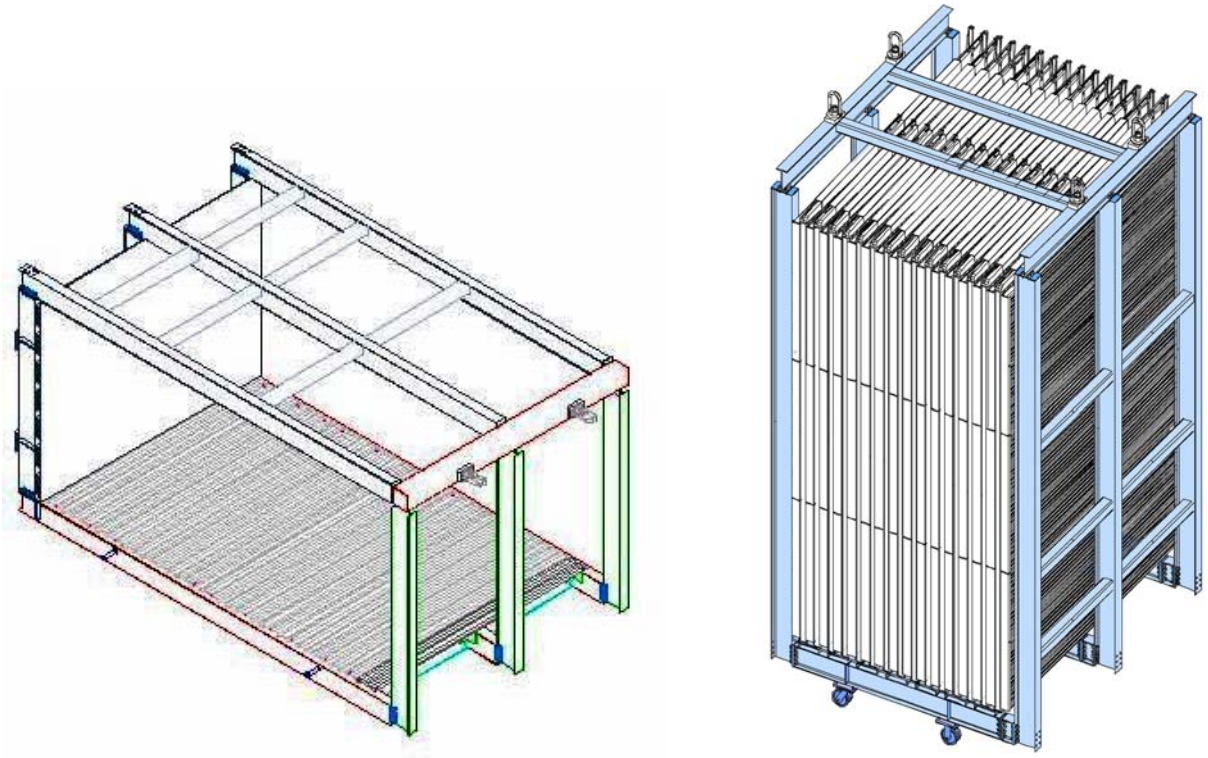

(a) (b)

Fig. 16.7: The block moving cradle. In (a) the cradle is empty to show its construction.Note that it is never fully configured in this manner in the horizontal position. In (b) it is loaded with a Near Detector block and raised to the vertical position.

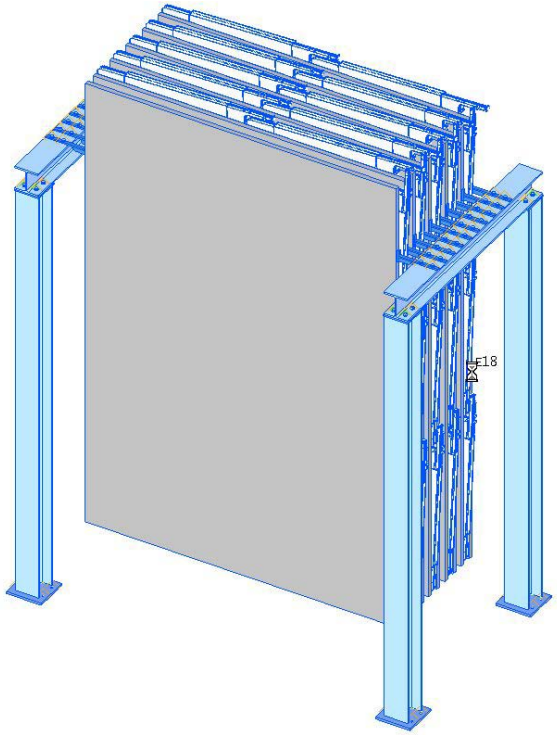

Fig 16.8. Conceptual design of the muon catcher section and its support structure.

16.3.4 Filling the Near Detector with Scintillator

The active detector planes will be filled with scintillator after they are assembled into a detector, i.e. they are empty while being moved. The plan is to fill the planes from a tanker on the surface and fitted with a shrouded pipe the length of the shaft, with a Far Detector like filling system (see Chapter 17) extending to the detector location. A pressure reducing valve will be used to reduce the liquid pressure from the 300' high vertical pipe. An approximately 50 gallon relaxation tank to allow static charge to neutralize will be placed at the bottom. The buildup of static charge in oil pumped through pipes has been determined to be a real problem in NOvA and is discussed in [3]; this relaxation tank provides an extra level of safety in the case of the long vertical drop. A separate pipe will vent pseudocumine vapor to the tanker. Details of the piping are given in [4].

Three precautions will be taken to prevent spilling of liquid scintillator as it travels down the shaft. The first is to protect the vertical pipe with a shroud. The second is to assert that there be no other activity in the shaft while filling is taking place. The purpose is to be sure that the filling pipe is not struck and ruptured. The final precaution is to place a secondary containment device at the bottom of the shaft. This commercial device is called a spill berm and one will similarly be placed under and around the filled detector. This device is similar to a plastic "kiddie pool." The sides form essentially a fence which is made high enough to contain a potential spill of the entire liquid scintillator volume. Beneath the shaft this is the volume of the pipe plus a small amount while in the ND cavern this is the entire volume of the detector.

16.3.5 Fire Protection

The liquid scintillator is mildly flammable, and thus the detector in the cavern will need fire suppressant. Flooding the cavern with an oxygen depleted atmosphere is straightforward. The cavern entrance and emergency escape way will have fire doors which will automatically close in case of a blaze.

16.3.6 Changes in the Near Detector Design and Assembly Since the CDR

The CDR contained few details about how the detector would be assembled. However at the time the CDR was prepared it was planned to construct the detector out of seven- and eight-plane segments, rather than 31-plane blocks. The entire detector can now be lowered down the shaft in 16 trips, six for the active blocks and ten for the steel/scintillator planes.

16.3.7 Work Remaining to Complete the Near Detector Design and Assembly Plan

Detailed configuration of the steel planes still needs to be established. The design will be based on the successful MINOS one.

The safeguards in and below the shaft during detector filling need to be worked out.

References

[1] Discussion of the NOvA Near Detector Location and an Alternate Location, V.D. Bogert, NOvA DocDB #1922, May 2007. This is a PowerPoint document; the decision to construct the ND cavern was made as a result of this presentation.
[2] Near Detector Parameters, K. Kephart, NOvA DocDB #1136, May 2007
[3] Liquid Scintillator Handling – Safety, M. Gebhard and J. Musser, NOvA DocDB #1118, November 2006
[4] Near Detector Scintillator Supply Pipe, D. Pushka, NOvA DocDB #2064, May 2007

17 Far Detector Assembly

17.1 Introduction

This Chapter describes the structural design of the NOvA far detector, the tooling and infrastructure required to assemble the detector at the Ash River site, and the detector assembly process itself. These tasks are the responsibility of WBS 2.9, which receives detector components from WBS 2.2 (liquid scintillator), 2.5 (PVC modules), 2.6 (electronics) and 2.7 (data acquisition) for assembly at the facility provided by WBS 2.1 (far detector site and buildings). The close coordination and integration of these Level 2 WBS activities is one of the most important detector assembly tasks. WBS 2.9 is responsible for designing and building several large semi-automatic machines, especially the adhesive dispenser and the block pivoter, used for assembling modules into blocks and installing blocks in the detector. The task includes the checkout and validation of completed sections of the detector and the transition to routine data acquisition operation. The detector installation requires the hiring and training of a crew of technicians that will perform the actual assembly work over a 2.5-year period, beginning with beneficial occupancy of the detector building and ending when the 15 kton detector is fully operational. WBS 2.9 is responsible for the design and operation of the liquid scintillator supply system, which receives scintillator from delivery tankers, subjects it to quality assurance testing and uses it to fill the detector modules. The overall structure of the far detector is shown schematically in Figure 17.1 and its design parameters are summarized in Table 17.1.

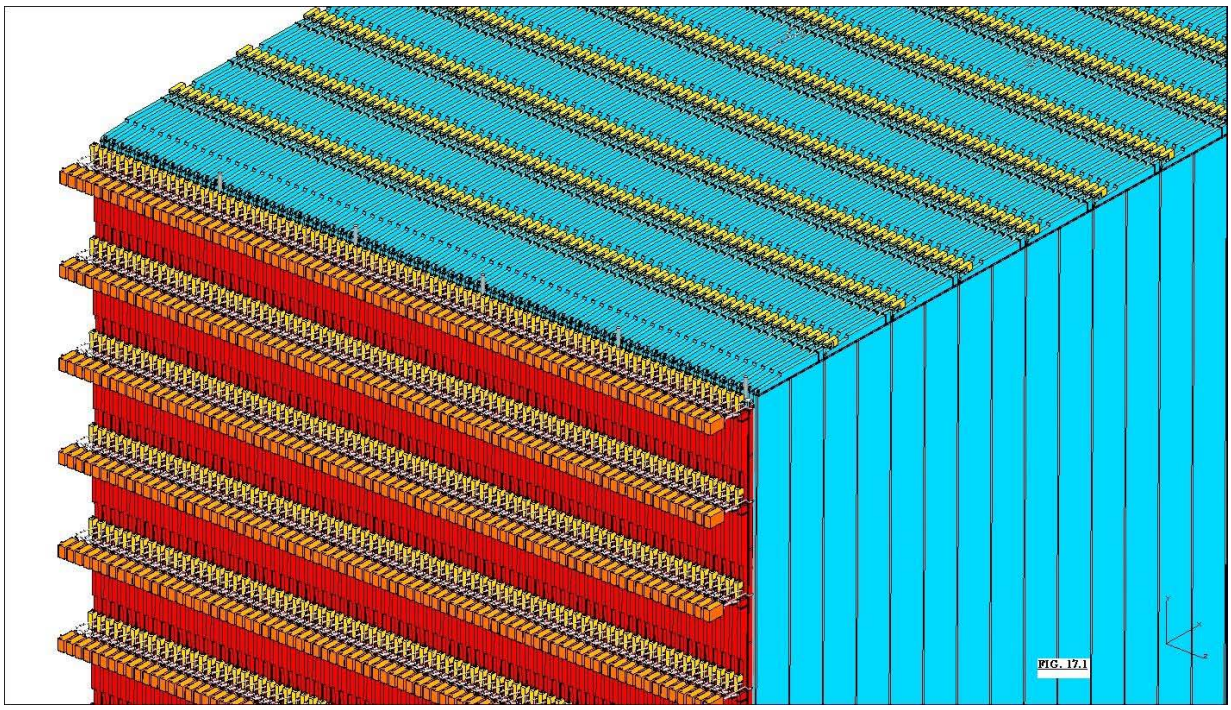

Fig. 17.1: Top quarter of one superblock of the NOvA far detector. Each superblock consists five 31-plane blocks. Blocks consist of alternating planes of twelve horizontal or twelve vertical modules. Superblocks begin and end with planes of vertical modules.

Total mass in active volume	15,004 metric tons (without manifolds, end seals, base pallets and bottom filler grout)
Mass of rigid PVC extrusions	4,501 metric tons
Mass of PVC edge stiffeners	1.328 metric tons
Mass of PVC expansion gap spacers	0.792 metric tons
Mass of liquid scintillator	10,376 metric tons (3,213,660 gallons)
Liquid scintillator	Mineral oil base with 4.1% pseudocumene as the scintillant, PPO and bis-MSB waveshifters added.
Active mass fraction	70%
Active height × width	15.494 m × 15.494 m
Detector length	66.9 m
Number of planes	1003 (505 vertical, 498 horizontal) 33 blocks (20 "A" and 13 "B") 32 blocks with 31 planes each, 1 block with 11 planes
Radiation length per plane	~ 0.15
Mass of adhesive between planes	121 metric tons
Mass of adhesive between module extrusions	0.557 metric tons
Mass of filler grout in active volume	3.031 metric tons
Modules per plane	12
Module outer wall thickness	3.3 mm in horizontal cells, 4.8 mm in vertical cells
Module inner web thickness	2.3 mm in horizontal cells, 3.3 mm in vertical cells
Module width	1.3 m
Module length	15.647 m
Maximum hydrostatic pressure in modules	18.79 psi (vertical), 1.58 psi (horizontal)
Cells per module	32
Cell interior width × depth, horizontal cells vertical cells	 3.71 cm × 5.94 cm 3.60 cm x 5.64 cm
Total number of cells	385,152
Total number of modules	12,036
Wavelength-shifting fiber	0.7 mm diameter double clad fiber with 300 ppm K27
Total WLS fiber length	13,000 km
Total WLS fiber mass	5 metric tons (0.735 tons is not displaced by scintillator)

Table 17.1: Summary of far detector parameters. See NOVA-doc-2066 for sources of parameters.

17.2 Technical Design Criteria

The detector assembly R&D task, WBS 1.8, has provided a structural design for the far detector that meets physics performance criteria and is mechanically stable during all stages of the assembly process and throughout the operational lifetime of the detector. The primary task for WBS 2.9 is to provide equipment and procedures for assembling the detector in a safe and environmentally responsible manner, including quality assurance procedures to ensure that the structure meets all performance and mechanical stability requirements. The completed detector will be stable against the long-term effects of PVC creep and aging of materials for a minimum of 20 years. Chapter 12, Section 12.5, describes the effects of creep on the strength of PVC extrusions in detail. An important aspect of the assembly process is the safe transfer of liquid scintillator (70% of the detector mass) from delivery tanker trucks to the detector modules, including quality assurance tests to ensure that contaminated scintillator is never put into the detector and that the origin of the scintillator in every detector module can be traced. Liquid scintillator spills and vapors will be carefully controlled throughout the assembly process.

The mechanical assembly of each 31-plane detector block consists of applying adhesive to the lower surfaces of all 12 PVC extrusion modules in every plane except the first (bottom) one. The modules will be precisely located and held in position while the adhesive cures, in order to achieve the design geometry and the adhesive bond strength used in the structural stability analyses. Each of the 33 blocks will be raised into place against the previously installed block. Blocks are sequentially filled with liquid scintillator and then outfitted with photodetectors and readout electronics as assembly proceeds. External light that could affect the photodetectors is prevented from entering the detector by the thickness of the vertical extrusions, by the opaque module manifolds and by black paint on the exposed surfaces of the thin-walled horizontal extrusions. After the final block is installed, the block pivoter is left in place to act as the north bookend. The last three blocks are then filled and outfitted.

The NOνA far detector is unique in its composition and scale, and many of the assembly tasks are beyond our direct experience. Lack of relevant experience at this size and scale presents technical, cost and schedule risks that can only be mitigated by acquiring relevant experience. A number of the first 16-cell NOνA extrusions are being used to build and test small-scale (a few meters by a few layers) prototype structures to verify finite-element analysis (FEA) predictions. Many of the 16-cell extrusions are being cut to our full 15.5 m length and will be used for realistic time and motion studies. Full length extrusions will be used to benchmark our procedures for assembling extrusion modules into planes. We will also use full length extrusions to build a full-height, partial-width, 2-block prototype that will be raised to the vertical position. A full-height, full-width, multi-plane prototype will also be assembled (but not raised) to optimize block assembly procedures and to measure manpower and time requirements. These studies will help us to understand the structural and handling details with appropriately sized objects and allow us to verify requirements for the block pivoter.

17.3 Overview of the Far Detector Assembly Procedure

Completed and fully tested PVC modules from the extrusion module factories are delivered to the far detector hall where they are assembled into blocks of alternating horizontal and vertical planes. Each plane consists of 12 extrusion modules. Thirty-one planes of modules are glued together into a strong structure of alternating vertical and horizontal layers called a block. There are two types of blocks, each weighing 127 metric tons. An “A” block begins and ends with planes of vertical modules. A “B” block begins and ends with planes of horizontal modules. Three “A” blocks and two “B” blocks (A-B-A-B-A) form a superblock. There are no spaces between the extrusions in adjacent blocks. There is a 2-cm expansion gap between adjacent superblocks to prevent superblocks from touching after they filled with scintillator. The full

detector consists of 33 blocks, arranged as six 5-block superblocks and one 3-block superblock (A-B-A).

The first block is erected and placed against the concrete bookend at the south end of the detector hall. Each subsequent block is placed against the previously erected block. The bookend structure is strong enough to resist any buckling deformation that could be exerted by the structural failure of blocks in the completed detector. The expansion gaps, which allow for swelling of the extrusions when they are filled with scintillator, are described in more detail below. Expansion gaps between superblocks are formed by gluing 2-cm-thick by 30-cm-high by 15.5-m-long PVC spacers between the top 30 cm of the blocks adjacent to the gap. Block spacer thicknesses are adjusted to maintain a vertical detector face as the assembly progresses. The deformations of empty blocks during raising, and of filled blocks in the completed detector, are limited by stiff steel base pallets that are built into each block as it is assembled.

The extrusion modules are handled using vacuum lifting fixtures attached to an overhead crane. Empty horizontal modules weigh 320 kg and vertical modules weigh 436 kg. An automatic adhesive dispenser rotates each module bottom-side-up, applies 32 beads of adhesive to the top surface, and rotates it back again so that the glue is on the bottom. A heavy roller presses each module accurately into position and spreads the glue out evenly. The requirements for the NOνA structural adhesive are described in NOVA-doc-145 and the requirements for the adhesive dispenser are described in NOVA-doc-144.

The planes are assembled horizontally on the same device that raises them to the vertical orientation and moves them against the previously erected block. The device is known as the "block pivoter" and looks like a giant fork-lift with a detachable steel block-base pallet instead of forks. The block pivoter is shown in the horizontal position in Figure 17.2 and in the vertical position in Figure 17.3

Cable trays, chilled water loops, power distribution boxes and other electronics infrastructure are installed on each set of two adjacent blocks after they are erected. This equipment does not interfere with the liquid scintillator filling process. Scintillator vapor vent lines and expansion tanks are also installed during this period.

The filling of a superblock with liquid scintillator begins as soon as the last block in the superblock is installed. Long before this operation is completed, the first block of the next superblock will be in place. It serves as a temporary "bookend" to control any unexpected transient movements during the filling process. Figure 17.4 shows the front-end electronics boxes mounted to module manifolds on the top and side of a superblock. After filling, each block is outfitted with APDs, front-end electronics boxes, and associated infrastructure. The final (11-plane) block of the detector is glued to the block pivoter during assembly. After it is erected, the pivoter remains in place to serve as the north bookend. Additional structural members are installed to strengthen it sufficiently to resist the forces resulting from any unanticipated block-buckling structural failure.

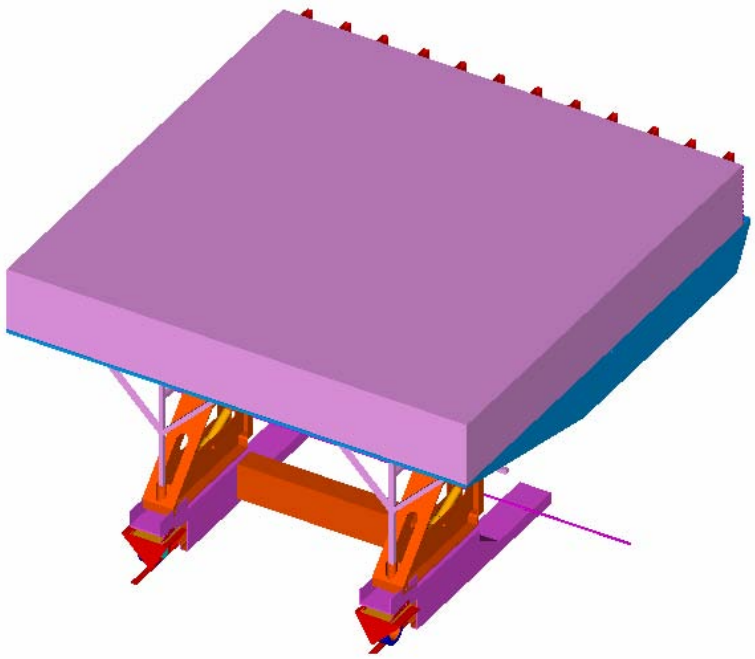

Fig. 17.2: The NOνA block pivoter, supporting an assembled block, in its horizontal position. The block pivoter is used in this position to assemble modules into alternating horizontal and vertical planes to form a 31-plane block. The edge of the block-base pallet is visible at the bottom edge of the block (top of figure).

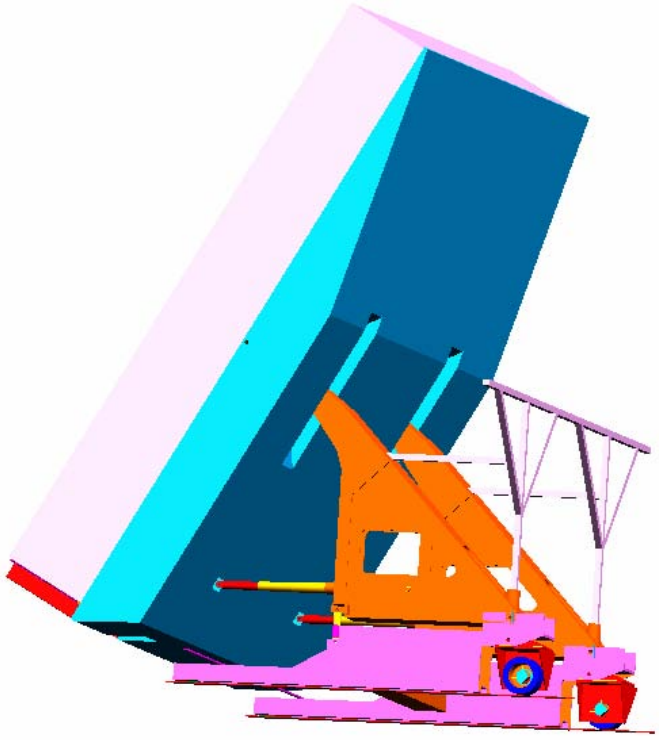

Fig. 17.3: The NOνA block pivoter in its vertical position. The steel block-base pallet on left side of the figure supports the block.

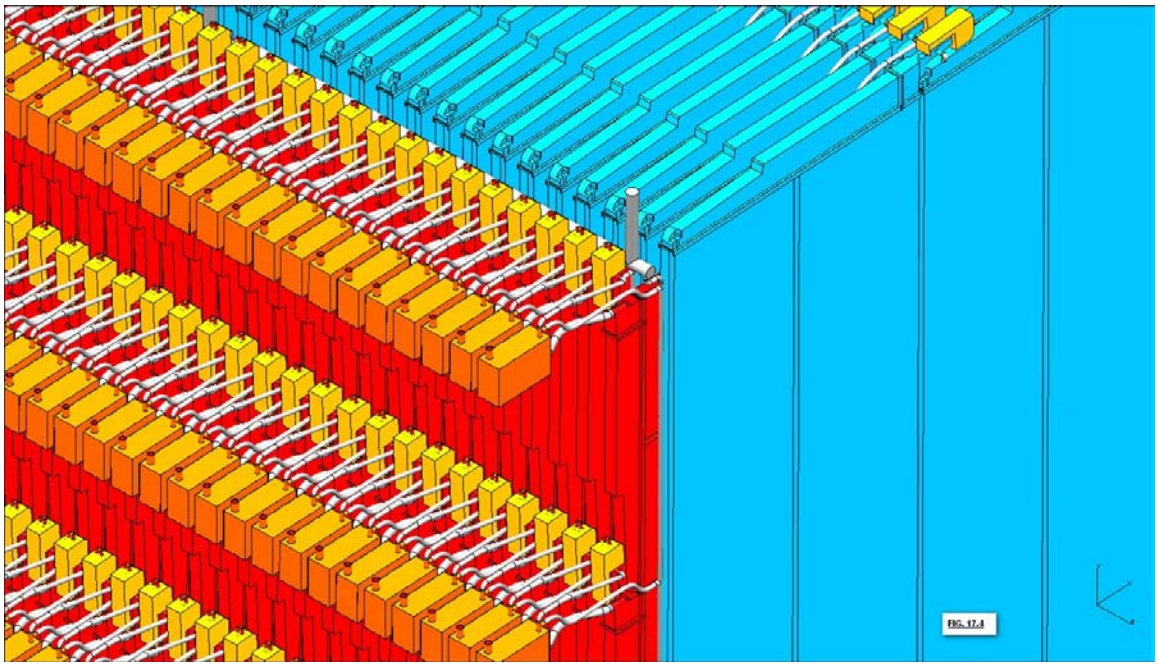

Fig. 17.4: Top corner of one block of a superblock, showing module manifolds and electronics boxes (L-shaped boxes on the top and sides) on alternating horizontal and vertical planes. The rectangular boxes on the left side of the drawing are the horizontal module expansion tanks.

17.4 Structural Issues

17.4.1 Introduction to the Structural Analysis

This section provides an executive summary of Sections 17.4, 17.5 and 17.6.

The primary structural requirement on the far detector is that it be mechanically stable at every stage of the assembly process and also throughout its nominal 20-year operating lifetime. A secondary requirement is that mechanical stability should not be compromised by filling the installed detector blocks with liquid scintillator while additional blocks are still being assembled and installed. Finite Element Analysis (FEA) calculations, performed with ANSYS, have been used to design a detector structure that meets these structural requirements without compromising physics sensitivity. We have checked the validity of the FEA techniques used in our detector model by using the same methods to predict the mechanical characteristics of many different types of prototype structures and comparing predictions with actual measurements of stresses and deformations.

The mechanical integrity of the detector structure depends critically on the strength of the adhesive bonds attaching horizontal modules to the adjacent planes of vertical modules that support their weight. Each horizontal module is fully supported by these bonds, since the lowest modules cannot support the accumulated weight of the upper modules. The Devcon 60 acrylic adhesive has been selected specifically because of its superior ability to support the shear and peel stresses within these bonds. The strength of this adhesive exceeds the maximum calculated stresses by a factor of five or more. We have interpreted “mechanical stability” of the assembled detector as a requirement for a safety factor of five against buckling, under conservative assumptions about the PVC modulus, the strength of adhesive bonds and the presence of isolated

anomalies such as failed adhesive bonds and leaky modules that cannot be filled with scintillator. The structural design described here meets these requirements.

Mechanical stability during the assembly period is assured by the stability of individual, freestanding 31-plane blocks, subject only to a "top-guided" constraint. Such a block has a safety factor against buckling of more than ten when empty and more than five for six months after filling. In practice, blocks are not completely filled until they are already substantially constrained by the close proximity of adjacent blocks, which increases the buckling safety factor significantly. Long-term stability is more complicated because creep effects can decrease the modulus of PVC under stress by as much as a factor of five over the 20-year operating lifetime of the experiment. In this case, stability is achieved by constraining the installed detector blocks between two strong bookend structures and by limiting the total accumulated space between all blocks to be less than about eight inches. After 20 years, creep weakened blocks will have deformed and partially filled the gaps between them. Eventually, the pressure that deformed blocks exert on each other (and on the bookends) will cause the webs of horizontal modules (the weakest structural element) to buckle, but this would not occur until long after the 20-year design lifetime.

The swelling of detector modules under hydrostatic pressure complicates the design of a structure that allows filling with liquid scintillator to begin before all blocks are installed. FEA calculations show that hydrostatic swelling propagates from plane to plane. This produces unacceptably high PVC stresses in the outside planes of structures with large numbers of planes in contact with each other. We have observed such propagation in multi-plane prototype structures and found it to be in agreement with predictions. The far detector design incorporates 2-cm expansion gaps every 155 planes (five blocks) to stop the propagation of swelling before very large stress levels are reached. The incorporation of expansion gaps between 5-block superblocks allows the filling of a superblock to begin as soon as its last block has been installed. The total length of all expansion gaps in the full detector must not exceed the limit imposed by long-term structural stability, as described above.

The stresses and deformations of the installed detector blocks will be measured continuously during the assembly and operation periods. The detector stability monitor system incorporates strain gauges, pressure sensors and laser position monitors to provide real-time data for comparison with FEA model predictions of detector mechanical characteristics. Detector filling would be suspended if significant deviations from predicted stress or deformation levels were detected. Filling could resume after the deviations were understood and corrective actions taken. In the worst case, the vertical modules in the remaining detector would be only partially filled to reduce hydrostatic swelling. In this case, detector filling would be completed only after block installation was complete and the second bookend had been installed.

The following sections describe in detail the calculations and prototype tests used to validate the mechanical characteristics of the far detector design.

17.4.2 Structural Design Strategy

The NOvA detector is constructed from alternating layers (planes) of 15.5-m long vertical and horizontal PVC extrusion modules, connected together by adhesive bonds between layers. The basic structural unit of the detector is a subassembly of 31 planes of PVC extrusion modules called a block. The modules in each block are glued together in a horizontal orientation on the block pivoter. Each of the 33 blocks in the 15 kton detector is rotated to a vertical orientation after the adhesive has cured. The far detector is constructed from two types of blocks. "A" blocks have planes of vertical modules on both outside faces, while "B" blocks have planes of horizontal modules on both outside faces. Sets of five sequential blocks, called superblocks, are separated by 2-cm expansion gaps, to accommodate the swelling of the PVC extrusions under hydrostatic pressure. Every superblock begins and ends with an A block, but A and B blocks alternate within

a superblock. Figure 17.1 shows one of six 5-block superblocks. In addition to these superblocks, a single 3-block superblock is required to complete the 33-block detector.

The bottom of each vertical module is subjected to 19 psi hydrostatic pressure after it is filled with liquid scintillator. The horizontal modules are supported by the vertical modules through the adhesive bonds. There is a small gap between the horizontal extrusions within a plane so there is no load transfer between them. The top of each horizontal module is at atmospheric pressure, so it needs to withstand only a small hydrostatic pressure plus the weight of its PVC and scintillator. The vertical extrusions have thicker walls than the horizontal extrusions in order to reduce stresses in the adhesive that connects them.

The use of plastic as a key structural element of such a large edifice presents a number of engineering challenges. The optimization of the far detector structural design, described in the remainder of this Section and in Section 17.5, is based on the following construction and stability conditions.

- During construction, the detector blocks are mechanically stable and act as independent, self-supporting structures.
- Individual blocks are filled with liquid scintillator as soon as possible, while installation of subsequent blocks is still in progress, in order to allow data taking to proceed.
- The expansion gaps between superblocks are large enough that the swelling of PVC extrusions under hydrostatic pressure is not transferred to adjacent superblocks.
- When the last block is in place, the second bookend is installed.
- The long-term stability of the detector against block buckling is achieved by limiting the amount of deformation any given block can have, by restraining the array of 33 blocks between the north and south bookends.
- Long-term deformations of the filled detector blocks could result from a decrease in PVC strength from plastic creep effects. If a block deforms or buckles to fill the neighboring expansion gaps, it is supported adequately to prevent any further deformation.

17.4.3 PVC and Adhesive Stresses

The strengths of the adhesive bonds between extrusions are critical to the success of this design. The PVC is the main structural element of the detector and is also required to provide a high level of reflectivity to ensure sufficient light output from the detector. In parallel with the structural design studies described here, NOvA engineers were developing a special PVC formulation with high reflectivity. Samples of the final NOvA PVC formulation were not available for most of the experimental tests described in the following sections, although all types of PVC tested to date have very similar mechanical properties. NOvA R&D studies of long-term creep effects in PVC (Chapter 12) give quantitative predictions that are incorporated into the structural design of the detector. The prediction of creep weakening of the PVC modulus based on measurements of PET-B PVC is the one we believe best reflects the properties of NOvA PVC over time. A second, more pessimistic prediction was derived from measurements of another early PVC formulation, NOvA-2.

Figure 17.5 and Table 17.2 show the predictions of PVC modulus variation over time for both of these models. For the structural design we have attempted to bracket our analysis between these two predictions. We believe that this technique, coupled with a requirement of a stability safety factor of five for both PVC and adhesive stresses, ensures structural stability against time dependent effects. Also, we have set a target of 600 psi as a maximum von Mises stress in the PVC at any point in time. (Von Mises stress is a measure of the combined stress that is calculated from the stress components provided by the FEA analysis.) Based on the Engineered Materials Handbook [1] we believe that if the PVC stress is kept below this value, then the PVC will remain in the viscoelastic range where the value of the modulus is not stress dependent and a single value of the modulus can be used to model the structure.

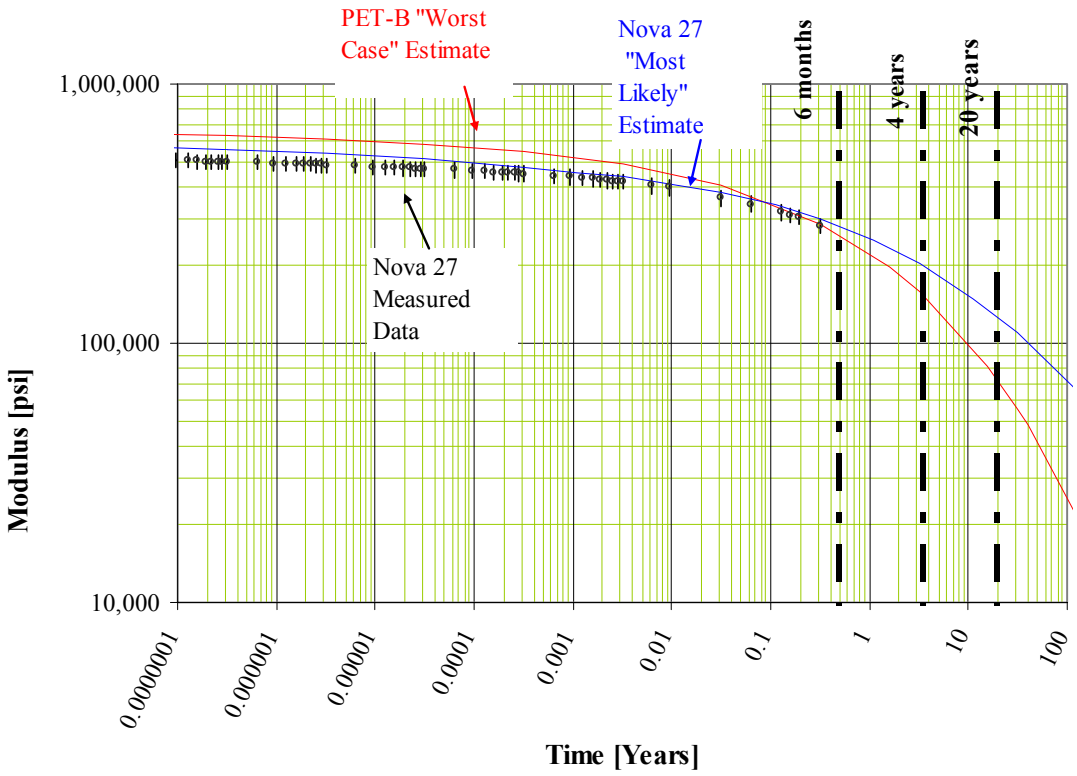

Fig. 17.5: Projected time variation of the PVC modulus caused by creep effects. "Most Likely Estimate" is the creep modulus in the middle of the range estimated by our consultant [2, 3]. Table 17.2 gives numerical values for the PVC modulus at important times on both curves. This figure is the same as Figure 12.24 in Section 12.6, which discusses it in more detail.

The adhesive between detector planes is also critical to the mechanical integrity of the structure. The adhesive will be applied over large surfaces, so ES&H concerns about vapor release and control have been important considerations in our selection of the plane adhesive. The adhesive must also have a work life of about 20 minutes to match the handling time estimates for PVC extrusion modules during far detector assembly. We have selected Devcon Plastic Welder 60, which is a special formulation of Devcon's Plastic Welder II, as the baseline adhesive. Devcon developed this formulation specifically to satisfy NOvA requirements for high shear and peel strength (average shear strength of 1200 psi and peel strength of 115 lb/in) and a work life of 30 minutes. Devcon 60 is substantially stronger than our earlier choice of 3M 2216 epoxy, and superseded it as our baseline adhesive as soon as we were convinced that ES&H concerns about Devcon's methyl methacrylate vapor control could be mitigated (Section 17.7.1).

Creep Condition	Year	Modulus (psi) for the "Worst Case Estimate" in Fig 17.5	Modulus (psi) for the "Most Likely Estimate" in Fig 17.5	Comments
Modulus at 6 Months	0.5	262,631	292,488	6 months in the maximum time over which creep can occur between the assembly of a superblock and completion of filling
Modulus at 2 years	2	183,244	235,341	2 years is the schedule for assembly of the detector
Modulus at 4 years	4	145,544	205,195	This TDR assumes the 140,000 psi value as a worst case where the assembly time might get extended to four years before the second bookend is in place.
Years between start of test station creep measurements and first assembly of Far Detector	Five	134,011	195,454	This means that we will know the first part of the creep curve for our specific PVC before construction begins. The error bars in Fig 17.5 indicate the two curves will be separated by about 2 standard deviations at that time.
Modulus at 20 years	20	72,046	136,965	This TDR assumes a 20 year "life" requirement for the detector and we use the lower "Worst Case" value of the modulus for structure performance at 20 years. This value translates into structural requirements for the bookends
Estimated year that the "Best Estimate" equals the "Most Conservative Prediction" 20 year value	120	n/a	n/a	If the "Most Likely Estimate" curve is correct, then our structure and bookend design may actually have a very long lifetime.

Table 17.2: Values extracted from Figure 17.5. This illustrates our conservative approach to the PVC structure design. One should not infer larger safety factors based on the ratio of "Best Estimate" to "Most Conservative Estimate" moduli since the modulus enters safety factor calculations in different ways depending on the failure mode analyzed.

Based on an evaluation of the published engineering literature on the design of plastic and adhesive structures, NOvA engineers have concluded that a safety factor of five is needed in a unique structure such as the NOvA far detector, which is constructed completely from PVC extrusion modules bonded together. Throughout the analysis, a safety factor of five for stress and buckling stability has been a design requirement.

Our analysis of the NOvA far detector structure is divided into four distinct stages:

- Analysis of individual extrusions determines the optimum extrusion profile.
- Analysis of 31-plane blocks and adhesive stresses ensures that individual blocks can be assembled and filled and will stand as independent structures during the detector assembly process. Separate analyses are performed for A-type and B-type blocks.
- Stability of independent 31-plane blocks is required during assembly and throughout the 20-year lifetime of the detector.
- Long-term stability of the entire structure is provided by expansion gaps between superblocks during assembly and filling, and by the second bookend that is installed at the end of the construction.

The following sections describe each of these stages of analysis.

17.4.4 Analysis of Individual Extrusions

The initial analysis examined individual PVC extrusions (Chapter 12), with the goal of optimizing the profile for extrudability, minimum PVC stress, and optimum reflectivity.

The pressure at the bottom of a vertical extrusion is 19 psi due to the 15.5-m head of the liquid scintillator. The horizontal extrusion modules are not subjected to this pressure because they are supported individually by adjacent vertical extrusions and there is no accumulation of weight from the extrusions above. Within the structure individual extrusions are adhered together and provide support to each other. The first stage of our analysis examines the properties of an individual vertical extrusion under internal hydrostatic pressure.

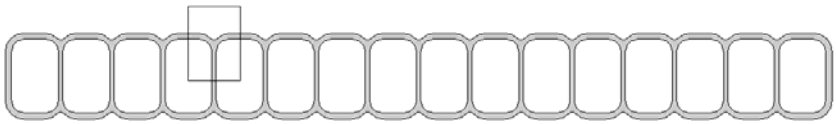

Fig. 17.6: Schematic representation of a PVC extrusion profile. The square box outlines the part of the extrusion used for the FEA calculations described in this section.

The geometry of the extrusions and cells was optimized to minimize the stress within an extrusion to approximately 600 psi when subjected to the maximum 19 psi hydrostatic pressure. The 600 psi stress was chosen based on initial understanding of the PVC creep as described above. The baseline extrusion geometry for horizontal modules has a 3.0-mm thick outer wall and a 2.0-mm thick inner web. Vertical module extrusions have 4.5-mm thick outer walls and 3.0-mm thick inner webs. The difference in wall thickness between vertical and horizontal extrusions minimizes adhesive stresses as described below. The internal radii reduce the stress concentrations in the corners of a cell. In addition, the outer scallops are required by the extruding process. The scallop geometry gives the same wall thickness all around the outer perimeter, which is important for uniform cooling in the final stages of the extrusion process. The ratio of the outer wall thickness to the inner web thickness was recommended by extruders as being optimal for reliable extruding. A PVC modulus used in this analysis, E = 150 ksi, is the predicted value of the modulus at 20 years (or at 10 years for the pessimistic prediction). Figure 17.7 shows the stress distribution within the PVC extrusion under the 19 psi internal pressure and Figure 17.8 shows the corresponding deflections.

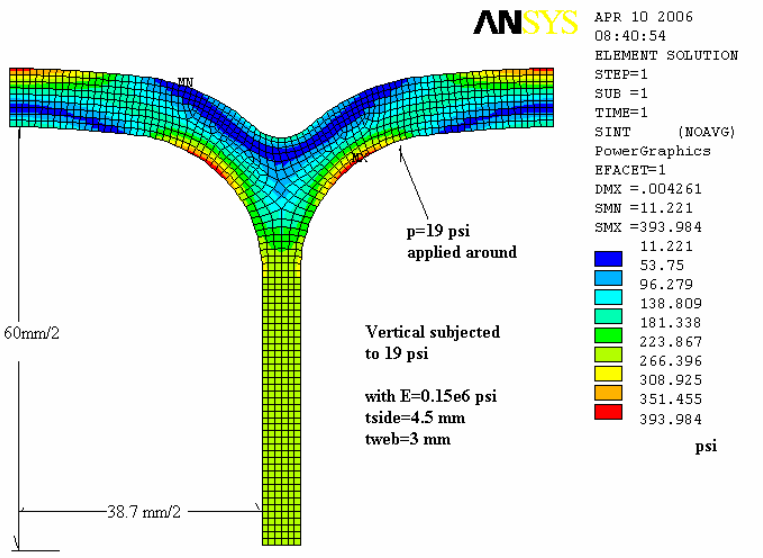

Fig. 17.7: Stress distribution for one vertical extrusion cell subjected to 19 psi with E = 150 ksi.

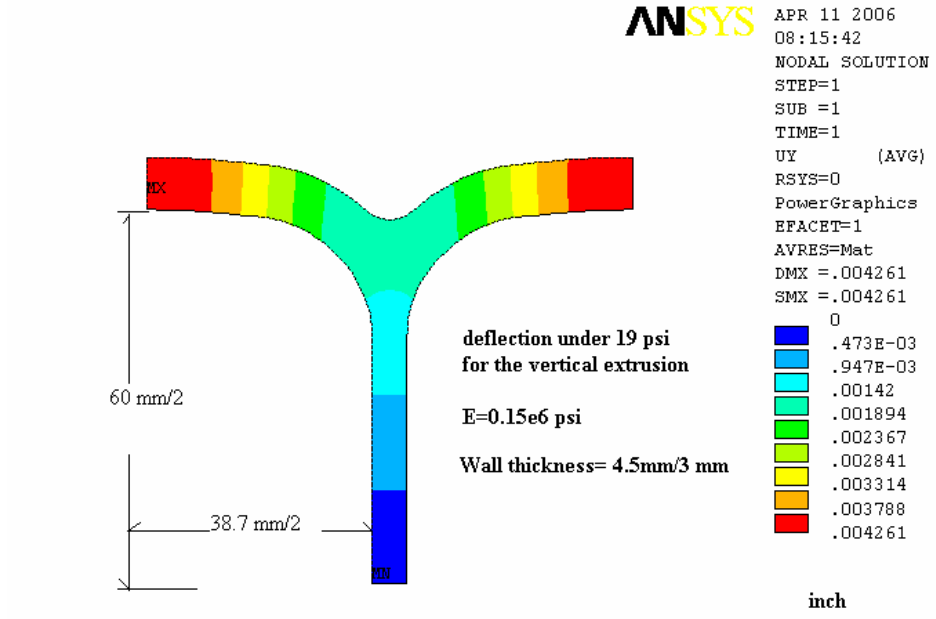

Fig. 17.8: Deflections in a single vertical extrusion cell subjected to 19 psi with E = 150 ksi.

17.4.5 Vertical Module Edge Stiffeners

Most of the surface area of vertical modules within a block is in contact with other modules and does not deform significantly under hydrostatic pressure. However, this is not the case for the outside edges of vertical module planes or for the edges of vertical modules within a plane that have gaps between them. The edges of outside vertical modules are strengthened by 3.2-mm thick by 4-cm wide by 7.3-m high PVC edge stiffeners, which are glued in place during module assembly, effectively increasing PVC thickness along these edges. NOVA-doc-1204 describes the design of the edge stiffeners. Gaps between vertical modules within a plane are filled with epoxy grout after each plane is assembled, as described in Section 17.6.8.

The end cell of PVC extrusion with a 3.88-cm x 6.0-cm cell size has a 6 cm span length, which is subjected to 19 psi hydrostatic load. With a 4.5 mm exterior wall, the maximum bending stress is around 1,200 psi. A 2-mm thick stiffener plate would bring the stress down to ~ 700 psi, similar to stresses in other parts of the structure. (Actual stiffeners make use of commercially available stock material, 3.2-mm thick.) The peak shear stress at the corner for the adhesive layer is around 581 psi, which is substantially below the average shear strength of ~1000 psi. The adhesive peeling force at the corner is 3.7 lbf/in, which is also below to the peeling strength of 19 lbf/in. The 20-year PVC modulus of 75 ksi is used for the design calculation described in NOVA-doc-1204. The stiffener reduces the end-cell stress from 1300 psi to 719 psi and the end-cell deflection from 0.088 inches to 0.034 inches.

Figure 17.9 shows the calculated deflection of an end cell with a 2-mm by 4-cm stiffener under 19 psi hydrostatic pressure. Figure 17.10 is a CAD drawing of the bottom of a vertical extrusion with an edge stiffener attached.

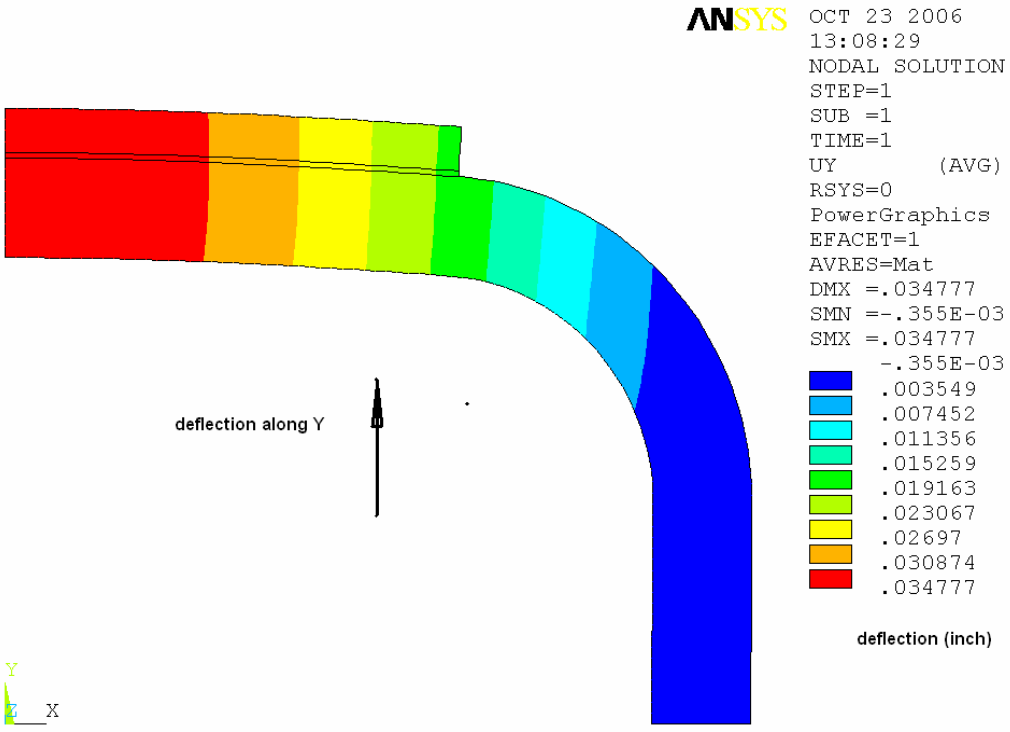

Fig. 17.9: Deflections in an outside vertical extrusion cell, with edge stiffener attached, subjected to 19 psi with a PVC modulus of E = 75 ksi.

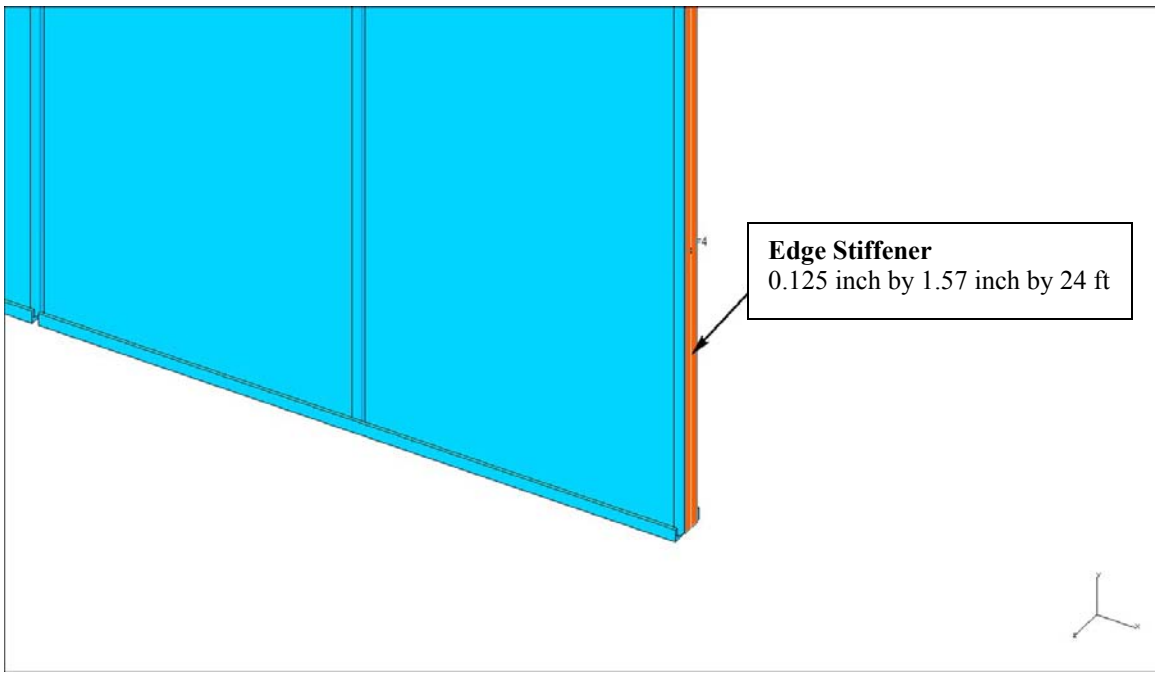

Fig. 17.10: CAD drawing of the bottom of an outside vertical module with edge stiffener attached.

17.5 Analysis of Detector Block Structure

Modeling a 31-plane block of PVC extrusion modules is challenging. In order to have accurate predictions of the structure's behavior from the FEA model, it is important to use a very high mesh density to get convergence of the solution. This requires state-of-the-art computer hardware and software because the number of degrees of freedom in the model is very large. The following sections describe the FEA models we have developed for the PVC extrusion modules and the adhesive bonds between them.

17.5.1 Modeling of Adhesive Joints

Optimizing the geometry of a single PVC extrusion to withstand the 19 psi hydrostatic pressure within the detector is a fairly straightforward analysis. However, once these extrusions are bonded together to form a monolithic structure, the structural analysis problem becomes much more complex. The buckling/stress/deflection analyses of the assembled detector that are described in the sections below depend on how the adhesive bond is modeled.

The analysis of an adhesive-bonded joint is considered to be a challenging FEA task. The difficulty arises from both the complex stress state within the adhesive and the constraints imposed by computational capacity on the modeling of a complicated geometry. Several methods including the average stress method, the maximum stress method and fracture mechanics method are discussed in detail in Reference [1]. However, application of this approach to our large structure, with a 3-D 0.25-mm adhesive bond, would result in an FEA model of formidable size.

As an alternative, two widely used approaches were considered in this study of the structure. One is to extract the nodal force by assuming the interface between the vertical and horizontal plane will move together with a connected node – merged node. The second approach is to model the adhesive layer as three spring elements, as suggested by Tahmasebi [4] and Zhu & Keyward [5]. Two springs account for the in-plane shear stiffness of adhesive and one models the normal stiffness of adhesive. This can be implemented by using a spring element (#14) in

ANSYS. Both of these methods were tried for NOvA adhesive bonds and yielded the same result. For the analysis presented below the spring element method was used.

Throughout the analysis the nodal forces area is extracted and divided by its element area to calculate the average shear and normal stress around that location. By using a Mohr's circle, a maximum shear stress (principal shear stress) can be obtained as

$$\tau_{\max} = \sqrt{(\frac{\sigma_{normal}}{2})^2 + \tau^2}$$

This maximum average shear stress over the area of the element is calculated and compared to the average shear stress for the adhesive measured in double-lap shear tests of NOvA adhesive bonds. The ratio of measured average shear stress at bond failure to the maximum average shear stress from the FEA model is taken as the safety factor (SF) on the adhesive strength. This approach is similar to that described in Reference [1].

The FEA model for a 31-plane NOvA block is very large and it is only possible to extract the average adhesive stresses from it due to the size of the elements used. However, we were concerned that stress concentrations along the edges of the bond areas would cause progressive structural failure to occur. Following the methodology outlined in Reference [1], a highly detailed model of the bond joint in the structure was created in order to calculate potential stress concentrations in the adhesive. Next, we created a detailed FEA model of the standard ASTM tests used to measure the average strength of actual adhesive bonds. The peak stresses found in the model of the ASTM tests and in the detailed model of the detector bond joint were then compared when loaded to the average failure stress. We found that the ratio of the maximum stresses (safety factor) was similar to the ratio of the average stresses under this loading condition. We therefore believe that the safety factor (SF) calculated for average stresses will provide a SF that is similar to that for the peak stresses.

Instead of using a single element over the adhesive pad area, a refined mesh with more elements was used to obtain the stress variation over the bond area. A peak stress at the adhesive bond termination is used as the maximum calculated stress. A corresponding safety factor is calculated as:

SF= Maximum measured (test) peak stress/maximum calculated stress.

The difficulty here is the lack of actual "maximum measured peak stress" values. Conventional measurements and most available technical data sheets give only average stress data. These data are obtained by applying a force to the ASTM test piece up to its breaking point. The shear strength is calculated by the dividing the force over the overlap area (F/A psi) or a width of the overlap to give a peeling strength (F/width lbf/in). There are no measured data related to how this stress is distributed within the bond area and what the failure peak stresses are at the bond edge. A calculation of the safety factor is not valid without this information to account for peak stresses. To overcome this shortcoming, a maximum stress approach is proposed by Reference [1]. The idea is to produce a "quasi" stress distribution by modeling both the test specimen and the actual structure with FEAs using the same mesh size and element type. The stress distribution and its peak stress value at the bond termination is highly dependent upon the element type and mesh size. This is because geometry in the model has a sudden change (sharp corner, no filler radius and so on) causing a stress singularity where dissimilar materials are joined together. As the mesh density increases, the peak stresses correspondingly increase. By applying a similar mesh density for both the test piece and the actual NOvA geometry, as suggested in Reference [1], a similar stress singularity state should be expected.

17.5.1.1 Modeling the ASTM Tests

Figures 17.11 to 17.13 show test geometries and the corresponding FEA models for three ASTM tests of NOvA bonds: the double-lap test for shear and the T-shape and cleavage tests for peel. The actual tests used 3M 2216 epoxy (before the change of baseline plane adhesive to

Devcon 60). The FEA model uses a 3-D element with a 20-node brick element (higher order). The mesh size is 0.0625 inches (1.57 mm). The tests measured the force at failure and a stress distribution/peak stress was calculated.

Next, we use the same element type (20-node brick) and a very similar mesh size for a mini 3-D model of the NOvA geometry, shown in Figure 17.14. The model represents a pair of vertical and horizontal cells joined by an adhesive layer. The mesh size of 0.064 inches (1.65 mm) resulted in 1,300 nodes for the adhesive area and 37,000 nodes for the whole model. A 19-psi pressure is applied to the vertical extrusion with a symmetry boundary over the sides. A "free to move" boundary condition is used for the horizontal side. Both shear and peeling forces are calculated.

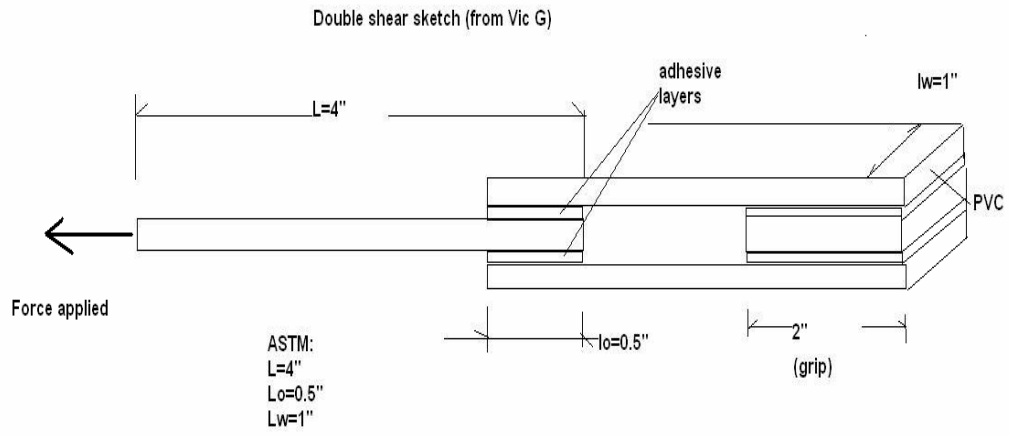

Fig. 17.11(a): Test specimen for double-lap test.

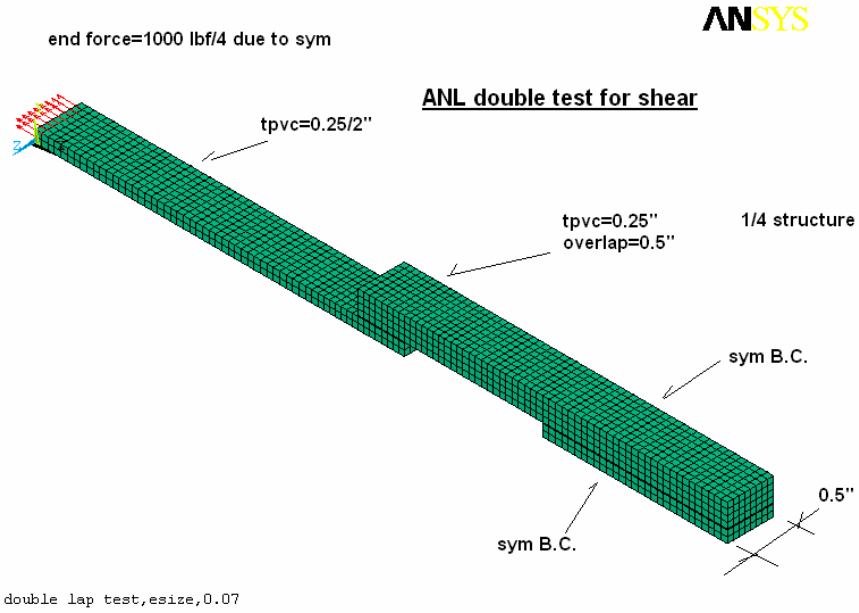

Fig. 17.11(b): FEA model for double-lap test.

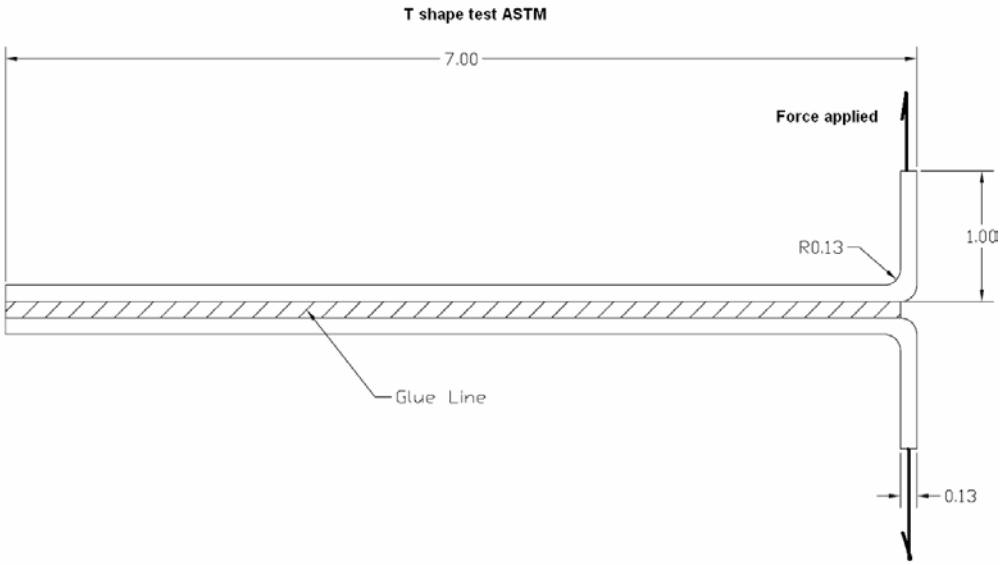

Fig. 17.12(a): T-shape test specimen.

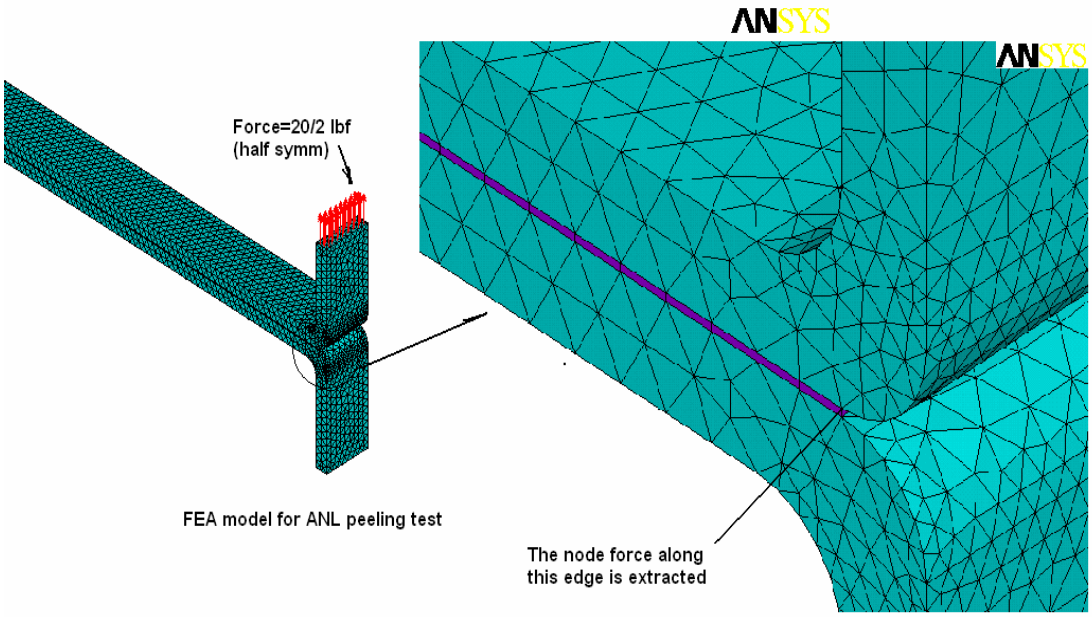

Fig. 17.12(b): FEA model for T-shape test.

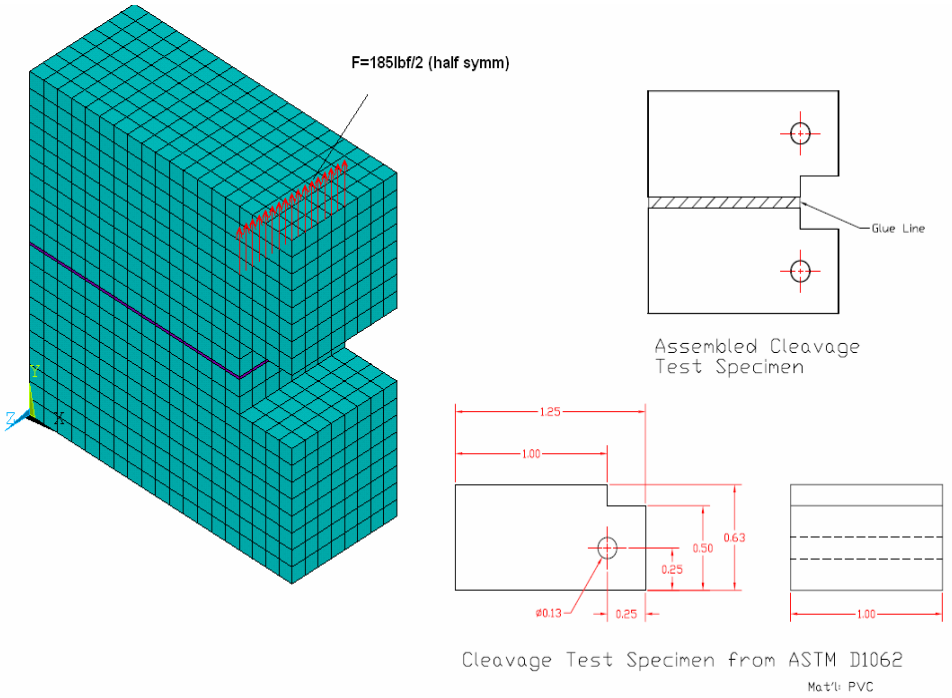

Fig. 17.13: The cleavage test specimen and FEA model.

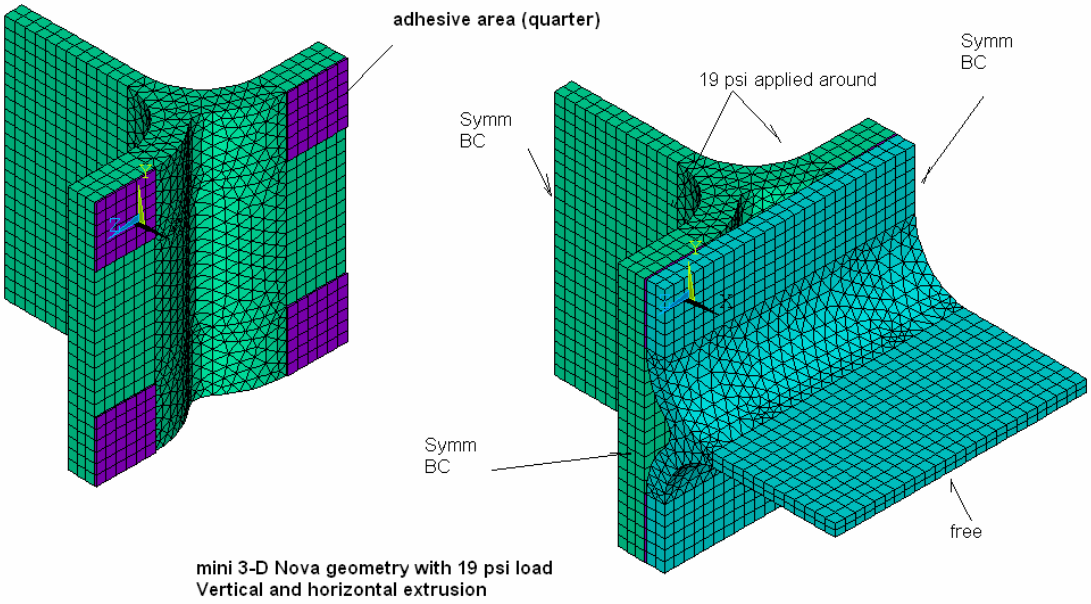

Fig. 17.14(a): Mini 3-D model for NOvA geometry.

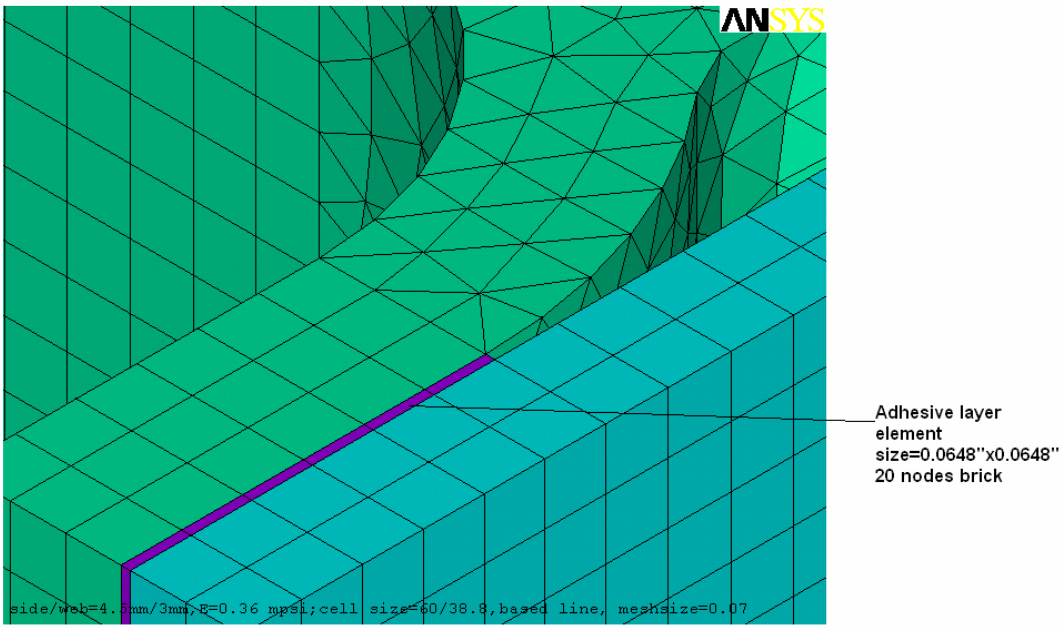

Fig. 17.14(b): The mesh over the adhesive layer in the NOvA mini 3-D model.

17.5.1.2 Peak Stresses in NOvA Structure Bond with ASTM Tests: Shear stress

Double-shear measurements of test specimens found that a force of 900 lbf was required to cause failure of the adhesive. This can be compared to a calculated peak stress of 4878 psi, using a mesh size of 0.0625 inches, as shown in Figures 17.15 and 17.16. With a similar mesh size for the mini 3-D model with 19 psi loading, the maximum shear stress is around 1130 psi, yielding a safety factor SF = 4878/1130 = 4.3. A detailed examination of the stress pattern showed that the peak stress of the double lap is mostly concentrated along the edge and is uniformly distributed along its width. However, the mini 3-D model shows that the peak stress is at the corner where the model has a sudden geometry change and dissimilar materials. The model calculation is therefore considered to be more severe in terms of the stress singularity, so the SF = 4.3 value calculated above is quite conservative.

Section 17.6.7 describes measurements of Devcon 60 shear strength in the actual detector geometry, using 3-layer assemblies of NOvA extrusions. The strengths found from standard ASTM tests closely match the strength measured in this test, indicating that these results are a good predictor of the strength that can be expected in the far detector geometry.

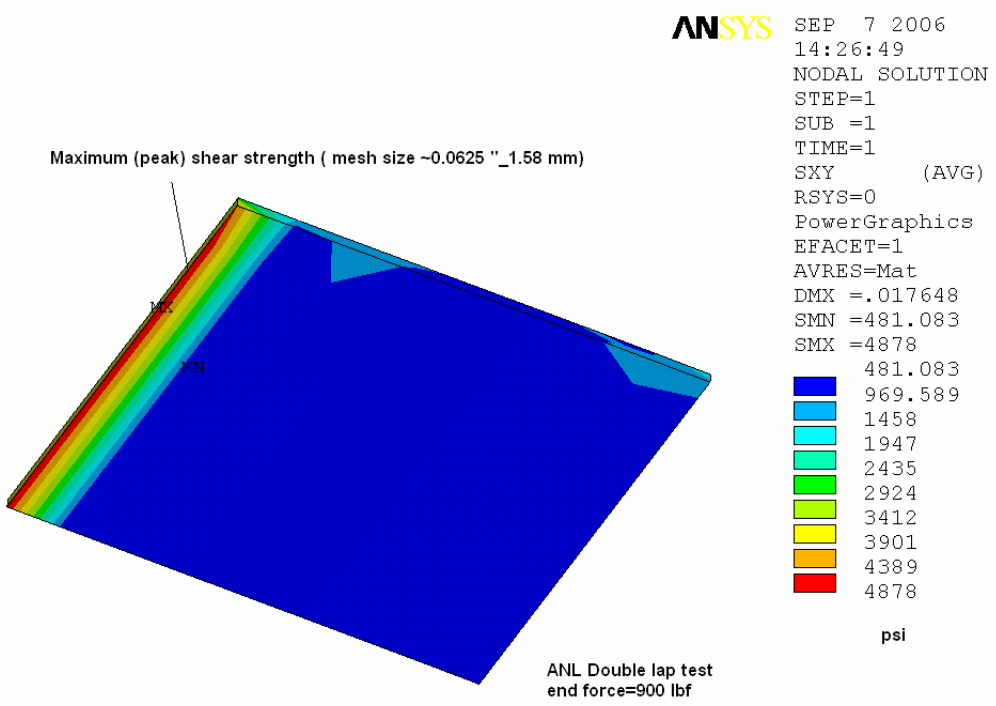


```
double lap test,esize,0.07
```

Fig. 17.15: The maximum shear strength calculation, based on the double-lap shear test.

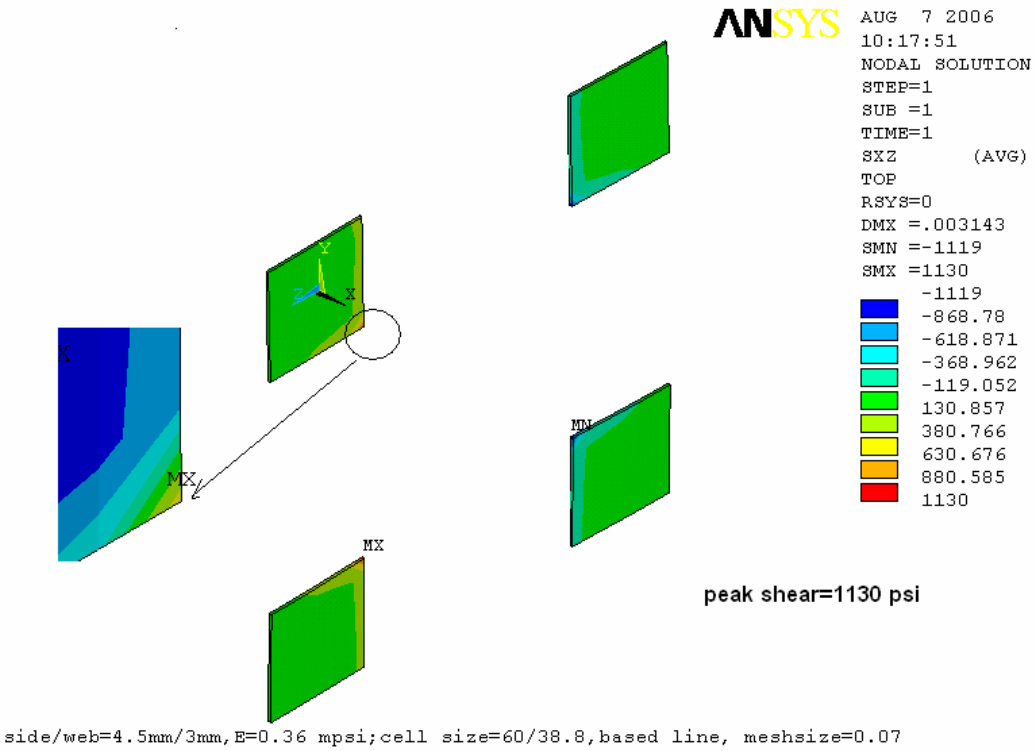


```
side/web=4.5mm/3mm,E=0.36 mpsi;cell size=60/38.8,based line, meshsize=0.07
```

Fig. 17.16: The calculated maximum shear stress, based on mini 3-D model.

17.5.1.3 Peak Stresses in NOvA Structure Bond: Peeling Force and Normal Stress

Our calculation of peak peeling force and normal stress begins with the FEA model for the T-shape and cleavage peel tests. The comparisons to test measurements are made as follows:

a) <u>The edge peeling force comparison</u>

We use a 3-D 20-node brick to model the T-shape test, in which a 20 lbf force was applied as shown in Figure 17.17. The element edge force along the bond termination line is extracted as shown in Figure 17.18. The maximum edge force is found to be 20 lbf/in. With a similar mesh size, an element edge (peeling) force is also extracted from the NOvA mini 3-D model shown in Figure 17.19. This gives 4.98 lbf/in, yielding a safety factor SF = 20/5 = 4.

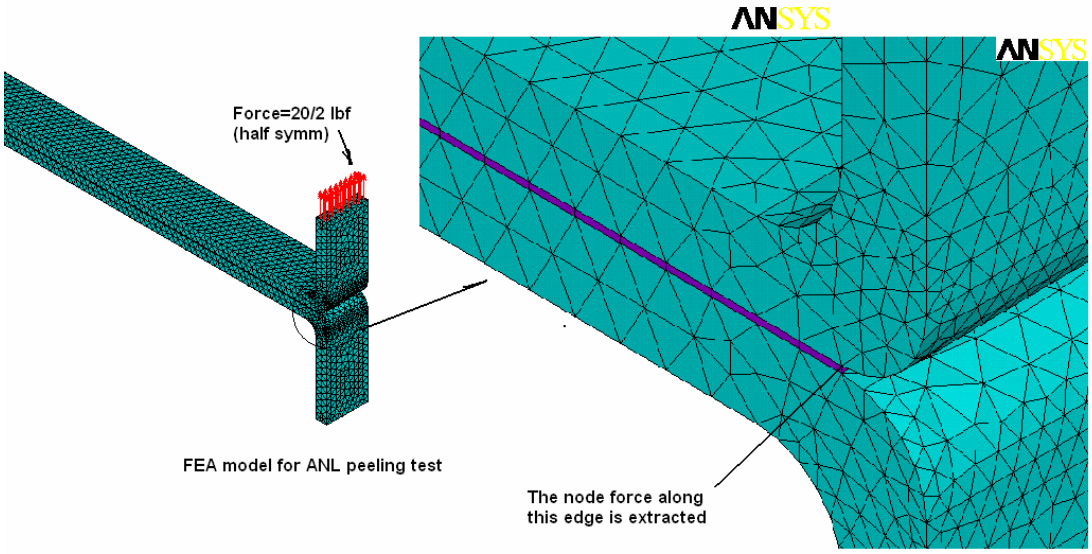

Fig. 17.17: The FEA model for peel test (F = 20/2 lbf applied).

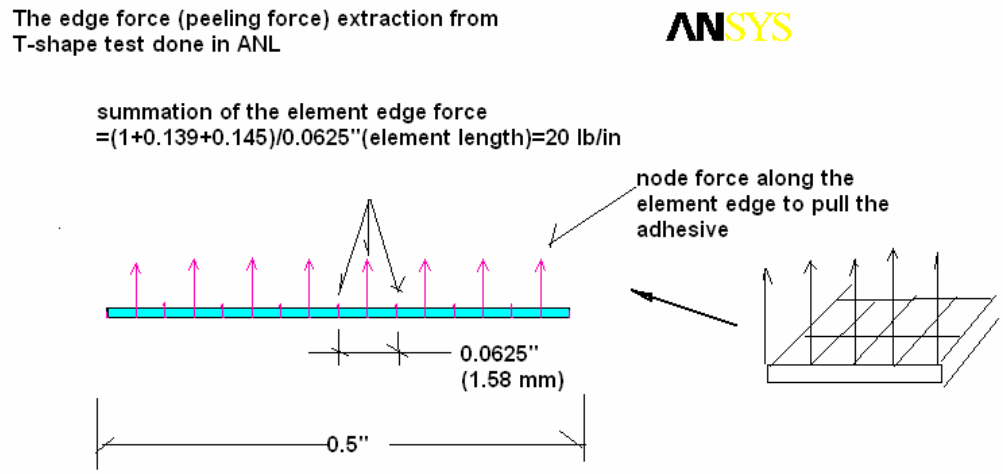

Fig. 17.18: The node force along the edge of the adhesive, extracted from T-shape test.

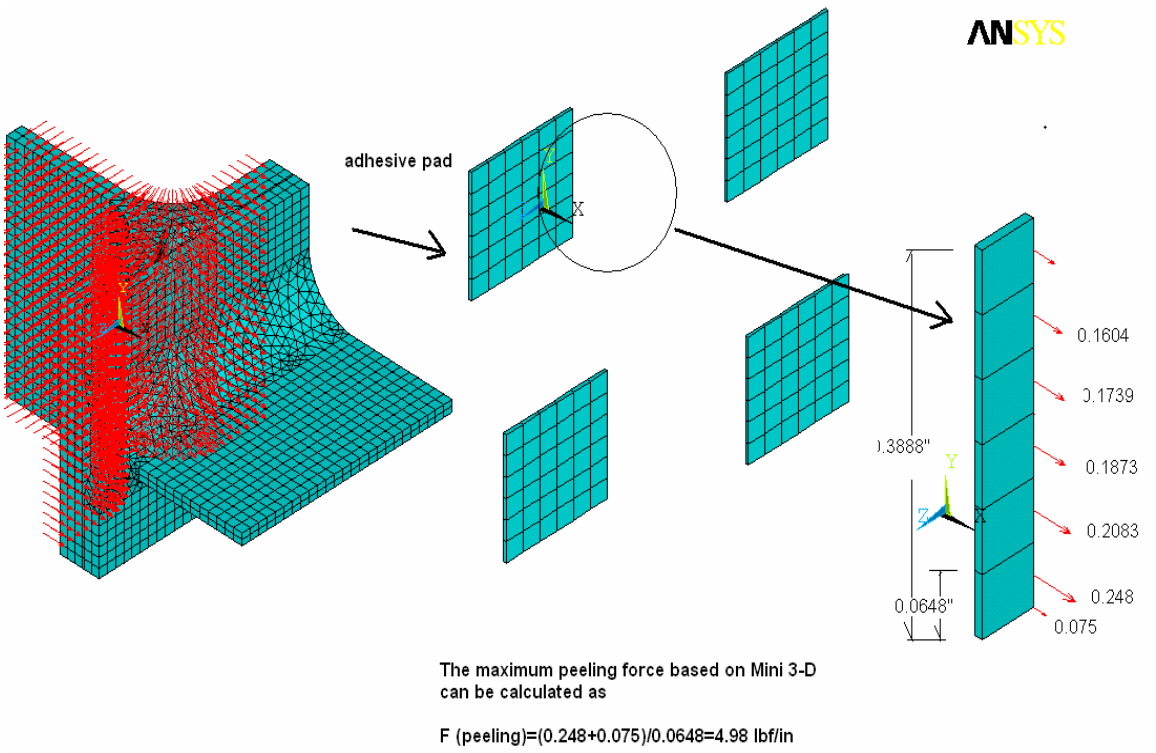

Fig. 17.19: The element edge force for the NOvA mini 3-D model.

b) <u>The normal stress comparison</u>

The calculation of normal adhesive stress in the T-shape test, shown in Figure 17.20, yields a peak value of 1661 psi. The peak stress is concentrated along the adhesive edge line and is uniformly distributed along its width. However, the normal stress in the mini 3-D model has a maximum value of 1300 psi, shown in Figure 17.21. This is concentrated in the corner where the stress singularity is more severe than in the actual T-shape test specimen. There are two ways to handle this difficulty. The first is to use the stress calculated one or two elements away from the corner, as shown in Figure 17.22. This gives a stress of 516 psi and a SF = 1661/516 = 3.2. The second method is to slightly modify the geometry for both T-shape and cleavage tests to produce a similar stress singularity pattern. Figure 17.23 shows the modified geometry, obtained by simply deleting a set of elements along the edge (about 0.0625 inches) to create two sides of the "geometry sudden change" effect, as in the mini 3-D model. A similar stress singularity pattern is observed. The peak stress is concentrated in the corner, rather than uniformly along the width. Figure 17.23 shows a normal peak stress of 3600 psi and a SF = 3912/1300 = 2.76.

A similar result is obtained from the cleavage test as shown in Figure 17.24. The edge force comparison yields SF = 19.8/5 = 4. The normal stress comparison with a slightly modified geometry similar to the T-shape yields a SF = 3912/1300 = 3.

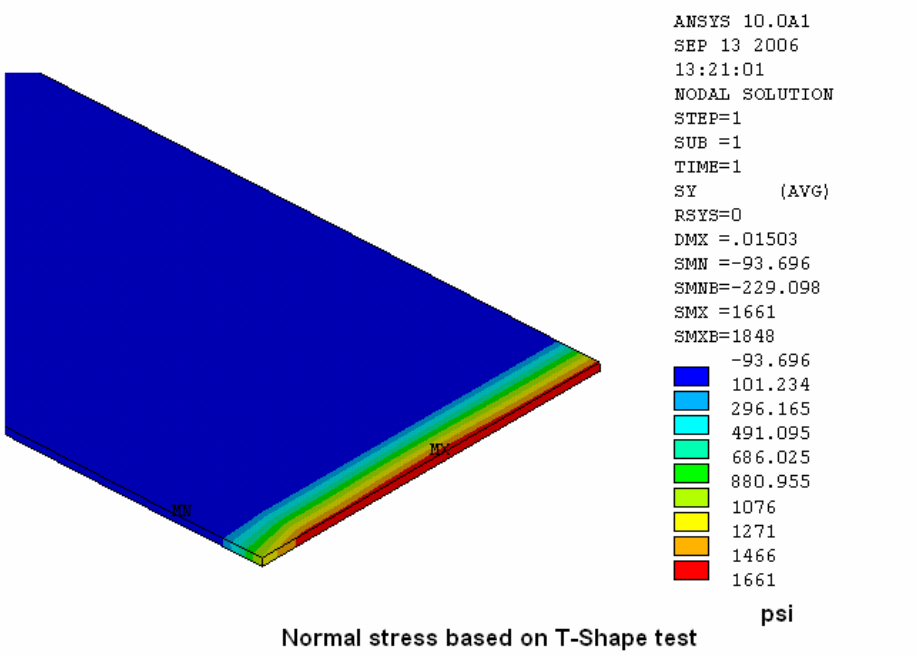

Fig. 17.20: Normal stress based on T-shape test.

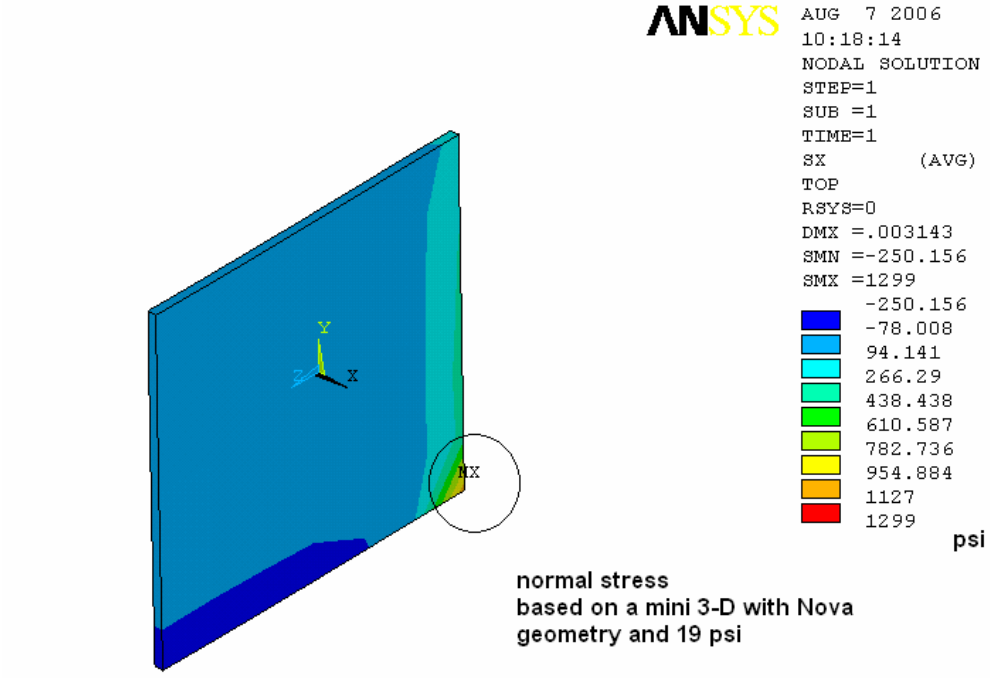

Fig. 17.21: Normal adhesive stress in the NOvA mini 3-D model with 19 psi.

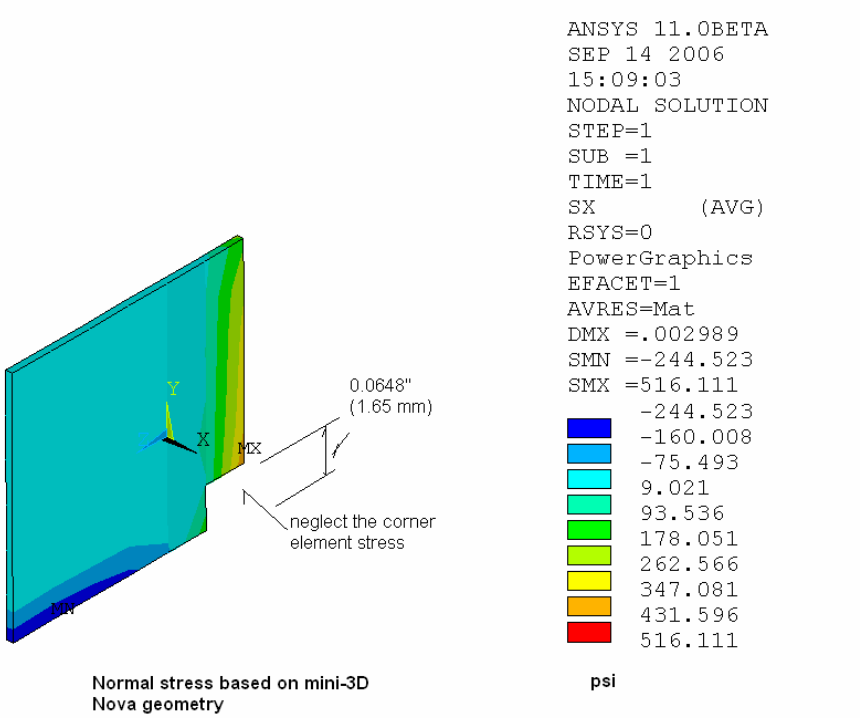

Fig. 17.22: Normal adhesive stress at 1.65 mm from the corner in the mini 3-D model with 19 psi.

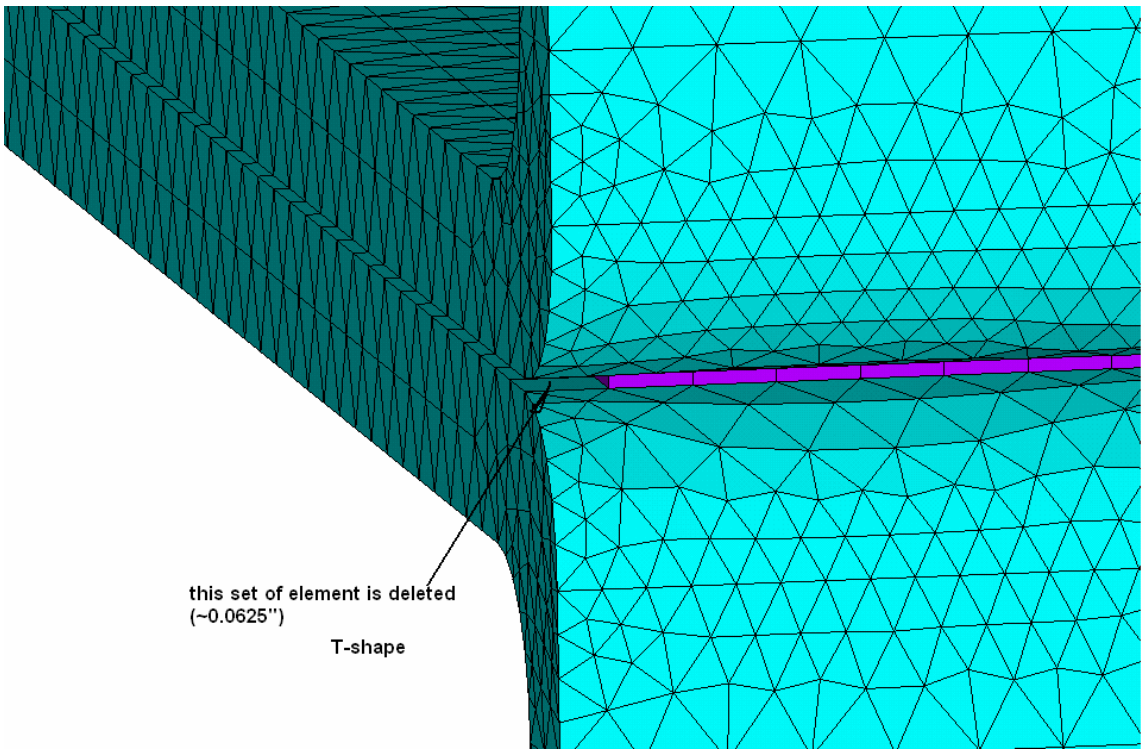

Fig. 17.23(a): The modified T-shape geometry.

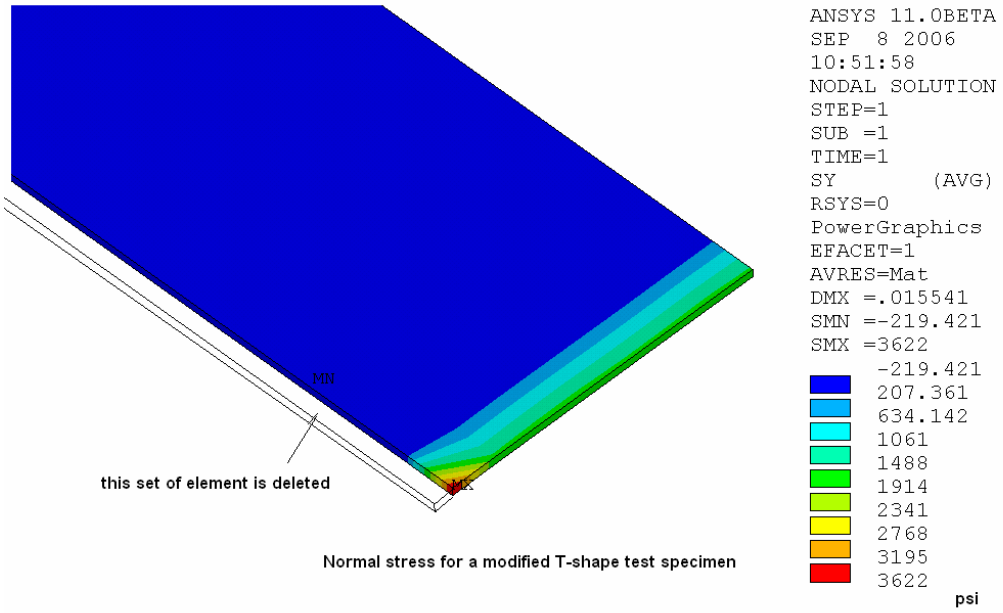

Fig. 17.23(b): Adhesive normal stress based on the slightly modified T-shape geometry.

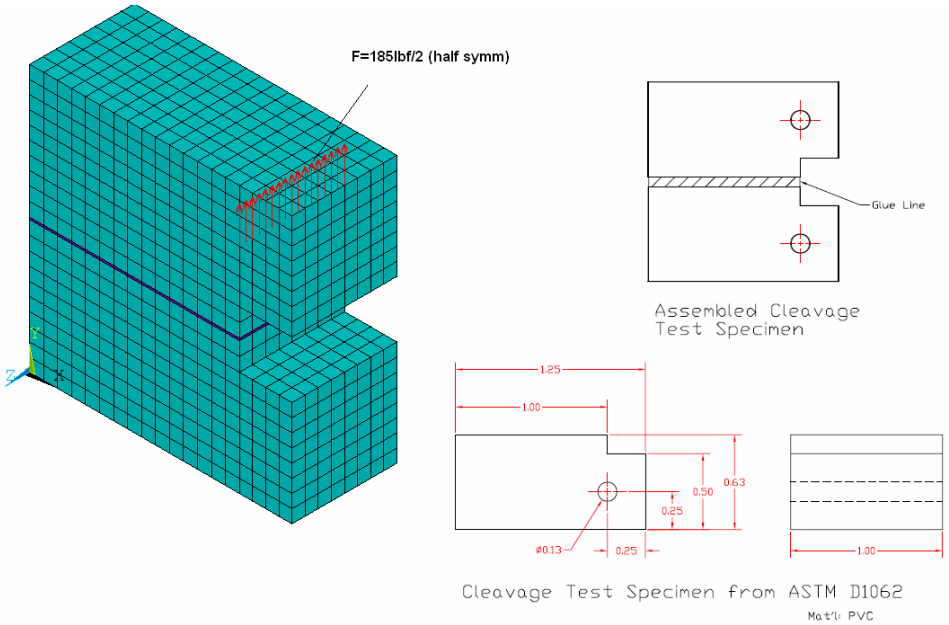

Fig. 17.24(a): The cleavage test geometry.

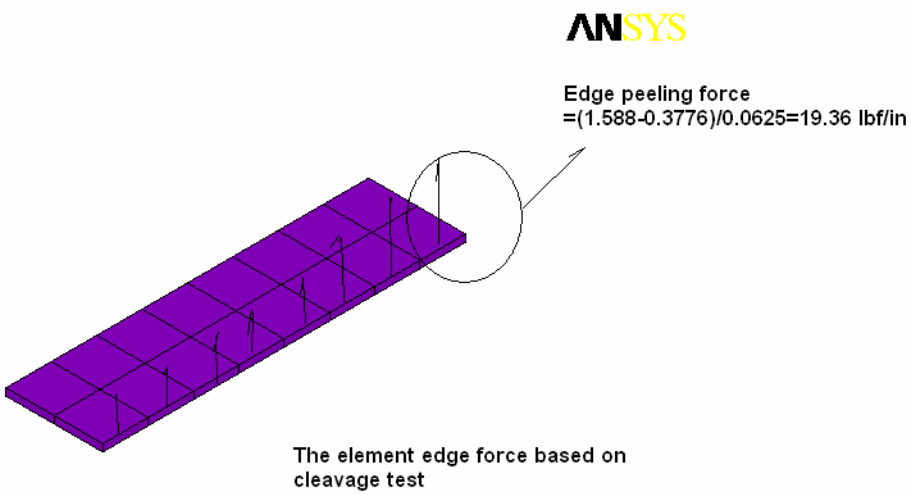

Fig. 17.24(b): The adhesive element edge force extraction from cleavage test.

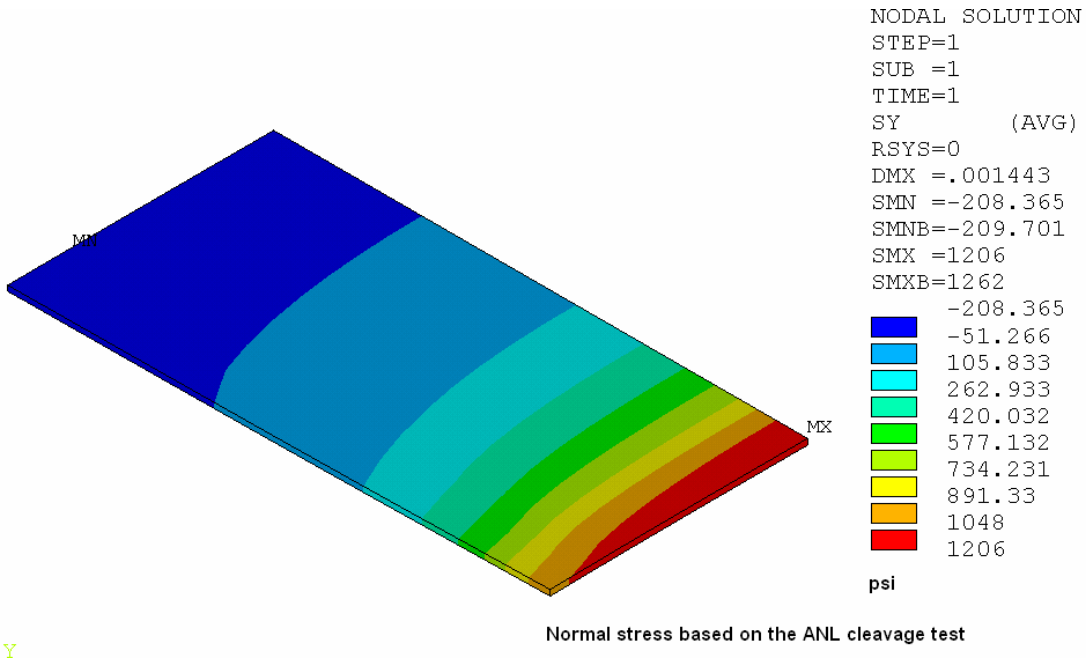

Fig. 17.24(c): Adhesive normal stress for cleavage test.

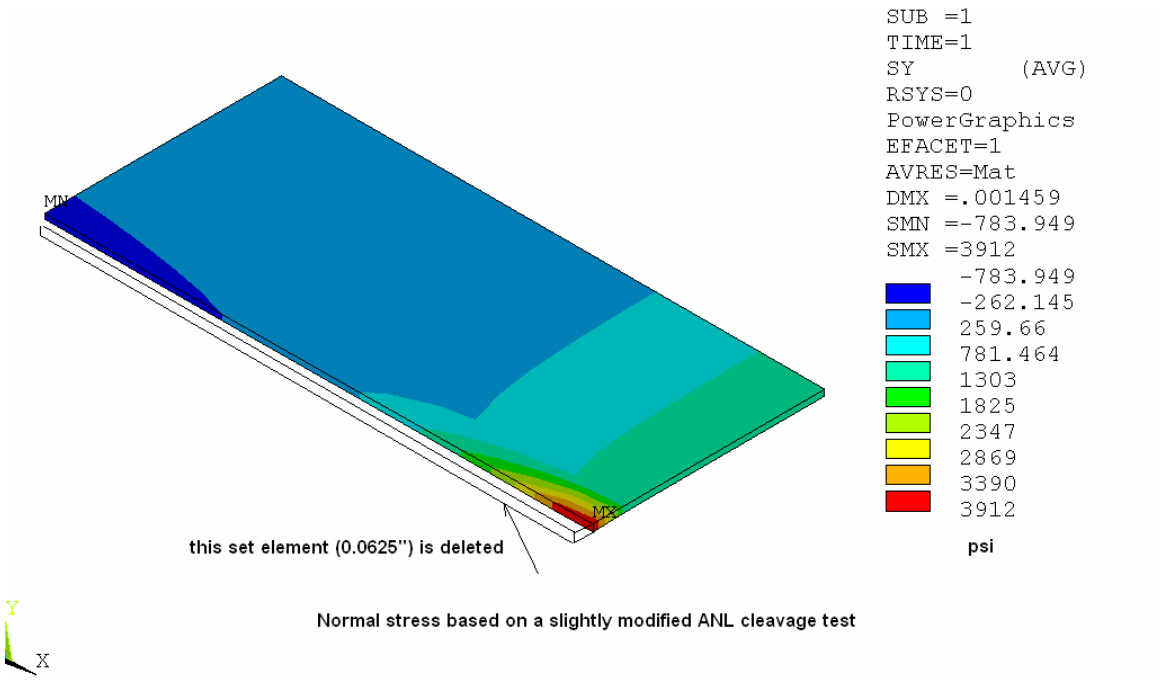

Fig. 17.24(d): Adhesive normal stress for slightly modified cleavage test.

17.5.1.4 Summary of Adhesive Bond Modeling

Tables 17.3, 17.4 and 17.5 summarize the results of shear and peel tests with 3M 2216 epoxy and compare them with FEA calculations to obtain adhesive bond strength safety factors. The safety factors for the shear and peel stresses are around 4.6 and 3, respectively, based on this refined mesh study. Since the adhesive stress analysis is considered to be very complex due to the complicated geometry being modeled and inability of the method to quantize the stress singularity at the bond termination, the analysis results are mainly used to provide guidelines for design optimization.

	Peak shear psi	Normal stress psi	Peeling force lbf/in	Von Mises stress psi	Mesh size 20 node brick
Mini 3-D (19 psi) Nova geometry	1130	1299 (or 500 psi, neglecting the corner)	4.98	2152	~0.0648 inch (~1.65 mm)

Table 17.3: Summary of results for mini 3-D model of NOvA geometry (19 psi, one pair of cells).

	Peak shear psi	Normal stress psi	Peeling force lbf/in	Von Mises stress psi	Mesh size
Double lap test for shear	4878			9564	~0.0625"
T-shape test for peeling		1661	20		~0.0625
Cleavage test for peeling		1206	19.8		~0.0625
Slightly modified T- shape geometry		3662			~0.0625
Slightly modified cleavage geometry		3912			~0.0625

Table 17.4: Summary adhesive strength results from shear and peel tests with 3M 2216 epoxy.

	SF peak shear stress	SF normal stress	SF Peeling force	SF Von Mises stress
Double-lap shear test	SF = 4878/1130 = 4.31			SF = 9564/2152 = 4.4
T-shape peel test		SF=1611/1300 =1.23	SF = 20/5 = 4	
Peeling strength from cleavage peel test		SF=1206/1300 =0.93	SF = 19.8/5 = 4	
Slightly modified T-shape peel test		SF = 3622/1300 = 2.76		
Slightly modified cleavage geometry		SF = 3912/1300 = 3.0		

Table 17.5: Summary of safety factor calculations from shear and peel tests for 3M 2216 epoxy.

17.5.2 Description of the FEA Model of Assembled Blocks

NOvA engineers have developed several finite element models for the NOvA far detector structure. An initial 2-D FEA model was used to calculate the stress due to 19 psi hydrostatic pressure in the vertical extrusions. Subsequently, a more complex model was developed to understand the complete block structure in terms of its stresses and stability. The actual PVC structure has a 15.5 m × 15.5 m cross section with 1003 layers of alternating horizontal and vertical PVC extrusion modules. The most efficient way to model this structure is to use the shell element (STIF 63/STIF 181 in ANSYS). This has characteristics similar to those of a beam element. To limit the size of the problem and reduce computational time, only a slice in the middle of the structure was modeled. A symmetry boundary condition was imposed on both sides to reflect the rest of the structure. The mesh size of the shell element is 0.5 inches to 0.7 inches, in a structure whose full height is ~600 inches. The resulting model has approximately 260,000 nodes and 6 degrees of freedom (DOF) per node, giving a total of 1.5 million DOF for a 31-plane block, without counting the spring elements used for the adhesive layers. We used "top free" and "bottom fixed" boundary conditions as a worst case. The hydrostatic load of 19 psi was applied linearly along the vertical extrusion and zero pressure was used for the horizontal extrusion. The density of PVC was increased to account for the weight of the liquid. This baseline model and its boundary conditions were modified many times to study the structural characteristics under different scenarios, as described in detail in NOVA-doc-1147, 1151, 1172, 1297, 1298, 1351, 1490 and 1876. Figure 17.25 shows basic structure of the FEA model.

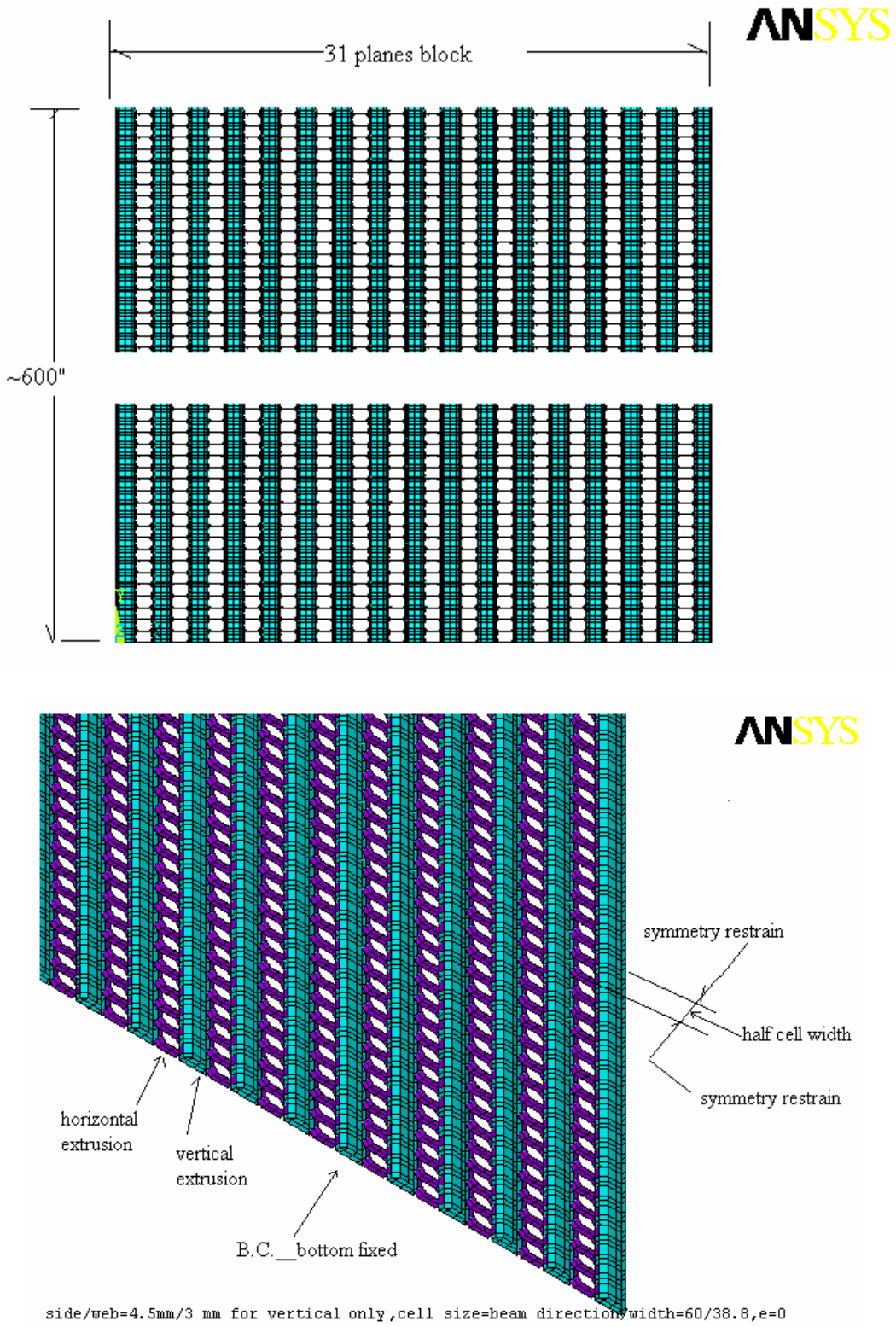

Fig.17.25: FEA model of the NOvA far detector with the shell element.

17.5.3 Analysis of a 31-Plane "A" Block

From a physics performance point of view, it is desirable to have as many planes of modules glued together into a block as possible. However, there are practical limits to how large a block can be, including the maximum physical size that can be constructed on the block pivoter, the allowable internal stresses within the block and the stability of the block.

We examined the stresses and deflections of the assembled planes, including stresses and deflections of the PVC and adhesive. This study used a PVC modulus for 4 years (E = 146 ksi), which is the maximum time period of the assembly, and for 20 years, which is the nominal operating lifetime of the detector. The analysis of A-type blocks, with planes of vertical modules on the outside faces, is treated in this section. Section 17.5.4 describes the analysis of B-type blocks, with planes of horizontal modules on the outside faces.

This initial series of analyses shows that the cumulative swelling at the bottom of the detector, due to the hydrostatic pressure in the vertical extrusions, increases with the number of planes in a block. This in turn increases the stresses in the PVC and in the adhesive supporting the horizontal extrusions. In order to keep the stresses within an acceptable range for the creep-weakened PVC, the number of planes within a block was limited to 31. The stresses in the PVC could be lowered further by reducing the number of planes within a block, however, below 31 planes the block buckling stability falls below the target safety factor of 5.

A second series of FEA models used a PVC modulus of 75 ksi as the worst case prediction for the modulus at 20 years. The calculation was done for 31, 59, 123 and 187 layers in a single block.

The results for 4-year and 20-year PVC modulus values are summarized in Tables 17.6 and 17.7, and in Figures 17.26 through 17.34. For 31 planes per block, the stresses and deflections for both PVC and adhesive are acceptable. As the number of planes per block increases, both the deflections and stresses of the PVC extrusions rise. The peel stress in the adhesive becomes unacceptably high for a block with more than 123 planes per block.

Figures 17.26 through 17.34 show that the maximum PVC stress occurs at the very bottom of the vertical extrusions. However, the FEA model does not include the support of extrusions by the module end seals. Therefore, the maximum stresses predicted by this analysis would not occur because of the additional strength provided to the vertical extrusions by the end seals. The remaining PVC stresses appear to be at an acceptable level after 20 years of PVC creep. However, the adhesive stresses were still of concern for 3M 2216 epoxy. The current baseline adhesive, Devcon Plastic Welder 60, provides 1200 psi shear strength and 115 lbs/in of peel strength, giving a safety factor of 5 for adhesive peel failure with 31 planes per block.

E=0.146 mpsi (4y)							
Number of the layers in a block	31	59	123	187	251	315	371
Total swelling (inch)	0.11	0.218	0.408	0.598	0.776	0.944	1.084
Von Mises stress (peak, psi)	776	866	969	1029	1071	1105	1129
Von Mises stress(excluding peak, psi)	497	564	644	691	726	752	772
Von Mises strain(peak, %)	0.53	0.6	0.66	0.7	0.73	0.75	0.77
Von Mises strain(excluding peak,%)	0.34	0.39	0.44	0.47	0.49	0.51	0.53
Adhesive shear stress (psi)	159	190	216	232	238	247	252
Adhesive Peeling force (lbf/in)	4.27	5,64	9.59	11.83	13.26	14.31	15.01

Table 17.6: Block properties versus number of planes/block for a 4-year PVC modulus.

E=0.075 mpsi (20 y)				
Number of the layers in a block	31	59	123	187
Total swelling (inch)	0.2	0.38	0.78	1.16
Von Mises stress(peak, psi)	776	866	969	1029
Von Mises stress(excluding peak, psi)	497	564	644	691
Von Mises strain(peak, %)	1	1.1	1.2	1.37
Von Mises strain(excluding peak,%)	0.6	0.7	0.8	0.9
Adhesive shear stress (psi)	162	188	217	233
Adhesive Peeling force (lbf/in)	4.31	5.23	9.52381	11.84

Table 17.7: Block properties versus number of planes/block for a 20-year PVC modulus.

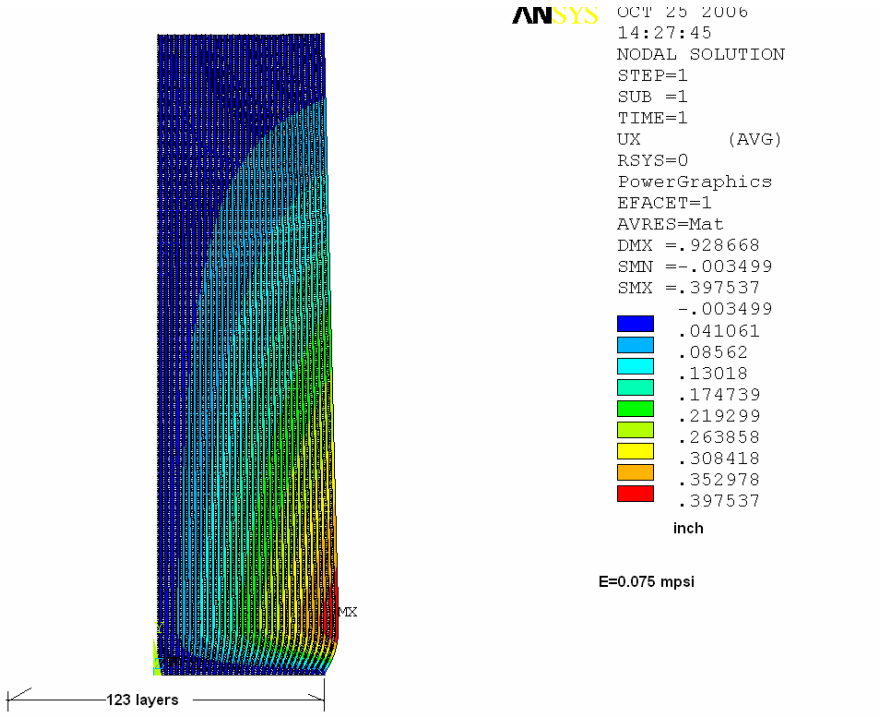

Fig. 17.26: The swelling shape for a NOvA A-type block at 20 years.

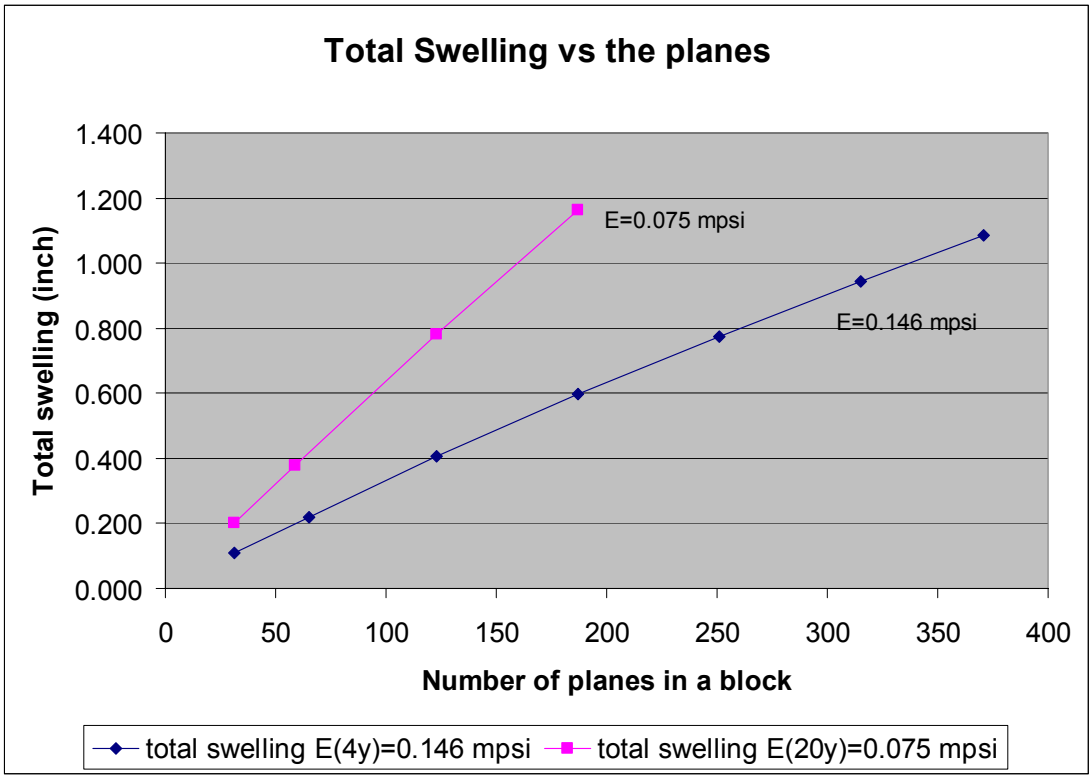

Fig. 17.27: Maximum swelling vs the number of planes per block.

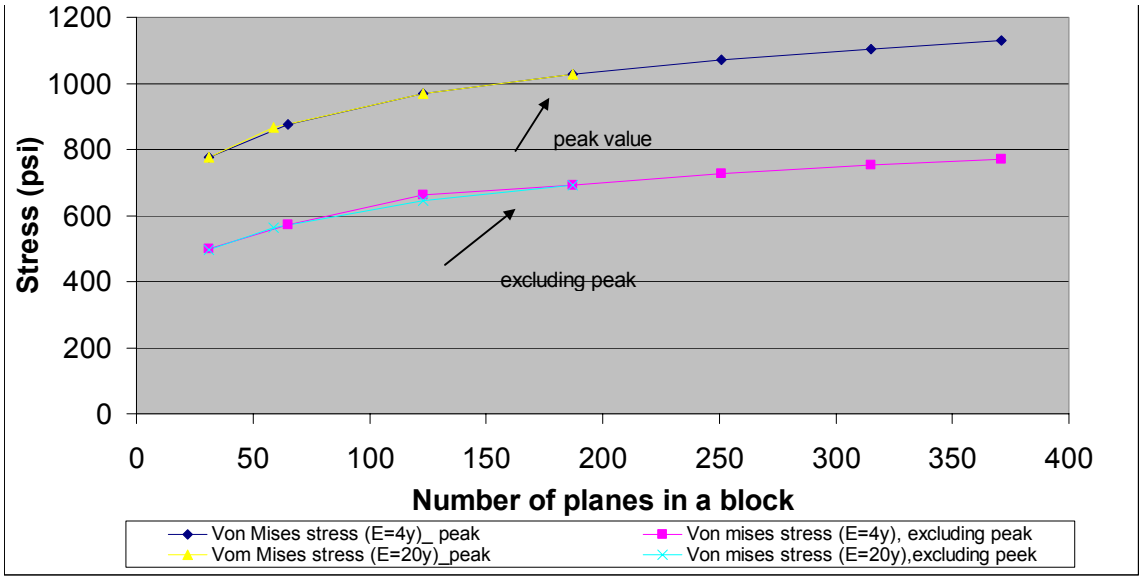

Fig. 17.28: Von Mises stress vs the number of planes per block at 4 years and 20 years.

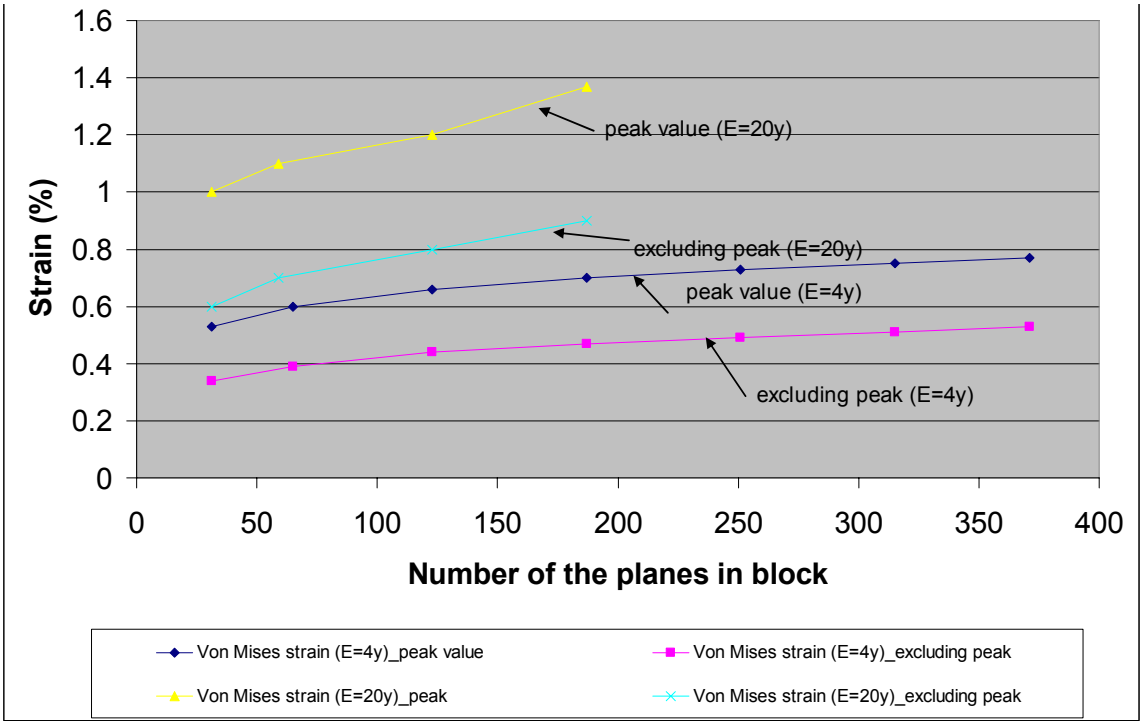

Fig. 17.29: Von Mises strain vs the number of planes per block at 4 years and 20 years.

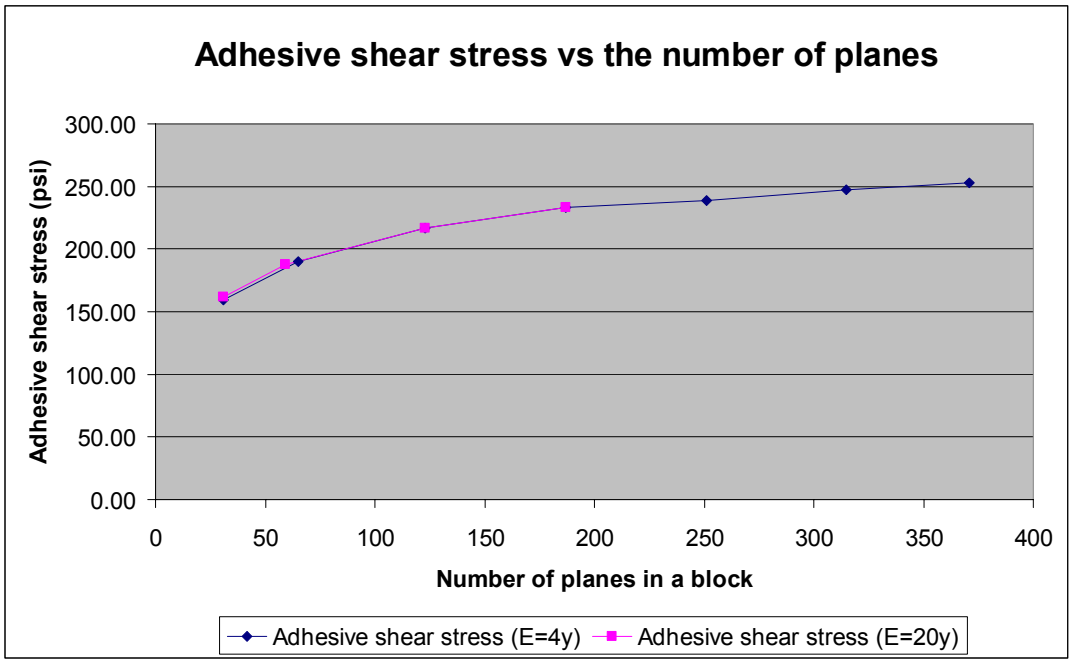

Fig. 17.30: Adhesive shear stress vs number of planes per block.

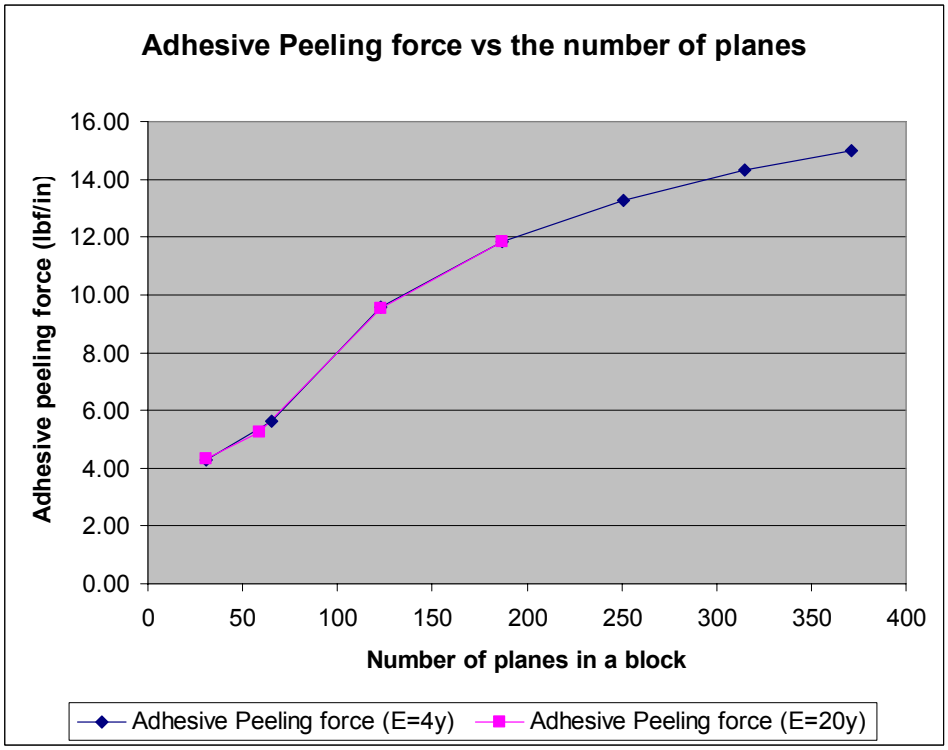

Fig. 17.31: Peeling force vs number of planes per block.

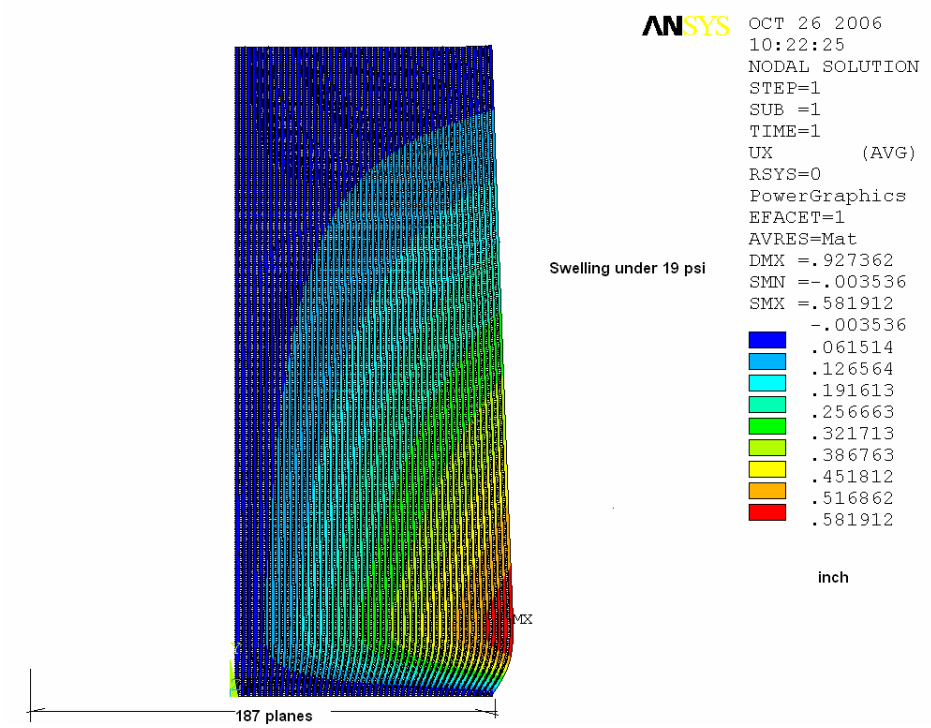

Fig. 17.32: Block swelling for 187 planes case at 20 years.

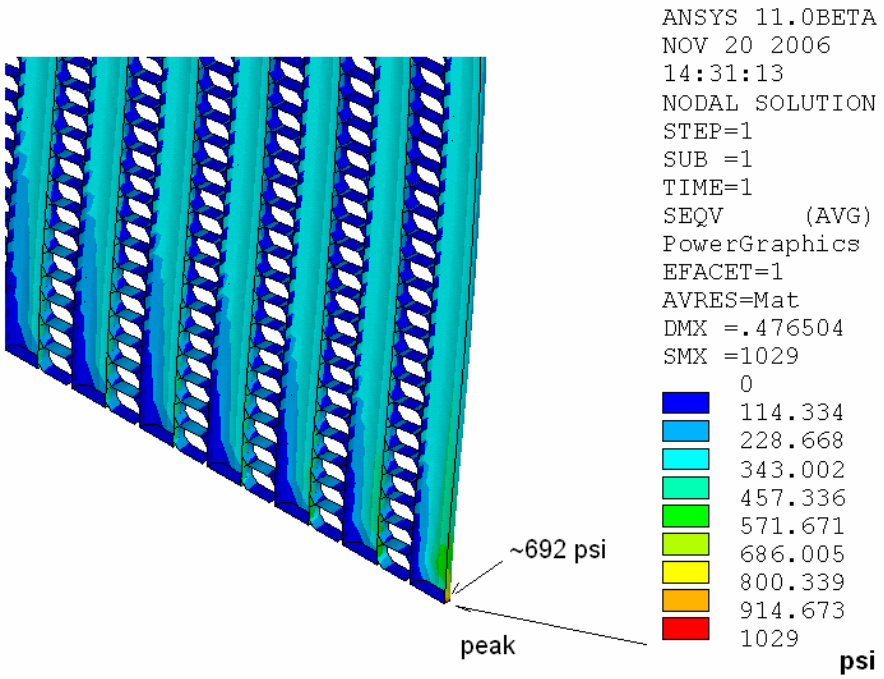

Fig. 17.33(a): Von Mises stress for a block with 187 planes at 4 years.

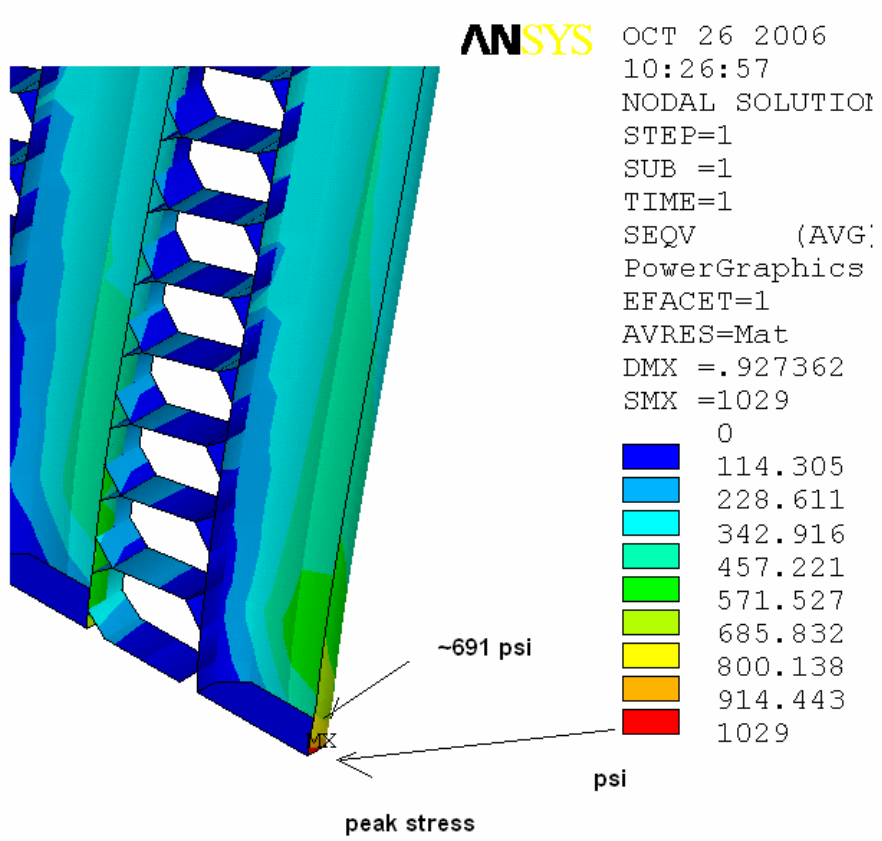

Fig. 17.33(b): Von Mises stress for a block with 187 planes at 20 years.

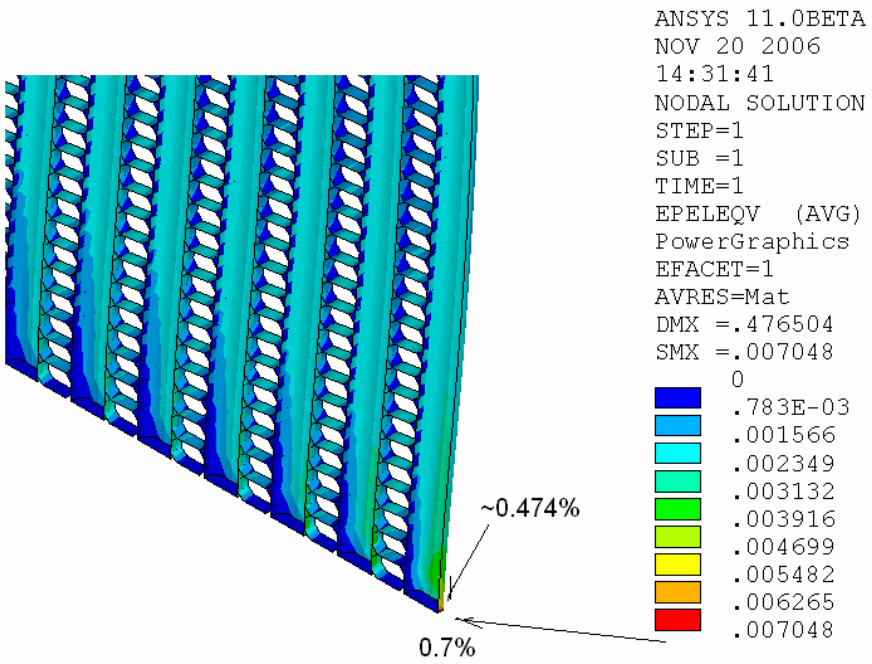

Fig. 17.34(a): Von Mises strain for a block with 187 planes at 4 years.

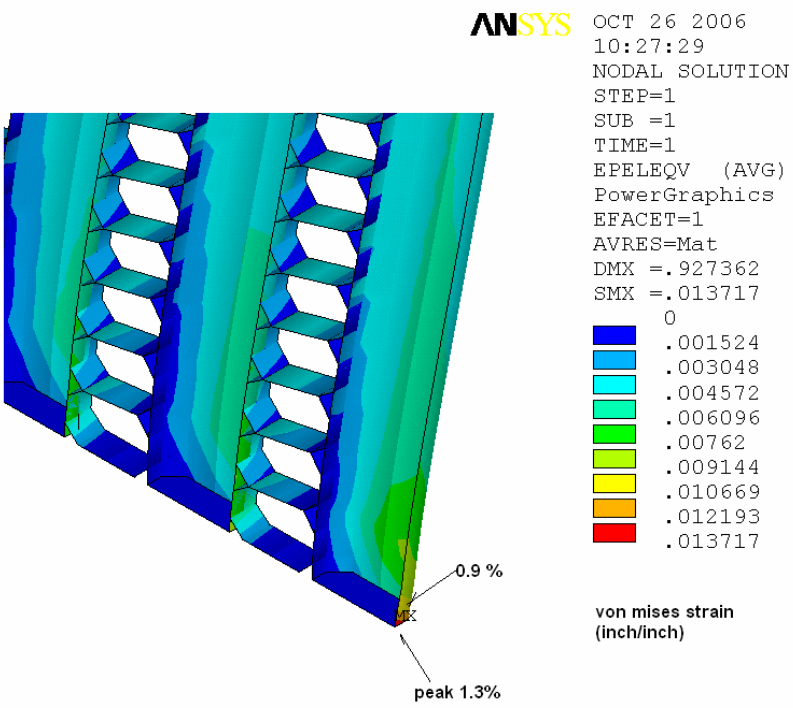

Fig. 17.34(b): Von Mises strain for a block with 187 planes at 20 years.

17.5.3.1 "A" Block Adhesive Strength Requirements

The model described in the previous sections was used to examine adhesive stresses in order to understand the strength requirements for the plane adhesive. The initial analysis examined 32 planes filled with scintillator. Figure 17.35 shows the distribution of the adhesive stresses from the bottom to the top of the detector and Figure 17.36 shows the location of the shear stresses in the FEA model. The maximum adhesive shear stresses occur at the bottom of the detector and are approximately 165 psi but are less than 140 psi throughout the remainder of the plane.

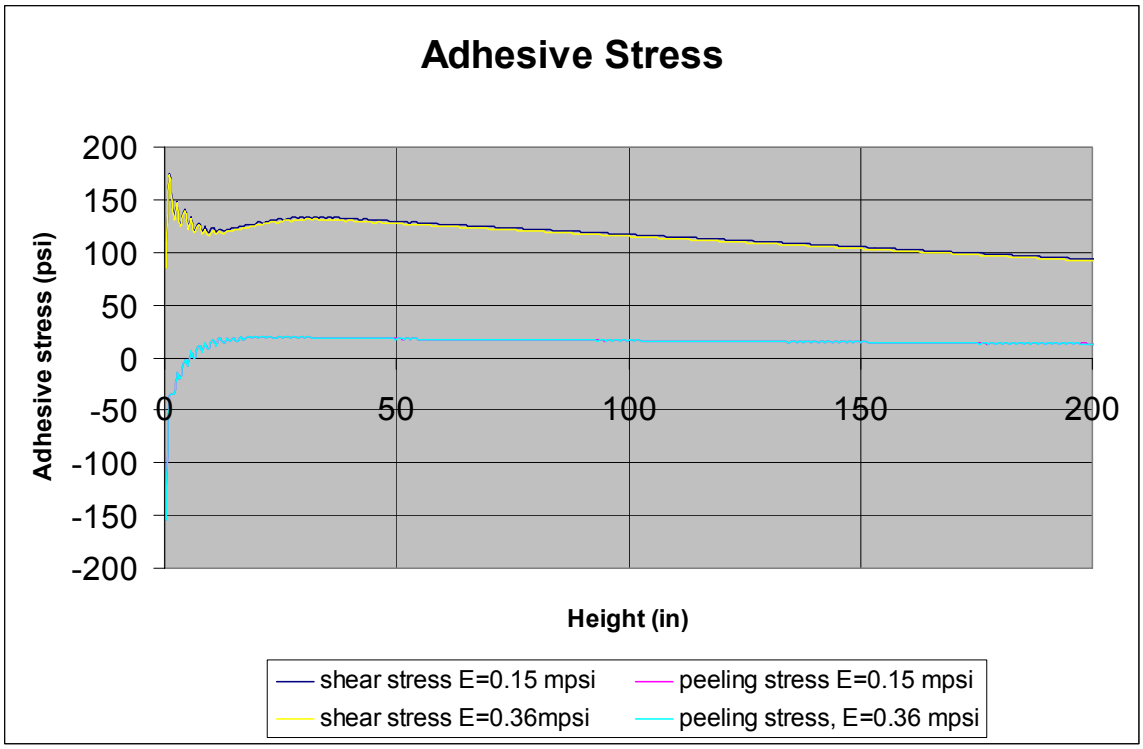

Fig. 17.35: Adhesive stress vs height.

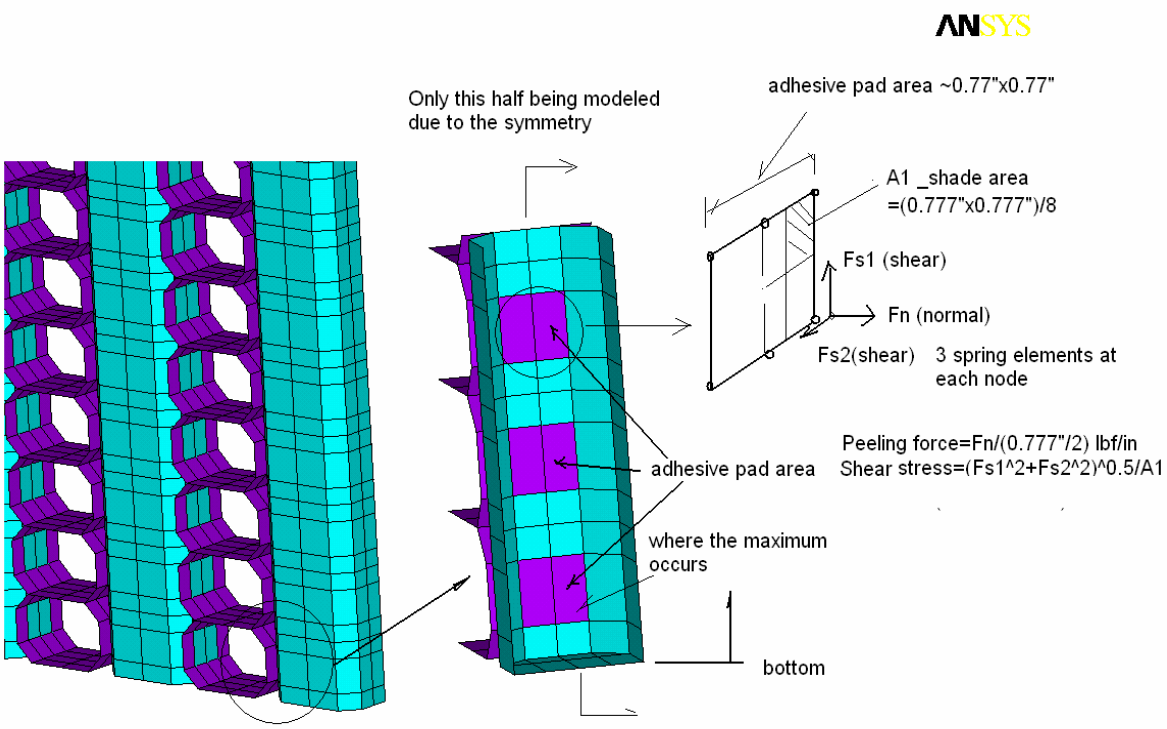

Fig. 17.36: Location of shear stresses in the FEA model.

Three components contribute to adhesive stresses. The (small) first component is due to the weight of the horizontal extrusions being transferred to the vertical extrusions. The second component is due to the stress from the PVC deformation under hydrostatic pressure. The third component is due to the differential strain between the vertical and horizontal extrusions from the weight of the extrusions and scintillator.

17.5.3.2 Buckling Analysis of a 31-Plane "A" Block

The stability of a 31-plane A-type block filled with liquid scintillator was examined in a number of different ways in order to gain confidence in the result. First, an eigenvalue analysis was done using the creep modulus at a particular time. Second, a static nonlinear analysis was performed. The modulus of the PVC at 20 years was used as input, an initial displacement was given to the block and the load was increased in steps until instability occurred. Finally, a time dependent nonlinear analysis was performed. The creep curve shown in Figure 17.5 above was input into the model, the block was given an initial deformation, and the deformation calculated as a function of time. These different analyses gave similar results for the time when block instability would occur.

17.5.3.2.1 Eigenvalue buckling calculation

The first calculation is done by using an eigenvalue linear analysis with a modulus at 4 years and 20 years. Four years was used because this is the time assumed for assembly of the detector and the maximum period through which blocks will have to stand as independent structures. Twenty years is the required lifetime of the detector. The 4-year and 20-year safety factors for a 31-plane block, calculated by the eigenvalue analysis, are summarized in Table 17.8. The boundary conditions used were "top free" and "top guided," as shown in Figure 17.37.

Year	E creep _1/D (mpsi)	SF _top guided	SF _ top free
4	0.146	2.626	2.02
20	0.0725	1.173	0.926

Table 17.8: Results of eigenvalue buckling analysis of block stability.

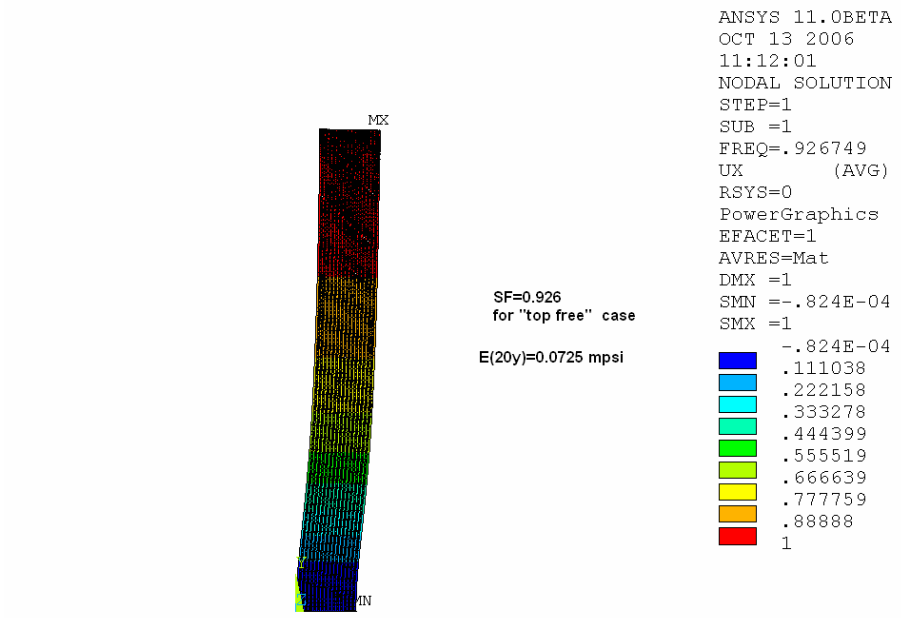

Fig. 17.37(a): Eigenvalue calculation for E(20y) = 0.0725 mpsi (top free).

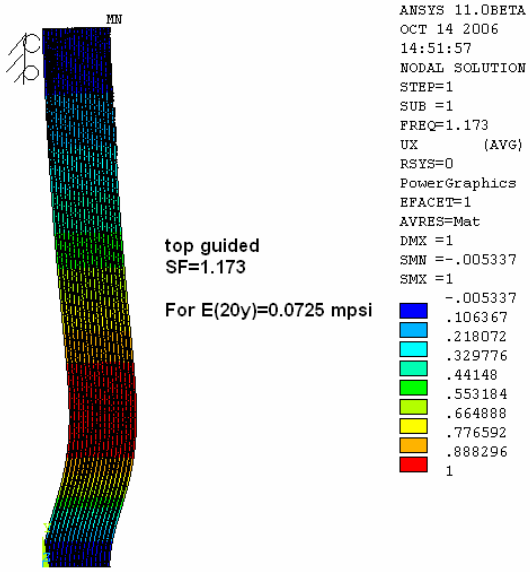

Fig. 17.37(b): Eigenvalue calculation for E(20y) = 0.0725 mpsi (top guided).

17.5.3.2.2 Buckling calculation using a static nonlinear analysis

The second analysis uses a static nonlinear large-deflection approach, with E(20 year) = 72.5 ksi. We assume that the structure has an initial 1-inch offset at its top or middle portion to simulate a worst-case initial condition, as shown in Figure 17.38. The load is increased gradually

to find the value at which the structure becomes unstable. Figure 17.39 shows that the deflection of a block increases rapidly for loads greater than 0.8 G in the "top free" case, and for loads greater than 1.1 G in the "top guided" condition. The results are consistent with the eigenvalue approach, as shown in Table 17.9.

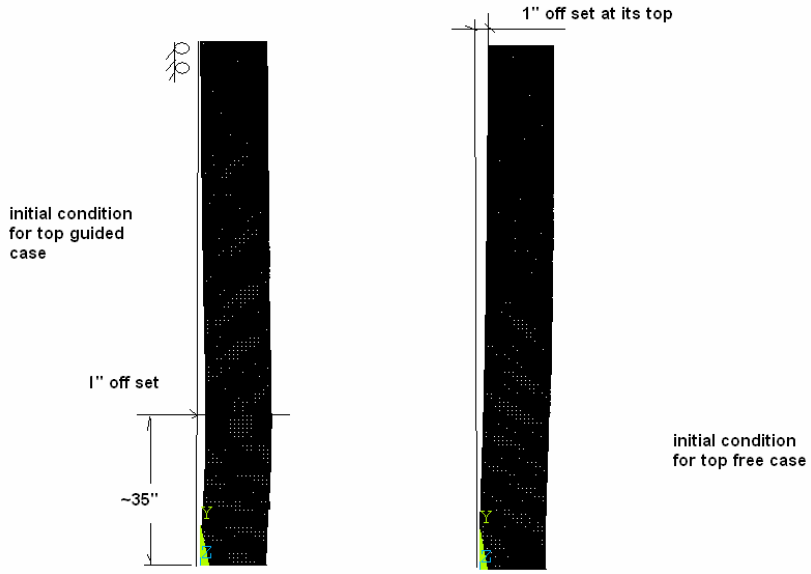

Fig. 17.38: FEA model for a top free and top guided case.

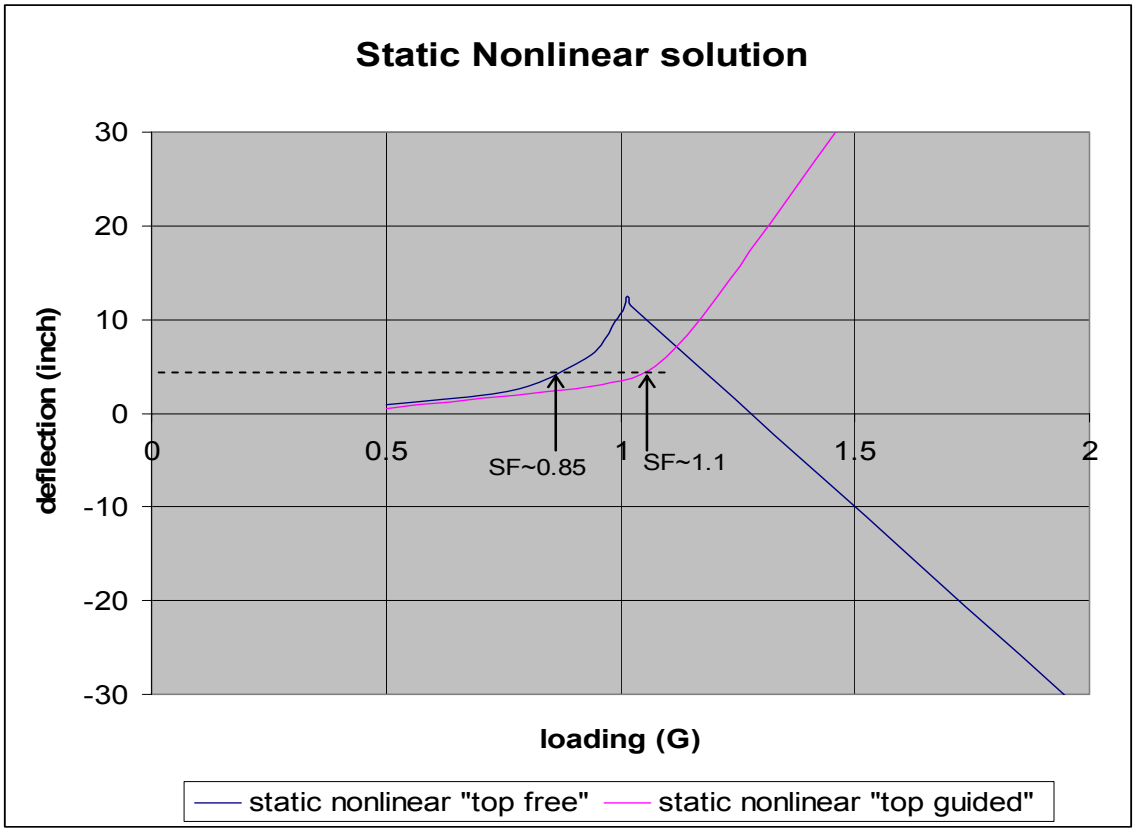

Fig. 17.39: Block deflection as a function of the G load.

E(20y)=0.0725 msi	Eigenvalue (Euler)	Static nonlinear large deflection
SF _ top guided	1.173	~1.1
SF _ top free	0.926	~0.85

Table 17.9: Comparison of eigenvalue and static nonlinear large deflection solutions with E(20y) = 72.5 ksi.

17.5.3.2.3 Time dependent of nonlinear large deflection analysis.

The two approaches described in the previous sections give an estimate of the additional force (ΔF) the structure may be able to withstand before it becomes unstable. However, it does not address how much time is needed to develop this excessive structural deformation for the structure under a constant load.

The FEA model described in the previous sections with top-free and top-guided cases was used to perform a time dependent nonlinear large deflection analysis. The result is shown in Figure 17.40. For the top-free case, the structure is stable up to ~17 years and then its deflection starts to accelerate. This is in agreement with the first two analyses, which gave SF ~0.8 for E(20y) = 0.0725 mpsi. For the top-guided case the critical time is around 22 years. Again, this is consistent with the predictions from first two approaches (SF~1.1).

Table 17.10 shows the PVC and adhesive stresses at 10 years since a single block is unstable at 20 years.

If PVC material is described by the pessimistic creep curve, the stability of individual blocks, constrained at the top, would limit their lifetime to less than 20 years. Section 17.5.5 describes how installation of the second bookend after four years guarantees that the 33-block detector is structurally stable for much longer than 20 years.

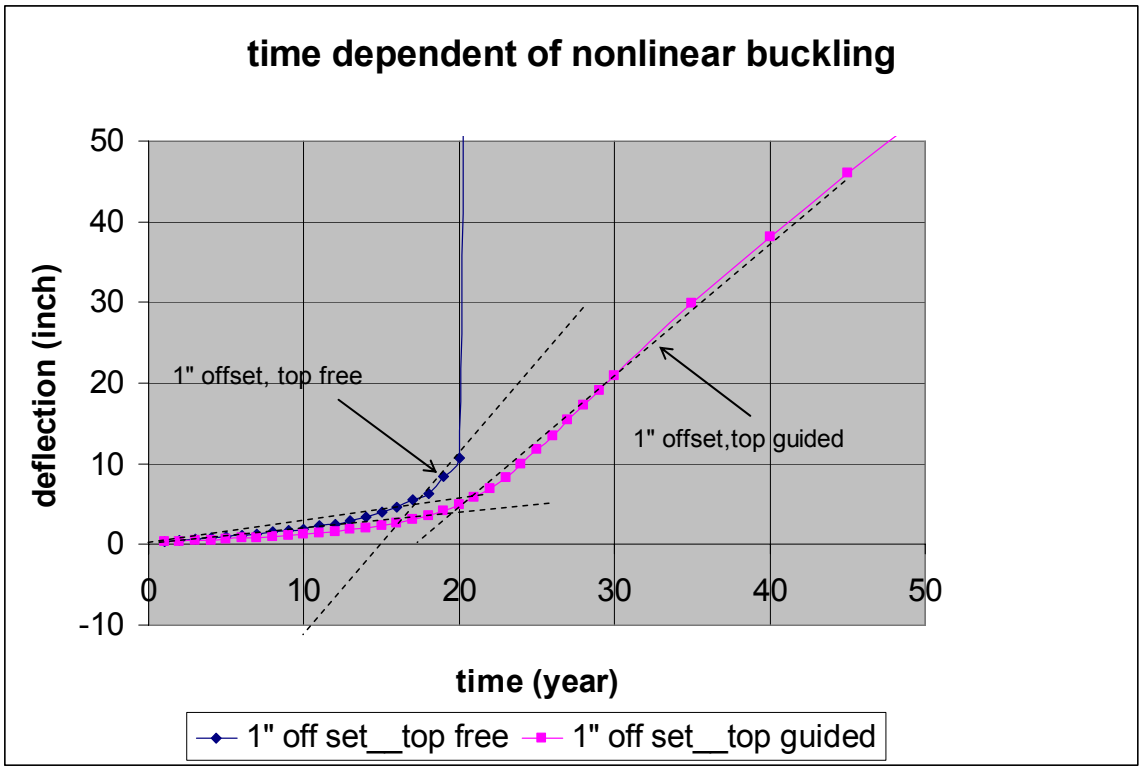

Fig. 17.40: Deflection as function of the time for first 50 years.

Time (year) t=10 year	Deflection (inch)	*Maximum stress (psi)	*Maximum Strain (%)	*Maximum adhesive Shear (psi)	*Maximum Adhesive Peeling force
Top free	1.92 (top)	858/561	0.85/0.55	173	5.1 (lbf/in)
Top guided	1.7 (~35" from bottom	896/598	0.88/0.59	178	8.8 (lbf/in)

Table 17.10: The stress and deflection at t = 10 years from the time dependent nonlinear large-deflection analysis.
* Note: The peak values listed in the stress and strain columns ignore the corner peak values, as illustrated in Figure 17.42 and 17.43. The shear stress is an average stress over the 1/8 of the adhesive pad area (0.777 inch x 0.777 inch).

The stresses and deflections of the block at 10 years are described in detail below to provide an example of the performance of a block.

Figures 17.41 and 17.42 show the regions of the maximum stress in the block for the top-free and top-guided cases, respectively. The maximum stress is approximately 858 psi and occurs at the bottom corner of the extrusions. The average stress in this region is much smaller and well within the limits of being considered viscoelastic which is important for insuring that creep is not a function of stress.

Figures 17.43 and 17.44 show the overall deformation of the block for both the top-free and top-guided cases, respectively. The deflections are less than 2 inches, which is insignificant compared to the size of the detector.

Figures 17.45 and 17.46 plot the height dependence of the adhesive peel and shear stresses within the detector, respectively. The maximum adhesive stresses occur at the bottom of the block in the outermost layers. The maximum peel stress is approximately 13 lbs/in, which is far below the adhesive peel strength of 115 lbs/in. The maximum shear stress is approximately 180 psi, which is also far below the 950 psi adhesive shear strength. The peel stresses shown in Figure 17.45 vary rapidly because the maximum peel force occurs at the edges of the contact pad between extrusions but is virtually zero in the center of the pad.

Finally, the top guided case is used to extract the edge-pulling force at t = 10 years. The result, shown in Figure 47, is a value of F (pulling) = 5514 lbf/total (or 18.48 lbf/in) at t = 10 years. With this pessimistic E(creep) curve, a block has no safety margin against the buckling for both top free and top guided cases after 20 years.

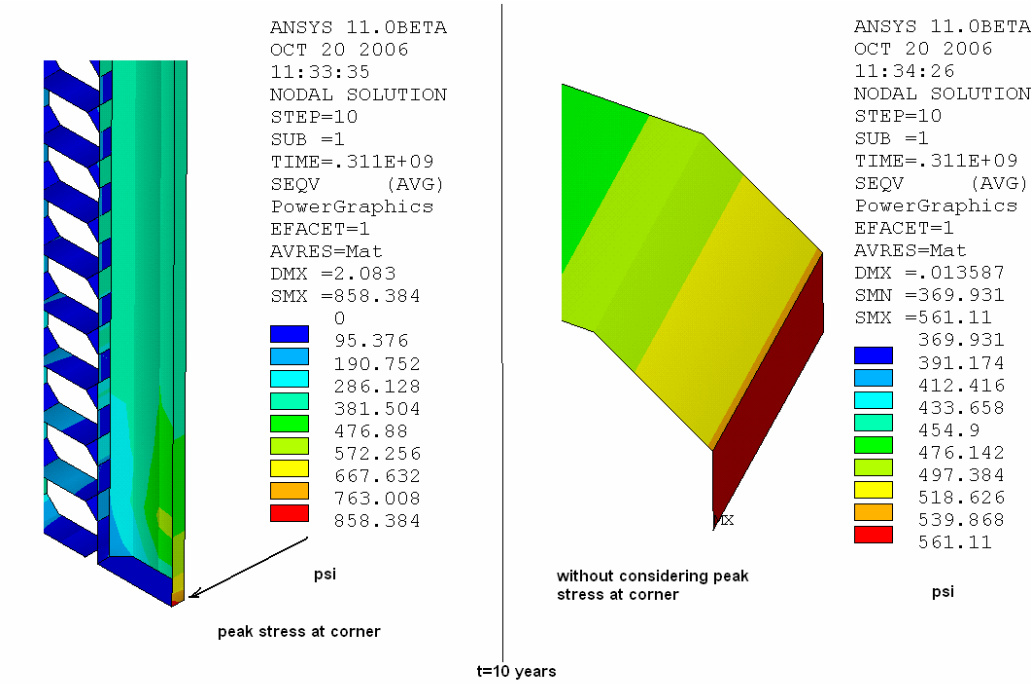

Fig. 17.41: Von Mises stress at t = 10 years for the top-free case.

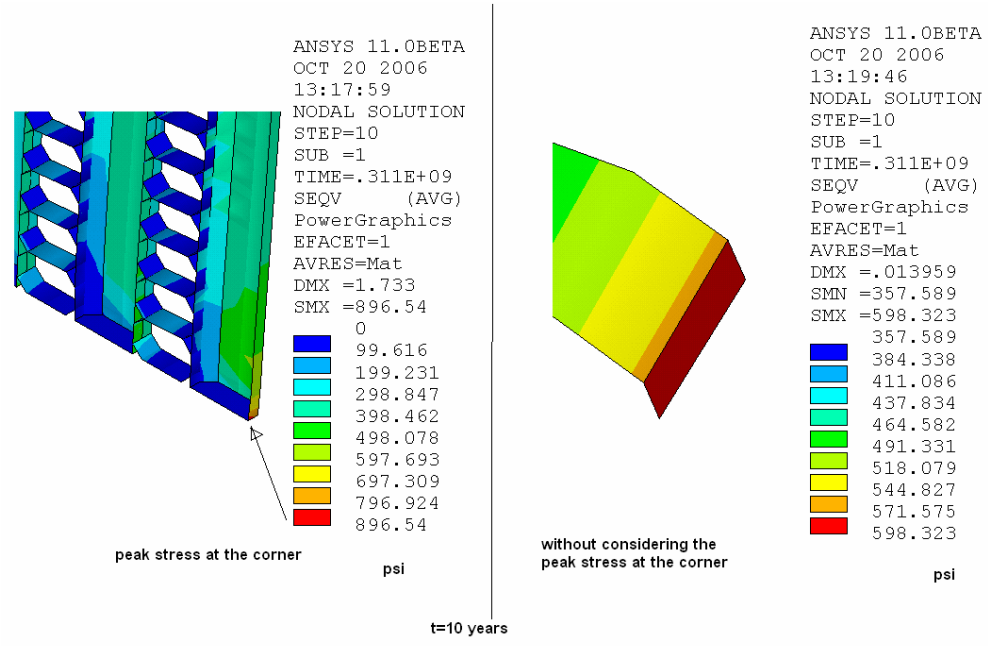

Fig. 17.42: Von Mises stress at t = 10 years for the top-guided case.

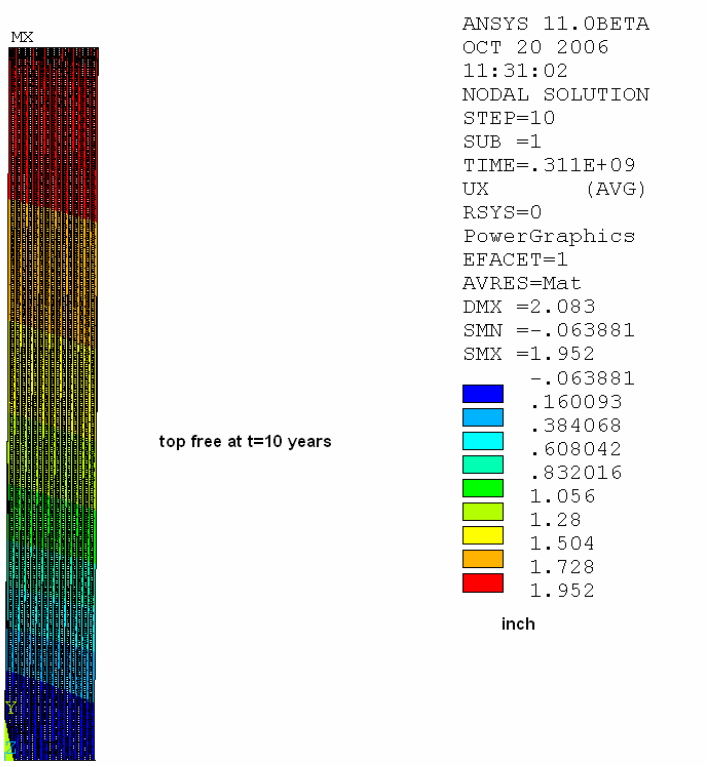

Fig. 17.43: Deflection at 10 years for top-free case.

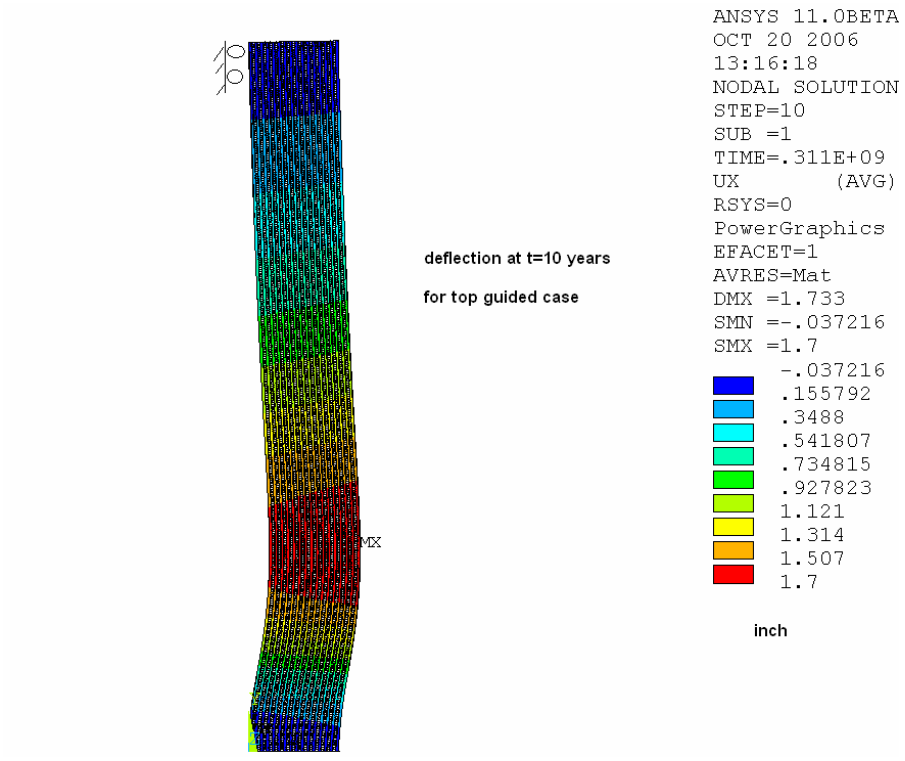

Fig. 17.44: Deflection at t = 10 years for top-guided case.

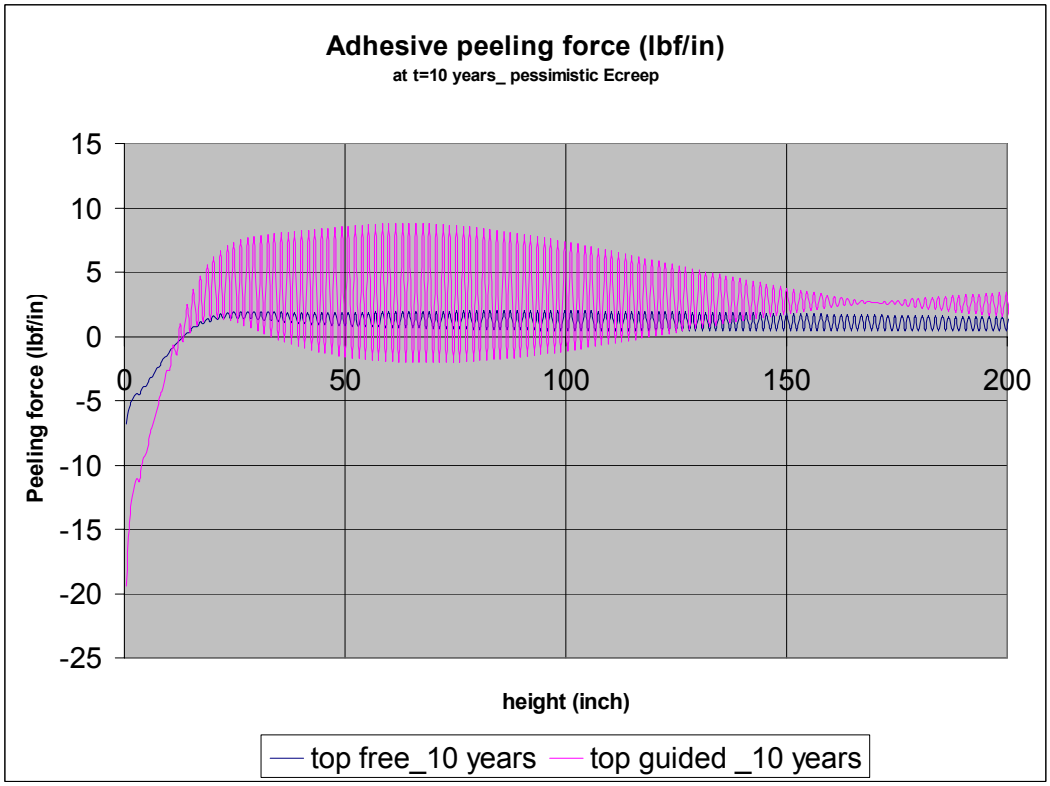

Fig. 17.45: Dependence of adhesive peel stress on height in the detector at t = 10 years.

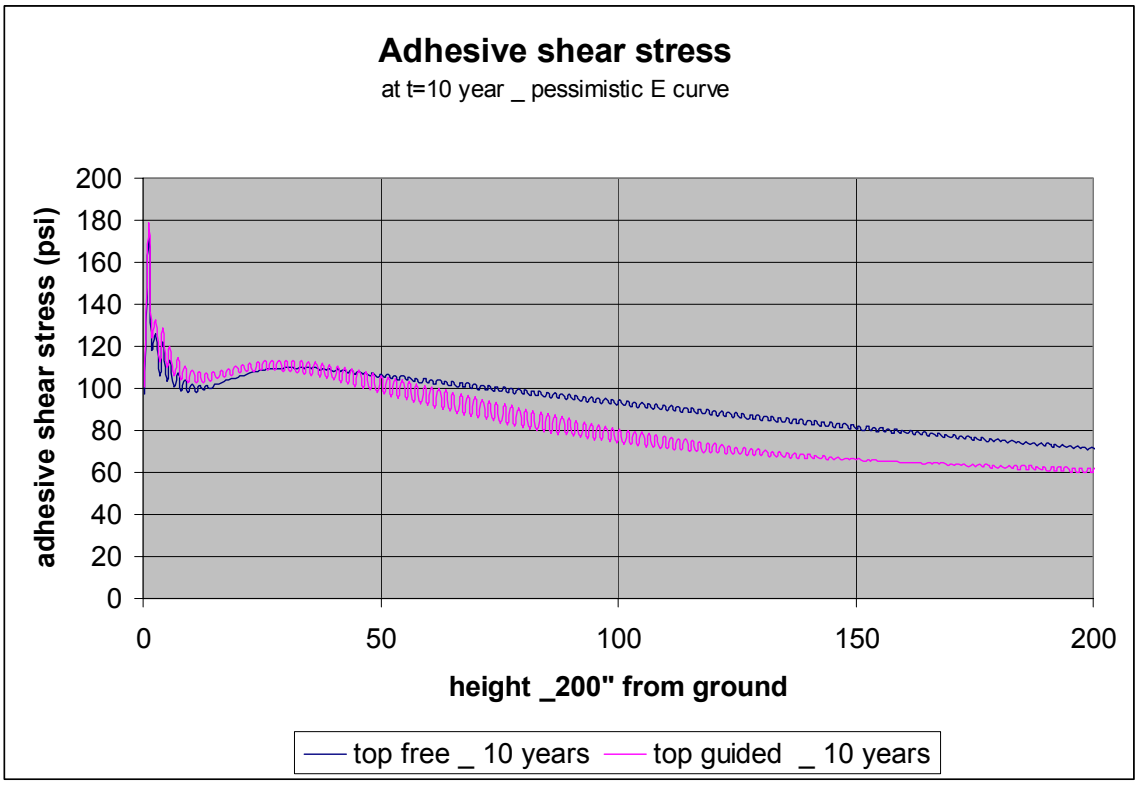

Fig. 17.46: Dependence of adhesive shear stress on height in the detector at t = 10 years.

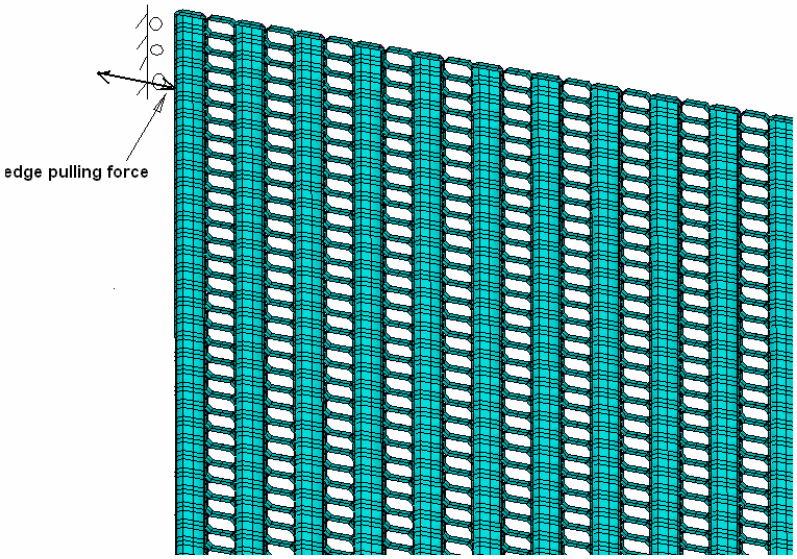

Fig. 17.47: Edge-pulling force extraction.

17.5.4 Analysis of a 31-Plane "B" Block

The construction of a B block is similar to that of an A block except that B blocks have planes of horizontal extrusions on the outside surfaces where A blocks have vertical extrusions. The layout of a B block is shown in Figure 17.48. This difference has a small impact on the maximum stresses in both the PVC and adhesive, which occur on the outside layers of the block. The buckling safety factors of A and B blocks are also different. The model of B blocks is very similar to that for A blocks. It was used to calculate the PVC and adhesive stress based on the both E = 145 ksi (4-year worst case PET B) and E = 75 ksi (20-year worst case PETB). The result is summarized in Table 17.11.

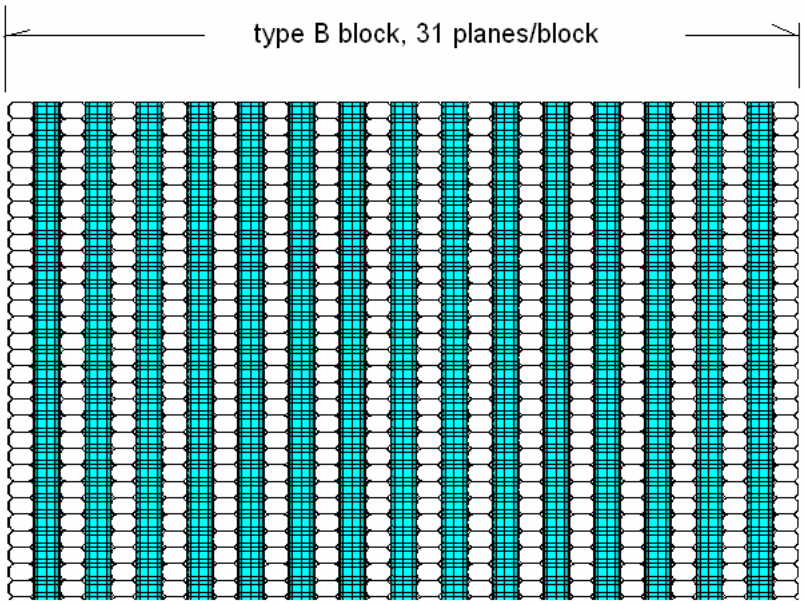

Fig. 17.48: Layout of a B block.

Number of planes In a block	31 planes _ B type	31 planes _ B type
Modulus E (ksi)	146	75
Total swelling (inch)	0.109	0.21
Stress peak (psi)	564	564
Excluding peak (psi)	533	533
Strain peak (%)	0.38	0.75
excluding peak (%)	0.36	0.71
Adhesive Peeling force (lbf/in)	4.78	4.83
Adhesive Shear stress (psi)	234	236

Table 17.11: Summary of FEA stress calculations for a B-type block.

17.5.4.1 "B" Block Adhesive Strength Requirements

Table 17.11 lists the shear and peel stresses in the adhesive for different values of modulus of the PVC. The maximum adhesive stresses occur in the outermost layers of the B block and at the bottom of the layer. The maximum peel stress is only 4.8 lbs/in which is far below the 115 lbs/in peel strength of the adhesive. However, the shear stresses are higher than in the A blocks because the outside horizontal modules are essentially hanging from the vertical extrusions. The maximum shear strength of the adhesive is 950 psi, which gives a safety factor in shear of 4.0 compared to the design goal of SF = 5.0.

17.5.4.2 Buckling Analysis of a 31-Plane "B" Block

The B-block buckling analysis is similar to the one for A blocks described in Section 17.5.3.2. In that section it was shown that the three approaches used to understand the buckling and long term stability of the blocks produced similar results. Table 17.12 shows the buckling

safety factor for the B blocks for the eigenvalue and nonlinear static approaches. B blocks have a slightly lower SF than A blocks. Figure 17.49 shows the deflection versus gravity load using the 20-year modulus. At the full gravity loading, the deflections increase dramatically, indicating that the structure is unstable. The long term stability of the detector is addressed in Section 17.5.5.

A time dependent nonlinear analysis was also done in which the actual pessimistic creep curve was used in the analysis and the deformation over time was calculated. Figure 17.50 below shows how the B block deformed over time. The free standing B block becomes unstable at approximately 15 years when the top is not guided and become unstable at approximately 18 years when the top is guided. The B blocks are therefore less stable than the A blocks, which become unstable at approximately 22 years. However, the long term stability of the detector is achieved by having adjacent block mutually support each other and being restrained between two bookends (Section 17.5.5).

E(20y) = 0.0725 mpsi	Eigenvalue (Euler)	Static nonlinear large deflection
SF_ top guided	1.056	0.95
SF_ top free	0.86	0.80

Table 17.12: Buckling safety factor (SF) for a B block with E(20y) = 72.5 ksi (pessimistic curve).

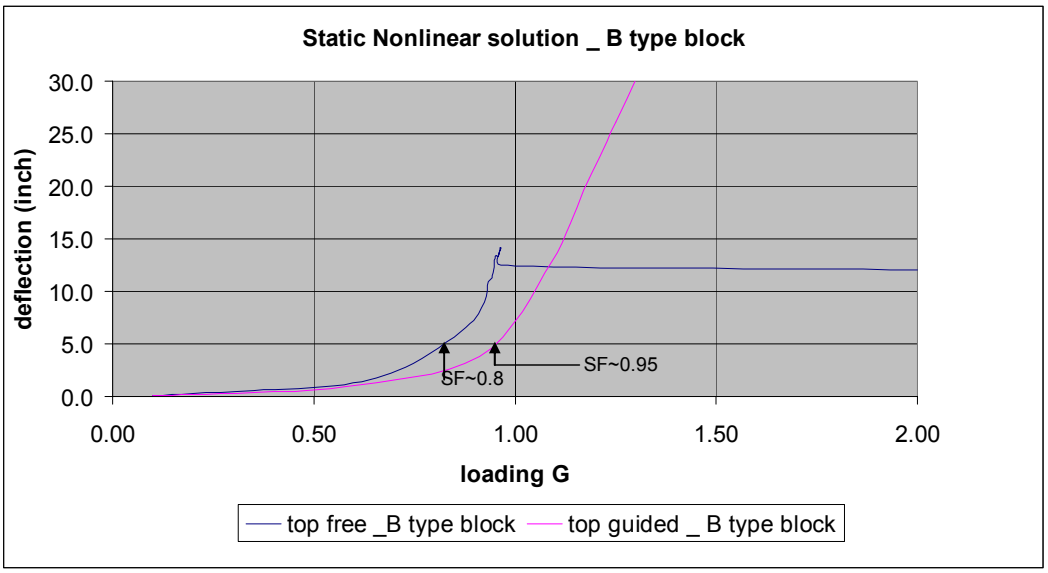

Fig. 17.49: B-type block deflection as a function of the G load for 75 ksi modulus (20 year).

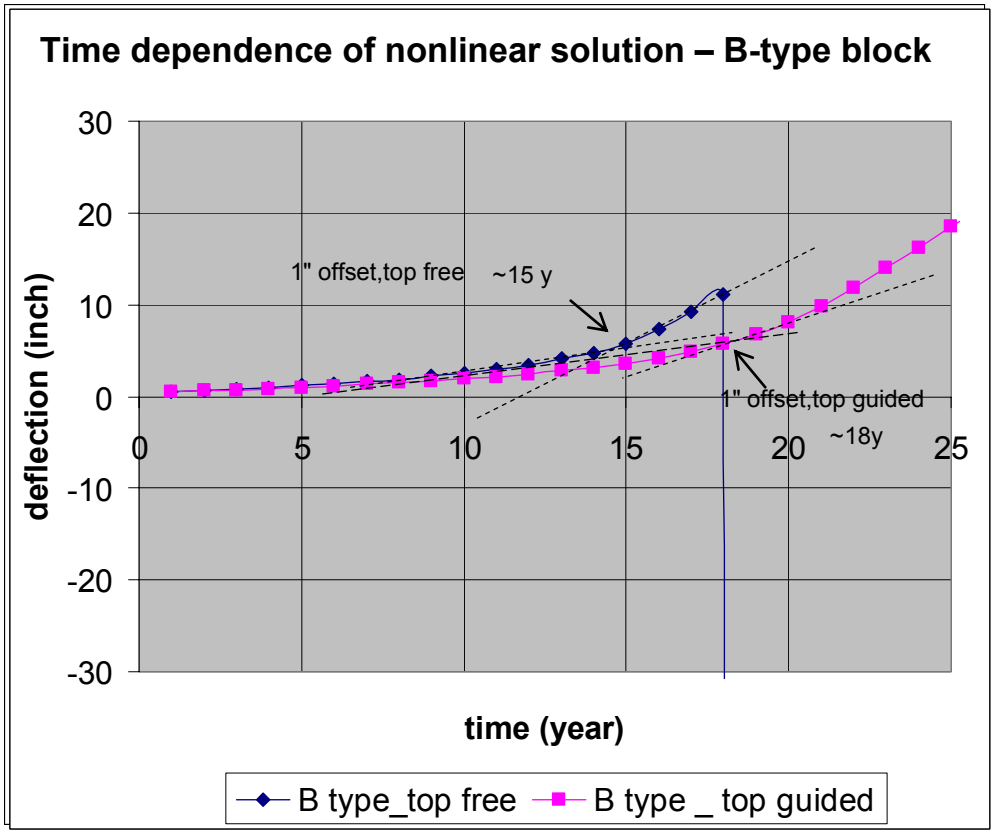

Fig. 17.50: B-type block deflection as a function of the time.

17.5.5 Long-term Structural Stability of the Detector

The buckling analysis of structurally independent blocks in Sections 17.5.3 and 17.5.4 showed that at 20 years (using the most pessimistic prediction for the PVC modulus), there is no safety factor against buckling. It also showed that during the 4-year period of detector construction, there is a safety factor of ten for empty blocks and of nearly three for filled blocks, assuming that a support is provided at the top of each detector block.

Long term buckling stability is achieved by installing the second (north) bookend at the end of the construction period and restraining the movement of the blocks between the two bookends. Once the second bookend is in place, a block can deform until it makes contact with an adjacent block. The total deflection of the blocks is limited by the spacing between blocks and the constraint provided by the two bookends. The bookends are designed to withstand the forces from cumulative block deformation after 25 years of PVC creep.

Blocks are assembled together in groups of five to form a superblock. Within a superblock, the blocks are pushed as close together as possible but they are not glued to each other. The 2-cm (0.75-inch) expansion gap between superblocks allows superblocks to be filled while detector installation is still in progress, before the second bookend is installed. Gaps between blocks within a superblock are made as small as possible to minimize the amount of space that a block can deform into over time. However, gaps between superblocks ensure that the swelling of filled blocks does not grow progressively larger as it propagates down the length of the detector. As shown above, the swelling of the blocks increases the stresses in the PVC and adhesive. The swelling within a superblock is within acceptable limits for stresses in the adhesive and PVC. Figure 17.51 shows the spacing of blocks and superblocks within the detector. In the worst case,

all blocks will deform in the same direction and make contact with one of the bookends. The block adjacent to that bookend will deform the least and the deformation of each successive block will increase. The space available for the block furthest from the bookend will be equal to the sum of all of the gaps between the blocks. The detector is stable as long as the buildup of forces acting between blocks that have deformed against each other can be supported by the PVC extrusions. When the forces exceed the buckling strength of the weakest member, the webs in the horizontal extrusions, structural failure occurs. The force between blocks is dependent on spacing between blocks and superblocks.

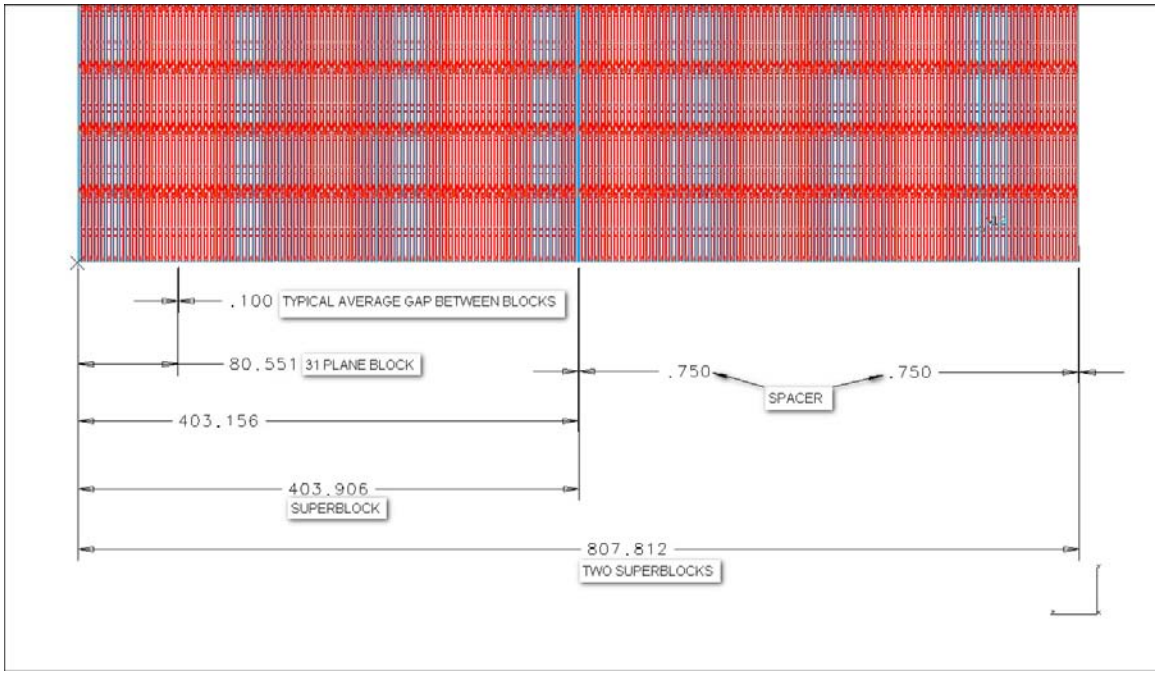

Fig. 17.51: Spacing of blocks and superblocks in the detector.

The analysis of the assembled detector is very computer intensive and requires several weeks to complete because it is an iterative process and because of the large model size. The initial analysis of the assembled detector was done using all A-type blocks in the detector. Several scenarios were examined in order to understand the forces between the blocks and on the bookends. Whereas the exact forces found in this analysis may not apply to the current arrangement of alternating B-A-B blocks, the dependency of the block forces on gap size is illustrative and therefore included in the Section 17.5.5.1 below. This section is followed by Section 17.5.5.2 which describes the forces acting on the blocks in the B-A-B super block arrangement. In this analysis only gap spacing of 0.1 inch between blocks within a super block and 0.75 inch between super blocks was examined because it was determined in Section 17.5.5.1 that this would result in the largest forces.

17.5.5.1 Analysis of Assembled Detector with "A" Blocks Only

The initial analysis of the assembled detector was done with only "A" blocks in the detector. The blocks make contact at the top and are completely constrained at the top between the bookends. As the blocks deform over time, contact will be made in the lower half of the detector. The contact area between blocks occurs approximately between 170 inches to 195 inches above the bottom of the vertical extrusions.

Figures 17.52, 17.53 and 17.54 show the forces acting at the top and middle of the blocks as they deform and make contact with each other. Block 40 is against the bookend and block 1 is the furthest from the bookend. The analysis assumes that all of the blocks deform in the same direction and buckle towards one bookend.

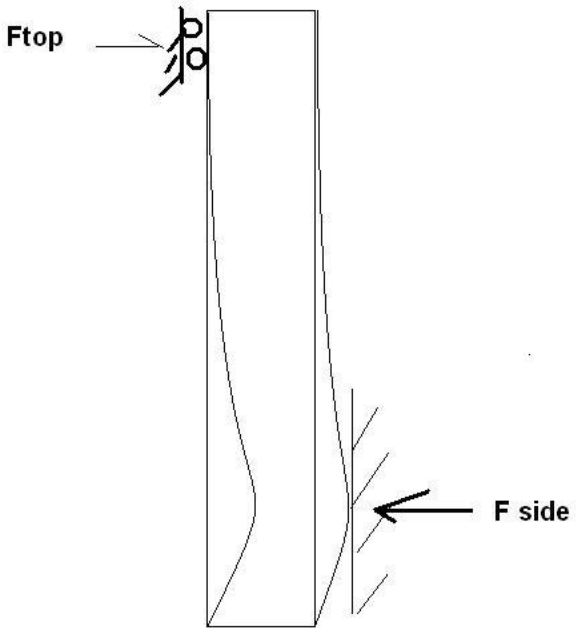

Fig. 17.52: Schematic of forces acting on a deformed block.

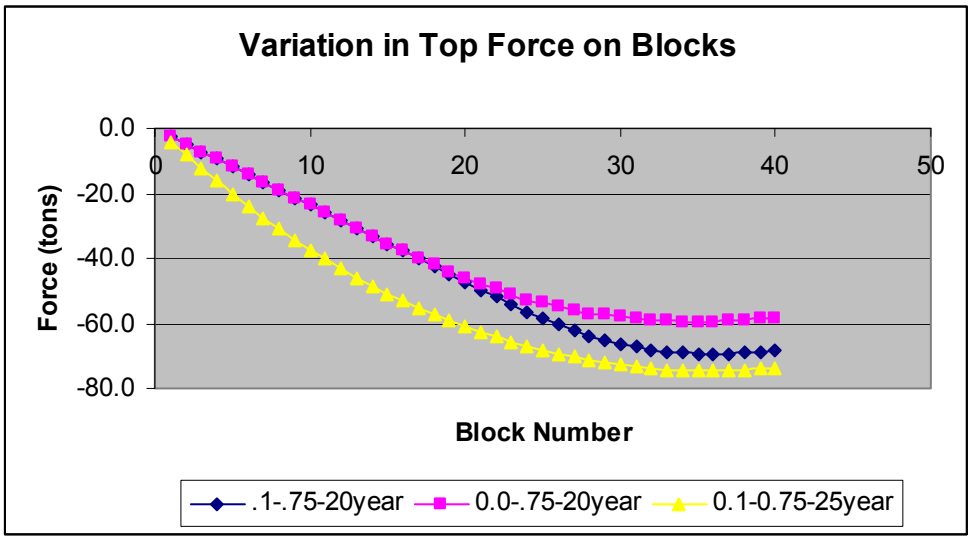

Fig. 17.53: Forces between the tops of blocks.

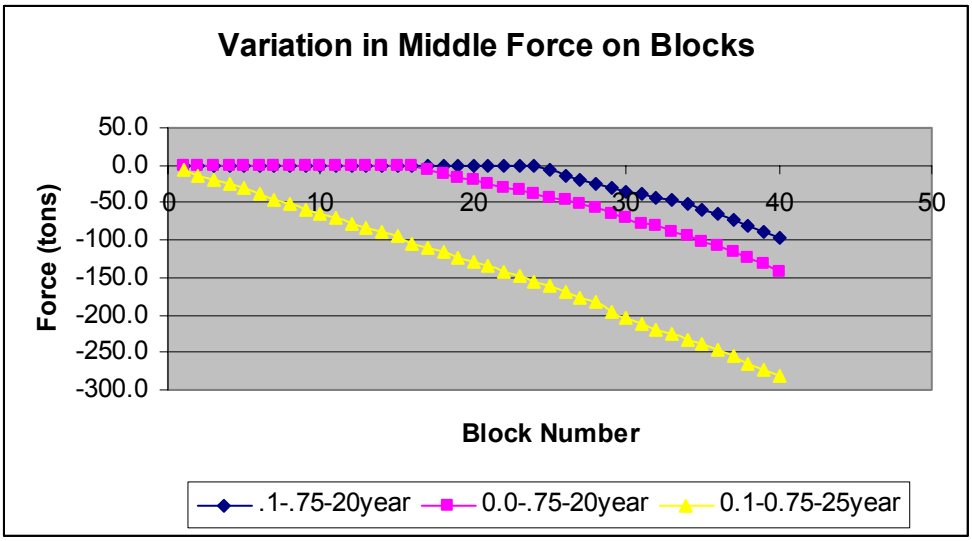

Fig. 17.54: Forces acting on block surface.

In Figures 17.53 and 17.54, the blue diamonds labeled "0.1-0.75-20year" show the analysis of the detector with a 0.1-inch gap between blocks within a superblock and a 0.75-inch gap between superblocks, using the PVC modulus at 20 years. The magenta squares labeled "0.0-0.75-20year" show the analysis when there is zero gap between blocks within a superblock and a 0.75-inch gap between superblocks, using the PVC modulus at 20 years. The yellow triangles labeled "0.1-0.75-25year" show the analysis of the detector with a 0.1-inch gap between blocks within a superblock, a 0.75-inch gap between superblocks, using the PVC modulus at 25 years from the pessimistic creep curve.

Figure 17.53 shows the forces acting at the tops of the blocks. The two curves with the same 20-year modulus follow each other until the point where blocks begin to make contact with each other. Blocks 1-23 do not make contact with each other and blocks 24-40 do contact each other, which is the point where these curves begin to diverge. In the block stability analysis discussed above, the blocks begin to become unstable after 20 years. This is reflected in the yellow curve which uses a modulus of 25 years. The deformation at 25 years becomes much larger and all of the blocks are now in contact.

In Figure 17.54, the force acting on the surface of the blocks is zero until contact is made at block 17 when there is a zero gap between blocks within a superblock, and at block number 24 when there is a 0.1-inch gap between blocks within a superblock. The force between blocks increases by nearly 50 tons when the gap between the blocks in each superblock is increased from zero to 0.1 inch. Figure 17.54 also shows that at 25 years the deformation of the blocks is unstable and all of the blocks are in contact. Use of the 25-year modulus increases the force between blocks dramatically, to a maximum of nearly 300 tons, which is three times the force at 20 years for the same gap between blocks. The bookends are designed to withstand the forces, shown in Figure 17.54, from cumulative block deformation after 25 years of PVC creep. The detector blocks will also withstand these forces at 25 years. Under the compressive forces shown in Figure 17.54, the 2-mm thick inner webs of the horizontal extrusions are the weakest detector component. NOVA-doc-1349 describes experimental measurements of the buckling strength of these webs and compares it to the FEA model of the test setup. The test and model results are in good agreement, giving confidence in the model predictions at 25 years with the lower PVC modulus.

Long term stability of the detector is ensured by restraining the blocks between two bookends. Each block is restrained at the top of the detector and the gaps between superblocks allow the detector to be filled while assembly is still in progress. During the years after the second

bookend is installed, the blocks will deform and fill these gaps, eventually making contact with adjacent blocks. These gaps between the lower surfaces of superblocks are small enough that the structure is stable, with an adequate safety factor, after 20 years of PVC creep. Although free-standing blocks are not stable at 20 years, the full detector structure is stable for much longer than 20 years because it is constrained between two bookends. The bookends limit the amount of deformation each block can undergo and therefore prevent the collapse of the detector or deformations that are large enough to cause excessively high stresses in the PVC or adhesive.

The PVC and adhesive stresses were examined within each block in the assembled detector at 20 years. Table 17.13 summarizes these stresses for the case of 0.1 inch between blocks and 0.75 inch between superblocks and a 75 ksi modulus at 20 years. The PVC and adhesive stresses are larger in the assembled detector that is making contact between blocks than it is for individual free standing blocks using the same modulus as shown in the sections above.

Block #	#16	#25	#26	#27	#28	#40
Max. deflection	4.507	3.013	3.013	3.013	3.013	0.8679
Pvc stress						
peak (psi)	996	924	925	925	925	803
excluding peak (psi)	684	622	623	624	624	521
adhesive stress						
Peeling (lbf/in)	14.30	11.16	11.21	11.26	11.26	6.31
shear (psi)	193.69	179.14	181.29	181.67	181.55	161.84

Table 17.13: Maximum PVC and adhesive deflections and stresses for different blocks in a 40-block detector at 20 years, with 0.75 inch expansion gaps between superblocks and 0.1 inch gaps between the blocks within a superblock.

17.5.5.2 Analysis of the Assembled Detector with A-B-A-B-A Superblocks

An analysis of the assembled detector was performed (NOVA-doc-1932) using the A-B-A-B-A organization of a superblock and taking advantage of what was learned in the initial analysis described in the section above. In this analysis a gap of 0.1 inch was set between blocks within a superblock and a gap of 0.75 inch was set between superblocks. In this analysis blocks are given a 1-inch initial offset to begin deformation, for A blocks this results in a 5.03-inch deflection and 6.5 inch for B due to its slightly weaker structure. See Figures 17.55 and 17.56. For two blocks with B+A together, the expected deflection is somewhere between A and B. The result shows that the deflection is about 5.5 inches, see Figure 17.57. Each superblock will have five single blocks in a pattern of A+B+A+B+A. This pattern suggests that the analysis can be accomplished by calculating A following by B+A. The gap size is assumed to be 0.1 inch between the blocks and 0.75 inch between superblocks. The modulus of E=0.075 mpsi (t = 20 years) is used based on the worst curve of PETB. An iterative process of calculating the force on the blocks and then transferring this force to the adjacent block can then be carried out in a manner similar to that described in Section 17.5.5.1 above.

The main conclusions of this analysis are:

- Blocks within the detector will not make contact with each other until #17 +#18 (B+A) where the available gap for the deformation is 5.5 inches.
- The force acting on the bookend/last extrusion is about 15% higher than the all-A case. Results are summarized on Table 17.14:
  Total force = 172 tons
  Total top force = 60 tons
  Total side force = 111.16 ton (between 120 inches ~190 inches from ground)

Max contact pressure = 6.8 psi

- Stress in PVC and adhesive seems similar to all straight A, except for adhesive shear. Results are shown in Table 17.15

Figure 17.58 shows schematically the forces acting on blocks as well as location and distribution of the forces.

The maximum shear stress appears to be much higher than for an A block assembly discussed in Section 17.5.5.1 above. However, after looking into this maximum shear further, we find that the value of 313 psi occurs in last interface (V+H) of B block. This peak drops rather quickly to ~220 psi after 1 cell in height and ~170 psi after 5 cells from bottom. The 313 psi peak shear is very localized (confined in one cell area) as shown in Figure 17.59 and poses no danger to the whole structure. In fact, 99% of adhesive shear stress is below to 200 psi under the worst scenario. Figure 17.60 shows the peak shear stress as a function of block (B) interface and indicates again that this peak only happens in the last interface.

		A	8	0.1	7.85	-5317.25	0.00	-41341.44	0	0.00	0.00	0.00	0.00
		B	9	0.1	7.75	-5317.25	0.00	-46658.69	0	0.00	0.00	0.00	0.00
		A	10	0.75	7.65	-5317.25	0.00	-51975.94	0	0.00	0.00	0.00	0.00
	3	A	11	0.1	6.90	-4718.98	0.00	-56694.91	0	0.00	0.00	0.00	0.00
		B	12	0.1	6.80	-5317.25	0.00	-62012.16	0	0.00	0.00	0.00	0.00
		A	13	0.1	6.70	-5317.25	0.00	-67329.41	0	0.00	0.00	0.00	0.00
		B	14	0.1	6.60	-5317.25	0.00	-72646.66	0	0.00	0.00	0.00	0.00
		A	15	0.75	6.50	-5317.25	0.00	-77963.91	0	0.00	0.00	0.00	0.00
	4	A	16	0.1	5.75	-4718.98	0.00	-82682.89	0	0.00	0.00	0.00	0.00
********		**B**	**17**	**0.1**	5.65	-5220.10	**0.00**	**-87902.98**	**0**	**0.00**	**0.00**	**0.00**	**0.00**
		A	18	0.1	**5.55**	-5220.10	-6081.48	-93123.08	-6081.48	162.40	156.80	5.60	**-1.81**
		B	19	0.1	5.45	-4978.94		-98102.02		0.00	0.00	0.00	
		A	20	0.75	**5.35**	-4978.94	-8160.31	-103080.97	-14241.79	164.80	156.40	8.40	**-2.83**
	5	A	21	0.1	4.60	-4292.04	-20595.15	-107373.01	-28755.46	175.79	165.00	10.79	**-4.44**
		B	**22**	**0.1**	**4.50**	-3883.78		-111256.79					
		A	23	0.1	4.40	-3883.78	-20382.26	-115140.56	-40977.41	171.59	152.20	19.39	**-3.52**
		B	**24**	**0.1**	**4.30**	-3503.39		-118643.95					
		A	**25**	**0.75**	**4.20**	-3503.39	-32935.37	-122147.33	-53317.63	**169**	**148**	**21.00**	**-4.23**
	6	A	**26**	**0.1**	**3.45**	-2549.76	-27798.84	-124697.09	-60734.21	**170.19**	**149.2**	**20.99**	**-4.82**
		B	**27**	**0.1**	**3.35**	-2232.35		-126929.44					
		A	**28**	**0.1**	**3.25**	-2232.35	-46171.08	-129161.79	-73969.92	**169.79**	**142**	**27.79**	**-4.44**
		B	**29**	**0.1**	**3.15**	-1907.33		-131069.11					
		A	**30**	**0.75**	**3.05**	-1907.33	-57670.20	-132976.44	-103841.28	**169.79**	**138.6**	**31.19**	**-5.55**
	7	A	**31**	**0.1**	**2.30**	-1035.26	-55886.28	-134011.71	-113556.48	**170.99**	**138.6**	**32.39**	**-5.84**
		B	**32**	**0.1**	**2.20**	-684.71		-134696.42					
		A	**33**	**0.1**	**2.10**	-684.71	-78605.88	-135381.13	-134492.16	**172.39**	**131.8**	**40.59**	**-5.52**
		B	**34**	**0.1**	**2.00**	-445.94		-135827.07					
		A	**35**	**0.75**	**1.90**	-445.94	-96237.00	-136273.00	-174842.88	**173.19**	**127.6**	**45.59**	**-6.39**
	8	A	**36**	**0.1**	**1.15**	388.53	-92314.68	-135884.47	-188551.68	**175.79**	**126.4**	**49.39**	**-6.36**
		B	**37**	**0.1**	**1.05**	743.35		-135141.13					
		A	**38**	**0.1**	**0.95**	743.35	-121166.28	-134397.78	-213480.96	**177.79**	**118.6**	**59.19**	**-6.01**
		B	**39**	**0.1**	**0.85**	964.26		-133433.52					
		A	**40**	**0.75**	**0.75**	964.26	-123426.36	**-132469.25**	-244592.64	**183.19**	**124**	**59.19**	**-6.89**

	total force (ton)	**top**
		-60.21
	Sum=top+side (ton)	
		-171.39

	Side
	-111.18

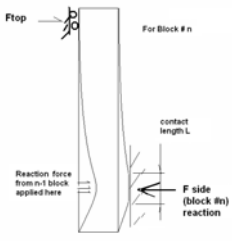

*Note: The sign of the reaction force
The sign of the reaction force acting on the extrusion is based on the Fig 2. For example, the side reaction for the extrusion is always positive which means toward the left as a compressive force for the extrusion. The sign for the top force is strictly depending upon the interpolation. Since the " guided " is imposed on its left side, negative sign for the top force means is a pulling force for the extrusion or it is compressive force if the "guided" is imposed on the right side. The magnitude will be the same.

Table 17.14: Side force acting between blocks.

	B+A	B+A
Block #	#14 (B) and 15 (A)	#39 (B) and 40 (A)
Max. deflection	5.625"	0.75"
PVC stress		
peak (psi)	1085	842
excluding peak (psi)	759	552
Adhesive stress		
Peeling (lbf/in)	17.62	6.32
shear (psi)	312.50	243.72

Table 17.15: PVC and adhesive stresses. Note: (1) #14+#15 (B+A) is the B+A block whose available gap size = 6.5 inches (no touching occurs on its side yet); (2) #39 and #40 is last B+A block in the detector.

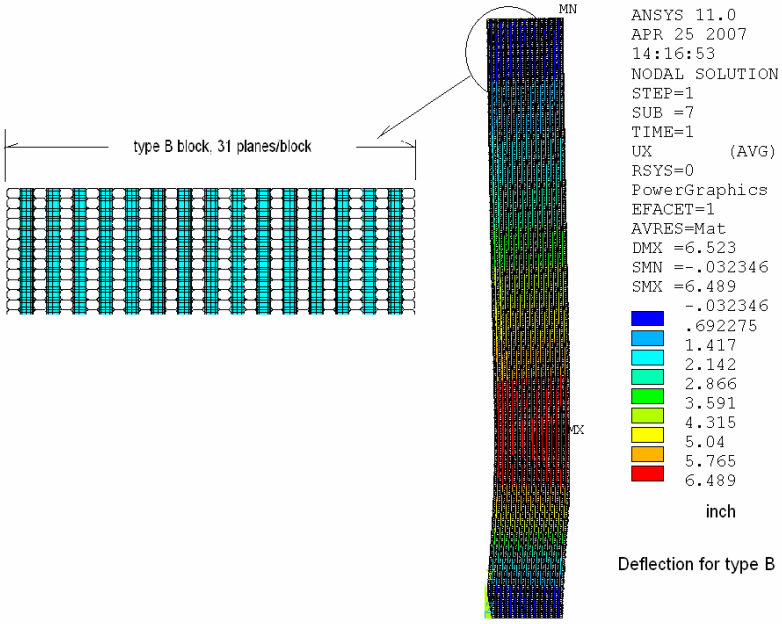

Fig. 17.55: Deflection of type B block with 31 planes.

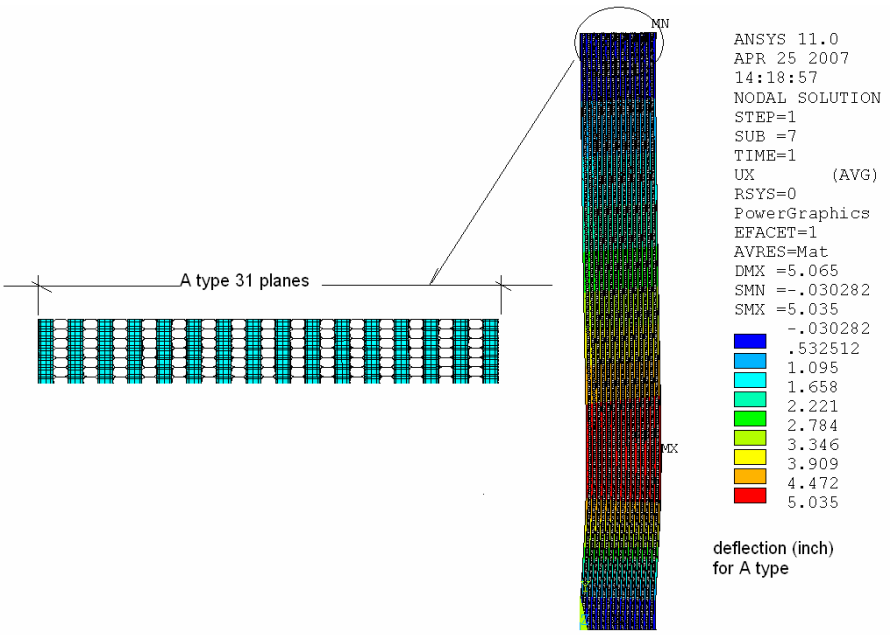

Fig. 17.56: Deflection of type A block with 31 planes.

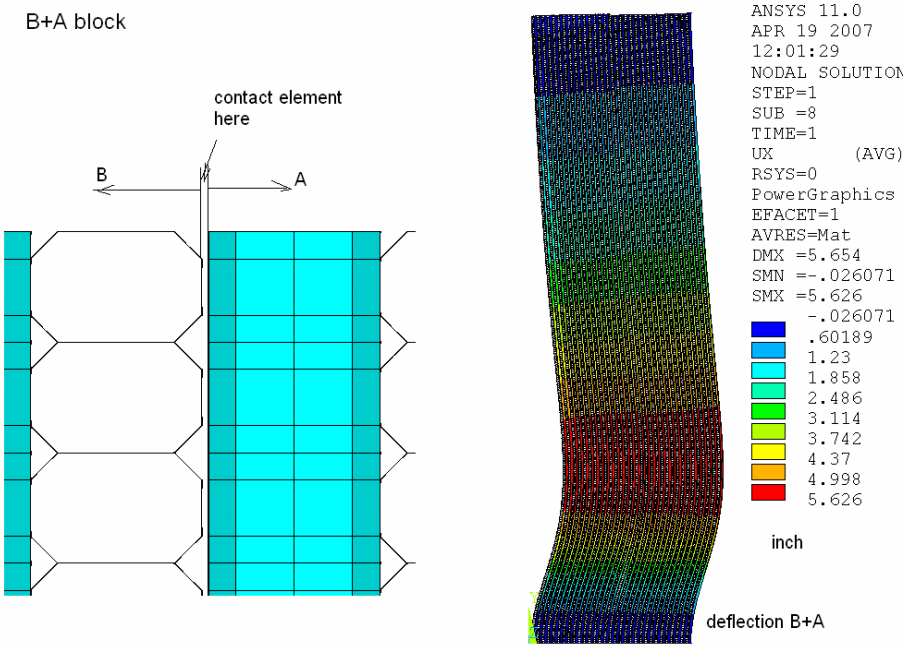

Fig. 17.57: Deflection of type B+A block with 31 planes.

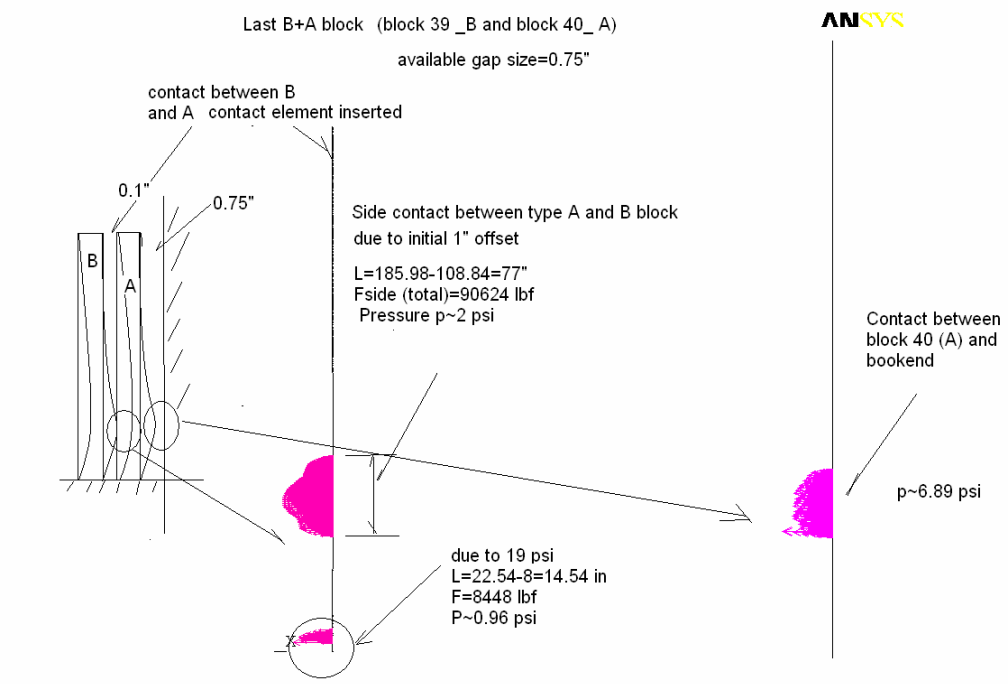

Fig. 17.58: Schematic representation of how contact occurs between blocks.

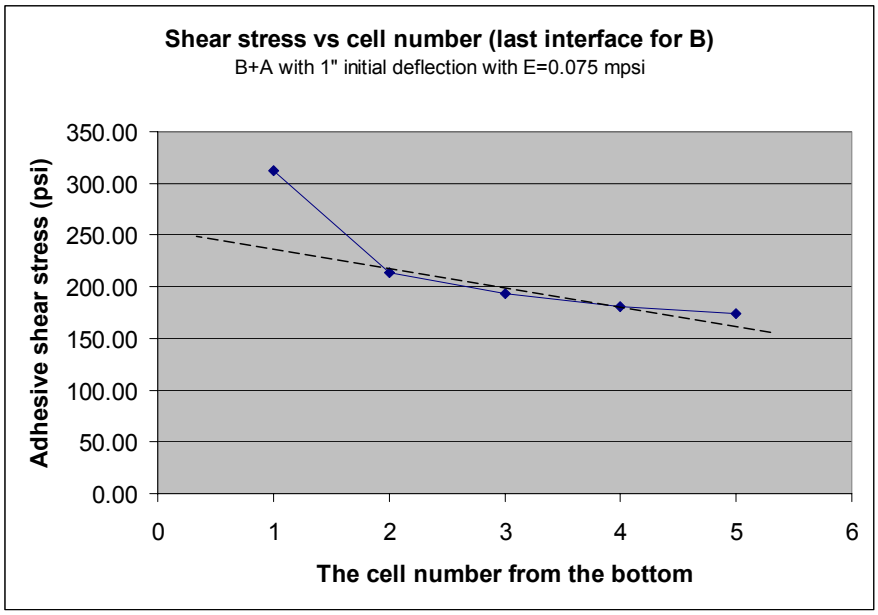

Fig. 17.59: Adhesive shear stress vs the cell number from the bottom.

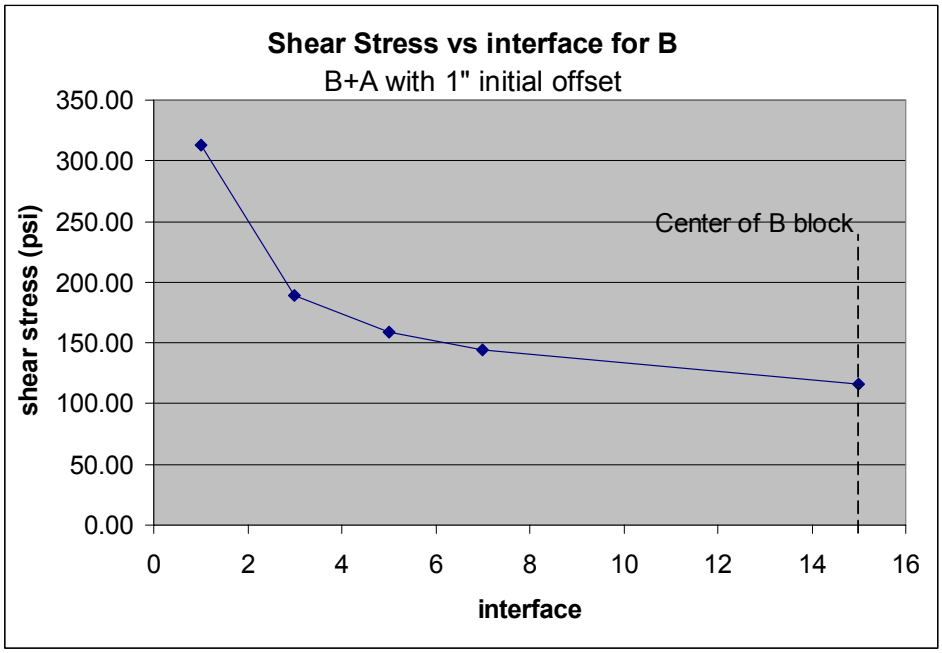

Fig. 17.60: Adhesive shear stress vs the plane interface. The dashed line indicates the block center.

17.5.6 Structural Considerations During Scintillator Filling

The far detector assembly plan calls for filling the modules in each superblock with liquid scintillator as soon as the last block in a superblock is installed (NOVA-doc-2510). Blocks within a superblock are filled one at a time, beginning with the south-most block. (NOVA-doc-2659 shows that structural stability is maintained regardless of the order of filling of blocks within a superblock.) Planes of horizontal modules within a block are completely filled before the filling of vertical modules begins (NOVA-doc-1298 and 2510). During the full-rate installation period, a new superblock will be completed every three months, and filling will be finished around the time that the next superblock has been installed. Significant PVC creep weakening begins during the installation and filling process, as stress on the PVC increases. We assume conservatively that the PVC modulus has been weakened by six months of creep when a superblock is completely full (Table 17.2). At that time, the "top guided" constraint condition is provided by the presence of the next superblock. NOVA-doc-2664 indicates that, after 6 months of PVC creep, the buckling safety factor for a filled A-type block will be about 5 and that a single filled B-type block has a safety factor of 4.7. Since the B blocks are in contact with A blocks on both sides, the "top-guided" constraint for the B blocks is conservative and the buckling safety factor for the filled superblock structure will be about the same as the SF = 5 result obtained for an A block alone.

17.5.7 Adhesive Requirements

We have required a safety factor of 5.0 on the adhesive stresses throughout the design process. Sections 17.5.3.1, 17.5.4.1 and 17.5.5.2 describe the adhesive stresses in the detector under a range of loading conditions. We have calculated the maximum shear and peel stresses at 20 years in the assembled detector using the pessimistic creep prediction. Table 17.15 shows that the maximum peel force (17.6 lbf/in) and shear stress (312 psi) both occur in blocks #14-15. However, as explained in Section 17.5.5.2, the peak adhesive shear stress is very localized and the most adhesive shear stresses are below 200 psi. Our SF = 5.0 constraint requires an adhesive peel strength of 88 lbf/in and shear strength of 1000 psi for the average stress in the block.

As described in Section 17.6.7 and NOVA-doc-1944, adhesive shear and peel strength decreases as the glue line thickness and open time increase. For an open time of 20 minutes and a

glue thickness of 0.030 inch, the measured adhesive shear strength of 508 psi is significantly less than our requirement of 1000 psi. In NOVA-doc-2419 we have therefore reassessed the stability of the structure using the measured adhesive shear strength instead of 1000 psi (which gives a safety factor of five). The calculation treats all the glue bond joints with SF <5, based on the 508 psi shear strength, as joint failure.

The results of the calculation for both A-type and B-type blocks are shown in Figures 17.61 and 17.62 respectively. For a B-type block, which has the highest peak stress, in the fully bonded case the peak shear of 233 psi appears at first few glue pads above the floor and decays very quickly. To have a SF = 5 based on the 500 psi strength, the shear working stress has to be limited to 100 psi or less. This condition is satisfied for all bonds that are 9 inches or more above the bottom of the block. The "adhesive bond missing" curves in Figures 17.61 and 17.62 show the results with adhesive joints below 9 inches deleted, to simulate the bond failure. The results for a B-type block are summarized in Table 17.16. By comparing with the fully bonded case, the impact on buckling safety factor is negligible. In fact, only 6 pads out of the total 328 pads, less than 2%, are treated as failures. The maximum adhesive stress is about 125 psi and ~5.45 lbf/in for the peeling force. The calculation was repeated for an A-type block and a similar conclusion was reached, as shown in Table 17.17. Finally, as an extension of this study, we have calculated the SF as a function of the distance above the floor below which glue bond failure occurs. Figure 17.63 shows that there will be no significant impact on the buckling safety factor until the glue bond failure length exceeds 30 inches from the bottom of the block. It is however essential to maintain the minimum adhesive strength of ~500 psi to achieve SF ~5, since the shear stress curve decreases faster than linearly as a function of the height after first 10-15 inches from block bottom. The 20-year PVC modulus of E = 0.146 mpsi was used for these calculations

	Maximum shear stress (psi)	Maximum peel stress (lbf/in)	SF (top free)	SF (top guided)
Fully bonded	234	4.78	1.86	2.46
Glue bonds fail 9" above the floor	~125	5.45	1.84	2.45

Table 17.16: Summary of shear and peel strength analysis for a B-type block.

	Maximum shear stress (psi)	Maximum peel stress (lbf/in)	SF (top free)	SF (top guided)
Fully bonded	167	4.28	2.02	2.63
Glue bonds fail 9" above the floor	~119	4.68	2.01	2.62

Table 17.17: Summary of shear and peel strength analysis for an A-type block.

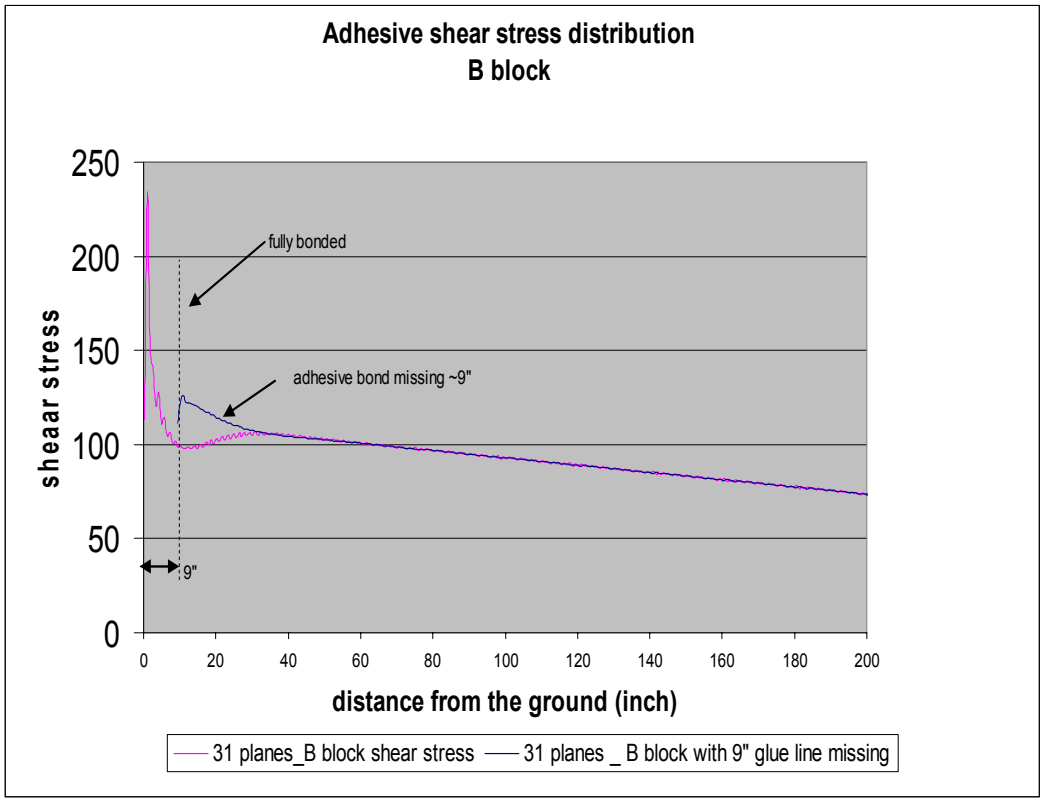

Fig. 17.61: Adhesive shear stress as function of the height above the bottom of a B-type block. The two curves show the stresses with all bonds intact and with all bonds below 9 inches deleted.

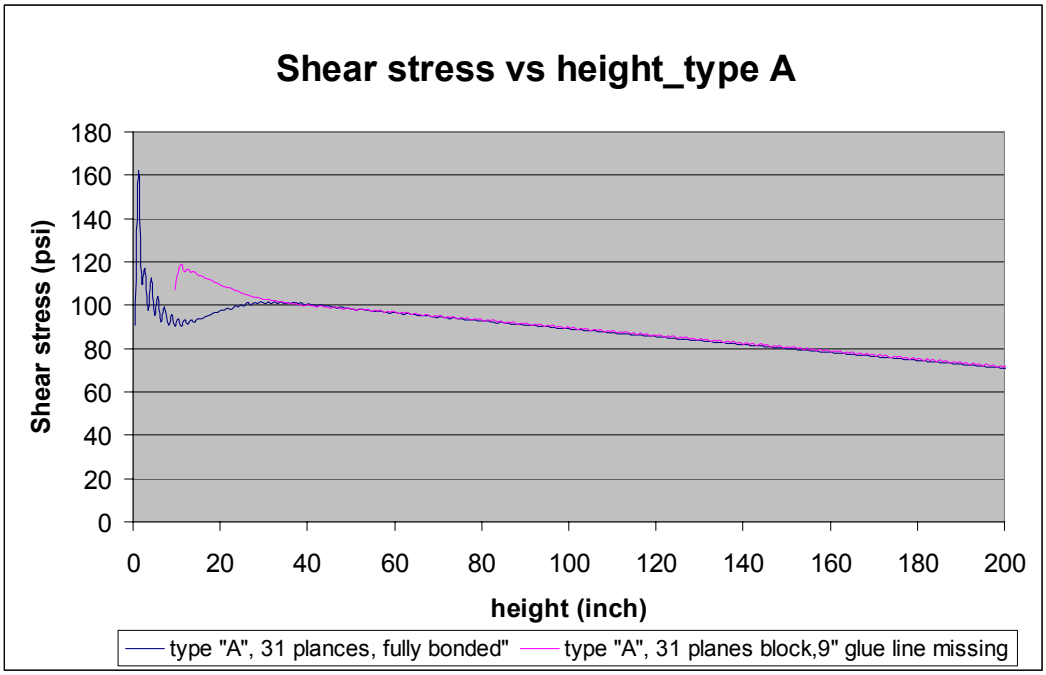

Fig. 17.62: Adhesive shear stress as function of the height above the bottom of an A-type block. The two curves show the stresses with all bonds intact and with all bonds below 9 inches deleted.

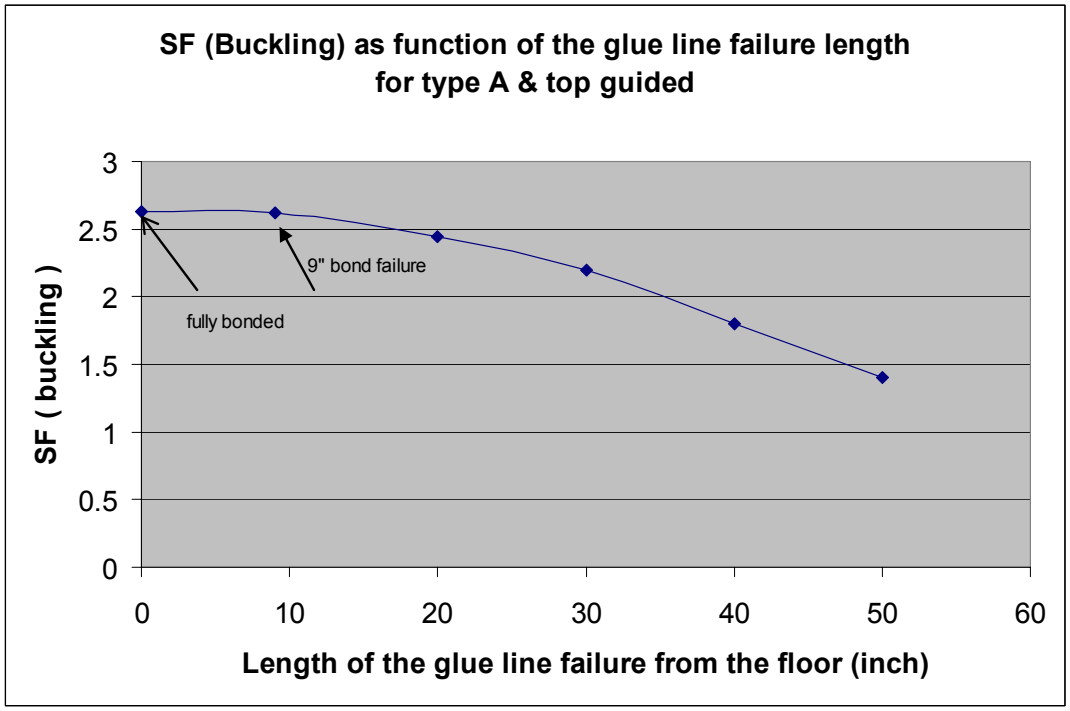

Fig. 17.63: Buckling safety factor as a function of the height below which all glue bonds fail. These calculations use the top-guided constraint for a type-A block.

17.6 Mechanical Prototypes

It is very important to perform extensive mechanical prototype studies of the NOvA structure using actual extrusions. The production of the first prototype extrusions that were useful for such studies began in September 2006. The purposes of the mechanical prototypes described in this section are (1) to test the ability of the FEA modeling to predict the performance of the PVC extrusions and adhesive, (2) to evaluate the assumptions that have gone into the model, and (3) to have a realistic test of the adhesive bond using the actual geometry.

To date the following prototype structures have been built and tested:

- 4-ft extrusion under internal pressure
- 3-Layer/single-extrusion prototype under internal pressure (3M 2216 adhesive)
- 7-Layer hydrostatic stress transmission test (3M 2216 adhesive)
- 11-Layer/single-extrusion prototype under internal pressure (Devcon 60 adhesive)
- 4-Plane IPND block prototype (Devcon 60 adhesive)
- 8-plane IPND block prototype (Devcon 60 adhesive)
- 3-layer extrusion prototype measurements of Devcon 60 shear strength

In addition, the full height structural engineering prototype is planned for 2008.

The sections below describe the results of the prototyping that has been done to date.

17.6.1 Four-Foot Extrusion Under Internal Pressure

Extensive analysis has been done on the NOvA structure. These calculations have been difficult to verify experimentally because actual PVC extrusions of the correct geometry were not available until September 2006. Currently a die for 16-cell extrusions has been made and is being used to produce prototype extrusions. These extrusions are now being used to perform

mechanical tests to confirm the structural analysis. The first test was simply to seal the ends of a 4-ft long extrusion and pressurize it to 19 psi (the operating hydraulic pressure at the bottom of the detector). Rosette strain gages have been placed on the surface of the extrusion to measure the stresses which are then compared to an FEA simulation. This prototype construction and test results are described in NOVA-doc-1120.

17.6.1.1 Test description

A 4-ft long extrusion had four rosette strain gages placed at the center of the length, at the locations shown in Figures 17.64 and 17.65. The rosettes are oriented as shown in Figure 17.66. The X direction is aligned with the direction of extrusion and the Y direction is aligned with the width of the extrusion. The pressure was applied using nitrogen from a tank. A pressure gage on the tank and on the extrusion confirmed the pressure within the extrusion. A barrier used by welders was placed around the extrusion as a precaution against failure of the extrusion or end seal. The extrusion was kept under pressure for five days and then released and allowed to relax for one day.

Future tests will use a temperature compensating gage to eliminate the effect of temperature on the measurements. A lack of data channels prevented the use of a temperature compensating gage on this test.

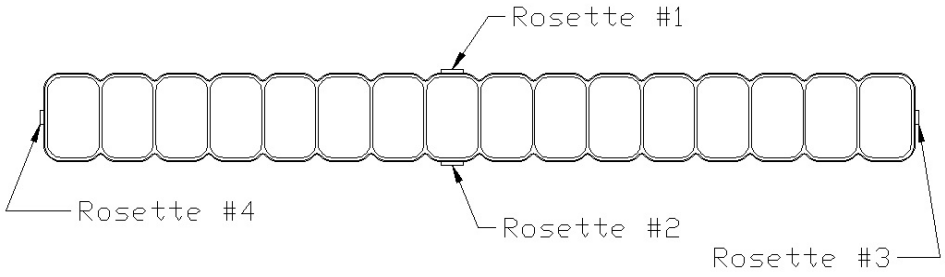

Fig. 17.64: Location of rosette strain gages on the 4-ft long extrusion.

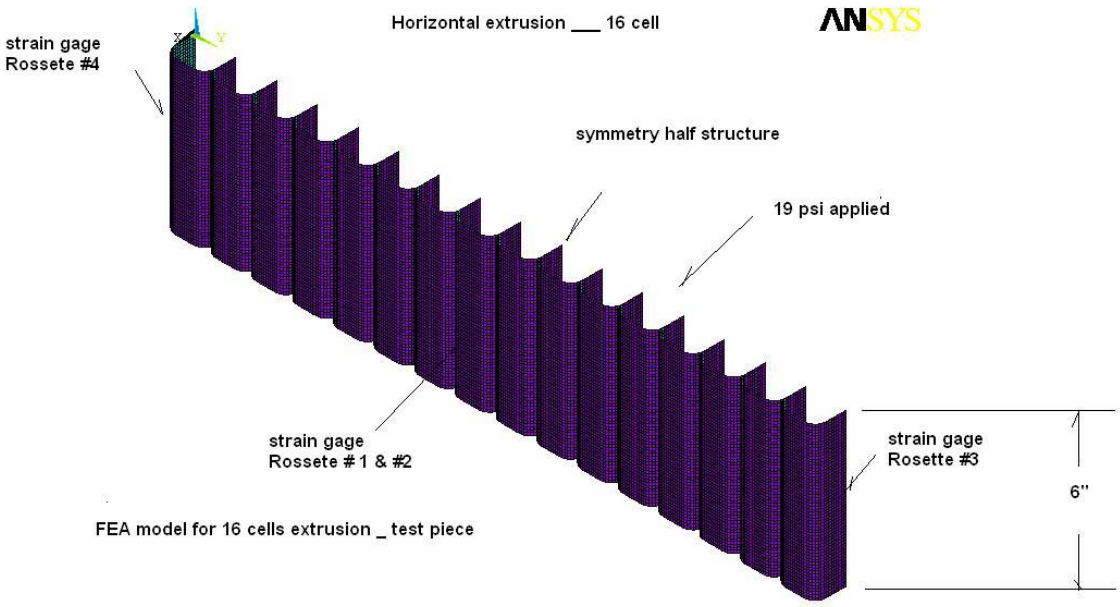

Fig. 17.65: Location of rosettes used for comparison to FEA model.

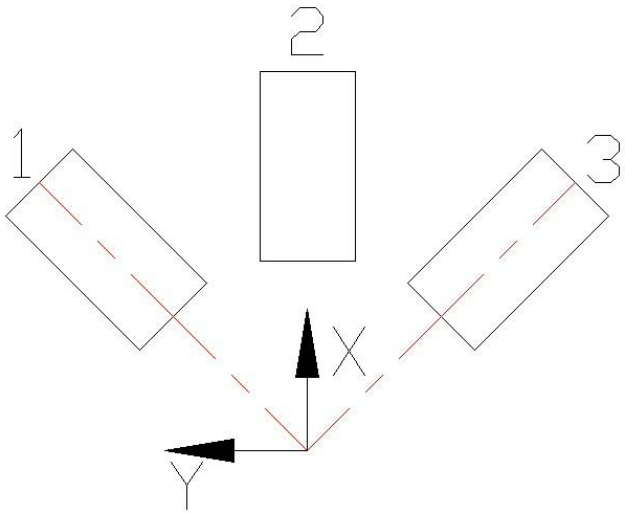

Fig. 17.66: Strain gage orientation and numbering within a rosette.

17.6.1.2 Test results

The strain gages output strains in the direction of their axis. Through geometry the strains in any direction can then be found. The strains from the rosettes were converted to strains in the X and Y directions for comparison to the FEA model.

In order to make a valid comparison between the FEA model and the test measurements the thickness of the webs and sidewalls of the extrusion and the modulus of the material must be taken into account. Initial tests on the PVC show that in the short term modulus of the PVC is on the order of 500 ksi. Measurements on the PVC extrusion showed that the wall thickness

averaged 1.5 mm for the web and 2.5 mm for the outside wall thickness. These values were used in the FEA model to compare to the experimental measurements.

NOVA-doc-1120 gives the detailed test results. Figure 17.67 shows the von Mises stress plotted versus time.

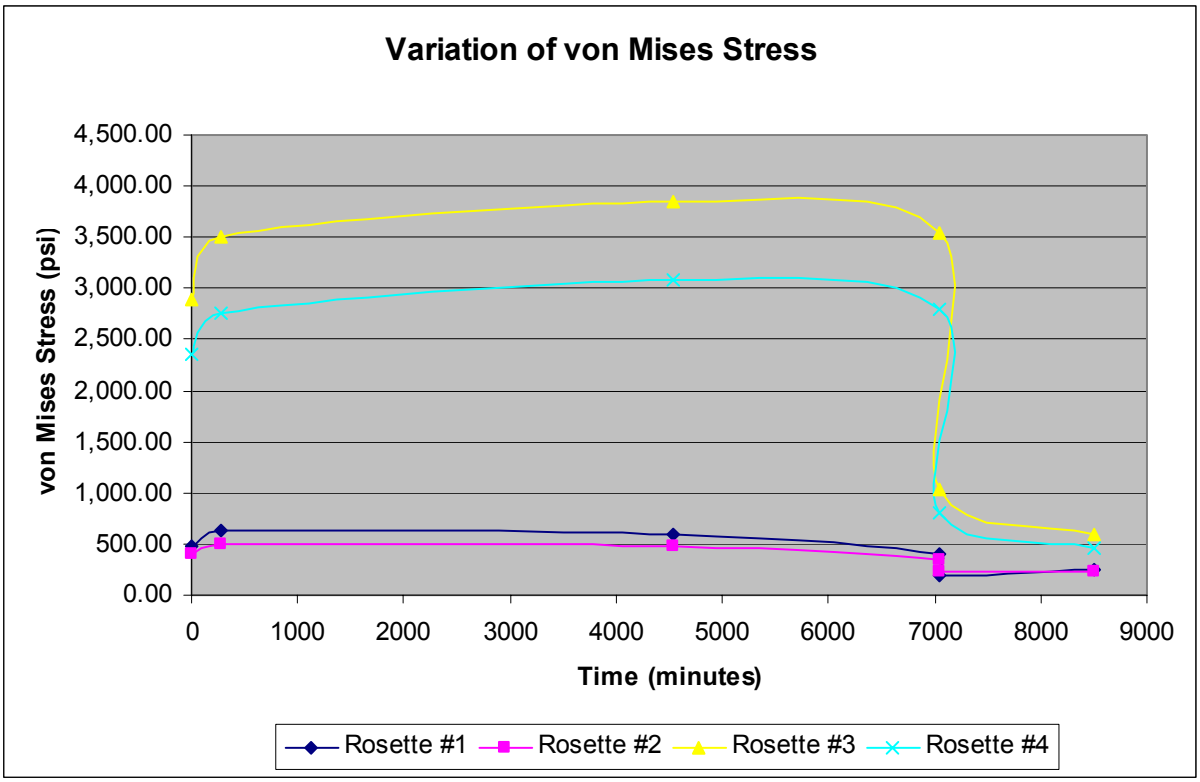

Fig. 17.67: Measured change in von Mises stress with time.

17.6.1.3 Evaluation of results

It can be seen in Figure 17.67 that the stresses increase over a short period of time from their initial values. This increase is most likely due to the initial high creep rate that occurs when PVC is stressed. The calculations of the von Mises stress used a constant modulus (550,000 psi) however the initial modulus was most likely higher and then declined over time. It is felt that the initial increase in stress is due to a high level of initial creep strain. The drop in stress at 7000 minutes is most likely due to temperature variation in the building. The temperature dropped about 15° F between these two measurements and we know that the PVC strain is dependent upon temperature.

It is significant however, that the stress did not return to zero after the pressure was released, and remained even after 24 hours.

The von Mises stress matches closely with the calculated stresses for a single extrusion under pressure, as seen in Figure 17.68. The initial von Mises stress in the side wall on the scallop averaged 437 psi but then increased to 566 psi over a short period. This matches well with the value of 698 psi calculated in the FEA model. The difference is attributed to the averaging affect of the gage over the area that it covers and variation of the thickness within the extrusion. The strain/stress varies rapidly in this region and the strain gage can only average over the 6mm area that it covers. The stress compares very well for the 66 mm sidewall. The gages

measured a von Mises stress of 2628 psi initially and this increased after a short period to 3129 psi, which compares well with the FEA result of 2982 psi. Table 17.18 shows a comparison of initial stresses and strains with the FEA results.

The dial indicator on the third scallop indicated an initial deformation INWARD of the scallop of 0.001 inches which increased to 0.008 inches by the end of the test. A similar type of deformation was found in the FEA model on the order of 0.002 inches as seen in Figure 17.66.

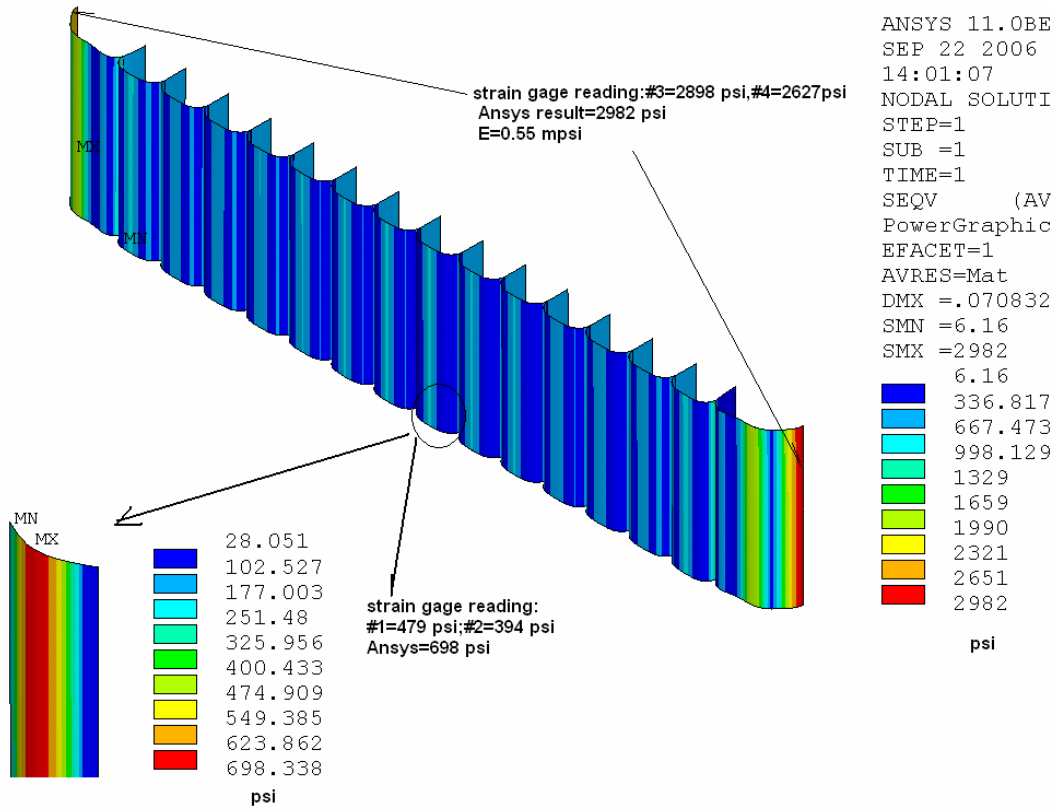

Fig. 17.68: Comparison of strain gage readings with FEA results.

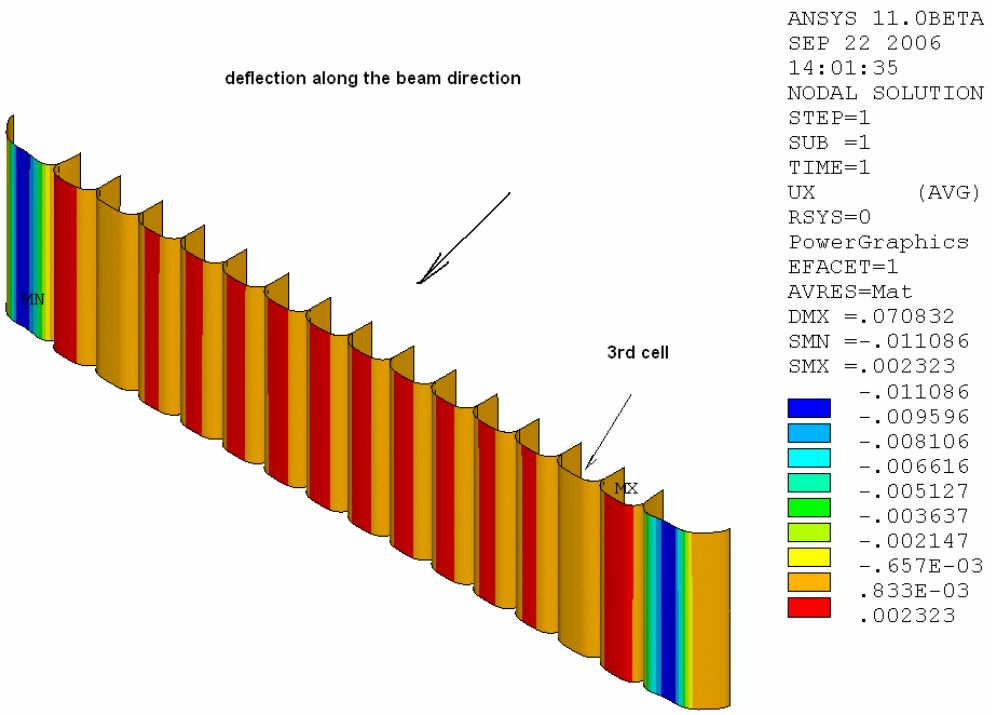

Fig. 17.69: Deformation of scallops predicted by FEA calculation.

	Test Results		FEA Model	
	Stress psi	Strain (Micro)	Stress psi	Strain (Micro)
Scallop side	**480**	872	**694**	1270
60 mm side	**2900**	5270	**2982**	5422

Table 17.18: Comparison of test results with FEA model for 4-ft extrusion prototype.

17.6.1.4 Conclusions from 4-ft extrusion prototype test

This initial test demonstrates that the FEA model can predict within reasonable accuracy the strains/stresses in a PVC structure. Variations in the material thickness and modulus, however, will introduce errors. Any future test will need to use the correct modulus from actual material measurements in order to have a valid comparison.

17.6.2 Three-layer/Single-extrusion X-Y Prototype

The second mechanical prototype constructed was a three layered structure designed to mimic a horizontal extrusion sandwiched between two vertical extrusions. It is described in detail in NOVA-doc-1194. This prototype was constructed using 3M 2216 epoxy with the surfaces of the extrusions roughened using an industrial sander. Figures 17.70 and 17.71 are photographs of

this prototype. The extrusions that simulate the vertical extrusions have end caps installed so that these extrusions can be pressurized. The middle extrusion does not have an end cap because the horizontal extrusions are nominally at atmospheric pressure.

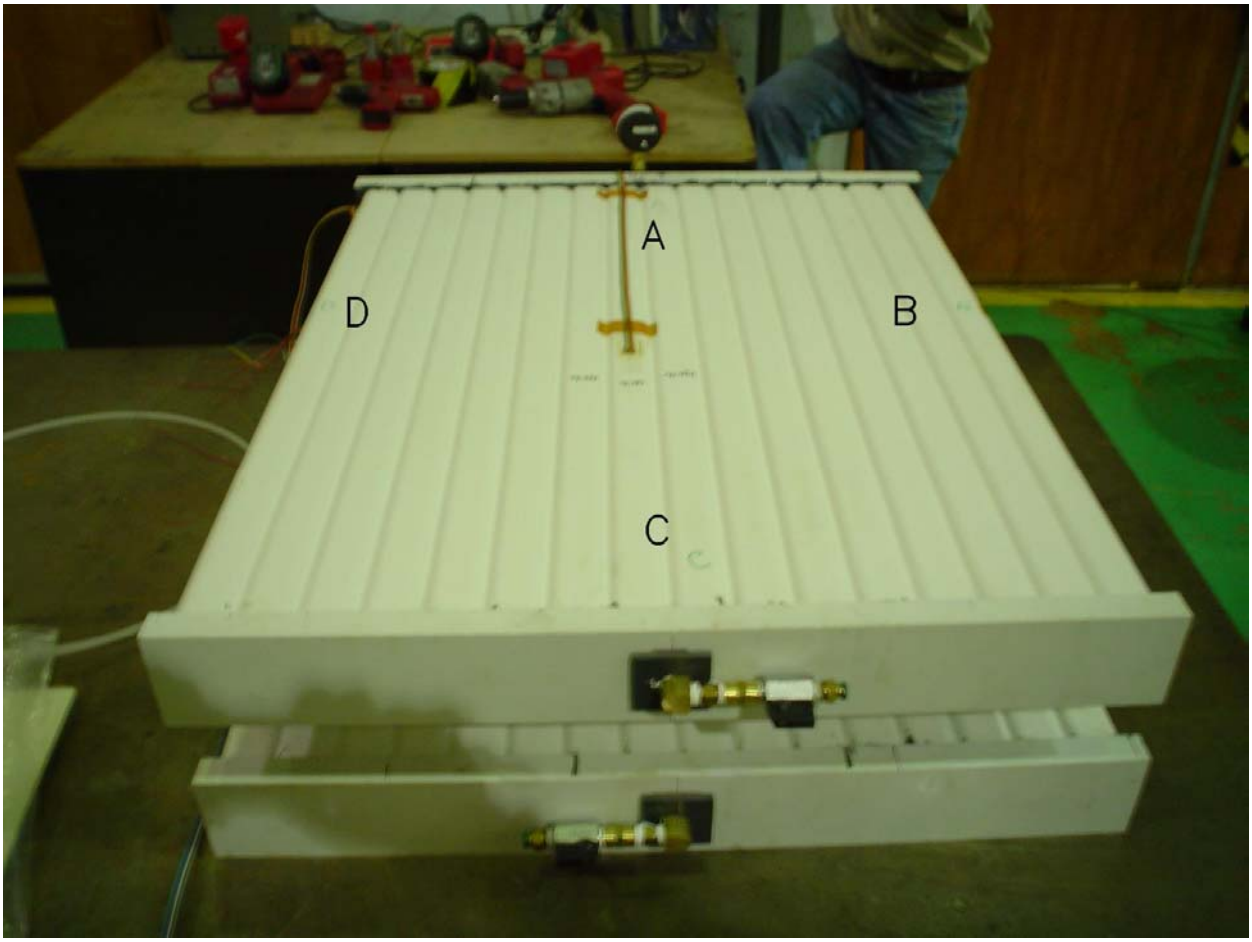

Fig. 17.70: Three-layer X-Y mechanical prototype showing the labeling of the sides. The "vertical" extrusions are on the top and bottom in the photograph.

Fig. 17.71: Three-layer X-Y mechanical prototype showing the top and bottom interfaces. The "vertical" extrusions are on the top and bottom in the photograph.

17.6.2.1 Experimental Setup Description

Strain gages were placed at the locations shown in Figure 17.72 on the outside extrusions being pressurized. The prototype was placed in a plywood box for protection in the event of catastrophic failure of the extrusion/end-seal while being pressurized. The pressure was increased to 20 psi and held for 1.5 hours. The pressure was then successively increased to 40 psi, 60 psi, and finally 80 psi and held at each of these pressures for 1.5 hours. At each pressure the readings of the strain gages were recorded.

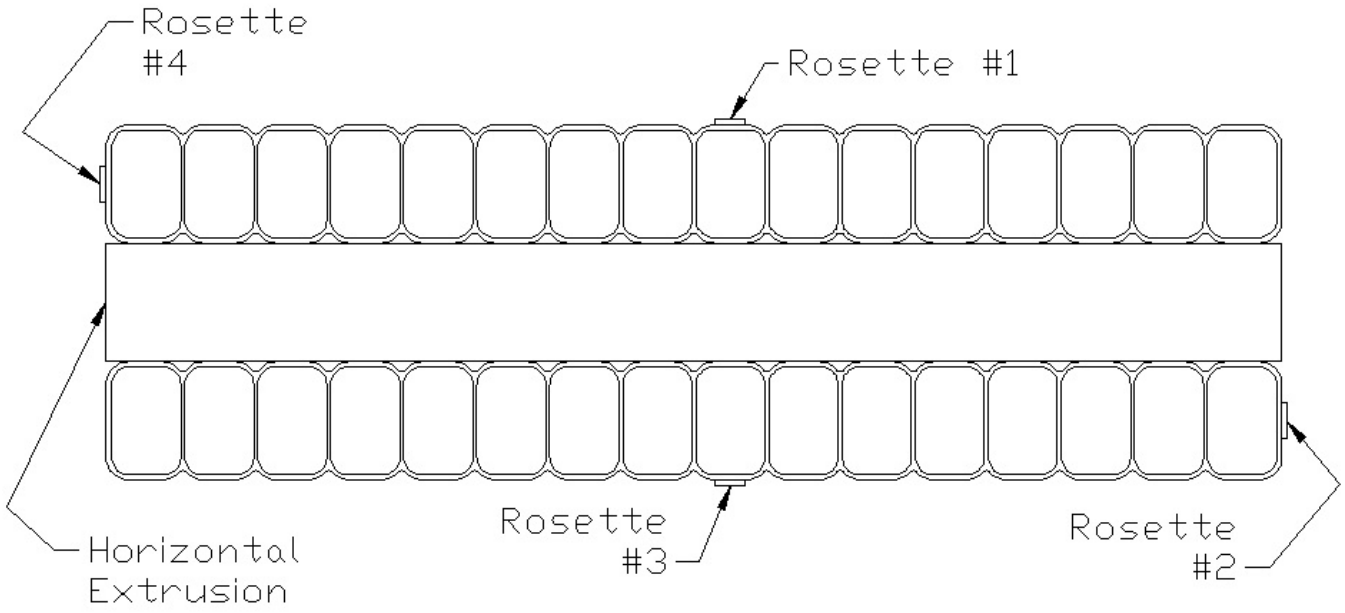

Fig. 17.72: Layout of rosettes on three-layer X-Y mechanical prototype. Figure 17.51 shows the layout and numbering of strain gages in a rosette.

17.6.2.2 Experimental Results

The strain gages output strains in the direction of their axis. Groups of three strain gages are called a rosette and are oriented as shown in Figure 17.66. The rosette was oriented so that the X direction was along the direction of extruding. Through geometry the strains in any direction can then be found. The strains from the rosettes were converted to strains in the X and Y direction for comparison to the FEA model. In order to make a valid comparison between the FEA model and the test measurements the thickness of the webs and sidewalls of the extrusion and the modulus of the material must be taken into account. Initial tests on the PVC show that in the short term modulus of the PVC is on the order of 500 ksi. Measurements on the PVC extrusion showed that the wall thickness averaged 1.5 mm for the web and 2.5 mm for the outside wall thickness. These values were used in the FEA model to compare to the experimental measurements.

NOVA-doc-1194 gives the strain gage readings obtained during the pressure test of the prototype. As the pressure was increased to 40 psi a series of popping noises was heard from the prototype after the pressure passed 35 psi. The popping noise stopped once the pressure stabilized at 40 psi. After 1.5 hours at 40 psi the pressure was increased to 60 psi and immediately the popping noise was heard again until the pressure stabilized again at 60 psi. The same noise was heard again when the pressure was increased from 60 psi to 80 psi. Unfortunately at 80 psi one of the end seals failed and pressure dropped before strain gage readings could be taken.

It is believed that the popping noise that was heard was from failure of the adhesive bonds. Since the prototype was inside the plywood box for protection it was impossible to observe what was happening directly.

A feeler gage 0.0015 inches thick was then used to investigate what bonds had failed. The gage was long enough to be inserted to a depth of 7 cells. Each side of the prototype was labeled as shown in Figure 17.70. At each cell location the feeler gage was inserted in order to measure the depth to which it could be inserted. NOVA-doc-1194 summarizes the measurements and the

number of cells the feeler gage was able to be inserted into the prototype. These are compared with the FEA model of this device in the next section.

17.6.2.3 FEA Model of Prototype

An FEA model for the 3-layer X-Y prototype was created as shown in Figures 17.73 and 17.74. The same type of shell element and the mesh size as a real detector model was used so that meaningful comparison can be established. The wall thickness of test piece is 2.5/1.5 mm (side wall/web) for both vertical and horizontal extrusions. The PVC module is 0.55e6 psi which is consistent with t = 90 min of creep predicted by the creep curve. The modulus for the adhesive is 0.5e6 psi with 10 mils thickness assumed. Figures 17.75 and 17.76 show the results for several loading cases. The maximum peeling force reaches 20 (lbf/in) for 40 psi loading, where the "popping sound" occurred. The calculation indicates this maximum peel occurs at the edge joint. Compared with earlier T-shape and cleavage test results, one would expect that some adhesive joints would fail at a peeling force of ~20 lbf/in (peeling strength) if 40 psi loading is applied to the test piece. The shear stress is still far below 1,000 psi (average shear strength from the double shear test and technical data sheet for 3M 2216 epoxy). Figures 17.77, 17.78, 17.79 and 17.80 show the model results used for the comparison between the FEA calculations and strain gage measurements. Table 17.19 summarizes the comparisons. The results agree within 11% for the 60 mm side. However, the FEA results give a higher stress/strain for the 38.8 mm side. It could be due to the thickness variation since an average thickness of 2.5/1.5 mm is used for the extrusion. A final cross check with a mini 3-D model shows that the peeling force along the edge reaches its capacity of 19.2 lbf/in for p = 40 psi with a wall thickness of 2.5 mm/1.5 mm for both vertical and horizontal extrusions, as shown in Fig 17.81 and Fig 17.82.

P=18 psi	Von Mises Strain (micro) (FEA)	Von Mises Stress (psi) (FEA)	Von Mises Strain (micro)(measured)	Von Mises psi (measured)
60 mm	4294	2358	3788	2170
38.8 mm	1145	624	588	323
E	0.55 mpsi is based on the E curve at t = 90 min			

Table 17.19: Comparison for the stress/strain in the 3-layer X-Y prototype.

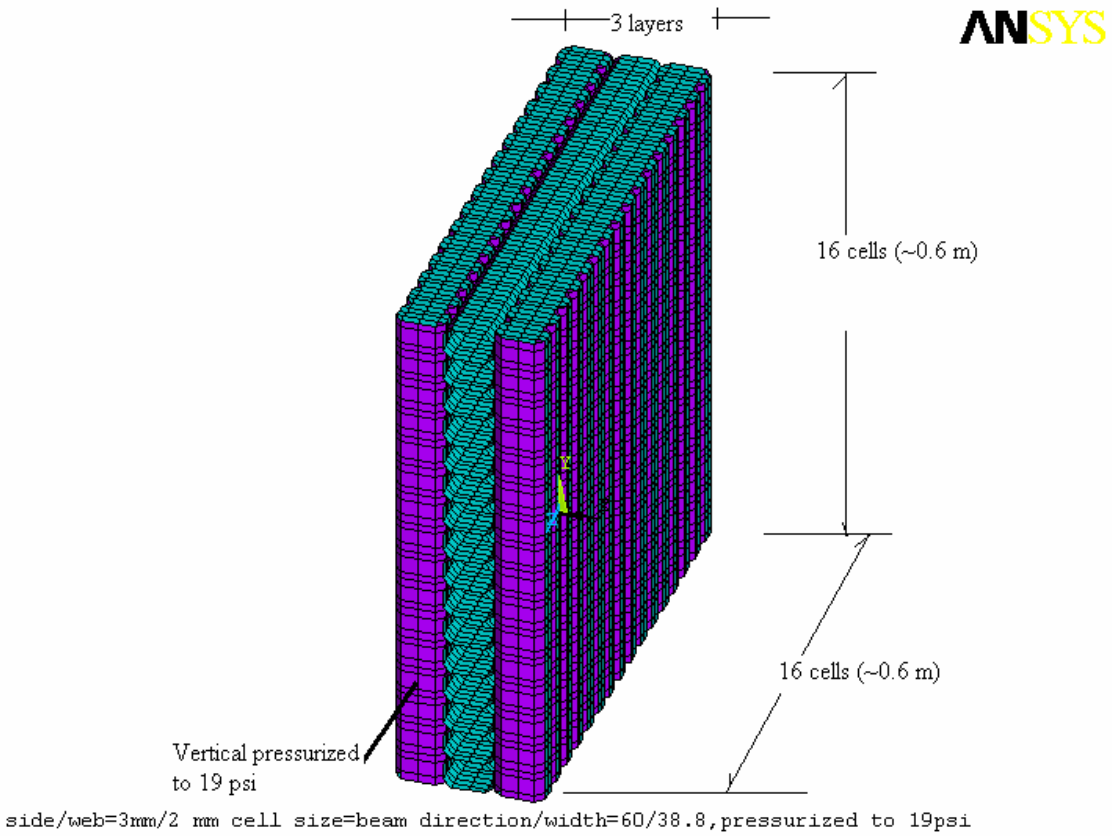

Fig. 17.73: FEA model of 3-layer X-Y prototype structure.

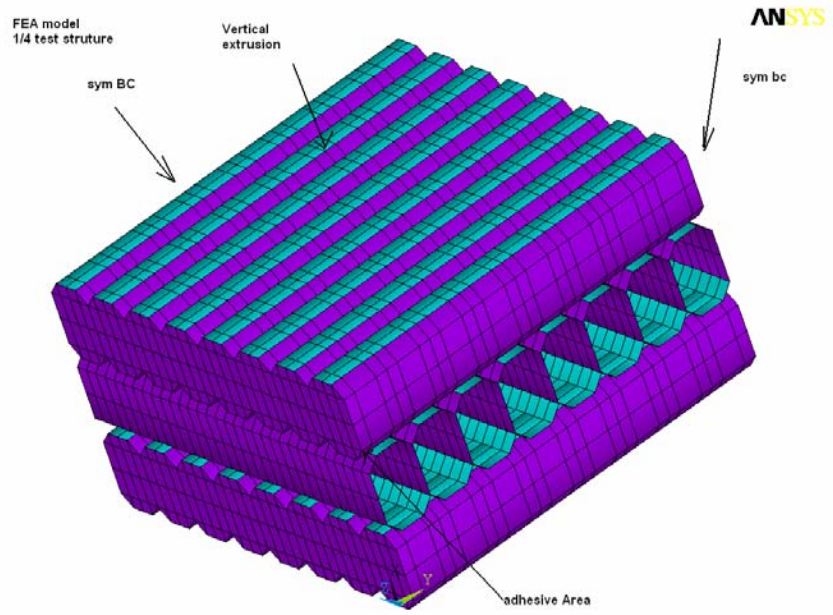

Fig. 17.74: FEA model of one quarter of 3-layer X-Y prototype, using symmetry.

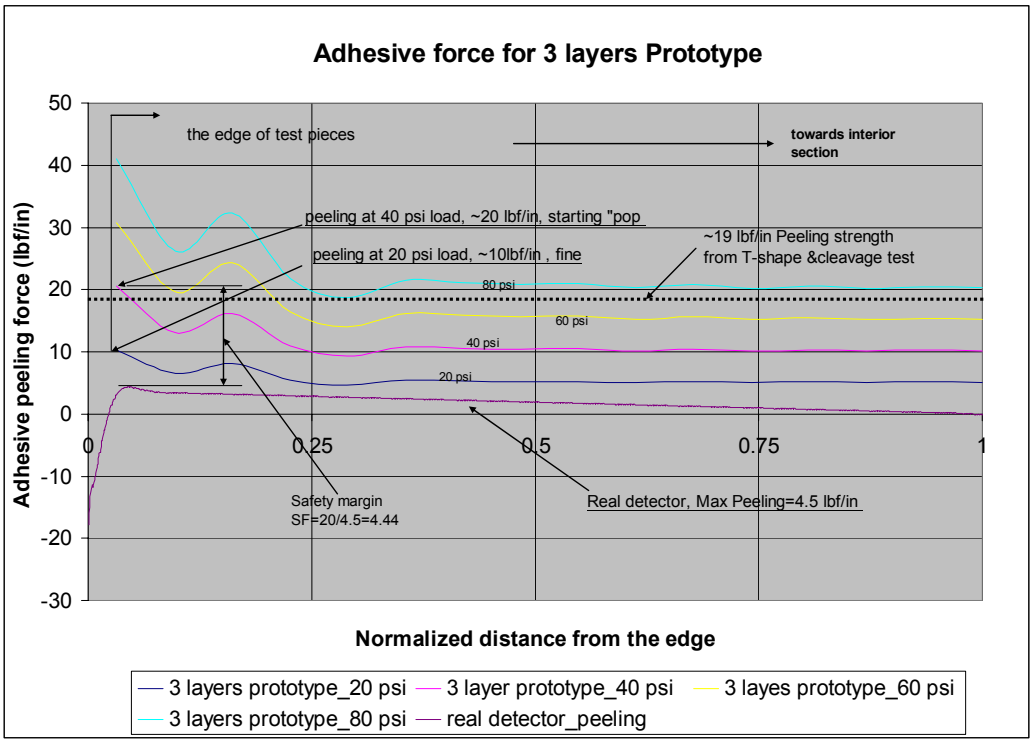

Fig. 17.75: The peeling force comparison. The X axis is a normalized length. The test piece is normalized to its half length, using symmetry, and the real detector is normalized to its full height.

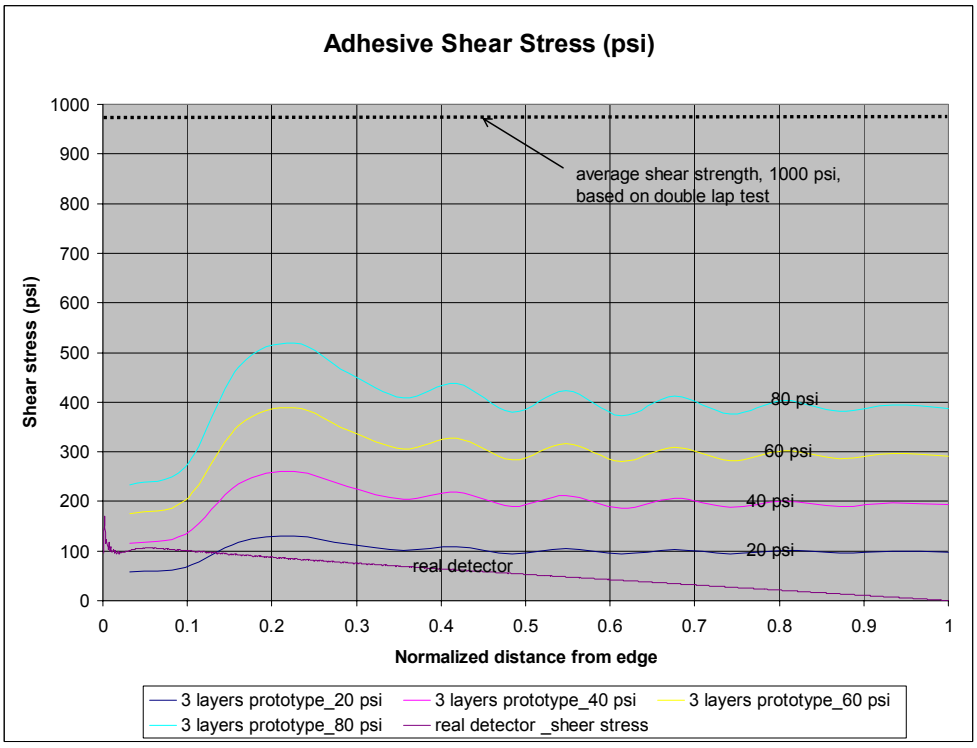

Fig. 17.76: Shear stress comparison. The X axis is a normalized length. The test piece is normalized to its half length, using symmetry, and the real detector is normalized to its full height.

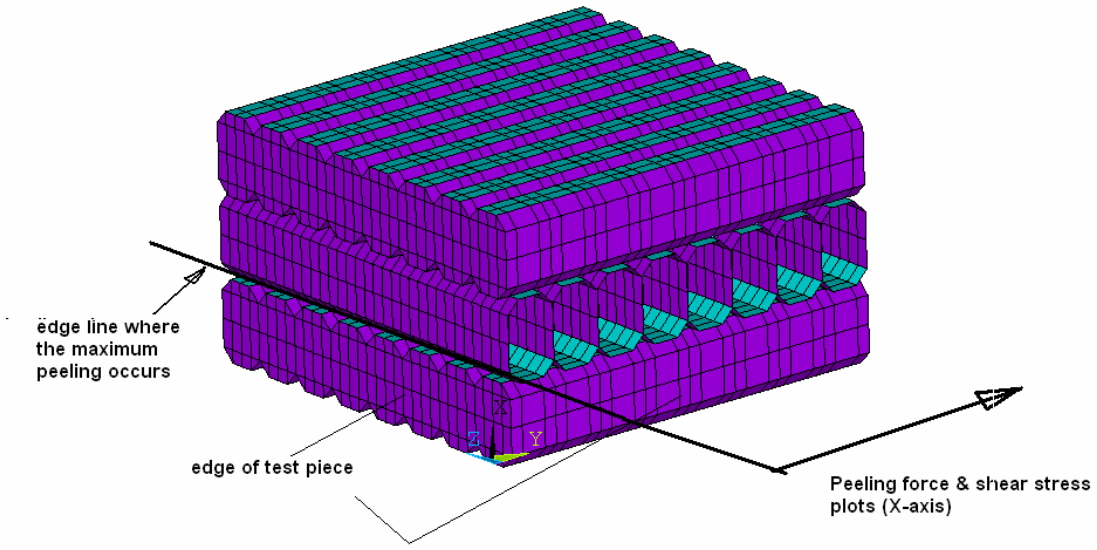

Fig. 17.77: Location of the maximum peeling force in the 3-layer X-Y prototype.

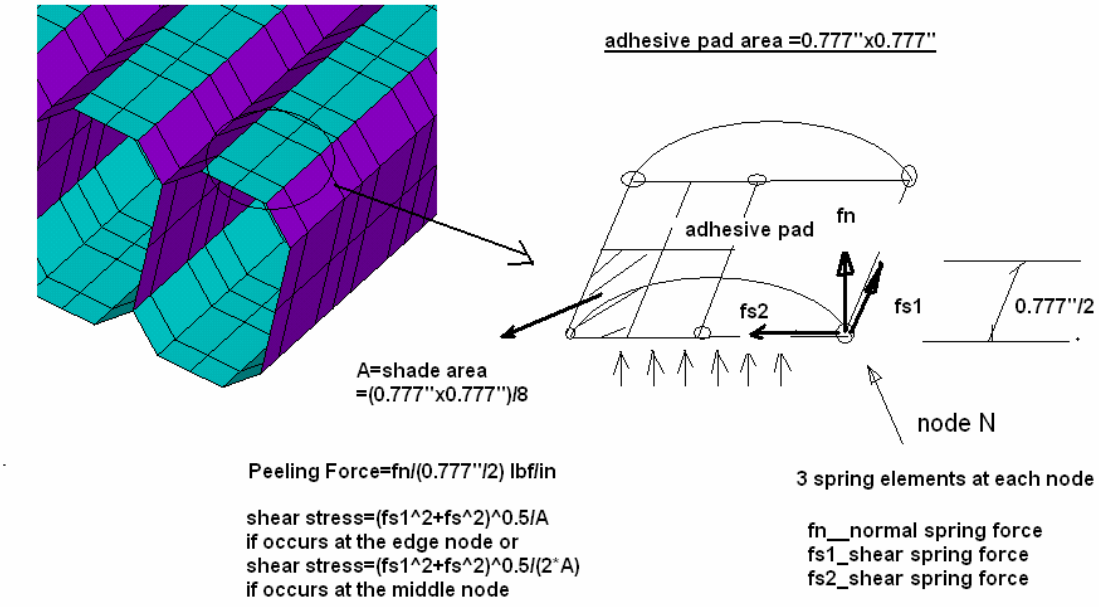

Fig. 17.78: The force extraction from the 3-layer X-Y prototype model.

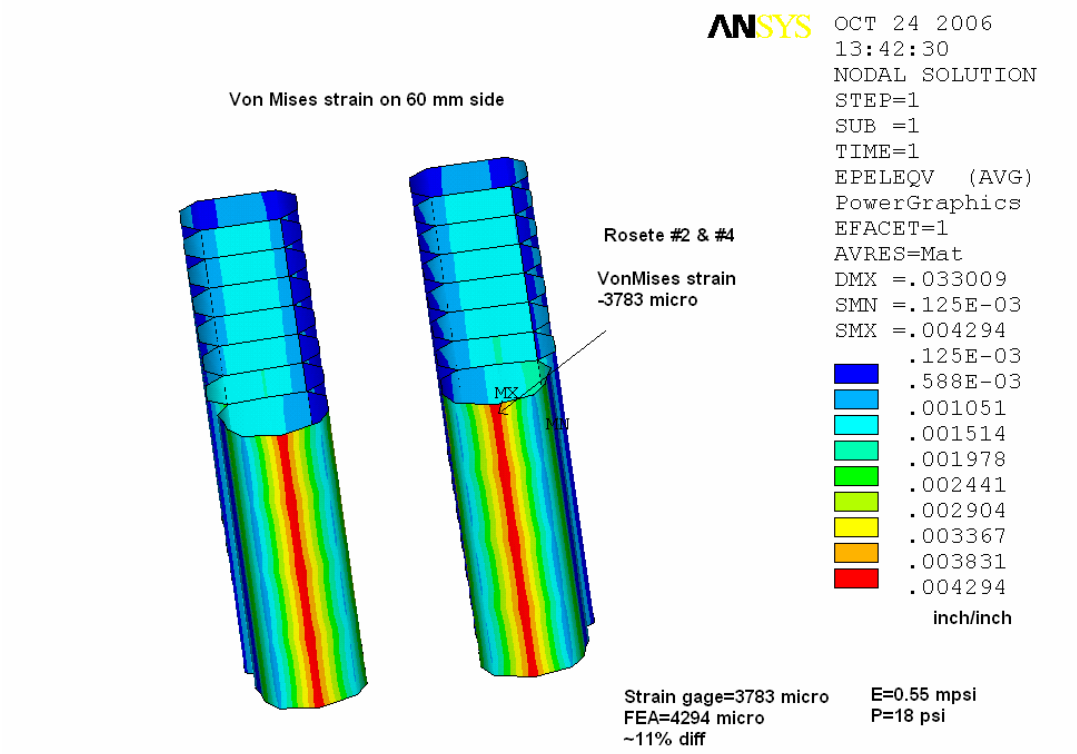

Fig. 17.79: Von Mises strain in the 3-layer X-Y prototype model.

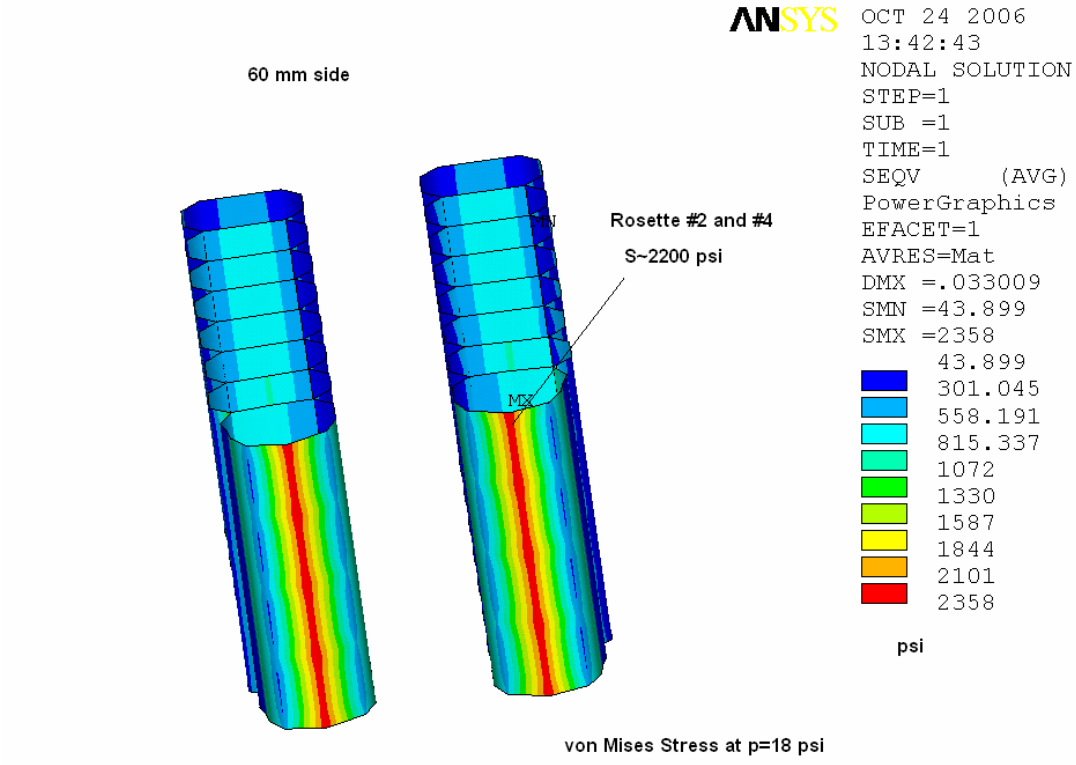

Fig. 17.80: Von Mises stress in the 3-layer X-Y prototype model.

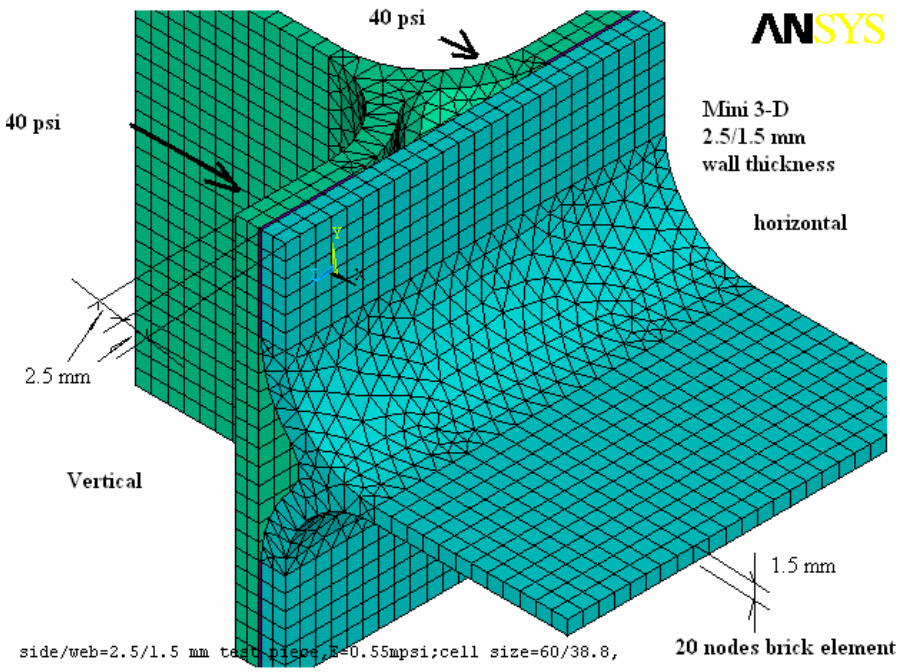

Fig. 17.81: Mini 3-D model for the adhesive peeling force in 3-layer X-Y prototype.

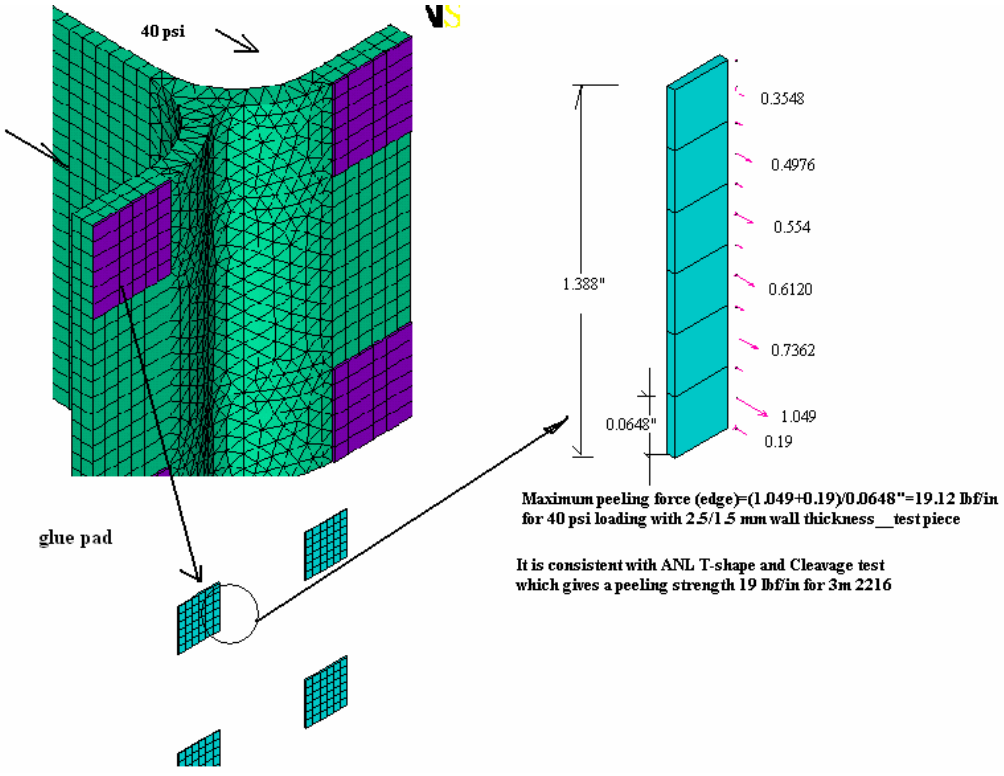

Fig. 17.82: Maximum peeling for p = 40 psi from mini-3D model of the 3-layer X-Y prototype.

17.6.2.4 Conclusions from the 3-layer X-Y Prototype

This initial mechanical test of assembled extrusions showed mixed results when compared to the FEA model. The FEA model showed that at 40 psi internal pressure the peel stresses approached the peel failure strength of the adhesive. However, not all of the bonds failed at this pressure and there were relatively few failed bonds even after the extrusions were pressurized to 80 psi. The FEA model also showed that the shear strength of the adhesive bond was far below the actual strength of the 3M 2216 epoxy. The strain gages showed very good agreement with the gages on outside edges of the extrusion on the 60 mm side. However, there was poor agreement with the strains measured on the scalloped surfaces. Similarly poor comparisons were also seen on the initial 4 ft pressured prototype. The poor comparison with the FEA could be explained by the high strain gradient in this region which could not be measured by the gages which actually only measure the strain averaged over the 0.125 inch individual gages and the 0.5 inch wide rosette.

17.6.3 Seven-layer Hydrostatic Stress Transmission Prototype

17.6.3.1 Experimental Setup

The purpose of this prototype was to check the FEA model prediction that the swelling resulting from filling the first cell of a NOvA X-Y structure propagates through the entire block thickness. To test this idea, a series of empirical tests were conducted. Cells were filled with water and deflections measured.

An assembly of early prototype NOvA 3-cell PVC extrusions was constructed with 4 vertical extrusions and 3 horizontal extrusions. The vertical extrusions are ten feet high while the horizontal extrusions are 5 inches long. The hydrostatic pressure at the bottom of the vertical extrusions was 4.32 psi. 3M 2216 epoxy was used to join the extrusions and one half inch thick plastic plugs where inserted and epoxied into the lower ends of the vertical extrusions. Figure 17.83 is a photograph of the setup.

This assembly is shown behind a ladder used when filling the vertical extrusions with water. Two dial indicators where set up to measure the deflections of the center cell of the outer vertical extrusions at a distance of twelve inches above the bottom. The assembly was placed on a steel plate but was not constrained by it other than by friction. The table and aluminum channel was used as a safety restraint; it did not constrain the extrusion assembly but would prevent the extrusion from moving if the extrusion were bumped. This test is described in more detail in NOVA-doc-1198.

Fig. 17.83: Photograph of the 7-layer X-Y prototype used to measure transmission of swelling from hydrostatic pressure.

17.6.3.2 Results

The vertical extrusions in the 7-layer structure were filled with water twice. A full water column height provides 3.9 psi on the extrusion at an elevation of 12 inches above the bottom (this corresponds to where the dial indicators were located). Figure 17.84 shows the cell numbering scheme. The order of cell filling changed with each filling, but the cell numbering remains

V11	Horz.	V8	Horz.	V5	Horz.	V2
V10		V7		V4		V1
V12		V9		V6		V3

Fig. 17.84: View looking down on the top of the 7-layer X-Y prototype assembly.

For the first test, cell V1 was filled first, then V2, then V3, etc. until cell V12 was filled last. For the second test, the center cells were filled first, and adjacent cells were filled from the center outwards. The detailed results of these tests are described in NOVA-doc-1198, and are compared with the results of an FEA analysis in the next section.

17.6.3.3 Comparison of 7-layer prototype results with FEA model

The seven-layer PVC structure is modeled with a shell element and a spring element was used for the glue layers. Figures 17.85, 17.86 and 17.87 show the details of the FEA model. This

is very similar to the approach used for the NOvA far detector structure, except that the cell geometry and wall thicknesses were modified to reflect the 3-cell extrusions used for this study. A linear distributed pressure is applied on the vertical extrusion with maximum value of 4.32 psi at the bottom. The bottom of extrusion is assumed to be fixed by the plastic end plug. The calculation reflects the filling sequences used for the measurements. A PVC modulus of E of 0.36 mpsi and 0.4 mpsi, based on a single layer 8-ft high extrusion test, is used in the calculation.

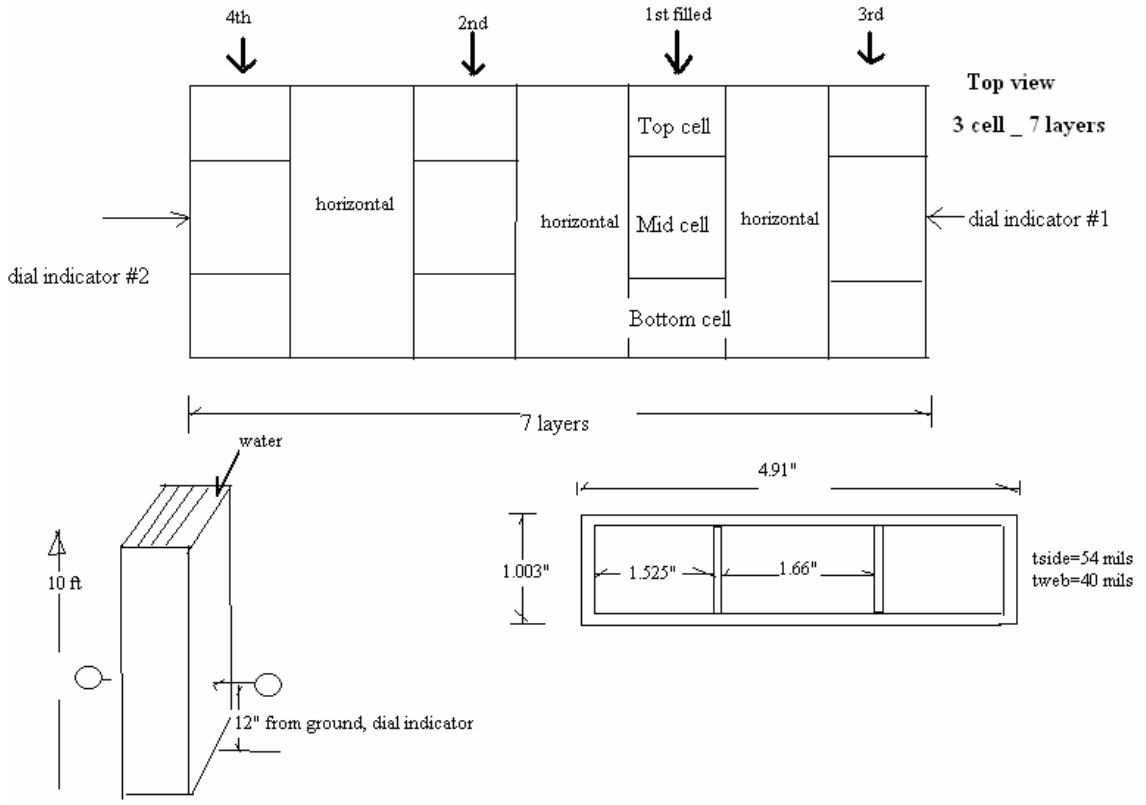

Fig. 17.85: Sketch of the geometry of the 7-layer prototype constructed of 3-cell extrusions.

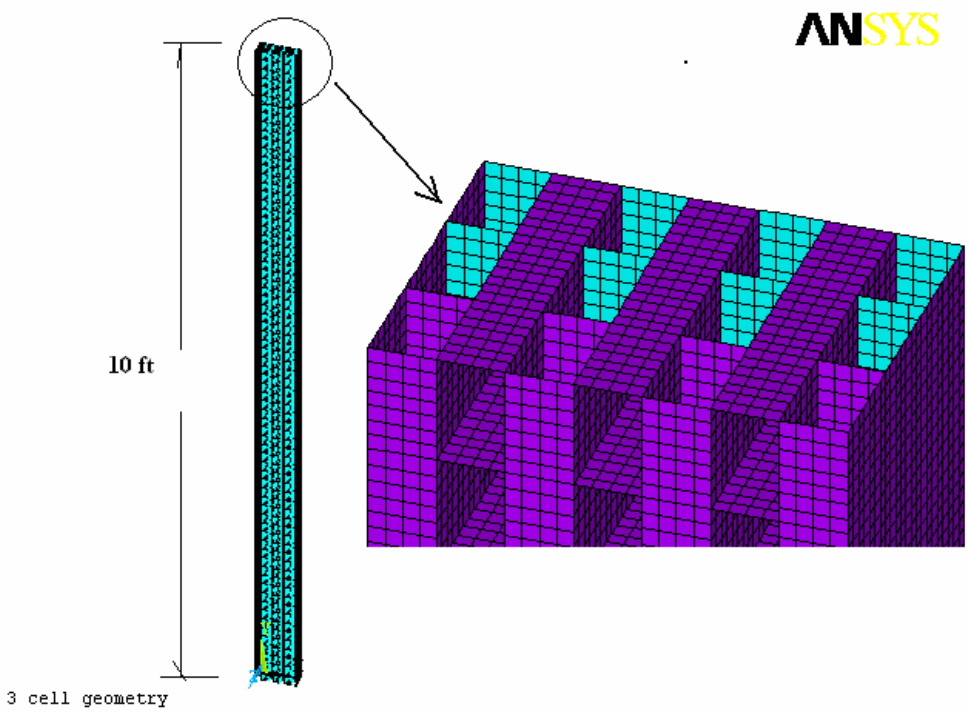

Fig. 17.86: FEA model of 7-layer prototype.

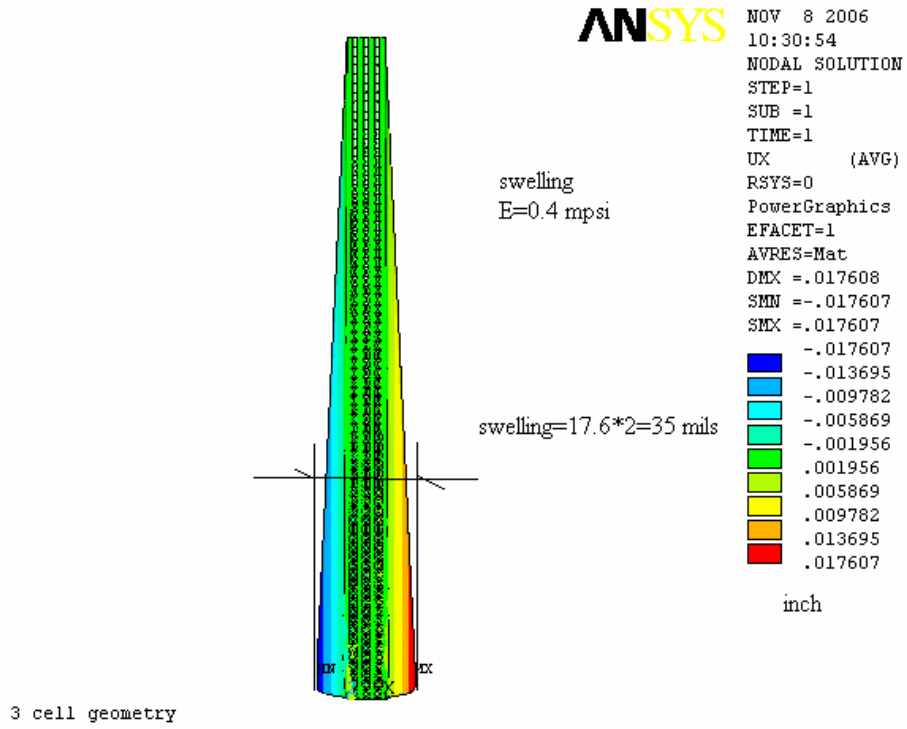

Fig. 17.87: Swelling results from the FEA model of the 7-layer prototype.

The results summarized in Table 17.20 and Figure 17.88 show good agreement between the measurement and FEA calculation. The deflection is relatively small when the first two layers are filled since these are internal layers with "double wall" thickness. When third and fourth layers are filled, the deflection is increased noticeably due the single wall for the exterior layers. With four layers completely filled, the FEA result gives a 33 mil deflection for E=0.4 mpsi and 36.6 mils for the E = 0.36 mpsi, respectively, in excellent agreement with the test result of 32.67 mils. It is interesting to note that the total deflection (swelling) can be approximated as

*Total deflection ~ Single-layer deflection (for two exterior surfaces) + double wall deflection * number of interior vertical layers.*

The second term represents accumulative nature of the swelling. For example, total swelling is 28.1 mils for a single-layer, 10-ft high extrusion. The double wall reduces its deflection by a factor of ~8, resulting in a 3.5 mil deformation. For a seven layer structure with two interior vertical layers, the total deflection is estimated as 28.1 + 3.5*2 = 35 mils. The FEA gives a deflection of 33 mils compared to the test result of 32.67 mils. The deflections in this 7-layer test structure are smaller than those in a structure with more planes glued together, where the second accumulative term would be larger.

Filled Layers		1	2	3	4
Mid cell (mils)		1	-8	21	33.5
Top cell (mils)		2	-10	18.5	33
Bottom cell (mils)		2	-11	20	31.5
Average (mils)		**1.67**	**-9.67**	**19.83**	**32.67**
FEA (E=0.4 mpsi) (mils)		**1.27**	**2.54**	**18.86**	**33.19**
FEA (E=0.36 mpsi) (mils)		**1.41**	**2.82**	**20.96**	**36.88**

Table 17.20: Comparison of 7-layer prototype hydrostatic swelling measurements with FEA model calculations.

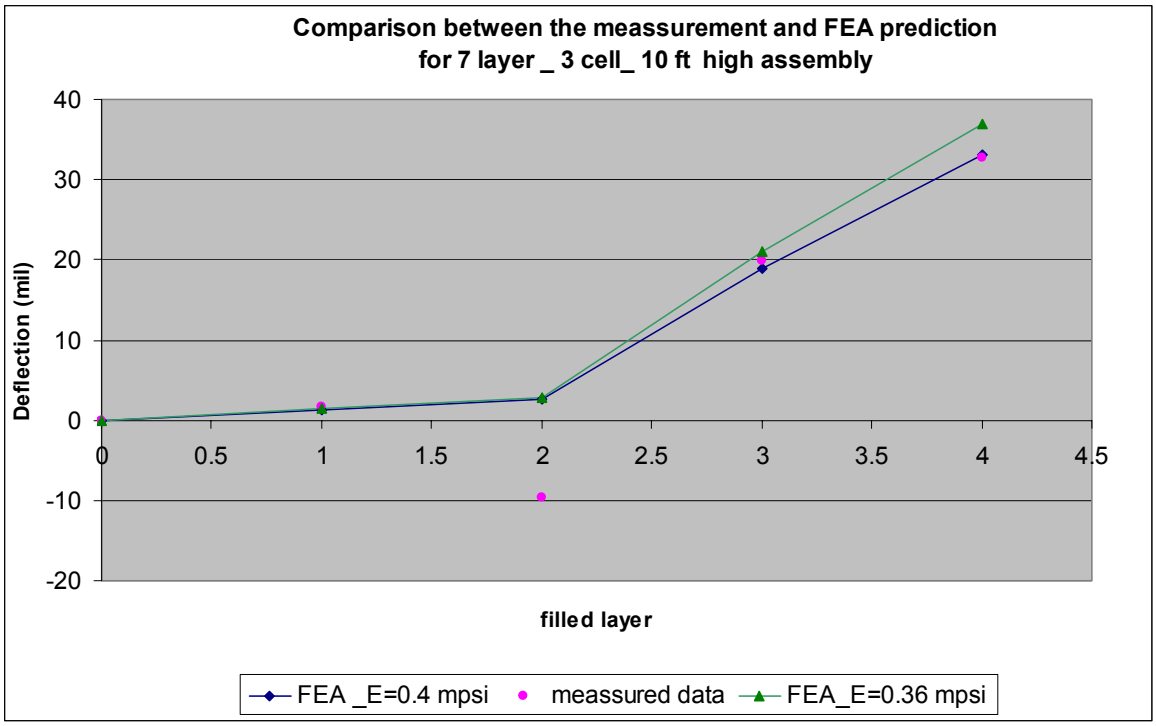

Fig. 17.88: Graphical comparison of the 7-layer test results and the FEA calculation.

17.6.4 Eleven-layer/Single-extrusion X-Y Prototype

The eleven-layer prototype was similar in size and construction to the three-layer prototype described in Section 17.6.2. As in the earlier prototype, the edges and outside surfaces were instrumented with strain gages and dial indicators. Figure 17.89 shows a photograph of the 11-layer prototype and its instrumentation. The initial test conducted on the 11-layer prototype was a progressive pressurization of its layers, progressing from the first to the second to the third, etc. The purpose of this test was to validate FEA calculations that predicted the propagation of hydrostatic swelling of one plane in a detector block to produce stresses and strains in subsequent layers. The strain gages in the prototype did not indicate any strain unless the extrusion on which it was mounted was itself subjected to pressure. The pressurization of one extrusion did not cause strain in adjacent layers. However, the dial indicators showed pressurization of one layer caused deformation of the extrusions in layers that were not pressurized. When only the first layer was pressurized, the eleventh layer moved 0.002 inch. It moved 0.004 inch when the first and third layers were pressurized and 0.006 inch when the first, third and fifth layers were pressurized, etc. The swelling of the pressurized layers simply expanded the entire assembly, moving adjacent layers as single bodies. These results are in agreement with FEA model predictions. Additional tests are planned in which the pressure will be increased above 19 psi until failure occurs in the adhesive bonds. Strain gage readings will then be compared to FEA model calculations.

Fig. 17.89: Photograph of the 11-layer prototype showing dial indicators (to measure PVC deformation) and strain gauges.

17.6.5 Four-layer IPND-Block Prototype

A four plane IPND mechanical prototype was constructed using extrusions produced during tuning of the 16-cell prototype extrusion die. This initial mechanical prototype did not have any end seals or manifolds and was intended to provide an initial experience gluing together large extrusions using the new adhesive. NOVA-doc-1369 describes this prototype in detail.

There were two vertical and two horizontal planes. Each vertical plane had four 16 cell extrusions and each horizontal plane had six 16 cell extrusions. Planes were glued together using Devcon 60 adhesive. The prototype block weighed approximately 600 kg.

The goals of this prototype were the following:

- Perform a large scale application of the Devcon adhesive.
- Perform ES&H measurements during the application of the Devcon adhesive in large quantities over a large area.
- Begin to get a feel for difficulty of handling large extrusions and placing them together into a block.
- Evaluate the need for compression on extrusions during gluing.

During the entire construction the air was monitored for volatiles from the adhesive. In addition, the two people applying the adhesive wore personal monitoring devices the entire time.

17.6.5.1 IPND Block Fabrication

Four planes of an IPND module were constructed. The block was constructed on the floor starting with a layer of horizontal modules. Devcon adhesive was applied to the next layer of vertical modules from 400-ml cartridges using a pneumatic powered gun. A glue line bead of approximately 0.125 inch diameter was placed down the center of each scallop. The vertical modules were staged on a set of supports so that they were at a convenient height to apply the adhesive. The extrusions were then flipped over by hand and placed in the appropriate position on the horizontal extrusions.

A series of right angle fixtures were mounted to the floor to be used for alignment of each plane. The fixtures consisted of Unistrut at right angles to the floor. A wire/survey was used to align all of the fixtures in the same plane and perpendicular to each other. The construction of each layer was begun by placing the first extrusion against the two sets of stops and then locating subsequent extrusions with respect to this initial one. This setup is a rough approximation of fixturing and tooling that will be on the block pivoter for locating the modules. Measurements showed that the fixtures were located within 0.040 inches of each other.

As each extrusion was placed in position a 75 lb roller was run over the surface of the extrusion to spread out the glue and obtain compression.

The top layer of the prototype was a vertical layer. The two outside vertical extrusions were placed as before. The center extrusions though were shrink wrapped and placed into the assembly. One of the shrink wrapped extrusions was rolled with the 75 lb weight while the second shrink wrapped extrusion had no compression. The purpose of the shrink wrapping is to allow the extrusions to be removed after the adhesive had cured in order to observe the glue pattern that was achieved.

Figures 17.90 (a), (b) and (c) show schematics of the assembly. Eight planes are shown in these figures because the same fabrication method will be used for the eight plane prototype that will be constructed using modules with end seals.

Figures 17.91, 17.92 and 17.93 are photographs of the assembly process.

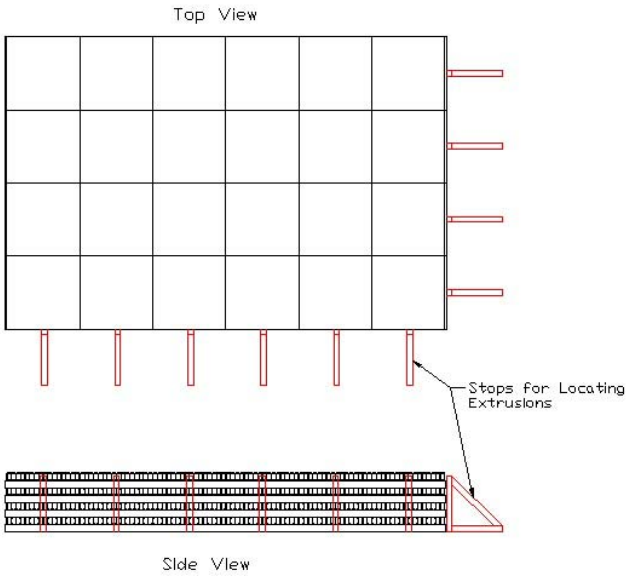

Fig. 17.90(a): View of IPND prototype block in construction orientation.

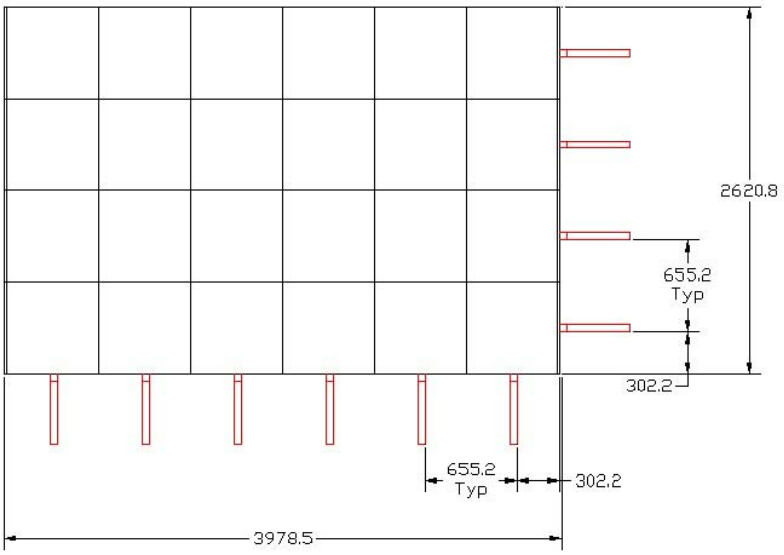

Fig. 17.90(b): Plan view of block during construction with location of fixtures.

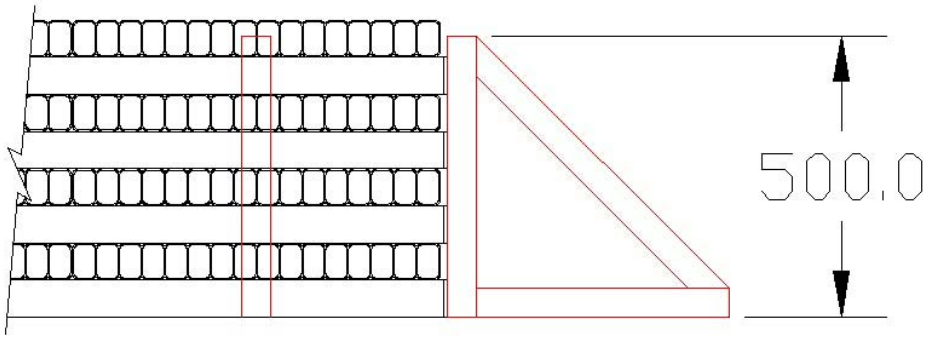

Fig. 17.90(c): Close-up view of block assembled against assembly fixture.

Fig. 17.91: Positioning an extrusion.

Figure 17.92: Applying the adhesive.

Fig. 17.93: Rolling the extrusion and applying pressure to remove the banana shape.

17.6.5.2 Results

During the construction the following were learned.

1. Alignment. It was difficult to get all of the extrusions within a plane to align perfectly parallel to each other and perpendicular to the previous plane. This was caused by non-perpendicular cuts on the bottom of the extrusions. Also, the sides of the extrusions do not appear to be parallel or straight. It was clear that some of the extrusions were straighter than others. On the first layer of verticals it was observed that the second vertical placed down had a banana shape that created a gap of approximately 1mm between extrusions. A force was applied to the extrusion and the banana shape was removed, however, after a few minutes the extrusion relaxed and assumed nearly its previous shape. The glue surface tension is clearly not enough to hold extrusions into place after they had been deformed.

It was also found that it was possible to move extrusions in order to align them after they had been placed. The adhesive surface tension was not so high that it became difficult to move the extrusions after placing them into position.

2. Extrusion thickness. The thickness of the extrusion at each cell was measured for each extrusion. Figure 17.94 shows the dedicated measurement fixture used. Figure 17.95 shows a plot of the variation in extrusion thickness for each cell.

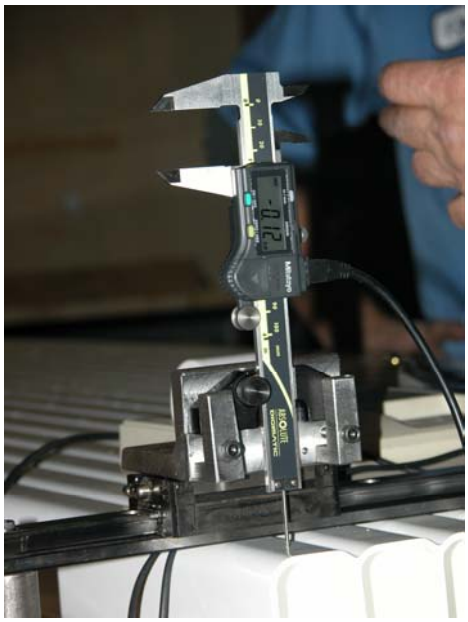

Fig. 17.94: Measuring fixture.

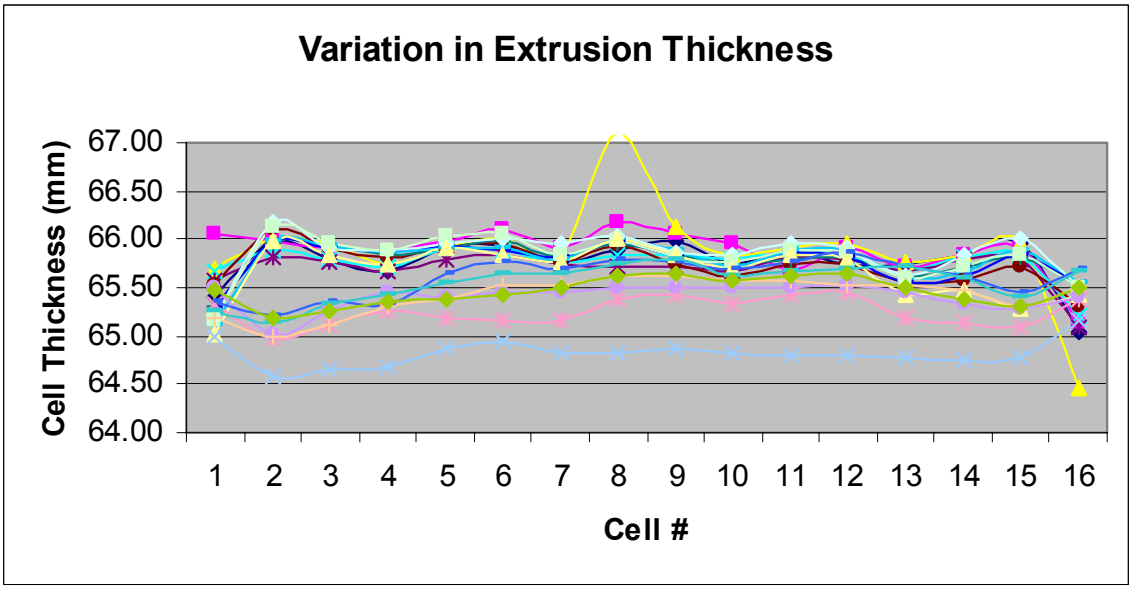

Fig. 17.95: Variation in extrusion thickness.

It can be seen in Figure 17.95 that the extrusions tended to be thinner at the outside cells. Also, whereas the overall thickness is less than the nominal thickness it is still within specification and tolerance variation that has been requested of the extruder.

3. Compression of modules. The 75 lb roller appeared to work well. The ends of the extrusions tended to bow upwards and lose contact. Repeated rolling of these areas tended to eliminate this problem and achieve compression. However, the second vertical extrusion on the second layer continued to bow upward after repeated rolling. After the third layer of horizontals was placed though and rolled the gap in this region closed and appears to made good contact.

After curing the top two vertical extrusions that were shrink-wrapped were removed and the glue line compression observed. It was clear that the adhesive did not spread out at all on the extrusions that had not been compressed. Figures 17.96 and 17.97 are close-up photographs of the compressed and non-compressed extrusions.

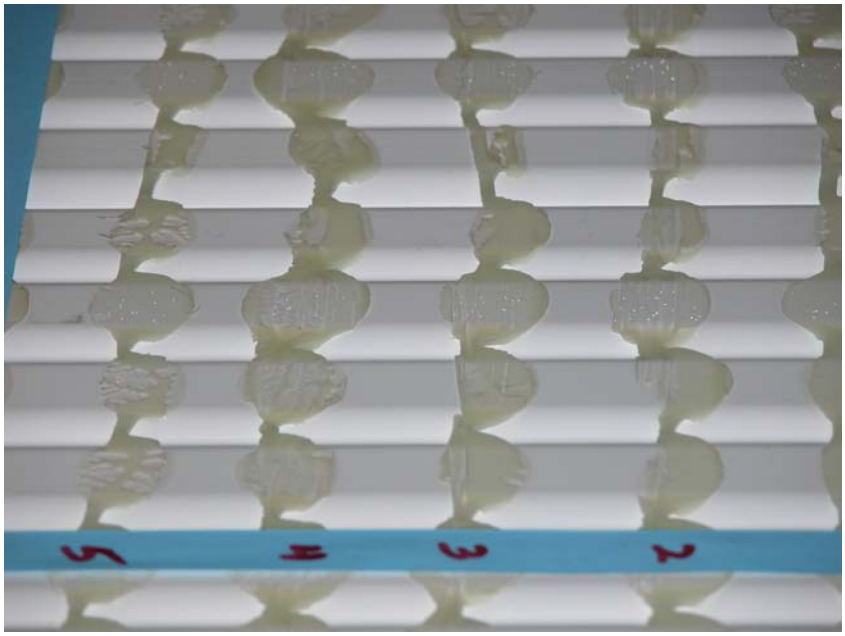

Fig. 17.96: Adhesive pattern under compressed extrusion.

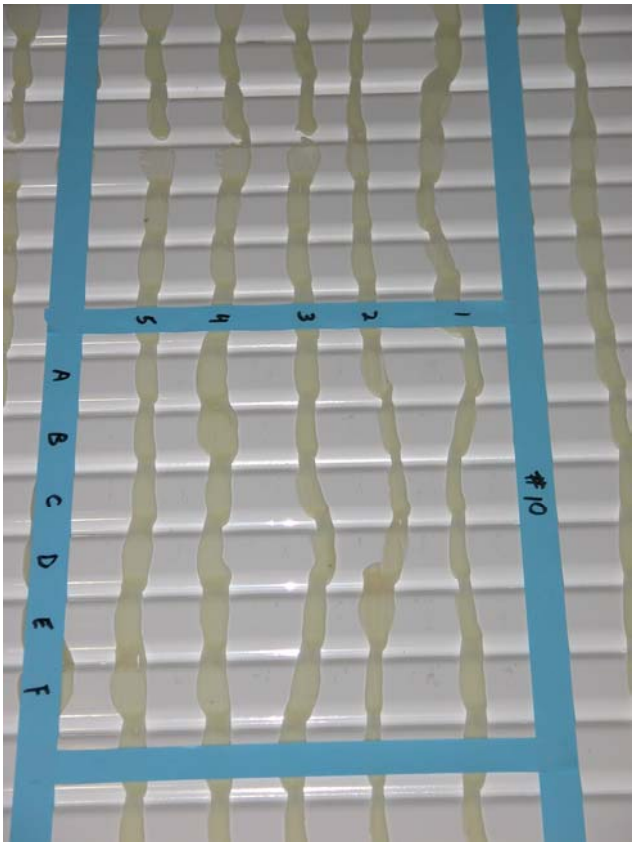

Fig. 17.97: Adhesive pattern under non-compressed extrusion.

These compression patterns showed clearly that that the adhesive was not as compressed along the first and 16th cells, which were not as thick as the other cells. The thickness of the extrusions played a role in the amount that the adhesive was compressed. Figure 17.98 shows the adhesive pattern in a region of the boundary between two extrusions. It is clear that along the first cell of one extrusion and the 16th cell of its neighbor that less compression occurred.

The exposed adhesive was divided into a grid as shown in Figure 17.99 and the glue line thickness was measured. Measurements were only recorded on an inside square that was two cells in from the outer edges of both the vertical and horizontal extrusions. This was done because of the obvious difference in compression along the outer edges of the extrusions and it was desired to obtain an average thickness that was not biased by the lack of compression on the edges due to the thinner extrusions in that area. Within each pad of adhesive there was sometimes significant variation in thickness if the adhesive bead had not been placed on the center of the scallop. In these cases the adhesive would be squeezed out towards the scallop and a radius would be formed in the adhesive. The average thickness of the compressed pads was 0.013 inch, which is similar to the 0.012-inch-diameter glass beads in the adhesive. The standard deviation was 0.004 inch, which is identical to the standard deviation of the extrusion thickness measurements. The non-compressed patterns had an average thickness of 0.024 inch with a standard deviation of 0.004 inch.

Fig. 17.98: Compression along boundary between adjoining extrusions.

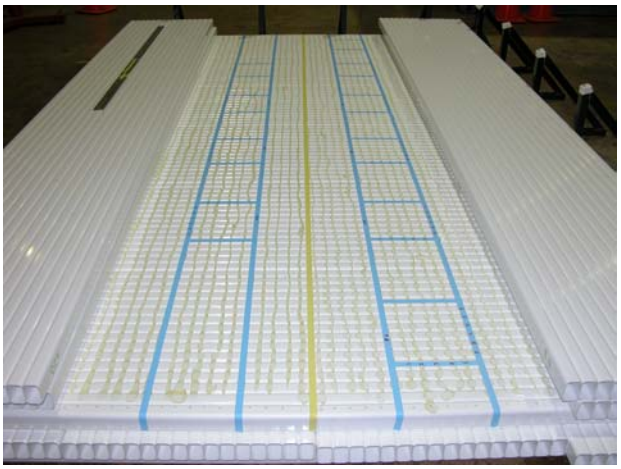

Fig. 17.99: Measurement pattern.

17.6.5.3 ES&H

During this test there was no direct air movement in the area of gluing (e.g., by fans) but the actual volume exchange in the building is not known. More important, the gluing occurred in a large high bay area with a very large volume of air over 1.5 hours so there was a very large volume for the methyl methacrylate vapors to dissipate into. Over time the concentration would likely have increased as the methyl methacrylate filled the volume of the building. There was clearly an unpleasant smell in the area, which was most intense in the area where gluing occurred and diminished away from the prototype area. A person working in the building 60 ft away could not smell the adhesive until he was within 30 ft of the prototype fabrication area.

Area monitors and personal monitors worn by the two people performing the gluing provided measurements of the integrated methyl methacrylate concentration during this

construction. The ES&H report is included in NOVA-doc-1347. The highest time weighted average concentration of methyl methacrylate was 21.3 ppm for one of the glue applicators but only 3.1 ppm in the area immediately next to the block being constructed. These are below the OSHA permissible exposure limit of 100 ppm and the 50 ppm 8-hr threshold limit value recommended by the American Conference of Governmental Industrial Hygienists. However, extrapolation of these values to the far detector assembly process at Ash River indicates that aggressive ventilation to remove adhesive vapor will be required around the adhesive dispenser and block pivoter assemble table.

17.6.5.4 Conclusions

The following conclusions were made:

- The use of rollers for compression looks promising.
- Need to do further tests to understand glue compression and coverage.
- It is possible to move modules once they have been placed.
- For assembly it would be best if any gaps due to banana were accepted and no effort was made to take them out.

17.6.6 Eight-layer/Single-extrusion X-Y Prototype

An eight plane IPND mechanical prototype block was constructed using extrusions produced during a tuning run with the 16-cell prototype extrusion die. This mechanical prototype was constructed with the "vertical" extrusions with end seals on both ends. There were no end seals on the "horizontal" extrusions. Figure 17.100 shows the completed prototype with some of the assembly crew. NOVA-doc-1981 describes the 8-layer prototype study in detail.

There were four vertical and four horizontal planes. Each vertical plane had four 16 cell extrusions and each horizontal plane had six 16 cell extrusions. The modules in each plane were glued into the block with Devcon 60 adhesive.

The prototype block weighed approximately 1200 kg.

The purpose of this prototype was:

- To perform a large scale application of the Devcon adhesive.
- To perform ES&H measurements of methyl methacrylate (MMA) vapor during the application of Devcon 60 adhesive in large quantities over a large area.
- To gain experience with the handling large extrusions and placing them accurately into a block.
- To evaluate the need for compression on extrusions during gluing.
- To construct a prototype that could be filled with liquid and loaded to simulate the stresses and deflections in a full height block.

During the entire construction process, the air in the assembly area was monitored for MMA vapor released by the adhesive. In addition, the two people applying the adhesive wore personal monitoring devices the entire time.

Fig. 17.100: Completed 8-plane prototype with assembly crew.

Eight planes of an IPND module were constructed. A procedure identical to that followed during the construction of the 4 plane IPND mechanical prototype was followed. The block was constructed on the floor starting with a layer of horizontal modules. Devcon adhesive was applied to the next layer of vertical modules from 400-ml cartridges using a pneumatic powered gun. A glue line bead of approximately 0.125-inch diameter was placed down the center of each scallop. The vertical modules were staged on a set of supports so that they were at a convenient height to apply the adhesive. The extrusions were then be flipped over by hand and placed in the appropriate position on the horizontal extrusions.

A series of right angle fixtures were mounted to the floor to be used for alignment of each plane. The fixtures consisted of Unistrut at right angles to the floor. A straight wire was used to align all of the fixtures in the same plane and perpendicular to each other. The construction of each layer was begun by placing the first extrusion against the two sets of stops and then locating subsequent extrusions with respect to this initial extrusion. This setup was a rough approximation of fixturing and tooling that will be on the block pivoter for locating the modules. Measurements showed that the fixtures were located within 0.040 inch of each other.

As each extrusion was placed in position a 75 lb roller was run over the surface of the extrusion to spread out the glue and obtain compression.

During construction the main observation was the alignment of modules and the bottom end seals. The 13-ft long vertical extrusions had a slight banana shape that could not be taken out. The edges of the verticals were aligned on two of the stops but the banana shape resulted in a misalignment of the bottom end seal. The bottom of the IPND will be grouted to fill gaps and

ensure uniform support of the load-bearing vertical module end seals before the structure is raised to the vertical position.

Area monitors and personal monitors worn by the two people performing the gluing were used to record any volatiles from the adhesive. Monitors were placed in the area of gluing and at the inlet and outlet of the ventilation fan. The ventilation fan had a 0.5-inch thick activated carbon filter on the inlet and approximately 2,000 cfm of air flow. The concentrations of MMA at the locations during gluing are summarized in Table 17.21. The concentrations are significantly lower than recorded during the earlier 4 plane IPND prototype construction where one person had a concentration of 14.7 ppm and the other had a concentration of 21.3 ppm (NOVA-doc-1369).

SAMPLE NO.	DATE	NAME/ BADGE NO.	LOCATION/ OPERATION	METHYL METHACRYLATE CONC. (PPM)
39751	4/23/2007	Area Air Sample	E of panels on floor (4 ft. above floor)	0.8
39752	4/23/2007	Area Air Sample	E end below glue table (12 in. above floor)	0.5
39753	4/23/2007	K. Kephart/ 03119N	Adhesive Application	1.5
39754	4/23/2007	M. Slabaugh/ 14132N	Adhesive Application	4.3
39755	4/23/2007	Area Air Sample	E end of glue table, 5 ft. above floor (16 ft. E of exhaust fan)	0.9
39756	4/23/2007	Area Air Sample	Fan exhaust, 3.5 ft above floor (2.5 ft. W of fan)	0.3
39757	4/23/2007	Area Air Sample	Fan inlet (4 in. from filter)	0.7
39758	4/23 & 24/2007	Area Air Sample (Overnight)	After Panel Assembly, N side on floor (4 in. from panels on floor, 3 in. above floor)	1.5
39759	4/23 & 24/2007	Area Air Sample (Overnight)	After panel Assembly, on top of panels (9 in. above panel)	0.6

Table 17.21: Concentrations of methyl methacrylate vapor measured during assembly of the 8-plane prototype.

The following conclusions were made from this study:

- A small amount of ventilation can reduce the concentration of MMA significantly.
- This test did not determine the effectiveness of the filter in removing MMA vapor.
- The use of rollers for compression looks promising.
- Additional tests are required to understand glue compression and coverage.
- It is possible to move glued modules immediately after placement in a block.
- For assembly it would be best if any gaps due to banana were accepted and no effort was made to take them out.

The next step of this prototype study will be to fill the gaps between extrusions and end seals at the bottom of the block with epoxy grout and then to raise it vertical. Strain gages will be applied to the prototype and the vertical modules will be filled with water. Additional air pressure will be applied to achieve 19 psi at the bottom of the vertical extrusions. Next, large weights will

be placed on top of the vertical modules in order to simulate the adhesive and PVC stresses in a full-height far detector block.

17.6.7 Adhesive Shear and Peel Strength Measurements

The structural integrity for the NOvA detector depends on the peel and shear strength of the Devcon 60 adhesive. NOVA-doc-1944 describes our measurements of the strength of the adhesive as measured using standard ASTM testing of actual extrusions glued together and subjected directly to shear and peel.

Standard double lap shear and T-peel tests have been used to measure the strength of the adhesive. Multiple samples were tested under different conditions to determine the strength of the adhesive under all conditions during assembly of the detector. Figures 17.101 and 17.102 show details of the double lap shear tests and Figures 17.103 and 17.104 show details of the T-peel test specimen. The glue line thickness and the open time of the adhesive play important roles in the actual shear and peel strengths achieved. During assembly the adhesive will be applied to modules in beads that could be left open to the air for as long as 20 minutes, between the time the first bead is applied and the time when the module in placed and the adhesive bead compressed. (The nominal open time during block assembly is designed to be less than 10 minutes.) Table 17.22 summarizes the test results for different glue line thickness and open times of the adhesive. The glue line thickness is nominally 0.012 inches, which is set by the size of the glass beads suspended in the adhesive.

	Zero Open Time			20 Minute Open Time		
Glue Line Thickness	**0.012”**	**0.030”**	**0.060”**	**0.012”**	**0.030”**	**0.060”**
Shear Stress (psi)	1132.3	1008.6	792.9	842.6	508.5	294.3
Shear Stress Std-Dev.	131.6	309.7	47.1	137.5	124.0	87.8
Peel (lbs/in)	99.12	125.1	122.9	87.1	64.8	84.1
Peel Std-Dev.	14.3	15.8	21.7	17.2	23.2	22.4

Table 17.22: Shear and peel strength measurements for Devcon 60 adhesive. Each result is based on measurements of 15 samples.

Table 17.22 shows that the shear strength of a bond declines significantly as the open times and glue line thicknesses increase, while the peel strength is affected much less.

The ASTM tests we have used are good indicators of the strength that we can expect from the adhesive. However, the actual strength of a joint also depends on the PVC surface preparation, the thickness of the PVC and the stiffness of the PVC extrusion. It is critical to determine the actual strength that can be achieved under realistic conditions. To this end, two tests were performed to evaluate the peel and shear strengths of adhesive bonds between extrusions. For each test setup, extrusions were glued together in the configurations described below. The effect of the amount of adhesive in the joint was evaluated by performing each test with both 6 cc and 3 cc of adhesive distributed over the 4 pads of contact between extrusions.

Figure 17.101 shows the test setup for the peel test. The outer vertical extrusions are rigidly clamped in the fixture and a load applied to the center vertical extrusion. The joints between extrusions are under shear but the loading is dominated by the peel forces that result. The peel force, calculated from statics, is plotted versus vertical displacement in Figures 17.102 and 17.103. The peel strength is significantly higher than that measured using the standard ASTM tests. This increase is attributed to the additional adhesive that flows into the scallops and forms a large radius at the point where the peel failure begins. We conclude that the filling of the scallops contributes significantly to the peel strength of NOvA adhesive bonds.

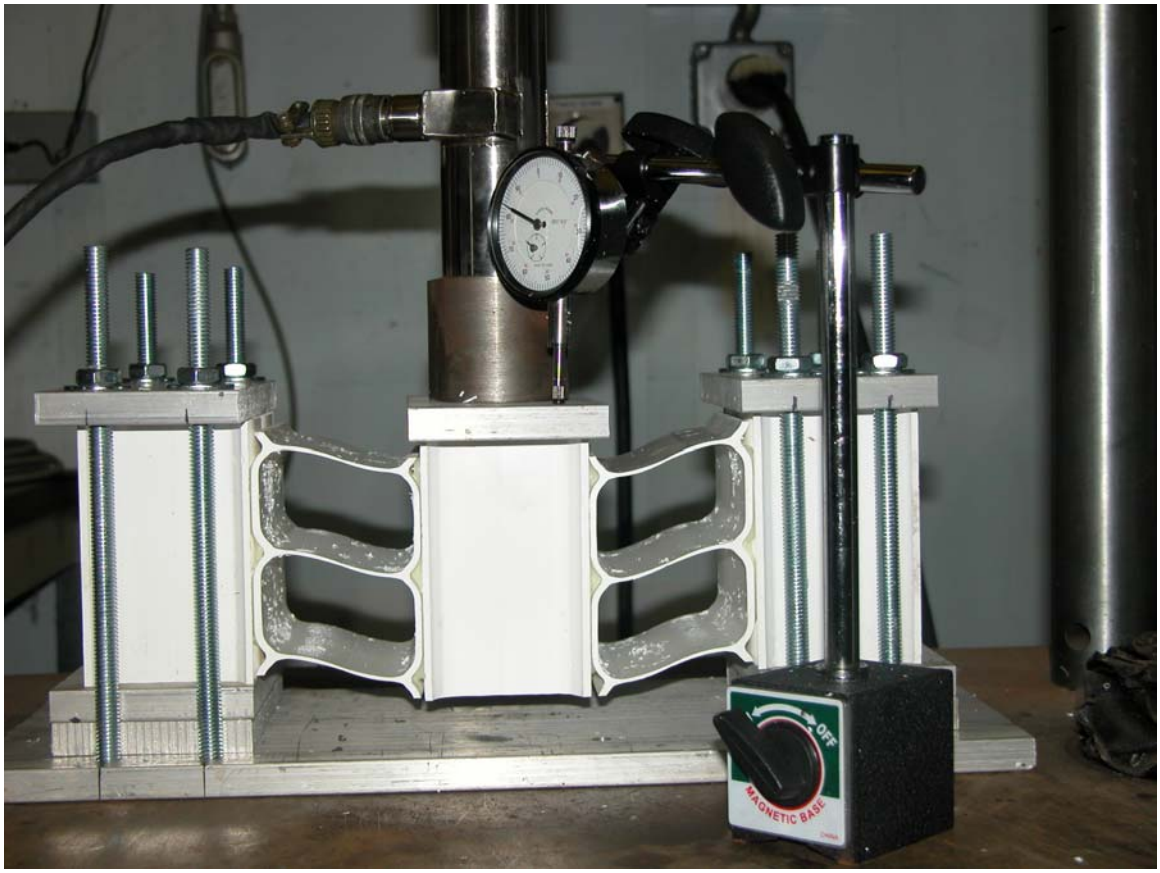

Fig. 17.101: Peel test of NOvA extrusion assemblies.

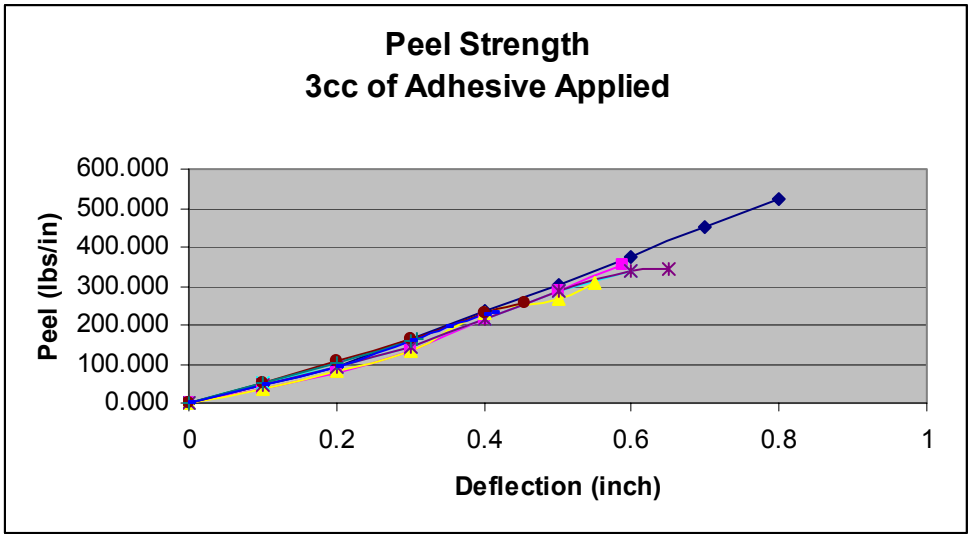

Fig. 17.102: Peel strength measured for bonds with 3 cc of adhesive.

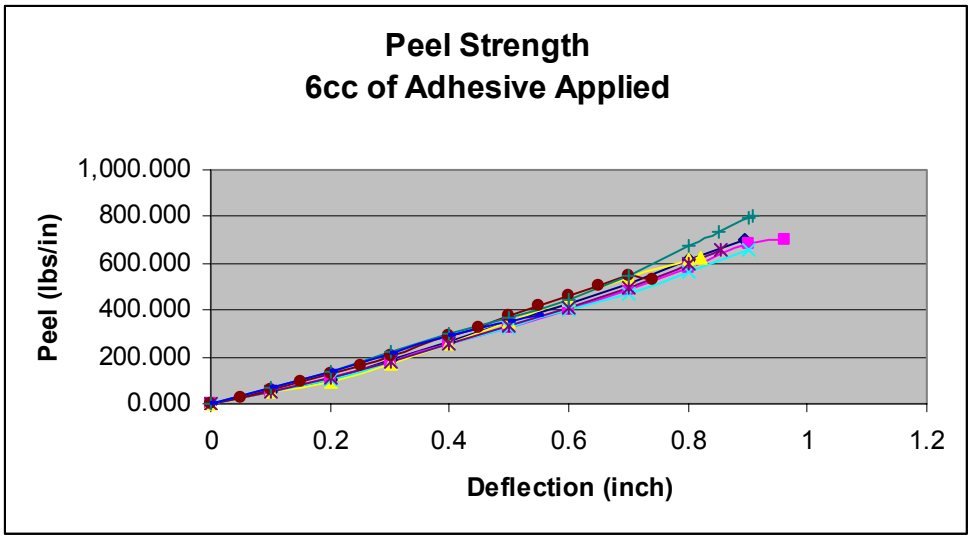

Fig. 17.103: Peel strength measured for bonds with 6 cc of adhesive.

Figures 17.104 through 17.107 show the second measurement of shear strength, in which the joint between the extrusions was subjected to nearly pure shear. Figure 17.104 is a schematic of the test pieces that were made. For the preliminary tests enough adhesive was applied to insure that entire area of contact between the horizontal and vertical extrusions was covered and that there was some minimal squeeze out into the scallop area. Figure 17.105 shows schematically how the extrusion setup was restrained and the force applied.

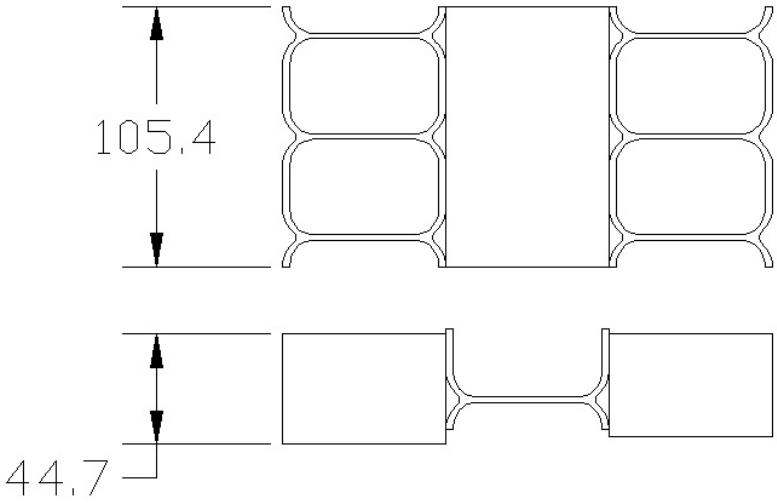

Fig. 17.104: Front and top views of the shear test extrusion assembly.

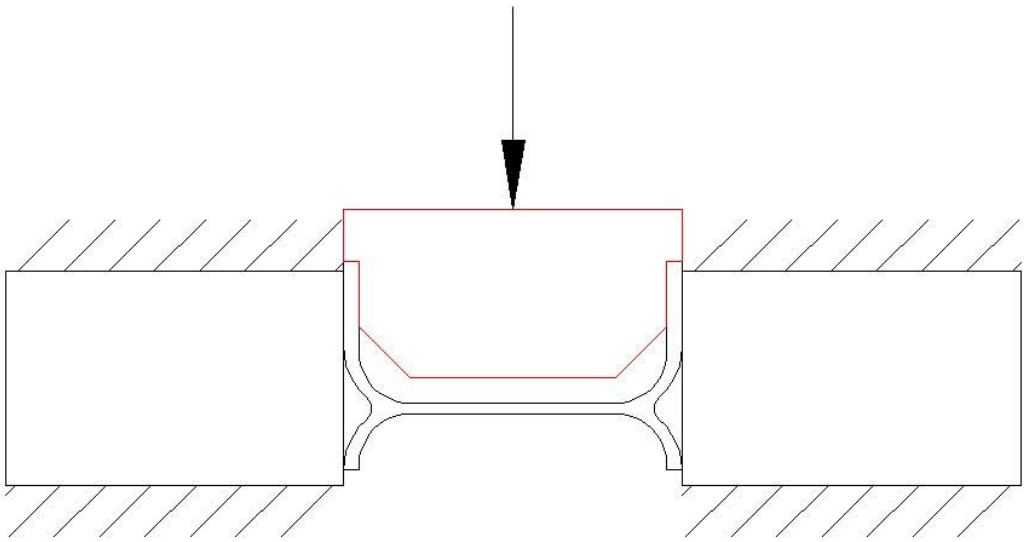

Figure 17.105 – Schematic of shear test restraint and force application.

In the shear test it is important that the force be applied directly to the side wall and that the side wall is restrained so that it cannot begin to peel due to deformation of the extrusions. The vertical extrusions were restrained to prevent motion and the plug resting in the horizontal extrusion ensured that the sidewalls could not move laterally in peel. The plug also insured that the force was applied directly in shear to the side walls. Figures 17.106 and 17.107 show the test setup.

Fig. 17.106: Extrusion assembly used for the shear strength measurement.

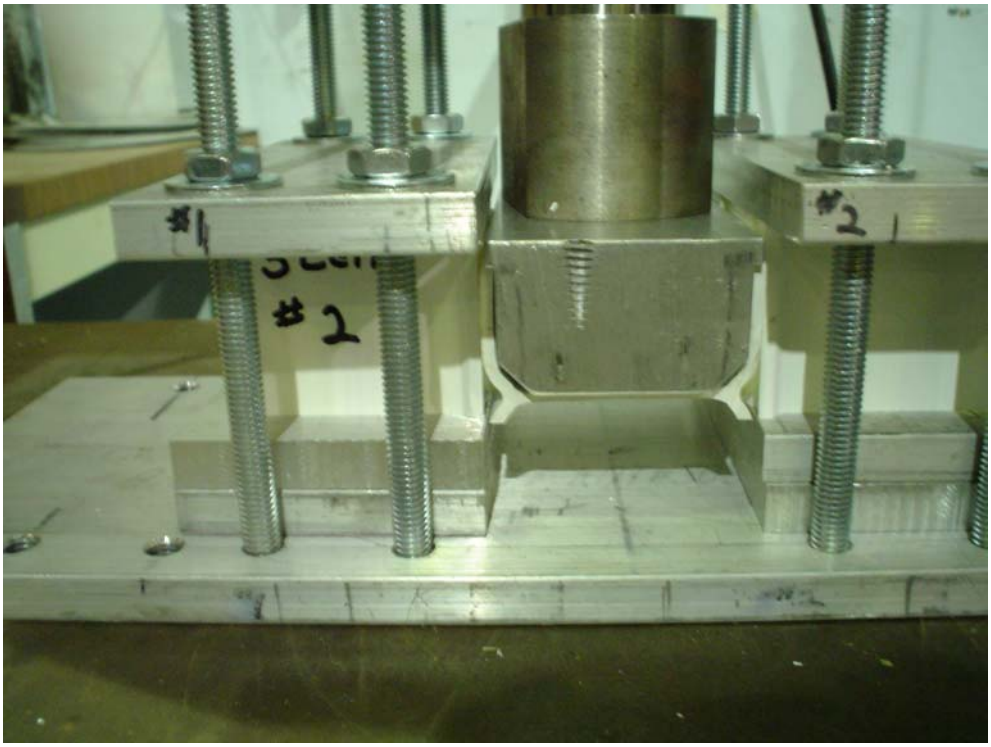

Fig. 17.107: Test setup used for the shear strength measurement.

The extrusions used in this test have 19 mm flats between the scallops so that bonded horizontal and vertical extrusions have bond areas of 19 mm x 19 mm = 361 mm^2 (0.56 in^2). In the extrusion setup used in this test, the applied force is resisted by four of these pads with a total area of 2.24 in^2.

Using this theoretical area, the shear stress in the adhesive was calculated and plotted versus deflection as shown in Figures 17.108 and 17.109.

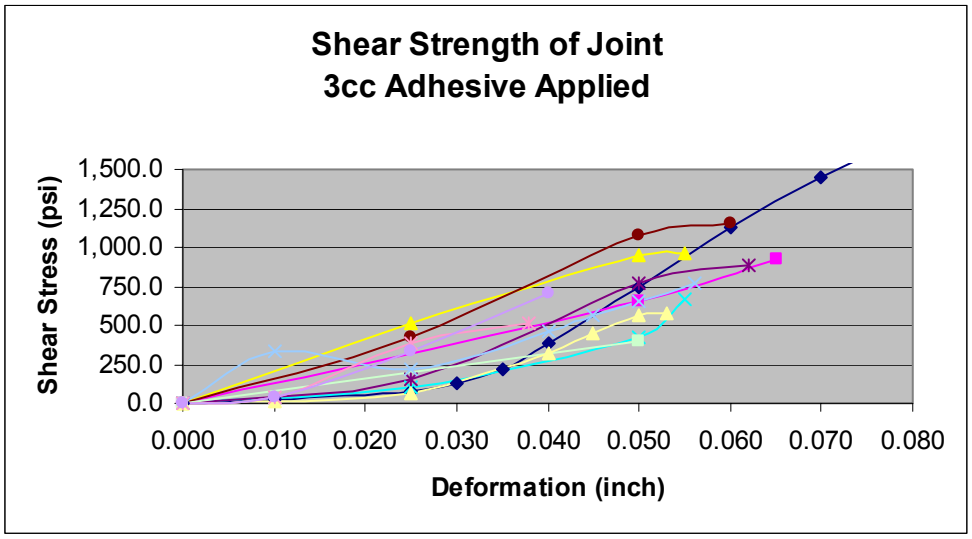

Fig. 17.108: Shear strength versus deformation of joint with 3 cc of adhesive per 4 contact pads.

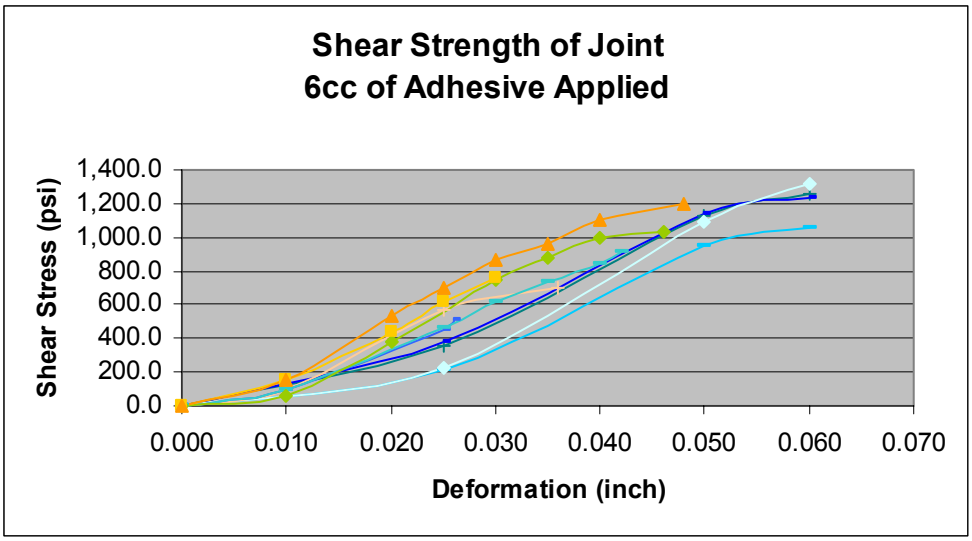

Fig. 17.109: Shear strength versus deformation of joint with 6 cc of adhesive per 4 contact pads.

Figures 17.108 and 17.109 show that the strength of adhesive joint is equal to or exceeds the strength found in the ASTM tests. Failure occurred at stresses above 1000 psi and after fairly large deformations of greater than 0.040 inches (1 mm).

Although ASTM and extrusion tests show that the adhesive joints can achieve the high strength needed for the NOvA structure, long adhesive open times and thick glue lines will degrade the shear strength. Studies are currently being conducted on the adhesive compression to evaluate how to achieve the optimum adhesive thickness of 0.012 inches. The 4-layer IPND mechanical prototype (Section 17.6.5 and NOVA-doc-1369) demonstrates how the glue line thickness depends on the uniformity of the extrusion thickness. Compressed lines of adhesive achieved the desired 0.012-inch thickness with a standard deviation of 0.005 inch, while uncompressed lines were on average 0.024 inch thick with a standard deviation of 0.005 inch.

The minimum thickness of glue bonds is constrained by the 0.012-inch diameter glass beads that have been incorporated into the adhesive mixture. Variation in the thickness of extrusion cells will add to this minimum thickness. Such variations can arise from variations within a single 16-cell extrusion and from any thickness differences that result from the gluing of two 16-cell extrusions into a single 32-cell unit (by WBS 2.5).

Figure 17.110 shows the results of systematic measurements of the cell thickness uniformity of NOvA-27 production extrusions. The two cells on either end of each extrusion are systematically thinner than the 12 central cells by about 0.015 inches. We anticipate that retuning of the die, which is now under way, will correct this effect. However, even if the thinner end cells are included, glue bond thickness would still remain less than 0.030 inches.

Figure 17.111 shows the difference in cell thicknesses obtained during initial studies of techniques for gluing two 16-cell extrusions together to form a 32-cell module. The variations measured should not result in bond thicknesses greater than 0.020 inches, even when the four edge cells are included in the measurement. Control of the thickness uniformity of 16-cell extrusions and of 32-cell extrusion assemblies within a single plane may require sorting of extrusions and pre-assembly assignment of modules to specific detector planes.

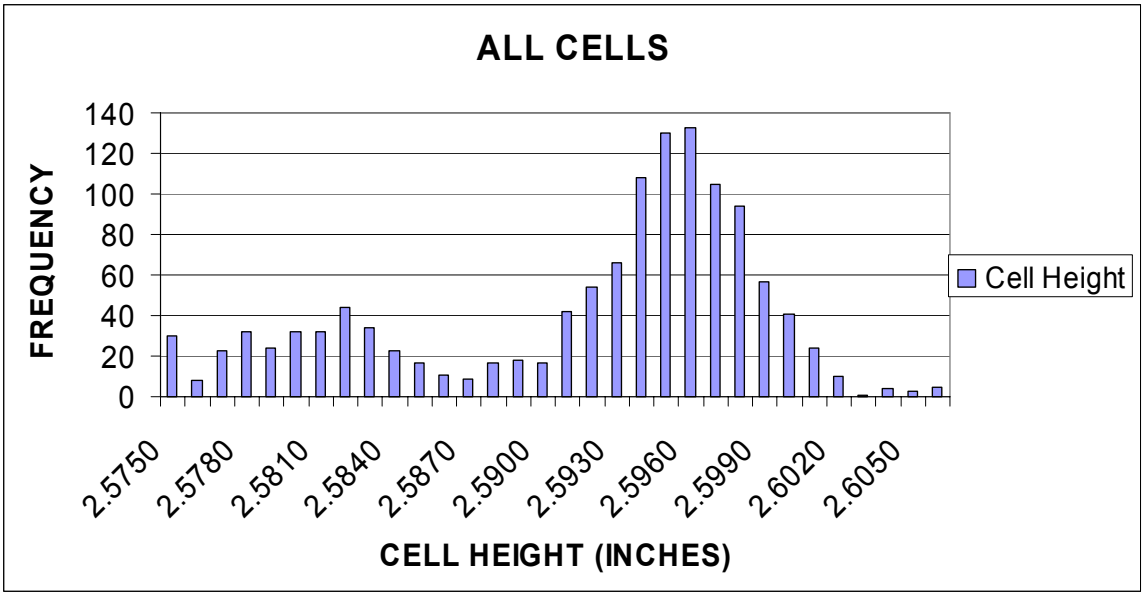

Fig. 17.110: NOvA-27 extrusion cell thickness uniformity. Cells #1, 2, 15 and 16, on the outside edges of the extrusions are responsible for the cluster of thin cells around 2.584 inches.

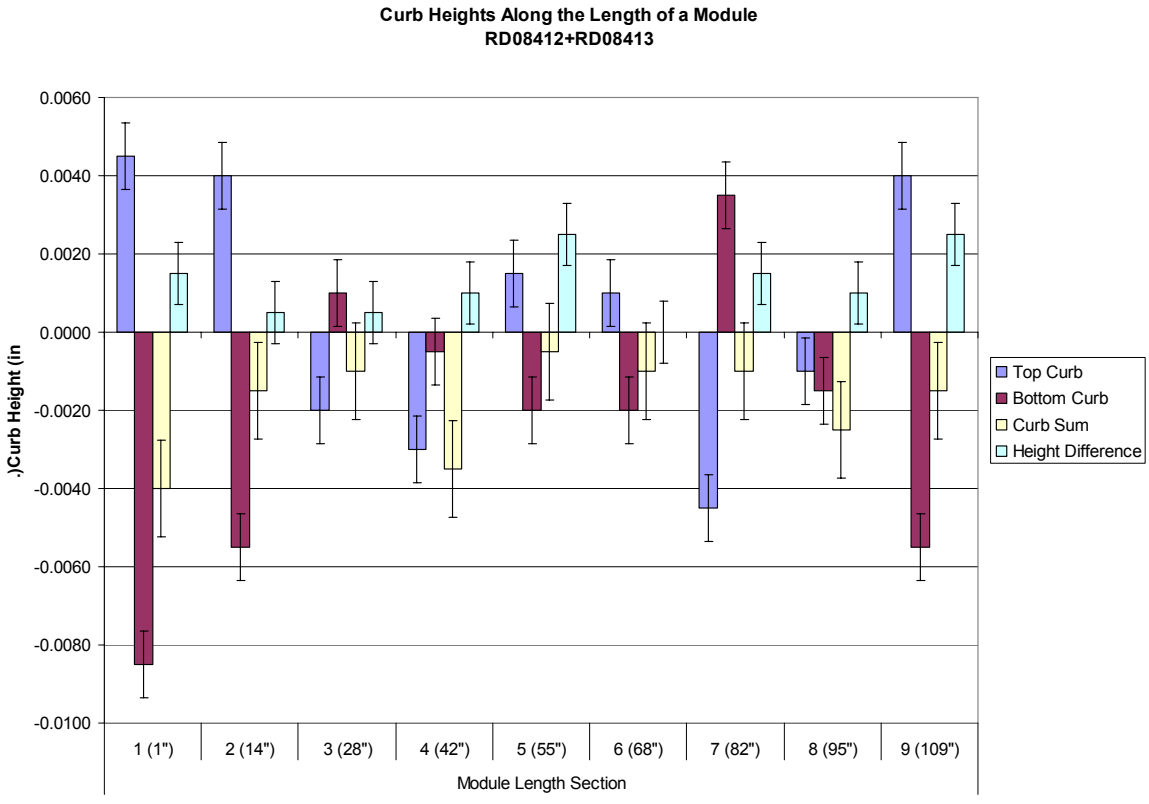

Fig. 17.111: Thickness offset of two 16-cell extrusions glued together to form a 32-cell module.

17.6.8 Block Base Filler Grout Studies

In order to insure that the bottom end seals of the vertical modules in far detector blocks are in full contact with the base pallet, a deep pour epoxy grout will be used to fill all gaps during block assembly (NOVA-doc-2609). The grout must be able to fill small gaps (~1 mm) and have sufficient compressive strength to withstand the loading of the filled detector. The grout will also be used to fill the gaps between vertical modules to insure that adjacent extrusions provide support for resisting the internal pressure.

Devcon's Deep Pour Grout was used to pot the base of the 8-plane IPND mechanical prototype block described in Section 17.6.6. This grout is an epoxy adhesive that consists of an epoxy base mixed with sand. It is self leveling and can fill small gaps while maintaining a high compressive strength. The work life of the grout is 40 minutes. The compressive strength is 2,500 psi.

The grout is needed to fill the gap between the bottom end seals of the vertical modules and the pallet of each far detector block. The current plan is to place the bottom of the end seals into full contact with the base pallet. However, due to distortion of extrusions it is possible that the end seal will not be in full contact with the pallet. For example, during the construction of the IPND 8-plane prototype, the extrusion of a vertical module was banana shaped. This distorted extrusion was brought into contact with adjacent vertical modules which resulted in the bottom end seal not being in line with the other end seals. Figure 17.112 below shows this distorted end seal.

For this first test of the filler grout technique, we used 12 gallons of grout on the 8-plane prototype block. Scaling this to the size of a far detector block, we find that an equivalent of 288 gallons/block would be needed. However, the average thickness of grout under the bottom end seals was 1 inch in the 8-plane prototype test. Correcting for the fact that a far detector block will have a much smaller gap (about 0.5 inch on average), we estimate a usage volume of 150 gallons per block.

After assembly of the 8-plane IPND prototype block, a dam was created along the bottom of the detector and filled with grout to form a continuous surface to support the IPND. Gaps like the one shown in Figure 17.113 must be filled with grout to insure that the weight of the filled FD is evenly distributed on the end seals and across the base pallet.

The horizontal modules will be slightly above the bottom end seals which forms a gap which can also be seen in Figure 17.112 and 17.113. It is desired to only transfer load from the detector structure to the pallet through the vertical modules and not through the horizontals. Therefore, this gap will be filled with an inexpensive, lightweight foam material to prevent the grout from filling this space. This technique worked well on the IPND prototype block. The foam serves the purpose of filling the gap but also has a low enough stiffness that it will not transfer any loading to the horizontal extrusions.

The grout easily poured and filled the gap between the dam and the bottom of the prototype. The prototype was successfully raised from the horizontal to the vertical orientation and placed on the grout. Figure 17.114 and 17.115 shows the module resting on the grout.

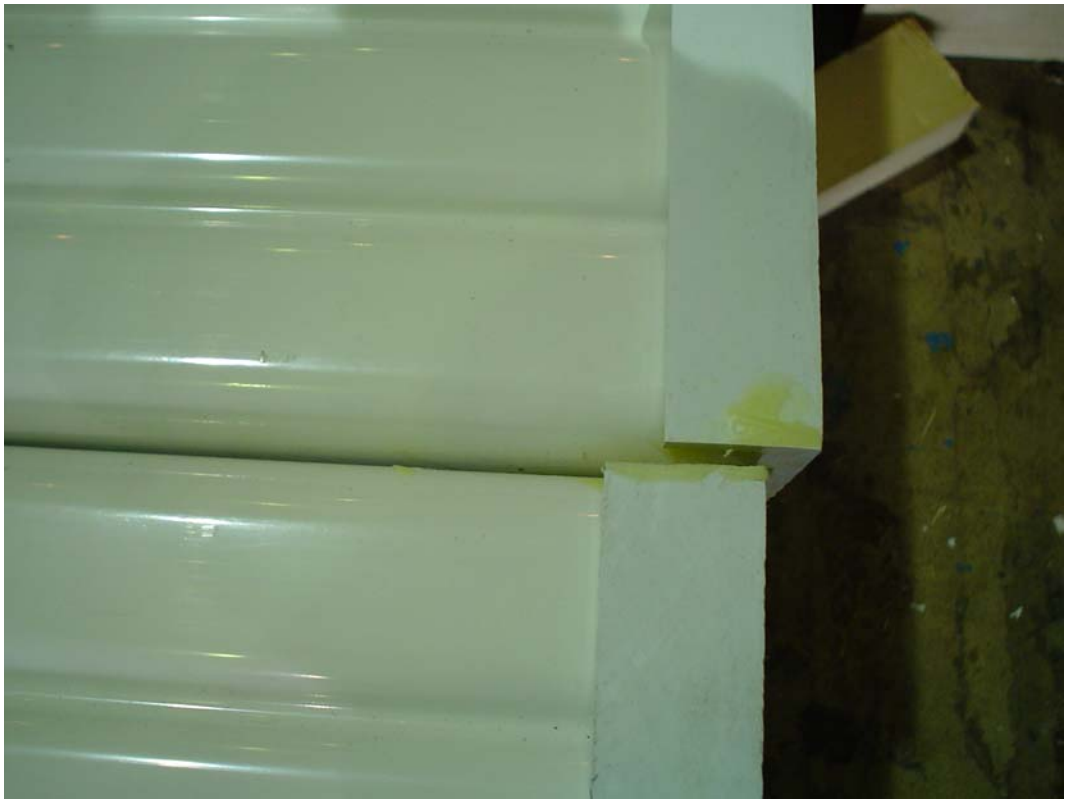

Fig. 17.112: Misalignment of end seals in IPND 8-plane prototype.

Fig. 17.113: Misalignment of end seals and gaps between vertical end seals and horizontal extrusions in IPND 8-plane prototype.

Fig. 17.114: Edge view of grout showing overfill of dam and leakage into the extrusion scallops.

Fig. 17.115: View of grout with IPND prototype in the vertical position. The blue material is foam used to fill the gaps under the bottom horizontal extrusions of the horizontal planes.

17.7 Far Detector Infrastructure

Far detector installation and operation make use of several large structures and equipment complexes that are specified and designed jointly by the WBS 2.1 and WBS 2.9 tasks. One or the other of these tasks has the primary responsibility for fabricating and installing a given system. The main infrastructure systems are described in the following sections.

17.7.1 Environmental Control Systems

17.7.1.1 Temperature and Humidity Specifications

The dimensions of PVC extrusion modules depend on both the temperature and humidity of their environment. The coefficient of thermal expansion of PVC is 7×10^{-5}/°C. At 20°C and 40% relative humidity, a temperature change of 3°C causes about three times the change in PVC dimension as a 1% change in relative humidity, as measured by strain gages on NOvA extrusions in an environmentally controlled chamber (NOVA-doc-1535).

The temperature and humidity in the assembly area where far detector blocks are constructed will be controlled to prevent significant changes in PVC dimensions as modules in a block are glued together over the course of several weeks. In addition, modules will be installed in blocks only after their dimensions have stabilized in the environment of the assembly area. Extrusion modules reach temperature equilibrium within 24 hours of being subjected to a large temperature change upon delivery to the far detector site, however they will require several days to come to equilibrium after a large humidity change. These considerations, weighed against the cost of controlling temperature and humidity in the assembly and loading dock areas at different seasons, have resulted in the following specifications. The temperature in both the loading dock and assembly areas will be maintained at 70±5°F, summer and winter. The relative humidity will be maintained at 50±10% during the summer and 15±10% during the winter. An initial analysis showed that these conditions are sufficient to limit the buildup of internal stresses during block assembly to acceptable levels. Detailed FEA calculations are now in progress to check this result.

After a block has been assembled and its adhesive has cured, its modules will expand and contract together as environmental conditions change, so PVC dimensional stability considerations are not the dominant factor in determining environmental specifications for the detector hall. Instead, the change in liquid scintillator volume with temperature sets these specifications. Since the volume coefficient of expansion of liquid scintillator is 3.5 times larger than that of PVC (NOVA-doc-344), a two liter liquid overflow volume is provided for each module to accommodate temperature increases in the detector hall. Similarly, detector modules will be initially overfilled by two liters to prevent liquid levels from dropping unacceptably low during negative temperature excursions. For vertical modules, this ±2-liter volume is provided by the module manifolds plus the length of vertical module extrusion that extends above the top of adjacent horizontal module plane. For horizontal modules, a separate 4-liter “expansion” tank is attached to each module manifold.

The humidity in the detector hall will be kept below a dewpoint of 50°F to prevent condensation on the chilled water plumbing to the APD thermoelectric coolers. These considerations require that the detector hall temperature be maintained at 70±5°F, summer and winter. Short-term fluctuations are of little consequence because of the large thermal inertia of the filled detector. The relative humidity will be kept below 45% (50°F dewpoint) during the summer and around 15% during the winter.

17.7.1.2 Ventilation Requirements

Nearly four tons of Devcon Plastic Welder 60 adhesive will be used in the assembly of each detector block. During the adhesive application and curing process, 1 to 3% of the adhesive

mass (depending on environmental conditions) is released into the surrounding environment as methyl methacrylate (MMA) vapor (NOVA-doc-1975, 1979, 1984). The block assembly area at the far detector site will include a substantial ventilation system in order to limit the exposure of far detector assembly workers to MMA vapor. NOVA-doc-1520 describes the design criteria for this system.

The American Conference of Governmental Industrial Hygienists Threshold Limit Values in 2006 for methyl methacrylate is an 8-hr time-weighted average concentration (Threshold Limit Value, or TLV) of 50 ppm (205 mg/ m^3 air). The OSHA Permissible Exposure Limit is 100 ppm. The target concentration for NOvA is set well below these values to protect the health of the assembly crew workers. For NOvA detector assembly, we have adopted the requirement that MMA vapor concentrations will be limited to 10 ppm. This specification is based on our review of literature on the health effects on workers exposed to MMA.

Calculations described in NOVA-doc-1520 lead to separate ventilation specifications for the two areas at the far detector site with the greatest potential for worker exposure to MMA vapor. To meet our 10 ppm limit, MMA-contaminated air will be removed from each of these areas at a rate of 10,000 cfm. These localized ventilation systems operate in parallel with the 13,000 cfm loading dock and assembly area HVAC systems. These MMA removal systems are expected to limit MMA vapor levels within 100 ft of the far detector building complex to less than 1 ppm.

Methyl methacrylate vapor levels were recorded during assembly of the 4-layer and 8-layer IPND-block prototypes, as described in Sections 17.6.5 and 17.6.6 (NOVA-doc-1369 and 1981). Additional, more detailed measurements of MMA vapor levels will be made during future large-scale gluing exercises, as IPND blocks and the far detector full-scale assembly prototype are constructed. These will provide experimental verification of the effectiveness of our ventilation requirements for controlling worker MMA exposure levels during far detector assembly. In addition, the adhesive dispenser design incorporates ventilation ductwork to remove MMA-contaminated air as close to the source as possible. Measurements made with the adhesive dispensers for the IPND and the full-scale assembly prototype will provide early opportunities to test this system and optimize its design for the more challenging environment of the far detector assembly areas.

17.7.2 The South Bookend

The first (south) bookend provides a strong, flat surface to which the first detector block is attached. The bookend is a reinforced concrete structure that is mounted against the south building wall. It is designed to resist the hydrostatic pressure of the first plane of vertical extrusions (19 psi at the bottom) and to withstand the forces exerted by a buckling failure of the completed, filled detector. These forces were calculated using a PVC modulus weakened by 25 years of creep and allowing the detector blocks to deform into the expansion gaps between superblocks as described in Section 17.5.5. In this Section, the worst case scenario is calculated where the blocks all buckle in the same direction, make contact with each other, and are prevented from collapsing because they are restrained by the bookend. The forces acting on the bookend are shown in Figures 17.53 and 17.54. The graph in the latter figure shows that the side force on the bookend is 255 tons. This is distributed over a distance of 108 inches starting at approximately 110 inches from the bottom of the detector. The top force of 67 tons is distributed over a distance of approximately 60 inches at the top of the detector.

The block located adjacent to the bookend will have a 20-mm thick spacer located in the calculated regions of contact. A survey will be made of the south bookend wall before installing the first block. Based on this survey the thickness of the nominal 20-mm thick spacer will be increased to account for the bookend's out of flatness in order to insure contact. The spacer has to be a minimum of 20-mm thick to insure that the manifolds which overlap the extrusions do not

make contact with the wall. The spacer thickness will be increased as needed based on the survey to insure contact. The first block will be placed into contact along the spacers with the south bookend wall when it is rotated vertical. It should be noted that the location of contact is significantly higher than the location where the swelling in the block occurs due to hydrostatic pressure. The 20-mm thick spacers will insure that the location where swelling occurs does not make contact with the bookend. This is important so that the stresses in the PVC and adhesive due to swelling are not increased.

The concrete bookend structure is constructed by WBS 2.1. WBS 2.9 is responsible for surveying the surface of the bookend, and for attaching PVC sheet material to it as necessary to make it smooth, flat and plumb to a tolerance of about 2 mm.

17.7.3 The North Bookend

The second (north) bookend provides a strong, flat surface against which the final detector block rests. Its mechanical strength requirements are the same as those for the south bookend.

After the detector assembly has been completed, the block pivoter is converted to a stationary object serving as the north bookend. This is accomplished by gluing the last (11-plane) block to the pivoter during assembly and leaving the pivoter in place after it is erected. The majority of the block pivoter structure will remain intact, with only the hydraulic cylinders disconnected and replaced with rigid structural members and the vertical loads transferred from the rolling elements to permanent cribbing.

Since the vertical side supports (Section 17.12) are not sufficient to transfer the entire horizontal load from the north bookend to the floor, additional structural steel column sections will be attached to the back side of the block pivot table and anchored to the building floor (Figure 17.116).

The north bookend is installed by the WBS 2.9 assembly crew. WBS 2.9 is responsible for the design and fabrication of the additional bracing structures.

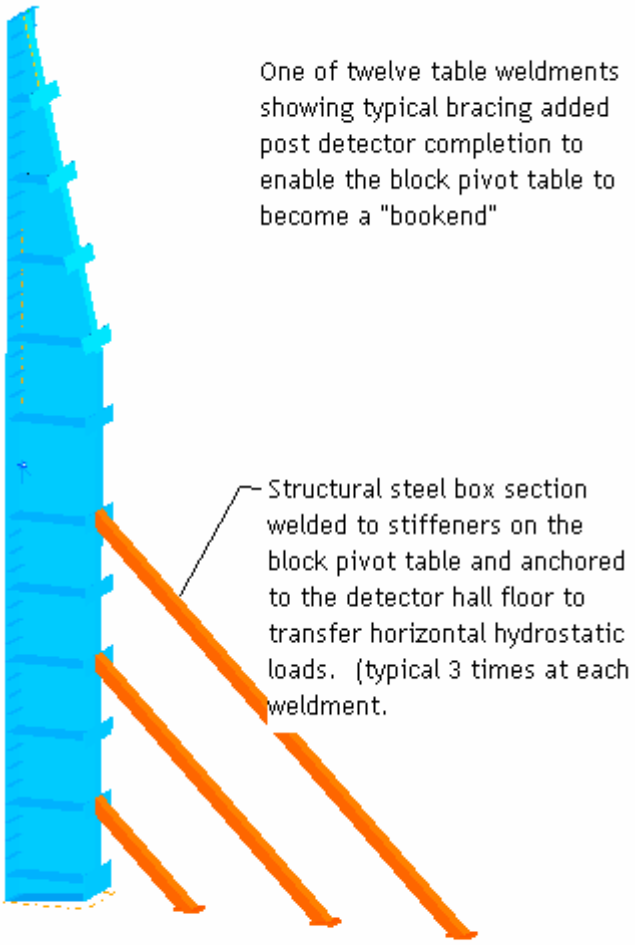

Fig. 17.116: Section through a portion of the block pivoter table showing the additional bracing needed to achieve the requirements of the bookend.

17.7.4 Detector Stability Monitor System

Over the 20-year lifespan of the NOvA detector, the PVC will continue to creep and the assembled detector blocks will move and deform. We will monitor the movement of the detector over time to ensure that it is following the expected deformation pattern and to provide a warning if the deformations become excessive, which could be indicative of potential failure and collapse of the detector. NOVA-doc-2339 describes the detector stability monitoring system in detail. The following paragraphs provide a brief summary.

FEA calculations have shown that the highest stresses will occur approximately 40 inches from the bottom of the detector on the outside planes of each superblock. During the assembly of the first and last blocks of a superblock, strain gages rosettes are placed on every other 16 cell extrusion (for a total of 12) on the outer most vertical extrusions of a superblock. Each rosette consists of three strain gages, so a total of 72 channels per superblock ($2\times3\times12 = 72$) are needed for readout. There are 7 superblocks for a total 504 strain gage channels to be monitored. The strain gages are read out by the detector control system (DCS) through monitoring electronics located in two relay racks. One relay rack is located one quarter of the detector length from the north end of the detector and the other is one quarter of the distance from the south end.

Blocks are in contact along the top of the detector. Thin pressure sensors such as Flexiforce sensors, which are less than 0.010-inch thick, are placed along the top of the detector to monitor the force along the top edge. The FEA model of the detector sets an acceptable range for the pressure along the top edge of the detector. If the monitored pressure exceeds this value, steps could be taken to relieve the pressure. A pressure sensor will be placed on the center of each module on the outside surface of each block. This results in 12 sensors per block and for 33 blocks and two bookends there are 34 interfaces, for a total of 408 sensors and channels that have to be read out. Simple electronic cards can be made to supply the voltage and op-amp for reading out these sensors. The electronics cards could be placed in the same racks as the strain gage instrumentation.

Over time we expect that blocks at the ends of superblocks will deform and make contact with each other. Calculations have shown that contact will first occur at a height between 130 and160 inches above the bottom of the detector. Pressure sensors such as Flexiforce sensors will be placed on the outermost extrusions. These sensors are only about 0.010-inch thick and the pressure between blocks would be measured as a change in voltage. Twelve sensors would be placed on each interface between superblocks (or superblocks and bookends).There are seven such gaps, resulting in a total of 84 channels.

The sensors described in previous paragraph are sensitive to the pressure between blocks within a superblock. It is also important to monitor the movement of superblocks relative to each other. Laser sensors will be mounted from the platforms to shoot beams across the width of the detector at several different heights of each expansion gap. Absolute block motion relative to the detector hall, above a set value, would be detected when a laser beam is broken.

The detailed FEA model of the assembled detector and full size testing will be used to determine locations of highest stress/pressure/motion. These areas will be monitored in a variety of ways, as described above, to insure that the stresses/pressure/motion stay within acceptable limits. If any of these monitored parameters exceed these limits, alarms will be raised and appropriate steps taken (i.e., emptying blocks) to ensure that the detector remains structurally stable.

17.7.5 Access to the Installed Detector Blocks

The detector assembly crew must have good access to the top and west side surfaces of the 52-ft high by 52-ft wide detector blocks in order to fill the blocks with liquid scintillator and to outfit them with electronics and DAQ hardware. Scintillator filling involves the manipulation of heavy transfer lines, through which large volumes of potentially hazardous liquid flow, near the top and side surfaces of the detector. Subsequent installation of photodetectors, front-end electronics, plumbing for the APD water cooling system and data acquisition cabling and hardware, involves careful alignment of delicate hardware in awkward locations, as well as manipulation of cable trays and pipes that could damage the detector modules. Cooling hardware, racks containing electronics hardware, and building utilities (mounted on the building walls) are also located close to the detector surfaces. Even after detector installation is completed, readout hardware maintenance requires occasional access to the top and side of the detector. These diverse requirements have motivated a substantial design effort aimed at providing safe and convenient access to the top and sides of detector blocks.

Access to the west side of the detector is provided by four walkways extending the full length of detector hall. These are shown in Figure 17.117. The 7-ft wide walkways are separated by approximately 14 ft in elevation. Each walkway accommodates a 3-ft wide egress path and an 8-inch wide space along the building wall that is allocated for building utilities and ventilation ducts.

The building floor and the bottom three walkways each give access to three levels of horizontal module manifolds, with movable stepladder platforms used to reach the upper

manifolds. The top walkway is located 14 inches above the top surface of the detector. It gives access to the rolling access platforms and also supports electronics power-supply racks and cooling-water chillers.

Two rolling access platforms, like the one shown in Figure 17.118, are supported by three rails attached to the concrete ceiling, like light-weight overhead crane bridges. Each platform gives access to the full width of the detector. The platforms are designed for both scintillator filling and to provide access for electronics outfitting. Each platform is suspended 14 inches above the top surface of the detector and can carry three workers.

Stairs provide safety egress from the building and allow personnel movement between walkways. Heavy equipment can be moved from the loading dock area to the top walkway and the elevator on the west side, as described in Section 17.9.

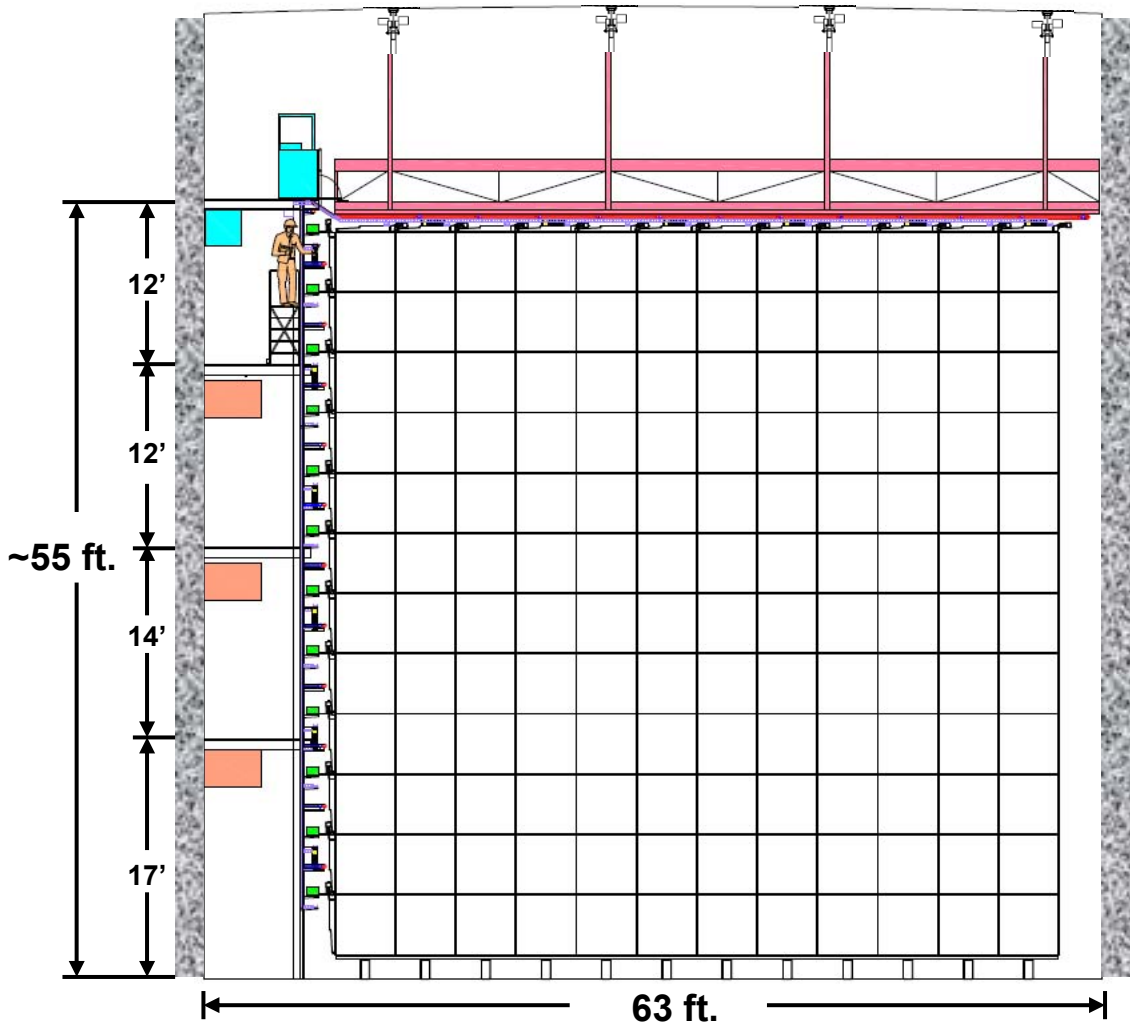

Fig. 17.117: Elevation view of the NOvA far detector, showing the four detector-access walkways on the west side. See Figure 17.118 for more a more detailed view.

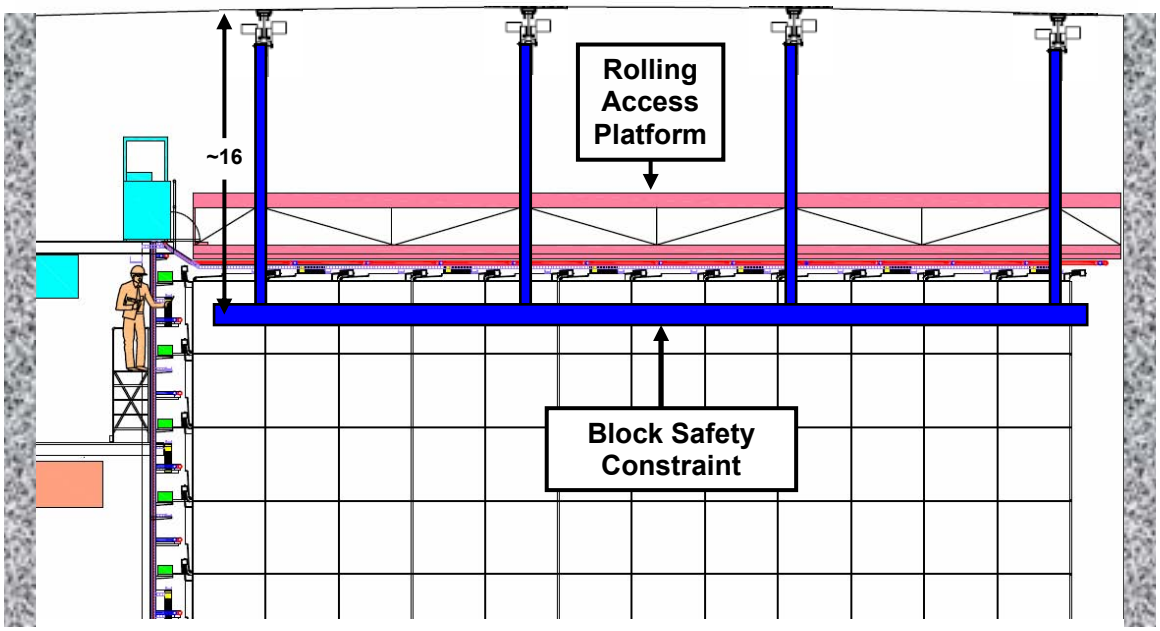

Fig. 17.118: Close-up elevation view of the top of the NOνA far detector, showing one of two rolling access platforms. These platforms are used for filling vertical modules with liquid scintillator, and for outfitting them with electronics and associated infrastructure. The block safety constraint beam, described in Section 17.13.5, is also shown in this view.

17.7.6 Detector Control Room

The detector control room and adjacent computer room are located on the west side of the detector hall near the elevator and the north end of the detector, as shown in Figure 17.119. This facility is the same as the same elevation as the top walkway on the west side of the detector. Cable trays connect the computer room to the top walkways and to the top and sides of the detector where the front-end electronics are located. WBS 2.7 and the Cooperative Agreement Operations tasks are responsible for the setup of the control room.

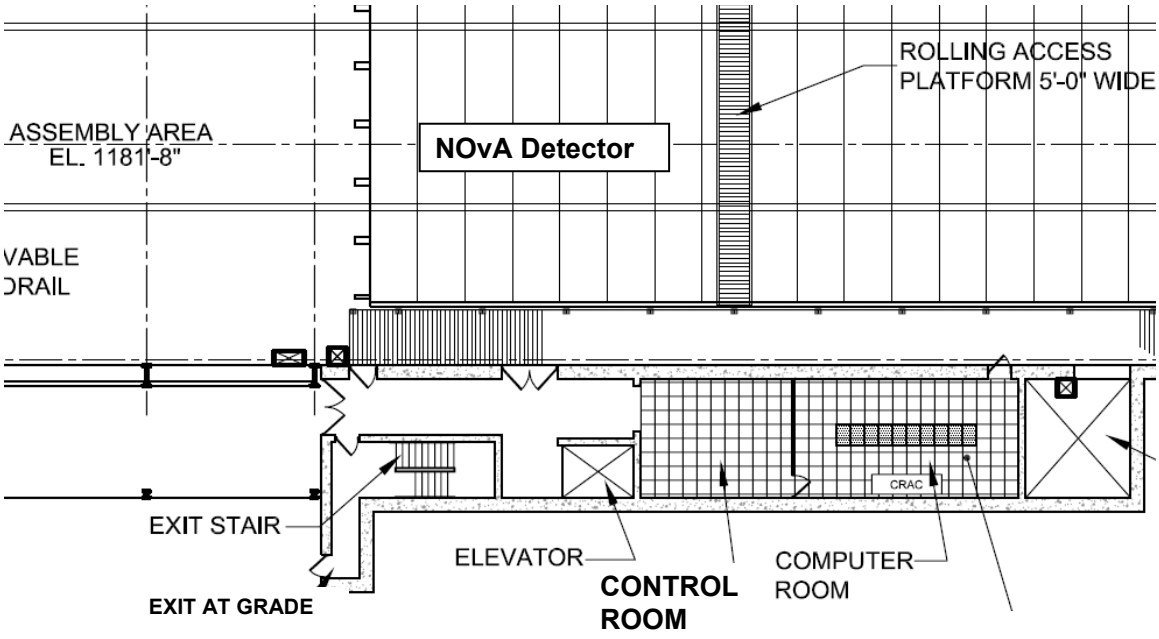

Figure 17.119: Plan view of the control room and computer room.

17.8 Liquid Scintillator Distribution and Supply System

17.8.1 Scintillator Distribution System

The scintillator distribution system is designed to accept scintillator from delivery tankers at a rate of roughly one tanker per day at the far site, and to deliver this oil to the modules being filled, in a safe and reliable manner. The sustained flow rates of roughly 24 gpm required to fill the detector at the same rate that blocks are lifted into position imposes a number of requirements on the distribution system, which we describe below. During the period of full-rate installation, blocks are installed at the rate of one every 2.6 weeks. Filling will occur during one 40-hour shift per week about 85% of the time. The scintillator delivery system includes components that ensure that the scintillator is delivered to the module at a precisely controlled temperature and flow rate. Thermal control is necessary to minimize post-filling changes to the scintillator volume as it comes to the ambient hall temperature.

The delivery system is designed to eliminate all possible hazards associated with static generation and charge accumulation resulting from the flow of a non-conductive fluid. As described in NOVA-doc-1118, an anti-static agent (Stadis 425) is added to the scintillator at a concentration that reduces the discharge time, and therefore, the steady state fluid charge, by orders of magnitude. The distribution system itself uses conductive plumbing fixtures at all points, bonded and discharged to ground. Finally, a vapor return system is included in the scope of the scintillator distribution system. During filling, this system returns the displaced gas volume to the tanker being discharged. During normal operation, this system maintains nominal pressure in the trapped gas volume in the detector modules as the scintillator volume changes due to temperature changes in the detector hall. For the horizontal modules, the vent system includes a 4 liter expansion tank that provides a 2 liter reservoir of scintillator at nominal hall temperature, allowing the full active volume to be maintained over decreases in hall temperature of as much as 5ºF. In addition, the expansion tank provides a take-up volume sufficient to accommodate increases in hall temperature of as much as 5º F.

This section presents a detailed description of the scintillator distribution and filling system, starting from the tanker and working towards the module filling hardware, and ending with a description of the vent system design.

17.8.2 Distribution Control System

Figure 17.120 shows a schematic representation of the scintillator distribution control system. It includes connections to the delivery tanker, pump, filter, thermal control system, as well as temperature, flow rate, and pressure monitoring. Figure 17.121 shows the connections between the distribution system and the scintillator delivery tanker yard. The scintillator in each tanker will be tested for light output, attenuation length and conductivity before the transfer line is attached to the tanker. The scintillator control system then ensures that the scintillator is filtered, temperature corrected, and at the correct pressure and flow rate for delivery to the detector.

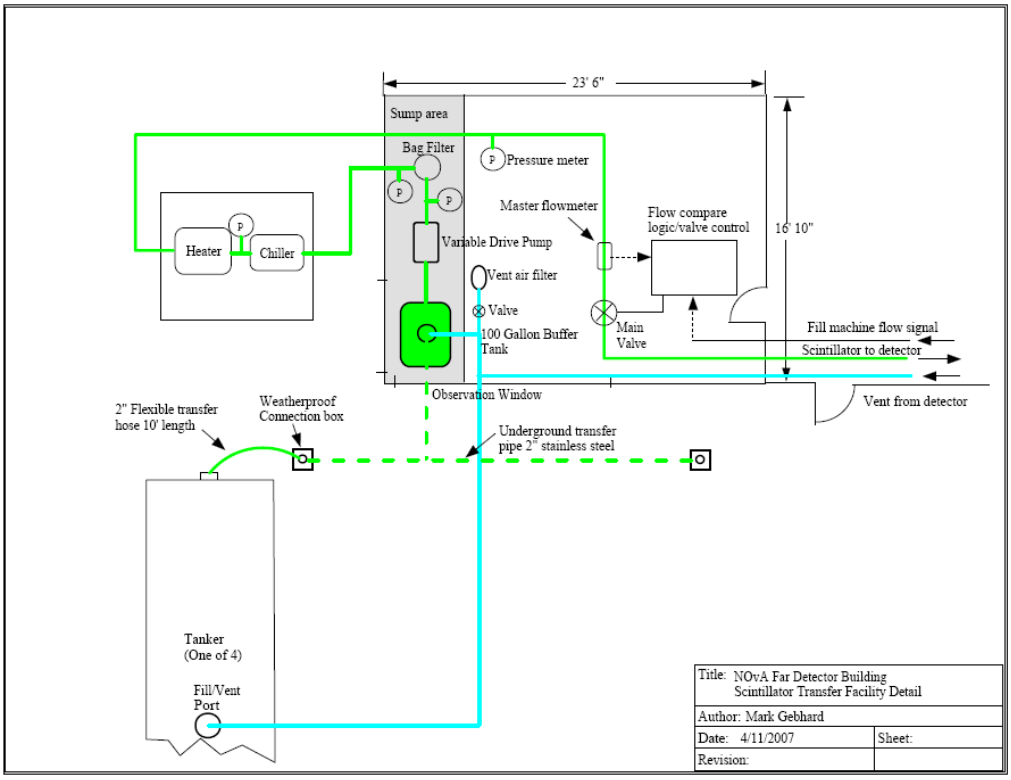

Figure 17.120: Scintillator distribution control system.

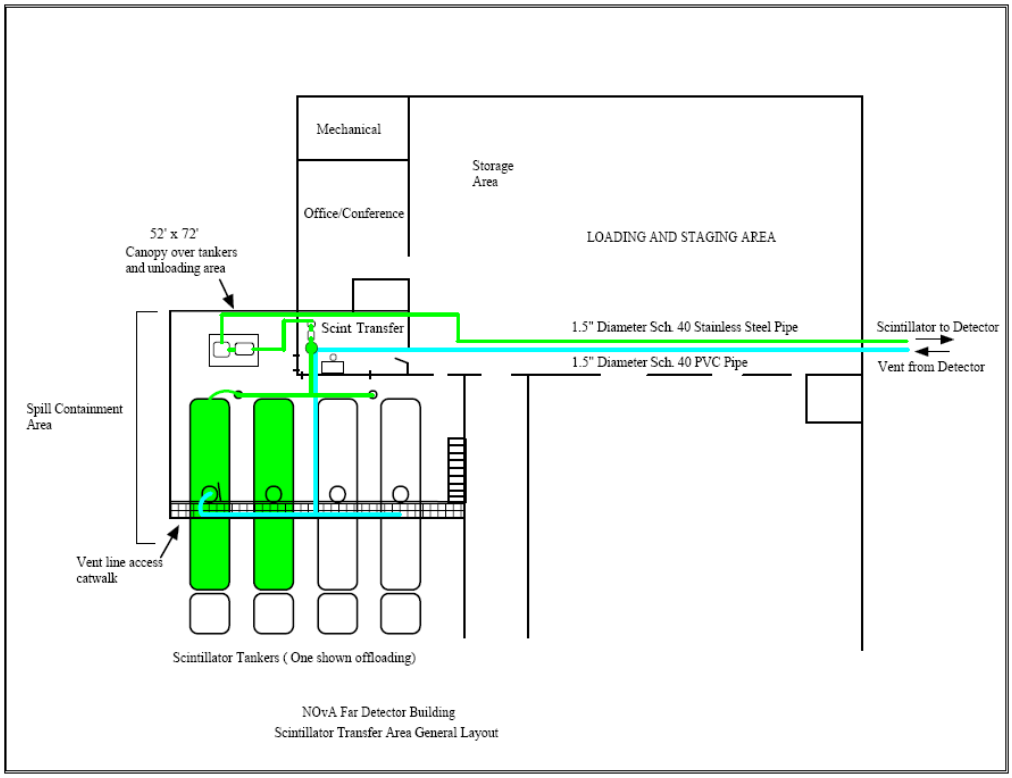

Figure 17.121: Scintillator transfer area layout.

The tanker location is elevated to a height that permits gravity feed of the scintillator out of the tanker, through a flexible 2-inch transfer hose and pipe leading to a 100 gallon buffer tank. This buffer tank is equipped with level sensors that close valves at the module fill stations when the delivery tanker is fully drained, and before air is allowed into the distribution plumbing. The tank is equipped with a valved vent line to allow venting of trapped air back into the tanker.

The distribution system pump is designed to provide 24 gpm of oil through a system flow impedance that includes the effects of the filter, heater, chiller, valves, piping, and hoses to the module manifolds. A variable frequency drive is used to control the motor speed driving the centrifugal pump. This drive is controlled by the fill machine operator, who soft starts the fill system and brings the pump up to the speed required to deliver 2.3 gpm to the eight manifolds being filled.

Following the pump, the scintillator makes one pass through a 10 micron filter, which is a standard size for oil filtration. A trade size 8 holder and bag are appropriate for the nominal flow rate of 24 gpm, assuming that the scintillator is relatively free of particulate matter. The pressure drop across the filter is measured and used to determine when replacement of the filter bag is necessary.

The tankers are preheated prior to shipment to ensure that they arrive at the far site at a known temperature. The thermal control system described below is designed to accommodate scintillator at the tanker that is within a ±10º C range about room temperature, and to deliver oil to the detector within 1º C of ambient hall temperature. The ±10º C temperature range of scintillator in the tanker is maintained by setting the temperature at the point of origin to compensate for the expected environment during transit. Under extreme conditions in which this input temperature range is exceeded, the scintillator flow rate (and consequently, detector fill rate), will be adjusted to compensate, allowing the distribution system's thermal subsystem to bring the scintillator to ambient hall temperature at the module.

From the filter, the scintillator passes to the heater, where the temperature of the scintillator is corrected as needed. The heater is designed to provide control to ±1° C of the output temperature at 24 gpm. The heater is followed by a chiller which again is designed to provide thermal control to ±1° C. A flow meter following the chiller serves as a master supply reference. If the supply flow in this meter does not equal the supply total flow of the 8 meters in the fill machine running at the extrusions, the flow master control in the fill machine will issue a halt command to the pump and terminate all filling to the 8 output lines. This avoids spills due to a catastrophic failure of the plumbing between the scintillator transfer facility and the fill machine.

17.8.3 Distribution Plumbing

Figure 17.122 shows a schematic for the distribution system plumbing. Liquid scintillator enters the detector hall plumbing filtered and temperature corrected and at a known pressure and flow rate. The scintillator is then delivered to the fill site through a combination of fixed and flexible stainless steel pipe (Figure 17.122). The mainline pipes for the distribution system in the detector hall are 1.5-inch diameter stainless steel. O-ring unions are used on all serviceable equipment to ease removal and replacement when required. Valves are used to isolate sections of the system for service and to ensure leak free hookups at the hydraulic quick disconnects in the system.

The top of the detector is serviced through a pipe located on the west wall of the detector hall at the top walkway level, with ports at six locations along the length of the detector, each having a valve and quick disconnect. A 30-ft long, 1-inch diameter flexible, conductive delivery hose is used to couple a quick-disconnect at this level to the rolling access platform, which provides access to the top of the detector. A 1-inch stainless steel pipe runs along the platform, with quick disconnects every 8 ft. A fill machine is located on this platform at all times and connected to one of six outlet ports with a conductive flexible hose.

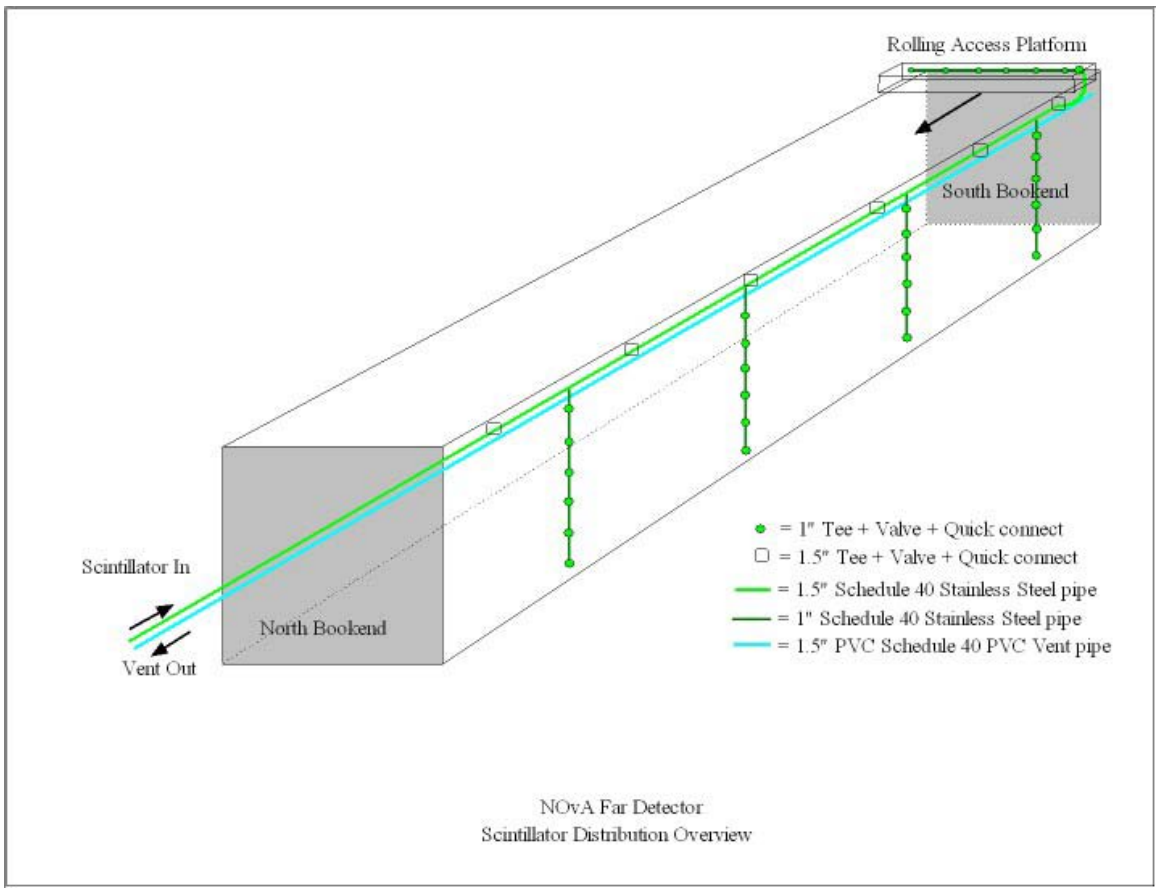

Figure 17.122: Scintillator distribution system plumbing.

The west side of the detector is serviced by four down-going fixed pipe runs. Each of these consists of a 1-inch diameter stainless steel pipe teed off from the 1.5-inch diameter mainline (on the top walkway level) and running to the ground floor level, with a quick disconnect installed at each walkway level. A 1-inch diameter conductive flexible hose connects the wall-mounted quick disconnect to an extension pipe, which in turn connects to a fill machine through a length of 1-inch diameter flexible conductive hose.

17.8.4 Scintillator Filling Machines

The fill machines, two for the west side and one for the top, are the final components of the delivery system. Figure 17.123 shows a schematic diagram of one fill machine. Each is mounted on a two-wheel hand truck, and consists of nine positive displacement oval gear GPI flow meters that control solenoid valves and provide a display of the total scintillator delivered to each extrusion. The ninth flow meter measures the total flow into the machine.

The NOvA extrusions must be filled to ±1 liter without visible feedback on a volume of 1,031 liters (horizontal) and 1,116 liters (vertical). The initial fill will be terminated well before the extrusion is completely filled, and the scintillator and extrusion allowed to come to thermal equilibrium. The final top-off of the extrusions is controlled by ultrasonic level sensors mounted on the exterior of the extrusion or horizontal expansion tanks. The final fill level will be accurate to ±1 cm. When the proper level is reached and detected, a signal will be issued to close a solenoid valve on the output line and terminate fill. The fill machine output lines are 4-ft flexible conductive 0.5-inch diameter hose ending in a custom fill nozzle, shown in Figure 17.124. The nozzle design is described in more detail in NOVA-doc-1525. While filling, precautions are taken

to terminate a fill if a nozzle should detach or begin to leak. Spill trays, also shown in Figure 17.124, are located directly under all active fill ports, and are equipped with optical liquid level detectors that terminate flow in response to the detection of standing oil in the tray.

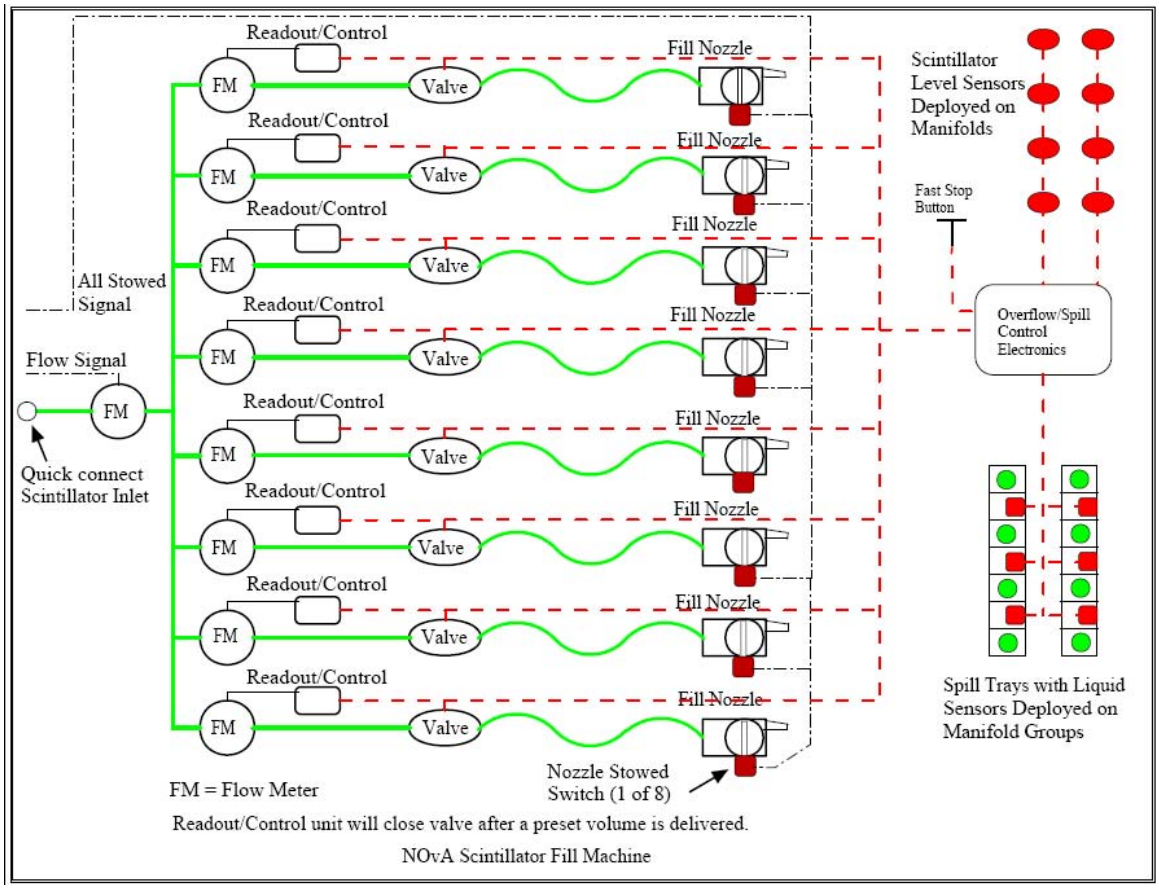

Figure 17.123: Schematic drawing of the fill machine.

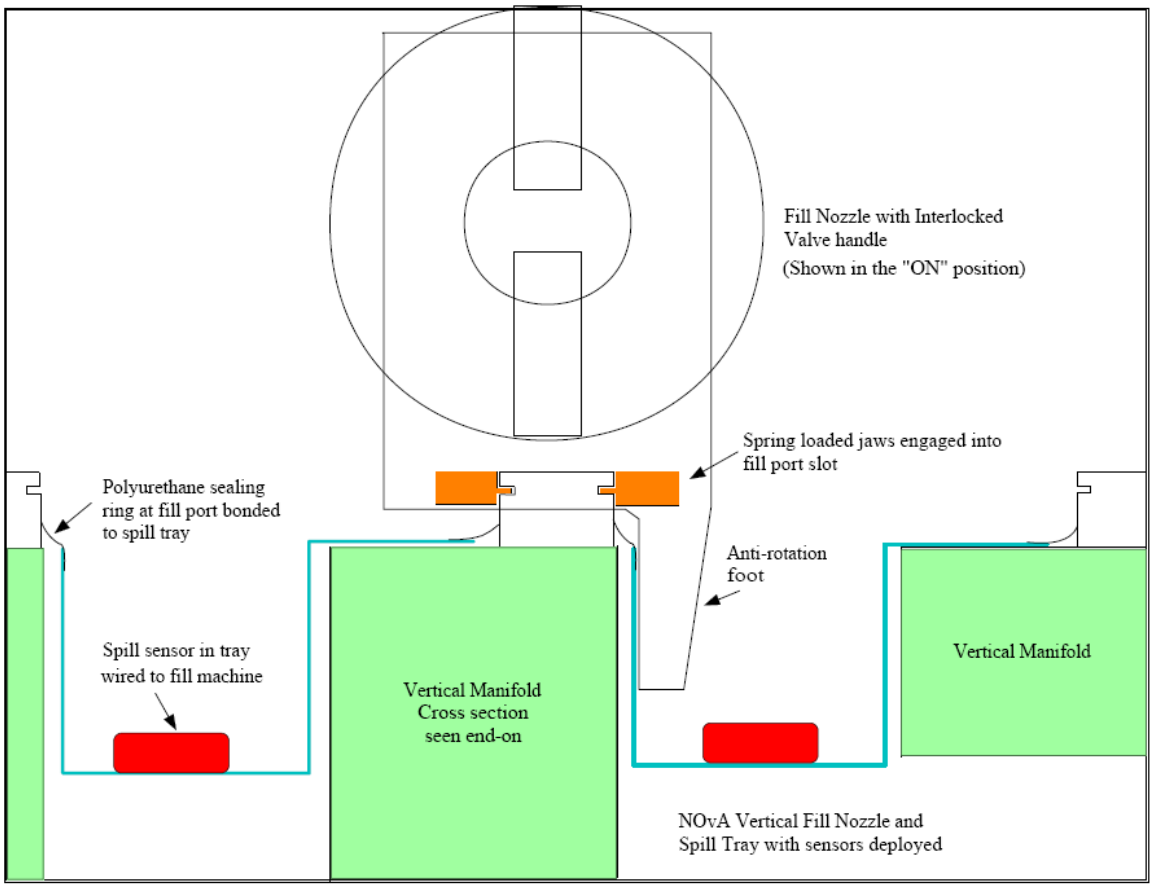

Figure 17.124: Schematic drawing of the fill nozzle and spill tray.

17.8.5 Vapor Recovery System

During filling, a large volume of scintillator-laden vapor is displaced from the extrusions, which must be vented from the hall and filtered before exhausting to the local environment. To accomplish this, a vapor transfer system is installed on the detector and plumbed out of the hall and to the off-loading delivery tanker. The vapor transfer lines consist of a black PVC tubing plenum servicing one plane. Connections to the plenum from tubing running from the module vent port are made by black nylon barbs with steel compression bands sealing each joint. Figure 17.125 shows the vent line layout for horizontal planes, where connections are made to both the manifold and expansion tank. Each plenum terminates at a manifold of 1.5-inch diameter black schedule-80 PVC pipe running along the length of each module, which in turn is connected to fixed pipe runs to the scintillator transfer room. During filling, the displaced vapor is returned to the unloading tanker. During normal operation, the vapor is exhausted to the air through a charcoal filter.

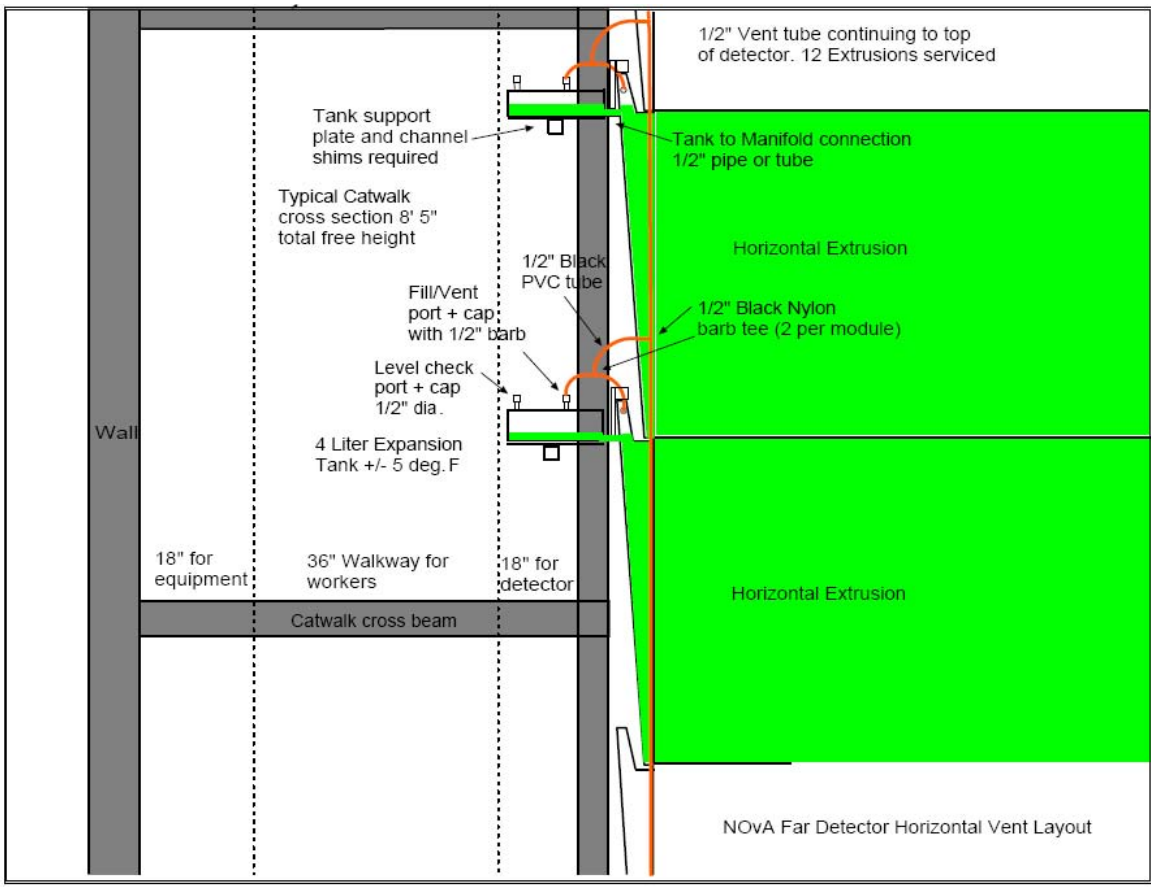

Fig. 17.125: Horizontal module vent layout.

17.8.6 Scintillator Distribution System Installation

The scintillator distribution and supply system is installed in three major pieces: the transfer facility, the distribution plumbing and the vapor recovery system. This work is performed during the ~10 months between beneficial occupancy and the time when the first block is ready to be filled. The scintillator technicians will require approximately 4-6 FTE-months to complete the non-block installation work. Figure 17.121 shows the scintillator transfer facility, which is located in a room next to the truck canopy where tankers deliver the premixed scintillator. This system is installed and tested by scintillator experts with help from the scintillator technicians. Installation may begin any time after beneficial occupancy of the building.

Installation of the rigid stainless steel distribution pipe begins immediately after beneficial occupancy of the far detector enclosure, as filler work for the scintillator technicians. This piping connects from the scintillator transfer facility to the distribution points needed around the detector. The 2-inch stainless steel mainline is located on the top walkway and is installed by the scintillator technicians and tested by the scintillator experts. There are four permanent 1-inch stainless steel pipes on the west side of the detector that feed the lower walkway levels, as described in Section 17.8.3. The rolling access platform is also installed with a rigid stainless steel pipe to feed the top of the detector. All pipes are fitted with shutoff valves and quick disconnects as needed. The exact location of these pipes in relationship to the building infrastructure has not yet been determined but they will be somewhere on the west detector hall wall.

The third part of the system is the scintillator vapor recovery. A schedule-40, 1.5-inch diameter, black PCV pipe runs down the west side of the detector hall back to the scintillator transfer facility. This mainline vapor pipe has fittings to connect to each of the detector blocks. It is located just under the top walkway to eliminate tripping hazards. The smaller flexible schedule-80 PVC pipes connect each module to 0.75-inch plane manifolds.

17.9 Far Detector Assembly Equipment

During the 12-week setup period, which begins immediately after beneficial occupancy of the far detector building, the first members of the assembly crew begin the setup of equipment needed to assemble and install detector blocks (Section 17.16). The assembly crew increases from 4 to 14 workers during this period. The setup work schedule includes time for the training of new crew members as they are hired and for safety reviews of equipment and procedures. The equipment is shipped to the site both from commercial suppliers and from NOvA institutions where it has been fabricated and tested prior to shipment. In the latter case, engineers and technicians who designed and built the equipment will travel to the far detector site to supervise and assist the assembly crew, and to provide training in operating it. The setup period is followed by a 15-week startup period, when the equipment is used to build and install the first three detector blocks while the installation crew ramps up to its full size of 26 workers. The following sections give detailed descriptions of the major items of equipment. Figures 17.126, 17.127 and 17.128 show the layouts of the loading dock and assembly areas at the north end of the detector hall, where most of this equipment is installed.

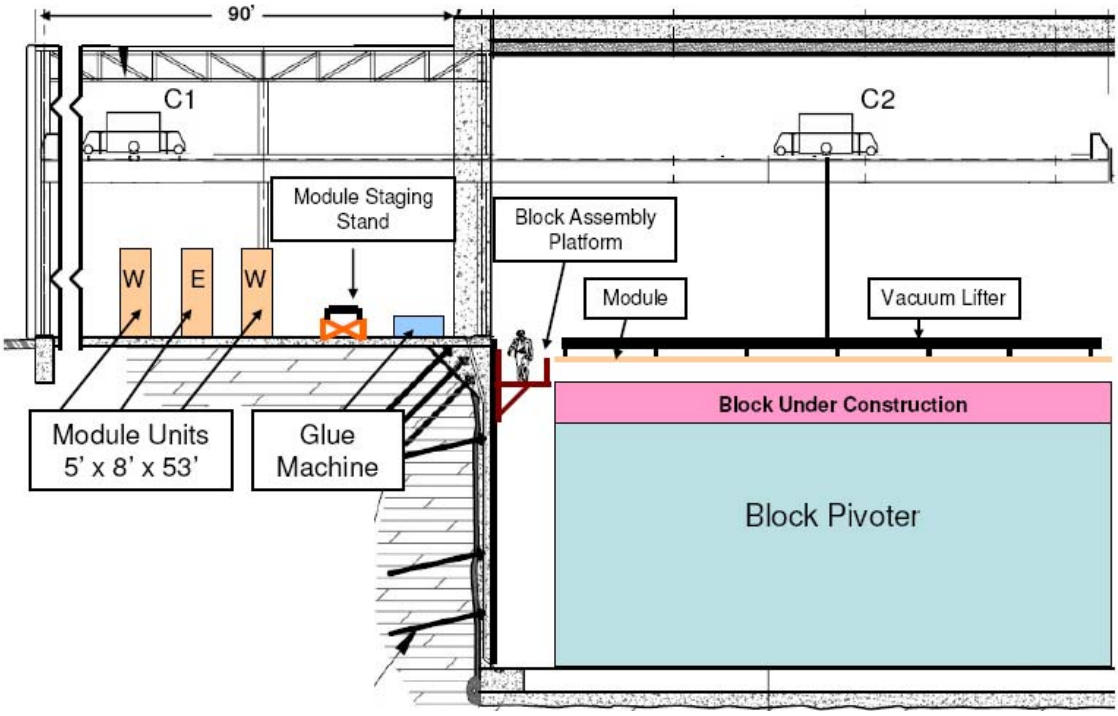

Fig. 17.126: Side view of the loading dock and assembly areas. The drawing shows a module being placed into the block under construction by a 10-ton bridge crane (C2). The 10-ton bridge crane (C1) is picking up a module that is ready for the adhesive dispenser. The elevation of the work surface of the block pivoter is ~16 feet below the loading dock. Access to all elevations below the loading dock level is provided by the block assembly platforms, which move vertically on rails mounted to the walls. Only the south block-assembly platform is shown in this view; the east and west platforms are not shown.

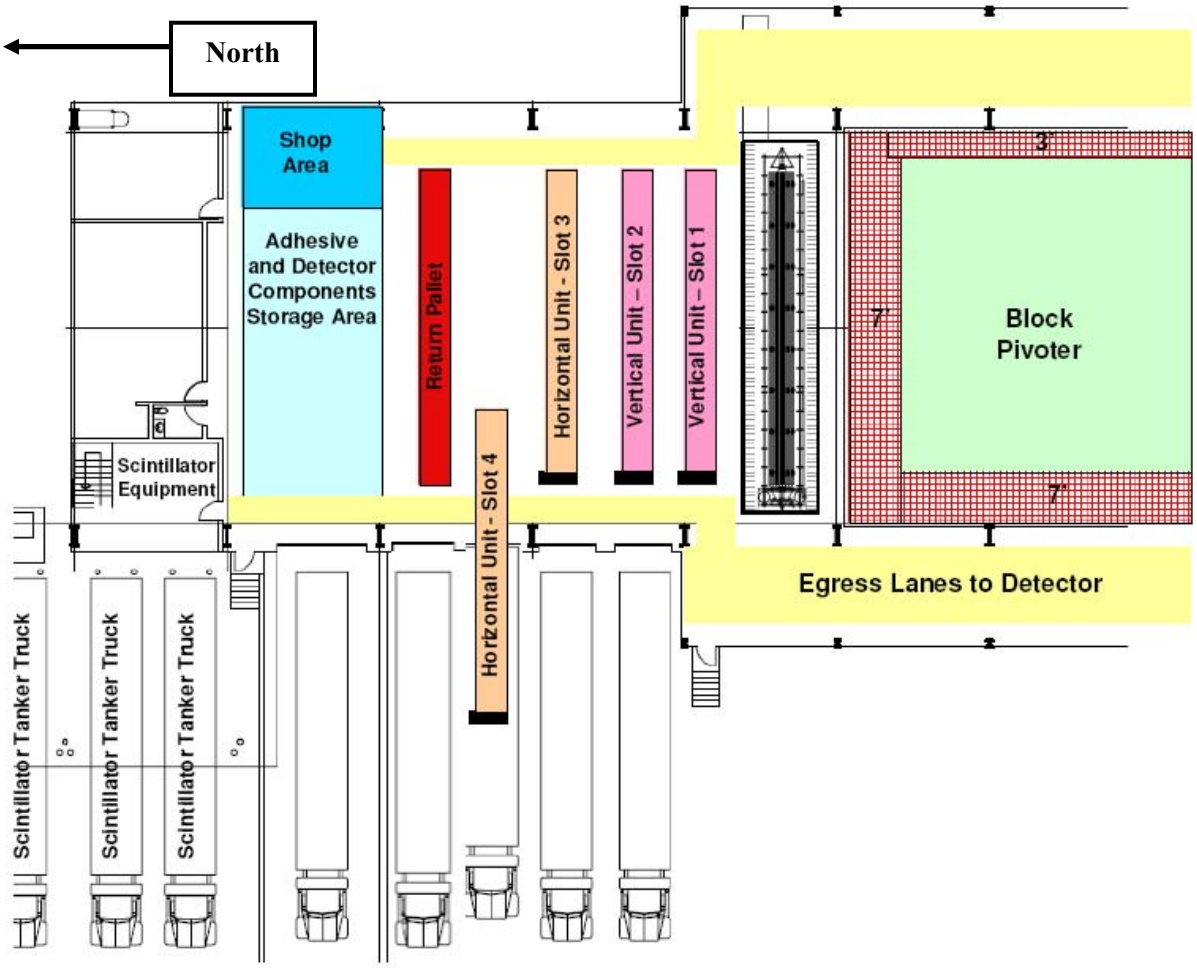

Fig. 17.127: Plan view of the loading dock area. Three module units are shown in the loading dock area and one (lower left) is being moved from an arriving delivery truck. Module units are prepared for testing after they have come to thermal equilibrium. A module unit weighs about 14 tons, including the custom pallet system, and is moved with a motorized pallet jack (NOVA-doc-1030 and 1038). The area at the left is used for temporary storage of pallets of glue, electronics and other items. It is shown in detail in Figure 17.128.

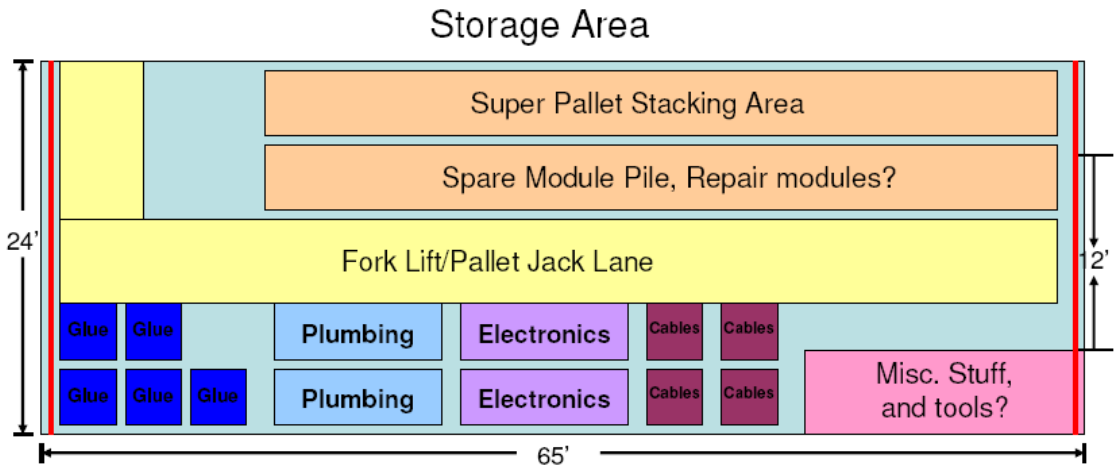

Fig. 17.128: Typical usage of the loading dock storage area for detector installation materials.

The list below gives an overview of the far detector assembly equipment. Most of this will be installed during the setup period.

- **Bridge cranes**
  Two 10-ton overhead bridge cranes run over the assembly area (block pivoter) and the loading dock on the same set of rails. They are used to move single modules to the adhesive dispenser, to place modules onto the block pivoter and to lower equipment to the main floor. They are operated by remote control units and also provide electrical power for module vacuum lifters suspended from their hooks. The cranes are purchased by WBS 2.1 and installed before the setup period begins.
- **Vacuum lifting fixture (NOVA-doc-1112)**
  The vacuum lifter (described in Section 17.10) is a 52-ft long vacuum spreader bar for moving single modules. It attaches to a module with long rectangular suction cups that line up with the flat cell surfaces of the extrusions.
- **Adhesive dispenser (NOVA-doc-1357)**
  The adhesive dispenser (described in Section 17.11) is located in the loading dock area adjacent to the block pivoter. A module is placed on the adhesive dispenser by the 10-ton bridge crane with a vacuum lifting fixture. The module remains stationary as the glue head with 16 nozzles lays beads of Devcon 60 adhesive along the top of each cell. The adhesive dispenser incorporates a module flipping device to orient each module glue-side-down before it is picked up by the south bridge crane and moved to the block pivoter.
- **Block pivoter (NOVA-doc-989)**
  The block pivoter (described in Section 17.12) is at the center of block assembly and installation. Its top surface is the block assembly table and it rotates completed blocks (Far Detector Parameter Sheet NOVA-doc-2066) from the horizontal to the vertical. It provides alignment fixtures for modules within a block, and ensures that blocks are plumb, level and square. NOVA-doc-1396 describes module and block survey and alignment requirements.
- **Block pivoter access platforms**
  These commercial platforms provide access to the east, west and north sides of the block assembly surface of the pivoter. Each one is a set of stairs on wheels with a work platform on top. They are used for personnel access to the top of the block under construction and to provide access to the sides of the block for outfitting, light proofing and alignment.

- **Scintillator handling equipment (NOVA-doc-1118, 1239, 1921)**
  The tanker truck hardstand and canopy, with room for four tankers and the liquid transfer conduit to the detector, is constructed by WBS 2.1. As described in Section 17.8, WBS 2.9 is responsible for installing the grounded metal supply pipes, the supply system plumbing, the vapor return system and the three filling machines. WBS 2.2 provides the scintillator test equipment used by the WBS 2.9 assembly crew.
- **Module unit mover (NOVA-doc-1030 and 1038)**
  Module units are stacks of 24 modules that are prepared and shipped from module factories to the detector site. A module unit is pulled out of the delivery truck on a set of long narrow air casters by a motorized pallet jack. The air casters are narrow enough to be placed on each side of the module pallets while still in the truck.
- **Module test equipment (NOVA-doc-1031)**
  WBS 2.5, 2.6 and 2.7 provide equipment used for quality assurance testing of arriving modules and electronics. These tasks also provide experts to train the assembly crew in the routine use of the equipment.

17.10 Module Vacuum Lifter

Figure 17.129 shows the vacuum lifting fixture (NOVA-doc-1320), which is a 52-ft long vacuum spreader bar for moving single modules. It has six cross bars, evenly spaced along its length, each with four rectangular vacuum cups that are easily aligned with the flat surfaces of a module's extrusion cells. The vacuum lifter is carried by an overhead crane that provides electrical power to operate the vacuum pump. It is a commercial lifting fixture that has been slightly modified for attaching to the NOvA modules. The simple modifications involve a change in the suction cups, lengthening of the main spreader beam, and the addition of guides to help locate the suction cups. These changes were incorporated into an existing fixture that was used in the MINOS experiment. Subsequent tests with prototype modules have verified the feasibility of this design. Figure 17.129 shows the full span of the lifting fixture with the vacuum pump and lifting point located in the center of the spreader beam and six cross supports containing the suction cups. The vacuum pump is operated by 120 VAC and is valve connected in a failsafe manner such that, in the event of electrical power loss, the vacuum is maintained long enough to allow a module to be lowered safely to the ground.

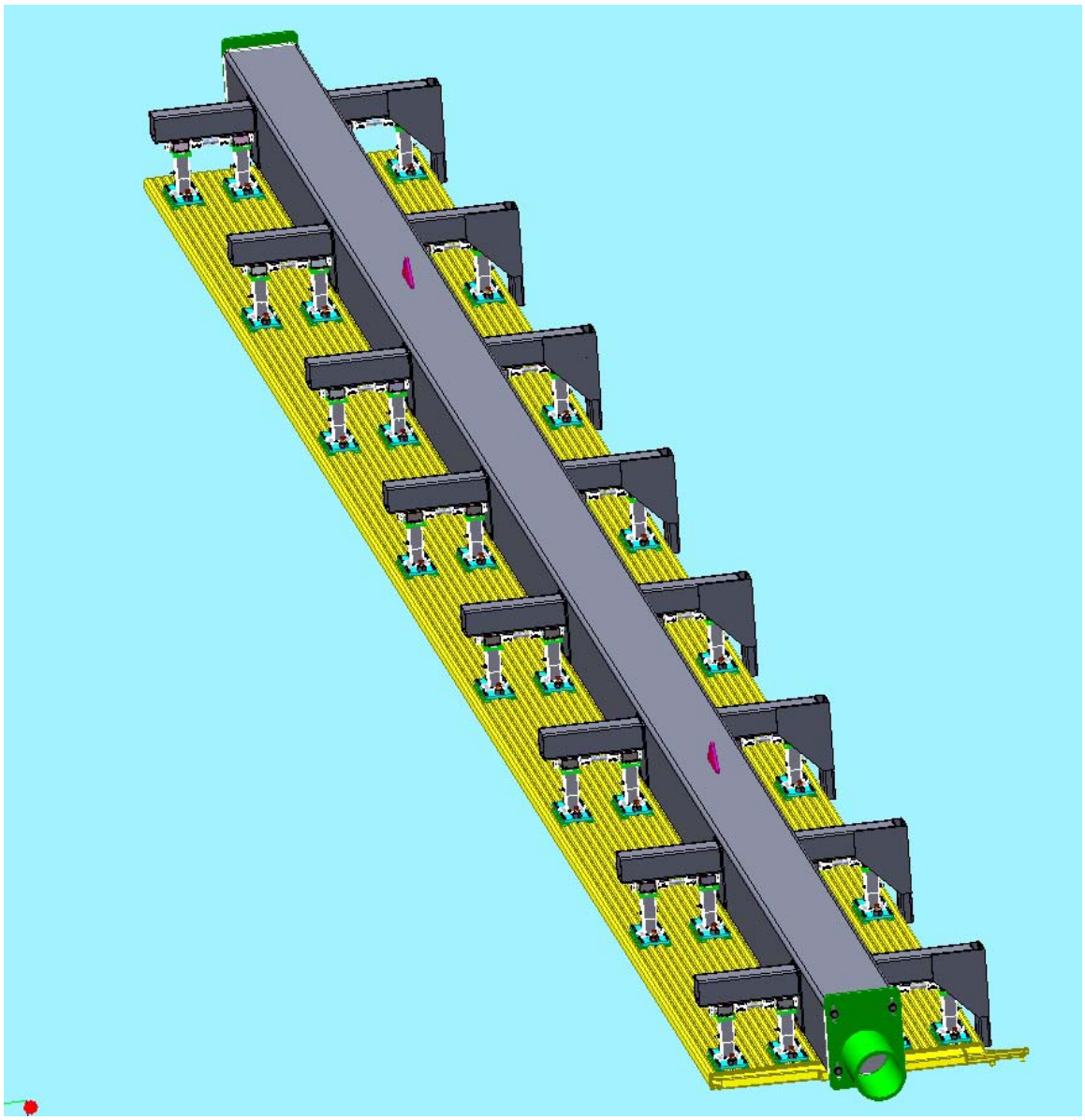

Fig. 17.129: Lifting fixture with module attached. The green cylinder on the right-hand end is the support pivot that mates with the adhesive dispenser.

Figure 17.130 shows some important features in greater detail. Because of the scalloped surface of the extrusion, narrow rectangular suction cups are needed to provide a reasonable area for the lift points without crossing into the troughs between extrusion cells. To ensure that the suction cups are located properly with respect to the troughs, a guide is built into the cross piece to properly locate the suction cups upon making contact with the side of the extrusion. (This guide piece has an additional structural function that is described in Section 17.11.) The suction cups are prevented from rotating into the troughs by connecting rods that pass through the suction cup mounts and are connected to the side guide. Finally shown in Figure 17.130 is a pivot shaft that projects out of the spreader beam near the center of gravity of the combined lifting fixture and module. This feature is also used by the adhesive dispenser, as described in Section 17.11.

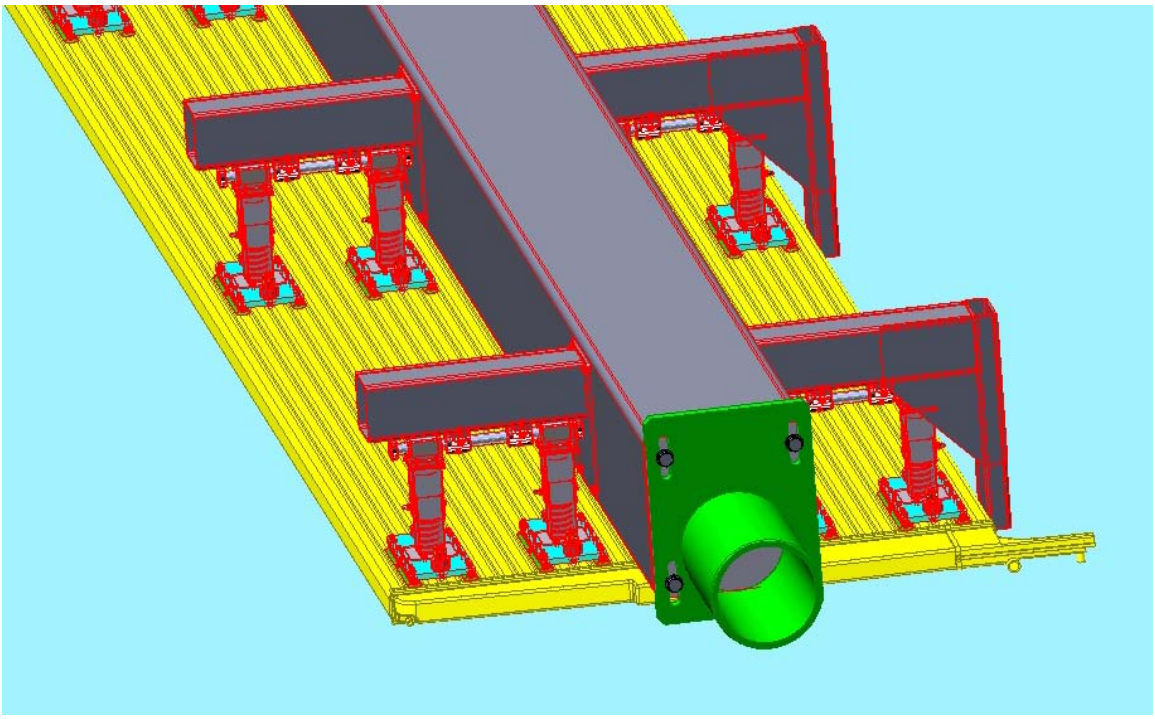

Figure 17.130: Close-up view of the vacuum lifting fixture suction cups and alignment guides. The guides are the extensions attached to the right-hand ends of the transverse beams. The green cylinder on the near end of the fixture is one end of the support pivot used by the adhesive dispenser.

17.11 The Adhesive Dispenser

The adhesive dispenser (NOVA-doc-2067) applies the adhesive to one surface of each extrusion module before it is installed in a block. The module is supported by the vacuum lifting fixture, allowing direct movement from the adhesive dispenser to the block pivoter. Figures 17.131 shows CAD-model overviews of the device. Figures 17.132(a), (b) and (c) show close-up views of the adhesive dispensing heads, the two 55-gallon drums containing the two components of Devcon 60 adhesive, and the eight adhesive pumps. The sequence of operations starts with an extrusion attached to the fixture being lowered onto the adhesive dispenser by the 10-ton bridge crane. The fixture is lowered until the two support pivot shafts (one on each side of main spreader beam, as described in Section 17.10) are set into the compliant bearing supports on the adhesive dispenser table. A drive mechanism is then connected to the pivot shaft and the fixture is rotated 180º to expose the unobstructed bottom surface of the module. As the fixture is rotated, the suction cups are still active and additional side support is provided by alignment guides described in Section 17.10. After this rotation is complete and the module is secured, the glue carriage (formerly parked out of the way at the base end of the table) travels across the table. The carriage contains the glue dispenser for the two part adhesive as well as two 55 gallon drums containing the adhesive components. The carriage includes 16 dispensing nozzles mounted to a bearing rail and a lead screw assembly. The latter allows the nozzle assembly to move transversely, by two extrusion cell widths, to cover the full module width. With 16 nozzles, the carriage makes two trips along the length of the module and returns to the park position upon completion. The module is then rotated by 180º so that the lifting hook is on top. The glued module is ready to be rigged to the block pivoter with adhesive applied to its bottom surface.

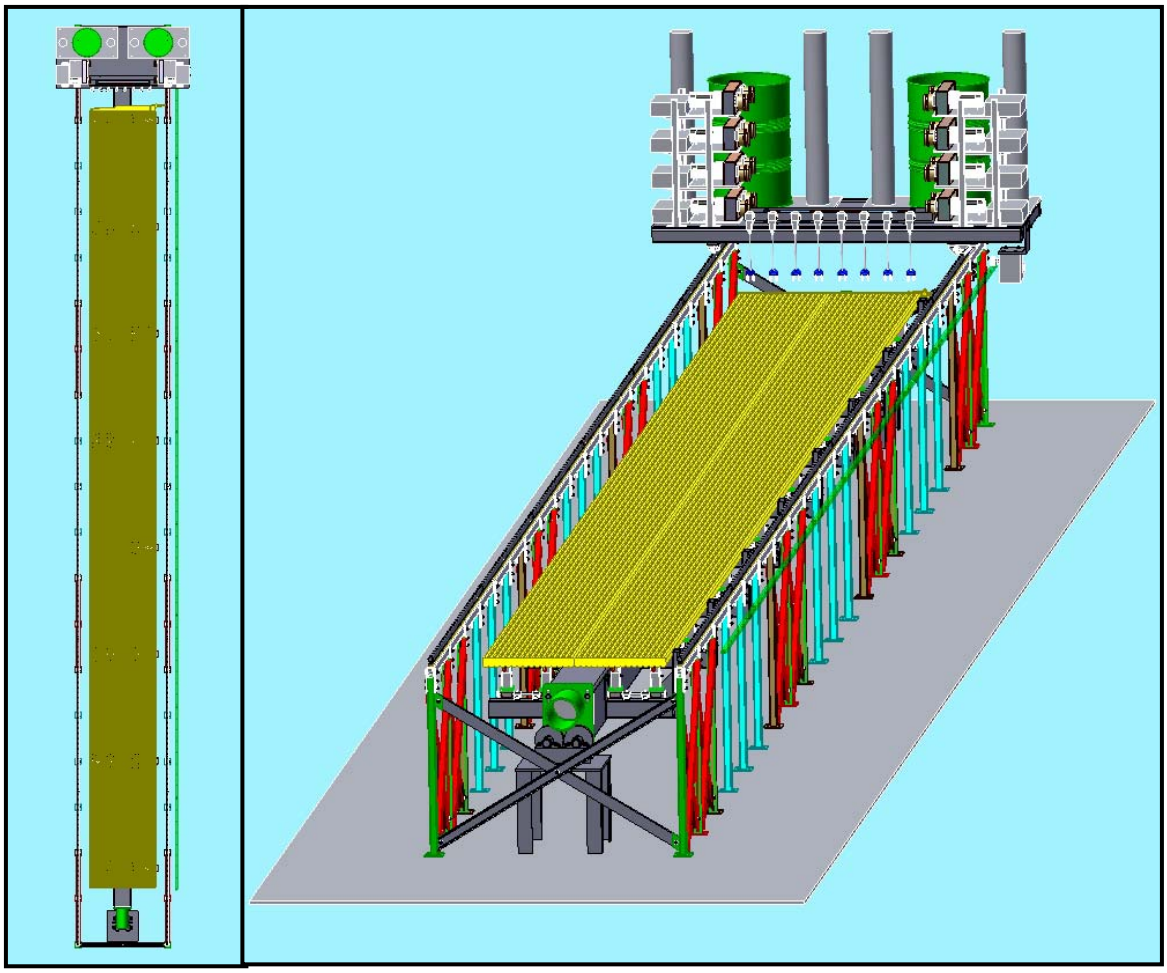

Fig. 17.131: CAD model overviews of the adhesive dispenser. A plan view is shown on the left and an isometric view is on the right. The adhesive dispensing mechanism is at the top in both drawings.

Figure 17.132(a), (b) and (c) show the adhesive dispenser in more detail. The carriage travels the length of the module supported by bearing rails that are mounted to the glue table. It is driven by servo motors using a rack and pinion system. The carriage and dispenser are specified to dispense adhesive and travel at 0.5 m/s. The adhesive dispenser uses a PLC for supervisory control of the carriage motion, dispenser actuation, fixture rotation, and safety monitoring. The operator is responsible for engaging the rotation mechanism and for initiating the various automatic sequences. Depending on the stiffness of the lifting fixture, intermediate supports for the modules may be needed to reduce module deflection while on the fixture. There are several possible methods for quickly attaching the rotation device to the fixture but further analysis is needed to select the optimal mechanism. The pivot points of the fixture are located very near the center of gravity of the combined module/lifting fixture. The thick-walled vertical modules weigh 36% more than the horizontals, resulting in locations for the centers of gravity that are 0.75 inch apart.

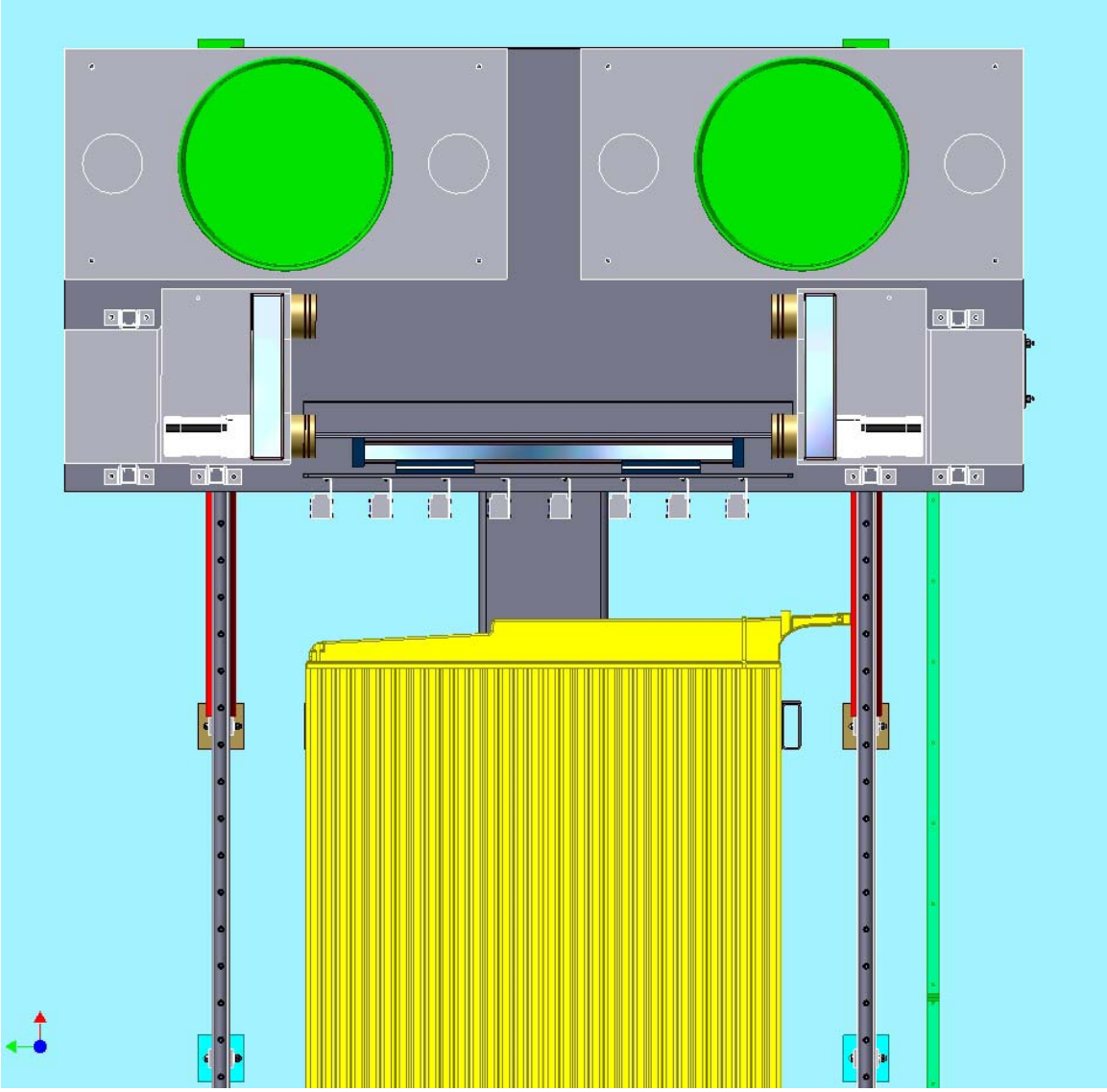

Fig. 17.132(a): Top view of a module (in yellow) mounted in the adhesive dispenser. The module has been rotated and is ready for adhesive deposition. The eight gray squares above the module manifold are the dispensing heads, seen from above.

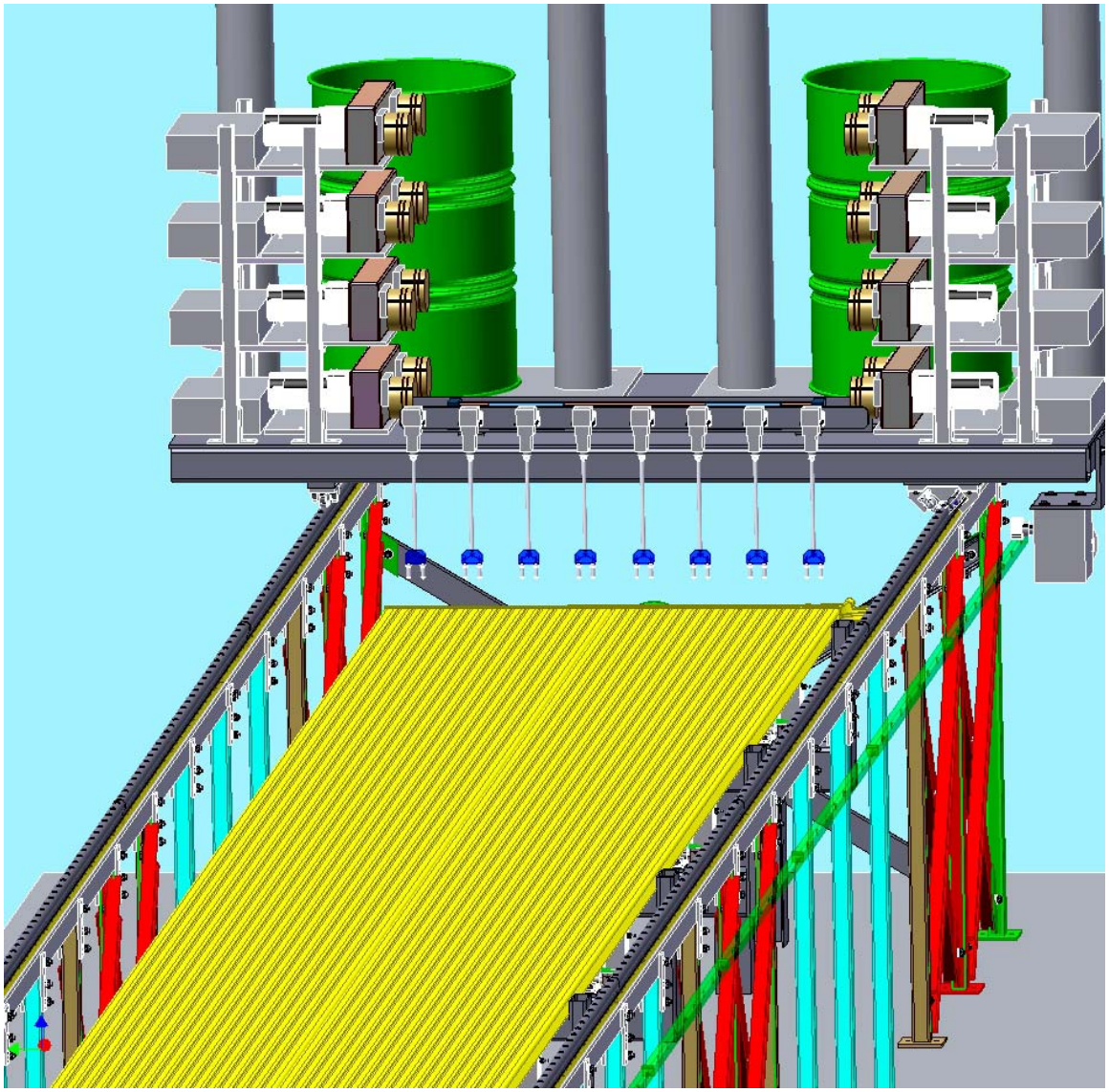

Fig. 17.132(b): Isometric view of a module (in yellow) mounted in the adhesive dispenser. The module has been rotated and is ready for adhesive deposition. Each 55-gallon drum (green barrels) holds one of the two adhesive components. Four adhesive dispensing pumps are shown in front of each 55-gallon drum. Each pump feeds both adhesive components to one of the eight mixing chambers (gray boxes). Each mixing chamber feeds mixed adhesive to two nozzles (below the blue fan-out chambers).

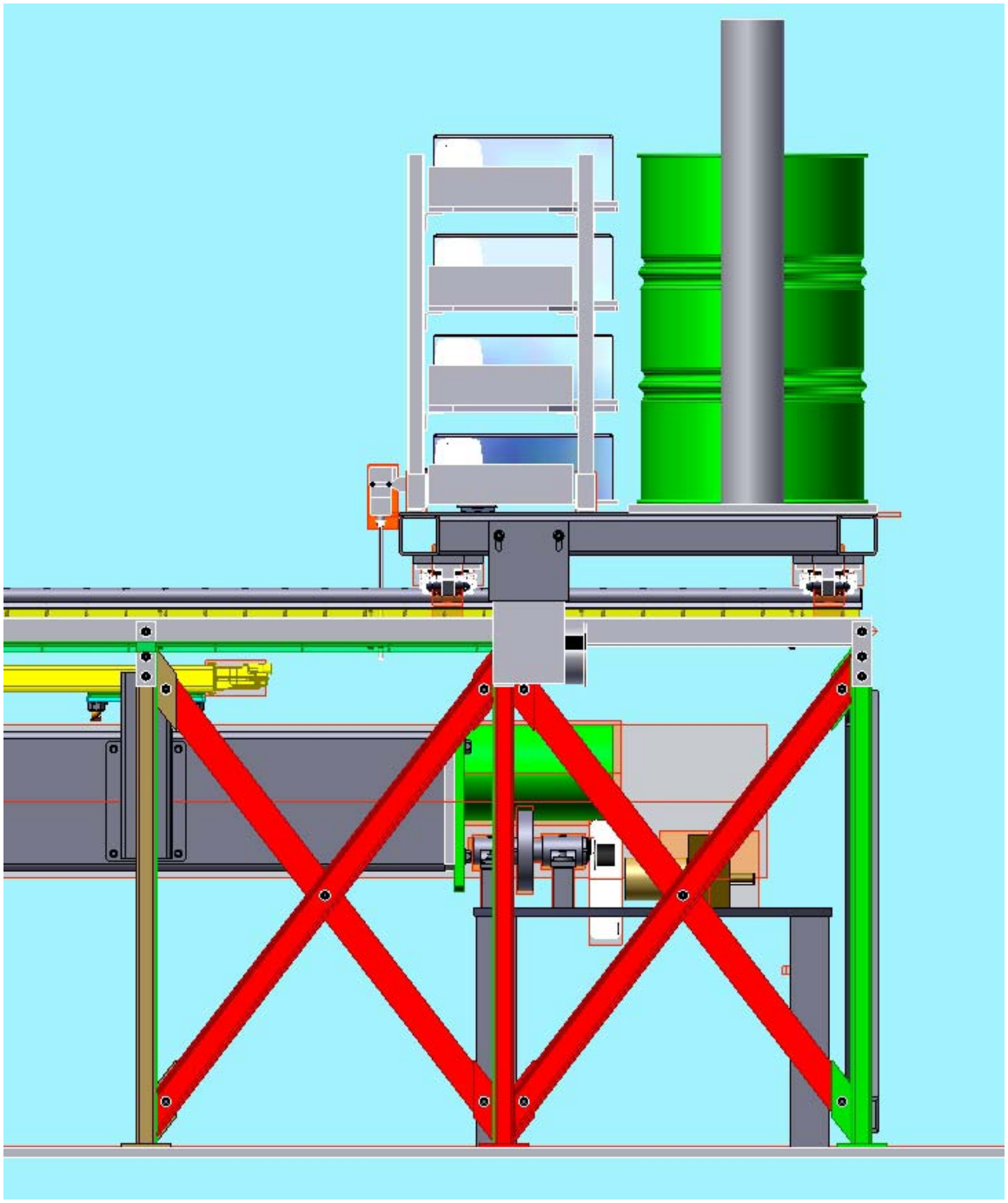

Fig. 17.132(c): Side view of the adhesive dispenser. The module has been rotated and is ready for adhesive deposition. The module (yellow) mounted on a vacuum lifting fixtures is shown edge-on at the middle left. The lifting fixture support pivot (green cylinder) is on the right-hand end of the lifting fixture, underneath the adhesive pumps. The module-rotating mechanism is immediately underneath and to the right of the support pivot.

17.12 Block Pivoter

The block pivoter (NOVA-doc-989) performs several functions during the installation process. First, the pivoter provides a flat surface for block assembly, including alignment fixtures and tooling to ensure that each block meets dimensional requirements. Second, it moves each completed block from the assembly area to the detector face. Third, the pivoter rotates the assembled block from the horizontal to a near vertical orientation and moves it approximately 9 meters to place it in the correct location in the detector. Finally, the pivoter rotates the block the last few degrees into a vertical orientation and then lowers the block and pallet approximately 2 to 3 centimeters onto the floor.

When the detector installation is complete, the block pivoter is permanently installed against the last block to serve as the north bookend.

The requirements for the block pivoter are described in NOVA-doc-113.

17.12.1 Block Pivoter – General Configuration

In Figure 17.133, the block is shown in violet, the block pivoter table is in blue and the structure that supports the pivoter table is shown in orange and purple. The pink structural steel shown above the drive wheels is provided to limit the table deflection when the table is in the horizontal position.

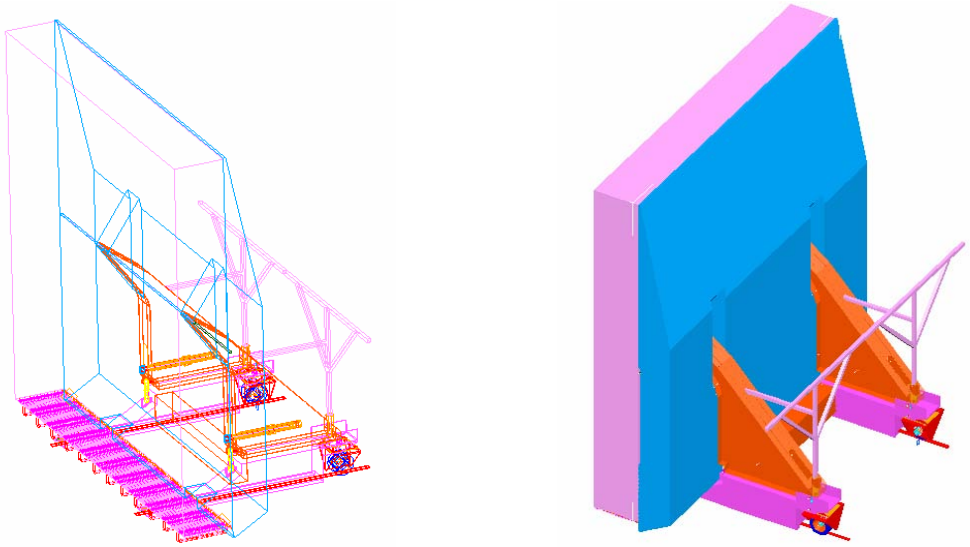

Fig. 17.133: Two isometric views of the block pivoter table shown in the vertical position.

17.12.2 Block Pivoter – Detector Assembly Table

Figure 17.134 shows the detector assembly table as a solid object for the simplicity of rendering the images. However, the detector assembly table will be fabricated from steel plate to provide a flat, relatively rigid surface for assembling the detector on, and at a minimum expense. Figure 17.135 shows an image of the block pivot table as viewed from below to show the plate

structure. The upper surface and each of the webs are made from 0.25-inch thick carbon steel plate. A structural grade material, ASTM A36 low alloy carbon steel, is suitable for this application because the deflections dominate the design criteria and not the overall strength. Higher strength steels will have the same deflection as A36, but will cost more to procure. The lower cord of the weldment is 0.75-inch thick, 12 inch wide A36 bar stock. The open structure allows access to the bottom of the top surface and the webs for welding.

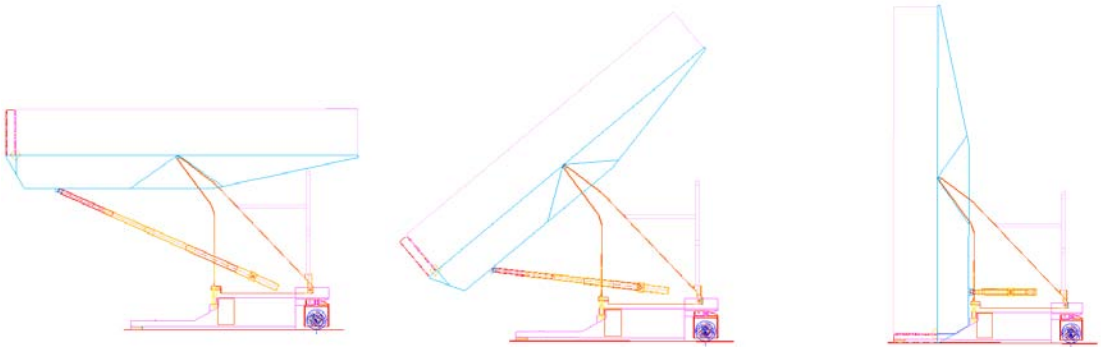

Fig. 17.134: Three side views of the block pivoter showing the block in the horizontal, intermediate, and vertical positions.

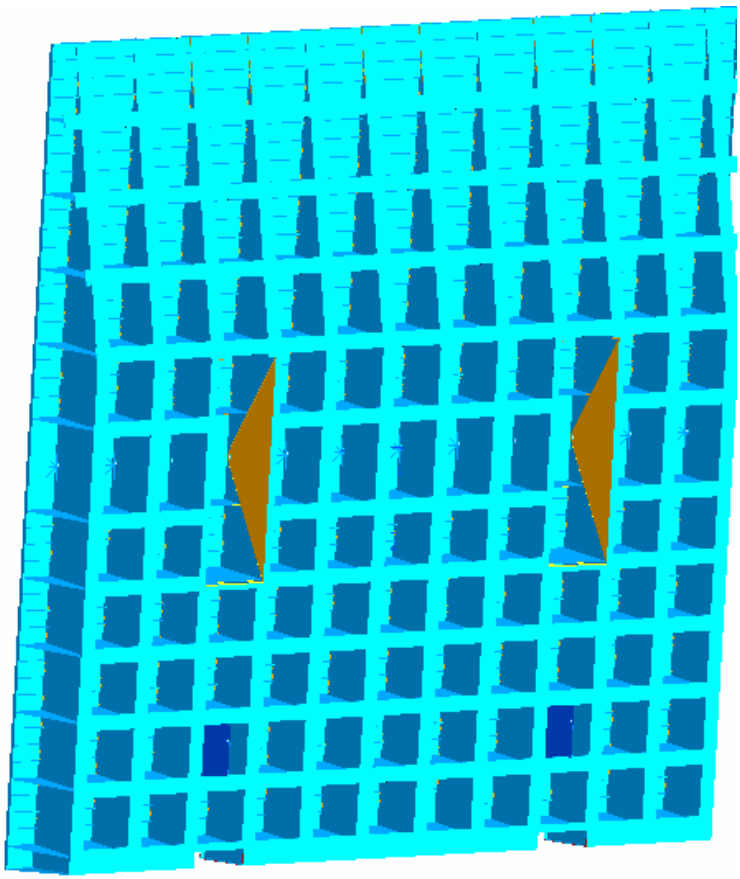

Fig. 17.135: View of the block pivoter table bottom surface when table is near vertical, showing the weldment structure.

In Figure 17.135, the two rectangular areas shown with the orange triangles are the locations where the arms of the upper vertical side supports fit into the table to allow the pivot location to be near to the top (when table is horizontal) surface. The two small cut-outs near the bottom edge are provided to allow clearance for the lower table support arms that allow rolling elements to be positioned under the assembled block for stability.

The top surface of the assembly table, when the table is horizontal, is 620 inches wide. When the able is vertical, it is 640 inches tall. Clearly, this exceeds the normal shipping dimensions, so the table will be made from 12 sections. Figure 17.136 depicts the table in a exploded view to show these sections. Two sections will be joined in the shop into an assembly approximately 104 inches wide, 60 inches tall, and 53.3 feet long. Weight of each two section assembly will be less than 20,000 pounds. Six truck loads will be required to transport the table sections to the far detector site.

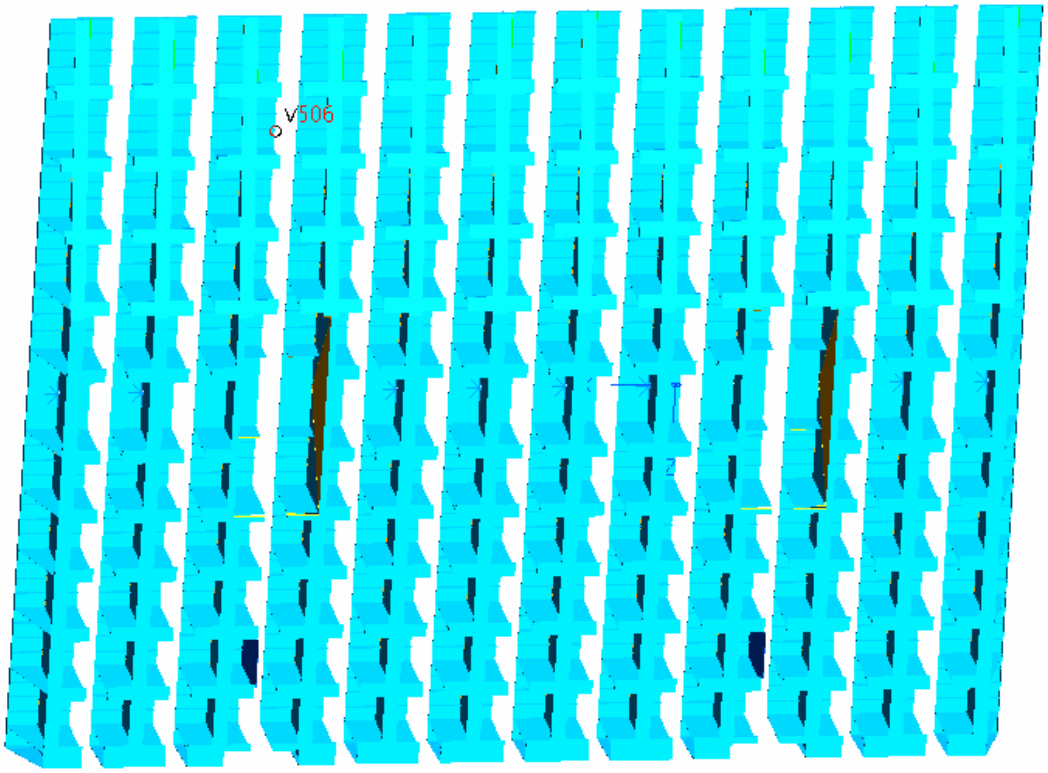

Fig. 17.136: Exploded view of the block pivoter table, showing the individual weldments.

Each of the weldment sections shown in Figure 17.136 is shop fabricated using the same techniques used to fabricate bridge girders used in highway overpass construction. This is a mature technology using standard welding practices and common low alloy carbon steel. The cost estimate for this table includes line item costs for the welding fixtures needed to achieve the required flatness of each weldment. FEA modeling of one weldment, described in NOVA-doc-2308 and 2328, has been performed and the deflections are shown in Figure 17.137. This analysis was performed using symmetric boundary conditions and a uniform pressure applied to the top surface of the detector of 0.82 psi. This pressure is the pressure that would be uniformly applied to the top surface of the table by the fully assembled detector block assuming that the PVC block has no stiffness. As such, this is a very conservative loading condition and over predicts the deflection and stresses on the table.

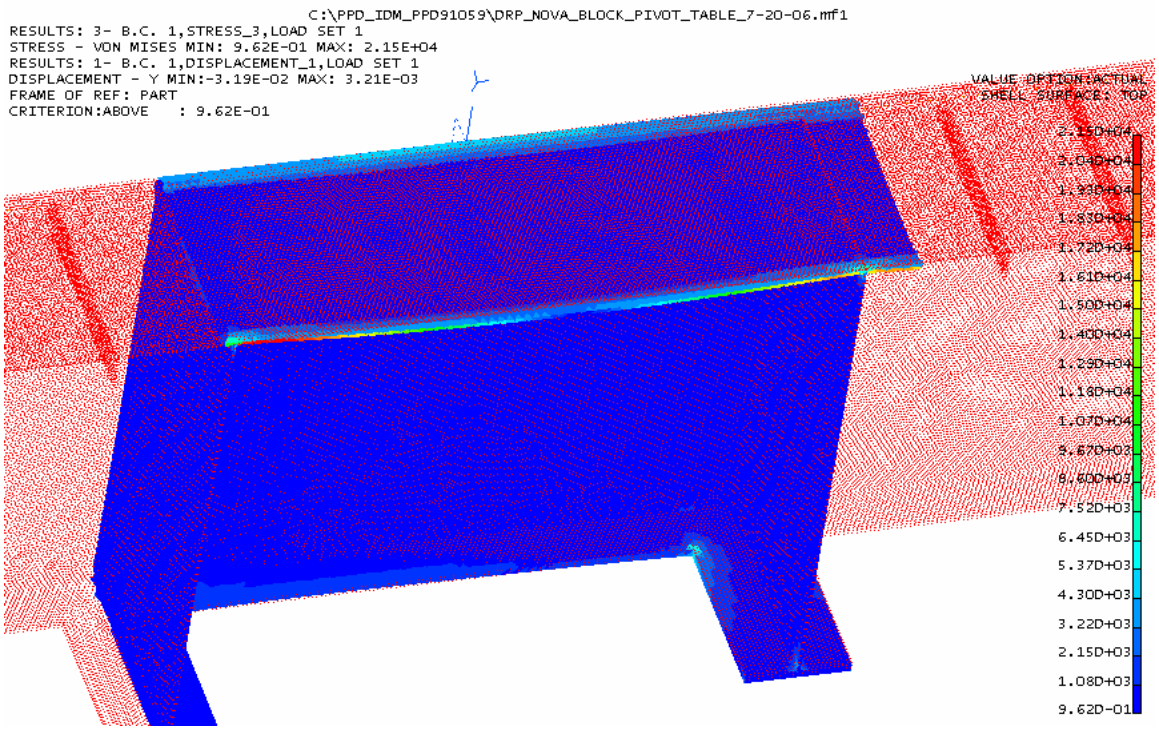

Fig. 17.137: FEA deflection results for loading on one weldment of the block pivoter table.

17.12.3 Block Pivoter – Pivoting Hydraulics

Figures 17.134 and 17.138 show the hydraulic cylinders used to push the pivoter table into the horizontal position. These cylinders retract to allow the table to pivot into the vertical position. Figure 17.138 shows that the pivot bearing is positioned very close to the top (when horizontal) of the assembly table.

There are several important considerations in the overall layout of the block pivoter:

- To provide a moving structure that is inherently stable and not prone to tipping.
- To place the pivot location as close as is possible to the center of gravity of the assembled block and table to reduce the loading during rotation.
- To shop fabricate the block pivoter components, preassemble and test the pivoter, partially disassemble the device and ship the components to the far detector location using commercial trucking. All components are designed to break down into parts that are easily shipped and are within the lifting capacity of the crane at the far detector.

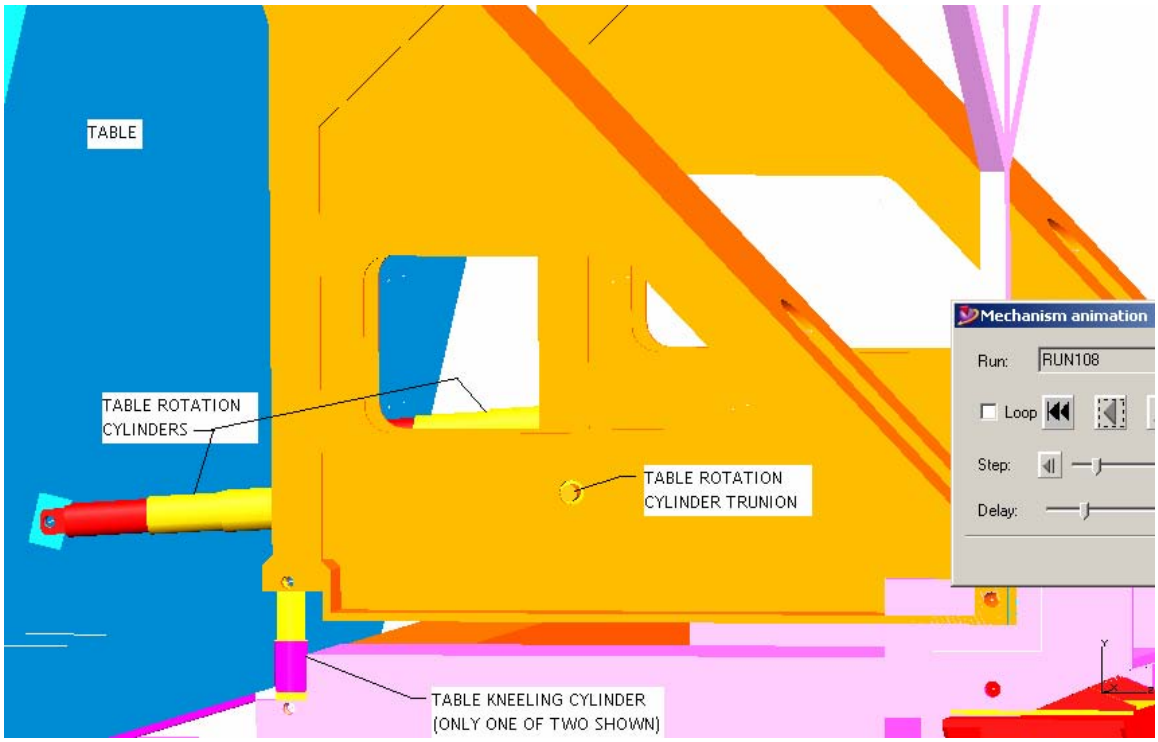

Fig. 17.138: Detail of the block pivoter showing the table approaching vertical, highlighting the table rotation cylinders and one table kneeling cylinder.

Stability of the block pivoter structure is maximized in several ways. First, the structural support (shown in purple in the Figures 17.133 and 17.134) is extended forward to the front side of the block (when the block is vertical) to maximize the wheel base and therefore the stability. Second, the maximum velocity of the pivoter is limited so that even if the loaded table were to stop immediately while moving at maximum velocity, the pivoter would not tip.

Two multistage, double acting, hydraulic cylinders control the rotation of the block pivoter table. These cylinders are commercially produced by several manufacturers and are available in strokes and capacities in excess of those needed for this application. The compressive load is shown as a function of cylinder extension in Figure 17.139.

When the block is fully assembled on the table and the table is horizontal, the cylinders exert a combined axial force of 25 tons. As hydraulic fluid is allowed to exit the cylinders and the table rotates, the axial force peaks at about 31 tons (15.5 tons per cylinder), returning to a combined value of 25 tons when the table is fully vertical. This is shown as the magenta line at the top of Figure 17.139.

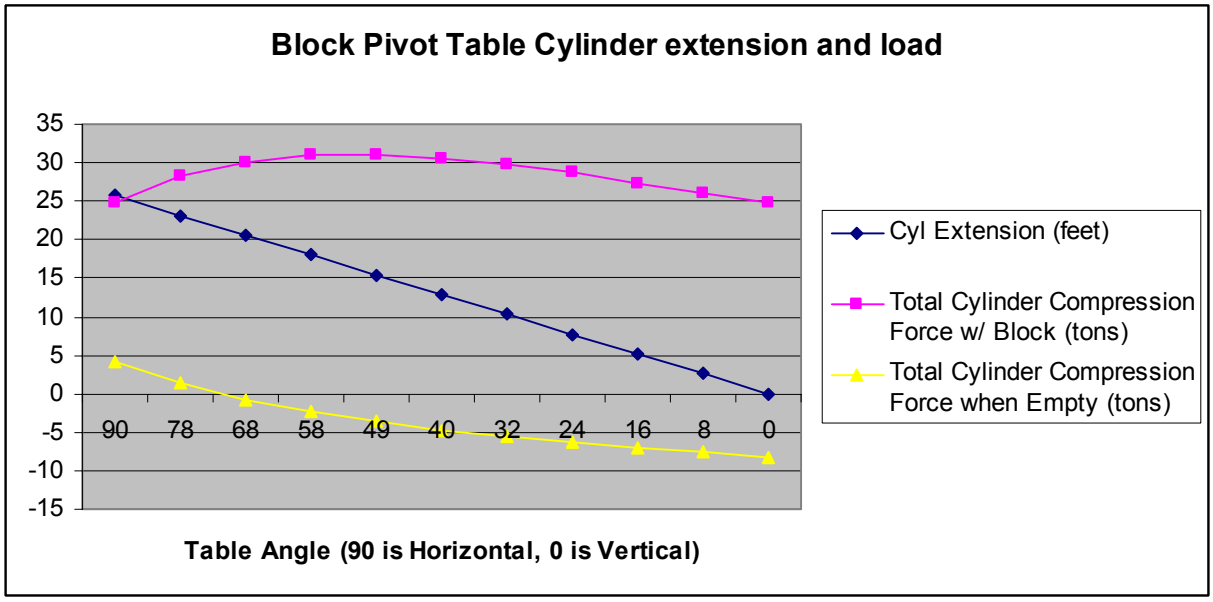

Fig. 17.139: Hydraulic cylinder extension (feet) and compressive load (tons) for the pivoter design using two cylinders and a pivot location near the block center of gravity.

As the block is lowered onto the concrete detector hall floor, the load on the hydraulic cylinders changes sign to become a tensile load. When the table is vertical and unloaded, the combined axial load on the cylinders is 8.3 tons in tension. This is why double acting cylinders are necessary. As fluid is pumped into the cylinders to allow the table to rotate to the horizontal position, the load steadily increases until reaching a maximum value of about 5 tons compression. As each module is positioned during block assembly, the load on the pivoter table rotation cylinders increases until it reaches 25 tons with the block fully assembled.

Figure 17.138 shows a detail of block pivoter table hydraulics with the key components labeled. The table is shown in the near vertical orientation and both of the table rotation cylinders can be seen, although the second cylinder is partially obscured by the orange table support structure. Also visible is one of the two kneeling cylinders that lower the entire table and block as the block is set down on the detector hall floor.

When the block is rotated to the vertical position, its weight is supported by the block base pallet, which is cantilevered from the block pivoter table surface. The pallet is shown in Figure 17.140 and described in NOVA-doc-2622. Each block has its own dedicated pallet that remains with the block after installation. The gaps below the pallet surface provide space for the pivoter's front support legs (Figure 17.133). They also serve as witness spaces so that any scintillator leaks from the modules can be observed and perhaps located. Irregularities in the detector hall floor are accommodated by setting each pallet in place on a grout bed as described in Section 17.12.5.

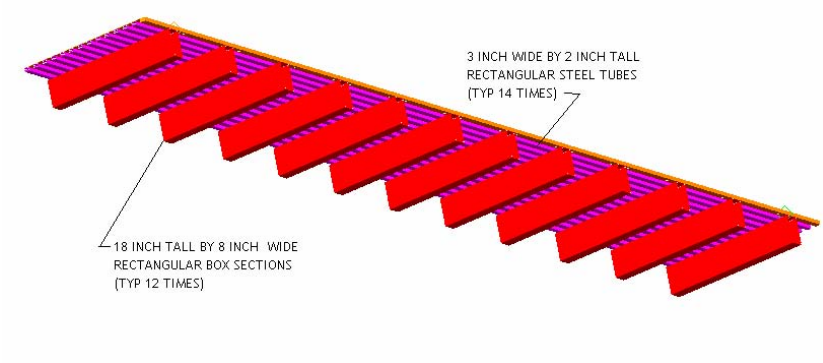

Fig. 17.140: Bottom view of a pallet with twelve 18-inch deep by 8-inch wide box beam cantilever members and fourteen 3-inch by 2-inch transverse stringers.

17.12.4 Block Pivoter – Propulsion Drive

Figure 17.141 shows the mechanism used to move the pivoter along the hall from the assembly area to the detector face. Hydraulic motors driving a planetary gear drive, directly attached to a solid urethane wheel, provide the traction effort to move the loaded block pivoter down the length of the detector hall. These commercially produced drive units are similar to those used on large earth moving equipment. The chief advantage of these units is that they can propel very heavy loads at steady but slow speeds. The disadvantage of these units is that the lead time to procure them is on the order of twelve months. Spare parts are available off the shelf because of the demands of the construction industry. Two units are used, one driving each side of the pivoter.

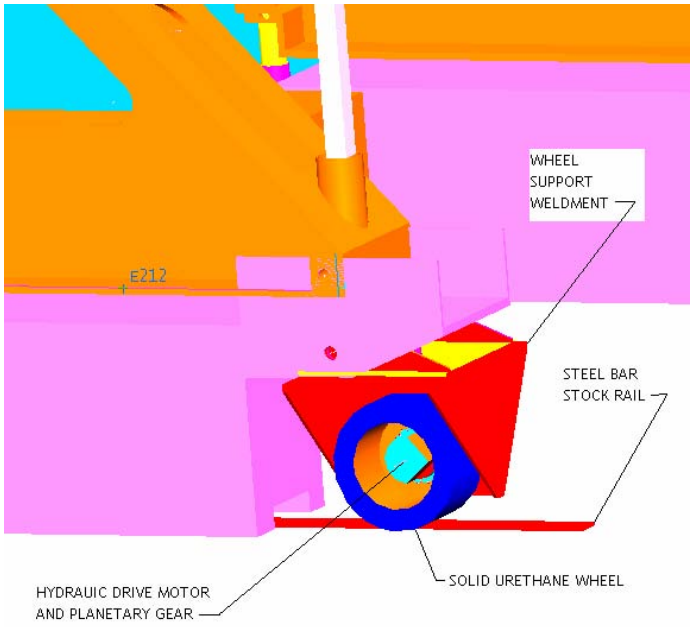

Fig: 17.141: Detail of block pivoter drive wheel mounting and hydraulic drive motor.

The pivoter moves on Hilman rollers for the non-driven rolling elements. These rollers include cam followers to allow the pivoter to follow the flat bar-stock rails. Hilman rollers are available in capacities above 300 tons, although 100-ton capacity units are used here. On each

lower side support, one roller is located at the tip of the extension of the lower side support. For stability reasons a second roller is located directly below the kneeling cylinder.

17.12.5 Block Pivoter – Block Base Pallet

Each detector block rests on a block base pallet (Figure 17.140 and NOVA-doc-2622) when installed in its final location in the detector hall. Prior to stacking the modules for each block, the pallet will be located in its final position on the detector hall floor, grouted to accommodate irregularities between the detector hall floor and the steel pallet weldment. Once the grout has cured, the pallet will be lifted off the grout with the block pivoter. The pivoter is then rotated to the horizontal position, taking the pallet to the vertical position, and moved to the detector assembly area.

Cantilevering the pallet from the block pivoter table introduces a moment into the table, causing a rotation. This rotation over the width of the pallet and the deflection of the pallet (cantilevered beam deflection) have been quantified and shown to induce an acceptable level of stress into the PVC extrusion modules in a block (NOVA-doc-1953). Figure 17.142 shows the result of a finite element analysis of the combined table and cantilevered pallet. Beam elements were used to model a 72-inch deep table and twelve 18-inch deep pallet members. Since twelve pallet members were used, the load applied to each member was 313,000 / 12 pounds (26,100 pounds). The calculation applies this load at a point in the center of the cantilevered pallet and assumes that the block has no stiffness. This conservative assumption gives an upper limit on the tip deflection.

In Figure 17.142, the dashed magenta line represents the deformed shape of the table and cantilevered pallet. The green lines indicate the original shape while the orange line segments indicate the beam elements. (The red dimension lines are artifacts remaining from the geometry creation.) Note that the deflection of the vertical magenta line representing the table is nearly indistinguishable from the original geometry.

This result indicates that the block pivoter design, with very deep members for the table and a pallet supported by 18-inch deep tubes, meets the block deflection criteria established to prevent damage to the vertical module end seals during block rotation (NOVA-doc-1860).

The 3 inch by 2 inch box sections between the 18-inch deep members also deflect when loaded by the detector weight. Figure 17.143 shows the deflection for the empty-block case under the assumption that the detector has no stiffness. The deflection is calculated to be 0.028 inches by the FEA and 0.024 inches using hand methods. While this deflection may be acceptable for the empty condition, the estimated maximum weight of a filled block is 1.2 million pounds. This gives a linear loading of 137 pounds per inch. Resulting stresses would be about 13 ksi and deflections would approach 0.1 inch.

NOVA-doc-2336 describes a full FEA calculation of the stresses on a bottom end seal of a filled extrusion module supported by a block base pallet. Maximum stresses in the end seal and its adhesive bond to the PVC extrusion are similar to those in other parts of a filled block. Calculations using a variety of boundary conditions give safety factors between 3.4 and 5.0 against failure of the end-seal bond.

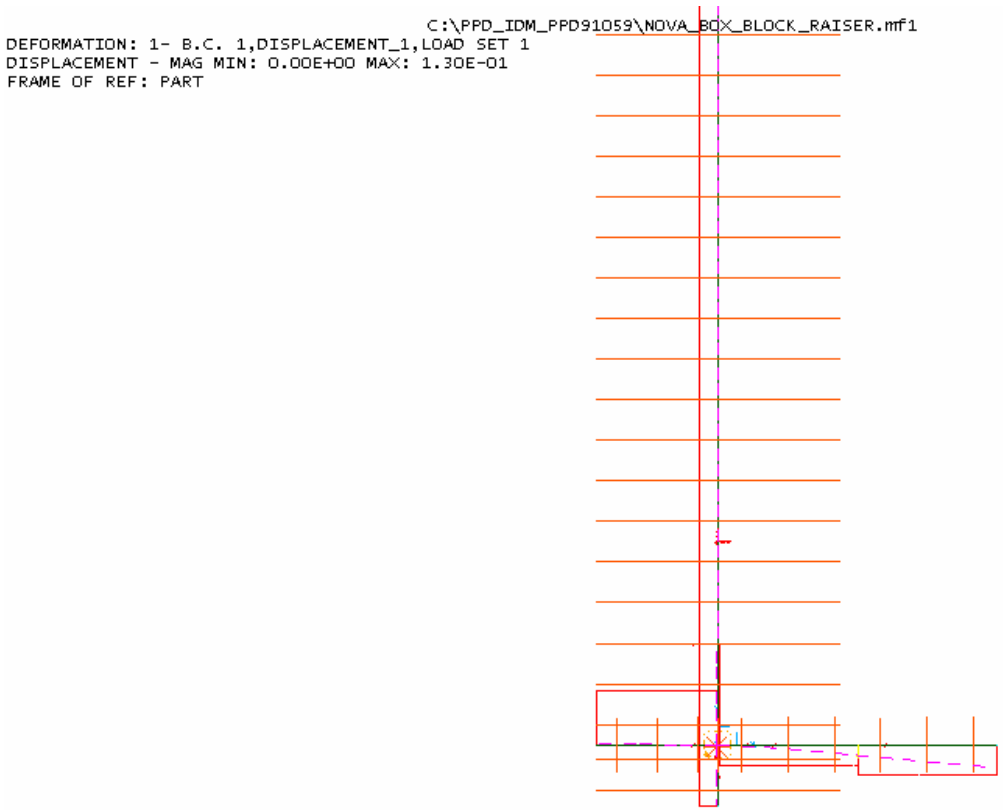

Fig. 17.142: Results of the FEA calculation of the deflection of a plate structure block pivoter table and cantilevered pallet. The deflection at the edge of the pallet is 0.13 inches.

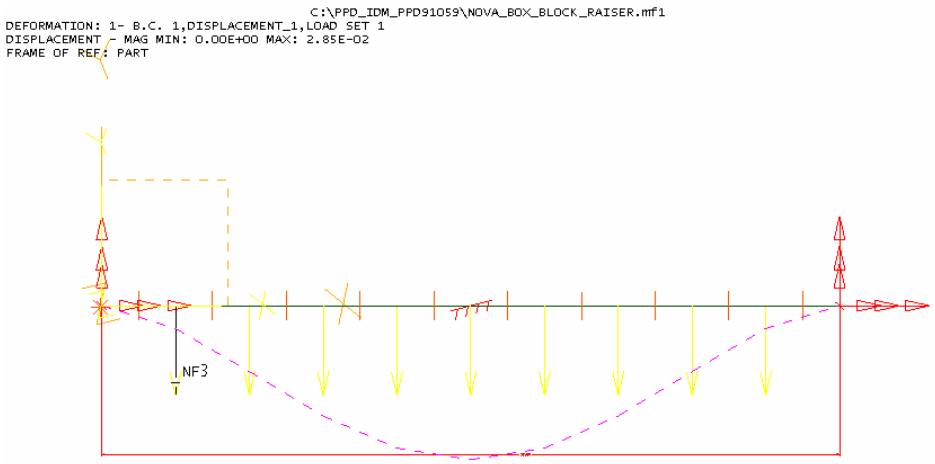

Fig. 17.143: Deflection of the transverse 3 inch by 2 inch stringer between each 18 by 8 inch box beam on the pallet due to a uniform 36 pounds per linear inch load. The total deflection is 0.028 inches.

17.12.6 Block Pivoter – Upper Table Support Weldment

The upper structural support (Figure 17.144) has been analyzed using Ideas and the results are shown as a screen-capture image in Figure 17.145. There are two upper side support members which transfer the weight of the table and the assembled block to the lower side support members. A 300,000 pound vertical load was applied to the table pivot bearing and vertical restraints were applied at the kneeling cylinder and rear cylindrical bearing. This 300,000 pound load is a conservative estimate of the combined table (150,000 pounds) and block weight (313,000 pounds) shared between two upper side supports. Stresses in the side support are less than 10,000 psi and the deflection at the bearing is approximately 0.2 inches. This weldment weighs about 32,000 pounds so it is shipped in sections that can be moved by one of the 10-ton bridge cranes in the far detector hall. The stresses and the deflections for a conservatively estimated load are acceptable.

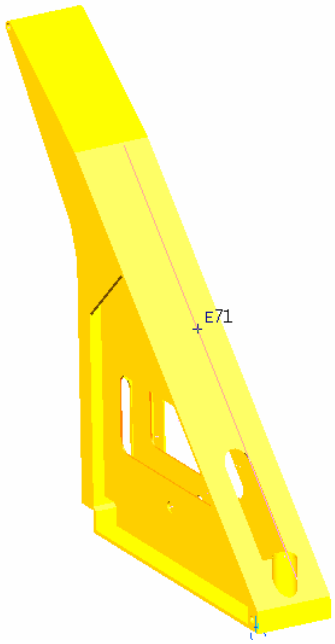

Fig. 17.144: Block pivoter upper side support weldment as viewed from the rear quarter.

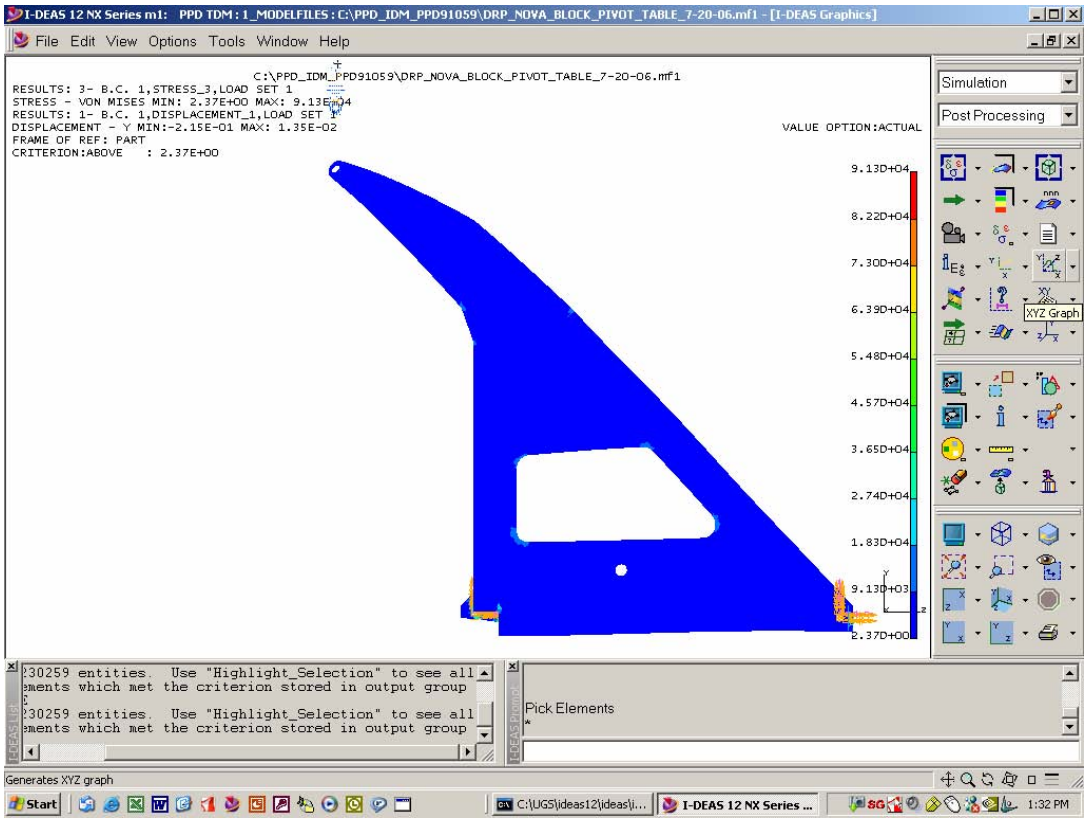

Fig. 17.145: Analysis image of the upper side support stresses and deflection.

17.12.7 Block Pivoter – Lower Table Support Weldment

The lower structural support is shown in Figure 17.146. This part transfers load from the upper structural support to the Hilman rollers and the hydraulic drive unit. The narrow portion shown in the lower left corner of Figure 17.143 extends below the table and pallet to ensure the stability of the entire loaded block pivoter.

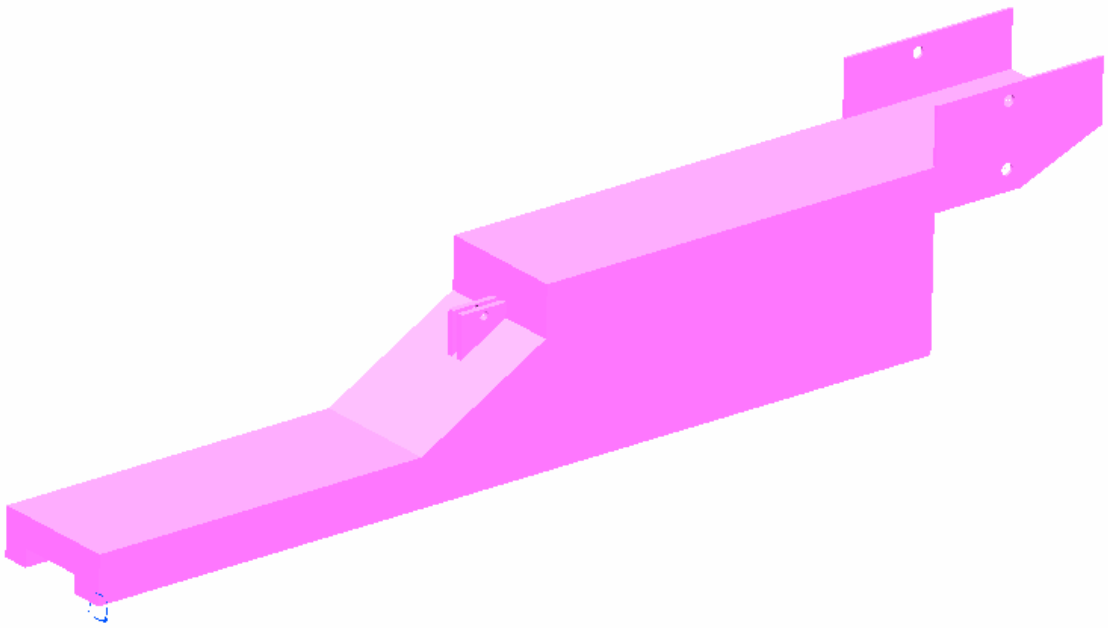

Fig. 17.146: Block pivoter lower structural support.

Figure 17.147 show the results of an FEA analysis of the lower structural support. This analysis was performed using a half section of the part and applying symmetric boundary conditions. The results indicate that the high stress region corresponds to where the kneeling jack applies its load while the bulk of the structure is very lightly stressed and the deflections are minimal. Each of the two lower structural supports currently weighs about 16,000 pounds (8 tons). Results of the analysis indicate that some of this weight can be removed by making the sections thinner, saving cost. However, optimizing the lower structural support is not an urgent design task as the design presented here works satisfactorily and meets the shipping and installation requirements.

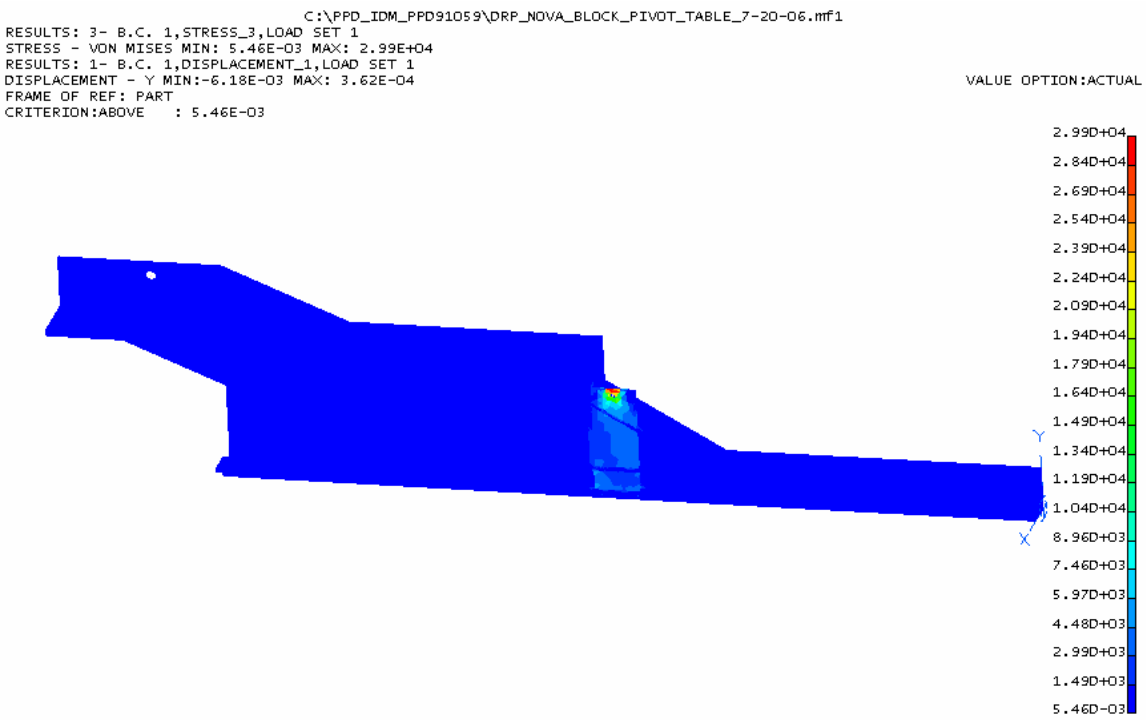

Fig. 17.147: Analysis image of the lower side support stresses and deflection.

17.12.8 Block Pivoter – Rear Table Support

The deflection of the detector assembly table can be minimized during the detector assembly by supporting the back end of the table when it is in the horizontal position. A simple structure provides this support and is shown in Figures 17.133, 17.134 and 17.148. This structure is fabricated from ordinary steel box sections ASTM A500 material and serves to limit the table bulk deflection changes while a block is being fabricated.

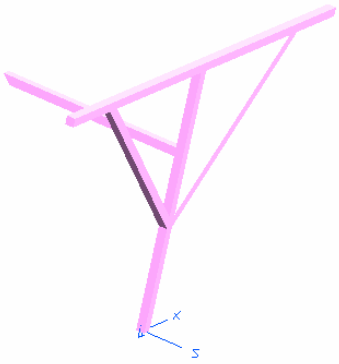

Fig. 17.148: Image of the rear table support.

17.12.9 Block Pivoter – Parameter Summary

Table 17.23 summarizes the most important parameters of the block pivoter.

PVC Extrusion Block Weight (estimated based on nominal extrusion)	313,000 pounds
Pivot Table Weight (estimated)	150,000 pounds
Depth of Pivot Table	6 feet
Distance from Table Surface to Pivot centerline	4 inches
Vertical Distance from Pivot to Cylinder Centerline (table vertical)	216 inches
Vertical Distance from Assembly Table top to Floor (table horizontal)	317 inches
Maximum Vertical Distance from Floor to top corner of 31 plane block (at nominal dimensions) when pivoting	651 inches
Lower Structural Support Weight (per unit – two units used), estimated	30,000 pounds
Upper Structural Support Weight (per unit – two units used), initial design, not final.	32,000 pounds
Pivot Bearing Size and Type	4” Plain Spherical
Pivot Bearing Capacities (static and dynamic), pounds, each	533,000 static, 173,000 dynamic
Number of Pivot Bearings Used	4
Forward Roller Capacity, metric tons	100 metric tons
Forward Roller Load, tons (estimated)	96 short tons
Pallet Weight (estimated)	10,000 pounds
Depth of Pallet	20 inches
Deflection of Pallet between18” by 8” members with empty block	0.028 inches
Deflection of Pallet between 18” by 8” members with full block	0.1 inches
Deflection of Pallet Cantilever with empty block	0.13 inches
Hydraulic Cylinder closed Length	76 inches
Hydraulic Cylinder Length when Table is Horizontal	309.02 inches
Kneeling Cylinder Load (with block on table), estimated	180 tons
Kneeling Cylinder Load (without block), estimated	70 tons

Table 17.23: Summary of block pivoter parameters.

17.13 Detector Assembly Sequence

17.13.1 Overview of the Detector Assembly Process

The installation task (NOVA-doc-2494) begins with beneficial occupancy of the far detector building and the hiring of that assembly crew administrative staff (the Detector Assembly Manager, the Assistant Detector Assembly Manager and a half-time Administrative Assistant). During an initial ~11 week “preparatory” period, this staff oversees civil construction “checklist” work, plans upcoming installation tasks in detail and interviews assembly crew job candidates. They also make preparations to hire and train the first assembly crew members.

The preparatory period is followed by a 12-week “setup” period, which is devoted to installing and commissioning installation equipment, including the block pivoter, the adhesive dispenser and the south bookend. The first four assembly crew workers are hired at the beginning

of this period. The on-site assembly crew size increases from four to fourteen workers during the setup period. The schedule includes time for training crew leaders and other workers after they are hired. The setup period is followed by a 15-week "startup" period, during which the first three detector blocks are built and installed. The startup period begins with safety tests of installation equipment and the review and approval of materials handling and block assembly procedures. During this period, physicist and engineer "experts" from WBS 2.2, 2.5, 2.6 and 2.7 assist in training the local assembly crew technicians. The crew size ramps up to 26 workers (plus the administrative staff) and the work schedule changes from one to two 8-hour shifts/day, five days/week during this time. The startup period is followed by 73 weeks of full-rate installation, with a full crew of 26 workers. During the full-rate period, all but the last two blocks are installed, with a new block completed every 2.6 weeks.

Two types of 31-plane blocks are used to construct a superblock. A blocks start and end with vertical module planes and B blocks start and end with horizontal module planes. There are no gaps between blocks within a superblock, but there is a 2-cm expansion gap between superblocks to prevent superblocks from touching after filling with liquid scintillator.

Electronics installation begins on each pair of blocks as soon as the second block of the pair is installed. With the exception of the vertical module electronics boxes, all electronics, chilled water and vapor return systems are installed before filling begins. Vertical module electronics boxes are installed only after a block has been completely filled. The filling of a superblock with liquid scintillator (NOVA-doc-1118 and 2510) begins as soon as the last block in the superblock is installed.

The full-rate period is followed by a 10-week ramp-down period, during which the last two blocks are installed and crew size is reduced to 14 workers. During a final 14-week period, the north bookend is installed and the remaining blocks are filled and outfitted with electronics. By the end of this period, the crew size has been reduced to three workers and the administrative staff. After the detector installation is complete, these people will join the operations crew that operates and maintains the detector during data taking.

The assembly crew installs blocks and readout hardware but WBS 2.6/2.7 engineers and collaboration physicists perform the initial turn-on and commissioning of the electronics and DAQ systems. Data taking with cosmic-ray and neutrino beam events begins as soon as the first block is commissioned. An operations crew (not part of WBS 2.9) operates the completed sections of the detector and is also responsible for building and site maintenance during detector installation. The first two superblocks (~5 kilotons) will be reading out approximately 16 months after the start of the installation setup period. A new superblock is completed every 3 months. The total detector installation time is 124 weeks or about 2.5 years.

During the full-rate detector assembly period the local assembly crew consists of: the following workers (in addition to the 2.5 person administrative staff):

- 4 crew bosses: supervise work crews and fill in for absent crew members
- 4 heavy equipment operators: operate the two bridge cranes and block pivoter
- 2 glue technicians: operate the adhesive dispenser
- 4 module technicians: feed modules to adhesive dispenser, move them to the block pivoter
- 8 block pivoter technicians: assemble modules into blocks
- 4 scintillator/outfitting technicians: install front-end electronics infrastructure, DAQ hardware; receive and test liquid scintillator, fill modules

An operations crew, hired under the Cooperative Agreement to maintain the building and site infrastructure and (eventually) to operate the detector, increases from two to five workers during the detector assembly period. The operations crew is not included in the WBS 2.9 task.

Section 17.16 describes the tasks performed by assembly crew members in detail.

17.13.2 Quality Control and Assurance

Quality control and assurance activities for the far detector include the checkout of detector components as they are delivered, block assembly, block erection, scintillator filling, installation of readout hardware and the commissioning of the detector.

Experts from other Level 2 tasks develop and document procedures to verify that delivered components, e.g., scintillator, modules and readout hardware, have not been damaged in transit. They also train assembly crewmembers to perform these tests, which eventually become routine. WBS 2.9 engineers develop and document procedures for testing critical commercial products to verify that they meet specifications: (1) the block assembly adhesive – NOVA-doc-2341, (2) the epoxy grout filler for the bottoms of blocks – NOVA-doc-2456, (3) the block base pallets – NOVA-doc-2455, (4) the block base pallet grout – NOVA-doc-2455 and (5) the horizontal module expansion tanks – NOVA-doc-2509. In addition, WBS 2.9 engineers develop and document procedures for applying and testing adhesive properties (as described in NOVA-doc-2341) during the block assembly process itself to ensure that the expected structural properties and overall mechanical stability of the detector are achieved.

The far detector assembly crew performs routine testing and maintenance of critical equipment, e.g., the block pivoter, adhesive dispenser and moving equipment, to ensure that they are operating properly. This includes testing each shipment of 55 gallon drums of Devcon 60 adhesive immediately after arrival. The crew administrative staff develops and documents operating procedures for this equipment and ensures that operators are properly trained in its use.

PVC modules are assembled and fully tested at remote module factories before the completed modules are shipped to the far detector hall. The modules are inspected at the far detector site to ensure that they have not been damaged in transport. The leak test described in Chapter 13 is repeated at the far detector site, before modules are assembled into planes, to ensure that there are no leaks. Filling the extrusion modules with liquid scintillator and verifying that they do not leak during filling is also a WBS 2.9 responsibility. The crew ensures that the liquid scintillator passes tests for attenuation length and light output before it is put into the detector, and also maintains a database that records the origin and history of the scintillator in every module. In the unlikely event that a module is found to leak while it is being filled, the filling will immediately stop. The module will be examined and a decision will be made to repair the module in-situ or to leave the module unfilled.

Alignment fixtures attached to the block pivoter assembly table ensure the accurate positioning of extrusion modules within each block during assembly (NOVA-doc-1396). This ensures that the weight of each block is uniformly supported on the bottom end seals of the vertical modules and also that the block is properly aligned to its neighbors and will fit within the available space. A positioning accuracy of about 1 cm is expected to be adequate to meet both of these requirements. Transverse alignment of cells is not critical for the physics performance of the far detector, which is essentially a tracking calorimeter. The transverse cell size is ~4 cm, so the required accuracy is about 4 cm/$\sqrt{12}$, or again about 1 cm. Multiple scattering arguments and the transverse size of the electron showers that propagate through the detector lead to similar conclusions. The plane assembly process works to achieve this accuracy over the full 15.5 m length. Tooling, fixtures and procedures are developed to achieve this goal. The same scale of accuracy is required between adjacent 31-plane blocks. The block pivoter is designed to satisfy this requirement. Care is also taken to ensure that each 31-plane block is erected square and plumb, and that it maintains a vertical detector face. Spacers between 31-plane blocks may be required to accomplish this.

Readout system cables, power distribution and water lines for cooling the far detector electronics are installed by the far detector installation team, which is responsible for ensuring that they operate properly and that water lines do not leak. The installation team is also

responsible for making the detector light tight and for initial checkout of module readout hardware after being trained by WBS 2.6 and 2.7 experts.

17.13.3 Detector Component Delivery

As a general rule, delivery is on a just-in-time basis because on-site storage is limited. Stores of all of the critical detector components are located within one day's travel of the Ash River site and larger stores are readily available from more distant suppliers. Scintillator oil is delivered in 6500-gallon tanker trucks to a canopy-covered area. There is room for as many as four tankers under the canopy. The scintillator transfer facility is equipped with cooling and heating capabilities to maintain scintillator oil close to 70º F. The scintillator in each arriving tanker undergoes quality assurance testing and is then pumped through the scintillator supply system into the detector modules.

Figure 17.127 shows the 24-ft by 70-ft foot storage and shop area which contains a work shop and inside storage for detector components other than modules. Some items that are not affected by temperature will be stored outside of the building in temporary trailers. The list below describes the most important detector components (other than modules and scintillator).

- **Block Base Pallet**

The block pallets (Figure 17.140) come in two types, for A-type and B-type blocks. Since each pallet weighs approximately 10,000 lbs, only four of them can be shipped on a flatbed trailer. The trailer is moved directly below the norht bridge crane, which picks it by lifting clevises attached to the top edge of the pallet. The trailer is stored outside and covered with tarps. It is moved into position the day before it is needed to bring the steel to building temperature.

- **Module Adhesive**

The module adhesive, Devcon 60, is shipped in 55-gallon drums. It is stored in a spill containment area at 55-75° F (to maintain maximum shelf life). Ventilation systems at the adhesive dispenser and block pivoter remove the MMA vapor released by Devcon 60 (Section 17.7.1 and NOVA-doc-1347). Usage is estimated at 33 gallons/plane so the consumption will be close to 500 gallons/week (which is also the manufacturer's batch size). The manufacturer performs strength tests on each batch of adhesive and also provides material, process, and strength QC data sheets to certify that the correct mixture and process was used to produce each batch. These tests will be repeated at Ash River before use. Section 17.13.2 and NOVA-doc-2341 provide more details. Eighteen to twenty 55-gallon drums are delivered every two weeks.

- **Filler Grout**

The pourable grout filler is also a Devcon product. It is delivered in 3.1-gallon buckets and is manufactured in batch sizes similar to those for Devcon 60 adhesive. Quality control is described in Section 17.13.2. Approximately 150 gallons are needed for each block so shipments of approximately 50 buckets will be needed every two weeks.

- **Consumables**

Consumables for block construction include mixing nozzles for the adhesive dispenser, mixing supplies, cleaning supplies and other small components, requiring approximately 50 sq. feet of storage space on shelving. Foam spacers used to fill the spaces under the bottom horizontal modules are also stored on shelves. The storage area is shown in Figure 17.127.

- **Electronics**
    - **Relay Racks and Chiller Units**

      Electronics are installed in two block segments and each requires a full-sized relay rack and a chiller unit. To minimize shipping costs, a large number of these will be shipped at once and placed on the upper level walkway after delivery.

- **Cable Trays**

  There are 14,440 linear feet of cable trays. The trays come in 10 foot lengths. On the sides these are supported by steel tubing or Unistrut. Since they cannot be installed prior to the block installation, they are stored in 10 ft by 4 ft racks until needed.
- **Plumbing**

  Chilled water manifolds and plumbing runs are stored in stacks since they are shipped in long boxes. These are made and tested off-site. At the Ash River site, they can be stored outside in an unheated/non-air-conditioned van.
- **Wiring Harnesses**

  Wiring harnesses are shipped in stackable boxes. Since they are pre-made and labeled off-site, the number in storage is kept to a minimum.

- **Module Units**

Module units are packaged in groups of either 24 horizontal modules or 24 vertical modules. Module units are pulled out of the trucks using an air caster system as described NOVA-doc-2011. Each module unit is packaged with a wood and foam module snout protector, wrapped in plastic and strapped to a "Super Pallet". The packaging is removed and modules are tested for leaks and fiber continuity. The fully automated tests require two assembly crew technicians to make all the connections. The 24-module test must run overnight and the test is recorded at the start of the next day. An average of six module units will be delivered to Ash River each week. NOVA-doc-2494 describes these procedures in more detail.

Module units use six 4-ft by 8-ft sheets of 1-inch rigid foam between modules to protect the manifolds. As each module is moved to the adhesive dispenser, the foam is hand carried and placed on the return pallet. Each return pallet holds three module units worth of packing material and is shipped back to the module factory in Minneapolis. Details on return pallets can be found in NOVA-doc-1433.

17.13.4 Block Assembly Process

Module installation in a block is described in detail in NOVA-doc-2494. This process requires the coordination of three independent teams of technicians, one at the adhesive dispenser, one to move modules and a third to install modules at the block pivoter. The two crew bosses direct the work of the three teams and stand in for workers who are sick or on vacation. Since the working lifetime of the Devcon 60 adhesive is approximately 20 minutes, the process cannot be stopped once the module has been processed by the adhesive dispenser. The main block assembly tasks are described in the list below. Both cranes run simultaneously during plane construction. Table 17.24 shows the crane moving sequence during the 10 minutes per module movement. This process is described in more detail below.

17.13.4.1 Block Pivoter Preparation

Before the first plane of modules can be laid, the block base pallet must be installed. The 5-ton block base pallet is moved off a truck in the loading dock using the 10-ton overhead crane. It is lowered to the block pivoter (Figure 17.149), which is located in the assembly area. It is leveled and squared to the work surface of the pivoter and bolted in place. The block pivoter is then moved to the location where the new block will be installed and placed on the detector hall floor. Irregularities in the floor are accommodated by setting each pallet on a grout bed and leveling it. The pivoter and block base pallet are then moved back to the assembly area to begin plane installation. This entire sequence takes ~ 12 hours of clock time but the grout must be cured overnight before the block pivoter is moved back into position. This task uses half of the 10 person installation team; the rest of the installation team is doing QC on module units, maintenance on the adhesive dispenser or other similar tasks.

Crane Moving Sequence

Minutes	1	2	3	4	5	6	7	8	9	10	11	12	13	14	15	16	17	18	19	20
Crane 1	Move module to adhesive dispenser				Move empty crane to North			Hook-up empty fixture			Move module to adhesive dispenser				Move empty crane to North			Pick up empty fixture		
Adhesive Dispenser				Unhook crane, glue module, hook-up crane										Unhook crane, glue module, hook-up crane						
Crane 2		Align module on block pivoter			Move Vacuum Fixture back				Move module to block pivoter			Align module on block pivoter			Move Vacuum Fixture back				Move Module	

Table 17.24: Crane moving sequence during module installation.

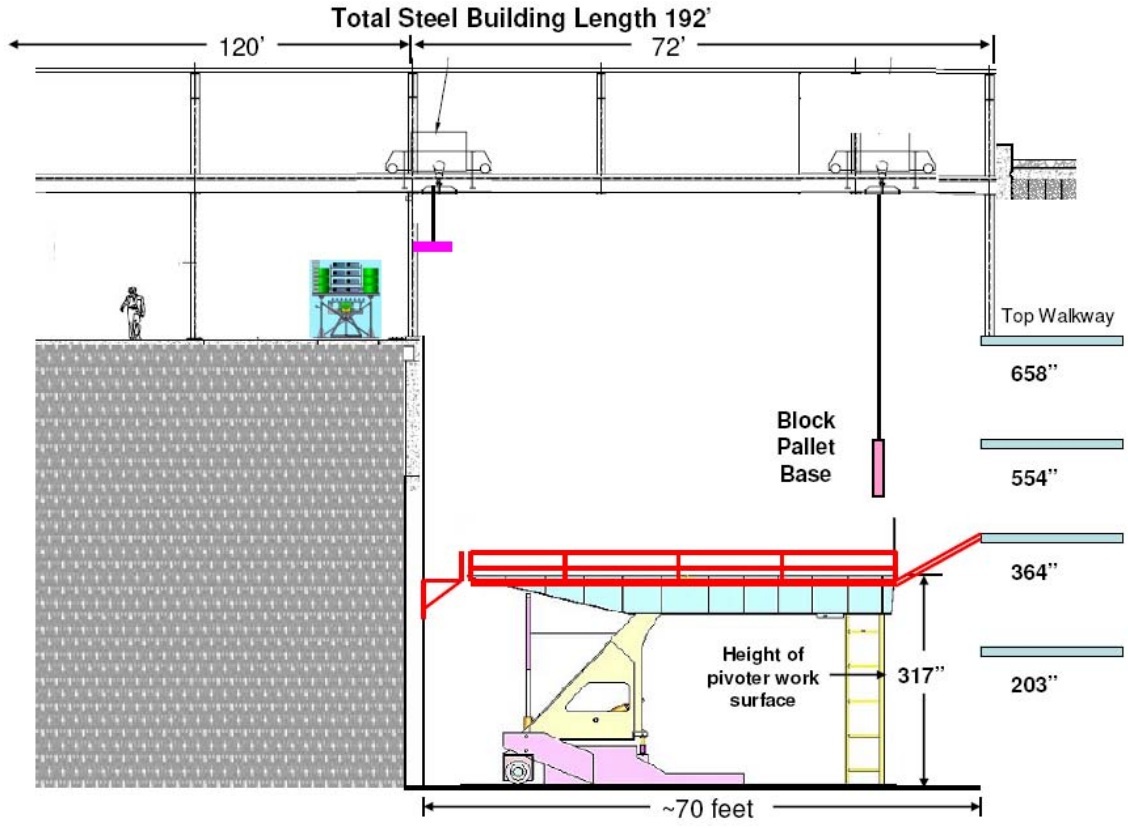

Fig. 17.149: Sketch of a block base pallet being lowered into place on the pivoter.

17.13.4.2 Module Movement

Block assembly time and motion studies (NOVA-doc-1954) of the gluing and assembly process will not be completed until early 2008. Current time estimates are based on the module movement and crane speeds achieved during the MINOS detector installation. The cost estimate

contingency allowance for the installation labor force is set high enough to allow additional workers and a third shift to be added if needed to maintain the baseline assembly schedule.

The modules are handled using vacuum lifting fixtures attached to an overhead crane. Empty horizontal modules weigh 320 kg and vertical modules weigh 436 kg. After placing the module on the adhesive dispenser, the vacuum lifting fixture is rotated about its long axis and thirty-two beads of adhesive are applied to what is now the top surface of each module, using an automatic system shown in Figure 17.131. Each time a module is placed in the adhesive dispenser, the AC power and the slings attached to the crane are disconnected. This entire task takes 5 minutes and is the key procedure in the 10-minute module moving sequence shown in Table 17.24.

Table 17.25 shows the time sequence of assembly crew tasks during the module handling process. The two 10-ton cranes move simultaneously. Crane 1 loads new modules into the adhesive dispenser and crane 2 places them on the block pivoter. The vacuum lifting fixture stays with each module. It is released from crane 1, and then reconnected to crane 2 after adhesive has been applied. Once the module has been placed onto the block, the empty vacuum lifter is moved to the module unit that has the next module to be installed. Figures 17.150, 17.151 and 17.152 illustrate the positions of the cranes during the module installation process.

	1 Adhesive Dispenser Technician 1 Crane Operator 1 Module Technician			1 Crane Operator, 1 Module Technician 1 Crew Boss			4 Block Pivoter Technicians	
Time-Min.	**Load Glue Table**	**Glue Process**	**Get Next Module**	**Move Module**	**Locate Module**	**Get Next Module**	**Position Modules**	**Roll Modules**
1	**3 min.**			**1 min.**				
2					**3 min.**			
3								
4		**5 min.**						
5			**6 min.**			**4 min.**		
6								
7								
8								
9				**3 min.**				
10								
11	**3 min.**							
12					**3 min.**			
13								
14		**5 min.**						
15			**6 min.**			**4 min.**		
16								
17								
18								
19				**2 min.**				
20								

Table 17.25: Module handling schedule for three assembly crews (which make up the "installation crew") for full rate assembly at ten minutes per module. The six workers shaded in gray in the first two columns are located at the loading dock level.

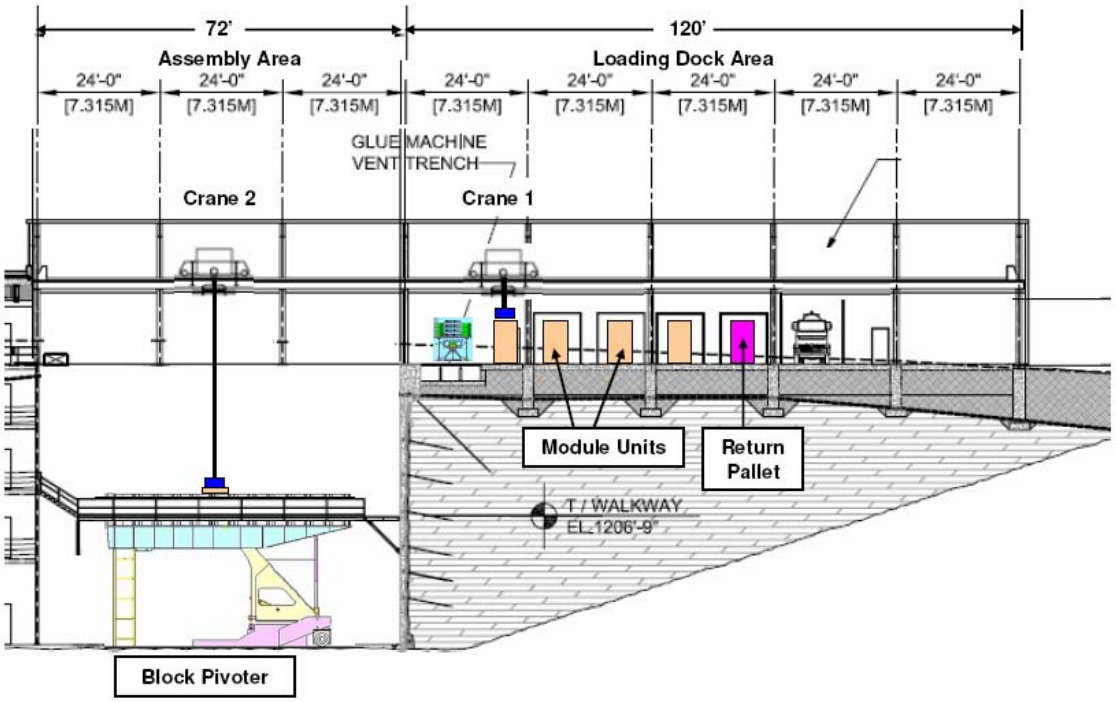

Minute 1-3

Fig. 17.150: Crane 1 removes a new module from a module unit and moves it to the adhesive dispenser. At the same time, crane 2 installs another module in the block.

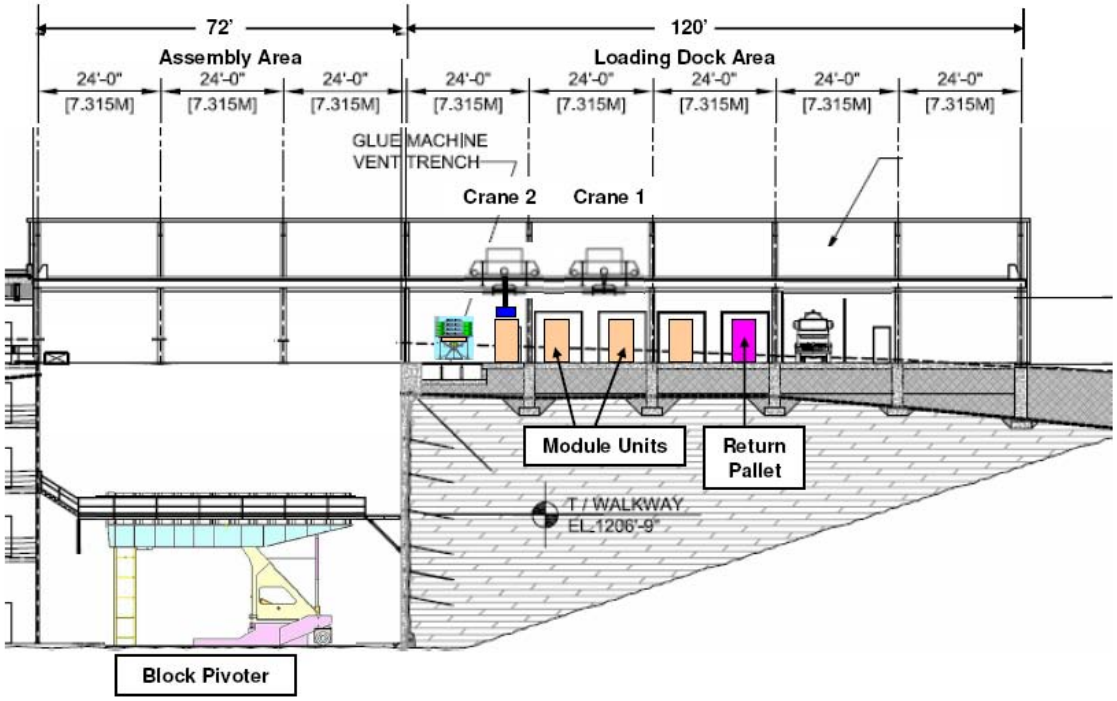

Minute 4-7

Fig. 17.151: Crane 2 moves the empty vacuum lifter back to the module unit while the other vacuum lifter is in the adhesive dispenser.

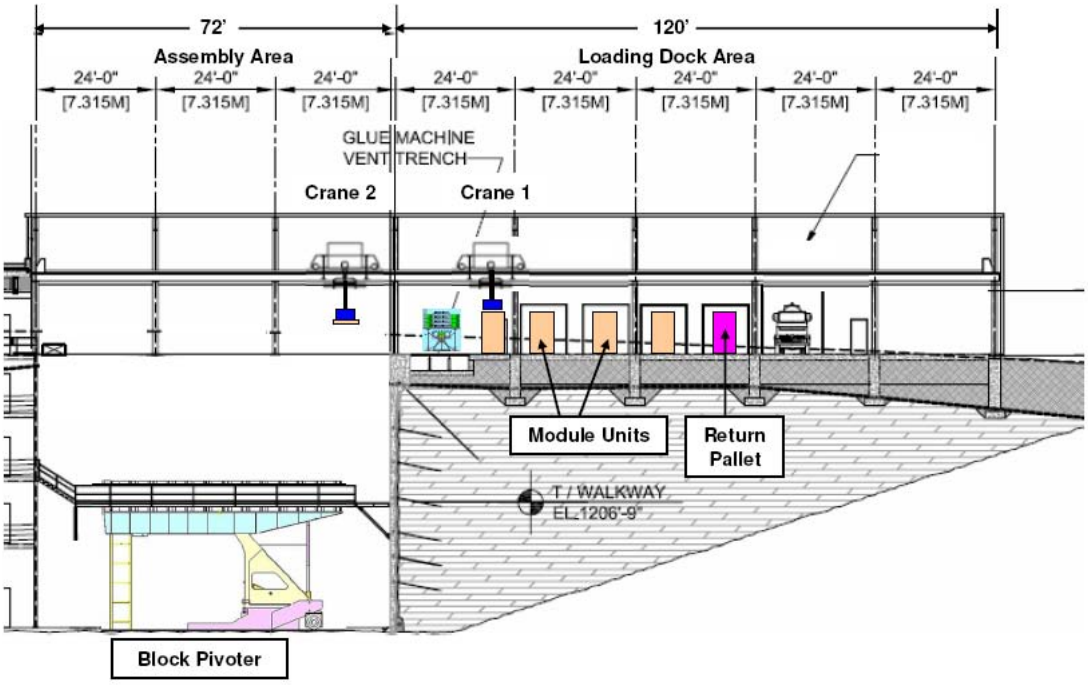

Fig. 17.152: Crane 2 picks up the module from the adhesive dispenser and moves it into position in the block. Vertical modules must be rotated 90 degrees. Crane 1 picks up the next module to be moved to the adhesive dispenser.

17.13.4.3 Module Alignment and Plane Completion

The first plane of each block is not glued, but its modules need to be rotated to the correct orientation and aligned. If it is a vertical plane is first (A-type block), the alignment fixtures are installed on the east side of the block pivoter. Modules are pushed tight against the block base pallet to the south and against the alignment fixture or module to the east. If the first plane is horizontal, the bottom module is aligned by spacers installed against the block base pallet. The module end seals are pushed tight against stops on the east side of the block pivoter.

After each module is placed in its final location, it is rolled with a 75-pound steel roller over its length to ensure a good bond to modules in the plane below. The module positioning and rolling tasks require four technicians working on the block pivoter, ~30 feet below the loading dock elevation.

After completion of each plane, a series of tasks taking about two hours is performed by the installation team shown in Table 17.25. Pourable epoxy grout is used to fill air gaps in the plane. On vertical planes, this includes the spaces between the module end-cap and the block base pallet and also any voids between modules in the lower 7 meters. The epoxy grout level extends to the upper surface of the plane. After each vertical plane is installed, a spacer is added to set the position of the first horizontal plane module, to separate it from the adjacent vertical-module end seal and to provide a positive alignment stop.

Module locations are measured to ±5mm and survey data are entered into the database. NOVA-doc-1396 describes module and block survey and alignment requirements. For the vertical modules, the module alignment fixtures located on the east side of the block pivoter have steel measuring tape holders that securely hold the tape to the "0" reference point. The centerline of the first cell in each module (closest to the module snout) has been marked with a target at the

module factory. Because of the long length of the modules, they are marked at the top manifold, bottom end cap and the middle. A total of 10 targets are measured on each module, so 240 measurements are taken after each plane is completed. A laptop computer is used to enter the numbers into a form which automatically checks for errors. This information is then downloaded into the main database. A similar technique is used for the horizontal modules, which are referenced off the block base pallets and horizontally centered about the detector axis. Horizontal modules are tilted at an angle of 2.5 mrad, with the manifold end raised above the end-seal end, to prevent air entrapment in extrusion irregularities.

After any schedule breaks longer than 10 minutes the mixing nozzles on the adhesive dispenser must be changed. After the completion of each plane there is a ~2 hour period when modules are not going through the adhesive dispenser, so additional cleaning can be done as needed. This is also the time period that "Super Pallets" are stacked on the return pallet and general cleanup of the work area takes place.

17.13.4.4 Block Completion

After the last plane of each block has been installed, the adhesive is allowed to cure for a minimum of 24 hours before the block is moved. During this time period, the module and block pivoter technicians spend two shifts cleaning and maintaining the adhesive dispenser and performing the following tasks on the assembled block:

- **Glue block spacer to the first block in a superblock**
  A PVC spacer board (2 cm x 30 cm x 15.5 m) sets the width of the expansion gap between superblocks and ensures adequate clearance between the manifolds on planes of vertical modules in adjacent superblocks. The adhesive dispenser is used to apply the adhesive to one side of the spacer board.
- **Remove module alignment stops**
  Remove module alignment stops as needed.
- **Install brackets to support the top cable trays**
  Brackets that support the cable trays and electronics distribution systems are glued in place.
- **Apply light-proofing paint**
  Measurements show (NOVA-doc-378) that the 4.5-mm side walls of the vertical modules are sufficient to block most of the light to which APDs are sensitive but this is not the case for the 3.0-mm thick walls of horizontal modules. NOVA-doc-140 describes the application of light-proofing paint to NOvA modules. PVC paint primer is applied by brush to exposed surfaces of horizontal modules and allowed to dry overnight. This is followed by a topcoat of black PVC paint that is also applied by brush.
- **Equipment maintenance**
  Maintenance of all block building equipment takes place during this period. Any extra manpower is used to assist with electronics outfitting work.

17.13.5 Raising and Securing a Block

The block moving and raising sequence takes approximately 8 hours.

- **Prepare block for movement**
  The block and pivoter top and side clearances are checked and the rails and floor area are checked for obstructions.
- **Move block pivoter**
  The block pivoter moves from the assembly area to about 30 ft away from the detector face at a maximum speed of 20 feet per minute.
- **Rotate pivoter**

The pivoter rotates the block to within a few degrees of a vertical orientation. Most of the 2-hour time allocation is for setup and safety checks. The actual rotation takes 10-15 minutes.

- **Move into final position**
  The pivoter moves the block the last 30 ft to within a few inches of the detector face. It then rotates the block last few degrees to a vertical orientation. After the location is checked, the pivoter moves the block against the detector face and sets it down on the floor of the detector hall.
- **Move block pivoter back to assembly area**
  The assembly crew detaches the block base pallet from the pivoter and moves the pivoter back until it is clear of the detector. They then rotate the pivoter to the horizontal orientation and move it to the assembly area where the process of installing the next block base pallet begins.
- **Install block safety constraint beam**
  After the block pivoter is clear of the detector face, the block safety constraint beam is moved against the last block (Figure 17.153). This device is supported by the same rails as the top-of-detector moving access platform. A hydraulic system presses the beam against the block. The beam is removed just before the next block is installed.
- **Survey newly installed block**
  The location of each block will be surveyed with the V-STARS Industrial Photogrammetry System [6], similar to that used on other Fermilab experiments.

17.13.6 Construction of a Superblock

A superblock consists of five blocks with no gaps between them. An A-type block, with vertical module planes on its outside faces, is the first to be installed. It is the only block with a spacer board attached, to set the expansion gap between superblocks.

The first block in the sequence has 31 planes, starting and ending with a vertical plane. This block is the only one with a 2-cm thick spacer glued to its south face. The remaining four blocks alternate between A and B types. A superblock contains a total of 1860 modules in 155 planes, 78 vertical planes and 77 horizontal planes. The 15 kton detector consists of 6 five-block superblocks and one three-block superblock. Figure 17.154 shows a completed superblock.

The steel block base pallets provide support for the vertical module planes, so the pallets for A-type blocks are wider than those for B blocks (with horizontal modules on their outside faces). The steel pallet widths must accommodate blocks that have the widest extrusions and thickest glue bonds between planes, so A-block pallets will generally extend a few inches beyond the south faces of these blocks. Within a superblock, this excess pallet width fits under the horizontal module plane of the adjacent B block. However, the pallet for the first block in each superblock is custom made, taking into account the thicknesses of modules in the block (which are known many weeks in advance of block assembly). The pallet in this first block of each superblock is not allowed to extend beyond the 2-cm width of the expansion gap to the adjacent superblock.

The last superblock is unique in that it contains only three blocks. The last of these blocks (A-type) consists of only eleven planes. It is mounted permanently on, and glued to, the block pivoter. After it is raised into position, the pivoter remains in place and is converted into the north bookend structure with the installation of additional structural braces.

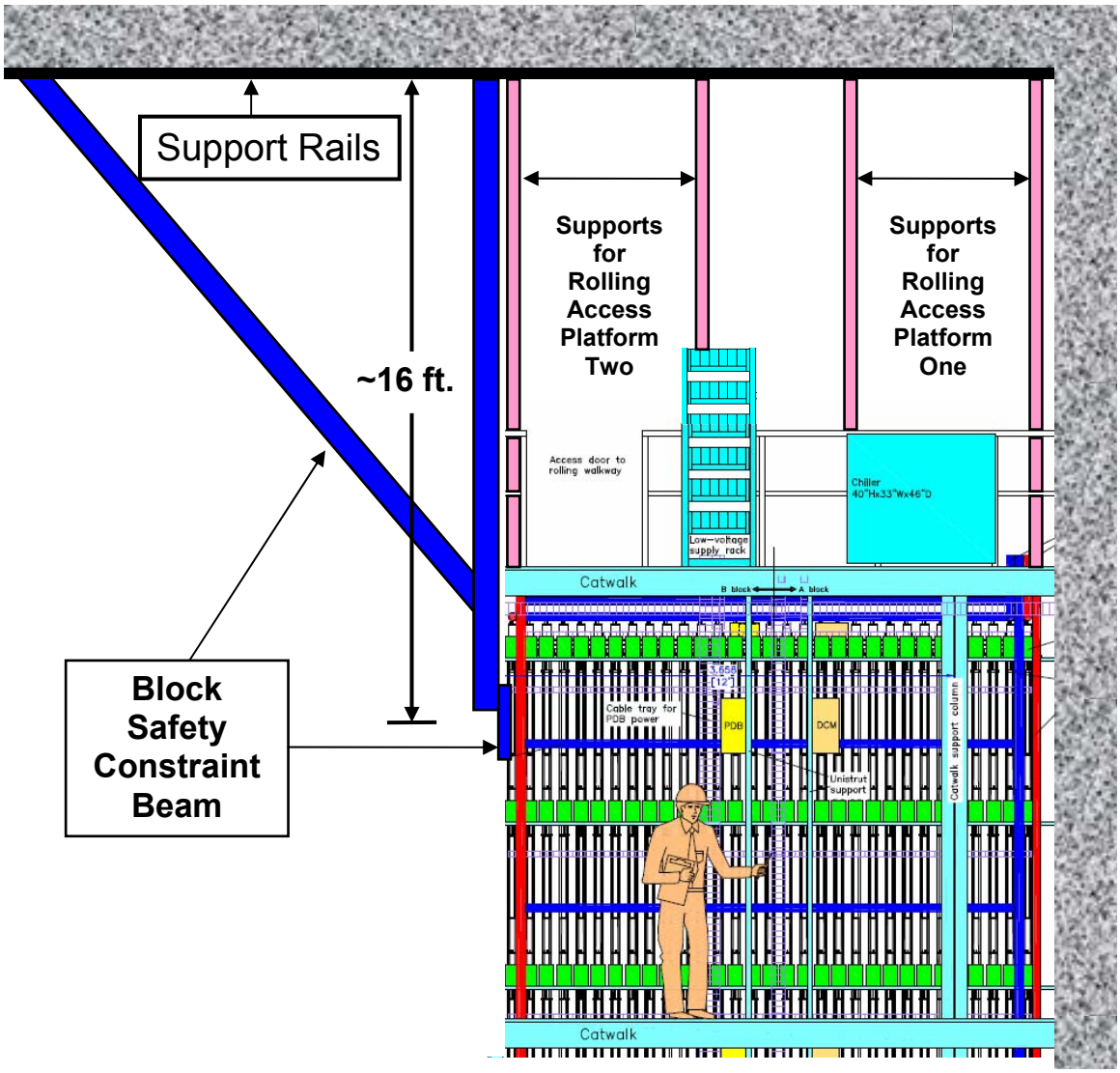

Fig. 17.153: Sketch of the block safety constraint beam and rolling access platform support rails.

17.14 Filling the Detector With Liquid Scintillator

Section 17.8 describes the liquid scintillator distribution and filling system in detail. The present section provides only a short summary.

The 33-block detector holds 10,370 tons (3.22 million gallons) of liquid scintillator. During the full-rate assembly period at the far site, one block (102,600 gallons) will be filled every 2.6 weeks (about 100 hours of working time), giving an average flow rate of about 24 gal/minute. Allowing time for the liquid level to equalize between the 32 cells in a module, this corresponds to filling 8 modules in parallel at an average flow rate of 3 gal/min. About one 6,500 gallon delivery tanker per day will be needed during this full-rate period. The scintillator receiving station can accommodate up to four tanker trucks under a gas-station-type canopy, so there is always a few-day buffer on hand. Empty tankers are sent back to the scintillator blending facility to be refilled.

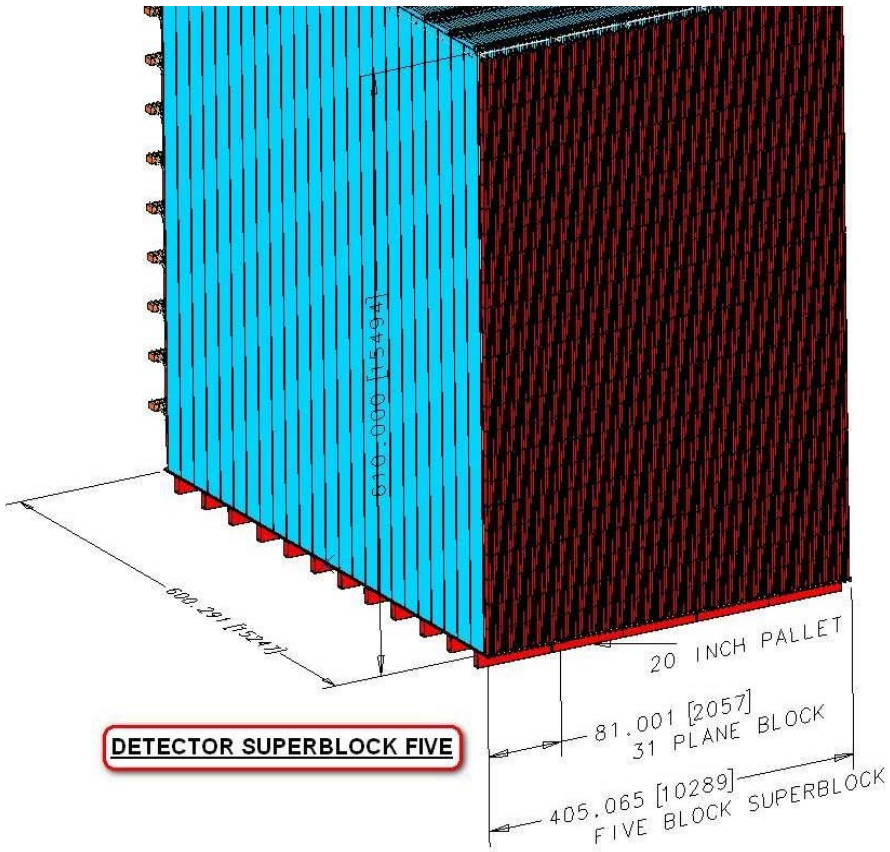

Fig. 17.154: CAD drawing of a superblock. Nominal dimensions are shown in inches and [mm].

The modules in each superblock are filled with liquid scintillator as soon as the last block in a superblock is installed. Blocks within a superblock are filled one at a time, beginning with the south-most block. Planes of horizontal modules within a block are completely filled before the filling of vertical modules begins (NOVA-doc-1298 and 2510).

Chapter 10 describes the liquid scintillator composition and properties, including the potential hazards resulting from electrostatic charge buildup during transfer operations. The scintillator handling procedures at the far detector site are designed to mitigate the risks associated with such charge buildup and possible sparking during the movement of scintillator in supply pipes and especially during the filling of vertical extrusion modules. Such sparking has the potential for causing personal injury, damaging equipment and igniting scintillator vapors or aerosols. NOVA-doc-1118 gives the detailed requirements for safely filling the detector.

NOVA-doc-1521 reports the results of a Minimum Ignition Energy (MIE) test of an aerosol of NOvA scintillator in air. The MIE was higher than standard test equipment could measure, so the buildup of static charge during vertical module filling poses no risk of fire or explosion. However, it is still important to reduce the risk of static electricity discharges that could damage equipment or injure workers, as described below.

Delivery tankers are grounded to earth and electrically bonded to the distribution system prior to the transfer of scintillator to the detector. The scintillator tanker area is equipped with a sump and spill-control berm that is sufficient to contain 100% of the liquid from a single tanker. The transfer process is controlled from the small scintillator control building located between the truck bays at the scintillator receiving station. Samples of scintillator from arriving tanker trucks are hand carried in small containers to the scintillator transfer facility located along the main

detector building. They are used for quality assurance measurements of attenuation length and light yield. These samples are saved and sent to Fermilab for archiving and possible additional testing.

After evaluating test results, the scintillator filling technicians connect an arriving tanker to the scintillator supply system through conductive hoses. Scintillator from a tanker is pumped directly into the detector modules through a 7.6-cm diameter electrically conductive pipe, permanently mounted and electrically bonded to the earth, with a resistance to ground less than 10 ohms. The temperature of the arriving liquid is raised or lowered by the heater or chiller unit at the scintillator receiving station, so that it is within 2° C of the 20° C temperature of the detector. It is pumped to the detector hall through an underground pipe and delivered to the detector through a flexible, conductive hose. The total flow rate from a tanker is limited to 40 gal/min.

At the detector, the fill system includes metering, level sensing and automatic safety shutoff valves. Fill system hoses are conductive and electrically bonded to the distribution system. Flow velocities in any given line are kept below 2 m/s in order to limit electrostatic charge buildup. Filling at the detector end makes use of 1.27-cm diameter or larger connections to vertical module manifolds or horizontal module expansion tanks.

All horizontal modules in a block are filled before vertical modules are filled. (Horizontal modules are installed at an angle of 2.5 mrad to the horizontal, with the manifold end raised about the end-seal end, to prevent air entrapment in extrusion irregularities.) Flow rates into each extrusion are metered, totalized and logged. A preset total is used as the primary means of determining when a module is full. Once this preset is reached, a "top-off" phase is initiated, in which ultrasonic sensors mounted on either side of the manifold/extrusion joint are monitored to determine when the final desired fluid level is obtained. Connections between the fill system and detector are made with hydraulic quick-disconnect fittings.

The flow of scintillator in the vertical extrusions is controlled to eliminate the formation of mist or aerosols by restricting flow to occur only along the walls of the extrusion, and with minimal free-fall and consequent breakup of the fluid stream. This is accomplished by distributing the flow to individual cells in the extrusion with a plenum interior to the manifold, with orifices on the plenum positioned and sized to ensure that the flow rate per cell is uniform, directed to the cell walls, and sufficiently low to avoid breakup and free-fall of the fluid stream.

The gas volume displaced during the fill process is returned to the delivery tanker through a vapor recovery system. A vapor-tight connection to each manifold vent is made using 1.27-cm diameter flexible hose, connecting to a rigid plenum pipe servicing one plane. Each plane's plenum is connected with flexible hose to a primary plenum running the length of the detector. During transfer of scintillator from a tanker, the vapor recovery hose connects to the tanker, replacing the volume of scintillator delivered with an equivalent volume of vapor. In the steady state detector operation, changes in the detector volume due to temperature fluctuations can result in vapor flow rates of up to 1 liter/s from the entire detector, containing up to 0.5 ml/s of pseudocumene. For the outflow, volatiles are removed from the vapor prior to venting to the atmosphere using a filter attached to the primary vent return. Intake air is also filtered.

During filling, flow rates on the liquid intake and vapor outlet sides of the distribution loop are monitored, in addition to the total fill rate, to detect an out-of-balance condition that would indicate a leak in the distribution loop. A solenoid valve at the distribution loop intake is closed if an out-of-balance condition is detected. This safety system is intended primarily to address catastrophic leaks in the distribution system. Two ultrasonic sensors mounted on the side of each manifold are used to detect "full" and "over full" conditions. The full condition is used to terminate filling on this extrusion. An overfull condition halts all filling operations. A spill pan is placed in position to catch spillage due to leakage of fittings, breaking of fittings, etc. An optical sensor mounted to the bottom of this pan senses liquid level, and shuts down all fill operations if a spill is detected.

Liquid scintillator similar to NOνA's is commonly used in laboratory settings and can be handled safely by following a few precautions. Chemically impervious gloves must be worn at all times when working with the scintillator. No smoking is allowed in or around the detector site. No welding should occur in close proximity to filling operations. All oil-soaked rags and absorbent materials will be stored in fire-proof covered steel containers. Chapter 9 and NOVA-doc-1021 describe the spill containment provided by the far detector hall itself.

The scintillator filling task requires two full-time scintillator technicians and a half-time crew boss (who is shared with the electronics outfitting task). The crew boss directs the work and also fills in for sick or vacationing technicians.

17.15 Detector Outfitting

17.15.1 Detector Readout Infrastructure

Detector outfitting refers to the installation of readout and liquid scintillator hardware on installed blocks. NOVA-doc-2538 describes this process in detail. A 3D I-DEAS CAD model is used to integrate the locations and installation sequences of electronics hardware and liquid scintillator supply and vent plumbing (Sections 17.8 and 17.14). Some of this hardware is installed on blocks while they are still on the pivoter, before being erected and installed. The remainder of the outfitting installation process is integrated with the module filling process. The installation of readout hardware after blocks are installed in the detector is performed on pairs of adjacent blocks (called di-blocks) to take advantage of the natural lengths of cable trays and chilled water pipes. There are three major systems to be installed:

- **Electronics**
  This includes relay racks, cable trays, power and signal cables, power distribution boxes, data concentrator modules, and detector control system sensors to monitor the power system. NOVA-doc-2239 lists the cable and cable tray sizes for all the power cable runs.
- **Chilled water**
  This system consists of the Tempest chiller units on the top walkway plus the plumbing that connects the chillers to the electronics. The system also includes sensors and electronics for remote monitoring and control of the chillers.
- **Scintillator plumbing**
  This includes the main feed pipes that supply the scintillator to the block filling stations, the scintillator vapor recovery piping and the horizontal-module expansion tanks.

Most of this equipment is installed as soon as each new pair of blocks is erected. Outfitting of the west side of the detector is done from the walkways and movable work platforms. A Unistrut frame supports the cable trays, PDBs, DCMs, and plumbing. Filling of horizontal modules with liquid scintillator is done through the individual module expansion tanks, which are located away from the vertical sides of the detector. The locations of the expansion tanks eliminates interference between outfitting and filling, so the sides of the detector can be fully outfitted, including electronics box installation, before modules are filled.

Outfitting the top surface of the detector is more difficult. The rolling access platforms shown in Figure 17.155 allow workers to reach the top detector surface and the vertical module manifolds by lying flat on the platform. The distance from the floor of an access platform is required to be less than 16 inches above the vertical module manifolds to make this operation possible. All outfitting top hardware except for the delicate electronics boxes is installed before the vertical modules are filled. The vertical module electronics boxes are installed only after filling is completed.

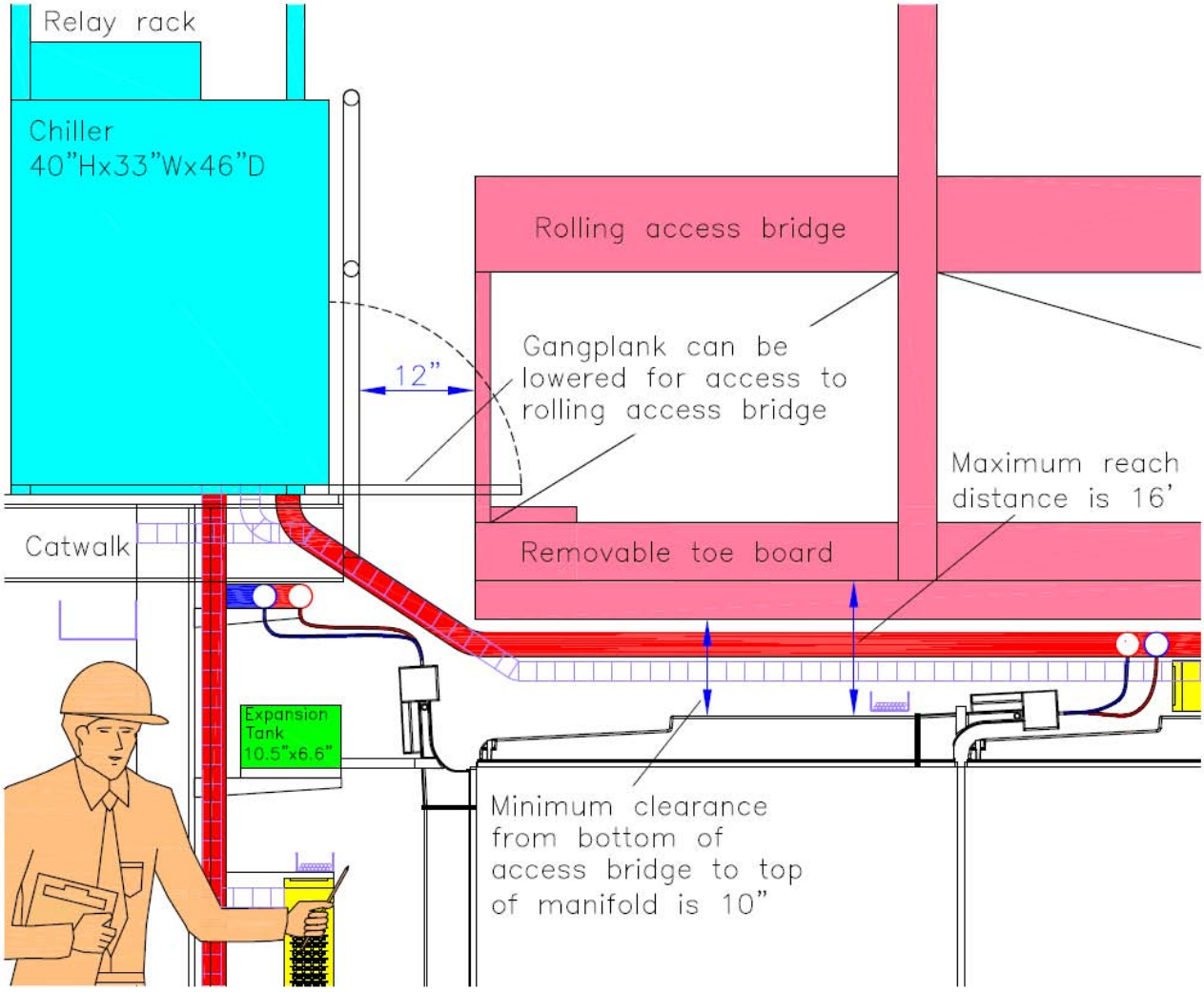

Fig. 17.155: View (looking north) of rolling access platform that allows access to the top of the detector.

17.15.2 Outfitting Components

The following hardware components are installed on the detector blocks during the outfitting process:

- **Electronics**
  - **Readout electronics racks**
    One relay rack contains all the power supplies and readout electronics for each di-block. Each has four 40 A, 208-230 V receptacles, two 20 A, 120 V receptacles (all quiet power) and one 20 A, 120 V convenience receptacle. The racks can be installed any time after beneficial occupancy since they do not interfere with access to the rolling access platforms. The detector also requires one high voltage power supply rack, located near the center of the detector.
  - **Cable trays**
    Cable trays are required in 2-inch x 2-inch, 4-inch x 2-inch and 8-inch x 4-inch sizes. These are installed on di-blocks as soon as they are added to the detector. Cable trays are stored in a rack in the loading dock area until they are needed. The top cable trays are mounted on clips that hold them in place on the flat

sections of the vertical module manifolds. Side cable trays are mounted to Unistrut frames attached to the walkway support columns.

- **Cable harnesses**
  Cable harnesses are configured specifically for the di-block areas that they service. They are removed from the shipping boxes and laid directly into the cable trays.
- **Power distribution boxes (PDBs)**
  Each di-block uses 12 PDBs, a total of 198 for the 33-block detector. Boxes are 9.14-inch D x 17-inch W x 5.3-inch H. PDBs on top of the detector lie on insulated shims. Those on the side of the detector are mounted to Unistrut frames that are supported by the side walkway columns. The power is supplied from the readout electronics racks via transverse 4-inch x 2-inch cable trays.
- **Data concentrator modules (DCMs)**
  Each di-block uses 12 DCMs, a total of 198 for the 33-block detector. Each box is 9.14-inch D x 17-inch W x 5.3-inch H. DCMs lie on insulated shims on the top of the detector and are mounted to the Unistrut frames on the west side of the detector.
- **Electronics boxes**
  The vertical module electronics boxes are installed after all other outfitting and scintillator filling are completed. Horizontal module electronics boxes are installed before expansion tanks are mounted and before scintillator filling. Once electronics boxes have been installed, all the electrical, data and chilled water connections are made.

- **Chilled water for APD TECs**
  - **Supply and return manifolds**
    The 1.25-inch diameter pre-insulated supply and return manifolds connect the chiller unit to the service manifolds. On the top of the detector, the elevations of these must be above the electronics boxes and service manifolds to minimize air blockages. They are manufactured in ~50-inch lengths to match the pitch of the modules.
  - **Supply and return service manifolds**
    The 0.75-inch diameter pre-insulated supply and return service manifolds run longitudinally to the di-blocks. Each one feeds 32 electronics boxes. Each 0.25-inch diameter hose has a valved disconnect, so that a TEC can be removed from the system and replaced without affecting the rest of the electronics. They are manufactured in ~80-inch lengths to match a single block.
  - **Chiller units**
    Each Tempest water-chiller unit has 2 tons of chilling capacity. Each is 40-inch H x 33-inch W x 46-inch D and weighs 600 lbs when full. One unit is required for each di-block and requires a 20 A, 230 V, 3Ø service.
- **Scintillator**
  - **Vapor return plumbing**
    A wall mounted 1.5-inch diameter white PVC schedule 40 pipe runs the length of the detector and back to the scintillator transfer station. A 0.625-inch acid-grade black PVC pipe is routed to each block where a tee is connected at each manifold and a short piece of hose is attached to the vent port on each module manifold. Figure 17.156 shows the general location of the vent plumbing.
  - **Horizontal module expansion tanks**
    The 5976 four-liter plastic expansion tanks, shown in Figure 17.156, are tested before being shipped in batches of ~ 1000 to Ash River. The tank dimensions, which are still being optimized, are 6.5-inch H x 4-inch W x 10.5-inch D. The

Unistrut frame that holds all the cable trays and chilled water also supports a sturdy shelf that the tanks rest on. Outfitting technicians need to lean on these shelves to work on the electronics boxes, so each is designed to support the weight of approximately 28 expansion boxes plus a person.

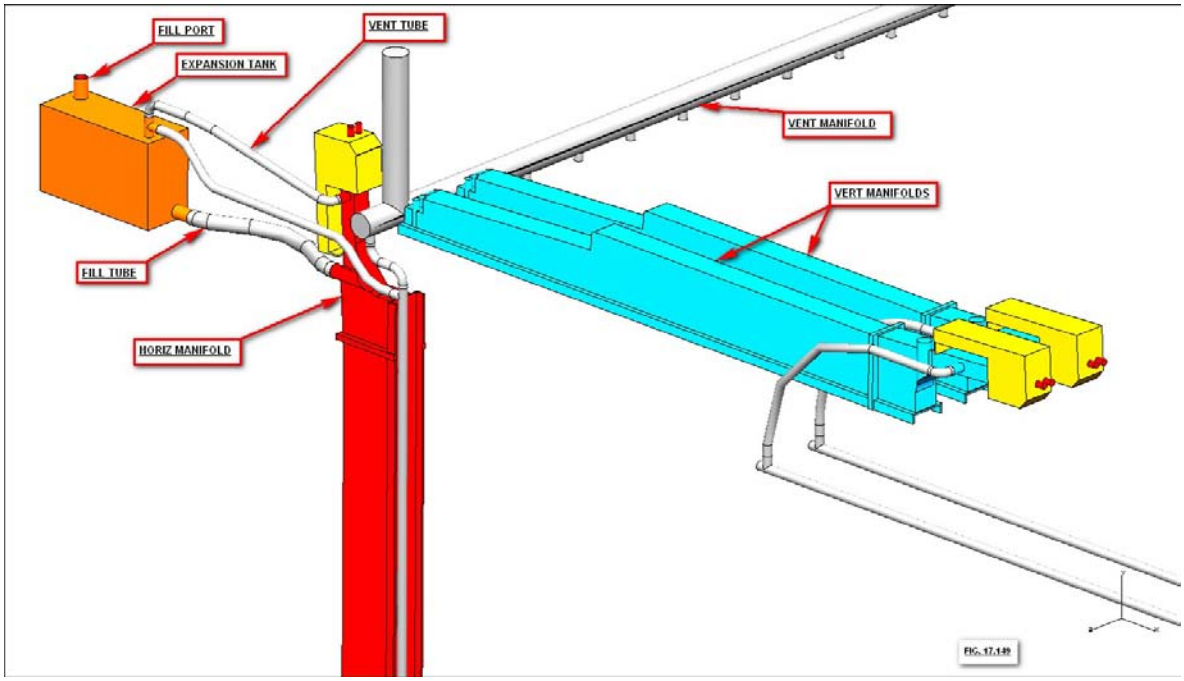

Fig. 17.156: Schematic diagram of the scintillator vent plumbing and expansion tank for a horizontal module at the top west corner of the detector. Two vertical module manifolds (blue) are shown in the right side of the figure. Electronics boxes are shown in yellow. Module extrusions are not shown in order to expose other features.

17.15.3 Outfitting Installation Sequence

A new outfitting sequence begins after each pair of blocks is installed in the detector. The Unistrut frame on the side of the detector cannot be installed until blocks are in place and the associated survey work has been completed. Components are installed in a highly structured pattern to maximize efficiency and minimize the risk of damaging components, e.g., to avoid threading long cables underneath previously installed items. Installation of electronics boxes on the top of the detector is delayed until both the initial filling and topping up of the vertical modules has been completed. For the horizontal modules, the electronics boxes are installed before the expansion tanks because access to the boxes is more difficult after tanks are installed.

- **Manpower**
  The long lengths of cable trays and pipes are installed by outfitting teams of one crew boss and two technicians. When scintillator filling is not taking place, both the day and afternoon shift outfitting and scintillator teams are available. Additional crew members may be available from the installation team (listed in Table 17.25). The two rolling access platforms allow two teams to work on the top of the detector and several on the side without interference. The outfitting task provides "filler" work for assembly crew members whose regular work is delayed by equipment failures or other problems.
- **Side support frame**
  Mounting holes or welded brackets to hold the Unistrut on the walkway support columns are completed before the blocks are in place, to minimize risk of damage to the modules.

This work can be a filler job during the start-up period when the installation teams are being trained. The Unistrut is pre-cut and drilled in the shop area of the loading dock. The cable safety railings along the walkways may be removed as the frame is installed by bolting it into place. The frame work should minimize interference of access to electronics boxes and is stiff enough to be stable. Figure 17.157 shows a possible layout.

- **Vapor return piping**
  The vapor return piping is the first item to be installed on both the top and the side of the detector. The 1.5-inch diameter vent manifold shown in Figure 17.157 is put in place first. This pipe connects to the main vent pipe that is attached under the upper walkway and runs back to the scintillator receiving station. Support brackets for the 1.5-inch PVC pipe can be attached to the Unistrut frame. The smaller 0.625-inch diameter pipe is located on top of the horizontal modules on the top, and against the vertical modules on the side. Simple self-sticking cable-tie holders are used to hold the pipe in place. All connections are pushed over barbed fittings and are held in place by spring clamps. The final connections to the expansion tanks are made after the rest of the side outfitting is completed. All vent plumbing is completed before filling begins.

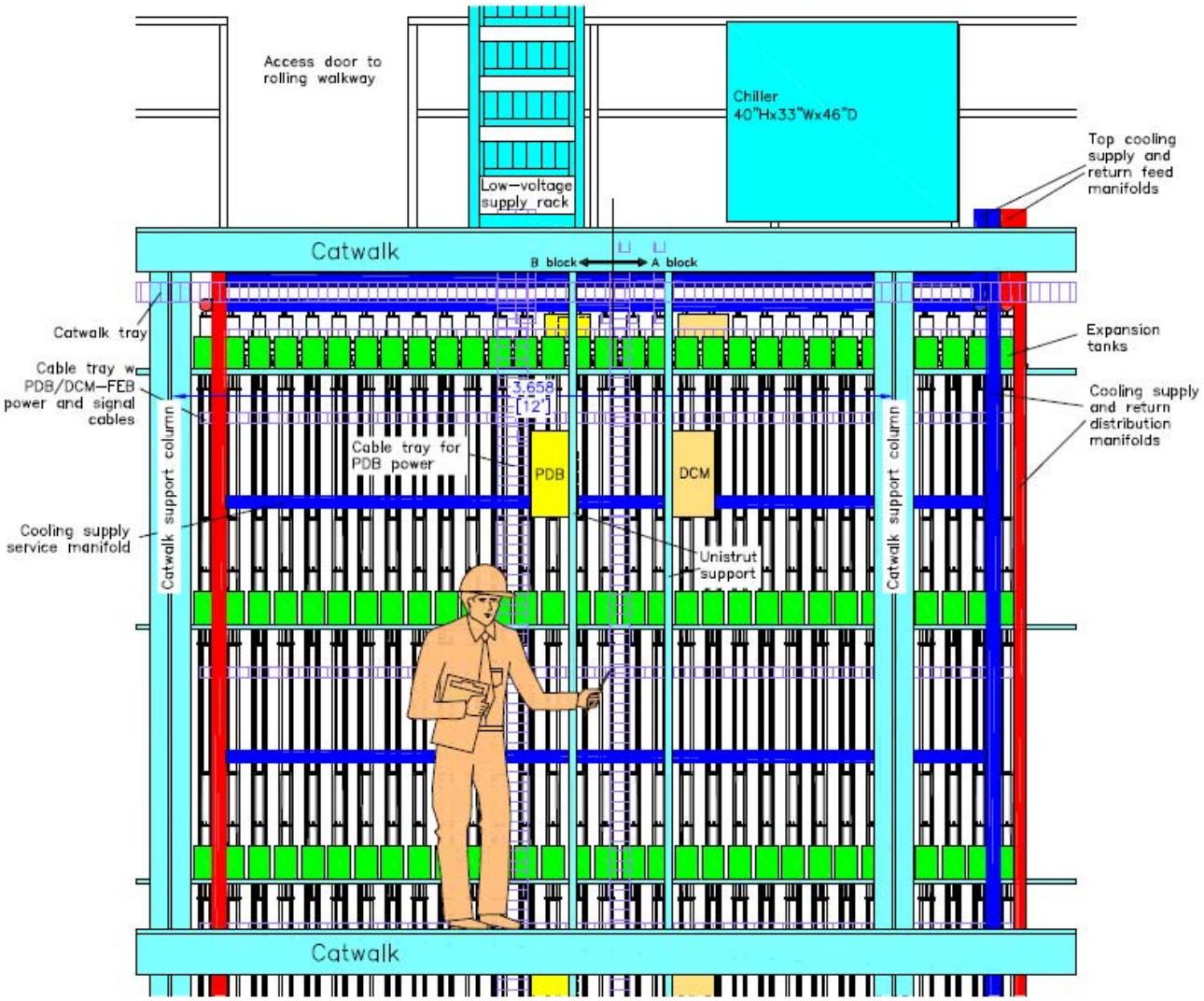

Fig. 17.157: View of the side of a di-block between walkways and the layout of a Unistrut frame.

17.15.4 Detector Top Outfitting

17.15.4.1 Access to the Top of the Detector

Access is provided by the two rolling access platforms. Usually one platform is set up for scintillator filling but it can be used for outfitting when not in use for filling. Access to the platform is via gates off of the top walkway, as shown in Figure 17.158. The final design will have gates located between the relay-rack and chiller units for each di-block. The spacing will be approximately every 162 inches since the locations of the relay racks are fixed to the pitch of the detector blocks to minimize cable length. Access to the rolling access platform is only from the west-side top walkway.

Workers lie on their stomachs and lean over the side of the access platform to install top outfitting hardware. Workers use safety harnesses during this procedure. Typically, the two technicians would be positioned lying down on the access platform and the crew boss would supply materials and move the platform as needed.

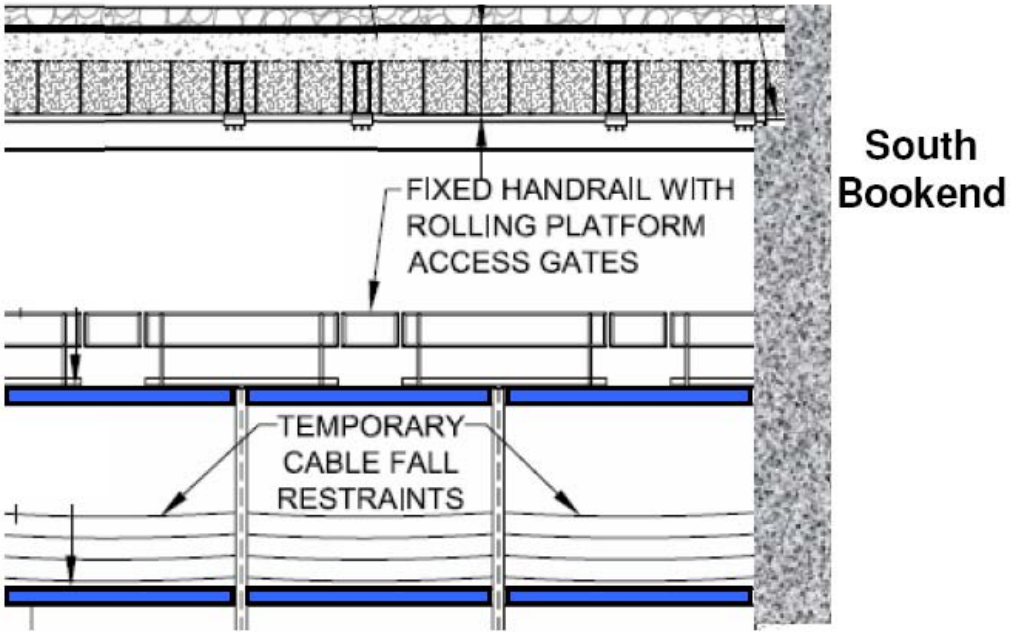

Fig. 17.158: Side view of the south end of the detector enclosure, showing access gates onto the rolling access platform and the cable fall-restraints along the mid-level walkways.

17.5.4.2 Top-of-Detector Installation Sequence

- **Vapor return piping**
  The vapor return piping is the first item to be installed on the top of the detector, as described in Section 17.15.3.
- **Longitudinal cable trays**
  The twelve 4-inch x 2-inch longitudinal trays are the first ones put in place. They are located just west of each module snout on the flat part of the manifold as shown in Figure 17.159. These trays provide support for other trays that cross them and for the chilled water pipes. A U shaped PVC saddle is placed over each vertical manifold to be used to clamp the tray in place and distribute the load evenly across the detector. The saddles are shimmed as needed to put them at the same elevation, to compensate for variations in module lengths.

- **PDBs and DCMs**
  The six power distribution boxes and the six data concentrator modules are placed on the same U shaped PVC saddles as the cable trays. They are located just west of the longitudinal trays. They are again shimmed to make a level support platform that the 9.14-inch D x 17-inch W x 5.3-inch H boxes are attached to. The saddles provide thermal insulation to protect the vertical module manifolds from heat. Each set of PDB and DCM boxes feeds two rows of vertical modules for a total of 64 or 62 electronics boxes. (Different numbers of boxes are needed for di-blocks with 2 A-type blocks and those with one A-type and one B-type block.)

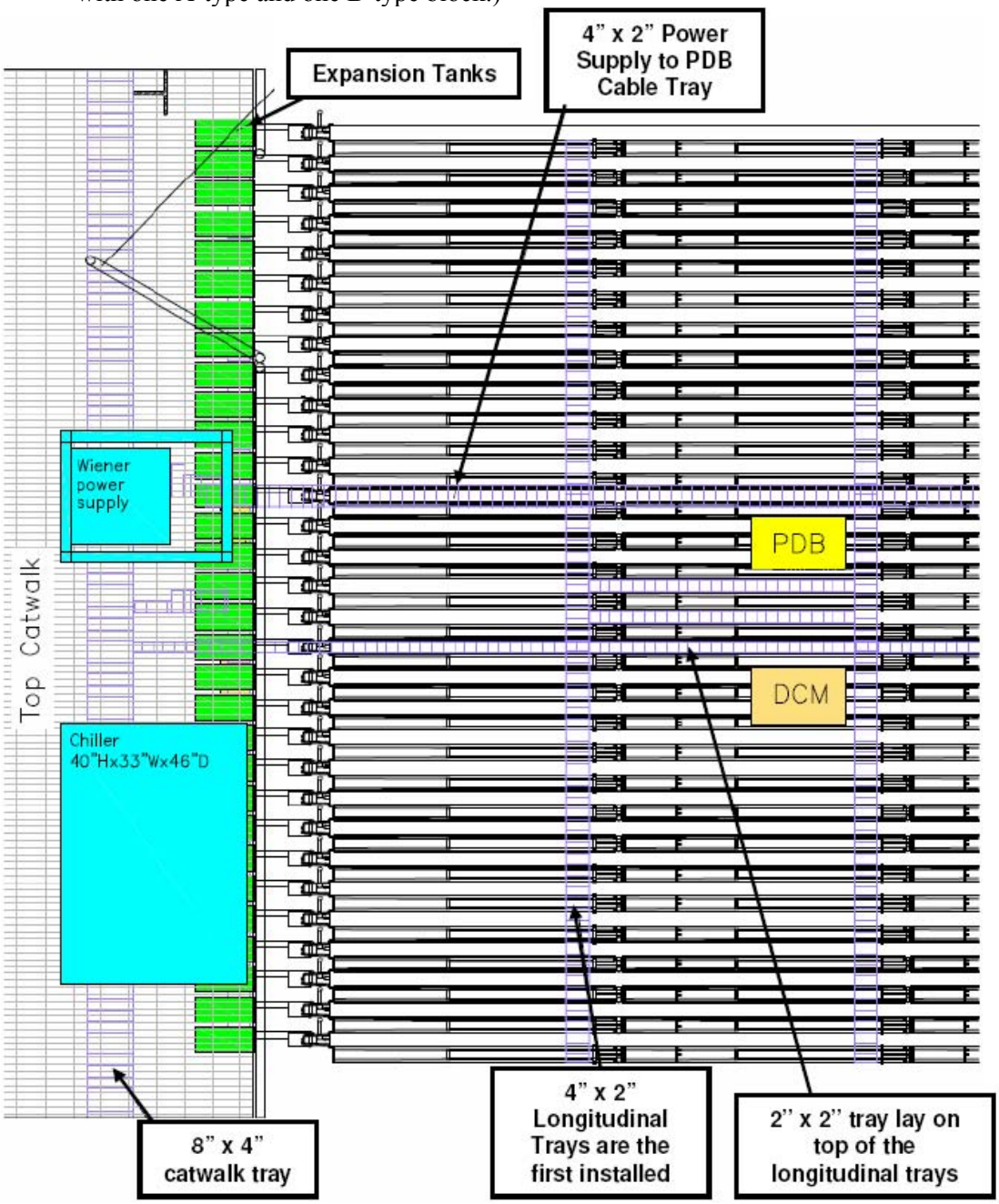

Fig. 17.159: Plan view of the top of the detector near the side walkway, showing the layout of detector outfitting components.

- **Power feed trays**
  The next trays to be put in place are the 4-inch x 2-inch power feed trays that run to the PDB and DCM boxes. These trays are mounted to brackets attached to the longitudinal trays and run under the top walkway to the 8-inch x 4-inch walkway tray. Once the trays are in place, the cables are installed and connected. The power feed cables are quite large and stiff, up to the 1-inch diameter 2AWG, 2C. No power is turned on until the system has been inspected and certified by experts.
- **PDB to FEB feed trays**
  These feed trays contain the electronics-box power and signal cables from the PDB and DCM boxes. Figure 17.160 shows the locations of both the longitudinal and transverse trays.
- **Electronics box power and signal cables**
  These cable harnesses are made and tested at the University of Virginia and are labeled specifically for each set of modules. Once the cable trays are installed, cables are routed into their final positions. Since the electronics boxes are not installed until after scintillator filling, the module ends of the cables remain in the cable tray out of the way. Cables may be connected to the PDB and DCM boxes at any time.

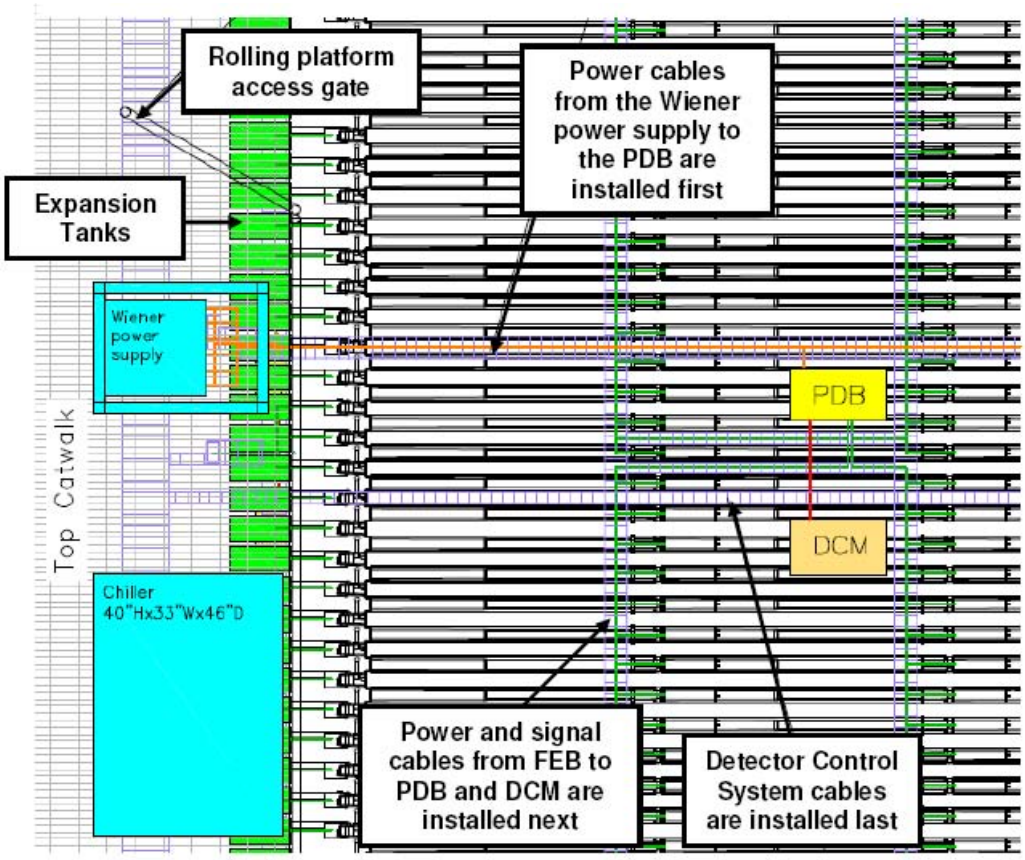

Fig. 17.160: Expanded plan view of a section of the top of the detector, showing the route of the cable harness runs to the electronics boxes from PDBs and DCMs. Each pair feeds 62 or 64 electronics boxes.

- **Detector control system (DCS) cables**
  These cables connect the PDB and DCM boxes for the detector control system. They run in the same cable trays as the power feeds.
- **Supply and return manifolds**
  The supply and return manifolds run from the chiller units to the di-block service manifolds. They are supported by rigid foam blocks that hold them above the electronics boxes. Each supply and return manifold tee has a shutoff so that service manifolds can be isolated. The sides of the manifold come in 12 sections ~50 inches long and are glued in place as they are installed. The end pieces are ~80 inches long. All of the pieces come pre-insulated but are wrapped at the fittings after they have passed their leak tests.
- **Supply and return service manifolds**
  Each supply and return service manifold comes in two ~80-inch pieces, which are attached to the shutoff valves in the main manifolds. Since these runs are longitudinal, rigid foam blocks are used hold them at the proper elevations. The cooling pigtails which attach to the electronics boxes have valves so that TECs can be replaced without shutting down an entire loop.
- **Water system testing**
  Since the entire system has valves at all key locations, it can be pressure tested before it is connected to the electronic boxes.
- **Scintillator filling**
  The filling sequence is described in NOVA-doc-2501. The electronics boxes are not installed on the top of the detector until filling is completed because they would interfere with the spill trays and filling process. Filling cannot begin until after each superblock is completed and at least one additional block has been added to the detector. Once a di-block has been filled and topped off, the final electronics work is completed on the top of the detector.
- **Electronics box installation**
  This is a very delicate operation and assembly crew workers will be trained by experts. There are eight steps in the process. Figure 17.161 shows the electronics box components.
    - Mount the electronics box base to the module snout with a bolted clamp system
    - Insert alignment pins, O-ring and shims
    - Install carrier board onto pins
    - Press heat sink holder surface until it meets cookie surface
    - Insert screws to hold clamshell together
    - Install ADC/heat-sink/TEC assembly and fasten to heat-sink holder
    - Install electronics box cover
    - Make all electrical and water connections.

  All electrical connections are to the module side of the electronics box. All chilled water connections are on the snout end of the electrical box. If the ADC/heat-sink/TEC assembly fails during operation, it can be replaced by removing the electronics box cover and sliding it out.

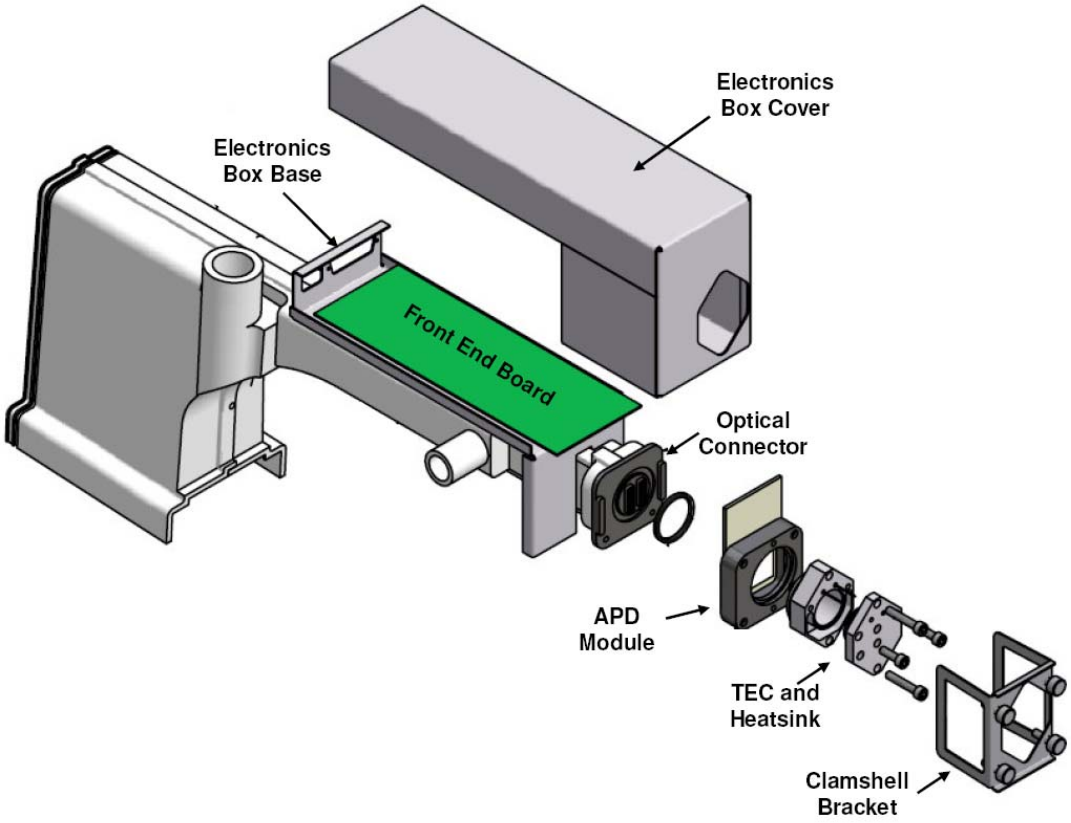

Fig. 17.161: Schematic diagram of the electronics box components to be assembled during installation.

17.15.5 Detector Side Outfitting

17.15. 5.1 Access to the Side of the Detector

The four walkways plus the detector hall floor provide access to the west side of the detector. The floor and the lower three walkways each service three levels of horizontal module manifolds. The walkways are wide enough to accommodate the movable work platforms, which allow workers to get to the upper manifolds and electronics boxes, without blocking the safety egress paths. Figure 17.162 shows a technician on the third level walkway accessing the power distribution box (PDB) from a movable work platform.

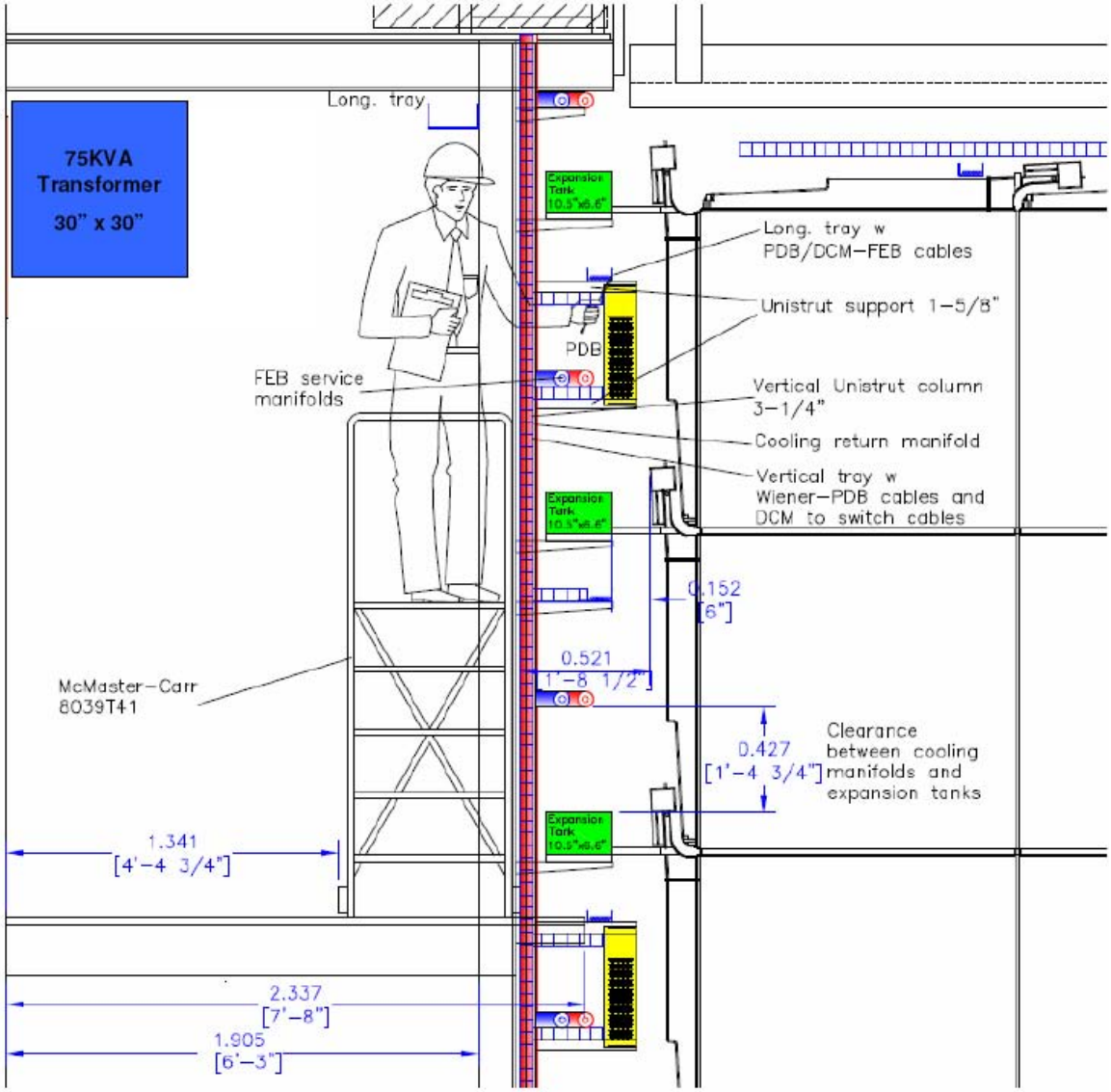

Fig. 17.162: Elevation view of the top west corner of the detector, looking north at a technician working on the detector from a movable work platform.

17.15.5.2 Side-of-Detector Installation Sequence

Once the detector survey work is completed, installation of the support structure can begin. Temporary cable fall restraints can be removed after installation of the Unistrut frame support structures, which also act as the safety railings. The walkway toe boards will remain in place during and after outfitting.

- **Support structure, shelves and brackets**
  All of these parts are pre-cut in the shop, located in the loading dock area.
- **Expansion tank**
  The expansion tanks come to Ash River pre-tested and are carefully inspected before installation. The plumbing to the fill port on the manifolds is done with rigid pipe and compression fittings to minimize any chance for leaks. The vent tubing is done in flexible tubing to the manifold. The 0.625-inch vent tube on the top of each tank is connected to

the main vent return pipe. The tank sits on a shelf that holds it in position at the proper elevation.

- **Electronics box installation**
  The horizontal module electronics boxes are installed before any of the cable trays or plumbing are put in place.
- **PDB and DCM boxes**
  The six power distribution boxes and the six data concentrator modules are bolted to the brackets installed for them.
- **Power feed trays**
  The 4-inch x 2-inch power feed trays are put in place next. The power cables that run to the PDB and DCM boxes are also installed at this time.
- **Longitudinal trays**
  These 12 trays that run from the PDB and DCM boxes feed the cables to the electronics boxes. The cables are installed at this time as well.
- **DCS cables**
  These cables connect the PDB and DCM boxes for the detector control system. They run in the same cable trays as the power feeds.
- **Supply and return manifolds**
  The supply and return manifolds run from the chiller unit to the supply and return service manifolds on each di-block. They need to be installed first, before the service manifolds.
- **Supply and return service manifolds**
  Each supply and return service manifold comes in two ~80-inch pieces and is attached to the main manifold at a shutoff valve.
- **Water system testing**
  Since the entire system has valves at all key locations it can be pressure tested before the system is attached to the electronics boxes.
- **Connections to electronics boxes**
  Cables can now be connected to the electronics box.
- **Scintillator filling**
  This task is detailed in NOVA-doc-2501. Filling of horizontal modules can begin as soon as the outfitting has been completed.

17.16 Assembly Crew and Rate of Detector Assembly

Section 17.13.1 provides an overview of the detector assembly process and the tasks performed by assembly crew workers. The present section describes these tasks and the assembly schedule in more detail. NOVA-doc-2494 describes the assembly crew work plan in much more detail. Table 17.26 summarizes the activities, schedules and effort levels during the different stages of the installation task.

17.16.1 Job Classifications

The effort levels shown below are for the full-rate installation period.

- **Crane operators (4 workers)**
  The two bridge cranes are operated by four certified heavy equipment operators. One crane carries modules to the adhesive dispenser the other moves glued modules to the block under construction.
- **Glue technicians (2 workers)**
  The glue technicians are responsible for operating the adhesive dispenser. They also disconnect and reconnect the crane hook and vacuum lifter AC power for every module.

- **Module technicians (4 workers)**
  Because the modules are so large and must be placed accurately, one module technician assists each crane operator during module movement, both into and out of the adhesive dispenser. They are also responsible for moving the packing material from the module units to the return super pallet as time permits.
- **Block pivoter technicians (8 workers)**
  Modules are rolled with a 75-pound steel roller to ensure good compression of the glue bond. The technicians who perform this work are also responsible for installing module alignment fixtures and for filling the gaps between modules with epoxy grout.
- **Outfitting/Scintillator technicians (4 workers)**
  The four outfitting/scintillator technicians share several tasks. They are responsible for installing electronics and cooling hardware, including cabling and plumbing for the outfitting task. They are also responsible for receiving and testing arriving shipments of scintillator, and for filling scintillator modules.
- **Crew bosses (4 workers)**
  One of the two crew bosses in each team supervises the block construction work and the other supervises the outfitting and scintillator tasks. They also serve as replacement workers when someone is sick or on vacation, or a position is temporarily vacant.
- **Administration (2.5 workers)**
  The assembly crew administrative team consists of the Detector Assembly Manager and a half-time secretary on the day shift, and the Assistant Detector Assembly Manager on the afternoon shift. This part of the staff begins employment at beneficial occupancy. They are the first assembly crew members hired and are responsible for hiring the rest of the crew.
- **Operations staff (4.5 workers)**
  During the installation period, additional staff is needed to operate the completed sections of the detector, to maintain computer networks, and to perform building maintenance and grounds-keeping tasks. The operations staff consists of the Laboratory Manager, the Laboratory Safety Officer, a computer networks technician, a groundskeeper/custodian and a half-time secretary. The operations staff is employed under the Cooperative Agreement and is not paid for by WBS 2.9. Most of these people will continue after installation is complete, as members of the experiment operations staff.

Installation stage	# of Blocks	Starting # of people	Ending # of people	Job Class distribution at end of the period
60 days – Setup		**4**	**14**	**2 Crane, 2 Crew Boss, 10 Tech**
75 days– Startup	**3**	**14**	**26**	**4 Crane,4 Crew Boss, 18 Tech**
364 days – Full rate	**28**	**26**	**26**	**4 Crane,4 Crew Boss, 18 Tech**
50 days – Ramp down	**1.3**	**26**	**14**	**2 Crane,2 Crew Boss, 10 Tech**
50 days – Install bookend, complete filling	**0**	**14**	**7**	**1 Crane, 2 Crew, 4 Tech**
20 days – Complete outfitting		**7**	**3**	**1 Crew, 2 Tech**
Total: 619 days (124 wks)	**32.3**			**26 workers in full-rate stage**

Table 17.26: Far detector installation stages and effort levels, not including the 2.5-person administrative staff.

17.16.2 Crew Size, Shift Schedule and Training

The work schedule for the full-rate installation period is based on two overlapping 8.5-hour shifts/day, five days/week. The half-hour shift overlap period gives time for information transfer and allows the adhesive dispenser to remain in continuous operation. One hour each shift is scheduled for lunch and coffee breaks. Another 1.5 hours/shift is allowed for work inefficiencies, unscheduled activities and shift overlap. Workers are paid for 8 hours per day. Installation rates are based on 6 hours of productive work each day. Table 17.26 shows the numbers of workers during the different stages of the installation process. Table 17.27 illustrates the breakdown into the different job classifications.

- **Training**
  Training falls into two major categories: task-related and safety. While standard industrial safety training is included for all tasks and procedures, additional first aid safety training is provided because of the remoteness of the site. All training is documented to provide a record of compliance. It is 45 miles to the closest hospital, so a one-hour travel time to expert medical assistance is assumed. The parking area on the north-west side of the building complex is large enough to land a life-flight helicopter.
  - **Procedures and tasks**
    The crew bosses and experts (physicists and engineers) for each of the systems conduct the training classes. A safety committee comprised of experts from Fermilab, the University of Minnesota and the assembly crew staff approves all procedures. Outside experts in specific fields like materials handling, adhesive usage and scintillator spill cleanup are brought to the site as needed. Most procedures are developed, documented and approved during full-scale prototype work at Fermilab or Argonne before far detector installation begins.
  - **Safety training**
    Due to the remoteness of the site, it is important to have several trained first responders or EMTs as members of the assembly crew. Personnel with such

training will be given preference during the hiring process. Equipment required for emergency medical treatment (paid for by the Cooperative Agreement) is kept on site. All personnel are trained in first aid, CPR, defibrillators and high-flow oxygen techniques. Specific safety training for dealing with scintillator spills, vapor control and other detector-related safety issues is provided, with refresher classes given each year. Except for assembly crew effort devoted to training, most costs associated with safety training (e.g., the cost of courses and equipment) are paid for by the Cooperative Agreement. Monthly safety meetings with specific training topics are mandatory for all workers.

Summary of Labor Breakdown

Task assignment	Day Shift	Afternoon Shift
Installation Team – 10 workers		
Crane Operators	**2**	**2**
Module Technicians	**2**	**2**
Glue Technicians	**1**	**1**
Block Pivoter Technicians	**4**	**4**
Crew Bosses	**1**	**1**
Outfitting Team – 3 workers		
Outfitting/Scintillator Technicians	**2**	**2**
Crew Bosses	**1**	**1**
Total	**13**	**13**
Grand Total 26 workers		

Table 17.27: Job classifications and effort levels during full-rate installation period.

17.16.3 Full-Rate Block Installation Schedule

The total assembly and installation time for each block is 2.6 weeks during the full-rate installation period. Three planes will be installed each working day. The schedule is based on an average 10-minute module handling time, which will be confirmed or revised following time-and-motion studies with the full-scale block assembly prototype (NOVA-doc-1954). The installation schedule and assembly crew effort levels may be modified (and labor contingency allocations reduced) as a result of these studies. Tables 17.28 to 17.30 show the 2.6 week full-rate schedule. Tasks like moving and testing modules are not shown, but will be performed as background work, as time permits, by members of the installation team. (Additional effort will be shifted to these tasks if they fall too far behind schedule.) An average of one module unit per day is delivered to the loading dock area. Since the scintillator filling and electronics outfitting teams work independently of the block installation teams, the former can be made available to help with module shipment unloading as needed. In addition to the assembly tasks shown in Tables 17.28 to 17.30, each crew member has approximately 80 hours (two weeks) of safety training during the first year of employment and 40 hours per year after that. Note that the shift schedule includes a weekly half-hour general safety meeting during the shift overlap period every Wednesday.

Week 1

	Mon.	Tues.	Wed.	Thurs.	Fri.
7:00	Start Meeting	Start Meeting	Start Meeting	Start Meeting	Start Meeting
7:30	Pivoter Prep	1:VM 1-3	4:HM 1-3	7:VM 1-3	10-HM 1-3
8:00		1:VM 4-6	4:HM 4-6	7:VM 4-6	10:HM 4-6
8:30		1:VM 7-9	4:HM 7-9	7:VM 7-9	10:HM 7-9
9:00	Break	Break	Break	Break	Break
9:30	Pivoter Prep	1:VM 10-12	4:HM 10-12	7:VM 10-12	10:HM 10-12
10:00		Survey & Stops	Survey & Stops	Survey & Stops	Survey & Stops
10:30					
11:00	Lunch	Lunch	Lunch	Lunch	Lunch
11:30	Pivoter Prep	Survey & Stops	Survey & Stops	Survey & Stops	Survey & Stops
12:00					
12:30		2:HM 1-3	5:VM 1-3	8:HM 1-3	11:VM 1-3
13:00	Break	Break	Break	Break	Break
13:30	Pivoter Prep	2:HM 4-6	5:VM 4-6	8:HM 4-6	11:VM 4-6
14:00		2:HM 7-9	5:VM 7-9	8:HM 7-9	11:VM 7-9
14:30		2:HM 10-12	5:VM 10-12	8:HM 10-12	11:VM 10-12
15:00 | 15:00	Start/End Shift	Start/End Shift	Safety Meeting	Start/End Shift	Start/End Shift
15:30	Pivoter Prep	Survey & Stops	Survey & Stops	Survey & Stops	Survey & Stops
16:00					
16:30					
17:00	Break	Break	Break	Break	Break
17:30	Pivoter Prep	Survey & Stops	Survey & Stops	Survey & Stops	Survey & Stops
18:00		3:VM 1-3	6:HM 1-3	9:VM 1-3	12:HM 1-3
18:30		3:VM 4-6	6:HM 4-6	9:VM 4-6	12:HM 4-6
19:00	Lunch	Lunch	Lunch	Lunch	Lunch
19:30	Pivoter Prep	3:VM 7-9	6:HM 7-9	9:VM 7-9	12:HM 7-9
20:00		3:VM 10-12	6:HM 10-12	9:VM 10-12	12:HM 10-12
20:30		Survey & Stops	Survey & Stops	Survey & Stops	Survey & Stops
21:00	Break	Break	Break	Break	Break
21:30	Pivoter Prep	Survey & Stops	Survey & Stops	Survey & Stops	Survey & Stops
22:00					
22:30					
23:00	Clean-up	Clean-up	Clean-up	Clean-up	Clean-up

Table 17.28: Full-rate installation schedule for week 1 of the 2.6-week block assembly period.

Week 2

	Mon.	Tues.	Wed.	Thurs.	Fri.
7:00	Start Meeting	Start Meeting	Start Meeting	Start Meeting	Start Meeting
7:30	13:VM 1-3	16:HM 1-3	19:VM 1-3	22-HM 1-3	25-VM 1-3
8:00	13:VM 4-6	16:HM 4-6	19:VM 4-6	22:HM 4-6	25:VM 4-6
8:30	13:VM 7-9	16:HM 7-9	19:VM 7-9	22:HM 7-9	25:VM 7-9
9:00	Break	Break	Break	Break	Break
9:30	13:VM 10-12	16:HM 10-12	19:VM 10-12	22:HM 10-12	25:VM 10-12
10:00	Survey & Stops	Survey & Stops	Survey & Stops	Survey & Stops	Survey & Stops
10:30					
11:00	Lunch	Lunch	Lunch	Lunch	Lunch
11:30	Survey & Stops	Survey & Stops	Survey & Stops	Survey & Stops	Survey & Stops
12:00					
12:30	14:HM 1-3	17:VM 1-3	20:HM 1-3	23:VM 1-3	26:HM 1-3
13:00	Break	Break	Break	Break	Break
13:30	14:HM 4-6	17:VM 4-6	20:HM 4-6	23:VM 4-6	26:HM 4-6
14:00	14:HM 7-9	17:VM 7-9	20:HM 7-9	23:VM 7-9	26:HM 7-9
14:30	14:HM 10-12	17:VM 10-12	20:HM 10-12	23:VM 10-12	26:HM 10-12
15:00 | 15:00	Start/End Shift	Start/End Shift	Safety Meeting	Start/End Shift	Start/End Shift
15:30	Survey & Stops	Survey & Stops	Survey & Stops	Survey & Stops	Survey & Stops
16:00					
16:30					
17:00	Break	Break	Break	Break	Break
17:30	Survey & Stops	Survey & Stops	Survey & Stops	Survey & Stops	Survey & Stops
18:00	15:VM 1-3	18:HM 1-3	21:VM 1-3	24:HM 1-3	27:VM 1-3
18:30	15:VM 4-6	18:HM 4-6	21:VM 4-6	24:HM 4-6	27:VM 4-6
19:00	Lunch	Lunch	Lunch	Lunch	Lunch
19:30	15:VM 7-9	18:HM 7-9	21:VM 7-9	24:HM 7-9	27:VM 7-9
20:00	15:VM 10-12	18:HM 10-12	21:VM 10-12	24:HM 10-12	27:VM 10-12
20:30	Survey & Stops	Survey & Stops	Survey & Stops	Survey & Stops	Survey & Stops
21:00	Break	Break	Break	Break	Break
21:30	Survey & Stops	Survey & Stops	Survey & Stops	Survey & Stops	Survey & Stops
22:00					
22:30					
23:00	Clean-up	Clean-up	Clean-up	Clean-up	Clean-up

Table 17.29: Module installation schedule for week 2 of the 2.6-week block assembly period.

Week 3

	Mon.	Tues.	Wed.	Thurs.	Fri.
7:00	Start Meeting	Start Meeting	Start Meeting	Start Meeting	Start Meeting
7:30	28:HM 1-3	31:VM 1-3	Final QC Checks	Pivoter Prep	1-HM 1-3
8:00	28:HM 4-6	31:VM 4-6			1:HM 4-6
8:30	28:HM 7-9	31:VM 7-9			1:HM 7-9
9:00	Break	Break	Break	Break	Break
9:30	28:HM 10-12	31:VM 10-12	Final QC Checks	Pivoter Prep	1:HM 10-12
10:00	Survey & Stops	Survey & Stops			Survey & Stops
10:30					
11:00	Lunch	Lunch	Lunch	Lunch	Lunch
11:30	Survey & Stops	Light Tighten	Move Block Pivoter	Pivoter Prep	Survey & Stops
12:00					
12:30	29:VM 1-3				2:VM 1-3
13:00	Break	Break	Break	Break	Break
13:30	29:VM 4-6	Light Tighten	Move Block Pivoter	Pivoter Prep	2:VM 4-6
14:00	29:VM 7-9				2:VM 7-9
14:30	29:VM 10-12				2:VM 10-12
15:00 15:00	Start/End Shift	Start/End Shift	Safety Meeting	Start/End Shift	Start/End Shift
15:30	Survey & Stops	Light Tighten	Move Block Pivoter	Pivoter Prep	Survey & Stops
16:00					
16:30					
17:00	Break	Break	Break	Break	Break
17:30	Survey & Stops	Light Tighten	Move Block Pivoter	Pivoter Prep	Survey & Stops
18:00	30:HM 1-3				3:HM 1-3
18:30	30:HM 4-6				3:HM 4-6
19:00	Lunch	Lunch	Lunch	Lunch	Lunch
19:30	30:HM 7-9	Light Tighten	Move Block Pivoter	Pivoter Prep	3:HM 7-9
20:00	30:VM 10-12				3:HM 10-12
20:30	Survey & Stops				Survey & Stops
21:00	Break	Break	Break	Break	Break
21:30	Survey & Stops	Light Tighten	Move Block Pivoter	Pivoter Prep	Survey & Stops
22:00					
22:30					
23:00	Clean-up	Clean-up	Clean-up	Clean-up	Clean-up

Table 17.30: Full-rate block installation schedule for week 3 of the 2.6-week period.

17.17 Changes in the Far Detector Assembly Since the CDR

1. Detector mass: decreased from 25 kton (64 blocks) to 15 kton (32.35 blocks).
2. Detector structure: 1-cm expansion gaps between all blocks changed to 2-cm gaps only between 5-block superblocks.
3. Block structure: All A-type blocks changed to alternating A-type and B-type blocks within superblocks.
4. Building size: decreased from 30 kton to 18 kton (40 blocks).
5. Building/detector orientation: rotated 180 deg so detector assembly starts at south end.
6. Top of detector access: roof support truss walkways changed to rolling access platforms.
7. Maximum assembly rate: one block/80 crew hours changed to one block/150 crew-hours.

8. Maximum assembly crew size: decreased from 39 to 26 plus 2.5 administrators.
9. Block raiser design: block raiser changed to block pivoter.
10. Block assembly location: moved from detector face to loading dock.
11. Detector component inventory: 30-day on-site buffer changed to just-in-time delivery.
12. Plane adhesive: changed from 3M 2216 epoxy to Devcon 60 acrylic adhesive.
13. Plane adhesive ventilation: Enhanced ventilation added around adhesive dispenser and block pivoter to exhaust methyl methacrylate vapor outside the building.
14. Plane adhesive application: applied by machine to each module before installation.
15. Liquid scintillator charge buildup mitigation: antistatic additive, grounded metal supply pipes, elimination of splash filling, slower fill rate.
16. Scintillator supply system: design simplified to match slower fill rate.
17. Detector readout geometry: All horizontal modules read out on the west side instead of alternate planes reading out on alternate (east or west) sides of the detector.
18. APD condensation control: dry nitrogen system replaced by local desiccant system.
19. Additional WBS 2.9 responsibilities: Scintillator supply system, horizontal module expansion tanks, block safety constraint beam, electrical installation from main building panels to all equipment and electronics.
20. Design improvements: structural design validation with 16-cell NOvA extrusion prototypes, adhesive application to modules, block pivoter design, block base pallet design, detector access platforms and walkways.

17.18 Work Remaining to Complete the Far Detector Assembly Design

1. Development of detailed module and block alignment and survey procedures.
2. Procedure validation, time-and-motion studies with full-scale block assembly prototype.
3. Structural design validation with full-height structural engineering prototype.
4. Long-term structural stability validation with ongoing creep and aging measurements of module and block materials.
5. Prototyping of the liquid scintillator supply and filling equipment.
6. Initial system integration and commissioning studies with IPND.

17.19 Chapter 17 References

[1] Engineered Materials Handbook - Adhesives and Sealants Volume 3, ASM International.
[2] E. Ray Harrell, Jr., “Modeling of the Creep Modulus of PVC 1111-BB for Predicting Creep at 20°C for 20 Years,” NOVA-doc-667, March 3, 2006.
[3] E. Ray Harrell, Jr., “Modeling of the Creep Modulus of NOvA 2P for Predicting Creep at 20°C for 20 Years,” NOVA-doc-667, July 25, 2006.
[4] F. Tahmasebi, PhD, “Finite Element Modeling of an Adhesive in a Bonded joint”, FEMCI, NASA Goddard Space Flight Center, July,1999.
[5] Y. Zhu and K. Keyward, “Method of Analysis and Failure Predictions for Adhesively Bonded Joints of Uniform and Variable Bond Line Thickness”, DOT/FAA/AR-05/12, Final Report, May, 2005.
[6] V-STARS Industrial Photogrammetry Systems, Geodetic Systems, Inc., 3D Industrial Measurement Systems, http://www.geodetic.com.

Appendix A. Guide and Links to Other NOνA Project Documentation

A.1 Introduction

In addition to this Technical Design Report, there are a large number of supporting documents for the NOνA project assembled by the Integrated Project Team. This Appendix serves as a guide to these documents. A short description of each document is provided and a link to each document is embedded in the text.

A.2 Department of Energy Documents

A.2.1 Critical Decision Zero, November 29, 2005

The DOE issued a Critical Decision Zero on November 29, 2005 calling for a program to study electron neutrino appearance. The document can be found at http://www.science.doe.gov/hep/Eva.pdf.

A.2.2 Neutrino Scientific Assessment Group (NuSAG) Report, February 28, 2006

NuSAG evaluated the physics potential and feasibility of various long baseline and reactor-based neutrino oscillation experiments including NOνA. Their report, *Recommendations to the Department of Energy and the National Science Foundation on a U.S. Program of Reactor and Accelerator-based Neutrino Oscillation Experiments* can be found at http://www.science.doe.gov/hep/NuSAG2ndRptFeb2006.pdf.

A.2.3 Critical Decision One Review Close-out, April 2006

A DOE Review of the NOνA Project was conducted in April 2006 to determine compliance with the requirements for Critical Decision One (CD-1). The committee recommended CD-1 approval. The final report from the committee is NOνA-doc-1302.

A.2.4 P5 Report, October 2006

The Particle Physics Project Prioritization Panel (P5) issued their report *The Particle Physics Roadmap* in October of 2006. The report discusses off-axis neutrino experiments and recommends the construction of NOνA. The report can be found at http://www.science.doe.gov/hep/P5RoadmapfinalOctober2006.pdf.

A.2.5 Acquisition Strategy

The Acquisition Strategy document for NOνA is a DOE document that provides a relatively high level description of the project including the technical objectives, alternatives, schedule range, cost range and management structure. The Acquisition Strategy is NOνA-doc-1361.

A.2.6 Critical Decision One

A.2.7 Project Execution Plan (PEP)

The Project Execution Plan (PEP) is a DOE document that establishes roles and responsibilities, and describes in detail the manner in which a project is to be managed and executed. The PEP is also the primary agreement between the DOE and NOνA on project planning and objectives, and is to be prepared, submitted, and approved by CD-2. The PEP for NOνA is NOνA-doc-130.

A.2.8 Environmental Assessment (EA)

The Environmental Assessment (EA) is a document that is submitted to the DOE that assesses the potential impact of the activities associated with NOνA on safety, health and the environment. The NOνA EA covers activities at Fermilab, Ash River and Universities engaged in NOνA Project work. This document goes together with the State of Minnesota Environmental Assessment Worksheet (NOνA-doc-205) to satisfy both Federal and State requirements. The EA is NOνA-doc-2646.

A.3 NOνA Project Office Documents

A.3.1 Project Management Plan (PMP)

The NOνA Project Management Plan follows from the Project Execution Plan and establishes roles and responsibilities within the NOνA Project and describes in detail the manner in which the project will be managed. The PMP is NOνA-doc-129.

A.3.2 NOνA Cost and Schedule

The NOνA cost and schedule currently only resides in Open Plan and is not generally accessible.

A.3.3 Quality Management Plan

NOνA's Quality Management Plan is described in NOνA-doc-1353.

A.3.4 Earned Value Management System (EVMS)

Fermilab's Earned Value Management System (EVMS) is a comprehensive system that develops and maintains the baseline, tracks project cost, schedule, and scope and provides for the

generation of timely performance measurement data and reports. Fermilab's EVMS system is described in NOνA-doc-1084.

A.3.5 Risk Management Plan

The Risk Management Plan (RMP) for NOνA provides a structured and integrated process for identifying, evaluating, tracking, abating, and managing project risks. The NOνA Risk Management Plan is described in NOνA-doc-185.

A.3.6 NOνA Risk Registry

The NOνA risk registry is a tool for Project Management to keep track of high risks items in the project. The risk registry is NOνA-doc-1323.

A.3.7 Security Vulnerability Assessment Report

A Preliminary Security Vulnerability Assessment was preformed for NOνA. The assessment is documented in NOνA-doc-1442.

A3.8 State of Minnesota Environmental Assessment Worksheet (EAW)

The Environmental Assessment Worksheet (EAW) is the form used by the State of Minnesota to assess potential impacts to the environment, safety and health. The NOnA EAW covers the activities that will be performed at the Far Detector site in Ash River, Minnesota during both the construction and operation phases. The EAW is NOνA-doc-205.

A.3.9 Hazard Analysis

The Fermilab Environmental, Safety and Health Manual (FESHM) requires projects to identify hazards and describe how the risks will be mitigated. The NOnA Hazard Analysis is described in NOνA-doc-618.

A.3.11 Preliminary Safety Assessment Document

NOνA has performed and documented a preliminary hazard/risk analysis for each phase of the project in order to systematically identify any hazards that may be present. The assessment can be found in NOνA-doc-598.

A.3.12 Contingency Analysis Rules

The rules for determining contingency for the NOνA Project are described in NOνA-doc-616.

A.3.13 NOνA Proposal, March, 2005

The NOνA Proposal is NOνA-doc-593.

A.3.14 NOνA Conceptual Design Report, March 2006

The NOνA Conceptual Design Report is NOνA-doc-536.

A.3.15 NOνA Configuration Management Plan

The NOνA Configuration Management Plan identifies the organization providing configuration control, defines what a configuration-controlled item is, describes the change control process, and identifies the plan for configuration status accounting and verification. The plan is described in NOνA-doc-131.

A.3.16 Acquisition Plan for NOνA Cost Drivers

The Acquisition Plan for NOνA describes the strategy for acquiring the relatively few items that drive the cost of the Project. The plan is described in NOνA-doc-1321.

A.3.17 Start-Up Test Plan for the NOνA Project

The Start-up Test Plan describes the strategy for System check-out and verification of performance for the various NOνA subsystems. The plan is described in NOνA-doc-2646.